NANOSTRUCTURES: PHYSICS AND TECHNOLOGY

17th International Symposium

Minsk, Belarus, June 22–26, 2009

Co-Chairs
Zh. Alferov
L. Esaki

PROCEEDINGS

Minsk, 2009

Published by
Ioffe Physical-Technical Institute
26 Politekhnicheskaya, St Petersburg 194021, Russia
http://www.ioffe.ru/

Publishing license ΛP No 040971 of June 16, 1999.

Copyright © 2009 by Ioffe Institute and individual contributors. All rights reserved. No part of this publication may be multiple copied, stored in a retrieval system or transmitted in any form or by any means, electronic, mechanical, photocopying, recording or otherwise, without the written permission of the publisher. Single photocopies of single articles may be made for private study or research.

ISBN 978-5-93634-051-2

The International Symposium "Nanostructures: Physics and Technology" is held annually since 1993. The first Symposium was initiated by Prof. Zh. Alferov and Prof. L. Esaki who are its permanent co-chairs. More detailed information on the Symposium is presented on the World Wide Web **http://www.ioffe.ru/NANO2009/**

The Proceedings include extended abstracts of invited talks and contributed papers to be presented at the Symposium. By tradition this book is published before the beginning of the meeting.

The volume was composed at the Information Services and Publishing Department of St Petersburg Physics and Technology Center for Research and Education of RAS from electronic files submitted by the authors. When necessary these files were converted into the Symposium style without any text revisions. Only minor technical corrections were made by the composers.

Design and layout: N. Vsesvetskii
Desk editor: E. Savostyanova

Information Services and Publishing Department
St Petersburg Physics and Technology Center for Research and Education of RAS
8, bld. 3 Khlopina, St Petersburg 194021, Russia
Phones: (812) 534-58-58
Fax: (812) 534-58-50

Printed in Republic of Belarus

The Symposium is held under the auspices of
the Russian Academy of Sciences

Organizers

B.I. Stepanov Institute of Physics of the National Academy of Sciences of Belarus
St Petersburg Physics and Technology Center for Research and Education of RAS
Ioffe Physical-Technical Institute

in association with

Branch of Physical Sciences of the Russian Academy of Sciences
National Academy of Sciences of Belarus
St Petersburg Scientific Center of the Russian Academy of Sciences
Ministry of Education and Science of the Russian Federation
RUSNANO, Russian Corporation of Nanotechnologies
Exhibition Company Belinterexpo of the Belarusian Chamber of Commerce and Industry

Acknowledgments

The Organizers gratefully acknowledge the following
for their contribution to the success of the Symposium:

Russian Academy of Sciences
National Academy of Sciences of Belarus
Belarusian Republican Foundation for Fundamental Research
St Petersburg Scientific Center of the Russian Academy of Sciences
RUSNANO, Russian Corporation of Nanotechnologies

Location and Date

Symposium is held in Minsk, Belarus June 22–26, 2009.

Advisory Committee

G. Abstreiter (*Germany*)
Zh. Alferov (*Russia*)
Y. Arakawa (*Japan*)
A. Aseev (*Russia*)
G. Bastard (*France*)
D. Bimberg (*Germany*)
L. Eaves (*United Kingdom*)
L. Esaki (*Japan*)
S. Gaponov (*Russia*)
E. Gornik (*Austria*)
Yu. Gulyaev (*Russia*)
N. Holonyak, Jr. (*USA*)
L. Keldysh (*Russia*)
G. Landwehr (*Germany*)
J. Merz (*USA*)
M. Shur (*USA*)
M. Skolnick (*United Kingdom*)
R. Suris (*Russia*)

Programme Committee

R. Suris, Chair (*St Petersburg, Russia*)
V. Evtikhiev, Secretary (*St Petersburg, Russia*)
A. Andronov (*Nizhny Novgorod, Russia*)
N. Bert (*St Petersburg, Russia*)
C. Chang-Hasnain (*Berkeley, USA*)
A. Chaplik (*Novosibirsk, Russia*)
V. Dneprovskii (*Moscow, Russia*)
V. Dubrovskii (*St Petersburg, Russia*)
A. Gippius (*Moscow, Russia*)
S. Gurevich (*St Petersburg, Russia*)
S. Ivanov (*St Petersburg, Russia*)
V. Kabanov (*Minsk, Belarus*)
P. Kop'ev (*St Petersburg, Russia*)
Z. Krasil'nik (*Nizhny Novgorod, Russia*)
V. Kulakovskii (*Chernogolovka, Russia*)
M. Kupriyanov (*Moscow, Russia*)
X. Marie (*Toulouse, France*)
I. Merkulov (*St Petersburg, Russia*)
V. Panov (*Moscow, Russia*)
O. Pchelyakov (*Novosibirsk, Russia*)
E. Poltoratskii (*Moscow, Russia*)
H. Sakaki (*Tokyo, Japan*)
N. Sibel'din (*Moscow, Russia*)
M. Stutzmann (*Garching, Germany*)
V. Timofeev (*Chernogolovka, Russia*)
P. Vitiaz (*Minsk, Belarus*)
V. Volkov (*Moscow, Russia*)
V. Ustinov (*St Petersburg, Russia*)

Organizing Committee

V. Kabanov, Chair (*Institute of Physics, NASB*)
V. Mashko, Vice-Chair (*Institute of Physics, NASB*)
A. Ponyavina, Secretary (*Institute of Physics, NASB*)
A. Chumakov (*Institute of Physics, NASB*)
V. Dubrovskii (*St Petersburg Physics and Technology Centre for Research and Education, RAS*)
I. Filatova (*Institute of Physics, NASB*)
S. Gaponenko (*Institute of Physics, NASB*)
A. Isaevich (*Institute of Physics, NASB*)
V. Komarov (*Institute of Physics, NASB*)
M. Kulagina (*Institute of Physics, NASB*)
N. Malashenok (*Institute of Physics, NASB*)
G. Malashkevich (*Institute of Physics, NASB*)
M. Mizerov (*Scientific Engineering Center for Microelectronics at the Ioffe Institute*)
N. Mukhurov (*Institute of Physics, NASB*)
V. Plavskii (*Institute of Physics, NASB*)
R. Shulyakovskii (*Institute of Physics, NASB*)
N. Sibeldin (*Lebedev Physical Institute, RAS*)
N. Tarasenko (*Institute of Physics, NASB*)
V. Zayats (*Branch of Physical Sciences of the RAS*)

Contents

Infrared and Microwave Phenomena in Nanostructures

Metal Nanostructures

Microcavity and Photonic Crystals

Nanostructure Technology

Nanostructure Characterization

Si-Ge Based Nanostructures

Nanostructures and Life Sciences

Transport in Nanostructures

Excitons in Nanostructures

Nanostructure Devices

2D Electron Gas

Tunnelling Phenomena

Spin Related Phenomena in Nanostructures

Wide Band Gap Nanostructures

Closing Plenary Session

Unprinted Papers

The papers listed below are included in the Symposium Programme, but not printed in the Proceedings, as the authors had not submitted electronic files in due time.

17th Int. Symp. "Nanostructures: Physics and Technology"
Minsk, Belarus, June 22–26, 2009
© 2009 Ioffe Institute

Nano-VCSELs for the terabus

D. Bimberg[1], S. A. Blokhin[1], *A. Mutig*[1], A. M. Nadtochiy[1], G. Fiol[1], P. Moser[1], D. Arsenijevic[1], F. Hopfer[1], V. A. Shchukin[2,*], J. A. Lott[2] and N. N. Ledentsov[2]

[1] Institut für Festkörperphysik und Zentrum für Nanophotonik, Technische Universität Berlin, 10623 Berlin, Germany
[2] VI Systems GmbH, 10623 Berlin, Germany
[*] presently at PBC Laser GmbH, 10717 Berlin, Germany

Abstract. High speed 850 nm oxide-confined vertical-cavity surface-emitting lasers (VCSELs) operating at bit rates up to 40 Gbit/s at room temperature and high temperature stable 980 nm oxide-confined VCSELs operating at 20 Gbit/s at temperatures up to 120 °C are presented. The 850 nm VCSELs contain InGaAlAs insertions that enable high speed operation. High temperature stability of the 980 nm VCSELs is due to our use of a sub-monolayer growth mode for the InGaAs active region and by an optimized device geometry and design.

Introduction

Moore's Law in data communications predicts a four-fold increase in the serial transmission speed each 5 years. Presently 3–8 Gbit/s transmission is becoming common not only in advanced networks, but also in consumer applications like USB 3.0, HDMI 1.3, PCIe, SDI,… Further upgrades are coming soon. At high bit rates beyond 10 Gbit/s the maximum length of copper wire-based links is limited to very short distances down to <1 m. In order to reach the bit rates required by the new standards for electrical interfaces like Fibre Channel FC16G (17 Gbit/s), Infiniband (20 Gbit/s) or FC32G (34 Gbit/s) for short reach ($\sim 0.3-300$ m) applications the use of fiber or plastic waveguide optics becomes indispensable. Vertical-cavity surface-emitting lasers (VCSELs) at 850 nm are very promising candidates for use in optical transmitters for such kind of applications [1]. They have established themselves as low-cost, reliable, low power consuming light sources. Single-mode 850 nm VCSELs under *external* modulation have been used to provide 40 Gbit/s error-free transmission over 2 km of photonic crystal fibre [2]. Error-free transmission up to 28 Gbit/s (850 nm) [3,4] and 35 Gbit/s (980 nm) [5] has been achieved for *directly modulated* VCSELs based on quantum wells (QWs). Here we report on the performance of *directly modulated* oxide-confined 850 nm AlGaAs VCSELs with InAlGaAs-based active regions that exhibit open optical eye diagrams at up to 40 Gbit/s.

Furthermore, chip-to-chip computer interconnects require temperature robust light sources with low integration costs capable to high bit rate operation beyond 10 Gbit/s [6] and VCSELs could serve also here as transmitter components [7]. Thus, the high temperature stability of the VCSELs can play a very important role here. Reliable operation of a module at 85 °C requires full functionality of the laser chip at 100 °C or even higher temperatures. In this work we report on 980 nm VCSELs showing clearly open eyes at 20 Gbit/s at temperatures up to 120 °C [8–10]. At the present moment no standards exist for computer optical interconnects. This gives some freedom in the choice of the emission wavelength, but the shorter wavelengths (850 and 980 nm) are preferred for the future standardization. Comparable to the common wavelength of 850 nm the wavelength of 980 nm gives some crucial advantages like better temperature stability due to suppressed escape of nonequilibrium carriers and transparency of the substrate. This is why this wavelength was chosen for the high temperature stable VCSELs presented here.

1. High temperature stable 20 Gbit/s 980 nm VCSELs

The epitaxial structure for 980 nm VCSELs was grown on an n^+ GaAs (100) substrate by molecular beam epitaxy. The active region consists of a triple stack of highly strained InGaAs layers grown in the sub-monolayer (SML) growth mode [11,12]. The active region was inserted into a thin GaAs region and centered within the low index $Al_{0.8}Ga_{0.2}As$ cavity. The cavity length was 3λ2-thick. Doped top/bottom distributed Bragg reflectors (DBRs) with 20/32 pairs and optimized electrical resistance

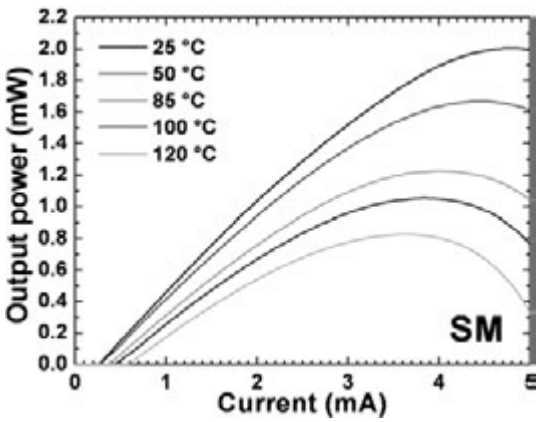

Fig. 1. L-I characteristics of the single mode 980 nm VCSEL at different temperatures.

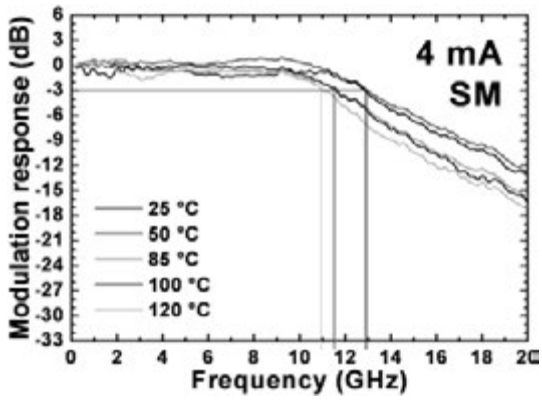

Fig. 2. Small signal modulation response at constant current for temperatures between 25 and 120 °C for the single mode 980 nm VCSEL.

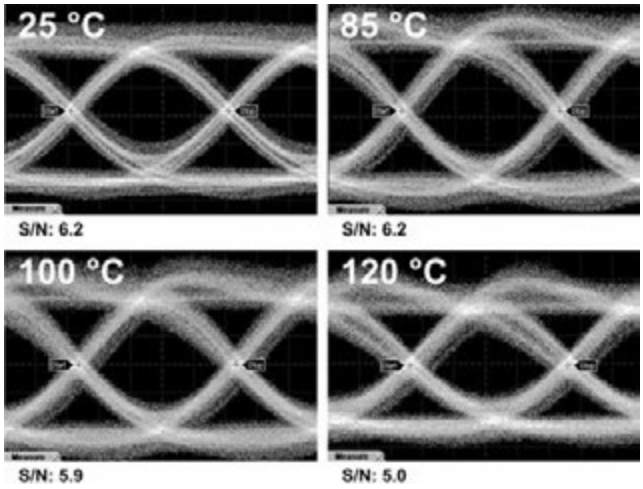

Fig. 3. 20 Gbit/s 2^7-1 PRBS back-to-back (with 3 m of OM3 multimode fiber) eye diagrams and signal-to-noise ratios between 25 and 120 °C for the same bias current and modulation voltage for the single mode laser.

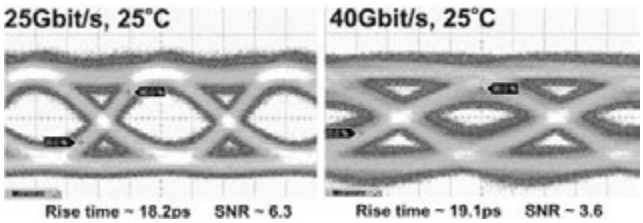

Fig. 4. BTB optical eye diagrams for an 850 nm VCSEL with 9 μm aperture at 25 and 40 Gbit/s modulation at fixed bias current and 20 °C.

were used. The oxide aperture was placed in a field intensity node on top of the microcavity on the p-doped side. In order to improve the temperature stability of the lasers, the cavity was red shifted from the peak gain at 25 °C by ∼20 nm. The shift of the peak gain with temperature is with ∼0.3 nm/K, identical to that of normal QWs. Devices with different aperture sizes were manufactured using an for high speed operation optimized design with high frequency ground-source-ground (GSG) contact pad configuration for easy on-wafer probe testing and taking into account a compromise between performance trade-offs related to effective heat dissipation/thermal conductivity, a reduction in electrical parasitic elements, and the ease/reliability of manufacture.

The static (continuous wave) characteristics for a single-mode (SM) 980 nm VCSEL with 2 μm aperture diameter are shown in Fig. 1. The maximum output power is about 2 mW at 25 °C and is still about 0.8 mW at 120 °C. The good temperature stability of the static properties of the VCSEL is a necessary condition for good temperature stability during high speed operation.

Fig. 2 shows the small signal modulation response of the same device in Fig. 4 for different temperatures. The $-3dB$ frequency is ∼13 GHz at room temperature and decreases by only 2 GHz between 25 and 120 °C.

Open eye diagrams of the same VCSEL measured using a 2^7-1 pseudo-random bit sequence (PRBS), non-return to zero (NRZ) pattern at 20 Gbit/s in a back-to-back (BTB) configuration (with 3 m of fiber) for temperatures between 25 °C

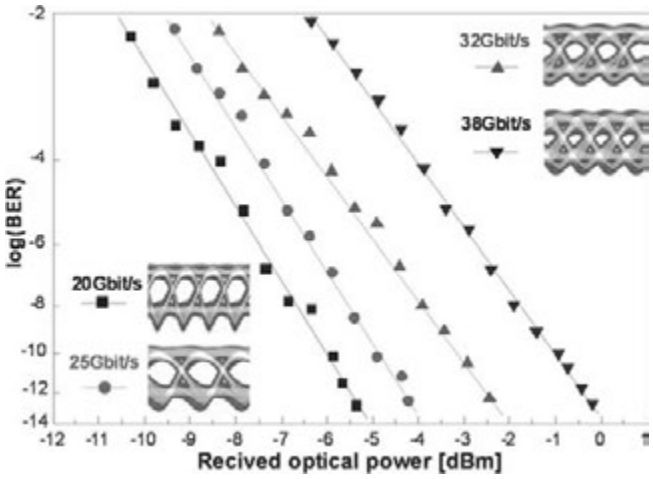

Fig. 5. 20 °C BER measurements in a BTB-configuration for 9 μm-diameter 850 nm VCSEL at 20, 25, 32, and 38 Gbit/s bit rates for a bias current of 9 mA and at 20 °C. Inset: corresponding optical eye diagrams.

and 120 °C are shown in Fig. 3. The measured signal-to-noise ratios (SNRs) are also given. The bias current and modulation voltage V_{P-P} were kept constant at 4.3 mA and 1.22 V for all measurements, respectively. The eyes are clearly open and error free at all temperatures from 25 °C up to 120 °C. The signal-to-noise ratio is 6.2 at 25 °C and 5.0 at 120 °C. Note that the rise and fall times of the traces are partly limited by the photoreceiver bandwidth, which was measured to be ∼10 GHz at 985 nm. Eye diagrams of the multimode device look almost identical up to 100 °C. These results confirm the high temperature stability of our 980 nm VCSELs.

2. High speed 850 nm VCSELs

Epitaxial wafers for oxide-confined 850 nm VCSELs were grown with conventional AlGaAs DBRs, and an InGaAlAs-based microcavity and active region by MOCVD. The epitaxial design was optimized for ultra-high speed operation. High speed devices with co-planar top contacts and different aperture diameters were processed using the processing similar to that for 980 nm VCSELs described above.

Large signal modulation experiments were carried out in a BTB configuration using a NRZ data pattern with a 2^7-1 PRBS. Room temperature optical eye diagrams with the corresponding SNRs and rise times for a VCSEL with a 9 μm-diameter oxide aperture are shown in Fig. 4. The eye remains open up to 40 Gbit/s. Note that the eye quality of the received signal is significantly affected by the imperfection of the electrical RF-signal applied to the devices. Hence, taking into account the detector saturation at higher average powers, one can conclude that the experimental set up limits the maximal data speed of error free transmission.

Bit error ratio (BER) measurements were also carried out for a 9 μm-diameter oxide aperture VCSEL and are presented in Fig. 5. The respective optical eye diagrams are shown as insets. The peak-to-peak modulation amplitude V_{P-P} was 0.8 V at 20 °C, while the bias current was fixed at 9 mA, and a back-to-back (BTB) configuration was used. The drive current corresponds to a current density of ∼10 kA/cm^2, which is low

enough to support degradation robustness of the device. The devices operate error free with a BER below 10^{-12} and no error floor is observed up to 38 Gbit/s. These results show the high speed potential of the 850 nm VCSELs.

Acknowledgements

This work was supported by the German Ministry for Education and Research bmb+f (AGENT), the Deutsche Forschungsgemeinschaft (Sfb 787), NoE SANDiE II, the State of Berlin (100×100 Optics), the European Community's Seventh Framework Programme (FP7/2007-2013) under *grant agreement* No. 224211 (FP7 "VISIT" Project), DLR, the Program of Fundamental Studies of the Presidium of the Russian Academy of Sciences ("Fundamental studies of nanotechnologies and nanomaterials") and by the Russian Federal Agency of Education ("Development of scientific potential of higher education institutions 2009-2010").

References

[1] D. Collins, N. Li, D. Kuchta, F. Doany, C. Schow, C. Helms, and L. Yang, "Development of high-speed VCSELs: 10 Gb/s serial links and beyond", Proc. SPIE 6908-09 (2008).

[2] H. Hasegawa, Y. Oikawa, T. Hirooka, M. Nakazawa, "40 Gbit/s-2 km photonic crystal fibre transmission with 850 nm single-mode VCSEL", *Electronics Letters* **43**, 642–644 (2007).

[3] P. Westbergh, J. S. Gustavsson, A. Haglund, and A. Larsson, "Large aperture 850 nm VCSEL operating at 28 Gbit/s", MB1, ISLC 2008, Sorrento, Italy.

[4] J. A. Lott, V. A. Shchukin, N. N. Ledentsov, A. Stintz, F. Hopfer, A. Mutig, G. Fiol, D. Bimberg, S. A. Blokhin, L. Y. Karachinsky, I. I. Novikov, M. V. Maximov, N. D. Zakharov, and P. Werner, "20 Gbit/s error free transmission with ∼850 nm GaAs-based vertical cavity surface emitting lasers (VCSELs) containing InAs-GaAs submonolayer quantum dot insertions. Proc. SPIE 7211-40 (2009).

[5] Y.-C. Chang, C. S. Wang, L. A. Coldren, "High-efficiency, high-speed VCSELs with 35 Gbit/s error-free operation", *Electronics Letters* **43**, 19 1022–1023, September 2007.

[6] A. F. Benner, M. Ignatowski, J. A. Kash, D. M. Kuchta and M. B. Ritter, "Exploitation of optical interconnects in future server architectures", IBM *J. Res.& Dev.* **49**, (4/5) 755 (2005).

[7] F. E. Doany, L. Schares, C. L. Schow, C. Schuster, D. M. Kuchta and P. K. Pepeljugoski, "Chip-to-chip optical interconnects", OFC, OFA3 (2006).

[8] F. Hopfer, A. Mutig, G. Fiol, M. Kuntz, V. A. Shchukin, V. A. Haisler, T. Warming, E. Stock, S. S. Mikhrin, I. L. Krestnikov, D. A. Livshits, A. R. Kovsh, C. Bornholdt, A. Lenz, H. Eisele, M. Dähne, N. N. Ledentsov and D. Bimberg, "20 Gb/s 85 °C Error Free Operation of VCSELs Based on Submonolayer Deposition of Quantum Dots", IEEE *J. Sel. Topics Quantum Electron.* **13**, 1302 (2007).

[9] F. Hopfer, A. Mutig, M. Kuntz, G. Fiol, D. Bimberg, N. N. Ledentsov, V. A. Shchukin, S. S. Mikhrin, A. R. Kovsh, N. D. Zakharov and P. Werner, "Single-mode submonolayer quantum dot vertical-cavity surface-emitting lasers with high modulation bandwidth", *Appl. Phys. Lett.* **89**, 141106 (2006).

[10] A. Mutig, G. Fiol, P. Moser, D. Arsenijevic, V. A. Shchukin, N. N. Ledentsov, S. S. Mikhrin, I. L. Krestnikov, D. A. Lifshits, A. R. Kovsh, F. Hopfer and D. Bimberg, "120 °C 20 Gbit/s operation of 980 nm VCSEL", IEEE *Electronics Letters* **44**, 22 1305–1306, October 2008.

[11] D. Bimberg, "Quantum dot based nanophotonics and nanoelectronics", IEEE *Electronics Letters* **44**, 33, 31 January 2008.

[12] I. L. Krestnikov, N. N. Ledentsov, A. Hoffmann, and D. Bimberg, "Arrays of two-dimensional islands formed by submonolayer insertions: growth, properties, devices", *Phys. Stat. Sol. (a)* **183**, 2 207–233 (2008).

17th Int. Symp. "Nanostructures: Physics and Technology"
Minsk, Belarus, June 22–26, 2009
© 2009 Ioffe Institute

Theory of high performance tunneling-injection quantum dot lasers

Levon V. Asryan
Virginia Polytechnic Institute and State University, Blacksburg, Virginia 24061, USA

Abstract. A semiconductor laser exploiting tunneling-injection of electrons and holes into quantum dots (QDs) from two separate quantum wells is discussed. Even in the presence of out-tunneling from QDs and recombination outside QDs, the tunneling-injection laser shows the potential for significant improvement of temperature-stability of the threshold current — the characteristic temperature remains very high (above 300 K at room temperature) and not significantly affected by the QD size fluctuations. The intensity of parasitic recombination outside QDs remains restricted with increasing injection current. As a result, the light-current characteristic becomes increasingly linear, and the slope efficiency grows closer to unity at high injection currents – a fascinating feature favoring the use of tunneling-injection of both electrons and holes into QDs for high-power lasing.

Introduction

High temperature-stability of the threshold current and high electrical-to-optical power conversion efficiency have always been among the main objectives of research on semiconductor lasers [1]. There is still much room for improvement even in the most advanced type of diode lasers — quantum dot (QD) lasers [2,3]. In the conventional design of QD lasers, the conductive optical confinement layer (OCL) transports mobile carriers to the QDs. Due to bipolar population in the OCL, a certain fraction of the injection current goes into the electron-hole recombination there. The parasitic recombination outside QDs is a major source of the temperature-dependence of the threshold current [4,5]. In addition, the carrier capture from the OCL into QDs is not instantaneous. For this reason, the carrier density in the OCL and hence the parasitic recombination rate rise, even above the lasing threshold, with injection current. This leads to sublinearity of the light-current characteristic (LCC) and limits the output power [6,7]. Suppression of the parasitic recombination would be expected to significantly enhance the temperature stability and the output optical power of a laser.

1. Tunneling-injection of electrons and holes into QDs

To improve the QD laser characteristics, tunneling-injection into QDs has been proposed. In [8,9], to minimize hot carrier effects, tunneling-injection of only electrons into QDs was proposed from a single quantum well (QW). In the structures of [8,9], bipolar carrier density and hence parasitic recombination still remain on the hole-injecting side. In [10], resonant tunneling was proposed from the bulk region (OCL) into the QD excited-state.

In [11–13], to suppress the recombination outside QDs and thus to improve the temperature-stability of the laser, tunneling-injection of both electrons and holes into QDs was proposed from two separate QWs (Fig. 1). There have been recent experimental developments [14–17] related to this concept. Compared to a conventional QD laser, tunneling-injection can efficiently improve the uniformity of QDs by selecting the QDs of the 'right' size [11–13]. Using tunneling-injection of both electrons and holes, the highest ground-state gain was reported for a single-layer InAs QD laser, thus allowing for ground-state lasing in short-cavity devices [15].

The energy band diagram of the structure of [11–13] is shown in Fig. 1. A single layer with QDs is clad on each side by a QW separated from the QDs by a thin barrier. Electrons (holes) are injected into QDs by tunneling from the left- (right-) hand-side QW. The key idea of the device is that the QWs are not connected by a current path that bypasses QDs. Fig. 1 shows the most optimum situation, when the lowest subband edge for majority carriers in the QW is in resonance with the energy level for the corresponding type of carrier in the average-sized QD, and hence the tunneling-injection rate is at its maximum.

In an ideal situation, there will be no second tunneling step, i.e., out-tunneling from QDs into the "foreign" QWs (electron-injecting QW for holes, and hole-injecting QW for electrons). Accordingly, there will be no electrons (holes) in the hole- (electron-) injecting side of the structure. As shown in [11–13], the total suppression of bipolar population and, consequently, of recombination outside QDs will lead to a virtually temperature-independent threshold current in a tunneling-injection QD laser. It will also lead to an ideal LCC [18].

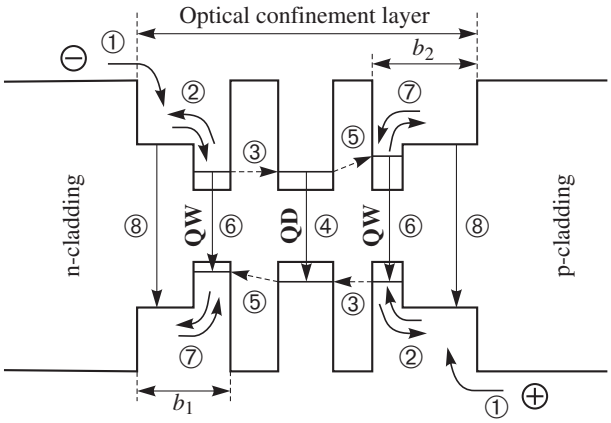

Fig. 1. Energy band diagram of a tunneling-injection QD laser. ("Reprinted with permission from [D.-S. Han and L. V. Asryan, Appl. Phys. Lett., Vol. 92, Issue 25, Art. No. 251113, 2008.] Copyright [2008], American Institute of Physics.")

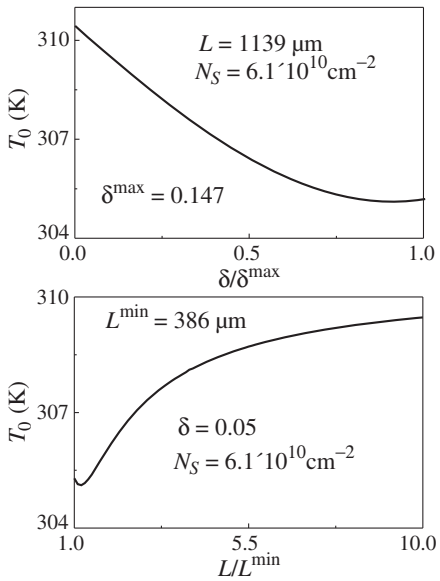

Fig. 2. Characteristic temperature versus normalized (a) root mean square of relative QD size fluctuations and (b) cavity length. In Figs. 2–4, the operating temperature is $T = 300$ K. ("Reprinted from Solid-State Electron., Vol. 52, No. 10, D.-S. Han and L. V. Asryan, Characteristic temperature of a tunneling-injection quantum dot laser: Effect of out-tunneling from quantum dots, Pages No. 1674–1679, Copyright (2008), with permission from Elsevier.")

2. Out-tunneling from QDs into the foreign QWs

Out-tunneling into the foreign QWs cannot be completely blocked in actual devices. Fig. 1 shows an optimized structure, in which the lowest subband edge for minority carriers in the QW is misaligned from the energy level for the corresponding type of carrier in the QD. Even in such a structure, there will be an indirect out-tunneling (shown by the inclined arrows in Fig. 1) — electrons (holes) as minority carriers will appear in the hole- (electron-) injecting QW. Then they will thermally escape to the right- (left-) hand side of the OCL where holes (electrons) are the majority carriers. As a result, a bipolar population will establish outside QDs, and parasitic recombination will occur. In [18,19], these processes were thoroughly studied and the potential of a realistic tunneling-injection QD laser for temperature-stable and high-power operation was studied. The model was based on a set of rate equations for electrons and holes in the layered structure of Fig. 1 and for photons. Here, some of the findings of [18,19] are discussed.

2.1. Characteristic temperature

Fig. 2 shows the characteristic temperature versus the QD structure parameters normalized to their critical tolerable values. As seen from the figure, T_0 is very high throughout the entire range of the parameters shown. As each of the parameters is changed toward its critical tolerable value, T_0 decreases. This decrease is however small — notice that even the lowest value of T_0 is above 300 K, i.e., well above (by a factor of more than three) the characteristic temperature of commercial telecommunication QW lasers. At the same time, if the structure parameters are reasonably far from their critical values, the threshold current densities [19] are well below those of telecommunication lasers.

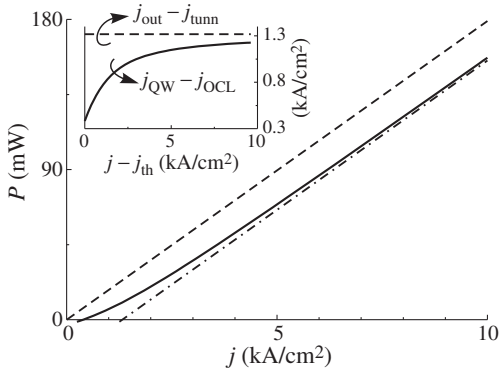

Fig. 3. LCC of a tunneling-injection QD laser (solid curve). The dashed line is the LCC of an ideal structure given by (2). The dash-dotted line is the asymptote given by (4). The inset shows the parasitic recombination current density (solid curve) and out-tunneling current density (horizontal dashed line) against excess injection current density. A GaInAsP heterostructure lasing near 1.55 μm is considered. ("Reprinted with permission from [D.-S. Han and L. V. Asryan, Appl. Phys. Lett., Vol. 92, Issue 25, Art. No. 251113, 2008.] Copyright [2008], American Institute of Physics").

2.2. Light-current characteristic

In terms of the excess of the injection current density over the current densities of spontaneous recombination in QDs, QWs, and OCL, the optical output power is

$$P = \frac{\hbar\omega}{e} S\Big(j - eN_{\rm S}\frac{f_{\rm n}f_{\rm p}}{\tau_{\rm QD}} - eB_{\rm 2D}n_{\rm QW}^{\rm L}p_{\rm QW}^{\rm L} - eB_{\rm 2D}n_{\rm QW}^{\rm R}p_{\rm QW}^{\rm R} - eb_1Bn_{\rm L}p_{\rm L} - eb_2Bn_{\rm R}p_{\rm R}\Big), \quad (1)$$

where $\hbar\omega$ is the photon energy, e is the electron charge, S is the cross-section of the junction, j is the injection current density, $N_{\rm S}$ is the surface density of QDs, $f_{\rm n,p}$ are the electron- and hole-level occupancies in QDs, $\tau_{\rm QD}$ is the spontaneous radiative lifetime in a QD, $n_{\rm QW}^{\rm L,R}$ and $p_{\rm QW}^{\rm L,R}$ are the two-dimensional (2-D) electron and hole densities in the left- and right-hand-side QWs (Fig. 1), $b_{1,2}$ are the thicknesses of the left- and right-hand sides of the OCL and $n_{\rm L,R}$ and $p_{\rm L,R}$ are the free-electron and -hole densities there (Fig. 1), and B and $B_{\rm 2D}$ are the spontaneous radiative recombination constants for the bulk (OCL) and 2-D region (QWs), respectively.

The sum of the last four terms in the brackets in (1) presents the parasitic recombination current density outside QDs.

If out-tunneling into the foreign QWs is completely blocked, there will be no minority carriers outside QDs ($p_{\rm L}$, $p_{\rm QW}^{\rm L}$, $n_{\rm QW}^{\rm R}$, $n_{\rm R} = 0$). The electron-hole recombination will occur only in QDs. Eq. (1) will read as

$$P^{\rm highest} = \frac{\hbar\omega}{e} S\left(j - eN_{\rm S}\frac{f_{\rm n}f_{\rm p}}{\tau_{\rm QD}}\right). \quad (2)$$

Hence, the LCC of an ideal tunneling-injection QD laser is linear and the slope efficiency is unity.

In an actual structure, there can be out-tunneling into the foreign QWs (Fig. 1). For this reason, the electron-hole recombination outside QDs cannot be completely suppressed. It is shown in [18] that the current density of parasitic recom-

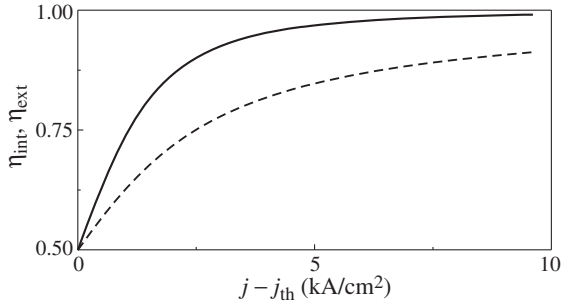

Fig. 4. Internal quantum efficiency (dashed curve) and slope efficiency (solid curve) against excess injection current density. ("Reprinted with permission from [D.-S. Han and L. V. Asryan, Appl. Phys. Lett., Vol. 92, Issue 25, Art. No. 251113, 2008.] Copyright [2008], American Institute of Physics.")

bination outside QDs is limited by the current density of out-tunneling of minority carriers from QDs to the foreign QWs,

$$eB_{2D}n_{QW}^{L}p_{QW}^{L}+eB_{2D}n_{QW}^{R}p_{QW}^{R}+eb_1Bn_Lp_L+eb_2Bn_Rp_R < ew_{p,tunn}^{L}p_1^{L,QW}N_Sf_p+ew_{n,tunn}^{R}n_1^{R,QW}N_Sf_n, \quad (3)$$

where $w_{p,tunn}^{L}$ and $w_{n,tunn}^{R}$ are the out-tunneling coefficients of holes and electrons from QDs to the left- and right-hand-side QWs, respectively (measured in units of cm^2/s), and the quantities $p_1^{L,QW}$ and $n_1^{R,QW}$ are related to the 2-D effective densities of states in the conduction and valence bands in the QWs.

The parasitic recombination current density [the left-hand side of (3)] and the out-tunneling current density [the right-hand side of (3)] are shown in the inset in Fig. 3 versus the excess of the injection current density j over the threshold current density j_{th}.

By using (3), the lower limit for the output power is obtained from (1),

$$P^{lowest}=\frac{\hbar\omega}{e}S\Big(j-eN_S\frac{f_nf_p}{\tau_{QD}} -ew_{p,tunn}^{L}p_1^{L,QW}N_Sf_p-ew_{n,tunn}^{R}n_1^{R,QW}N_Sf_n\Big). \quad (4)$$

Since $f_{n,p} \le 1$, the last three terms in the brackets in (4) remain restricted with increasing j.

As seen from (4), the lower limit for the LCC is linear (dash-dotted line in Fig. 3) and its slope efficiency is unity. It is parallel to the upper limit [given by (2) and shown by the dashed line in Fig. 3] and shifted from the latter by the amount of the out-tunneling current density. Hence, the actual LCC (obtained from the solution of the rate equations and shown by the solid curve in Fig. 3) is confined between the two parallel lines given by (2) and (4) (dashed and dash-dotted lines in Fig. 3). Since the parasitic recombination current density (solid curve in the inset in Fig. 3) remains restricted, the fraction of the excess injection current density $j - j_{th}$ that goes into the stimulated emission (the internal quantum efficiency) rises with increasing j (Fig. 4) — the LCC approaches the straight line given by (4) (Fig. 3).

3. Conclusion

Even in the presence of out-tunneling from QDs and recombination outside QDs, the characteristic temperature of a laser exploiting tunneling-injection of both electrons and holes into QDs remains very high (above 300 K at room temperature) and not significantly affected by the QD size fluctuations, which is a clear manifestation of robustness of such a device. The LCC of the laser becomes more and more linear, and the slope efficiency grows closer to unity with increasing injection current. Such a feature is due to the fact that the current paths connecting the opposite sides of the structure lie entirely within QDs — in view of the three-dimensional confinement in QDs, the out-tunneling fluxes of carriers from dots (which are the source of parasitic recombination) are limited.

Acknowledgements

This work was supported by the U.S. Army Research Office under Grant No. W911-NF-08-0462.

References

[1] Zh. I. Alferov, *Rev. Mod. Phys.* **73**, 767 (2001).
[2] Y. Arakawa and H. Sakaki, *Appl. Phys. Lett.* **40**, 939 (1982).
[3] N. Kirstaedter, N. N. Ledentsov, M. Grundmann, D. Bimberg *et al*, *Electron. Lett.* **30**, 1416 (1994).
[4] L. V. Asryan and R. A. Suris, *Semicond. Sci. Technol.* **11**, 554 (1996).
[5] L. V. Asryan and R. A. Suris, *IEEE J. Quantum Electron.* **34**, 841 (1998).
[6] L. V. Asryan, S. Luryi, and R. A. Suris, *Appl. Phys. Lett.* **81**, 2154 (2002).
[7] L. V. Asryan, S. Luryi, and R. A. Suris, *IEEE J. Quantum Electron.* **39**, 404 (2003).
[8] K. Kamath, D. Klotzkin, and P. Bhattacharya, *Proc. IEEE LEOS 10th Annual Meeting* **2**, 498 (1997).
[9] P. Bhattacharya, X. Zhang, Y. Yuan, K. Kamath, D. Klotzkin, C. Caneau, and R. J. Bhat, *Proc. SPIE* **3283**, 702 (1998).
[10] Y. Arakawa, *Solid-State Electron.* **37**, 523 (1994).
[11] L. V. Asryan and S. Luryi, *IEEE J. Quantum Electron.* **37**, 905 (2001).
[12] L. V. Asryan and S. Luryi, *Solid-State Electron.* **47**, 205 (2003).
[13] L. V. Asryan and S. Luryi, *U.S. Patent 6,870,178 B2* (2005).
[14] T. Chung, G. Walter, and N. Holonyak, *Appl. Phys. Lett.* **79**, 4500 (2001).
[15] G. Walter, T. Chung, and N. Holonyak, *Appl. Phys. Lett.* **80**, 1126 (2002).
[16] G. Walter, T. Chung, and N. Holonyak, *Appl. Phys. Lett.* **80**, 3045 (2002).
[17] P. K. Kondratko, S.-L. Chuang, G. Walter, T. Chung, and N. Holonyak, *Appl. Phys. Lett.* **83**, 4818 (2003).
[18] D.-S. Han and L. V. Asryan, *Appl. Phys. Lett.* **92**, Art. No. 251113 (2008).
[19] D.-S. Han and L. V. Asryan, *Solid-State Electron.* **52**, 1674 (2008).

17th Int. Symp. "Nanostructures: Physics and Technology"
Minsk, Belarus, June 22–26, 2009
© 2009 Ioffe Institute

Power conversion efficiency in stacked quantum dot lasers

A. E. Zhukov[1,2,3] and M. V. Maximov[3,2,1]

[1] Academic Physics and Technology University of RAS, St Petersburg, Russia
[2] St Petersburg Physics and Technology Centre for Research and Education RAS, St Petersburg, Russia
[3] Ioffe Physical-Technical Institute, St Petersburg, Russia

Abstract. We present a theoretical model for the initial stage of epitaxial growth of semiconductor nanowires by the so-called vapor-liquid-solid mechanism. It is shown that there are two characteristic diameters of drops, one relating to the drops lying on the substrate surface and another to the minimum diameter when the growth proceeds. The model also allows one to obtain the nanowire shape at the initial stage. Theoretical results are compared to the available experimental data on the Au-assisted molecular beam epitaxy of GaAs nanowires on the GaAs(111)B substrates at different growth conditions.

Introduction

Diode lasers operating in the 1.2–1.3 μm based on InAs/InGaAs self-organized quantum dots (QDs) are capable of achieving extremely low threshold current densities [1], high characteristic temperatures [2] and low internal loss [3]. However, optimization of QD lasers for high power conversion efficiency is a quite difficult task because of a complicated dependence of threshold current density on optical loss. To date the highest conversion efficiency of 1.3 μm QD lasers is 56% [4], while it exceeds 70% in quantum well lasers [5,6]. In the present work a model is evolved in order to optimize variable parameters of a QD diode laser for achieving the highest possible power conversion efficiency at a given output power.

1. Maximization of power conversion efficiency

The aim of our analysis is to find out a combination of laser's variable parameters (cavity length L, stripe width W and facer reflectivity R) for a prescribed output power level P which provides the maximum power conversion efficiency $\eta_C^{\max}(P)$ possible for a family of diode lasers fabricated of a given epitaxial wafer. Power conversion efficiency can be approximated as [7,8]:

$$\eta_C \approx \frac{\eta\,(I - I_{th})}{I^2 R_S + I U_0}, \tag{1}$$

where I — diode current, I_{th} — threshold current, η — slope efficiency, R_S and U_0 — diode series resistance and turn-on voltage. Eq. (1) is convenient to present in the following form:

$$\eta_C(p,a) = \frac{p}{i(p,a)\,[i(p,a)\rho_S + U_0]},$$

where $p = P/S$ is optical power per diode area, a — output loss, $i(p,a) = p/\eta(a) + j_{th}(a)$ — current density required for power level P, $j_{th}(a)$ — threshold current density, ρ_S — specific series resistance.

It is seen that conversion efficiency is a function of two independent variables (p and a). The maximum efficiency is achieved at certain optimal values of normalized power (p_0) and output loss (a_0) for which extremum conditions ($\partial\eta_C/\partial a = 0$ and $\partial\eta_C/\partial p = 0$) are jointly satisfied. Particularly, optimum p_0 and a_0 are found from the following equation:

$$p_0 = p_1(a_0) = p_2(a_0),$$
$$p_1(a) = \eta(a)\sqrt{j_{th}^2(a) + j_{th}(a)U_0/\rho_S},$$

$$p_2(a) = \eta^2(a)\,\frac{dj_{th}(a)/da}{d\eta(a)/da}. \tag{2}$$

The maximum power conversion efficiency is:

$$\eta_C^{\max} = \frac{\eta(a_0)}{U_0}\,\frac{x_0}{\left(1+\sqrt{1+x_0}\right)^2}, \tag{3}$$

where $x_0 = U_0/(j_{th}(a_0)\rho_S)$. Eq. (3) is a generalized form of a peak conversion efficiency of an individual laser [7,8]. The maximum conversion efficiency, optimum output loss and optimum normalized power can be considered as some inherent parameters for the whole family of diode lasers fabricated of a given epitaxial wafer.

In order to satisfy the maximum conversion efficiency at a prescribed output power P, the laser's variable parameters (L, W and R) should be chosen to provide the required output loss $a_0 = (2L)^{-1}\ln(R^{-1})$ and normalized power $p_0 = P/(LW)$. Ideally, the maximum conversion efficiency can be realized for any output power. In practice, its possible range is restricted by limits of variation of W, L and R in laser diodes.

2. Power conversion efficiency in case of quantum dots

Eq. (3) is applicable for any kind of diode lasers. Effect of a laser's active region can be considered through specific dependences of the threshold current density $j_{th}(a)$ and slope efficiency $\eta(a)$ on output loss. QD lasers are characterized by low transparency current density j_{tr}, while the optical gain is restricted by its saturated value G_{sat}. As output loss approaches the saturated gain in order to maximize the slope efficiency, the threshold current density of a QD laser sharply increases. Therefore, high values of power conversion efficiency in QD lasers are questionable.

In the present work it is assumed that internal slope efficiency η_{in} and internal loss α_{in} are independent of output loss so that the slope efficiency is described by well known formula $\eta(a) = \eta_{in}(a/(a+\alpha_{in}))$ Threshold current density is approximated by empirical equation [9]

$$a + \alpha_{in} = G_{sat}\left[1 - \exp\left(-\gamma(j_{th} - j_{tr})/j_{tr}\right)\right],$$

where γ is non-ideality (fitting) parameter.

The only variable parameter of a QD active region is assumed to be a number of QD planes N_{QD}. Successive deposition of several planes of InAs/InGaAs QDs separated by

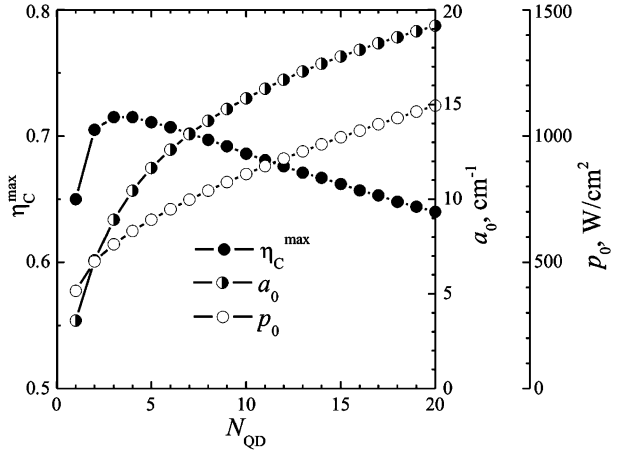

Fig. 1. Dependence of maximum power conversion efficiency η_C^{max}, optimum output loss a_0 and optimum normalized output power p_0 on number of quantum dot planes N_{QD} in laser's active region.

unstrained (GaAs or AlGaAs) spacer layers results in proportional increase of the transparency current density $j_{tr}(N_{QD}) \approx N_{QD} j_0$, as well as the saturated gain $G_{sat}(N_{QD}) \approx N_{QD} G_0$.

3. Power conversion efficiency of stacked QD laser

The following internal parameters of 1.24 μm QD lasers are assumed: $G_0 = 5$ cm^{-1}, $j_0 = 8$ A/cm^2, $\gamma = 0.65$, $\eta_{in} = 0.99$ W/A, $\alpha_{in} = 1$ cm^{-1}, $\rho_S = 1.6 \times 10^{-4}$ $\Omega \times$ cm^2, $U_0 = 1.02$ V, which, in fact, are averaged over the best published values [10]. Calculated maximum power conversion efficiency, optimum output loss and optimum normalized output power are shown in Fig. 2 as functions of quantum dot planes in laser's active region. It is seen that the maximum power conversion efficiency exceeds 70% as it is achieved at certain optimum number of QD planes (about 2–7 for parameters under consideration). Such number of planes can be realized in practice by means of various methods of quantum dot stacking. The optimum normalized power ranges from 500 to 750 W/cm^2; the optimum output loss is about 9–13 cm^{-1}.

The highest output power, for which the maximum conversion efficiency can be achieved, is limited by the lowest possible value of the facet reflectivity. Suggesting that R can be as low as 0.1% and W can be 250 μm, the maximum output power is estimated to be 5 W. The laser's cavity length should be about 3–4 mm which is quite acceptable.

The lowest output power, for which the maximum conversion efficiency can be achieved, is limited by the shortest possible cavity length. Suggesting that L can be as short as 200 μm and W can be 1 μm, the lowest output power is about 1 mW. To provide the required optimum output loss, the facet coating should be $R \sim 66\%$.

4. Conclusion

It is demonstrated that proper optimization of quantum dot active region (optimum number of QD planes) and optimization of laser diode itself (optimum output loss and normalized output power) can provide the power conversion efficiency as high as 70% for a wide range (1 mW–5 W) of output power level.

Acknowledgements

The work is supported in different parts by Russian Federal Agency of Education ("Development of scientific potential of higher education institutions in 2009-2010"), Russian Foundation for Basic Research, Programs of Fundamental Studies of the Presidium of RAS, Physical Department of RAS and St Petersburg Scientific Center of RAS.

References

[1] I. R. Sellers *et al*, *Electron. Lett.* **40**, 1412 (2004).
[2] S. Fathpour *et al*, *Appl. Phys. Lett.* **85**, 5164 (2004).
[3] A. R. Kovsh *et al*, *Electron. Lett.* **38**, 1104 (2002).
[4] S. S. Mikhrin *et al*, *Semicond. Sci. Technol.* **20**, 340 (2005).
[5] M. Kanskar *et al*, *Electron. Lett.* **41**, 245 (2005).
[6] A. Knigge *et al*, *Electron. Lett.* **41**, 250 (2005).
[7] R. G. Waters *et al*, *Appl. Phys. Lett.* **51**, 1318 (1987).
[8] D. P. Bour *et al*, *J. Appl. Phys.* **66**, 2813 (1989).
[9] A. E. Zhukov *et al*, *Semicond. Sci. Technol.* **14**, 118 (1999).
[10] A. E. Zhukov *et al*, *Quant. Electron.* **38**, 409 (2008).

17th Int. Symp. "Nanostructures: Physics and Technology"
Minsk, Belarus, June 22–26, 2009
© 2009 Ioffe Institute

Graphene terahertz laser

V. Ya. Aleshkin[1], A. A. Dubinov[1] and V. I. Ryzhii[2]

[1] Institute for Physics of Microstructures RAS, 603950, Nizhny Novgorod, Russia
[2] University of Aizu, Aizu-Wakamatsu 965-8580, Japan and Japan Science and Technology Agency, CREST, Tokyo 107-0075, Japan

Abstract. We have developed a device model for terahertz laser based on optically pumped graphene as the active media and suggested waveguide structure. Using this model, we calculate the spectral dependences the dynamic conductivity of the optically pumped graphene associated with the interband and intraband transitions, estimate the pumping optical power required for lasing, and demonstrate the feasibility of realization of such a laser.

Introduction

Recent progress in formation of different graphene-based structures not only by pealing method but also by various epitaxial techniques indicates that exceptional electronic properties of graphene can utilized in real optoelectonic devices. Due to the gapless energy spectrum in graphene and rather small energy gaps in graphene nanoribbons and graphene layers grown on substrate, such optoelectonic devices can operate in the terahertz (THz) range of spectrum. Graphene has important advantage comparing with other narrow band semiconductor: due energy-momentum conservation the Auger recombination is suppressed in graphene with linear dependence of electron energy on momentum or is forbidden in graphene with Dirac electron spectrum. As shown [1] the optically pumped graphene can exhibit negative dynamic THz conductivity associated with the interband population inversion and domination of the interband emission over the intraband Drude absorption. This can be used for creation of lasers generating THz electromagnetic radiation. However, the crucial point in realization of a graphene THz laser is the feasibility of a waveguide system which could provide sufficiently low loses of THz radiation.

In this work, we consider a model for graphene THz laser with optical pumping which includes a graphene with linear or Dirac electron dispersion and a waveguide system. The latter consists of a thinned Si substrate of thickness 10–50 μm with Au film on one side and a SiO_2 layer of thickness 300 nm on the other followed by 80 nm SiC layer. The graphene layer is sandwiched between the SiC layer and 300 nm layer of SiO_2. This structure (see Fig. 1) is akin to that fabricated in Ref. [2].

1. Conductivity of optically excited graphene

Under optical excitation, electrons and holes are photogenerated with the energy $\varepsilon_0 = \hbar\Omega/2$. Here $\hbar\Omega$ is the energy of the incident photons. The electron-electron and electron-phonon interactions thermalize the distributions of photogenerated electrons and holes. So the electron and hole energy distributions are close to the Fermi distributions with quasi-Fermi energies $F > 0$. We shall use this simplified distributions for conductivity estimations. Note that the electron and hole distribution functions, $f_e(\varepsilon)$ and $f_h(\varepsilon)$, exceed 1/2 in certain energy ranges near the bottom of the conduction band and the top of the valence band. This implies the population inversion of the states in these energy ranges. In the optically pumped ungated and undoped graphene the equilibrium electron and hole concentrations are equal to each other, the Fermi distributions of electrons and holes are characterized by the same Fermi energy F and the effective temperature T:

$$f_e(\varepsilon) = f_h(\varepsilon) = \left[1 + \exp\left(\frac{\varepsilon - F}{k_B T}\right)\right]^{-1}, \qquad (1)$$

where k_B is the Boltzmann constant. For simplicity we disregard the difference between electron (hole) and lattice temperatures. The real part of the dynamic conductivity $\mathrm{Re}\,\sigma(\omega)$ which determines the absorption coefficient of photons with the frequency ω, comprises the contributions of both the interband and intraband transitions:

$$\mathrm{Re}\,\sigma(\omega) = \mathrm{Re}\,\sigma(\omega)^{\mathrm{inter}} + \mathrm{Re}\,\sigma(\omega)^{\mathrm{intra}}. \qquad (2)$$

Taking into account that the graphene band structure includes two nonequivalent valleys in the K points of the Brillouin zone and the spin degeneracy, as well as considering that the value of the interband momentum matrix element is equal to vm_0 for electron spectrum $\varepsilon(p) = \pm\sqrt{E_g^2/4 + v^2p^2}$ (where E_g is the gap, m_0 is the free electron mass, $v \simeq 10^8$ cm/s is the characteristic velocity of electrons and holes in graphene, p is the electron momentum), one can derive the following formula for the interband conductivity:

$$\mathrm{Re}\,\sigma(\omega)^{\mathrm{inter}} = \frac{e^2}{2\hbar}\tanh\left(\frac{\hbar\omega - 2F}{4k_B T}\right)\theta\left(\hbar\omega - E_g\right). \qquad (3)$$

here $\theta(x)$ is theta function ($\theta(x) = 1$ for $x > 0$ and $\theta = 0$ otherwise).

For $\mathrm{Re}\,\sigma(\omega)^{\mathrm{intra}}$ one can use the Drude formula

$$\mathrm{Re}\,\sigma(\omega)^{\mathrm{intra}} = \frac{2e\mu n}{\left(1 + \omega^2\tau^2\right)}, \qquad (4)$$

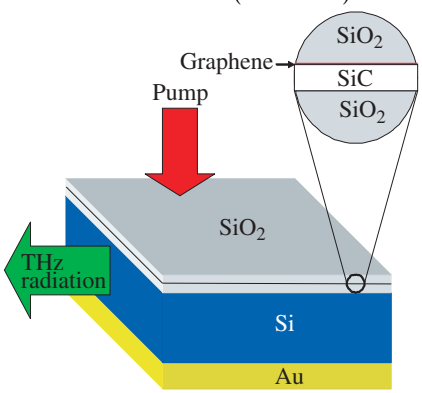

Fig. 1. Schematic view of the device structure.

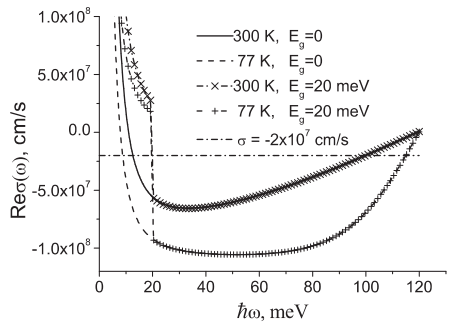

Fig. 2. Real part of the dynamical conductivity $\sigma(\omega)$ vs photon energy $\hbar\omega$.

here e is the electron charge, μ is the electron and hole mobility in graphene, τ is the momentum relaxation time of electrons and holes associated with their scattering, n is the electron concentration.

Figure 2 shows the real part of the dynamic conductivity Re σ_ω as a function of the photon energy $\hbar\omega$ calculated for the Fermi energy $F = 60$ meV, $\mu = 2 \times 10^5$ [3] at two values of the temperature ($T = 77$ and 300 K) and two values E_g. The momentum relaxation time was assumed to be $\tau = 10^{-12}$ s. The horizontal line corresponds to the threshold conductivity $\sigma = -2 \times 10^7$ cm/s for excitation TM_0 mode (see text below and [4]).

2. Laser waveguide

The calculated spatial distributions of the electric field of the TE_0 and TM_0 modes and the refractive index for frequency $\omega/2\pi = 2$ THz are shown in Fig. 3a. The Si layer width was chosen to provide the minimal generation threshold of these modes. The threshold conductivity (when gain and losses are equal) dependencies on Si layer width are shown in Fig. 3b for three frequencies 2, 4 and 6 THz. From Fig. 3b it is clear that the minimal threshold conductivity (corresponding to a optimal Si layer width) increases with the radiation frequency growth. It is due to absorption growth in SiO_2 layers. From Fig. 3b one can conclude that the absolute value of the threshold conductivity for TM_0 less than 2×10^7 cm/s for frequency range 2–6 THz. Calculations show that the absorption coefficient of electromagnetic modes in such a waveguide is about 4 cm^{-1}. So, as follows from Fig. 2, the gain coefficient for the laser under consideration is about 10–15 cm^{-1}.

Let us estimate the incident optical power required to obtain $F = 60$ meV at $T = 300$ K. This occurs when $n \simeq 4.2 \times 10^{11}$ cm^{-2} for $E_g = 0$ and $n \simeq 4.1 \times 10^{11}$ cm^{-2} for $E_g = 20$ meV. The required rate of photogeneration is equal to $G = n/\tau_R$, where τ_R is the recombination time. By now, there is no clear understanding of the nonradiative recombination mechanisms in graphene with relatively high electron and hole concentrations. It is reasonable to suppose that Auger recombination is dominant mechanism for case $E_g = 0$. Assuming that $\tau_R \simeq 2$ ps [5], considering that graphene absorbs only $2\pi e^2/\hbar c$ part of the incident radiation power and that in the waveguide structure under consideration there the pumping optical radiation twice passes through graphene, for the optical power required for lasing one obtains $G \approx 2.1 \times 10^{23}$ cm^{-2}s^{-1}. If the pumping is provided by CO_2 laser with the photon energy about 120 meV, the pertinent power should be about 4×10^4 W/cm^2. As was mentioned above in graphene with non zero gap the direct Auger recombination is forbidden by the energy-momentum conservation law. If this prohibition rises recombination time on two orders then excitation power is reduced to 400 W/cm^2. Latter value can be provided in cw generation regime.

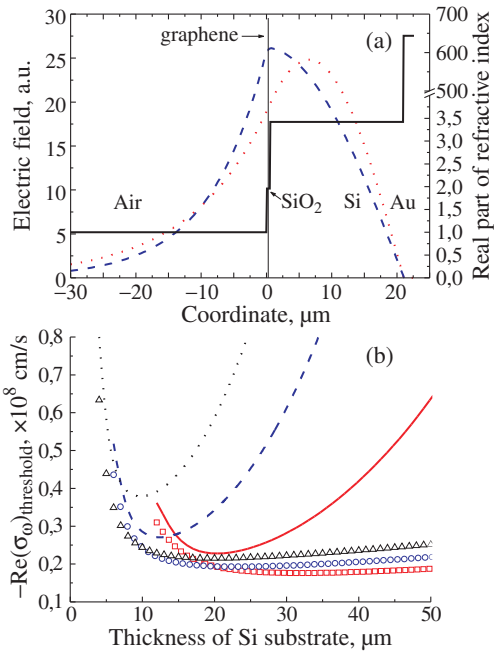

Fig. 3. (a) Spatial distributions of the refractive index (solid line) and ac electric fields of TE_0 mode (dotted line) and TM_0 mode (dashed line) in waveguide for frequency 2 THz. Horizontal arrow indicates the graphene layer position (vertical line). (b) Dependencies of the threshold conductivity for the TE_0 and TM_0 modes on the thickness of Si substrate in this structure for frequencies $\omega/2\pi = 2$ THz ($\hbar\omega \approx 8.27$ meV, solid curve corresponds to the TE_0 mode and open squares correspond to the TM_0 mode) and $\omega/2\pi = 4$ THz ($\hbar\omega \approx 16.54$ meV, dashed curve corresponds to the TE_0 mode, open circles correspond to the TM_0 mode), $\omega/2\pi = 6$ THz ($\hbar\omega \approx 24.81$ meV, dotted curve is for the TE_0 mode whereas open triangles are for TM_0 mode).

Acknowledgements

This work was in part financially supported by the Program of Russian Academy of Sciences "Physical and technologic investigations of semiconductor lasers directed on achievement of extreme parameters" and by the Japan Science and Technology Agency, CREST, Japan.

References

[1] V. Ryzhii, M. Ryzhii, and T. Otsuji, *J. Appl. Phys.* **101**, 083114 (2007).

[2] M. Suemitsu, Y. Miyamoto, H. Kanda, and A. Konno, *e-Journal of Surf. Sci. and Nanotechnol.*

[3] S. V. Morozov, K. S. Novoselov, M. I. Katsnelson, F. Schedin, D. C. Elias, J. A. Jaszczak, and A. K. Geim, *Phys. Rev. Lett.* **100**, 016602 (2007).

[4] V. Ya. Aleshkin, A. A. Dubinov, V. I. Ryzhii, *Pis'ma v ZhETF* **89**, 70 (2009).

[5] F. Rana, *Phys. Rev. B* **76**, 155431 (2007).

17th Int. Symp. "Nanostructures: Physics and Technology"
Minsk, Belarus, June 22–26, 2009
© 2009 Ioffe Institute

Wannier–Stark laser based on GaAs/$Al_xGa_{1-x}As$ superlattices with weak barriers

A. A. Andronov, *D. I. Zinchenko*, E. P. Dodin, Yu. N. Nozdrin
Institute for Physics of Microstructures, Russian Academy of Sciences, Nizhny Novgorod GSP-105 603600, Russia

Abstract. Basing on superlattice transport experiments and theoretical calculations and considerations, we propose THz Wannier–Stark laser on GaAs/$Al_xGa_{1-x}As$ superlattices with weak barriers. The amplification in such laser is due to population inversion between the first and the second Wannier–Stark levels situated two-three SL periods apart in the electric field region of *positive* differential conductivity. Calculated amplification coefficient can reach value of about hundreds of cm^{-1} for 10^{16} cm^{-3} doping level with high tunability by applied voltage. Such lasers could well compete with existing quantum cascade lasers due to simplicity of the superlattices used and high tunability.

Introduction

The idea of using semiconductor superlattices (SLs) to generate electromagnetic radiation with frequency tunable by changing applied electric field appeared [1] soon after the idea of superlattices themselves [2]. However, it was soon established that the field configuration in such structure will be unstable due to existence of low-frequency (static) negative differential conductivity (NDC) in the working region of proposed device, leading to formation of domains of inhomogenious electric fields. And such simple generator has been never built. To prevent field instabilities, different schemes were put forward, and one of them led to creation of Quantum Cascade Lasers (QCLs) [3]. Design of these lasers was constantly improved, and now they cover almost all frequencies in mid and far IR bands. However, their working principle (wavefunction engineering with aligning system of energy levels in required positions) leads to limited frequency tuning capacity (voltage drop on single cascade should remain constant to maintain energy levels alignment), and they require high precision growth technology for production. In this paper alternative design of laser based on semiconductor SLs with weak barriers is presented [4]. In this case, lasing should appear due to natural inversion between population of 1st and 2nd Wannier–Stark levels in different wells of the superlattice (cf. [1]), and the frequency of such transition depends on the voltage drop on one period of SL, that makes it possible to tune the laser frequency substantially wider as compared to QCLs. The calculation of amplification coefficient for such structure, based on the calculation of matrix elements for transitions between Wannier–Stark levels, is presented.

1. Experimental

In this work, several different SL samples with weak (short $\sim$1$-$1.5 nm and low $<$100 meV) potential barriers and minigap not exceeding 20 meV has been studied [4]. Here the results for 2 such SLs, samples 426 and 816, are presented. Table 1 shows some properties of these samples, here E_1 is the bottom of the first miniband, ΔE_1 is the width of 1-st miniband, $E_{\rm gap}$ is the width of the 1-st minigap, E_2 is the bottom of the 2-nd miniband, ΔE_2 is the width of 2-nd miniband, d, w and b are SL period, well and barrier widths, correspondingly, and N is the number of SL layers.

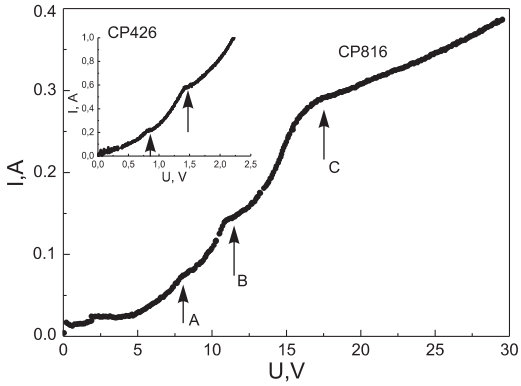

Fig. 1. I–V curves for samples SL 426 and SL 816.

In Fig. 1, the experimentally observed I–V curves (studied on $n^+ - \mathrm{SL} - n^+$ mesas) for these SL samples are presented. The curves for the both SLs exhibit several different regions: first, narrow region of Ohmic conductivity, then single-miniband transport with the region of static NDC with current oscillations (lowering part of I–V curve), and then the growth region, corresponding to inter-miniband tunneling of electrons. In this last region, there are some pronounced peculiarities (arrows) that are attributed to resonant tunneling between Wannier–Stark levels of different wells, located several SL periods apart [6].

2. Wannier–Stark laser

The peculiarities in I–V curves and their identification as due to inter-Wannier–Stark level tunneling [4,5] point to the existence of long-range (several SL periods) spread of electron

Table 1. Sample parameters.

Sample	426	816
E_0 (meV)	3.2	7.4
ΔE_1 (meV)	11.2	9.8
E_1 (meV)	14.4	17.2
$E_{\rm gap}$ (meV)	7.1	16.8
E_2 (meV)	21.3	33.9
ΔE_2 (meV)	34.9	32.5
$d = w + b$, μm	185+10	160+20
N	100	1000

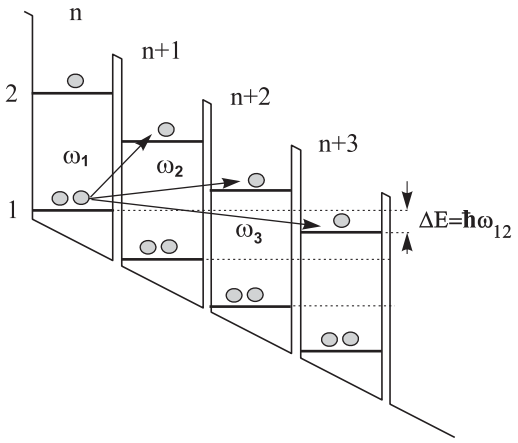

Fig. 2. Scheme of energy levels in SL and transitions between them, circles represent relative population of levels.

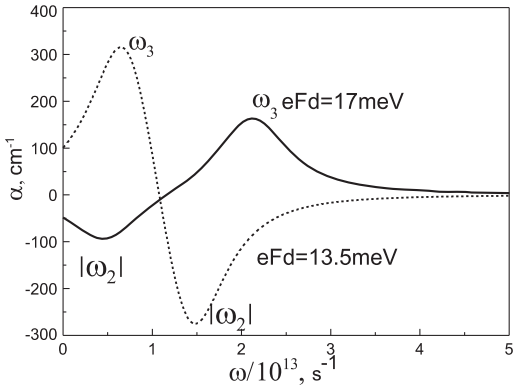

Fig. 3. Frequency dependence of amplification coefficient for 2 different values of voltage drop on one SL period.

wavefunction in superlattices studied. This implies that the wavefunctions of Wannier–Stark levels in such structures can be extended to long distances near the resonance values of electric field which correspond to aligning of Wannier–Stark levels originating from different minibands. In such resonant situation matrix elements of transitions between aligned levels become large due to long distance between wells where these levels are located. On the other hand, there is natural inversion between levels of first Wannier–Stark ladder (originating from first miniband) and levels of second ladder, when the level of first ladder lies higher than the level of second ladder located in another well (Fig. 2, arrow labeled ω_3).

In Fig. 3 the results of calculation of amplification coefficient for two different field values are presented. Two transitions labeled ω_2 and ω_3 in Fig. 2 were taken into account, and the amplification coefficient was calculated with matrix element values for these transitions found in [5], population inversion values from quasiclassical Monte-Carlo simulation [6] and fixed effective scattering rate $\nu = 5 \times 10^{12}\ \mathrm{s}^{-1}$ for electron concentration $10^{16}\ \mathrm{cm}^{-3}$. Calculated values of amplification coefficient α reach several hundreds of cm^{-1} for such parameters, which makes it possible to use $n^+ - \mathrm{SL} - n^+$ resonators to achieve lasing. We believe this scheme could well compete with the QCLs.

The SLs studied were undoped with electron concentration about $1-3\times10^{14}\ \mathrm{cm}^{-3}$. The amplification coefficient for such doping level is not enough to overcome losses in n^+ regions even for 1000 periods SL816 sample.

Acknowledgements

The authors are grateful to A. A. Padalitsa and A. A. Marmalyuk for growing the SL samples, M. N. Drozdov and Yu. N. Drozdov for SIMS and X-Ray characterization of the samples and to I. Yu. Shuleshova for samples processing.

References

[1] R. F. Kazarinov, R. A. Suris, *Sov. Phys. Semicond.* **5**, 707 (1971).
[2] L. Esaki and R. Tsu, *IBM J. Res. Dev.* **14**, 61 (1970).
[3] J. Faist *et al*, *Science* **264**, 553 (1994).
[4] A. A. Andronov, E. P. Dodin, Yu. N. Nozdrin, D. I. Zinchenko, *Semiconductors* **43**, 228 (2009).
[5] A. A. Andronov, E. P. Dodin, Yu. N. Nozdrin, D. I. Zinchenko, *Phys. stat. sol. (c)* **5**, 190 (2008).
[6] A. A. Andronov, I. M. Nefedov, and A. V. Sosnin, *Semiconductors* **37**, 360 (2003).

17th Int. Symp. "Nanostructures: Physics and Technology"
Minsk, Belarus, June 22–26, 2009
© 2009 Ioffe Institute

Absorption and emission of radiation by hot carriers in Sb-based laser structures

L. E. Vorobjev[1], V. L. Zerova[1], D. A. Firsov[1], G. Belenky[2], L. Shterengas[2], G. Kipshidze[2], D. Wang[2], T. Hosoda[2], S. Suchalkin[2] and M. Kisin[2]

[1] St Petersburg State Polytechnic University, 195251 St Petersburg, Russia
[2] SUNY, Stony Brook, New York 11794, USA

Abstract. Dynamics of interband photoluminescence was studied in structures with InGaAsSb quantum wells and different barriers under wide range of the temperatures and optical excitation intensities. Carrier lifetime in quantum wells was determined at different temperatures and pumping levels. Increasing the recombination rate in structures with deep electron quantum wells was found and related to resonant Auger recombination. Recommendation were given to use quinternary solid solutions as a material for the barriers in laser structures for 3–4 μm spectral range. Emission from laser structure with quantum well shifted to p-cladding layer for reducing the waveguide losses was studied.

Introduction

Sb-based structures with InGaAsSb/InAlGaAsSb quantum wells (QW) in semiconductor injection lasers allow to extend their spectral range to 3–4 μm. Characteristics of lasers are strongly determined with recombination processes in such structures and internal losses in waveguide. The present paper is devoted to the study of the recombination processes and optical losses in the structures used for the development of the lasers with record characteristics [1,2].

1. Recombination studies

Recombination was studied in the structures of two types containing 4 $In_{0.54}Ga_{0.46}As_{0.24}Sb_{0.76}$ QWs. The barriers were formed with $Al_{0.35}Ga_{0.65}As_{0.03}Sb_{0.97}$ for type 1 structure and $In_{0.25}Al_{0.20}Ga_{0.55}As_{0.03}Sb_{0.97}$ for type 2 structure. The use of quinternary solid solution in barriers described in [2] allowed to improve laser characteristics. We studied time resolved photoluminescence (PL) at photon energy corresponding to maximal PL signal at different temperatures and intensities of the optical pumping using up-conversion technique with time resolution of 1 ps.

The curves of PL decay measured in structure of type 1 at $T_0 = 300$ K are shown in Fig. 1. It should be noted that the excitation conditions differed significantly for structures of types 1 and 2. The barrier direct energy gap for the structure of type 1 was approximately equal to the photon energy of excitation $E_g^\Gamma \approx h\nu$, as a result the absorption coefficient was relatively small. In the structures of type 2 $E_g^\Gamma < h\nu$ and the absorption of pumping radiation can be influenced with the dynamic Burshtein–Moss effect. So, in order to bring the nonequilibrium electron concentration and the pumping level in the correlation, we calculated PL intensity that corresponds approximately to the maximal point of PL decay curve as a function of electron concentration. The results of calculations and the corresponding experimental dependence of PL signal at the maximum of decay curve on the pumping level are shown in Fig. 2 for the structure of type 1.

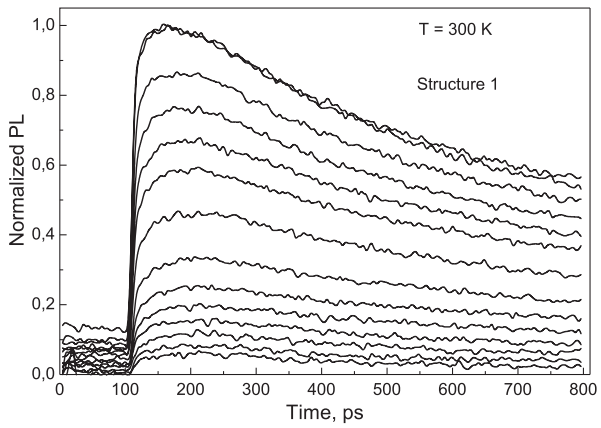

Fig. 1. Dependences of PL signal on time for the structure of type 1 ($In_{0.54}Ga_{0.46}As_{0.24}Sb_{0.76}$/ $Al_{0.35}Ga_{0.65}As_{0.03}Sb_{0.97}$) measured at different pumping levels.

Experimentally determined dependences of PL signal J_{PL} on time and dependences of PL signal in maximum of decay curves on pumping level I_{pump} allowed to calculate the total recombination rate as a function of electron concentration:

$$-R(n_0) = \frac{1}{n_0}\frac{dn_0}{dt} = \frac{1}{I_{pump}}\frac{dI_{pump}}{dJ_{PL}}\frac{dJ_{PL}}{dt} = \frac{1}{I_{pump}}\left(\frac{dJ_{PL}}{dI_{pump}}\right)^{-1}\frac{dJ_{PL}}{dt}. \quad (1)$$

The results of the calculation of recombination rate R for the structure of type 1 are presented in Fig. 3. The quadratic dependence of $R(I_{pump})$ observed at increasing the temperature correspond to significant contribution of Auger recombination. We found that Auger recombination is more significant in structure of type 1 with quaternary barrier. The electron temperatures were estimated from the power balance equations taking into account the LO phonon accumulation. These values are shown in Fig. 3. Heating the electrons is connected with the energy transfer from Auger electron ($E \simeq E_g$) to the carriers in low subbands due to *e-e*, *e-h* and *e-h* collisions. Electron temperature T_e increases up to 390 K. The difference between T_0 and T_e was also observed in [3] where T_e was determined from PL spectra.

Auger recombination coefficient C can be estimated from Fig. 3 if we subtract linear term corresponding to the radiative

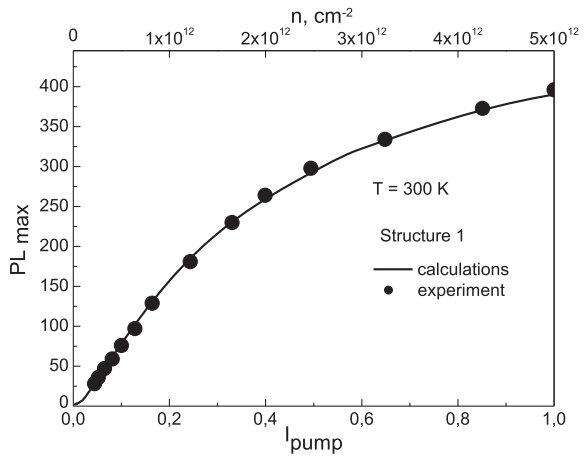

Fig. 2. Calculated and experimentally found dependences of PL signal in maximum of decay curves.

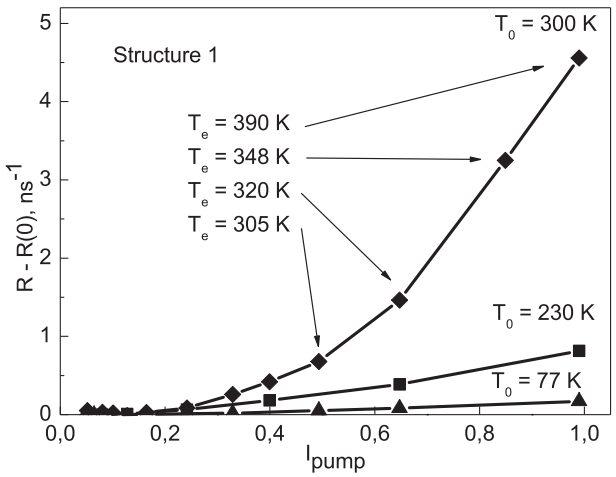

Fig. 3. Recombination rate as a function of pumping intensity.

recombination from the total recombination rate:

$$C = \frac{R(n) - R(0) - Bn}{n^2} = \frac{1}{\tau_{\text{Auger}} n^2}. \qquad (2)$$

At $T_0 = 300$ K, $T_e = 390$ K: in the type 1 structure $C \approx 2 \times 10^{-16}$ cm^4/c, in the type 2 structure $C \approx 4 \times 10^{-17}$ cm^4/c.

The enhancement of Auger recombination rate in structure of type 1 can be explained with resonant Auger recombination. As it follows from calculations, the incorporation of In in barrier solid solution of type 2 structure leads to the decrease of electron QW depth and to the increase of hole QW one. In structures where the depth of electron QW exceeds the energy gap, the excited electron energy levels can serve as a final states for Auger electrons. So, in addition to the ordinary CHCC Auger processes the resonant Auger processes accompanied with vertical electron transitions are possible in such structures [4]. The probability of resonant Auger processes is comparatively high, so the total recombination rate increases.

In case the quinternary solid solution is used for the barriers of laser structure (structure of type 2) the depth of electron QW is less than E_g and resonant Auger processes are impossible. In case the quaternary solid solution is used (structure of type 1) possible resonant Auger processes lead to the decrease of internal efficiency. So, structures of type 2 are preferable

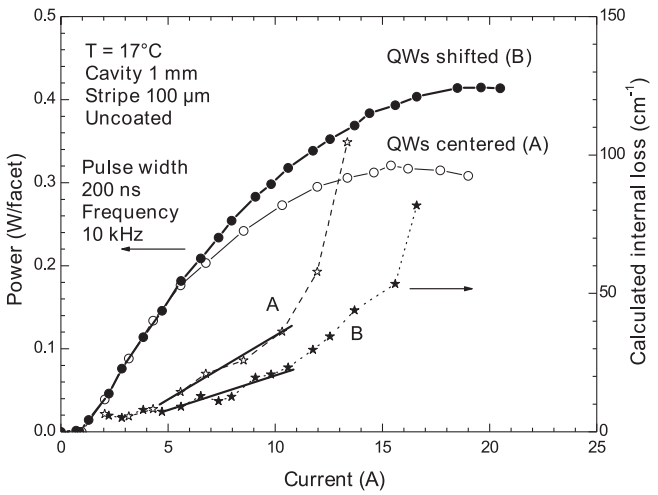

Fig. 4. Left axis: pulse mode light-current characteristics for 1 mm long, 100 μm wide stripe uncoated lasers of two types at 17 °C. Right Y-axis: calculated internal loss against peak current.

for the improved laser operation. The analysis of laser characterizes [1,2] confirms this conclusion.

2. Waveguide losses

The further progress in enhancing the laser characteristics under high pumping level is related to minimizing the waveguide losses connected to free carrier light absorption [5,6]. Two laser structures were grown. Quantum wells were centered in waveguide in structure A. In contrast, quantum wells were shifted to p-cladding in structure B. Holes injected to waveguide give the main contribution in absorption and the optical losses in structure B were expected to be less due to low hole concentration in waveguide in comparison to structure A. Some results are presented in Fig. 4.

It should be noted that at the current exceeding the threshold one by a factor of five, the radiation power from structure B is more. The internal losses found from the analysis of experimental data for structure A are more than for structure B. This is a main reason of increasing the radiation power due to the shift of QWs to p-cladding layer.

Acknowledgements

This work is supported by the grants of RFBR, Ministry of Education and Science of Russian Federation and US National Science Foundation under grant DMR071054.

References

[1] T. Hosoda, G. Belenky, L. Shterengas, G. Kipshidze, M.V. Kisin, *Appl. Phys. Lett.* **92**, 091106 (2008).
[2] L. Shterengas, G. Belenky, G. Kipshidze, T. Hosoda, *Appl. Phys. Lett.* **92**, 171111 (2008).
[3] D.-J. Jang, M. E. Flatté, C. H. Grein, J. T. Olesberg, T. C. Hasenberg, Thomas F. Boggess, *Phys. Rev. B* **58**, 13047 (1998).
[4] L. V. Danilov, G. G. Zegrya, *Semiconductors* **42**, 550 (2008).
[5] K. A. Bulashevich, V. F. Mymrin, S. Yu. Karpov, D. M. Denisov, A. L. Ter-Martirosyan, *Semicond. Sci. Technol.* **22**, 502 (2007).
[6] B. S. Ryvkin, E. A. Avrutin, *J. Appl. Phys.* **97**, 113106 (2005).

17th Int. Symp. "Nanostructures: Physics and Technology"
Minsk, Belarus, June 22–26, 2009
© 2009 Ioffe Institute

High-speed (~40 Gbit/s) oxide-confined 850 nm VCSELs

S. A. Blokhin[1,2,3], J. A. Lott[4], G. Fiol[1], N. N. Ledentsov[2,4], M. V. Maximov[2,3], A. Mutig[1], A. M. Nadtochiy[1,2,3], *L. Ya. Karachinsky*[1,2,3], I. I. Novikov[1,2], V. A. Shchukin[2,4] and D. Bimberg[1]

[1] Institute of Solid-State Physics and Center of Nanophotonics, Technical University Berlin, EW 5-2, D-10623, Berlin, Germany
[2] Ioffe Physical-Technical Institute, St Petersburg, Russia
[3] St Petersburg Physics and Technology Centre for Research and Education RAS, St Petersburg, Russia
[4] VI Systems GmbH, Hardenbergstrasse 7, D-10623, Berlin, Germany

Abstract. Oxide-confined 850 nm range vertical-cavity surface-emitting lasers with InGaAs-based active region suitable for open-eye operation up to 40 Gbit/s and error-free transmission up to 39 Gbit/s at current densities ~10 kA/cm^2 are realized. The deconvoluted rise time of the device is below 10 ps and remains hardly temperature sensitive up to 100 °C.

Introduction

Future development of local (LAN) and storage (SAN) area networks requires high-speed optical components. Vertical-cavity surface-emitting lasers (VCSELs) emitting at 850 nm are reliable, low-cost, low power consumption components for optical transmission at 0.1–10 Gbit/s in data communication networks [1]. With modern industrial photonic crystal fibers single mode 850 nm VCSEL applied to demonstrate 40 Gbit/s error-free transmission over 2 km distance under external electrooptic modulation [2]. However, developing of current-modulated VCSELs reliable to degradation free operation at data rates beyond 10 Gbit/s is challenging. To overcome the problem for the 980–1100 nm spectral range devices with the active area based on InGaAs strained quantum well or quantum dots (QDs) were introduced [3,4,5]. More recently error-free transmission at bit rates >20 Gbit/s was achieved at 850 nm wavelength [6,7,8].

In this paper we report on oxide-confined 850 nm GaAs-based VCSELs with InGaAs-based quantum-sized active region suitable for open-eye operation up to 40 Gbit/s and error-free transmission up to 39 Gbit/s, both numbers being limited by the experimental set-up and not by the optical components. The VCSELs deconvoluted rise time measured at current densities ~10 kA/cm2 was found to be <10 ps and hardly temperature dependent up to 100 °C.

1. Experiment

Epitaxial wafers for oxide-confined 850 nm VCSELs composed conventional $Al_{0.15}Ga_{0.85}As$-$Al_{0.9}Ga_{0.1}As$ distributed Bragg reflectors (DBRs), (Al,Ga)As-based cavity and an InGaAlAs-based active region. Epitaxial structure design was optimized for ultra-high speed operation including appropriate doping and composition profiles in the DBR regions. The VCSEL wafer was processed into a high frequency ground-source-ground (GSG) contact pad configuration for on-wafer probe testing as described in [8].

The FC-connector multimode fiber pigtailed *p-i-n*-diode module (VIS D30-850M) with a rise time below 7 ps (20%–80%) was used as a photodetector. Large signal modulation experiments were performed using a non-return to zero (NRZ) data pattern with $(2^7 - 1)$ pseudorandom bit sequence (PRBS) from SHF 12100B bit pattern generator (rise time of 8 ps). The optical signal was sent to the photodetector in back-to-back (BTB) configuration. The optical eye diagrams and the bit error ratio (BER) were studied using 70 GHz Agilent 86100C digital oscilloscope and SHF 11100B error analyzer, respectively. More detailed experimental set-up description is presented in [8].

2. Static characteristics

Fig. 1 shows the typical light-current (L-I) characteristics of the 6 μm oxide aperture device for temperatures between 20 and 100 °C. The inset displays the emission spectrum at 20 °C and 5 mA indicating a trend of multimode operation around 860 nm. The root mean square (RMS) spectral width is less than 0.55 nm for all temperatures. The peak slope efficiency is hardly temperature dependent and reduces insignificantly from 0.83 W/A at 20 °C to 0.73 W/A at 85°C.

3. Dynamic characteristics

Fig. 2 shows eye-diagrams for 6 μm oxide-confined VCSEL recorded in BTB-configuration at 10 Gbit/s at pump current 5 mA and different temperatures. Except of the slightly reduction in the signal-to-noise ratio caused by smaller optical modulation amplitude (OMA) at higher temperatures, no further significant changes were revealed. The ripples in the eye diagram originate from the original BERT signal oscillations broadened by the jitter related to amplifiers and connectors and

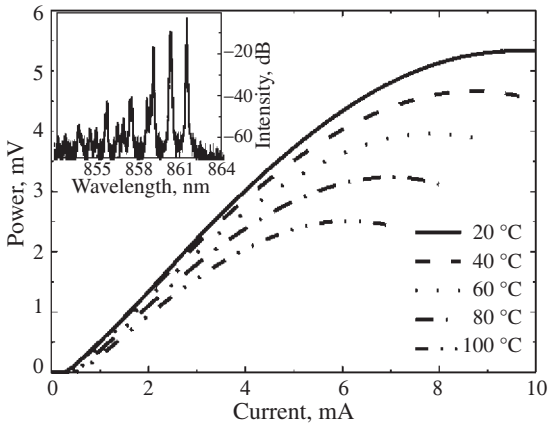

Fig. 1. L-I curves for 6 μm oxide-confined InAlGaAs VCSEL in 20–100 °C temperature range. Inset: Optical spectrum at 20 °C and 5 mA pump current.

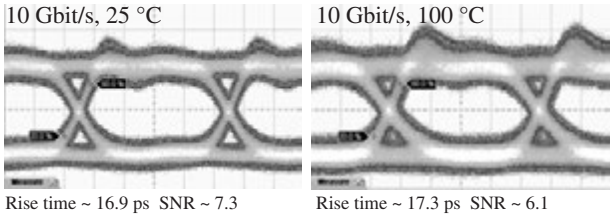

Fig. 2. 10 Gbit/s eye diagrams in BTB-configuration and corresponding rise time for 6 μm oxide-confined InAlGaAs VCSEL at 25 and 100 °C different temperatures.

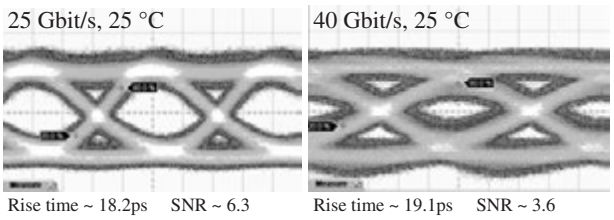

Fig. 3. BTB optical eye diagrams for 6 μm InAlGaAs VCSEL at 25 and 40 Gbits/s modulation at fixed bias current and 25°C.

reproduced by the VCSEL with a similar periodicity. The signal rise time in the eye diagram remains hardly affected up to 100 °C and is defined predominantly by the convoluted BERT and amplifier rise times (11 ps). The deconvoluted VCSEL rise time is found to be below 8-10 ps at all temperatures.

Eye diagrams remain open up to 40 Gbit/s as it is shown in Fig. 3. Note that the eye quality of the received signal is significantly affected by the imperfection of electrical RF-signal applied to the devices (jitter, noise, additional rise times, ringing in the BERT signal). Additionally OM3 fiber tests at 20 Gb/s were performed at 20 °C for 6 μm VCSELs. No significant changes in the eye diagrams were found for the fiber lengths up to 100 m. In spite of the fiber intermodal dispersion resulted in degradation of the eye quality and the SNR-ratio, the error-free transmission was still achieved at all distances, which is acceptable for future standards. The link penalties at a transmission distance of 50 m, 100 m and 150 m were found around 0.5 dBm, 1.6 dBm and 3 dBm, respectively.

It was also found that VCSELs having larger oxide apertures could also operate at similar bit rates but at even lower current densities. Larger aperture devices are important because they provide improved reliability. The results of the BER studies carried out for 9 μm oxide aperture VCSEL are presented in Fig. 4. The modulation amplitude Vp-p was 0.8 V at 20 °C and 0.6 V at 85°C, while the bias current was fixed at 9 mA (BTB-configuration was used). The drive current corresponds to a current density of 10 kA/cm^2, low enough to support degradation robustness of the device. The devices operate error free with a BER below 10^{-12} and no error floor is observed up to 38 Gbit/s. The highest error free transmission rate measured was 39 Gbti/s, but at a significant power penalty of 3 dB. Temperature increase for the same modulation voltage was reducing the OMA and extinction ratio and the required optical power to reach the same error rate was higher. The penalty due to the increased temperature (85°C) was 1.5 dB and 2 dB for 20 and 30 Gbit/s bit rates, respectively, as compared to the BTB error rates at 20 °C.

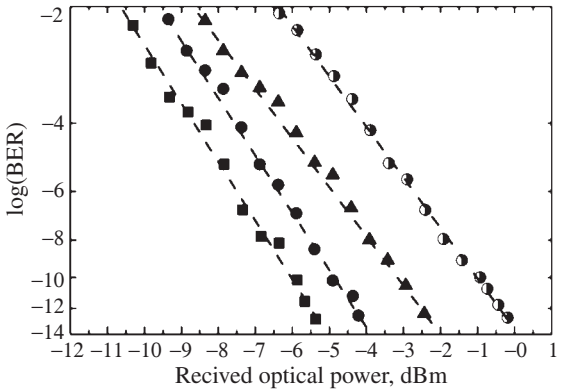

Fig. 4. BER measurements in BTB-configuration for 9 μm oxide-confined InAlGaAs VCSEL at 20 (squares), 25 (filled circles), 32 (triangles), 38 Gbit/s (semi-filled circles) bit rates for the bias current of 9 mA and 20 °C.

4. Conclusion

Oxide-confined 850 nm VCSELs were fabricated and studied. Open eye diagrams and error-free transmission up to 40 Gbit/s and 39 Gbit/s, respectively, both being limited by our current experimental set up, were demonstrated. Power penalty for high temperature (85°C) error free transmission at 30 Gbit/s was found to be around 2 dB. The VCSELs have the deconvoluted rise times <8–10 ps up to the highest temperature (100 °C) at sufficiently low current densities (10 kA/cm^2). Obtained results clearly indicate that current-modulated VCSELs can be applied in the near future for reliable ultrahigh-speed data transmission in short distance optical data networks and optical cables.

Acknowledgements

This work was supported in different parts by the RFBR, EU Project "VISIT" (FP7-ICT-2007-2-224211), Program of the Presidium RAS "Fundamental studies of nanotechnologies and nanomaterials", joint RFBR-DFG project, Grant from St Petersburg Scientific Centre RAS, Purpose-oriented program of Russian Federal Agency of education "Development of scientific potential of higher education institutions (2009–2010)".

References

[1] D. Collins *et al*, *Proc. SPIE* 6908, 690809-1 (2008).
[2] H. Hasegawa *et al*, *Electron. Lett.* **43**, 642 (2007).
[3] Y.-C. Chang *et al*, *Electron. Lett.* **43**, 1022 (2007).
[4] A. Mutig *et al*, *Electron. Lett.* **44**, 1345 (2008).
[5] N. N. Ledentsov *et al*, *Proc. IEEE* 95, 1741 (2007).
[6] P. Westbergh *et al*, *Electron. Lett.* **44**, 907 (2008).
[7] R. Johnson and D. Kuchta, *Proc. CLEO* 2008, paper CPDB2.
[8] J. A. Lott *et al*, *Proc. SPIE* 7211, paper 721140P-1 (2009).

17th Int. Symp. "Nanostructures: Physics and Technology"
Minsk, Belarus, June 22–26, 2009
© 2009 Ioffe Institute

Erbium-doped nano-glass-ceramics: spectral and informational characteristics

V. Aseev[1], *M. Khodasevich*[2], A. Klementeva[1], E. Kolobkova[3], N. Nikonorov[1], G. Sinitsyn[2] and Y. Varaksa[2]

[1] St Petersburg State University of Information Technology, Mechanics, and Optics, St Petersburg, Russia
[2] B. I. Stepanov Institute of Physics, NASB, Minsk, Belarus
[3] St Petersburg State Technological Institute, St Petersburg, Russia

Abstract. Fluoride erbium-doped nano-glass-ceramics is shown to be an attractive host for broadband optical fiber amplifier. It combines good luminescent properties of erbium ions in crystallites and good fiberizability. Spectroscopic characteristics of transparent nano-glass-ceramics obtained at different durations of secondary thermal treatment of virgin glass are studied. Spectral and informational characteristics of fiber amplifiers made of these nano-glass-ceramics are calculated. Benefits of new host material for optical fiber amplifiers used in broadband communication systems are discussed. The results received show that 12 hours annealed fluoride nano-glass-ceramics doped by erbium ions with 0.5 mol.% concentration displays the best spectroscopic, informational and gain characteristics.

Introduction

The rare-earth (RE) ions doped materials with the abundant energy levels structure have now the extensive applications in high density optical data reading and storage, fiber sensors, viewers and indicators, color displays and so on. In particular, the erbium ion has received recently much attention because its 1.5 μm emission plays an important role in communication systems.

Continuous growth of modern communication systems requires the investigation of new materials for fiber amplifiers, e.g. other RE-doped glasses such as praseodymium-doped ones, holmium-doped ones, thulium-doped ones and glasses doped by combinations of RE ions including erbium and ytterbium as sensitizer. Ions of other metals (e.g. bismuth or chromium) can be used as dopants for different wavelength regions of transparency of optical fibers. Another field of investigation is the search for the new host materials for erbium-doped fiber amplifiers (EDFA). Stark splitting of metastable and ground levels of dopant ions is dependent on the ions' environment. Therefore the shape and peak value of absorption and emission cross-sections of erbium ions depend on the host material of fiber.

Tellurite and oxygen-free glasses can be emphasized among other glasses as attractive hosts for broadband optical amplifiers. Moreover, these glasses possess also a wide infrared transmittance, high solubility for RE ions and good chemical durability. However there are the essential drawbacks for their use as hosts for active fibers. For example, tellurite glasses are liable to spontaneous crystallization that complicates the fiber drawing technique. Furthermore, tellurite glasses have high enough refraction index (>2) that makes the splicing with standard silicate fiber difficult. For oxygen-free glasses there is not the drawing technique for the long enough spans (>5 m).

One of the possible new materials free from foregoing drawbacks is transparent fluoride nano-glass-ceramics doped with RE ions. Fluoride glasses are characterized by low maximum phonon energy [1]. This nano-glass-ceramics combines good luminescent properties of dopant ions in crystallites and good fiberizability. In such structures up to 200 nm sized crystallites are controllably grown in glass host during secondary thermal treatment. The structure and optical properties of nano-glass-ceramics depend on the secondary thermal treatment regime.

The virgin material in our study is the $30SiO_2$-$18PbF_2$-$7.5Al_2O_3$-$5ZnF_2$-$29CdF_2$ glass doped with erbium and ytterbium ions. The concentration of erbium ions is 0.5 molar percent (1.4×10^{19} cm^{-3}). During secondary thermal treatment of virgin glass at 520 °C transparent nano-glass-ceramics have been formed, containing crystallites with the size of 15–200 nm depending on the treatment duration. The purpose of the current work is the finding of optimal duration of secondary thermal treatment of virgin glass to achieve the maximum capacity of EDFA.

1. Figures of merit of host materials for EDFA

The conventional figures of merit of host materials for EDFA are spectroscopic characteristics of the materials. We consider these characteristics hereinafter too. However the informational characteristics of EDFA are more convenient for comparison of fiber materials with respect to the functional application of EDFA [2,3]. Capacity C of EDFA has been proposed to use as the most adequate informational figure of merit [3]. Capacity C of EDFA is the maximum speed of information transmission and depends on the frequency band used ($\Delta\nu$), optical signal-to-noise ratio at the input of EDFA ($SNR(0)$) and the minimum optical noise figure of the amplifier ($F_0^{\min}$):

$$C = \int_{\Delta\nu} \log_2\left(1+\frac{SNR(0)}{F_0^{\min}}\right) + \frac{SNR(0)}{F_0^{\min}}\log_2\left(1+\frac{F_0^{\min}}{SNR(0)}\right) d\nu.$$

The value of noise figure substantially depends on the amplifier regime. In the high gain regime the minimum noise figure is independent of the spectral characteristics of erbium ions for quasi-two-level and three-level pumping. However at quasi-two-level pumping scheme in unsaturated gain regime, when the pump power is considerably higher than the total signal and amplified spontaneous emission powers, the minimum noise figure shows dependence on spectroscopic parameters of the

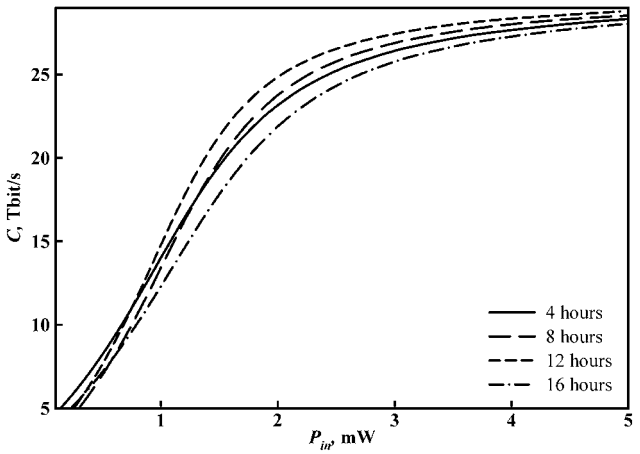

Fig. 1. Capacity of EDFA on the basis of nano-glass-ceramics versus input pump power.

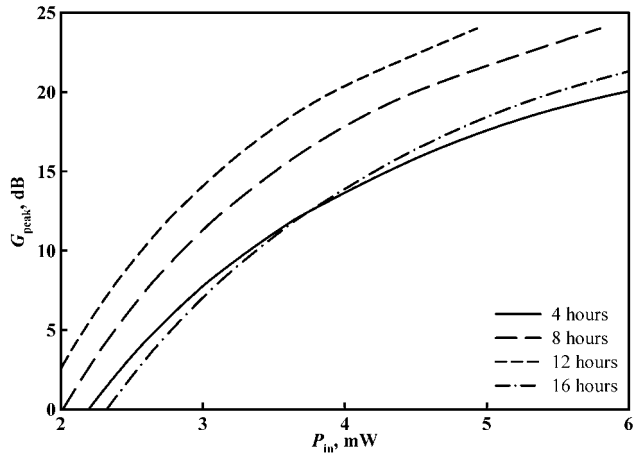

Fig. 2. Peak gain of EDFA on the basis of nano-glass-ceramics versus input pump power.

host material and on the concentration of dopant ions [4]. We compare here the capacity for unsaturated gain regime of quasi-two-level pumped EDFA made of nano-glass-ceramics with different duration of secondary thermal treatment (from 4 to 16 hours annealing at 520 °C).

2. Comparison results

Some spectroscopic characteristics usually applied for comparison of EDFA host glasses are presented in the Table 1 for the samples studied [5].

Two samples of nano-glass-ceramics obtained at 8 and 12 hours annealing are preferable by the value of emission spectrum width, the latter has the bigger peak value of emission cross-section and therefore the greater value of product of peak value and the half-width of emission cross-section. Capacity (in C-band, i.e. 1535–1565 nm) of EDFA made of considered nano-glass-ceramics is presented in Figure 1. One can see that nano-glass-ceramics obtained at 12 hours annealing at 520 °C has the best characteristics too.

Furthermore, we have considered the gain spectra of EDFA. Despite large widths of emission cross-sections spectra of nano-glass-ceramics, their substantial nonuniformity leads to the reduction of gain spectra widths of EDFA on the basis of these materials compared to virgin glass. Large nano-glass-ceramics gain ripple compared to virgin glass is due to crystalline environment of the large portion of erbium ions.

Along with the width of gain spectra the peak gain value is an essential characteristic of fiber amplifiers at specified pump power level. The peak gain of EDFA is presented in Figure 2. One can see that in the whole range of input pump powers an EDFA on the basis of 12 hours secondary thermal treated nano-glass-ceramics has the largest value of the peak gain. Moreover, this sample is characterized by the maximum effectiveness of pump power conversion, and the virgin glass is the worst according to this criterion.

Table 1.

Sample (annealed)	Half width of emission cross-section spectrum, nm	Peak value of emission cross-section, 10^{-21} cm^2	Product of peak value and the half-width of emission cross-section, 10^{-32} m^3
4 hours	63.2	6.54	4.13
8 hours	64.0	7.55	4.83
12 hours	64.1	7.97	5.11
16 hours	59.5	7.47	4.44

3. Conclusions

Thus, on the basis of the results received we can conclude that 12 hours annealed nano-glass-ceramics displays the best spectroscopic characteristics. Informational and gain characteristics of fiber amplifiers made of this material are also the best among the samples of nano-glass-ceramics obtained at different durations of secondary thermal treatment of erbium-doped virgin glass.

Further we plan to optimize simultaneously the concentration of erbium ions and the regime of secondary thermal treatment of nano-glass-ceramics. This may allow obtaining superior informational characteristics of EDFA compared to currently used host glasses for EDFA.

Acknowledgements

The authors are thankful to Belarusian Republican Foundation for Fundamental Research and Russian Foundation for Fundamental Research for the partial support of this work.

References

[1] B. Layne *et al*, *Phys. Rev. B* **16**, 10 (1977).
[2] M. A. Khodasevich *et al*, *Opt. Spectr.* **101**, 757 (2006).
[3] Y. A. Varaksa *et al*, *Opt. Spectr.* **104**, 130 (2008).
[4] E. Desurvire. *Erbium-Doped Fiber Amplifiers, Principles and Application*. New York: Wiley-Interscience, 1994. 770 p.
[5] V. A. Aseev *et al*, International Conference *"Laser Optics 2008"*, St Peterburg, Russia, **ThR1** p. 57.

17th Int. Symp. "Nanostructures: Physics and Technology"
Minsk, Belarus, June 22–26, 2009
© 2009 Ioffe Institute

Broaden flat gain spectra in the asymmetric multiple-quantum-well $Ga_{0.47}In_{0.53}As/Ga_{0.18}In_{0.82}As_{0.4}P_{0.6}$ heterostructures

D. V. Ushakov[1] and V. K. Kononenko[2]

[1] Belarussian State University, Independence Ave., 4, 220030 Minsk, Belarus
[2] B. I. Stepanov Institute of Physics NASB, Independence Ave., 70, 220072 Minsk, Belarus

Abstract. For asymmetric multiple-quantum-well heterostructures based on the $Ga_{0.47}In_{0.53}As/Ga_{0.18}In_{0.82}As_{0.4}P_{0.6}$ compounds, the analysis of widen modal gain spectra is carried out in the framework of the four-band $\mathbf{k} \times \mathbf{p}$ method. Effective procedure of obtaining the broaden and practically flat gain spectrum is offered. Various designs of semiconductor sources with different sets of nonuniform excited QWs, giving a broaden gain spectrum in the 1.28–1.52 and 1.36–1.60 μm ranges, are approved.

Introduction

The problems of coherent laser spectroscopy, fiber-optic communications, chemical analysis, metrology, and environment monitoring require the use of efficient tunable lasers covering the spectral range from 1.3 to 1.6 μm. Lasing in this region can be obtained in asymmetric multiple-quantum-well (QW) heterostructures based on ternary and quaternary $Ga_xIn_{1-x}As/Ga_xIn_{1-x}As_yP_{1-y}$ compounds [1–3] with a set of nonuniformly excited QWs of different widths.

The idea of nonuniform excitation of QWs in $GaAs/Al_xGa_{1-x}As$ compounds was proposed in [4,5], where the broadband gain spectrum was obtained in the wavelength range of 0.79 to 0.85 μm. The emission wavelength of interband transitions in QW lasers depends on the thickness of active layers. QWs of different widths amplify radiation in different wavelength ranges and therefore the total gain spectrum of a multiple QW heterostructure with such QWs can cover a rather broad spectral range.

Using ternary and quaternary compounds with a narrower energy gap lying in the IR region can increase the width of the gain spectrum. In this paper, we study the modal gain spectra of asymmetric multiple-QW heterostructures based on the $Ga_{0.47}In_{0.53}As$ QWs and $Ga_{0.18}In_{0.82}As_{0.4}P_{0.6}$ barrier layers matched with an InP substrate.

1. Theoretical calculation

Calculations of modal gain spectra were carried out in some steps. At the first step on the basis of a four-band $\mathbf{k} \times \mathbf{p}$ method [6,7] are calculated energy levels, wave functions and gain coefficient spectra at various excitation levels for QWs of width from 2 to 15 nm. The gain coefficient at the light frequency ν and a definite TE or TM polarizations in the QW of the width d_i is defined as follows [8, 9]

$$k(\nu) = \frac{e^2}{\varepsilon_0 c m_e^2 n_0 \nu d_i} \sum_{n,m} \int L\left(h\nu - E_{cv}\right) dE_{cv}$$
$$\times \int |\mathbf{M}_{nm}|^2 \left[f_e\left(E_{cn}(k_\parallel)\right) + f_h\left(E_{vm}(k_\parallel)\right) - 1 \right]$$
$$\times \frac{dk_\parallel}{(2\pi)^2} \delta\left(E_{cv} - E_{cn}(k_\parallel) + E_{vm}(k_\parallel)\right),$$

where n_0 is the refractive index of the active region, f_e and f_h are Fermi–Dirac functions for electrons and holes, $E_{cn}(k_\parallel)$ and $E_{vm}(k_\parallel)$ are energies of the states involved in the optical transitions, $|\mathbf{M}_{nm}|^2$ is the squared matrix element of the dipole transitions between electron and hole subbands with the quantum numbers n and m accordingly, $L(h\nu - E_{cv})$ is the Gaussian function of spectral line broadening.

The received database was applied on the second step by optimization of excitation level of semiconductor system from several QWs of various widths with the purpose of reception of a wide and flat modal gain spectrum in a required wavelength range. Numerical results of such calculation for the $Ga_{0.47}In_{0.53}As/Ga_{0.18}In_{0.82}As_{0.4}P_{0.6}$ system with the 2(2)–3–7 and 3(2)–4–15 sets of QWs are shown in Fig. 1. Received waveguide gain spectrum is nearly flat on the intervals of 1.28–1.52 and 1.36–1.60 μm.

At the final step on the basis on the Poisson and current continuity equations [5] electrophysical characteristics were defined. Also the doping levels and thicknesses of barrier layers corresponding of necessary excitation level in the QWs are established. Two important effects that appeared in asymmetric multiple-QW heterostructures have been taking into account [5]. One is the blocking of the electron and hole transport from one QW into another adjacent QW. The second one is the electron-optical interactions between the QWs resulting in synchronization of emission and populations for different QWs.

2. Conclusions

We have calculated the modal gain spectra of the asymmetric multiple-QW heterostructures in the $Ga_{0.47}In_{0.53}As/Ga_{0.18}In_{0.82}As_{0.4}P_{0.6}$ system taking into account the mixing of the subbands of the valence band in the four-band $\mathbf{k} \times \mathbf{p}$ method approximation. An almost flat and broad modal gain spectrum is obtained upon nonuniform excitation of QWs of different widths. By using different sets of QWs, flat tunable regions are received between 1.28 and 1.52 μm and between 1.36 and 1.60 μm. The proposed designs of asymmetric multiple-QW heterostructures in the $Ga_{0.47}In_{0.53}As/Ga_{0.18}In_{0.82}As_{0.4}P_{0.6}$ system can be used for widen tunable elements of optoelectronic and photonic integrated circuits.

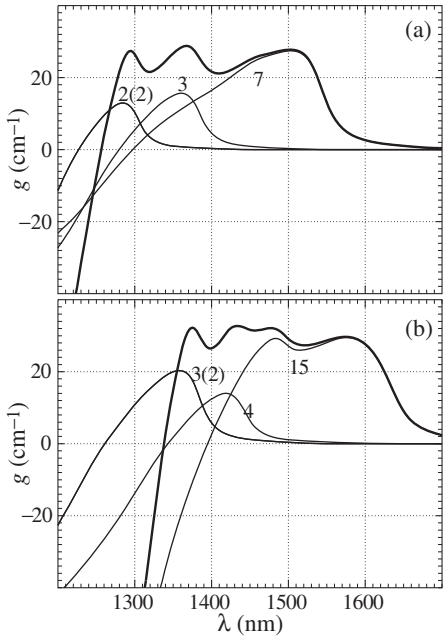

Fig. 1. Modal gain spectra $g(\lambda)$ at the TE mode for the asymmetric multiple-QW $Ga_{0.47}In_{0.53}As/Ga_{0.18}In_{0.82}As_{0.4}P_{0.6}$ heterostructure with four QWs with the sets of widths (a) 2(2)–3–7 nm and (b) 3(2)–4–15 nm upon nonuniform excitation of QWs. The bold curve describes the total modal gain. The numbers at the curves denote QW widths d: (a) two QWs with $d = 2$ nm, $\Delta F = 1.01$ eV, $\Gamma = 2.4 \times 10^{-3}$; $d = 3$ nm, $\Delta F = 0.97$ eV, $\Gamma = 3.6 \times 10^{-3}$; $d = 7$ nm, $\Delta F = 0.96$ eV, $\Gamma = 8.4 \times 10^{-3}$; $U = 1.015$ V, $j = 355$ A/cm^2. (b) two QWs with $d = 3$ nm, $\Delta F = 0.99$ eV, $\Gamma = 3.9 \times 10^{-3}$; $d = 4$ nm, $\Delta F = 0.92$ eV, $\Gamma = 5.2 \times 10^{-3}$; $d = 15$ nm, $\Delta F = 0.89$ eV, $\Gamma = 19.7 \times 10^{-3}$; $U = 0.987$ V, $j = 373$ A/cm^2.

Acknowledgements

The Belarussian Republican Foundation for Fundamental Research supported this work.

References

[1] O. Issanchou, J. Barrau, E. Idiart-Alhor, M. Quillec, *J. Appl. Phys.* **78**, 3925 (1995).
[2] T. Yamatoya, S. Mori, F. Koyama, K. Iga, *Jpn. J. Appl. Phys.* **38**, 5121 (1999).
[3] Zhao Hong-Quan, Yu Li-Juan, Huang Yong-Zhen, *J. Appl. Phys.* **100**, 023513 (2006).
[4] V. K. Kononenko, I. S. Manak, S. V. Nalivko, *Spectrochimica Acta. Part A.* **55**, 2091 (1999).
[5] V. K. Kononenko, A. A. Afonenko, I. S. Manak, S. V. Nalivko, *Opto-Electron. Rev.* **8**, 241 (2000).
[6] J. M. Luttinger, W. Kohn, *Phys. Rev.* **97**, 869 (1955).
[7] G. E. Pikus, G. L. Bir, *Fiz. Tverd. Tela* **1**, 1642 (1959).
[8] K. Nakamura, A. Shimizu, M. Koshiba, K. Hayata, *IEEE J. Quantum Electron.* **25**, 889 (1989).
[9] S. V. Nalivko, I. S. Manak, A. L. Chizh, *Lithuanian J. Phys.* **39**, 365 (1999).

17th Int. Symp. "Nanostructures: Physics and Technology"
Minsk, Belarus, June 22–26, 2009
© 2009 Ioffe Institute

Violation of steady-state stability and dynamics of a dual-wavelength vertical external cavity surface-emitting laser

Yu. A. Morozov, M. Yu. Morozov and V. V. Popov
Kotelnikov Institute of Radio Engineering and Electronics (Saratov Branch), RAS, 410019, Saratov, Russia

Abstract. The analysis of a steady-state operation point and its stability for a dual-wavelength vertical external cavity surface-emitting laser (VECSEL) is fulfilled. This operation point is shown to be unconditionally stable for a VECSEL including the uncoupled gain areas with non-identical quantum wells. If the VECSEL's gain regions are coupled owing to absorption of short-wavelength emission in the deeper quantum wells, the violation of a steady-state stability and the pulse dynamics could be observed. It is obtained that the pulse train period coincides approximately with the external cavity round-trip time and an excitation of oscillations at both wavelengths occur nearly in-phase.

Introduction

Despite essential success of quantum-cascade lasers (QCLs) in mid- and far-infrared generation, there are both fundamental and technical problems hindering further progress of these devices. As far as we know, the attempts undertaken to observe a room-temperature continuous wave operation of QCLs at wavelengths exceeding 10 microns didn't succeed yet [1].

We believe that the alternative approach based on non-linear frequency conversion in semiconductor lasers could be discussed as a promising one as compared to the quantum-cascade principle of operation [2,3]. Since the dual-wavelength vertical external cavity lasers (VECSELs) have been made [4,5], a realizable possibility for highly efficient frequency conversion hopefully appears. Indeed, these lasers generate two coaxial gaussian beams in the fundamental transverse modes of a high cross section and thus of a high power. Besides, the dual-wavelength VECSELs allow for a non-linear crystal to be placed inside the laser cavity. Intracavity non-linear optical interaction is far more effective as compared with extracavity one, provided the other parameters are the same [6]. The intracavity sum-frequency generation of high efficiency has been recently observed in the dual-wavelength VECSEL [7]. It should be noted, that most of usual non-linear crystals are opaque in the far-infrared range. Fortunately, isotropic quasi-phase-matched GaAs crystals are transparent and can be applied to non-linear frequency conversion in the range reaching up to 17 microns [8].

Two different modifications of a dual-wavelength VECSEL with the wavelength separation about 60–80 nm in the near-infrared range (∼1000 nm) have been proposed in [4,5]. Both VECSELs comprise of two active regions with the non-identical quantum wells (QWs) included. The main distinction of these two VECSELs consists in the method of absorption's decrease for the short-wavelength radiation in the deeper quantum wells. In the first variant of a VECSEL [4], the deeper QWs are located in the nodes of the short-wavelength radiation. The gain areas of the second choice of a VECSEL [5] are separated by the dichroic Bragg mirror. This mirror is highly reflective to the short-wavelength optical field while being transparent to the long-wavelength one. Moreover, the long-wavelength gain region is grown deeper in the structure and the short-wavelength gain region is located close to the surface of the device. Both varieties of the VECSELs show either a continuous wave or a pulse regime of operation depending on a pump power value.

1. Steady state operation point and its stability

The rate equations for both variants of the dual-wavelength VECSEL can be written as follows:

$$\begin{aligned} \dot{S}_i &= v_g \left[\sum_{j=1}^{2} \Gamma_{ij} g_{ij} - \alpha_i + \frac{1}{2L_i} \ln\left(\frac{S_{i\tau}}{S_i}\right) \right] S_i \\ \dot{N}_i &= \frac{J_i}{t_w} - \frac{N_i}{\tau_r} - \frac{v_g}{m_i t_w} \sum_{j=1}^{2} \Gamma_{ji} g_{ji} L_j S_j, \end{aligned} \qquad (1)$$

here i is the index corresponding to the short- ($i = 1$) and the long-wavelength ($i = 2$) radiation; S_i is the photon density, the quantity with index τ corresponds to the time moment $t - \tau_{\text{ext}}$; Γ_{ij} and g_{ij} are the confinement factor and the gain of the i-th optical field in the j-th equivalent QW; v_g is the light group velocity; L_i is the sub-cavity length; N_i is the carrier density in the i-th equivalent QW; τ_{r} and τ_{ext} are the carrier lifetime and the round-trip time in the external cavity, respectively; J_i is the pumping carrier flux density to the i-th equivalent QW; t_w is the width of QW; m_i is the number of QWs in the corresponding gain area. The overall loss factor can be defined as

$$\alpha_i = \alpha - \frac{1}{L_i} \ln\left[r_{\text{ext}} (1 - r_{\text{ar}}^2) r_i \right],$$

where α is the material loss factor; r_{ext}, r_{ar} and r_i are the external mirror reflectivity, the sub-cavity facet reflectivity and the reflectivity of the DBR mirror inside the structure, respectively. When deriving Eqs. (1), a few simplifying assumptions have been adopted. First of all, we assume that the gain coefficient of the i-th active region with m_i QWs can be lumped to a single equivalent QW. This can be done by the corresponding increase of the confinement factor Γ_{ij}. Second, we neglect the effect of spontaneous emission to the laser modes and the effect of noisy carrier generation-recombination. Third, we didn't account for the gain saturation for the time being.

Note, that the active areas appear uncoupled if the reciprocal confinement factors $\Gamma_{12} = \Gamma_{21} = 0$, the quantity Γ_{12} playing the main role in their coupling. The effect of Γ_{21} is negligible because of a small value of the gain coefficient g_{21} for the

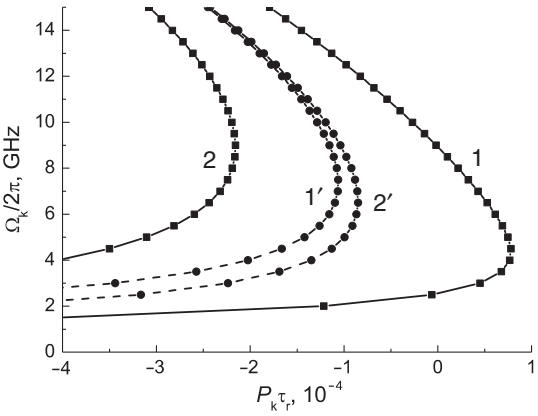

Fig. 1. Roots of the characteristic equation on the complex plane.

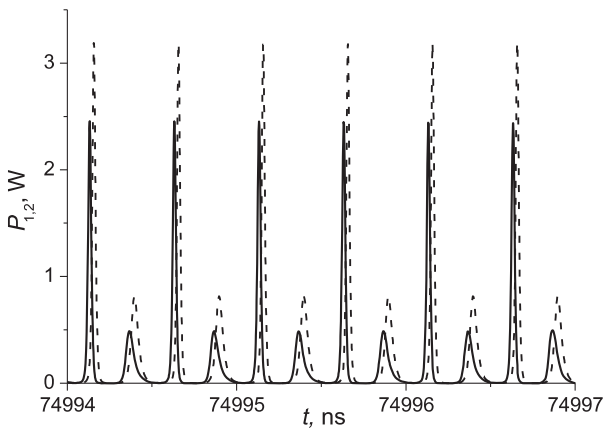

Fig. 2. Dynamics of the dual-wavelength VECSEL's output power on the selected time interval.

long-wavelength optical field in the shallow equivalent QW. Thereafter, we suppose $\Gamma_{21} = 0$.

By setting the derivatives zeros in (1) one obtains the steady-state operation point $W_{\rm st} = (S_{10}, N_{10}, S_{20}, N_{20})^T$. It is convenient to carry out the analysis of the steady-state stability by applying the Laplace transformation to a linear ODE system written in terms of small deviations from the above steady state values. Then, the corresponding characteristic equation reads

$$\det(\hat{M}(p)) = 0, \qquad (2)$$

where the matrix $\hat{M}(p)$ contains the parameters defined in the steady-state operation point. The roots of Eq. (2) are complex and consist of four branches:

$$\begin{aligned} p_k^{(1,3)} &= P_k^{(1)} \pm j\Omega_k^{(1)}, \\ p_k^{(2,4)} &= P_k^{(2)} \pm j\Omega_k^{(2)}, \end{aligned}$$

where P_k and Ω_k denote the increment (or the decrement) and the characteristic frequency of deviations from the stea-dy-state operation point. Fig. 1 shows the roots of the characteristic equations, branches $1'$, $2'$ and 1, 2 correspond to the uncoupled ($\Gamma_{12} = 0$) and the coupled ($\Gamma_{12} = 0.1\Gamma_{11}$) active regions, respectively. The positions of the roots are shown by the squares and circles. The simulation has been performed with the following parameters: $L_1 = L_2 = 10\ \mu$m, $\Gamma_{11} = \Gamma_{22} = 0.0112$, $\alpha_1 = \alpha_2 = 10\ {\rm cm}^{-1}$, $\tau_{\rm ext} = \tau_{\rm r} = 2$ ns, $t_w = 7$ nm, $m_1 = m_2 = 8$, $r_{\rm ext}^2 = 0.98$. The pump power $P_{\rm in}$ and its beam diameter at the onset of the structure are 1 W and 100 μm. We assumed $In_{0.14}Ga_{0.86}As/GaAs$ and $In_{0.25}Ga_{0.75}As/GaAs$ QWs to be used for the short-wavelength and the long-wavelength gain areas. One can see, that the steady-state operation point is stable provided the gain areas are uncoupled. The steady-state stability could be violated if some coupling between those areas exists: branch 1 has the maximal value of $P_k > 0$. In our opinion, the main origin of the instability is saturable absorption of the short-wavelength emission in the deep QWs. Note, the adjacent root values of the branches are spaced by the inverse of the external round-trip time, i.e. $\Delta\Omega_{k,k+1}/2\pi \approx \tau_{\rm ext}^{-1}$.

2. Dynamics of the dual-wavelength VECSEL

Violation of the steady-state results in self-pulsations of VECSEL's output radiation. Fig. 2 displays the dynamics of the VECSEL on the selected time interval. Incident pump power $P_{\rm in}$, the external-cavity round-trip time $\tau_{\rm ext}$ and the reciprocal confinement coefficient Γ_{12} are taken to be 1 W, 0.5 ns and $0.1\Gamma_{11}$, respectively. The graphs of the short-wavelength and the long-wavelength emission power are shown by the solid and dotted lines. As it follows from the graphs, the pulse train is characterized by the time period which nearly equals the external-cavity round-trip time $\tau_{\rm ext}$. The duration of the pulses is about tens of picoseconds. Initial part of the pulse sequence demonstrates the rise time of instability and the subsequent variation of the pulse magnitude on the time scale of tens of microseconds (simulated but not shown here). Fig. 2 shows that the short-wavelength and the long-wavelength pulses occur nearly in phase. This feature is of principal importance for efficient intracavity non-linear different frequency generation in the dual-wavelength VECSEL. The high power of radiation combined with the nearly perfect spatial and temporal overlapping of the gaussian beams are promising for mid- and far-infrared semiconductor sources based on non-linear frequency conversion.

Acknowledgements

This work has been supported in part by the RFBR grant No. 08-02-90007-Bel-a.

References

[1] M. Beck, D. Hofstetter, T. Aellen, J. Faist *et al*, *Science* **295**, 301 (2002).

[2] Yu. A. Morozov, I. S. Nefedov, T. Leinonen, M. Yu. Morozov, *Semiconductors* **42**, 463 (2008).

[3] B. N. Zvonkov, A. A. Biryukov, A. V. Ershov, S. M. Nekorkin *et al*, *Appl. Phys. Lett.* **92**, 021122 (2008).

[4] T. Leinonen, Yu. A. Morozov, A. Härkönen, M. Pessa, *IEEE Phot. Techn. Lett.* **17**, 2508 (2005).

[5] T. Leinonen, S. Ranta, A. Laakso, Yu. Morozov *et al*, *Optics Express* **15**, 13451 (2007).

[6] V. G. Dmitriev, L. V. Tarasov, *Applied nonlinear optics*, Moscow, Physmatlit, 2004.

[7] A. Härkönen, J. Rautiainen, T. Leinonen, Yu. A. Morozov *et al*, *IEEE Phot. Techn. Lett.* **19**, 1550 (2007).

[8] O. Levi, T. Pinguet, T. Skauli, L. Eyres *et al*, *Optics Lett.* **27**, 2091 (2002).

17th Int. Symp. "Nanostructures: Physics and Technology"
Minsk, Belarus, June 22–26, 2009
© 2009 Ioffe Institute

Calculation of the threshold pump power for electron beam excited lasers based on multilayer heterostructures

M. M. Zverev[1], N. A. Gamov[1], E. V. Zdanova[1], V. B. Studionov[1], *D. V. Peregoudov*[1], S. V. Ivanov[2], S. V. Sorokin[2], I. V. Sedova[2], S. V. Gronin[2] and P. S. Kop'ev[2]

[1] Moscow State Institute of Radio Engineering, Electronics and Automations, Moscow, 117454, Russia
[2] Ioffe Physical-Technical Institute, St Petersburg, Russia

Abstract. The dependences of threshold current density on the position of quantum well in the waveguide for electron-beam-pumped semiconductor lasers based on ZnSe heterostructures are calculated. It is shown that for low electron beam energies the optimal position of quantum well moves from the center of waveguide to the free surface.

Electron-beam-pumped (EBP) green pulsed semiconductor lasers based on ZnSe can be successfully used for numerous applications, such as, optical communications, medicine, navigational systems etc. Fabrication of low-threshold EBP green RT lasers pumped by electron beam with energy of 4–25 keV based on alternately-strained superlattice waveguide has been reported [1]. The efficiency up to 8.5% and peak pulsed power up to 12 W from one facet has been measured [2].

To decrease the threshold current density and improve the laser power and efficiency one has to optimize the collection of non-equilibrium carriers in the active zone and to achieve the maximum interaction of carriers and electromagnetic field. This calls for choose the optimum design of laser structure.

In the present paper we calculate the threshold pump power of EBP lasers based on multi-layered heterostructures, taking into account the spatial distribution of carriers in semiconductor structures at different values of electron beam energy and spatial distribution of electromagnetic field of different cavity modes.

We consider a laser with transverse pumping. Usual rate equations have the form [3]

$$\dot{n} = W(N-n) - Bqn - n/\tau, \quad \dot{q} = VBqn - q/\tau_c.$$

Here n is number of non-equilibrium carriers in laser, W is pumping (probability of non-equilibrium carrier excitation), N is maximal possible concentration of non-equilibrium carriers in a laser, B is a radiation rate, q is the number of photons in a laser, τ is the lifetime of non-equilibrium carrier, V is a volume occupied by mode inside the active region, τ_c is the photon lifetime in a laser. These equation yield the following expression for threshold pumping

$$W = \frac{1}{\tau\tau_c BVN}.$$

Usual rate equations don not however take into account the details of non-equilibrium carriers distribution in the waveguide. In the lasers under consideration the distribution of carriers is sharply heterogeneous: the majority of carriers are localized in thin quantum wells and these are the carriers participating in generation. It may happen that the well is situated in the node of the light mode and in this case there will be no generation despite the large over-all number of non-equilibrium carriers. Thus we assume that the threshold is determined not with the mode volume itself but with an integral

$$\int nE^2\, d^3r.$$

Electric field distribution with depth was calculated using the equation [4]

$$\frac{\partial^2 E}{\partial x^2} - \left(\beta^2 - k_0^2\varepsilon(x)\right) E = 0,$$

where β is wave vector along the waveguide axis, $k_0 = 2\pi/\lambda$ is wave vector in vacuum, λ is a wavelength, $\varepsilon(x)$ is the depth-dependent dielectric constant. We used the simplest waveguide model: the layer between two half-spaces. The first half-space is vacuum, the second — lower cladding, in this model we neglect thin upper cladding. Mode calculation for this model is reduced to a simple transcendent equation [5].

Non-equilibrium carriers distribution was calculated as the solution of the following equation

$$\frac{\partial n}{\partial t} = \frac{\partial}{\partial x} D(x) \frac{\partial n}{\partial x} + \frac{\partial}{\partial x} n \frac{\partial U(x)}{\partial x} - n/\tau(x) + W(x,t).$$

Here n is concentration of carriers, $D(x)$ is diffusion coefficient, $D = L^2/\tau$, L is a diffusion length, $\tau(x)$ is lifetime of carriers, $W(x,t)$ is pumping, $U(x)$ is effective potential arising from difference of band gaps in different layers. The function $W(x)$ reflecting the distribution of electron beam energy losses with depth in ZnSe was taken from [6].

The model presented allows to calculate the dependence of threshold on different parameters of heterostructure: the number and positions on quantum wells, the thicknesses of waveguide and claddings, for different modes and electron-beam energies. The calculations show that for the structures with single quantum well the optimal position of the well depends both on the mode shape and electron energy. The dependences of threshold current density on the position of quantum well for different values of electron-beam energy and different size of waveguide are shown in Fig. 2. The structures consisted of a bottom $Zn_{0.90}Mg_{0.10}S_{0.15}Se_{0.85}$ cladding layer followed by a $ZnS_{0.14}Se_{0.86}$/ZnSe superlattice waveguide. ZnSe QW was centered with the CdSe QD-sheet and placed in waveguide. The parameters of structure for calculations correspond to [1]. One can see that the optimal distance between quantum well and surface decreases with the electron energy. For

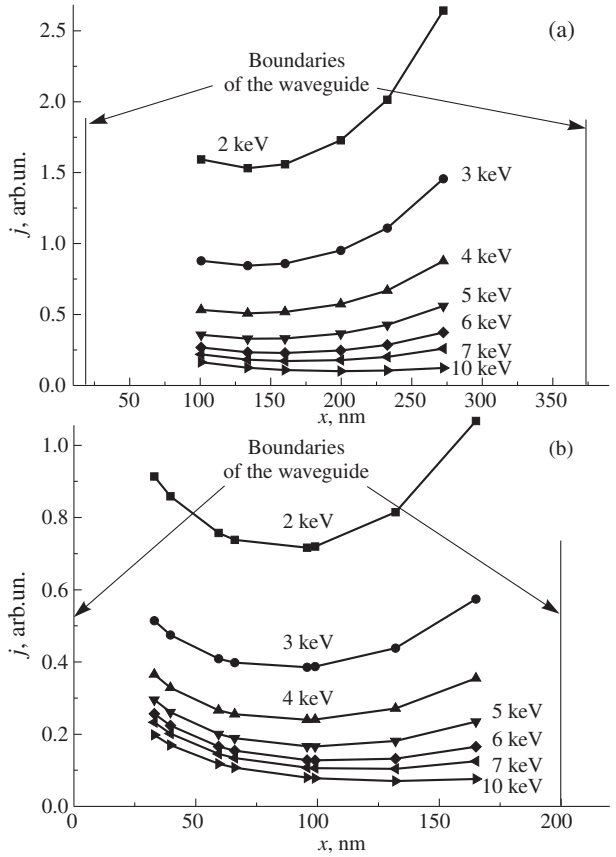

Fig. 1. The dependence of threshold current density on the position of quantum well for different values of electron-beam energy: (a) the width of waveguide is about 380 nm, the width of upper cladding is 20 nm; (b) the width of waveguide is 200 nm, the upper cladding is absent.

minimization of beam energy it is desirable to make waveguide approximately as thick as the wavelength (inside structure, approximately 200 nm) and use the structures without upper cladding. Similar calculations allow to determine optimal geometry for multi-well heterostructures.

Acknowledgements

This work was partially supported by ISTC project #3754.

References

[1] M. M. Zverev, N. A. Gamov, E. V. Zdanova, D. V. Peregoudov, V. B. Studionov, I. V. Sedova, S. V. Gronin, S. V. Sorokin, S. V. Ivanov, and P. S. Kop'ev, *Tech. Phys. Lett.* **33** (24), 1 (2007).

[2] M. M. Zverev, N. A. Gamov, D. V. Peregoudov, V. B. Studionov, E. V. Zdanova, I. V. Sedova, S. V. Gronin, S. V. Sorokin, S. V. Ivanov, and P. S. Kop'ev. *Semiconductors* **42** (12), 1472 (2008).

[3] O. Svelto, *Principles of lasers*, Springer, 1998.

[4] M. J. Bergmann and H. C. Casey, Jr., *J. Appl. Phys.* **84**, 1196 (1998).

[5] L. D. Landau, E. M. Lifshitz, *Quantum mechanics (non-relativistic theory)*, Moscow: Nauka, 1989.

[6] E. N. Donskoj, E. V. Zhdanova, A. N. Zalyalov *et al*, *Quantum electronics* **38**, 1097 (2008).

17th Int. Symp. "Nanostructures: Physics and Technology"
Minsk, Belarus, June 22–26, 2009
© 2009 Ioffe Institute

K_2O-Nb_2O_5-SiO_2 nanostructured glasses with low silica content producing second harmonic generation

V.N. Sigaev[1], V.S. Ryzjenkov[1], N.V. Golubev[1], S.V. Lotarev[1], S.Yu. Stefanovich[2] and G.E. Malashkevich[3]

[1] Mendeleev University of Chemical Technology of Russia, Miusskaya sq. 9, 125190 Moscow, Russia
[2] L. Ya. Karpov Institute of Physical Chemistry, Vorontzovo pole 10, 103064 Moscow, Russia
[3] B. I. Stepanov Institute of Physics, NASB, Minsk Pr. Nezavisimosti, 71, Belarus

Abstract. Glasses of Me_2O-Nb_2O_5-X_nO_m system where Me = Li, Na, K and X_nO_m = SiO_2, B_2O_3, P_2O_5, GeO_2 are of great interest for photonics because second-order optical nonlinearity and promising electro-optic properties based on Pockels effect may be initiated in them by thermal d.c. poling. Quadratic nonlinearity is expected to increase both with niobium content growth and nanostructuring of glasses by nonlinear-optic crystals. In the present work, glassy plates of compositions $(1-x)$ $KNbO_3 - -xSiO_2$ with very low SiO_2 content up to 12 mol. % were prepared and nano-inhomogeneities formation for initial stages of amorphous phase separation and crystallization of glasses as well as their influence on second-order optical nonlinearity were examined. The x-T range of obtaining transparent SHG-active glasses in the K_2O-Nb_2O_5-SiO_2 system which are promising for elaboration of highly efficient electro-optic modulators by thermal d.c. poling was determined.

Introduction

A lot of attempts to initiate second-order optical nonlinearity (SON) in glasses by thermal d.c. poling were carried out during the last decade. The main objects of those studies were homogeneous glasses of two types: silica glass doped with Ge, OH^-, alkaline cations [1] and the multicomponent glasses containing alkali and high-polarizable cations (Ti, Nb, Te, Pb, etc.) [2,3]. Thermal d.c. poling of Nb-containing glasses produces a nonlinear-optical (NLO) layer up to several micrometers thick with high second harmonic generation (SHG) efficiency. The second-order optical susceptibility $\chi^{(2)}$ reaches ~5 pm/V within this layer [4], i.e. not too small in comparison with that in $LiNbO_3$ and other NLO crystals. Promising ways to increase SON in glasses are niobium concentration increase and nanostructuring the glass by Nb-containing crystalline phases. It is claimed that glass nanostructuring leads to appreciable SON growth [5], but according to [6] glass nanostructuring has insignificant influence on $\chi^{(2)}$.

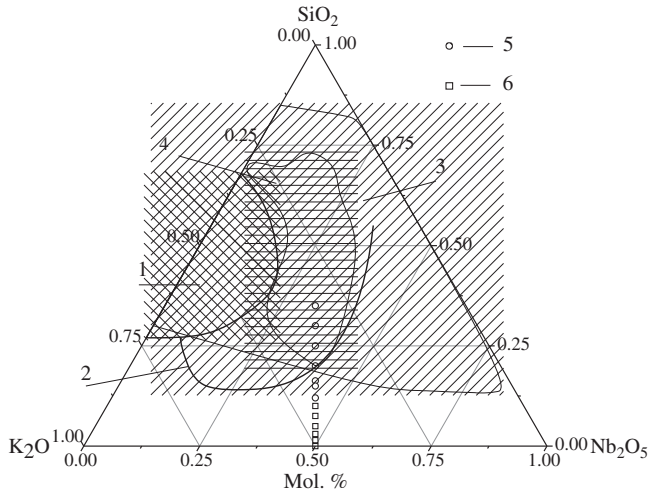

Fig. 1. Glass forming area in K_2O-Nb_2O_5-SiO_2 system for various cooling conditions: (1) area of glasses with low chemical stability [13]; (2) pressing melt between metal plates [13] (melting in quartz crucible); (3) cooling of several grams of melt in platinum crucible in the air [14]; (4) the composition studied in work [15]. The glasses studied in the present work for K_2O/Nb_2O_5=1 obtained by pressing (5) and melt blowing (6).

The hypotheses explaining high SON of Nb-containing glasses subjected thermal poling are based on the occurrence of poling-induced charge migration and presence in glass deformed niobium polyhedrons [7–9]. It is known, that high polarizability of Nb-containing glasses is connected with large anisotropy of NbO_5 and NbO_6 polyhedrons due to huge (up to 0.55 Å) scatter of Nb-O bond length [10,11]. Therefore it is naturally to assume that poling possibilities in formation of high SON raise with growth of deformed niobium polyhedrons content. Glass formation areas in systems Me_2O-Nb_2O_5-SiO_2 (B_2O_3, P_2O_5, GeO_2) reach ~20 mol.% of glass former. However, the majority of researches have been performed for composition containing more than 40 mol.% of SiO_2 and B_2O_3 [12–13].

In our opinion, in order to increase of poling influence on SON it is very important to initiate SON in as-quenched glass along with increase of niobium content. As it is shown in [14] SON is initiated in alkali-niobium-silicate glasses during amorphous phase separation at temperatures near T_g. It is quite probable that the thin plates of glass convenient for studying crystallization behavior, optical and NLO properties, for carrying out thermal poling can be obtained and at lower content of glass-former by faster cooling of samples. However there is little information about glass formation and crystallization of such glasses. Minimization of glass-former content keeping technologically acceptable conditions of glass producing seems rather interesting for better understanding of the fundamental mechanisms of $\chi^{(2)}$ origin in glasses as well as for fabrication of highly effective glass-based NLO materials.

In this study, we focus our attention on the glass formation, the crystallization behavior and SHG of K_2O-Nb_2O_5-SiO_2 glasses with molar ratio K_2O/Nb_2O_5=1 and less than 40 mol.% of SiO_2.

1. Experimental

The compositions of the investigated glasses can be expressed by the general formula $(1-x)KNbO_3 - xSiO_2$ (where x changes from 0.35 to 0). These composition (open circles) and glass formation areas according to [13–15] are present in

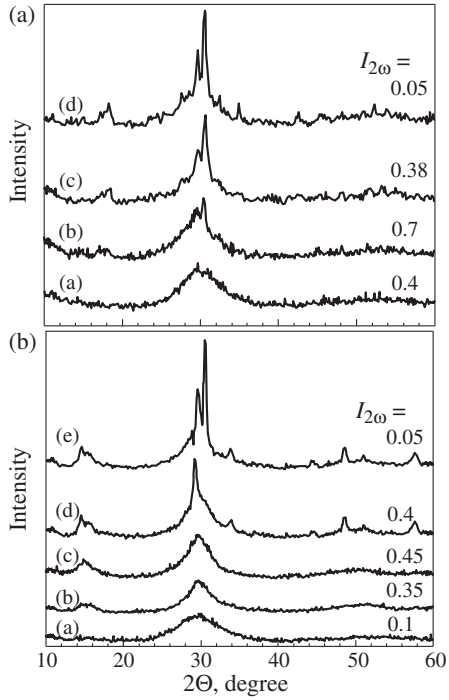

Fig. 2. (Top) XRD patterns and SHG ($I_{2\omega}$) of KNS-15 samples: as-quenched (a) and heat-treated at 590 °C for 24 h (b), 36 h (c) and 48 h (d). (Bottom) XRD patterns and SHG ($I_{2\omega}$) of KNS-25 samples: as-quenched (a) and heat-treated at 610 °C for 24 h (b), 36 h (c), 48 h (d) and 60 h (e).

Fig. 1. The glasses were melted in platinum crucibles at 1250–1400 °C depending on SiO_2 content. Then they were quenched by pouring out the melt on a cooled massive metal plate and then pressing by another metal plate up to thickness of about 1 mm. X-ray diffraction (XRD) was used to verify amorphous nature of as-quenched glasses and identify crystalline phases precipitated. The SHG experiments were performed using a Nd:YAG solid-state pulsed laser operating at wavelength of 1.064 μm in the Q-switching mode at frequency of 12.5 Hz at room temperature. The reported SHG signal, $I_{2\omega}$ indicates the ratio of SHG intensity of a tested sample to that of a reference α-quartz powder standard with a dispersity of approximately 3–5 μm. The background and facilities of the SHG evaluation technique have been described in more detail elsewhere [16]. Microstructure of the glasses has been studied by JSM 7500 FA JEOL scanning electron microscope.

2. Results and discussion

Plates of glasses without signs of crystallization were obtained by pressing melt for a series of compositions with $x = 0.35 - 0.12$. They were shown to be fully amorphous according to XRD curves (Fig. 2). However electron microscopy of these samples revealed some inhomogeneities whose concentration increased in the samples with less SiO_2 percentage. Typical electron microscopy images ($x = 0.15$) are shown at Fig. 3 and show approximately 5 nm large nanoinhomogeneities evenly distributed in the glass bulk. This initially inhomogeneous structure is a reason of second harmonic generation of about 0.4 relative to α-quartz powder standard. The situation is the same for the glasses with other x values. SHG efficiency depending on the heat-treatment duration is shown at Fig. 4. As

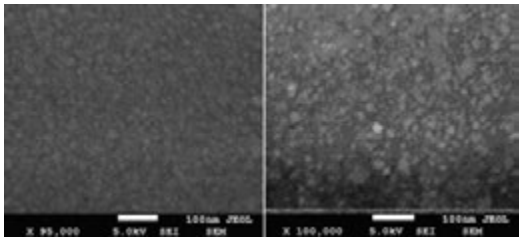

Fig. 3. EM images of as-quenched (left) and heat treated at 610 °C for 4 h (right) KNS-15 samples.

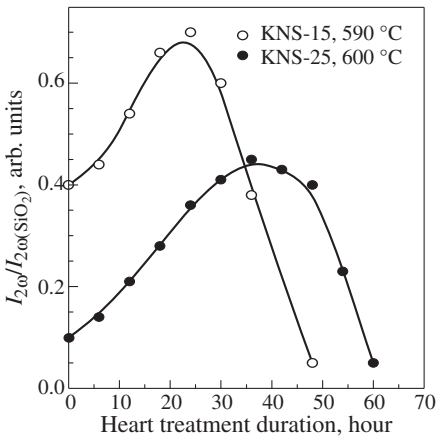

Fig. 4. SHG efficiency vs. heat-treatment time.

heat-treatment becomes longer nanoinhomogeneities grow and phase boundaries become more distinct. That results in SHG increase until the glass starts loosing transparency and once the size of inhomogeneities increases up to 30–50 nm SHG diminishes rapidly due to opalescence, decrease of transparency and centrosymmetric structure of crystallizing inhomogeinities.

Thus in the wide range of compositions, temperatures and heat-treatment durations KNS system allows obtaining nanostructured glasses with low SiO_2 percentage possessing reasonable SHG. These glasses are promising for developing active elements of electro-optical modulators by thermal d.c. poling.

Acknowledgements

The present work was supported partially by Russian and Belorussian Foundations for Basic Research, grant # 08-03-90038, and Russian Foundations for Basic Research, grant # 09-03-00104.

References

[1] Y. Quiquempois *et al*, *Cur. Opinion in Solid St. and Mater. Sci.* **7**, 89 (2003).
[2] B. Ferreira, *J. Non-Cryst. Solids* **343**, 121 (2004).
[3] H. Nasu, *J. Non-Cryst. Solids* **217**, 182 (1997).
[4] M. Dussauze *et al*, *Opt. Exp.* **13**, 4064 (2005).
[5] N. Tamagawa *et al*, *Opt. Comm.* **217**, 387 (2003).
[6] A. Malakho *et al*, J. Solid State Chem. **178**, 1888 (2005).
[7] H. Tanaka *et al*, *J. Optic. Mat.* **22**, 71 (2003).
[8] R. C. C. Figueira *et al*, *J. Non-Cryst. Solids* **354**, 5162 (2008).
[9] Kazansky *et al*, *J. Opt. Commun.* **101**, 611–614 (1994).
[10] M. P. Crosnier *et al*, *J. Ferroelectrics* **124**, 61 (1991).
[11] M. P. Crosnier *et al*, *J. Solid State Chem.* **98**, 128 (1992).
[12] Bh. Rao, *J. Glass Techn.* **5**, 67 (1964).
[13] M. Imaoka *et al*, *J. Cer. Assoc. Japan* **12**, 215 (1963).
[14] V. N. Sigaev *et al*, *J. Non-Cryst. Solids* **306**, 238 (2002).
[15] D. E. Vernacotola *et al*, *J. Phys. Chem. Glasses* **35**, 123 (1994).
[16] S. Yu. Stefanovich *et al*, *J. Glass Phys. Chem.* **21**, 253 (1995).

17th Int. Symp. "Nanostructures: Physics and Technology"
Minsk, Belarus, June 22–26, 2009
© 2009 Ioffe Institute

Diffraction-free and dispersion-free pulsed beams formation by means of multicircular diaphragm

E. E. Ushakova[1] and *S. N. Kurilkina*[2]

[1] Belorussian State University, 4 Independence Ave., Minsk 220050, Belarus
[2] B. I. Stepanov Institute of Physics of NAS Belarus, 68 Independence Ave., Minsk 220072, Belarus

Abstract. Special type of diffraction-free and dispersion-free pulsed beams, existing in the vicinity of lens focus, generated by means of the multicircular diaphragm and the lens has been investigated. Influence of diaphragm and lens parameters on behavior dynamics of the light fields has been analysed. Criterion of stable interference structure formation has been found.

Introduction

Nowadays rapt attention of scientists is attracted to the problem of diffraction-free and dispersion-free light fields formation and propagation [1–3]. Pulsed light Bessel beams, belonging to the mentioned objects class, posess a number of unique properties such as propagation invariance, ability for profile selfreconstruction after meeting the obstackle have found a wide application spectrum, including laser cutting and welding, atmosphere and biological objects probing, systems of information transmittance, processing [4–6]. By the present time generated by means of an axicon, hologram light fields have been investigated both in experimental and theoretical aspects [7,8]. However, there exists rather perspective method [9] that allow one to generate diffraction-free and dispersion-free pulsed light Bessel beams. This technique applying multicircular diaphragm and the lens for obtaining pulsed light Bessel beams is good in view of investigation of the objects in process of their formation as well as during further propagation. In the present extended abstract influence of multicircular diafragm and lens characteristics on the forming optical diffraction-free and dispersion-free pulsed Bessel beams properties is analysed.

1. Results of the investigation

Possibility of pseudodiffractionless pulsed Bessel light beams formation using multicircular diaphragm and the lens is shown in accordance with [10]:

$$\varepsilon(r,z)=\int_{R-\Delta}^{R+\Delta}\int_{\omega_0-2\pi/t_0}^{\omega_0+2\pi/t_0}\frac{\omega}{czf\left(\frac{1}{z}-\frac{1}{F(\omega)}+\frac{1}{fn(\omega)}\right)}$$
$$\times\exp\left[-ik(\omega)\left(z+\frac{r^2}{2z}+\frac{f}{n(\omega)}-\frac{r^2}{2z^2\left(\frac{1}{z}-\frac{1}{F(\omega)}+\frac{1}{fn(\omega)}\right)}\right)\right]$$
$$\times\varepsilon_0(r')\exp\left[-\frac{i\omega r'^2}{2cf}\left(1-\frac{1}{fn(\omega)\left(\frac{1}{z}-\frac{1}{F(\omega)}+\frac{1}{fn(\omega)}\right)}\right)\right]$$
$$\times J_0\left(\frac{\omega r' r}{czf\left(\frac{1}{z}-\frac{1}{F(\omega)}+\frac{1}{fn(\omega)}\right)}\right)r'\xi\,(\omega-\omega_0)\,dr'd\omega.$$

During estimating how the the diaphragm and lens parameters affect obtaining light field it is established a number of important results. To the first, the more the number of diaphragm rings is the more intensively narrowing and increase of the central maximum accompanied by suppression of the secondary maxima takes place. In Fig. 1 there are illustrated transverse intensity distributions of pulsed Bessel light beams formed by means one-, two-, three-circular diaphragm and lens. This is evidence of a stronger light energy localisation close to the pulsed beam axes accompanying by substantial loss decrease, which represents significant achievement due to the reason that namely the central maximum behavior is of great interest. Moreover, having varied diaphragm parameters central maximum can be diminished to submicron size. To the second, behavior of light pulsed beams in space nearby lens focus is investigated, transformation of light field structure retracing in dynamics. Criterion of stable interference structure formation is found. Accoding to calculations both transverse intensity distribution and envelope form appear to be the same as those for pulsed Bessel light beams up to distances $0.003F$ after the focal plane of the lens. It should be noted such an interesting peculiarity that the form of the envelope proves to be insensitive to verifying of the inner diaphragm ring radius that is shown in Fig. 2. Finally, it should be emphasized that the pulsed beams under consideration, that is those light fields existing in the vicinity of lens focus distance, are related to the objects of special type. Therefore their investigation carried out contributes particular interest and also due to range of possible applications in communication systems, probing.

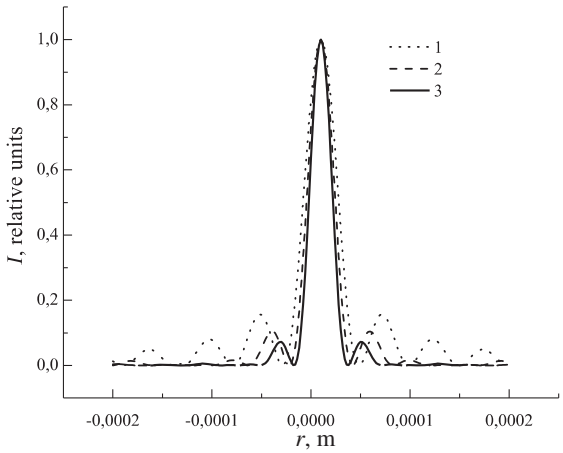

Fig. 1. Normalised intensity distributions of the pulsed Bessel beam obtained by means of 1 — one-, 2 — two-, 3 — threecircular diaphragm.

References

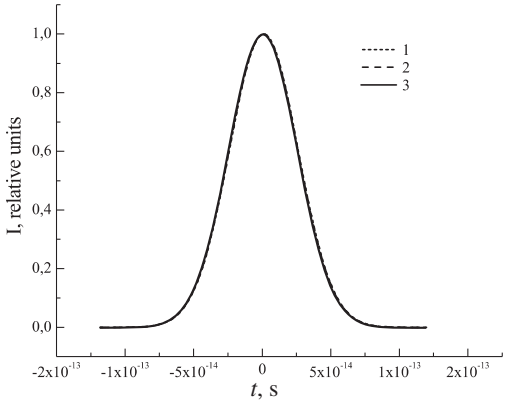

Fig. 2. Normalised intensity of the envelope form obtained with the help of twocircular diaphragm with inner rings radia 1 — 1.50 mm, 2 — 0.50 mm, 3 — 0.05 mm.

[1] M. A. Kaliteevski, S. Brand, R. A. Abram, A. J. Gallant and J. M. Chamberlain, *Opt. Express* **16**, 14582 (2008).
[2] M. Zamboni-Rached, K. Z. Nobrega, H. E. Hernandez-Figueroa, E. Recami, *Opt. Comm.* **226**, 15 (2003).
[3] L. N. Pyatnitskiy, V. V. Korobkin, *Proceedings of Common Physics Institute* **57**, 59 (2000).
[4] J. Lu, Sh. He, *Opt. Comm.* **161**, 187 (1999).
[5] G. Milne, K. Dholakia, D. McGloin, K. Volke-Sepulveda and P. Zemanek, *Opt. Express* **15**, 13972 (2007).
[6] L. Paterson, E. Papagiakoumou, G. Milne, V. Garces-Chavez, T. Briscoe, W. Sibbett, L. Dholakia and A. Riches, *J. Biomed. Opt.* **12**, 054017 (2007).
[7] M. A. Porras, I. Gonzalo, *Opt. Comm.* **217**, 257 (2003).
[8] H. Sonajalg, M. Ratsep, P. Saari, *Opt. Lett.* **22**, 310 (1997).
[9] E. Recami, *Physica A* **252**, 586 (1998).
[10] S. A. Akhmanov, S. U. Nikitin, *Physical Optics*, (M.: Science) 654, 2004.

17th Int. Symp. "Nanostructures: Physics and Technology"
Minsk, Belarus, June 22–26, 2009
© 2009 Ioffe Institute

Quantum optics with nanowires and quantum dots

V. Zwiller, N. Akopian, M. van Weert, M. van Kouwen, U. Perinetti, S. Dorenbos and L. Kouwenhoven
Quantum Transport, Kavli Institute of Nanoscience, TU Delft, Delft, The Netherlands

Nanowires grown by epitaxial methods enable the fabrication of complex semiconducting heterostructures where composition, size, position and doping can be controlled with unprecedented freedom. We study the optical properties of single nanowires containing single quantum dots with the aim of interfacing the world of quantum transport and quantum optics. We have demonstrated the operation of a single nanowire light emitting diode. Photocurrent measurements on gated quantum dots were performed to probe the energy levels of a single quantum dot in a nanowire. The polarization properties of nanowire heterostructures will also be discussed and photoluminescence measurements done in different orientations demonstrate that vertical nanowire devices enable the extraction of any polarization. We show that vertical nanowires enable the generation and readout of any exciton spin orientation and we demonstrate optical access to single spins in nanowire quantum dots. Because both zincblende and wurtzite crystal phases are stable in nanowires, a novel type of charge confinement where quantum dots composed of the same material than the surroundings is possible. We will present recent results obtained on InP quantum dots in InP nanowires.

We have recently coupled the emission from a single quantum dot to a rubidium vapor and we will discuss the potential advantages of solid state — atomic vapor coupling for a wide range of quantum optics experiments.

For detection, we are developing superconducting nanowire detectors and implementing them into single photon experiments. We will also discuss the possibility of detecting single plasmons and performing 'quantum optics on a chip' using superconducting nanowires for detection and semiconducting nanowires for emission.

17th Int. Symp. "Nanostructures: Physics and Technology"
Minsk, Belarus, June 22–26, 2009
© 2009 Ioffe Institute

Dynamics of excited states in PbS quantum dots

M. S. Gaponenko[1], K. V. Yumashev[1], A. M. Malyarevich[1], S. A. Tihomirov[2], O. V. Buganov[2] and A. A. Onuschenko[3]

[1] Institute for Optical Materials and Technologies, BNTU, Belarus
[2] B. I. Stepanov Institute of Physics, NASB, Belarus
[3] Research and Technological Institute of Optical Materials Science, Russia

Abstract. Transient bleaching of the first excitonic absorption band of PbS quantum dots in glasses was investigated by means of a femtosecond pump-probe spectroscopy. We demonstrate that bleaching is in strong competition with the induced excited-state absorption and report on the measured decay times of the exciton excited states.

Introduction

The optical properties of semiconductor nanocrystals or quantum dots (QDs) have been extensively investigated over a past decade and still attract a growing interest from both fundamental and applied points of view. Because of quantum confinement, QDs possess size-dependent discrete exciton energy levels. The latter allows to change the spectral position of the absorption and emission bands of QDs by varying their size and makes them candidates for tunable absorbers and emitters in applications such as light-emitting devices [1,2] and biomedical fluorescent labeling [3]. Lead sulfide (PbS) QDs have emerged recently as an interesting semiconductor low-dimensional system. Narrow band gap (0.41 eV at room temperature) and large exciton Bohr radius (18 nm) make them attracting candidates for investigating strong quantum confinement effects. From a technological perspective, glasses doped with PbS QDs are of interest as saturable absorbers for lasers because they are among the few materials that can provide tunable electronic transitions in the range of 0.8–3 μm [2]. Thus, the knowledge and understanding of absorption bleaching and related relaxation dynamics in glasses doped with PbS QDs are of great importance.

In the present work, we report on the femtosecond time-resolved study of the bleaching dynamics in glasses doped with PbS QDs of different sizes.

1. Experimental

The samples under investigation have been prepared using a SiO_2-Al_2O_3-NaF-Na_2O-ZnO glass system. The glass preparation method was described elsewhere [4]. The chosen conditions of a glass thermal treatment allowed obtaining the samples with uniformly distributed PbS QDs with average radii of 2 nm, 2.4 nm, 2.8 nm, and 3 nm for samples #1, 2, 3, and 4, respectively. The samples room-temperature absorption spectra are presented in Fig. 1.

Nonlinear transient absorption was investigated by means of a femtosecond pump-probe absorption spectroscopy. The experimental setup [5] based on a home-made original femtosecond Ti:saphire pulsed oscillator and a regenerative amplifier system operated at 10 Hz repetition rate. The Ti:sapphire master oscillator was synchronously pumped with a doubled output of a feedback controlled mode-locked pulsed Nd:YAG laser. The pulse width and energy of Ti:sapphire system after the amplifier were 150 fs and 0.5 mJ, respectively, tunable over the spectral range 760–820 nm. The fundamental output of the Ti:sapphire system (790 nm output wavelength was set for present study) split into two beams in the ratio 1:4. The more intense beam passed through a controlled delay line and was utilized for sample pumping. The second beam of fundamental frequency was used for generation of a femtosecond supercontinuum (by focusing into a 1 cm path length quartz plate) which served as the probe radiation. The continuum probe light was split with a beam splitter into two pulses (reference and signal), identical in intensity, and was focused on the sample by mirror optics. The spectra of both reflected pulses were recorded for every laser flash by a polychromator equipped with a silicon CCD matrix and transferred to the computer. Time resolution of the setup is limited by the pump and probe pulse duration and estimated as 0.2 ps. For measurements in spectral range 1–1.6 μm an IR array detector based on InGaAs was used.

2. Results

Pump pulse excites a group of the higher-energy excitonic transitions in QDs (denoted as $\langle 2 \rangle$ in the Fig. 2). Following pumping, the excited charge carriers relax to the first excited state $\langle 1 \rangle$ with consequent exciton recombination. The excited-state absorption may likely occur as from the first excited state $\langle 1 \rangle$, as well as from the initially pumped states $\langle 2 \rangle$. Differential absorption spectra recorded at different delay times for sample #1 are presented in Fig. 3. Transient deferential absorption

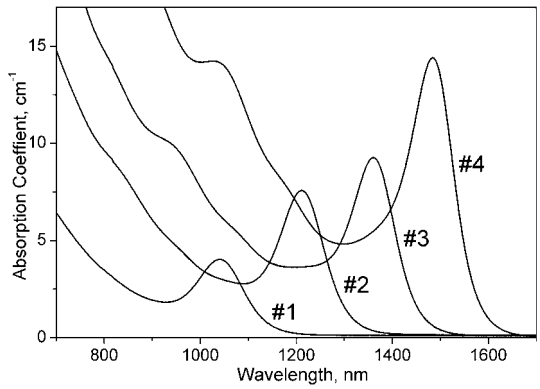

Fig. 1. Absorption spectra of glasses doped with PbS QDs of different size. The average radii of QDs are 2 nm, 2.4 nm, 2.8 nm, and 3 nm for samples #1, 2, 3, and 4, respectively. The distinguished first excitonic absorption band corresponds to the transition $\langle 0 \rangle$–$\langle 1 \rangle$ at the energy level scheme on Fig. 2.

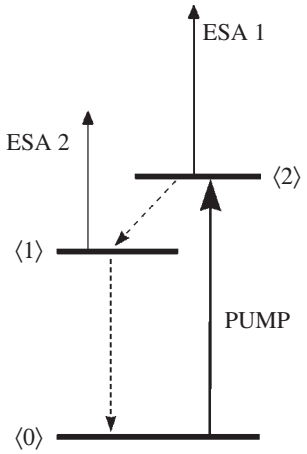

Fig. 2. Sketch of the exciton levels in PbS QDs. Level ⟨0⟩ corresponds to the absence of exciton.

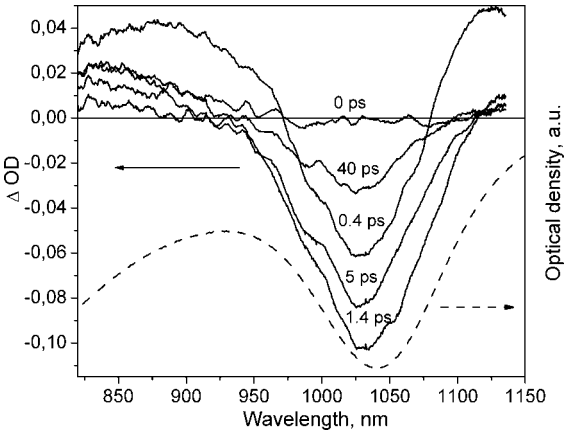

Fig. 3. Deferential absorption spectra of the sample #1 measured at different delay times. Negative values of Δ OD corresponds to the bleaching, positive — to the induced absorption. Dashed line shows the linear absorption spectrum of the sample.

kinetics measured at different wavelength for sample #1 are presented in Fig. 4. The next main features are clearly observed:

1) The induced absorption at wavelengths around 880 nm appears immediately just after excitation, reaches its maximum at 0.4 ps time delay and then starts to non-exponentially decay with characteristic time constants of 0.8 ps and 16 ps.
2) The bleaching of the first excitonic absorption band (corresponds to transitions between levels ⟨0⟩ and ⟨1⟩) at wavelengths around 1110 nm reaches its maximum at 1.5 ps with follow-up decay characterized by time constant of 15 ps.
3) The induced absorption at wavelengths near 1100 nm reaches its maximum at 0.4 ps (similar to what is observed with induced absorption near 880 nm), but turns into bleaching after 1 ps and again to induced absorption after 12 ps. Such behavior indicates that competitive processes of induced absorption and bleaching take place.

The observed features give rise to suggest the following excited carriers dynamics in PbS QDs. Excitation to the levels

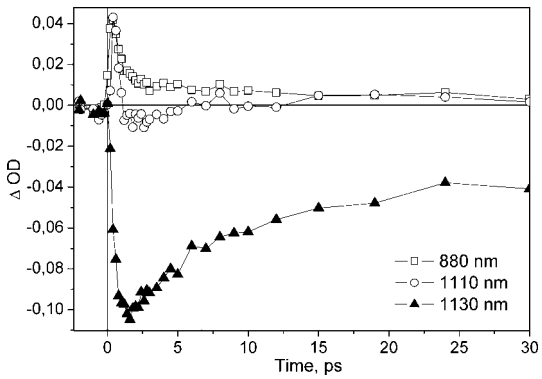

Fig. 4. Deferential absorption kinetics measured at different wavelengths along the first excitonic absorption band for the sample #1. Negative values of Δ OD corresponds to the bleaching, positive — to the induced absorption.

⟨2⟩ turns on the first channel of the excited-state absorption ESA1 (Fig. 2). Carrier's relaxation from levels ⟨2⟩ to ⟨1⟩ with decay time of 0.8 ps leads not only to the absorption saturation in the channel ⟨0⟩–⟨1⟩, but also to the emergence of the second channel of the excited-state absorption ESA2. The characteristic decay time of level ⟨1⟩ is determined to be ∼15 ps. Thus one may conclude, that dynamics of the bleaching of the first excitonic transition in PbS QDs has a complicated form due to the competition between the absorption saturation of the band and the induced excited-state absorption.

The results obtained with samples containing PbS QDs of larger size shows similar tendencies and will be discussed.

References

[1] A. M. Malyarevich, K. V. Yumashev, A. A. Lipovskii, *J. Appl. Phys.* **103**, 081301 (2008).
[2] E. U. Rafailov, M. A. Cataluna, W. Sibbett, *Nature Photonics* **1**, 395 (2007).
[3] B. N. G. Giepmans, S. R. Adams, M. H. Ellisman, R. Y. Tsien, *Science* **312**, 217 (2006).
[4] A. A. Onushchenko, A. A. Zhilin, G. T. Petrovskii, E. L. Raaben, M. S. Gaponenko, A. M. Malyarevich, K. V. Yumashev, V. V. Golubkov, *J. Opt. Technol.* **73**, 576 (2006).
[5] A. P. Blokhin, F. Gelin, O. V. Buganov, S. A. Tikhomirov, G. B. Tolstorozhev, *Zh. Prikl. Spektrosk.* **70**, 66 (2003).

17th Int. Symp. "Nanostructures: Physics and Technology"
Minsk, Belarus, June 22–26, 2009
© 2009 Ioffe Institute

Hole cyclotron resonance absorption in strained InGaAs/GaAs quantum wells under high magnetic fields

O. Drachenko[1], D. V. Kozlov[2], K. V. Maremyanin[2], A. V. Ikonnikov[2], V. Ya. Aleshkin[2], *V. I. Gavrilenko*[2], B. N. Zvonkov[3], M. Goiran[4], J. Leotin[4], G. Fasching[5], S. Winnerl[1], H. Schneider[1], J. Wosnitza[1] and M. Helm[1]

[1] Dresden High Magnetic Field Laboratory and Institute of Ion-Beam Physics and Materials Research, Forschungszentrum Dresden-Rossendorf, P.O. Box 510119, 01314 Dresden, Germany
[2] Institute for Physics of Microstructures of Russian Academy of Sciences, 603950 N.Novgorod, Russia
[3] Physico-Technical Research Institute of the Lobachevskii N. Novgorod State University, 603950 N. Novgorod, Russia
[4] Laboratoire Nationale des Champs Magnetiques Pulses, 143 Av. de Rangueil, 31432 Toulouse, France
[5] Zentrum für Mikro- und Nanostrukturen, TU Wien, 1040 Wien, Austria

Abstract. Hole cyclotron resonance (CR) absorption in strained InGaAs/GaAs quantum wells (QWs) was studied in quantizing magnetic fields up to 55 T. A remarkable CR line splitting was evidenced when the resonant field exceeded 20 T. The observed CR line positions proved to be in a good agreement with those calculated using 4×4 Luttinger Hamiltonian including strain and QW potentials for the linear interpolation of the Luttinger parameters for InGaAs solid solution. On the other hand, the spectral weight distribution of the CR split components suggests an inverted position of the two first Landau levels compared to the single-particle model.

Introduction

Nowadays strained-layer InGaAs/GaAs quantum well (QW) heterostructures remain potentially interesting for many applications, such as high-frequency electronics, solar cells, and infrared lasers (see for review Ref. [1]). The built-in strain removes the valence degeneracy and shifts the light-hole (lh) band down with respect to the heavy-hole (hh) one, which becomes the uppermost (lowest hole energy), thus resulting in low values of hh in-plane effective masses that has been confirmed by cyclotron resonance (CR) measurements [2–4]. Since the energy separation between lh and hh subbands is relatively small, the dispersion of the hh band is expected to be strongly nonparabolic [5]. However, the situation with the band dispersion remains unclear yet (cf. [6,7]). The present work is devoted to a systematic study of CR in p-type InGaAs/GaAs QWs under high magnetic fields up to 55 T in wide spectral range from 420 to 65 μm. The CR frequency is shown to depend highly nonlinearly on the magnetic field and a pronounced splitting of the absorption line is discovered in the magnetic fields over 20 T.

1. Experimental

The sample under study is a p-type $In_{0.14}Ga_{0.86}As$/GaAs MOCVD grown on a semi-insulating GaAs(001) substrate. It consists of 50 InGaAs QWs 70 Å wide sandwiched between 500 Å wide GaAs barriers. The barriers contain two carbon delta layers separated from each QW by a 150 Å thick spacer. The nominal hole concentration is 4.5×10^{11} cm^{-2} per QW. All CR experiments were performed in pulsed magnetic fields in Faraday configuration. Most of the measurements were carried out in the Dresden High Magnetic Field Laboratory (HLD). The magnet produces roughly 150 ms long pulses with a rise time close to 12 ms. The excitation light was guided by a polished stainless steel waveguide to the sample mounted in the center of the coil. The transmitted light was detected by a Ge:Ga crystal.

As the main excitation source we used the free-electron laser (FEL) facility at the Forschungszentrum Dresden–Rossendorf [8] that delivers a continuous train of short Fourier-limited pulses with 13 MHz repetition rate ($4 < \lambda < 230\,\mu$m). In addition to the FEL, semiconductor quantum cascade lasers (QCLs) operating at wavelengths 75 and 100 μm in a pulsed mode with 500 ns pulse width and 20 kHz repetition rate was used. Experiments above the longest wavelength available at FEL were performed at the Toulouse High Magnetic Field Laboratory (LNCMP). This laboratory is equipped with a long-pulse coil, delivering magnetic fields up to 40 T with a total pulse length of 800 ms. On the optical side, at the LNCMP several CO^2 pumped gas lasers emitting in far infrared range are available. The experimental setup is very similar to the one in Dresden. All measurements were carried out at $T = 4.2$ K.

2. Method of calculations

To analyze the data the hole Landau levels (LLs) and the CR transition energies were calculated using a 4×4 Luttinger Hamiltonian in the axial approximation that includes also strain and QW potentials [9]. As for Luttinger parameters for InGaAs alloy, both linear [10] and nonlinear [11–13] interpolations from the values of the parent binary compounds [10] were proposed. We found much better agreement with the experiment when the linear interpolation scheme is used.

3. Results and discussion

Fig. 1 represents a set of typical transmission spectra. Up to approximately 20 T the position of the CR absorption line scales nearly linearly with magnetic field (cf. [6]). Above this value the CR line splits into two well resolved components with strongly nonlinear magnetic field dependencies. In the Fig. 2, we summarize the experimentally obtained energies of

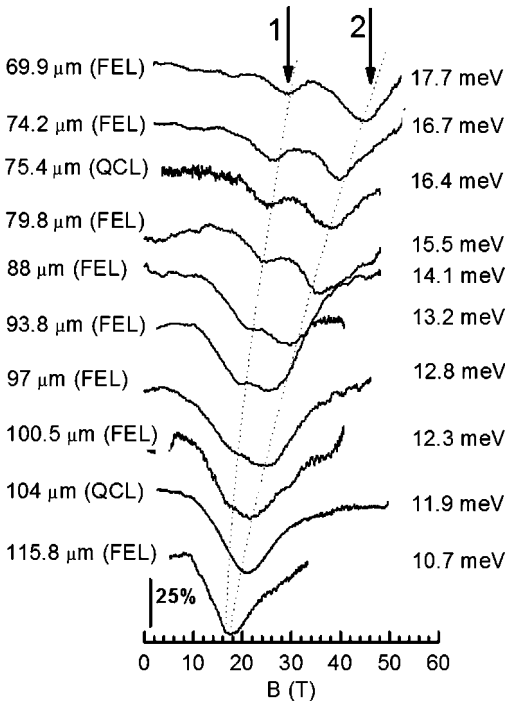

Fig. 1. Selected transmission curves versus the magnetic field, measured under FEL and QCL excitation. Arrows 1 and 2 point to minima corresponding to the transitions $0s \rightarrow 1s$ and $3a \rightarrow 4a$, respectively.

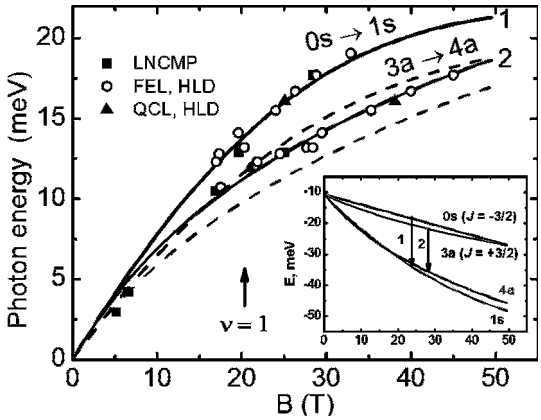

Fig. 2. Energies of cyclotron resonance transitions as a function of magnetic field, calculated (lines) and measured (symbols). Solid (dashed) lines correspond to the calculations made with linearly (nonlinearly) interpolated Luttinger parameters. The inset shows the energies of the four lowest Landau levels versus magnetic field calculated using linearly interpolated Luttinger parameters. Arrows 1 and 2 indicate the transitions corresponding to lines 1 and 2 on the main figure, respectively.

all resonances versus the magnetic field. The inset of Fig. 2 shows the energies of the first four LLs. In our model the LLs in the first subband of size quantization are characterized by the level number n and the in-plane symmetry called s for symmetric and a for antisymmetric states.

For the given carrier density, the filling factor unity corresponds to a magnetic field about 20 T. On the other hand, since the energy separation between the first two LLs, $0s$ and $3a$, is comparable to k_BT both of them should be populated. We then attribute the two CR absorption lines observed at high magnetic fields (see Fig. 1) to the CR transitions $0s \rightarrow 1s$ and $3a \rightarrow 4a$ (arrows 1 and 2 in Figs. 1,2, respectively). The lines in Fig. 2 show the calculated transition energies 1 and 2 calculated according to our model using linear (solid lines) and nonlinear (dashed lines) interpolation schemes. We found excellent agreement between the measured and calculated transition energies without any fit parameters when linear interpolation scheme was used.

As easy to see in Fig. 1, the low-field line ($0s \rightarrow 1s$ transition) has a lower spectral weight than the high-field line ($3a \rightarrow 4a$ transition). In contrast, our calculations show that the LL $0s$ lies above (i.e., lower hole energy) the LL $3a$. This implies a higher hole occupation of the $0s$ state and, therefore, a larger spectral weight of the corresponding transition $0s \rightarrow 1s$ (assuming the oscillator strengths are similar) while our experiment shows the opposite behavior. We attribute this unusual behavior to the crossover of the first two LLs, $0s$ and $3a$. In terms of our model, the crossover point shifts to the lower fields when the Luttinger parameter κ reduces. The linearly interpolated value $\kappa = 2.2$ results to the crossover in magnetic field of 50 T, while the value $\kappa = 1.5$ would shift the crossover point toward 20 T.

Surprisingly, use of the nonlinear interpolation scheme, which gives significantly smaller value of $\kappa = 1.62$, does not help so much since the changes in the other Luttinger parameters γ_i result into strong deviation of the calculated transition energies from the experiment (see dashed lines in Fig. 2). Changes in the κ parameter can also be provoked by hole-hole interaction similar to the exchange enhancement of the effective electron g factor (see, for example, Ref. [14]). The importance of hole-hole interaction in strained InGaAs/GaAs structures was evidenced earlier by Warburton *et al* [6]. Detailed analysis of the present effect, however, requires additional studies and is beyond the topic of the present report.

Acknowledgements

We are grateful to S. Barbieri and C. Sirtori (University Paris VII) and K. Unterrainer and G. Strasser (TU Wien) for providing terahertz QCLs. This work was financially supported by RFBR (Grants 08-02-01126, 09-02-00752), BRHE (Grant Y5-P-01-03) and Russian Academy of Sciences. Part of this work has been supported by EuroMagNET under the EU contract No. RII3-CT-2004-506239.

References

[1] H. Morkoc, *Proc. IEEE* **81**, 493 (1993).
[2] J. E. Schirber *et al*, *Appl. Phys. Lett.* **46**, 187 (1985).
[3] S. Y. Lin *et al*, *Appl. Phys. Lett.* **55**, 666 (1989).
[4] D. Lancefield *et al*, *Surf. Sci.* **229**, 122 (1990).
[5] G. C. Osbourn *et al*, *Appl. Phys. Lett.* **49**, 731 (1986).
[6] R. J. Warburton *et al*, *Phys. Rev. B* **43**, 14124 (1991).
[7] S. Y. Lin *et al*, *Appl. Phys. Lett.* **67**, 2170 (1995).
[8] http://accelconf.web.cern.ch/AccelConf/f04/papers/MOAIS04/MOAIS04.pdf
[9] V. Y. Aleshkin *et al*, *Phys. Rev. B* **66**, 155336 (2002).
[10] I. Vurgaftman *et al*, *J. Appl. Phys.* **89**, 5815 (2001).
[11] M. M. Rieger and P. Vogl *Phys. Rev. B* **48**, 14276 (1993).
[12] P. Lawaetz *Phys. Rev. B* **4**, 3460 (1971).
[13] R. Winkler *et al*, *Phys. Rev. B* **53**, 10858 (1996).
[14] T. Ando and Y. Uemura *J. Phys. Soc. Jpn.* **36**, 1044 (1974).

17th Int. Symp. "Nanostructures: Physics and Technology"
Minsk, Belarus, June 22–26, 2009
© 2009 Ioffe Institute

Illumination effect on multiple quantum well heterostructure visualization with scanning spreading resistance microscopy

D. E. Sviridov and V. I. Kozlovsky
P. N. Lebedev Physical Institute of RAS, 119991 Moscow, 53 Leninsky pr., Russia

Abstract. In this work we carried out SSRM investigation of undoped multiple QW (MQW) heterostructure. Insight into visualization mechanism has been presented. Illumination from built-in AFM red laser and halogen lamp (HL) influence on the data obtained has been studied.

Introduction

Subsequent reduction of semiconductor devices active regions demands new informative and reliable methods capable of providing information about their internal structure with high spatial resolution. Scanning spreading resistance microscopy (SSRM) is relatively new atomic force microscopy (AFM) based technique developed for obtaining information about surface resistivity distribution and accordingly carrier concentration and their drift mobility with resolution about 5–20 nm. Resistivity of a sample under investigation ρ can be derived from measured resistance in the case of flat, pure ohmic tip-sample contact with radius a by equation $R_s = \rho/4a$. The carrier concentration n, electron and hole mobility μ_e, μ_h and resistivity ρ related by $\rho = 1/e(n\mu_e + p\mu_h)$, where e is the charge of an electron.

Different kinds of semiconductor devices have been studied with SSRM [1,2]. In particular F. Giannazzo [3] and K. Maknys [4] reported the results of quantum well (QW) heterostructure SSRM investigations. They have shown that the carrier concentration in QW and mobility can be measured with help of calibration technique. Both studies dealt with doped heterostructures and visualization mechanism has been attributed to electron accumulation in the QWs [5] and hole concentration in the QWs greater relatively barriers [4].

1. Experimental

The GaInP/AlGaInP (lattice matched) structure with distributed Bragg reflector (DBR) has been grown by metal-organic vapor-phase epitaxy (MOVPE) on n^+-doped GaAs substrate. 7 nm thick 25 QWs have been separated by 186 nm thick barriers. DBR consisted of 37.5 pairs of AlAs/ AlGaAs layers, grown between substrate and the MQW structure. The structure was undoped. Indium has been evaporated on the top AlGaInP layer in vacuum to form the second electrical contact. Measurements have been carried out on a freshly cleaved surface using an AFM Solver P47 Pro. We used N doped diamond coated probes with a force constant ranging from 2.5 to 22.5 N/m. In order to study an effect of built-in laser ($\lambda = 650$ nm, $I < 1$ mW) influence on the SSRM images we switched it off and on during the scanning process and set the value of feedback (FB) gain coefficient to zero to prevent piezoscanner retraction. The laser spot diameter was approximately 50 μm leading to radiation intensity 35 W/cm^2.

Topographical and current images obtained in SSRM mode under -8 V sample bias are shown in Fig. 1. In the left part of the first section on topographical image one can see 9 pairs of AlAs/AlGaAs layers with thicknesses 51.5 and 46 nm respectively. This region of the cleavage is 10 nm higher than the rest of the surface because of DBR and MQW structure materials have different oxidation rates [5,6].

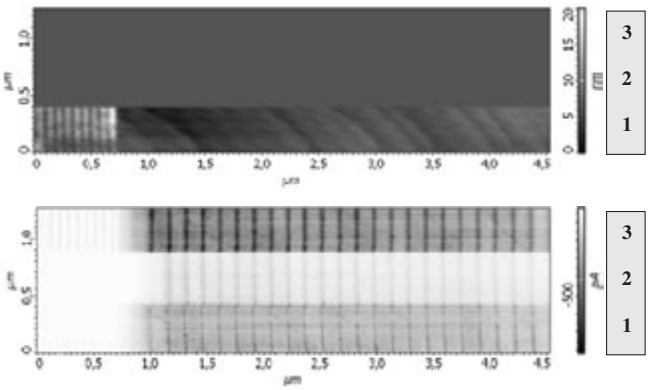

Fig. 1. Topographical (top) and current (bottom) cleavage surface images obtained in SSRM. $U = -8$ V: 1) Built-in laser on, FB gain = 2, 2) Built-in laser off, FB gain = 0, 3) Built-in laser off, FB gain = 0, HL on.

In the first section of current image (Fig. 1) one can see 23 QWs 30 nm wide. They represent areas of high carrier concentration and mobility. Resistivity of DBR region is high. During the second and third section image acquisition built-in laser was off, FB gain = 0, that made information about relief obtaining impossible. However tip still has been in contact with the sample. And in the second section of the current image 23 QWs clearly resolved as before, but their resistivity increased. Additional experiment has shown that ρ increase is not due to FB gain value changes but due to built-in laser switching on and off. During the scanning in the third section built-in laser was off, FB gain = 0 besides illumination with HL radiation took place that caused substantial decrease in resistivity value of QWs, barriers and DBR. Average value of QWs width increased to 45 nm. We could obtain current images under negative biases only when $U < -6$ V. Under positive biases visualization became possible only under HL illumination and $U > 9$ V.

The data presented shows that sample illumination with HL radiation results in non-equilibrium carriers generation both in QWs and in barrier layers, decreasing their resistivity. Although photon energy of the built-in laser (1.9 eV) is smaller then band gap energy of booth GaInP QW (1.97 eV) and barrier layer it, nevertheless, also generate non-equilibrium carriers

due to Franz–Keldysh effect.

Since current can flow only under negative applied voltages to the sample in dark, we suggest Schottky barrier formation at both tip-sample and back contact-semiconductor interface. Assuming that the conductivity of our sample is slightly n-type, we attribute the visualization of QWs in dark to electron accumulation. Additional illumination of the sample results in carriers generation and as a consequence current increase.

Acknowledgements

We thank M. D. Tiberi from Principia LightWorks Inc. for the GaInP/AlGaInP structures. Work is supported by the Russian Foundation for Basic Research (Gr. 07-02-01139), the Program of Scientific Schools of Russia (Gr. NSh-3168.2008.2), the Program of basic research of the Physics Department of the Russian Academy of Science "Physics of new materials and structures" and Educational Scientific Complex of P. N. Lebedev Physical Institute.

References

[1] L. Zhang, K. Ohuchi, K. Adachi, *Appl. Phys. Lett.* **90**, 192103 (2007).
[2] P. De Wolf, T. Clarysse, and W. Vandervorst *et al*, *J. Vac. Sci. Technol.* **B 16(1)**, 355 (1998).
[3] F. Giannazzo and V. Raineri, *Appl. Phys. Lett.* **88**, 043117 (2006).
[4] K. Maknys, O. Douheret, and S. Anand *et al*, *Appl. Phys. Lett.* **83**, 2184 (2003).
[5] F. Reinhardt, B. Dwir, and E. Kapon *et al*, *Appl. Phys. Lett.* **68**, 3168 (1996).
[6] P. A. Dementyev, M. S. Dunaevskii, A. V. Ankudinov *et al*, *Appl. Phys. Lett.* **89**, 081103 (2006).

17th Int. Symp. "Nanostructures: Physics and Technology"
Minsk, Belarus, June 22–26, 2009
© 2009 Ioffe Institute

The energy spectrums of both free charge carrier and exciton states in the nanoparticle which was shaped lake a paraboloid of revolution

V. P. Dzyuba, I. V. Dzyuba, Yu. N. Kulchin and A. M. Bururuev
Institute of Automation and Control Processes, Far East Division, RAS, Vladivostok, 690041 Russia

Abstract. In this report is presented a analytical estimation of the energy spectrums of both coupled charge carriers and free charge carriers in the nanoparticle, which was shaped lake a paraboloid of revolution. For the nanoparticle with the height 40 nm and the base width 40 nm, the exciton's spectrum in the nanoparticles is formed by a practically continuous 0.1-eV-wide band adjoined to the bottom of the conduction band from below and by discrete levels localized deeply in the band gap at the energies 0.2 eV and larger below the bottom of the conduction band. The energy spectrum of charge carriers in the conduction band also can involve the discrete levels $E_{n,m}$.

One of the most important informative optical characteristics of the electronic structure and physical mechanisms controlling the optical and electrical properties of nanoparticles is presented by the transmittance and absorption spectra of an ensemble of nanoparticles. The processes responsible for the transmittance spectrum are directly related to the energy spectrum of both free charge carriers and charge carriers bound in exciton pairs in the nanoparticle. The energy spectrum of charge carriers is directly dependent on the nanoparticle's shape. In this report is presented a analytical estimation of the energy spectrum of both coupled charge carriers and free charge carriers in the nanoparticle, which was shaped lake a paraboloid of revolution. To this end, we choose the model of the infinitely deep potential well confined by a paraboloid of revolution and by the dimensions of workable nanoparticles. The exciton binding energies in the spectrum are estimated by considering only the Coulomb electron-hole interaction and the size-quantization effect in the effective mass approximation, which proves to be correct for comparatively small nanoparticels [1–3]. The exciton wave function $\Psi(\eta, \xi, \varphi)$ in the parabolic coordinates with the origin at the center of mass of the electron-hole pair satisfies the equation [4]

$$\frac{4}{(\xi+\eta)}\left[\frac{\partial}{\partial\xi}\xi\frac{\Psi}{\partial\xi}+\frac{\partial}{\partial\eta}\eta\frac{\partial\Psi}{\partial\eta}\right]+\frac{1}{\xi\eta}\frac{\partial^2\Psi}{\partial\varphi^2}+2\left(E+\frac{2}{\xi+\eta}\right)=0. \quad (1)$$

In Eq. (1), we use relative units; i.e., Planck's constant and the charge are equal to unity; the electron's mass m_e the hole's mass m_h and the exciton's mass $\mu = m_e m_h/(m_e+m_h)$ are chosen in the effective mass approximation, and the unit's length is the exciton's Bohr radius in the material of the nanoparticle, $a_{ex} = \varepsilon_2\eta^2/\mu e^2$. The parabolic coordinates are related to the Cartesian coordinates by the following relations: $x = \sqrt{\xi\eta}\cos\varphi$, $y = \sqrt{\xi\eta}\sin\varphi$ and $z = (\xi-\eta)/2$. The paraboloid of revolution about the $0z$ axis in the parabolic coordinates is defined by the equation $\eta = \eta_0$, and the plane $z = z_0$ corresponding to the nanoparticle's base is defined by the expression $\xi = 2z_0 + \eta$. The coordinates of the points at the nanoparticle's surface satisfy the two equations $\eta = \eta_0$ and $\xi = 2z_0 + \eta$. The condition of the corresponding edge superimposed on the wave function at the surface of the potential well is $\Psi(\eta_0, \xi = 2z_0 = \eta, \varphi) = 0$. The solution of this problem is expressed in terms of degenerate hypergeometric functions as

$$\Psi(\eta,\xi,\varphi) = C\frac{1}{n^2|m|!}\sqrt{\frac{(\alpha+|m|)!\,(\beta+|m|)!}{\alpha!\beta!}}$$
$$\times F\left(-\alpha, |m|+1, \frac{\xi}{\eta}\right)\times F\left(-\beta, |m|+1, \frac{\eta}{n}\right)$$
$$\times\exp\left(-\frac{\xi}{2n}-\frac{\eta}{2n}+im\varphi\right)\times\left(\frac{\xi\eta}{n^2}\right)^{|m|}. \quad (2)$$

The number n specifies the exciton's energy levels $E_n = \mu e^4/(2\varepsilon_2\eta^2 n^2)$ and satisfies the relation $n = \alpha+\beta+|m|+1$. The edge condition at the side surface of the paraboloid of revolution $\eta = \eta_0$ corresponds to the ground state, in which $\beta = 1$, $\alpha = 0$, and $n(|m|+1) = \eta_0$. In this case, $n = (|m|+1)/2 \pm \sqrt{(|m|+1)^2/4 + \eta_0/(|m|+1)}$, and each quantum number m corresponds to two energy levels. The value of $m = 0$ corresponds to the exciton moving in the plane parallel to the $0z$ axis. According to [5], the effective electron mass and hole mass in Al_2O_3 are $m_e = 0.4m_0$ and $m_h = 6.2m_0$, respectively. With these masses, for the nanoparticle with the height 40 nm and the base width 40 nm, the quantity η_0 expressed in relative units is 13, and, correspondingly, the energies of the exciton's ground state ($m = 0$) are 0.07 and 0.04 eV. Assuming that the kinetic energy of the exciton as a whole is negligible, we find that the exciton's energy levels are in the band gap at the energies 0.07 and 0.04 eV below the bottom of the conduction band. The second doublet of levels corresponding to $m = 1$ is moved away from the conduction band deep into the band gap by 0.05 and 0.21 eV. For $m = 2$, 3, and 4, the exciton's levels are, correspondingly, at 0.03 and 0.58 eV, 0.04 and 1.36 eV and 0.02 and 4.06 eV below the bottom of the conduction band. In the spectrum of these lines, one can notice the clearly pronounced effect of geometric amplification of the electron-hole interaction. The edge condition in the plane $\xi = 2z_0 + \eta$ corresponds to the excited state, for which $\beta = 0$, $\alpha = 1$, and $n = (|m|+1)/2 \pm \sqrt{(|m|+1)^2/4 + (2z_0+\eta)/(|m|+1)}$. In this state, the energy of the levels depends on the coordinate ηg that varies from zero to η_0. This dependence is representative of the effect of the shape of the potential well's surface on the exciton's energy spectrum. In general, the character

of the exciton's energy spectrum remains the same as before. The spectrum consists of two regions, of which one is practically continuous and adjoined to the bottom of the conduction band from below, and the other is discrete and located deep in the band gap. In the effective mass approximation, the wave function $\Psi(\eta, \xi, \varphi)$ written in the parabolic coordinates for a particle freely moving within the potential well satisfies Eq. (1) without the Coulomb term. The solution of this equation, finite at the origin of coordinates, is known and expressed in terms of the Bessel functions

$$\Psi(\eta, \xi, \varphi) = C J_{m/2} \frac{k}{2} \eta J_{m/2} \frac{k}{2} \xi \exp(im\varphi).$$

The energy spectrum of a free particle is defined as

$$E_{n,m} = \frac{2\eta^2}{m_{\mathrm{e,h}}} \frac{1}{\eta_0^2} + \frac{1}{(2z_0 + \eta)^2} \alpha_{n,m}^2.$$

Here, $\alpha_{n,m}$ is the nth root of the Bessel function of the order $m/2$; the coordinates η_0 and z_0 are measured in nanometers. Similarly to the exciton's spectrum, the energy spectrum of free charge carriers depends on the variable η. Thus, taking into account the natural and thermal broadening of levels, we can state that the exciton's spectrum in the nanoparticles under consideration is formed by a practically continuous 0.1-eV-wide band adjoined to the bottom of the conduction band from below and by discrete levels localized deeply in the band gap at the energies 0.2 eV and larger below the bottom of the conduction band. The energy spectrum of charge carriers in the conduction band also can involve the discrete levels $E_{n,m}$.

We assume that there exist energy levels of free charge carriers. Such levels are conditioned by spatial confinement of the quantization volume and by sufficient-longlived excitons that make a noticeable contribution to the polarization of the nanoparticle. This requires that the nanoparticles be in the condition of weak confinement ($a^{\mathrm{ex}} < a$). For the electron's (hole) energy levels $E_{n,m}$ to be formed due to spatial confinement of the quantization region, the energies $E_{n,m}$ must exceed the energy of interaction of charge carriers with the field $U(a)$ of polarization produced at the nanopartice-matrix interface. This interaction energy depends on the nanoparticle's shape and dimensions and on the dielectric properties of the medium surrounding the nanoparticle. Therefore, the determination of this energy for irregular asymmetric nanoparticles presents a nontrivial problem [6]. To estimate this energy, we can make use of the expression given in [10] for a spherical particle of radius a,

$$U(a) \approx \frac{e^2\beta}{2\varepsilon_2 a}, \qquad \text{where} \quad \beta = \frac{\varepsilon_1 - \varepsilon_2}{\varepsilon_1 + \varepsilon_2}.$$

Then the condition for the formation of discrete energy levels due to spatial confinement of the quantization levels is $E_{n,m} \gg e^2\beta/(2\varepsilon_2 a)$. In the case of the above-considered nanoparticle with the height 40 nm and the base width 40 nm, this condition is satisfied. For example, with the electron's effective mass $0.4m_0$, the lowest electron levels are at the energies $E_{1,0} \approx 0.95$ eV and $E_{1,1} \approx 0.49$ eV, much larger than $U(a) \approx 10^{-3}$ eV for the 40 nm Al_2O_3 nanoparticle in the vacuum oil matrix. For nanoparticles embedded in an insulator medium, it is essential that the nanoparticle's dimension a should not exceed the threshold dimension $a_c = 6|\beta|^{-1}a_{\mathrm{e,h}}$, where $a_{\mathrm{e,h}}$ are the Bohr radii of an electron or a hole in the material of the nanoparticle [1–3].

References

[1] N. A. Efremov *et al*, *Sov. Phys. Solid State* **27**, 27 (1985).
[2] N. A. Efremov *et al*, *Sov. Phys. Solid State* **32**, 1697 (1990).
[3] A. Efremov *et al*, *Sov. Phys. Solid State* **33**, 1607 (1991).
[4] L. D. Landau *et al*, *Quantum Mechanics: Non-Relativistic Theory.* Nauka, Moscow, 1989.
[5] T. V. Perevalov *et al*, *JETP Lett.* **85**, 165 (2007).
[6] S. I. Pokutnyi, *Semiconductors* **40**, 217 (2006).

17th Int. Symp. "Nanostructures: Physics and Technology"
Minsk, Belarus, June 22–26, 2009
© 2009 Ioffe Institute

Anomaly of baric coefficients of photoluminescence spectra for InAs/GaAs-and InAs/AlAs-heterostructures

V. A. Gaisin[1], B. S. Kulinkin[1,2] and T. S. Shamirzaev[3]

[1] Physics Department, St Petersburg State University, 198504 St Petersburg, Russia
[2] Petersburg State Medical University. Academician I. P. Pavlov 197022 St Petersburg, Russia
[3] Institute of Semiconductor Physics, pr. Lavrentieva 13, 630090 Novosibirsk, Russia

Abstract. The data on abnormal dependences of baric coefficients for InAs quantum dots (QDs) are presented. The baric coefficients of photoluminescence lines shift varied in the range from 4 to 10 meV/kbar for InAs/GaAs QDs and from -1.5 to -6 meV/kbar for InAs/AlAs QDs. The observed effect is explain (i) by the dependence of carrier wave functions on the QD zise, (ii) by the change of energy band structure of bulk InAs under the stress caused by the difference of the InAs lattice constant and of that of barriers, and (iii) by the penetration of wave functions of the localized in QD carriers into the barrier layers.

Introduction

Heterostructures are perspective materials for optoelectronics. The hydrostatic pressure technique is used to obtain the additional data on energy structure of quantum dots (QDs). Baric coefficients (BCs) for InAs/GaAs QDs has been measured in Ref. [1] where it was found that BC $= 8$ meV/kbar for optical transition energy $E = 1.2$ eV, which is considerably smaller of those for both bulk InAs (11.6 meV/kbar) and bulk GaAs (10.3 meV/kbar). Results of our studies have confirmed the observed effect [2]. Besides we observed the BCs in range from 10 to 4 meV/kbar depending on the optical transition energy [2]. We also studied InAs/AlAs QDs and found the negative dependence of BCs on transition energy. They varied from -1.5 meV/kbar up to -6 meV/kbar [3]. As an example, Figure 1 shows the dependence for InAs/AlAs QDs taken from Ref. [3].

1. Results and discussion

In this paper, an attempt to explain observable anomaly of BCs in the investigated structures is made. The large deviation of BCs for the QDs from those for bulk materials is assumed to be caused by the following reasons.

First, we take into account the penetration of the carrier wave functions in the barrier layers. This effect is already discussed for quantum wells [4]. According to the analysis, the BCs in quantum wells of the small well thickness coincide with that for barrier layers and coincide with that of the quantum well material for wide wells. The authors of Ref. [4] explained this effect by different localization of the carriers, namely, by the strong localization for wide quantum wells and by the penetration of the carrier wave functions in the barriers for narrow wells.

We consider similar effect for QDs. In the case of small InAs QDs, the BC should be equal to that for barrier. Our experiments [2,3] support this conclusion. However in the case of large InAs QDs, there is the principal difference between the experiment and the theory. Indeed, the BC for large QDs should approach that of bulk InAs, i.e., should be large. At the same time, our extrapolation of the experimentally determined energy dependence of BCs in InAs/GaAs heterostructure to the large QD sizes gives rise to value 4 meV/kbar. Similar extrapolation for InAs/AlAs structure gives BC $= -6$ meV/kbar. Both the values considerably smaller than that for for bulk InAs, BC $= 11.6$ meV/kbar [1].

We attribute so small BC value to the presence of initial deformation of InAs QDs due to large difference of lattice constant for InAs crystal and that of barriers. This deformation considerably changes the energy structure of bands, which form the carrier states in QDs. In particular, the energy gaps between valley $\Gamma 8$ and split-off valley $\Gamma 7$ as well as valleys $L4$, $L5$, and $L6$ are decreased with deformation because of small BC for $\Gamma 8$ valley relative to those for other valleys [4]. Similar changes occur in the conduction band where the $X6$ and $X7$ valleys are shifted towards the $\Gamma 6$ valley in energy due to the negative BCs.

While modeling the energy states of QDs, it is necessary to take into account the contribution of all band states. We assume that the BCs in this case should have some average values of those for the valleys contributed the QD states. Because of smaller (or even negative) values of BCs for all the valleys contributed that those for $\Gamma 8$ and $\Gamma 6$ valleys, the BCs for QDs should be smaller that for bulk crystal.

As an example we consider the InAs/AlAs QDs. The BCs for the small QDs should be initially negative due to the penetration of the carrier wavefunction in the AlAs barriers because

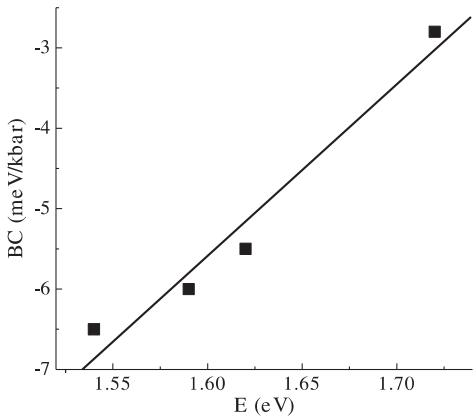

Fig. 1. Dependence of BC on the energy of optical transtions in InAs/AlAs QDs [3].

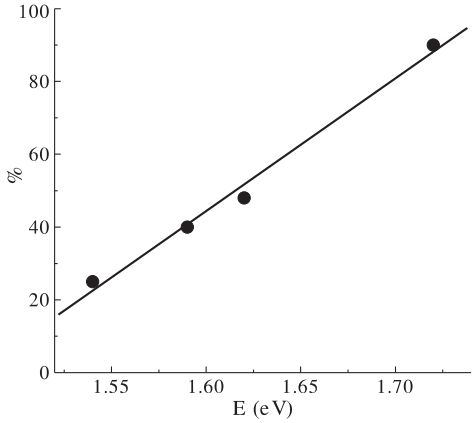

Fig. 2. Per cent content of wave function in barrier layers as a function of the optical transition energy.

the AlAs crystal is indirect semiconductor with negative BC.

We explain the reduction of BC up to −6 meV/kbar for large QDs as follows. First we can estimate the pressure caused by the difference of lattice constants of InAs and AlAs crystals using the blue shift of optical transitions for large InAs QDs relative to that for bulk InAs. The energy gap, E_g, for these QDs increases up to 1.2–1.3 eV, that corresponds to pressure ∼100 meV/kbar. As a result, the band scheme for InAs/AlAs QDs is essentially changed relative to bulk InAs. One can expect, that, at so large pressure, the $X6$, $X7$-valleys should almost coincide in energy with $X6$ valley in conduction band. Correspondingly, the BC for electronic states in these QDs should be small. In the valence band, Γ7 valley should be shifted higher than Γ8 so that the BC for hole states should be positive. As a result, the BC for optical transitions should be negative. Our estimates based on effective masses of the valleys contributed to the QD states gives rise to BC values, which are close to that observed experimentally for large QDs.

In the case of QDs of intermediate size, all the factors, namely, the initial deformation, the band mixing due to the sized quantization effect, and the delocalization of carriers may affect the BC. We consider here only the last effect. For this purpose, we use the linear interpolation for the per cent content of carrier wave function in barriers assuming it to be zero for large QDs and 100% for small ones. The respective results are shown in Fig. 2.

Acknowledgements

The work was supported by the Russian Foundation for Basic Research (Grants No. 07-02-00134-a and No. 08-02-00954-a) and by the program of Presidium of RAS (grant No. 320).

References

[1] I. E. Itskevich, M. Henini, H. A. Carmona, L. Eaves, P. C. Main, D.K. Maude, J. C. Portal, *Appl. Phys. Lett.* **70**, 505 (1997).
[2] V. A. Gaisin *et al*, Proc. 15th Int. Symp. Nanostructures: Physics and Technology, St Petersburg, 212 (2007).
[3] T. S. Shamirzaev *et al*, Proc. 12th Int. Symp. Nanostructures: Physics and Technology, St Petersburg, 262 (2004).
[4] Y. Tang *et al*, *Phys. Lett. A* **336**,434 (2005).

17th Int. Symp. "Nanostructures: Physics and Technology"
Minsk, Belarus, June 22–26, 2009
© 2009 Ioffe Institute

Strain distribution in quantum dot structures with linear gradient of composition: analytical solution

A. V. Nenashev and A. V. Dvurechenskii

Institute of Semiconductor Physics, 630090, Novosibirsk, Russia
Novosibirsk State University, 630090, Novosibirsk, Russia

Abstract. The strain distribution in a structure consisting of infinite matrix with a polyhedral-shaped inclusion (a quantum dot) is obtained analytically, assuming that the lattice mismatch between matrix and inclusion is a linear function of the radius vector (that corresponds to a linear gradient of composition in the quantum dot). Both matrix and quantum dot materials are assumed to be elastically isotropic, and to have the same Young's modulus and Poisson's ratio. This problem was solved by a method based on a formal analogy between problems of elasticity theory and of electrostatics. Strain tensor is shown to be a sum of contributions of inclusion faces, edges, and vertices. Each of these contributions has a simple geometrical meaning.

Introduction

Self-assembled quantum dots are three-dimensional inclusions of one material in another one (a matrix). Usually there is a lattice mismatch between materials of an inclusion and a matrix. The lattice mismatch gives rise to a built-in inhomogeneous elastic strain which in turn produces significant changes in the electronic band structure. Therefore knowledge of the strain distribution is of crucial importance for electronic structure studies. Especially important is the strain distribution for type-II quantum dots where the confining potential for one type of carriers is mainly due to the strain inhomogeneity.

As a rule, composition of quantum dots is non-homogeneous (see, for example, Ref. [1]), due to surface segregation and/or intermixing during overgrowing process. But an analytical solutions of elastic inclusion problem are known either for homogeneous inclusions [2] or for simple (ellipsoidal) inclusion shapes [3]. Here we consider an non-homogeneous inclusion of arbitrary polyhedral shape. We assume simplest form of inhomogeneity-namely, a linear gradient of lattice mismatch (that corresponds to linear gradient of composition). Our aim is to find an analytical expression for strain tensor as a function of co-ordinates, both inside and outside the inclusion. For simplicity, both matrix and quantum dot materials are assumed to be elastically isotropic, and to have the same Young's modulus and Poisson's ratio.

1. Analogy between elasticity and electrostatics

To solve this problem, we used a method developed in Ref. [4]. This method utilizes the fact that the *displacement vector* $\mathbf{u}$ induced by an infinitely small inclusion in isotropic medium, $\mathbf{u}(\mathbf{r}) \sim \mathbf{r}/r^3$, is proportional to the *electric field* of a point charge. Therefore, from the mathematical point of view, the inclusion problem in elasticity theory is analogous to the electrostatics problem expressed by Poisson's equation. More strictly, there is the following relation between strain tensor $\varepsilon_{\alpha\beta}(\mathbf{r})$, induced by an inclusion, and a solution $\tilde{\varphi}(\mathbf{r}) = \int \varepsilon_0(\mathbf{r}')d\mathbf{r}'/|\mathbf{r}-\mathbf{r}'|$ of Poisson's equation with charge density $\varepsilon_0(\mathbf{r})$:

$$\varepsilon_{\alpha\beta}(\mathbf{r}) = -\frac{1+\nu}{4\pi(1-\nu)}\frac{\partial^2\tilde{\varphi}(\mathbf{r})}{\partial x_\alpha \partial x_\beta} - \varepsilon_0(\mathbf{r})\chi(\mathbf{r}), \qquad (1)$$

where ν is the Poisson's ratio, and $\chi(\mathbf{r})$ is 1 inside the inclusion and 0 outside.

In Ref. [4], we propose a simple geometrical way of obtaining second derivatives $\partial^2\tilde{\varphi}/\partial x_\alpha \partial x_\beta$ for *constant* misfit strain ε_0 and arbitrary polyhedral shape of the inclusion. This way consists in establishing some relations between four kinds of potential functions (see Fig. 1):

(1) $\varphi(\mathbf{r})$ — a potential of uniformly charged inclusion:

$$\varphi(\mathbf{r}) = \int_V \frac{1}{|\mathbf{r}-\mathbf{r}'|}\,d^3\mathbf{r}', \qquad (2)$$

where V is the inclusion volume;

(2) $\Psi_i(\mathbf{r})$ — a potential of uniformly charged i-th face of inclusion surface:

$$\Psi_i(\mathbf{r}) = \int_{S_i} \frac{1}{|\mathbf{r}-\mathbf{r}'|}\,d^2\mathbf{r}'; \qquad (3)$$

(3) $\Omega_i(\mathbf{r})$ — a potential of i-th face uniformly covered by dipoles[1]:

$$\Omega_i(\mathbf{r}) = \int_{S_i} \frac{\mathbf{n}^i(\mathbf{r}-\mathbf{r}')}{|\mathbf{r}-\mathbf{r}'|^3}\,d^2\mathbf{r}', \qquad (4)$$

where $\mathbf{n}^i$ is an outward normal vector to this face;

(4) $\Phi_k(\mathbf{r})$ — a potential of uniformly charged k-th edge of inclusion surface:

$$\Phi_k(\mathbf{r}) = \int_{L_k} \frac{1}{|\mathbf{r}-\mathbf{r}'|}\,dl' = \log\frac{r_1+r_2+l}{r_1+r_2-l}, \qquad (5)$$

where r_1 and r_2 are distances from the point $\mathbf{r}$ to ends of this edge, l is the edge length.

It was found in Ref. [4] that derivatives $\partial\varphi/\partial x_\alpha$ are linear combinations of functions Ψ_i. In their turn, derivatives $\partial\Psi_i/\partial x_\beta$ are linear combinations of Ω_i and Φ_k. Therefore, if ε_0 is constant (and, consequently, $\tilde{\varphi} = \varepsilon_0\varphi$), then second derivatives of $\tilde{\varphi}$ contributing to Eq. (1) can be expressed via functions Ω_i and Φ_k. This gives a closed-form analytical solution for strain tensor $\varepsilon_{\alpha\beta}(\mathbf{r})$, as functions Ω_i and Φ_k have explicit representations in a closed form.

[1] Its absolute value $|\Omega_i(\mathbf{r})|$ has a simple geometrical meaning: it is equal to a *solid angle* subtended by the i-th face from the point $\mathbf{r}$.

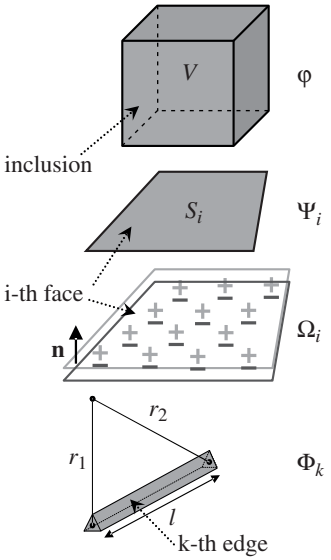

Fig. 1. Potentials φ, Ψ_i, Ω_i, and Φ_k (see Eqs. (2)–(5)).

Now we generalize this approach to the case of linearly varied lattice mismatch, $\varepsilon_0(\mathbf{r}) = \mathbf{A}\mathbf{r} + B$. Note that the potential $\tilde{\varphi}(\mathbf{r})$, contributing to Eq. (1), differs from $\varphi(\mathbf{r})$ given by Eq. (2) only by additional factor $\varepsilon_0(\mathbf{r}')$ in the integrand. In the analogous way, we introduce potentials $\tilde{\Psi}_i(\mathbf{r})$, $\tilde{\Omega}_i(\mathbf{r})$, and $\tilde{\Phi}_k(\mathbf{r})$ by putting $\varepsilon_0(\mathbf{r}')$ into integrands of Eqs. (3–5). We found the following relations between functions $\tilde{\varphi}$, $\tilde{\Psi}_i$, $\tilde{\Omega}_i$, and $\tilde{\Phi}_k$ (assuming linear lattice mismatch):

— derivatives $\partial\tilde{\varphi}/\partial x_\alpha$ are combinations of $\tilde{\Psi}_i$ and φ;
— derivatives $\partial\tilde{\Psi}_i/\partial x_\beta$ are combinations of $\tilde{\Omega}_i$, $\tilde{\Phi}_k$, and Ψ_i;
— $\tilde{\Omega}_i$ can be expressed via Ω_i and Φ_k;
— $\tilde{\Phi}_k$ can be expressed via Φ_k and $(r_1 - r_2)$ — difference between distances from the point $\mathbf{r}$ to the ends of k-th edge.

As a result, one can reduce second derivatives of $\tilde{\varphi}(\mathbf{r})$ (and, consequently, the strain tensor $\varepsilon_{\alpha\beta}$ via Eq. (1)) to combinations of functions Ψ_i, Ω_i and Φ_k. As these functions have closed-form analytical representations, this solves the problem of evaluating $\varepsilon_{\alpha\beta}(\mathbf{r})$ in a closed form.

2. Results

Using the method described in Sec. 1, we obtained a closed-form analytical expression for the strain tensor $\varepsilon_{\alpha\beta}(\mathbf{r})$ induced by a polyhedral-shaped inclusion (a quantum dot) with linearly varied latice mismatch ε_0: $\varepsilon_0(\mathbf{r}) = \mathbf{A}\mathbf{r} + B$. Strain tensor is represented as a sum of contributions of faces, edges, and vertices of the dot surface:

$$\begin{aligned}\varepsilon_{\alpha\beta}(\mathbf{r}) &= \sum_i \left[P^i_{\alpha\beta}\Psi_i(\mathbf{r}) + (Q^i_{\alpha\beta} + R^i_{\alpha\beta\gamma}x_\gamma)\Omega_i(\mathbf{r}) \right] \\ &+ \sum_k (S^k_{\alpha\beta} + T^k_{\alpha\beta\gamma}x_\gamma)\Phi_k(\mathbf{r}) \\ &+ \sum_m U^m_{\alpha\beta}|\mathbf{r} - \mathbf{r}_m| - (\mathbf{A}\mathbf{r} + B)\chi(\mathbf{r})\delta_{\alpha\beta}.\end{aligned}$$

There the indices i, k, m run over faces, edges and vertices, correspondingly. $\Psi_i(\mathbf{r})$, $\Omega_i(\mathbf{r})$ and $\Phi_k(\mathbf{r})$ are functions introduced in Sec. 1 (all of them can be written in a closed form). $\mathbf{r}_m$ is a position vector of m-th vertex. $\chi(\mathbf{r})$ is equal to 1 if the point $\mathbf{r}$ lies inside the dot, otherwise $\chi(\mathbf{r}) = 0$. $\delta_{\alpha\beta}$ is the Kronecker delta. Coefficients $P^i_{\alpha\beta}$, $Q^i_{\alpha\beta}$, $R^i_{\alpha\beta\gamma}$, $S^k_{\alpha\beta}$, $T^k_{\alpha\beta\gamma}$, $U^m_{\alpha\beta}$ are defined by geometry of the inclusion; explicit expressions for them will be presented below.

We will use the following notations. $\mathbf{n}^i$ is an outward normal vector to i-th face of the inclusion surface. $\mathbf{n}^{k1}$ and $\mathbf{n}^{k2}$ are two of these vectors which correspond to faces intersecting at k-th edge. $\mathbf{l}^k$ is an unit vector along k-th edge. $\mathbf{b}^{k1}$ is an unit vector perpendicular to k-th edge and to $k1$-th face and directed out of this face; the vector $\mathbf{b}^{k2}$ is defined in the same way. $\mathbf{r}^i$ and $\mathbf{r}^k$ are arbitrarily chosen points in i-th face and k-th edge, correspondingly. A tensor $\gamma^k_{\alpha\beta}$ is defined as $n^{k1}_\alpha b^{k1}_\beta + n^{k2}_\alpha b^{k2}_\beta$. A value Λ is equal to $-(1+\nu)/4\pi(1-\nu)$, where ν is the Poisson's ratio.

With these notations, the coefficients $P^i_{\alpha\beta}\ldots U^m_{\alpha\beta}$ are

$$\begin{aligned}P^i_{\alpha\beta} &= \Lambda\left(n^i_\alpha n^i_\beta n^i_\gamma A_\gamma - n^i_\alpha A_\beta - n^i_\beta A_\alpha\right), \\ Q^i_{\alpha\beta} &= \Lambda n^i_\alpha n^i_\beta\left[\left(\mathbf{A}\mathbf{n}^i\right)\left(\mathbf{r}^i\mathbf{n}^i\right) + B\right], \\ R^i_{\alpha\beta\gamma} &= \Lambda n^i_\alpha n^i_\beta\left[A_\gamma - \left(\mathbf{A}\mathbf{n}^i\right)n^i_\gamma\right], \\ S^k_{\alpha\beta} &= \Lambda\gamma^k_{\alpha\beta}\left[\mathbf{A}\mathbf{r}^k - \left(\mathbf{A}\mathbf{l}^k\right)\left(\mathbf{r}^k\mathbf{l}^k\right) + B\right] \\ &\quad + \Lambda n^{k1}_\alpha n^{k1}_\beta\left(\mathbf{A}\mathbf{b}^{k1}\right)\left(\mathbf{r}^k\mathbf{n}^{k1}\right) \\ &\quad + \Lambda n^{k2}_\alpha n^{k2}_\beta\left(\mathbf{A}\mathbf{b}^{k2}\right)\left(\mathbf{r}^k\mathbf{n}^{k2}\right), \\ T^k_{\alpha\beta\gamma} &= \Lambda\gamma^k_{\alpha\beta}l^k_\gamma\left(\mathbf{A}\mathbf{l}^k\right) - \Lambda n^{k1}_\alpha n^{k1}_\beta n^{k1}_\gamma\left(\mathbf{A}\mathbf{b}^{k1}\right) \\ &\quad - \Lambda n^{k2}_\alpha n^{k2}_\beta n^{k2}_\gamma\left(\mathbf{A}\mathbf{b}^{k2}\right), \\ U^m_{\alpha\beta} &= -\Lambda\sum_k \gamma^k_{\alpha\beta}\left(\mathbf{A}\mathbf{l}^k\right).\end{aligned}$$

In the last expression, summation is over edges converging at m-th vertex, and unit vectors $\mathbf{l}^k$ are directed from m-th vertex toward adjacent vertices.

Summary

In conclusion, we have obtained an analytical expression for strain distribution inside and around a polyhedral quantum dot with linear gradient of lattice mismatch. The quantum dot is assumed to be buried in an infinite, elastically isotropic matrix, and to have the same elastic moduli as the matrix. The generalization to semi-infinite matrix is possible by mirror image method developed by Davies [5]. This solution can be a useful tool for calculations of electronic structure, and for simulation of stacking process in multilayered quantum-dot structures.

Acknowledgements

This work was supported by the Dynasty foundation.

References

[1] P. Offermans, P. M. Koenraad, J. H. Wolter, K. Pierz, M. Roy, and P. A. Maksym, *Phys. Rev. B* **72**, 165332 (2005).
[2] H. Nozaki and M. Taya, *J. Appl. Mech.* **68**, 441 (2001).
[3] T. Mura and N. Kinoshita, *Phys. Stat. Solidi (a)* **48**, 447 (1978).
[4] A. V. Nenashev and A. V. Dvurechenskii, arXiv:0707.2183 (2007).
[5] J. H. Davies, *J. Appl. Mech.* **70**, 655 (2003).

17th Int. Symp. "Nanostructures: Physics and Technology"
Minsk, Belarus, June 22–26, 2009
© 2009 Ioffe Institute

Optical absorption lines of combined magnetoexciton-cyclotron resonance in quantum well structures

S. A. Moskalenko[1], M. A. Liberman[2] and I. V. Podlesny[1]

[1] Institute of Applied Physics, Academy of Sciences of Moldova, 5, Academiei str., MD-2028, Chisinau, Republic of Moldova
[2] Department of Physics, Uppsala University, Box 530, SE-751 21, Uppsala, Sweden

Abstract. A theory of combined exciton-cyclotron resonance in the quantum well structures is developed for a strong magnetic field. The absorption band structure is calculated for optical quantum transitions with circularly polarized radiation creating a two-dimensional exciton and simultaneously exciting one of the resident electrons from the lowest to the first Landau level.

Introduction

Fundamental many-body elementary and combined processes occurring in the presence of two-dimensional electron gas (2DEG) are displayed in optical spectra, such as shakeup processes [1,2], where e-h pair recombination is accompanied by transition of the second electron to a higher energy state. A closely-related phenomenon of combined exciton-cyclotron resonance (ExCR) was recently discovered in low-density 2DEG system of a semiconductor quantum well heterostructure [3,4]. Here, an incident photon creates a Wannier–Mott exciton and simultaneously excites one of the resident electrons from the lowest to a higher Landau level (LL). The ExCR line shifts linearly with the magnetic field strength with a slope comparable to the electron cyclotron frequency. The intensity of the ExCR line increases for higher illumination intensity, i.e. for larger $n_{\rm el}(\rho)$, whereas the exciton lines remain insensitive. It was found [3,4], that the ExCR line is strongly σ^- polarized. Influence of the magnetic field and Coulomb interaction on the combined ExCR was considered in different theoretical descriptions [3–5], based on the first order perturbation theory of the electron-photon interaction. Here we present a rigorous theory of the ExCR on the base of the dipole-active quantum transitions in the frame of the second order perturbation theory using as perturbations the electron-radiation interaction and the electron-electron Coulomb interaction.

1. Optical orientation, spin polarization and alignment of 2D magnetoexcitons in the presence of background electrons

According to [3,4] the incident photon creates an electron-hole pair with different Landau quantum numbers $n_{\rm e}$ and $n_{\rm h}$, so that the optically created hole with $n_{\rm h} = 0$ together the background electron in the initial state with $n_{\rm e} = 0$ form the magnetoexciton $X_{0,0}$, whereas the optically created electron with $n_{\rm e} = 1$ becomes a background electron in the final state with the same quantum number. In semiconductor quantum well structure of the type CdTe, the electrons belong to s-type conduction band with spin projections $s_z = \pm 1$, whereas the heavy-holes are formed in p-type valence band with orbital momentum projection $M = \pm 1$. The heavy holes with total momentum projections $j_z = \mp 3/2$ and electrons with spin projection $s_z = \pm 1/2$ form electron-hole pairs with $F = s_z + j_z = \mp 1$ coinciding with the orbital quantum number M. Without a magnetic field the band-to-band quantum transitions are of allowed type whereas in the presence of a strong perpendicular magnetic field they are dipole active when the created e-h pair has the same Landau quantum numbers $n_{\rm e} = n_{\rm h}$, and are quadrupole-active when the quantum numbers differ by 1, i.e. $n_{\rm e} = n_{\rm h} \pm 1$. In the later case the probability of quantum transition is proportional to $|\vec{Q}_{\rm 2D}|^2$, where $\vec{Q}_{\rm 2D}$ is the projection of the light wave vector $\vec{Q}$ on the layer surface, which vanishes in the Faraday geometry of excitation.

We consider a strong magnetic field such that the distance between the Landau levels is larger than the exciton Rydberg and the magnetic length $l_0 = \sqrt{\hbar c/eH}$ is smaller than the Bohr radius $a_{\rm B} = \varepsilon\hbar^2/me^2$, otherwise assuming small concentration of the resident electrons, which does not influence structure of the magnetoexcitons [3–6]. Let the light with a given circular polarization $\vec{\sigma}_{\vec{Q}}$ creates an electron-heavy-hole pair with equal Landau quantum numbers $n_{\rm e} = n_{\rm h} = 0$ and circular polarization $\vec{\sigma}_M$ in the presence of a background electron. The amplitude of this matrix element is proportional to $(\vec{\sigma}^*_{\vec{Q}} \times \vec{\sigma}_M)$ and depends essentially on the reciprocal spin orientations of the optically created electron defined by the value M and background electron. On the second step of the perturbation theory these two electrons undergo the Coulomb scattering process, and as a result one of them remains on the lowest Landau level and the second electron is transferred on the final state $n_{\rm e} = 1$. Because the Coulomb direct and exchange interactions this scattering process depends on the mutual spin orientations of two electrons.

To calculate the probability of the transitions we use the matrix elements of the electron-photon interaction obtained in [8] between the initial and the intermediate states expressed in the terms of the matrix element of the band-to-band transition, and matrix elements of the electron-electron Coulomb interaction obtained in [7]. The later do not vanish only between the intermediate and final states with the same quantum number M because the light is not involved and does not influence symmetry of the 2D layer.

The probabilities of quantum transitions depend on the reciprocal orientation of the photon and exciton circular polarization vectors $\vec{\sigma}^{\pm}_{\vec{k}}$ and $\vec{\sigma}_M$ expressed by the factor $|(\vec{\sigma}^{\pm}_{\vec{k}} \times \vec{\sigma}_M)|^2$. In the Faraday geometry light propagates along the magnetic field, $\vec{Q}_{\rm 2D} = 0$ and $\vec{\sigma}^{\pm}_{\vec{Q}}$ coincides with $\vec{\sigma}_M$, so that $\vec{\sigma}^{+}_{\vec{Q}} = \vec{\sigma}_1$ and $\vec{\sigma}^{-}_{\vec{Q}} = \vec{\sigma}_{-1}$. This means spin polarization of the e-h pair

because the magnetoexciton with $M = -1$ is composed of the heavy-hole with $j_z = -3/2$ and electron with $s_z = 1/2$ whereas the magnetoexciton with $M = +1$ is composed of the heavy-hole with $j_z = 3/2$ and electron with $s_z = -1/2$. Two electrons with $s_z = 1/2$ in the intermediate state interdependently participate in the quantum transition being identical, so that a direct and exchange terms are involved. On the contrary, two electrons with different spins participate separately in the transition. This difference essentially influences probability of the combined quantum transition, which is expressed in additional factor 4, with participation of two electrons with parallel spins compared to the probability with participation of two electrons with antiparallel spin projections. The transition probability is strongly enhanced if the circularly polarized light excites an e-h pair so that the electron polarization of the magnetoexciton and of the background electrons are the same.

The momentum conservation for the magnetoexciton-photon quantum transition is implemented by the equality $\vec{k}_{\rm ex} = \vec{Q}_{\rm 2D}$, whereas the combined quantum transition is governed by the conservation law for only one component of the involved momenta. It reflects the symmetry properties of 2D e-h system in a strong magnetic field [5,6,9,10].

Spectral functions determining the absorption band shapes for two circular light polarizations in the Faraday geometry have the same maximal spectral width corresponding to the ionization potential I_l of the magnetoexciton $X_{0,0}$ at $k = 0$. This means that all points of the magnetoexciton band take part in the quantum transition due to participation of the background electrons. The maximum width of the band shapes is the same for both circular polarizations because this feature is due exclusively to the momentum conservation law in x in-plane direction in the Landau gauge description. The transition probabilities depend on magnetic field as $H^{-1/2}$ for a given filling factor, or as $H^{-3/2}$ for a given concentration of background electrons. The widths of the band shapes are due to inhomogeneous broadening arising from the dispersion law of the magnetoexciton energy band. The band shapes corresponding to different circular polarizations in the Faraday geometry can be distinguished experimentally.

Strong circular polarization of the ExCR line in the PLE spectrum revealed by the authors of [3] is clearly seen as different intensities of spectral lines in Fig. 2b of Ref. [3], where the curves (c) and (d) correspond to σ^- and σ^+ polarized excitations. The ratio of spectral line intensities is approximately 4, which is in a good agreement with the present calculations.

For the probability of quadrupole-active transition its angular dependences on the light circular polarization vector as well as on the magnetic field are the same as in the dipole-active transitions. In the Voight geometry of excitation both types of optical quantum transitions as dipole-active as well as quadrupole-active can take place simultaneously.

Acknowledgements

This work was supported by the grant # 08.820.05.033RF offered by the Academy of Sciences of Moldova and RFBR as well as by the grant # 08.819.05.07F of the Academy of Sciences of Moldova for the young scientists. One of the authors (S. A. M) greatly appreciates support of the Wenner–Gren Foundation during his stay in Uppsala.

References

[1] I. Bar-Joseph, *Semicond. Sci. Technol.* **20** 6, R29–R39 (2005).
[2] G. Finkelstein, H. Shtrikman, I. Bar-Joseph, *Phys. Rev. Lett.* **74**, 976 (1995).
[3] D. R. Yakovlev, V. P. Kochereshko, R. A. Suris, H. Schenk, W. Ossau, A. Waag, G. Landwehr, P. C. M. Christianen, and J. C. Maan, *Phys. Rev. Lett.* **79**, 3974 (1997).
[4] V. P. Kochereshko, D. R. Yakovlev, R. A. Suris, G. V. Astakhov, W. Faschinger, W. Ossau, G. Landwehr, T. Wojtowicz, G. Karczewski, J. Kossut, in *Optical properties of 2D systems with interacting electrons* (NATO Science Series, 2002) 125 p.
[5] A. B. Dzyubenko, *Phys. Rev. B* **64**, 241101(R) (2001).
[6] A. B. Dzyubenko and A. Yu. Sivachenko, *Phys. Rev. Lett.* **84**, 4429 (2000).
[7] S. A. Moskalenko, M. A. Liberman, P. I. Khadzhi, E. V. Dumanov, Ig. V. Podlesny and V. V. Boţan, *Physica E* **39**, 137 (2007).
[8] S. A. Moskalenko, M. A. Liberman, and I. V. Podlesny, *Phys. Rev. B* (2008) (accepted).
[9] L. P. Gor'kov and I. E. Dzyaloshinskii, *Zh. Eksp. Teor. Fiz.* **53**, 717, (1967) [*Sov. Phys. JETP* **26**, 449 (1968)].
[10] H. A. Nickel, T. M. Yeo, A. B. Dzyubenko, B. D. McCombe, A. Petrou, A. Yu. Sivachenko, W. Schaff, and V. Umansky, *Phys. Rev. Lett.* **88**, 056801 (2002).

17th Int. Symp. "Nanostructures: Physics and Technology"
Minsk, Belarus, June 22–26, 2009
© 2009 Ioffe Institute

Microscopic model of quantum dot: quantum Langevin approach

A. V. Savelyev and A. E. Zhukov

Academic Physics and Technology University RAS
St Petersburg Physics and Technology Centre for Research and Education RAS, St Petersburg, Russia

Abstract. Langevin approach to quantum dynamics of a multi-electron system with discrete energy levels has been developed. It allows obtaining an equation of motion of all system operators in Markowian approximation when relaxation mechanism is known. Langevin noise sources have been calculated. Proposed theory can be applied to calculation of optical properties of zero-dimensional nanostructures such as emission spectrum, homogeneous broadening, gain spectrum, field correlation functions and photon statistics. As an application of the theory all these properties have been calculated for four-level single semiconductor quantum dot under continuous nonresonant excitation.

Semiconductor zero dimensional nanostructures (ZDN) such as self-organized quantum dots (QDs) have been an area of intensive studies for the last decade. Among the most important results are creation of single-photon emitters [1] and realization of quantum dot lasers with outstanding characteristics [2]. Understanding optical properties of ZDN is closely connected with the investigation of a charge carriers dynamics. Namely carriers statistics determines emission intensity and gain while carrier coherence determines emission spectrum and correlation functions. Therefore application of quantum theory of carrier dynamics in ZDN is essential to calculate its optical properties. Appropriate theory should include interaction with the environment for two reasons: it is crucially important for coherency of quantum states and plays major role when external injection of carriers is discussed.

The first effective approach to quantum dynamics of ZDN has been introduced by Lax in terms of quantum Langevin forces and quantum master equation for reduced density matrix [3]. These results were widely utilized afterwards including the works on semiconductor properties [4]. However, Lax's theory was oriented to maser like applications and described single electron dynamics in multilevel systems. When discussing optics of semiconductor ZDN at least two carriers (electrons and holes) are of interest. Thus there is need to develope multilevel multi-electron approach to quantum carrier dynamics in ZDN embedded in the environment. The goal of current paper is to formulate this theoretical approach and, as an implementation of it, calculate optical properties of ZDS-gain spectra, two-time correlation functions and photon statistics. Presented approach is of significance for quantum dot physics because it establishes connections between carrier dynamics in QD and QD's optical properties. This allows to interprete single quantum dot experiments [1] in clear physical terms such as carrier relaxation/escape times and injection rate. Also it is important for QD laser theory as a tool to calculate QD homogeneous broadening and noise properties.

We start with the hamiltonian of the system in rotating wave approximation:

$$\begin{aligned}\hat{H} &= \hat{H}_0 + \hat{V}_1 + \hat{V},\\ \hat{H}_0 &= \sum \hbar\epsilon_\alpha \hat{a}^+_\alpha \hat{a}_\alpha + \sum \hbar\omega_q \hat{b}^+_q \hat{b}_q,\\ \hat{V} &= \sum_{\alpha,\beta,q} \left(g_{\alpha\beta}\hat{a}^+_\alpha \hat{a}_\beta \hat{b}^+_q + g^*_{\alpha\beta}\hat{a}^+_\beta \hat{a}_\alpha \hat{b}_q \right),\ \alpha < \beta, \quad (1)\end{aligned}$$

where $\hat{H}_0$ — free hamiltonian for electrons and phonons (photons), $\hat{V}_1$ — interaction with external fields, $\hat{V}$ — interaction between electrons and phonons that rules the relaxation, $\hat{a}$ — Fermi destruction operators of the system and $\hat{b}$ — Bose destruction operators of phonon (photon) field.

Using conventional approach to weak system-bath interaction and Markowian approximation one can obtain equation of motion for arbitrary system operator $\hat{X}$ in the form:

$$\frac{d}{dt}\langle\hat{X}\rangle = -\frac{1}{2}\sum_{\beta>\alpha}\Gamma_{\alpha\beta}\left\{ n^t_{\alpha\beta}\left([\hat{\sigma}^-_{\alpha\beta}, [\sigma^+_{\alpha\beta}, \hat{X}]] + \dots \right.\right.$$

$$\left.\left. + [\hat{\sigma}^+_{\alpha\beta}, [\sigma^-_{\alpha\beta}, \hat{X}]]\right) + \hat{\sigma}^+_{\alpha\beta}[\hat{\sigma}^-_{\alpha\beta}, \hat{X}] + [\hat{X}, \hat{\sigma}^+_{\alpha\beta}]\hat{\sigma}^-_{\alpha\beta} \right\} + \hat{N}_X(t), \quad (2)$$

where $\hat{\sigma}^{\pm}_{\alpha\beta} = \hat{a}^+_\alpha \hat{a}_\beta$ ($\alpha \gtrless \beta$), $\Gamma_{\alpha\beta} = 2\pi \left|g_{\alpha\beta}\right|^2 D(|\epsilon_\alpha - \epsilon_\beta|)/\hbar$ — transition rates between levels α and β, $D(E)$ — DOS of phonons (photons) and $n^t_{\alpha\beta} = (\exp(|\epsilon_\alpha - \epsilon_\beta|/T) - 1)^{-1}$. The Langevin noise source is denoted as $N_X(t)$ and Markowian noise correlations $\langle \hat{N}_X(t_1)\hat{N}_Y(t_2)\rangle = 2D_{XY}\delta(t_1 - t_2)$ are assumed. All diffusion coefficients can be calculated from (2) with Einstein rules [3].

As an example, equation of motion for level filling operators $\hat{f}_i = \hat{a}^+_i \hat{a}_i$ and current operators $\hat{j}^+_{\alpha\beta} = \hat{a}^+_\alpha \hat{a}_\beta$ can be presented in the form:

$$\frac{d}{dt}\hat{f}_n = \sum_\alpha \Gamma_{\alpha n} n^t_{\alpha n}\left(\hat{f}_\alpha - \hat{f}_n\right) + \sum_{\alpha>n}\Gamma_{\alpha n}\left(1 - \hat{f}_n\right)\hat{f}_\alpha - \dots$$

$$- \sum_{\alpha<n}\Gamma_{\alpha n}\left(1 - \hat{f}_\alpha\right)\hat{f}_n, \quad (3)$$

$$\frac{d}{dt}\hat{j}_{mn} = -\frac{1}{2}\left(\hat{\gamma}^{\mathrm{S}}_{mn} + \hat{\gamma}^{\mathrm{T}}_{mn}\right)\hat{j}_{mn}, \quad (4)$$

$$\hat{\gamma}^{\mathrm{T}}_{mn} = \sum_{\alpha\neq n}\Gamma_{\alpha n} n^t_{\alpha n} + \sum_{\alpha\neq m}\Gamma_{\alpha m} n^t_{\alpha m},$$

$$\hat{\gamma}^{\mathrm{S}}_{mn} = \Gamma_{mn}\mathrm{sign}(n-m) + \sum_{\alpha<m}\Gamma_{\alpha m}(1 - \hat{f}_\alpha) + \dots \quad (5)$$

$$+ \sum_{\alpha<n}\Gamma_{\alpha n}(1 - \hat{f}_\alpha) + \sum_{\alpha>n}\Gamma_{n\alpha}\hat{f}_\alpha + \sum_{\alpha>m}\Gamma_{m\alpha}\hat{f}_\alpha. \quad (6)$$

Equation (3) is obviously agree with rate master equation that can be obtained from non-quantum treatment [5]. However expressions (4–6) that establish connection between polarization damping rate and kinetic constants are presented at our best knowledge for the first time.

To demonstrate an application of developed approach let us now discuss a quantum dot with excited states 'ce', 've' and ground states 'c', 'v' for electrons and holes respectively (Fig. 1a). Presence of excited levels in our model is essential to take into account an injection and its influence onto optical properties in non-empiric way. While discussing non-resonant pumping we assume that filling operators of the pumping levels 'ce', 've' are not correlated with the ones of radiation levels 'c','v'. This means $\langle \hat{f}_{\rm ce}\hat{f}_{\rm c}\rangle = \langle \hat{f}_{\rm ce}\rangle\langle \hat{f}_{\rm c}\rangle$. This is true always when $\langle \hat{f}_{\rm ce}\rangle \ll 1$, in other words when excited states are far from saturation. This is quite general case for quantum dot lasers and single-photon emitters operation. That way we replace $\hat{f}_{\rm ce}$, $\hat{f}_{\rm ve}$ operators by c-numbers (in (3–6) for example). All remaining quantum operators describe two-level quantum system and can be presented as a superposition of the following ones: $\hat{f}_{\rm c}$, $\hat{f}_{\rm v}$, $\hat{S} = \hat{f}_{\rm c}\hat{f}_{\rm v}$, $\hat{j} = \hat{a}_{\rm v}^{+}a_{\rm c}$, $\hat{j}^{+}$, $\hat{E}$ — unit operator. For example spontaneous emission intensity is proportional to $\hat{I} = \hat{f}_{\rm c} - \hat{S}$. The time evolution of those 6 operators can be written down in the following linear form:

$$\frac{d}{dt}\vec{X} = \mathcal{A}\vec{X},\ \vec{X}^{\rm T} = \left(\hat{f}_{\rm c},\ \hat{f}_{\rm v},\ \hat{S},\ \hat{J}^{+},\ \hat{J}^{-},\ \hat{E}\right), \qquad (7)$$

$$\mathcal{A} = \begin{pmatrix} -\gamma_{\rm c} & 0 & R & -iE & iE & R_{\rm c} \\ R & -\gamma_{\rm v} & -R & iE & -iE & R_{\rm v} \\ R_{\rm v} & R_{\rm c} & -\gamma_{\rm S} & 0 & 0 & 0 \\ -iE & iE & 0 & i\Delta - \gamma_j/2 & 0 & 0 \\ iE & -iE & 0 & 0 & -i\Delta - \gamma_j/2 & 0 \\ 0 & 0 & 0 & 0 & 0 & 0 \end{pmatrix}$$

$$\gamma_j = \Gamma_{\rm v} n_{\rm v}^{t} + \Gamma_{\rm c} n_{\rm c}^{t} + \Gamma_{\rm v}(1 - f_{\rm ve}) + \Gamma_{\rm c} f_{\rm ce} + R,$$
$$R_{\rm c} = \Gamma_{\rm c}\left(n_{\rm c}^{t} + 1\right) f_{\rm ce}\,,\ R_{\rm v} = \gamma_{\rm v} n_{\rm v}^{t} f_{\rm ve}\,,\ \gamma_{\rm S} = \gamma_j - R,$$
$$\gamma_{\rm c} = \Gamma_{\rm c}\left(n_{\rm c}^{t} + f_{\rm ce}\right) + R\,,\ \gamma_{\rm v} = \Gamma_{\rm v}\left(n_{\rm v}^{t} + 1 - f_{\rm ve}\right), \qquad (8)$$

where we introduce interaction with a coherent classical external field in the form $\hat{V}_{\rm I} = pE(\hat{J}^{+} + \hat{J}^{-})$, where p — dipole matrix element of 'c-v' optical transition, $2E$ — external field amplitude, $\hat{J}^{+} = \exp(i\Delta t)\hat{j}^{+}$ and Δ — frequency detuning between optical transition frequency and frequency of the light. The linear equation of motion, together with calculated diffusion coefficients, completely determine quantum statistical properties of the system.

Equation (7), together with quantum regression theorem [6], allow to calculate correlation functions in close analytical form: the most important are the first order correlation function $G^{(1)}(\tau) = \langle \hat{J}^{+}(t+\tau)\hat{J}^{-}(t)\rangle$ and the second order correlation function $g^{2}(\tau) = \langle : \hat{I}(t+\tau)\hat{I}(t) :\rangle / \langle \hat{I}(0)\rangle^{2}$. The first one determines spectral width of gain and luminescence while $g^{(2)}(\tau)$ determines photon statistics. The peak gain and luminescence intensity can be found by solution of stationary equation $\mathcal{A}\vec{X} = 0$. Lineshape of luminescence ($E = 0$) is Gaussian with full width at half maximum $\delta\omega_{\rm L} = \sqrt{2}\gamma_j$. From (8) it is clear that $\delta\omega_{\rm L}$ is power dependent especially at low temperatures: higher injection makes line wider (see Fig. 1c, line A). The same result is correct for gain linewidth $\delta\omega_g = \delta\omega_{\rm L}$ in the weak driving field when no gain saturation occurs. In the strong driving field saturation itself depends on Δ thus interaction of QD with external field becomes nonlinear and original gain concept fails.

At Fig. 1b time dependence of $g^{(2)}(\tau)$ is demonstrated. For $\tau = 0$ $g^{(2)}$ goes to zero that means clear photon antibunching

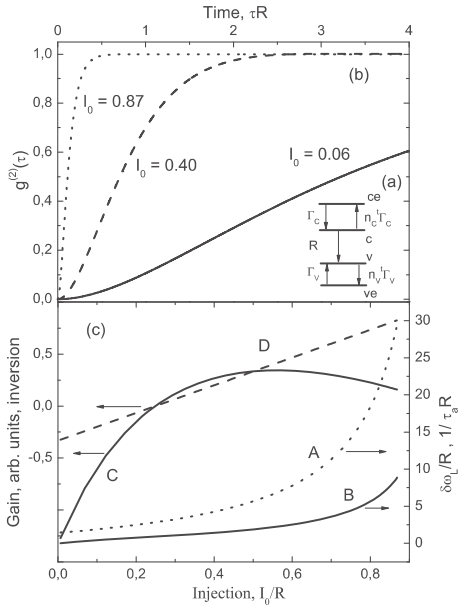

Fig. 1. (a) Scheme of QD levels and relaxation processes. (b) Function $g^{(2)}(\tau)$ at different injection levels, $I_0 = \langle \hat{I}(0)\rangle / R$. (c) A — luminescence linewidth $\delta\omega_{\rm L}$, (B) — reciprocal characteristic time $1/\tau_{\rm a}$ (see text for details), (C) — peak gain value of single QD, (D) — population inversion in dependence of injection intensity I_0. $\Gamma_{\rm c} = \Gamma_{\rm v} = 100R$ and $n_{c,v}^{t} = 0$ were assumed in calculations.

and $g^{2} \to 1$ for $\tau \to \infty$. The characteristic antibunching time $\tau_{\rm a}$ that can be defined as $g^{(2)}(\tau_{\rm a}) = 0.5$ is also power dependent as presented at Fig. 1c, line B.

The maximum gain (at $\Delta = 0$) of a single QD is shown in Fig. 1c (line C) — that quantity is relevant to SQD placed in the microresonator that is working in laser regime. It demonstrates unusual behavior: with injection rate high enough gain decreases. This effect is due to gain broadening with power as mentioned above. Though inversion increases (Fig. 1c, line D) broadening leads to reducing the peak gain value.

In conclusion general theory proposed above can be utilized to the simple scheme that describes all the main QD optical properties in the frame of one linear model (7,8). Complications that are relevant to more realistic QD model such as spin degeneracy of energy levels can be taken into account in the same way. In earlier works polarization damping has been treated in empiric way indepently from charge carrier dynamics [7]. We suppose that proposed model can be the starting point to calculate dynamical properties of quantum dot emitting devices such as lasers, microlasers and single quantum dot emitters.

Acknowledgements

This work was supported by the program of Presidium of RAS, the program of Section of Physical Science RAS and the grant of Federal Agency of Education.

References

[1] C. Becher *et al*, *Phys. Rev. B* **63**, 121312(R) (2001).
[2] V. M. Ustinov, *Semiconductors* **38**, 923 (2004).
[3] M. Lax, *Phys. Rev.* **145**, 110 (1965).
[4] Y. Yamamoto, S. Machida, *Phys. Rev. A* **34**, 4025 (1986).
[5] M. Grundmann and D. Bimberg, *Phys. Rev. B* **55**, 9740 (1997).
[6] M. Lax, *Phys. Rev.* **157**, 213 (1967).
[7] C. Geis *et al*, *Phys. Rev. A* **75**, 013803 (2007).

17th Int. Symp. "Nanostructures: Physics and Technology"
Minsk, Belarus, June 22–26, 2009
© 2009 Ioffe Institute

Mechanism of carriers capture in InAs/AlAs quantum dots

T. S. Shamirzaev[1], K. S. Zhuravlev[1], F. Trojánek[2], B. Dzurňák[2] and P. Malý[2]

[1] Institute of Semiconductor Physics, pr. Lavrentieva 13, 630090 Novosibirsk, Russia
[2]Charles University in Prague, Faculty of Mathematics and Physics,
Ke Karlovu 3, 121 16 Prague 2, Czech Republic

Abstract. Carriers capture in InAs self-assembled quantum dots (QDs) embedded in AlAs has been studied by transient photoluminescence (PL). Low temperature PL measured by up-conversion technique demonstrates the same rise time dynamics in whole spectral region that does not depend on excitation power density. The experimental results evidence in phonon-mediated mechanism of carriers capture in QD, which provides the same carriers capture time for QDs of any sizes.

Introduction

Self-assembly of semiconductor quantum dot (QDs) heterostructures with strong three-dimensional confinement is currently considered for fabrication of novel devices [1]. A special attention was fixed to study process of carriers collection in QDs that is required to construct optoelectronic devices [2]. The majority of the studies reported so far have concentrated on In(Ga)As/GaAs material system. Several mechanisms there are proposed to explain effective carriers capture in QD: Auger carrier-carrier scattering [3–5], and phonon mediated processes such as multi-phonon emission [3,6] and relaxation of carriers on continuum tail of the energy states extended down to QD's ground state [7]. However, carriers captured in QDs in technologically similar system of InAs/AlAs QDs has not been studied yet. Meanwhile, energy structure of InAs/AlAs QDs is quite different from that of In(Ga)As/GaAs QDs. Actually, stronger electronic confinement in the InAs/AlAs QDs leads to direct-indirect transition of the lowest state of conduction band within type I band alignment [8], and to significant change in their electronic and optical properties as compared with the In(Ga)As/GaAs QDs system [9]. Here carriers capture in InAs/AlAs QDs has been studied by transient photoluminescence.

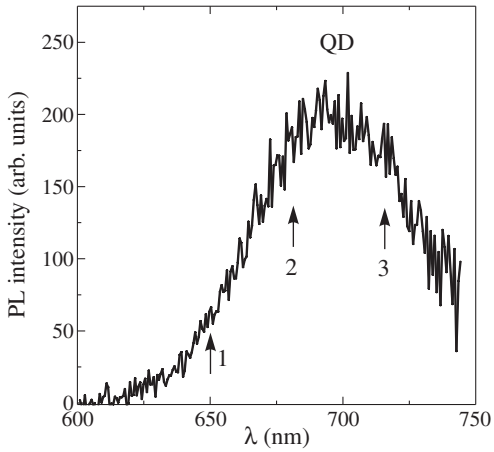

Fig. 1. Low temperature (8 K) PL spectrum of structure InAs/AlAs QDs at a time delay related to maximum of PL signal from QDs. Numbers mark energies where PL dynamics presented in Fig. 2 was measured: 1 — 1.91 eV, 2 — 1.82 eV, 3 — 1.73 eV.

1. Experimental

The samples of InAs QDs in an AlAs matrix studied in this work were grown by molecular beam epitaxy in a Riber-32P system. The samples consisted of twenty layers of the QDs divided by 20 nm thick layers of AlAs grown on top of a 200 nm buffer GaAs layer. The nominal amount of deposited InAs in each layer was equaled to 2.5 monolayers. A 20 nm GaAs cap layer was grown on top of the sandwich in order to prevent oxidation of AlAs. The ultrafast luminescence dynamics were measured using standard up-conversion technique. The excitation source was a frequency-doubled Ti:sapphire laser (Tsunami, Spectra Physics). Parameters of excitation pulses were: wavelength 405 nm, time duration 90 fs, average power 2–20 mW at spot size of about 20 nm, and repetition rate 82 MHz. Luminescence light from the sample and the switching femtosecond pulse at the fundamental laser wavelength were focused into a nonlinear BBO crystal to produce the light at the sum-frequency. The time resolution of our set-up was about 250 fs.

2. Results

Figure 1 demonstrates a PL spectrum of the multi-layer structure with InAs/AlAs QDs detected by up-conversion technique at a time delay related to maximum of PL signal from QDs. The spectrum is a wide band marked in figure as QD with linewidth typical for InAs/AlAs QDs [8]. PL dynamics curves measured at different energies along the QD band are shown in Fig. 2.

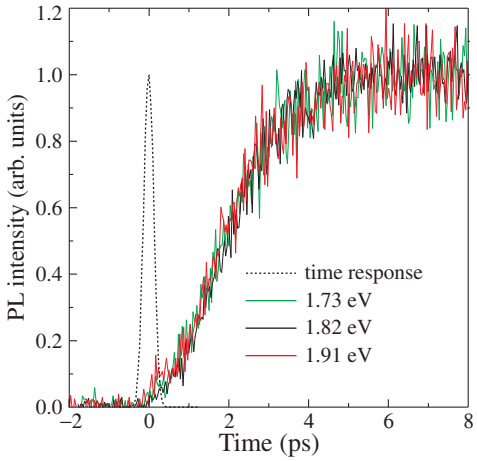

Fig. 2. Normalized PL dynamics of structure with InAs/AlAs QDs at different PL energies mark in Fig. 1.

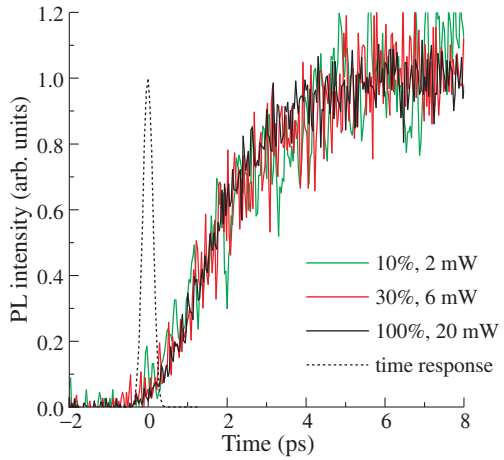

Fig. 3. Normalized PL dynamics of InAs/AlAs QDs at energy of 1.73 eV as a function of excitation power.

One can see that the rise time of PL equals a few picoseconds and is the same at any spectral point. In our previous works we demonstrated that for excitation by strongly absorbable in AlAs light the PL intensity of InAs/AlAs QW and QD do practically not depend on thickness of AlAs layers [8,10]. Therefore, the number of carriers photoinduced in matrix and then captured by InAs QD or QW does not depend on nonradiative centers in AlAs which amount increases with increasing in thickness of AlAs layers. Therefore short rise-times observed here is not a result of non-radiative recombination in AlAs layer and carriers generated in AlAs are captured by QDs. Since energy of PL transition is determined by QD's size we conclude that similar rise time of PL in whole spectral region denotes the carriers capture time is the same for QDs of any sizes. PL rise times at different excitation power densities are presented in Fig. 3. One can see that PL rise time does not depend on excitation power density. Since Auger capture mechanism results in rise time acceleration with increase in excitation density [3,5], we can exclude this mechanism. Therefore carriers are captured in InAs/AlAs QD via phonon mediated processes. We assume that the short capture time, which is in several times smaller than that in InAs/GaAs QDs [5], and its independence from QDs size are result of strong interaction phonons with electrons in X value of InAs conduction band.

Acknowledgements

This work was supported by the RFBR (grant No. 07-02-00134) and by the Program of Fundamental Studies of the Presidium of RAS (grant No. 32).

References

[1] D. Bimberg, M. Grundmann, and N. N. Ledentsov, *Quantum Dot Heterostructures* Wiley, New York, 1999.
[2] J. J. Finley *et al*, *Appl. Phys. Lett.* **73**, 2618 (1998).
[3] J. Siegert *et al*, *Phys. Rev. B* **72**, 085316 (2005).
[4] G. Narvaez *et al*, *Phys. Rev. B* **74**, 075403 (2006).
[5] C. Lobo *et al*, *Phys. Rev. B* **62**, 2737 (2000).
[6] B. Ohnesorge *et al*, *Phys. Rev. B* **54**, 11 532 (1996).
[7] E. W. Bogaart *et al*, *Phys. Rev. B* **72**, 195301 (2005).
[8] T. S. Shamirzaev *et al*, *Phys. Rev. B* **78**, 085323 (2008).
[9] T. S. Shamirzaev *et al*, *JETP Lett.* **77**, 389 (2003).
[10] T. S. Shamirzaev *et al*, *Phys. Rev. B* **76**, 155309 (2007).

17th Int. Symp. "Nanostructures: Physics and Technology"
Minsk, Belarus, June 22–26, 2009
© 2009 Ioffe Institute

Ultra-fast carrier exchange in tunnel-injection structures with nano-bridges. Tuning by an external electric field

V. G. Talalaev[1,2,3], A. V. Senichev[3], J. W. Tomm[1], N. D. Zakharov[2], P. Werner[2], U. Gösele[2], B. V. Novikov[3], Yu. B. Samsonenko[4,5,6], A. D. Bouravleuv[4,5], I. P. Soshnikov[4,5] and G. E. Cirlin[4,5,6]

[1] Max-Born-Institut für Nichtlineare Optik und Kurzzeitspektroskopie, 12489 Berlin, Germany
[2] Max-Planck-Institut für Mikrostrukturphysik, 06120 Halle (Saale), Germany
[3] Fock Institute of Physics, St Petersburg State University, 198504 St Petersburg, Russia
[4] Ioffe Physical-Technical Institute, St Petersburg, Russia
[5] St Petersburg Physics and Technology Centre for Research and Education RAS, St Petersburg, Russia
[6] Institute for Analytical Instrumentation RAS, 190103 St Petersburg, Russia

Abstract. InGaAs tunnel-injection nanostructures (TINs) consisting of a single quantum well (QW) as injector and a quantum dots (QDs) layer as emitter are embedded into pin-junctions and studied under external electric field by steady-state (cw) and time-resolved (TR) photoluminescence (PL) spectroscopy. The tunnel vicinity of QW increased the QD cwPL intensity by one order. The behavior of TRPL is found different for the TINs with and without nano-bridges (NBs) between QD apex and QW layer. Such point contacts are detected by transmission electron microscopy. For TINs with NBs the tunneling between QW and QDs takes place within a few ps. The field dependence of tunneling time reflects a passage of electron ground states in size-distributed QDs arrays across the resonance with single QW level. For TINs with NBs this dependence could be characterized as a threshold one.

Tunnel-injection nanostructures (TINs) offer additional degrees of freedom for the gain region design in diode lasers. A selective population of the lasing ground state allows to reduce electron heating in the light emitter (QDs) by direct injection of cold electrons from the separated carrier injector (QW) performed by tunneling. It potentially results in reduced internal losses, increased quantum efficiency, decreased diffusion capacitance, and decreased response time of TIN-based devices.

Earlier [1] we demonstrated the unique optical and transport properties of InGaAs TINs with inversion of the nanolayers; specifically a quantum well (QW) layer, an injector, was grown after quantum dot (QD) layer, an emitter, which were spaced by GaAs barrier. For TINs with a thin GaAs barrier (<5 nm) the tunneling between QW and QDs was short (about 10 ps), and it deviated from semiclassical dependence of the tunneling time versus barrier thicknesses. These deviations are attributed to the formation of nano-bridges (NBs) across the tunneling barriers. In that way the NBs form the channels for a fast carrier transport from QW to QDs layer.

In the current work we present a further investigation of inverted InGaAs TINs with NBs. The QD-QW TINs were embedded into pin-junctions and studied under external electric field.

TINs are grown by solid-source molecular beam epitaxy with the following sequence of layers: InAs QDs (2 monolayers), GaAs spacer (variable thickness determined by TEM), and a single 11 nm thick $In_{0.15}Ga_{0.85}As$ QW; all embedded into i-region of GaAs pin-junctions. Reference TINs in the undoped GaAs matrix and a sample containing exclusively QDs layer are grown as well. Structural information (morphology of QD and QW, local chemical composition) is provided by TEM. For thin GaAs barrier the TEM techniques detected the NBs between QD apex and QW layer, as shown in Fig. 1. The NBs had a 1–2 nm size and variable In content (0.1–0.4). The $In_{0.6}Ga_{0.4}As$ QDs had a 18 nm diameter and a 4 nm height (standard deviation was about 10%). Using this information the calculations within the framework of the effective mass approximation were performed. The calculated electronic structure of TINs has been experimentally confirmed by Arrhenius analysis of cwPL intensities versus measurement temperature. A scheme representing conduction bands structure of TINs (with and without NBs) is shown in Fig. 2a.

First, we analyzed the influence of the QW on the QD PL intensity. In the flat band conditions the tunnel vicinity of QW increased the QD cwPL intensity by one order in relation to the reference sample containing only QD layer. This advantage of TINs is explained by a larger cross section and a higher rate of electron capture for the QW than for the QDs, as well as by an effective electron tunneling from QW to the QDs. Therefore, we studied tunneling in TINs, particularly in TINs with NBs. Previously obtained values of tunneling time (10 ps) in such structures [1] were limited by the time response of the streak-camera system. Currently used up-conversion time-resolved PL setup with ps-resolution allowed to evaluate the tunneling

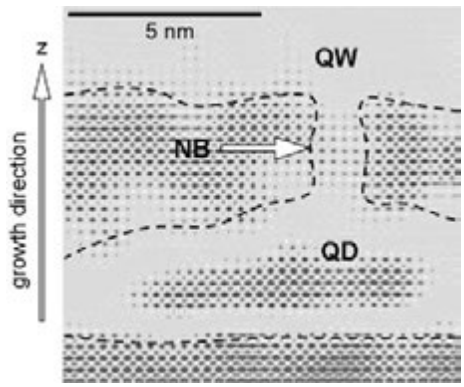

Fig. 1. High-resolution TEM of TIN with 3.1 nm barrier thickness. The dash contour was drawn over the contrast corresponding to 0.15 indium content.

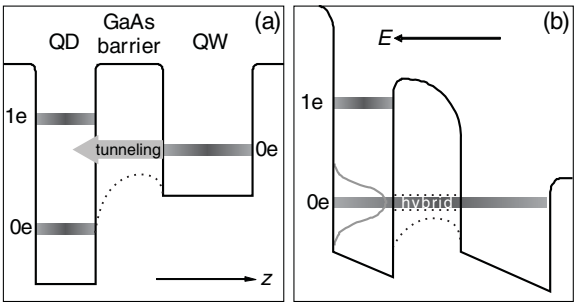

Fig. 2. Scheme of TINs conduction bands: (a) TIN in undoped GaAs matrix (or TIN embedded into pin-junction in the flat band conditions), (b) TIN embedded into pin-junction with built-in electric field E. Dotted line denotes the case of TINs with NBs, when GaAs barrier is lowered and the formation of a hybrid electronic state for QD and QW is possible.

time in TINs with NBs as a few ps depending on the barrier thickness. In these measurements a new limiting factor has become evident, namely the inhomogeneity of QD sizes. Since barrier thickness is determined as a gap between QD apex and QW, the formation of NBs takes place primarily for the large QDs. Thus the QD array is divided into two parts: with NBs and without NBs.

In order to control the emission properties of TINs (with and without NBs) we investigated the QD PL of TINs under external electric field. Fig. 2b presents the energy scheme of TIN embedded into the pin-junction. The field-induced behavior of QD PL is shown in Figs. 3,4. Initially, at zero-bias and low PL excitation, most electron states of QDs are above QW level. Such states are empty due to the tunnel sweep-out of electrons from QDs. At the increase of forward bias the Gaussian-distributed densities of QD states pass a resonance with QW level. The QDs having the appropriate sizes are filled up with electrons and become active for PL. Correspondingly, the parameters of QD PL band change as follows: PL peak shifts in the high-energy direction (Fig. 3a), full width at half maximum (FWHM) increases (Fig. 3b). These changes stop at the flat band conditions (Fig. 2a). The absence of saturation for the intensity of QD PL band (Fig. 4a) is explained by the contribution of injection component. The field-induced saturation of PL intensity for reference QD sample (open squares in Fig. 4a) once more confirms a high efficiency of QD pumping via QW. Field-induced scanning of Gaussian-distributed QD states relatively to the QW level provides a selective electron charging of the large-size QD array part, which makes it active in the PL spectrum (Fig. 3a,b). The possibility to control density of active QDs gives an opportunity to use TINs as single electron emitters.

Fig. 4b shows processed data from TRPL measurements of TINs at forward bias. In comparison with cwPL the transient PL gives more information about the dynamics of carrier exchange between QDs and QW. In particular, the decay time of QD PL band (Fig. 4b) represents the competition of radiative recombination in QDs and tunneling between QDs and QW. Thus the field dependence of tunneling time reveals notable difference between TINS with and without NBs. For TINs with NBs this dependence could be characterized as a threshold one, differently from a gradual increase of tunneling

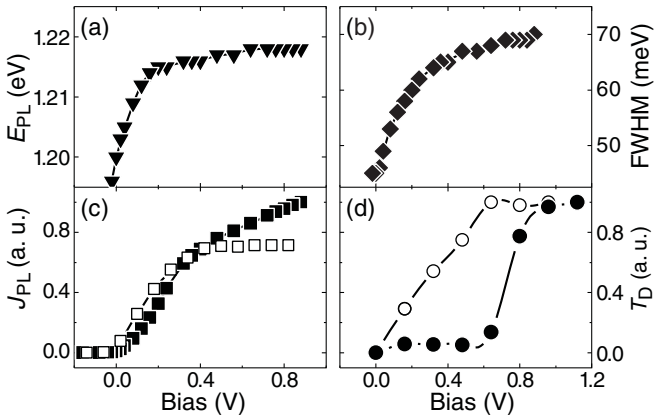

Fig. 3. (Steady-state PL data of QD band for TIN with 3-nm barrier *versus* external bias: (a) PL peak position (E_{PL}), (b) FWHM. T = 10 K.

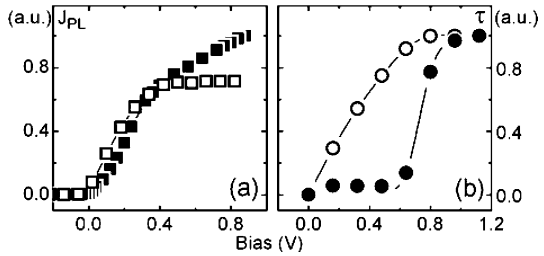

Fig. 4. (QD PL data for different TINs *versus* external bias: (a) integrated steady-state PL intensity (J_{PL}). Full squares relate to the TIN with 3-nm barrier; open squares denote the reference QD-sample; (b) normalized PL decay time (τ) deduced from TR spectra. Full circles correspond to the TIN with NBs (3-nm barrier); open circles represent the TIN without NBs (7.5-nm barrier). T = 10 K.

time for TINs without NBs. The threshold obviously reflects the transition from levels of large QDs with NBs to the states of smaller QDs without NBs in the same QD array passing through the resonance with QW level.

Pre-threshold carrier exchange between QDs and QW through the NB is ultra-fast and field-independent. These facts in combination with data of the PL excitation spectroscopy allow to propose the following energy model of NB. The NB lowers the barrier between QD apex and QW down to its disappearance (Fig. 2b). It results in the formation of a hybrid electronic state from half-pined states of QD and QW, which is similar to the Fano resonance. A hybrid wave function assumably has a node centered at NB, and it provides an ultra-fast carrier exchange between QW and QDs layers. This mechanism has a high potential for novel TINs.

Acknowledgements

This work has been supported by the Russian Foundation for Basic Research, Programs of RAS "Fundamentals of Nanotechnologies and Nanomaterials" and "Fundamentals of Epitaxial Nanotechnologies Development".

References

[1] V. G. Talalaev *et al*, *Appl. Phys. Lett.* **93**, 031105 (2008).

17th Int. Symp. "Nanostructures: Physics and Technology"
Minsk, Belarus, June 22–26, 2009
© 2009 Ioffe Institute

Subband structure in ultra-thin silicon films

V. A. Sverdlov[1,2], O. Baumgartner[1], S. Tyaginov[3,4], Th. Windbacher[1] and S. Selberherr[1]

[1] Institute for Microelectronics, TU Wien, Gußhausstraße 27-29, A-1040 Wien, Austria
[2] V. A. Fock Institute of Physics, Universitu of St Petersburg, Ulyanovskaya 1, 198904 Petrodvorets, St Petersburg, Russia
[3] Christian Doppler Laboratory for TCAD at the Institute for Microelectronics,TU Wien, Gußhausstraße 27-29, A-1040 Wien, Austria
[4] Ioffe Physical-Technical Institute, St Petersburg, Russia

Introduction

Silicon is composed of nuclei with predominantly zero spin and is characterized by a negligible spin-orbit interaction. Silicon is therefore attractive for spintronic applications. Coherent spin transport through a silicon wafer of 350 μm length was demonstrated in a recent ground-breaking experiment [1]. However, since the conduction band consists of six equivalent valleys, the valley degeneracy is a potential source of increased decoherence and must be removed. Biaxial stress lifts the degeneracy by moving two of the valleys down. Various experiments provide a controversial insight on the splitting between the two remaining valleys. Conductivity measurements on an electron system composed of thin silicon films in Si-SiGe heterostructures in magnetic field reveal a small valley splitting [2]. From the other side, recent experiments on the conductance through a point contact created by additionally confining a quasi-two-dimensional electron system in lateral direction demonstrate a splitting between equivalent valleys larger than the spin splitting [2]. In this work we address the controversy based on a two-band $\mathbf{k}\times\mathbf{p}$ model for the conduction band. We also demonstrate that a large splitting between the two unprimed subbands with the same number can be induced by a shear strain component.

1. Method

The two-band $\mathbf{k}\times\mathbf{p}$ Hamiltonian is employed to describe the conduction band in presence of shear strain ε_{xy} [3,4]. For the unprimed subbands of a [001] silicon film the following equation for y_n is obtained [5]:

$$\sin(k_0 t y_n) = \frac{\eta y_n \sin\left(k_0 t \frac{1-\eta^2-y_n^2}{1-y_n^2}\right)}{\sqrt{(1-y_n^2)(1-\eta^2-y_n^2)}}, \qquad (1)$$

with t being the layer thickness, $k_0 = 0.15(2\pi/a)$ is the position of the valley minimum with respect to the X point, and $\eta = m_l|D\varepsilon_{xy} - \hbar^2 k_x k_y/M|/k_0^2$ [5]. Note, that for $\eta = 0$ the quantized momentum $y_{0n} = \pi n/(k_0 t)$ is for both subbands.

2. Results

The dependencies of the subband quantization energy vs. η of for a film of the thickness $t = 5.43$ nm obtained solving (1) numerically are shown in Fig. 1. Degeneracy between the subbands is removed resulting in a splitting which becomes large at high strain values. Fig. 2 shows that the dependence of the splitting is not necessarily monotonous. The effective masses

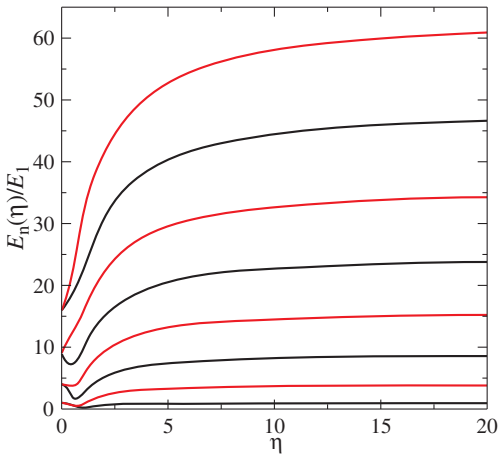

Fig. 1. Normalized positions of the subband minima with respect to the strain-dependent conduction band minimum as function of dimensionless shear strain for a film of thickness $t = 5.43$ nm.

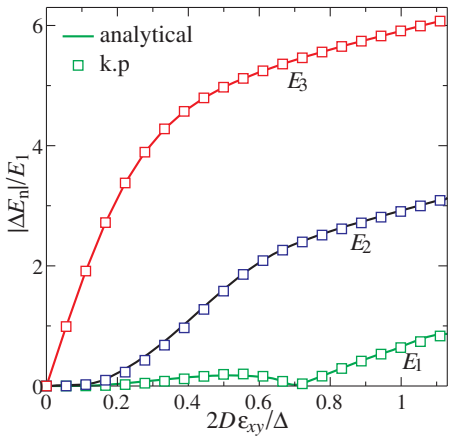

Fig. 2. Strain-dependent splitting between the minima of the unprimed subbands with the same n.

of the two ground subbands are depicted in Fig. 3. It was revealed that in ultra-thin films without strain the masses of the two ground subbands are not equal. The contour plots of the dispersions of the subbands are shown in Fig. 4. The two-band model provides the dependence on the film thickness of the effective mass in the first primed subband shown in Fig. 5 in comparison to first-principle results [6]. In order to demonstrate the unusual behavior we solve (1) by perturbation, which

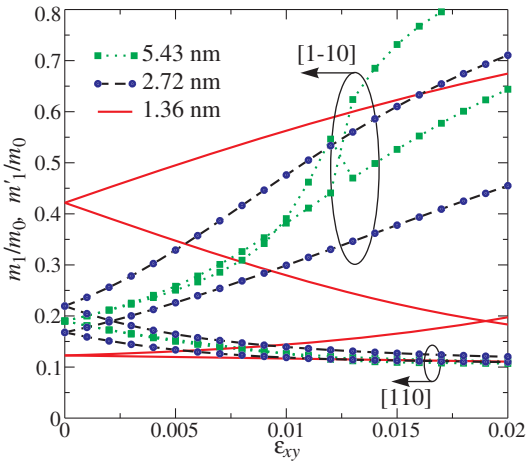

Fig. 3. Effective masses of the two ground subbands. In ultra-thin films the effective masses of the two ground subbands are different even without stress.

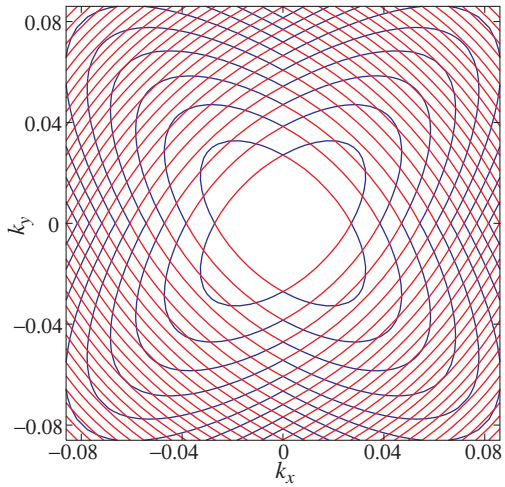

Fig. 4. Dispersions of the two ground subbands for a film thickness of 1.36 nm. The lower subband dispersion is described by the unification of the two ellipses with different masses, while the second subband is described by their intersection.

results in the dispersion relation:

$$E_n^{\pm} = \frac{\hbar^2 k_0^2 y_{0n}^2}{2m_l} + \frac{\hbar^2\left(k_x^2+k_y^2\right)}{2m_t} \pm \frac{y_{0n}^2\left|D\varepsilon_{xy} - \frac{\hbar^2 k_x k_y}{M}\right|}{\left|1-y_{0n}^2\right|}\sin(k_0 t), \tag{2}$$

providing that without strain ($\varepsilon_{xy} = 0$) the two ground subbands is characterized by different masses in [110] direction. Such a difference results in the splitting between the subbands linear vs. the magnetic field and in the enhanced splitting between the two different subbands for the case of a [110] point contact. The strain-induced subband splitting increases rapidly with decreased film thickness (Fig. 6).

3. Conclusions

We have shown that the two-fold degeneracy of the unprimed subbands is eliminated in thin films. This results in a subband splitting proportional to the strength of the perpendicular magnetic field. The valley splitting can be enhanced in [110] oriented point contacts, while it is suppressed in a [100] point contact. Finally, one controls and makes the valley splitting larger than the Zeeman splitting with shear strain. Therefore silicon appears to be very attractive for spintronic applications.

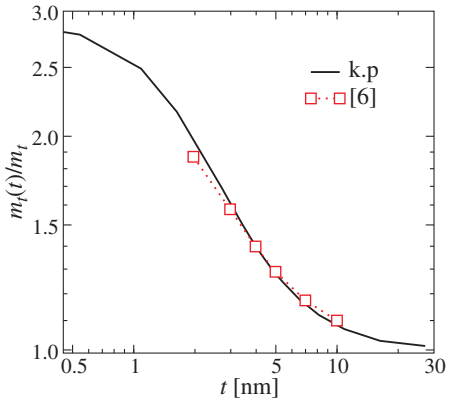

Fig. 5. The thickness dependence of the effective mass of the lowest primed subbands computed with the two-band $\mathbf{k}\times\mathbf{p}$ model (solid line) is in excellent agreement with the full-band calculations [6] (symbols).

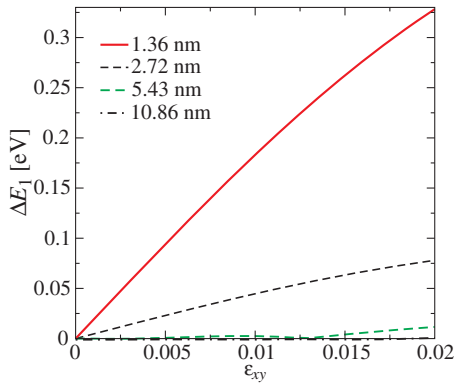

Fig. 6. Shear strain induced splitting of the ground subbands, for several film thicknesses. In ultra-thin films the splitting is larger than kT already for moderate stress.

Acknowledgements

This work was supported by the Austrian Science Fund (FWF) project P19997-N14.

References

[1] I. Appelbaum *et al*, *Nature* **447**, 295 (2007).
[2] S. Goswami *et al*, *Nature Physics* **31**, 41 (2007).
[3] G. L. Bir and G. E. Pikus, Symmetry and Strain-Induced Effects in Semiconductors, J. Willey & Sons, NY 1974.
[4] J. C. Hensel *et al*, *Phys. Rev.* **138**, A225 (1965).
[5] V. Sverdlov *et al*, *Sol. State Electron.* **52**, 1861 (2008).
[6] J. van der Steer *et al*, *IEEE Transactions on Electron Devices* **54**, 1843 (2007).

17th Int. Symp. "Nanostructures: Physics and Technology"
Minsk, Belarus, June 22–26, 2009
© 2009 Ioffe Institute

Anisotropy of phonon-plasmon modes in GaAs/AlAs (100) and (311) superlattices: Raman studies

V. A. Volodin

Institute of Semiconductor Physics of SB RAS, pr. ak. Lavrentjeva 13, Novosibirsk 630090, Russia
Novosibirsk State University, Pirogova street, 2, 630090, Novosibirsk, Russia

Abstract. Raman spectroscopy technique was applied to study phonon-plasmon coupled modes in Si doped set of GaAs/AlAs superlattices (SLs), grown on (100), (311)A and (311)B substrates. Anisotropy in dispersion of phonon-plasmon modes with wavevector normal to SL layers and in SL layers was observed for (100) SLs. Additional lateral anisotropy of the phonon-plasmon modes was observed for SLs grown on nano-corrugated (311)A surface. The observed anisotropy supposed to be result of charge carrier mass anisotropy appearing due to structural anisotropy.

Effects of interaction of phonons with electrons in bulk semiconductors and semiconductor superlattices (SLs) have long been under study of wide community of researchers [1] but are actual up today. The analysis of dispersion of phonon-plasmon modes in SLs can be express and non-destructive tools for measurements of charge carrier concentration and effective mass anisotropy [2].

The studied SLs were grown using molecular beam epitaxy technique on (311)A-(1×8) reconstructed GaAs substrate and (001)-(2×4) reconstructed GaAs substrate at temperature 550 °C. The control of reconstruction was carried out *in situ* with the use of reflection of high energy electron diffraction. In the case of (311) substrates the angle disorientation of the substrates from (311) direction was less than 15′.The flux of As_4 molecules was 5×10^{14} molecules/cm^2 per second, the growth rate was about 0.3 m/h for GaAs and 0.32 m/h for AlAs. All SL-satellites on (001) and (311)B GaAs substrates were grown in the same growth procedures "side by side". The (311)A and B surfaces were detected using anisotropy of chemically etching. The set of $GaAs_n/AlAs_m$ SLs were grown, data are shown in Table 1. To achieve electron concentration at room temperature 2×10^{18} cm^{-3}, the impurity (Si) concentration in doped SLs was 2.5×10^{19} cm^{-3}. Impurity of Si can be both acceptor and donor, but in chosen growth condition it give the n-type material.

The Raman spectra were registered at room temperature in backscattering geometry in various polarization geometries. The line 514.5 nm of Ar^+ laser was used as a light source. The triple spectrometer T64000 (Horiba Jobin Yvon) equipped with cooled CCD camera and micro-Raman setup was used. Polarization resolved Raman spectra were registered using polarization optics.

It is known, that in polar semiconductors the phonon-plasmon interaction takes place. It leads to coupling of phonon-plasmon modes and to shift and broadening of Raman peaks [1]. According to calculations to register effects phonon-plasmon modes anisotropy, the wavenumber of these modes should be about 10^6 cm^{-1}. So, one should use both "normal" scattering the wavevector of light is normal to SL, and "in-plane" geometry, shown in Fig. 1. The using of micro-Raman system allows to focus laser beam into SL edge in sport about 1 micrometer.

Table 1. Specifications of the studied SLs $GaAs_nAlAs_8$. 1 ML in 311 direction = 1.7 angstrom.

Substrate			GaAs	AlAs	Periods
311A	311B	100	thickness Å	thickness Å	
1A	1B	1	1.7	13.6	400
2A	2B	2	3.4	13.6	300
3A	3B	3	6.8	13.6	200
4A	4B	4	10.2	13.6	100

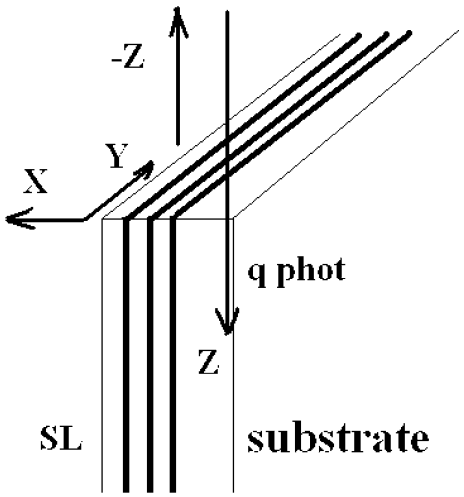

Fig. 1. Scheme of "in-plane" Raman geometry.

The Raman spectra of (100) GaAs/AlAs SLs for "normal" geometry are shown in Fig. 2.

One can see shift of LO^+ phonon-plasmon modes versus variation of GaAs layer thickness. The peaks at 240–280 cm^{-1} are due to scattering on localized optic phonons in GaAs layers. One can see also longitudinal optic (LO) bulk modes from GaAs substrate. It should be noted, that scattering on transverse optical (TO) phonons is forbidden in this geometry, but its appear supposal due to resonance phenomena.

In Fig. 3 one can see Raman spectra of (100) SLs registered in Z(YY)-Z geometry, Wavevector of initial light was parallel to Z axe, wavevector of scattered light was anti-parallel to Z axe, vector of polarization of light was parallel to SL layers (see Fig. 1). In the case of (100) SLs axe X is along (100), axe Y is along $(01-1)$, and axe Z is along (011) directions.

It should be noted, that the spectra in this "in-plane" geometry practically do not depend on polarization of light (the configurations Z(XX)-Z and Z(XY)-Z were also used).

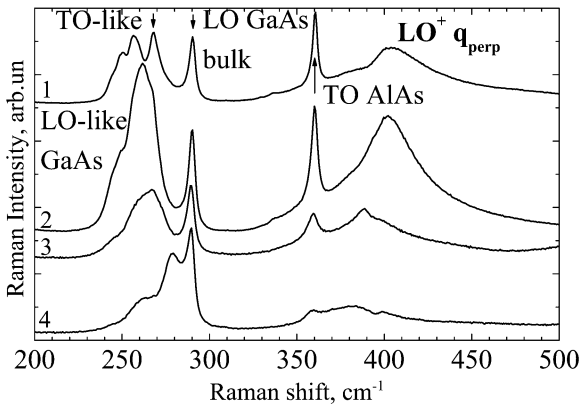

Fig. 2. Raman spectra in "normal" geometry for (100) SLs, curves 1–4 correspond to samples 1–4 in Table 1.

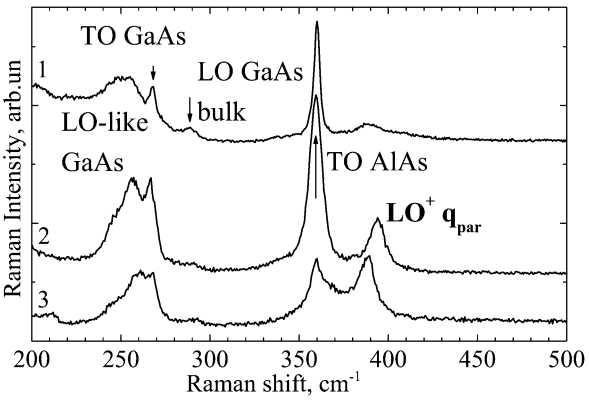

Fig. 3. Raman spectra in "in-plane" geometry for (100) SLs 1–3.

If one compare the spectra of the same (100) SLs but in various geometry (Figs. 2 and 3), the anisotropy of phonon-plasmon modes is clearly seen. The wavevector is perpendicular to SL layers in Fig. 2 and wavevector is parallel to SL layers in Fig. 2.

On Fig. 4 one can see an example of lateral anisotropy of (311)A SLs. It is known, that in some growth condition in (311)A surface GaAs form quantum well wire (QWW) like structure [3]. The (311)A surface is nano-corrugated with lateral period 3.2 nm along $(01-1)$ direction. So, it is possible to form structure with QWWs elongated along (-233) direction. In the case of (311) SLs axe X' is along $(01-1)$, axe Y' is along (-233), and axe Z' is along (311) directions. Solid line in Fig. 4 corresponds to Z'(X'X')-Z' geometry, dashed line corresponds to Y'(X'X')-Y' geometry, dot line corresponds to X'(Z'Z')-X' geometry. It should be noted, that axes X', Y', and Z' do not correspond to axes X, Y, and Z shown in Fig. 1.

One can see in Fig. 4 anisotropy for "in-plane" geometry. Wavevector can be parallel to QWWs (dashed line) or wavevector can be perpendicular to QWWs (dot line) in Fig. 4. In the last case the spectrum more like on spectrum in "normal" geometry (wavevector is also perpendicular to QWWs — solid line).

It is known, that structural lateral anisotropy is not so pronounced in the case of (311)B SLs [3]. The Raman experiment was also carried out for 2B SLs (see Table 1). Solid line in Fig. 5 corresponds to Z'(X'X')-Z' geometry, dashed line corresponds to Y'(X'X')-Y' geometry. One can see anisotropy for

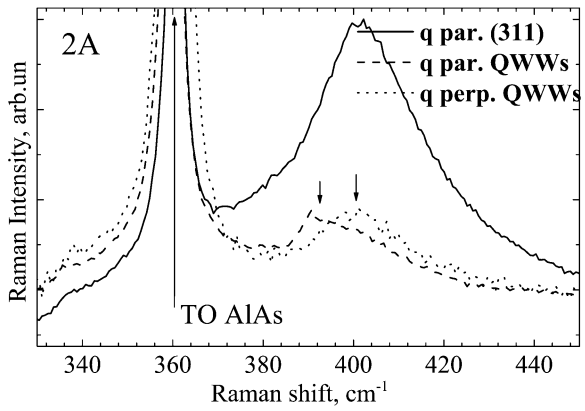

Fig. 4. Raman spectra in "normal" and "in-plane" geometries for 311A SL (sample 2A see Table 1). Arrows show the lateral anisotropy effect.

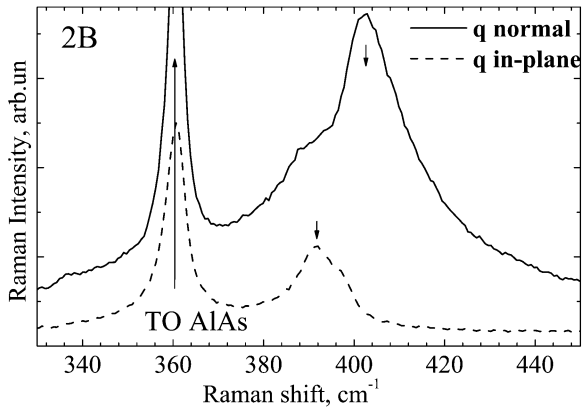

Fig. 5. Raman spectra in "normal" and "in-plane" geometries for 311B SL (sample 2B see Table 1). Arrows show the anisotropy effect.

"normal" and "in-plane" geometries. But for lateral effects, SLs (311)B were more like on (100) SLs without pronounced lateral anisotropy.

So, as it was predicted in calculations [2], the anisotropy in dispersion of phonon-plasmon modes, supposed due to effective mass anisotropy, was observed. The lateral anisotropy for (311)A SLs grown on nano-corrugated surfaces was observed.

Acknowledgements

Author is grateful to Drs. Preobrazhenskiy and Semyagin for growth of the SLs.

References

[1] M Cardona *et al*, *Light Scattering in Solids IV.Electronic Scattering, Spin Effects, SERC, and Morphic Effects*, Berlin, Germany 1982.

[2] V. A. Volodin *et al*, *Phys. Low-Dim. Strut.* **5/6**, 109 (2003).

[3] N. N. Ledentsov *et al*, *Journal of Electronic Materials* **30** (5), 463 (2001).

17th Int. Symp. "Nanostructures: Physics and Technology"
Minsk, Belarus, June 22–26, 2009
© 2009 Ioffe Institute

Emission of terahertz radiation from two-dimensional electron systems in semiconductor nano-heterostructures

Taiichi Otsuji[1,4], Yuki Tsuda[1], Hiromi Karasawa[1], Tetsuya Suemitsu[1,4], Maki Suemitsu[1,4], Eiichi Sano[2,4], and Victor Ryzhii[3,4]

[1] RIEC, Tohoku University, Sendai 980-8577, Japan
[2] RICIQE, Hokkaido University, Sapporo 060-8628, Japan
[3] CNEL, University of Aizu, Aizu-Wakamatsu 965-8580, Japan
[4] JST-CREST, Tokyo 102-0075, Japan

Abstract. This paper reviews recent advances in emission of terahertz radiation from two-dimensional (2D) electron systems in semiconductor nano-heterostructures. 2D plasmon resonance is first presented to demonstrate intense broadband terahertz emission from InGaP/InGaAs/GaAs material systems. The device structure is based on a high-electron mobility transistor and incorporates authors original doubly interdigitated grating gates. Second topic focuses on graphene, a monolayer carbon-atomic honeycomb lattice crystal, having attracted attention due to its peculiar carrier transport and optical properties holding massless and gapless energy spectrum. Stimulated terahertz emission from femtosecond laser pumped epitaxial graphene is experimentally observed, reflecting the occurrence of population inversion.

Introduction

In the research of modern terahertz (THz) electronics, development of compact, tunable and coherent sources operating in the THz regime is one of the hottest issues [1]. Two-dimensional (2D) plasmons in semiconductor nano-hetero-structures like electron channels in high-electron mobility transistors (HEMT) have attracted much attention due to their nature of promoting emission of THz electromagnetic radiation [2,3]. On the other hand, linear dispersion relations for the perfect 2D electrons and holes with zero energy bandgap in graphene [4–6] provide nontrivial features like negative-dynamic conductivity in the THz spectral range [7,8], which may bring a new type of THz lasers. This paper reviews recent advances in emission of terahertz radiation from 2D electron systems in semiconductor nano-heterostructures promoted by those unique features.

1. THz emission from 2D plasmon resonance

We are proposing our original 2D-plasmon-resonant microchip emitter as a new terahertz light source [9-14]. The structure is based on a HEMT and featured with interdigitated dual-grating gates. The dual grating gates can alternately modulate the 2D electron densities to periodically distribute the plasmonic cavities (100-nm width in microns distance) along the channel, acting as an antenna [9]. The device was fabricated using InGaP/InGaAs/GaAs material systems. The 2D plasmon layer is formed with a quantum well in the InGaAs channel layer. The dual grating gates are formed with an upper-deck semiconducting layer in place of a standard metallic layer to improve the conversion efficiency [9,13].

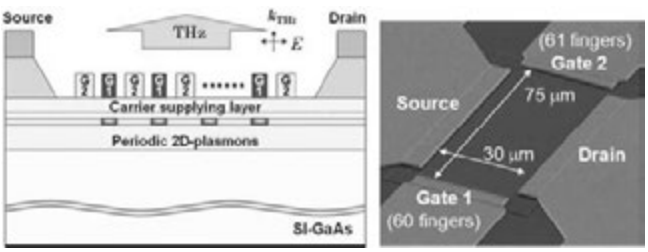

Fig. 1. Structure and image of the plasmon-resonant HEMT.

The field emission property of the fabricated chip was characterized by using a Fourier-transformed far-infrared spectrometer (FTIR). The detector was a 4.2 K-cooled Si bolometer. As shown in Fig. 2, the device emits 0.5-to-6.5 THz radiation with microwatt power at 300 K under appropriate bias conditions. Such a broadband emission with threshold/super-linear dependence on the drain bias is analytically interpreted as the excitation of multimode plasmons: thermal excitation of incoherent plasmons [12,15] and instability-driven and/or transit-time-driven self-exc-itation of coherent plasmons [2,16].

The fabricated sample was introduced to a FTIR system as a microchip THz source. Water-vapor absorption spectrum was successfully observed at 300K, which is proven to the standard data provided by NASA (see Fig. 3) [14]. Next, we measured the transmission spectra of two different types of sugar groups: honey and maple syrup, both of which contain their finger prints of featured spectrum in the THz region. The measured spectra were compared with the results for their main components measured by RIKEN (see Fig. 4). The results fairly exhibit identical spectral features for both materials [14]. To the best of the authors' knowledge, this is the first-time demonstration of THz sensing/spectroscopic applications utilizing room-temperature

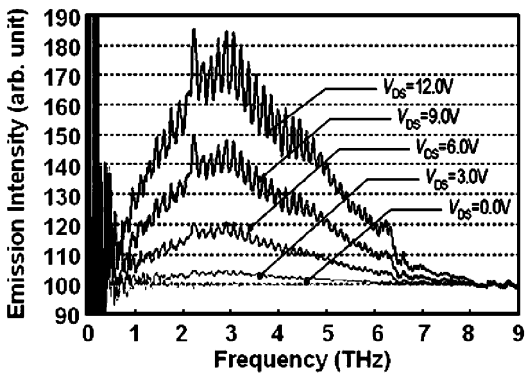

Fig. 2. FTIR measured emission spectra for a fabricated device.

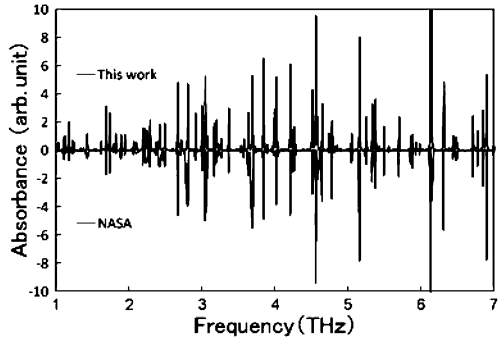

Fig. 3. Measured absorption spectrum of atmospheric water vapor in comparison with the data provided by NASA.

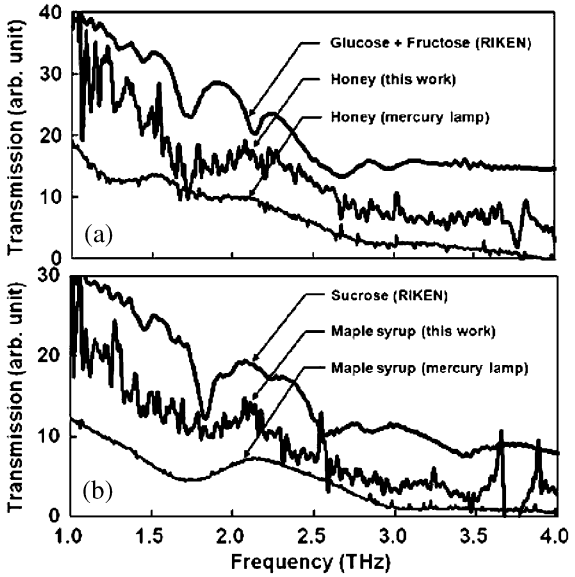

Fig. 4. Transmission spectra of sugar groups measured by using a plasmon-resonant emitter (this work) and by using a high-pressure mercury lump, and their main ingredient(s) provided by RIKEN. (a) honey vs. glucose and fructose, and (b) maple syrup vs. sucrose.

operating THz solid-state micro-light. Further improvements on its emission power enable the device to be of promising candidate as a new THz light source.

2. THz stimulated emission from epitaxial graphene on silicon

When graphene is pumped with the photon energy $\hbar\Omega$ electrons and holes are photogenerated via interband transitions. Due to a very short time of the optical phonon emission $\tau_0 \approx 10^{-12}$ s, the photogeneration of electrons and holes leads to the emission of a cascade of optical phonons, so that the photoelectrons and photoholes occupy the states with the energies close to $\varepsilon_N = \hbar(\Omega/2 - N\omega_0) < \hbar\omega_0$, where $\hbar\Omega$ the pumping photon energy, $\hbar\omega_0$ the optical phonon energy, and N the number of emitted optical phonons. As a consequence, photoelectrons/holes recombine to radiate THz photons with the energy $\hbar\omega = 2\varepsilon_N$ (see inset in Fig. 5) [7]. The incident photon spectra will reflect on the THz photoemission spectra as a proof of occurrence of such a process.

The real part of the net ac conductivity $\mathrm{Re}\,\sigma_\omega$ is proportional to the absorption of photons with frequency ω and comprises the contributions of both interband and intraband transitions.

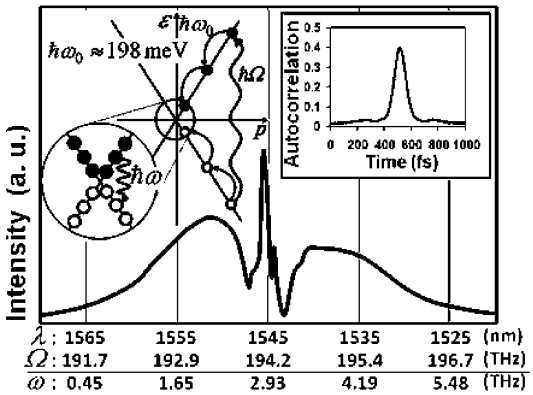

Fig. 5. Autocorrelation (inset) and spectral profiles for the pump&probe laser pulse. Carrier relaxation and recombination processes in graphene are also depicted.

$$\mathrm{Re}\,\sigma_\omega = \mathrm{Re}\,\sigma_\omega^{\mathrm{inter}} + \mathrm{Re}\,\sigma_\omega^{\mathrm{intra}}. \tag{1}$$

When graphene is weakly pumped ($\varepsilon_\mathrm{F} < k_\mathrm{B}T$), where $k_\mathrm{B}T$ the thermal energy, $\mathrm{Re}\,\sigma_\omega$ becomes [7]

$$\mathrm{Re}\,\sigma_\omega \cong \frac{e^2 g}{8\hbar}\left[1 + \frac{3}{2}\left(\frac{\omega - \bar{\omega}}{\omega}\right)^2 - \frac{I_\Omega}{\bar{I_\Omega}}\right], \tag{2}$$

where

$$\bar{g} = \left(\frac{4\ln 2}{\pi}\right)^{1/3}\left(\frac{\hbar}{k_\mathrm{B}T\tau}\right)^{1/3}, \bar{\omega} \approx \left(\frac{k_\mathrm{B}T\tau}{\hbar}\right)^{1/3}\frac{1.5}{\tau}, \tag{3}$$

τ the momentum relaxation time of electrons and holes. When the pumping intensity exceeds the threshold: $I_\Omega > \bar{I_\Omega}$, the conductivity becomes negative in a certain range around the minimum ω, $\omega \approx \bar{\omega}$. When $T = 300$ K, $\tau = 10^{-11}$, $\bar{I_\Omega} = 0.30(1 - 100)$ W/cm^2 for recombination time of $10^{-7\sim-9}$ s. Assuming a practical device size of 100×100 μm with a relatively intensive $10 \sim 100$-mW pumping intensity gives the negative dynamic conductivity, which is feasible.

We observed the carrier relaxation and recombination dynamics in optically pumped epitaxial graphene hetero-structures using THz emission spectroscopy [17]. An ultra-thin graphene layer was grown by the thermal decomposition of an 80-nm-thick 3C-SiC film heteroepitaxially grown on a B-doped Si(110) substrate [18]. Its 2D-band Raman spectra proven the existence of monolayer and bilayer of graphene, and the G-band spectra at 1595 cm^{-1} corresponds to the optical phonon energy of 198 meV [19]. A 1550-nm, 20-MHz, 80-fs pulsed fiber laser beam (Fig. 5) was impinged to the sample (normal to the surface). Its frequency spectra exhibit non-exponentially bumped big side-lobes apart from the main-lobe (Fig. 5).

Time-resolved electric-field intensity originated from the THz photon emission was electrooptically sampled by a Cd-Te crystal placed on the sample in total-reflection geometry [6]. Measured temporal profile (inset in Fig. 6) exhibited frequency-up/down chirped relaxation oscillation, and was damped in an exponential decay on the order of $\sim$10 ps corresponding to the relaxation of radiative electron-hole recombination. Its Fourier spectrum roughly traces the pumping photon spectrum (Fig. 6) [17]. The spectral drop below 2 THz in the lower side-lobe might be caused by the band-gap opening due to existing

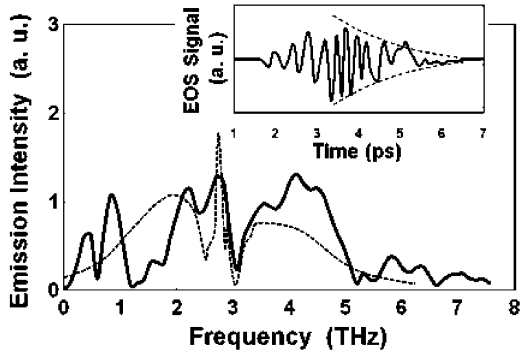

Fig. 6. Measured temporal profile (inset) and its Fourier spectrum (solid line). An image of the pumping photon energy spectrum is also shown with a dashed line.

bilayer graphene with the built-in vertical potential slope arisen at the heterointerface.

In conclusion, we successfully observed coherent, stimulated THz emission owing to the fast relaxation and relatively slow recombination dynamics of photogenerated electrons/holes in an epitaxial graphene heterostructure. The result well supports the occurrence of negative dynamic conductivity leading to the population inversion enabling a new type of THz lasers.

Acknowledgements

The authors would like to thank M. Dyakonov and M. Shur for valuable discussion. They also thank W. Knap, Y. M. Meziani, A. El Fatimy, D. Coquillat, A. Satou, V. V. Popov, T. Nishimura, and Y. Tsuda, for their contributions to the study on plasmon resonance, and H. Fukidome, H. Handa, Y. Miyamoto, T. Komori, T. Watanabe, and M. Ryzhii for their contributions to the study on graphene. This work has been suported in part by the Grant-in-Aid for BR(S) from JSPS. Japan, and by the JST-CREST, Japan.

References

[1] M. Tonouchi, *Nature Photon.* **1**, 97 (2007).
[2] M. Dyakonov and M. Shur, *Phys. Rev. Lett.* **71**, 2465 (1993).
[3] N. Dyakonova, F. Teppe, J. Lusakowski, W. Knap, M. Levinshtein, A. P. Dmitriev, M. S. Shur, S. Bollaert, and A. Cappy, *J. Appl. Phys.* **97**, 114313 (2005).
[4] A. K. Geim and K. S. Novoselov, *Nat. Mater.* **6**, 183 (2007).
[5] K. S. Novoselov, A. K. Geim, S. V. Morozov, D. Jiang, M. I. Katsnelson, I. V. Grigorieva, S. V. Dubonos, and A. Firsov, *Nature* **438**, 197 (2005).
[6] P. Kim, Y. Zhang, Y.-W. Tan, H. L. Stormer, *Nature* **438**, 201–204 (2005).
[7] V. Ryzhii, M. Ryzhii, and T. Otsuji, *J. Appl. Phys.* **101**, 083114 (2007).
[8] V. Ryzhii, M. Ryzhii, and T. Otsuji, *Phys. Stat. Sol. (c)* **5**, 261 (2008).
[9] T. Otsuji, M. Hanabe, T. Nishimura and E. Sano, *Opt. Express* **14**, 4815 (2006).
[10] T. Otsuji, Y. M. Meziani, M. Hanabe, T. Ishibashi, T. Uno, and E. Sano, *Appl. Phys. Lett.* **89**, 263502 (2006).
[11] T. Otsuji, Y. M. Meziani, M. Hanabe, T. Nishimura, and E. Sano, *Solid State Electronics* **51**, 1319 (2007).
[12] Y. M. Meziani, H. Handa, W. Knap. T. Otsuji, E. Sano, V. V. Popov, G. M. Tsymbalov, D. Coquillat, and F. Teppe, *Appl. Phys. Lett.* **92**, 201108 (2008).
[13] T. Otsuji, Y. M. Meziani, T. Nishimura, T. Suemitsu, W. Knap, E. Sano, T. Asano, V. V. Popov, *J. Phys.: Condens. Matters.* **20**, 384206 (2008).
[14] Y. Tsuda, T. Komori, T. Watanabe, T. Suemitsu, and T. Otsuji, *J. Opt. Soc. America B* (*in press*).
[15] V. V. Popov, G. M. Tsymbalov, and N. J. M. Horing, *J. Appl. Phys.* **99**, 124303 (2006).
[16] V. Ryzhii, A. Satou, M. Ryzhii, T. Otsuji, and M. S. Shur, *J. Phys.: Condens. Matters.* **20**, 384207 (2008).
[17] H. Karasawa, T. Komori, T. Watanabe, M. Suemitsu, V. Ryzhii, and T. Otsuji, *Conf. Tig. of CLEO/Europe-EQEC (Munich,2009)*, European Physical Society, CF8.3, 2009.
[18] M. Suemitsu, Y. Miyamoto, H. Handa, and A. Konno, *e-J. Surface Sci. and Nanotech.* (*in press*).
[19] Y. Miyamoto, H. Handa, E. Saito, A. Konno, Y. Narita, M. Suemitsu, H. Fukidome, T. Ito, K. Yasui, H. Nakazawa and T. Endoh, *e-J. Surface Sci. and Nanotech.* **7**, 107 (2009).

17th Int. Symp. “Nanostructures: Physics and Technology”
Minsk, Belarus, June 22–26, 2009
© 2009 Ioffe Institute

Plasmonics: science and terahertz applications

Viacheslav Muravev and Igor Kukushkin
Institute of Solid State Physics RAS, Chernogolovka, Moscow district, Institutskaya 2, 142432 Russia

Abstract. There has been an increasing interest in the basic properties of robust collective phenomena such as plasma excitations in low-dimensional electron systems. Compared with, for example light waves, plasma excitations offer powerful additional degrees of freedom to alter the dispersion, since the plasmon velocity is easily tuned through the application of a magnetic field or by changing the electron density. For this reason different wave phenomena such as interference and tunable band gap formation could be investigated on a single semiconductor nanostructure. The plasmon properties are greatly affected by the dielectric properties of matter in the immediate vicinity of the two-dimensional electron system. This fact gives a convenient tool to manipulate with the plasmon dispersion low and gives rise to a whole series of unconventional plasma modes. An important impetus to study plasma waves in nanostructures comes from potential applications. The fact that resonant plasmon frequency falls into the terahertz frequency range make it possible to build a new generation of low-cost, tunable giga-terahertz “on-chip” detectors-spectrometers. Matrix cameras can be easily created on the basis of the single detector. The cameras may be used for terahertz vision.

17th Int. Symp. "Nanostructures: Physics and Technology"
Minsk, Belarus, June 22–26, 2009
© 2009 Ioffe Institute

Trapped oblique plasmon modes and tremendous shrinking of terahertz plasmon resonance in a multichannel nanotransistor

V. V. Popov

Kotelnikov Institute of Radioengineering and Electronics (Saratov Branch), Saratov, 410019, Russia

Abstract. Terahertz radiation impinging on a multichannel high-electron-mobility transistor (MC-HEMT) excites oblique plasmons modes that can be trapped within two-dimensional rectangular microcavities in the gated region of the MC-HEMT channel, which prevents leakage of the gated plasmon energy into the ungated plasmon reservoir. These results can explain significant shrinking of the gated plasmon resonance linewidth in MC-HEMT.

Introduction

Plasmon oscillations excited under the gate contact (gated plasmons) in a high-electron-mobility transistor (HEMT) can be used for tunable resonant detection of terahertz (THz) radiation [1]. The plasmon resonance linewidth characterizing the selectivity of the resonant plasmon detector is determined by plasmon damping via all possible damping mechanisms. Electron scattering in two-dimensional (2D) electron channel contributes to the full width at half maximum (FWHM) of the plasmon resonance line as $1/\tau$, where τ is the electron momentum relaxation time. However, measured FWHM of the plasmon resonance in InGaAs/InAlAs HEMT with a sub-100-nm-long gate [2] amazingly exceeded the $1/\tau$-contribution by an order of magnitude. This broadening of the plasmon resonance linewidth was interpreted in [3] in terms of the effect of intermode plasmon-plasmon scattering leading to the leakage of the gated plasmon energy into continuum of the ungated plasmons excited in the ungated access regions of 2D electron channel. Such considerable broadening might vastly deteriorate the selectivity of HEMT based plasmon detectors of THz radiation.

Recently, Refs. [4] and [5] reported on a dramatic reduction of the plasmon resonance linewidth down to the $1/\tau$-contribution in a InGaAs/InAlAs multichannel HEMT (MC-HEMT). In this MC-HEMT, an initially wide 2D electron channel was etched through and divided into many narrow separate nanochannels (55 separate nanochannels in Refs. [4] and [5]) leaving rectangular gated-channel nano-cavities with area of 200×200 nm^2 and 500-nm repetition distance athwart the channel. In this paper, the staggering shrinking of the plasmon resonance in MC-HEMT is interpreted in terms of the effect of trapping of the oblique plasmons excited in the MC-HEMT by incoming THz radiation within the gated-channel nanocavities.

1. Discussion

In conventional HEMTs, the channel width is much larger than the gate length (typically, by two or even three orders of magnitude). Due to long-scale homogeneity along the device width, the transverse in-plane component of the wavevector (athwart the channel) is conserved in the course of the linear (one-photon) electromagnetic process of interaction between THz radiation and plasmons in the HEMT channel. Therefore, THz radiation incident at normal direction upon the HEMT structure (with no in-plane component of the THz-radiation wavevector) can only excite gated plasmons with wavevectors directed along the channel. The electric field of the incident THz radiation has to be polarized in this direction (or, at least, has a nonzero component of the electric field in this direction) in order to couple with the gated plasmons. In a simplified model implying that the nodes of the plasmon current are located directly under the gate contact edges, the wavevectors q of the gated plasmons can be estimated as $q = m\pi/l$, where l is the gate length with m being an integer ($m = 1, 2, 3, \ldots$). (In a real HEMT structure, the boundary conditions at the gate edges are different due to a fringing-field effect, which can be taken into account by introducing an effective gate length $l_{\text{eff}} > l$ [6]). Note that only the gated plasmon modes with odd m-th ($m = 1, 3, 5, \ldots$) can be excited by THz radiation because those with even m-th ($m = 2, 4, 6, \ldots$) have zero net dipole moment and, hence, do not couple to THz radiation.

Strictly speaking, in the case of obliquely incident THz radiation (e.g., in an uncollimated THz beam), there might be some deviation in the direction of the gated plasmon wavevector caused by nonzero in-plane component of the THz-radiation wavevector. However, this effect is very small because the THz radiation wavevector is much smaller (typically by three orders of magnitude) than the plasmon wave-vector. Hence, the oblique gated plasmon modes (i.e., plasmon modes traveling athwart the channel along the gate finger [7]) cannot normally be excited by THz irradiation of the HEMT with a wide channel (unless the homogeneity athwart the channel is broken due to small uncontrollable corrugations of the structure). Of course, the converse statement is also correct: the oblique plasmon modes once excited either by a stimulated [7] or thermal mechanism in a HEMT with a wide channel cannot be emitted from the structure in the form of THz radiation without relying on special coupling elements (such as grating couplers with periodicity athwart the channel).

The transverse in-plane component of the plasmon wavevector also conserves during the process of intermode plasmon-plasmon scattering so that both the gated and ungated plasmons may be considered having zero in-plane component of the wavevector athwart the channel in a HEMT with a wide channel. In general, wavevectors of the ungated plasmons differ from those of the gated plasmons (typically, the wavevectors of ungated plasmons are smaller). In this case, an umk-

lapp process of the plasmon intermode transformation, leading to significant broadening of the gated plasmon resonance linewidth [3], becomes possible only due to abrupt discontinuities at the edges of the gate contact.

In contrast to the case of a wide homogeneous electron channel, the oblique plasmon modes can be excited by THz irradiation of the MC-HEMT because a periodic sequence of the separate nanochannels breaks the homogeneity of the structure along the gate finger, hence, making the THz excitation of the oblique plasmon modes possible. The frequencies of the gated plasmon modes in each rectangular gated-channel nanocavity having length l and width w are

$$\omega_{mn} = s\sqrt{q_x^2 + q_y^2} \quad (m, n = 1, 2, 3, \ldots)\,, \tag{1}$$

where $q = m\pi/l$ and $q = m\pi/w$ are the longitudinal and transverse in-plane components of the gated-plasmon wavevector along and athwart the channel, respectively, and s is the plasma wave velocity, which can be changed by varying the gate voltage.

Each of the plasmon modes with the spectra described by Eq. (1) with a given wavevector component q_x can be understood as the superposition of two *oblique plasmon modes* with counter-directed wavevectors q_y and $-q_y$ traveling athwart the channel. Let us consider the oblique gated-plasmon mode with wavevector (q_x, q_y) incident upon the boundary between the gated and ungated regions of the channel. The HEMT structures studied in Ref. [4] and [5] also have highly doped cap layers above the ungated regions of the channel, which screen the ungated plasmons [8] yielding a linear plasmon dispersion in these capped regions

$$\omega = \hat{s}\sqrt{\hat{q}_x^2 + \hat{q}_y^2}\,, \tag{2}$$

which is similar to that of the gated plasmons given by Eq. (1), with $\hat{q}_x$ and $\hat{q}_y$ being the longitudinal and transverse components of the ungated plasmon wavevector, respectively. The phase velocity of the ungated plasmons $\hat{s}$, is controlled by the electron density in ungated access regions of the MC-HEMT channel, which does not depend on the gate voltage.

Because the transverse in-plane component of the plasmon wave-vector conserves ($\hat{q}_y = q_y$), Eq. (2), subject to $q_y = \omega \sin\theta/s$, can be rewritten as

$$\hat{q}_x = \frac{\omega}{s}\sqrt{\left(\frac{s}{\hat{s}}\right)^2 - \sin^2\theta}\,, \tag{3}$$

where θ is the angle of incidence of the oblique gated plasmon upon the gate edge in the 2D channel plane (x-y plane). Since the phase velocity of the gated plasmons is typically smaller then that of the ungated plasmons, the expression under radical in Eq. (3) becomes negative if $\sin\theta > (s/\hat{s})$, which yields pure imaginary wavevector component $\hat{q}_x$ of the ungated plasmon wavevector. In this case the oblique gated plasmons are totally reflected from the boundaries between the gated and ungated regions of the channel, being trapped within the gated-channel nanocavities. Because of this the intermode plasmon-plasmon scattering becomes suppressed.

Our estimates show that the plasmon total reflection angle, $\theta_R = \sin^{-1}(s/\hat{s})$ is about 38° in experiments [4,5]. In a gated-channel nanocavity of the MC-HEMT, the components of the gated plasmon wavevector can be estimated as $q_x = m\pi/l$ and $q_y = n\pi/w$ so that the angle of incidence of the gated plasmons upon the gate edge is $\theta = \tan^{-1}(nl/mw)$. Considering the lowest-order plasmon mode having indexes $m = 1$ and $n = 1$ one has $\theta = 45°$ for nearly squared ($l \approx w \approx 200$ nm) gated-channel nanocavities of the MC-HEMT structure studied in Refs. [4] and [5]. In this case, $\theta > \theta_R$ and, hence, the total internal reflection of the gated plasmons prevents the intermode plasmon scattering, which can explain significant shrinking of the gated plasmon resonance linewidth (down to the $1/\tau$-contribution) in the MC-HEMT [4,5] compared to that in a conventional HEMT with a single wide channel [2].

2. Conclusions

In conclusion, the excitation of oblique plasmon modes in a multichannel HEMT by incoming THz radiation can suppress the intermode plasmon-plasmon scattering due to the total internal reflection of the gated plasmons from the gate edges. This effect must lead to significant shrinking of the gated plasmon resonance line, which is very important for increasing the selectivity of HEMT based plasma wave detectors of THz radiation.

Acknowledgements

This work has been supported by the GDR-E project "Semiconductor Sources and Detectors for Terahertz Frequencies", the Russian Foundation for Basic Research (Grant Nos. 06-02-16155 and 09-02-00395), and the Russian Aca-demy of Sciences Program "Basic Research in Nanotechnology and Nanomaterials".

References

[1] M. Dyakonov and M. Shur, *IEEE Trans. Electron. Devices* **43**, 380 (1996).
[2] A. El Fatimy *et al*, *Appl. Phys. Lett.* **89**, 131926 (2006).
[3] V. V. Popov *et al*, *Appl. Phys. Lett.* **93**, 263503 (2008).
[4] S. Boubanga-Tombet *et al*, *Appl. Phys. Lett.* **92**, 212101 (2008).
[5] A. Shchepetov *et al*, *Appl. Phys. Lett.* **92**, 242105 (2008).
[6] V. V. Popov *et al*, *J. Appl. Phys.* **98**, 033510 (2005).
[7] M. I. Dyakonov, *Semiconductors* **42**, 984 (2008).
[8] V. Ryzhii *et al*, *J. Appl. Phys* **99**, 084507 (2006).

17th Int. Symp. "Nanostructures: Physics and Technology"
Minsk, Belarus, June 22–26, 2009
© 2009 Ioffe Institute

Impurity-assisted terahertz emission from GaAs quantum wells and GaN epilayers at lateral electric field

V. A. Shalygin[1], L. E. Vorobjev[1], D. A. Firsov[1], V. Yu. Panevin[1], A. N. Sofronov[1], G. A. Melentyev[1], A. V. Andrianov[2], A. O. Zakharyin[2], N. N. Zinov'ev[2], A. E. Zhukov[2], V. S. Mikhrin[2], A. P. Vasil'ev[2], S. Suihkonen[3] and H. Lipsanen[3]

[1] St Petersburg State Polytechnic University, 195251 St Petersburg, Russia
[2] Ioffe Physical-Technical Institute, St Petersburg, Russia
[3] Helsinki University of Technology, FI-02150 Espoo, Finland

Abstract. Emission of terahertz radiation from n-GaAs quantum wells (QWs) and n-GaN epilayers was observed at lateral electric field exceeding impurity breakdown threshold. The experimental spectra demonstrate several types of emission lines. In doped GaAs QWs some of these lines can be assigned to optical electron transitions between resonant and localized states of the donors. In GaN epilayers the major lines can be attributed to intracenter electron transitions and to transitions between conduction band and the ground state of donors (Si and O). The structures investigated can be suitable for development of electrically pumped THz emitters.

Introduction

In terahertz (THz) spectral range electrically pumped emitters based on semiconductors with shallow impurities are promising low-cost alternative to quantum cascade lasers. Over the past few years, many investigations were devoted to the development of an impurity-doped silicon laser. Firstly, THz lasing from phosphorus-doped bulk silicon has been observed via optical pumping [1]. Intense spontaneous THz emission from P-, B- and Ga-doped silicon devices has also been achieved via electrical pumping [2–4]. It has been shown in [4] that the maximal operating temperature of THz emitters based on intracenter optical transitions in bulk Si should not exceed $T \sim 40$ K.

Stimulated emission in the THz range has been observed from uniaxially stressed p-type germanium at strong external electric fields [5,6]. Spontaneous THz emission has been also studied from p-GaAsN/GaAs microstructures containing built-in strain at the conditions of electric breakdown of the shallow impurity [7]. In papers [5–7] the major contribution to the emission spectrum is attributed to the optical transitions between the resonant and localized impurity states.

In the present paper we report on the observation of spontaneous THz emission from n-GaAs quantum wells and n-GaN epilayers at lateral electric field. At first we present current-voltage characteristics and field dependencies of integrated emission intensity in the spectral range from 50 to 130 μm measured by means of liquid-helium-cooled Ge:Ga detector. Then we discuss emission spectra which were measured using a Fourier spectrometer operating in step-scan mode, as described in [8]. In the latter case THz radiation was detected by liquid-helium-cooled Si bolometer using lock-in technique.

1. GaAs quantum wells

The structures were grown by molecular beam epitaxy on (001) SI-GaAs substrate and contained 200 periods of GaAs/AlGaAs quantum wells. Well and barrier widths were 30 and 7 nm respectively. Central part of each QW was doped with Si, so that the electron sheet concentration was 10^{11} cm^{-2}. Two ohmic contacts with a separation of 4.6 mm were produced on the top surface of QW structure.

At the temperature $T = 4.2$ K all impurities are frozen, but in the fields exceeding 10 V/cm super-linear increase of the current is observed (Fig. 1) due to impurity breakdown processes. Simultaneously THz emission appears. The THz emission spectra at different values of electric fields are shown in Fig. 2. One can see that the line with a maximum at 13.6 meV dominates the THz emission spectrum at relatively weak electric field ($E = 34$ V/cm). This line can be attributed to optical transition of *hot* electrons from the $n = 1$ subband of the conduction band to the donor ground state ($e1 - 1s$ transitions). Two less intensive emission lines at 5.8 and 7.3 meV are also seen in the spectrum, they can be assigned to optical transitions between localized states of the donor impurity in QWs ($np_{x,y} - 1$ s optical transitions). The spectral positions of these lines are close to that expected from numerical simulation [9].

With increase of electric field the major emission line gets broader and its maximum slightly shifts to higher energies (see Fig. 2). At the same time the new features appear in the THz emission spectra, namely: the lines at 11.5 and 18.6 meV emerge in the spectra at higher electric fields. The results of calculations [9] allow to attribute them to optical transitions from resonant donor state $2p_z$ (the donor state which hits upon continuum of the $e1$ subband) to localized donor states ($2s$ and $1s$). It is important to note that these optical transitions are similar to that were proposed in [6] as the scheme for lasing at THz frequencies.

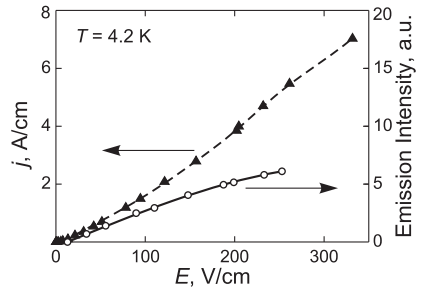

Fig. 1. Current density (left axis) and integrated THz emission intensity (right axis) versus electric field in n-GaAs QWs.

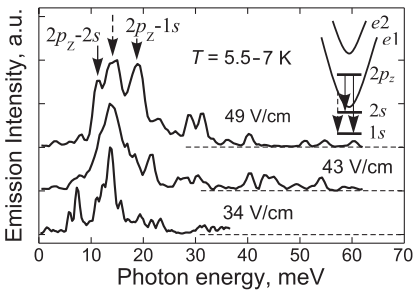

Fig. 2. Spectra of THz emission from n-GaAs QWs for different electric fields. Solid arrows denote intracenter optical transitions from resonant state $2p_z$ in accordance with theoretical simulation [9]. Dashed arrows correspond to hot electron transitions $e1 - 1s$.

2. GaN epilayers

Gallium nitride epitaxial layers of 4 μm thickness were grown on sapphire substrate by means of MOCVD method. The GaN layers were intentionally undoped but they contained residual shallow donors (Si and O) providing electron concentration of 6×10^{16} cm^{-3} at room temperature. Electron mobility was about 230 cm^2/V s. Two Ti/Au contacts with a separation of 4.6 mm were produced on the top surface of GaN epilayer.

At liquid helium temperature all shallow donors are frozen out and current-voltage characteristic demonstrates impurity breakdown behavior in the electric field range from 500 to 2000 V/cm (Fig. 3), at fields exceeding 3000 V/cm one can see sub-linear $j - E$ dependence due to electron mobility decrease caused by carrier heating. The phenomenon of THz electroluminescence in n-GaN epilayers has threshold character. The THz emission arises at electric field of about 600 V/cm close to shallow impurity breakdown threshold (Fig. 3).

At the temperature of 77 K the majority of Si and O donors is still not ionized in the absence of electric field. In the case of Si less than 20% of donors are thermally ionized due to relatively small density of states in the conduction band of GaN (one valley with the effective mass of $0.2m_0$). That is why at this temperature the impurity breakdown processes start under high enough electric fields causing THz emission. Experimental spectra analysis allows to attribute observed THz emission to optical electron transitions from GaN conduction band to the ground donor state ($c - 1s$) and to intracenter transitions from excited donor state to the ground one ($2p - 1s$), see Fig. 4. For Si (O) donors the energies of these transitions are 30.4 and 22.5 meV (33.2 and 24.9 meV), respectively [10].

The experimental results on THz emission from n-GaN epi-

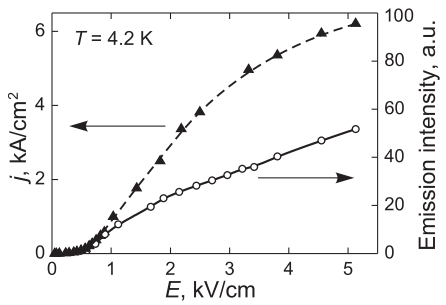

Fig. 3. Current density (left axis) and integrated THz emission intensity (right axis) versus electric field in n-GaN epilayer.

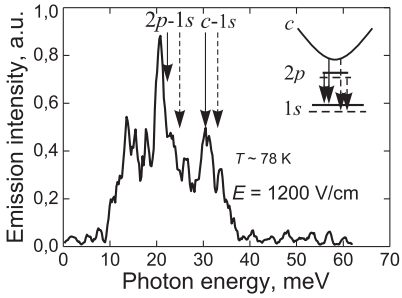

Fig. 4. Spectra of THz emission from n-GaN epilayers at $T \sim 78$ K. Solid and dashed arrows denote optical transitions to ground state of Si and O donors, respectively.

layers are promising for development of THz emitters operating at $T \geq 77$ K. Structures based on n-GaN also provide at $T \sim 4$ K much more effective THz electroluminescence than n-GaAs QW structures. In the former case emission intensity is about one order of magnitude larger at the same applied electric power.

Acknowledgements

This work is supported by the Academy of Finland (grant 118542), RFBR and Ministry of Education and Science of Russian Federation.

References

[1] S. G. Pavlov *et al*, *Phys. Rev. Lett.* **84**, 5220 (2000).
[2] P. -C. Lv *et al*, *Appl. Phys. Lett.* **85**, 22 (2004).
[3] P. -C. Lv *et al*, *Appl. Phys. Lett.* **85**, 3660 (2004).
[4] S. A. Lynch *et al*, *Appl. Phys. Lett.* **87**, 101114 (2005).
[5] I. V. Altukhov *et al*, *JETP Lett* **59**, 476 (1994).
[6] M. A. Odnoblyudov *et al*, *Phys. Rev. Lett.* **83**, 644 (1999).
[7] V. A. Shalygin *et al*, *Appl. Phys. Lett.* **90**, 161128 (2007).
[8] A. V. Andrianov *et al*, *JETP Lett* **79**, 365 (2004).
[9] M. Helm *et al*, *Phys. Rev. B* **43**, 13983 (1991).
[10] P. P. Paskov *et al*, *Phys. Stat. Sol. (c)* **4**, 2601 (2007).

17th Int. Symp. "Nanostructures: Physics and Technology"
Minsk, Belarus, June 22–26, 2009
© 2009 Ioffe Institute

Terahertz difference frequency generation in dual-frequency InGaAsP/InP laser with InGaAs quantum wells

A. A. Dubinov and V. Ya. Aleshkin
Institute for Physics of Microstructures RAS, 603950, Nizhny Novgorod, Russia

Abstract. The scheme of a semiconductor laser with quantum wells for simultaneous generation of TE_0 and TM_0 modes with different near-IR frequencies is proposed. The effective terahertz difference frequency generation is studied theoretically in such laser. It is shown that the power of the difference mode in the 1–8 THz range generated by 1-W near-infrared modes in a 100-μm-wide laser at room temperature can be $\sim$1 μW.

Introduction

One way of terahertz frequency generation is a difference frequency generation ($\omega = \omega_2 - \omega_1$) resulting from mixing two near-IR fields at frequencies ω_1 and ω_2 [1] in a quadratically nonlinear ($\varepsilon^{(2)}$) semiconductor structure A_3B_5 [2]. Since the wave intensities in semiconductor laser cavities are large, difference frequency generation can be realized directly in theirs [3]. In this case two problems should be solved. First problem is dual-frequency semiconductor laser creation. Second problem is realization of phase-matching condition for difference frequency generation. The scheme of butt-joint diode laser can be used for simultaneous dual-frequency generation [4]. However, the production of such laser is complex in comparison with one-chip laser and the butt-joint diode laser doesn't permit generation of near frequencies so that laser gain regions recover. Stable dual-frequency generation in one-chip laser was found for TE_0 and TE_1 modes at liquid nitrogen temperature only [5].

In this work we propose a new scheme for simultaneous dual-frequency generation in semiconductor laser. The use of different polarization modes (TE_0 and TM_0) is suggested in order to avoid absorption of the radiation with smaller wavelength in deepest quantum well. In accordance with selection rules [6], the type of upper hole subband in quantum well determines the generated mode polarization. The quantum well with upper heavy hole subband generates TE mode. The quantum well with upper light hole subband generates TM mode mainly.

The control of the upper hole subband type can be realized by quantum well deformation in grown plane. If a quantum well is strained in grown plane, than there is upper light hole subband for not very small quantum well thickness. If a quantum well is not strained or is griped in grown plane, than there is upper heavy hole subband. Probably, the simple control of quantum well deformation can be realized in InP/$In_xGa_{1-x}As$ heterostructure, where $In_xGa_{1-x}As$ layer is a quantum well. The lattice constant of $In_{0.53}Ga_{0.47}As$ coincides to that of InP [7]. The lattice constant of $In_xGa_{1-x}As$ increases with indium part growth.

So the InP-based laser scheme is proposed in this work for simultaneous near-IR TE_0 and TM_0 mode generation. Near-IR modes will spread in $In_{0.77}Ga_{0.23}As_{0.5}P_{0.5}$ layer and two different quantum wells will take up position in the center of this layer. The quantum wells will generate two fundamental modes with different frequencies and polarizations. The active region for the TE_0 mode generation is quantum well $In_{0.57}Ga_{0.43}As$ with thickness 5 nm ($\hbar\omega_1 \approx 0.819$ eV), and the active region for the TM_0 mode generation is quantum well $In_{0.4}Ga_{0.6}As$ with thickness 9 nm ($\hbar\omega_1 \approx 0.831$ eV). The layer parameters of the laser, in which difference frequency is generated, is shown in Table 1.

The phase-matching condition, which is necessary for effective difference frequency generation, is satisfied for two fundamental modes by thickness selection of $In_{0.77}Ga_{0.23}As_{0.5}P_{0.5}$. This condition consists to the equality the phase velocities of the polarization wave, produced by nonlinearity-induced interaction between near-IR modes, and the difference frequency propagating mode. It is significant that it is possible by small refractive index dispersion of $In_{0.77}Ga_{0.23}As_{0.5}P_{0.5}$ in wavelength region of stimulated radiation in this laser [8]. InP has sufficiently large second order nonlinearity in terahertz frequency range, which exceeded 3 times that in GaAs [8]. The use of semiinsulated substrate for suggested laser will reduce difference frequency absorption by optical phonons and free carriers significantly, because difference mode will propagate in the substrate mainly, and substrate will play a role of the oversize cavity.

1. The calculation of the difference frequency power

In the case when the laser waveguide is grown on the (001)-plane substrate and the near-IR modes propagate along the [110] direction, the nonlinear polarization in $In_{0.77}Ga_{0.23}As_{0.5}P_{0.5}$ has planar and normal to the plane of layers components and the TE and TM mode is generated at the difference frequency, correspondingly. The z-axis is directed along the crystallographic direction [001].

Polarization difference of the near-IR modes suppresses ab-

Table 1.

#	Layer composition	Type conductivity	Carrier concentration, cm^{-3}	Layer thickness, μm
1	InP	semiinsul.	–	150
2	InP	n	10^{18}	0.1
3	InGaAsP	n	10^{18}	0.8
4	InP	p	2×10^{18}	4
5	InP	p	10^{19}	0.2
6	Au	–	–	0.2

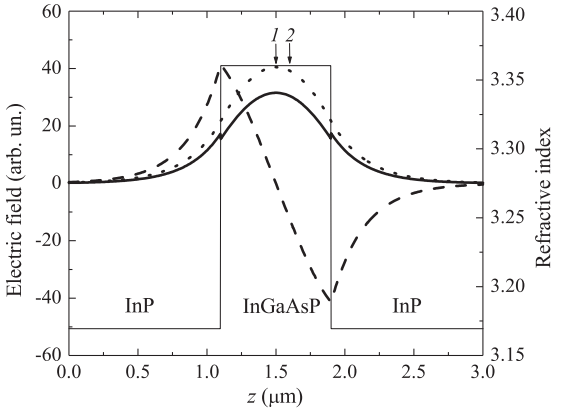

Fig. 1. Refractive index for $\hbar\omega_1 = 0.819$ eV (thin solid line) and electric fields versus coordinate z in laser with parameters from Table 1: E_{1y} — dotted curve, E_{2z} — solid curve, E_{2x} — dashed curve. Arrows indicate place of quantum wells: 1 — $In_{0.57}Ga_{0.43}As$, 2 — $In_{0.4}Ga_{0.6}As$.

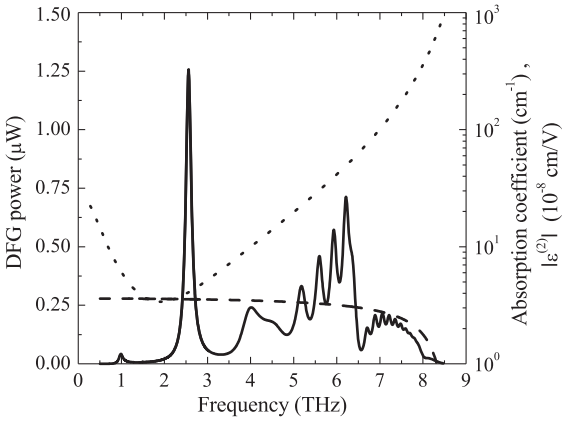

Fig. 2. The difference frequency generated power (solid curve) and absorbtion coefficient (dotted curve) versus the difference frequency in laser with parameters from Table 1 at room temperature ($\hbar\omega_1 = 0.819$ eV). Dashed curve corresponds to the dependence of the module of $\varepsilon^{(2)}$ in InP on the difference frequency.

sorption of the electric field's z-component (directed normal to structure layers) with frequency ω_2 in frequency ω_1 generated quantum well. If frequency ω_1 generated quantum well is placed to a node of the electric field's x-component (directed along wave propagation) with frequency ω_2, the absorption of this component can be suppressed. These conditions will permit to realize dual-frequency generation in proposed laser. Indeed, in this case fundamental TM_0 mode has one magnetic field's y-component (directed along structure layers and normal to wave propagation) only. The magnetic field's component H_{2y} and electric field's component E_{2x} are connected by next ratio: $E_{2x}(z) = -i(c/\varepsilon(z,\omega_2)) \times (dH_{2y}/dz)$. Where c — the light velocity in vacuum, $\varepsilon(z,\omega)$ — the permittivity of structure layers. So E_{2x} component has a node in a loop of the H_{2y} component, and overlap integral of fields E_1 and E_2 is substantially smaller overlap integral of fields E_1 and E_{2z} (see Fig. 1). So we considered TE-polarization of difference frequency wave only.

The difference frequency power is calculated as approximation, that $\alpha L \gg 1$ (α — the absorption factor by difference frequency, L — laser length). In this case the difference frequency power doesn't depend on L. In the calculation next parameters are used: waveguide wide is 100 μm and power of each near-IR modes is 1 W.

The calculated difference frequency power for suggested diode laser is shown in Fig. 2. The smallest frequency for a near-infrared mode ω_1 is fixed in our calculation. The frequency of the difference mode is changed by variation of the frequency of another near-IR mode. The spectral dependence of power features a number of resonance peaks. Each peak corresponds to oversize waveguide mode, for which the phase-matching condition is satisfied. The results of our calculations indicate that the difference mode can be generated with a power of $\sim$1 μW in the ranges 1–8 THz. It is significant, that the difference frequency mode propagates in InP substrate for the most part, and near-IR modes interaction takes place in $In_{0.77}Ga_{0.23}As_{0.5}P_{0.5}$ layer, which was grown by this InP substrate. Figure 2 shows that the difference frequency radiation power has maximum about frequency 2.6 THz, caused by the minimum of the absorption in proposed structure. In the frequency region smaller than 2.6 THz a growth of the absorption with frequency reduction is caused by the free carriers absorption in doped structure layers. In the frequency region larger than 2.6 THz a growth of the absorption with frequency growth is caused by the optical phonons absorption in the structure. Moreover, the reduction of $\varepsilon^{(2)}$ happens with frequency growth.

2. Conclusions

The results of our calculations indicate that for near-IR modes power around 1 W, the difference mode can be generated with a power of $\sim$1 μW in the ranges 1–8 THz in InP/InGaAsP/InGaAs laser with 100-μm-wide waveguide at room temperature.

Acknowledgements

This work has been supported by grants from the RFBR (07-02-12177, 07-02-00486, 08-02-90054, 08-02-97034, 09-02-97025), the RAS Programs "Modern problems of Radiophysis" and "Physical and technologic investigations of semiconductor lasers directed on achievement of extreme parameters".

References

[1] I. R. Shen, *The principles of the nonlinear optics.*, (M.: Nauka, 1989).

[2] C. Flytzanis, *Phys. Rev. B*, **6**, 1264 (1972).

[3] V. Ya. Aleshkin, A. A. Afonenko, N. B. Zvonkov, *Semiconductors* **35**, 1203 (2001).

[4] B. N. Zvonkov, A. A. Biryukov, A. V. Ershov, S. M. Nekorkin *et al*, *Appl. Phys. Lett.* **92**, 021122 (2008).

[5] V. Ya. Aleshkin, A. A. Biryukov, A. A. Dubinov, B. N. Zvonkov, S. M. Nekorkin, *Technical Physics* (2009).

[6] F. Bachmann, P. Loosen, R. Poprawe, *High power diode lasers. Technology and applications.*, (New York: Springer Science+Business Media, 2007).

[7] I. Vurgaftmana, J. R. Meyer, L. R. Ram-Mohan, *J. Appl. Phys.* **89**, 5815 (2001).

[8] O. Madelung, *Semiconductors: Data Handbook.*, (New York: Academic Press, 1998).

17th Int. Symp. "Nanostructures: Physics and Technology"
Minsk, Belarus, June 22–26, 2009
© 2009 Ioffe Institute

Effects of electron-electron interaction on cyclotron resonance in InAs/AlSb QW heterostructures in quantizing magnetic fields

A. V. Ikonnikov[1], S. S. Krishtopenko[1], Yu. G. Sadofyev[1], V. I. Gavrilenko[1] and M. Orlita[2]

[1] Institute for Physics of Microstructures RAS, 603950 Nizhny Novgorod, Russia
[2] Grenoble High Magnetic Field Laboratory, CNRS, Grenoble, France

Abstract. Cyclotron resonance in InAs/AlSb quantum well heterostructures in quantizing magnetic fields up to 13 T was studied. CR line splitting into 3 components at noninteger values of Landau level filling factor ν was discovered. The observed splitting nearby even ν was shown to exceed significantly the calculated value, the discrepancy being increased with the magnetic field. The discovered effects are attributed to the exchange electron-electron interaction.

Introduction

According to Kohn theorem [1], cyclotron resonance (CR) frequency in a translational invariant system is not affected by electron-electron (e-e) interaction. However, e-e interaction effects on the CR can be expected if the translational symmetry is broken, e.g. due to a strong band nonparabolicity and/or to the presence of disorder that was shown both experimentally [2,5,6] and theoretically [2,3,4]. Despite the results obtained, up to now there is no clear understanding how e-e interaction manifests itself in the CR, so further explorations are still urgent. The present work is devoted to the search of e-e interaction effects on the CR in InAs/AlSb quantum well (QW) heterostructures. In addition to a strong conduction band nonparabolicity these structures exhibit a number of remarkable properties such as low electron effective masses in InAs QWs down to $0.03m_0$, high electron mobility up to 9×10^5 cm^2/V s at $T = 4.2$ K [7] and strong bipolar persistent photoconductivity (PPC) effect [8,9], which allow to reversibly change electron concentration in InAs QW in a wide range.

1. Experimental

InAs/AlSb heterostructures under study were grown by MBE technique on semi-insulating GaAs(100) substrates on thick metamorphic GaSb layer followed by a ten-period smoothing GaSb/AlSb superlattice. The active part of the structure consists of a lower AlSb barrier 12 nm wide, an InAs QW with a nominal thickness of 15 to 18 nm, an upper AlSb barrier 30 to 40 nm wide and a GaSb cap layer 6 nm wide. The electron concentration in the dark at $T = 4.2$ K was about 7×10^{11} cm^{-2} and the mobility $\sim 4 \times 10^5$ cm^2/V s. CR spectra were measured with Bruker 113V FT spectrometer. We used square samples with the area 5×5 mm^2 with two strip ohmic contacts for magnetoresistance measurements. The samples were mounted in the light-pipe insert in the liquid helium cryostat in the center of superconducting solenoid, the sample can be illuminated by blue LED. All measurements were carried out at $T = 2$ K. The radiation transmitted through the structure was detected with a Si composite bolometer. Transmission signals measured in magnetic fields were normalized to that measured in the absence of the magnetic field. The two-terminal magnetoresistance of the samples was recorded to determine the two-dimensional (2D) electron concentration.

2. Theory

To calculate Landau levels (LLs) for the self-consistent QW profile we used 8×8 $k - p$ Hamiltonian [10] accounting the deformation [11]. The calculations were performed using the transfer matrix technique neglecting in the Hamiltonian the terms proportional to the square of the hole wavevector. The self-consistent potential takes into account the Hartree potential, ionized impurity fields and the image potential. The InAs lattice constant in the plane of the structure was assumed to be equal to that of GaSb. We found that the band bending as well as deformation term affects LLs spectra less than 0.5%.

3. Results and discussion

Typical CR spectra are given in Fig. 1. A remarkable CR line splitting (into 2 or 3 lines) is clearly seen. The measured CR transition energies as well as calculated ones between the lowest LLs versus the magnetic field are presented in Fig. 2. It is clearly seen that the experimental data correspond qualita-

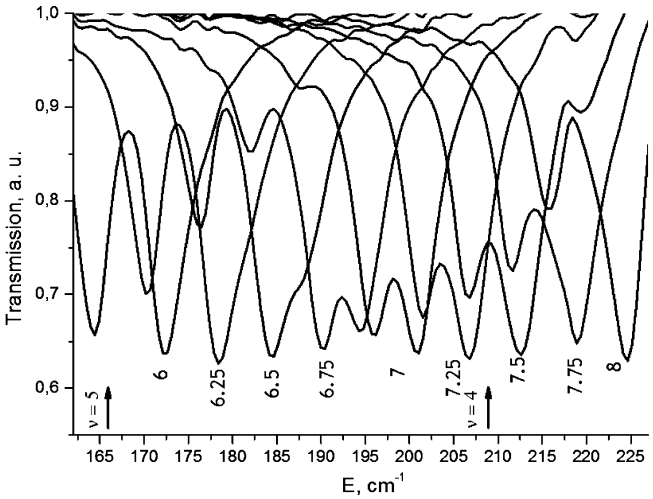

Fig. 1. CR spectra in the sample 038 ($d_{\mathrm{QW}} = 18$ nm, $n_s = 6.6 \times 10^{11}$ cm^{-2}) measured at different magnetic fields (the field values in Tesla are given below the curves). Arrows indicate integer values of the LL filling factor ν.

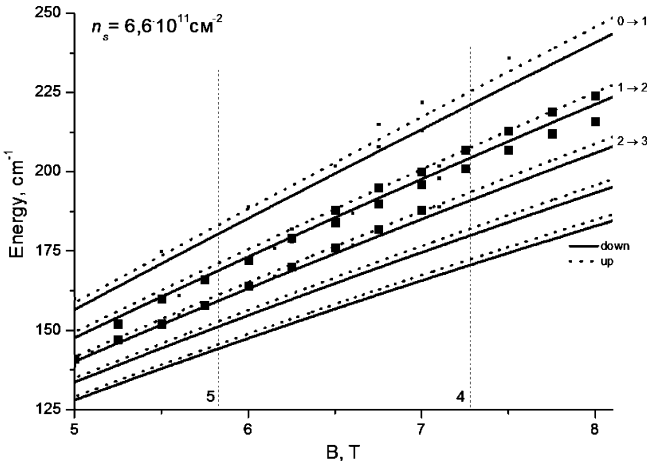

Fig. 2. Spectral positions of the observed CR absorption lines in the sample C038 with the electron concentration 6.6×10^{11} cm^{-2} versus the magnetic field. Lines correspond to calculated CR transitions between the lowest LLs.

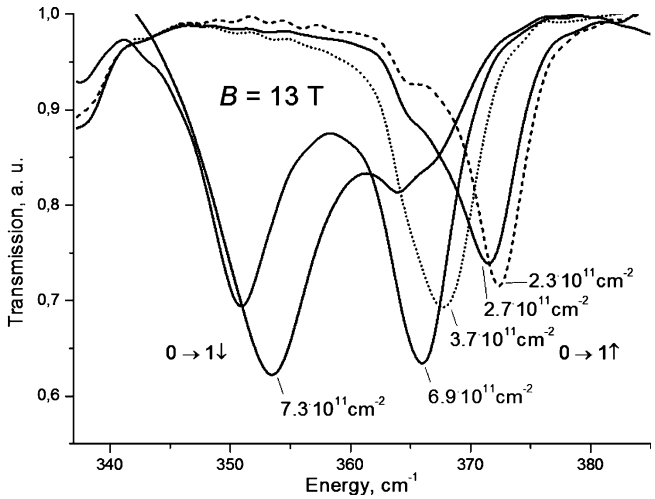

Fig. 3. CR spectra in the sample 040 ($d_{\mathrm{QW}} = 15$ nm) at $B = 13$ T for different electron concentrations.

tively farly well to the calculation results. That allows us to identify all the CR transitions corresponding to the observed absorption lines. At $B \sim 6$ T (filling factor $\nu \sim 5$) CR absorption results from $2^{\uparrow} \to 3^{\uparrow}$ and $1^{\downarrow} \to 2^{\downarrow}$ transitions and the observed splitting is caused by nonequidistant LL spacing (Δm^*-splitting). In the magnetic fields near 7.5 T ($\nu \sim 4$) CR results from $1^{\downarrow} \to 2^{\downarrow}$ and $1^{\uparrow} \to 2^{\uparrow}$ transitions and the splitting is due to the different effective g-factor at the 1-st and the 2-nd LLs (Δg^*-splitting). In the magnetic field of 6.75 T the CR line splitting into 3 components is clearly seen: $2^{\uparrow} \to 3^{\uparrow}$, $1^{\downarrow} \to 2^{\downarrow}$ and $1^{\uparrow} \to 2^{\uparrow}$ transitions. The same effect was discovered in this sample at different electron concentrations as well as in another sample ($d_{\mathrm{QW}} = 15$ nm). Earlier a possibility of CR line splitting into 3 components was discussed but actually was not seen probably because of a worse quality of samples (see, for example [12]).

An unusual high splitting of $1 \to 2$ CR transition was observed at $\nu < 5$ ($B > 7$ T). As easy to see in Fig. 2 the measured $1^{\downarrow} \to 2^{\downarrow}$ transition energy becomes significantly less than that calculated in the single-electron model with the magnetic field increase. At the same time, the energy of $1^{\uparrow} \to 2^{\uparrow}$ transition remains in a good agreement the calculated value. The same discrepancy was observed in other samples and it significantly exceeds the measuring accuracy.

Another CR peculiarity was discovered in the spectral range above phonon apsorption band in GaAs (Fig. 3). In the maximum available magnetic field 13 T in this spectral range the spin-split $0 \to 1$ transitions are observed. At $n_s = 7.3 \times 10^{11}$ cm^{-2} ($\nu \approx 2.4$), there are two lines in CR spectra: the left line corresponding to the $0^{\downarrow} \to 1^{\downarrow}$ transition and the weaker right one corresponding to the $0^{\uparrow} \to 1^{\uparrow}$ transition. Under the illumination by blue LED the concentration goes down (and the filling factor decreases), so the left line decreases in the amplitude while the right line increases. At the same time, the left line shifts to the lower energies and the right one to the higher energies, though in single particle model CR transitions energies should not depend on the concentration. At further decrease of the concentration only the right line remains in the spectra and its position still shifts to higher energies.

We speculate that the observed unusual dependences of the CR frequencies on the LL filling are provoked by the exchange e-e interaction which was not taken into account in our calculations. The model calculations of the e-e interaction effects on hybridization of CR spin-split transitions demonstrate that depending on electrons distribution between initial states either the merging or the repulsion of two CR lines can take place [13]. Effects of electron-phonon interaction on the CR should be observed in a spectral range near InAs LO phonon frequency only [6]. In our experiments abnormal CR splitting was observed in a wide spectral range, so the most likely the reason is the effect of exchange e-e interaction.

Acknowledgements

This work was financially support by RFBR (grants 07-02-01382, 08-02-92503, 09-02-00752), CRDF (grant Y5-P-01-03) and by Russian Academy of Sciences. The measurements at GHMFL are supported by EC from the 6-th framework program Transnational Access Specific Support Action, contract No. RITA-CT-2003-505474.

References

[1] W. Kohn, *Phys. Rev.* **123**, 1242 (1961).
[2] T. Ando *et al*, *Rev. Mod. Phys.* **54**, 437 (1982).
[3] C. Kallin *et al*, *Phys. Rev. B* **31**, 3635 (1985).
[4] A. H. MacDonald *et al*, *Phys. Rev. B* **40**, 5795 (1989).
[5] C. M. Hu *et al*, *Phys. Rev. B* **52**, 12 090 (1995).
[6] X. G. Wu *et al*, *Phys. Rev. Lett.* **84**, 4934 (2000).
[7] C. Nguyen *et al*, *J. Electron. Mater.* **22**, 255 (1993).
[8] Ch. Gauer *et al*, *Semicond. Sci. Technol.* **8**, S137 (1993).
[9] V. Ya. Aleshkin *et al*, *Semiconductors* **39**, 30 (2005).
[10] E. O. Kane, *J. Phys. Chem. Solids* **1**, 249 (1957).
[11] G. L. Bir, G. E. Pikus, *Symmetry and Strain-Induced Effects in Semiconductors.* Wiley, New York, (1974).
[12] M. J. Yang *et al*, *Phys. Rev. B* **47**, 1681 (1993).
[13] K. Asano, T.Ando *et al*, *Phys. Rev. B* **58**, 1485 (1998).

17th Int. Symp. "Nanostructures: Physics and Technology"
Minsk, Belarus, June 22–26, 2009
© 2009 Ioffe Institute

Investigations into THz impurity photoconductivity relaxation in GaAs/$In_{0.1}Ga_{0.9}As_{0.8}P_{0.2}$ and Ge/GeSi quantum well heterostructures

S. V. Morozov, K. V. Maremyanin, D. I. Kuritsin, S. M. Sergeev, A. V. Antonov, I. V. Erofeeva and V. I. Gavrilenko

Institute for Physics of Microstructures RAS, 603950 Nizhniy Novgorod, Russia

Abstract. In *n*-GaAs/InGaAsP and *p*-Ge/GeSi quantum well heterostructures excited by picosecond broad band pulses of THz radiation the relaxation times of the impurity photoconductivity were measured for the first time.

Introduction

Nowadays there is a growing interest to the nonequilibrium phenomena and possibilities to produce the intra-band population inversion in semiconductor nanostructures doped with shallow impurities. In order to design THz laser operating at the optical transitions involving shallow impurity states direct information on lifetimes of carriers both excited into conduction (valence) band and captured by excited impurity states is required. The pa-per is devoted to the exploration of relaxation kinetics of impurity photoconductivity in *n*-GaAs/$In_{0.1}Ga_{0.9}As_{0.8}P_{0.2}$ and *p*-Ge/$Ge_{1-x}Si_x$ quantum well (QW) heterostructures excited by broadband THz emission generated by optical rectification of femtosecond laser pulses.

1. Experimental

n-GaAs/$In_{0.1}Ga_{0.9}As_{0.8}P_{0.2}$ heterostructures under study were MOCVD grown on GaAs(001) semi-insulating substrates and contained 30 GaAs QWs separated by 400 Å wide $In_{0.1}Ga_{0.9}As_{0.8}P_{0.2}$ barriers. QW widths d_{QW} were 200 Å in the structure #4147 and 90 Å in #4236 one. Silicon delta-layer was introduced in the center of each QW. The donor concentration measured by Hall effect was 3.3×10^{10} cm^{-2} per well. Strained *p*-Ge/$Ge_{1-x}Si_x$ heterostructures with residual acceptors were CVD grown on Ge(111) substrates. The structure #306 ($x = 0.12$) contained 162 Ge QWs 200 Å wide and #308 one ($x = 0.09$) contained 80 Ge QWs 355 Å wide. The residual acceptor concentration was about 3×10^{14} cm^{-3}. The photoconductivity spectra were measured using BOMEM DA3.36 Fourier-transform spectrometer at $T = 4.2$ K. Two strip ohmic contacts 4 mm apart were deposited onto a sample surface 5 × 5 mm in size. The samples were biased by a d.c. voltage. Impurity photoconductivity spectra of *n*-GaAs/$In_{0.1}Ga_{0.9}As_{0.8}P_{0.2}$ samples contain a broad long-wave band in between 27 and 150 cm^{-1} corresponding to transitions from the ground donor state into excited states and to the continuum. In the photoconductivity spectra of Ge/GeSi samples #306 and #308 broad band in between 20 and 40 cm^{-1} and around 60 cm^{-1} respectively are observed. The binding energy of shallow acceptor is known to depend on the impurity position in QW [1]. These spectra due to the built-in strain in the Ge/GeSi heterostructures differ significantly from the impurity photoconductivity spectrum of bulk *p*-Ge where the maximum is located nearby 100 cm^{-1}. Investigations of impurity photoconductivity relaxation kinetics were carried out at the excitation by picosecond broadband (0.5 to 3 THz) THz pulses. THz radiation was generated by optical rectification in ZnTe crystal of 100 fs long laser pulses ($\lambda = 800$ nm). The photoconductivity signal was registered with averaging by a digital oscilloscope with a resolution of 1 ns.

2. Results and discussion

Typical oscillograms of the photoresponse in two GaAs/InGaAsP samples are given in Figs. 1,2. In both cases a significant increase of the photoresponse relaxation time with the bias voltage U decrease: was observed from 2 up to 5 ns in the sample #4147 and from 2 up to 3 ns for #4236 one. We attribute

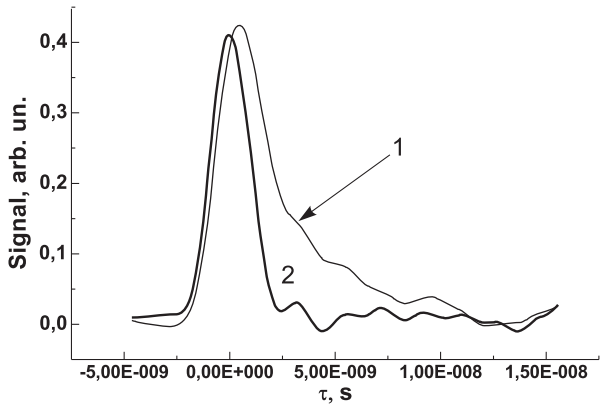

Fig. 1. Oscillograms of the photoresponse in GaAs/InGaAsP sample #4147 ($d_{QW} = 200$ Å) at $U = 2$ V (curve 1) and $U = 10$ V (curve 2).

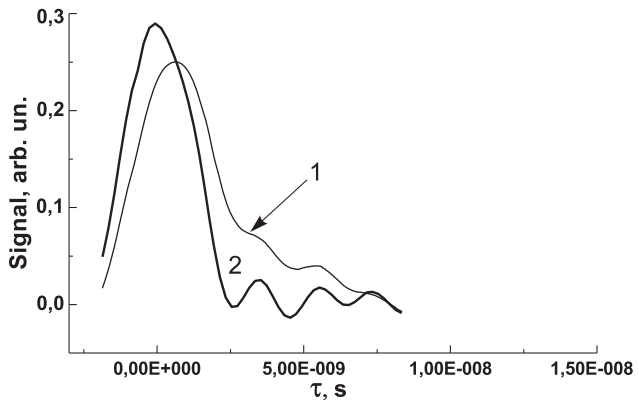

Fig. 2. Oscillograms of the photoresponse in GaAs/InGaAsP sample #4236 ($d_{QW} = 90$ Å) at $U = 2$ V (curve 1) and $U = 10$ V (curve 2).

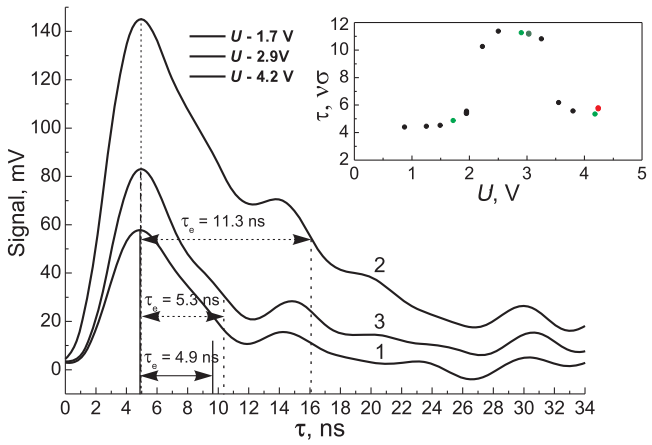

Fig. 3. Oscillograms of the photoresponse in Ge/GeSi sample #308 (d_{QW} = 355 Å) at U = 1.7 V (curve 1), U = 2.9 V (curve 2) and U = 4.2 V (curve 3). In the insert: photoresponse relaxation time versus bias voltage.

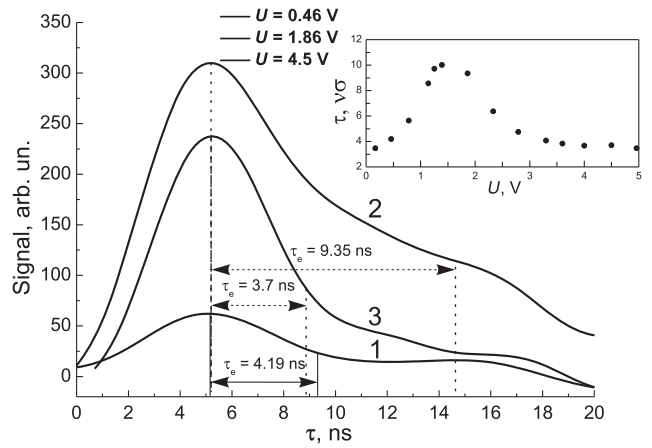

Fig. 4. Oscillograms of the photoresponse in Ge/GeSi sample #306 (d_{QW} = 200 Å) at U = 0.78 V (curve 1), U = 1.86 V (curve 2) and U = 4.5 V (curve 3). In the insert: photoresponse relaxation time versus bias voltage.

this effect to the transition from the free-carrier photoconductivity at the impurity breakdown regime (U = 10 V) to the impurity photoconductivity (U = 2). The impurity photoconductivity decay observed at low bias voltages are governed by processes of free electron capture by impurities. We attribute the observed decrease of the relaxation time from 5 down to 3 ns at reducing GaAs QW width from 200 Å down to 90 Å to an increase of the matrix element of electron-acoustic phonon interaction (emission of acoustic phonon is necessary for free electron capture by impurity). This matrix element is proportional to the wavevector of the acoustic phonon to be emitted and hence to the phonon energy. And a shallow impurity binding energy is known to in-crease with decreasing QW width. Oscillograms of the photoresponse in two Ge/GeSi samples with residual acceptors are given in Figs. 3,4. For both samples #308 and #306 with different quantum well width the increase of the bias voltage results in the rise of the impurity photoresponse decay time (from 4.9 to 11.3 ns and from 4.19 to 9.35 ns, correspondently). We relate this effect to the "switching-off" the excited impurity states from the cascade hole capture mechanism [2] due to their impact ionization. At further increase of the bias voltage the decay time decreases (from 11.3 down to 5.3 ns and from 9.35 down to 3.7 nanoseconds, respectively, see inserts in Figs. 3,4) just as in the case of shallow donors (Figs. 1,2). The latter again is explained by a transfer from the impurity photo-conductivity mechanism of the photoresponse to the free carrier one because of the impurity breakdown.

Acknowledgements

The work has been financially supported by RFBR (#05-02-17374) and RFBR-CNRS (#07-02- 01307) projects and by Russian Academy of Sciences.

References

[1] A. A. Reederet *et al*, *IEEE J. Quant. Electron.* **24**, 1690 (1998).
[2] V. N. Abakumov *et al*, *Ion-radiative recombination in semiconductors*, St Peterburg, Nauka, (1997), (in Russian).

17th Int. Symp. "Nanostructures: Physics and Technology"
Minsk, Belarus, June 22–26, 2009
© 2009 Ioffe Institute

Identification of nitrogen centers in nanodiamonds: EPR studies

A. A. Soltamova[1], I. V. Ilyin[1], P. G. Baranov[1], A. Ya. Vul'[1], S. V. Kidalov[1], F. M. Shakhov[1], G. V. Mamin[2], S. B. Orlinskii[2] and M. Kh. Salakhov[2]

[1] Ioffe Physical-Technical Institute, St Petersburg, Russia
[2] Kazan State University, Federal Center of Shared Usage for Physicochemical Measurements, Kazan, 420008 Russia

Abstract. Single isolated nitrogen donor N^0 and nitrogen pair N_2^+ have been observed by means of high-frequency electron paramagnetic resonance (EPR) in natural nanodiamond powder. The structure and parameters of these centers were determined. For the first time the nitrogen centers were observed in synthetic detonation nanodiamond. Hence, it was proved that single nitrogen atoms occupy stable sites in the lattice of nanodiamod particles with a size of grains smaller than 10 nm.

Introduction

The properties of carbon nanostructures are to date of the great interest among other nanomaterials. Numerous theoretical studies [1] have shown that structure of intrinsic and impurity defects in nanodiamonds (ND) differ from those in bulk diamonds. In particular, theoretical studies have shown that nitrogen impurities in ND are metastable.

Nitrogen single defects and clusters are generally believed to be dominant defects in diamonds. One of the major paramagnetic center is N^0 ($g = 2.0024$) which is a substitutional nitrogen atom in diamond lattice often referred to as P1 center [2]. Electronic structure of nitrogen donors is well studied by methods of EPR and electron nuclear double resonance (ENDOR) as well as the wave function of unpaired donor electron. The primary cluster is the pair of adjacent substitutional nitrogen atoms N_2^+ labeled in [3] as W24 center. EPR spectra were observed in type Ia diamonds under ultraviolet illumination and disappear after illumination was switched off.

1. Experimental

Experiments were carried out on two types of ND samples: sample I was a ND powder with characteristic size of the particles $\leq$250 nm. The samples were produced by fragmentation of natural microdiamond crystals with following centrifuge division into fractions. The maximum of the size distribution for the samples I was 150 nm. Some of the samples were annealed for 20 minutes at the tempetature 700 °C.

Samples II were produced by sintering the detonation NDs at the temperatures 1500–1700 °C and the pressure 6–7 GPa. According to the results of the X-ray diffraction the average size of the particles was 8.5 nm.

Continuous-wave (cw) electron paramagnetic resonance (EPR) and electron-spin echo (ESE) at both X-band (9.3 GHz, cw) and W-band (94 GHz, cw and ESE) frequencies were used in studies. Low temperature X-band EPR measurements were made using custom-made gas flow helium cryostat within temperature range 4–300 K. All spectra were recorded without accumulation. The simulations were performed using the Brucker software "Simfonia".

2. Results and discussions

Figure 1 shows the X-band EPR spectra in sample I NDs. Spectrum 1 was registered at 30 K before annealing, spectra 2 and 3 after annealing at temperatures 30 K and 40 K respectively. All spectra have a very strong broad central line at $g = 2.0027$ and three sets of weak satellites symmetrically disposed on each side. One can notice that intensity ratio between central line and satellites changes after annealing — the contribution of central line decrease significantly.

Similar EPR spectra were observed in natural microdiamond powder (size of ≥ 1 μm) [4]. Satellites closest to the central line were related to hyperfine (hf) interaction with single nitrogen atom N^0. The dashed line shows the calculated spectra for the hf interaction with N^0 with hf parameters same as for bulk diamonds with regard to averaging of the EPR spectra over all orientations. Two pairs of distant satellites (marked with asterisk), were related in [4] to anisotropic hf interaction between surface centers and ^{13}C, as the intensity ratio of these satellites to the central line was close to the natural abundance of ^{13}C (1.1%). This interpretation is fallacious and was due to impossibility to distinguish centers with close values of g factors. The assignment of these hf lines (marked with asterisk on Fig. (1) have changed several times later on and in Ref. [3] they were assigned to the nitrogen pairs in microdiamonds with size of 50 μm. Thus, the assignment of the hf structure of EPR signals remains contradictory due to the overlapping of the ni-

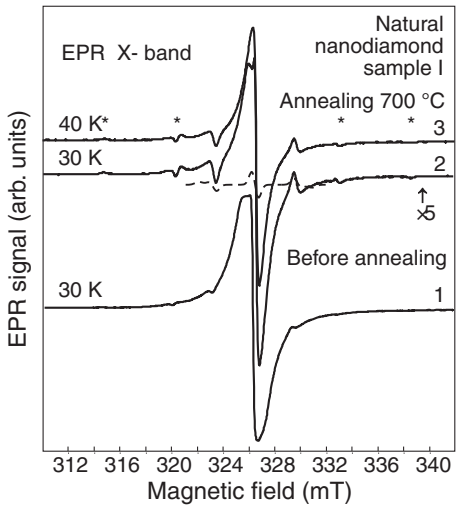

Fig. 1. Low temperature X-band EPR spectra in natural ND powder (sample I ND) before (1) and after (2,3) annealing and calculated EPR spectra (dashed line) for N^0 centers.

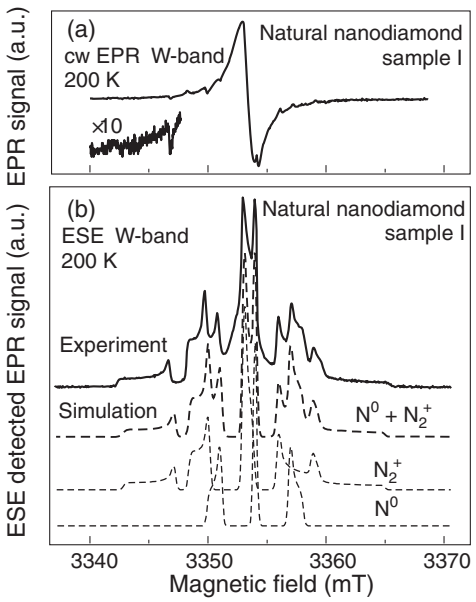

Fig. 2. (a) — W-band (94 GHz) cw EPR spectra and (b) ESE-detected EPR spectra in natural sample I NDs with sizes ≤250 nm and simulated spectra for single nitrogen atoms (N^0), nitrogen pairs N_2^+ and their sum.

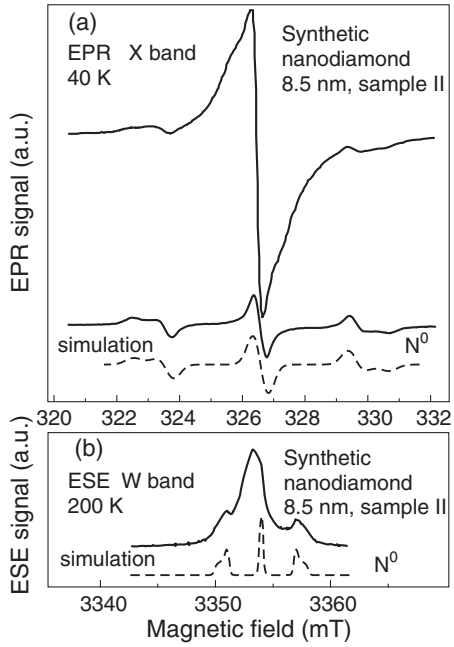

Fig. 3. (a) X-band EPR spectrum in synthetic detonation sample II ND (size of 8.5 nm)-top; EPR spectrum in microdiamond powder (size app 100 μm) and simulated spectra (dashed line) for N^0 centers — bottom; (b) W-band ESE detected EPR spectra in sample II and simulated spectra (dashed line) for N^0 centers.

trogen EPR lines and what is more the EPR signal of the surface centers masks the main EPR lines. Not to mention that these problems were not yet discussed in NDs.

To determine the actual nature of EPR signals, observed in X-band, high-frequency cw EPR (94 GHz) investigations were carried out in sample I NDs before annealing (see Fig. 2(a)). The W-band EPR spectrum consists of strong central line and several pairs of weak satellites in low and high fields, the number of satellites has increased. It is well-known that the central line is assigned to surface dangling bonds in micro- and NDs [4,5]. The number of the surface centers reduces notably after annealing (see Fig. 1).

ESE studies allowed to reduce the EPR signal of surface centers due to the short relaxation times of these centers. Figure 2(b) shows ESE detected EPR spectrum, measured in idem sample (sample I before annealing). This spectrum can be explained by presence of two types of nitrogen centers: single nitrogen atom N^0 and nitrogen pair N_2^+. On the Fig. 2(b) simulated spectra for N^0, N_2^+ and their sum are shown; parameters used for the simulation almost coincide with the corresponding spin Hamiltonian parameters in bulk diamonds and are the following: $g_\parallel = g_\perp = 2.0024$, $A_\parallel = 40.7$ G, $A_\perp = 29$ G for N^0 and $g_\parallel = 2.00245$, $g_\perp = 2.0030$, $A_\parallel = 55.38$ G, $A_\perp = 29$ G for N_2^+, the linewidth was 3 G. The excellent agreement between simulation and experimental data unambiguously proves that this type of EPR signal relate to N^0 and N_2^+ centers. These results allow to determine the concentration of N^0 and N_2^+ centers in these crystals and can be used as a reference point to control the concentration of paramagnetic nitrogen in NDs.

One of the most significant results is the anisotropy of g factors for nitrogen pairs N_2^+ (quite small to be detected in X-band) and isotropy of g factors for single nitrogen atoms (N^0). For the first time the EPR lines assigned to nitrogen centers were distinguished due to the high frequency used in measurements.

Figure 3 shows the cw X-band (a) and W-band ESE detected (b) EPR spectra observed in synthetic detonation NDs with the size of 8.5 nm after sintering at high temperature under high pressure (sample II). For comparison the EPR spectra in microdiamond powder (size of 100 μm) and the simulated spectra (X- and W-band, dashed line) are shown for N^0 centers. It is clear that hf structure of EPR signals can be assigned to N^0 center. This gives a ground to conclude that single nitrogen substitutional atoms occupying a stable state in ND particles with the size of 8.5 nm.

Thus, the EPR signals of substitutional nitrogen atoms and nitrogen pairs were measured in ND with the sizes smaller than 250 nm, their structure and parameters are identified by method of high frequency EPR. For the first time the EPR spectra of nitrogen centers in frittered synthetic ND with the sizes of 8.5 nm were observed.

Acknowledgements

This work has been supported by Federal Agency for Science and Innovations under the Contract No. 02.513.12.3031, the Programs of RAS "Spin-Dependent Effects in Solids and Spintronics", "Support of Innovations and Elaborations" and "Basic Researches of Nanotechnologies and Nanomaterials" and by the Russian Foundation for Basic Research under Grants No. 09-02-01409-a and No. 09-02-00730-a.

References

[1] A. S. Barnard *et al*, *Diam. Relat. Mat.* **16**, 2078 (2007).
[2] J. A. van Wyk *et al*, *J. Phys. C: Solid State Phys. Diam. Relat. Mat.* **16**, 1501 (1983).
[3] O. D. Tucker *et al*, *Phys. Rev. B* **50**, 15586 (1994).
[4] N. D. Samsonenko *et al*, *Pis'ma Zh. Eksp. Teor. Fiz.* **5**, 304 (1967).
[5] A. I. Shames *et al*, *J. Phys. Chem. Solids* **63**, 1993 (2002).

17th Int. Symp. "Nanostructures: Physics and Technology"
Minsk, Belarus, June 22–26, 2009
© 2009 Ioffe Institute

Diode and "topological" Hall Effects in magnetic nanostructures

A. A. Fraerman
Institute for physics of microstructures RAS, (603950) Russia, Nizhny Novgorod, GSP-105

Investigations of spin and spatial degrees of freedom for electrons and their interplay in conducting ferromagnets are of great interest from both theoretical and practical points of view [1]. For collinear distribution of magnetization, spatial and spin degrees of freedom for current carriers are independent. But for noncollinear distribution, the motions of electron in real and spin spaces are coupling. This can lead to the peculiarities of transport properties for noncollinear magnetic systems. In general case, distribution of magnetization in laterally-confined magnetic multilayer is noncollinear and, what is more — non coplanar. In the report I am going to discuss connection between magnetic states and transport properties of such systems. The report consists of three parts. In the first part the influence of an exchange interaction on transport properties of a magnetic nanostructures is concerned from a phenomenological point of view. Possible transport phenomena arising due to an exchange interaction are discussed. Namely, it is demonstrated that in a medium with non-coplanar magnetization distribution an additional contribution to the Hall Effect ("topological" Hall Effect) and rectification effects can arise. The second part of the work is devoted to a microscopic theory of the above mentioned phenomena in systems with vortex and spiral magnetization distribution. In third part, I am going to discuss some experimental methods for creation of noncoplanar distributions of magnetization in nanostructures.

The phenomenological theory is based on the assumption that an exchange interaction dominates in a medium. This leads to an independence of medium characteristics on a simultaneous rotation of all the magnetic moments in the system on the same angle. Therefore a conductivity tensor should be invariant with respect to a magnetization rotation [2]. Using such an assumption it is possible to find conductivity tensor describing transport phenomena occurring due to an exchange interaction. Indeed, common expression for electrical current including quadratic (respect to electrical field E) term has the form

$$j_i = \sigma_{ik} E_k + \gamma_{ikn} E_k E_n + \dots \qquad (1)$$

Magneto depending part of linear conductivity in the formula is

$$\sigma_{ik} = N\left(\frac{\partial \vec{M}}{\partial x_i}\frac{\partial \vec{M}}{\partial x_k}\right) + K_{\mathrm{H}}\left(\vec{M}\left[\frac{\partial \vec{M}}{\partial x_i}\times\frac{\partial \vec{M}}{\partial x_k}\right]\right) + \dots \qquad (2)$$

$\vec{M}$is a local magnetization. The first term in formula (2) describes well-known effect of giant magnetoresistance [3] and second term is additional contribution in Hall conductivity predicted by Aharonov and Stern [4]. It is seen that the tensor of Hall conductivity is non zero only in a medium with non-coplanar magnetization distribution. For example, "topological" Hall Effect appears in a magnetic nanoparticle with "vortex" magnetic structure [5]. A reason for "topological" Hall Effect is breaking of time reversal symmetry due to an exchange interaction. If a magnetization distribution is also asymmetric with respect to a spatial inversion, rectification effects can occur. Tensor of nonlinear conductivity in (1) has the form

$$\gamma_{ikn} = \gamma_0\left(\vec{M}\left[\frac{\partial \vec{M}}{\partial x_i}\times\frac{\partial^2 \vec{M}}{\partial x_k \partial x_n}\right]\right). \qquad (3)$$

In the work the above mentioned phenomena are considered also from a microscopic point of view. Theory of the rectifying effect is built for the particular case of non-coplanar system — magnetic spiral. Formalism of Boltzmann equation is used for the calculations. It is shown that in the region of a low frequency of an external electric field there are two mechanism of the diode effect. First is an asymmetry of a group velocity, which arises due to a spectrum asymmetry [6]. The second mechanism is a scattering asymmetry. It arises due to the non-trivial form of an electron wave function in the noncoplanar magnetic spiral. In the region of resonant frequencies corresponding to the energy gap between two spin subbands one more mechanism of the diode effect occurs. This mechanism connected with the transitions of electrons from one spin subband to another spin subband under the impact of an alter-

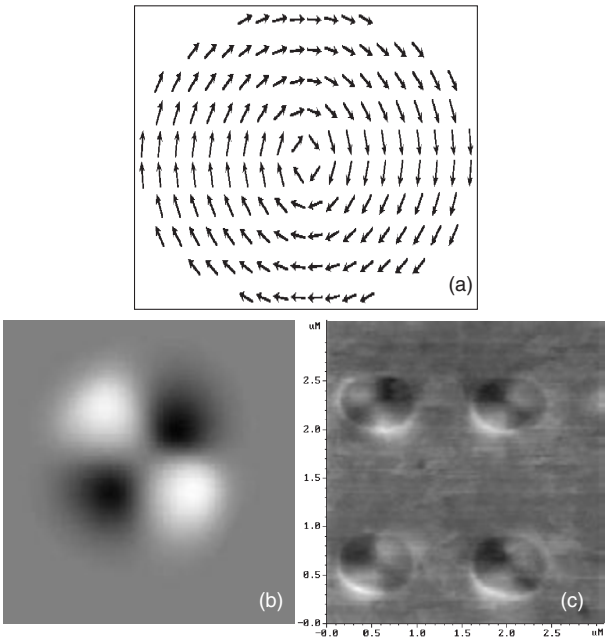

Fig. 1. Vortex state in ferromagnetic nanoparticles: a) — schematic pictures of the vortex distribution, b) — simulated MFM contrast for vortex particle, c) — experimental MFM image from single Co nanodisks with different chirality.

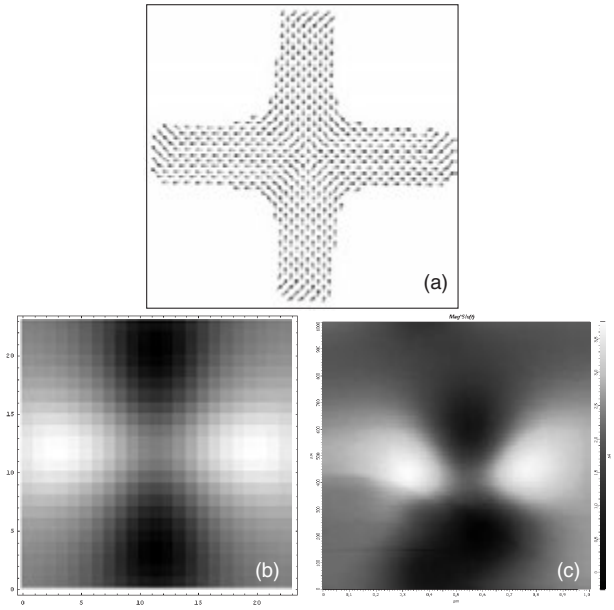

Fig. 2. Antivortex state in ferromagnetic cross: a) — schematic pictures of the antivortex distribution, b) — simulated MFM contrast for antivortex cross, c) — experimental MFM image from single Co cross.

native external field [7]. The resonant mechanism is stronger than two mechanisms mentioned above, but it exists only in the narrow frequency range. I am going to discuss of quasiclassical approach for topological Hall effect in magnetic vortex also. Estimation made on the base of the theory shows that for 100 nm Co particle "topological" Hall Effect gives dominant contribution to the Hall conductivity if a magnetic field is less than 200 Oe.

Magnetic vortex is ground state of ferromagnetic nanodisc. The state is result of interplay between magnetostatic interaction and exchange energy. Distribution of magnetization and Magnetic Force Microscopy (MFM) image of magnetic vortex in ferromagnetic particles are presented on the Fig. 1. It is interesting that topological Hall effect not dependence on vortex chirality and determined only core polarization (see, formula (2)). Another possible distribution of magnetization for observation of topological Hall effect is so-called antivortex in ferromagnetic cross (Fig. 2). Recently [8], using MFM, we had shown that helix state is ground state in laterally confined magnetic multilayers containing three magnetic layers separated by nonmagnetic spacers. The spiral state in the system originates from the magnetostatic interaction taking into account interplay between nearest and next nearest neighboring magnetic layers (Fig. 3). The structure is appropriate for observation of diode effect.

Acknowledgements

The work is supported by RFBR under grant No. 07-02-01321-p and Program of RAS "Nanostructures".

References

[1] I. Zutic, J. Fabian, S. D. Sarma, *Rev. Mod. Phys.* **76**, 323 (2004).
[2] L. D. Landau and E. M. Lifshitz, *Electrodynamics of Continuous Media*, 2nd ed., Course on Theoretical Physics, Vol. 8, Pergamon, New York, 1984.

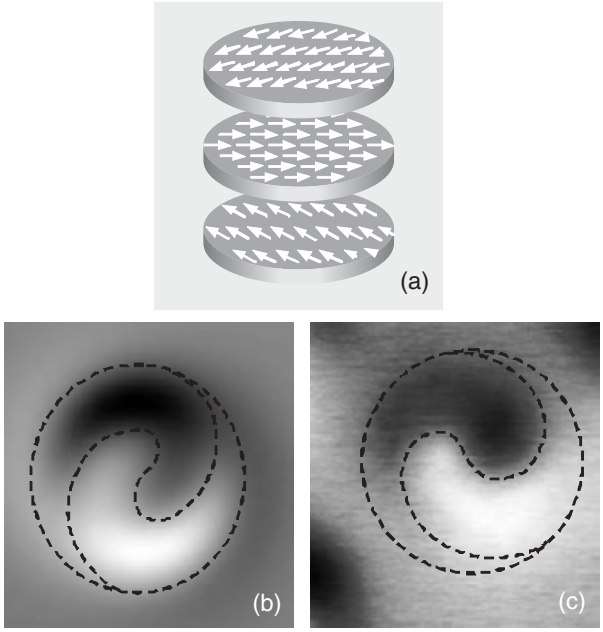

Fig. 3. Spiral state in multilayer nanomagnet: a) — schematic pictures of the noncollinear magnetic helix in the three disks system, b) — simulated MFM contrast for a triple nanodisk, c) — experimental MFM image from triple Co nanodisk. The dashed lines separate the regions with dark and bright contrast to emphasize the spiral symmetry of MFM contrast.

[3] http://nobelprize. org/nobel_prizes/physics/laureates/2007/index.html
[4] Ya. Aharonov, A. Stern, *Phys. Rev. Lett.* **69** 25, 3593 (1992).
[5] R. P. Cowburn, D. K. Koltsov, A. O. Adeyeye *et al*, *Phys. Rev. Lett.* **83**, 1042 (1999).
[6] A. A. Fraerman, O. G. Udalov, *Phys. Rev. B* **77** 9, 094401–094404 (2008).
[7] A. A. Fraerman, O. G. Udalov, *JETP Letters* **87** 3, 159–163 (2008).
[8] A. A. Fraerman, B. A. Gribkov, S. A. Gusev *et al*, *J. Appl. Phys.* **103**, 073916 (2008).

17th Int. Symp. "Nanostructures: Physics and Technology"
Minsk, Belarus, June 22–26, 2009
© 2009 Ioffe Institute

Light-matter interaction in metal-dielectric nanostructures

S. V. Gaponenko[1] and D. V. Guzatov[2]

[1] B. I. Stepanov Institute of Physics, NASB, Minsk 220072, Belarus
[2] Y. Kupala Grodno State University, Grodno 230023, Belarus

Abstract. Basic physical ideas and technological implementations are discussed of strong enhancement of light-matter interaction in plasmonic nanostructures. Experiments with quantum dots and molecules on enhanced luminescence and Raman scattering are considered. The theory of so-called "hot spots" is proposed based on simultaneous enhancement of incident field and photon density of states near metal nanobodies.

Introduction

Nanostructures with characteristic surface relief of the order of 10–100 nm are known to modify spatial distribution of incident electromagnetic field. Local field enhancement results in enhanced absorption of photons by molecules or nanocrystals adsorbed at the surface. The effect is extremely pronounced in metal-dielectric structures because of surface plasmon resonance. A systematic application of the field enhancement in Raman scattering enhancement (Surface Enhanced Raman Scattering, SERS) and in photoluminescence (PL) enhancement with respect to molecular probes is followed nowadays by application of the effect with respect to nanocrystals (quantum dots) adsorbed at metal-dielectric nanotextured surfaces. It is the purpose of the present contribution to review mechanisms of Raman scattering and photoluminescence enhancement factors in the context of their application to enhanced luminescence of molecules and quantum dot and Raman scattering. We consider not only the local field enhancement in terms of excitation process but also photon density of states enhancement effect on photon emission processes with Raman and Rayleigh scattering as specific photon emission processes. In this consideration, scattering of light experiences enhancement as spontaneous emission does. Therefore field enhancement and density of states effects should manifest themselves in the same manner in photoluminescence and scattering processes. Differences in scattering and luminescence enhancement are due to quenching processes which are crucial for PL and less pronounced for scattering.

1. Theoretical background

In terms of quantum electrodynamics, spontaneous emission of photons by a really excited quantum system and spontaneous scattering of photons by a virtually excited system are considered alike in a sense that the number of emitted/scattered photons $I_0(\omega')$ into a mode with frequency ω' per unit time for both type of processes is directly proportional to the incident photon flux $I_0(\omega)$ with ω being the frequency of incident electromagnetic radiation, and density of photon states $D(\omega')$. In other words, one can write an expression

$$I\left(\omega'\right) = I_0\left(\omega\right)\left[\text{Interaction Term }\right] D\left(\omega'\right). \qquad (1)$$

Interaction term is to be explicitly calculated for every specific process taking into account interaction cross-section, quantum yield (for spontaneous emission) for a given quantum system and quantum process under consideration. In a specific case of resonant (Rayleigh) scattering one has always $\omega = \omega'$.

The role of photon density of states (DOS) in spontaneous emission of photons is well established and recognized [1,2]. Since the pioneering paper by Purcell [3] predicting modification of spontaneous decay rates for radiofrequencies and first experiments in the optical range by K. H. Drexhage in 1970, modification of spontaneous decay rate because of spectral/spatial redistribution of photon density of states have been demonstrated for a number of mesoscopic structures with molecules, ions, and quantum dots used as elementary probe quantum systems. A non-exhaustive list includes microcavities, photonic crystals, heterostructures and interfaces, dielectric slabs, biomembranes. However photon density of states effects on spontaneous scattering of light in mesoscopic structures has been involved into consideration only recently [4–6]. Introduction of photon DOS effects into consideration of giant Raman signals in surface enhanced spectroscopy should noticeably contribute to the value of experimentally observed enhancement factors.

2. Field enhancement factor

Surface plasmon resonances inherent in metal nanoparticles embedded in a dielectric ambient medium promote development of high local light intensity in the close vicinity of a particle. In coupled nanoparticles and in purposeful arrangement of particles as well as with purposeful shaping of particles the electromagnetic field enhancement can further be magnified. This phenomenon forms the basic pre-requisite effect in linear and non-linear spectroscopies including metal nanotextured surface-enhanced and metal tip-enhanced fluorescence and Raman scattering among linear optical phenomena as well as nonlinear phenomena like, e.g. second harmonic generation, hyper-Raman scattering an others.

Surface plasmon oscillations give rise to local increase in light intensity after some time the light enters the vicinity of a metal nanoparticle. The local areas of higher light intensity coexist with other areas where light intensity is not enhanced and even may be depleted as compared to propagation of light in a continuous dielectric medium. Even for a single isolated particle the thorough electrodynamical calculations to be performed are very cumbersome and can be realized only numerically. It is the general opinion that the ideal case would be a small particle (preferably a prolate ellipsoid or spheroid as well as cone-like or other sharp tip) or, better, a couple of par-

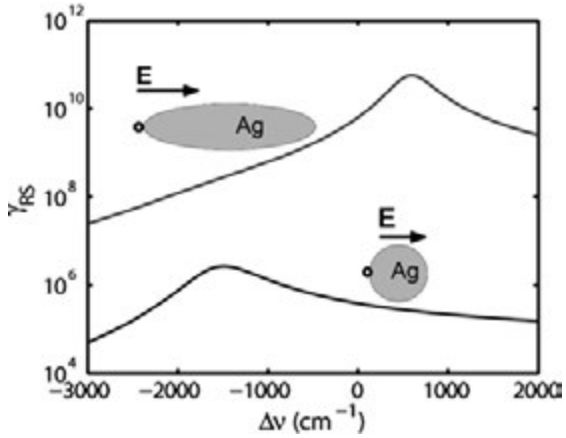

Fig. 1. Raman scattering cross-section enhancement factor due to local incident field enhancement as a function of spectral shift.

ticles of material with low damping rate and minor interband transitions.

Coupled particles ("plasmonic dimers") show higher enhancement in the area between particles, the enhancement factors being strongly dependent on electric field orientation with respect to a dimer axis 10^4 intensity enhancement was predicted between two silver spherical particles of 30 nm diameter and 2 nm spacing at wavelength of 520 nm [7].

A transition from a single particle to dimers provides a hint towards engineering of plasmonic nanostructures with enormous enhancement of electromagnetic field. Further steps can be made based on more complex geometries. In more complex self-similar metal nanostructures the local fields around the smallest nanosphere are enhanced by a factor of 10^3 for the field amplitude [8].

In the recent work [6] the enhancement of Raman scattering from the local incident field enhancement has been examined theoretically in the near field of a spherical and a spheroidal prolate silver particle (Fig. 1). Raman scattering cross-sections have been calculated for a hypothetical molecule with polarizability 10^3 Å^3 placed in a close vicinity near a silver prolate spheroid with length 80 nm and diameter 50 nm and near a silver spherical particle with the same volume. Polarization of incident light has been chosen so as the electric field vector is parallel to the axis connecting a molecule and the center of the silver particle. Maximal enhancement has been found to occur for molecule dipole moment oriented along electric field vector of incident light. The position of excitation wavelength for maximal values of Raman cross-section is approximately determined by the position of maximal absolute value of nanoparticle's polarizability. For selected silver nanoparticles it corresponds to 383.5 nm and 347.8 nm for spheroid, and 354.9 nm for sphere. It was shown that a prolate spheroid can give nearly 10^{11}-fold enhancement of Raman response.

3. Density of states contribution

In case of complex heterogeneous structures with big local variation in dielectric permittivity of materials involved like individual, coupled or aggregated metal nanoparticles or nanorods, explicit evaluation of photon density of states (DOS) is not so obvious and straightforward. In such cases the discussion in terms of the DOS concept should be replaced by the *local* DOS

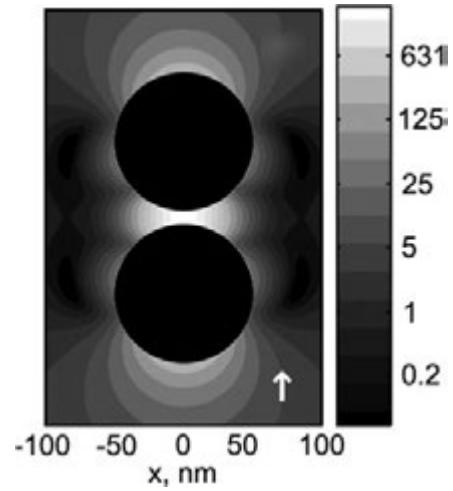

Fig. 2. Mapping of radiative decay rate of a probe dipole near a couple of silver spherical nanoparticles.

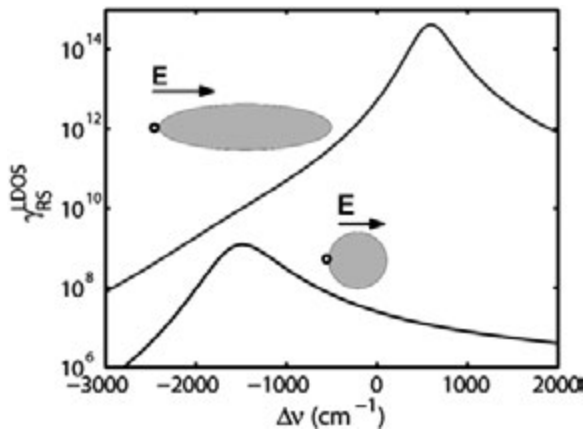

Fig. 3. Raman scattering rate for a molecule near a spheroidal and spherical silver nanopartilce. All parameters are the same as in Fig. 2 but additionally, the local density of states was included in calculations.

(LDOS) value. The latter is currently under debates with respect to correct calculations and experimental determination. Imaging using scanning near-field optical microscope (SNOM) in the illumination mode seems to provide reasonable insight on local DOS over a surface under examination similar to tunneling current in scanning tunneling microscopy which is sensitive to local electron DOS for complex surfaces. Recently an efficient computational technique has been developed for spontaneous decay rate calculation in complex metal dielectric structures [9]. Fig. 2 presents application of the technique to a couple of identical spherical particles. Notable is nearly 3 order of the magnitude enhancement of decay rate in the region between nanoparticles. The enhancement is strongly dependent on dipole orientation.

The similar approach is applicable to calculation of the Raman scattering rate based on the assumption that both processes are governed by the density of states enhancement. Fig. 3 presents the results where both local incident field enhancement and local density of states enhancement is thoroughly accounted for a spherical nanopartilce and for a prolate spheroid. When comparing Fig. 3 with Fig. 1, a contribution form the local DOS enhancement is evident. Notably, the resulting en-

hancement exceeds 10^{14} and is capable to explain ultimate single molecule Raman detection which remained unexplained from 1998 [7] till recent paper [6].

Note that such huge enhancement is by no means feasible for spontaneous emission of photons because of finite lifetime of excited states and inevitable non-radiative decay promoted by a metal proximity. Therefore, the optimal distance of an emitter from a metal body has to be chosen to get the positive net balance of the three factors: field enhancement, radiative rate enhancement and luminescence quenching. Therefore, to the best of our knowledge luminescence enhancement factors are limited by the values of 10^1–10^2 [10].

4. What is a "hot spot"?

The proposed model sheds light on the so-called "hot points" as such places on a nanotextured metal surface or near metal nanobodies where simultaneous spatial redistribution of electromagnetic field occurs both at the frequency of the incident radiation ω and at the frequency of scattered radiation ω'. Recalling the original Purcell's idea on Q-fold enhancement of spontaneous emission rate in a cavity [3], local DOS enhancement can be treated as high Q-factor development in certain portion of space near a metal nanobody. Therefore, a hot point in SERS can be treated as a place where high Q-factor develops simultaneously at the incident light frequency and emitted light frequency.

Local DOS enhancement in a sense accounts for concentration of electromagnetic field at the scattered frequency. This statement unambiguously implies *probe*, non-existing field. However, concentration of real field by many authors was anticipated to offer $|E(\omega')|^2$ enhancement factor by analogy to $|E(\omega)|^2$ factor for input light intensity. That anticipation is by no means justified because for both incident and scattered light enhancement occurs only in the close subwavelength-scale vicinity of a nanobody. Therefore enhancement of scattered field by no means can contribute to light harvesting in typical far field experiments. LDOS enhancement means immeasurable concentration of vacuum electromagnetic field rather than emitted light concentration. The latter can actually contribute to SERS but only as *induced* Raman scattering (I_0 term in Eq. (1)).

Local field enhancement for incident light can not be interpreted as surface redistribution of incident light, i.e. as a kind of local light "microfocusing" as commonly anticipated by many authors. Surface enhanced Raman scattering (as well as surface enhanced photoluminescence) are considered within the framework of linear light-matter interaction contrary to e.g. surface enhanced second harmonic generation. Therefore the overall Raman signal harvesting from a piece of area containing statistically large number of molecules will be the same independently of surface redistribution of light intensity because total incident light intensity integrated over the piece of area remains the same. Within the framework of linear light-matter interaction, Raman signal enhancement by means of incident field enhancement can only be understood in terms of high local Q-factors for incident light, i.e. in terms of light *accumulation near the surface* rather than light *redistribution over the surface*. Q-fold rise up of light intensity then occurs near hot points as it happens in microcavities and Fabry–Perot interferometers. However, accumulation of light energy needs certain time. Therefore huge Raman signals can develop only after certain time which is necessary for transient processes to finish resulting in steady increase of incident light intensity near hot points as compared to average light intensity in incoming light flux. Transient SERS experiments are therefore to be performed to clarify Q-factor effects in hot points formation.

Conclusion

Enhancement of spontaneous emission and scattering of photons is proposed to be considered alike in terms of simultaneous enhancement of incident field and photon density of states. Both effects are considered in terms of field redistribution near metal nanobodies. While incident field concentration occurs for real field and takes the finite time to happen, density of states concentration imply redistribution of imaginary, probe field and also can be viewed as local concentration of electromagnetic vacuum.

References

[1] W. L. Barnes, *J. Mod. Opt.* **45**, 661 (1998).
[2] V. P. Bykov, *Radiation of Atoms in a Resonant Environment*, World Scientific, Singapore, 1993.
[3] E. M. Purcell, *Phys. Rev.* **69**, 681 (1946).
[4] S. V. Gaponenko, *Phys. Rev. B* **65**, 140303(R) (2002).
[5] V. S. Zuev *et al*, *J. Chem. Phys.* **122**, 214726 (2005).
[6] D. V. Guzatov, S. V. Gaponenko, in: Borisenko V. E. *et al*, (Eds.) *Physics, Chemistry and Applications of Nanostructures*, World Scientific, Singapore, 2009.
[7] K. Kneipp *et al*, (Eds.) *Surface-Enhanced Raman Scattering*, Springer-Verlag, Berlin, 2006.
[8] K. Li *et al*, *Phys. Rev. Lett.* **91**, 227402 (2003).
[9] V. V. Klimov, D. V. Guzatov, *Phys. Rev. B* **75**, 024303 (2007).
[10] O. S. Kulakovich *et al*, *Nanotechnology* **17**, 5201 (2006).

17th Int. Symp. "Nanostructures: Physics and Technology"
Minsk, Belarus, June 22–26, 2009
© 2009 Ioffe Institute

Aharonov–Bohm effects in nanostructures

V. L. Gurtovoi, A. V. Nikulov and *V. A. Tulin*

Institute of Microelectronics Technology, Russian Academy of Sciences, 142432 Chernogolovka, Moscow region, Russia

Abstract. Measurements of the Little–Parks oscillations at measuring current much lower than the persistent current give unambiguous evidence of the dc current flowing against the force of the dc electric field because of the Aharonov–Bohm effect. This result can assume that an additional force is needed for description of the Aharonov–Bohm effect observed in semiconductor, normal metal and superconductor nanostructures in contrast to the experimental result obtained recently for the case of the two-slit interference experiment.

Introduction

Y. Aharonov and D. Bohm have shown in 1959 [1] that according to the universally recognized quantum formalism magnetic flux can act on quantum-mechanical state of charged particles even if the flux is enclosed and the particles do not cross any magnetic field lines [2]. The Aharonov–Bohm effect proposed [1] and observed [3] first for the two-slit interference experiment becomes apparent in numerous mesoscopic quantum phenomena observed in semiconductor and metal nanostructures [4–12]. This effect has fundamental impotence and is considered [13] as one of the most remarkable attainment in the centenarian history of quantum physics. The influence of the magnetic vector potential A on the phase φ of the wave function $\Psi = |\Psi| \exp i\varphi$ results directly from the universally recognized interpretation of the phase gradient $\nabla\varphi$ as a value proportional to the canonical momentum $\hbar\nabla\varphi = p = mv + qA$ of a particle with the mass m and the charge q. But the non-local force-free quantum momentum $p = \hbar\nabla\varphi$ transfer implied in the Aharonov–Bohm effect provokes debates [14–16] which is bucked up in the last years [17,18]. Because of the phase shift $\Delta\varphi = q\Phi/\hbar$ observed in this phenomenon it is seem that magnetic forces can act on charged particles such as electrons — even though the particles do not cross any magnetic field lines [17]. Some authors assume such forces [16]. The direct experimental test [18] has give unambiguous evidence that the Ahranov-Bohm effect in the case of the two-slit interference experiment can not be connected with a force which could shift the phase $\Delta\varphi = q\Phi/\hbar$.

One of the consequence of the Aharonov–Bohm effect in nanostructures is the persistent current observed in semiconductor, normal metal and superconductor loops [2,7–9,19–21]. The persistent current is observed in agreement with the theories [22–24] obtained in the limits of the universally recognized quantum formalism. But its observations in the loops with non-zero resistance call in question the force balance as well as in the case of the Ahranov-Bohm phase shift in the two-slit interference experiment [1–3,14–16]. Both these problems can not be considered as solved. The experimental evidence of the absence of time delays associated with forces of the magnitude needed to explain the Aharanov–Bohm phase shift [18] rather makes the problem more urgent than solves it. In the case of the Aharonov–Bohm effect in nanostructures the problem can be made more manifest because of the possibility of a dc potential difference V on loop halves with non-zero resistance $R > 0$. The observation of the persistent current $I_p \neq 0$ in this case could mean that it can flow against the force of electric field $E = -\nabla V$ if it can be considered as a direct circular equilibrium current. The progress of nanotechnology allows to make such investigation which together with the investigation of the two-slit interference experiment [17,18] can give new information on paradoxical nature of the Aharonov–Bohm effect. Semiconductor and metal nanostructures could be used for this investigation. We use superconductor nanostructure consisting system of aluminum rings with radius $r \approx 1$ μm.

1. Experimental evidence of the persistent current as a direct circular equilibrium current

First of all one should note that the persistent current is observed as a direct circular equilibrium current in many experiments [7,8,19–21,25]. The periodical change of sign and magnitude of the magnetization $M = SI_p$ [7,8,19] and the dc voltage $V_p \propto I_p$ [20,21,25] with the period of magnetic field H_0 corresponding to the flux quantum $\Phi_0 = 2\pi\hbar/q$ inside the loop with the area S gives unambiguous evidence that the persistent current has clockwise or anti-clockwise direction depending on magnetic field magnitude H. The amplitude $I_{p,A}$ of the $I_p(H) \approx I_{p,A}2(n - \Phi/\Phi_0)$ oscillations, increasing with loop perimeter l decreasing [8], does not exceed $I_{p,A} = 1$ nA in semiconductor and normal metal loop with the perimeter $l \approx 4$ μm [19]. In superconductor loop the $I_{p,A}$ value is much higher even above superconducting transition $T > T_c$ [7], where $R > 0$ and the persistent current is observed because of the thermal fluctuations. Magnetization measurements of aluminum rings with section $s = 6000$ nm^2 (110-nm-wide 60-nm-thick) have revealed at $T = T_c$ the oscillations $I_p(H)$ with the amplitude $I_{p,A} \approx 700$ nA at radius $r = l/2\pi \approx 0.5$ μm, $I_{p,A} \approx 200$ nA at $r \approx 1$ μm [7] corresponding to the theoretical prediction [24]. Our measurements of the critical temperature shift ΔT_c induced by the external current and the persistent current have collaborated these results in order of value, Fig. 1.

2. Measurements of the Little–Parks oscillations at low measuring current

In order to observe the Little–Parks oscillations $R(H)$ [26] the ring resistance is found as the relation $R = V/I_{ext}$ of the potential difference V measured on ring halves to the measuring current I_{ext} [25]. The dc electric filed $E = -\nabla V$ measured on both ring halves is directed from left to right or from right to left depending on the I_{ext} direction. The circular persistent current (and the total current $I = I_p - I_{ext}/2$

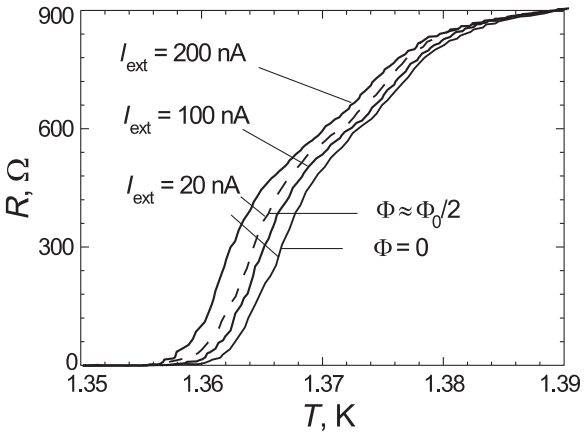

Fig. 1. The resistive transition $R(T) = V/I_{\rm ext}$ of a system of 110 aluminium rings connected in series with radius $r \approx 1$ μm and half-ring sections $s_n = 4000$ nm^2 (200-nm-wide 20-nm-thick) and $s_n = 8000$ nm^2 (400-nm-wide 20-nm-thick) measured at different values of the measuring current $I_{\rm ext} = 20$ nA; 100 nA; 200 nA and the persistent current $I_{\rm p} = 0$ at $\Phi = 0$, $I_{\rm p} \approx 100$ nA at $\Phi = \Phi_0/2$. The $R(T)$ shift $-\Delta T_{\rm c} \approx 0.0025$ K induced by the persistent current $I_{\rm p}$ with maximum value observed at $\Phi = \Phi_0/2$ is large than the one $-\Delta T_{\rm c} \approx 0.0015$ K induced by the external current $I_{\rm ext} = 100$ nA and smaller than $-\Delta T_{\rm c} \approx 0.004$ K induced by $I_{\rm ext} = 200$ nA.

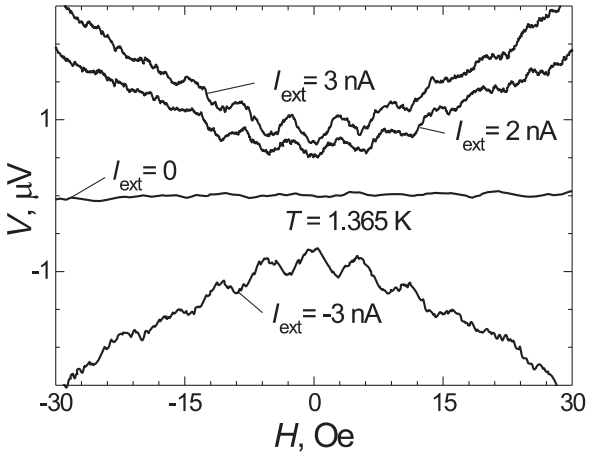

Fig. 2. The Little–Parks oscillations of the potential difference $V = RI_{\rm ext}$ measured on a system of 110 aluminium rings connected in series at low measuring current $I_{\rm ext} = -3$ nA, 0 nA, 2 nA, 3 nA and the temperature $T \approx 1.365$ K corresponding to the lower part of the resistive transition $R(T)$. The resistance $R = V/I_{\rm ext}$ oscillations in magnetic field $R(H)$ do not depend on sign and magnitude of the measuring current $I_{\rm ext}$ and is consequence $\Delta R(H) \propto I_{\rm p}^2(H)$ of the persistent current oscillations $I_{\rm p}(H)$ with the amplitude $I_{{\rm p},A} \approx 100$ nA. The period of the oscillations $H_0 = 5.2$ Oe corresponds to the flux quantum inside the ring with the area $S = \pi r^2 = 4$ μm^2.

at $I_{\rm ext} < 2I_{\rm p}$) is directed against the force of the dc electric field $E = -\nabla V$ in one of the ring halves since the $I_{\rm p} \neq 0$ is observed at a magnetic flux $\Phi \neq n\Phi_0$ constant in time $d\Phi/dt = 0$. In order to observe the Little–Parks oscillations at low measuring current $I_{\rm ext} \ll I_{\rm p}$ we used a system with great number of rings connected in series [25]. We could not observe the $R(H)$ oscillations at $I_{\rm ext} < 50$ nA in [25] because of a noise. Additional shielding has allowed us the measure $R(H)$ at $I_{\rm ext} = 2$ nA $\ll I_{{\rm p},A} \approx 100$ nA, Fig. 2. These results give unambiguous evidence of the dc current $I = I_{\rm p} - I_{\rm ext}/2 \approx I_{\rm p}$ flowing against the force of the dc electric field $E = -\nabla V \approx -RI_{\rm ext}/\pi r$ because of the Aharonov–Bohm effect. The Aharonov–Bohm effect in this case can not be explained without an additional force in contrast to the result [18] obtained for the case on the two-slit interference experiment.

Acknowledgements

This work has been supported by a grant "Possible applications of new mesoscopic quantum effects for making of element basis of quantum computer, nanoelectronics and micro-system technic" of the Fundamental Research Program of ITCS department of RAS, the Russian Foundation of Basic Research grant 08-02-99042-r-ofi and a grant of the Program "Quantum Nanostructures" of the Presidium of RAS.

References

[1] Y. Aharonov and D. Bohm, *Phys. Rev.* **115**, 485 (1959).
[2] S. Olariu and I. I. Popescu, *Rev. Mod. Phys.* **57**, 339 (1985).
[3] R. G. Chambers, *Phys. Rev. Lett.* **5**, 3 (1960).
[4] Doing-In Chang *et al*, *Nature Phys.* **4**, 205 (2008).
[5] F. Loder *et al*, *Nature Phys.* **4**, 112 (2008).
[6] R. Matsunaga *et al*, *Phys. Rev. Lett.* **101**, 147404 (2008).
[7] N. C. Koshnick *et al*, *Science* **318**, 1440 (2007).
[8] N. A. J. M. Kleemans *et al*, *Phys. Rev. Lett.* **99**, 146808 (2007).
[9] V. M. Fomin *et al*, *Phys. Rev. B* **76**, 235320 (2007).
[10] V. L. Campo Jr. *et al*, *in Proceedings of 15th International Symposium "Nanostructures: Physics and Technology"* St Petersburg: Ioffe Institute, 2007, p. 236.
[11] O. A. Tkachenko *et al*, *in Proceedings of 14th International Symposium "Nanostructures: Physics and Technology"* St Petersburg: Ioffe Institute, 2006, p. 250.
[12] D. V. Nomokonov *et al*, *in Proceedings of 13th International Symposium "Nanostructures: Physics and Technology"* St Petersburg: Ioffe Institute, 2005, p. 197; O. A. Tkachenko *et al*, *idid*, p. 205.
[13] D. Kleppner and R. Jackiw, *Science* **289**, 893 (2000).
[14] M. Peshkin and A. Tonomura, *The Aharonov–Bohm Effect*, Springer, New York, (1989).
[15] M. Peshkin, *Foun. Phys.* **29**, 481 (1999).
[16] T. H. Boyer, *Foun. Phys.* **30**, 893 (2000); *Foun. Phys.* **32**, 41 (2002).
[17] A. Tonomura and F. Nori, *Nature* **452** 298 (2008).
[18] A. Caprez, B. Barwick, and H. Batelaan, *Phys. Rev. Lett.* **99**, 210401 (2007).
[19] B. Reulet, M. Ramin, H. Bouchiat, and D. Mailly, *Phys. Rev. Lett.* **75**, 124 (1995); R. Deblock *et al*, *Phys. Rev. Lett.* **89**, 206803 (2002).
[20] V. L. Gurtovoi *et al*, *in Proceedings of 16th International Symposium "Nanostructures: Physics and Technology"* Vladivostok, Institute of Automation and Control Processes, 2008, p. 247.
[21] S. V. Dubonos *et al*, *in Proceedings of 15th International Symposium "Nanostructures: Physics and Technology"* St Petersburg: Ioffe Institute, 2007 p. 60.
[22] I. O. Kulik, *Zh. Eksp. Teor. Fiz.* **58**, 2171 (1970); *Pisma Zh. Eksp. Teor. Fiz.* **11**, 407 (1970) (*JETP Lett.* **11**, 275 (1970)).
[23] F. von Oppen and E. K. Riedel, *Phys. Rev. Lett.* **66**, 587 (1991).
[24] F. von Oppen and E. K. Riedel, *Phys. Rev. B* **46**, 3203 (1992).
[25] A. A. Burlakov *et al*, *Pisma Zh. Eksp. Teor. Fiz.* **86**, 589 (2007) (*JETP Lett.* **86**, 517 (2007)).
[26] M. Tinkham, *Introduction to Superconductivity*. McGraw-Hill Book Company (1975).

17th Int. Symp. "Nanostructures: Physics and Technology"
Minsk, Belarus, June 22–26, 2009
© 2009 Ioffe Institute

Quantum oscillations of the critical current of asymmetric superconducting rings and systems of the rings

V. L. Gurtovoi[1], M. Exarchos[2], R. Shaikhaidarov[2], V. N. Antonov[2], *A. V. Nikulov*[1], and V. A. Tulin[1]

[1] Institute of Microelectronics Technology, Russian Academy of Sciences, 142432 Chernogolovka, Moscow region, Russia
[2] Physics Department, Royal Holloway University of London, Egham, Surrey TW20 0EX, UK

Abstract. The quantum oscillations in magnetic field of the critical current of asymmetric superconducting rings with different widths of the half-rings are shifted to opposite sides for measurement in the opposite direction. The value of this shift found before equal half of the flux quantum for single ring with radius 2 μm has smaller value at lower critical current and for system of the rings with smaller radius.

Introduction

Quantum mechanics was developed for description of paradoxical phenomena observed on the atomic level with typical size <1 nm $= 10^{-9}$ m. In our everyday word with typical size >0.1 mm $= 10^{-4}$ m quantum phenomena are not observed. One may say that nanostructures appertain to a region of boundary between the quantum and classical worlds. For example, according to the Bohr' quantization of the angular momentum of electron $rp = rmv = \hbar n$ postulated in 1913 the energy difference between permitted states $E_{n+1,n} = mv_{n+1}^2/2 - mv_n^2/2 \approx \hbar^2/2mr^2 \approx 5.5 \times 10^{-21} J \approx k_B 400$ K at the orbit radius $r \approx 1$ nm and $E_{n+1,n} \approx k_B 0.0004$ K at $r \approx 1$ μm $= 1000$ nm. Therefore atom orbits with $r < 1$ nm are stable at the room temperature $T \approx 300$ K whereas the persistent current, the quantum phenomena connected with the Bohr' quantization, can be observed in semiconductor [1] and normal metal [2] ring with $r \approx 1$ μm only at very low temperature $T < 1$ K. In the rings with radius $r \approx 10$ nm made recently [3] this phenomenon was observed up to $T = 4.2$ K.

The persistent current is observed because of the influence of the magnetic vector potential A on the phase φ of the wave function $\Psi = |\Psi| \exp i\varphi$ the gradient of which $\nabla\varphi$ is proportional to the canonical momentum $\hbar\nabla\varphi = p = mv + qA$ of a particle with the mass m and the charge q. The minimum permitted value of the velocity $\oint_l dlv = m^{-1} \oint_l dl(\hbar\nabla\varphi - qA) = m^{-1}(2\pi\hbar n - q\Phi)$ should be periodical function of the magnetic flux Φ inside the ring since the $\Psi = |\Psi| \exp i\varphi$ must be single-valued at any point of the ring circumference. The period of oscillations in magnetic field H_0 corresponds to the flux quantum $H_0 S = \Phi_0 = 2\pi\hbar/q$ inside the ring with the area $S = \pi r^2$.

1. Quantum oscillations of the persistent current

The energy difference between permitted states of any real superconductor ring $\Delta E_{n+1,n} \gg k_B T$ since superconducting condensate moves as whole and superconducting pairs can not change the integer quantum number n individually [4]. Therefore the persistent current $I_p = sj_p = sqn_s v$ is observed even above superconducting transition [5]. The $n - \Phi/\Phi_0$ value in the relation

$$I_p = I_{p,A} 2\left(n - \frac{\Phi}{\Phi_0}\right) \qquad (1)$$

for the permitted value of the persistent current corresponding to minimum energy $E_n \propto (n - \Phi/\Phi_0)^2$ changes between $-1/2$ and 1/2 with the Φ variation from $(n+0.5)\Phi_0$ to $(n+1+0.5)\Phi_0$ and jumps from 1/2 to $-1/2$ at $(n + 0.5)\Phi_0$ [6]. The state with minimum energy gives predominant contribution to the thermodynamic average value $\overline{I_p}$. This value equals zero $\overline{I_p} = 0$ not only at $\Phi = n\Phi_0$ but also at $\Phi = (n + 0.5)\Phi_0$ where the persistent current I_p have equal magnitude and opposite direction in the two states $n - \Phi/\Phi_0 = \pm 1/2$. In agreement with (1) the magnetization $M \propto \overline{I_p}$ [5] and the rectified voltage $V_{dc} \propto \overline{I_p}$ [7,8] equal zero at $\Phi = n\Phi_0$ and $\Phi = (n + 0.5)\Phi_0$. The Little–Parks oscillations of the resistance $\Delta R \propto \overline{I_p^2} \propto \overline{(n - \Phi/\Phi_0)^2}$ have minimum at $\Phi = n\Phi_0$ and maximum at $\Phi = (n + 0.5)\Phi_0$ [9].

2. Shift of the critical current oscillations measured on asymmetric rings

The magnetic dependencies of the critical current $I_c = I_{c0} - 2|I_p|$ measured on symmetric ring [10] agree also with the persistent current oscillations (1) predicted with the universally recognized quantum formalism. The maximums of $I_c(\Phi/\Phi_0)$ are observed at $\Phi = n\Phi_0$ and minimums at $\Phi = (n+0.5)\Phi_0$ [10]. But we have discovered that the $I_{c+}(\Phi/\Phi_0)$ and $I_{c-}(\Phi/\Phi_0)$ oscillations of the critical current measured on asymmetric rings with different widths of the half-rings are shifted to opposite sides for measurement in the opposite direction [10]. This shift results to the anisotropy of the critical current $I_{c,an}(\Phi/\Phi_0) = I_{c+}(\Phi/\Phi_0) - I_{c-}(\Phi/\Phi_0) = I_c(\Phi/\Phi_0 + \Delta\phi/2) - I_c(\Phi/\Phi_0 - \Delta\phi/2) \neq 0$ explaining the rectification effect [8] observed on asymmetric superconducting rings [7]. But the observation of the $I_{c+}(\Phi/\Phi_0)$, $I_{c-}(\Phi/\Phi_0)$ maximums at $\Phi = (n \pm \Delta\phi/2)\Phi_0$ and their minimums at $\Phi = (n + 0.5 \pm \Delta\phi/2)\Phi_0$ is in an irreconcilable contradiction with the prediction (1) of the universally recognized quantum formalism. Because of possible fundamental importance of this contradiction we have measured the shift observed on ring with different radius and on system with different number of rings.

Our previous measurements [10] of single ring with radius $r \approx 2$ μm and widths of the half-rings $w_w = 0.25$ μm, $w_n = 0.2$ μm; $w_w = 0.3$ μm, $w_n = 0.2$ μm; $w_w = 0.35$ μm, $w_n = 0.2$ μm; $w_w = 0.4$ μm, $w_n = 0.2$ μm have shown that the value of the shift $\Delta\phi \approx 0.5$ independently of the value of

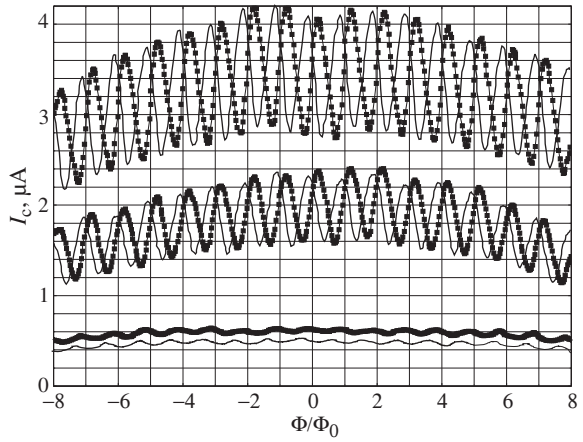

Fig. 1. Magnetic field dependencies of the critical current of a single asymmetric ring with radius $r \approx 2$ μm and widths of the half-rings $w_w = 0.3$ μm and $w_n = 0.2$ μm measured in the positive I_{c+} (solid lines) and negative I_{c-} (black squares) directions at $T = 0.986T_c$ ($I_c(T) = 4.3$ μA); $T = 0.990T_c$ ($I_c(T) = 2.5$ μA) and $T = 0.996T_c$ ($I_c(T) = 0.6$ μA). $T_c = 1.294$ K. The $I_{c+}(\Phi/\Phi_0)$ dependence for $T = 0.996T_c$ is vertically shifted on -0.1 μA. The period of oscillations in magnetic field $H_0 = \Phi_0/S = 1.44$ Oe corresponds to the rings area $S = \pi r^2 = 14.4$ μm^2 and the radius $r \approx 2.1$ μm.

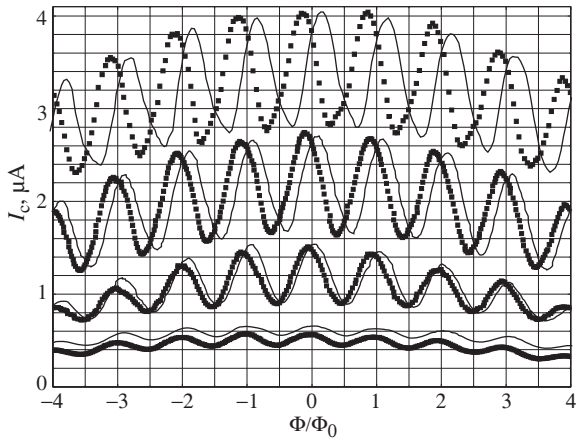

Fig. 2. Magnetic field dependencies of the critical current of an system of 110 asymmetric ring with radius $r \approx 1$ μm and widths of the half-rings $w_w = 0.4$ μm and $w_n = 0.2$ μm measured in the positive I_{c+} (solid lines) and negative I_{c-} (black squares) directions at $T = 0.968T_c$ ($I_c(T) = 4.1$ μA); $T = 0.975T_c$ ($I_c(T) = 2.8$ μA); $T = 0.981T_c$ ($I_c(T) = 1.6$ μA) and $T = 0.989T_c$ ($I_c(T) = 0.7$ μA). $T_c = 1.345$ K. The $I_{c-}(\Phi/\Phi_0)$ dependence for $T = 0.996T_c$ is vertically shifted on -0.1 μA. The period of oscillations in magnetic field $H_0 = \Phi_0/S \approx 5.2$ Oe corresponds to the rings area $S \approx 4$ μm^2 and the radius $r \approx 1.1$ μm.

the ring anisotropy w_w/w_n in the interval 1.25–2 and of the critical current value $I_c(T)$. More careful measurements have confirmed this result for the critical current $I_c(T) > 10$ μA. But at the higher temperature, where the $I_c(T)$ is lower, we have found a weak decrease of the shift value: $\Delta\phi \approx 0.4$ at $I_c(T) \approx 8$ μA; $\Delta\phi \approx 0.35$ at $I_c(T) \approx 4.3$ μA; $\Delta\phi \approx 0.3$ at $I_c(T) \approx 2.5$ μA; $\Delta\phi \approx 0.25$ at $I_c(T) \approx 0.6$ μA, Fig. 1. A more visible decrease of the shift is observed at measurement of system of 110 rings with radius $r \approx 1$ μm; $\Delta\phi \approx 0.3$ at $I_c(T) \approx 4.1$ μA; $\Delta\phi \approx 0.16$ at $I_c(T) \approx 2.8$ μA; $\Delta\phi \approx 0.1$ at $I_c(T) \approx 1.6$ μA;

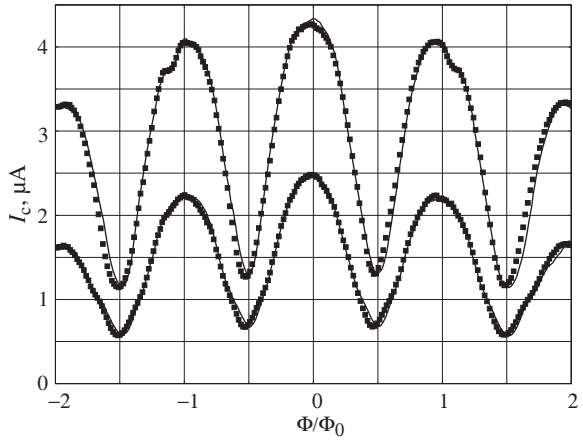

Fig. 3. Magnetic field dependencies of the critical current of an system of 667 asymmetric ring with radius $r \approx 0.5$ μm and widths of the half-rings $w_w = 0.2$ μm and $w_n = 0.15$ μm measured in the positive I_{c+} (solid lines) and negative I_{c-} (black squares) directions at $T = 0.955T_c$ ($I_c(T) = 4.3$ μA) and $T = 0.960T_c$ ($I_c(T) = 2.5$ μA). $T_c = 1.327$ K. The period of oscillations in magnetic field $H_0 = \Phi_0/S = 22.6$ Oe corresponds to the rings area $S \approx 0.92$ μm^2 and the radius $r \approx 0.54$ μm.

$\Delta\phi \approx 0.08$ at $I_c(T) \approx 0.7$ μA, Fig. 2. Only insignificant discrepancy is observed between the magnetic dependencies $I_{c+}(\Phi/\Phi_0)$, $I_{c-}(\Phi/\Phi_0)$ of the critical current measured in opposite directions on system of 667 asymmetric ring with radius $r \approx 0.5$ μm, Fig. 3.

Acknowledgements

This work has been supported by the Russian Foundation of Basic Research grant 08-02-99042-r-ofi, a grant "Possible applications of new mesoscopic quantum effects for making of element basis of quantum computer, nanoelectronics and microsystem technic" of the Fundamental Research Program of ITCS department of RAS and a grant of the Program "Quantum Nanostructures" of the Presidium of RAS.

References

[1] D. Mailly, C. Chapelier, and A. Benoit, *Phys. Rev. Lett.* **70**, 2020 (1993); B. Reulet *et al*, *Phys. Rev. Lett.* **75**, 124 (1995); W. Rabaud *et al*, *Phys. Rev. Lett.* **86**, 3124 (2001); R. Deblock *et al*, *Phys. Rev. Lett.* **89**, 206803 (2002); R. Deblock *et al*, *Phys. Rev. B* **65**, 075301 (2002).

[2] L. P. Levy *et al*. *Phys. Rev. Lett.* **64**, 2074 (1990); V. Chandrasekhar *et al*, *Phys. Rev. Lett.* **67**, 3578 (1991); E. M. Q. Jariwala *et al*, *Phys. Rev.Lett.* **86**, 1594 (2001).

[3] N. A. J. M. Kleemans *et al*, *Phys. Rev. Lett.* **99**, 146808 (2007).

[4] A. V. Nikulov, *AIP Conference Proceedings*, **1101** *Foundations of Probability and Physics-5*, 2009, p. 134.

[5] N. C. Koshnick *et al*, *Science* **318**, 1440 (2007).

[6] M. Tinkham, *Introduction to Superconductivity*. McGraw-Hill Book Company (1975).

[7] S. V. Dubonos *et al*, *Pisma Zh. Eksp. Teor. Fiz.* **77**, 439 (2003) [*JETP Lett.* **77**, 371 (2003)].

[8] V. L. Gurtovoi *et al*, *Zh. Eksp. Teor. Fiz.* **132**, 1320 (2007) [*JETP* **105**, 1157 (2007)].

[9] A. A. Burlakov *et al*, *Pisma Zh. Eksp. Teor. Fiz.* **86**, 589 (2007) [*JETP Lett.* **86**, 517 (2007)].

[10] V. L. Gurtovoi *et al*, *Zh. Eksp. Teor. Fiz.* **132**, 297 (2007) [*JETP* **105**, 262 (2007)].

17th Int. Symp. "Nanostructures: Physics and Technology"
Minsk, Belarus, June 22–26, 2009
© 2009 Ioffe Institute

Size effects and metal nanoparticle near-field enhancement

R. A. Dynich and *A. N. Ponyavina*
Institute of Physics, National Academy of Sciences of Belarus, Minsk, Belarus

Abstract. Extinction and near-field scattering efficiency factors of silver-contained nanospheres and nanoshells was examined theoretically on the basis of the extended Mie theory and with consideration of the metal permittivity size-dependence. Numerical simulations were made in the spectral range close to the localized surface plasmon absorption resonances. High sensitivity of near-field enhancement to intrinsic size effects is shown. Characteristic parameters providing a strong near-field enhancement are determined.

Introduction

Materials containing noble-metallic nanoparticles are well known for their attractive properties associated with an existence of localized surface plasmon absorption (LSPA) resonances and strongly enhanced optical fields near metal nanoparticles. Electron confinement effects in nanostructures offer a possibility to modify luminescent properties of matter and to develop novel nanostructured luminophores with enhanced efficiency [1]. However, as a rule the field enhancement near metalline nanoparticles is regarded without the internal size effect consideration. At the same time the additional free electron damping gives rise not only to the metal permittivity size dependence but also to the strong modification of nanoparticle absorption and scattering efficiency. Here we analyze the size effect on the near-field enhancement of silver nanospheres and nanoshells.

1. Method

Metal nanoshells are among the most promising plasmonic nanostructures since they are characterized by two well-controlled LSPA resonances corresponding to the both metal surfaces of a shell. Spectral position of the LSPA resonances and extinction maxima values are shown to be strong sensitive to the change of a core volume fraction [2]. Here the simulations for all-silver and silver-coated spheres were made with the use of the extended Mie theory. We have developed special codes to analyze not only extinction, absorption and scattering efficiency factors, but also a local field distribution near metalline nanoparticles, as well as the efficiency scattering factor at a near-field zone, with consideration of the metal permittivity size-dependence.

Efficiency scattering factors at a near-field zone is determined by the following relation [3]:

$$Q_{\mathrm{NF}} = \frac{\xi^2}{\pi r^2 I_0} \int_0^{2\pi} \int_0^{\pi} E_s E_s^* \sin\theta \mathrm{d}\theta \mathrm{d}\varphi|_{\xi},$$

where E_s — electrical field of scattered wave at a near zone, I_0 — intensity of incident light, ξ – radius of a spherical surface that corresponding to a surface of integration. The value of Q_{NF} shows a scattered light intensity summarized along the sphere of integration. It is worthwhile to note that with growing of ξ a value of Q_{NF} tends asymptotically to a value of Q_{sca}.

The size dependence of metal shell optical constants has been calculated in the framework of the limitation of electron mean free path model [4] based at the model proposed by Kreibig for all-metal nanospheres [5]. The principle of the model is that the limitation of mean free path causes an additional collision damping. By this means the size-dependent damping factor is:

$$\gamma_R = \gamma_0 + \frac{v_{\mathrm{F}}}{L},$$

where v_{F} — the Fermi velocity, L — an effective electron mean free path determined by collisions with the boundary, γ_0 — the bulk damping factor.

At the case of nanoshells we have the following expression for the effective electron mean free path:

$$L(R,a) = R\left[\frac{1}{1+a^2} - \frac{a}{2} - \frac{1}{4}\frac{(1-a^2)}{1+a^2}(1-a)\ln\frac{1-a}{1+a}\right],$$

where $a = r/R$ and $0 < a < 1$. As it is clear, L depends on the radius of a particle as a whole (R) as well as on the radius of a dielectric core (r). When $r \to 0$ the relation transforms into $L = R$ that is the well-known formula for all-metal spheres [5].

2. Results and discussion

In our numerical simulation we restricted our consideration to the specific case of $n_0 = n_{\mathrm{core}}$. Besides, we analyzed efficiency of extinction (Q_{ext}) and near-field scattering (Q_{NF}) at the maximum of the long-wavelength LSPA resonance of nanoshells ($\lambda_{\max}$), since it was much more pronounced than the short-wavelength LSPA resonance. This fact makes the spectral range about $\lambda_{\max}$ the most promising to expect strong near-field enhancement. It is worthwhile to note also that the value of $\lambda_{\max}$ increases rapidly when a dielectric core size tends to a nanoshell external size.

In Fig. 1 one can see that without size effects consideration the values of $(Q_{\mathrm{ext}})_{\lambda_{\max}}$ and $(Q_{\mathrm{NF}})_{\lambda_{\max}}$ oscillate when a core volume fraction increases. Oscillations were observed at any considered combinations of $n_{\mathrm{core}} = n_0$ although were damping when this value grows. The core volume fractions at the oscillation peaks correspond to values about 0.1, 0.35, 0.5, 0.68 and 0.84 for all considered values of n_{core}, n_0.

According with Fig. 2, when handling with size-depen-dent optical constants, the absolute maxima of $(Q_{\mathrm{NF}})_{\lambda_{\max}} = 1460$ is reached at all-silver nanoparticles with the external radius of 12.8 nm (for $\lambda_{\max} = 440$ nm). Corresponding value calculated without size dependence is about 5000 [6]. Besides, consideration of metal permittivity size dependence leads to practically whole smoothing the $(Q)_{\max}$ oscillations via a core volume fraction.

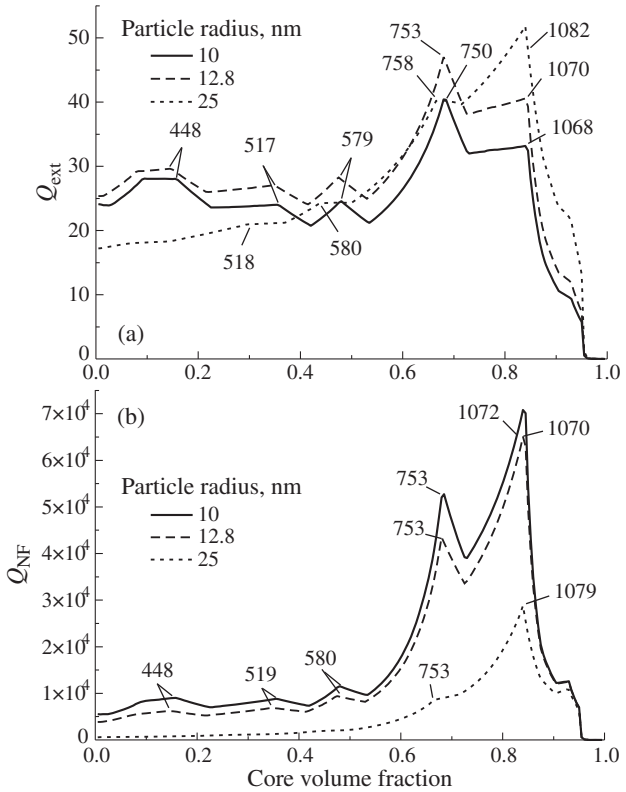

Fig. 1. Nanoshells efficiency factors at the LSPA band maximum via the core volume fraction: (a) — $(Q_{\text{ext}})_{\lambda_{\max}}$, (b) — $(Q_{\text{NF}})_{\lambda_{\max}}$. Numbers near peaks are equal to the LSPA band maximum wavelengths $\lambda_{\max}$ at a corresponding core volume fraction. Calculations were made without consideration of optical constant size dependence, $n_{\text{core}} = n_0 = 1.5$.

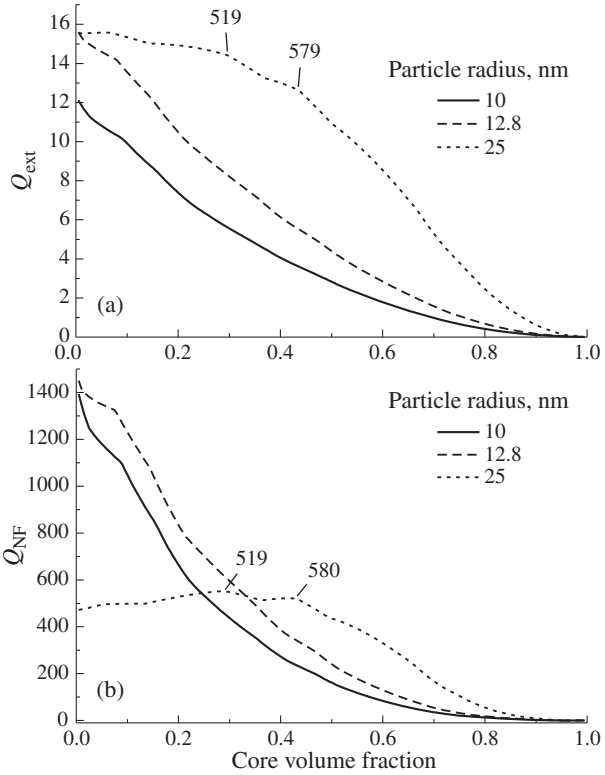

Fig. 2. Nanoshells efficiency factors at the LSPA band maximum via the core volume fraction: (a) — $(Q_{\text{ext}})_{\lambda_{\max}}$, (b) — $(Q_{\text{NF}})_{\lambda_{\max}}$. Numbers near peaks are equal to the LSPA band maximum wavelengths $\lambda_{\max}$ at a corresponding core volume fraction. Calculations were made with consideration of optical constant size dependence, $n_{\text{core}} = n_0 = 1.5$.

This is the effect of strong additional damping that connected with collisions of free electrons with both metal shell surfaces. The smaller is a particle size and the thinner is metal shell, the stronger is smoothing. For example, when the nanoshell external radius is smaller then 25 nm the additional damping gives rise the $(Q_{\text{NF}})_{\lambda_{\max}}$ decreasing just after the dielectric core appears. For nanoshells with the external radius of 25 nm and larger, the $(Q_{\text{NF}})_{\lambda_{\max}}$ depends on a core volume fraction nonmonotonically even for size-dependent optical constant (see Fig. 2b) but its maximal value is not very high (about 500 at $\lambda_{\max} = 519$ nm). Nevertheless, this value is an order of magnitude larger than the maximal value Q_{NF} reached at this wavelength for all-silver nanoparticles ($R = 45$ nm).

Conclusion

The results obtained demonstrate primarily an importance of size-dependent optical constants consideration at regarding near-field enhancement by metal nanospheres and nano-shells. Correct evaluation of near-field scattering efficiency shows that the all-silver nanospheres are more effective than nanoshells at the short-wavelength range. At the same time the use of nanoshells may give a considerable gain at the red and near IR spectral ranges, where all-metal nanospheres are not enough effective from the point of view of the near-field enhancement.

References

[1] V. A. Shubin *et al*, *J. of Lightwave Technology* **17**, 2183 (1999).

[2] A. Ivinskaya, R. Dynich, A. Ponyavina, *Proccedings of the 8th Conference on Electromagnetic and Light Scattering by Non-spherical Particles: Theory, Measurements, and Applications* (Salobrena, Spain), 132, 2005.

[3] B. J. Messinger, K. U. von Raben, R. K. Chang, P. W. Barber, *Phys. Rev. B* **24**, 649 (1981).

[4] S. M. Kachan, A. N. Ponyavina, *J. Mol. Struct.* **267**, 563 (2001).

[5] U. Kreibig, M. Voller, *Optical Properties of Metal Clusters*, (Berlin, Springer-Verlag) 533, 1995.

[6] R. A. Dynich, A. N. Ponyavina, *J. Appl. Spectr.* **75**, 831 (2008).

17th Int. Symp. "Nanostructures: Physics and Technology"
Minsk, Belarus, June 22–26, 2009
© 2009 Ioffe Institute

Ultrafast spectral dynamics and electric properties of Cu/SiO_2 nanocomposites around the percolation threshold

O. A. Buganov[1], S. M. Kachan[1], A. N. Ponyavina[1], I. A. Svito[2], J. A. Fedotova[2], A. K. Fedotov[2] and *S. A. Tikhomirov*[1]

[1] Institute of Physics, National Academy of Sciences of Belarus, Minsk, Belarus
[2] Belorussian State University, Minsk, Belarus

Abstract. Surface plasmon resonance response in reflectance spectra of dense Cu/SiO_2 nanocomposites has been studied by methods of stationary and femtosecond time-resolved spectroscopy. We examined the samples in the range of copper nanoparticle concentrations around the percolation threshold defined from resistivity measurements. We also analysed the correlation between ultrafast time-resolved optical response of dense nanocomposites and their electrical conducting properties depending on concentration changes.

Introduction

Recent progress in study of metal-dielectric nanostructures opens new opportunities for development of functional spectral-selective materials with ultrafast and tunable optical response. Spectral properties of nanoscale metal objects are specified by the localized surface plasmon resonances (SPR) resulting in strong absorption bands in the visible. The reason of the SPR resonances is coherent collective oscillations of free electrons under electromagnetic wave excitation, which are confined by the nanoparticle surface. The relaxation characteristics of plasmon and electron excitations in metal nanoparticle arrays have already been established to be dependent on nanoparticle size and shape, as well as on metal and matrix materials [1–3].

Additional way of controlling both surface plasmon decay and electron thermalization/cooling rates can be associated with collective interactions of different natures in dense arrays of metal nanoparticles. The aim of our work was to study dynamics of electron excitations in nanocomposites made of close-packed Cu nanoparticles embedded in SiO_2 matrix. Using the time-resolved reflection spectroscopy technique enabled us to examine nanocomposites with high nanoparticle concentrations which have strong absorbance at optical wavelengths.

1. Experimental

The samples are Cu/SiO_2 nanogranular films placed on the strip glass-ceramic (sitall) substrates. The film thickness and the copper atomic concentration x are the increasing functions of the film length. The size of nanogranules is about 50 nm and concentration x varies from 30 to 75 at.%, as estimated by scanning electron microscopy. Reflectance spectra of the samples were measured both by stationary and femtosecond time-resolved spectroscopy techniques. In the last case we employed the original experimental setup [4] based on the femtosecond Ti:sapphire pulsed oscillator and the regenerative amplifier system operated at 10 Hz repetition rate. The Ti:sapphire master oscillator was synchronously pumped with doubled output of feedback controlled mode-locked pulsed Nd:YAG laser. Plasmon modes of the nanocomposites were excited by second harmonic of working frequency of Ti-sapphire laser. The pump beam with the 400 nm wavelength had power of 30 μJ for 140 fs pulse duration and was focused into the 2 mm spot. We also examined resistivity of all the samples at room temperature.

2. Results and discussion

Stationary reflection spectra of the nanocomposite show a maxima at 600 nm which can be explained by the SPR excitation (see Figure 1). An increase in concentration of the copper granules causes the red shift of this maximum. This fact is an evident spectral appearance of electrodynamic coupling on the scale of short-range order in arrays of close-packed metal nanogranules [5]. Maxima in the short-wavelength region (220–270 nm) originate from Cu interband absorption.

Electrical conductive properties of nanocomposites show the percolation behavior in the concentration range $x = 55$–65 at.% (see Figure 2). Near the percolation threshold metal nanogranules interconnect into the continuous current-conducting clusters and the binary nanocomposite as a whole changes its electric properties from dielectric to metallic. In this situation, as it is well-known, physical properties of nanocomposites become very sensitive to external actions.

In Figure 3 we show the differential spectra of transient reflectance measured for the sample with nanoparticle concentration near the percolation threshold ($x = 60$ at.%). One can

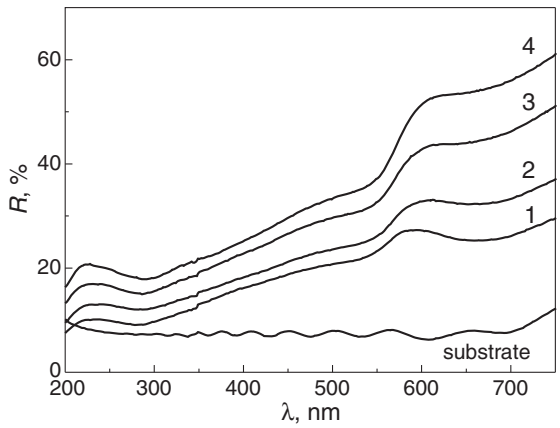

Fig. 1. Stationary reflectance spectra of $Cu_x(SiO_2)_{1-x}$ nanocomposites with different atomic concentratrion of copper: (1) 50, (2) 60, (3) 65, (4) 70 at.% (detecting reflection angle $\alpha = 20°$).

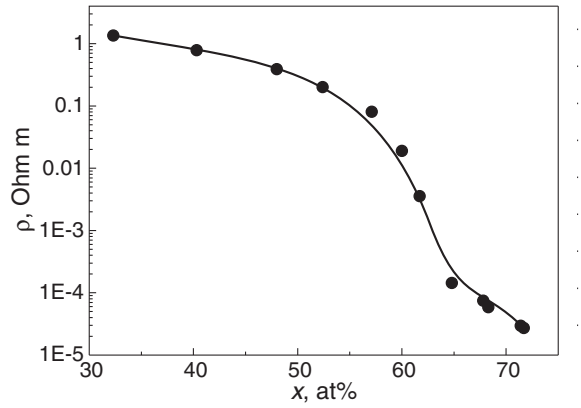

Fig. 2. Resistivity of nanogranular films $Cu_x(SiO_2)_{1-x}$ as a function of Cu atomic concentration measured at the temperature $T = 295\,^{\circ}\mathrm{C}$.

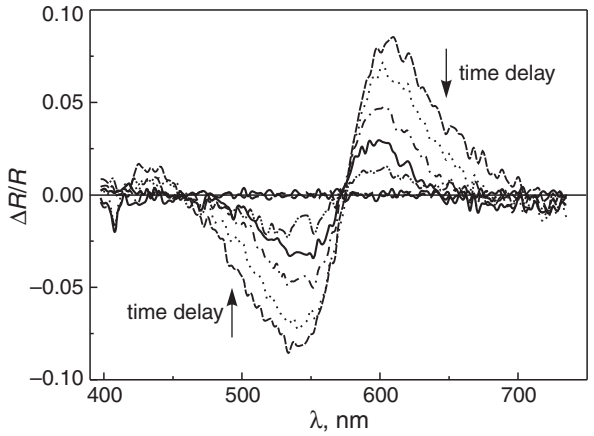

Fig. 3. Differential spectra of transient reflectance of $Cu_{0.6}(SiO_2)_{0.4}$ nanocomposite in the range of time delay up to 10 ps, minimal step $\Delta t = 100$ fs.

see that femtosecond pulse excitation of Cu nanogranular films gives rise to the significant transformation of reflectance band within the SPR range.

The features of the presented differential reflectance spectra indicate a spectral shift and a decrease in the SPR band intensity due to excitation of the sample by a femtosecond pulse. We should note that a higher value of x in granular films hardly transforms the typical view of the differential spectra but it has appreciable influence on the amplitudes of induced changes and characteristic relaxation rates at time-resolved pump-probe interactions. The reason of these effects is the competition of several processes, which are responsible for electron heating and thermalization (such as electron-electron scattering, electron-phonon interaction, dynamic Coulomb screening etc. [1–3]).

From our point of view, together with these base mechanisms there is another important contribution to the induced response associated with the concentration dependence of the efficiency of free electron tunneling between close-packed nanogranules. Apparently, tunneling in nanogranular composites is additionally stimulated by femtosecond pump pulses and causes electron collectivization on the particular scale L, which is essentially larger than a metal nanogranule's size [6].

The induced changes demonstrate fast relaxation rates. Actually, we recorded almost mono-exponential relaxation with the characteristic time of the order of 2 ps at the maximum.

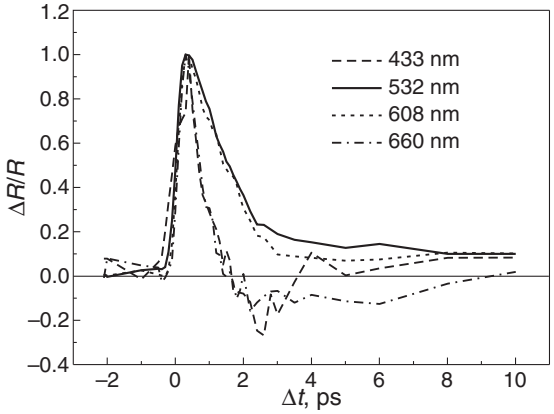

Fig. 4. Kinetics of induced changes in reflectance of the $Cu_{0.6}(SiO_2)_{0.4}$ nanocomposite.

There is also low-intensive long-term (about 100 ps) component with concentration-dependent characteristics, which is related to energy excess transport into the matrix. It is important to note that even shorter relaxation times (down to subpicosecond) were measured at the differential band edges.

Detection of high-intensive ultrafast transient response in reflectance spectra of dense Cu/SiO_2 nanocomposite thin films at their femtosecond-pulse excitation is of great practical interest due to the relevant problem of the development of ultrafast optical modulators which are capable to operate in the reflective regime.

References

[1] J. Y. Bigot, V. Halte, J. C. Merle, and A. Daunois, Electron dynamics in metallic nanoparticles, *Chem. Phys.* **251**, 181–203 (2000).

[2] S. Link and M. A. El-Sayed, Optical Properties and Ultrafast Dynamics of Metallic Nanocrystals, *Annu. Rev. Phys. Chem.* **54**, 331–366 (2003).

[3] S. -K. Eah, H. M. Jaeger, N. F. Scherer, X. -M. Lin, and G. P. Wiederrecht, Femtosecond transient absorption dynamics of closed-packed gold nanocrystal monolayer arrays, *Chem. Phys. Lett.* **386**, 390–395 (2004).

[4] A. P. Blokhin, M. F. Gelin, O. V. Buganov, V. A. Dubovskii, S. A. Tikhomirov and G. B. Tolstorozhev, Femtosecond Dynamics of Optically Induced Anisotropy of Complex Molecules in the Gas Phase, *J. Appl. Spectrosc.* **70**, 70–78 (2003).

[5] S. M. Kachan and A. N. Ponyavina, Spectral properties of close-packed monolayers consisted of silver nanospheres, *Journ. Phys.: Cond. Matter.* **14**, 103–111 (2002).

[6] L. V. Lutsev, M. N. Kopytin, A. V. Sitnikov, O. V. Stogne, Properties of nanogranular metal-dielectric composites in strong electric fields and cluster electron states, *Fizika tverdogo tela (in Russian)* **47**, 2080–2090 (2005).

17th Int. Symp. "Nanostructures: Physics and Technology"
Minsk, Belarus, June 22–26, 2009
© 2009 Ioffe Institute

Plasmonic resonances in photonic crystal slabs

André Christ[1], *Nikolai A. Gippius*[2,3] and Sergei G. Tikhodeev[3]

[1] Nanophotonics and Metrology Laboratory, École Polytechnique Fédéral de Lausanne, Lausanne, Switzerland
[2] LASMEA, UMR 6602 CNRS, Université Blaise Pascal, 24 av. des Landais, 63177 Aubière, France
[3] A. M. Prokhorov General Physics Institute, RAS, 119991, Moscow, Russia

Abstract. The properties of the plasmonic resonances in photonic crystal slabs made of arrays of metallic nanowires will be overviewed. The special attention will be paid to the formation of collective polaritonic states in such systems, the effects of near-field and far-field interactions, the ways to control the optical strength and width of the resonances.

Resonant metallic nanostructures supporting localized particle plasmons play a remarkable role in current nanoscience, where their optical properties are the subject of considerable research efforts [1]. When illuminated at their resonance frequency, extremely strong and confined optical fields can be generated to alter light-matter interactions on the nanoscale. In ordered arrays of metallic nanostructures, i.e., *metallic photonic crystal slabs*, even more possibilities are opened to control the plasmonic resonances and their interactions. In our talk the properties of the plasmonic resonances in photonic crystal slabs made of arrays of metallic nanowires will be overviewed. We will discuss the formation of waveguide-plasmon polaritons in a grating of metallic nanowires on top of a dielectric waveguide [2,3], the interaction between the localised and delocalised plasmons in a grating of metal nanowires on top of metal film [4], controlling of the subradiant and radiant plasmonic modes in a system of interacting metal nanowires gratings [5,6].

As an example, we discuss the effect of structural asymmetry in a system of two displaced gold nanowire gratings (see in Fig. 1) [5,6]. It is an important example, because periodically arranged metallic wire pairs mimic so-called magnetic atoms [7]: they demonstrate a strong diamagnetic response at optical frequencies. We show that optically inactive (i.e., optically dark) particle plasmon modes of the symmetric wire lattice are immediately coupled to the radiation field, when a broken structural symmetry is introduced. Such higher order plasmon resonances are characterized by their subradiant nature. They generally reveal longer lifetimes and smaller absorption losses than the optically active (radiant) modes. It is shown that the near-field interaction strongly determines the subradiant and radiant modes.

Figure 1 shows the scheme of two displaced gold nanowire gratings. The S-matrix calculations [8] were done for 100 × 15 nm^2 gold wires with horizontal period $d_x = 200$ nm, variable vertical spacings $L_{\rm sp}$ and horizontal displacements d_s. Figure 2(a) shows the calculated reflection spectra of the two gratings for $d_s = 0$ (dotted curve) and for intermediate symmetric alignment $d_s = 100$ nm (solid curve), $L_{\rm sp} = 30$ nm. The dashed line shows the reflection of a single grating. The narrow dip in the two-grating spectra is the subradiant asymmetric mode (with oppositely oriented dipole moments of the top and bottom wires at $d_s = 0$), the wider maximum is approximately the position of the radiant mode (with collinear dipoles). The spectral shape of the reflection can be fitted using

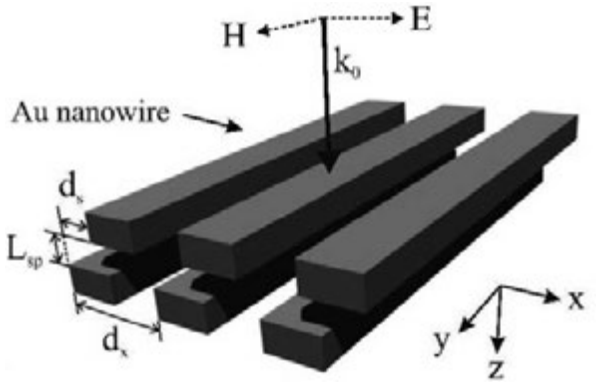

Fig. 1. A schematic picture of two displaced gratings of gold nanowires.

a Fano-type formula for amplitude reflection coefficient [5,6]

$$r(\omega) = a_r - \sum_{j=s,a} \frac{b_j \Gamma_j e^{i\Phi_j}}{\hbar\omega - E_j + i\Gamma_j}, \qquad (1)$$

where a_r ar specifies the amplitude of a constant background, and b_j and Φ_j characterize the amplitude and phase of the two localized surface plasmon eigenmodes. The spectral position and the linewidth of the individual resonances are specified by E_j and Γ_j, respectively. Figure 2(b) shows the fitted spectra. For the single-layer reference spectrum, the fit includes only a single resonance at $E_s = 1.75$ eV with a total linewidth $\Gamma_s = 250$ meV. In the case of $d_s = 0$, excellent agreement is found using two resonances: a symmetric (antisymmetric) mode at $E_s = 1.93$ eV ($E_a = 1.38$ eV) with $\Gamma_s = 380$ meV ($\Gamma_a = 60$ meV), and $\Phi_s = 0$ ($\Phi_a = 0.98$). This quantitative analysis provides important information on the coupling mechanism. For example, a lattice displacement of $d_s = 100$ nm affects the spectral positions of both resonances, and E_s (E_a) is shifted to 1.6 eV (1.76 eV). Furthermore, while the linewidth of the subradiant mode Γ_a is not modified, Γ_s is increased to 450 meV. Figure 2(c) shows the extracted dependencies of the E_a on d_s for different $L_{\rm sp}$.

As numerical analysis of the electromagnetic near-field distributions shows (see, e.g., in [3]), the electric field in the proximity of the metallic wire can be modelled as the field of an electric dipole with alternating induced charges on opposite vertical walls of the wire. Interestingly, this electrostatic analogy works quite well: the energy level shifts of the coupled plasmonic modes with changing d_s and $L_{\rm sp}$ can be modelled

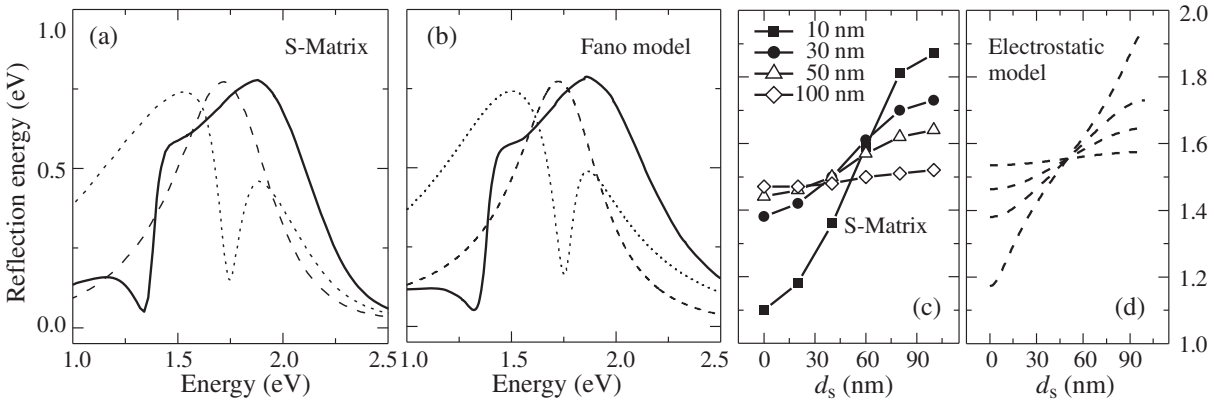

Fig. 2. Calculated (panel a) and fitted by the Fano formula (panel b) reflection spectra of the system of two gold nanowire gratings. $L_{\rm sp} = 30$ nm. Dotted and solid curves are for $d_s = 0$ and 100 nm, respectively. Dashed line is the reflection spectra of a single grating. Panel (c) shows the fitted energy of the subradiant mode E_a (see in Eq. (1)) as a function of the horizontal displacement d_s for different vertical distances $L_{\rm sp}$ between the gratings. Panel (d) shows the electrostatic energies of a system of interacting charged cylinders, as explained in the text.

within an electrostatic model as

$$\Delta E_a \propto \sum_{n,m} Q_n^u Q_m^b \log|\mathbf{r}_n^u - \mathbf{r}_m^b|,$$
$$n = 0, 1, \quad m = 0, \pm 1, \ldots . \tag{2}$$

Here $\mathbf{r}_n^u = (nd, 0)$ and $\mathbf{r}_m^d = (nd + d_s, L_{\rm sp})$ are the 2d radius-vectors of the vertical wire walls of the upper and bottom gratings, respectively, and $Q_{2n}^u = -Q_{2n}^b = -Q_{2n+1}^u = Q_{2n+1}^b$ are induced effective electrostatic charges on the upper and bottom wires (per unit wire length). The energy shifts calculated by this model are shown in Fig. 2(d) by dashed lines, they are in a reasonable agreement with the fitting of the scattering matrix calculations in Fig. 2(c). One has to bear in mind that the electrostatic model does not work for large distances $\Delta r \gg \lambda$. Also at small h the finite wire hight becomes important and the logarithmic approximation in the above formula becomes invalid.

Acknowledgements

We acknowledge support from the Russian Academy of Sciences, the Russian Ministry of Science, the Russian Foundation for Basic Research, and the ANR Chair of Excellence Program.

References

[1] U. Kreibig and M. Vollmer, *Optical Properties of Metal Clusters* (Springer, Berlin, 1995).

[2] A. Christ, S. G. Tikhodeev, N. A. Gippius, J. Kuhl, and H. Giessen, *Phys. Rev. Lett.* **91**, 183901 (2003).

[3] A. Christ, T. Zentgraf, J. Kuhl, N. A. Gippius, S. G. Tikhodeev, and H. Giessen, *Phys. Rev. B* **70**, 125113 (2004).

[4] A. Christ, T. Zentgraf, S. G. Tikhodeev, N. A. Gippius, J. Kuhl, and H. Giessen, *Phys. Rev. B* **74**, 155435 (2006).

[5] A. Christ, Y. Ekinci, H. H. Solak, N. A. Gippius, S. G. Tikhodeev, and O. J. F. Martin, *Phys. Rev. B* **76**, 201405 (2007).

[6] A. Christ, O. J. F. Martin, Y. Ekinci, N. A. Gippius, and S. G. Tikhodeev, *Nano Lett.* **8**, 2171 (2008).

[7] V. Podolskiy, A. Sarychev, V. J. Shalaev, *Nonlinear Opt. Phys. Mater.* **11**, 65 (2002).

[8] S. G. Tikhodeev, A. L. Yablonskii, E. A. Muljarov, N. A. Gippius, and T. Ishihara, *Phys. Rev. B* **66**, (2002).

17th Int. Symp. "Nanostructures: Physics and Technology"
Minsk, Belarus, June 22–26, 2009
© 2009 Ioffe Institute

Non-equilibrium and equilibrium features of polariton Bose–Einstein condensates in semiconductor microcavities

D. N. Krizhanovskii[1], A. P. D. Love[1], K. Lagoudakis[2], B. Pietka[2], D. M. Whittaker[1], R. A. Bradley[1], K. Guda[1], S. Al Rizeiqi[1], R. Bouchekioua[1], D. Sanvitto[3], P. R. Eastham[5], M. S. Skolnick[1], M. Wouters[2], B. Deveaud[2], M. Richard[4], R. Andre[4] and Le Si Dang[4]

[1] Department of Physics & Astronomy, University of Sheffield, Sheffield S3 7RH, UK
[2] Ecole Polytechnique Fédérale de Lausanne (EPFL), Station 3, CH-1015 Lausanne, Switzerland
[3] Dep. Fisica de Materiales, Universidad Autonoma de Madrid, 28049 Madrid, Spain
[4] Institut Néel, CNRS and Université J. Fourier, 38042 Grenoble France
[5] Department of Physics, Imperial College, London SW7 2AZ, UK

Abstract. Here we investigate fundamental quantum properties of the CdTe polariton BEC such as temporal and spatial coherence. Above threshold, condensation into several polariton levels with different energies and k-vectors is observed, which arises from a non-equilibrium character of the polariton system. The specific k-vectors at which condensation is triggered are determined by local potential landscape. Individual modes exhibit long-range spatial coherence comparable to their size and long coherence times (100–200 ps) for the first and the second order correlation functions, which are two orders of magnitude longer than polariton lifetime (∼2 ps). The effects of interactions between polaritons play essential role in the coherence of polariton BEC.

Introduction

Strong exciton-photon coupling in semiconductor microcavities with embedded quantum wells results in formation of two-dimensional (2D) polaritons with a very small effective mass. As a result, polariton condensation can be achieved at high temperatures and relatively small optical excitation densities. Macroscopically occupied states have been recently observed in CdTe [1] microcavities under conditions of non-resonant excitation. Polariton condensates exhibit the characteristic properties of a Bose–Einstein condensate, such as long range spatial coherence [1], reduced number of fluctuations at threshold [2] and the quantization of vortices [3]. There is evidence for equilibrated polariton distributions [1]. However, polariton condensates are far from thermodynamic equilibrium and originate from a dynamical balance of pumping and losses in the system. Non-equilibrium BEC is the well established terminology for such an interacting system, which can be described by both microscopic calculations and generalization of the Gross–Pitaevskii equation [4,5,6].

1. Multi-mode structure of polariton BEC

The sample employed here is a piece from the CdTe-based microcavity wafer used in Ref. [1], where BEC with extended spatial coherence was reported. The excitation is non-resonant using a CW diode laser at 685 nm. The size of the excitation spot is around 20 μm. Spectrally and spatially resolved images were recorded using spectrometer and a CCD camera.

Fig. 1 shows polariton emission from the bottom of the lower polariton (LP) branch in Energy-Momentum (E-k_y) space recorded at $k_x = 0$. The excitation power $P = 16$ mW is well above the threshold ($P_{\rm th} \approx 4$ mW) for polariton condensation. The emission consists of 4 narrow peaks with energy separation 0.080–0.2 meV. Two higher energy peaks are also observable at k_x away from zero. The peaks are quite narrow (FWHM ≈ 60 meV, resolution limited). Remarkable spectral narrowing and super-linear increase of the intensity of each single mode with excitation power indicates the build-up of coexistent macroscopically occupied states (polariton condensate).

The multi-mode structure of the stimulated emission originates from polariton interaction with fluctuations of transverse photonic potential, which typically occurs on a length scale of 2–4 μm with an amplitude of 0.5–0.7 meV in CdTe samples. To reveal the role of the potential on the formation of spectrally narrow coexisting condensates, we recorded spectrally and spatially resolved 2D images in momentum and real space.

Figure 4 (a–f) shows 2D images recorded in momentum space. The first ground state mode emitting at 1.675176 eV is localised around $k = 0$ within ± 0.5 μm^{-1}. The second mode emitting at energy of 1.675281 meV already consist of two lobes at ($k_x = 0$ μm^{-1}, $k_y = +1.2$ μm^{-1}) and ($k_x = 0$ μm^{-1}, $k_y = -1.2$ μm^{-1}), respectively. The pattern of the higher energy modes 3 to 6 becomes more complicated: each mode has k-vectors distinct from zero, which corresponds to the momentums of propagating LP states at the same energy. We note, that modes 3 and 6 consist of two strong maxima

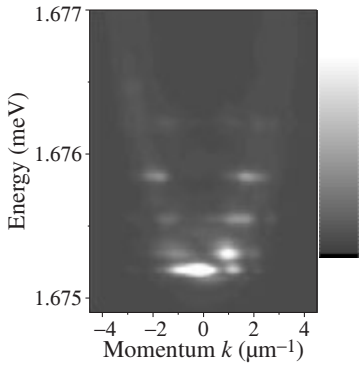

Fig. 1. Image of polariton condensate emission above threshold in energy-momentum (E-k) space. Condensation into states with different k-vectors is observed.

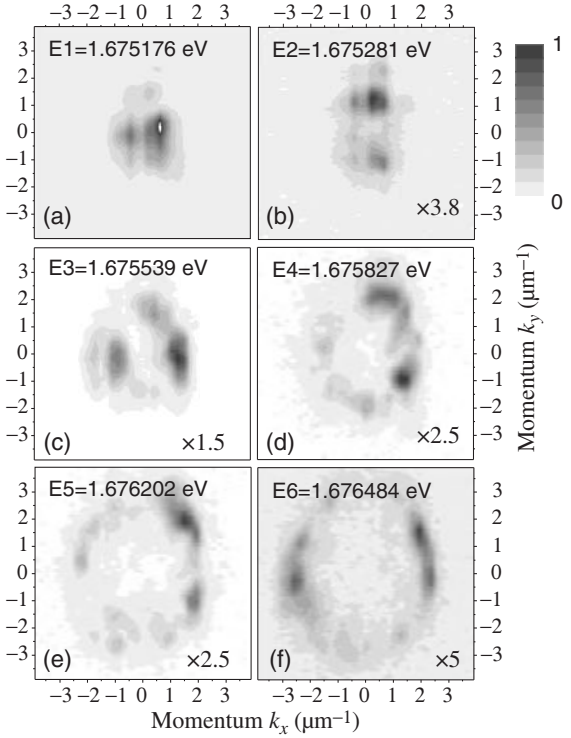

Fig. 2. Spectrally resolved k-space images of polariton condensate emission.

with opposite k-vectors at ($k_x = \pm 1.15\ \mu\text{m}^{-1}$, $k_y = 0$) and ($k_x \approx \pm 2.3\ \mu\text{m}^{-1}$, $k_y = 0$), respectively, suggesting efficient backscattering by local photonic potential disorder.

Spectrally resolved images in real space revealed that mode 1 is strongly localised within area of $5 \times 3\ \mu$m, whereas the wavefunctions of the higher energy polariton states consist of several maxima separated by 3–4 μm and are extended over a length scale of 10–20 μm. Moreover all the modes shows strong spatial overlap, indicating coexistence of the condensed phases.

A distinctive feature of BEC is formation of long range spatial coherence. Spatial coherence between the spatially separated regions of the spectrally distinct condensates was studied using standard Michelson interferometry. Above threshold an interference pattern is observed between the emissions from separated areas across the samples. Such observation indicates polariton modes have coherence lengths comparable to their size.

In a true equilibrium BEC system condensation is expected to occur only into a single ground state with its resultant massive occupation below a critical temperature, whereas the population for the higher energy states should obey Boltzmann distribution with a certain temperature. Polariton system is different from an equilibrium. At powers much below threshold, polariton relaxation toward the ground state due to polariton-phonon scattering is very inefficient, and hence polaritons are not thermalised. By contrast, with increasing excitation power, polariton-exciton scattering from the reservoir of exciton states toward the LP states becomes dominant. Such scattering enables simultaneous macroscopic occupation of several polariton modes with different k-vectors. Above threshold a dynamical balance is formed between losses in the condensed polariton modes and the gain due to relaxation from the reservoir.

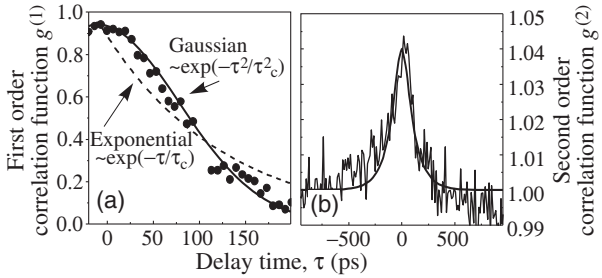

Fig. 3. Decay of the first (a) and the second (b) order correlation function of an individual polariton BEC mode.

Therefore, there is a close analogy between the phenomena of polariton condensation and laser, with a one significant difference that no population inversion is required to obtain a macroscopic occupation, because stimulated relaxation is ensured by the bosonic nature of polaritons.

The k-vectors at which polariton condensation is triggered are determined by the spatial fluctuations of the photonic potential. These fluctuations result in the formation of discrete localised polariton levels. Above threshold condensation into each localised level occurs resulting in a multi-mode stimulated polariton emission. Nevertheless, the higher energy polariton condensates, which have energies 0.7–1 meV above the polariton ground state and thus above the fluctuations in photonic potential, arise from delocalised polariton states. These propagating condensed polariton modes also interact with the potential and particles with particular k-vectors determined by a pattern of local potential may undergo coherent backscattering, which minimizes in-plane losses and triggers condensation into the states with these specific k-vectors.

2. Temporal coherence

We studied temporal coherence [7] of individual BEC modes and observe coherence times of 100–200 ps for both the first order phase correlation function, $g^{(1)}$, and the second order intensity correlation function, $g^{(2)}$ as shown in Fig. 3. The $g^{(1)}$ function is found to have a Gaussian shape and a decay time which saturates with increasing numbers of particles in the condensate.

The coherence times of the condensate are nearly two orders of magnitude longer than the polariton lifetime below threshold (2 ps), demonstrating a strong slowing of the decay processes in the coherent regime. Such slowing occurs because stimulated scattering from the polariton reservoir into the condensate dominates over spontaneous processes.

We model the system using a laser-like treatment, with a saturable gain term, to which we add the short range interactions of an atom system. Physically, the gain is provided by stimulated scattering from the reservoir of polaritons in high momentum states, which offsets the cavity losses, maintaining dynamic equilibrium. This model explains quantitatively the slowing down of the decay of the $g^{(2)}$ function. More importantly, it shows that, as a result of the slowing down, the system is in a new regime where the decay of $g^{(1)}$ is determined by the effects of interactions between polaritons in the coherent state. The interactions cause spontaneous number fluctuations in the coherent state to be translated into random energy variations, leading to decoherence. The signature of this regime is a Gaus-

sian decay for the $g^{(1)}$ function, as observed experimentally, with a decay time dependent on the interaction strength, which is in good agreement with the measured values.

Exactly this decoherence process would occur in a true equilibrium system, so our results demonstrate that the polariton condensate can behave like an equilibrium BEC on timescales much longer than the cavity lifetime. Indeed, the same physics has been predicted to occur in atomic BEC, but has yet to be observed experimentally. This is because the coherence of atom BECs is measured in atom-laser experiments, where the coherence is limited by the lifetime in the trap, as opposed to the intrinsic interaction effects we observe here.

References

[1] J. Kasprzak, M. Richard, S. Kundermann, A. Baas, P. Jeambrun, J. M. J. Keeling, F. M. Marchetti, M. H. Szymanska, R. André, J. L. Staehli, V. Savona, P. B. Littlewood, B. Deveaud and Le Si Dang, *Nature* **443**, 409–414 (2006).

[2] J. Kasprzak, M. Richard, A. Baas, B. Deveaud, R. André, J. - Ph. Poizat, and Le Si Dang, *Phys. Rev. Lett.* **100**, 067402 (2008).

[3] K. G. Lagoudakis, M. Wouters, M. Richard, A. Baas, I. Carusotto, R. André, Le Si Dang, B. Deveaud-Plédran, *Nature Physics* doi:10. 1038/nphys1051.

[4] M. Wouters and I. Carussoto, *Phys. Rev. Lett.* **99**, 140402 (2007).

[5] M. H. Szymanska, J. Keeling, and P. B. Littlewood, *Phys. Rev. Lett.* **96**, 230602 (2006).

[6] J. Keeling and N. G. Berloff, *Phys. Rev. Lett.* **100**, 250401 (2008).

[7] A. P. Love, D. N. Krizhanovskii, D. M. Whittaker, R. Bouchekioua, D. Sanvitto, S. Al Rizeiqi, R. Bradley, M. S. Skolnick, P. R. Eastham, R. André, and Le Si Dang, **Phys. Rev. Lett. 101**, 067404 (2008).

17th Int. Symp. "Nanostructures: Physics and Technology"
Minsk, Belarus, June 22–26, 2009
© 2009 Ioffe Institute

Single photons propagation in finite one-dimensional photonic crystals

A. S. Maloshtan and S. Ya. Kilin

B. I. Stepanov Institute of Physics NASB, Nazalezhnasti ave. 68, Minsk Belarus

Abstract. We present theoretical approach for description of an atom-field interaction for a system of two level atoms in one dimensional finite photonic crystal (PC). Atoms are interacting with a quantized light field mode propagating thought the photonic crystal. By using this model it is possible to consider time-spatial excitation distribution and the single photon shape transformation by finite one-dimensional PC.

Introduction

A quantum network [1] utilizes matter quantum bits (qubits) to store and process quantum information at local nodes, and light qubits (photons) for long-distance quantum state transmission between different nodes. Quantum networks can be used for distributed quantum computing or for large scale and long distance quantum communications between spatially remote parties. There are several physical systems based on cavity quantum electrodynamics (cavity-QED), which could be used for quantum networks with high success probability for quantum-state transfer or processing. One of them is the semiconductor quantum dot (QD)-cavity system [2]. Single-photon single-atom quantum interface can be implemented in micropillar microcavity where the distributed Bragg reflectors (DBR) and the transverse index guiding provide the three-dimensional confinement of light. In this work we develop the model of quantized light propagation is finite one-dimensional photonic crystal (PC) systems.

1. The model description

Let's consider the classical field inside 1d photonic crystal. Assume that the photonic crystal consists of layers with equal optical lengths. Thus if the light source with constant amplitude is placed inside 1d PC the electric field is changed at times divisible by layer traveling time (τ). For simplicity we consider the linear polarized light. The positive-frequency electric-field amplitude of a monochromatic component at frequency can be written as follows [3]:

$$E^{(+)}(z,\omega) = \sum_{n}^{\text{layers}} rect_n(z) \times \left[A^n_{\rightarrow}(\omega)\vec{e}^n_{\rightarrow} \exp\left(ik^n_{\rightarrow}(z-z_{n0})\right) + B^n_{\leftarrow}(\omega)\vec{e}^n_{\leftarrow} \exp\left(-ik^n_{\leftarrow}(z-z_{n0})\right)\right],$$

where $A^n_{\rightarrow}(\omega)$, $B^n_{\leftarrow}(\omega)$ — forward and backward propagating waves amplitudes, $\vec{e}^n_{\leftrightarrow}$ — polarization vector, $\pm\exp(ik^n_{\leftrightarrow} \rightarrow (z-z_{n0}))$ — spatial local mode configuration corresponding to bulk material with refractive index n_{layer} ($k^n = \omega n_{\text{layer}}/c$), $rect_n(z)$ — unit function which is one inside the n-layer and zero otherwise. The modes of adjacent are coupled via reflection and transmittion coefficients. Mathematically each boundary can be considered as a "beam splitter" which transforms left and right input waves to output waves. Amplitudes of local layers modes are transformed according the following rule:

$$\begin{aligned} A^{\text{right}}_{\text{out}} &= T_{l/r} A^{\text{left}}_{\text{in}} + R_{r/l} B^{\text{right}}_{\text{in}}, \\ B^{\text{left}}_{\text{out}} &= T_{r/l} B^{\text{right}}_{\text{in}} + R_{l/r} A^{\text{left}}_{\text{in}}. \end{aligned}$$

Taking into account that field amplitudes change at discrete time moments (time moments divisible by τ) one can suggest following evolution scheme. During τ period the modes inside the layer are freely evolve according the Maxwell equation without coupling to others layers modes. Then the boundaries act like a beam splitters on adjacent layers modes thus coupling the modes. Then the evolution cycle is repeated. This scheme gives the precise result for the field generated by constant amplitude source. The main approximation is that the source amplitude changes at discrete time moments divisible by τ.

To work with quantum field one needs to replace complex field amplitudes by bosonic operators inside each layers for forward and backward propagating waves. If the two level emitter is placed inside a layer it interacts with local modes only. Thus, each layer described by it's own Hamiltonian: "free

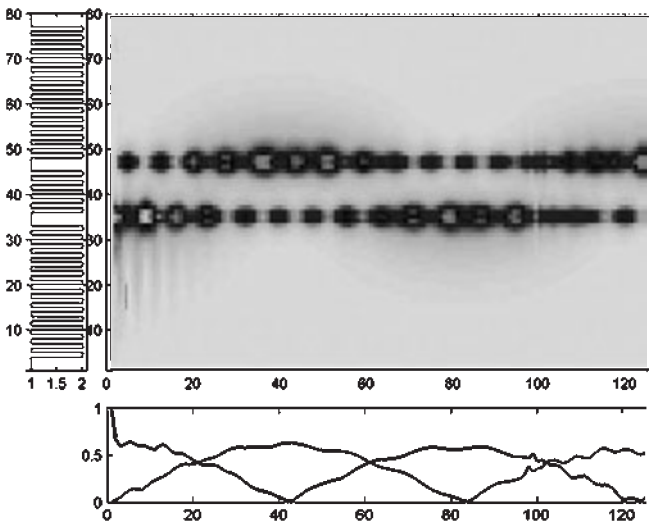

Fig. 1. Evolution of two TLA inside PC. Left panel — PC index profile. The atoms are placed at geometrical defects. Center panel — spatially related light intensity (single photon "intensity distribution"). Bottom panel — excited levels population. The frequencies of both atoms are in PC band gap.

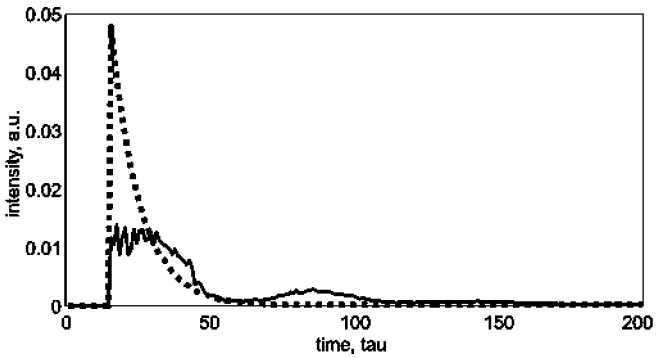

Fig. 2. Single photon shape: TLA emits photon is free space (dotted), TLA emits in finite PC (solid line). TLA frequency is out of the PC band gap.

field" or "free field + two level atom". System Hamiltonian is:

$$H = \sum_{\text{free layers}}^{l} H^l_{\text{free}} + \sum_{\text{TLA layers}}^{l} H^l_{\text{TLA}}.$$

If we consider the one excitation subspace the wave function represented as follows:

$$|\Psi(t)\rangle = \sum_{k}^{\text{TLA}} f^k |\uparrow^k\rangle + \sum_{k}^{\text{layers}} \left(c^n_k |1^{\rightarrow n}_k\rangle + d^n_k |1^{\leftarrow n}_k\rangle\right).$$

For such an approach interfaces between layers work like "beam splitters" acted on local field oscillators amplitudes [4].

$$BS_l |1^{\rightarrow n}_l\rangle = r^{l+1}_l |1^{\leftarrow n}_l\rangle + t^{l+1}_l |1^{\rightarrow n}_{l+1}\rangle,$$
$$BS_l |1^{\leftarrow n}_{l+1}\rangle = t^{l}_{l+1} |1^{\leftarrow n}_l\rangle + r^{l}_{l+1} |1^{\rightarrow n}_{l+1}\rangle.$$

So, one can suggest the following evolution scheme for quantum case. Evolution of layer's dynamic variables during single layer light propagation time are governed by layer Hamiltonian. At time moments divisible by single layer light propagation time "beam splitters" act on adjacent layers modes, thus coupling the field oscillators. By applying corresponding time evolution scheme the full dynamics of different two level emitters placed inside finite PC with quantized electromagnetic field can be obtained.

2. Scheme applications

The example of model application is shown on Fig. 1. Two TLA are placed inside PC with two geometrical defects. One of TLA is initially excited. If the TLA frequencies are in PC band gap the population oscillations between TLA are observed.

By using this model also it is possible to consider the single photon shape transformation by finite one-dimensional PC. The example is shown on Fig. 2. The model is reliable for modeling double-sided microcavities with few quantum dots at single photon level.

Acknowledgements

Text of aknowledgements here. The authors gratefully acknowledge partial financial support by EU under EQUIND project of 6FP IST-034368 and BRFFI.

References

[1] J. I. Cirac, P. Zoller, H. J. Kimble, and H. Mabuchi, *Phys. Rev. Lett.* **78**, 3221 (1997).
[2] T. Wilk, S. C. Webster, A. Kuhn, and G. Rempe, *Science* **317**, 488 (2007).
[3] J. Perina Jr., M. Centini, C. Sibilia, M. Bertolotti, M. Scalora, *Phys. Rev. A* **73**, 033823 (2006).
[4] H-A. Bachor, T. C. Ralph, *A Guide to Experiments in Quantum Optics* (Wiley-VCH, 2 ed.) 2004.

17th Int. Symp. "Nanostructures: Physics and Technology"
Minsk, Belarus, June 22–26, 2009
© 2009 Ioffe Institute

Photon localization in non-absorbing disordered nanostructures

V. P. Dick
Institute of Physics, Academy of Sciences of Belarus, F. Scaryna Avenue 68, 220072 Minsk, Belarus

Abstract. The conditions of light localization according to Ioffe–Regel criterion are investigated. The analysis is carried out for dispersive media formed of nanosized spherical particles. It is shown that light localization in non-absorbing dispersive media can be observed only if relative refractive index of particles has a value $n > 2.7$. The values of particle size parameter and particle volume concentration fulfilling the Ioffe–Regel criterion are determined for media with $n = 3.0$ and $n = 3.5$.

Introduction

During the last two decades an increasing attention has been focused on investigations of classical wave localization phenomena in disordered structures. These studies have been carried out for structures with regular arranged inhomogeneities (so called photonic and phononic crystals), as well as for disordered media where inhomogeneities were randomly distributed.

Wave localization in media with randomly distributed inhomogeneities, often called Anderson localization, is characteristic feature of disordered structures with anomalously high scattering, where mean free path l is of the order of the wavelength λ. The wave propagation in such structures is impossible, wave is "frozen", localized in a disordered medium. It is assumed, that wave with wavenumber k will be localized, if the condition $kl \leq 1$, known as Ioffe–Regel criterion, is fulfilled [1].

Wave localization can be realized in disordered media with high concentration of inhomogeneities. To analyze the wave propagation in such media one should solve the problem of wave propagation in many-body system. The exact analytical solution of this problem is not feasible. Therefore, approximate solutions are necessary. One of such solutions is a well known quasi-crystalline approximation(QCA) [2].

In this paper the QCA is used for analysis of light localization in nonabsorbing dispersive media formed of monosized homogeneous spherical particles. The conditions for realization of Ioffe–Regel criterion are analyzed. The last is represented in the form:

$$\varepsilon_k \geq 1, \tag{1}$$

where $\varepsilon_k = 1/kl$ is the normalized extinction coefficient.

1. Method

It is well known, that an optical wave in dispersive media can be decomposed into two parts: attenuated incident wave and multiply scattered wave. In the multiple wave scattering theory the attenuated incident wave is called a coherent wave. In case of the plane wave incident on a dispersive layer the coherent wave can be written in the form:

$$\langle E \rangle = E_0 \exp\left(-i(\omega t - Kz)\right), \tag{2}$$

where K is the wave number that characterizes the propagation of the coherent wave in dispersive media. Generally K is a complex value, with its real part, Re K, characterizing the velocity of the coherent wave, and the imaginary part, Im K, describing the attenuation of the coherent wave. The relation between K and ε_k is given by obvious equation $\varepsilon_k = 2\mathrm{Im}\,(K/k)$.

In this paper, the wave number K was found by numerical solution of the matrix integral equation employing QCA approximation:

$$\bar{B}\exp\left(i\mathbf{K}\times\mathbf{r}_1\right) = \bar{A}\exp\left(i\mathbf{k}\times\mathbf{r}_1\right) + N\int q(\mathbf{r}_1-\mathbf{r}_2) \times\bar{\bar{\sigma}}(\mathbf{r}_1-\mathbf{r}_2)\bar{\bar{T}}\,\bar{B}\exp\left[i\mathbf{K}(\mathbf{r}_2-\mathbf{r}_1)\right]\mathrm{d}^3\mathbf{r}_2, \tag{3}$$

where $\bar{A}$ is the matrix-column of the expansion coefficients of the incident wave into vector spherical wave functions, $\bar{B}$ is the matrix-column of the expansion coefficients of the coherent wave into vector spherical wave functions, $q(\mathbf{r})$ is the radial distribution function of the particles, $\bar{\bar{\sigma}}(\mathbf{r})$ is the translation matrix for vector spherical wave functions, $\bar{\bar{T}}$ is the so-called T-matrix describing the scattering of light by an individual particle, $\mathbf{k}$ is the light wave vector in the binding medium.

2. Results

Fig. 1 show normalized extinction coefficient ε_k calculated in the QCA for nonabsorbing dispersive media formed of monosized spherical particles. It can be seen, that extinction coefficient is nonmonotonic function of the particle concentration c_v and of the particle size parameter $x = \pi d/\lambda$. The number of peaks on the whole $\varepsilon_k(x, c_\mathrm{v})$-map roughly corresponds to the number of maxima of the $\varepsilon_k(x, c_\mathrm{v})$ at low c_v. From Fig. 1 it also follows, that extinction coefficient $\varepsilon_k(x, c_\mathrm{v})$ reaches its global maximum $\varepsilon_k^{\max}$ at some values of particle volume concentration and particle size parameter, that we denote as $c_\mathrm{v}^{\max}$ and $x^{\max}$, respectively. Values of the $\varepsilon_k^{\max}$, $x^{\max}$ and $c_\mathrm{v}^{\max}$ do essentially depend on the particle relative refractive index n.

Fig. 2 shows dependence of the $\varepsilon_k^{\max}$, $x^{\max}$ and $c_\mathrm{v}^{\max}$ on the n. It is noteworthy, that maximum light extinction is realized at relatively low concentration of particles. At $n = 2.5$ the volume concentration of particles $c_\mathrm{v}^{\max} = 0.129$. With increasing n the particle volume concentration $c_\mathrm{v}^{\max}$ slowly increases and reaches its value $c_\mathrm{v}^{\max} = 0.141$ at $n = 3.5$.

As follows from Fig. 2, the value of the $x^{\max}$ rapidly decreases with increase of the n. It is straightforward to write an approximated expression for $x^{\max}(n)$. Indeed, as follows from Fig. 1, the values of the $x^{\max}$ are approximately the same as values of x for the second Mie resonance. Therefore, at high n values $x^{\max}$ can be given by approximate equation:

$$x^{\max} = 4.49/n. \tag{4}$$

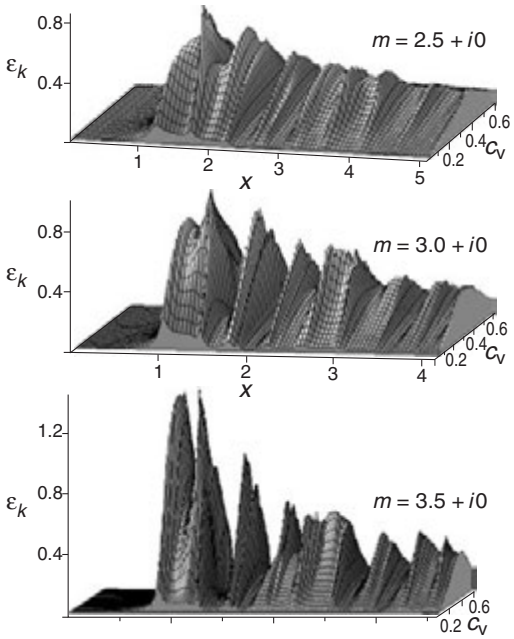

Fig. 1. Normalized extinction coefficient ε_k as function of the particle size parameter x and of the particle volume concentration c_v, at relative refractive indexes of particles $m = 2.5 + i0$, $m = 3.0 + i0$ and $m = 3.5 + i0$.

The values of the x^{max}, calculated according to Eq.(4), are shown on Fig. 2(a) as dashed curves. Comparison of these values with exact solution (Fig. 2(a), solid line) shows that, despite of relative simplicity of Eq.(4), it provide accurate description of x^{max} at $n \geq 2.5$.

From Fig. 2(b), showing dependence of the normalized extinction coefficient ε_k^{max} on the particle relative refractive index n, it follows that the highest possible extinction coefficient ε_k^{max} increases quickly when n increases, and reaches $\varepsilon_k^{max} = 1$ value at $n = 2.7$. Correspondingly, $n = 2.7$ is the lowest relative refractive index for non-absorbing monosized spherical particles for which Ioffe–Regel criterion is realized.

At $n = 2.7$ condition of the light localization ($kl \geq 1$) is realized only at $x = x^{max}$ and $c_v = c_v^{max}$. At $n > 2.7$, as can be seen, e.g., in Fig. 1, the condition is realized within certain range of x and c_v values, that becomes wider as n increases. Values of the x and c_v at which the light localization occurs in case of particles with $n = 3.0$ and $n = 3.5$ are shown in Fig. 3. In case of $n = 3.0$ the conditions for the light localization are realized within single narrow region of x and c_v values, with values of x being close to the second Mie resonance (at $n = 3.0$ the second Mie resonance takes place at particle size parameter $x_{res} = 1.43$), and values of c_v from $c_v \approx 0.13$ to $c_v \approx 0.16$. In contrast, for $n = 3.5$ condition $\varepsilon_k \geq 1$ is realized within two much wider regions of x and c_v. The first one is at values of x being close to the first Mie resonance ($x_{res} = 0.86$), the second one is at values of x being close to the second Mie resonance ($x_{res} = 1.24$).

The data shown in Fig. 3 corresponds to dispersive media formed of monosized spherical particles. Nonsphericity and polydispersity of particles will likely change and narrow the regions of x and c_v at which the light localization occurs. We speculate, however, that the best conditions for light localization will be realized in media with average particle size parameter $\bar{x}$ being close to x^{max} and the particle volume concentration c_v being close to c_v^{max}, i.e. at $\bar{x} \approx 4.49/n$ and $c_v \approx 0.14$. This assumption is supported by results of Ref. [3], where propagation of the microwave radiation in system of regularly arranged, but irregularly shaped scatterers with $n = 3.5$, has been investigated experimentally. In such a system, as shown in Ref. [3], essentially complete localization occurs at scatterer volume concentration $c_v \approx 0.14$.

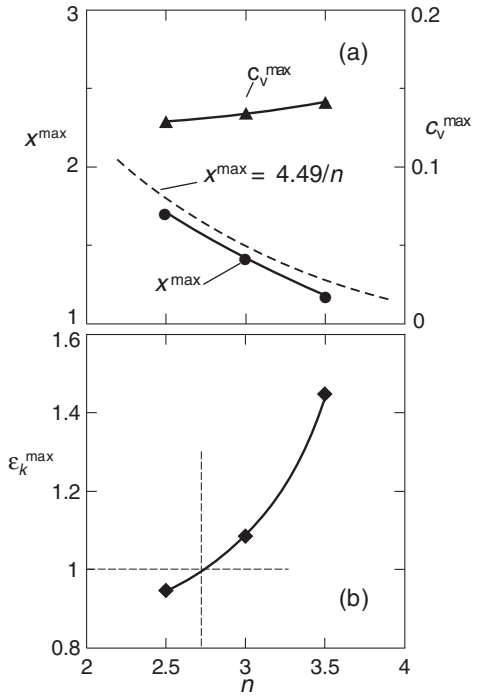

Fig. 2. Particle size parameter x^{max}, particle volume concentration c_v^{max} and normalized extinction coefficient ε_k^{max} as function of the particle relative refractive index n. Symbols are results of the calculation in the QCA; dashed curve is results of the calculation according to formula $x^{max} = 4.49/n$.

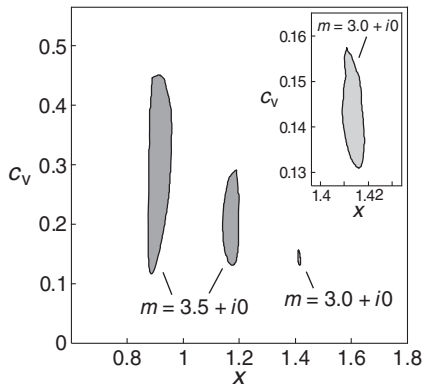

Fig. 3. Hatched regions represent ranges of x and c_v for which the light localization conditions are fulfilled for nonabsorbing dispersive media formed of monosized spherical particles with relative refractive indexes $m = 3.0 + i0$ and $m = 3.5 + i0$.

References

[1] A. F. Ioffe *et al*, *Prog. Semicond.* **4**, 237 (1960).
[2] M. Lax, *Phys. Rev.* **85**, 621 (1952).
[3] E. Yablonovitch *et al*, *Phys. Rev. Lett.* **63**, 1950 (1989).

17th Int. Symp. "Nanostructures: Physics and Technology"
Minsk, Belarus, June 22–26, 2009
© 2009 Ioffe Institute

Stop band shift in the phase transition-governed opal-VO_2 photonic crystals in NIR spectral range

S. A. Grudinkin, S. F. Kaplan, D. A. Kurdyukov, A. N. Poddubny, A. B. Pevtsov and V. G. Golubev
Ioffe Physical-Technical Institute, St Petersburg, Russia

Abstract. Three-dimensional film opal-VO_2 photonic crystals were synthesized by the chemical bath deposition technique. In the near infrared region the spectral shift of the photonic stop band governed by the semiconductor-metal phase transition as high as 150 meV was achieved. The theoretical analysis showed that in the spectral range of $\lambda \geq 1.2$ μm, where the real part of dielectric constant of VO_2 in the metallic phase is negative, the photonic stop band shifts toward the short-wave range or long-wave range depending on the VO_2 filling factor of opal pores.

Introduction

Three-dimensional (3D) photonic crystals (PhC) are prospective materials for nanophotonics. The possibility of the effective control of light in 3D PhC based on opal-VO_2 composites resulting from the shift of spectral position of a photonic stop band (PSB) was demonstrated [1–4]. This shift is governed by the semiconductor-metal phase transition in vanadium dioxide. At the same time the position and spectral shift of the PSB are defined by the lattice constant of PhC under investigation and the change of the dielectric constant of VO_2 at the phase transition. The reversible PSB shift in opal-VO_2 composites was obtained in the visible range when the real part of the dielectric constant of VO_2 is positive in the semiconductor and metal phase [1–4]. The maximum value of the shift of about 60 meV was attained. The measured value of the PSB shift can be described by using the classic Bragg relation ($\lambda = 2d_{111}\sqrt{\langle\varepsilon\rangle - \sin^2\theta}$, where λ — wavelength, $d_{111} = 0.816D$ — the interplane distance of the composite in the [111] direction, D — the silica spheres diameter, θ — the incident angle, $\langle\varepsilon\rangle$ — the average dielectric constant of the photonic crystal). It should be noted that VO_2 possesses strong dielectric constant dispersion [5]. In the spectral range of $\lambda > 1.2$ μm the real part of dielectric constant of VO_2 in the metallic phase becomes negative that must exert influence on the PSB shift controlled by the semiconductor-metal phase transition in this spectral range. Some complications appear at the estimation of the effective dielectric constant of the medium containing metal inclusions (VO_2 particles in the metallic phase in our case). In the present work, the experimental and theoretical results on investigation of the PSB shift in the film 3D PhC based on opal-VO_2 composite governed by the phase transition in the near infrared (1.2–1.8 μm) range (NIR) are presented.

1. Experimental

The opal films composed of close-packed silica spheres were grown by the vertical deposition method on a fused silica substrate [6]. The silica spheres formed a face-centered cubic (fcc) opaline matrix with the (111) plane parallel to the substrate surface. The silica sphere diameter was $D = 630$ nm. The opal pores were initially filled with V_2O_5 by the chemical bath deposition technique. The V_2O_5 was reduced to VO_2 by annealing in a hydrogen atmosphere at 550 °C and constant total pressure of 1 bar. The average filling factor of opal pores with VO_2 in the films was equal to 60 %vol. The composite structural perfection was studied by atomic forced microscopy, x-ray diffraction and Raman spectroscopy. It was found that nanocrystalline VO_2 was synthesized in the opal pores. The reflection spectra were measured by Ocean Optics NIR256 spectrometer.

2. Results and discussion

Fig. 1 presents the reflection spectra at the incident angle 13° from the opal film filled with VO_2. The spectra were measured at two temperature values: below the phase transition temperature at $T = 30$ °C (the semiconductor phase) and above it at $T = 90$ °C (the metallic phase). The observable wide peaks, which are due to the Bragg diffraction of electromagnetic waves by the periodic structure of the sample, characterize the PSB in the [111] direction. The sample heating leads to the phase transition in VO_2 and the shift of the Bragg diffraction peak position toward the short-wave region by about 0.15 eV. The value of shift appreciably exceeds ones observed for the opal-VO_2 with the PSB in the visible range [2]. It should be noticed that the Bragg reflection spectrum in the "metallic phase" becomes broader and its intensity becomes higher as compared to the Bragg line in the "semiconductor phase".

Such behavior of the Bragg line seems to be related with the negative value of real part of the VO_2 dielectric constant in the

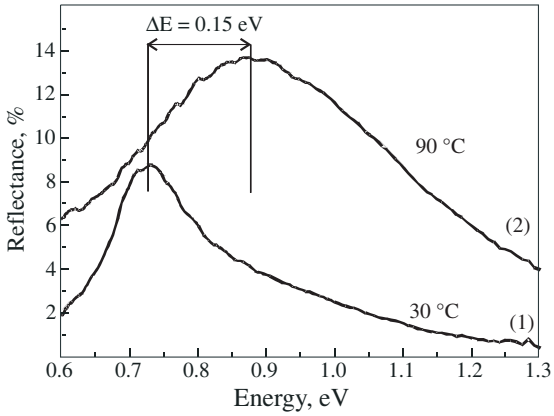

Fig. 1. Calculated dependence of the photonic stop band shift on VO_2 filling factor of opal pores for the silica spheres diameter $D = 250$ nm (PSB is located in the visible range) and $D = 630$ nm (PSB is located in the near infrared range).

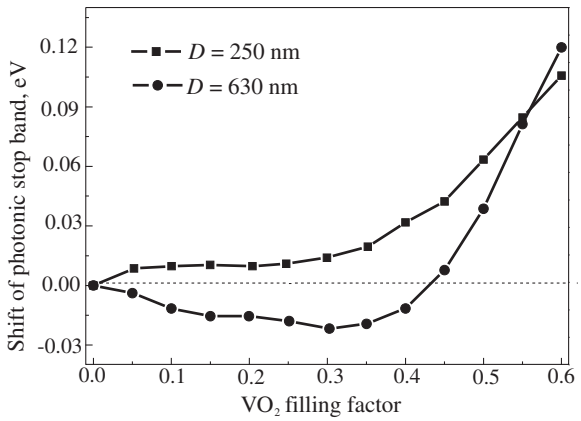

Fig. 2. Calculated dependence of the photonic stop band shift on VO_2 filling factor of opal pores for the silica spheres diameter $D = 250$ nm (PSB is located in the visible range) and $D = 630$ nm (PSB is located in the near infrared range).

metallic phase and differs from early observed changes in the visible range, where the real part of the VO_2 dielectric constants in the semiconductor and metallic phases are positive.

In order to estimate the value of the PSB shift the effective dielectric constant of opal pores filled with VO_2 metallic particles should be determined. The concept of the effective dielectric constant (ε_{eff}) is reasonable to use since the characteristic size of the pores is much smaller than the light wavelength. However, it was demonstrated that universal formula for the calculation of ε_{eff} of composite medium valid at any concentration of the metallic inclusions with arbitrary value of the dielectric constant does not exist [7]. The traditional way to determine the value of ε_{eff} of the granular composite medium is the so-called symmetrical Maxwell–Garnett's formula [7]. The two possible structure configurations are taken into account within the framework of this approach: (i) the grain of VO_2 surrounded by air and (ii) the air pore in VO_2. The relative fractions of these configurations P_1 and P_2, respectively, strongly depend on the VO_2 fill factor in the pores f. They are explicitly given by $P_1 = 1/\{1 - [(1 - f)^{-1/3} - 1]^3\}$ and $P_2 = 1 - P_1$, so that $P_1 = 1$, $P_2 = 0$ at $f = 0$ (empty pores) and $P_1 = 0$, $P_2 = 1$ at $f = 1$ (filled pores). The effective-medium theory is based on the assumption that the average dipole moment of the medium is zero, leading to the following equation [7]

$$P_1 \frac{\varepsilon_{\text{eff}} - \varepsilon_1}{2\varepsilon_{\text{eff}} + \varepsilon_1} + P_2 \frac{\varepsilon_{\text{eff}} - \varepsilon_2}{2\varepsilon_{\text{eff}} + \varepsilon_2} = 0, \qquad (1)$$

where ε_1 and ε_2 — the effective dielectric constants calculated by using classic Maxwell-Garnett's formula for 1 and 2 configurations, respectively. This formula takes into account both the resonance interaction of electromagnetic field with metallic particles and a percolation junction at exceeding of metallic particles concentration of a certain threshold.

The relation (1) has been used to calculate the effective dielectric constant of pores filled with VO_2. Note that the real part of the effective dielectric constant of the pores is positive even at high fill factor $f = 0.6$. Afterward we have undertaken the calculation of the Bragg reflection spectra of PhC by the Korringa–Kohn–Rostoker method with the given dielectric constant of the silica spheres and pores before and after the phase transition. Fig. 2 presents the calculated shift of the PSB caused by change of dielectric constants due to the phase transition in VO_2 as a function of the filling factor of pores with VO_2 for the PhC PSB position both in the visible ($D = 250$ nm) and the NIR ($D = 630$ nm) ranges. For the filling factor of about 60% the calculated data satisfy experimental results. We would like to draw attention on nonmonotonic behavior of the theoretical dependence of the PSB position shift versus the filling factor in the NIR spectral range. As the filling factor increases the Bragg line position shifts toward the long-wave range, value of the shift attains maximum, after that one intersects zero and at the high filling factor the Bragg line position shifts toward the opposite (short-wave) range.

3. Conclusion

The film 3D photonic crystals based on opal-VO_2 nanocomposites were prepared. The high shift of photonic stop band (0.15 eV) in the actual for practical application NIR spectral region (1.5 μm Telecom Standard) has been demonstrated. The mechanism of an influence of the VO_2 metallic filler on optical properties of the opal-like photonic crystal has been established. The calculation of the photonic stop band position of opal-VO_2 composite was done taking into consideration the effective dielectric constant of the opal pores averaged with symmetrical Maxwell-Garnett's formula. It is possible to create the photonic crystals based on the opal-VO_2 composite where photonic stop band governed by the semiconductor-metal phase transition will shift toward the short-wave range or long-wave range depending on the filling factor of pores with vanadium dioxide.

Acknowledgements

This work has been supported by the Dynasty Foundation — "ICFPM", RAS and RFBR.

References

[1] V. G. Golubev *et al*, *Appl. Phys. Lett.*, **79**, 2127 (2001).
[2] V. G. Golubev *et al*, *Semiconductors* **36**, 1043 (2002).
[3] D. A. Mazurenko *et al*, *Appl. Phys. Lett.* **86**, 041114 (2005).
[4] A. B. Pevtsov *et al*, *Phys. Rev. B* **75**, 153101 (2007).
[5] H. W. Verleur *et al*, *Phys. Rev.* **172**, 788 (1968).
[6] P. Jiang *et al*, *Chem. Mater.* **11**, 2132 (1999).
[7] A. P. Vinogradov *et al*, *UFN* **178**, 511 (2008).

17th Int. Symp. "Nanostructures: Physics and Technology"
Minsk, Belarus, June 22–26, 2009
© 2009 Ioffe Institute

Spectral characteristics of the 2D photonic crystals with active medium and nano-size roads

O. N. Kozina[1] and L. A. Melnikov[2]

[1] Institute of Radio Engineering and Electronics (Saratov Branch), RAS 410019 Saratov, Russia
[2] Saratov State University, 410026 Saratov, Russia

Abstract. We presented the theoretical and numerical approach to the computation of the optical characteristics of two-dimensional photonic crystal structure with active medium and metallic nano-roads. The results of calculations of the spectral characteristics of these structures are presented. The plane wave expansion method has been used.

Introduction

As well known, a photonic crystal (PC) is the dielectric material with a periodic modulation of the dielectric constant that strongly perturbs optical modes and causing photonic band gaps (PBG) to occur. The presence of gain or loss in PC dielectrics can change its characteristic [1–3]. Namely, leads to the amplification or losses depending on the sign of the imaginary part of the refraction index [4,5]. It was shown numerically for nonlinear 1D PBG structure that more than five times increase of transmission in one direction relatively to the opposite direction should be possible using realistic materials and intensities [5]. Exploration of nonlinear properties of photonic band-gap (PBG) materials may open new applications of PC for all-optical signal processing and switching [5–8]. Firstly, we investigated one-dimensional photonic crystal structure with active medium by the transfer matrix formalism method [6–8]. In that investigation the model of active medium corresponds to Nd^{+3} doped glass. We have shown the noticeable enhancement of the transmission at wavelength near 1.06 μm occurs, when unsaturated gain is about 10 cm^{-1}. The lazing optimum condition was determined. Secondly, we observed the 2D PC based on activated glasses which consists of the Nd^{3+} doped glass roads (refraction index $n_1 = 1.58 - i0.0001$) and glass tubes (refraction index $n_2 = 1.5$) with air holes ($n_3 = 1$) [9]. We assumed that this 2D PC structures is close-packed roads and observe it like 1D band structure in first approach. Using the same theoretical method we calculated the transmission coefficient for 2D PC structures vs normalized frequency. We have shown like for 1D PC [6-8], the noticeable enhancement of the transmission at wavelength near 1.06 μm occurs ($K \approx 6$). This fact, as before, means amplification. We have shown that parameters of photonic crystal laser can choose by aforementioned method. In this paper we investigate the finite-thickness 2D PC by the plane wave expansion method [10]. Firstly we consider the 2D PC slab having regular placed air holes in doped glass medium. Secondly — 2D PC slab whit metallic nono-roads. The results of the calculations of the optical characteristics of light propagation throw such structures will be present here.

1. Theory

As well known, the plane-wave expansion method [10] is based on the Fourier expansion of the internal field and the dielectric function, and is applicable to any 2D photonic crystal as long as the wave vector of the incident plane wave lies in the 2D x–y plane. Although its convergence becomes poor and it is not practical when the contrast of the dielectric constant is larger than 4:1. The model of the 2D PC is shown on Fig. 1. The external plane wave in region 1 is incident on the left (front) surface of the specimen located in region 2, which consists of N layers of circular rods with a radius r and the background dielectric. The lattice constant is denoted by a in the x–y direction (a square lattice) and the distance between the surface and the first layer of the rods is denoted by d.

As well known, these two kinds of eigenfunctions represent two independent polarizations; one is called the E polarization for which the electric field is parallel to the z axis, and the other is called the H polarization for which the magnetic field is parallel to the z axis. We consider the E polarizations when the electric field is parallel to z axis. The electric field for TE waves in the region 2 satisfies:

$$\nabla^2 E_2(r) + \left(\frac{\omega}{c}\right)^2 \varepsilon(r) E_2(r) = 0. \qquad (1)$$

Since photonic crystals may be regarded as periodic gratings, the magnetic field in region 1 is the superposition of the incident plane wave and the reflected Bragg waves, whereas that in region 3 is composed of the transmitted Bragg waves, as follow:

$$E_1(r) = E_0 \exp(ik_i r) + \sum_n R_n \exp(ik_i r), \qquad (2)$$

$$E_3(r) = \sum_n T_n \exp(ik_t(r - L)), \qquad (3)$$

where the E_0, R_n, T_n are the amplitudes of the electric field of the incident wave, the reflected Bragg waves and the transmitted Bragg waves, respectively; n is the Bragg wave order. Then we can expand the field equation and dielectric function

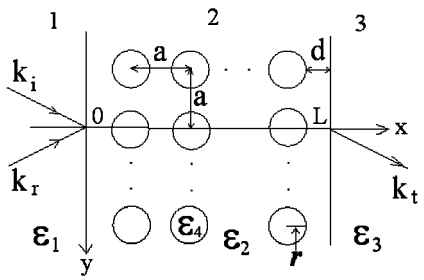

Fig. 1. The model of the 2D PC, a cross-section.

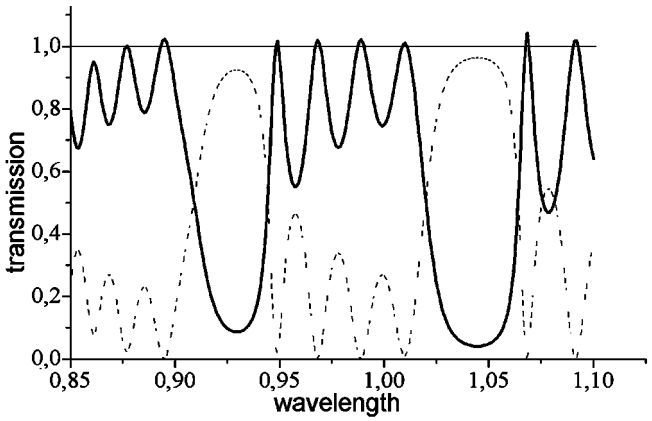

Fig. 2. The transmission and reflection spectrums of the 2D air-Nd^{3+} doped glass PC. Solid line is the transmission coefficient, dashed line — reflection. TE modes.

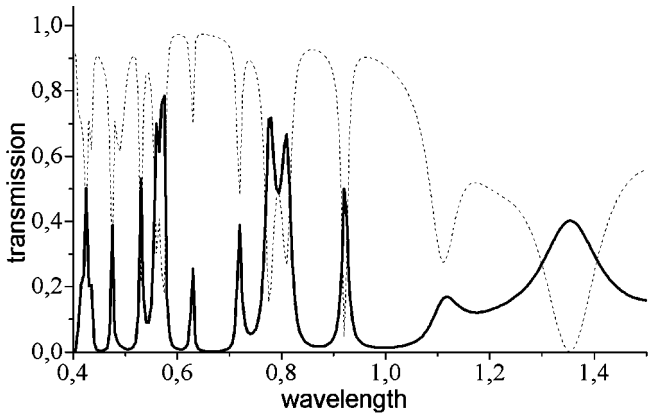

Fig. 3. The transmission and reflection spectrums of the 2D PC with nono-size metallic roads. Solid line is the transmission coefficient, dashed line — reflection. TM modes.

in Fourier series

$$\psi(x, y) = \sum_n \sum_m A_{nm} \exp(ik_y y) \sin\left(\frac{m\pi x}{L}\right), \quad (4)$$

$$\frac{1}{\varepsilon(x, y)} = \sum_n \sum_m \kappa_{nm} \exp\left(iG_y y + \left(\frac{m\pi x}{L}\right)\right), \quad (5)$$

Where the field equation $\psi(x, y)$ contains the boundary conditions [10]. The equation for H polarization can be writing on the analogy of E polarization [10].

2. Calculation and results

Using this method we calculated the transmission and reflection spectra of 2D photonic crystals. As known, the transmission spectra of photonic crystals reflect their band structure directly. They are often used for the experimental characterization of real specimens. Firstly, we investigate the spectral characteristics of the 2D air-Nd^{3+} doped glass PC. The dielectric constant of the rods is $\varepsilon_4 = 1$, for simplicity, and the background is $\varepsilon_2 = (1.58 - i0.0001)^2$ and corresponds to Nd^{3+} doped glass; $\varepsilon_1 = \varepsilon_3 = 2.48$. The parameters of structure as follow: $L = 14.5$ μm, $a = 0.25$ μm, $r = 0.125$ μm, $d = 0.25$ μm. We found the transmission coefficient behaves like we expect. Maximum peak is observed near the band gap edge and the increasing of the thickness of PC leads to the increase of its magnitude. The noticeable enhancement of the transmission occurs at $\lambda = 1.06$ μm (Fig. 2).

This method allows calculate the nonlinear deformation of the field distribution along the structure due to gain and refraction index saturation too. Then we observed the 2D photonic crystals with nano-size metallic roads. We consider the PBG system a two-dimensional square array of infinitely long metallic cylinders of radius $r = 20$ nm with $\varepsilon_4 = -9.55 + i0.309$. The lattice constant $a = 50$ nm a nd total width $L = 3000$ nm. The PC dielectric structure with permittivity $\varepsilon_2 = 2.25$ is surrounded by dielectric material with permittivity $\varepsilon_1 = \varepsilon_3 = 2.24$, for exception of the total boundary reflection. The base optical characteristics of these structures have been investigated for TE and TM modes. The results of the calculation the reflection and transmission coefficients vr wavelength for TM modes is present on the Fig. 3. Easy to see, the reflection and transmission coefficients oscillate. The partial photonic band gaps occur for TM mode. The influence of the metallic roads for TE modes comes to reflection and transmission decreasing due to losses. We compare those results with the result of calculation spectral characteristics for think dielectric film (with the same dielectric constant) without metallic embedment's. Estimated that result, we can conclude, that the interference wave can by ignorable.

So, in this paper, we have presented the theoretical and numerical approach to the computation of the amplification characteristics of two-dimensional photonic crystal structure with active medium. The model of active medium corresponds to Nd^{3+} doped glass or glasses with other doped. The results of calculations of the spectral characteristics (transmission) of these structures are presented. We present the transmission and reflection spectrums of the 2D PC with nono-size metallic roads too.

References

[1] A. Sukhorukov, Y. Kivshar *et al*, *Phys. Rev. Letters* **87**, 083901(4) (2001).
[2] S. John, *Photonic Band Gap Materials*, (Ettore Majorana Center, Erise) 241, 2000.
[3] K. Sakoda *et al*, *Opt. Express* **4**, 167 (1999).
[4] J. Fogel, J. Bendickson, M. Tocci *et al*, *Pure Appl. Opt.* **7**, 393 (1998).
[5] K. P. Dowling, M. Skarola, M. J. Bloemer, *J. Appl. Phys.* **75**, 1896 (1994).
[6] L. A. Mel'nikov, O. N. Kozina, *Opt. Spectrosc.* **94**, 411 (2003).
[7] L. A. Mel'nikov, O. N. Kozina, *Laser Physics* **14**, 1 (2004).
[8] O. Kozina, L. Melnikov. *Journal of Non-Crystalline Solids* **353** 968 (2007).
[9] O. N. Kozina, L. A. Mel'nikov *et al*, *Proceedings of 16th. Int. Symp. "Nanostructures: Physics and Technology" (Vladivostok, Russia, July 15–19, 2008)*, 253, 2008.
[10] K. Sakoda *et al*, *Optical properties of photonic crystals.*, (New York Springer-Verlag Berlin Heidelberg), 2001.

17th Int. Symp. "Nanostructures: Physics and Technology"
Minsk, Belarus, June 22–26, 2009
© 2009 Ioffe Institute

Light scattering by a plane-parallel layer with spatial correlation of particles

A. V. Loiko[1] and V. V. Berdnik[2]

[1] Institute of Physics of the NAS of Belarus, 220072 Minsk, Belarus
[2] Techniques of hydrogeological investigation, 420015 Kazan, Russia

Abstract. We propose a model of light propagation in a layer of partially ordered particles. It is based on the radiative transfer equation and the doubling method. The interference approximation is used to take into account collective scattering effects.

A rigorous description of scattering in the layer with spatial correlation of particles requires the use of the multiple scattering waves theory. As a rule, publications devoted to analysis of the propagation of radiation in close-packed media with spatial correlation of particles are confined to an analysis of either the attenuation of a parallel beam of light or the angular structure of singly scattered light. In most cases, such investigations are based on the equations of wave transport and numerical simulation by the Monte Carlo method.

The structure factor $S_3(\gamma, w)$, which takes into account the effect of light interference occurring in a system of correlated particles, is used to find differential scattering coefficient, scattering coefficient, and the extinction coefficient for a medium consisting of identical spherical particles [1].

For a system with a hard sphere potential, the structure factor was calculated in the Percus–Yevick approximation [2]

$$S_3(\gamma, w) = 1 + 4\pi n \int_0^\infty [g(r, w) - 1] \frac{\sin zr}{zr} r^2 dr, \quad (1)$$

where n is the number of particles in a unit volume; $g(r, w)$ is the radial distribution function characterizing the spatial arrangement of particles; $z = 4x \sin\gamma/2$.

The function

$$u = \int_0^\pi p_l(\gamma) S_3(\gamma, w) \sin\gamma d\gamma \quad (2)$$

characterizes the degree of optical interaction of particles. Calculations show that the magnitude u decreases monotonically with increasing particles concentration and the spectral dependence has maximum. The peak value of spectral dependence increases with the concentration increasing.

The value of the phase function at small scattering angles decreases with increasing of the volume concentration of particles w. At fairy large concentrations, the phase function acquires a characteristic maximum at a nonzero scattering angle. Upon an increase in the value of w, the maximum is displaced towards large angles, while an increase in the particle size displaces maximum towards small angles. Note, that at certain values of the particle radius and concentration of particles the asymmetry parameter of the phase function may be equal to zero, or attain the negative values.

The spectral dependence of the optical thickness of the layer with non absorbing particles is presented by the expression

$$\tau_0 = A\lambda^{-k(\lambda)}, \quad (3)$$

where A is a constant, $k(\lambda)$ is the exponent, which sometimes referred as "wave exponent"

$$k(\lambda) = \frac{d(\ln\tau_0)}{d(\ln\lambda)}. \quad (4)$$

The wave exponent for diffusely scattered light

$$k_d = \frac{d(\ln(-\ln T(\mu_0)))}{d(\ln\lambda)}, \quad (5)$$

where $T(\mu_0)$ is the transmission coefficient determined by the layer doubling technique. In the case of small optical thicknesses $k = k_d$.

Spectral dependence of transmitted light for a layer of non-absorbing optically soft fine particles is investigated. At small volume concentration of the particles the week spectral dependences of wave exponents for coherently transmitted and diffuse light are observed. It is shown that in a layer with large volume concentration of particles the wave exponent can exceed considerably the value of four, which takes place for the Rayleigh particles. The dependence of wave exponents for coherently transmitted and diffuse light on the refractive index and concentration of particles is investigated in details. Multiple scattering of light results in the reduction of the exponent. The quantitative results are presented and discussed. It is shown that there is a range of wavelengths where the negative values of the wave exponent at the regime of multiple scattering are implemented.

The results were used to describe some specific features observed experimentally in liquated glasses, where the value of exponent more than four is implemented.

The developed model is applicable for disordered photonic crystals, composite liquid crystal materials, polymer-dispersed liquid crystal cells, liquated glasses, porous glasses and other disperse systems, where ordering or partial ordering of particles takes place.

Acknowledgements

This work has been supported in part by the "Photonics" programm.

References

[1] V. V. Berdnik *et al*, *J. Quant. Spectr. Rad. Transfer* **88**, 111 (2004).
[2] V. V. Berdnik *et al*, *Quantum electronics* **36**, 1016 (2006).

17th Int. Symp. "Nanostructures: Physics and Technology"
Minsk, Belarus, June 22–26, 2009
© 2009 Ioffe Institute

Resonant multiple diffraction of light in three-dimensional photonic crystals

V. G. Fedotov[1,2], *A. V. Sel'kin*[1,2], A. Yu. Men'shikova[3], N. N. Shevchenko[3] and A. V. Yakimanskiy[3]

[1] Ioffe Physical-Technical Institute, St Petersburg, Russia
[2] Faculty of Physics, St Petersburg State University, 198504 St Petersburg, Russia
[3] Institute of Macromolecular Compounds, RAS, 199004 St Petersburg, Russia

Abstract. Propagation of electromagnetic field in spatially confined three-dimensional photonic crystals with high dielectric contrast is studied for the case when the regime of multiple diffraction is of importance. Comparison of the eigenmode energy spectrum of spatially confined photonic crystals with measured and calculated reflectance contours is performed in details. The complicated structure of the Bragg reflection spectra is shown to be shaped due to the additional eigenmodes excited resonantly by diffraction of light on the crystal planes inclined to the lateral ones.

Introduction

Interaction of electromagnetic field with spatially-periodic solid state structures which permittivity changes with spacing comparable with the wavelength of light is accompanied by a number of striking diffractive optical phenomena that can be matched with strong modification of the eigenmode energy spectrum [1]. Heightened interest to such structures called photonic crystals (PhC) is associated with a possibility of effective control of light propagation inside PhC and with new perspective applications in laser techniques and optoelectronics using nanostructured materials [2]. Being a nontrivial object of scientific research, PhC make it possible to study important fundamental problems of light interaction with condensed matter [3].

In this work, the electromagnetic wave propagation in 3D PhC for the case when the multiple Bragg diffraction (MBD) [4] regime is of importance is performed. Special attention is given to the theoretical analysis of the complicated structure of the Bragg reflection contour. On this, the resonant phenomena due to the photonic band gap (PBG) structure modification with an account of the MBD effects are discussed.

1. Results

The distinctive feature of a number of opal-like PhC possessing high dielectric contrast (strong spatial modulation of refraction index) is an existence of the doublet structure in the Bragg reflection spectra for *s*-polarized light in some range of the incidence angles θ (for example, see Ref. [3]). As detailed measurements show, such doublet structure is shaped by the dip that moves to the long-wave region (contrary to the Bragg's law) with θ increasing. Arising the Bragg reflection contour doublet structure indicates the 3D character of the PhC periodicity (simultaneous diffraction on the non-parallel crystal planes takes place).

General diffraction phenomena associated with the 3D periodicity of PhC can be described (not only qualitatively, but also quantitatively) in the framework of truncated Bloch state formalism [5]. Such formalism imply Bloch amplitude extension by minimal number of G_{hkl} vectors of reciprocal lattice characterized by (h, k, l) indexes of the face centered cubic (f.c.c.) lattice crystallographic planes. These vectors make main (resonant) contribution to the light scattering. In the case of our calculation the vectors G_{000}, G_{111}, and $G_{\bar{1}11}$ should be used. Numerical calculations of the spectra are performed using characteristic values of structural and dielectric parameters of an opal-like PhC [3] made up from spherical polystyrene particles.

Bragg reflection spectra (*s*-polarization) calculated for a semi-infinite opal-like PhC with (111) reflecting (lateral) surface are shown in Fig. 1 (left column). The spectra are calculated for the case when the incidence plane is perpendicular to the $(\bar{1}11)$ crystal plane. These spectra are compared with the eigenmode energy spectra calculation for the same values of angles θ (right column).

Calculated curves of the reflection coefficient demonstrate a striking effect caused by the multiple character of diffraction: a dip in the reflection spectrum in a narrow range of light incidence angles. As shown in Fig. 1, the dip moves to the long-wave region with θ increasing when the Bragg reflection band moves to the short-wave region. This fact completely correlates with the results of experiment.

2. Discussion

Physical interpretation of the discussed phenomena becomes clear as a result of comparison of the reflection spectra (Figure 1(a), (b), (c)) with the corresponding energy spectra of eigenmodes in semi-infinite PhC ((a′), (b′), (c′)). As can be seen from Fig. 1, the dip in the reflection contour arises when additional modes (curves 2) associated with the contribution of the $(\bar{1}11)$ crystal planes inclined to the lateral surface of PhC in the Bragg diffraction of light are excited.

Exclusion of the oblique crystal planes from calculations results in disappearance of the spectral dips in reflecttance. Then the reflection contour is shaped by modes of type 1 and 3. The contour has the form of a band with 100% plateau in maximum, which occupies spectral range corresponding to the PGB width of the trivial 1D Bragg structure.

Excitation of additional modes in the 3D PhC structure means the energy transfer in the PBG range inside PhC. The additional modes appear in main PBG between dispersion curves 1 and 3. In this case additional diffraction of light along directions, different to ones defined by the standard reflection-refraction law arises. A part of incident energy flow goes

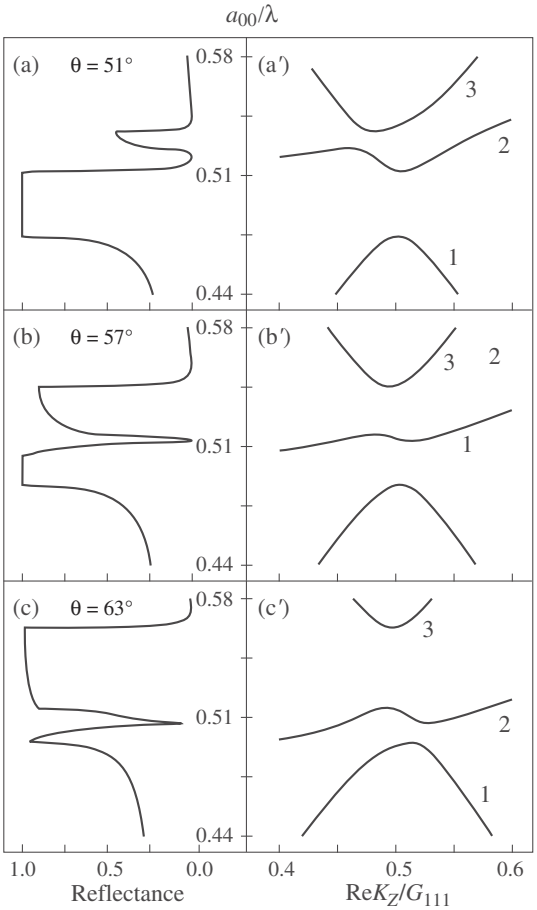

Fig. 1. Calculated Bragg reflection spectra (a), (b), (c) and the corresponding dispersion dependences (a′), (b′), (c′) for the electromagnetic field eigenmodes of a semi-infinite photonic crystal with the reflecting surface (111) at the different incidence angles θ subject to simultaneous diffraction by the two systems of crystal planes (111) and $(\bar{1}11)$ (three-band mixing approximation). a_{00} is the distance between the neighboring spherical particles of the specimen, λ is the wavelength of light in vacuum, Re K_Z is the projection of the real part of the mode wavevector onto the normal to the surface, and G_{111} is the length of the reciprocal-lattice vector in the [111] direction (Z axis).

through the crystal interface and thereby attenuates the reflected flow. As a result, the reflection coefficient becomes less than unity and a spectral dip appears in the reflection contour at the frequencies where the type 2 modes are excited most efficiently.

It is interesting to note that there exists the spectral region where the group velocity for the eigenmodes 2 (Fig. 1) is negative. This means that the opal-like medium under consideration is characterized by the negative refraction index, i.e. such a medium is expected to exhibit specific properties of metamaterials [6].

Spectral position $\lambda_{(\min)}$ of the dip in the calculated Bragg reflection contour for the ideal f.c.c. lattice can be estimated within the approximation of the weak spatial modulation of the PhC permittivity (the "empty lattice" approximation):

$$\lambda_{(\min)} = a_{00}\sqrt{2/3}\left(\sqrt{2}\sin\theta + \sqrt{\varepsilon_0 - \sin^2\theta}\right), \qquad (1)$$

where $\varepsilon_0 = \varepsilon_a f + \varepsilon_b(1-f)$ is the average permittivity of PhC,

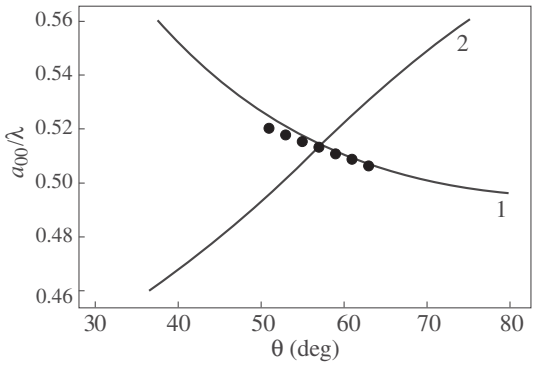

Fig. 2. Spectral positions of the dips (curve 1, symbols) and the peaks (curve 2) of the Bragg reflection against the light incidence angle θ: 1 — calculation based on the analysis of the dispersion curves of the eigenmodes stimulated by oblique planes, 2 — in accordance with the Bragg's formula (diffraction by the (111) planes), symbols — from the calculated reflection spectra.

consisting of the spheres with permittivity ε_a (for polystyrene $\varepsilon_a = 2.522$) and "cavities" with permittivity ε_b (for vacuum $\varepsilon_b = 1$), and f is the filling factor of the PhC structure (filling by contacting spheres). In fact, in the same approximation the Bragg's formula for spectral position $\lambda_{(\max)}$ of the reflection peak can be obtained:

$$\lambda_{(\max)} = a_{00}\sqrt{8/3}\left(\sqrt{\varepsilon_0 - \sin^2\theta}\right). \qquad (2)$$

In Fig. 2 the solid curves show calculated (using Eq. (1) and Eq. (2)) dependences of ratios $a_{00}/\lambda_{(\min)}$ (curve 1) and $a_{00}/\lambda_{(\max)}$ (curve 2) against θ. In this figure the points represent the dip spectral position dependence taken from the calculated Bragg reflection spectra like shown in Fig. 1 (left column). As can be seen, the points are located sufficiently close to the solid curve plotted by using Eq. (1). When analyzing experimental data according to the formula (1) we have to take into account actual experimental errors in the angle and dip position measuring (especially, when due to the PhC structure imperfection the spectral singularities are expressed not as clear as in Fig. 1). So, it is reasonable to assert that, within the limits of experimental error, the simple analytical approach based on Eq. (1) describes well the MBD spectral dip position and is of significant practical importance for diagnostic and characterization of opal-like PhCs.

Acknowledgements

This work has been supported in part by the Presidium of the Russian Academy of Sciences, by the Physical Sciences Division of the Russian Academy of Sciences, by the St Petersburg Scientific Center of the Russian Academy of Sciences, and by the Russian Foundation for Basic Research.

References

[1] S. John, *NATO ASI Series B* **340**, 523 (1995).
[2] C. Lopez, *Adv. Mater.* **15**, 1679 (2003).
[3] A. G. Bazhenova *et al*, *Phys. Solid State* **49**, 2010 (2007).
[4] H. M. van Driel and W. L. Vos, *Phys. Rev. B* **62**, 9872 (2000).
[5] A. V. Sel'kin, *Proc. of 12th Int. Symp. "Nanostructures: Physics and Technology"*, St Petersburg, Russia, 2004, p. 111.
[6] J. B. Pendry *et al*, *Phys. Rev. Lett.* **85**, 3966 (2000).

17th Int. Symp. "Nanostructures: Physics and Technology"
Minsk, Belarus, June 22–26, 2009
© 2009 Ioffe Institute

Green's function asymptotic in two-layered periodic medium

I. Starkov[1,2], S. Tyaginov[1,3] and T. Grasser[1]

[1] Institute for Microelectronics, TU Vienna, Guß hausstraße 27–29, A-1040 Vienna, Austria
[2] Academic Physics and Technology University, St Petersburg, Russia
[3] Ioffe Physical-Technical Institute, St Petersburg, Russia

Abstract. Green's function asymptotic properties of the wave field in a two-layered periodic medium is analytically examined. The solution is constructed by the stationary phase method. It is shown that some singularities occur in this approach. Namely, the Green's function asymptotical form is proportional to the distance from a source as $R^{-5/6}$, instead of the expected R^{-1} behavior. Thus, the power flux density in this directions decreases very slowly (as $R^{-5/3}$) and as a consequense there exists a set of ultra-propagation power channels. We focus on the description of the vicinity of a singular cone where the usual stationary phase method fails and determined a smooth transition from the standard asymptotic form to the new one. Finally, a detailed analysis of the obtained results is given.

Introduction

The Green's function method applied to periodic structure has theoretical significance, but studying propagation and scattering of waves is one of the most effective methods to investigate systems with periodically varying in space properties [1,2]. This method is widely adopted in investigations of liquid crystals [3] and photonic band structures [4]. Here we study the field of a point source, i.e. the Green's function in a two layered medium (a_1, a_2) with a step-like spatial variation of wave numbers (k_1, k_2) and one-dimensional periodicity for large distances from the source (Fig. 1). It is important to point out that the specified formulas do not depend on size and other structural parameters. It is shown that forbidden zones exist in such a media. The results are illustrated by numerical calculations.

1. Green's function integral representation

We consider a scalar field and are not interested in polarization effects. The Green's function $G(z, z_1, \mathbf{r}_\perp)$ is the solution of the equation

$$\left(\Delta + k^2(z)\right) G(z, z_1, \mathbf{r}_\perp) = -\delta(\mathbf{r} - \mathbf{r_1}),$$

which satisfies the limiting absorption principle. Taking advantage of the known integrated representation of the one-dimensional Green's function [5,6] we receive the following asymptotic representation

$$G(z, z_1, \mathbf{r}_\perp) \approx -\frac{1}{\sqrt{8\pi^3 r_\perp}} \int \frac{V(z_>)V^-(z_<)}{W(q)} \sqrt{q} \times \exp\left(i(qr_\perp + p(q)|z - z_1| - \pi/4)\right) dq. \quad (1)$$

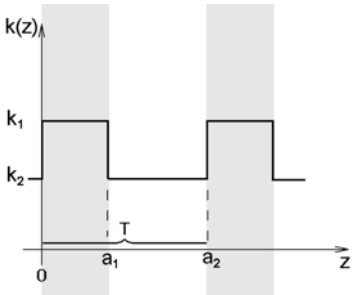

Fig. 1. Considered structure. The values a_1, a_2, k_1, k_2 are the layer widths and the wave numbers of the medium. T is the periodicity.

2. Method of a stationary phase

The asymptotic form of the Green's function in the far zone is to be considered, thus we calculate the integral (1) by the method of the stationary phase. In order to perform this it is necessary to find stationary points. The equation for definition of stationary points in polar coordinates (the origin is combined with a source $r_\perp = R\cos\varphi$, $|z - z_1| = R\sin\varphi$) looks like

$$p'(q) = -\mathrm{ctg}\varphi. \quad (2)$$

A typical quasi-momentum derivative curve $p'(q)$ is represented in Fig. 2.

Let the polar angle vary in the sector $\varphi_* + \epsilon < \varphi < \pi/2$, where $\epsilon > 0$. Then the Green's function asymptotic is defined by the unique stationary point $q = q_1$ and can be presented in the form

$$G(z, z_1, \mathbf{r}_\perp, q_1) \approx -\frac{V(z_>)V^-(z_<)}{2\pi W(q_1)} \sqrt{\frac{q_1}{p''(q_1) r_\perp |z - z_1|}} \times \exp i\left(q_1 r_\perp + p(q_1)|z - z_1| + \pi/4(\mathrm{sign}(p''(q_1)) - 1)\right). \quad (3)$$

3. Green's function singularities

Received asymptotic (3) becomes inapplicable in a vicinity of $q = q_*$, $p'(q_*) = -\mathrm{ctg}\varphi_*$. At this point the function $p''(q)$ is zero (special direction). In order to construct a smooth asymptotic form we rewrite (3) as

$$G(z, z_1, \mathbf{r}_\perp, q_i) = A(z, z_1, r_\perp, q_i) \times \exp\left(iF(z, z_1, r_\perp, q_i)\right),$$

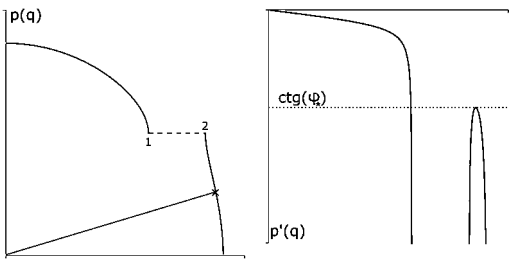

Fig. 2. The dispersion diagram $p(q)$ and quasi-momentum derivative curve $p'(q)$. The 1–2 dotted line shows the forbidden zone. It is visible, that the equation (2) has a unique root at $\mathrm{ctg}\,\varphi < \mathrm{ctg}\,\varphi_*$, two roots at $\mathrm{ctg}\,\varphi = \mathrm{ctg}\,\varphi_*$ and three roots in other cases. The angle φ_* is defined by the structure parameters.

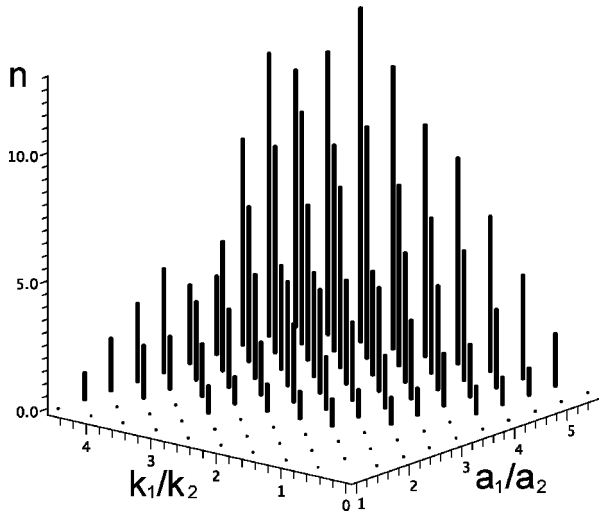

Fig. 3. The dependence of the forbidden zone number (n) on the relative layers width and the wave numbers. One can see that by varying the structure parameters in a certain way we obtain a different number of forbidden zones, i.e. number of special directions.

where $F(z, z_1, r_\perp, q_i) = q_i r_\perp + p(q_i)|z - z_1|$

$$A(z, z_1, r_\perp, q_i) = -\frac{e^{-i\frac{\pi}{4}}}{2\pi}\sqrt{\frac{q_i}{p''(q_i) r_\perp |z-z_1|}}\frac{V(z_>)V^-(z_<)}{W(q_i)}.$$

In this form the smooth asymptotic may be written as

$$G_s(z, z_1, \mathbf{r}_\perp, q_{(2,3)}) = e^{i\phi}\left(C_1 Ai(\psi) + C_2 Ai(1, \psi)\psi^{-1/2}\right),$$

where

$$\phi = (F(q_3) + F(q_2))/2,\ \psi = (3/4\,(F(q_3) - F(q_2)))^{2/3},$$
$$C_1 = \sqrt{\pi}\psi^{1/4}\,(A(q_3) + A(q_2)),$$
$$C_2 = i\sqrt{\pi}\psi^{1/4}(A(q_3) - A(q_2)).$$

Therefore, in the sector $0 < \varphi < \varphi_* + \epsilon$ the Green's function is the sum of two items

$$G(z, z_1, \mathbf{r}_\perp) = G\,(z, z_1, \mathbf{r}_\perp, q_1) + G_s\left(z, z_1, \mathbf{r}_\perp, q_{(2,3)}\right).$$

Here q_i are the roots of the equation (2). Similar expressions arise at the description of a wave field in the vicinity of a caustic. In our case this asymptotic form describes the complex interference picture in the far zone. It is possible to derive an expression for the power flux density if we define it as $P = i(G\nabla G^* - G^*\nabla G)/2$. In this case power propagation features the special directions, but proportional to $R^{-5/3}$ rather than R^{-2}. Results of numerical calculations of the Green's function and power flux density are represented in Fig. 4.

Thus, in contrast to a homogeneous medium, the Green's function for the periodic layered structure has a number of features. There are areas in which the wave field is described not only by a single wave, but by a sum of wave fields with the maximal number is defined by the properties of the structure and does not exceed number of extending normal waves for a wave guide consisting of two layers with periodic boundary conditions. Also, there exist allocated directions in which there is an occurrence or disappearance of an additional beam summand. The asymptotic of the wave field for these directions is

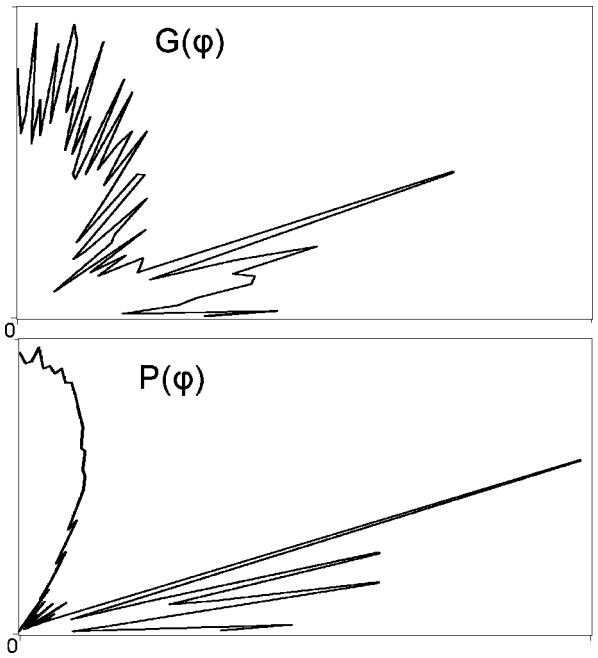

Fig. 4. Directional patterns of the Green's function $G(\varphi)$ and the power flux density $P(\varphi)$. The presence of the allocated directions corresponding to slower decrease are clearly visible.

described through the Airy function and in these directions the Green's function and the power flux density decreases slowly.

Such a structure can be used as an attractive optical material for controlling and manipulating the light flow. The obtained results offer additional features leading to new device concepts (e.g. microscale structure for the lightconfinement with radically different characteristics compared to conventional optical fiber [7]), when some technological aspects such as manufacturability and principal difficulties such as disorder are being under control.

References

[1] M. S. Tomas, *Phys. Rev. A.* **51**, 2545 (1995).
[2] E. V. Aksenova, V. P. Romanov and A. Yu. Val'kov, *Phys. Rev. E.* **59**, 1184 (1999).
[3] V. A. Belyakov, *Diffraction Optics of Periodic Media with a Layered Structure* (Berlin: Springer-Verlag), 1992.
[4] K. M. Leung, *J. Opt. Soc. Am. B* **10**, 303 (1993).
[5] L. Brillouin and M. Parodi, *Propagation des Ondes dans les Milieux Périodiques* (Paris:Masson et cie editeurs,Dunodediteurs), 1956.
[6] L. Felsen and N. Marcuvitz, *Radiation and Scattering of waves* (New Jersey: Prentice Hall), 1973.
[7] J. D. Joannopoulos, S. Johnson, J. Winn and R. Meade, *Photonic Crystals: Molding the Flow of Light* (Princeton NJ: Princeton University), 2008.

17th Int. Symp. "Nanostructures: Physics and Technology"
Minsk, Belarus, June 22–26, 2009
© 2009 Ioffe Institute

Photonic quasicrystals based on multiple-quantum-well structures

M. M. Voronov, A. N. Poddubny and E. L. Ivchenko
Ioffe Physical-Technical Institute, St Petersburg, Russia

Abstract. A theory of light propagation through resonant photonic quasicrystals and deterministic aperiodic structures based on multiple quantum wells (MQWs) has been developed. The general expression for the structure factor of a one-dimensional (1D) quasicrystal has been derived. Special attention is paid to quasiperiodic Fibonacci chains and Thue–Morse structures with the QW exciton resonance frequency tuned to the Bragg diffraction resonance. The dispersion equation for exciton polaritons is obtained in the two-wave approximation, and the effective allowed and forbidden bands are found. The reflection spectra from the proposed structures are calculated as a function of the well number and detuning from the Bragg condition.

Introduction

Quasicrystals (QCs) belong to a wide class of aperiodic systems possessing long-range order and allowing coherent Bragg diffraction of electron or electromagnetic waves [1,2]. In case of light waves such structures are photonic QCs termed as "resonant" or "active" if the constituting materials have dipole-like excitations [3–4]. The special kind of 1D resonant photonic QCs is the structure based on excitonic resonances in semiconductor MQWs, aperiodically arranged in dielectric matrix. This system has been proposed in [3] and experimentally realized in [4].

Here we, firstly, present an original equation for the structure factor of an arbitrary 1D QCs composed of two segments and, secondly, develop a general approach to desribe linear optical properties of resonant deterministic aperiodic structures (DAS), including QCs.

1. Structure factor of 1D quasicrystals

There are three different but consistent approaches to the concept of quasicrystals which refer to: (i) the incommensurate chains, (ii) the substitution rules and (iii) the cut-and-project method. In general case, the coordinates of the QWs centers, constituting a QC (see Fig. 1), can be written in the form

$$z_m = z_0 + m\bar{d} + \Delta\left\{\frac{m}{t} + \varphi\right\}, \qquad (1)$$

where $\bar{d}$ is the mean period of the lattice, z_0 is an arbitrary shift of the lattice as a whole, and Δ, t and φ are the structure parameters, with t being irrational and φ being noninteger. At vanishing Δ Eq. (1) specify a simple periodic lattice with the period $\bar{d}$. In case of rational t, the structure is still periodic but has a compound supercell, whereas for irrational values of t Eq. (1) leads to a deterministic aperiodic chain termed also as "modulated crystal" [2]. For z_m defined according to Eq. (1) the spacings $z_{m+1} - z_m$ take one of the two values, $a = \bar{d} + \Delta/t$ and $b = \bar{d} + \Delta(1/t - 1)$, from where $\bar{d} = (b - a)/t + a$.

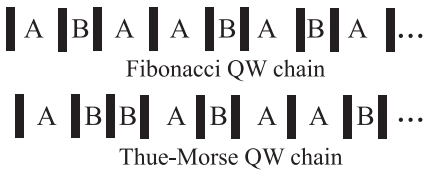

Fig. 1. Fibonacci and Thue–Morse QW chains shown for the first $N = 8$ wells.

Moreover, the ratio N_B/N_A of numbers of the spacings a and b in an infinite lattice is related with t by $N_B/N_A = t - 1$.

Under the certain conditions imposed upon the values of t and φ the QW arrangement can be also obtained by the substitution rules acting on the segments A,B as follows: $A \to \sigma(A) = A_1A_2\ldots A_{\alpha+\beta}$, $B \to \sigma(B) = B_1B_2\ldots B_{\gamma+\delta}$. Here each of the symbols A_k and B_k stands for A or B, α and β denote the numbers of letters of A and B in $\sigma(A)$, and γ and δ are the numbers of A and B in $\sigma(B)$ [5]. The correspondence between the two definitions is established by the relation $t = 1 + (\lambda_1 - \alpha)/\gamma$ between a value of t and indices α, β, γ, δ, where $\lambda_1 = (l + \sqrt{l^2 + 4n})/2$, $l = \alpha + \delta$ and $n = \beta\gamma - \alpha\delta$. For the quasicrystals n must be equal to ± 1 [5].

The optical properties of the chains (1) are described by the structure factor $f(q)$ which in case of an infinite quasicrystal [2] consists of δ-peaks corresponding to the Bragg diffraction and characterized by two integer numbers h and h' with the diffraction vectors $G_{hh'}$ filling the wavevector axis in a dense quasicontinuous way, so that

$$f(q) = \sum_{h,h'=-\infty}^{\infty} \delta_{2q,G_{hh'}} f_{hh'}, \quad G_{hh'} = \frac{2\pi}{\bar{d}}\left(h + \frac{h'}{t}\right). \qquad (2)$$

We remind that in the periodic lattice ($\Delta = 0$) the structure factor has non-zero peaks at the single-integer diffraction vectors $G_h = 2\pi h/\bar{d}$ with $|f_h| = 1$. One can show that, for irrational values of t and $\Delta \neq 0$, the structure-factor coefficients are given by

$$f_{hh'} = \frac{\sin S_{hh'}}{S_{hh'}} e^{i\theta_{hh'}},\ \theta_{hh'} = (z_0 + \Delta\{\varphi\})\, G_{hh'} + S_{hh'},$$

$$S_{hh'} = \frac{\pi\Delta h}{\bar{d}} + \pi h'\left(1 + \frac{\Delta}{t\bar{d}}\right) = \pi h' + \frac{\Delta}{2} G_{hh'}.$$

The above equations for the structure factor are valid for the arbitrary value of the phase φ in Eq. (1). For the specific case when $\varphi = 0$ they can be obtained by the transformation of the result presented in [6].

We also study a correlated disordered structure, defined by $z'_m = z_m + \delta z_m$, where δz_m are independent and identically distributed random variables so that $\langle \delta z_m \rangle = 0$, $\langle \delta z_m^2 \rangle = \sigma_z^2$. The structure factor in such lattice averaged over disorder realization has a form

$$\langle f(q) \rangle = \sum_{h,h'} \delta_{2q,G_{hh'}} f_{hh'} e^{-(q\sigma_z)^2/2}. \qquad (3)$$

The dispersion of the structure factor tends to zero when $N \to \infty$, so it turns out that Eq. (3) provides a good estimation of the structure factor for any realization of disorder for $N \gtrsim 10$. The long-ranged correlations of QW positions are still preserved in such a structure, so Bragg diffraction is possible with the same diffraction vectors as in the periodic lattice. However, the peak values of the structure factor drop drastically with the increasing of σ_z in analogy with the Debye–Waller factor in the theory of the diffraction in the crystals.

2. Resonant Bragg condition

The structure under consideration consists of N semiconductor QWs with their centers positioned at points $z = z_m$ ($m = 1, \ldots, N$) arranged in an aperiodic lattice. The electric field of the light wave propagating in the MQW structure satisfies the following wave equation

$$\left(-\frac{d^2}{dz^2} - q^2\right) E(z) = 2q\xi(\omega) E(z) \bar{d} \sum_m \delta(z - z_m), \quad (4)$$

with resonant factor $\bar{d}\xi(\omega) = \Gamma_0/(\omega_0 - \omega - \mathrm{i}\Gamma)$, where ω_0, Γ_0 and Γ are the exciton resonance frequency, radiative and nonradiative decay rates. Assuming the resonant Fibonacci MQWs to contain a sufficiently large number N of wells we will replace the structure factor $f(q, N)$ by its limit $f(q)$ given by Eq. (2). This allows one to present solutions of Eq. (4) as a superposition of the "Bloch-like" waves

$$E_K(z) = \sum_{h,h'} e^{i(K - G_{hh'})z} E_{K - G_{hh'}}. \quad (5)$$

We consider a QW quasicrystal tuned to the resonance

$$\omega_0 n_b/c \equiv q_0 = G_{h,h'}/2. \quad (6)$$

Note that this condition is valid for any QC and DAS with arbitrary number of indices $h, h', h'', \ldots$. For instance, for the Thue–Morse chain (see Fig. 1), which is not a QC, but still have Bragg peaks at $G_h = \pi h/\bar{d}$, where $\bar{d} = (a + b)/2$, it is written as $q_0 = G_h/2$.

Then, in the two-wave approximation, only two space harmonics K and $K' = K - G_{hh'}$ are taken into account in the superposition (5) and we come to approximate system of two coupled equations

$$\begin{aligned} &(q - K + \xi) E_K + \xi f^*_{hh'} E_{K'} = 0, \\ &\xi f_{hh'} E_K + (q + K - 2q_0 + \xi)\, E_{K'} = 0. \end{aligned} \quad (7)$$

Since $|\omega_0 - \omega| \ll \omega_0$ then the validity criterium of this approximation is inequality $|q_0 - K| \ll q_0$. In this case an admixture of other space harmonics has no remarkable influence on the propagation of the exciton polaritons in the QW Fibonacci chain. One can show that it is valid when

$$\max\{|\omega_0 - \omega|, \Gamma\} \gg \Gamma_0 \max\left\{\sqrt{1 - |f_{hh'}|^2}/q_0\bar{d}, 2q_0\bar{d}/|f_{hh'}|\right\}. \quad (8)$$

The edges, $\omega^{\pm}_{\mathrm{out}}$ and $\omega^{\pm}_{\mathrm{in}}$, of two symmetrical band gaps are obtained from Eq. (7) by setting $K^{(\pm)} = q_0$ and defined by the following expressions:

$$\omega^{\pm}_{\mathrm{out}} = \omega_0 \pm \Delta \sqrt{\frac{1 + |f_{hh'}|}{2q_0\bar{d}}}, \; \omega^{\pm}_{\mathrm{in}} = \omega_0 \pm \Delta \sqrt{\frac{1 - |f_{hh'}|}{2q_0\bar{d}}}, \quad (9)$$

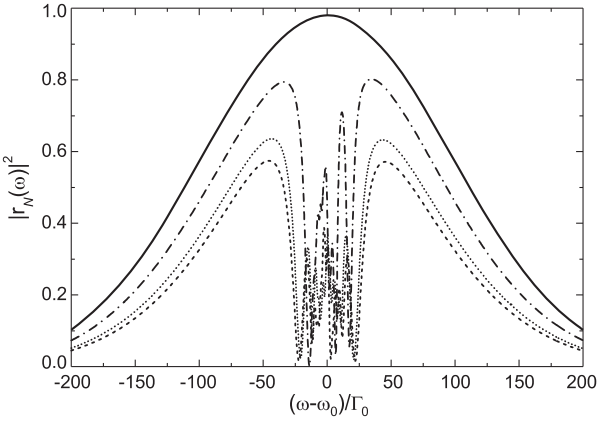

Fig. 2. Reflection spectra calculated for four MQWs, containing $N = 100$ wells, and tuned to the resonant Bragg condition $2\bar{d} = \lambda(\omega_0)$: Fibonacci chain (dotted curve), with $a/b = (\sqrt{5} + 1)/2$ [$(h, h') = (1, 0)$]; Thue–Morse chain (dashed) with $a/b = 3/2$ ($h = 2$); periodic (solid), with $a \equiv b \equiv \bar{d}$; and weakly disordered periodic (dashed-and-dotted) with $\delta x = \lambda_0/20$. Calculated for $\hbar\Gamma_0 = 50$ μeV, $\hbar\omega_0 = 1.533$ eV and $\Gamma = \Gamma_0$.

where $\Delta = \sqrt{2\Gamma_0\omega_0/\pi}$.

Fig. 2 depicts typical reflection spectra from a QW QCs and DASs with average period satisfying any of resonant Bragg condition like (7). Three spectra, corresponding to nonperiodic MQWs, have two prominent wide peaks related to the two band gaps whose edges are defined by (9). The fourth graph belongs to a periodic MQW where $|f_h| = 1$, therefore it shows a single band gap.

In order to derive an analytical expression for the reflection coefficient r_N from an N-well quasicrystalline chain sandwiched between the semiinfinite barriers (material B) we write the field in the three regions, the left barrier, the MQWs and the right barrier and impose the boundary conditions which are continuity of the electric field $E(z)$ and its first derivative $dE(z)/dz$ at the points $z_1 = 0$ and z_N. The straightforward derivation results in a surprisingly simple expression for the reflection coefficient

$$r_N = \frac{\xi f_{hh'}}{q_0 - q - \xi - \mathrm{i}Q \cot(QN\bar{d})}, \quad (10)$$

where $Q = \sqrt{(q_0 - q - \xi)^2 - \xi^2 |f_{hh'}|^2}$. Zeros of the denominator in Eq. (10) represent the eigenfrequencies of the QW structure, which are valid under condition (9).

In conclusion, we have demonstrated that the aperiodic long-range-ordered MQW structures tuned to the Bragg resonance have high reflectivity due to the constructive interference suppressing the effects of nonperiodicity.

Acknowledgements

We acknowledge the support by RFBR and the "Dynasty" Foundation — ICFPM.

References

[1] D. Levine *et al*, *Phys. Rev. Lett.* **53**, 2477 (1984).
[2] C. Janot, Quasicrystals. A Primer (Clarendon Press, Oxford, UK, 1994).
[3] A. N. Poddubny *et al*, *Phys. Rev. B* **77**, 113306 (2008).
[4] J. Hendrickson *et al*, *Opt. Express* **16**, 15382 (2008).
[5] X. Fu *et al*, *Phys. Rev. B* **55**, 2882 (1997).
[6] M. C. Valsakumar *et al*, *Pramana* **26**, 215 (1986).

17th Int. Symp. "Nanostructures: Physics and Technology"
Minsk, Belarus, June 22–26, 2009
© 2009 Ioffe Institute

Surface magnetostatic waves anisotropic diffraction in 1D magnonic crystal

S. L. Vysotsky[1], *Yu. A. Filimonov*[1], S. A. Nikitov[2], N. N. Novitskii[3] and A. I. Stognij[3]

[1] Kotelnikov Institute of Radio Engineering and Electronics (Saratov Branch), RAS, 410019, Saratov, Russia
[2] Kotel'nikov Institute of Radio Engineering and Electronics, RAS, Moscow, Russia
[3] Scientific-Practical Materials Research Centre of NAS of Belarus, Minsk, Belarus

Abstract. Diffraction of surface magnetoststic waves in yttrium-iron garnet film with surface 1D periodic groove structure was investigated depending on the angle α betwen the direction of excited wave and the groove's axis. It was found that at deviation of α from 90° (in the plane of the film) the diffraction condition is fulfilled for greater wavelenght in contrast with Bragg–Wolf prediction. The reason is associated with non-collinearity of the group and phase velocities of surface magnetostatic waves propagating at $\varphi \neq 90°$ where φ is the angle between wave vector and the direction of bias magnetic field.

Introduction

Magnetostatic (both surface and volume) waves propagation in ferrite films with 1D surface periodic system of grooves or gratings has been investigated to design tuneable microwave filters (see [1] and references therein). Also surface magnetostatic waves (SMSW) propagation in yttrium iron garnet (YIG) film with 2D periodic structure include etched holes was reported [2]; the forbidden gap found in the frequency spectra was attributed as a result of Bragg reflection of SMSW from the surface periodic structures. To our knowledge all the results were obtained at angle α between wave vector and reflected plane of periodic structure equals to 90 degrees (except for [2] where another direction was mentioned without detailed discussion). At this condition both incident and reflected waves' propagation is isotropic one. At the same time in tangentially magnetised magnetic film waves propagating at arbitrary angle to the bias magnetic field H_0 demonstrate non-collinearity of the group and phase velocities. So it can be assumed that at $\alpha \neq 90°$ Bragg condition would be changed. The paper presents the results of investigation of SMSW reflection from the 1D array of grooves depending on the angle α between the direction of excited wave and the groove's axis and their discussion.

1. Experimental

The investigated array includes 70 μm width 0.66 μm deep grooves separated by 30 μm lands was formed in 4 μm thick YIG film using low energy oxygen ion-beam etching through alumina mask. The structure was placed in microstrip delay line with 4 mm distance between microstrip transducers. Tangential bias magnetic field H_0 was applied along the transducers providing SMSW exciting. The Figure demonstrates the amplitude-frequency characteristic obtained at $\alpha = 90°$ (corresponding to SMSW wave vector directed perpendicular to groove axis, $H_0 = 742$ Oe) including two forbidden gaps marked 1 and 2. Wavelength corresponding to gaps frequencies were defined using phase-response characteristic analogously [2] as 210 μm and 108 μm demonstrating good agreement with Bragg–Wolf condition

$$2d \sin\alpha = n\lambda, \qquad (1)$$

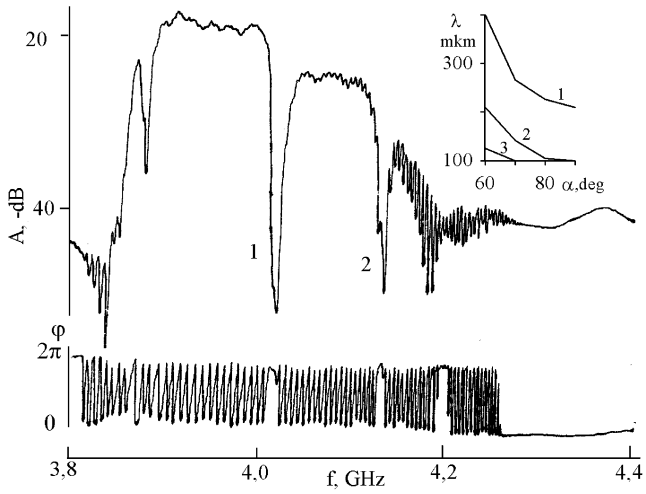

Fig. 1. The amplitude-frequency characteristic obtained at $\alpha = 90°$.

where d is array period (100 μm).

Note that (1) predicts the decreasing of λ at decreasing of α. The inset to the Figure demonstrates the $\lambda_i(\alpha)$ dependence where marks near curves correspond to number of forbidden gap. One can see that decreasing of α leads to increasing λ of in contrast to (1). Note that in addition to gaps marked 1 and 2 on the Figure one more gap became observable as a result of shift to region where SMSW losses are less than at very short waves region. It was shown that increasing of λ_i at $\alpha \neq 90°$ could be explained by consideration of diffraction process "step by step".

Acknowledgements

This work has been supported by RFBR grants 08-07-00119-a and 09-07-00186-a.

References

[1] A. Maeda and M. Susaki, *IEEE Trans. on Magn.* **42**, 3096 (2006).
[2] Yu. V. Gulyaev, S. A. Nikitov *et al*, *JETP Lett.* **77**, 567 (2003).

17th Int. Symp. "Nanostructures: Physics and Technology"
Minsk, Belarus, June 22–26, 2009
© 2009 Ioffe Institute

Phase formation and phase transitions in nanowires of III–V compounds

F. Glas, J. C. Harmand and G. Patriarche

CNRS — Laboratoire de Photonique et de Nanostructures, Route de Nozay, 91460 Marcoussis, France

Abstract. III–V compounds of cubic zinc-blende structure tend to adopt a defective hexagonal wurtzite structure when grown as nanowires from catalyst particles. After briefly recalling the origin of this behavior, we show that this structure can be changed to zinc blende by burying the nanowires with material growing epitaxially from the non-activated substrate. Burying is achieved by changing the growth temperature and eliminates all the pre-existing planar defects. We discuss the thermodynamics and the kinetics of this process, in particular the driving force for the phase transformation and its kinetic limitation by dislocation glide.

Introduction

Free-standing wires with diameters ranging from a few to hundreds of nanometers are nowadays commonly fabricated from a large range of semiconductor materials. These nanowires (NWs) have remarkable physical properties and many potential applications, yet the control of their growth and characteristics is still far from optimal. The NWs of III–V compounds present a case in point, in that even the control of their crystal structure has proven particularly elusive.

Indeed, all bulk N-free III–V semiconductors crystallize in the cubic sphalerite structure, also known as zinc blende (ZB). However, the NWs of these materials very often adopt the hexagonal wurtzite (WZ) structure. This is observed for most ZB III–V materials and growth techniques [1,2,3]. Here, we consider the common case of NWs growing on a $(\bar{1}\bar{1}\bar{1})$ ((111)B) oriented III–V substrate from pre-deposited catalyst particles, in the Vapor-Liquid-Solid (VLS) mode.

ZB and WZ are closely related structures. Both are periodic stacks along a given direction (e.g. [111]B in ZB) of identical biatomic planes, or monolayers (MLs), which differ by their transverse positions. Three such positions (A, B and C) are allowed. The unit sequences of ZB and WZ are ABC and AB, respectively. ZB and WZ can be identified by transmission electron microscopy (TEM) techniques In particular, in high resolution TEM (HREM) images, the 2-ML stacking periodicity of WZ (Fig. 1(b)) is clearly distinguished from the 3-ML periodicity of ZB (Fig. 1(d)).

We previously explained why the unusual WZ structure may form in NWs of cubic III–V compounds [4]. Our explanation is based on the kinetics of formation of the 2D nuclei of each new ML in WZ lateral position rather than in ZB position, and recognizes that nucleation should occur at the triple phase (VLS) line. We showed that WZ formation also requires a high supersaturation in the liquid catalyst.

Despite further theoretical investigations [5] and recent experimental progress [6,7], it remains very challenging to fabricate reproducibly single-phase III–V NWs. The present work explores an alternative route to phase control in III–V NWs. Namely, we describe and discuss a method to transform highly faulted WZ NWs into perfect ZB ones [8].

1. Epitaxial burying of the nanowires

We illustrate our method in the case of GaAs. Growth is performed by molecular beam epitaxy. To bury previously grown NWs, we deliberately alter the relative growth rates of the NWs and of the non-activated substrate by changing the growth temperature T_G. Whereas in our standard conditions the NWs grow faster than the non-activated substrate for $T_G \leq 620$ °C, the reverse holds for 620 °C $\leq T_G \leq$ 650 °C; any previously grown NW then gets buried by the substrate.

The standardly-grown NWs have the WZ structure with a high density of stacking defects (Fig. 1(a)). We first wrap them in a nm-thick protective $Al_xGa_{1-x}As$ shell to prevent their disappearance at elevated temperature. Since it nucleates on the NW sidewalls, the shell also adopts the WZ structure. By increasing the growth temperature, we then shift to a regime where the non-activated cubic GaAs substrate grows faster than the NWs, effectively burying them.

The samples were studied by TEM at various stages of the burying process. The burying layer naturally adopts the cubic ZB structure of the GaAs substrate from which it grows. In partially buried NWs (Fig. 1(b)), the part emerging from the burying layer is unaltered: it is still WZ with stacking defects. However, below the level of the top of the burying layer, the material is entirely of ZB structure. This implies that the buried portion of any NW has changed to ZB. Hence, the growing non-activated substrate transforms the buried portion of the NW from WZ to ZB. This phase transformation must be very

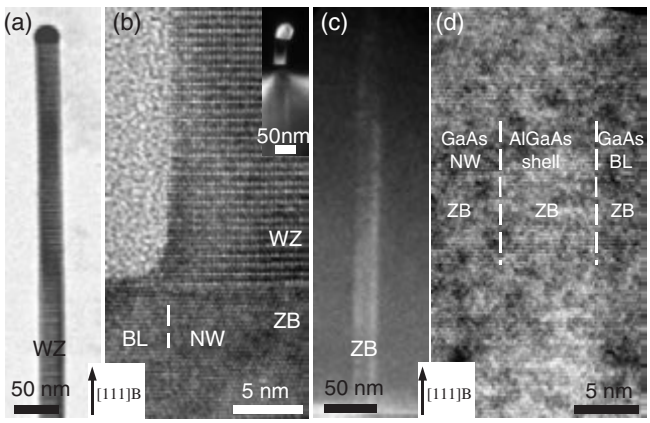

Fig. 1. (a) TEM image of an unburied NW. Horizontal striation is due to stacking defects. (b) HREM image of a partially buried NW, with lower resolution inset. Dashes mark the lateral interface between burying layer (BL) and NW. (c) A fully buried NW. Note the absence of striation. (d) HREM image of the interface between NW, shell and burying layer, after complete burying.

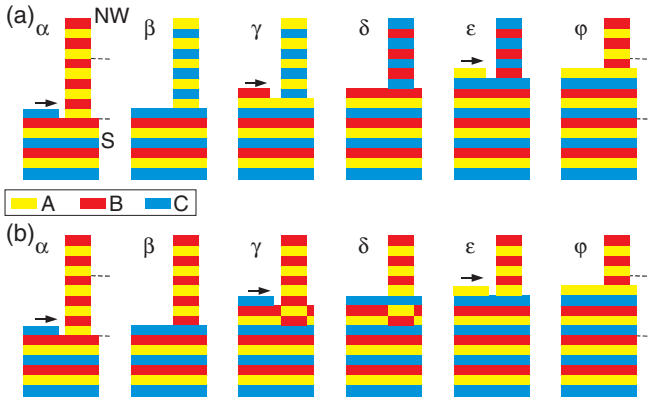

Fig. 2. Type I (a) and II (b) processes transforming a WZ NW into ZB. Greek letters label the stages of each process. Each rectangle represents a ML of the substrate (S) or NW; its color codes its lateral position (insert). Arrows give the step flow direction.

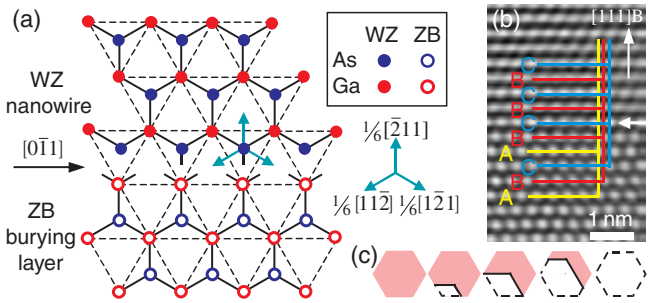

Fig. 3. (a) Top ML of the ZB burying layer meeting an out-of-registry NW ML (top view). The resulting partial dislocation (along arrow) can be annihilated by any of three translations of the NW ML (green arrows, ZB indices). (b) Filtered HREM image of the interface between the transformed and untransformed parts of a NW (side view), with ML positions and topmost ML in the ZB sequence (horizontal arrow) indicated. (c) Transformation of a NW ML from WZ to ZB positions (top view). The area not yet translated is colored. Solid lines track the glide of the partial dislocation initially formed (dashes) at the NW sidewall.

fast, since the phase boundary is flush with the top ML of the burying layer (Fig. 1(b)).

Further growth leads to complete burying of the NWs. Each NW can still be localized thanks to its AlGaAs shell (Fig. 1(c)). HREM confirms that the whole sample is pure ZB (Fig. 1(d)); moreover, all stacking defects have disappeared (Fig. 1(c,d)). We thus end up with perfect cubic NWs embedded in a cubic matrix.

2. Mechanism of the WZ → ZB phase transformation

Our observations of partly buried NWs show that, when the burying material reaches the sidewall of a NW, it transforms the latter's WZ structure into its own ZB one (Fig. 1(b)). Let us consider the burying process more closely. First recall that, along the ZB [111]B or WZ [0001] direction, a group-III atom sits right above the underlying group-V atom. The A, B, or C character of a III–V ML is therefore determined by the lateral position of its group-V atoms [4]. Let us assume that the burying layer has already transformed the lower part of the NW to its ZB stacking (Fig. 2(a,b), stage α) and consider how the next sequence of six yet unburied WZ MLs (between the dashed lines) may transform into ZB.

When the advancing top ML of the burying GaAs reaches the NW sidewall, the burying ML may be out of lateral registry with the corresponding ML of the NW (Fig. 3(a)). This fault in the NW (with respect to ZB) can be eliminated by a rigid shift of the whole emerging part of the NW (As plane included), which brings two more MLs in ZB position (Fig. 2(a), β). When the burying layer reaches the level of the next fault, two MLs above the previous one (Fig. 2(a), γ), the process repeats (Fig. 2(a), δ), and so on every other ML. Three such shifts transform the six MLs (Fig. 2(a), φ). We call "type I" this transformation mechanism.

The lateral contact between the top burying ML and the out-of-registry NW ML produces a glide set Shockley partial dislocation, albeit only partly surrounded by material (Fig. 3(a)). Since our NWs have vertical sidewalls parallel to the six $\{10\bar{1}0\}$ WZ ($\{\bar{2}11\}$ ZB) planes, the edges of the NW ML are $\langle 1\bar{1}0\rangle$-oriented. The Burgers vector of the partial dislocation is one of three translations allowed at each stage, namely $1/6\left[\bar{2}11\right]$, $1/6\left[1\bar{2}1\right]$ or $1/6\left[11\bar{2}\right]$ (or the complementary set, depending on the ZB variant). As the dislocation glides along the (111)B plane into the NW, the As atoms shift into ZB position. The translation of the whole As layer fully eliminates dislocation and stacking defect.

We also considered a type II process, whereby only one or two NW MLs are translated at each stage (Fig. 2(b)). The same partial dislocation forms initially (Fig. 2(b), α) but now only the NW ML that it borders gets shifted (Fig. 2(b), β), which produces a twin-like ABCBA sequence [9]. The next two NW MLs cannot shift before the third one, which occurs when the burying layer reaches its level and creates a double-twin BCBAC sequence (Fig. 2(b), γ,δ). Finally, the two already buried NW MLs may transform (Fig. 2(b), ε).

These two types of transformation of WZ into ZB can be distinguished by HREM via differences in stacking sequences at the interface between the untransformed and transformed parts of the NW. We first identify the topmost NW MLs that have already adopted the ZB stacking (Fig. 3(b)). At any stage of a type I process (Fig. 2(a)), the next NW MLs repeat the last two MLs of the ZB sequence (e.g. ABCABC/BCBC… at stage δ) whereas in a type II process (Fig. 2(b)) the same sequence is found only at stages α or φ (CABCAB/ABAB…), other (twin-like) sequences occurring at stages β to ε. Our HREM images only display the single stacking sequence characteristic of the type I process (Fig. 3(b)) and never the specific type II sequences. This indicates that, at least for GaAs, type I is the dominant transformation mechanism, and probably the only one.

3. Thermodynamic analysis

The driving force for the type I phase transformation is the joint elimination of the partial dislocation that forms at the NW/burying material lateral boundary (Fig. 3(a)) and change of structure of the NW from WZ to ZB. The length of the partial dislocation and the area of the faulted interface between the transformed and untransformed parts of the NW determine the system energy. Fig. 3(c) shows schematically how these change during the transformation of each ML. As overgrowth proceeds, the hexagonal-shape NW ML gets surrounded by the top burying ML (which extends by step flow) and the partial

dislocation forms at the lateral edge of this NW ML. As soon as the dislocation forms along at least two sides of the hexagon, it can glide inward without increasing its length and, therefore, its energy. The area of the NW ML swept by the dislocation adopts a ZB lateral position with respect to the underlying portion of the NW. The energy decrease γ upon eliminating the fault is 28 mJ m^{-2} [9]. Hence, the total energy decreases continuously during each elementary step of the transformation.

Of course, when a NW ML is already in ZB position, no dislocation is created and hence no driving force for translating the upper part of the NW. This happens in particular when there is a stacking defect in the yet unburied WZ NW, so that all such defects (Fig. 1(a)) get eliminated (Fig. 1(c)). The same holds for a pre-existing ZB sequence.

According to this analysis, there is no energy barrier to the transformation (and no critical NW radius). The reason why the transformation occurs upon burying but not in unburied NWs, although the same energy γ would be gained by eliminating the stacking defect, is the following. In the partly buried NW, a partial dislocation forms when the burying layer reaches the NW (clearly, leaving a gap between burying and NW MLs would lead to a higher energy). Conversely, in the free-standing case, the cost of forming the same dislocation offsets the gain γ procured by eliminating the stacking defect, which leads to a critical radius for the dislocation loop and an energy barrier to the transformation. The latter situation is akin to the WZ $\leftrightarrow$ ZB transformations in bulk samples, where there is a barrier for the nucleation of a transformed domain of critical size [10].

NW geometry is very favorable to a type I process, since nothing hinders the translation of the top part of the NW. Conversely, the last step of a type II process, during which two NW MLs must switch stacking positions (Fig. 2(b), δ to ε), can only occur if these MLs are not yet entirely surrounded by the burying MLs or if they can exchange atoms. This makes this process less likely than the type I process.

4. Kinetic considerations

The simple analysis of Sec. 3 shows that there is no thermodynamic barrier to the transformation. However, dislocation glide is kinetically limited. We can assess the impact of this kinetic limitation by comparing the dislocation glide velocity with the growth rate of the NWs.

The dislocation velocity at temperature T is given by:

$$v = v_0 \, (\tau/\tau_0)^m \exp\left(-Q/k_B T\right), \qquad (1)$$

where v_0, τ_0, m and Q are constants depending on material and dislocation type, k_B is Boltzmann's constant and τ the stress that induces the dislocation glide [11]. In the III–Vs, the velocity depends in particular on the α or β character of the dislocation, determined by the type of the core atoms.

Evaluating the dislocation velocity from Eq. (1) raises many questions. A standard partial dislocation loop is composed of α and β segments [11]. However, this configuration need not be relevant here, since the NW ML is not necessarily fully surrounded by the burying ML during dislocation glide, so that an open configuration with a reduced number of segments may occur (Fig. 3(c)). On the other hand, since group-III and group-V terminations occur alternatively on consecutive edges of a given NW ML, the first segment formed may be of either α or β character. Finally, there seems to be no published data about the mobility of individual partial dislocations in III–V compounds.

For lack of further information, we simply computed the mobilities of standard (dissociated) α and β dislocations via Eq. (1) by using the parameters given by Yonenaga [11]. The stress was evaluated as follows. Calling z the NW axis, the dislocation glides in the xy plane due to the existence of shear stresses $\sigma_{xz} = \sigma_{yz} = \tau$, induced by the planar fault at the WZ/ZB (111)B interface. If a dislocation segment of length L moves by δu, the work produced is $(F/L)L\delta u$, where F/L is the glide force per unit length. This work also equals $\gamma L \delta u$, with γ the areal fault energy (Sec. 3). Using Peach and Kohler's formula [12], that states that $F/L = \chi b \tau$, with b the modulus of the Burgers vector and χ a geometrical factor of the order of 1, we find that the stress verifies $\tau \gtrsim \gamma/b$.

From Eq. (1), we can now evaluate the dislocation velocities. We find very high velocities in GaAs at the burying temperature $T = 640$ °C, of the order of 0.4 m s^{-1} and 0.01 m s^{-1} for α and β dislocations. Even for NWs 100 nm wide, the time needed to traverse the NW would be at most 10^{-5} s, to be compared with the growth time of a ML, of the order of 1 sec. This accounts for the high efficiency of the process in GaAs, manifested by the complete transformation of the NWs (Fig. 1(c)), the abrupt WZ/ZB interface right at the level of the top burying ML (Fig. 1(b)) and the absence of partial dislocations frozen at the interface.

On the contrary, burying transforms InP NWs only partially. There are however two major differences with GaAs: the burying temperature is about 200 °C lower and the fault energy, and hence the stress, are also much lower [9]. For InP, we calculate dislocation velocities of only a few tens of μm s^{-1}, four orders of magnitude smaller than in GaAs. Although this rough calculation does not strictly forbid the phase transformation, it suggests that the difference noted is indeed due to the much lower dislocation velocities in InP. Moreover, sidewall-induced image forces might hinder the inward glide of the dislocations and reduce their velocities.

Acknowledgements

We thank L. Largeau, G. Cirlin, C. Sartel and V. Dubrovskii.

References

[1] M. Koguchi, *et al*, *Jpn. J. Appl. Phys.* **31**, 2061 (1992).
[2] A. I. Persson, *et al*, L. R. Wallenberg, *Nature Mater.* **3**, 678 (2004).
[3] J. C. Harmand, *et al*, *Appl. Phys. Lett.* **87**, 203101 (2005).
[4] F. Glas, J. C. Harmand and G. Patriarche, *Phys. Rev. Lett.* **99**, 146101 (2007).
[5] V. G. Dubrovskii, *et al*, *Phys. Rev. B* **78**, 235301 (2008).
[6] H. Shtrikman, *et al*, *Nano Lett.* **9**, 215 (2009).
[7] P. Caroff, *et al*, *Nature Nanotechnol.* **4**, 50 (2009).
[8] G. Patriarche, *et al*, *Nano Lett.* **8**, 1638 (2008).
[9] F. Glas, *J. Appl. Phys.* **104**, 093520 (2008).
[10] M. B. Geilikman, *Phys. Chem. Minerals* **8**, 2 (1982).
[11] I. Yonenaga, *J. Phys. III France* **7**, 1435 (1997).
[12] J. P. Hirth and J. Lothe, *Theory of dislocations, 2nd ed.*, (New York: Wiley) 91, 1992.

17th Int. Symp. "Nanostructures: Physics and Technology"
Minsk, Belarus, June 22–26, 2009
© 2009 Ioffe Institute

Non-linear growth kinetics of semiconductor nanowires

V. G. Dubrovskii[1,2], N. V. Sibirev[1], G. E. Cirlin[1,2], I. P. Soshnikov[1,2], W. Chen[3], R. Larde[3], E. Cadel[3], P. Pareige[3], T. Xu[4], B. Grandidier[4], J.-P. Nys[4], D. Stievenard[4], M. Moewe[5], L. C. Chuang[5], C. Chang-Hasnain[5], J. C. Harmand[6] and F. Glas[6]

[1] St Petersburg Physics and Technology Centre for Research and Education RAS, St Petersburg, Russia
[2] Ioffe Physical-Technical Institute, St Petersburg, Russia
[3] Universite et INSA de Rouen, France
[4] Institut d'Electronique, de Microelectronique et de Nanotechnologie CNRS, Lille, France
[5] Department of Electrical Engineering and Computer Sciences, University of California, Berkeley, California, USA
[6] LPN CNRS, Marcoussis, France

Abstract. Self-standing semiconductor nanowires (NWs) are promising building blocks for future nanoelectronic, nanophotonic and nanosensing devices. In this work we discuss some growth-related aspects of NW formation, in particular, non-linear growth effects, the maximum length and the length-diameter dependences of Si and III–V NWs obtained by the Au-assisted MBE and MOCVD techniques.

A rapidly growing interest in semiconductor NWs ranges from fundamental physics to many promising applications in nanoelectronics and nanophotonics. NWs are usually grown by MOCVD or MBE via the so-called vapor-liquid-solid (VLS) mechanism [1] on the surfaces activated by the drops of a metal catalyst (e.g., Au). Despite a rapid progress in fabrication technologies, many fundamental growth processes are not completely understood so far. This applies to the control over the position, radius, length, shape and uniformity of NWs, the crystal structure (zincblende, wurtzite or polytype) and many other issues. In this work we present new data concerning the growth properties of Si and III–V NWs. In particular, we discuss the interplay between the Gibbs–Thomson (GT) [2] effect and the adatom diffusion [3], the kinetic growth model, different non-linear growth effects, the length-diameter dependences of MOCVD grown Si, InP and MBE grown GaAs NWs and the possibilities for the control over the crystal phase of III–V NWs.

We first discuss the kinetic growth model schematized in Fig. 1a. The model accounts for different kinetic factors: direct impingement, adatom diffusion on the substrate and sidewalls and the GT effect in the drop seated at the NW top. In stationary growth mode with a constant radius R, the exact solution for the NW vertical growth rate can be presented in the form

$$\frac{dl}{dh} = \frac{BU(l) + C}{U'(l)} + A\,, \qquad l(h=0) = l_0. \qquad (1)$$

Here, $l \equiv L/\lambda_f$ is the normalized NW length and $h \equiv H/\lambda_f$ is the normalized deposition thickness, l_0 is the initial length of pre-existing NW. The R-dependent coefficients A, B and C stand for the direct impingement onto the drop surface, the adatom diffusion from the sidewalls and from the substrate, respectively. Due to the GT effect in the drop, coefficiencts A, B and C could be of *either signs*. The function $U(l)$ is given by

$$U(l) = \sinh(l) + F\,[\cosh(l) - 1]\,, \qquad (2)$$

where F is a positive coefficient depending on the ratio R/λ_s.

Analysis of Eq. (1) in the diffusion-induced mode ($A \to 0$) yields four possible growth scenarios:

(I) Infinite growth at $R > \max(R_B, R_C)$.
(II) Negative growth at $R < \min(R_B, R_C)$.
(III) Averaging growth at $R_C < R < R_B$.
(IV) Continuing growth at $R_B < R < R_C$.

The characteristic radii are determined by $R_B = R_{GT}/\theta_{fl}$; $R_C = R_{GT}/\theta_{sl}$, with R_{GT} as the characteristic GT radius, and θ_{fl} and θ_{sl} as the effective activities of sidewall and surface adatoms with respect to the bulk liquid phase.

We then consider our experimental data on the Au-assisted MBE of GaAs NWs on the GaAs(111)B substrates and show that (i) non-trivial scenario (II) clearly happens during a high temperature annealing on GaAs NWs under the arsenic flux and (ii) non-trivial scenario (IV) can promote high-temperature growth on the initially pre-existing NWs at a low supersaturation. The latter is important from the viewpoint of fabrication of zincblende NWs without stacking faults.

Analysis of kinetic growth equation shows that the length-diameter dependences are generally the functions with one maximum. This is explained by the combined effect of GT elevation of chemical potential in the small drop and the adatom diffusion, and is supported by previous findings [4]. We derive simplified equations for the NW growth rate in MOCVD and

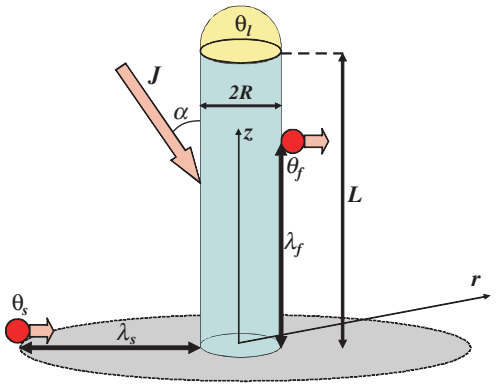

Fig. 1. NW growth model: J is the impinging flux, θ_s, θ_f are the activity of surface (s) and sidewall (f) adatoms, θ_l is the activity of semiconductor material in the drop (modified by the GT effect), λ_f and λ_s are the diffusion lengths on the sidewalls and the surface.

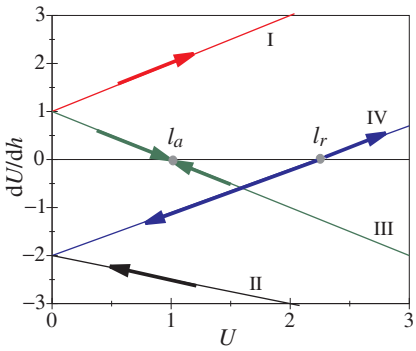

Fig. 2. Illustration of the growth modes described in the text: I — infinite growth, II — negative growth, III — averaging growth with attractive stationary point l_a such that all NWs tend to a finite length l_a, IV — continuing growth with repulsive stationary point l_r such that NWs with initial length $l_0 < l_r$ decay and longer NWs with $l_0 > l_r$ grow infinitely.

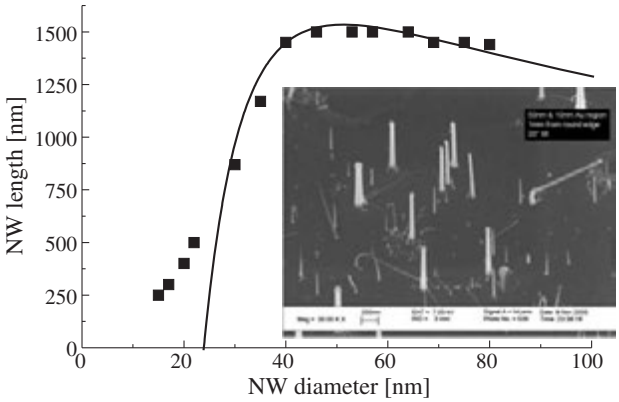

Fig. 3. Experimental length-diameter dependence of MOCVD grown InP NWs (black squares) and theoretical curve (solid line) obtained at $R_{GT} = 4$ nm, $\theta_{sl} = \theta_{fl} = 1.4$ and $\lambda_f = 50$ nm.

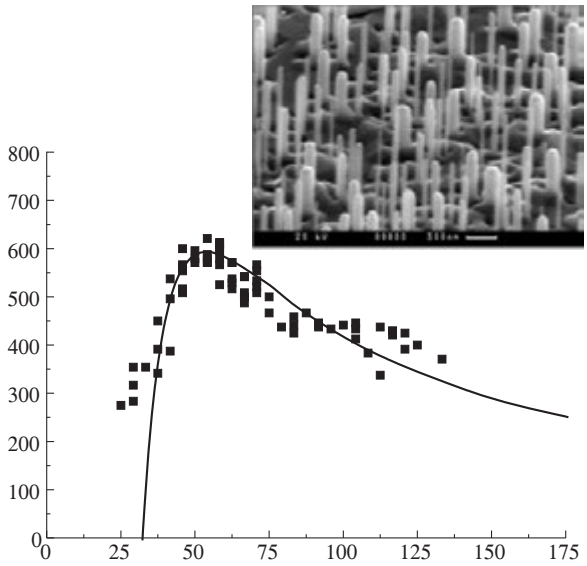

Fig. 4. Experimental length-diameter dependence of MBE grown GaAs NWs (black squares) and theoretical curve (solid line) obtained at $R_{GT} = 3.5$ nm, $\theta_{vs} = 2.20$, $\theta_{sl} = 1.24$ and $\lambda_s = 95$ nm.

MBE technique. To study the growth kinetics of NWs in different material systems, we perform three sets of experiments.

InP NWs are grown on the GaAs(111)B substrates using colloidal Au nanodrops as catalysts in a MOCVD reactor under the VLS growth mode. The mole fractions of the group V (tertiarybutylphosphine) and group III (trimethylindium) sources were 1.91×10^{-5} and 1.17×10^{-3}, respectively, in a 12 l/min hydrogen carrier gas flow yielding a V/III ratio of 61. The growth temperature was 470 °C and the growth time was 3 min. The size of Au drops ranges from 10 to 160 nm. Analysis of high-resolution scanning electron microscopy (SEM) images was used to study the length-diameter dependences, presented in Fig. 3, with a typical SEM image shown in the insert.

Si NWs are grown from Si (111) substrates by MOCVD techniques with Au nanodrops as catalyst. The Au was deposited in-situ by controlling the evaporation flow. The evaporation pressure is 7.98×10^{-10} mbar and the deposition time is 4 min. The growth temperature and time were 500 °C and 30 min respectively. The total pressure was 1.1 mbar and SiH_4 was diluted by H_2 with the ratio of 1:150. Measurements from SEM images and theoretical length-diameter dependences (not presented here) show the performance similar to that of Fig. 3, however, the numerical values of kinetic parameters during the growth are different.

GaAs NWs were grown by MBE on the GaAs(111)B substrates. First, the substrate was placed in the growth chamber of a MBE setup, where the oxide was removed from the substrates and the GaAs buffer layer was deposited. Second, the samples were transferred from the MBE setup to the vacuum chamber equipped with an Au electron beam evaporator. In the vacuum chamber, a thin Au film was deposited onto the sample surface. Third, the samples were transferred back to the MBE growth chamber and baked out at the temperature of 610 °C during 5 min. After that, the GaAs layer with the effective thickness of 420 nm was deposited at the deposition rate of 1 monolayer per second and the substrate temperature of 585 °C. The visualization of surface morphology was performed by applying SEM technique. Analysis of SEM image led to the length-diameter curve shown in Fig. 4, with a corresponding SEM image shown in the insert.

As seen from the results presented in Fig. 3 and 4, theoretical and experimental results are in reasonable agreement, apart from the discrepancy for very short NWs (whose growth can not be described by the simplified equations mentioned). From fitting experimental and theoretical curves, we can work out the estimates of some important kinetic parameters during the NW growth. In particular, the diffusion length of sidewall In atoms equals 50 nm in MOCVD, while the diffusion length of surface Ga atoms amounts to 95 nm in MBE.

Acknowledgements

This work was partially supported by RFBR grants, scientific programs of of Presidium RAS and the Russian Federal Agency for Science and Innovation.

References

[1] R. S. Wagner and W. C. Ellis, *Appl. Phys. Lett.* **4**, 89 (1964).
[2] E. I. Givargizov, A. A. Chernov, *Kristallografiya* **18**, 147 (1973).
[3] V. G. Dubrovskii *et al*, *Phys. Rev. B* **71**, 205325 (2005).
[4] E. Fröberg *et al*, *Phys. Rev. B* **76**, 153401 (2007).

17th Int. Symp. "Nanostructures: Physics and Technology"
Minsk, Belarus, June 22–26, 2009
© 2009 Ioffe Institute

Effect of diameter and density of the catalyst on GaAs nanowires growth by Au-assisted metal-organic chemical vapor deposition

Xiaomin Ren, Hui Huang, Xian Ye, Yisu Yang, Qi Wang, Yongqing Huang and Xia Zhang
Key Laboratory of Optical Communication and Lightwave Technologies (Ministry of Education), Institute of Optical Communication and Optoelectronics, Beijing University of Posts and Telecommunications, P.O. Box 66, Beijing 100876, China

Semiconductor nanowires (NWs) are intensively studied due to their great potential for nanoscale electronics and photonics [1,2]. Great efforts have been made on the vapor-liquid-solid (VLS) growth of the freestanding nanowires in a bottom-up manner [3]. In our laboratory, NWs are adopted to enable high quality heteroepitaxial growths and the NWs-based 2-dimensional superlattices with complex unit cell (as well as the quantum-wells-based 1-dimensional and quan-tum-dots-based 3-dimensional ones) are also pursued. In this paper, the VLS growth of the GaAs NWs on GaAs (111)B substrate with Au particles as catalyst is reported. Particularly, the interesting dependences of NWs growth rate on the diameter and density of Au particles have been investigated and discussed.

The epitaxial growth was performed by metal-organic chemical vapor deposition (MOCVD) with a Thomas Swan CCS-MOCVD system at a pressure of 100 Torr. Trimethylgallium and arsine were used as the precursors. Three samples (A, B and C) were prepared. Each of the them was prepared by firstly depositing an Au film on a GaAs (111)B substrate, then annealing the Au-coated GaAs substrate in the MOCVD reactor at 645 °C to form Au nanoparticles as catalyst and finally growing the GaAs NWs at 464 °C for 10 min with V/III ratio of 70. The Au film thickness for Sample A, B and C was 1.0 nm, 2.0 nm and 4.0 nm, respectively. And, The NWs for all the samples were simultaneously grown in one procedure and, in other words, under the exactly same condition.

Figure 1 shows the atomic force microscopy(AFM) images of Au nanoparticles on the GaAs substrate after annealing. The average diameter of Au nanoparticles is 45 nm, 70 nm and 160 nm for Sample A, B and C, respectively, and the corresponding density of Au nano-particles is 1.64×10^{10} cm^{-2}, 1.26×10^{10} cm^{-2} and 2.2×10^{9} cm^{-2}. As shown in Fig. 1, there is a rather broad distribution of the Au particle diameter in each sample.

Figure 2 shows the scanning electronic microscopy(SEM) images of the GaAs NWs. It can be found that the lengths of all the GaAs NWs for each sample are almost the same although the NWs diameters determined by the corresponding Au particle diameters are quite different. In other words, the growth rate of NWs was nearly independent on their diameters. The NWs length for Sample A, B and C is about 5.3 μm, 5.5 μm and 6.2 μm, respectively (the corresponding growth rate was 8.8 nm/s, 9.2 nm/s and 10.3 nm/s). So it could be concluded that the lower the density of the Au particles, the higher the growth rate and thus the longer the NWs might be. In comparison with theoretical result reported by V. G. Dubrovskii [4], it can be concluded that the NWs growth was mainly governed by catalysed chemical reaction and had neglectable contribution from adatom diffusion.

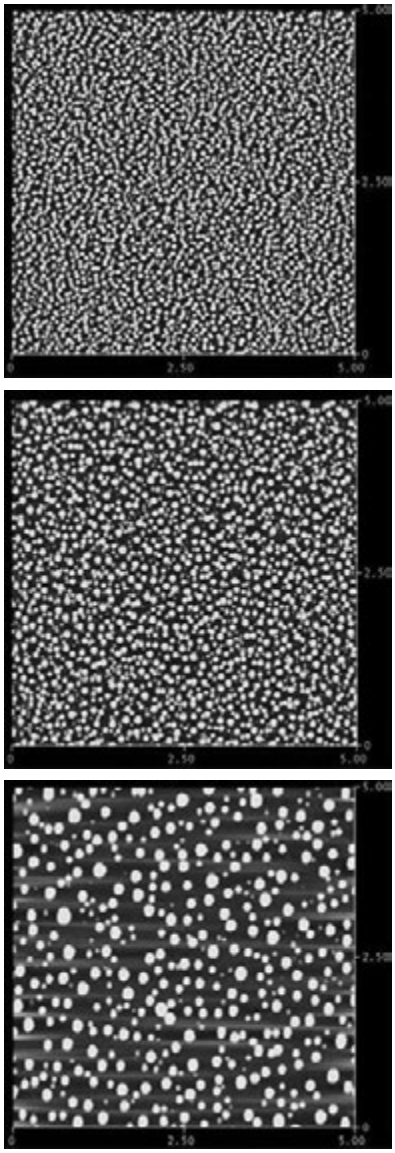

Fig. 1. AFM image of Au nanoparticles for (a) Sample A, (b) Sample B, and (c) Sample C.

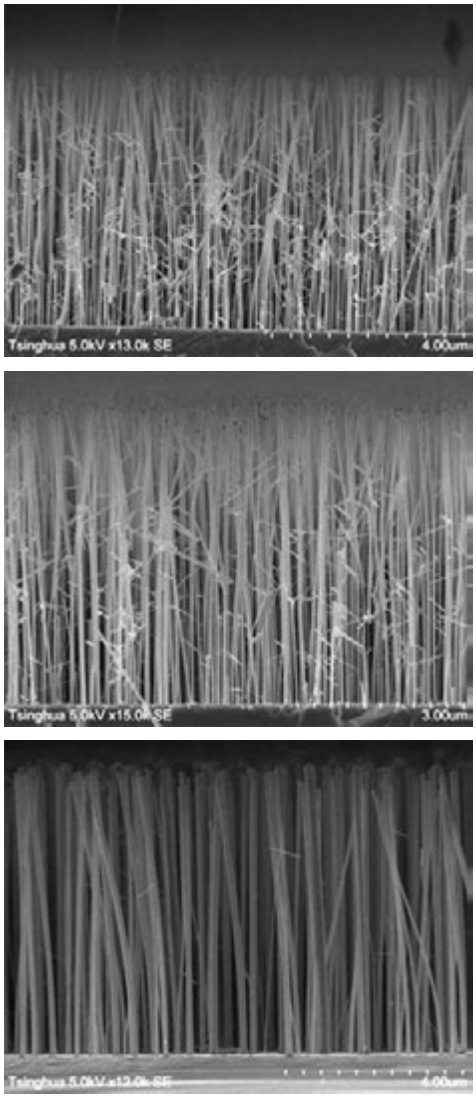

Fig. 2. SEM image of the GaAs NWs for (a) Sample A, (b) Sample B, and (c) Sample C.

Acknowledgements

This work was supported by grants from National Basic Research Program of China (No. 2003CB314901), the 111 Program of China (No. B07005), Program of Key International Science and Technology Cooperation Projects (No. 2006DFB 11110) and the Program for Changjiang Scholars and Innovative Research Team in University (No. IRT0609).

References

[1] J. Hu, T. W. Odom and C. M. Lieber, *Acc. Chem. Res.* **32**, 435 (1999).
[2] L. Samuelson, *Mater. Today.* **10**, 22 (2003).
[3] R. S. Wagner, W. C. Ellis, *Appl. Phys. Lett.,* **4**, 89 (1964).
[4] V. G. Dubrovskii, G. E. Cirlin *et al*, *Phys. Rev. B* **71**, 205325 (2003).

17th Int. Symp. "Nanostructures: Physics and Technology"
Minsk, Belarus, June 22–26, 2009
© 2009 Ioffe Institute

A3B5 coherent nanowires on silicon substrates: MBE growth and properties

G. E. Cirlin[1,2,3], Yu. B. Samsonenko[1,2,3], A. D. Bouravleuv[1,2], I. P. Soshnikov[1,2], N. V. Polyakov[1,2,3], N. V. Sibirev[2], V. G. Dubrovskii[1,2], M. Tchernycheva[4] and J.-C. Harmand[4]

[1] St Petersburg Physics and Technology Centre for Research and Education RAS, St Petersburg, Russia
[2] Ioffe Physical-Technical Institute, St Petersburg, Russia
[3] Institute for Analytical Instruments RAS, St Petersburg, Russia
[4] LPN CNRS, Marcoussis, France

Abstract. A variety of A3B5 semiconductor nanowires (NWs) can be coherently (i.e. the crystallographic directions are transferred from the substrate to the NWs) grown on silicon substrates using molecular beam epitaxy (MBE). Two different approaches are examined: Au-assisted growth for GaAs, AlGaAs, InAs, InP NWs, and GaAs, GaN/AlN self-catalyst Ga-terminated growth. All the A3B5/Si NWs are optically active, which may open a new way to combine Si-based microelectronics with A3B5-based optical parts on the same Si wafer.

Introduction

Over last few decades one of the most important tasks in optoelectronics is to merge Si-based microelectronics with A3B5 components serving as light emitters and/or detectors. Different approaches were examined so far, however with a limited success. In the case of direct growth of A3B5 on silicon several physical reasons (lattice mismatch, thermal expansion difference, phase-anti-phase boundary issues, different crystal structure etc.) are the key factors introducing structural defects at the A3B5 material/Si substrate interface. The way to decrease the sizes of A3B5 structures is now seen as one of the most promising to overcome the intrinsic problem. The object studied in this work is the A3B5 semiconductor NWs grown by MBE directly on Si substrates. It has been recently theoretically shown [1] that NWs can be grown on lattice mismatched surfaces without the formation of the structural defects (e.g., dislocations) due to the ability to accumulate for strain in two dimensions. We will also show that, together with commonly used external Au-catalyzed NWs formation, a self-catalyst Ga-terminated growth method can also be applied to A3B5 NWs fabrication directly on Si.

1. Experimental

Growth experiments are carried out using EP1203 and Riber 32P setups equipped with effusion Au cell to get Au-metal droplets at the high vacuum conditions. During the growth we have used Si(100) and Si(111). After the desorption of an oxide layer in the growth chamber we did not grow the buffer layer but, according to *in situ* reflection high energy electron diffraction (RHEED) patterns, the surface was atomically smooth. After that, the deposition of Au or Ga layer (0.1–1 nm) was applied. In the case of nitrogen-content NWs, AlN nanoscale islands were deposited on Si(111) substrate prior to the NW growth. The substrate was then set above the eutectic melting point of a corresponding alloy with Au in order to form seed drops. After this stage the grown of NW with desirable chemical composition was initiated. The growth temperature of NWs, V/III flux ratio and growth rate were varied during our experiments depending on the material. Formation of cubic, polytype or wurzite crystal phases at different stages was clearly observed from RHEED patterns. After the growth, the samples were characterized by scanning electron microscopy (SEM) and photoluminescence (PL) methods.

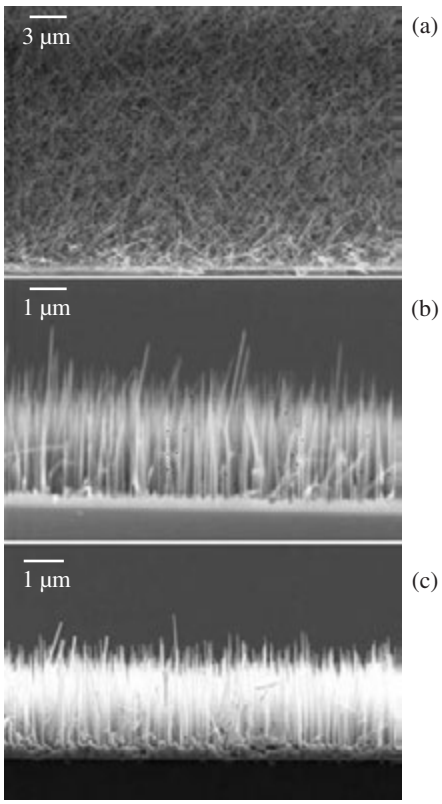

Fig. 1. SEM images of different A3B5 NWs grown on Si substrates. (a) — InAs/Si(100), (b) — GaAs/Si(111), (c) — AlGaAs/Si(111).

2. Results

We first discuss the Au-assisted MBE growth of NWs. The GaAs, AlGaAs, InP, InAs NWs were successfully synthesized on Si(111) and Si(100) surfaces. As typical examples, SEM images of InAs, GaAs, and AlGaAs and NWs grown on different Si substrates are presented in Fig. 1.

The temperature ranges for the growth of A3B5/Si NWs are

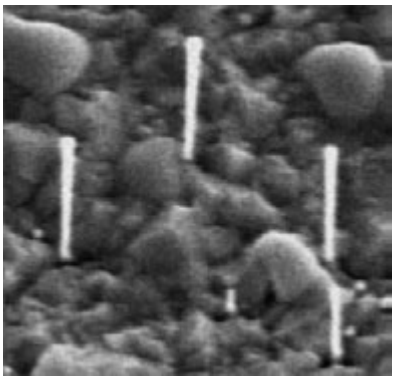

Fig. 2. SEM image of GaAs self-catalyzed NWs grown on Si(111) substarte.

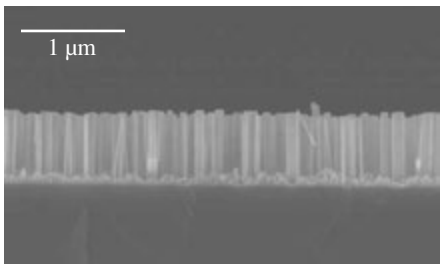

Fig. 3. SEM image of GaN self-catalyzed NWs grown on Si(111) substarte.

found to be quite different for the different material systems. The broadest temperature range (380–540 °C) corresponds to the cases of GaAs/Si(111) and AlGaAs/Si(111). In opposite, InAs and InP NWs can be growth within a very narrow temperature windows, (370–380 °C) and (390–410 °C), respectively.

An interesting phenomenon has been detected from the dynamic monitoring of the RHEED patterns. At the beginning of growth, the NWs (independently on the material deposited) have a pure cubic phase, however, it has been rather quickly converted to the wurzite or polytype lattice. As the NWs growth continued, the RHEED pattern (at least, partially) has been transformed back to the cubic phase. This is in opposite to the case A3B5 NWs growth on the own substrates, e.g., GaAs/GaAs(111)B, where the wurzite phase does not change in time after the first transformation from cubic to wurzite (except for the very top of the NW) [2]. According to our preliminary PL measurements of GaAs/Si(111) and InAs/Si(111) NWs [3,4], the dominant PL peak can be attributed to the cubic phase. This is also confirmed by the transmission electron microscopy studies.

In addition, we have studied the possibility of NW formation using the self-catalized method, where one of the element of the NW (e.g., Ga) is used as a growth catalyst. The use of Ga instead of Au allows one to avoid an unintentional Au doping during the growth. It is well established that Au incorporates during the growth of Si NWs, for A3B5 materials this is still not obvious. In the case of GaAs/Si(111), we use Si substrate covered with a thin (∼20 nm) oxide layer. In Fig. 2 we present the SEM image of GaAs NWs grown without external catalyst. The shape of these NWs is also different from those obtained on the GaAs(111)B surface. In particular, a negative tapering towards the NW foot is clearly seen in Fig. 2. The density and diameter of NWs are determined by the density of the openings in SiO layer and can be controlled by the thickness of the latter as well as by the duration of deoxidation process.

Finally, we grow GaN NWs on Si(111) substrates with predeposited AlN nanoscale islands. These islands serve as the nucleation sites for the subsequent NWs growth. Typical SEM image of GaN NWs is presented in Fig. 3. These NWs exhibit pure wurzite phase with a very low concentration of structural defects. GaN NWs has a strong PL up to the room temperature in spectral range of 3.4–3.6 eV.

In conclusion, we have demonstrated the possibility to grow epitaxial, dislocation-free A3B5 NWs on different Si substrates. All of them exhibit a bright light emission thus opening a new way for monolithic integration of A3B5 components on silicon substrates.

Acknowledgements

This work was partially supported by RFBR grants and scientific programs of Presidium RAS.

References

[1] F. Glas, *Phys. Rev. B* **74**, 121302(R) (2006).
[2] H. J. Fan, I. P. Soshnikov *et al*, *Phys. Sol. St.* **47**, 2213 (2005).
[3] B. V. Novikov *et al*, *this volume*.
[4] Cun-Zheng Ning, *private communication*.

17th Int. Symp. "Nanostructures: Physics and Technology"
Minsk, Belarus, June 22–26, 2009
© 2009 Ioffe Institute

Self-catalyzed MOVPE growth of GaAs whiskers

A. D. Bouravleuv[1,2,3], G. Statkute[3], G. E. Cirlin[1,2,4]
and H. Lipsanen[3]

[1] Ioffe Physical-Technical Institute, St Petersburg, Russia
[2] St Petersburg Physics and Technology Centre for Research and Education RAS, St Petersburg, Russia
[3] Helsinki University of Technology, FIN-02150 Espoo, Finland
[4] Institute for Analytical Instrumentation, 190103 St Petersburg, Russia

Abstract. Self-catalyzed metal organic vapor phase epitaxial growth of GaAs whiskers on GaAs(111)B wafers is demonstrated. In situ deposited Ga droplets are used as a seeds for a growth. The structure of the whiskers is characterized by the electron microscopy measurements. The crystal structure of whiskers is found to be dependent on the growth parameters. The maximum length of whiskers obtained is equal to 40 μm.

Introduction

One dimensional nanostructures, such as nanowhiskers or nanowires have recently attracted increasing attention due to a wide variety of their properties and versatile device applications [1,2]. Up to day the general technique for their growth is based on the vapor-liquid-solid (VLS) mechanism [3]. According to this method, the formation of the nano-whiskers occurs due to the adsorption of the gas-phase reactants by liquid droplets that are formed from pre-deposited metal nanoparticles, so called catalyst. The most commonly used catalyst is gold. The sizes and the positions of nanowhiskers depend directly on the diameters and the positions of the droplets. It is well known that nanowhiskers can be unintentionally contaminated by metal used as a catalyst for the growth and in many cases such contaminations can lead to the degradation of the device's properties. Therefore, the methods of the growth of one-dimensional nanostructures without the use of any foreign catalysts are of great practical consequence.

Recently, related methods have been demonstrated by both molecular beam epitaxy (MBE) [4–6] and metal organic vapor phase epitaxy (MOVPE) [7–9].

Here we report on the investigation of the self-catalyzed MOVPE growth (or self-catalytic) of GaAs whiskers using atoms of group III as a catalyst.

1. Experimental

GaAs whiskers were grown on GaAs(111)B substrates with the horizontal atmospheric pressure MOVPE reactor manufactured by Thomas Swan Scientific Equipment Ltd. using trimethylgallium (TMGa) and tertiarybutylarsine (TBAs) precursors as sources for gallium and arsenic, respectively. The carrier gas used was hydrogen. The steel bubblers were held in temperature-controlled baths. The halogen lamp was used to heat the graphite susceptor, whose temperature was measured by a thermocouple placed inside it. The preliminary annealing of GaAs wafers was carried out at 700 °C to eliminate native oxide overlayer. Then Ga droplets were created on the substrate surface by introducing TMGa into reactor for 30 s. Nanowhisker growth was initiated after reducing the temperature. The duration of growth was equal to 360 s. The growth of GaAs nanowhiskers was performed in the temperature range from 420 to 510 °C. The input V/III ratio in all growth experiments was 21, except for a growth at 510 °C, there it was equal to 30. Immediately after the completion of the growth, TMGa line was closed, whereas TBAs line remained open while the temperature of the susceptor was decreasing down to 400 °C.

Sample characterization was carried out using Zeiss Supra 40 Scanning Electron Microscope (SEM).

2. Results

The formation of Ga droplets on GaAs(111)B surface has been performed immediately after the annealing step, i.e. at the same temperature, to be ensure that they would create an alloy with substrate material. The relatively big sizes of in-situ deposited Ga droplets, as it is shown in Fig. 1, seem to be caused primarily by both the high rate of TMGa flow and the time of deposition process. We have done preliminary investigations and obtained smaller Ga droplets as well.

Figure 2 demonstrates SEM image of the sample with GaAs whiskers grown at 480 °C. It should be particularly emphasized, that the grow rate of GaAs whiskers obtained in turn also was reasonable high taking into account the time of the growth. The length of whiskers averages between 10 and 12 μm with the width of the basements are of the order of 4 μm. The sizes of whiskers can be substantially changed by the controlling of the sizes of deposited Ga droplets.

GaAs whiskers grow along $\langle 111 \rangle$ crystallographic direction and show pronounced tapering. It is well known, that the tapering itself indicates the presence of radial growth. If we take also into account the fact, that contrary to MBE, the growth of GaAs whiskers at our technological parameters was not accom-

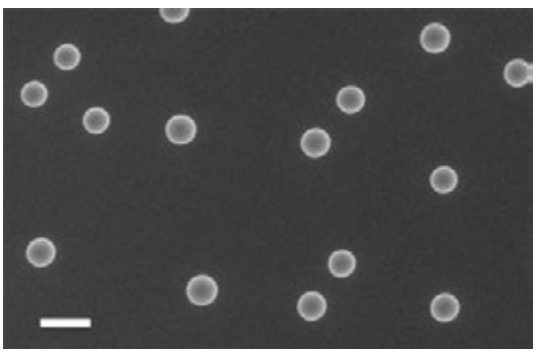

Fig. 1. SEM image of Ga droplets. The scale bar corresponds to 10 μm.

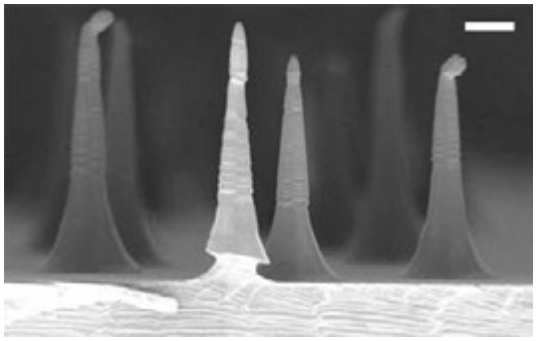

Fig. 2. The cross-sectional SEM image of the sample with GaAs whiskers grown at 480 °C. The scale bar corresponds to 2 μm.

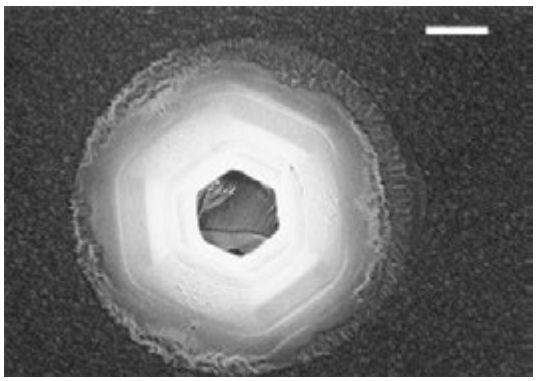

Fig. 3. SEM image of the broken individual GaAs whisker that was grown at 480 °C. The scale bar corresponds to 1 μm.

panied by the growth of GaAs wetting layer, one can suggest that the places for the effective decomposition of the precursors are the whiskers' nucleation sites instead of the substrate surface. Most likely, on the initial stage, clusters of Ga atoms play their role, whereas at the beginning of the growth, the precursors decompose at the side walls of the GaAs whiskers.

As it can be seen in Fig. 2, all GaAs whiskers translate the symmetry of the substrate surface. The edges of the whiskers are perpendicular to the ⟨110⟩ crystallographic orientations of the substrate. Figure 3 shows the SEM image of the individual whisker, which has been broken close to his basement. One can see, that the whiskers grown at 480 °C have hexagonal symmetry. As at the lower temperatures of the growth, whiskers have C_3 — type of symmetry (Fig. 4), which can be caused by non-equilibrium growth conditions, since this type of atomic packing for GaAs compounds is less favorable than hexagonal one. It might be well to point out, that usually GaAs with zinc-blend (ZB) crystal structure has C_3 — type of symmetry. Figure 2 indicates the presence of different segments along the whisker's axis. It can be result of the transition between wurtzite (WZ) and ZB crystal phases. The realization of such WZ–ZB polytypic structures may lead to interesting effects. Some of the whiskers grown at 500 °C seem to have pure WZ structure. However, to prove that an additional detailed investigation of the samples by transmission electron microscopy (TEM) is needed. By and large the geometrical sizes of nanowhiskers obtained in the temperature range between 420 and 500 °C are similar in sizes with small variations.

In addition, we have grown GaAs whiskers on GaAs(111)B surface at different TBAs flow (Fig. 5). In that case, the input

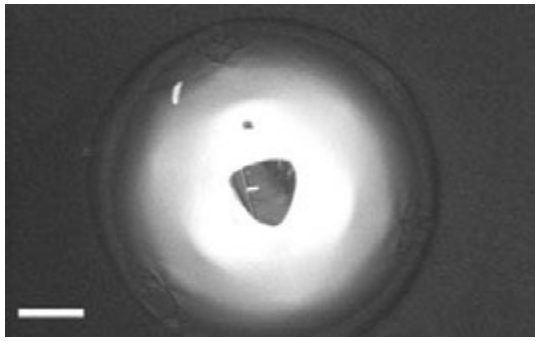

Fig. 4. SEM image of the broken individual GaAs whisker that was grown at 420 °C. The scale bar corresponds to 1 μm.

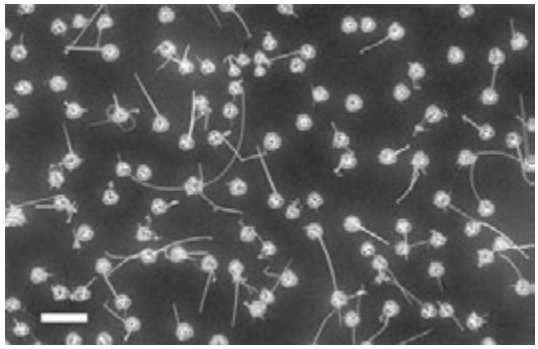

Fig. 5. The top view of the sample grown at 510 °C. The scale bar corresponds to 10 μm.

V/III ratio was equal to 30. The maximum length of whiskers obtained is around 40 μm. The shape of whiskers also differs from obtained in the previous described experiments. The mechanism of their formation is still an open question that requires an additional clarification.

Acknowledgements

The authors aknoweledge Dr. I. P. Soshnikov for a helpful discussions. This work was supported by Academy of Finland (grant No. 117280) and different grants of RFBR and the Presidium of RAS.

References

[1] W. Lu *et al*, *J. Phys. D: Appl. Phys.* **39**, R387 (2006).
[2] H. J. Fan *et al*, *Small* **2**, 700 (2006).
[3] R. S. Wagner and W. C. Ellis, *Appl. Phys. Lett.* **5**, 89 (1964).
[4] A. Fontcuberta i Morral *et al*, *Appl. Phys. Lett.* **92**, 063112 (2008).
[5] F. Jabeen *et al*, *Nanotechnology* **19**, 275711 (2008).
[6] A. D. Bouravleuv *et al*, *J. Phys.: Conf. Ser.* **100**, 052052 (2008).
[7] J. Noborisaka *et al*, *Appl. Phys. Lett.* **86**, 213102 (2005).
[8] C. J. Novotny *et al*, *Appl. Phys. Lett.* **87**, 203111 (2005).
[9] M. Mattila *et al*, *Appl. Phys. Lett.* **89**, 063119 (2006).

17th Int. Symp. "Nanostructures: Physics and Technology"
Minsk, Belarus, June 22–26, 2009
© 2009 Ioffe Institute

Ordered states engineering in nanostructures

A. A. Gorbatsevich
St Petersburg Physics and Technology Centre for Research and Education RAS, St Petersburg, Russia

Abstract. It is shown that a new type of ordered state — ferrotoroic state can be realized in heterostructures with the help of methods of band-structure engineering. This state corresponds to the ordering of toroidal moments. Compact description of toroidal moments which can be formed either by orbital currents or by localized spins is presented. In equilibrium toroics spontaneous electric currents exist on a scale of elementary cell with no net macroscopic current. Such macroscopic current emerges under non-equilibrium conditions and manifests itself as anomalous photogalvanic effect. Analogously macroscopic transport spin-currents can exist in non-equilibrium systems with broken spin-orbit symmetry.

Introduction

States with broken symmetry are traditionally in the focus of condensed matter physics researches. Lowering of macroscopic symmetry is accompanied as a rule by the formation of some kind of an ordered state. Generally breaking of the time-reversal symmetry results from magnetic moments ordering while spatial symmetry transformation can be caused by both charge carrier redistribution and magnetic moments ordering. Widely adopted description of phase transitions is based on the notion of an "order parameter" which is a physical quantity whose symmetry reflects symmetry change at the transition [1]. In ferroelectrics the order parameter is electric polarization vector $\mathbf{P}$, in ferromagnets — vector of magnetization $\mathbf{M}$. Polar vector $\mathbf{P}$ which invariant under time-reversal and axial t-odd vector $\mathbf{M}$ realize two of the four admissible vector representations of the group formed by operations of time and space inversions [2]. The two others are polar t-odd vector $\mathbf{T}$ and axial t-even vector $\mathbf{G}$ which characterize more exotic types of long range order and can be related to the ordering of toroidal moments [3] and spin currents [4].

Exotic orderings can emerge in bulk materials as a result of complex interelectron correlations and can be realized under stringent conditions on the parameters of interelectron interactions. However modern heterostructure technologies provide the possibility to control not only band structure and wave-function parameters but macroscopic symmetry of a system as well. While the former applications are well known as band structure or wave-function engineering the latter can be considered as *ordered states engineering*. State with given magnetic symmetry can be realized in nanostructures by means of traditional methods of wave-function engineering combined with application of external magnetic field [5,6]. A scale of physical effects observed in such systems is determined by characteristic length of nanostructure and can be large compared with analogous effects in bulk materials. In this report we describe a novel type of an ordered state — toroidal ordered state which can be created using methods of ordered states engineering.

1. Toroidal moment and toroidal order parameter

Toroidal moments are the third independent family of electromagnetic multipoles equally with electric and magnetic multipoles [7,8] which has been overlooked for a long time. Toroidal dipole emerges in the same order of multipole expansion as magnetic quadrupole. It's geometrical image is a torus with electric currents flowing only in the poloidal direction (the short way) around the torus (currents flowing in the long way around the torus are called toroidal currents and they determine the magnetic moment) or a closed loop of magnetic moments. Magnetic field produced by electric currents is enclosed inside the torus.

The toridal moment of a given electric current distribution $\mathbf{j}(\mathbf{r})$ is defined as [8,9]:

$$\mathbf{T} = \frac{1}{10c}\int \left(\mathbf{r}\,(\mathbf{r}\mathbf{j}(\mathbf{r})) - r^2\,\mathbf{j}(\mathbf{r})\right) d\mathbf{r}. \tag{1}$$

Using the relationship between current and magnetization $\mathbf{j} = c\,\mathrm{rot}\,\mathbf{M}$ one gets from (1) the expression for the toroidal dipole in terms magnetic moment distribution:

$$\mathbf{T} = \frac{1}{2}\int (\mathbf{r}\times\mathbf{M}(\mathbf{r}))\,d\mathbf{r}. \tag{2}$$

From (2) and definition of magnetic quadrupole moment [10] it follows that a system of two opposite magnetic moments oriented perpendicular to the line connecting them possesses both toroidal and magnetic quadrupole moments. At the same time a system of three or more magnetic moments forming a closed loop possesses only toroidal moment. The expression of current in terms of toroidal moment density distribution takes the form:

$$\mathbf{j}(\mathbf{r}) = c\,\mathrm{rot}\,\mathrm{rot}\,\mathbf{T}(\mathbf{r}) \tag{3}$$

In the expression for interaction energy W of a system with electromagnetic field toroidal dipole moment describes interaction with total current $\mathbf{j} = c/4\pi\,\mathrm{rot}\,\mathbf{B}$ including both transport and displacement currents:

$$W = -\int \mathbf{T}\mathrm{rot}\,\mathbf{B}d\mathbf{r}. \tag{4}$$

Independently polar t-odd vector emerged in the studies of ordered states with so called imaginary order parameter which was related to spontaneous current ordering [11,12] in the model of excitonic insulator [13]. Soon it was recognized [3,14] that the true order parameter which characterizes symmetry change at the phase transition point in such systems is the toroidal moment density. According to (4) total current plays the role of the conjugated field for the toroidal order parameter. Using this fact we can define operator of toroidal current density as

$$\hat{\mathbf{T}} = -\frac{c}{4\pi}\,\frac{\delta\hat{H}}{\delta\mathbf{j}} \tag{5}$$

and obtain expression for the toroidal current in a more simple way then the standard multipole expansion procedure. Consider Hamiltonian of N-particle system with arbitrary interparticle interactions depending only on particle coordinates:

$$\hat{H} = \sum_{i=1}^{N} \frac{1}{2m_i} \left(\hat{\mathbf{p}}_i - \frac{e}{c} \mathbf{A}(\mathbf{r}_i) \right)^2 + V(\mathbf{r}_1 \ldots \mathbf{r}_i \ldots \mathbf{r}_N). \quad (6)$$

It follows from Maxwell equation for the current

$$\text{rot rot } \mathbf{A}(\mathbf{r}) = \frac{4\pi}{c} \mathbf{j}(\mathbf{r}), \quad (7)$$

that for slowly varying current $\mathbf{j}$ vector-potential $\mathbf{A}(\mathbf{r})$ can be represented as a bilinear function of coordinates x_j. It is convenient to consider transversal vector-potential. Then there exist two bilinear in x_j transversal functions satisfying the equation (7):

$$\text{rot rot } (\mathbf{r} \times (\mathbf{r} \times \mathbf{j})) = 6\mathbf{j} \quad \text{and} \quad \text{rot rot } \mathbf{r}^2 \mathbf{j} = -4\mathbf{j}.$$

Taking into account the relations:

$$\text{div } (\mathbf{r} \times (\mathbf{r} \times \mathbf{j})) = 2(\mathbf{rj}) \quad \text{and} \quad \text{div } \mathbf{r}^2 \mathbf{j} = 2(\mathbf{rj})$$

we arrive at the following representation for the vector-potential:

$$\mathbf{A}(\mathbf{r}) = \frac{2\pi}{5c} \left((\mathbf{r} \times (\mathbf{r} \times \mathbf{j})) - \mathbf{r}^2 \mathbf{j} \right). \quad (8)$$

Substituting (8) into (6) one gets from (5) and (6):

$$\hat{\mathbf{T}} = \frac{e}{10c} \sum_{i=1}^{N} \frac{1}{m_i} \left((\mathbf{r}_i \times (\mathbf{r}_i \times (\hat{\mathbf{p}}_i - \frac{e}{c} \mathbf{A}(\mathbf{r}_i)))) - \mathbf{r}^2 \left(\hat{\mathbf{p}}_i - \frac{e}{c} \mathbf{A}(\mathbf{r}_i) \right) \right). \quad (9)$$

Averaging of (9) results in the substitution

$$\frac{e}{m_i} \left(\hat{\mathbf{p}}_i - \frac{e}{c} \mathbf{A}(\mathbf{r}_i) \right) \to \mathbf{j}.$$

Then passing from the summation over point charges to the integration we arrive at the classical expression for toroidal moment (1). Analogous procedure can be applied to derive the expression for the toroidal moment of spin system with the Hamiltonian:

$$\hat{H} = 2 \sum_{i=1}^{N} \mu_{\mathrm{B}} \hat{\mathbf{S}}_i \mathbf{H}, \quad (10)$$

where μ_{B} — is Bohr magneton. Magnetic field $\mathbf{H}$ can be expressed from Maxwell equation as

$$\mathbf{H} = \frac{4\pi}{c} \frac{1}{2} (\mathbf{j} \times \mathbf{r}). \quad (11)$$

Substituting (11) to (10) we arrive from (5) at the definition:

$$\hat{\mathbf{T}}_{\mathrm{S}} = \sum_{i=1}^{N} \mu_{\mathrm{B}} \left(\hat{\mathbf{S}}_i \times \mathbf{r}_i \right), \quad (12)$$

which is quantum analog of (2). Hermicity of (9) and (12) is obvious from their definition (5).

Materials with toroidal ordering are called "toroics" or "ferrotoroics" [15,16]. The symmetry of toroidal moment is the same as the symmetry of Pointing vector: $\mathbf{T} \sim (\mathbf{E} \times \mathbf{H})$. Therefore there must exist magnetoelectric effect in ferrotoroics:

$$\mathbf{P} \sim (\mathbf{T} \times \mathbf{H}) \quad \text{and} \quad \mathbf{M} \sim (\mathbf{H} \times \mathbf{T}) \quad (13)$$

where $\mathbf{P}$ — is electric polarization. From (13) it follows that vector $\mathbf{T}$ is dual to the antisymmetric part of magnetoelectric tensor. Measuring of magnetoelectric tensor asymmetry emerging at the transition point was used to identify the ferrotoroic state in [17,18] which soon has been observed in a number of materials [19] with spin magnetic ordering. Recently ferrotoroic domain structure which is an essential property of any ferroic material was observed [20]. The qualitative difference of ferrotoroics from other magnetoelectrics (with symmetrical magnetoelectric tensor) follows from the fact that at the ferrotoroic transition point a special type of response-function — the response function to the external current diverges.

2. Equilibrium and nonequilibrium currents in orbital toroics

Within the framework of equilibrium thermodynamics the structure of the Landau free energy functional doesn't distinguish between orbital and spin toroics. The main difference is in the values of the coefficients entering the functional with symmetry invariants. In spin toroics magnetoelectric effect is caused by spin-orbit interactions and is small. In orbital toroics it can be much larger. A special interest to orbital ferrotoroics was attracted because of the possible existence there of large diamagnetism without superconductivity (superdiamagnetism) [3,21] caused by orbital current precession in external magnetic field. Symmetry of vector $\mathbf{T}$ coincides with the symmetry of current $\mathbf{j}$. But the existence of spontaneous current $\mathbf{j} \sim \mathbf{T}$ is forbidden by guage invariance requirement [21]. On the microscopic level it is provided by a special velocity sum rule which forces macroscopic current to be zero for any distribution function depending only on energy of charge carriers. Existence of nonzero orbital toroidal moment density manifests itself on the microscopic level of description in the asymmetry of elementary excitations spectrum in quasimomentum $\mathbf{k}$: $E(\mathbf{k}) \neq E(-\mathbf{k})$, because the product $(\mathbf{Tk})$ is invariant under symmetry transformations. Hence the velocity is not an odd function of quasimomentum: $v(\mathbf{k}) \neq -v(-\mathbf{k})$ and contributions of states with opposite quasimomentum into the current don't cancel each other. However in the expression for the current

$$\mathbf{j} = -2 \frac{e}{(2\pi)^3} \int \frac{1}{\hbar} \frac{\partial E(\mathbf{k})}{\partial \mathbf{k}} f(\mathbf{k}) d\mathbf{k} \quad (14)$$

terms under the integral sign turn into the full derivative and the whole integral turns into zero if the distribution function depends only on energy $f(\mathbf{k}) \equiv f(E(\mathbf{k}))$. Under non-equilibrium conditions this is not already true and one can expect that the current emerges which is proportional to toroidal order parameter:

$$\mathbf{j} = \eta \mathbf{T}. \quad (15)$$

Here η is a dissipation constant depending on material parameters as well as on relaxation characteristics which determine the

peculiar form of non-equilibrium distribution function. In particular even under non-equilibrium conditions the current (15) turns into zero for quasi-Fermi distribution.

The current (15) exists in the absence of electrochemical potential gradient and therefore can be attributed to the class of anomalous photogalvanic effects (APE). Analogous currents were intensively studied in nonmagnetic systems without inversion center [22,23] where their origin is related to the asymmetry of intra- and interband scattering processes. Such asymmetry results in the formation of asymmetric in quasimomentum component of distribution function which is constant in alternating electromagnetic field. This component produces constant current in a system with **k**-odd charge carrier velocity. To obtain such a component of distribution function from kinetic equation it is necessary to go beyond the limits of Born approximation which is not the case for toroidal APE.

Recently an interest boosted in studying spin currents in the systems with spin-orbit interactions motivated by the demands of emerging spintronics field [24]. Bright manifestation of spin currents is spin Hall effect [25,26]. Very much alike APE there exist extrinsic (related to spin-dependent scattering of carriers) [26] and intrinsic (related to dissipationless spin currents) [27] contributions. Standard model system for studying these effects is Rashba Hamiltonian where it was shown [28] that dissipationless spin currents exist even in equilibrium. However as was stressed in [27] they are not transport currents. Spin current in Rashba model doesn't depend on the value of Fermi energy. It results from the cancelation of contributions from energy branches corresponding to different chirality which is an analog of the sum-rule for spontaneous electric currents (14). As studies of APE in ferrotoroics show dissipationless non-transport currents become transport currents under non-equilibrium conditions. Hence to observe real transport spin currents in systems with broken spin-orbit symmetry it is necessary to introduce non-equilibricity say by pumping with electromagnetic field. Non-equilibricity can destroy aforementioned cancelation and result in spin currents much larger then their intrinsic component.

3. Design of heterostructures for spontaneous currents observation

In [5,6] it was shown that a system with nonzero toroidal moment density accompanied by energy spectrum asymmetry can be constructed on the basis of asymmetric heterostructure with in-plane magnetic field **H**. Vector **T** in such system is determined as $\mathbf{T} \sim (\mathbf{l} \times \mathbf{H})$ where **l** is a polar vector oriented in growth direction of heterostructure. Heterostructure asymmetric can be achieved by composition variation. Any such system in magnetic field possesses magnetic moment formed by edge currents. The currents forming magnetic moments are antisymmetrically distributed in space in respect to the middle part of the heterostructure. In asymmetric heterostructure this current distribution is not antisymmetric. Toroidal moment is formed by currents which determine the deviation from perfectly antisymmetric current distribution. In homogeneous system Landau functions are degenerate with respect to the location of Landau orbital which is determined by transverse quasimomentum. In heterostructure potential Landau function energy depends upon position in space and therefore dispersion in quasimomentum emerges which means that in asymmetric heterostructures this dispersion is asymmetric as well. It is important that different quantum states correspond to Landau-like orbitals located in different space regions. Hence action of external field is different for different states and it explains microscopic mechanism of giant APE and in-plane magnetoelectric effects observed in [29,30]. In systems with broken spin-orbit symmetry asymmetric heterostructure can serve to spatially separate different components of spin currents as well which then can be easily unbalanced by external electromagnetic field.

References

[1] L. D. Landau and E. M. Lifshits, *Statistical Physics, part 1* (3-ed, Pergamon) 562 p., 1980.
[2] E. Ascher, in: *Magnetoelectric Interaction Phenomena in Crystals*, eds, A. Freeman and H. Schmid (New York) 1975.
[3] V. L. Ginzburg *et al*, *Solid St. Commun.* **143**, 339 (1984).
[4] A. A. Gorbatsevich and Yu. V. Kopaev, *Pis'ma ZhETF* **39**, 558 (1984).
[5] A. A. Gorbatsevich, V. V. Kapaev and Yu. V. Kopaev, *Pis'ma ZhETF* **57**, 565 (1993).
[6] A. A. Gorbatsevich, V. V. Kapaev and Yu. V. Kopaev, *Ferroelectrics* **161**, 303 (1994).
[7] V. M. Dubovik and L. A. Tosunyan, *Fiz. Elem. Chastits At. Yadra* **14**, 504 (1983).
[8] V. M. Dubovik and V. V. Tugushev, *Phys. Rep.* **187**, 145 (1990).
[9] N. A. Spaldin, M. Fiebig and M. Mostovoy, *J. Phys.: Condens. Matter.* **20**, 434203 (2008).
[10] L. D. Landau and E. M. Lifshits, *The Classical Theory of Fields* (ed., Pergamon) 428 p., 2000.
[11] B. A. Volkov and Yu. V. Kopaev, *Pis'ma ZhETF* **27**, 10 (1978).
[12] B. I. Halperin and T. M. Rice, *Solid St. Phys.* **21**, 115 (1968).
[13] L. V. Keldysh and Yu. V. Kopaev, *FTT* **6**, 2791 (1964).
[14] B. A. Volkov, A. A. Gorbatsevich and Yu. V. Kopaev, *ZhETF* **86**, 1870 (1984).
[15] D. G. Sannikov, *Pis'ma ZhETF* **41**, 229 (1985).
[16] H. Schmid, *Ferroelectrics* **252**, 41 (2001).
[17] Yu. F. Popov *et al*, *ZhETF* **114**, 263 (1998).
[18] Yu. F. Popov *et al*, *Pis'ma ZhETF* **89**, 302 (1999).
[19] C. Ederer and N. A. Spaldin, *Phys. Rev. B* **76** 214404 (2007).
[20] B. B. Van Aken *et al*, *Nature* **449** 702 (2006).
[21] A. A. Gorbatsevich, *ZhETF* **95**, 1467 (1989).
[22] E. L. Ivchenko and G. E. Pikus, *Superlattices and Other Heterostructures. Symmetry and Optical Phenomena* (Berlin: Springer) 1997.
[23] V. I. Belinicher and B. I. Sturman, *Usp. Fiz. Nauk* **130**, 415 (1980).
[24] I. Zutic *et al*, *Rev. Mod. Phys.* **76** 323 (2004).
[25] M. I. Dyakonov and V. I. Perel, *Pis'ma ZhETF* **13**, 467 (1971).
[26] J. E. Hirsch, *Phys. Rev. Lett.* **83** 1834 (1999).
[27] J. Sinova *et al*, *Phys. Rev. Lett.* **92** 126603 (2004).
[28] E. I. Rashba, *Phys. Rev. B* **68** R241315 (2003).
[29] V. I. Tsebro *et al*, *Phys. Low-Dim. Struct.* **1/2** 25 (1997).
[30] O. E. Omeljanovskii, V. I. Tsebro and V. I. Kadushkin *Pis'ma ZhETF* **63** 197 (1996).

17th Int. Symp. "Nanostructures: Physics and Technology"
Minsk, Belarus, June 22–26, 2009
© 2009 Ioffe Institute

Fabrication of opal-semiconductor photonic crystals from melts

D. A. Kurdyukov, N. F. Kartenko, and V. G. Golubev
Ioffe Physical-Technical Institute, St Petersburg, Russia

Abstract. A technique for filling pores of bulk and film silica opals with melts of AgI and V_2O_5 having relatively high melting points (T_m = 600–700 °C) using capillary forces is suggested. Pore filling degrees of 70–4% vol. for V_2O_5 and 97–3% vol. for AgI have been achieved.

Introduction

Nanocomposites based on opals, infiltrated with semiconductors and ionic crystals attract considerable attention of researchers. These nanocomposites and inverted composites based on them are used, for instance, as three-dimensional photonic crystals (3D PCs) [1,2]. The commonly employed techniques of opal pore filling are solution-based techniques [2]. They are used for infiltration of pores of both bulk opals [2] and opal films [3]. These techniques can result in 90% opal pore filling, however, multiple infiltrations, up to several dozens of infiltration runs, are needed [2].

Some authors reported the use of melts of metals [4], semiconductors [5], and organic materials [6] for opal pore filling. The infiltration with non-wetting melts (contact angle $\theta > 90°$) is carried out under an external hydrostatic pressure (Pb [4], InSb [5]) to overcome the negative capillary pressure ($P < 0$) that tends to reject a fluid from pores. This technique allows a complete pore filling in bulk opals during one infiltration run, however, special high-pressure equipment is needed [4]. It is unsuitable for infiltration of opal films because the sample surfaces are damaged when the embedded opal is taken out of the surrounding bulk material by using, for example, a jeweler's saw [4].

Wetting melts ($\theta < 90°$) can be introduced into pores under the action of capillary forces because positive capillary pressure ($P > 0$) forces a fluid to be drawn into the pores (capillaries). This means that opal pores can be infiltrated with melts by using the techniques similar to those using solutions. For example, ribose (T_m = 87 °C) was introduced into an opal film pores under the action of capillary forces [6]. To prevent formation of a bulk material layer at the opal film surface, a thin polydimethylsiloxane slab was pressed onto the surface of the opal film filled with liquid ribose [6].

This paper shows that melts of AgI and V_2O_5 having relatively high melting points ($T_m \leq$ 700 °C) can be introduced into pores of bulk and film opals under the action of capillary forces. The nanocomposites thus obtained can be used as tunable 3D PCs. V_2O_5 in opal pores can also be used as a precursor for the synthesis of VO_2 [7] to obtain ultrafast tunable 3D PCs as we have shown earlier [8].

1. Experimental

The opal samples were close-packed beads of amorphous SiO_2 310±10 nm in diameter synthesized by the Stöber technique [9]. Typical sizes of bulk opals were $5 \times 5 \times 1.5$ mm^3; the substrate sizes for the opal film were $15 \times 8 \times 1.5$ mm^3, the film thickness was 3 μm, and the film surface was parallel to the (111) planes of the SiO_2 beads. The opal film was grown by the vertical deposition technique [10].

Infiltration with V_2O_5 was performed in a fused silica vial under ambient conditions, and infiltration with AgI was carried out in an evacuated sealed silica vial to prevent reaction of these compounds with oxygen of the air. AgI and V_2O_5 were introduced into bulk opal pores, V_2O_5 was also infiltrated into pores of the opal film. The vial containing an opal sample and weighted portion of the infiltrating material was placed into a furnace and heated at a rate of 10 °C/min to the temperature T_{inf} exceeding by approximately 10–20% the melting temperature T_m (for V_2O_5: T_m = 690 °C, T_{inf} = 750 °C; for AgI: T_m = 557 °C, T_{inf} = 600 °C). Infiltration of the opal film with the V_2O_5 melt occurred in the lateral direction, similar to the technique for film infiltration with aqueous solutions of salts we developed earlier [3]. The bulk and film opal samples were kept under isothermal conditions at T_{inf} in contact with the melt during 0.5 and 3 hours, correspondingly. Then the samples were cooled at a rate of 10 °C/min to T_m of the infiltrating material, were kept at this temperature during 30 min, and then were cooled to room temperature at the same rate. SiO_2 beads were etched from the opal-AgI composite by diluted (1%) aqueous solution of HF to obtain an inverted composite.

2. Results and discussion

The contact angle values measured by the sessile drop technique at fused silica surface were 40° for AgI and 25° for V_2O_5, thus the compounds wet the SiO_2 surface ($\theta < 90°$), and hence they can penetrate into opal pores due to $P > 0$.

X-ray diffraction (XRD) studies have shown that the crystal structures of AgI and V_2O_5 remain unaltered after these compounds are introduced into opal pores (Fig. 1). Crystal lattice parameters of the fillers are close to those of bulk compounds.

The pore filling degrees of the composites synthesized by using bulk opals measured by the gravimetric technique were 70–4% vol. for V_2O_5 and 97–3% vol. for AgI. Therefore, the pore infiltration with AgI was nearly complete, and the degree of filling with V_2O_5 was well below 100%. Since wetting fluids completely filled capillaries (opal pores), the degrees of opal pore filling with the melts of these compounds were equal and amounted to 100%vol. at T_m. The filling degree of pores with a solid depends on a change in the density of the filler at solidification and on changes in densities of fillers and opal beads at cooling from $T_m$to room temperature (RT). The densitiy of solid V_2O_5 (3.371 g cm^{-3}) at RT exceed considerably the density of this compound in the liquid state (2.34 g cm^{-3})

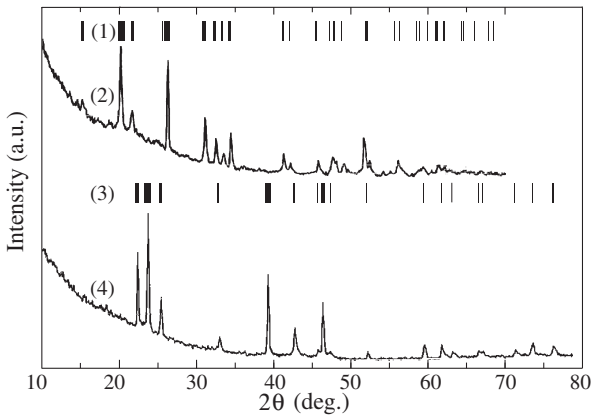

Fig. 1. XRD patterns. (1) —V_2O_5 (JCPDS 9-387); (2) — opal-V_2O_5; (3) — AgI (JCPDS 9-0374); (4) — opal-AgI.

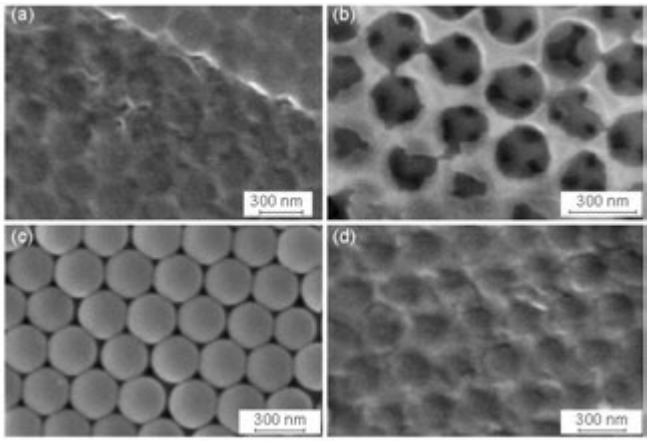

Fig. 2. SEM images: (a) bulk opal-V_2O_5; (b) inverted bulk opal-AgI; (c) film opal-V_2O_5; (d) film opal-V_2O_5 without the upper SiO_2 bead layer.

at T_m. For this reason, the filling degree of opal pores with V_2O_5 on solidification and cooling decreases to 70% vol. Densities of liquid and solid AgI are nearly equal (5.63 g cm^{-3} and 5.68 g cm^{-3}, correspondingly), and the pore infiltration with this filler at RT is nearly complete.

Fig. 2 shows Scanning Electron Microscope (SEM) images of opal-V_2O_5 and inverted opal-AgI composites. The photographs in Fig. 2a,b show that the pores in bulk opals are infiltrated. As seen from Fig. 2b, AgI is polycrystalline. No filler is seen in the upper layer of the opal film after infiltration with V_2O_5 (Fig. 2c). Fig. 2d shows an image of the film opal-V_2O_5 composite from which the upper layer of beads was removed. It is evident that the pores in the composite are filled, thus the filler is absent only in the upper film layer (Fig. 2c). This effect is likely to be due to a considerable increase in the V_2O_5 density at solidification (see above). Probably, the V_2O_5 melt moves into the sample depth and tends to minimize the number of voids arising between infiltrated regions in pores because of a decrease in the V_2O_5 molar volume at solidification. Formation of voids leads to an increase in the filler surface area and, hence, to an increase in the free surface energy, which is energetically unfavorable.

The composites we synthesized demonstrate properties characteristic of PCs [1]. Fig. 3 shows, as an example, spectra of the initial (uninfiltrated) opal film (curve 1) and the film infiltrated with V_2O_5 (curve 2) measured at normal light incidence. The broad bands in the spectra are due to Bragg diffraction of electromagnetic waves from a spatially periodic PC structure. They point to the existence of a photonic band gap (PBG) for the photonic states in the light propagation direction [1]. The energy position of the PBG is determined by diameters of the a-SiO_2 beads forming the opal film and its mean dielectric permittivity that depends on the filling degree of opal film pores with V_2O_5. In addition to the Bragg bands, the spectra of the initial opal film and opal-V_2O_5 composite contain distinct interference fringes because of light reflection from two plane-parallel film surfaces.

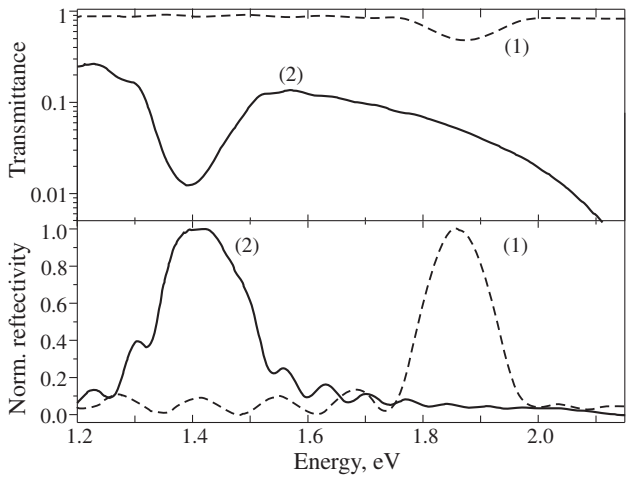

Fig. 3. The spectra of transmission and reflection of a bare opal film (1) and the opal film filled with V_2O_5 (2).

3. Conclusion

To summarize, a technique for infiltration of silica colloidal crystals with liquid AgI and V_2O_5 under the action of capillary forces has been developed. No special equipment is needed for this technique, infiltration occurs in either a sealed (AgI) or open (V_2O_5) fused silica vial at the temperature exceeding by 10–20% the melting temperature of the infiltrating compound. The process of infiltration of an opal film with the melt in the lateral direction, which ensures the absence of bulk material at the outer surface, has been implemented for the first time. The technique described here can be suitable for nearly complete filling of opal pores to provide for a synthesis of semiconductor 3D PCs.

Acknowledgements

We thank Dr. S. F. Kaplan for opal film fabrication, Dr. S. I. Troshkov for SEM measurements and Dr. S. A. Grudinkin for optical characterization of the samples. This work was supported by the RAS and the RFBR (project 08-02-00450).

References

[1] C. López, *Adv. Mater.* **15**, 1679 (2003).
[2] J. C. Lytle *et al*, *Ann. Rev. of Nanoresearch* **1**, 1 (2006).
[3] S. A. Grudinkin *et al*, *J. Phys. Chem. C* **112**, 17855 (2008).
[4] A. E. Aliev *et al*, *Physica C* **453**, 15 (2007).
[5] S. G. Romanov *et al*, *Appl. Phys. Lett.* **69**, 2897 (1996).
[6] F. Fleischhaker *et al*, *Chem. Mater.* **18**, 5640 (2006).
[7] V. G. Golubev *et al*, *Appl. Phys. Lett.* **79**, 2127 (2001).
[8] A. B. Pevtsov *et al*, *Phys. Rev. B* **75**, 153101 (2007).
[9] W. Stöber *et al*, *J. Colloid Interface Sci.* **26**, 62 (1968).
[10] P. Jiang *et al*, *Chem. Mater.* **11**, 2132 (1999).

17th Int. Symp. "Nanostructures: Physics and Technology"
Minsk, Belarus, June 22–26, 2009
© 2009 Ioffe Institute

Focused ion and electron beam lithography fabrication of three-terminal ballistic junction devices in InGaAs/InP and Si-based structures

Ivan Maximov[1], Fantao Meng[1], Jie Sun[1], Mariusz Graczyk[1], Martin Frimmer[2] and H. Q. Xu[1]

[1] Division of Solid State Physics/Nanometer Structure Consortium, Lund University, Box 118, S-221 00, Lund, Sweden
[2] Now at: FOM Institute for Atomic and Molecular Physics, P.O. Box 41883, 1009 DB Amsterdam, The Netherlands

Abstract. We present fabrication technology of InGaAs/InP and Si Three-Terminal Ballistic Junction (TBJ) devices. This technology is based on focused ion beam lithography and selective wet etching and electron beam lithography and dry etching, respectively. This approach allows us to make TBJ-devices with lateral dimension of about 50 nm. Electrical characterisation of the TBJ-devices is reported.

Introduction

Three-Terminal Ballistic Junction (TBJ) devices [1,2] are novel structures which show non-linear electrical properties and can be used in a variety of areas, e.g. for realisation of logic functions [3]. Earlier we have demonstrated technology of the InGaAs/InP TBJ-devices and circuits using electron beam lithography (EBL) [3] and nanoimprint [4] for high-resolution patterning. In this work we present a novel fabrication technology which is based on local implantation of 30 keV Ga^+ by focused ion beam and selective wet etching of the implanted areas to form the TBJ-devices. We also demonstrate fabrication of a Si-based TBJ-device using EBL and dry etching techniques.

1. Results and discussion

The $In_{0.75}Ga_{0.25}As$/InP 2DEG MOVPE-grown wafer with sheet electron concentration of 4×10^{11} cm^{-2} and mobility of 9×10^3 cm^{2}V^{-1}s^{-1} at room temperature was used as starting material. The InGaAs QW was positioned 40 nm under surface of the structure which made is easily accessible for the 30 keV Ga^+ ions as modeled by a freely available SRIM simulation program [5]. For focused ion beam implantation we used FEI Nova NanoLab 600 dual beam system controlled by lithographic stream files. The stream files control deflection of the ion beam to form single-pixel lines, which define the TBJ-devices with different geometry. The optimal line implantation dose was found to be about 2.5×10^8 cm^{-1}. After the implantation the InGaAs/InP sample was etched in 10% HF solution for 20 min to remove the implanted areas [6]. The etching results in formation of 50 nm wide and 30–40 nm deep trenches, which correspond to the thickness of the InP cap layer. The final processing steps included formation of mesas, metal evaporation and annealing of ohmic contacts. Figure 1 depicts a schematic of the local implantation and selective wet etching of the implanted areas. Scanning electron microscope (SEM) image of the TBJ-device fabricated with this process is shown in Figure 2.

The TBJ-devices were measured at room temperature in so-called push-pull fashion $V_L = -V_R$, where V_L and V_R are the voltages on the left and right branches, respectively. The voltage at the central branch, V_C, is recorded by a voltage meter and plotted against V_L. Some results of our measurements are presented in Figure 3. As it can be seen from this figure, the fabricated devices showed non-linear down-bending behavior of the devices, which is a signature of ballistic electron transport [1]. Electrical characterization of the devices in an

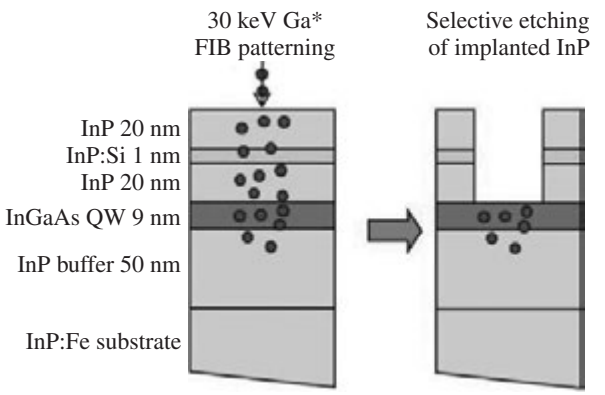

Fig. 1. Schematic of the local implantation of Ga^+ by focused ion beam and selective wet etching of the implanted areas to form the TBJ-devices.

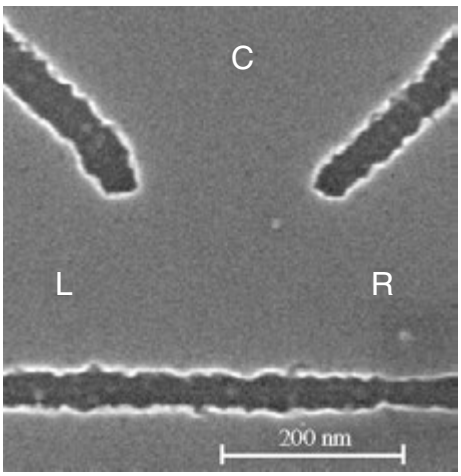

Fig. 2. SEM image of the InGaAs/InP TBJ device after the FIB implantation and HF-etching. Trenches 50 nm wide and 30–40 nm deep have been produced after the wet etching step.

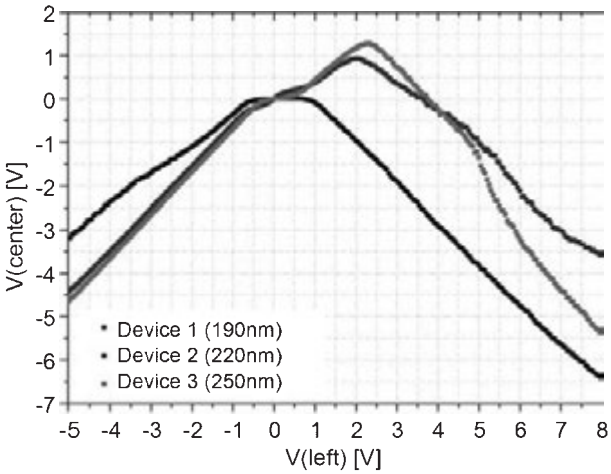

Fig. 3. Electrical characterisation of the FIB-formed TBJ-devices with 3 different geometrical widths (190, 220 and 250 nm). Some asymmetry in the curves is attributed to astigmatism of the focused ion beam.

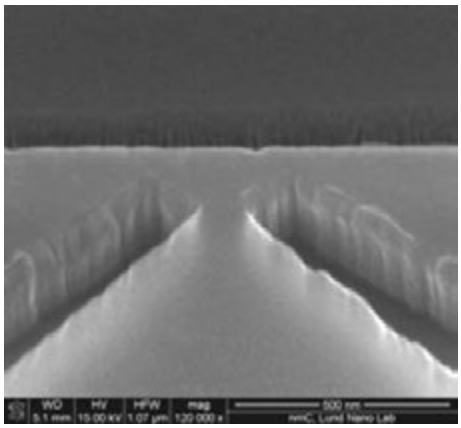

Fig. 4. An example of Si-based TBJ-device made using EBL and reactive ion etching. The typical width of the constriction is about 75 nm.

asymmetric configuration with V_L (or V_R) being fixed at certain voltage, while sweeping V_R (or V_L) and monitoring V_C voltage, also showed asymmetric behavior consistent with assumption of ballistic electron transport in the formed devices [7]. Details of the transport properties of the fabricated TBJ-devices are described elsewhere [8].

Figure 4 demonstrates an example of Si-based TBJ-device made using the EBL and Inductively Coupled Plasma Reactive Ion Etching (ICP-RIE). As starting material, silicon-on-insulator (SOI) wafer was used. The SOI structure was patterned by a high-resolution EBL to produce Cr etch mask and later etched by the ICP-RIE using CF_4 and O_2 as etch gases. Figure 4 shows a SEM image of a Si-TBJ-device structure with a lateral constriction of about 75 nm. The electrical characterization of the device is underway.

Acknowledgements

This work was partly supported by the Swedish Research Council (VR), the Swedish Foundation for Strategic Research (SSF) through the Nanometer Structure Consortium at Lund University, and EU program SUBTLE. M. Frimmer gratefully acknowledges financial support through Dr. Anna Fontcuberta i Morral's Marie Curie Excellence Grant "SENFED".

References

[1] H. Q. Xu, *Appl. Phys. Lett.* **78**, 2064 (2001).
[2] H. Q. Xu, *Physica E* **13**, 942 (2002).
[3] I. Shorubalko *et al*, *IEEE Electron Device Lett.* **23**, 377 (2002).
[4] I. Maximov *et al*, *Nanotechnology* **13**, 666 (2002).
[5] J. Ziegler *et al*, *The Stopping and Range of Ions in Matter* (SRIM 2008), computer program, http://www.srim.org.
[6] H. König *et al*, *Jpn. J. Appl. Phys.* **38**, 6142 (1999).
[7] H. Q. Xu, *Appl. Phys. Lett.* **80**, 853 (2002).
[8] M. Frimmer *et al*, *Appl. Phys. Lett.* **93**, 133110 (2008).

17th Int. Symp. "Nanostructures: Physics and Technology"
Minsk, Belarus, June 22–26, 2009
© 2009 Ioffe Institute

Nanocrystalline Si films grown by LEPECVD on non-crystalline substrates

P. L. Novikov[1], A. Le Donne[2], S. Cereda[2], Leo Miglio[2], S. Pizzini[2], S. Binetti[2], M. Rondanini[3], C. Cavallotti[3], D. Chrastina[4], T. Moiseev[4], H. von Känel[4], G. Isella[4] and F. Montalenti[4]

[1] Institute of Semiconductor Physics, Novosibirsk, 630090 Novosibirsk, Russia
[2] Dipartimento di Scienza dei Materiali and L-NESS, Università di Milano-Bicocca, 20125 Milan, Italy
[3] Dipartimento di Chimica, Materiali, Ingegneria Chimica "G. Natta", Politecnico di Milano, 20131 Milan, Italy
[4] Dipartimento di Fisica and L-NESS, Politecnico di Milano, 22100 Como, Italy

Abstract. A joint theoretical and experimental analysis of the crystalline fraction profile in nanocrystalline films grown by low-energy plasma enhanced chemical vapor deposition on non-crystalline substrate is presented. The effect of key growth parameters such as temperature, silane flux, and hydrogen dilution ratio is analyzed and modeled at the atomic scale, introducing an environment-dependent crystallization probability. It is shown, that at the initial stage of growth a thin amorphous buffer layer is formed, followed by the growth of nanocrystalline structure. A qualitative agreement is found between experimental and theoretical dependence of the buffer layer thickness upon the growth rate.

Introduction

Plasma enhanced chemical vapor deposition PECVD (including its low energy version LEPECVD) is a popular technique for growing Si films. The high growth rates (>1 nm/s), obtained by exploiting the presence of reactive radicals in the gas phase, make this technique of industrial interest, allowing for the fast deposition of thin films even at moderately low temperatures [1,2,3]. By tuning the growth parameters, PECVD can be used to grow epitaxial, amorphous, and micro- or nanocrystalline nc films. Being promising for the production of solar cells with a good efficiency/cost ratio [4], nc-Si films attracted wide attention.

The enhanced degree of complexity introduced by the presence of the plasma makes the understanding of PECVD less advanced with respect to more academic techniques such as molecular beam epitaxy. Recently, some significant advances were made in trying to identify some key processes at the atomic scale. Importantly, the reason why hydrogen promotes crystallinity was understood. By using DFT calculations [5,6], indeed, we showed that, in surface regions covered by hydrogen, an adsorbed SiH_3 radical can be incorporated into epitaxial sites surmounting a barrier of only ∼1 eV, provided that an incoming H atom hits the radical etching out one of the silyl hydrogens. Further study of LEPECVD Si growth on a crystalline Si(001) substrate was carried out by Monte-Carlo modeling, which has shown quantitative agreement between experimentally measured and simulated crystallinity fractions of the films [7]. In the present work we report the results of LEPECVD study for the case of non-crystalline substrate.

1. Experimental

The nc-Si samples were deposited on 4 in. ITO/glass wafers by LEPECVD [8]. The growth temperature ranged between 100 and 300 °C, while the silane dilution in the hydrogen-silane process gas mixture,

$$d = \frac{\Phi_{SiH_4}}{\Phi_{H_2} + \Phi_{SiH_4}} \qquad (1)$$

was varied between 1% and 50%. Silane fluxes Φ_{SiH_4} ranged between a few sccm (sccm denotes cubic centimeter per minute at STP) and a maximum of 20 sccm, while the maximum H_2 flux Φ_{H_2} was 50 sccm. In some cases, nc-Si layers were deposited at the same dilution factor $d = 50\%$ but using different SiH_4 and H_2 fluxes. The crystalline volume fraction χ_c of the samples was studied by Raman spectroscopy, using as reference an amorphous sample grown at 200 °C and $d = 100\%$.

According to that procedure, a scaled Raman spectrum obtained from the reference a-Si sample is subtracted from the Raman spectrum of the nc-Si film providing the only contribution of the crystalline part. The crystalline fraction can then be determined as follows:

$$\chi_c = \frac{A_c}{A_c + \sigma A_{am}}, \qquad (2)$$

where A_c and A_{am} are the areas of the crystalline part of the nc-Si film and of the TO peak of the a-Si film, respectively, and σ is the ratio between the cross sections of the c-Si and the a-Si [9]. Measurements were carried out at room temperature with a Jobin Yvon LabRAM micro-Raman system in backscattering configuration, equipped with a liquid-nitrogen-cooled charge coupled device camera, using an Ar^+ laser at 488 nm. Crystallinity depth profiles were also obtained combining the powerful properties of the confocal optics with a more penetrating He-Ne laser at 633 nm. However, the crystallinity depth profiles do not provide the real depth of the detected film region with respect to the surface, since in the case of a confocal microscope, the optical sectioning thickness strongly depends on the refractive index of examined material.

2. Monte-Carlo modeling

Film growth was simulated by Kinetic Monte Carlo (KMC), imposing a diamond lattice. The details of the model are described elsewhere [7]. Briefly, we considered deposition from the gas phase of the three most important species [2]: SiH_3(g), SiH_2(g), and H(g). When SiH_3(g) sticks, it is assumed to be bound to a dangling bond and to be completely surrounded

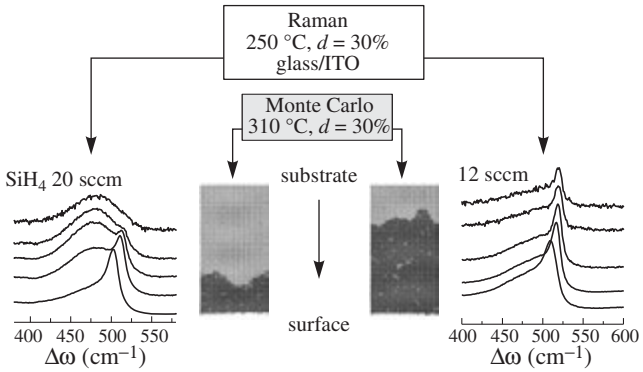

Fig. 1. Effect of silane flux on the buffer layer thickness for films grown on non-crystalline substrate (Raman and MC data).

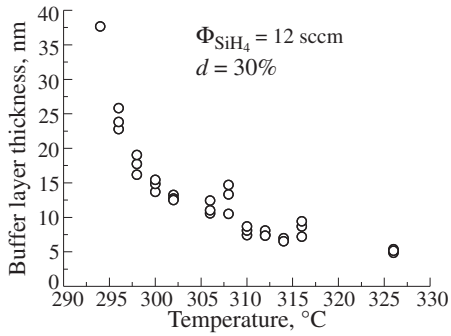

Fig. 2. Thickness of the amorphous buffer layer as dependent on temperature (KMC simulation data).

by H-saturated sites (configuration 2Ha in [6]). At the deposition of SiH_2(g) it captures one of the surface H, transforming into the very same configuration here above discussed for SiH_3. It is important to recall that such initial adsorption site is not epitaxial [6], incorporation into crystalline positions being possible only after an incoming H(g) etches out one of the adsorbed-radical hydrogens. For simplicity we shall call this etching-following configuration SiH_2. If SiH_2 is created, the radical will incorporate into an epitaxial site with a rate $k = \nu_0 \exp[-(E_{in}/k_B T)]$, where E_{in} is the incorporation barrier, ν_0 a frequency prefactor here set to the usual 10^{13}s^{-1} value, and k_B the Boltzmann constant. If incorporation is successful, we create a new crystalline site, which can be further covered by other species during growth. For an isolated radical adsorbed on the Si(001)(1 × 2):H surface, $E_{in} \equiv E^0_{in} \sim 1$ eV [6], but deviations should be expected in the presence of amorphous regions. Based on the idea that occupying a crystalline site must be easier in a crystalline environment, in our code we set $E_{in} = E^0_{in} + N_{nn} \times E_{nn}$ where N_{nn} is the number of amorphous nearest neighbors (located one layer below), each contributing to the incorporation barrier with an additional term E_{nn}, which we used as an adjustable parameter to fit the experimental data. Results shown in this paper refer to the value $E_{nn} = 0.21$ eV. When incorporation occurs, we transform also the amorphous nearest neighbors into crystalline ones.

3. Results and discussion

Fig. 1 presents the effect of growth rate on the uniformity of film crystallinity. Raman spectra, corresponding to different film depths, are vertically shifted. The upper curves characterize the substrate-film interface region, while the lower ones are related to the surface. For the flux $\Phi_{SiH_4} = 12$ sccm the peak at 520 cm^{-1} is present in all spectra, while for $\Phi_{SiH_4} = 20$ sccm it disappears near the interface region. This gives an evidence of an amorphous buffer layer formation at the initial stage of a faster growth. The buffer layer is reproduced by MC simulation. The thickness of a buffer layer decreases with the decrease of growth rate, which is demonstrated by two cross-section views of simulated films (light field is a-Si, dark field is c-Si). In terms of our phenomenological model the formation of nanocrystals on an amorphous surface is much less favorable in comparison with that on the crystalline one, since the barrier of incorporation is significantly higher. For that reason at the first stage of growth film has an amorphous structure. However, the probability of nanocrystalline clusters formation on an amorphous surface still is not zero, and after a certain time (which determines the buffer layer thickness) a big enough crystal nucleous is to be formed, giving rise to the growth of nc-Si film. Low growth rate favors nanocrystallite formation due to a longer time available for a SiH_2 to be incorporated (before being capped with the next layer deposited). Our model predicts dramatic reduction of the buffer layer thickness with the increase of temperature (Fig. 2). Since the first crystal nucleus formation is a random event, the buffer layer thicknesses are scattered within a certain range. Increase of H content in silane gas mixture also leads to decrease of the buffer layer thickness. In all cases the increase of the buffer layer thickness results in the decrease of the crystallinity of nc-Si film formed above.

References

[1] A. Matsuda, *Jpn. J. Appl. Phys.* **43** 1, 7909 (2004).
[2] D. Maroudas, *Adv. Chem. Eng.* **28**, 251 (2001).
[3] C. Cavallotti, M. D. Di Stanislao, and S. Carrá, *Prog. Cryst. Growth Charact. Mater.* **48**, 619 (2004).
[4] A. Shah *et al*, *Science* **285**, 692 (1999).
[5] S. Cereda *et al*, *Phys. Rev. B* **75**, 235311 (2007).
[6] S. Cereda *et al*, *Phys. Rev. Lett.* **100**, 046105 (2008).
[7] P. L. Novikov *et al*, *Appl. Phys. Lett.* **94**, 051904 (2009).
[8] C. Rosenblad *et al*, *J. Vac. Sci. Technol.* **A16**, 2785 (1998).
[9] C. Smit *et al*, *J. Appl. Phys.* **94**, 3582 (2003).

17th Int. Symp. "Nanostructures: Physics and Technology"
Minsk, Belarus, June 22–26, 2009
© 2009 Ioffe Institute

Production of nanoparticle suspensions by laser ablation of solid materials in liquids as a new sampling technique for optical emission spectrochemical analysis

M. Belkov, V. Burakov, V. Kiris and S. Raikov
Institute of Physics, 68 Nezavisimosty Ave., 220072 Minsk, Belarus

Abstract. A new rapid method of direct spectrochemical analysis of solid-state materials is proposed on the basis of a tandem technique of pulsed laser ablation of a sample in deionised water with on-line transportation of a suspension of nanoparticles in analytical volume of inductively-coupled plasma of optical emission spectrometer. In result, all instrumentation and methodical advantages of the standard equipment in combination with calibration procedure by standard aqueous solutions are provided.

Introduction

The first step in any spectrochemical analysis is to prepare the samples and standards for introduction to the analytical volume. This step depends on the physical and chemical characteristics of the samples and runs the gamut from simple dilution to a complex series of chemical reactions and other preparation steps. Such widespread and well-known technique as optical emission spectroscopy with inductively coupled plasma (OES-ICP) has the routine application at the analysis of liquid samples. The simplest way of the analysis of solid-state materials is based on a direct dissolution of an analyzed sample or its fragment. Unfortunately, often this approach requires additional time and labour, frequently significant, uses a sealed pressure vessels for holding strong mineral acids or alkalis at temperatures well above normal boiling points, does not allow carrying out microanalysis of samples.

OES with a sample atomization in ICP combined with preliminary laser ablation (LA) of a solid sample in a carrier gas (LA-ICP-OES) is at present the most conventional and suitable direct method for the elemental spectrochemical microanalysis of any solids with minimum or no sample preparation as well as of any materials that are difficult to dissolve. Nevertheless, this high-sensitive technique is till now very limited by the availability of solid-state certificated reference materials with necessary matrices and chemical elements.

We have realized the tandem technique of a direct laser sampling of any solid material in deionised water with on-line analysis of prepared by such way aqueous suspension of nanoparticles with the help of conventional OES-ICP. Such approach makes it possible to achieve a combination of all advantages of LA-ICP-OES and a routine calibration by standard reference aqueous solutions usually available for any element of interest. On the other hand, laser ablation of a solid material in a liquid medium is at present a well established technique of nanoparticle production for various purposes. Generally speaking, the main problem in the described approach consists in revealing and discrimination of possible specific features of evaporation and atomization in ICP of such specific solutions (suspensions) containing nanoparticles in comparison with the real aqueous solutions.

1. Experimental

The instrumentation employed in our work is at present quite standard and maximally suitable for a routine practice (Fig. 1). The fundamental (1.06 μm) or the second harmonic (0.53 μm) of a nanosecond Q-switched Nd:YAG laser (LS-2134 U, Lotis, Belarus) with a pulse duration of 6–8 ns (depending on wavelength and energy) and 10-Hz pulse repetition rate is employed for ablation of solids immersed in a cell with deionised water. The laser used is an improved version with variable reflectivity mirrors (VRM). This model provides a high stability of the emitted radiation. The VRM resonator gives excellent harmonic conversion efficiency due to an increased spatial uniformity of the output beam, a low divergence and a short pulse duration. The laser beam, with an aperture of $\leq$ 6 mm and a beam divergence of $\leq$6 0.8 mrad, is sharply focused on the sample surface by a 50 mm focal length plano-convex lens. The laser spot diameter on a target surface is about 50 μm. A sample is fixed at the X, Y, Z translation holder, which enables precise adjustment of focusing on a sample surface. The laser pulse energy can be varied from 10 to 270 mJ with an energy stability of $\pm$3%. Thorough optimization of laser output parameters, mainly pulse power density on a target surface and a number of pulses (usually 50) were carried out at the microanalysis of metallic and dielectric reference samples with known compositions. Comparatively small amounts of prepared aqueous suspensions (usually 10–15 cm^3) were on-line (to avoid possible nanoparticle agglomeration) analyzed by OES-ICP (IRIS Intrepid II, Thermo-Electron, USA) in accordance with a conventional reliably fulfilled procedure of analysis of liquid samples and calibration by aqueous standards.

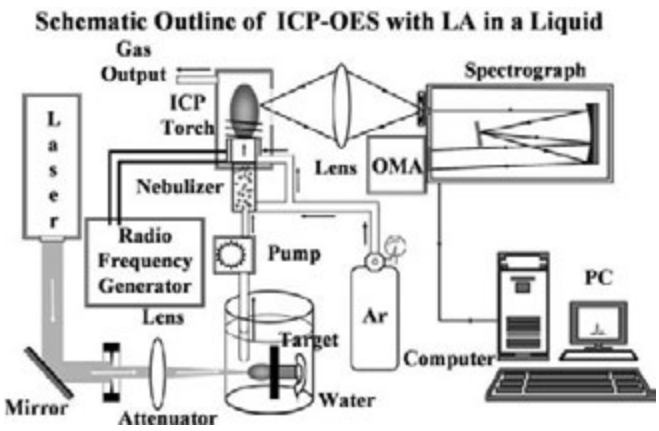

Fig. 1. Schematic outline of OES-ICP with LA of a solid in a liquid.

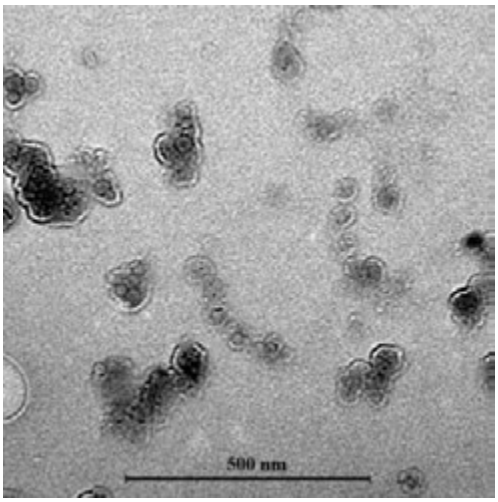

Fig. 2. TEM photograph of nanoparticles produced by LA of the glass sample in deionised water.

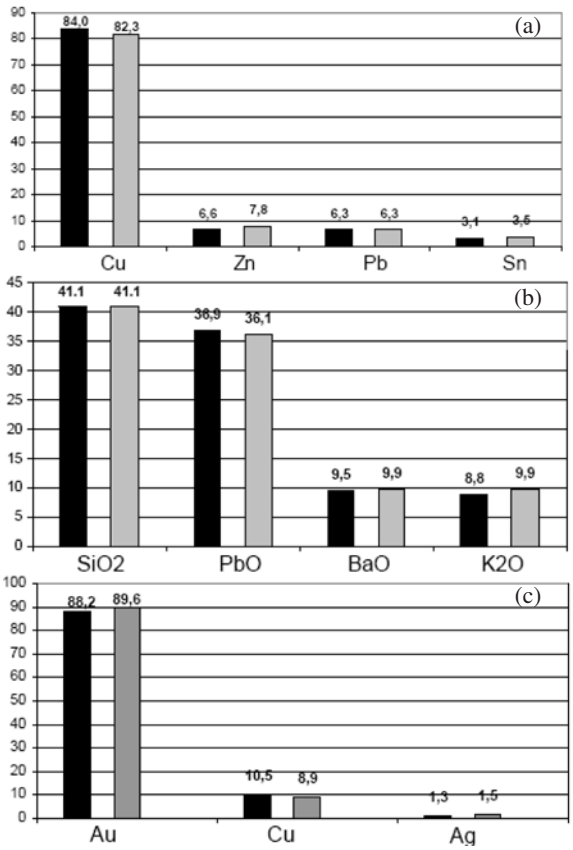

Fig. 3. Composition of the a — bronze alloy, b — glass, c — gold alloy, % (black — reference data; grey — measured data).

2. Results and discussion

Fig. 2 shows the TEM images (LEO 906E) of the trapped products of LA of a glass sample in a water.

Experimental results are presented in Fig. 3. As a whole, the satisfactory quantitative conformity of measured and reference data for all analyzed materials is received. Nevertheless, the further detailed optimization of ablation procedure, in particular, wavelengths of laser radiation, power density on a target surface, focusing conditions number of laser shots is necessary. The results obtained have confirmed the suitability of the proposed approach and have proved its potential for the direct and high-sensitive microanalysis of any solid materials with minimum sample consumption and without certificated reference materials. All instrumentation and methodical advantages of standard equipment in combination with calibration procedure by standard water solutions are provided.

17th Int. Symp. "Nanostructures: Physics and Technology"
Minsk, Belarus, June 22–26, 2009
© 2009 Ioffe Institute

Plasma-assisted synthesis and modification of $CuFeS_2$ nanoparticles for the development of froth flotation techniques

N. A. Savastenko[1], V. Brüser[1], N. V. Tarasenko[2], V. S. Burakov[2], A. V. Butsen[2], and F. May[1]

[1] Leibniz-Institute for Plasma Science and Technology, 2 Felix-Hausdorff-Strasse, 17489 Greifswald, Germany
[2] B. I. Stepanov Institute of Physics, NASB, 68 Nezavisimosty Ave., 220072 Minsk, Belarus

Abstract. The $CuFeS_2$ nanoparticles were successfully fabricated for the detailed investigation of the physical and chemical mechanisms involved in the flotation process. This technique is based on the different wettability of the minerals. Due to the high surface/volume ratio and reactivity of nanoparticles, they are ideal model systems for the study of processes leading to a change in wettability of materials. The nanoparticles were obtained by laser ablation of chalcopyrite ($CuFeS_2$) in water. The $CuFeS_2$ nanoparticles and bulk chalcopyrite were modified by Ar:O_2 RF-plasma. The nanoparticles were characterized by UV-visible spectroscopy, EDX, XRD, IR-spectroscopy and AFM.

Introduction

The main goal of this work was to gain fundamental scientific knowledge required for the development of a flotation technique for the separation of chalcopyrite ($CuFeS_2$) and pyrite (FeS_2).

Flotation is a mineral separation process, which takes place in water-mineral slurry. The surfaces of selected minerals are made hydrophobic (water-repellent). The hydrophobic particles become attached to air bubbles that are introduced into the pulp and are carried to a froth layer above the slurry thereby being separated from the hydrophilic (wetted) particles.

In conventional flotation technique, the wettability of materials is changed by conditioning with selective reagents. We propose a new approach which is based on non-thermal plasma treatment of minerals. Detailed investigation of plasma-minerals interaction is needed to optimize the plasma treatment conditions. Due to the high surface/volume ratio and reactivity of nanoparticles, they are ideal model systems for the study of processes leading to a change in wettability of materials.

In this paper, we have synthesised the $CuFeS_2$ nanoparticles by pulsed laser ablation in liquid (PLAL) method. Nanoparticles thus produced have been characterized by UV-visible spectroscopy, EDX and XRD. The $CuFeS_2$ nanoparticles and bulk chalcopyrite were modified by Ar:O_2 RF-plasma. IR-spectroscopy and AFM have been applied to investigate the changes caused by plasma treatment.

1. Experimental

1.1. Synthesis of nanoparticles

The $CuFeS_2$ nanoparticles were synthesized by focusing of radiation of a Nd:YAG laser (LOTIS TII, LS2131), operating at 1064 nm (energy 60 mJ/pulse, repetition rate 10 Hz, pulse duration 12 ns), on the surface of chalcopyrite target placed in the cell filled with distilled water. The laser ablation of chalcopyrite was accompanied by the presence of a small plasma plume above the target surface. A visible coloration of the solution was observed after several minutes of the beginning of the ablation experiment. The synthesized particles were obtained as a colloidal solution.

1.2. Plasma treatment of nanoparticles

Plasma treatment was performed in inductively coupled radio frequency (RF) plasma generated in a vibrating bed reactor. The reactor is described in detail elsewhere [1–4]. Before the treatment, the reactor was evacuated to a pressure of 10^{-3} Pa. The gas flow rate was 30 sccm. Plasma treatment was performed at RF-power of 80 W for 2 min at a total pressure of 10 Pa under gas flow conditions (Ar:O_2= 15 sccm:15 sccm). Before the exposure the vacuum chamber was flushed with the Ar:O_2 gas mixture for 5 min.

1.3. Characterization of nanoparticles

Atomic force microscopy (AFM) was used to investigate the morphology of both untreated and plasma-treated nanoparticles. The AFM measurement was conducted with the CP-II SPM from Veeco Co. at atmosphere and ambient temperature. In each case, an area of 5×5 μm was scanned using the non-contact mode.

The optical absorption spectra of the formed colloids were measured by UV-visible spectrophotometer (CARY 500).

The powder formed after the drying of colloidal solutions was examined by X-ray diffraction analysis (XRD). Powder phase composition, its crystalline structure, lattice parameters and grain size were determined using X-ray diffraction

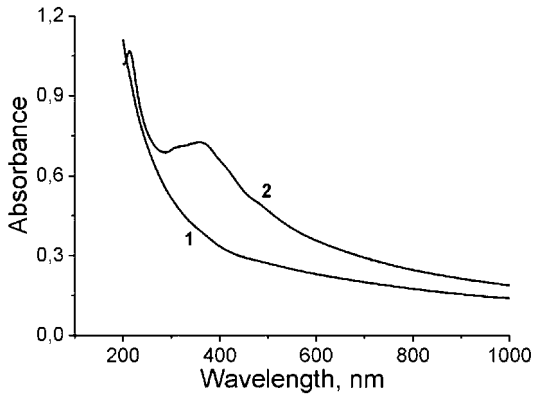

Fig. 1. UV-Vis optical absorption spectra of colloidal solutions prepared by laser ablation of chalcopyrite (1) and pyrite (2) in distilled water.

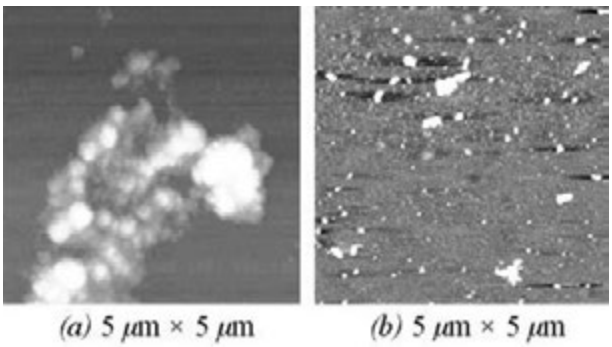

Fig. 2. AFM images of nanoparticles before (a) and after (b) nanoparticles treatment.

at Cu K_α (0.154 nm). The X-ray diffractometer D8-Advance (Bruker, Germany) was used.
The elemental composition of the powder deposited on the substrate was detected using energy dispersive X-ray (EDX) spectrometer attached to the scanning electron microscope (SUPRA 55WDS, Carl Zeiss, Germany).

2. Results and discussion

2.1. UV-visible absorption spectroscopy

The optical absorption spectrum of as-prepared colloidal chalcopyrite solution is illustrated in Fig. 1 (curve 1). It is rather featureless and exhibits a broad absorption band edge in the UV spectral range. For comparison the typical absorption spectrum of the colloid obtained by pulsed laser ablation of a pyrite (FeS_2) sample in water (curve 2) has an absorption peak at 362 nm.

2.2. EDX Analysis

The EDX spectrum of powder formed after the drying of the colloidal $CuFeS_2$ solution showed the presence of iron, copper, sulfur, as well as oxygen and carbon of the substrate material. The ratio of atomic contents Fe:Cu:S determined from EDX spectrum was found to be close to the stoichiometric ratio of the $CuFeS_2$ phase.

2.3. XRD Analysis

As it followed from the XRD pattern the synthesized product was composed of tetragonal chalcopyrite $CuFeS_2$ phase with lattice constants $a = 5.286$ nm, $b = 5.286$ nm and $c = 10.410$ nm, orthorhombic valleriite $Cu_2Fe_4S_7$ phase with lattice constants $a = 6.130$ nm, $b = 9.810$ nm and $c = 11.400$ nm, and copper iron sulfide $CuFe_2S_3$ phase with lattice constants $a = 6.467$ nm, $b = 11.117$ nm and $c = 6.231$ nm. No oxides phases were detected.

2.4. AFM

AFM images of chalcopyrite nanoparticles deposited on the glass substrate before and after nanoparticles treatment are presented in Fig. 2. It is clearly seen that the dispersion behaviour of nanoparticles is improved after plasma treatment.

3. Summary

In summary, our experiments show that PLAL provides a convenient way for fabrication of $CuFeS_2$ nanoparticles. These nanoparticles are ideal model systems for the detailed investigation of plasma-chalcopyrite interaction. The information obtained from these experiments helps optimize the flotation technique.

References

[1] V. Bruser *et al*, *Plasma Proc. and Polymers* **4**, 94 (2007).
[2] I. Herrmann *et al*, *Electrochemic. Society* **152**, 2179 (2005).
[3] N. A. Savastenko *et al*, *J. Power Sources* **165**, 24 (2007).
[4] F. Harnisch*et al*, *J. Power Sources* (2009) [in press].

17th Int. Symp. "Nanostructures: Physics and Technology"
Minsk, Belarus, June 22–26, 2009
© 2009 Ioffe Institute

The behavior of different types of materials under AFM overload regime

S. A. Chizhik, *A. L. Khudoley* and T. A. Kuznetsova
A. V. Luikov Heat and Mass Transfer Institute, Minsk, Belarus

Abstract. It is proposed use AFM overload regime for studies of the behavior of different types of materials. It is shown that removing material layers of thickness from 1 to several tens of nanometers allows to study the structure and to analyze the properties of the material in depth.

Introduction

Atomic force microscopy (AFM) is the main instrument in the field of nanotechnology, which allows not only to examine the morphology and to measure the surface topography in the nanometer range, but also to affect the surface. It is a contact AFM probe impact on the surface that enables the measurement of mechanical and tribological properties of the material for the elastic behavior of the material. Typical AFM scanning regime is carried out with probe loads up to 50% that, as a rule, do not change the surface performances and provides a long-term use of the AFM probe. We believe that a critical behavior of the material must be studied under the overload AFM conditions which are being accompanied by the plasticity deformation.

Aim of the work study of the behavior of different types of materials under AFM overload regime.

1. Materials

In this paper we studied surfaces of different materials such as silicon, glass, mica, pyrolytic graphite, silicon coated with mono- and multilayer LB-films of polivinilpiridin with the thickness up to 10 nm and about 10 nm cathode sputtering golden film on a glass substrate.

2. Methods

AFM studies were performed with the atomic force microscope "NT-206" (Microtestmachines Ltd., Belarus) and a program software "Surface Scan 169". This technique allowed to control the load and movement trajectory of the tip under the surface scanning process. In this study we used standard silicon probes of the "NT-MDT" company (Russia) with the tip radius of 10 nm. The load on the probe was 72–80%. Constant ("Set Point") and increasing ("Distance") load modes were used. Movement trajectory of a probe was set as a square ("Size of Square"). The repeated passage of a probe along one line and the surface was used. The topography of the real trace of the set trajectory of probe after the exposure to the same probe was studied. The force spectroscopy of the material was also performed.

3. Results and discussion

We show that the result of repeated pass of the probe depends on the nature of the tested material. Golden film with protruding crystallites is cleaned from the crowned elements (element size) after the probe action.

The form of the trace on the surface depends on the probe speed and on the material. While carrying out the operations on silicon with high-speed silicon probe, a slippage occurs on the silicon surface in the movement process, which leads to the formation of rhomb rather than a square. In this case, the probe hardness is equal to the hardness of the material.

The probe speed, which depends on the perimeter of the path, is a critical parameter for obtaining the desired type of trace on silicon. Thus, the reduction of the pathway of the probe to 50 × 50 nm at 100 rass per 30 s, instead of pricks formation leads to the opposite effect.

Instead of cavity on the trace some picks of 5–10 nm height appear, formed by tribochemical reactions. The increase in the trajectory to 100 × 100 nm with the same number of passes and the same length leads to the initial stage of formation of

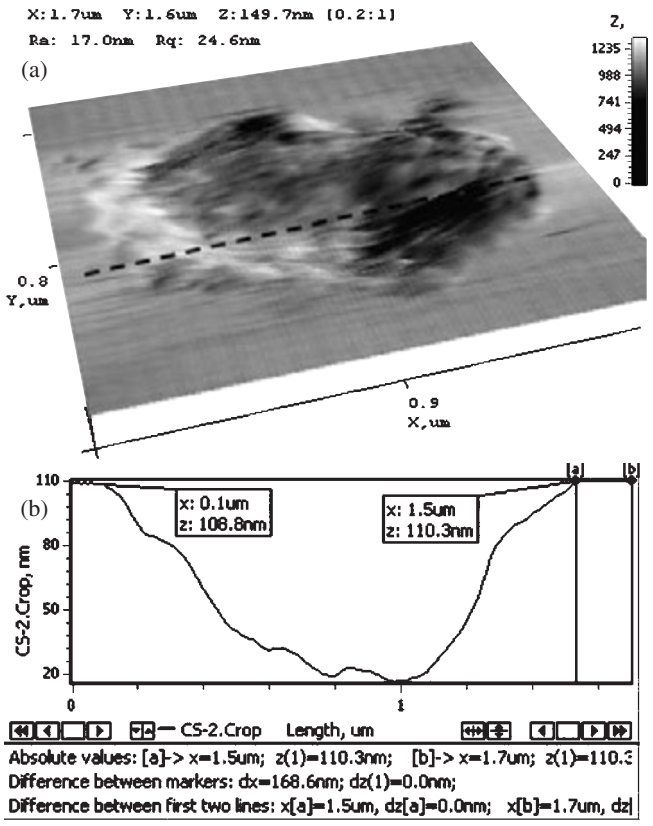

Fig. 1. Results of the AFM overload regime for mica ("Size of Square" 500 × 500 nm, "Delay" 100): a) Surface topography after "Set Point" action, imaging region 1.4 × 1.4 μm; b) cross-section profile of the path "a".

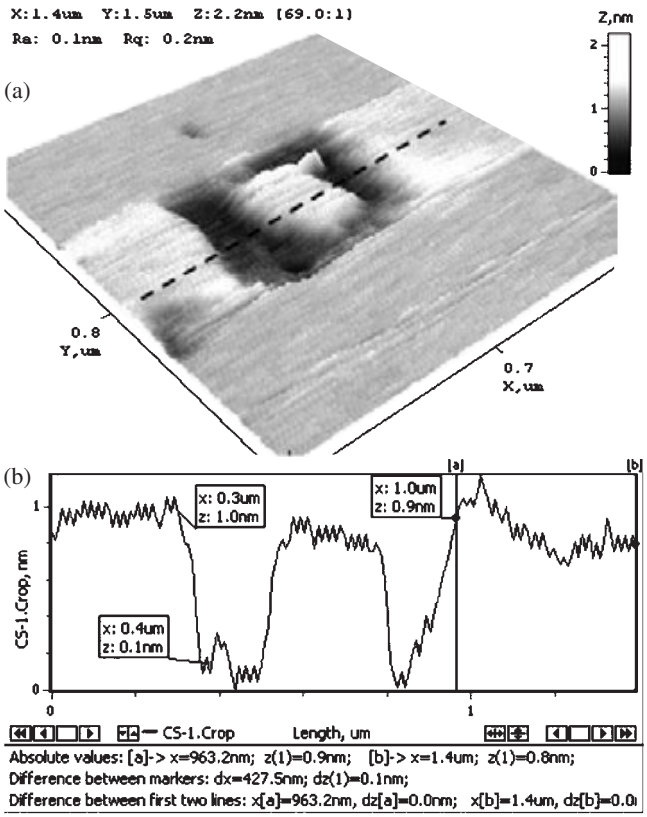

Fig. 2. Results of the AFM overload regime for mica ("Size of Square" 500 × 500 nm, "Delay" 100): a) Topography of the surface after "Distance" action, imaging region 1.6 × 1.6 μm; b) cross-section profile of the path "a".

oxidized material convexities into the pricks. Oxidized material at this stage takes no more than a quarter of the deepening square. The effect of convexities formation of the oxidized material on silicon instead of depressions with the movement parameters is possible only while using the new probe with 10 nm tip radius. Blunting of the probe to 40 nm increases the contact area, reduces the contact pressure and temperature. In this case, only hollows appear.

The impact of the probe on a soft surface (such as mica, graphite) distorts the shape and trace that is often oval. At mica needle "breach" material to a depth of 120–140 nm (Fig. 1). The reduction of the probe speed promotes the formation of the square with sides (Fig. 2), parallel to the field of scanning. For graphite we observed some formation along the contour of the pit of the bulk material, "removed" from the pit. The amount of graphite formed in bulk is bigger than the material volume in the hollow. The depth of the trace was 360 nm and height in bulk was 443 nm.

Using reproducibility and the height of the resulting bulk the plastic properties of the studied material can be qualitatively evaluated. Thus the value of constantly generated graphite bulks is much higher than the value for mica bulk. From this we can conclude that the plasticity of the surface layers of graphite is higher than that of mica.

When we impacted by the probe on glass surface under the overload regime, convexities with the size and shape similar to the structural elements on the original surface are formed.

The proposed method allows to investigate the properties of soft biological tissue and thin films of polymers by volume at the expense of possibility to use minor loads in the "Set-point" mode. Removing material layers of thickness from 1 to several tens of nanometers it is possible to study the structure and analyze the properties of the material in depth. The follow-up AFM imaging in the Torsion mode of the results of the impact of the treated surface identifies sites with the different mechanical properties.

Thus, using the AFM overload regime allows to receive new data about characteristics of different types of materials and investigate the behavior of surfaces under the contact destruction for nanovolumes that is very important for nanotribology and advanced materials.

17th Int. Symp. "Nanostructures: Physics and Technology"
Minsk, Belarus, June 22–26, 2009
© 2009 Ioffe Institute

Hollow SnO_2 formation by oxidation of Sn nanoislands

Peter I. Gaiduk[1] and A. Nylandsted Larsen[2]

[1] Belarusian State University, prosp. Nezavisimosti, 4, 220030, Minsk, Belarus
[2] Department of Physics and Astronomy, University of Aarhus Ny Munkegade, DK-8000 Aarhus C, Denmark

Abstract. Hollow tin-dioxide nanoislands are formed as a result of thermal oxidation of MBE deposited Sn. Microstructure, phase composition, size distribution, and surface morphology of the nanoislands were studied by transmission electron microscopy and electron diffraction. It is found that the formation of voids and their evolution into large holes depend on thickness of the deposited Sn, on temperature of thermal oxidation and on content of oxygen in the atmosphere. The results are discussed on the basis of the Kirkendall effect.

Introduction

Recently, the use of nanocrystalline particles with a high surface-to-volume aspect ratio made it possible to improve the properties of devices such as gas-sensing and optoelectronic devices which are mainly influenced by the surface region of the particles [1–3]. From an application point of view, it is important to obtain nanoparticles with specific size and morphology. Thus, control of size, shape and morphology of the nanoparticles are among the most important issues in the synthesis of nanomaterials. There is, in particular, an increasing interest in fabrication of core-shell and hollow nanostructures due to their potential applications as photonic crystals, sensors, and chemical reactors [4,5].These hollow structures generally consist of metal oxides. Tin dioxide (SnO_2), an n-type semiconductor with a wide bandgap ($Eg = 3.62$ eV), is one of the most important materials used in different technological applications [2,3]. Recent developments in this area show that hollow structures can be produced during direct solid evacuation with Ostwald ripening [6] or formed from self-assembly of grains due to hydrophobic interactions [7]. There are some evidences that hollow structures are created during thermal oxidation of Sn nanoislands as a consequence of the Kirkendall effect [8]. Thus, the mechanisms of hollow structure formation as a result of oxidation processes are still poorly understood. In the present work, the oxidation behavior of Sn nanoparticles and the formation of hollow SnO_2 nanoislands are investigated by transmission electron microscopy (TEM).

1. Experimental

Chemically cleaned 100 mm, p-type (001) Si wafers of resistivity 1.8–2.2 Ω cm were used as substrates. Prior to molecular beam epitaxial (MBE) deposition, uniform and pure SiO_2 layers of thicknesses between 10 to 50 nm were thermally grown in a pure oxygen (O_2) ambiance. About 1 nm of this SiO_2 layer was removed from the top surface layer prior to Sn deposition *in-situ* the MBE chamber using a Si flux of 0.035 nm s^{-1} with the wafer held at 850 °C as described in detail elsewhere [9]. A Sn layer of average thickness between 2 and 20 nm was then deposited on the SiO_2 covered Si wafers, with a rate of 0.3 nm/min at 75–250 °C. The samples of $Si/SiO_2/Sn$ were subsequently cut *ex-situ* and heated in an O_2 ambiance at 200–950 °C for 1–30 minutes. The structure and phase composition of the samples were characterized by TEM in plan-view and cross-sectional geometries.

2. Results and discussion

It is established by TEM that the structure and morphology of the layers depends on the thickness of initially deposited Sn and on oxidation conditions (temperature, atmosphere).

A. Low temperature oxidation. MBE deposited layer of 8-nm-thick, contains circular Sn nanoislands of average diameter of about 20–70 nm in planar direction (Fig. 1(a)) and 5–20 nm in vertical direction. According to selected area electron diffraction (SAED) pattern (inset in Fig. 1(a)) as-deposited layer consist of tetragonal β-Sn. Fig. 1(b,c) show bright-field (b) and dark-field (c) TEM images of the nanoislands after thermal oxidation at 200 °C for 20 min.

It is well seen that the low temperature oxidation results in appearance of narrow shells, bordered the Sn islands. The shells are grey in bright-field TEM image (Fig. 1(b)). In addition to tetragonal β-Sn phase, SAED pattern has some rings coming out due to diffraction on SnO phase (inset in Fig. 1(b)). Dark-field TEM image (Fig. 1(c)), acquired in SnO rings, exhibits fine-grain contrast which proves that islands have core-

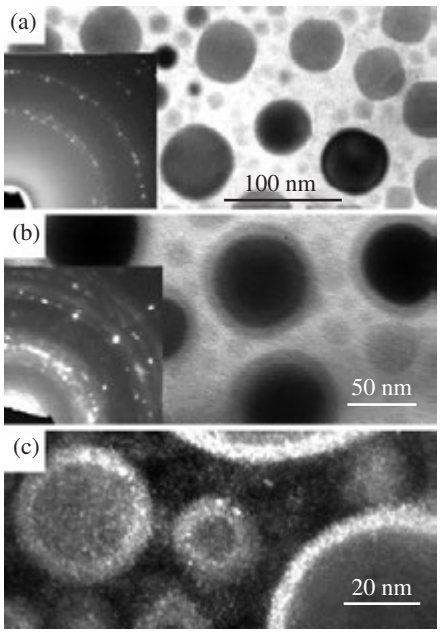

Fig. 1. Bright-field (a,b) and dark-field (c) TEM images of 8 nm Sn layers as deposited (a), and oxidized at 200 °C (b,c). Insets in (a) and (b) are corresponding SAED patterns. DFTEM (c) is obtained in SnO diffraction ring.

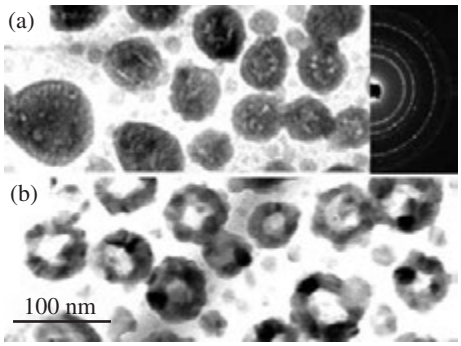

Fig. 2. BFTEM images of SnO_2 layers, thermally oxidized at 400 °C (a) or 650 °C (c) for 20 min. Inset in (a) shows the corresponding SAED pattern.

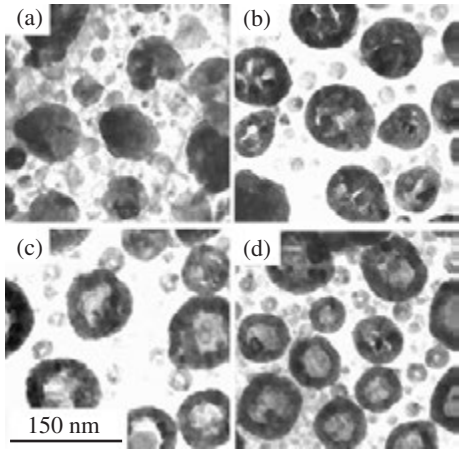

Fig. 3. BFTEM images of hollow SnO_2 nanoislands fabricated by MBE deposition of Sn followed by thermal oxidation at 650 °C for 20 min in an ambiance of of O_2 and N_2. The concentration of O_2 was: (a) — 5 vol.%, (b) — 20 vol.%, (c) — 50 vol.% and (d) — 90 vol.%.

shell structure of central Sn nanoisland surrounded with the shell of SnO phase.

B. High temperature oxidation. An increase of oxidation temperature results in strong change of TEM contrast (compare Figs. 1 and 2). It is registered that high temperature oxidation results in transformation of the nanoislands into tin oxide. A typical SAED pattern, inserted in Fig. 1(a), demonstrates that the diffraction rings belong to the tetragonal SnO_2 phase. It is well resolved that the islands acquire small bright features (spots) concentrated in their central part. An analysis of the TEM contrast in under- and over-focused, two-beam diffraction condition of image formation shows that the bright features inside the islands are open-volume defects or voids. Thus, it might be concluded that high-temperature oxidation results in hollow SnO_2 nanoislands formation.

C. Effect of oxidation ambient. Very intriguing dependence of SnO_2 island hollow morphology on the composition of the oxidizing atmosphere (the concentration of oxygen varying from 5 to 90 vol.%) is clearly seen in Fig. 3. No visible indication for void (hollows) formation is found after oxidation of Sn islands in the atmosphere with low (5 vol.%) concentration of oxygen (Fig. 3(a)). Enrichment of the atmosphere with oxygen up to 20 vol.% and then to 50–90 vol.% results in a sequential formation of small voids (Fig. 3(b)) and large holes (Fig. 3(c,d)). As it follows from the comparison of SAED patterns (similar to inset in Fig. 2(a) but not shown here), both low and high oxygen concentrations do result in the formation of an identical tin oxide phase: the only difference is in the average size of the grains which is larger in the layers oxidized in a diluted ambiance with a low content of oxygen.

D. Effect of thickness. It follows from the TEM study (not shown) that both the hollow structure and the morphology of the SnO_2 nanoislands depends strongly on the average thickness of initial Sn layer. The layers studied were of 2.5 nm, 7 nm and 20 nm followed by thermal oxidation at 650 °C for 20 min. After oxidation of these layers, the SnO_2 islands are formed without (2.5 nm) and with (7–20 nm) hollow structure. In addition, the island-density versus island size displays a bimodal distribution in the case of an initially thick Sn layer, which indicates a contribution of Ostwald ripening for island formation when the larger islands grow at the expense of smaller ones.

It can be concluded from analysis of TEM data that the formation of the voids in the center of SnO_2 particles is mainly a result of the Kirkendall effect [8] associated with a faster outward diffusion of Sn atoms as compared to the inward diffusion of oxygen atoms in the process of the formation of a surface oxide layer. This leads to the formation of a high density of vacancies at the metal side of the metal/oxide interface. Vacancies transform to vacancy clusters which then aggregate into holes. It might be expected from this model that the increase of oxygen content in the ambiance will result in the promotion of an inward diffusion of oxygen atoms into the Sn particles, and therefore, suppress (or at least keep at the same level) the formation of holes.

Acknowledgements

This work was supported by Belarusian Research Foundations (grants No. 20061216 and T08P-184) and by NATO Collaborative Linkage Grant CBP.EAP.CLG 982384. Special thanks to John Lundsgaard Hansen for the MBE growth of the structures.

References

[1] M. Law *et al*, *Angew. Chem. Int. Ed* **41**, 2405 (2002).
[2] R. E. Presley *et al*, *Appl. Phys. D* **37**, 2810 (2004).
[3] S. de Monredon *et al*, *J. Mater. Chem.* **12**, 2396 (2002).
[4] Y. Sun *et al*, *J. Am. Chem. Soc.* **126**, 3892 (2004).
[5] Y. Cao *et al*, *Chem. Mater.* **12**, 3445 (2000).
[6] H. G. Yang *et al*, *J. Phys. Chem* **108**, 3492 (2004).
[7] S. Park *et al*, *Science* **303**, 348 (2004).
[8] A. D. Smigelskas *et al*, *Trans. AIME* **171**, 130 (1947).
[9] P. I. Gaiduk *et al*, *Appl. Phys. Lett.* **928**, 193112 (2008).

17th Int. Symp. "Nanostructures: Physics and Technology"
Minsk, Belarus, June 22–26, 2009
© 2009 Ioffe Institute

Droplet to Stranski–Krastanov growth mode transition in indium epitaxy on (001)GaAs substrate

A. A. Lyamkina[1,2], *Yu. G. Galitsyn*[1], D. V. Dmitriev[1], V. A. Haisler[1], S. P. Moshchenko[1] and A. I. Toropov[1]

[1] Institute of Semiconductor Physics SB RAS, Acad. Lavrent'eva Ave. 13, 630090, Novosibirsk, Russia
[2] Novosibirsk State University, Pirogova 2, 630090, Novosibirsk, Russia

Abstract. In this work we investigate indium dose dependence of optical properties of quantum dot fabricated by droplet epitaxy. Photoluminescence measurements demonstrate red shift to 1.3 μm and considerable change of a dot spectra form with peak number increase. The Gaussians decomposition analysis revealed some characteristic peak widths corresponded to different QD groups. One width is close to Stranski–Krastanov growth mode value, measured on our analogical samples. It indicates that since some indium amount there is transition of droplet to SK growth mode.

Introduction

Some important advanced devices as single-photon emitter require quantum dots with low-density and long-wave spectrum [1]. Droplet epitaxy is often implemented in QDs growth experiments and seems to be a perspective line of this research [2]. Recently it was demonstrated that low-density QDs can be obtained by using of ultra-low InAs growth rate in combination with proper growth interruption time [3]. Ostwald-type ripening occurring during growth interruption time is considering the most significant reason for QDs size enlarging and density decrease. In droplet epitaxy there are more growth parameters and so there can be different modes due to elastic tension, the ripening, and other processes combination.

In this work indium dose dependence on droplet QDs formation is investigated. This dependence is of great interest because with indium amount increase QDs should enlarge and red-shift with corresponding density decrease. Besides the mechanism of QD formation can change because of elastic tension ascending role. So indium dependence data are useful for understanding of the QDs formation mechanisms. In this work InAs/GaAs QDs were fabricated by droplet epitaxy with temperature (about 500 °C) during the growth.

1. Experimental

The nanostructures investigated below were grown by molecular beam epitaxy on semi-insulating (001)-oriented GaAs substrates using a Riber 32P system with gate arsenic source. For avoiding possible effects of excess arsenic atoms, proper amount of Ga was deposited to the substrate surface at first. After it was applied to the GaAs surface, 2.1 ML of In was deposited without As_4 flux and the sample was exposed to a beam equivalent pressure (BEP) of 1.5×10^{-5} Torr of As_4. For fabricating the samples with varying indium layer width following constructive feature of growth installation was used. During growth time the sample is disposed angularly to indium source, so there is a gradient of indium flux along axis of symmetry, resulting in difference in indium dose approximately in two times. Analyzing an evolution of photoluminescence spectra measured along the sample, we can investigate changes of quantum-optical properties of our system. For PL measurements layer of QDs was capped between AlGaAs/GaAs layers. Second layer of QDs was grown uncapped to investigate it with surface sensitive methods like AFM imaging. The excitation power of laser with wavelength of 533 nm was 100 W/cm^2.

2. Results and discussion

In Fig. 1 photoluminescence spectra, measured at room temperature, are presented from up to down in order of increasing indium dose. At upper spectrum one can observe the only peak which corresponds to QDs, originated from small drops with wide size distribution. The next spectrum was measured at a point of the sample with bigger amount of indium. As it is seen from spectrum shift to long-wave region, dots enlarge and almost don't change their distribution, because this peak is quite similar to the previous one. Lower spectrum corresponds to further increased indium dose, that is supposedly over some critical value, as considerable qualitative changes take place. Here some pronounced peaks with rather well-defined vertexes are obtained.

It would appear reasonable to describe complex spectrum consisting of several peaks by sum of the Gaussians. With such description width is particularly important parameter of approximation, because amplitude and center position depends on QDs density and sizes, whereas width is a feature of some distribution and is a characteristic for a group of dots, formed by the same mechanism. Its significant change, if happens to be, associates with principal modification in dots forming process of so it should be investigated in details. Besides amplitudes, widths and center positions the area under peak depending on a density of states is important parameter, which also can be compared and investigated.

In the short-wave region of spectra there was obtained wide peak with large area. It corresponds to big amount of small dots with wide distribution. It can be expected that with growth interruption time increase these small dots would intensively evaporate or ripe to larger ones so this peak center position would considerably shifts. In point of fact such effect is not obtained, that means, that spectra change is connected with QDs formation kinetics during growth interruption time.

It was found that there are peaks with significantly different widths, that was not obvious before such mathematic expansion. One of these width value is close to one, which was observed before and attributed to the small drops. Besides the half width peaks which are characteristic for Stranski–Krastanov growth mode (it was measured before at analogical samples,

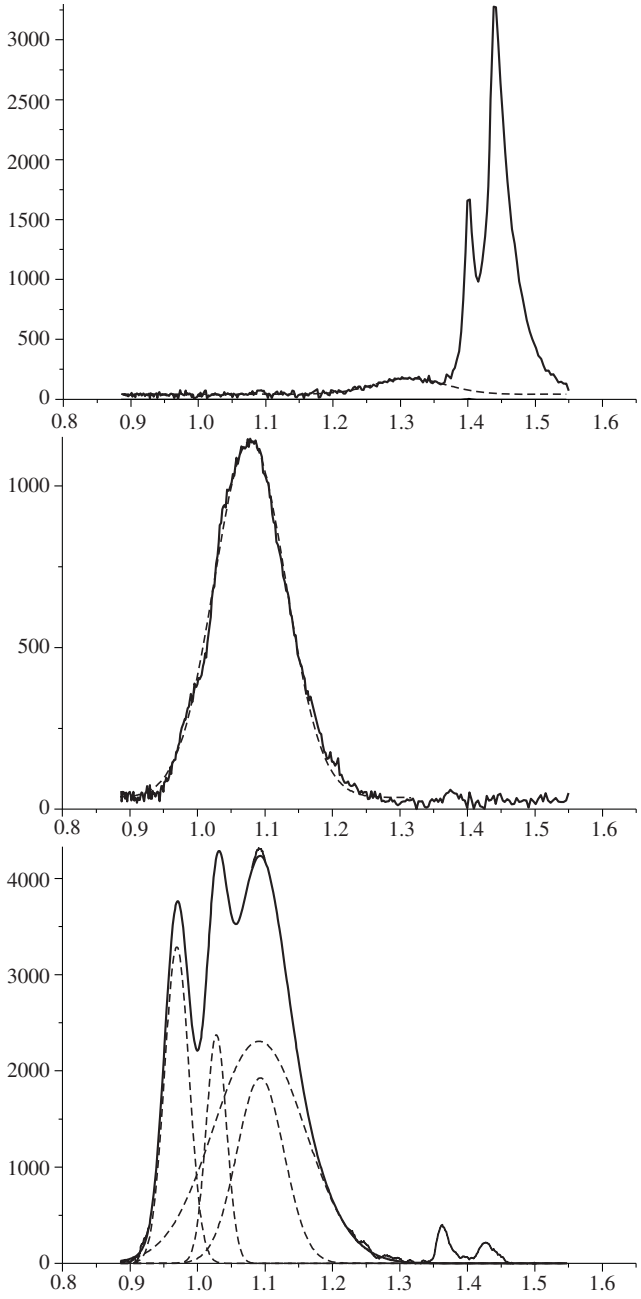

Fig. 1. PL spectra corresponding to increase of indium amount (from the top down). The decomposition by Gaussians is presented by dashed line. X-coordinate is energy (eV), y-coordinate is PL intensity (arbitrary units).

fabricated in the same conditions by this mode) appear accompanied by some even more narrow ones.

As it follows from general nucleation theory, drop sizes must obey some distribution like normal one. It might be expected from physicochemical considerations that this distribution would be rather wide, because it forms in the absence of strong interactions. At the same time in last spectrum there is the peak with considerably lesser width, than was observed in all previous ones. The presence of several peaks can be interpreted as the ground state and an excited state of QDs, but for such significant difference in width (few times) this explanation is not reasonable.

So we conclude, that over some critical indium dose value new group of dots appears. It forms after different than droplet mechanism and for this reason has different distribution. This threshold is planned to be obtained in further investigation. We suppose that the group with the most narrow distribution formed under the influence of an additional external force, that has significantly decreased size dispersion and consequently the width of distribution. Probably, it is surface tension of the drop force, which is distinctive feature exactly for the droplet growth mode. It is confirmed by AFM imaging with obtained dots groups with distinctly distinguishable drop symmetry (high center and some smaller dots around), as it was described in our previous paper [4]. It is interesting to note that obtained distribution width value is in numerical agreement with data of paper [5].

The presence in a spectrum of characteristic for Stranski–Krastanov growth mode width means that such idealized mechanism is not implemented per se. It can be supposed that under some critical size of metal drop the elastic stress relaxion by Stranski–Krastanov (usual for continuous film) is realized even on the drop area. During this, because of extra tension force, which is absent in case of continuous film, size distribution is expected to be significantly more narrow, what is in perfect agreement with analytic results of experimental spectra.

Acknowledgements

AAL thanks Federal Education Agency of Education and Science Ministry for financial support (AVCP, grant 3H-312-09).

References

[1] M. Sholz, S. Buttner, O. Benson, A. I. Toropov, A. K. Bakarov, A. Lochmann, E. Stock, O. Schulz, F. Hopfer, V. A. Haisler and D. Bimberg, *Optics Express* **15**, 9107 (2007).

[2] S.-S. Huang, Z.-C. Niu, H.-Q. Ni, F. Zhan, H. Zhao, Z. Sun and J.-B. Xia, *Chin. Phys. Lett.* **24**, 1025 (2007).

[3] L. H. Li, N. Chauvin, G. Patriarche, B. Alloing and A. Fiore, *J. Appl. Phys.* **104**, 083508 (2008).

[4] A. A. Lyamkina, S. P. Moshchenko, V. A. Haisler, Yu. G. Galitsyn and A. I. Toropov, *Proc. of 16th Int. Symp. Nanostructures: Physics and Technology (Vladivostok, 2008)*, Ioffe Physico-Technical Institute, 154, 2008.

[5] R. Heitz, F. Guffarth, K. Potschke, A. Schliwa, and D. Bimberg, *Phys. Rev. B* **71**, 045325 (2005).

17th Int. Symp. "Nanostructures: Physics and Technology"
Minsk, Belarus, June 22–26, 2009
© 2009 Ioffe Institute

Role of sp^3-hybridization in metastability of solid GeO films

E. B. Gorokhov[1], K. N. Astankova[1], V. A. Volodin[1,2] and M. Vergnat[3]

[1] Institute of Semiconductor Physics of SB RAS, pr. ak. Lavrentjeva 13, Novosibirsk 630090, Russia
[2] Novosibirsk State University, Pirogova street, 2, 630090, Novosibirsk, Russia
[3] Laboratoire de Physique des Materiaux, Nancy-Universite, CNRS, Boulevard des Aiguillettes B.P. 239, 54506 Vandouvre les Nancy, France

Abstract. The process of formation of solid films of germanium monoxide from GeO vapor was studied using physical and chemical approaches. A model clarifying the metastability of solid GeO is developed. According the model, the structure of atomic orbitals (σ- and π-bonds) of a GeO molecule causes the stability of GeO in gaseous phase. After condensation: GeO(gas) $\longleftrightarrow$ GeO(solid), the atomic orbitals of Ge are transformed in lowest energy sp^3-hybridized configuration, this configuration is universal both for Ge and for GeO_2. The decomposition of GeO(solid) into Ge and GeO_2 is caused by relaxation of deformation energy appearing due to big difference of Ge-Ge and Ge-O bond length.

The nanometer-sized semiconductor nanocrystals (NCs), embedded in wide-gap insulating matrices, have shown significant promises for a wide range of nanoelectronics and optoelectronics applications. To develop technology of formation of Ge- and Si- quantum dots (QDs) in dielectric films (GeO_2 or consequently SiO_2), it is important to study role of Ge or Si monoxides (GeO or SiO) in this formation [1,2]. GeO or SiO can be in the films both in solid or gas phase and react, for example, like that (Ge + GeO_2 $\longleftrightarrow$ 2GeO). There is lack of understanding of the monoxides from point of view of physical chemistry. This work is aimed to study of one of unresolved property of solid Ge monoxide — thermo-dynamical metastability of it.

Under heating of Ge/GeO_2 heterosystem, the process consisting of 3 subsequent reactions is easily realized (see Fig. 1): I — formation of vapor germanium monoxide GeO(g) ($T > 400 - 500$ °C); II — condensation of GeO vapor and formation of metastable solid germanium monoxide GeO(s) ($T \sim 350 - 650$ °C); III — decomposition of GeO(s) and formation of solid matrix from glassy GeO_2 with encapsulated Ge nanoclusters (amorph. or crystal.; $T > 250$ °C). One example of such film is shown in Fig. 2a. There are two surprising points in this subsequence. First — that the Ge/GeO_2 heterosystem, passed complex cycle of chemical and structural transformations, recover into initial structural state. Second — that GeO molecules in gas state is very stable, whereas in solid state of GeO, some germanium atoms are able to broke the bond with oxygen atoms without any remarkable activation energy, at temperatures close to room temperature. The apparent contradiction of these effects can be clarified using model of structure of metastable GeO(s) and studying the processes of formation of the structure.

It is known, that in atomic lattices of germanium and GeO_2 (hexagonal syngony, type of α-quartz) atomic orbitals of Ge-atoms are sp^3-hybridized. So, the elementary unit of germanium lattice is tetrahedron, in which each Ge atom in similar tetrahedron of lattice of hexagonal GeO_2 (Fig. 1b) is bonded by sp^3-hybridized atomic orbitals with four atoms (in GeO_2 oxygen is half-possessed to one of neighbor tetrahedron). The lattices of amorphous germanium and GeO_2 are built from elementary tetrahedrons, as also their crystalline modifications. During heating of any Ge/GeO_2 heterosystems to temperatures higher than 400 °C, the thermodynamically stable gaseous germanium monoxide (GeO(g)) is formed. The bond length in Ge-O molecule in gaseous state is $\sim 1.647 - 1.652$ Å [3]. For sp^3-hybridization of Ge-atomic orbitals four any atoms are needed in tops of proper tetrahedron arranged round Ge-atom, therefore in biatomic molecule GeO(g) such orbital structure is impossible. According to data [3] in GeO(g) molecule atom of Ge is bonded with O-atom by one σ-bond and one π-bond, so, it is possible, that atomic orbital of germanium in this case is sp^2-hybridized (Fig. 1c). Transformation of electron wave functions from sp^3-hybridized states (inherent to Ge(s) and GeO_2(s)), into sp^2-hybridized state (inherent to GeO(g) molecules), demands heating to temperature >400 °C and takes energy $\Delta H_{298} \sim 54$ kcal/mole [4]. Therewith, the quite good stability of atomic orbital configuration of a GeO(g) molecule is characterized by quite high energy of its dissociation — $\Delta H^0 \sim 159$ kcal/mole [4].

Stability of GeO(g) molecules is in sharp contrast with thermodynamic instability of germanium monoxide in solid state, when during deposition from GeO vapor (Fig. 1, reaction II), a formed GeO(s) film without any heating and additional stimulation is easily transformed into Ge(s) + GeO_2(s) mixture (Fig. 1, reaction II). It is obvious, that the reason of such strong changes of material properties is caused by radical transformation its atomic structure during changing into other phase state. As we consider, the important thing is that in solid state distances between separate GeO molecules are order of atom. In this case the conditions for formation of permanent net from these molecules is appeared. The Ge- and O-atoms can bond into 3D chains. And due to exchange interaction the atomic orbitals can be sp^3-hybridized (Fig. 1d).

Based only from approach of stoichiometry such structure can be interpreted as bonded tetrahedrons (Fig. 1d), where each atom of germanium is bonded with two other Ge-atoms and two O-atoms. And each O-atom bonds as a bridge two Ge-atoms in neighboring tetrahedrons. The driving force of such transformation can be free energy gain due to change types of atomic orbitals of germanium from σ- and π- bonds on sp^3-hybridization. But the length of Ge-Ge bonds in germanium ~ 2.45 Å (Fig. 1a) is strongly varied from the length of Ge-O bonds in GeO_2 and GeO(s) ~ 1.65 Å (Fig. 1b,d). Therefore, the elemental tetrahedron in GeO(s) lattices is strongly deformed with strongly distorted bond angles. Strong deformation of

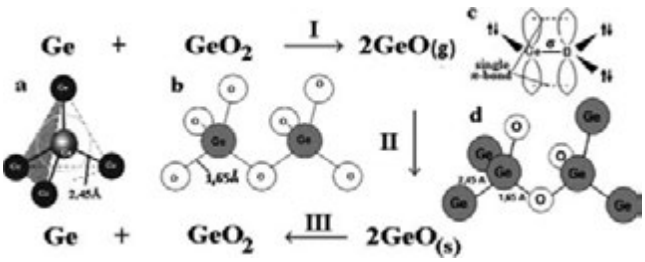

Fig. 1. Scheme of formation of GeO_2 film with Ge-QDs.

tetrahedron oriented sp^3-hybridized valence electron orbitals is source of remarkable atomic net stress energy. This deformation can also lead to lack of long range order in solid GeO films. These films are usually amorphous, but there is data concerning formation of crystalline phase of GeO(s) [5] with monoclin syngony. So, shown in Figure 1d structure of GeO(s) is not compact and has no minimized energy state for atomic net stablility. It is the reason of GeO(s), instability, even in amorphous state it can not save long time its form and under very soft thermal impact decomposes to phases with more stable net with sp^3-hybridized Ge and GeO_2.

IR spectroscopy of annealed GeO(s) films revealed peculiarities, confirming our supposition about GeO(s) structure. IR spectrum of absorbance of undecomposed GeO(s) film is characterized by peak with maxima at 770 cm^{-1} (Fig. 2b, curve 1). The peak is connected with valence asymmetric vibrations of oxygen atoms in Ge-O-Ge bridge [6]. IR spectrum of absorbance of fully decomposed GeO(s) film is characterized by peak with maxima at 870 cm^{-1} (Fig. 2b, curve 5). And peak with maxima at 770 cm^{-1} is absent, showing that the process of decomposition of GeO(s) into GeO_2 and Ge is finished. After the annealing with low temperature one can suppose the growth of the peak at 870 cm^{-1} and lowering of peak at 770 cm^{-1}. It is logically because one can expect the growth of GeO_2 part and lowering of GeO(s) part. But experimental data are different from this supposition. With the growth of annealing temperature the absorbance peak connected with the valence asymmetric vibrations of oxygen atoms is smoothly shifted from start position 770 cm^{-1} to direction of peak at 870 cm^{-1}, with consequent growth of its intensity (Fig. 2b. curves 2–4). It is difficult to explain such modifications of observed IR spectra because when the peak of the infrared absorption is between 770 and 870 cm^{-1}, it can not be attributed to any known compounds of germanium with oxygen. From other side modification of films during annealings can not be explained by any modification without decomposition GeO(s). Moreover, according to Raman scattering data, initial films do not contain Ge-Ge bonds. And after annealings at 260 °C higher broad peak at 275–280 cm^{-1} appeared in Raman spectra. This peak is connected to scattering on Ge-Ge bond vibrations in amorphous Ge clusters.

According to proposed model, the GeO(s) homogeneous material under thermal impact of annealings is decomposed into two stable phases. These phases are built from the regular tetrahedrons making up a cubic lattice of Ge and hexagonal lattice of GeO_2 based on sp^3-hybridized Ge-atoms. After decomposition GeO(s) film is transformed into Ge:GeO_2 heterostructure with Ge nanoclusters. The formation of this structure is going on by two steps. First is formation of metastable GeO(s)

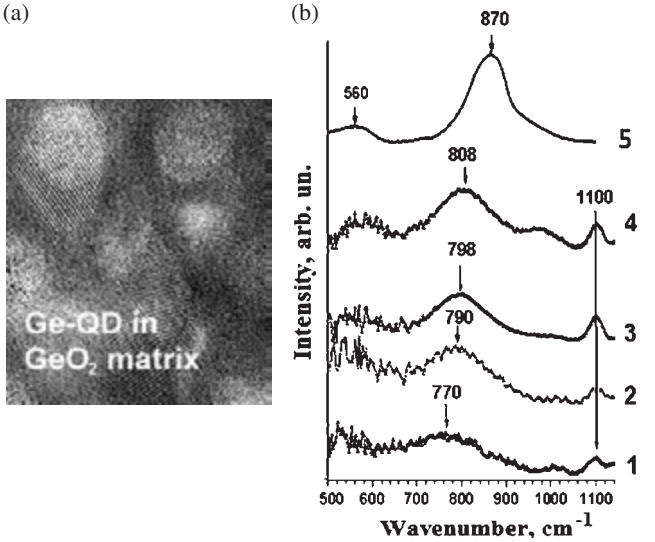

Fig. 2. a) HRTEM image of Ge-QDs in GeO_2 matrix; b) IR absorption spectra of GeO(s): 1 — as-deposited; 2, 3, 4, 5 annealed at: 260 °C 6 min; 290 °C 4 min; 320 °C 4 min; 600 °C 10 min.

films after condensation of GeO(g) molecules from vapor (this is relatively rapid process). Second (and more slowly) process is growth of Ge nanoclusters and formation of glassy GeO_2 matrix. This process we have studied using transformation of Raman and IR spectra after annealings.

The diffusion of germanium atoms in volume of matrix is not so free. This is not only diffusion of interstitial germanium or oxygen atoms and diffusion of vacancies, but diffusion of vacant valence bonds in not stable atomic net. Glassy film due to a great number of vacant valence bonds in its own net has low viscosity.

With the annealing beginning the Ge clusters start to grow. Initially these clusters are separated by GeO_x areas with $0 \leq x \leq 2$. Because the frequency of vibrations of oxygen atoms in Ge-O-Ge bridge depends also on neighboring surroundings (and certainly on stoichiometry parameter x), the IR peak is shifted (Fig. 2b, curves 2–4).

So, due to sp^3-hybridization the similar-type tetrahedron structure of atomic orbitals of Ge-atoms is appeared for each three materials — Ge, GeO_2 and GeO(s). This allows to explain not stability of GeO(s) and also mechanism of structural transformations of GeO(s) during its decomposition into Ge and GeO_2.

Acknowledgements

The work was supported by RFBR-grant # 07-08-00438.

References

[1] V. A. Volodin *et al*, *Solid State Phenomena*, **108–109**, 84 (2005).
[2] M. Molinari *et al*, *Appl. Phys. Lett.* **82**, 3877 (2003).
[3] I. V. Tanaev *et al*, *Himiya germaniya* (1967).
[4] M. Jolly *et al*, *J. Amer. Chem. Soc.* **74**, 5757 (1952).
[5] N. A.Vasyutinskii *et al*, *Inorganic Materials* **1** 7, 1057 (1965).
[6] D. Jishiashvili *et al*, *Georgian Eng. News.* **3**, 109 (2005).

17th Int. Symp. "Nanostructures: Physics and Technology"
Minsk, Belarus, June 22–26, 2009
© 2009 Ioffe Institute

InP nanowires with various morphologies formed by Au-assisted metal-organic chemical vapor deposition

Hui Huang, Xiaomin Ren, Xian Ye, Yisu Yang, Qi Wang and Yongqing Huang

Key Laboratory of Optical Communication and Lightwave Technologies (Ministry of Education), Institute of Optical Communication and Optoelectronics, Beijing University of Posts and Telecommunications, P.O. Box 66, Beijing 100876, China

Great potential of semiconductor nanowires (NWs) for various applications have attracted world-wide scientists to work on this subject [1–3]. In this paper, the vapor-liquid-solid (VLS) growth of the InP NWs on InP (100) substrate with Au particles as catalyst is reported. The NWs exhibit various morphologies such as straight, L-branch, Y-branch, K-branch, bottle-shape, cone-shape, needle-shape, etc. These abundant morphologies would have many potential applications in photonic integration.

The epitaxial growth was performed by metal-organic chemical vapor deposition (MOCVD) with a Thomas Swan CCS-MOCVD system at a pressure of 100 Torr. Trimethyl-indium and phosphine were used as the precursors. The sample was prepared by firstly depositing an 4.0 nm Au layer on an InP (100) substrate, then annealing the Au-coated InP substrate in the MOCVD reactor at 645 °C to form Au nanoparticles as catalyst and finally growing the InP NWs at 450 °C for 10 min with V/III ratio of 150. Morphologies of the NWs was investigated with scanning electronic microscopy (SEM), further transmission electron microscopy (TEM) analysis will be supplied.

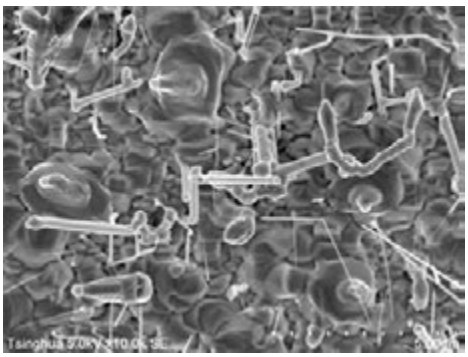

Fig. 1. SEM image of planar views of the InP NWs.

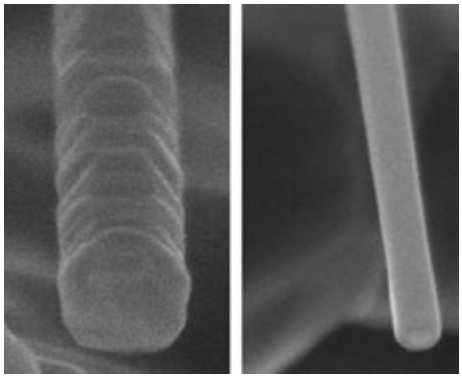

Fig. 2. Hexagonal and cylindric NWs.

Figure 1 shows the SEM images of the InP NWs. It is shown that the NWs exhibit various morphologies. As shown in Fig. 2, there are two kinds of straight NWs, i.e., cylindric shape with smooth sidewall and hexagonal shape with many microfacets. Fig. 3 shows the NWs exhibit morphologies such as T-branch, L-branch, Y-branch and K-branch. The branches maybe caused by precipitate the In droplet on the NWs sidewall or by bridge of two NWs grown along different directions during growth. Fig. 4 shows the NWs with pillar-shape, needle-shape, bottle-shape and cone-shape. Further indepth analysis by using TEM will be supplied. We believe these morphologies of the NWs would has many potential applications in photonic integration such as nano-waveguide for optical interconnections and novel optoelectronic devices.

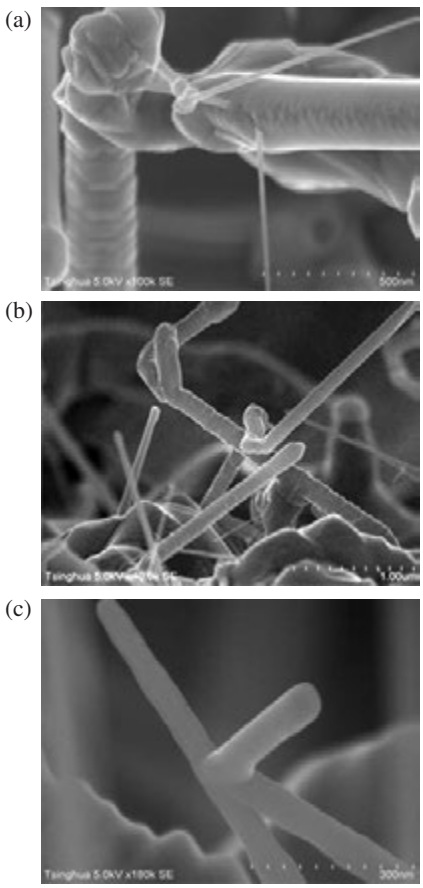

Fig. 3. The NWs exhibit morphologies such as (a) T-branch, (b) L- and Y-branch, and (c) K-branch.

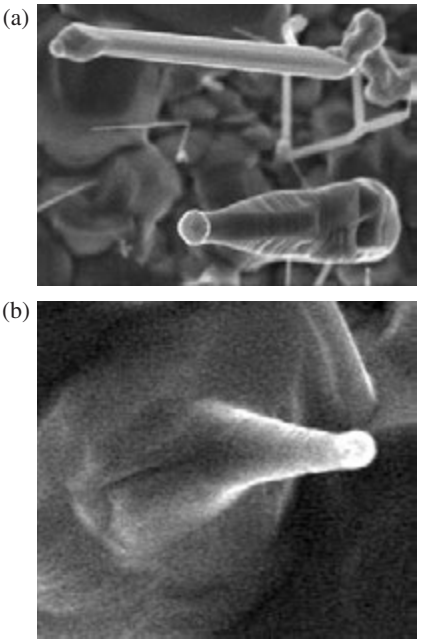

Fig. 4. The NWs with (a) needle-shape, pillar-shape and bottle-shape, and (b) cone-shape.

Acknowledgements

This work was supported by grants from National Basic Research Program of China (No. 2003CB314901), the 111 Program of China (No. B07005), Program of Key International Science and Technology Cooperation Projects (No. 2006DFB 11110), New Century Excellent Talents in University of China (NCET-05-0111) and the Program for Chang-jiang Scholars and Innovative Research Team in University (No. IRT0609).

References

[1] J. Hu, T. W. Odom, C. M. Lieber, *Acc. Chem. Res.* **32**, 435 (1999).
[2] L. Samuelson, *Mater.Today.* **10**, 22 (2003).
[3] R. S. Wagner, W. C. Ellis, *Appl. Phys. Lett.* **4**, 89 (1964).

17th Int. Symp. "Nanostructures: Physics and Technology"
Minsk, Belarus, June 22–26, 2009
© 2009 Ioffe Institute

Modification of luminescent Si nanostructures by irradiation with swift heavy ions

G. A. Kachurin[1], S. G. Cherkova[1], V. A. Skuratov[2], D. V. Marin[1] and A. G. Cherkov[1]

[1] Institute of Semiconductor Physics of SB RAS, pr. ak. Lavrentjeva 13, Novosibirsk 630090, Russia
[2] Joint Institute for Nuclear Research, Dubna, Russia

When swift heavy ions (SHI) penetrate in solid-state targets, their stopping in thin near-surface layers occurs mostly at the expense of ionization losses. If the stopping rate exceeds ∼1 keV/nm, tracks are forming with the nm-scale diameters, where the carrier concentrations may reach $\sim 10^{22}$ cm^{-3}. Temperature inside the tracks may exceed 5000 K for 10^{-13}–10^{-11} s. Thus, defect formation and ultra-short pulse treatments should proceed in the targets.

In our study thin SiO_2 layers were implanted with 140 keV Si ions to the dose of 10^{17} cm^{-2}. Two types of the samples were employed for irradiation with 130 MeV Xe ions: as-implanted with Si, and those subjected to post-implantation annealing at 1100 °C to form Si nanocrystals. The doses of Xe ions were ranging from 3×10^{12} to 10^{14} cm^{-2}. HREM and photoluminescence were used for the characterizations. In the as-implanted layers HREM revealed after Xe irradiations the 3–4 nm-size dark spots, whose number and size grew with increase in Xe ion dose (Fig. 1). In some of them lattice fringes may be distinguished, indicating their crystal character. The interplanar spacing matched those of silicon. Photoluminescence band at 660–680 nm was found in such samples (Fig. 2a). At first its intensity dropped with the Xe dose, but more prolonged bombardment caused the emission to grow. Passivation by hydrogen quenched the band and promoted emission at ∼780 nm, typical of Si nanocrystals (Fig. 2b). In spectra of 1100 °C-annealed layers strong ∼780 nm peak was observed at once. Under Xe bombardement its intensity fell rapidly, followed by appearance and growth of the 660–680 nm band (Fig. 3a). Passivation partly restored the emission at ∼780 nm (Fig. 3b). The obtained experimental results are interpreted as the emission at ∼660–680 nm belongs to the damaged Si nanocrystals. Analysis of both ionization and nuclear losses of Si and Xe ions allowed to conclude, that ionization losses of Xe ions are mainly responsible for the formation of new Si nanostructures in hot ion tracks, whereas nuclear losses mainly introduce the radiation defects, which quench the luminescence. Changes in spectra with growth of Xe ion dose are accounted for the difference in the diameters of Xe ion tracks (∼5 nm) and the displacement cascades (∼50 nm).

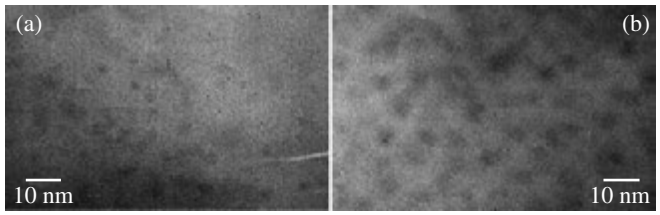

Fig. 1. HREM images of the Si-implanted SiO_2 layers after Xe ion bombardment to the doses of 3×10^{12} (a) and 10^{14} cm^{-2} (b).

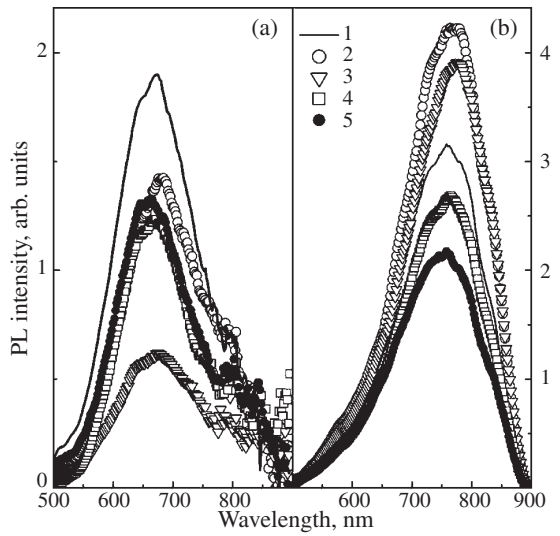

Fig. 2. a) PL spectra of the layers implanted with Si ions before (1) and after (2–5) irradiation with Xe ions. Doses, 10^{12} cm^{-2}: 2–3, 3–10, 4–30, 5–100. b) The same after passivation.

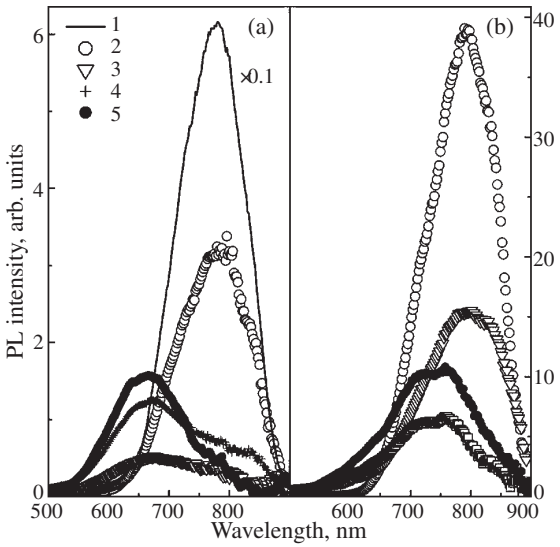

Fig. 3. a) PL spectra of the layers with embedded Si-ncs before (1) and after (2–5) irradiation with Xe ions. Doses, 10^{12} cm^{-2}: 2–3, 3–10, 4–30, 5–100. b) The same after passivation.

Acknowledgements

The work has been supported by the Grants # 08-02-00221 (Russian Foundation for Basic Researches), and # 06-02-72003 (Russian Foundation for Basic Researches, and Ministry of Science and Technology, Israel).

17th Int. Symp. "Nanostructures: Physics and Technology"
Minsk, Belarus, June 22–26, 2009
© 2009 Ioffe Institute

Transformation of art pigments to colloidal solution of nanosized particles as the sampling procedure for quantitative elemental analysis

E. V. Klyachkovskaya, E. V. Muravitskaya, V. A. Rozantsev, E. M. Torkailo, E. A. Ershov-Pavlov and M. V. Belkov

B. I. Stepanov Institute of physics NASB, 220072 Minsk, Belarus

Abstract. Transformation of art pigments to colloidal solution of nanosized particles can be good solution for sample preparation in the process of quantitative elemental compositions measurements with ICP-AES for such pigments that have low dissolubility in acids. In this work dependence of various characteristics of laser sampling procedure on the heat-chemical properties of art pigments was investigated.

Introduction

Nowadays, atomic emission spectrometry (AES) using inductively coupled plasma (ICP) as an excitation source of the emission spectra is one of the most powerful techniques for the quantitative analysis of chemical elemental compositions of various materials [1]. Traditional techniques of the sample preparation for the ICP-AES measurements is based on the material dissolving in the 1M nitric acid. In this case, among main requirements to the samples are their solubility in acids and homogeneity of the resulting analyte solution. Moreover obviously, ICP spectrometers demand particles in the solution to be lower a micrometer level [2]. However, some solid materials including many art pigments have low solubility in acids, and thus they can not be proper analyzed by the ICP-AES in a common way. Earlier, laser ablation in liquids has been proposed as a sample preparation technique for the ICP-AES measurements of an elemental composition of art materials [3]. Here we present results of our further study of the laser sampling in water for ICP-AES quantitative elemental analysis of art pigments with more detailed consideration of the sample transformation procedure.

1. Experimental

Ultramarine blue (No. 45010 PB 29.77007, Kremer, Germany) and Cinnabar (No. 42000 PR 106, Kremer, Germany) have been chosen as model samples for the measurements. These art pigments can not be dissolved in acids, and to our knowledge, their elemental composition could not be proper measured using ICP-AES and a traditional technique of the sample preparation. The Nd:YAG Q-switched double pulse laser has been used in the following operation regime: the laser wavelength is 1064 nm, laser pulse energy is 50 mJ, the pulses duration and the repetition rate are 12 ns and 10 Hz, respectively, a delay between the pulses in the double-pulse mode is 12 s. The double-pulse mode of the laser operation has been chosen due to the ablation rate significant increase in comparison with the common single-pulse regime [4].

From the art pigments chosen, dry layers of 1–2 mm thickness have been deposited on perspex plates. The plates have been immersed in a 15 ml beaker filled with de-ionized water. The laser beam has been focused in a spot onto the layer surface. After 30 laser shots the beaker with the sample has been moved to a new position. The Ablated sample material has distributed uniformly in the water forming a suspension. After 1–2 minutes exposition, the resulting colloidal solution has been diluted with de-ionized water up to 10 ml and ready for the ICP-AES measurements.

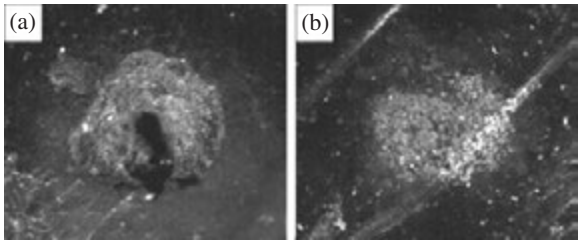

Fig. 1. Ablation craters produced by 30 laser double pulses on the ultramarine blue surface (a) in air and (b) in water.

2. Results and discussion

Ablation craters produced by the action of 30 laser double pulses on the ultramarine blue surface in air and in water are shown in Fig. 1a and b, respectively. Additionally, Fig. 2 presents in-depth profiles of the craters, which have been measured using Carl Zeiss LMA-1 optical microscope. One can see from the figures, that comparatively to the craters obtained

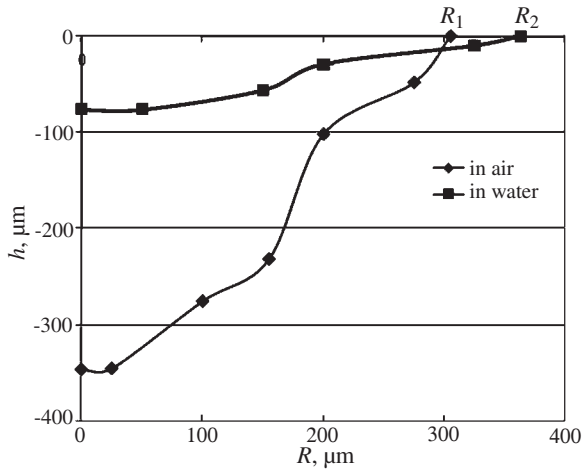

Fig. 2. In-depth profiles of the ablation craters produced in air and in water, which radii on the sample surface are R1 and R2, respectively.

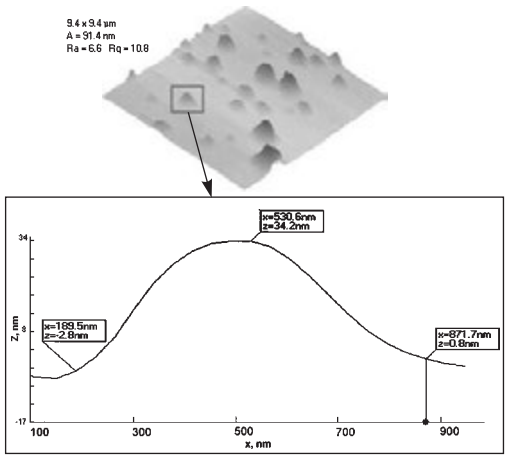

Fig. 3. A fragment of the film surface 3D topography showing distribution of the sample particles (right) and the profile of topography of selected particle (left).

in air, ones in water are shallower and do not have any rim around the crater, which is characteristic for the air case. It shows a difference of the ablation processes in liquid and in air, due to which ablated material of the sample comes into the ambient liquid more efficiently, and less or no re-solidification is observed [3]. Also, a rather large part of laser pulse energy is absorbed in water. It results in a decrease of the crater depth and, generally, in volume lowering of the craters comparatively to the air case.

Thin film of the suspension has been deposited on a very smooth Si-plate to study the suspension. The topography of the film surface has been examined with the atomic forth microscope NT-206. A fragment of the film surface 3D image is shown in Fig. 3. One can see a rather uniform distribution of separated particles immersed in a thin layer. The particles are of different sizes within limits around 200–700 nm. The particle dimensions are larger, than those measured previously [3]. It can be due to their agglomeration with time, as far as the suspension film was examined two days after it was prepared. Nevertheless even at this stage, the particles in the colloidal solution prepared from the art pigments by the laser ablation satisfy by their sizes to the requirements of ICP-AES spectrometer and can be used for the elemental composition measurements.

Table 1. Data of elemental composition measurements of ultramarine blue pigment using different preparation modes and evaluation results by chemical formula $2Na_2O \cdot Al_2O_3 \cdot 6SiO_2 \cdot 2Na_2S$.

El	Sample preparation mode				Evaluated by chemical formula
	Laser ablation		Chemical digestion		
	%	% RSD	%	% RSD	
Al	6.41	2.12	2.93	0.04	7.27
Ca	7.14	4.58	1.41	0.7	–
Fe	0.30	10.51	0.06	0.55	–
K	2.03	5.03	0.24	5.43	–
Mg	1.15	5.85	0.05	0.33	–
Na	26.21	4.94	3.58	1.64	24.77
S	8.53	1.03	2.93	0.03	8.64
Si	6.45	5.85	0.75	0.04	22.70
Zn	1.76	3.10	0.01	4.27	–
O	–	–	–	–	36.63

Table 2. Data of elemental composition measurements of cinnabar pigment using different preparation modes and evaluation results by chemical formula HgS.

El	Sample preparation mode				Evaluated by chemical formula
	Laser ablation		Chemical digestion		
	%	% RSD	%	% RSD	
Ca	–	–	0.36	1.02	–
Cu	0.02	2.74	0.07	7.27	–
Hg	68.91	0.37	1.53	2.28	86.22
K	–	–	0.35	3.12	—
Mg	0.01	1.07	0.06	3.17	—
P	0.39	4.01	—	—	—
S	17.79	0.30	0.67	9.47	13.78
Zn	0.05	0.50	0.50	10.61	—

Also, samples of the art pigments under consideration have been prepared with the common chemical digestion technique, and the ICP-AES measurements have been performed for the both sets of the samples. Details of the chemical digestion technique use for the sample preparation one can find elsewhere [5]. Using the results, one can make a comparative analysis of the techniques potential. The quantitative data of elemental compositions for ultramarine blue and cinnabar measured in the samples prepared with both technique (chemical digestion and laser ablation in water) are presented in the Table1 and Tablbe2, respectively.

According to the results, a correlation of the elements content in the samples prepared by laser ablation in liquid is in a better agreement with the data calculated using chemical formulas of the pigments. As far as these pigments dissolve badly in the acids, sediments have been formed in the analyte solution during the sample preparation using the chemical digestion, and the accuracy of the quantitative measurements has been decreased.

3. Conclusion

Thus, since a lot of art pigments have low solubility in acids, their transformation to colloidal solution of nanosized particles by means of the laser ablation in water can be a good solution for the sample preparation in the ICP-AES analysis.

References

[1] G. A. Meyer *et al*, *Inductively coupled plasmas in analytical atomic spectrometry*, VCH Publishers, New York, 473–516 (1992).

[2] IRIS Intrepid II ICP Spectrometer, *Operator's guide, part No. 14459300. Thermo electron* (2003).

[3] E. V. Klyachkovskaya *et al*, *SPIE Proceedings* **6735**, 673513 (2007).

[4] E. Ershov-Pavlov *et al*, *2nd Euro-Mediter. Symp. on LIBS (Book of abstracts)*, Hersonissos, Crete, Greece, 12 (2003).

[5] E. V. Muravitskaya *et al*, *Spectrochim. Acta, Part B* **64**, 119–125 (2009).

17th Int. Symp. "Nanostructures: Physics and Technology"
Minsk, Belarus, June 22–26, 2009
© 2009 Ioffe Institute

Two-stage nucleation of indium drops on GaAs(001) substrate

A. A. Lyamkina[1,2], Yu. G. Galitsyn[1], D. V. Dmitriev[1], S. P. Moshchenko[1] and A. I. Toropov[1]

[1] Institute of Semiconductor Physics, Acad. Lavrent'eva Ave. 13, 630090 Novosibirsk, Russia
[2] Novosibirsk State University, Pirogova 2, 630090, Novosibirsk, Russia

Abstract. The indium drops formation on GaAs as initial stage of droplet epitaxy was investigated. The drop density of 5×10^7 cm^{-2} allows to produce low-density quantum dots. Well-defined bimodal character of height distribution is revealed. We suppose that additional nucleation centers appeared on the surface during indium deposition time. They are supposed to be surface defects caused by arsenic evaporation from GaAs. The time of defect appearing was estimated on the base of two dot groups volume difference.

Introduction

The important problem facing advanced devices engineering is fabricating of nanostructures with specified qualities. For single-photon emitter it is required to produce low-density quantum dots [1], and now this problem is extensively investigated. Droplet epitaxy seems to be a perspective line of this research and now it is often implemented in the experiments [2]. We decided to focus on the initial stage of this method and to study the distribution and some properties of metal drops, which are the centers of following QDs formation.

Recently it was demonstrated that low-density QDs can be obtained by using of ultra-low InAs growth rate in combination with proper growth interruption time [3]. Occurring during growth interruption time Ostwald-type ripening is considering the most significant reason for QDs size enlarging and density decrease. We can suppose that in liquid indium drops this ripening can be held even more effective due to capillary forces. As drop properties are determined by formation and ripening processes, their investigation is useful for understanding of the mechanisms of indium redistribution on the surface.

1. Experimental

The phase of metal drops primarily is a part of QDs growth, so for its investigation conditions close to ones using in practical QDs fabricating should be chosen. We used the parameters with which in our previous experiments QDs with long-wave spectra were reproducibly obtained. Such condition choice is due to bring the system as close to the state like directly before dots formation as possible.

The drops were grown by molecular beam epitaxy on semi-insulating (001)-oriented GaAs substrates using a Riber32P system with gate arsenic source. Before indium deposition proper amount of Ga was applied to saturate excess arsenic atoms on the substrate surface. Necessary gallium deposition time was tuned in preliminary test on working substrate, according amount was 1.5 ML. Then 2.1 ML of indium with rate of 0.04 ML/s was applied to the GaAs surface without As_4 flux and immediately quenched. The growth was conducted at temperature of 500 ° C.

The morphology of the surfaces was studied *ex-situ* by the atomic force microscopy (AFM), using the scanning probe microscope Solver-P47H (NT-MDT). Standard silicon cantilevers were used for imaging by AFM.

2. Results and discussion

Typical AFM image is represented in Fig. 1. As it is seen, the drops are rather large and have a density of 5×10^7 cm^{-2}. It means that provided with such growth mode indium drops can be used to fabricate low density QDs. It is interesting to notice that two kinds of the drops are seen differing by the height. To study this interesting effect the data from hundreds μm^2 were got. Because of low density and small drop sizes eliminating allowed AFM resolution it is a kind of problem to get enough drops statistics.

Experimental AFM images were processed by particle analysis and then received data were handled by statistic analysis resulting in the information about geometrical parameters of the drops. Height and radius distribution histograms are presented in Fig. 2. The distribution was described by a sum of Gaussians, as it is seen from histogram, there are two well-defined drop groups with quite different height values. As

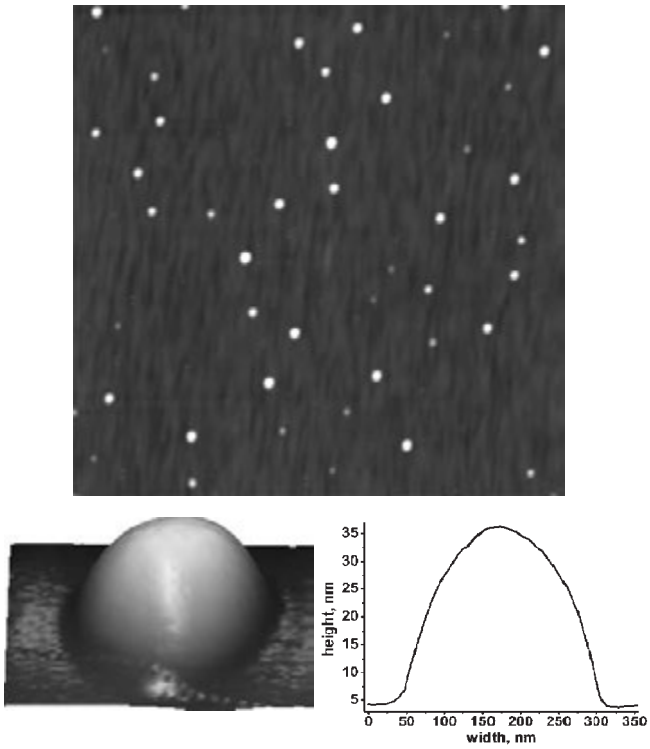

Fig. 1. AFM images of the sample with indium drops. Upper: 10 × 10 μm AFM of the surface with low-density drops. Lower: 3D view of a single drop and its height profile.

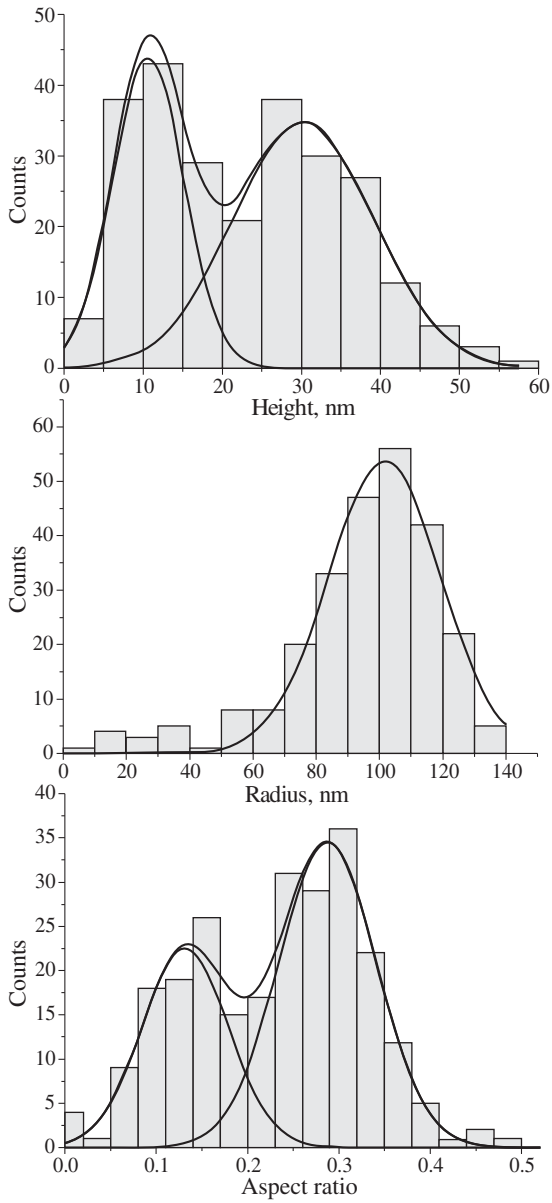

Fig. 2. The histograms of height and radius distribution are presented. The last histogram is aspect ratio distribution, which is rough estimation of drop wetting angle. All histograms are described by Gaussians (solid line).

it is illustrated in Fig. 2, height distribution has pronounced double-mode type, at the same time radius distribution can be well approximated by the only peak.

Of some interest is the lowest histogram, describing aspect ratio distribution. Comparing with height distribution, it has more pronounced bimodal character. So we can suppose that drop geometry is the same within one group, but quite different in two obtained groups.

The presence of two groups of drops can be explained by occurrence of different drop formation mechanisms or by changing of formation conditions during growth process. Both hypotheses should be investigated in details, but some conclusions can be made immediately. It follows that at some instant of indium deposition time additional nucleation centers appear on the surface.

Obtained experimental data allow us to make an estimation of this time. Considering that radii of two observed groups are close and heights differ in two times, it can be supposed that extra defects appear approximately in the second third of indium deposition time interval.

The instant and reasons of arising of these centers are a question of great importance for the growth. Probably, these defects are caused by arsenic evaporation from GaAs and consequent modifications of original surface. So this effect can be managed by the rate of indium deposition. We suppose that after rate increasing in two-three times an amount of smaller drops will decrease very significantly.

Acknowledgements

We are grateful to A. V. Prinz and V. A. Seleznev for the help with AFM measurements.

References

[1] M. Sholz, S. Buttner, O. Benson, A. I. Toropov, A. K. Bakarov, A. Lochmann, E. Stock, O. Schulz, F. Hopfer, V. A. Haisler and D. Bimberg, *Optics Express* **15**, 9107 (2007).

[2] S.-S. Huang, Z.-C. Niu, H.-Q. Ni, F. Zhan, H. Zhao, Z. Sun and J.-B. Xia, *Chin. Phys. Lett.* **24**, 1025 (2007).

[3] L. H. Li, N. Chauvin, G. Patriarche, B. Alloing and A. Fiore, *J. Appl. Phys.* **104**, 083508 (2008).

17th Int. Symp. "Nanostructures: Physics and Technology"
Minsk, Belarus, June 22–26, 2009
© 2009 Ioffe Institute

Influence of annealing on the capacitance properties $Si/SiO_2/Si$ structures with Ge nanocrystals

V. V. Malyutina-Bronskaya[1], V. B. Zalesskii[1], E. N. Pshenichnyii [2], V. S. Malyshev[2] and E. N. Gaiduk [2]

[1] B. I. Stepanov Institute of Physics NASB, 220072 Minsk, Belarus
[2] "Plant of Semiconductor Devices" Unitary Enterprise, 220108 Minsk, Belarus

Abstract. Samples containing $Si/SiO_2/Si$ layers with Ge nanocrystals, which average dimensions are in the range from 20 nm to 60 nm, obtained by the LPCVD method were investigated. Surface morphology studies during the thin films acquisition process are presented. Capacitance-voltage characteristics of the obtained samples in dependence of annealing mode are analyzed.

Introduction

Main elements for the creation of single-electron devices are semiconductor or metallic nanoclusters [1]. Self-organizing systems are a promising alternative for the acquisition of structures with dimensions lower than 10 nm. Ge nanocrystals embedded in the MOS transistor gate and placed on the tunneling distance from the channel region can be used in electronic memory devices [2,3]. Investigations and developments of memory devices with embedded arrays of self-organizing nanocrystals are presently carried out using three main approaches: 1) ion implantation, 2) deposition of hyperstoichiometric oxide layers and 3) deposition of multilayered structures with consequent oxidation [4,5].

1. Experimental

The LPCVD method was used in this work for the deposition of $Si_{x-1}Ge_x$ layers. A deposition of polycrystalline silicon thin films was carried out in the isothermal zone of low pressure horizontal reactor with hot walls of "Izotron 4-150" type in the temperature range from 520 to 620 °C. 100% monosilane and 5% mixture of monogermanium with hydrogen have been used in our experiments. Silicon wafers of KDB-12 type with 100 mm and crystallographic orientation (100) were used as substrates. Thermal silicon oxide layer with thickness 30 nm was preliminary grown on the wafers. Working pressure changed in the range 24 to 35 Pa. A pyrogenic oxidation of the deposited $Si_{x-1}Ge_x$ film in a diffusion furnace at temperatures 850 and 1000 °C have been carried out with a goal of Ge supplantation on the interface of film-silicon oxide. Structures with $Si_{x-1}Ge_x$ having thickness from 20 to 30 nm were used for the studies of $Si_{x-1}Ge_x$ oxidation process. Thereafter an annealing of the obtained structure was carried out in diffusion furnace in the nitrogen at temperature region from 850 to 900 °C. An additional annealing was made on air at temperatures 450–1000 °C.

Structural investigations of the obtained thin film samples were performed by means of transmission electron microscopy on the EM-125 set up. Capacitance-voltage characteristics were measured on the obtained nanostructures at room temperature by means of E7-20 immitance meter.

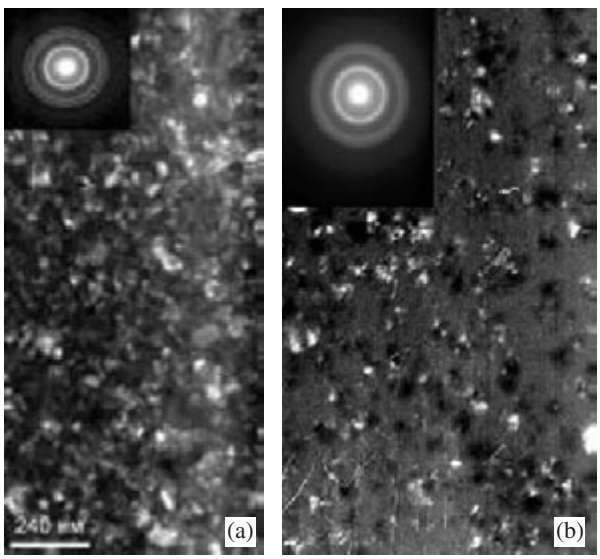

Fig. 1. The structure of $Si_{1-x}Ge_x$ thin films deposited at temperatures 520 °C, average grain size 22–60 nm (a) and at temperatures 560 °C, average grain size 25 nm (b).

2. Morfology and capacitance properties $SI/SiO_2/SI$ structures with Ge nanocrystals

The results of $Si_{1-x}Ge_x$ thin films structure analysis are presented in Fig. 1. The investigations did not reveal any substantial influence of deposition temperature on a grain size, except that at 520 °C (Fig. 1a) a somewhat larger range of grain sizes was observed as compared to the films deposited at temperatures 560 to 620 °C. At deposition temperatures 560 °C (Fig. 1b) and lower the deposition of amorphous undoped silicon films takes place. Most impact on the grain size is made by the deposited film thickness. With an increase of the film thickness average grain size rises. Formation of Ge nanocrystals can be realized by oxidation of $Si_{1-x}Ge_x$ films by means of different rates of oxidation of Si and Ge. Two oxidation modes

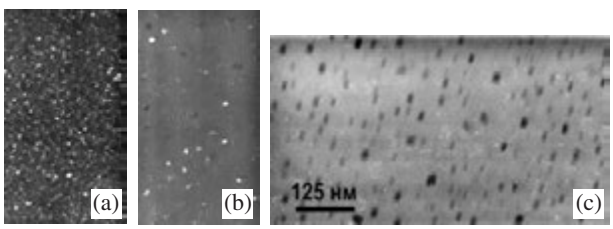

Fig. 2. SEM images of the structure of as-deposited $Si_{1-x}Ge_x$ films (a), the films which were oxidized during 25 min (b) and a bright-field image of Ge nanoclusters in a SiO_2 film (c).

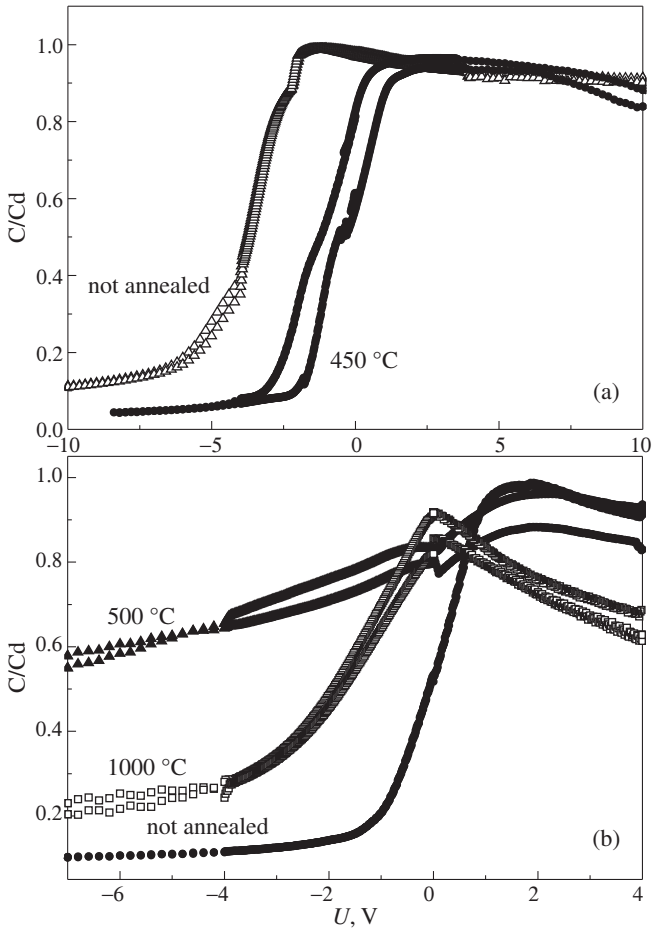

Fig. 3. C–V haracteristics of MOS-capacitors on the base of $Si/SiO_2/Si$ structures with Ge nanocrystals, measured at 100 kHz: not annealed samples and the samples annealed at 450 °C (a), at 500 °C and 1000 °C (b).

have been probed: a dry one at 1000 °C and a pyrogenic one at 850 °C. Samples with $Si_{1-x}Ge_x$ films having thickness 20 nm and Ge content of about 5 at.%. At the dry oxidation process during 30 min the film was completely oxidized. At the pyrogenic oxidation its duration varied in the range from 7 to 25 min (Fig. 2a,b). The initial sample had a polycrystal structure with a grain size in the region from 10 to 20 nm. After the oxidation during 7 min a large quantity of polycrystal material is left in the film. After the oxidation during 25 min amorphous film (silicon oxide) is formed with inclusions of Ge nanoclusters having sizes in the range from 10 to 15 nm (Fig. 2c).

Measurements of capacitance-voltage characteristics have been carried out on the obtained nanostructures. The obtained results which are characteristic for the overall series of annealed structures are presented in Fig. 3. It is observed from the experimental dependences that a large hysteresis, which is desirable for the acquisition of memory effect, does not occur on the structure which has not been annealed additionally (Fig. 3). After additional annealing at temperatures from 450 to 500 °C a hysteresis of about 1 V is observed on the capacitance-voltage characteristics (Fig. 3). A maximal hysteresis was obtained for the annealing at 500 °C. Capacitance modulation area and the value of dielectric capacitance change with annealing temperature variation as well (Fig. 3b). It has been noticed that during illumination by an electric filament lamp a change of capacitance value (by the absolute magnitude) and the increase of hysteresis are observed. With temperature rise this photoeffect diminishes. The observation of the above described effects enable us to point out that the annealing temperature influences formation of surface states on the interface and the surface states concerned with Ge nanoclusters (which average size is in the range from 20 to 60 nm). At the annealing temperature growth an increase of nanocluster sizes take place which leads to a formation of additional series capacitance, as a result of which capacitance decreases. Calculations have shown that such a reduction of capacitance is possible at the acquisition of a layer with a size of about 100 nm, which can be compared to sizes of Ge nanoclusters. From the obtained results one can suppose that the capacitance-voltage characteristics behavior depends on oxidation time and annealing temperature of experimental samples.

References

[1] I. I. Abramov, E. G. Novik *et al*, *Numerical modeling of metallic single-electron transistors*, Minsk, "Bestprint", (2000).
[2] H. Hanafi *et al*, *IEEE Trans. Electron Dev.* **43**, 1553 (1996).
[3] L. Guo *et al*, *Science* **275**, 649 (1997).
[4] P. Normand *et al*, *Electrochem. Solid State Letters* **1**, 88 (1998).
[5] S. Tiwari *et al*, *Appl. Phys.* **A71**, 403 (2000).

17th Int. Symp. "Nanostructures: Physics and Technology"
Minsk, Belarus, June 22–26, 2009
© 2009 Ioffe Institute

Monte Carlo simulation of growth condition effect on nanowhisker characteristics

A. G. Nastovjak, I. G. Neizvestny and N. L. Shwartz
Institute of Semiconductor Physics RAS SB, Novosibirsk, 630090, Russia

Abstract. Morphology of single-component nanowhiskers in relation to growth conditions and mechanisms was investigated by Monte Carlo simulation. It was found that nucleation at the drop-whisker interface can be mono- or polycentric depending on deposition conditions and catalyst drop diameter. Growth activation energy was estimated on the base of nanowhisker growth rate dependence on temperature. It was demonstrated that for drop-seed, possessing large contact angle with whisker material, the hollow nanowhisker (nanotube) formation is possible at appropriate deposition parameters.

Introduction

Nanowhiskers (NW) are one-dimensional vertical crystals that offer many opportunities for modern opto- and nanoelectronic devices [1]. The basic method of semiconductor NW formation is vapor-liquid-solid (VLS) growth activated by catalytic seed particle (generally Au) [2,3]. Since study of growth kinetics especially at the initial stage is rather complicated experimental task, such investigation may be carried out using simulation. Monte Carlo technique enables to investigate growth process at the atomic scale level. First Monte Carlo model of NW growth on the base of VLS mechanism was realized earlier [4]. The present work is an outgrowth of atomic scale investigation of nanowhisker growth.

1. Monte Carlo model

Simulation was carried out using program package SilSim3D based on lattice Monte Carlo model. For simulation of NW growth three-component system was considered (Fig. 1): whisker material (Si), catalyst (for example, Au) and precursor (for CVD process). Silicon atoms or precursor molecules containing silicon were deposited on Si(111) surface activated by gold. Flux particles were deposited on the substrate either perpendicular (similarly to MBE) or at arbitrary angles (CVD). Dissociation of precursor molecules could be catalytic or non catalytic. Deposited matter reached the drop both by direct flux impingement and due to diffusion from the substrate. Two mechanisms were responsible for NW growth: (i) Si dissolution into the drop with following crystallization at the whisker-drop interface (classic VLS mechanism); (ii) Si incorporation along whisker-drop interface perimeter due to weak wetting of silicon with catalyst material. Silicon crystallization at the drop-whisker interface was realized like that: by exchange diffusion silicon atoms reached the interface where they were either incorporated into growing silicon facet or dissolved back into the drop. Such realization of crystallization process provided layer-by-layer NW growth: silicon nuclei were formed at the drop-whisker interface with following lateral enlargement. Range of gold drop diameter d_0 in the model was 3–20 nm according to experimental values for CVD grown whiskers [5]. The distance between whiskers was less than adatom diffusion length.

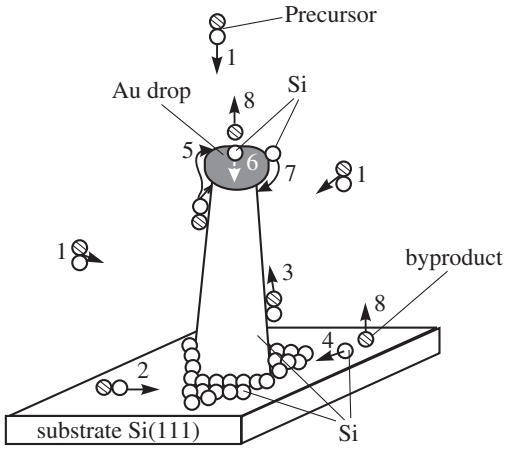

Fig. 1. The model system and possible component movement: 1 — precursor (P) flux; 2 — P diffusion along substrate surface; 3 — P diffusion along NW side wall; 4 — Si diffusion along substrate surface; 5 — P diffusion along drop surface; 6 — Si diffusion through the drop; 7 — Si diffusion along drop surface; 8 — evaporation of byproducts.

Physicochemical system of catalyst-whisker was determined by energy parameters of the model. The main energy parameters were: covalent energies: $E_{\mathrm{Si-Si}} = 1$ eV, $E_{\mathrm{Au-Si}} = 0.6$ eV, $E_{\mathrm{Au-Au}} = 1$ eV; activation energy of precursor diffusion $E_{\mathrm{P}} = 0.7$ eV; activation energy of precursor dissociation $E_{\mathrm{diss}} = 0.6$ eV; activation energy of Si exchange diffusion through the gold drop $E_{\mathrm{exdif}} = 1$ eV.

2. Results and discussion

Effect of growth conditions on NW characteristics and morphology was analyzed using proposed model. The dependences of NW morphology and growth rate on temperature, deposition rate and initial diameter of drop-seed were obtained. According to deposition parameters and drop diameter the growth of each silicon layer at the whisker-catalyst interface could be mono- or polycentric. The problem of mono- and polycentric nucleation has been considered theoretically in [2,6]. Fig. 2 shows cross-sections of drop-whisker interface at different growth conditions and diameters of catalyst drop. Under given growth conditions ($T = 800$ K, $F = 0.05$ ML/s) nucleation was monocentric for small drop diameter (Fig. 2a). Drop diameter increasing resulted in polycentric nucleation (Fig. 2b). Transition from polycentric nucleation to monocentric one for given drop diameter was possible either due to temperature increasing (Fig. 2c) or flux decreasing (Fig. 2d).

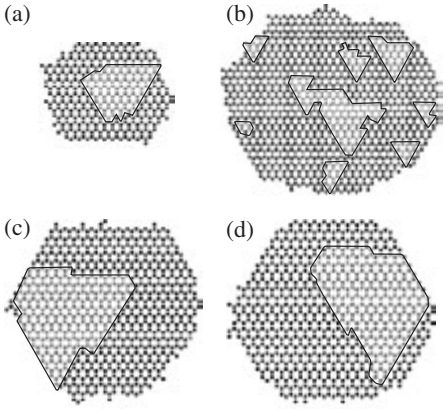

Fig. 2. Cross-sections of drop-whisker interface: mono- (a,c,d) and polycentric (b) nucleation. Au is marked with dark-grey color, Si with light-grey color. Diameter of catalyst drop $d_0 = 6$ nm (a), $d_0 = 9$ nm (b–d); $T = 800$ K (a,b,d), $T = 950$ K (c); $F = 0.05$ ML/s (a–c), $F = 0.001$ ML/s (d).

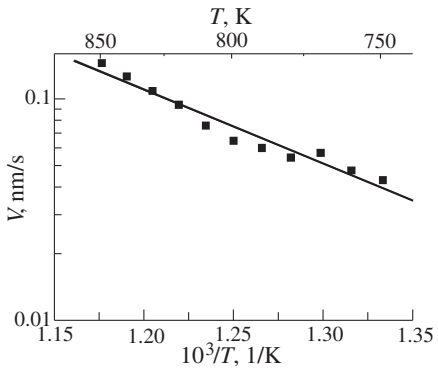

Fig. 3. NW growth rate V versus temperature ($F = 0.05$ ML/s, $d_0 = 6$ nm).

Temperature dependence of NW growth rate in semilogarithmic scale is shown in Fig. 3. As is evident from Fig. 3 the growth rate exponentially increases with temperature rise. For given physicochemical system at flux $F = 0.05$ ML/s activation energy of the process was estimated as 0.6 eV.

Simulation demonstrated that for large contact angle between whisker and drop the growth of tube-like NW was possible. Formation of whisker with cavity oriented along growing axes was possible if the number of atoms incorporated along interface perimeter was higher than the number of atoms crystallized by VLS mechanism. The cavity was created due to formation of silicon ring preventing further matter incorporation under the drop. Ring width as well as cavity diameter was depended on growth conditions. Flux rising resulted in increasing of tube inner diameter. Dependences of cavity diameter on flux in a range from 0.01 to 0.05 ML/s were obtained. At $F = 0.01$ ML/s cavity was absent and with flux rise from 0.02 to 0.05 ML/s cavity cross-section increased in 4 times. Fig. 4 illustrates variation of tube diameter depending on flux value. It was demonstrated that combination of VLS mechanism and Si incorporation along perimeter of Si-drop interface results in straight NWs with uniform diameter. This means that such combination is optimal for growth of NWs suitable for device application. Transition from one mechanism to another is determined by choice of whisker and catalyst material

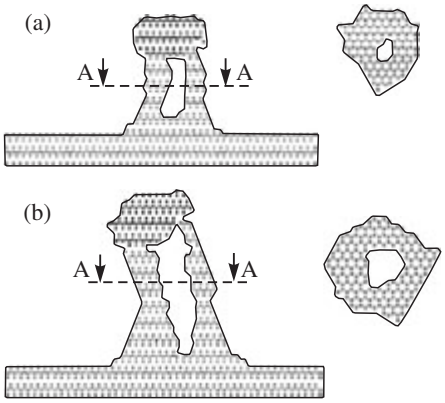

Fig. 4. Tube-like NWs (side view and cross-section along A-A) at different flux F: a — 0.025 ML/s; b — 0.045 ML/s ($T = 800$ K, $d_0 = 4.8$ nm, deposition time $t = 53$ s).

that imposes constraints on material choice for growth of NWs suitable for practice utilization.

3. Summary

Dependence of single-component nanowhisker morphology on growth conditions was studied. Nucleation of silicon layer at the drop-whisker interface could be mono- or polycentric according to growth conditions and drop diameter value. It was shown that combination of classic VLS growth mechanism with silicon incorporation along perimeter of drop-whisker interface is optimal: formation of straight and uniform whiskers at rather high growth rate. Possibility of tube-like whiskers formation under certain deposition conditions was demonstrated.

Acknowledgements

This work was supported by RFBR grant (08-02-00068) and the project "Growth mechanisms and characteristics of Si and SiGe nanowhiskers" according to basic research RAS Presidium program 27.

References

[1] O. Hayden, R. Agarwal, W. Lu, *Nano Today* **3**, 5–6, 12 (2008).
[2] E. I. Givargizov, *J. Crystal Growth* **31**, 20 (1975).
[3] V. G. Dubrovskii, N. V. Sibirev, *J. Crystal Growth* **304**, 504 (2007).
[4] A. G. Nastovjak, N. L. Shwartz, Z. Sh. Yanovitskaja, A. V. Zverev, *Proc. of 15-th Int. Symp. "Nanostructures: Physics and Technology" (Novosibirsk, Russia, 2007)*, Ioffe Physico-Technical Institute, 179, 2007.
[5] J. Kikkawa, Y. Ohno, S. Takeda, *Appl. Phys. Lett.* **86**, 123109 (2005).
[6] V. G. Dubrovskii, N. V. Sibirev, G. E. Cirlin, J. C. Harmand, V. M. Ustinov, *Phys. Rev. E* **73**, 021603 (2006).

17th Int. Symp. "Nanostructures: Physics and Technology"
Minsk, Belarus, June 22–26, 2009
© 2009 Ioffe Institute

Si nanowhiskers passivation by Ti-based dielectrics

Yu. V. Nastaushev, *O. V. Naumova*, T. A. Gavrilova, F. N. Dultsev, L. V. Sokolov and A. L. Aseev
Institute of Semiconductor Physics, SB RAS, Novosibirsk, Russia

Abstract. For the first time, plasmachemical oxidation and nitridation of Ti nanolayers evaporated onto the MBE-grown Si nanowhiskers was used for their chemical and electrical passivation.

Introduction

Attention to Si nanocrystals (nanowhiskers) is stimulated by 3D silicon electronics and environmental control perspectives [1,2]. An essential problem is chemical and electronic passivation of Si nanocrystal surface [3]. In this work, we used high-k dielectrics, based on Ti nanolayers treated with oxygen or nitrogen plasma, for the passivation of MBE-grown Si nanowhiskers [4].

1. Experimental

The Ti metal layer was deposited onto the 4-inch epi-ready Si (001) wafers in high vacuum (10^{-5}–10^{-7} Pa) using the e-beam sputtering technique. A 5 nm thick Ti layer was e-beam sputtered in an ANGARA molecular-beam epitaxy (MBE) unit. The deposition rate of the metal layer was 10 nm min^{-1}.

We used plasmachemical oxidation or nitridation of Ti nanolayers on flat Si surface to obtain TiO_x or $TiON_x$ nanolayers, respectively. Plasmachemical treatment was performed in O_2 or N_2 gas at a pressure of 0.8 Torr, RF power 150 W, at radio frequency 13.56 MHz ("MATRIX"), at room temperature for 2–20 min.

High-resolution transmission electron microscopy (HRTEM) of $TiON_x$-Si interface was carried out by means of JEM 4000 EX (Jeol Ltd). A thin sub layer of natural SiO_2 was detected on the silicon surface (Fig. 1). We observed very smooth, glassy surface of TiO_x and $TiON_x$ by means of AFM — technique (Fig. 2).

For the passivation of Si nanowhiskers surface the Ti metal layer was deposited onto the molecular-beam epitaxy (MBE) grown Si nanowhiskers in high vacuum (10^{-5}–10^{-7}) Pa using the e-beam sputtering technique. A detailed description of the growth procedure of nanowhiskers is given elsewhere [5]. A 5 nm Ti layer was e-beam sputtered in an ANGARA molecular-beam epitaxy (MBE) unit. The deposition rate of the metal layer was 10 nm min^{-1}.

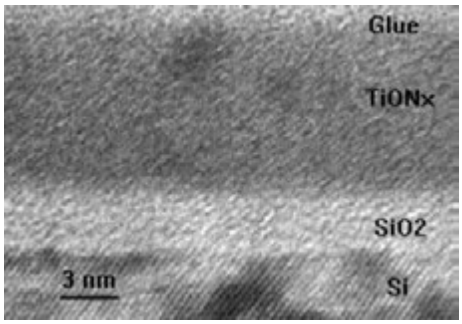

Fig. 1. HRTEM image of nanolayers on bulk-Si after plasmachemical nitridation of Ti film for 16 min.

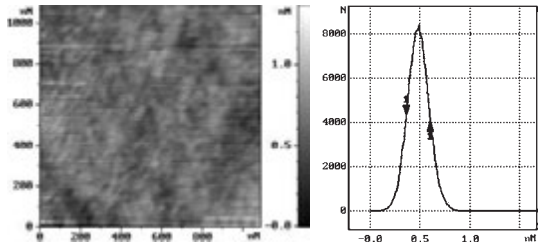

Fig. 2. AFM image of $TiON_x$ surface after 16 min plasma-chemical nitridation of 5 nm Ti nanolayer.

We used several different passivation regimes of Si nanowhiskers. Titanium oxidation on nanowhiskers was carried out at the substrate temperature of 0 °C, at the RF power 200 W for 10 min ("hard" regime) and at the RF power 70 W for 5 min ("soft" regime), oxygen pressure was 0,6 Torr. Plasma chemical treatment was carried out for 1 min with a break for 5 min for cooling (total time of treatment in plasma was 25 min).

Figure 3 shows the result obtained with TiO_x cover under the oxidation of Ti nanolayer. It is seen that Si nanowhiskers for "hard" regime of oxidation look like sharp cones with height up to 500 nm and with 300 nm base diameter. The plasma-chemical "soft" oxidation of Ti cover doesn't cause a damage of Si nanowhiskers. Base diameter of nanowhiskers is about 200 nm.

Titanium nitridation of nanowhiskers was carried out at the substrate temperature of 0 °C, at the RF power of 100 W for 1 min with a break for 5 min for cooling (total time of treatment in plasma was 25 min), nitrogen pressure was 0,2 Torr. A SEM-image of Si nanopillars with $TiON_x$ cover after "soft" plasma nitridation is shown in Fig. 4.

The electrical characteristics of silicon nanowhiskers passivated in different regimes were investigated. The current-voltage characteristics of nanowhiskers at room temperature are shown in Fig. 5. We used aluminum deposited on a poly-

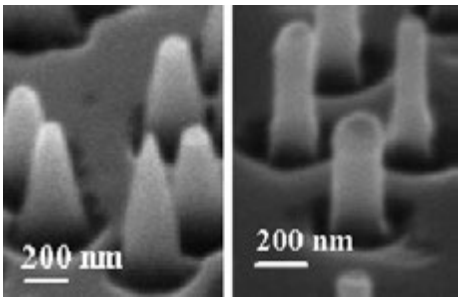

Fig. 3. SEM images of Si nanowhiskers with TiO_x cover after plasma-chemical "hard" (left) and "soft" (right) oxidation of 5 nm Ti nanolayers.

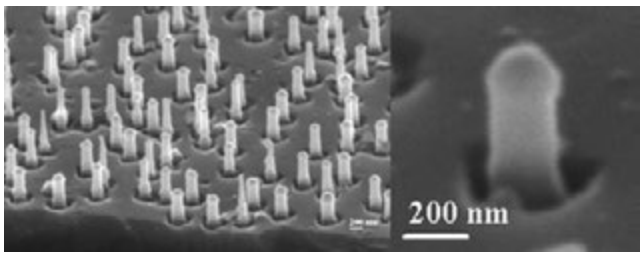

Fig. 4. SEM image of Si nanowhiskers with $TiON_x$ cover after "soft" plasma nitridation.

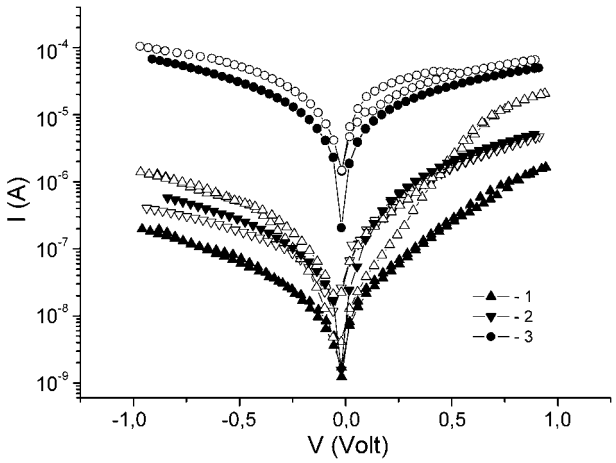

Fig. 5. Current-voltage characteristics of silicon nanowhiskers at room temperature in the dark (solid points) and under IR irradiation (open points): 1 — "hard" regime of Ti oxidation, 2 — "soft" regime of Ti oxidation, 3 — nitrided Ti (titanium oxynitride).

mer (PMMA) as the electric contact to nanowhiskers [4]. The electrical measurements were performed by applying voltage to the Si substrate, while the top Al contact was held at a constant potential. One can see that the highest conductivity of nanowhiskers was detected for the coating of titanium oxynitride obtained by plasma nitridation of the titanium layer 5 nm thick.

Fig. 6 shows the temperature dependencies of current through nanowhiskers covered by TiO_x and $TiON_x$ lfilms in "soft" regime. The $I(T)$ curves show that (1) the current through nanowhiskers exponentially decreases with the temperature ($I \sim \exp(E_a/kT)$) in the two intervals — from 300 to 150 K and from 150 to 78 K, and (2) the activation energy of conductivity, E_a, is almost independent of the type of covering layer. This allows us to conclude that the passivation regime has a strong effect on the conductivity of nanocrystals, especially at low voltage (Fig. 5), because it changes their surface state and does not modify the volumetric properties of whiskers.

Acknowledgements

Work was partly supported by RFBR under Project No. 07-02-01250. We are grateful to Dr. A. K. Gutakovskiy for HRTEM microscopy, to Dr. D. V. Sheglov and to Prof. A. V. Latyshev for AFM-measurements.

References

[1] T. Bryllert, L.-E. Wernersson, T. Lowgren and L. Samuelson, *Nanotechnology* **17**, S227 (2006).

[2] O. Hayden, R. Agarwal, W. Lu, *Nano Today* **3**, 12 (2008).

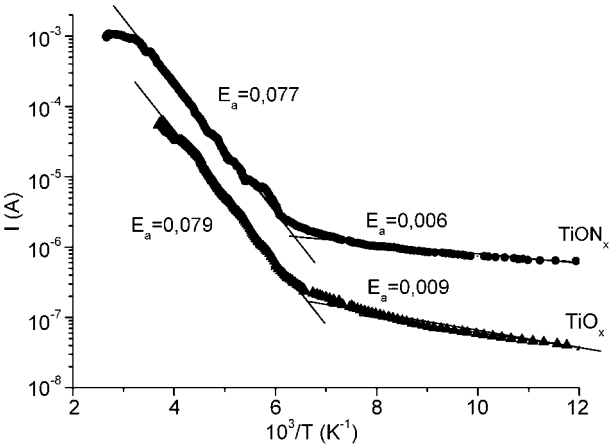

Fig. 6. Temperature dependencies of current measured at bias voltage $V = -5$ (V) through nanowiskers with $TiON_x$ and TiO_x cover prepared in "soft" regime. Solid lines: simulation with the activation energy E_a (eV) shown near a curve.

[3] D. Shir, B. Z. Liu, A. M. Mohammad, K. K. Lew, S. E. Mohney, *J. Vac. Sci. & Techn. B* **24**, 1333 (2006).

[4] O. V. Naumova, Yu. V. Nastaushev, S. N. Svitasheva, L. V. Sokolov, N. D. Zakharov, P. Werner, T. A. Gavrilova, F. N. Dultsev and A. L. Aseev, *Nanotechnology* **19**, 225708 (2008).

[5] L. Schubert, P. Werner, N. D. Zakharov, G. Gerth, F. M. Kolb, L. Long and U. Gösele, *Appl. Phys. Lett.* **84**, 4968 (2004).

17th Int. Symp. "Nanostructures: Physics and Technology"
Minsk, Belarus, June 22–26, 2009
© 2009 Ioffe Institute

Ge wetting layer thickness on Si(001) surface

A. I. Nikiforov, V. V. Ulyanov, V. A. Timofeev and O. P. Pchelyakov
Rzhanov Institute of Semiconductor Physics SB RAS, Lavrent'eva 13, 630090 Novosibirsk, Russia

Abstract. The influence of parameters of germanium deposition on wetting layer thickness was studied during the growth on the Si(100) surface. A non-monotone dependence of the thickness on growth temperature was discovered and accounted for by changing the mechanism of the layer-by-layer growth: from the growth and coalescence of 2D islands to the two-dimensional mechanism due to propagation of the monoatomic steps. The conclusion was supported by changing the mode of oscillations of the RHEED specular beam.

The germanium on silicon heterosystem is an ideal object for studying the heteroepitaxial growth and the 2D to 3D growth mode transition (the Stranski–Krastanow mechanism). The silicon structures with germanium quantum dots is of interest to practical optoelectronic applications due to their potential covering the regions from IR through the wavelengths used in fiber-optic communications.

Reflection high-energy electron diffraction (RHEED) is the most used technique in MBE. This technique enabled oscillations of the in-plane lattice constant to be detected for the Ge film growing according to the 2D mechanism on the silicon surface. There are available numerous papers that report studies of early stages of Ge growth on the Si(100) surface but only few data on the influence of deposition parameters on the wetting layer thickness. The growth of pure Ge on the Si(100) surface is described in most detail in Refs. [1, 2]. The phase diagram of the morphological state of Ge films on the Si(100) surface was obtained, the explicit dependence of the wetting layer thickness on temperature being not discovered though. Probably, this was because the attention was mainly paid there to boundaries of the formation of variously shaped islands.

A Katun-C MBE installation equipped with two electron beam evaporators for Si and Ge was used for synthesis. Diffraction patterns were monitored during the growth using a CCD camera on line with PC. The software allowed both the whole images and chosen fragments of the diffraction patterns to be monitored at the rate of 10 frames/s. Ge grew at the rate of 0.3-10 ML/min, temperature was varied from 250 to 700 °C.

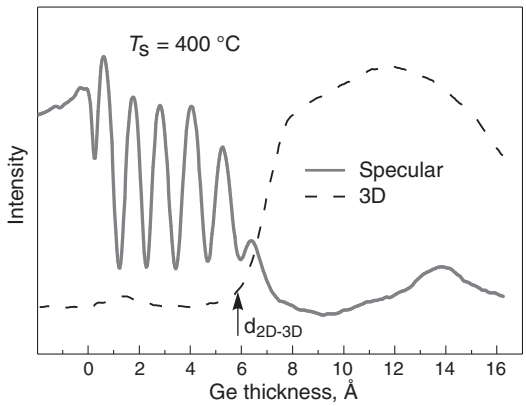

Fig. 1. Variations of the profile intensity along zero spot in the diffraction pattern in the course of the Ge layer growth on the Si(100) surface.

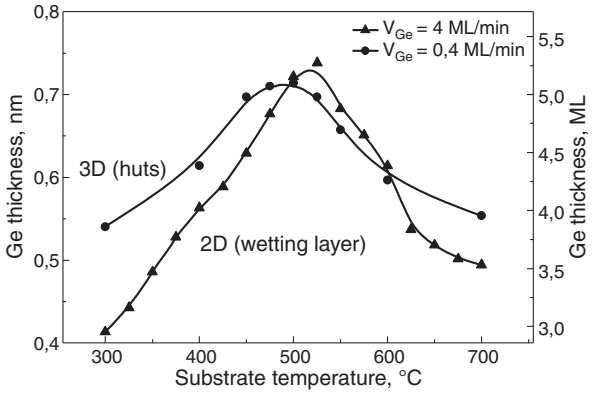

Fig. 2. Wetting layer thickness versus substrate temperature and growth rate.

As the thickness of the deposited layer increases, elastic strains induced by mismatching of the Si and Ge lattice constants also increase. Starting with some critical thickness, the 2D to 3D transition is observed, a part of strains being relaxed that is energetically favorable due to a decrease in the free energy of the system. Fig. 1 shows variations in the profile intensity along zero reflection in the diffraction pattern in the course of the Ge layer growth on the Si(100) surface. Along with oscillations of the specular reflection, a three-dimensional reflection becomes observable at a certain moment of time. The point of 2D to 3D transition is detected at an abrupt increase in the signal of 3D object towards the specular reflection in the diffraction pattern.

Thus, identifying the moment of 2D to 3D transition at various temperatures in the range of 300–700 °C allowed the wetting layer thickness to be determined as a function of temperature and growth rate [see Fig. 2]. This is a non-monotone dependence with the maximum at 500 °C. Parts of adatoms, due to their low mobility at low temperatures, do not reach edges of 2D islands that continue to grow by filling in the next monolayer on the 2D island surface. When so, multilevel islands may form to cause the high surface roughness and transform further into "hut"-clusters. When the temperature rises, the density of the multilevel islands (and, as a result, surface roughness) decrease that leads to an increase in the wetting layer thickness. As the temperature approaches 500 °C, the process is accompanied by the appearance of intensity oscillations of the RHEED electron specular beam. Oscillations of the maximal intensity and period number fall into the range of maximum in Fig. 3. The further elevation of the growth tem-

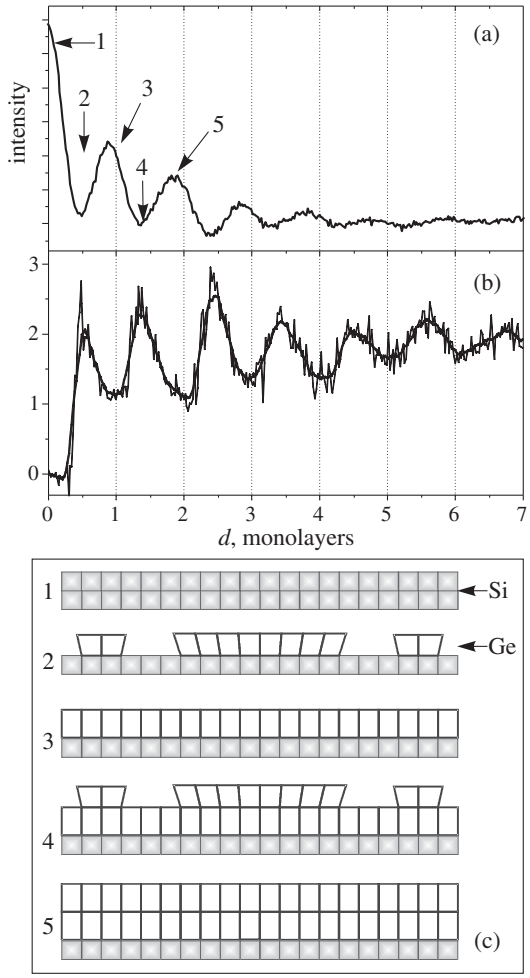

Fig. 3. Variations in specular beam intensity (a) and in-plane lattice constant (b) during growth of Ge film on Si(100). (c) — schematic representation of variations of in plane lattice constant.

perature leads to a progressive decrease in the thickness related to the 2D–3D transition. The observed gradual fading of oscillations of the specular reflection indicates the transition of the two-dimensional growth mechanism due to the growth and coalescence of 2D islands to the two-dimensional mechanism due to propagation of the monoatomic steps. It is shown [3] that the two-dimensional islands can deform to increase the relaxation of elastic strains (Fig. 3). The in-plane constant oscillates in the same manner as the specular beam intensity but is half period shifted. Variations in the in-plane lattice constant at the stage of 2D growth are caused by elastic deformation of edges of two-dimensional islands. A decrease in the density of the two-dimensional islands results in a decrease in the relaxation degree that is the reason for a decrease in the observed thickness related to the transition from 2D to 3D growth mechanism. The further temperature elevation results in a complete transition to the growth mechanism by step propagation. In this case the stains can only relax at the step edges but their density change only slightly with temperature.

Experimental studies were carried out both at low and at high growth rates. The changes follow the same way but the bend point shifts towards low temperatures in the plot as the rate decreases. The reason is that the molecular beam flux is lower at a low rate. Hence, the surface diffusion path lengthens and the transition to the step propagation mechanism is observed at a lower temperature. The shift of the bend point upon variations in the growth rate indicates the validity of the suggested interpretation of the non-monotone temperature dependence of the wetting layer thickness.

Acknowledgements

This work has been supported by the Russian Foundation for Basic Research (Grants Nos. 09-02-01262 and 08-02-92008).

References

[1] A. I. Nikiforov, V. A. Cherepanov, and O. P. Pchelyakov, *Mat. Sci. Engineering B* **89**, 180 (2002).
[2] V. Cimalla, and K. Zekentis, *Phys. Rev. Lett.* **77**, 1452 (2000).
[3] O. P. Pchelyakov, V. A. Markov, A. I. Nikiforov, and L. V. Sokolov, *Thin Solid Films* **306**, 299 (1997).

17th Int. Symp. "Nanostructures: Physics and Technology"
Minsk, Belarus, June 22–26, 2009
© 2009 Ioffe Institute

Properties of floating gate capacitors with incorporated Ge nanoclusters: effect of oxidation ambient

Andrei G. Novikau and Peter I. Gaiduk
Belarusian State University, prosp. Nezavisimosti, 4, 220030, Minsk, Belarus

Abstract. A 2D layer of spherical, crystalline Ge nanodots embedded in SiO_2 was formed by low pressure chemical vapor deposition combined with furnace oxidation and rapid thermal annealing. The samples were characterized structurally by using transmission electron microscopy and Rutherford backscattering spectrometry, as well as electrically by measuring CV and IV characteristics. It was found that formation of a high density Ge dots took place due to Ge segregation induced by oxidation. Strong evidence of oxidation ambient effect on charge storage in crystalline Ge-nanodot layer is demonstrated by the hysteresis behavior of the high-frequency CV curves.

Introduction

Group IV element nanoclusters (NCs-Si, Ge) embedded in SiO_2 have attracted much attention due to possible applications in integrated optoelectronic devices and high density nonvolatile memories [1,2]. It has been shown that such NCs contained in thin gate oxides exhibit charge storage effect with nonvolatile or DRAM-like memory behaviour [3,4]. Due to discrete charge traps, the use of a floating gate composed of isolated nanodots reduces the problems of charge loss encountered in conventional flash memories. Thus, it is possible to achieve the lower operating voltages, better endurance and faster write/erase speeds by using thinner injection oxides.

Self-assembling of silicon or germanium NCs in SiO_2 layers fabricated by low-energy ion implantation and different deposition techniques has been studied by several groups [5–8]. A strong memory effect in MOS devices using oxides with such NCs was reported [5,7]. However, implantation of Ge at the silicon — tunnel oxide interface creates trap sites and results in degradation of device performance [5]. The growth technique, using MBE deposition of 0.7–1 nm thick Ge layer, followed by rapid thermal processing was implemented in [9,10]. An alternative method for Ge NCs production has been recently proposed [11]. The method utilizes the following steps: low pressure chemical vapor deposition (LPCVD) of thin SiGe layer, thermal wet or dry oxidation, and thermal treatment in inert ambient (reduction). The oxidation step seems to be the most important in this approach as it determines the efficiency of Ge segregation and formation of Ge NCs. In this paper an effect of oxidation ambient is investigated.

1. Experimental

Wafers of n-type (001) Si were used as substrates. The uniform SiO_2 layer of 6-nm-thick (tunnel oxide) was first grown in a dry oxygen ambiance. A SiGe layer of 22-nm-thick was then deposited in LPCVD chamber at 560 °C. The sandwiched $SiGe/SiO_2/Si$ samples were thermally oxidized in either wet or dry oxygen ambiance at 850–900 °C for 10–90 min; i.e. at the temperature lower than Ge melting point (937 °C). Finally, thermally oxidized structures were heated in dry nitrogen ambient at 900 °C for 30 s. A reference sample of 6-nm-SiO_2/Si with no incorporated Ge NCs was prepared for comparison.

The structures were investigated by transmission electron microscopy (TEM) in plan-view and cross-section geometries with a Philips CM20 instrument operating at 200 keV. The composition and structure of the samples were measured by Rutherford backscattering spectrometry (RBS) using a 1.0–1.5 MeV He^+ beam and the spectra were analyzed by the RUMP program. Aluminium gates (area 500×500 μm^2 and separation distance of 100 μm between the neighbouring capacitors) have been fabricated for high-frequency capacitance-voltage (CV) measurements.

2. Results and discussion

The RBS and XTEM investigations of as grown and thermally oxidized samples testify the segregation process and the Ge pile up at the SiO_2/SiGe interface. An oxidation process might be described in terms of classical theory of binary alloy oxidation. The comparative analysis of RBS data (not shown here) reveals that Ge segregation depends on oxidation ambient. In particular, neither evaporation nor diffusion of Ge in SiO_2 layer takes place during thermal oxidation in *dry* O_2. On the contrary, *wet* oxidation results in strong loss (about 30%) of Ge from the SiO_2 layer, probably because of evaporation.

The results of plan-view TEM investigations correlate well with RBS data. Spherical and well-separated Ge clusters embedded in the SiO_2 layer are clearly observed after thermal treatment (inset in Fig. 1). Average size and aerial density of Ge NCs were obtained from plan-view and cross-section bright-field images and estimated to be 4–20 nm and 2×10^{11} cm^{-2}

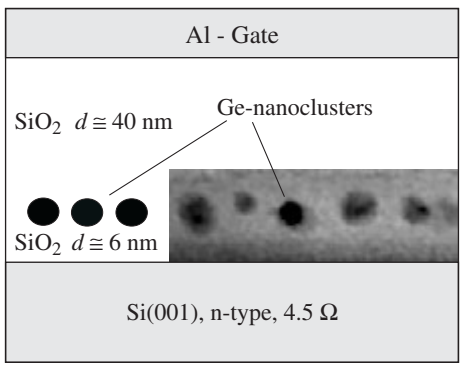

Fig. 1. Sketch of MOS capacitor prepared for CV and IV measurements. The inset shows bright field XTEM microphotograph of the Ge NCs embedded into SiO_2.

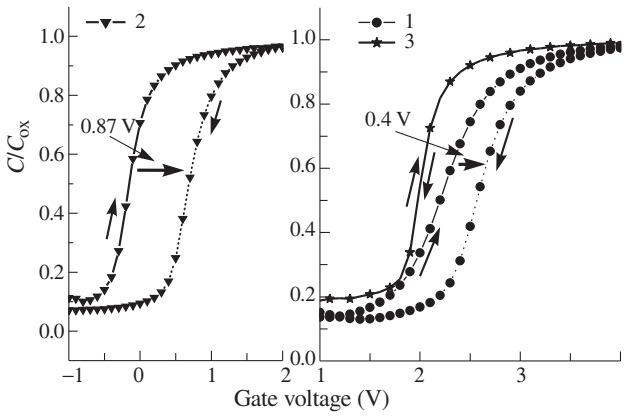

Fig. 2. High-frequency capacitance vs voltage curves of samples, oxidized: (1) — in *wet* O_2 at 850 °C for 25 min, (2) — in *dry* O_2 at 850 °C for 60 min. Oxidation step is followed by reduction at 900 °C for 30 s in N_2. The CV curve from reference sample of pure SiO_2 is shown (3).

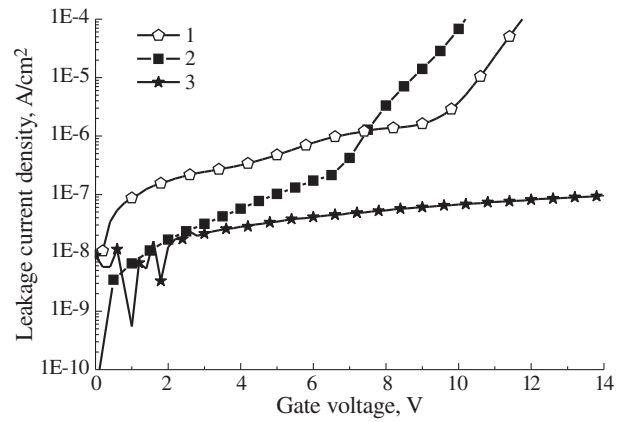

Fig. 3. Leakage current vs gate voltage characteristics obtained from wafers oxidized in either wet (1) or dry (2) conditions at 850 °C. The IV curve from reference sample of pure SiO_2 is shown (3).

respectively. The conditions of oxidation and reduction were optimized taking into account Ge segregation via the Si/SiO_2 interface, dot density $<10^{12}$ cm^{-2} and the largest possible charge storage capability.

The influence of oxidation ambient on efficiency of charge storage was studied by high-frequency CV measurements. The difference in hysteresis values of the CV characteristics was found for the structures, oxidized in wet and dry O_2 (Fig. 2). The maximum voltage shift was obtained in *dry* O_2 oxidation ambient and was measured to be 0.87 V for $V_g = 5$ V. On the contrary, it's clearly observed, that in the case of *wet* oxidation the maximum value is less then 0.4 V. High positive gate voltages force the CV curves to be shifted in the direction of stored negative charges. The charge trapping occurs through electron injection from the substrate into the oxide. Increasing of V_g sweep up to 5 V resulted in a gradual increase of the flat-band voltage shift. No flat-band voltage shift was observed for the reference sample prepared from wafer with pure SiO_2, oxidized at 850 °C for 60 min in O_2 ambiance. Thus, we assume that the effect of charge storage is Ge NCs related.

One of the major reasons for loss of charge in floating gate structures is leakage current. The measured IV curves from wafers oxidized in both wet and dry ambient are shown on Fig. 3. It's observed that the dry oxidation leads to almost one magnitude less leakage current at $V_g = 5$ V, than that of the wet oxidation samples. Typical value of leakage current for the dry oxide containing Ge NCs is measured to be at the level of 10^{-7} A/cm^2. We suppose that low value of leakage current was achieved due to high quality dry thermal growth of both tunnel and capping oxides compared to the deposited oxides, used in the other methods of MOS capacitor formation [12].

Acknowledgements

This work is a part of the Belarusian Scientific Research Program "Electronics" and is funded as Electornics 1.06 projekt.

References

[1] L. Rebohle *et al*, *Appl. Phys. B* **71**, 131 (2000).
[2] Y. H. Kwon *et al*, *Appl. Phys. Lett.* **80**, 2502 (2002).
[3] S. Tiwari *et al*, *Appl. Phys. Lett.* **68**, 1376 (1996).
[4] S. Tiwari *et al*, *Appl. Phys. Lett.* **69**, 1232 (1996).
[5] P. Normand *et al*, *Appl. Phys. Lett.* **83**, 168 (2003).
[6] V. Beyer *et al*, *Phys. Rev. B* **77**, 014107 (2008).
[7] T. Baron *et al*, *Appl. Phys. Lett.* **83**, 1444 (2003).
[8] W. K. Choi *et al*, *Appl. Phys. Lett.* **80**, 2014 (2002).
[9] A. Kanjilal *et al*, *Appl. Phys. Lett.* **82**, 1212 (2003).
[10] A. Kanjilal *et al*, *Appl. Phys. A* **81**, 363 (2005).
[11] A. G. Novikau *et al*, *Proc. of ICMNE* **O3–O2** (2007).
[12] Zerlinda Tan *et al*, *Appl. Phys. Lett.* **86**, 013107 (2004).

17th Int. Symp. "Nanostructures: Physics and Technology"
Minsk, Belarus, June 22–26, 2009
© 2009 Ioffe Institute

Fabrication of functional tungsten films on silicon by CVD-process: structural self-organization of the nanosystem and process optimization

S. V. Plyushcheva, A. V. Andreeva, G. M. Mikhailov and L. G. Shabelnikov
Insitut of Microelectronic Technology RAS, 44221 Chernogolovka, Russia

Abstract. It was discovered that the selflimited sublayer (20 nm) of W_5Si_3 silicide was formed on the W/Si interface at CVD-process as a result of the system self-organization. The self-organization processes in reaction zone are applied to optimization of CVD-method of fabrication of thin tungsten films with high adhesion and the specific resistivity 8×10^{-6} Ωcm.

Introduction

The employment of tungsten as a current-carrying material for metallization of ICs is of growing interest owing to its unique properties; as electronic devices become smaller, this material continues to withstand progressively greater current densities. Despite the fact that a tungsten layer has higher electrical resistance than an aluminum layer, in the production of semiconductor ICs the former offers a number of advantages to the process of metallization [1].

Tungsten films are to a smaller degree prone to electromigration, and they differ but little in their thermal-expansion coefficient from silicon and silica, which are most often used in technology. Knowledge of the basic laws that govern film-substrate interface interactions in the specific structures and feasibility of control over these processes with the use of various growth methods and different film growth conditions serve as a physical foundation in the manufacture of electronic devices. Moreover, the conditions at the interlayer boundary, by and large, dictate the useful life of the devices.

The main difficulty in fabricating film microstructures lies in spalling of metal layers. The film formed should have a good adhesion to silicon and chemical changes during a long on time the interface film-substrate should be minimal.

The aim of this work is to optimize the chemical vapor deposition (CVD) technique by matching it with the processes of internal structural self-organization of system. This allow to obtain high-conducting, structurally stable nanostructures of refractive metals on Si substrates.

1. Experimental

The films were prepared by [2]:

1) chemical vapor deposition of W via hydrogen reduction of WF_6;
2) the same CVD process with plasmachemical and RF stimulation of hydrogen;
3) magnetron sputtering of W layers.

The interaction of silicon and tungsten was investigated by thin film X-ray diffraction.

2. Results

It was found that the silicide W_5Si_3 forms on the interface at W chemical vapor deposition onto silicon. The absence of W_5Si_3 on the films prepared by magnetron sputtering and chemical vapor deposition of W onto a SiO_2 substrate suggests that W_5Si_3 is formed by the reaction:

$$WF_6 + Si \Rightarrow W_5Si_3 + SiF_4.$$

It was found that the thickness of the W_5Si_3 sublayer self-formed during CVD-process did not exceed 20 nm irrespective to the upper tungsten film thickness. This nanometer self-limited W_5Si_3 sublayer structurally correlates both with W and Si and acts as an adhesion promoter and efficient diffusion barrier. The presence of this sublayer leads to the system stabilization and the formation of high quality functional structure.

The observed regularities are related to the process of structure self-organization and are determined by the composition and relations of WF_6-Si-H in the reaction zone [3]. The energy nanosystem stabilization and formation of low-energy coherent interfaces are driving forces of the CVD-process.

Interface design methods, thermodynamic considerations and analysis of self organization processes of reaction zone are applied to optimization of chemical vapour deposition of thin tungsten films on silicon substrate.

As a result a procedure to fabricate high-conductivity, structurally stable, chemically and thermally stable tungsten thin films of high adhesion and resistivity 8×10^{-6} Ωcm was developed.

References

[1] V. Kireev, A. Stolyarov, *Microelectronics technologies. Chemical vapor deposition.* Moscow, Technosfera, 2006, 190.
[2] S. V. Plyushcheva, G. M. Mikhailov, L. G. Shabelnikov, S. Yu. Shapoval, *Inorganic Materials* **45** 2, 140–144 (2009).
[3] S. V. Plyushcheva, A. V. Andreeva, *Advanced materials* (in publishing).

17th Int. Symp. "Nanostructures: Physics and Technology"
Minsk, Belarus, June 22–26, 2009
© 2009 Ioffe Institute

Formation and optical properties of bimetallic nanoparticles of noble metals in thin film oxide matrices

G. P. Shevchenko[1], L. T. Potapenko[1], Yu. V. Bokshits[1], S. V. Vashchenko[2] and G. E. Malashkevich[2]

[1] Physico-Chemical Research Institute, Belarusian State University, Minsk, Belarus
[2] B. I. Stepanov Institute of Physics, NASB, Minsk, Belarus

Abstract. The processes of forming bimetallic nanoparticles of noble metals (Ag-Au) in thin film oxide matrices upon air-heating were investigated. Optical properties of the bimetallic nanoparticles formed, their structure, sizes and stability to oxidation were found to be substantially governed by the matrix ability to interact with the bimetallic nanoparticles forming. On doping the films with europium ions, Eu^{3+} luminescence is observed to be sensitized, the effectiveness of the sensitization being governed by the nature of the oxide matrix.

Introduction

Metal nanoparticles in various dielectric matrices are nowadays the subject of intensive studies in the context of fundamental scientific problems and the prospects of using this sort of materials in different fields of technique and technology. The interest in producing nanoparticles of noble metals such as silver, gold, palladium etc. in oxide matrices is due to nonlinear optical properties demonstrated by composites of this kind [1,2]. Nanocomposite "bimetal-oxide" systems are even more promising, the nonlinear optical properties being closely related to the frequency of surface plasmon resonance (SPR) of metals, and the presence of two metals in different molar ratios results in a shift of SPR frequency and thus in nonlinear optical properties of the system being modified. In addition, an increase in the intensity of luminescence of europium ions was observed in GeO_2-Eu_2O_3-Ag-Au films [3].

The present work was aimed at the investigation of the processes of forming bimetallic nanoparticles of noble metals in thin film oxide matrices upon air-heating and of the influence of the matrix nature on their optical and spectral-luminescent properties.

1. Experimental

The films in hand were formed by spin-coating the oxide Al_2O_3, GeO_2, SiO_2, SiO_2-GeO_2 sols doped with silver and gold ions layer-by-layer onto quarz substrates, each layer being air-dried at 150–300 °C for 5 min, and successively annealed at temperatures ranging from 300 to 900 °C (30 min at each of the temperatures) [4].

Optical absorbance spectra were registered in the wavelength range from 300 to 800 nm using the two-beam spectrophotometer (SPECORD M 40 UV-Vis). The luminescence and luminescence excitation spectra were obtained using an SDL-2 spectrofluorimeter. Luminescence spectra were excited at $\lambda = 280$ nm, and luminescence excitation spectra were recorded at $\lambda = 615$ nm. All spectral measurements were performed at 298 K. To determine the size and shape of the particles by TEM method, an instrument EM-125 K was used.

2. Results and discussion

For the systems SiO_2-Ag-Au, GeO_2-Ag-Au and SiO_2-GeO_2-Ag-Au on air-heating in the temperature range from 300 to 400 °C nanoparticles of Ag-Au alloys are formed, as evidenced by a broad plasmon band appearing in optical spectra, which is intermediate ($\lambda_{max} = 470$–490 nm, depending on the matrix nature) between the plasmon bands of nanoparticles of the individual metals (Fig. 1a). Heating the films in the temperature range 500–600 °C presumably results in silver oxidation in the alloy to give silver silicate and (or) germanate. Their thermolysis at 700 °C for SiO_2-Ag-Au and SiO_2-GeO_2-Ag-Au and at 900 °C for GeO_2-Ag-Au films causes silver nanoparticles to form, which shows up in absorbance spectra of the films as a double-peak feature with the maxima characteristic for the plasmon absorption of individual silver and gold nanoparticles. According to electron microscopic data, the particle sizes in the films range from 10 to 50 nm, depending on the heating temperature.

Neither Ag-Au alloy nanoparticles nor individual silver nanoparticles are observed to form in Al_2O_3-Ag-Au system. In absorbance spectra of these films, no matter what the heating temperature up to 900 °C, an absorption band characteristic of gold nanoparticles is registered, the position of the maximum changing to only a small extent from 525 to 540 nm (Fig. 1b). The size of the nanoparticles forming grows from 15 to 40 nm with temperature.

When SiO_2-Ag-Au and GeO_2-Ag-Au films are doped with europium ions on heating at 900 ° C, the luminescence intensity of Eu^{3+} ions is substantially increased (Fig. 2), due to complex optical centers being formed, which include Eu^{3+} ions, Ag^+ ions and/or oligomeric silver clusters Ag_m^{n+} located on the surface of Ag-Au alloy nanoparticles.

In samples based on Al_2O_3, silver ions are strongly bound with the oxide matrix, and only gold nanoparticles are present in the film at all heating temperatures. No optical centers responsible for effective sensitization of europium ion luminescence are therefore formed.

The present results allow one to conclude that the formation processes and properties (optical ones, particle sizes, stability to oxidation) of bimetallic nanoparticles in oxide systems upon air-heating are substantially determined by the chemical nature of oxide matrices. Thus in SiO_2 and GeO_2 films either individual metal nanoparticles (Ag,Au) or bimetallic Ag-Au alloy ones are formed, depending on the heating temperature. It is due to the chemical transformations proceeding in these systems at different temperatures: low-temperature decomposition of

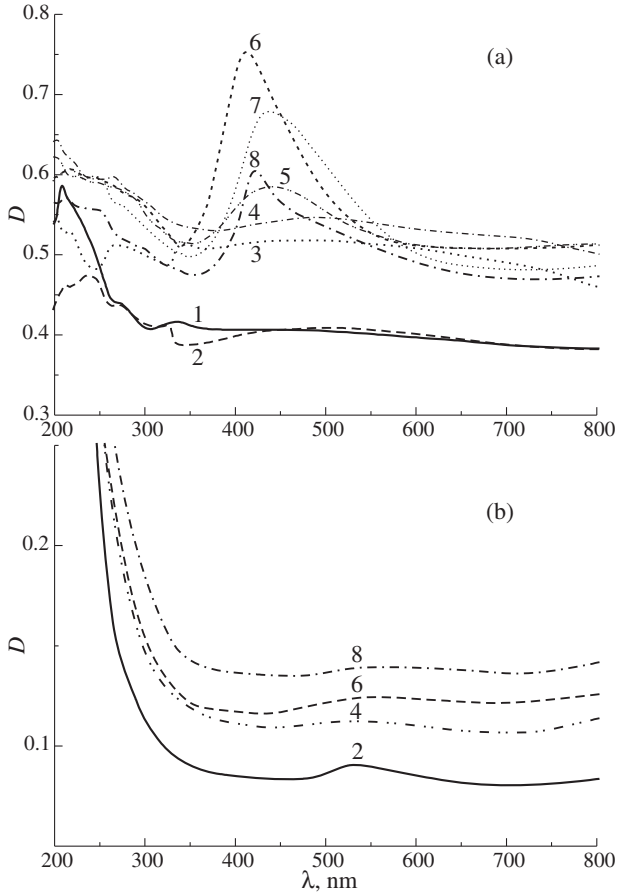

Fig. 1. Optical absorbance spectra for the films (mol.%) 89.7SiO_2-10Ag-0.3Au (a) and 89.7Al_2O_3-10Ag-0.3Au (b), air-heated at the temperatures, °C: 150 (1), 300 (2), 400 (3), 500 (4), 600 (5), 700 (6), 800 (7), 900 (8).

the initial metal compounds with the formation of bimetallic Ag-Au alloy nanoparticles in SiO_2(GeO_2)-Ag-Au films; subsequent high-temperature oxidation of silver in the alloy and silver interaction with the oxide matrix to give silver germanate (silicate) phases, followed by thermolysis of the latter yielding silver and the oxide. The silver nanoparticles formed are stable to subsequent oxidation, being incapsulated by the oxide. Au nanoparticles are more stable to oxidation and thus do not interact with the matrix. The absence of silver nanoparticles in Al_2O_3-Ag-Au films throughout the temperature interval is due to strong Al-O-Ag bonds formed on the stage of their formation, preventing silver from being separated as an individual phase.

The formation of metallic nanoparticles in oxide films was also found to affect the structural-phase transformation of the matrix itself, reducing the temperatures of tetragonal GeO_2, α-quarz, cristobalite and γ-Al_2O_3 formation.

The increased intensity of luminescence of europium ions in Eu-containing oxide films with Ag and Au nanoparticles makes them promising for development of new laser active media, fluorescent displays and sensors.

Acknowledgements

The work is supported by the Belarus Foundation for Basic Research (project Kh08D-002).

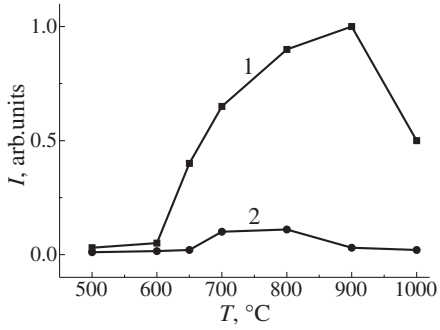

Fig. 2. Integrated luminescence intensity of Eu^{3+} versus the temperature of heat treatment for the films (mol.%): 79.7GeO_2-10Eu_2O_3-10Ag-0.3Au (1) and 79.7Al_2O_3-10Eu_2O_3-10Ag-0.3Au (2), λ_{ex} = 280 nm.

References

[1] P. Mazzoldi *et al*, *J. Nonlin. Opt. Phys. Mat.* **5**, 285 (1996).
[2] R. Magruder *et al*, *J. Non-cryst. Sol.* **176**, 299 (1994).
[3] G. E. Malashkevich *et al*, in *The 2nd International Conference on Physics of Laser Crystals*, Yalta, Crimea (2005), p. IOT4.
[4] G. P. Shevchenko *et al*, in: *Chemical problems of development of new materials and technologies*, Iss. 3, ed. by O. A. Ivashkevich (BGU, Minsk), 10–23 — in Russian.

17th Int. Symp. "Nanostructures: Physics and Technology"
Minsk, Belarus, June 22–26, 2009
© 2009 Ioffe Institute

Initial stage of semiconductor nanowire growth: theory and experiment

N. V. Sibirev[1], V. G. Dubrovskii[1, 2], G. E. Cirlin[1, 2, 3], Yu. B. Samsonenko[1, 2, 3] and M. V. Nazarenko[1]

[1] St Petersburg Physical Technological Center for Research and Education RAS, 194021 St Petersburg, Russia
[2] Ioffe Physical-Technical Institute, St Petersburg, Russia
[3] Institute for Analytical Instrumentation RAS, 190103 St Petersburg, Russia

Abstract. We present a theoretical model for the initial stage of epitaxial growth of semiconductor nanowires by the so-called vapor-liquid-solid mechanism. It is shown that there are two characteristic diameters of drops, one relating to the drops lying on the substrate surface and another to the minimum diameter when the growth proceeds. The model also allows one to obtain the nanowire shape at the initial stage. Theoretical results are compared to the available experimental data on the Au-assisted molecular beam epitaxy of GaAs nanowires on the GaAs(111)B substrates at different growth conditions.

Semiconductor nanowires (NWs) have gained a continuously growing interest due to many promising applications in nanoelectronic, nanophotonic and nanosensing devices as well as from the viewpoint of fundamental physics of the growth processes. The generally accepted mechanism of NW formation is usually referred to as the vapor-liquid-solid (VLS) growth [1]. This VLS mechanism is promoted by a metal seed drop (e.g., Au) sitting at the NW top. The drop acts as a chemical or physical catalyst collecting semiconductor material from the vapor phase, the substrate and the sidewalls and thus facilitating the NW nucleation and growth from the liquid alloy. Despite a very impressive progress in NW epitaxial fabrication, many growth-related aspects in this field are not completely understood so far. In this work we study theoretically and experimentally the initial stage of NW formation, in particular, the critical size of the seed drop from which the NW would grow and the geometrical shape of NW foot.

There are two different reasons for the existence îf a minimal size of drop below which the NW would not grow: the Gibbs–Thomson (GT) effect [2,3] and the substrate overgrowth (SO) [4]. While considering the minimum drop size promoting the VLS growth, most authors study the drop already sitting on the NW top [2–5]. It is clear, however, that the contact angle of the drop on the NW top (α_0) and the contact angle of the drop on the substrate surface (α') are generally different. Corresponding SEM images in the case of Au-assisted molecular beam epitaxy (MBE) of GaAs NWs on the GaAs(111)B substrates are presented in Fig. 1. Since $\alpha' > \alpha_0$, the radius of the drop on the NW top (r') is less then the radius of the drop on the substrate (r_0). Under the simplifying assumption of a constant amount of Au and semiconductor materials in the both drops considered, the radius of the drop r at given contact angle α can be obtained from the equation

$$r = \sqrt[3]{3V/\pi f(\alpha)}. \qquad (1)$$

Here, V is the constant volume of the droplet, and

$$f(\alpha) = \frac{(1-\cos\alpha)^2(2+\cos\alpha)}{\sin^3\alpha}.$$

On the other hand, the Young's relation for the drop in the geometry shown in Fig. 2c yields $\gamma_{SV}\sin\beta = \gamma_{LV}\sin\alpha$ and

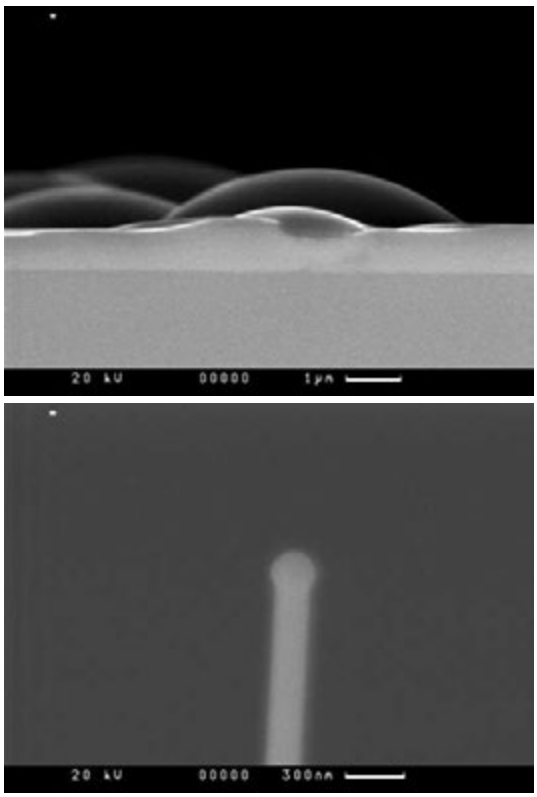

Fig. 1. SEM images of an Au-GaAs drop on the substrate surface (a) and on the top of the GaAs NW (b).

$\gamma_{SV}\cos\beta = \gamma_{LV}\cos\alpha + \gamma_{SL}$, with γ_{SV}, γ_{LV} and γ_{SL} as the surface energies of solid-vapor, liquid-vapor and solid-liquid boundaries, respectively. The angle β describes the sidewall inclination at the top. From geometrical considerations one obtains

$$\frac{dr}{dH} = -\frac{\cos\alpha + \gamma_{SL}/\gamma_{LV}}{\sin\alpha}, \qquad (2)$$

with H as the height of the nanowire. Comparing Eqs. (1) and (2), we arrive at the following equation for the NW shape:

$$\frac{d\alpha}{dH} = \frac{3f(\alpha)}{f'(\alpha)}\frac{\cos\alpha + \gamma_{SL}/\gamma_{LV}}{\sin\alpha}\sqrt[3]{\frac{\pi f(\alpha)}{3V}}. \qquad (3)$$

Numerical integration of Eq. (3) provides the NW shape $H(R)$. Typical shape for the parameters of Au-assisted MBE of GaAs

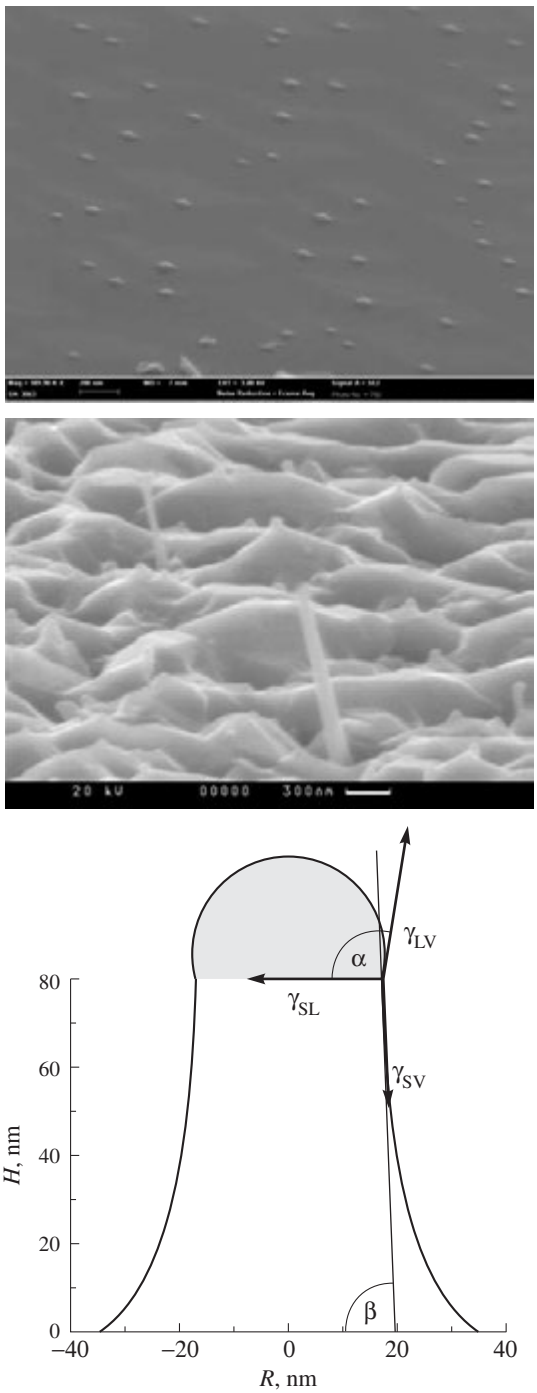

Fig. 2. SEM images of the floating drops on the GaAs surface (a); the shape of short GaAs NWs (b) and theoretical shape of the NW foot obtained from numerical solution of Eq. (3) for the parameters of the GaAs/GaAs(111)B-Au material system.

NWs on the GaAs(111)B substrate is presented in Fig. 2c.

The analysis of Eqs. (1) and (2) together with considerations for the size-dependent GT and SO effects gives numerical values of the two critical radii. The first critical radius relates to the drops that would be completely buried in the surface layer. The second critical radius describes the floating drops lying on the growing substrate surface. We present some numerical estimates for these critical radii in the case of Au-assisted MBE of GaAs NWs on the GaAs(111)B substrates. In particular, Fig. 2a presents the SEM images of such floating drops that would not initiate the vertical NW growth but, rather, lift up at a rate of the substrate. Fig. 2b demonstrates the initial shape of GaAs NWs which is in a qualitative agreement with theoretical calculations in Fig. 2c.

Acknowledgements

This work has been partially supported by the Russian Foundation for Basic Research.

References

[1] R. S. Wagner and W. C. Ellis, *Appl. Phys. Lett.* **4**, 89 (1964).
[2] L. E. Fröberg, W. Seifert and J. Johansson, *Phys. Rev. B* **76**, 153401 (2007).
[3] V. G. Dubrovskii, N. V. Sibirev, J. C. Harmand and F. Glas, *Phys. Rev. B* **78**, 235301 (2008).
[4] V. G. Dubrovskii and N. V. Sibirev, *Technical Physics Letters* **32**, 12, 1047,(2006).
[5] E. I. Givargizov and A. A. Chernov, *Crystallography*, **18**, 147 (1973).

17th Int. Symp. "Nanostructures: Physics and Technology"
Minsk, Belarus, June 22–26, 2009
© 2009 Ioffe Institute

Growth of GaAsN nanowhiskers by magnetron sputtering deposition

I. P. Soshnikov[1,2], G. E. Cirlin[1,2,3], A. M. Nadtochii[2], V. G. Dubrovskii[1,2], M. A. Bukin[4], V. A. Petrov[4], V. V. Busov[2] and S. I. Troshkov[2]

[1] St Petersburg Physics and Technology Centre for Research and Education RAS, St Petersburg, Russia
[2] Ioffe Physical-Technical Institute, St Petersburg, Russia
[3] Institute for Analytical Instruments of RAS, St Petesrburg, Russia
[4] St Petersburg State Polytechnical University, St Petersburg, Russia

Abstract. A possibility to grow of $GaAs_{1-x}N_x$ nanowhiskers (NW) with typical size from 10 to 200 nm in diameter and up to 3000 nm in length by magnetron sputtering deposition is demonstrated. Dependence of NW size on various parameters (size of initial catalytic particles, deposited rate, crystal orientation of substrate, growth temperature) is studied. It is found that the of length of the NW is inversionally proportional on their diameter showing a diffusion mechanism of NW growth. A composition of nitrogen up to 2.7% is reached at growth temperature from 400 to 500 °C. At the higher growth temperatures, a composition of nitrogen is reduced down to 0.3%.

Dependence of photoluminescence (PL) peak position on nitrogen composition and growth temperature is studied. The PL intensity of GaAsN NW is 5–10 times higher then for planar layer. The effect can be explained by dislocation free structure of NWs.

Solid solutions $GaAs_{1-x}N_x$ are perspective materials for many applications in opto-, micro-, and nanoelectronics [1–3]. However, the realization planar layers with low density of defects is hardly possible thus reduces potentials of the material use in devices [1–3]. Recently, F. Glas [4] show that heteroepitaxial NW having a diameter lower then critical may be grown without dislocations. This work is devoted to the investigation of the growth of GaAsN NWs by magnetron sputtering deposition on GaAs(111)B and Si(111) substrates.

Growth of GaAsN NWs is realized by the procedure described in detail in [5], which includes three stage: deposition of Au ultrathin film ($\sim$ 1 nm), formation of an array of disperse Au-Ga seeds and the formation of GaAsN NWs by sputtering of GaAs target in Ar-N_2 magnetron plasma in VUP-5M setup. The substrates used are industrial polishing epiready GaAs (111)B and Si(111) wafers with thickness 350–450 μm and different doping. For GaAs target, industrial GaAs wafers AGCHO having Sn doping $n \sim 10^{18}$ cm^{-3} is used. A mixture of Ar-N_2 with a ratio of 70:30 is used as a working gas. Purity of the materials (gases and Au) is better then 99.99%.

Surface morphology of the samples is investigated by scanning electron microscope CamScan 4-90FE. The excitation of PL is realized by YAG:Nd-laser with a wave length $\lambda = 532$ nm and total power of order of 330 mW. PL spectra are registered by a cooling InGaAs detector.

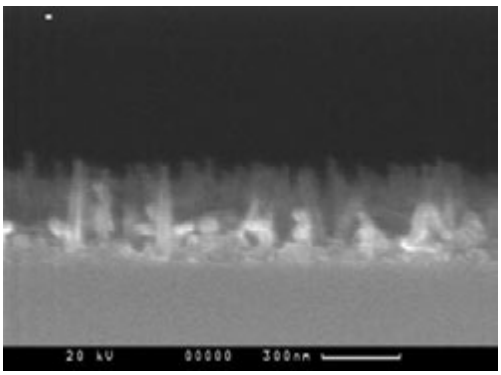

Fig. 1. Electron micrograph of surface morphology with GaAsN nanowhiskers grown on GaAs(111)B.

The typical morphology with GaAsN NWs on GaAs (111)B surface is presented on Fig. 1. The nanowhiskers are mostly oriented along (111)B direction. The density of nanowhiskers varies on different samples (dependently on the growth conditions) in the range between 10^7 and 10^9 cm^{-2}.

The typical size of GaAsN NWs is varied from 100 to 2000 nm in length and about 50 nm in diameter close to the base. The diameter near the top of NWs is varied from 10 to 60 nm.

On our case, the typical length is proportional to the total amount of the material deposited and may exceed up to 10 times then the mean thickness. As a result, we observe diffusion — induced mechanism of NW growth [6]. Fig. 2 demonstrates typical dependence of the NWs length on their diameter, showing a inverse proportional behavior [6]. Increasing of deposition rate from 0.5 to 2 ML/s leading to the formation of texture layer, which may be explained be a significant radial growth of NWs at low of diffusion length [6,7].

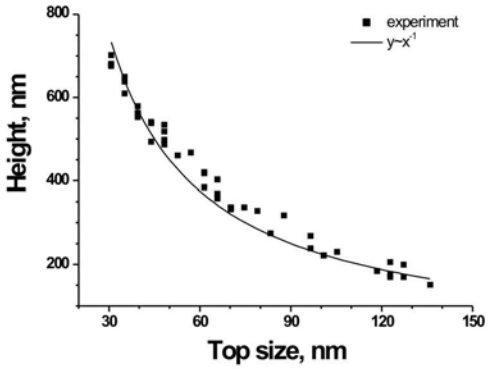

Fig. 2. Interdependence of length on diameter of GaAsN nanowhiskers grown on GaAs(111)B by magnetron sputtering deposition at $T = 470$ °C $v = 0.4$ ML/s $t = 150$ nm.

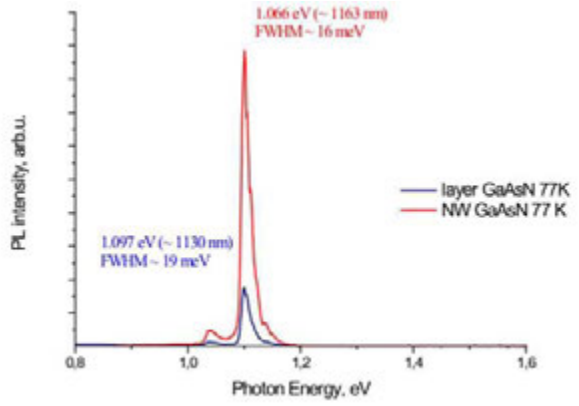

Fig. 3. PL spectra of samples with GaAsN planar layer and GaAsN nanowhiskers grown on GaAs(111)B by magnetron sputtering deposition $T = 470$ °C $v = 0.4$ ML/s $t = 150$ nm.

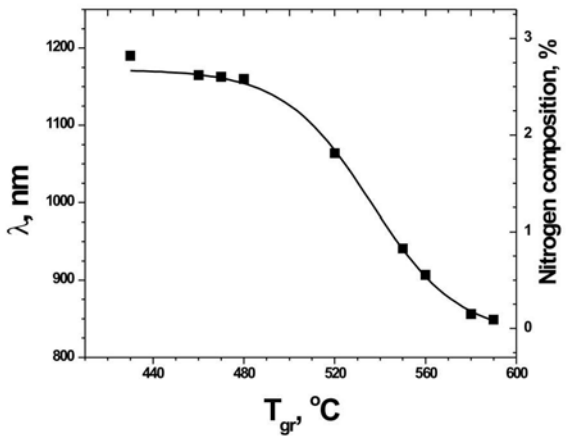

Fig. 4. Dependence of PL peak position of GaAsN nanowhiskers at 77 K on growth temperature.

At growth temperature about 560 °C we find cone habitués of the nanowhiskers. Further increasing of the growth temperature up to 585 °C leads to the formation of droplets on the surface. This behavior is explained by the effective escape of the adatoms from nanowhiskers surface [8].

Typical photoluminescence spectrum from an array of GaAsN NWs is given in Fig. 3. The PL peak in the range 1.0–1.2 eV is found for samples grown at temperature of 400–500 °C thus having different nitrogen content. FWHM of the peaks is about 40–60 nm at room temperature and 10–20 nm at 77 K. The peak position is weakly dependent on material and crystal orientation of the substrate. Estimation of the nitrogen composition gives 2.7% [1,2]. The increasing of growth temperature up to 550–570 °C leads to the shift of Pl peak to 1.3 eV, corresponding to the nitrogen composition $x \sim 0.5\%$ [1,2]. Comparison of PL spectra for NWs and planar layers grown separatively shown that spectral position is the same for the same N content. At the same time, the intensity of GaAsN peak from NWs is 5–10 times larger. This effect may be attributed to the reducing of the density of non-radiative defects (dislocations) and higher luminescence efficiency for the structures having larger surface area [9].

To conclude, we have demonstrated the possibility to grow a $GaAs_{1-x}N_x$ ($x = 0$–3%) nanowhiskers using magnetron sputtering deposition. It is shown that growth of the nanowhiskers proceeds via diffusion-induced growth mechanism. We have found that nitrogen composition is stable at growth temperature from 400 up to 500 °C and may exceed 2.7%. Reducing of nitrogen composition (down to 0.5%) is typical for higher growth temperatures (530–600) °C. PL intensity of an array of GaAsN NWs is higher ~10 times in comparison with planar layers having similar N content.

Acknowledgements

The work is supported by RFBR, and program of RAS of "Quantum nanostructures", and "Quantum macrophysics". Authors are greatly S. I. Troshkov and V. V. Busov for SEM examination of samples.

References

[1] I. A. Buyanova *et al*, *MRS Internet J. Nitride Semicond. Res.* **6**, 2 (2001).
[2] M. Henini (Ed.), *Dilute Nitride Semiconductors*, 630 p., 2005.
[3] I. P. Soshnikov and J. Chi *et al*, *Semicond. Sci. Technol.* **19**, 501 (2004).
[4] F. Glas, *Phys. Rev. B* **74**, 121302(R) (2006).
[5] I. P. Soshnikov, *Tech. Phys. Lett.* **31**, 35 (2005).
[6] G. E. Cirlin *et al*, *Semiconductors* **39**, 587 (2005).
[7] V. G. Dubrovskii *et al*, *Phys. Rev. B* **71**, 205325 (2005).
[8] L. L. Chang and K. Ploog (Eds.) *Molecular Beam Epitaxy and Heterostructures*, (Springer) 728 p., 1985.
[9] D. Harvey, *Modern Analytical Chemistry*, (Boston:McGraw-Hill) 798 p., 2000.

17th Int. Symp. "Nanostructures: Physics and Technology"
Minsk, Belarus, June 22–26, 2009
© 2009 Ioffe Institute

Ultrathin α-MoO_3 nanobelts: synthesis, micromorphology and structure

I. B. Troitskaia, *V. V. Atuchin*, T. A. Gavrilova and L. D. Pokrovsky
Institute of Semiconductor Physics, SB RAS, Novosibirsk, Russia

Abstract. Ultrathin α-MoO_3 nanobelts are obtained under the $T = 450$ °C treatment of molybdenum formate precursor crystals. The final product has been characterized by the X-ray diffraction (XRD), scanning electron microscopy (SEM) and transmission electron microscopy (TEM) methods. The obtained nanobelts were as thin as 10 nm and had the length of 10 μm and width of 200 nm. The model of $HCOOMo_4O_{12}OH \rightarrow \alpha$-$MoO_3$ transformation has been proposed on a basis of experimental results obtained by differential thermal analysis (DTA), IR- and Raman spectroscopies of precursor crystals and α-MoO_3 nanocrystals.

Introduction

Fabrication of non-isotropic materials both as a nanosized crystals [1,2] and as an two-dimencional subjects [3,4] is of interest in modern material science. It is caused by the not uniform properties of such materials on an direction which would become stronger owing to nano range. The orthorhombic α-MoO_3 phase possesses a strongly anisotropic layered structure formed by bilayers consisting of two sheets of MoO_6 octahedra stacked by Van der Vaals forces [5]. This phase is suitable for use as a sensing material for different gases [6], cathode material in batteries [7], conductive glass-fiber, catalyst [8] and many other. Wide range of applications leads to numerous efforts to prepare nanosized α-MoO_3 by such methods as vapor deposition [9], calcination under various conditions [10] and hydrothermal method [11]. In this study the preparation way of ultrathin α-MoO_3 nanobelts is presented. The structural and morphologic characteristics of the crystals obtained are established and transformation model from precursor crystals to final product is determined.

1. Experimental

Samples of α-MoO_3 nanobelts shown on Fig. 1 were fabricated by annealing of molybdenum formate precursor crystals under $T = 450$ °C during 3 hour. As a result the white crystals were formed. Their dimensions were of up to 10 μm length, 200 nm width and 10 nm thickness. White precursor crystals

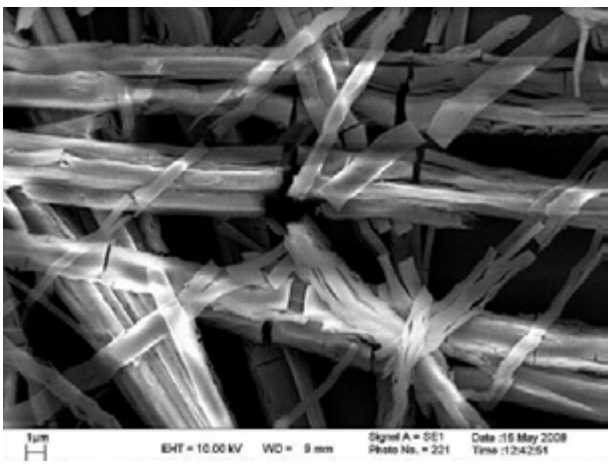

Fig. 1.

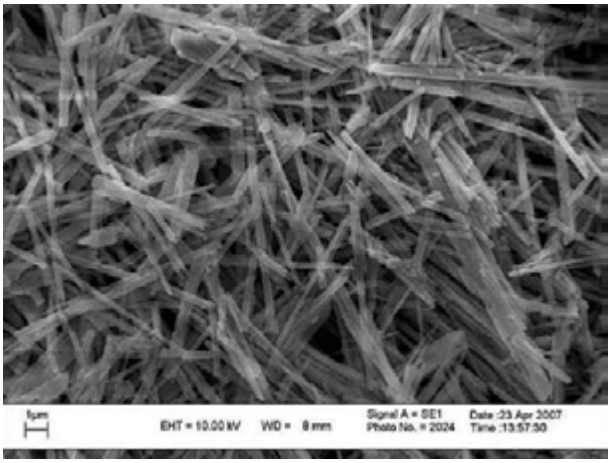

Fig. 2.

were obtained by precipitation from mother solution of formic acid and ammonium paramolybdate under room temperature during 30 days. Those were as the microrods with about 100 and 1 μm of length and diameter respectively. In Fig. 2 the bursting and aliquation of precursor crystals is evident.

Phase composition of the final product as α-MoO_3 (JCPDS 5-0508, *Pbmn*) has been confirmed by XRD and TEM analysis. Typical TEM pattern is shown in Fig. 3. Ellipsoidal character of that and variation of reflex intensity are appeared by primary layout of nanobelts on the substrate. The results of TEM analysis confirm the presence of pure α-MoO_3.

IR-spectra recorded for both final and precursor crystals consist of the bands accorded to modes of inner MoO_6 octahedrons vibration. The IR-spectrum of final product shows an adsorbtion line at 996 cm^{-1} which is a characteristic of α-MoO_3 srtructure and confirm bonding between octahedra bilayers. This band is absent in the IR-spectrum of precursor crystals. IR-spectrum of precursor crystals shows bands which confirm availability of -O-C-O- groups localized between the MoO_6 octahedra layers. Besides this, the spectrum shows doubling of lines related to hydroxil groups adsorption by crystals surface. The positions of Raman lines recorded for these crystals confirm the presence of MoO_6 octahedra in their structure too. On a basis of DTA curves the general formula of precursor was estimated as $HCOOMo_4O_{12}OH$. In Fig. 4 the model of $HCOOMo_4O_{12}OH \rightarrow \alpha$-$MoO_3$ transformation is shown. The model is determined on a basis of detailed analysis of IR-,

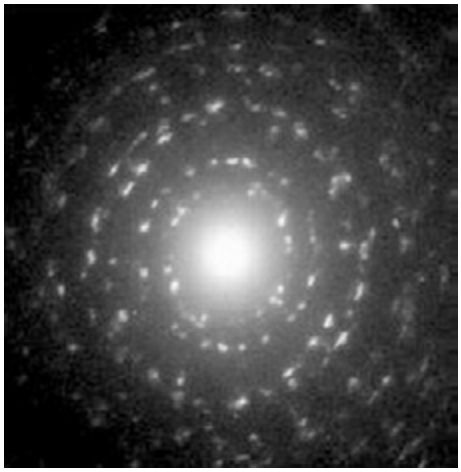

Fig. 3.

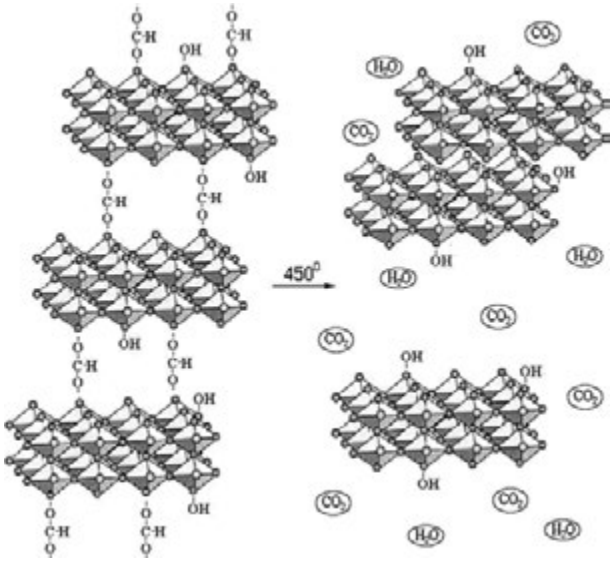

Fig. 4.

Raman-spectroscopy and DTA data of final oxide and precursor crystals.

References

[1] V. V. Atuchin, T. A. Gavrilova, V. G. Kostrovsky, L. D. Pokrovsky, I. B. Troitskaia, *Inorg. Mater.* **44**, 622 (2008).

[2] C. V. Ramana, V. V. Atuchin, I. B. Troitskaia, S. A. Gromilov, V. G. Kostrovsky, G. B. Saupe, *Solid State Commun.* **149**, 6 (2009).

[3] C. V. Ramana, V. V. Atuchin, V. G. Kesler, V. A. Kochubey, L. D. Pokrovsky, V. Shutthanandan, U. Becker, R. C. Ewing, *Appl. Surface Sci.* **253**, 5368 (2007).

[4] C. V. Ramana, V. V. Atuchin, L. D. Pokrovsky, U. Becker, C. M. Julien, *J. Vac. Sci. Technol. A* **25**, 1166 (2007).

[5] M. Itoh, K. Hyakawa, Sh. Oishi, *J. Phys.: Condens. Mater.* **13**, 6853 (2001).

[6] A. M. Taurino, A. Forleo, L. Francioso, P. Siciliano, *Appl. Phys. Lett.* **88**, 152111 (2006).

[7] W. Li, F. Cheng, Z. Tao, J. Chen, *J. Phys. Chem. B.* **110**, 119 (2006).

[8] W. E. Farneth, F. Ohuchi, R. H. Staley, U. Chowdhry, A. W. Sleight, *J. Phys. Chem.* **89**, 2493 (1985).

[9] H. C. Zeng, *J. Crystal Growth* **186**, 393 (1998).

[10] Q. P. Ding, H. B. Huang, J. H. Duan, J. F. Gong, S. G. Yang, X. N. Zhao, Y. W. Du, *J. Crystal Growth* **294**, 304 (2006).

[11] X. W. Lou, H. C. Zeng, *Chem. Mater.* **14**, 4781 (2002).

17th Int. Symp. "Nanostructures: Physics and Technology"
Minsk, Belarus, June 22–26, 2009
© 2009 Ioffe Institute

Surface plasmon resonance of metal nanoparticles in glasses

O. A. Usov[1], A. I. Sidorov[2], A. V. Nashchekin[1], O. A. Podsvirov[3], N. V. Kurbatova[4], V. A. Tsekhomsky[2] and N. V. Nikonorov[5]

[1] Ioffe Physical-Technical Institute, St Petersburg, Russia
[2] SPb ITMO State University, Kronverkskii 49, 194021 St Petersburg, Russia
[3] SPb Polytechnical State University, Polytechnicheskaya 29, 194021 St Petersburg, Russia
[4] Zavoisky Physical-Technical Institute, Sibirsky tract,10/7, 420029 Kazan, Russia
[5] Vavilov State Optical Institute, Birzhevaya line 12, 119034 St Petersburg, Russia

Abstract. Silver nanoparticles (NPs) with diameter about 4–8 nm were shown to be formed in the subsurface layer of photothermorefractive (PTR) glasses after high electron beam irradiation with subsequent heat treatment [1]. The type of MNPs depends on the composition of the PTR glass, the size distribution and NP concentration depend on irradiation dozes and heat treatment temperatures. The report will present the technology of silver NP fabrication, experimental measurements of optical absorption spectra, TEM image and Raman scattering for characterization of NP size distribution, and also simulation of spectral characteristics of the structures using extended Mie theory [2].

Introduction

Noble metals such as Ag, Au, Cu are widely used for fabrication of metal-dielectric photonic nanostructures named metamaterials due to unusual optical properties and opportunity of manipulation, guiding and localization of light at nanoscale [3]. Noble metal NPs embedded in a glass matrix exhibit a very intense color related to the resonance oscillation of the free conduction electrons known as surface plasmon resonance (SPR), which have great application potential in ultra-sensitive chemical and biomolecular detection [3]. The SPR is the main feature of the optical response for MNPs and usually regarded as a fingerprint feature of MNPs, e.g. spherical Ag nanoparticles with diameters from 1 to 50 nm dispersed in SiO_2 matrix show SPR peaks in the wavelength range between 380 and 470 nm depending on particle size, shape, concentration and its environment [4]. From the application point of view, optimization of the plasmonic device efficiency requires an investigation of the interaction of MNPs with the environment and quantum size effect of MNPs, which has strong influence on the spectral characteristics of SPR. The report will present the technology of fabrication of MNPs in the PTR glasses, optical absorption spectra, TEM image and low frequency Raman scattering characterization of shape and size of nanoparticles, and simulation of spectral characteristics of the obtained structures.

1. Technology and fabrication

The MNPs in the PTR glasses were fabricated using technology described by Dotsenko *et al* [5]. The size, shape and concentration of MNPs (Ag, Cu, Au etc.) precipitated in a glass subsurface layer depend on glass composition, type and intensity irradiation (UV, electron etc.) and thermal treatment [1]. To fabricate thin subsurface layer about 50 nm thickness with Ag nanoparticles in the diameter range about 4–8 nm the samples of PTR glasses containing Ag ions were irradiated by electron beam. The samples were exposed at RT using scanning electron microscope CamScan Series 4 DV 100 with electron energy 5–30 keV, current 2 nA, the size of exposed area being as large as 270×350 μm^2 and dose of irradiation about 11.4 $mKcm^{-2}$ [1]. This process is supposed to be related with diffusion of silver ions from the volume of the glass to the charged region and following reduction and aggregation. After subsequent heat treatment at 540 °C free electrons are captured by metal ions and neutral atoms being aggregated due to diffusion into colloidal particles. The MNPs were shown to have specific space distribution which explained by heterogeneous photo-thermal induced crystallization [1].

2. Results and discussion

The samples with Ag MNPs showed specific peaks in the optical absorption spectra in the range between 410–450 nm which relate to localized surface plasmon resonance (SPR). The absorption spectrum shown in Fig. 1 was obtained with Carry UV-vis-NIR spectrophotometer in the range between 300 and 1500 nm in dual mode. The plasmon resonant peaks and line widths are known to be sensitive to the size, shape, metal species and surrounding medium of the MNPs. This spectrum is supposed to be related with the spherical shape and weakly coupled Ag MNPs in dielectric matrix [4] and therefore analysis of the spectrum based on the Mie scattering theory, which defines the extinction, i.e. scattering and absorption, of light by spherical NPs [2]. For NPs small compared with the wavelength of light only the dipole absorption contributes to the extinction cross section (ECS). Therefore Mie equation for ESC in quasi-static or dipole approximation used for estimating the

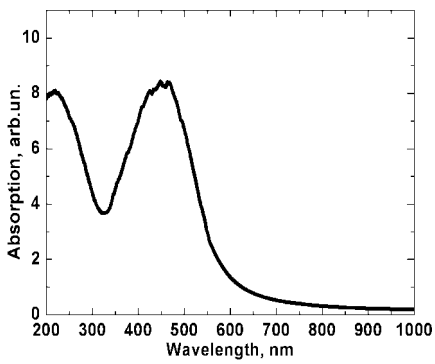

Fig. 1. Absorption spectrum of silver nanoparticles embedded in a photothermorefractive glass matrix.

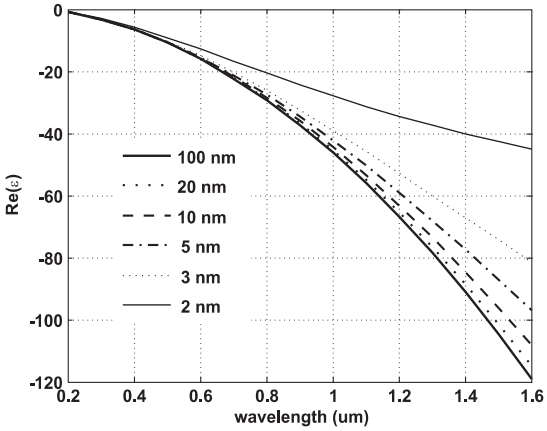

Fig. 2. The dependence of real part of silver permittivity on light wavelength for selected radii of silver nanoparticles.

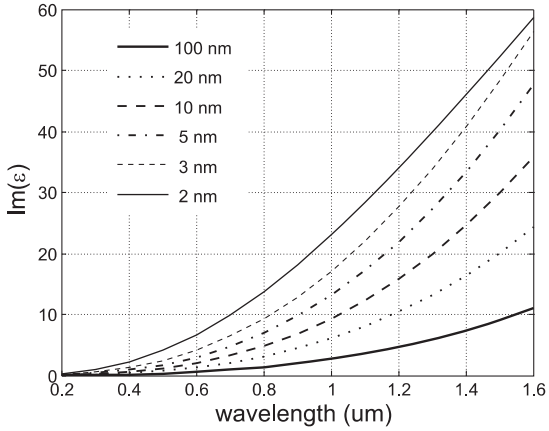

Fig. 3. The dependence of real part of silver permittivity on light wavelength for selected radii of silver nanoparticles.

absorption [2] in the form:

$$\sigma_{\text{ext}} = \frac{9V(R)c^{-1}\epsilon_{\text{g}}^{3/2}\omega\epsilon_2}{\left(\epsilon_1 + 2\epsilon_{\text{g}}\right)^2 + \epsilon_2^2}, \tag{1}$$

where V(R) is the spherical particle volume, c is the speed of light, ω is the angular frequency of the light, and ϵ_{g} is the dielectric constant of glass, ϵ_1 and ϵ_2 denote real and imaginary part, respectively, of the experimental dielectric function or Drude model function [2] of bulk or MNPs , i.e. $\epsilon(\omega) = \epsilon_1(\omega) + i\epsilon_1(\omega)$, which depends on light frequency. The parameters of Drude model were obtained by fitting model function to experimental data [2].

Within the dipole approximation there is no size dependence of MNP dielectric constant but only intensity depends on the NP size due to volume $V(R)$. But the size dependence of the plasmon bandwidth and peak position observed experimentally for small MNPs which is treated now as an effect which arises when the NP size approaches the mean free path length of the conduction electrons. So it was taken into account as a size dependent of damping frequency due to an alteration in the electron mean free path which is then incorporated into the modified or extended Drude model as follows:.

$$\epsilon(\omega, R) = 1 - \frac{\omega_{\text{p}}^2}{\omega^2 + \gamma(R)^2} + i\,\frac{\omega_{\text{p}}^2\gamma(R)^2}{\omega\left(\omega^2 + \gamma(R)^2\right)}, \tag{2}$$

where ω_{p} and $\gamma(R)$ are the plasma and damping or collision frequencies, respectively, the damping frequency being assumed to take the form:

$$\gamma = \gamma_{\text{b}} + \frac{V_{\text{f}}}{R}, \tag{3}$$

where γ_{b} is a bulk damping frequency, V_{f} is the Fermi velocity, which is about 0.005 c. The calculated size dependence of silver permittivity on radius of Ag NPs, ranging from 2 to 100 nm, is shown in Figs. 2 and 3. The figures indicate that the magnitude of permittivity and the collision frequency increase as the dimension decreases due to the reduction of the mean free path of electrons. Therefore, the kinetic energy is dissipated as heat, which results in an increase in the optical loss. Analysis of the experimental extinction spectrum shown in Fig. 1 with Eqs. (1–3) used for evaluation diameter and size distribution of the Ag NPs. The mean size of silver NPs were found at about 4–8 nm, which correlates with the NP size distribution obtained from TEM image analysis of the same samples.

3. Conclusions

The technology of fabrication of Ag MNPs in the subsurface layer of PTR glass has been developed and localized SPR peaks of the optical absorption spectra in the range about 410–480 nm were observed. From the analysis of the experimental absorption spectrum with extended Mie scattering model, the mean size of Ag NPs at about 4–8 nm was obtained which supported by the TEM image analysis and low frequency Raman scattering characterization.

Acknowledgements

This work is supported in part by the grant #10155 "Fundamental Science for Medicine" of the Presidium of the RAS and by the President of the RF grant #2951.2008.2.

References

[1] N. V. Nikonorov *et al*, *Tech. Phys. Let.* **35** 7, 35 (2009).
[2] C. F. Bohren, and R. R. Hoffman, *Absorption and Scattering of Light by Small Particles*, NY, Wiley-Interscience, 1998.
[3] A. Boltasseva *et al*, Fabricating Plasmonic Components for Nano- and Meta-Photonics, pp. 209–221 in *Metamaterials and Plasmonics: Fundamentals, Modelling, Applications*, Zouhdi Said, Sihvola Ari, Vinogradov A. P., Eds., Springer, Netherlands 2009.
[4] Jinlian Hu *et al*, *Nanotechnology* **18**, 185710 (2007).
[5] A. V. Dotsenko *et al*, *Physics and Chemistry of Photochromic Glasses*, CRC Press LLC, 1998.

17th Int. Symp. "Nanostructures: Physics and Technology"
Minsk, Belarus, June 22–26, 2009
© 2009 Ioffe Institute

Transformations of atomic structure and electronic properties at Sb/GaAs(001) and Cs/Sb/GaAs(001) interfaces

A. G. Zhuravlev[1,2], K. V. Toropetsky[1,2] and V. L. Alperovich[1,2]

[1] Institute of Semiconductor Physics, 630090 Novosibirsk, Russia
[2] Novosibirsk State University, 630090 Novosibirsk, Russia

Abstract. The effect of antimony adsorption on the atomic structure and electronic properties of the Sb/GaAs(001) and Cs/Sb/GaAs(001) interfaces is experimentally studied. The conversion of the (4 × 1) Ga-stabilized surface reconstruction to the (2 × 4) Sb-stabilized reconstruction is observed. Transformations of the surface reconstructions, band bending and photovoltage under Cs adsorption and subsequent annealing are compared for the Sb-rich, As-rich, and Ga-rich GaAs(001) surfaces.

Introduction

The preparation of atomically flat III–V semiconductor surfaces with controlled atomic structure and electronic properties is an important prerequisite for the basic research in the field of surface science, for the fabrication of nanostructures, and for the development of ultra-high vacuum (UHV) semiconductor devices. One of such UHV devices is a negative electron affinity (NEA) photocathode, which contains (Cs,O) activation layer of subnanometer thickness deposited on GaAs or another III–V semiconductor in order to reduce the work function down to the state of NEA and, thus, to maximize the quantum efficiency of photoemission. An opportunity for the improvement of the photocathode parameters consists in the control of the surface atomic structure and electronic properties of the initial clean surface and of the interface with (Cs,O) activation layer. The properties of the III–V semiconductor surface can be controlled by isoelectronic substitution of the top atomic layer with group III and V elements different from those constituting the semiconductor bulk. For GaAs a suitable isovalent adsorbate is antimony, which replaces arsenic on the GaAs surface and forms a Sb-stabilized (2 × 4) surface reconstruction. This reconstruction is stable up to higher temperatures as compared to the As-rich (2 × 4) reconstruction [1]. The goal of the present paper is to study the effect of antimony on the atomic structure and electronic properties of the Sb/GaAs(001) and Cs/Sb/GaAs(001) interfaces.

1. Experimental

The surface atomic structure and electronic properties were studied on epitaxial GaAs(001) layers in UHV conditions. Atomically clean GaAs surface with various reconstructions was prepared by the chemical removal of oxides and transfer to the UHV set-up in the inert nitrogen atmosphere with subsequent annealing in vacuum [2,3]. Surface composition and atomic structure were determined by x-ray photoelectron spectroscopy and low-energy electron diffraction (LEED), respectively. The electronic properties were studied by means of photoreflectance (PR) spectroscopy [4,5], which enabled us to measure the evolution of the surface electric field and band bending (by Fourier transform of Franz–Keldysh oscillations) and surface photovoltage (from the amplitude of PR spectra) under the adsorption and thermodesorption of Sb and Cs. To provide uniform electric field near the surface, epitaxial UP^+ structures with thin (∼100 nm) undoped surface layers were used [4]. A modification of the PR spectroscopy technique to a "real-time" version allowed us to measure the band bending evolution during the process of adsorption with a high precision [5].

2. Results and discussion

The antimony-stabilized GaAs(001)-(2 × 4) surface was prepared earlier by deposition of Sb on the As-rich GaAs(001)-(2 × 4) surface and subsequent annealing [1]. An opportunity to prepare Sb-stabilized surface starting from the Ga-rich surface was not explored before. Figures 1(a–c) show LEED patterns which illustrate transformations of the GaAs(001) surface atomic structure under deposition of antimony on the Ga-rich surface and subsequent annealing. The atomically clean Ga-rich GaAs(001)-(4 × 1) surface (Fig. 1a) was prepared by chemical treatment and annealing in vacuum at 540 °C. Deposition of Sb at room temperature leads to surface reconstruction disordering (Fig. 1b). Anneals of the surface with Sb coverage $\theta_{Sb} \sim 1$ ML forms the Sb-stabilized GaAs(001) surface with (2 × 4) reconstruction, starting from the annealing temperature of approximately 450 °C. This (2 × 4) reconstruction was stable at least up to $T \approx 560$ °C (Fig. 1c). Thus, the initial cation-terminated III–V semiconductor surface was converted to the anion-terminated surface by means of Sb deposition and subsequent annealing at relatively low temperatures. This is the first observation of such a conversion induced by the isovalent adsorbate.

It was shown earlier by the PR spectroscopy that the surface electronic properties, namely, the surface band bending and photovoltage evolved differently under Sb deposition on the As-rich and Ga-rich GaAs(001) surfaces [6]. In the present study it is found that subsequent anneals of the Sb-covered surfaces lead to the decrease of band bending and photovoltage down to the values, which are lower than on the initial surface. This effect may be considered as "electronic passivation" of the surface states, which are responsible for the band bending and photovoltage formation. The temperature dependences of the band bending and photovoltage are universal and do not depend on the composition and structure of the initial GaAs(001) surface, in accordance with the formation of the stable Sb-rich GaAs(001) surface.

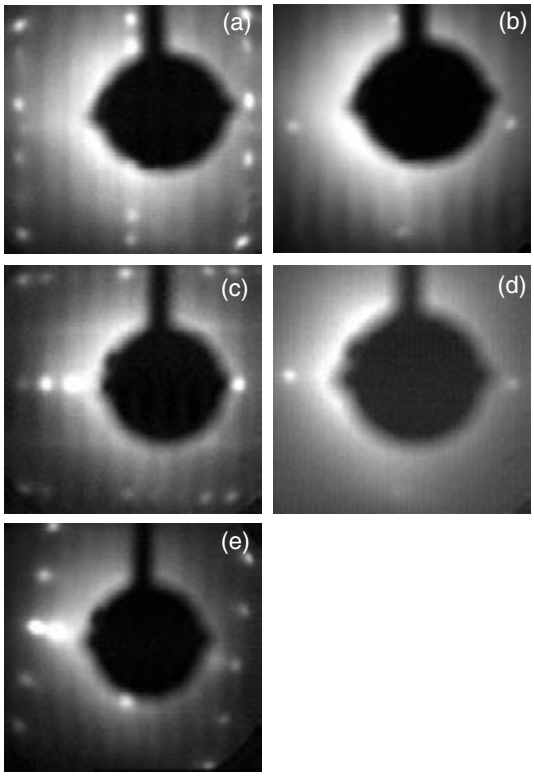

Fig. 1. LEED patterns: (a) clean Ga-stabilized GaAs(001)-(4 × 1) surface; (b) after deposition of 0.5 ML Sb on (a); (c) (2 × 4) surface reconstruction obtained after annealing of the surface with 1 ML of Sb at T=560 °C; (d) after deposition of 0.3 ML Cs on (c); (e) (2 × 4) reconstruction after annealing (d) at T=500 °C.

The first stage of the semiconductor photocathode activation is the deposition of cesium, so we studied transformations of the Sb-stabilized GaAs(001) surface structure, band bending and photovoltage under deposition of cesium and subsequent annealing. LEED patterns in Figures 1(c–e) illustrate Cs-induced transformations of the atomic structure. It is seen from Fig. 1d that deposition of 0.3 ML of Cs led to the destruction of the surface reconstruction, in qualitative agreement with the behavior of the As-stabilized surface structure under Cs adsorption [4]. Subsequent annealing at $T \approx 500$ °C again produced the (2 × 4) reconstruction. This observation differs qualitatively from the effect of Cs-induced conversion from the (2 × 4) to (4 × 2) reconstruction observed under Cs deposition on the As-rich surface and subsequent annealing at reduced temperatures $T \leq 500$ °C [4] and again confirms the stability of the Sb-rich surface as compared to the As-rich surface. It should be noted, however, that the spot intensity distribution of the LEED pattern in Fig. 1e differs considerably from that in Fig. 1c, indicating substantial changes in the Sb-rich surface structure produced by the Cs deposition and annealing.

As it was shown earlier, the dose dependences of the band bending are qualitatively different under Cs deposition on the As-rich and Ga-rich surfaces [5], while the dependences for the anion-terminated (Sb-rich and As-rich) surfaces are similar [6]. It is shown in the present study that repeated Cs depositions on the Sb-rich surface with subsequent anneals at successively increased temperatures produce the similar shapes of the band bending dose dependences $\varphi_S(\theta_{Cs})$ (Fig. 2a). This fact is in

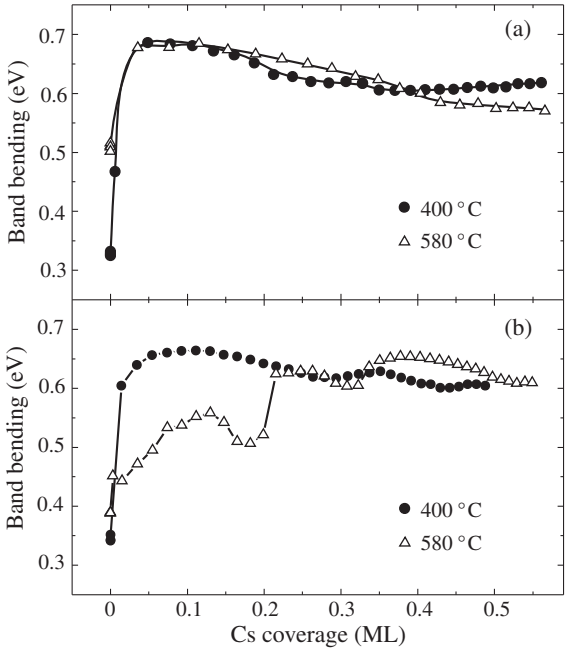

Fig. 2. Band bending evolution under Cs deposition on the initial Sb-rich (a) and As-rich (b) GaAs(001) surfaces, obtained by annealing at $T = 400$ °C (circles) and by Cs deposition and annealing at $T = 580$ °C (triangles).

distinction with the results of a similar procedure applied to the As-rich surface, at which the increase of annealing temperature leads to radical transformation of the $\varphi_S(\theta_{Cs})$ dependence from a simple shape with one maximum to the complex shape with a "fine structure" consisting of several maxima and minima (Fig. 2b). Thus, antimony stabilizes both the atomic structure and the electronic properties of the GaAs(001) surface.

In conclusion, we studied experimentally the transformations of the atomic structure and electronic properties at the Sb/GaAs(001) and Cs/Sb/GaAs(001) interfaces. The conversion of the cation-terminated III–V semiconductor surface to the anion-terminated surface induced by isovalent adsorbate was observed.

Acknowledgements

This work was supported by the Russian Foundation for Basic Research (grant No. 08-02-01236) and by the Russian Academy of Sciences (program "Spin phenomena in nano-structures and spintronics").

References

[1] F. Maeda, Y. Watanabe and M. Oshima, *Phys. Rev. B* **48**, 14733 (1993).

[2] O. E. Tereshchenko, S. I. Chikichev and A. S. Terekhov, *J. Vac. Sci. Technol. A* **17**, 2655 (1999).

[3] V. L. Alperovich, O. E. Tereshchenko, N. S. Rudaya, D. V. Sheglov, A. V. Latyshev and A. S. Terekhov, *Appl. Surf. Sci.* **235**, 249 (2004).

[4] O. E. Tereshchenko, V. L. Alperovich, A. G. Zhuravlev, A. S. Terekhov and D. Paget *Phys. Rev. B* **71**, 155315(7) (2005).

[5] A. G. Zhuravlev and V. L. Alperovich *JETP Letters* **88**, 702 (2008).

[6] A. G. Zhuravlev and V. L. Alperovich, *Proceedings 16th Int. Symp. Nanostructure: Physics and Technology, Vladivostok*, 2008, p. 173–174.

17th Int. Symp. "Nanostructures: Physics and Technology"
Minsk, Belarus, June 22–26, 2009
© 2009 Ioffe Institute

Control of a doping element distribution in sol-gel fabricated nano-composites using the atomic emission spectroscopy of laser erosion plasma

V. I. Zhuravleva[1], V. A. Rozantsev[1], E. A. Ershov-Pavlov[1], A. A. Boiko[2] and E. N. Poddenezhny[2]

[1] Institute of Physics, NASB 68, Nezalezhnastsi Ave. 220072 Minsk, Belarus
[2] P.O. Sukhoi Gomel State Technical University 48 Oktyabrya Ave. 246746 Gomel, Belarus

Abstract. It has been shown that the analysis of ratios of silicon and cerium spectral lines allows evaluating a homogeneity rate of the doping element distribution in nano-composites, which differ by their preparation technology. Particularly, the analytical pair of the lines of Ce II 385.31 nm / Si III 254.18 nm appears to be reliable enough to characterize the dopant distribution in sol-gel samples. The results obtained can be used for a control of technology processes at a production of new materials including sol-gel glasses, optical composites, as well as components for the nano-electronics.

Introduction

Technologies of the sol-gel synthesis are nowadays widely used for the fabrication of new materials. Particularly using a sol-gel technology, one can form nano-composites having predicted contents of doping elements, and thus necessary properties. For example, rare earth elements being introduced into quartz sol-gel glasses change their optical luminescence properties. The latter ones depend strongly on homogeneity of a spatial distribution of the doping elements. In its turn, the distribution is determined by the technology used [1]. That is why the techniques for in situ evaluation and control of the doping element content and distribution in sol-gel materials must be developed.

In this work, the atomic emission spectroscopy of laser erosion plasma has been used to determine the doping element distribution in sol-gel materials. The technique is based on an excitation of atoms/ions of the considered sol-gel material by the laser radiation focused on the sample surface, and on the following line intensity measurements in the resulting emission spectra. The doping element content can be analyzed using intensity ratio of spectral lines of the doping and basic materials. The doping element distribution and its homogeneity rate can be evaluated using two pairs of lines ratios in chosen points on the surface [2]. In such a way, we have studied results of the techniques used for the doping element incorporation. Two ways (pre-doping and post-doping methods) have been considered for introduction of particles of the filling component (aerosil A-175) with cerium oxide nano-particles (15–40 nm) deposited on their surfaces.

1. Experimental

A Q-switched double pulse Nd:YAG laser has been used for the study. Parameters of the laser radiation used for the emission spectra excitation have been taken as follows: 1064 nm wavelength, 10 ns duration and 0.05 J energy of the laser pulse, 8 μs time interval between the doubled pulses. The laser beam has been focused onto the material surface up to a spot of 60 μm diameter giving the irradiation power density of 1.7×10^{10} W/cm^2. Emission spectra of the resulting erosion plasma have been recorded using grating spectrometers with CCD detectors. Every spectrum has been formed as a result of 20 laser shots in one surface point. The sample has been moved point by point along a chosen direction with 1 mm interval to obtain a set of the spectra necessary for the analysis. The laser sampling spatial resolution is determined with dimensions of the total (after 20 laser shots) erosion crater on the sample surface having around 600 μm diameter and 200–250 μm depth [3]. Spectral lines of silicon and cerium have been used for the study to characterize the basic and doping components, respectively: Si I 252.41 nm, Si I 252.85 nm, Si I 288.16 nm, Si I 298.76 nm, Si III 254.18 nm, Ce II 385.31 nm, Ce II 390.69 nm, Ce III 305.56 nm, Ce III 308.53 nm.

The technique of the homogeneity evaluation is based on a comparison of ratio distributions of Si and Ce spectral lines for the basic and doping materials, respectively. A ratio of two Si spectral lines has been used to control the measurement error, and a ratio of Ce/Si lines has served to characterize a distribution of the doping element. The lines with close values of the excitation energy have been used for the base/doping lines ratio minimizing its dependence on the measurement conditions. We have determined a standard deviation S_1 and S_2, respectively, for the both ratio values. The homogeneity rate has been evaluated using F-criterion, where $F = S_2^2/S_1^2$ [2,4]. The value has been compared to a table value F_1 taken for the measurements at the chosen probability (0.99).

A distribution has been considered as homogeneous one,

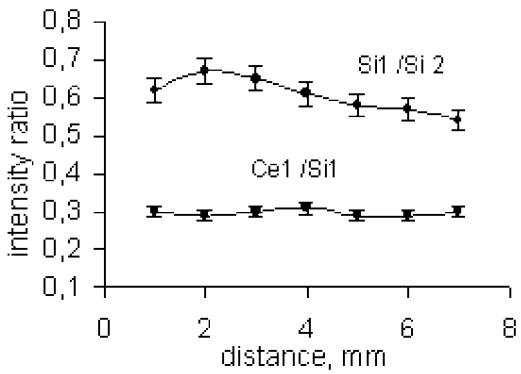

Fig. 1. Intensity ratios for Ce 308.53/Si 254.18 and Si 254.18/Si 252.85 lines measured for the homogeneous sample 1.

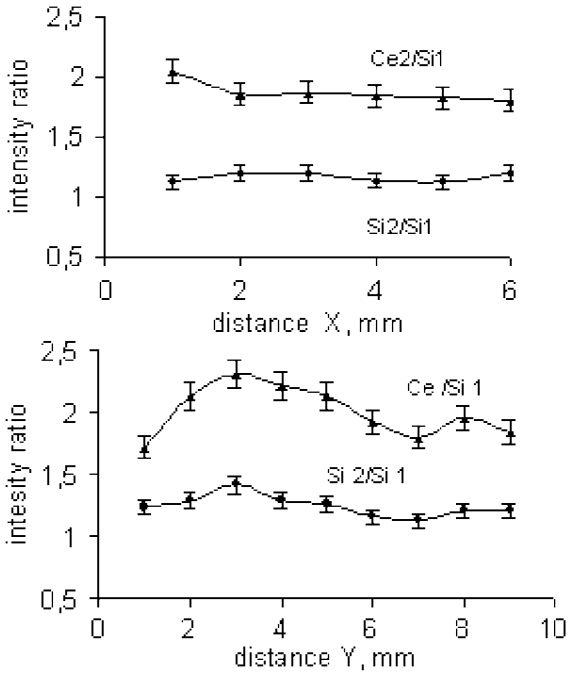

Fig. 2. Spatial distribution of ratios of Ce 385.31/Si 254.18 and Si 252.41/ Si 254.18 lines along X (top) and Y (bottom) directions for sample 2.

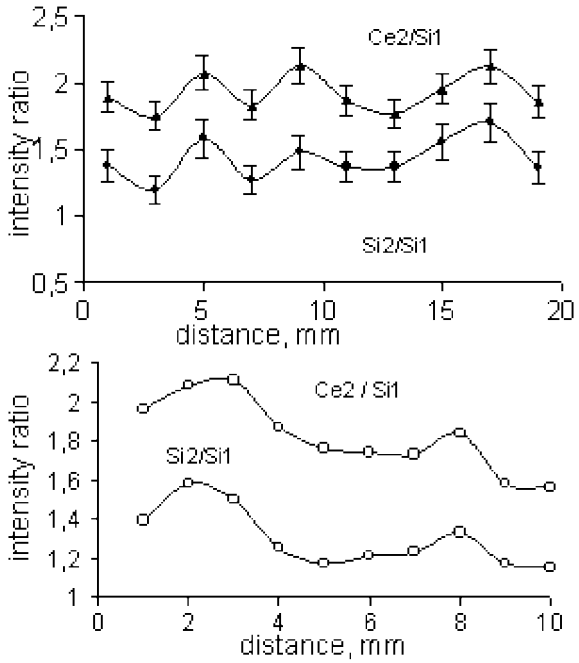

Fig. 3. Spatial distributions of line ratios Ce 385.31/Si 254.18 and Si 252.41/Si 254.18 measured for the sample 3 (top) and 4 (bottom).

when $F < F_1$. A mean standard deviation of 5% has been evaluated for Si lines ratio.

Four samples have been used in the study. Among them, one sample (1) has Ce distribution, which is known to be homogeneous. Distributions of Ce in the rest samples are unknown. Also, the samples have been prepared using different technologies. Samples 1, 3, 4 have been obtained using a pre-doping technique, and a post-doping one has been used to prepare sample 2.

2. Results and discussion

Spatial distributions of the ratios of Ce III 308.53 nm to Si III 254.18 nm lines (Ce1/Si1) and of two silicon Si III 254.18 nm/ Si I 252.85 nm lines (Si1/Si2) measured for the sample 2 are shown in Fig. 1. One can see that Ce1/Si1 ratio changes very little, which corresponds to the homogeneous Ce distribution in this sample. Fig. 2 shows measured distributions of Ce II 385.31/Si III 254.18 (Ce2/Si1) lines and Si I 252.41/Si III 254.18 (Si2/Si1) lines along two perpendicular directions X, Y on the sample surface. It is seen from the figure that Ce distribution along Y axis is more homogeneous, and it shows a certain increase of Ce content to the sample edge. Line ratios distributions of Ce II 385.31/Si III 254.18 (Ce2/Si1) and of Si I 252.41/ Si III 254.18 (Si2/Si1) shown in Fig. 3 for the samples 3 (top) and 4 (bottom) clearly demonstrate homogeneity of Ce distribution along their surfaces. Thus from various silicon lines tested for the comparative measurements, we have chosen Si III 254.18 nm line of silicon ion, which use allows determining better details of Ce distributions in the samples. The distribution difference can be due to changes in the doping element content, as well as because of inevitable measurement errors. Nevertheless, the results obtained show that the analytical pair of Ce II 385.31/Si III 254.18 lines chosen is reliable enough to characterize a distribution of the doping element in sol-gel samples.

3. Conclusion

It is shown that the analysis of ratios of silicon and cerium spectral lines allows evaluating a homogeneity rate of the doping element distribution in nano-composites, which differ by their preparation technology. The results obtained can be used for a control of technology processes at a production of new materials including sol-gel glasses, optical composites and nano-electronics components.

References

[1] E. N. Poddenezhny *et al*, *Zol-gel synthesis of optical quartz glasses*. (in Russ.) P.O. Sukhoi Gomel State University, Gomel, (2002), 210 pp.

[2] T. Terek *et al*, *Emission spectral analysis* **2** (1985).

[3] V. I. Zhuravleva *et al*, *XVIII Int. School-Seminar "Spectroscopy of Molecules and Crystals"*, Beregove, Crimea, Ukraine, 281–282 (2007).

[4] K. Doerfel, *Statistics in analytical chemistry* (1969) 247 pp.

17th Int. Symp. "Nanostructures: Physics and Technology"
Minsk, Belarus, June 22–26, 2009
© 2009 Ioffe Institute

Atomic scale analyses of nanostructures for a better understanding of their properties

P. Pareige, D. Blavette and B. Deconihout

Groupe de Physique des Matériaux Université et INSA de Rouen — UMR CNRS 6634
Faculté des Sciences, Université de Rouen 76801 Saint Etienne du Rouvray, France

Richard P. Feynman said in the late 50's "There's plenty of room at the bottom…". Nowadays, in France, more than 4000 researchers, engineers, post doc and PhD students are tracking matter at the nanometre scale in the field of nanoscience. However, among this population less than 10% are currently working in the field of scientific instrumentation to develop the new generation of tools that will allows to "see" and to "understand" what is going on down there!

Over the last 15 years, the three dimensional atom probe (3DAP) has undergone continuous improvements and it is now a well established and widely used nanoanalysis tool in material science. Due to its ability to map out in 3D the distribution of atoms in the real space on a nearly atomic scale, it has been extensively applied for the investigation of a large variety of materials, allowing a better understanding of physical phenomena involved in material science. In 2004, our group proposed to use femtosecond laser pulses to field evaporate the materials in the 3DAP. The large electrical field required for the field evaporation of atoms at the sample surface (few V/Å) is then given by a non linear component of the laser field. Thanks to this latest development it is now possible for the first time, to investigate semi-conductors at the atomic scale.

Principle and physics of the three dimensional atom probe
When a positive electric field of several volts per angstrom is applied to a metal surface, the surface atoms evaporate in the form of ions. This physical process, called field evaporation was used by E. W. Muller in 1968 [1]. Such intense fields can be obtained by applying a few kV on a specimen prepared in the form of a very sharp tip with an end radius R in the range of 50 to 100 nm. Due to the spherical shape of the extremity of specimen, field evaporated ions follow a quasi-stereographic projection from the surface on a position-sensitive detector (PSD). The magnification of this microscope is very high. It is simply given by the ratio $[L/(m+1)R]$ where L is the flight path of ions (about $10 < L < 40$ cm) and m a constant accounting for the projection features of the tip (see reference [2] for details). The position from which atoms originate at the surface is then accurately measured from their position onto the PSD. In order to get an accurate knowledge of the moment at which atoms are removed from the surface, a fraction of the high-voltage is applied by means of high voltage pulses (rise time 1 ns) allowing their chemical identification by time of flight mass spectrometry. During the analysis the material is evaporated atom by atom and atomic layer after atomic layer allowing an in-depth investigation of the chemistry of a material. The knowledge of the original position of ions in the material and their chemical identities allow a three dimensional reconstruction on a nearly atomic scale. With the advent of fast timing electronics and the development of increasingly powerful PSD, today the field of view of the technique can reach 100×100 nm^2.

Since its emergence in 1988 the 3D atom probe (3DAP) has been extensively applied to the investigation of a wide range of materials. However, because high voltage (HV) pulsed are required to get a time controlled evaporation of atoms, the 3DAP has been for long time limited to metals or materials with a sufficient electrical conductivity. When the specimen is highly resistive, HV pulses cannot be efficiently transmitted to the specimen apex. Due to the temporal degradation of the HV pulse, the material is removed by cluster of atoms or in the form of complex molecular ions making a clear assignment of chemical nature of elements close to impossible.

The extension of the field of application of the 3DAP to poor conductive materials has been of main concern since the emergence of the former one dimensional atom probe. The main difficulty is to bring fast pulsed field to a specimen surface whatever its conductivity. In addition, the pulse has to be short enough to avoid a large energy spread of emitted ions that would lead to a degradation of the mass resolution.

In 2004, our group demonstrated that the use of ultrafast laser pulses makes possible to field evaporate surface atoms [3,4]. As expected, the very short duration of the pulse significantly weakens the ion energy distribution leading to a high mass resolution without the need of time focusing or energy compensating ion optics [5]. In addition, the ability to resolve atomic terraces at the surface strongly suggests that the generated pulsed field lies in the very first atomic layers.

The physic of the interaction of ultrafast laser pulses (about 100 fs) with an object having sub wavelength dimensions is complex and still debated. However, we have shown that the evaporation of ions cannot be thermally activated even if the tip apex is heated after the illumination. We have shown that when the linear polarization of the wave is set parallel to the tip axis, the rectification of the optical field at the surface generates an ultrafast pulsed field that causes the evaporation of surface atoms in the form of ions [6,7]. This effect can only takes place at the surface of the specimen where the electronic density of states is highly asymmetrical. It means that the pulsed field lies in the very first atomic layers preserving the unique in-depth atomic resolution of the technique. This effect has also been proved to take place in the case of Si based materials [8–10]. This open the technique to new type of materials and in particular to the investigation of nanostructured devices such as magnetic multilayers, nanocontacts silicides, silicon nanowires, oxide layers…

As an example, by controlling the density of Au islands and their size, it is possible to subsequently grow single verti-

cally oriented Si nanowires on top of (111)-oriented silicon micropillar and analyze their chemical composition at the atomic scale with the femtosecond laser assisted tomographic atom probe. Three-dimensional images of the atom distribution in the nanowire, in particular, the distribution of boron impurities, are obtained and can be compared to the intended impurity concentration. A uniform doping distribution is observed in the core of the nanowire and ranges between 2600 and 3000 ppm. Such concentration agrees well with the ratio of the flow rates between silane and diborane and corresponds to an impurity concentration of $1.3 \pm 0.3 \times 10^{20}$ B cm^{-3} [11].

Another example of the application of the 3D Atom Probe is the dopant metrology in nano-electronic devices. The dopant implantation and annealing process is a crucial step for the creation of source/drain junctions in CMOS nano-devices. As far as p^+/n junctions are concerned, boron is the most commonly used dopant due to its high solid solubility in Si. However, its critical redistribution at high concentrations is a major drawback to comply with the international technology roadmap for semiconductors specifications and is generally associated with two problems: (1) the transient enhanced diffusion linked to the interactions between the intrinsic point defects and implanted impurities, and (2) the boron activation anomalies related to defect evolution during post-implantation annealing process.

Intensive experimental and theoretical work has been reported on the agglomeration of self-interstitial silicon atoms and the formation of the so called "boron interstitial clusters" (BICs) in crystalline or pre-amorphized Si [12,13]. With the lack of direct experimental information on these small size defects due to the limitation of nowadays analysis techniques, several models have been developed to predict the formation and the dissolution of the BICs, essentially based on atomistic simulations. Previous works, from ab initio calculations, show that only few atoms (from 2 up to 5 B atoms associated to interstitials-Si) are expected to be found in those clusters [14,15]. However, based on weak-beam-dark-field investigations, Cristiano *et al* recently presented a detailed analysis on large BICs formation after a high-fluence ultra-low energy boron implantation followed by low-temperature annealing [16]. More recently, Boninelli *et al* presented studies focusing on the thermal evolution of BICs in crystalline silicon and showed large clusters containing hundreds of atoms (with a B:Si ratio of $\sim$4) in thin highly-doped boron-enriched layers [17].

In a recent work, we gave a new insight into this clustering observation. In order to provide a direct evidence of these BICs in highly boron-doped Si, the laser-assisted wide-angle tomographic atom probe (LAWATAP) instrument was used. This is to date the only atomic scale imaging technique which is capable to chemically reveal this clustering phenomenon [18].

References

[1] E. W. Müller, J. A. Panitz, S. B. Mclane, Rev. Sci. Instrum. **39**, 1, 83–86 (1968).

[2] M. K. Miller, *Atom Probe Tomography*, Kluwer Academic/Plenum, New York, (2000).

[3] B. Deconihout, F. Vurpillot, B. Gault, G. Da Costa, M. Bouet, A. Bostel, A. Hideur, G. Martel, M. Brunel and D. Blavette, *Surface and Interface Analysis*, 38–40 (2006).

[4] B. Gault, F. Vurpillot, A. Bostel, A. Menand, and B. Deconihout, *Appl. Phys. Lett.* **9**, 86–88 (2005).

[5] B. Gault, F. Vurpillot, A. Vella, M. Gilbert, A. Menand, D. Blavette and B. Deconihout, *Review of Scientifics Instruments* **4**, 77–85 (2006).

[6] A. Vella, F. Vurpillot, B. Gault, A. Menand and B. Deconihout, *Phys. Rev. B.* **165416**, 73–80 (2006).

[7] A. Vella, M. Gilbert, A. Hideur, F. Vurpillot and B. Deconihout, *Appl. Phys. Lett.* **25**, 89–92 (2006).

[8] M. Gilbert, F. Vurpillot, A. Vella, H. Bernas, and B. Deconihout, *Ultramicroscopy* in press (2006).

[9] B. Gault, A. Menand, F. De Geuser, R. Danoix, and B. Deconihout, *Appl. Phys. Lett.* **11**, 88–91 (2006).

[10] K. Hoummada, E. Cadel, D. Mangelinck, C. Perrin-Pellegrino, D. Blavette and B. Deconihout, *Appl. Phys. Lett.* **18**, 89–92 (2006).

[11] T. Xu, J. P. Nys, B. Grandidier, D. Stiévenard, Y. Coffinier, R. Boukherroub, R. Larde, E. Cadel, and P. Pareige, *J. Vac. Sci. Technol. B* **26** (6), Nov/Dec 2008.

[12] P. A. Stolk, H. J. Gossman, D. J. Eaglesham, D. C. Jacobson, C. S. Raerty, G. H. Gilmer, M. Jaraiz, J. M. Poate, H. S. Luftman, T. E. Haynes, *J. Appl. Phys.* **81** 6031–6050 (1997).

[13] C. J. Ortiz, P. Pichler, T. Fühner, F. Cristiano, B. Colombeau, N. E. B. Cowern, A. Claverie, *J. Appl. Phys.* **96** 4866–4877 (2004).

[14] W. Luo, P. Clancy, *J. Appl. Phys.* **89** 1596–1604 (2001).

[15] L. Pelaz, M. Jaraiz, G. H. Gilmer, H. J. Gossmann, C. S. Rafferty, D. J. Eaglesham, J. M. Poate, *Appl. Phys. Lett.* **70** 2285–2287 (1997).

[16] F. Cristiano, X. Hebras, N. Cherkashin, A. Claverie, W. Lerch, S. Paul, *Appl. Phys. Lett.* **83** 5407–5409 (2003).

[17] S. Boninelli, S. Mirabella, E. Bruno, F. Priolo, F. Cristiano, A. Claverie, D. De Salvador, G. Bisognin, *Appl. Phys. Lett.* **91** 031905 (2007).

[18] M. Ngamo, S. Duguay, F. Cristiano, K. Daoud-Ketata, P. Pareige, *Journal of Applied Physics*, accepted for publication 2009.

17th Int. Symp. "Nanostructures: Physics and Technology"
Minsk, Belarus, June 22–26, 2009
© 2009 Ioffe Institute

Structural and electrical characterizations of ZnO nanorods doped by Cr and enhancement-mode field-effect transistor fabricated from them

O. V. Kononenko[1], A. A. Firsov[1], D. V. Matveev[2], E. E. Vdovin[1], G. N. Panin[1,5], V. T. Volkov[1], M. V. Shestakov[3] and A. N. Baranov[4]

[1] Institute of Microelectronics Technology, RAS, 142432 Chernogolovka, Moscow region, Russia
[2] Institute of Solid State Physics, RAS, 142432 Chernogolovka, Moscow region, Russia
[3] Moscow State University, Department of Materials Science, 119992 Moscow, Russia
[4] Moscow State University, Chemistry Department, 119992 Moscow, Russia
[5] QSRC, Department of Physics, Dongguk University 26, Seoul 100-715, Korea

Abstract. ZnO:Cr nanorods were synthesized from NaCl-Li_2CO_3 salt mixture with a solution-processed Zn-containing precursor using a freeze-drying method combined with a milling technique. Crystallographic structure was studied using transmission electron microscopy. Optical properties of nanorods were investigated by cathodoluminescence spectroscopy. The nanorods were transferred onto oxidized silicon substrates. E-beam lithography was used to pattern aluminum electrodes contacting a single nanorod. I–V curves were measured using two point structures. Si back gate FET fabricated from the ZnO:Cr nanorod demonstrated n-channel enhance-mode behavior.

Introduction

Zinc oxide is one of the most important functional semiconductor oxides with a direct wide band gap (3.37 eV) and a large exciton binding energy (60 meV) [1]. ZnO-based nano scale materials such as nanorods or nanowires have attracted great interest due to its unique combination of optical, electrical and piezoelectric properties. In recent years, the attention has focused on spindependent phenomena in dilute magnetic zinc oxide in which stoichiometric fraction of the zinc atoms are replaced by transition metal (TM) (Mn, Cr, V, Ti, Fe, Co, Ni, Cu) impurities. In spite of theoretical predictions of room temperature ferromagnetism originated by carrier-induced interaction between TM atoms in ZnO, the experimental results have been strongly contradictory. Ferromagnetism in the oxide material remains poorly understood experimentally. Several recent studies on $ZnO : Mn$, $ZnO : Co$ and $ZnO : Fe$ showed that ferromagnetism depends strongly on methods and preparation conditions used [2,4,5]. Magnetic ordering in ZnO-based DMS appears sensitive to point defects such as vacancies [3,6] which can supply electrons (holes) and can effect considerably on both magnetic and electric properties.

Quasi-1D nanostructures have unique feature to growth with single crystal structure without second phase. Moreover the density of surface point defects in nanowires with high surface-to-volume ratio is expected to be significant. It may affect their magnetic and electronic properties. The ZnO nanorods doped with Mn, Fe, Sn and Li were reported [7,8] to show ferromagnetic behavior. For example, the $Zn_{1-x}Mn_xO$ nanorods with $x < 0.01$ show hysteresis curves with the coercitive field of 200 Oe at 300 K [8]. In this work, we report on structure, optical and electrical properties of ZnO nanowires doped by Cr.

1. Experimental

ZnO nanorods with diameters from 40 to 150 nm were grown from NaCl-Li_2CO_3 salt mixture with a solution-processed Zn-containing precursor using a freeze-drying method combined with a milling technique, as described previously [9].

ZnO nanorods were grown from the as-prepared powder mixture with $0.5g\,Zn_2(OH)_2CO_3 \times xH_2O/9g\,NaCl/\ 1g\ Li_2CO_3$ weight ratio in an alumina crucible in a muffle furnace in air at 600–700 °C for 1–6 h. Cr doping occurred during the stage of zinc carbonate hydroxide synthesis.

To examine the samples a XL 30S field emission gun high-resolution scanning electron microscope (HRSEM) with a Mono CL system for cathodoluminescence (CL) spectroscopy was used. The light emitted from the sample can be directed into the slits of the monochromator, which is mounted on the SEM. The high-resolution transmission electron microscope JEOL 4000 FX was used for structure analysis of nanorods.

Devices for transport measurements of ZnO nanorods were fabricated using standard photo- and electron beam lithography and a lift-off technique. Nanorods were transferred onto the surface of thermally oxidized silicon chips with Au pads and lanes. E-beam lithography and a lift-off process were used

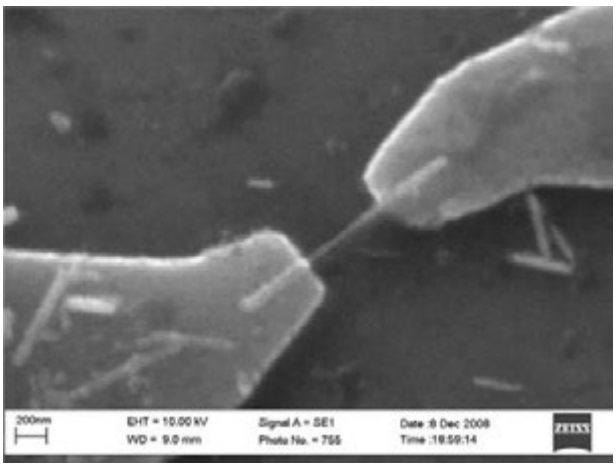

Fig. 1. SEM image of a two-terminal structure which was used for I–V measurements.

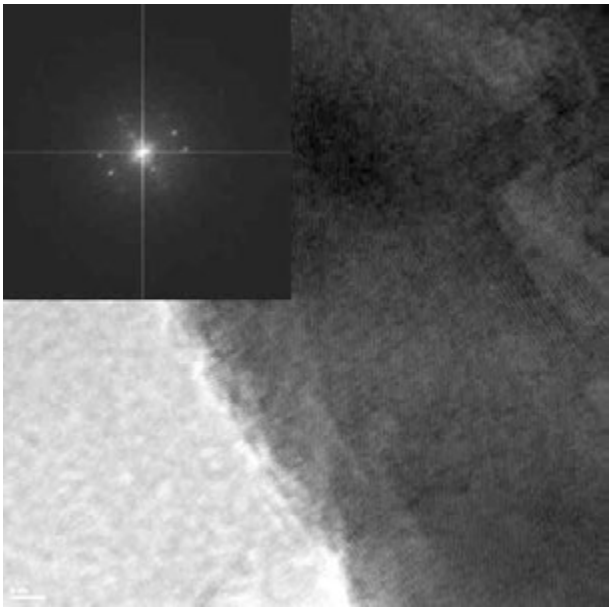

Fig. 2. HRTEM image of ZnO:Cr nanorods grown from NaCl-Li_2CO_3 salt mixture.

to pattern e-beam evaporation deposited aluminum electrodes contacting single nanorods. Two-terminal structures were used for measurements of I–V characteristics (Fig. 1).

2. Results and Discussions

Fig. 2 shows HRTEM image of ZnO:Cr nanorods grown from NaCl-Li_2CO_3 salt mixture. The selected area diffraction patterns have shown the nanorods to be single crystal with wurtzite structure. Crystal C-axis is directed along longitudinal axis of the nanorods. The diameters of ZnO:Cr nanorods were found to be in the range of 25–80 nm. A surface of the nanorods is corrugated.

The CL spectra for the ZnO nanorods synthesized in this work demonstrate three broad peaks at around 322 nm, 379 nm and 514 nm. The luminescence at 322 and 379 nm corresponds to the near band gap transition of small and large rods, respectively. The small rods also show the confinement effect and higher energy of a free bound exciton. Quantum confinement in our nanorods seems to be observed due to additional confinement by surface states as well as by good barrier separation of nanorods from each other in our method of preparation. The bands corresponding to 322 and 379 nm peaks are related to the different nanorod size. The 514 nm peak is the broad deep-level related emission (or trap-state emission) in the visible range that is attributed to the surface defects of the crystal. Intensity of the deep-level emission is determined by the surface states and concentration of surface defects [10].

Resistivity of the nanorod obtained from the I–V characteristics is about 1 Ω cm in the dark. The I–V curves exhibit rectify behavior indicating the Schottky-like barrier formation. The nanorod showed a strong, reversible response to above band gap ultraviolet light, with the UV-induced current being approximately a factor of 10 larger than the dark current at a given voltage.

Electrical transport measurements were performed on ZnO:Cr nanorod Field Effect Transistor using Si back gate. Figure 3

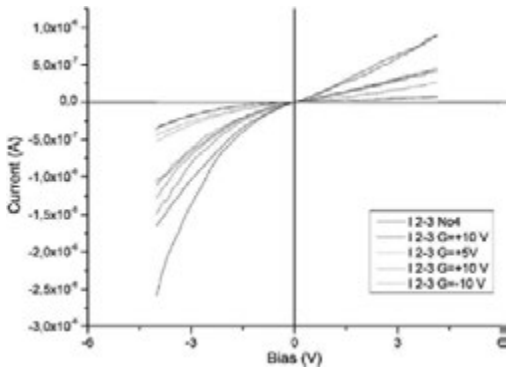

Fig. 3. I–V curves under different back gate voltages.

shows the typical I–V curves of the n-type ZnO nanorod under different back gate voltages ranging from −10 to 10 V. The conductance of nanowire increases with increasing back gate voltage which can be explained using energy band bending caused by back gating [11]. The positive back gate potential increases electron concentration and bends the conduction band towards the Fermi level. The result of that is increasing of conductance. The negative back gate depletes the electron concentration. The conduction band bends from the Fermi level, yielding lower conductance.

We obtain from plot of drain-source current as function of gate voltage (drain-source voltage is 1 V) that threshold voltage is about +5 V. It indicates that ZnO:Cr nanorod n-channel FET demonstrates enhancement-mode behavior. The trapping of carrier electrons in trap states can cause electron depletion in the channel. The depletion width in small diameter nanorods can be comparable to the diameter size of nanorod. In our case ZnO:Cr nanorod is completely depleted under the no gate bias condition due to the larger depletion region than the nanorod diameter.

In conclusion, ZnO nanorods doped by Cr were synthesized by heating the mixture of solution processed Zn precursor with NaCl-Li_2CO_3 salt. The nanorods have single crystalline structure and blue-green luminescence. Resistivity of the nanorod is about 1 Ω cm in the dark. The strong UV response of the nanorods is observed. Si back gate Field Effect Transistor fabricated from ZnO:Cr nanorod is n-channel and demonstrates enhancement-mode behavior.

Acknowledgements

This work has been supported in part by the Russian Foundation for Basic Research, grant No. 07-08-00514-a.

References

[1] S. J. Pearton *et al*, *Progr. in Mat. Science*, **50**, 293 (2005).
[2] K. Ueda *et al*, *Appl. Phys. Lett.* **79**, 988 (2001).
[3] D. C. Kundaliya *et al*, *Nature Mater.* **3**, 709 (2004).
[4] P. Sharma *et al*, *Nat. Mater.* **2**, 673 (2003).
[5] P. Wu *et al*, *Appl. Phys. Lett.* **89**, 012508 (2006).
[6] N. A. Spaldin, *Phys. Rev. B* **69**, 125201 (2004).
[7] G. N. Panin *et al*, *AIP Conf. Proc.* **893**, 743 (2007).
[8] G. Panin *et al*, *Mater. Res. Soc. Symp. Proc.* **957**, 0957-K04-06 (2007).
[9] A. N. Baranov *et al*, *Nanotechnology* **15**, 1613 (2004).
[10] I. Shalish *et al*, *Phys. Rev. B* **69**, 245401 (2004).
[11] S. J. Tans *et al*, *Nature* **393**, 49 (1998).

17th Int. Symp. "Nanostructures: Physics and Technology"
Minsk, Belarus, June 22–26, 2009
© 2009 Ioffe Institute

Adsorption and electronic structure of single $C_{60}F_{18}$ molecule on Si(111)-7×7 surface

A.I. Oreshkin[1,6], R.Z. Bakhtizin[2,6], V. Kumar[3,6], P. Murugan[4,6], J.T. Sadowski[5], Y. Fujikawa[6], Y. Kawazoe[6] and T. Sakurai[7]

[1] Moscow State University, Department of Physics, Moscow 119991,Russia
[2] Department of Physical Electronics, Bashkir State University, Ufa 450074, Russia
[3] Dr. Vijay Kumar Foundation, 1969 Sector 4, Gurgaon 122001, Haryana, India
[4] Functional Materials Division, Central Electrochemical Research Institute, Karaikudi, 630006, India
[5] Center for Functional Nanomaterials, Brookhaven National Laboratory, Upton, NY 11973 USA
[6] Institute for Materials Research, Tohoku University, Sendai 980-8577, Japan
[7] WPI Research Center Advanced Institute for Material Research (WPI-AIMR), Tohoku University, Sendai 980-8577, Japan

Abstract. Scanning tunneling microscopy has been used to spatially image individual fluorofullerene $C_{60}F_{18}$ molecule on Si(111)-7 × 7 surface. The images have been interpreted with the help of *ab initio* calculations. It is found that the fluorinated fullerene molecules interact with the 7 × 7 reconstructed (111) surface with F atoms pointing down towards the surface. The large electric dipole moment of the molecule induces strong polarization on the surface but there is a little charge transfer. A comparison of the experimental and calculated images implies that during STM image acquisition, there is a tendency of some F atoms to migrate from fluorofullerene molecule to the surface due to twice higher binding energy of F atoms to the Si surface than to C_{60} molecule.

Introduction

Self-organized nanostructures and thin films of organic materials compatible with Si-based semiconductor systems are currently of great interest for expanding micro-electronic technologies to nanoscale range and for applications in optoelectronic devices [1]. Among them, carbon fullerenes and their derivatives are very promising for the fabrication of electroactive elements in photovoltaic solar cells, active layers in organic field-effect transistors [2], and as building blocks for chemical manipulation in nano-science applications to develop new functionalities [3]. Therefore several studies have been done to understand crystal structures [4], and electronic properties of fullerenes [5]. The most stable fullerene derivatives are endohedral metallofullerenes and exohedral fullerene fluorides. The latter have been synthesized in a variety of compositions $C_{60}F_n$ ($n = 18 - 48$). Recently $C_{60}F_{18}$ has been obtained in high abundance and even a crystalline phase has been developed.

1. Experimental

Here we present the results of scanning tunneling microscope (STM) imaging of molecular level detection of $C_{60}F_{18}$ deposited on Si(111)-7 × 7 surface combined with *ab initio* calculations to obtain the atomic arrangement and electronic structure of these supported molecules.The structure of the molecule has been determined to have all the eighteen fluorine atoms bound to only one hemisphere of C_{60}. Following the notations in the Schlegel diagram in Ref. [6], the calculated C-C bond distances lie in the range of 1.37 to 1.68 Å and agree well with the experimental values. The shortest bonds are associated with sp^2 bonded carbon atoms while the longest bonds are associated with C-C bonds in pentagons having F atoms. The calculated highest occupied-lowest unoccupied (HOMO-LUMO) molecular orbital gap of $C_{60}F_{18}$ is 2.41 eV as compared to 1.65 eV for pure C_{60} while the average calculated binding energy of each F atom on C_{60} is 3.6 eV. Therefore $C_{60}F_{18}$ is a very stable molecule. The depositions of $C_{60}F_{18}$ molecules have been performed from Knudsen cell on a Si(111)-7 × 7 surface kept at room temperature. The deposition rate was in the range of 0.05–0.1 ML/min. All experiments were carried out at room temperature using a home-built ultra high vacuum field ion-scanning tunneling microscope (base pressure 2×10^{-11} Torr) equipped with standard surface preparation facilities [7]. A P-doped Si(111) wafer with resistivity of 1.6 Ω cm was cut into pieces of $20 \times 7 \times 0.5$ mm^3 (the nominal doping concentration was about 8×10^{17} cm^{-3}) to prepare the samples that were

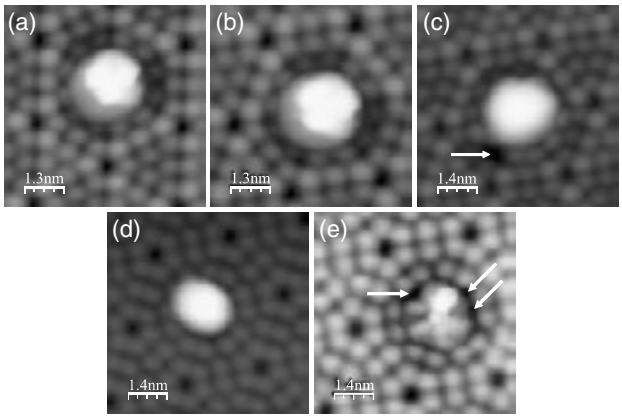

Fig. 1. STM images of a single $C_{60}F_{18}$ molecule adsorbed on a corner site of Si(111)-7 × 7 surface at constant tunneling current $I_t = 20$ pA. (a),(b),(c) — filled states images at a bias voltage $Us = -1.8$ V, −2.0 V and −2.0 V respectively. Fig. 1(c) shows an STM image obtained some time later than STM image represented in Fig. 1(b); (d),(e) — empty states images at $U_s = +1.8$ V. STM image presented in Fig. 1(e) was obtained some time later than STM image represented in Fig. 1(d). White arrows in Fig. 1(c),(e) indicate of some F atoms leaving $C_{60}F_{18}$ molecule and getting adsorbed on the surface during measurements.

ultrasonically washed in acetone and distilled water. The samples were mounted on a tantalum sample holder using "Ni-free" tools and the surface was cleaned by outgassing overnight at 650 °C and then flashing at 1250 °C for 5 s followed by slow cooling. In situ STM measurements were carried out at room temperature by using electrochemically etched W tips as well as commercial Pt-Ir tips. From our STM data we conclude that the initial nucleation of deposited $C_{60}F_{18}$ molecules occurs on three different positions of the Si(111)-7 × 7 surface unit cell, namely the unfaulted half, faulted half, and the corner hole. In this work we have focused on the study of $C_{60}F_{18}$ adsorption on a corner hole of the Si(111)-7 × 7 surface unit cell. Figures 1(a),(b) and (c) show STM images of the filled states of a $C_{60}F_{18}$ molecule located above a corner hole of Si(111)-7 × 7 surface at −1.8 V (Fig. 1(a)) and −2.0 V bias (Fig. 1(b),(c)), respectively. A bright spot with three lobes surrounded by Si corner hole adatoms, is clearly seen in place of the corner hole of the Si(111)-7 × 7 surface in Fig. 1(a) and (b). The images look similar but the bright spot in Fig. 1(a) is distinctly smaller in comparison with that in Fig. 1(b). Fig. 1(c) shows the image at −2.0 V bias taken after some time later than STM image presented in Fig. 1(b). One can observe the appearance of black spot in this STM image. STM images of the unoccupied states taken at +1.8 V bias are shown in Fig. 1(d) and (e). STM image presented in Fig. 1(e) was obtained some time later than the STM image presented in Fig. 1(d). The central part of the STM image changes drastically with the applied bias. There is a small spot of high intensity and five spots of much lower intensity. One can also notice the appearance of some black spots in the image depicted in Fig. 1(e). The black regions in Fig. 1(c) and (e) increase with time and are indicative of some F atoms leaving $C_{60}F_{18}$ molecule [8] and getting adsorbed on the surface (as illustrated by white arrows).

2. Calculations

The details of the spatially varying charge density as observed in our high-resolution STM images were analyzed from *ab initio* pseudopotential density functional calculations using plane wave projector augmented wave method. In order to further elucidate the STM images obtained experimentally, we calculated the total and the partial densities of states (DOS) for the bottom orientation case (the case of maximum adsorption energy) and these are shown in Fig. 2. It can be seen that the Fermi energy (E_F) lies in a band of states of Si(111)-7 × 7 surface, while the occupied and the unoccupied states of the $C_{60}F_{18}$ molecule are energetically well separated with a gap of about 2.1 eV. The 2p states of F atoms are fully occupied and lie more deeply as compared to the highest occupied 2p states of C atoms. Therefore STM images from the filled states in our experiments arise mainly from C-2p and Si-3p orbitals. From our calculations, no $C_{60}F_{18}$ state lies between E_F and $E_F - 2.0$ eV (see the bottom two curves) but some states exist between 2.1 and 3.9 eV below E_F predominantly on C atoms (some differences in the calculated and observed values of energies are possible due to the band gap problem in GGA). Accordingly the STM image of the filled states of the adsorbed $C_{60}F_{18}$ molecule at −2.0 V is largely due to C-2p states. We calculated the STM images by accumulating charge density from states in the energy range of $E_F - 2.1$ eV to E_F and it is shown in Fig. 3. The non-uniform electronic charge density distribution is similar to that seen in experiments (Fig. 1(a) and (b)). Our results of the DOS further confirm that F atoms in $C_{60}F_{18}$ molecule are orientated towards the surface. If F atoms would be on the top position, then we shall see no current in STM images at this bias. Our results also show that by reducing the bias, the image should reduce as there are no occupied states from C or F atoms within 2 eV below the E_F and this agrees with the reduction in image intensity in going from −2.0 eV to −1.8 eV.

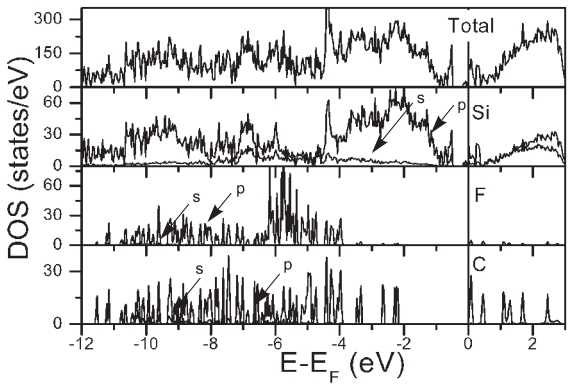

Fig. 2. Total and the partial electronic densities of states (DOS) of bottom oriented $C_{60}F_{18}$ molecule adsorbed on Si(111)-7 × 7 surface. Zero of energy is the Fermi level. The partial density of states on F atoms lies mostly about 4 eV below E_F and therefore no STM image is expected from F atoms for the bias voltage used in our study. Arrows indicate to s- and p-orbitals partial DOS of the respective atoms.

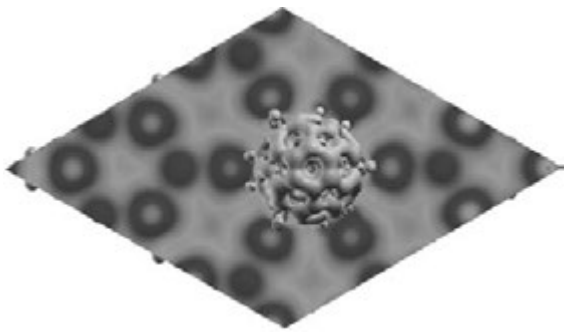

Fig. 3. Simulated STM image of a single $C_{60}F_{18}$ molecule on Si(111)-7 × 7 surface at $U_s = -2.14$ V (isosurface value = 0.01 electrons/Å).

Acknowledgements

AO, RB and VK gratefully acknowledge the hospitality at IFCAM, IMR. We thank the staff of CCMS, IMR for their support and for allowing the use of Hitachi supercomputer. The work was partially supported by RFBR grants and by the National Grant for technical regulation and metrology.

References

[1] F.-J. Meyer zu Heringdorf *et al*, *Nature* **412**, 517 (2001).
[2] R. Haddon *et al*, *Appl. Phys. Lett.* **67**, 121 (2005).
[3] Y. Lin *et al*, *Chem. Phys.* **331**, 85 (2006).
[4] J. M. Hawkins *et al*, *Science* **252**, 312 (1991).
[5] R. C. Haddon *et al*, *Nature* **350**, 320 (1991).
[6] I. S. Neretin *et al*, *Angew. Chem. Int. Ed.* **39** 18, 3273 (2000).
[7] T. Sakurai *et al*, *Prog. Surf. Sci.* **33**, 3 (1990).
[8] J. T. Sadowski *et al*, *Journal of Crystal Growth* **229**, 580 (2001).

17th Int. Symp. "Nanostructures: Physics and Technology"
Minsk, Belarus, June 22–26, 2009
© 2009 Ioffe Institute

Optical properties of GaAs nanowires studied by low temperature photoluminescence

B. V. Novikov[1], S. Yu. Serov[1], N. G. Filosofov[1], I. V. Shtrom[1], V. G. Talalaev[1], O. F. Vyvenko[1], E. V. Ubyivovk[1], Yu. B. Samsonenko[2,4], A. D. Bouravleuv[2,3], I. P. Soshnikov[2,3], N. V. Sibirev[2], V. G. Dubrovskii[2,3] and G. E. Cirlin[2,4]

[1] St Petersburg State University, Physical Faculty, St Petersburg, Russia
[2] St Petersburg Physics and Technology Centre for Research and Education RAS, St Petersburg, Russia
[3] Ioffe Physical-Technical Institute, St Petersburg, Russia
[4] Institute for Analytical Instruments RAS, St Petersburg, Russia

Abstract. Self-standing III–V nanowires (NWs) are promising building blocks for future optoelectronic devices, in particular, LEDs, lasers, photodetectors and solar cells. In this work we present the results of low temperature photoluminescence (PL) characterization of GaAs NWs grown by Au-assisted molecular beam epitaxy (MBE) on the GaAs(111)B and Si(111) substrates. PL spectra contain exciton peaks from zinc blende (ZB) and wurtzite (WZ) crystal structures of GaAs, influenced by the quantum confinement effects. Theoretical estimates for the exciton radiation peaks depending on the crystal structure and the NW radius are presented and compared to the experimental data.

Introduction

A rapidly growing interest in semiconductor NWs ranges from fundamental physics of their growth and optical phenomena to many promising applications in nanoelectronics and nanophotonics. NWs are usually grown by MOCVD or MBE via the so-called vapor-liquid-solid (VLS) mechanism [1] on the surfaces activated by the drops of a metal catalyst (e.g., Au). Due to ability to accumulate for strain in two dimensions, NW geometry is ideal for monolithic integration of materials with different lattice constants. This is very important for the growth of III–V compounds on silicon surface. Study of optical properties of III–V NWs is paramount for applications. In this work we present new data concerning optical characterization of MBE grown GaAs NWs by the PL technique and discuss various physical effects influencing the energy of exciton luminescence.

1. Experimental

Growth experiments are carried out using EP1203 and Riber 32P MBE setups equipped with effusion Au cell to form the Au drops at high vacuum conditions. During the growth we have used the GaAs(111)B and Si(111) substrates. After the desorption of an oxide layer and the growth of buffer layer (in the case of GaAs substrate), the deposition of a thin ($\sim 0.2-1$ nm) Au layer is applied. The substrate is then set above the eutectic melting point of a corresponding semiconductor alloy with Au in order to form the seed drops. After this stage, the grown of GaAs NWs by the conventional MBE from atomic Ga and As_4 beams is started. The growth temperature of NWs was 550 °C, the V/III fluxes ratio = 3 and the equivalent deposition rate = 1 ML/s. The samples were characterized by transmission and scanning electron microscopy (TEM and SEM) and PL methods.

2. Results and discussion

Typical SEM images of GaAs NWs on the GaAs(111)B (sample 1) and Si(111) (sample 2) substrates are presented in Fig. 1. Analysis of SEM images shows that NWs with smaller radii grow faster than thicker ones for the both samples studied. This confirms the diffusion-induced mode of VLS growth discussed previously [2,3]. In situ analysis of growing NWs by reflection high energy electron diffraction (RHEED) clearly demonstrates the presence of ZB and WZ sequences in GaAs NWs, however, ZB phase appears to be prevalent.

PL measurements were performed at $T = 5$ K. Results of PL characterization of different GaAs NWs are given in Fig. 2 [4]. Fig. 2 a is the PL spectra from the GaAs(111)B substrate. Weak peak at 819 nm is associated with the free exciton and the line at 830 nm is usually explained by the recombination of band-acceptor pairs with carbon acceptors. PL spectra from GaAs NWs on the GaAs substrate (sample 1

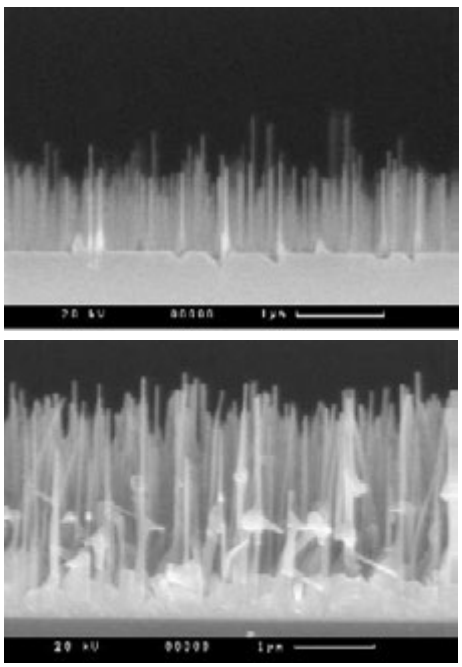

Fig. 1. SEM images of GaAs NWs on the GaAs(111)B (a) and Si(111) (b) substrates.

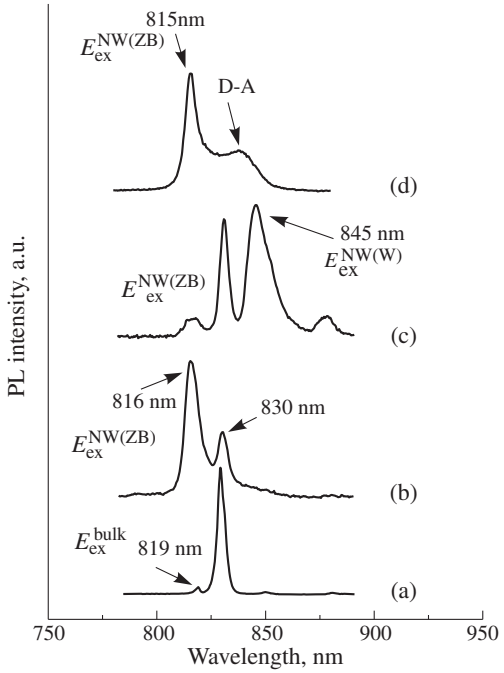

Fig. 2. PL spectra from GaAs substrate (a), ZB GaAs NWs on GaAs(111)B (b), ZB and WZ GaAs NWs on GaAs(111)B (c) and ZB GaAs NWs on Si(111) (d).

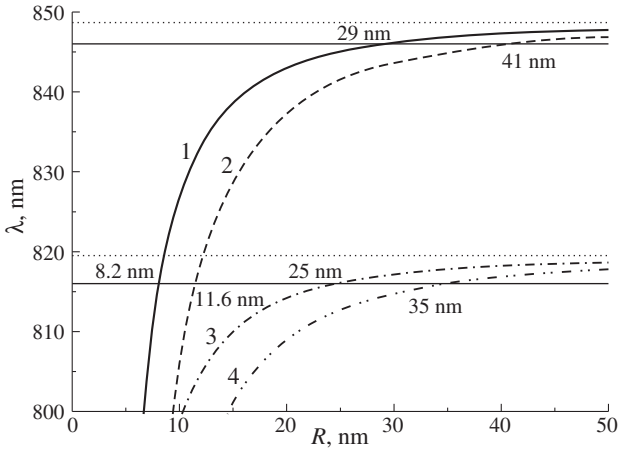

Fig. 3. Theoretical calculations of PL wavelength λ as function of NW radius R: 1 — WZ GaAs NW, 5 eV carrier at the sidewalls; 2 — WZ GaAs NW, infinite barrier; 3 — ZB GaAs NW, 5 eV barrier at the sidewalls; 4 — ZB GaAs NW, infinite barrier. Dotted horizontal lines are the exciton wavelengths for the bulk WZ (849 nm) and ZB (820 nm) GaAs. Solid horizontal lines are the PL peaks from Fig. 2 (846 nm for WZ NWs and 816 nm for ZB NWs).

in Fig. 1a), shown in Fig. 2b, contain two peaks: 815 nm line from ZB NWs and the C-associated line at 830 nm. PL spectra from another part of sample 1 (Fig. 2c) demonstrate the peak at 845 nm, which we presumably attribute to the exciton radiation from WZ GaAs NWs. The position of WZ line is in agreement with theoretical calculations of Ref. [4] and also with our own estimates given below. PL spectra from GaAs NWs grown on the Si(111) substrate (sample 2 in Fig. 1b), shown in Fig. 2d, indicate the presence of ZB NWs only, while the right impurity peak is most probably associated with the donor-acceptor pairs (Si atoms in GaAs NWs and/or defects). This follows from the analysis of the dependence of this line on the temperature and excitation power and is in agreement with the data of Ref. [5].

In order to analyze the positions of PL peaks from ZB and WZ NWs, we perform theoretical calculations of the energy of exciton luminescence, E_{ex}. The expression for E_{ex} under the assumption of infinite barrier for electrons and holes at the NW sidewalls is given by

$$E_{ex} = E_{ex}^{\infty} + \frac{\hbar^2}{m_0}\left(\frac{1}{m_h} + \frac{1}{m_e}\right)\left(\frac{x_{00}^2}{R^2} + \frac{\pi^2}{H^2}\right). \qquad (1)$$

Here, E_{ex}^{∞} is the energy of the bulk GaAs (having ZB or WZ crystal phase) $m_h = 0.51m_0$, $m_e = 0.063m_0$ are the effective masses of holes and electrons, respectively, m_0 is the electron mass, $x_{00} = 2.4048$ — the first zero of the Bessel function J_0, R is the radius and H is the height of cylindrical NW. In view of $R \ll H$, the quantum confinement is dictated by the radius of NW. Results of theoretical calculations for the dominant PL wavelengths, λ, are presented in Fig. 3, where we use Eq. (1) as well as a more complex approximation with a finite barrier at the NW sidewalls of 5 eV. We also utilize the data of Ref. [6] for the values of E_{ex}^{∞} of ZB and WZ GaAs crystal. Comparison of theoretical calculations with the measured PL spectra allows one to estimate the range of radii relating to the observed blue shift due to the quantum confinement effect. These ranges amount to 29–41 nm for WZ and 25–35 nm for the ZB NWs, which is slightly larger but within the reasonable agreement with the results of TEM analyses.

In conclusion, we have demonstrated the possibility for the growth of GaAs NWs on the GaAs and Si substrates by the Au-assisted MBE and perfirmed a detailed PL characterization of these NWs. The results of PL measurements demonstrate the presense of ZB and WZ phase and are with agreement with theoreritical calculations.

Acknowledgements

This work was partially supported by different RFBR grants, different scientific programs of RAS and the contract with the Russian Federal Agency for Science and Innovation. Authors are greatly S. I. Troshkov and V. V. Busov for SEM characterization.

References

[1] R. S. Wagner and W. C. Ellis *et al*, *Appl. Phys. Lett.* **4**, 89 (1964).
[2] V. G. Dubrovskii *et al*, *Phys. Rev. B* **71**, 205325 (2005).
[3] V. G. Dubrovskii *et al*, *Phys. Rev. B* **78**, 235301 (2008).
[4] Z. Zanolli *et al*, *Phys. Rev. B* 75, 245121 (2007).
[5] H. J. Joyce *et al*, *Adv. Funct. Mater.* **18**, 1 (2008).
[6] A. Dargys and J. Kundrotas, *Handbook on Physical Properties of* Ge, Si, GaAs *and* InP, Vilnius, Science and Encyclopedia Publishers, 1994.

17th Int. Symp. "Nanostructures: Physics and Technology"
Minsk, Belarus, June 22–26, 2009
© 2009 Ioffe Institute

Dynamic force spectroscopy for characterization of material properties on nanoscale

S. O. Abetkovskaia and S. A. Chizhik
A. V. Luikov Heat and Mass Transfer Institute, Minsk, Belarus

Abstract. A method for the characterization of material properties on nanoscale based on the dynamic force spectroscopy (DFS) is represented. The advantages of the method in comparison with the prevalent dynamic indentation are showed. An alternative interpretation of the experimental curves of DFS for the two types of materials is proposed.

Introduction

DFS mode of atomic force microscope (AFM) is very promising for the study of local properties of nanostructured materials. The method is based on the properties of the high sensitivity of AFM-tip, oscillating near the surface of the investigated material. The amplitude and phase shift of oscillations microcantilever probe is changed under the influence of interaction of the tip probe with surface layers of materials on nanosize area. The issue of data interpretation, dynamic spectroscopy is relevant [1,2]. This paper presents experimental data DFS in two materials, it is conditionally "hard" and "soft", and the option of interpretation, which allows to separate the influence of elastic and adhesive interactions.

1. Materials

Selected for the experiment, test samples with known values of Young's modulus of material: single crystal silicon wafer and a sample of polyurethane with a pronounced elastic properties. AFM probe is standard silicon dynamic NSC11 (Micromash Co, Lithuania), with a force constant of 48 N/m.

2. Methods

The experiment was carried out using atomic force microscope, NT-206 (Microtestmachines Co., Belarus) dynamic indentation (Spectroscopy in point), and DFS-analysis. DFS-analysis allows us to record the values of amplitude A and phase shift φ during approaching the probe and the sample, not only at a frequency close to resonance, but for a whole range of vibration frequencies of the probe (f) from 0 to 400 kHz (Fig. 1). This allows to keep track of whether the shift of resonant frequency of probe during its interaction with the surface. The shift in resonant frequency may be responsible for the sharp decrease in the amplitude of oscillations of the probe.

3. Results and discussion

The amplitude-frequency-approach and phase shift-frequency-approach of the profile section is selected by frequency, the corresponding maximum peaks of the probe oscillation amplitude for the data analysis procedure DFS-graphs. Fig. 2 presents the profiles of amplitude and phase shift of oscillations probe made to the resonant frequency of 377.8 kHz. As Fig. 1, phase oscillations of the probe makes the jump with the resonant frequency, changing the value from 360° to 0° at the B_1B_2 corresponding probe-sample distance before their contact.

Probe-sample contact occurs in point of B_2 and on there is jumping decrease of amplitude and phase of the probe oscillations for the B_2B_3. However, the resonant frequency shift in the further probe-sample approaching is not observed (Fig. 1, line B_3B_4).

Mathematical simulation showed that such jumps are caused by confrontation attractive and repulsive interactions of the probe and the sample and occur when switching between attraction and repulsion [1,3]. Two or more switches caused by a sufficiently high adhesive interaction can occur in the process of tip-sample approach [4].

In this experiment, a sharp increase in oscillation amplitude of the probe is observed as for the "soft" polyurethane, and for the "hard" silicon after the fall during 10–20 nm from the beginning of contact with the sample. This can be explained by the significant interaction of adhesive polyurethane and silicon probe in the first case and the high surface energy of contact interaction silicon-silicon. Attraction forces lead to increase the amplitude of oscillations of the probe by switching to a higher "branch" oscillation (so-called bi-stability) [1]. This

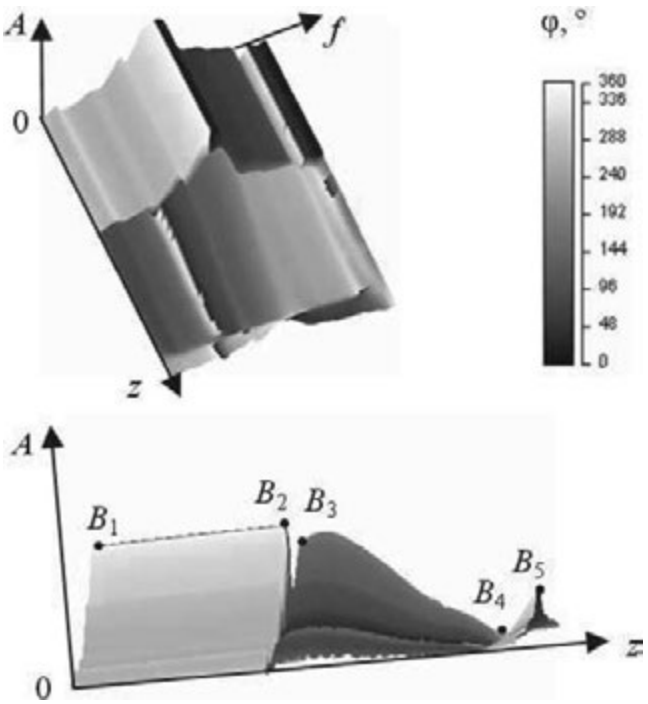

Fig. 1. Example results of monocrystal silicon DFS-analysis. Mixed 3D images of AFM probe oscillation amplitude with a color scheme imposed from the file of probe shift phase.

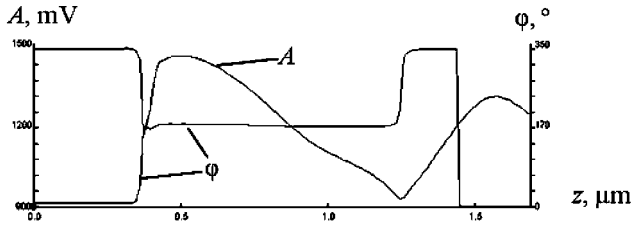

Fig. 2. Profile diagrams of monocrystal silicon DFS-analysis.

is negative for the material imaging in dynamic AFM in the most common mode of amplitude modulation, as in the process of scanning a surface approximation z is always changing in order to keep the amplitude of oscillation constant as the probe parameter feedback.

4. Conclusions

The presented results of the DFS experiment show its advantage over dynamic indentation, which does not allow control changes in the amplitude recorded as a result of the shift of probe resonant frequency. The influence of adhesion forces in DFS-curves on the probe oscillations is evidence of existence the uncontrolled switches of the probe oscillation modes at certain probe-sample distances during the scanning process of the silicon and polyurethane surfaces and the quality of images will be lower. It may be recommended the use of a probe with less force constant or greater probe-sample distance to avoid those switching. The oscillation amplitude of a soft probe will be less responsive to the attractive adhesive interactions, since the elastic properties of the material sample will provide a more significant influence, and vibrations will occur only in mode of the lower branches of the probe oscillation amplitude.

References

[1] R. Garcia and R. Pérez, *Surface Sci. Rep.* **47**, 197 (2002).
[2] S. O. Abetkovskaia and S. A. Chizhik, *J. of Engineering Physics and Thermophysics* **80/2**, 173 (2007).
[3] S. O. Abetkovskaia, A. P. Pozdnyakov, S. V. Siroezkin and S. A. Chizhik, *Recent Advances in Mechatronics* (Berlin Heidelberg: Springer) 551–555, 2007.
[4] S. O. Abetkovskaia and S. A. Chizhik *Proc. Heat and Mass Transfer*, 2007 (Minsk, 2007) 323, 2007.

17th Int. Symp. "Nanostructures: Physics and Technology"
Minsk, Belarus, June 22–26, 2009
© 2009 Ioffe Institute

Fano resonances in photocurrent spectra of InGaAs/GaAsP heterostructure and bulk GaAs doped with shallow acceptors

V. Ya. Aleshkin[1], A. V. Antonov[1], V. I. Gavrilenko[1], *L. V. Gavrilenko*[1] and B. N. Zvonkov[2]

[1] Institute for Physics of Microstructures RAS, Nizhny Novgorod, GSP-105, 603950, Russia
[2] Pysico-Technical Research Institute of the Nizhny Novgorod State University, Nizhny Novgorod, 603950, Russia

Abstract. Fano resonances were detected and investigated in impurity photocurrent spectra of *p*-InGaAs/GaAsP multiple quantum well heterosructure and *p*-GaAs sample series. Moreover in *p*-GaAs photocurrent spectra excited acceptor states concerned Fano resonances were detected.

Introduction

Investigation of phonon induced Fano resonances in photocurrent (PC) spectra of semiconductors doped with shallow impurities is attractive not only as theoretical knowledge but as practical way to determine phonon energy too. These features are more evident in PC spectra of polar material. But the shape of Fano resonance in polar semiconductors are strongly affected by dielectric permittivity behavior nearby phonon energies. This fact complicates identification of Fano resonance features in PC spectra of polar material. By now impurity PC spectra of *p*-GaAs are investigated thoroughly [1] excepting the restrahlen region between optical transversal (TO) and longitudinal (LO) phonon energies, where Fano resonance is expected to be.

Considering Fano resonances are induced by complicated resonance state "hole at acceptor ground state plus LO-phonon". These resonant states appear when wavefunctions of acceptor ground state and continuum states are mixed by means of hole-phonon interaction. In this case Fano resonances manifest themselves in the PC spectra as asymmetric features in the range of LO-photon energy. But excited state wavefunction can be mixed with continuum states wavefunctions too. In that case we will see features in the PC spectra at LO-phonon energy plus inter-level transition energy.

In this paper we report on Fano resonance detection and investigation in PC spectra of quantum well (QW) heterostructure *p*-InGaAs/GaAsP and *p*-GaAs (C, Be, Zn).

1. Experimental results

The PC spectra were measured on InGaAs/GaAsP heterostructures and on a bulk *p*- and *n*-GaAs samples. Parameter of bulk GaAs samples are listed in Table 1. The heterostructures under investigation were grown on semi-insulating GaAs substrate and contains 30 periods of 173 Å wide $In_{0.06}Ga_{0.94}As$ quantum wells separated by 180 Å wide $GaAs_{0.9}P_{0.1}$ barriers. The hole concentration measured by Hall effect at room temperature was 2×10^{11} cm^{-2} per quantum well. The photocurrent spectra were measured by using the BOMEM DA3.36 Fourier-transform spectrometer at 4.2 K.

Figure 1. represents overview of photocurrent spectra for all investigated samples. Impurity photocurrent spectra can be conditionally divided into two bands: long-wave band (180–260 cm^{-1}) corresponds to inter-level hole transitions while short-wave band contains restrahlen region where Fano resonance is expected. The long-wave band helps us to characterize samples purity and acceptor species. For example, *GA* sample only demonstrates pronounced peaks fit with inter-level transition lines of GaAs:Zn. At the short-wave region one broad peak is detected at LO-phonon energy. But dielectric permittivities vary sharply in that region, so electric field strength has features close to phonon energies.

Table 1. Bulk GaAs sample parameters.

Name	Impurity	Concentration, cm^{-1} (300 K)	Doped layer thickness, μm
GA	–	2×10^{15}	13
5636	Zn	1.6×10^{16}	3–3.5
5638	Be	1.2×10^{16}	3–3.5
5640	C	1.1×10^{16}	3–3.5
n-GaAs	Si	8.3×10^{14}	70

2. Impurity photocurrent spectra behavior at the restrahlen band

In polar semiconductor dielectric permittivities dramatically changes with frequency at restrahlen region due to light interaction with transversal optical phonons

$$\kappa(\omega) = \kappa_\infty + \frac{(\kappa_0 - \kappa_\infty)\,\omega_{\mathrm{TO}}^2}{\omega_{\mathrm{TO}}^2 - \omega^2 - i\omega\gamma}, \qquad (1)$$

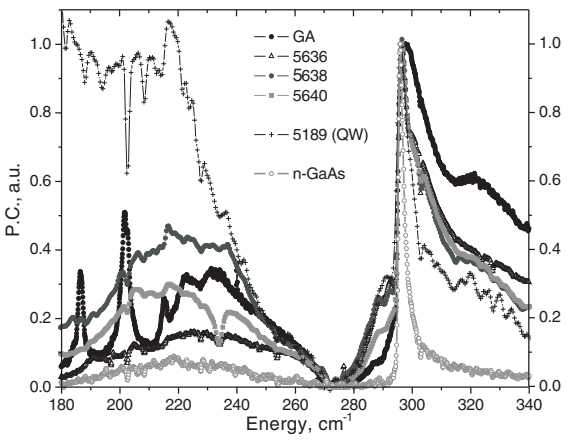

Fig. 1. Photocurrent spectra measured on InGaAs/GaAsP QW heterostructure and *n*- and *p*-GaAs samples.

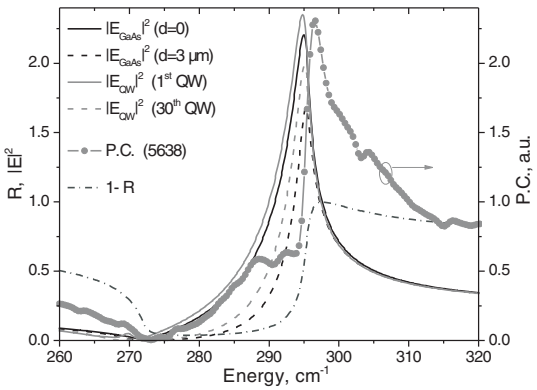

Fig. 2. Spectra of $|E|^2$ for semi-infinite GaAs layer at distance d of interface and also for 1-st and 30-th QWs in InGaAs/GaAsP heterostructure. Spectra of transmitted intensity and photocurrent are labeled as $1-R$ and PC, respectively.

where ω_{TO} and γ are the frequency and reverse time of the TO phonon decay, respectively. For simplicity sake let us considerate first normal dip of electromagnetic waves to the interface of bulk GaAs sample. In that case the electric field strength of transmitted wave is

$$E_{GaAs}(\omega) = \frac{2}{1+\sqrt{\kappa_{GaAs}(\omega)}}\,E_0, \qquad (2)$$

Note that photocurrent value is proportional to the electric field strength squared modulus $|E|^2$ instead of transmitted wave intensity $I = I_0(1-R(\omega))$ as considered in [2]. Both values $|E|^2$ and $1-R$ are presented in Fig. 2. At the restrahlen band behavior of $|E|^2$ and $1-R$ are different.

Therefore, to correctly calculate photocurrent spectrum is necessary to take into consideration electric field strength dependency.

$$J(\omega) = B\,|E_{GaAs}(\omega)|^2\,W(\omega)\int_L^d exp\,[-\eta(\omega)x]\,dx, \qquad (3)$$

where B is some constant, $W(\omega)$ is dipole hole transitions probability, L and d is the thickness of surface depletion region and of the doped layer, correspondingly, $\eta(\omega)$ is the absorbtion coefficient

$$\eta(\omega) = 2\omega Im\left(\sqrt{\kappa(\omega)}\right)/c,$$

and c is electromagnetic constant.

With the help of (3) we can calculate $W(\omega)$ for measured photocurrent spectra on bulk GaAs. As to GaAsP/InGaAs heterostructure we used transfer-matrix method to calculate electric field strength in QW layers. Spectra of $W(\omega)$ for QW heterostructure and p- and $n-GaAs$ are shown in Fig. 3. The region between 270 and 280 cm^{-1} is inconclusive because of division photocurrent by small value. It is seen that in dipole hole transition probability of p-type GaAs Fano resonances manifest themselves as dips, in contrast to n-type GaAs.

As it was mentioned above GA sample the only one of the series demonstrates impurity peaks in PC spectra. Therefore one can expect to detect Fano resonances connected with excited acceptor states on that sample. Indeed, Fig. 4 shows the sequence of narrow dips at energies 449 cm^{-1}, 470 cm^{-1}, 482 cm^{-1}, 498 cm^{-1} which conforms to sum of LO-phonon energy and energies of hole transitions between $1S_{3/2}$ state and

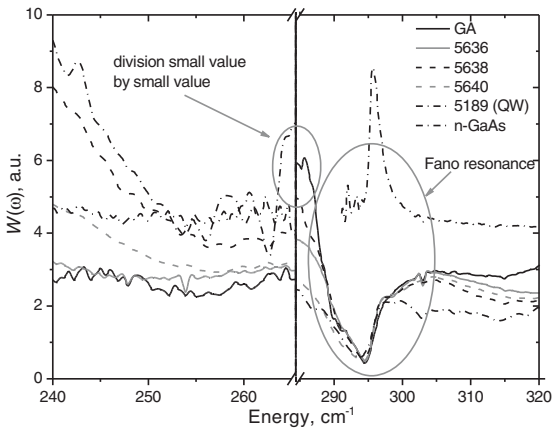

Fig. 3. $W(\omega)$ spectra for QW heterostructure and p-, n-GaAs.

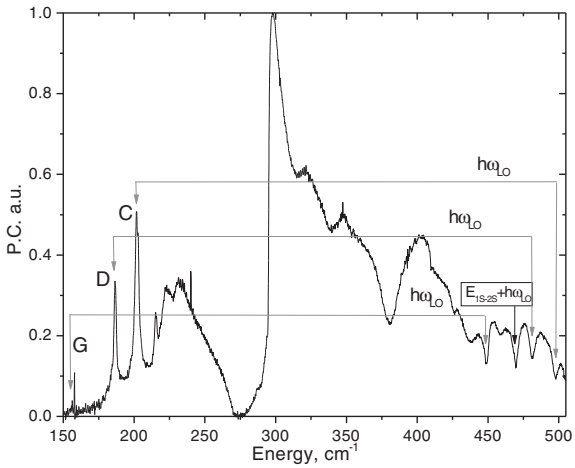

Fig. 4. Photocurrent spectra of GA sample.

excited states $2P_{3/2}(1\Gamma_8^-)$, $2S_{3/2}$, $2P_{5/2}(2\Gamma_8^-)$, $2P_{3/2}(1\Gamma_7^-)$. Resembling features were measured on p-Si [3].

In conclusion note that Fano resonances in p-type GaAs and QW heterostructure were detected. The shape of the spectral feature was investigated and shown that in dipole hole transition probability of p-type GaAs Fano resonances manifest themselves as dips, in contrast to n-type GaAs.

Acknowledgements

This work has been supported by RFBR grants (07-02-00549, 08-02-01126) and Russian Federation President grant MK-4580.2008.2 (for L. Gavrilenko).

References

[1] R. F. Kirkman, R. A. Stradling, P. J Lin-Chung, *J. Phys. C: Solid State Phys.* **11**, 419 (1978).

[2] V. Ya. Aleshkin, A. V. Antonov, L. V. Gavrilenko and V. I. Gavrilenko, *Phys. Rev. B* **75**, 125201 (2007).

[3] H. R. Chandrasekhar, A. K. Ramdas, and S. Rodriguez, *Phys. Rev. B* **14**, 2417 (1976).

17th Int. Symp. "Nanostructures: Physics and Technology"
Minsk, Belarus, June 22–26, 2009
© 2009 Ioffe Institute

Grazing-incidence X-ray reflectometry for structural characterization of samples containing Ge/Si quantum dots

L. I. Goray[1,2], N. I. Chkhalo[3] and Yu. A. Vainer[3]

[1] St Petersburg Physics and Technology Centre for Research and Education RAS, St Petersburg, Russia
[2] Institute for Analytical Instrumentation, RAS, 190103 St Petersburg, Russia
[3] Institute for Physics of Microstructures, 603950 Nizhny Novgorod, Russia

Abstract. High-resolution grazing-angle X-ray reflectometry measurements have yielded experimental and theoretical intensities of specular and diffuse reflection from MBE grown structures with single-layer unburied and multi-layer buried Ge/Si quantum dots (QD). The face slopes measured with a high precision ($\pm 0.1°$) from the position of diffuse scattering peaks in direct space have supported the validity of the known model of QD formation within wells with a structure of inverted pyramids with $\{11n\}$, $n = 7$–11 faces.

Introduction

While transmission electron microscopy, atomic force microscopy (AFM) and near-field scanning optical microscopy do enjoy wide use in analysis of nanosized objects, their application in comprehensive structural studies of quantum dot (QD) systems meets with difficulties. X radiation finds increasing recognition as an integral nondestructive probe for studying nanosized multilayered structures, including atomic-scale roughness of interfaces and interdiffusion. The methods of X-ray diffractometry and reflectometry based on analysis of the specular and diffuse X-ray scattering components in both reciprocal and direct spaces provide rich information for analysis of QD heterostructures.

A recent high-resolution grazing-angle X-ray reflectometry (HRXRR) study has analyzed X-ray scattering from samples with multiple QD ensembles MBE-grown in the In(Ga)As/GaAs system [1]. The position of the experimentally observed diffuse-scattering intensity peaks was found to be totally determined by the slope angle α of the QD pyramid faces (the so-called diffraction grating blaze condition), which had been theoretically predicted earlier [2]. A comparison with the results of numerical modelling of scattering based on the boundary integral equation method suggests that a straightforward geometric condition $2\alpha = \theta_{\rm inc} \pm \theta_{\rm dif}$ permits one to accurately derive α from the position of the intensity peak whose shape depends on many parameters [3]. Besides, the position and amplitude of the Bragg peaks can be employed to deduce the roughness/interdiffusion of an interface and the QD height.

We are reporting here on characterization of MBE-grown structures with one-layer unburied and multilayered buried Ge/Si QDs with the use of experimental and theoretical data on the specular and diffuse scattering intensity.

1. Experimental and numerical

Samples with Ge quantum dots were MBE grown on the vicinal Si(001) surface on a BALZERS UMS 500P setup [4]. Single-layer #1 and #2 samples with Ge QDs without capping layer were produced by Ge deposition at 700 °C on a stressed SiGe layer with 10 and 20% Ge content which was grown on a 100-nm thick Si buffer. A multilayered #3 sample with dome QDs and 20 Ge/Si superlattice layers with a period of 30 nm was grown at 650 °C on a 50-nm thick Si buffer layer and had the same capping layer. A multilayered sample #4 with pyramid and hut QDs and 20 layers of Ge/Si superlattice with a period of 11.7 nm was grown at 550 °C on a 50-nm thick Si buffer layer and had the same capping layer.

Surface morphology of the substrates and grown structures was studied with AFM. This method was used to investigate the size, shape and surface density of the self-organizing nanoislands, as well as to quantify surface roughness of the substrates and Si buffer layers. The AFM measurements were performed *ex situ* in air, in semi-contact mode on Solver PRO and Nanoscope III microscopes.

The specular and non-specular scattering measurements by HRXRR were conducted on a Philips Expert Pro reflectometer with a four-crystal Ge monochromator in $\theta/2\theta$ rocking curve scanning mode, and in θ and 2θ modes when studying diffuse scattering indicatrix. The measurements were performed at a wavelength $\lambda(\mathrm{CuK}_{\alpha 1}) = 0.154$ nm. The detector was a gas-discharge counter with an extremely low intrinsic noise, of the order of 0.1 quantum/s, with an entrance slit adjustable in width [1]. The distance to the sample was 20 mm, the slit width at the crystal monochromator was 100 μm to obtain a strong signal in measurements of scattered light, slit height was 1–5 mm, and the scan step was chosen in the $0.001 - 0.005°$ interval, depending on the desired resolution for an angular beam divergence of 0.003°. The detector slit could be varied from 0.1 to 3 mm.

The calculations based on rigorous electromagnetic theory were performed using a modified method of boundary integral equations (MIM) [5], which turned out to provide high accuracy and fast convergence at large ratios of the characteristic period D and height h of QDs to wavelength λ [6]. The error of the calculations estimated from the energy balance was $\sim 1.E-6$ for 400–1600 collocation points at each boundary of the modeled structures. The time taken up by calculations of a scattering intensity curve with one statistical set of parameters on a workstation with two Quad-Core Intel® Xeon® 2.66 GHz processors, 8 MB L2 Cache, 1333 MHz Bus Clock and 16 GB RAM is ~2 min when operating on Windows Vista® Ultimate 64-bit and employing eightfold paralleling.

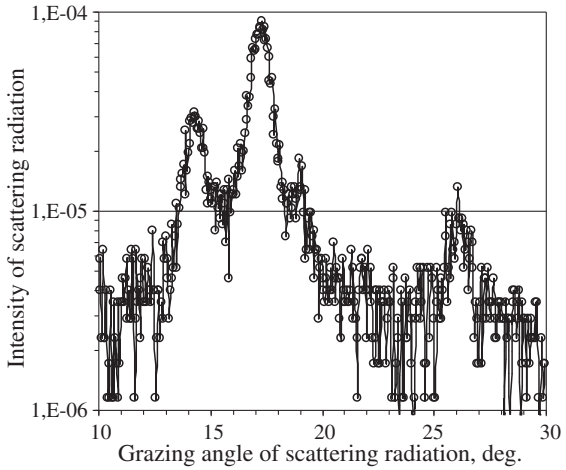

Fig. 1. Measured non-specular reflectance of #2 for 0.154-nm wavelength and 0.304° grazing incidence vs. grazing diffraction angle with +5° deviation from [110] or [1–10].

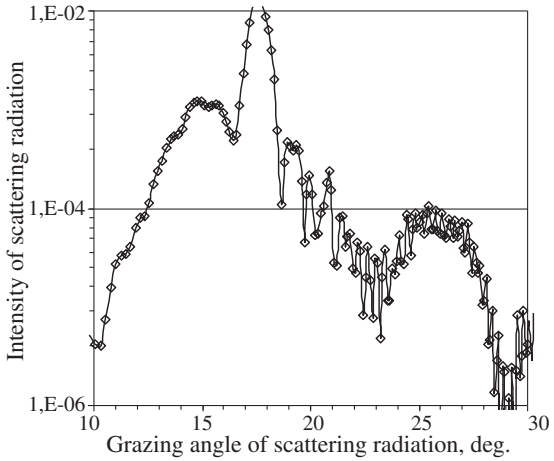

Fig. 2. Calculated diffuse reflectance of #2 for 0.154-nm wavelength and 0.304° grazing incidence vs. grazing diffraction angle.

2. Results and discussions

The QD face slopes measured with a high precision (±0.1°), primarily along the [110] and [1–10] directions from the position of the diffuse scattering peaks in direct space have yielded supportive evidence for the validity of the known model of QD formation inside wells having an inverted pyramid structure with {11n}, $n = 7 - 11$ faces, as well as proved the possible existence of similar faces in dome QDs [7, 8]. We observed these reflections reliably both in single-layer samples and in multilayered samples with a capping layer, structures which can be identified with those of the pyramid and hut and also the dome QDs. Inverted pyramids in the base of the QDs of the samples under study were observed also by AFM.

We have observed and studied a small deviation (by a few degrees) of central normals to the reflecting faces from the [110] and [1–10] directions, which affects noticeably the peak scattering intensity variation. The experimental HRXRR studies of the wells and QD faces have revealed that (1) long-range order in the distribution of self-organizing QDs in different samples grown on vicinal (001) substrates with a Si buffer layer is practically absent in the [100] or [010] directions, and (2) the corresponding faces may be not flat [9]. The AFM data were used to refine the MIM-based model to include generation of reasonable boundary profiles and to optimize the number of points to be arranged.

Typical experimental and theoretical curves of diffuse scattering intensity obtained with the use of HRXRR are shown graphically in Figs. 1 and 2 for the #2 structure. The position and shape of the main peaks in both graphs correlate well; to compare their amplitudes, however, one should reduce the three-dimensional scattering problem to the two-dimensional one [1]. Thus, the traditional use of HRXRR in determination of the layer parameters and of boundary imperfection has been extended in the method considered to include the geometry of QDs epitaxially grown in different systems. To eliminate the effect of factor (1), one should grow QDs with periodic masks, and to reduce the impact of (2), the temperature of deposition of the capping layer should be reduced.

Acknowledgements

The authors are indebted to A. Novikov (IPM) for providing the samples and fruitful discussions. This work has been supported in part by the Russian Foundation for Basic Research through 06-02-17331.

References

[1] L. I. Goray, N. I. Chkhalo and G. E. Cirlin, *Technical Physics* **79**, 117 (2009).
[2] L. I. Goray, G. E. Cirlin, E. Alves, Yu. B. Samsonenko, A. A. Tonkih, N. K. Polyakov and V. A. Egorov, *Proc. 15th Int. Symp. Nanostructures: Physics and Technology*, Novosibirsk, Russia 2007, 118.
[3] L. I. Goray, *Proc. SPIE* **6617**, 661719 (2007).
[4] N. V. Vostokov, Yu. N. Drozdov, D. N. Lobanov, A. V. Novikov, M. V. Shaleev, A. N. Yablonskii, Z. F. Krasilnik, A. N. Ankudinov, M. S. Dunaevskii, A. N. Titkov, P. Lytvyn, V. U. Yukhymchuk and M. Ya. Valakh, *Quantum Dots: Fundamentals, Applications, and Frontiers*, B. A. Joyce *et al*, eds. (Springer, Netherlands) 333–351, 2005.
[5] L. I. Goray, J. F. Seely and S. Yu. Sadov, *J. Appl. Phys.* **100**, 094901 (2006).
[6] L. I. Goray, *Nucl. Inst. and Meth. A* **536**, 211 (2005).
[7] O. P. Pchelyakov, Yu. B. Bolkhovityanov, A. V. Dvurechenskii, L. V. Sokolov, A. I. Nikiforov, A. I. Yakimov and B. Voigtlander, *Semiconducters* **34**, 1229 (2000).
[8] G. Bauer and F. Schaffler, *Physica Status Solidi (a)* **203**, 3496 (2006).
[9] J. Stangl, V. Holy and G. Bauer, *Rev. Mod. Phys.* **76**, 725 (2004).

17th Int. Symp. "Nanostructures: Physics and Technology"
Minsk, Belarus, June 22–26, 2009
© 2009 Ioffe Institute

Electrical properties of single-walled carbon nanotubes selectively grown by low pressure CVD method

O. V. Kononenko[1], V. N. Matveev[1], V. T. Volkov[1], A. A. Firsov[1], D. V. Matveev[2], S. I. Bozhko[2], Yu. A. Kasumov[1], I. I. Khodos[1]

[1] Institute of Microelectronics Technology, RAS, 142432 Chernogolovka, Moscow region, Russia
[2] Institute of Solid State Physics, RAS, 142432 Chernogolovka, Moscow region, Russia

Abstract. Single-walled carbon nanotubes were selectively grown on oxidized silicon substrates by low pressure CVD method. SWCNTs were investigated using high-resolution scanning electron microscope (HRSEM) and Scanning Probe Microscopy. Pd electrodes were prepared to SWCNTs to fabricate two terminal structures for SWCNTs resistance measurements. Contact potential difference between Pd electrode and SWCNT was measured using Kelvin mode of Scanning Probe Microscopy.

Introduction

Single-walled carbon nanotubes (SWCNTs) have attractive properties for using as a building blocks for future nanoelectronics devices due to the outstanding electrical, mechanical, physical, and optical properties of the typical one-dimensional (1D) materials. In recent years, many studies have been performed on single-walled carbon nanotubes for their promising applications in future nanoelectronics and nanodevices such as SWCNT field effect transistors (FETs) [1–3], logic devices [4–6], resonators [7,8], field emitters [9,10] and sensors [11–13].

Catalytical CVD [14] is one of the main techniques of carbon nanotubes (CNTs) synthesis and is very important for many applications [15,16]. Recently we reported on a new technique for CVD synthesis of carbon nanotubes under very low pressure of acetylene (about 0.4 torr) without any gas flow. The good quality of obtained nanotubes is confirmed by TEM observation and electron diffraction patterns, Raman spectroscopy and electron transport measurements [17].

Selective growth of CNTs on substrates is utterly desirable for fabrication of nanoelectronic devices. In this work we report on selective growth of SWCNTs on oxidized silicon substrates, fabrication of two terminal devices on the basis of SWCNTs and characterization of SWCNTs by high-resolution scanning electron microscope (HRSEM) and Scanning Probe Microscopy.

1. Experimental

The carbon nanotubes were synthesized on oxidized silicon substrates as follows. At first, a platinum film with chrome underlayer was deposited by e-beam evaporation on oxidized silicon wafer using photolithography mask to form contact pads and lanes. Then the wafer was cut up to obtain chips. 10 nm Al/1 nm Fe bilayer catalyst was selectively deposited by e-beam gun onto the chips using electron beam lithography and a lift-off technique. After that the chips with deposited bilayer catalyst were heated in a furnace in air atmosphere for 2 min in order to form Fe nanoparticles. The nanotube synthesis proceeds as follows. The samples are placed in a quartz tube reactor, which is pumped down to a pressure about 10^{-6} torr and then inserted into a furnace preheated up to 910 °C. When the samples are heated to the reaction temperature, acetylene is admitted into the quartz tube up to pressures of 0.4 torr for 5 s and then pumped out and extracted from the furnace. Results of the growth were controlled with aid of high-resolution scanning electron microscope SUPRA 50VP (Carl Zeiss) (Fig. 1).

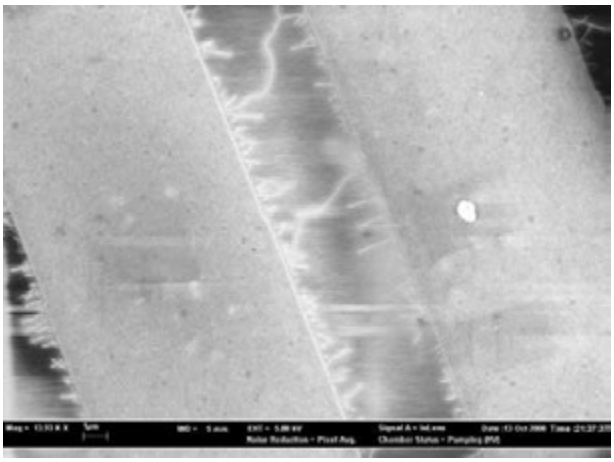

Fig. 1. SEM image of SWCNTs.

E-beam lithography (on the basis of Scanning Electron Microscope EVO 50 Carl Zeiss with NanoMaker system) and a lift-off process were used to pattern e-beam evaporation deposited palladium electrodes contacting nanotubes. Two-terminal structures were used for measurements of electrical properties of SWCNTs (Fig. 2). SWCNTs were also investigated with aid of Scanning Probe Microscopy (SOLVER P47H-PRO NT-MDT).

2. Results and Discussions

Figure 1 shows SEM image of SWCNTs grown on the oxidized silicon substrate with 10×30 μm^2 catalyst layers. SWCNTs can be visualized in SEM due to the electron-beam stimulated field emission from single-walled carbon nanotubes on an insulating substrate [18]. It is seen that SWCNTs grow far away from the edge of catalyst layer along the substrate surface. The angle between the edge of catalyst layer and SWCNTs in many cases is close to 90°. Such arrangement of SWCNT's gives us possibility to fabricate contacts to selected SWCNTs. The example of six nanotubes contacted between two Pd electrodes is shown in Fig. 2.

Resistance of four two-terminal structures containing from three to eight SWCNTs parallel connected between Pd contacts

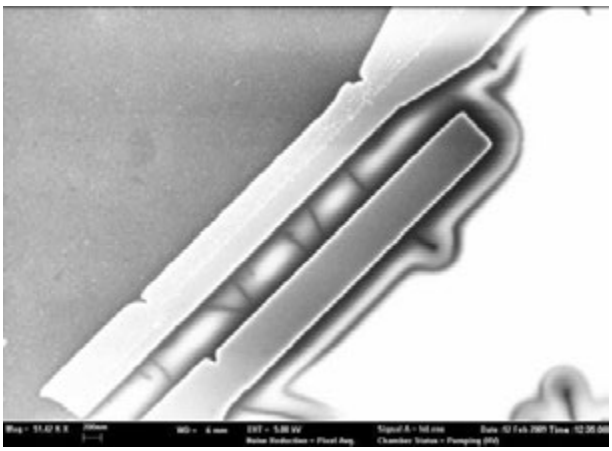

Fig. 2. SEM image of two-terminal structure for electrical characterization of SWCNTs.

was measured. The resistance was in the range from 15 to 50 kOhm.

SWCNTs were investigated in the scanning probe microscope SOLVER P47H-PRO NT-MDT using AFM semicontact mode and Kelvin mode. For investigation we used a cantilever with conductive probe coated by 10 nm Pd.

We have found that it is very difficult to visualize SWCNTs in the scanning probe microscope using AFM regime. It took additional processing of AFM image in order to display SWCNTs. Diameters of the SWCNTs have been found to be 1 nm.

Kelvin mode is based on the two-pass technique. In the first pass the topography is acquired using standard semicontact mode. In the second pass this topography is retraced at a set lift height from the sample surface to detect the electric surface potential $\Phi(x)$. Thus, we have information about Contact Potential Difference distribution along the sample surface.

Figure 3 shows images obtained in AFM and in Kelvin modes. It is seen that Kelvin mode give us possibility to visualize SWCNTs easily. The same place of sample is shown in Fig. 2 and Fig. 3.

As far as contact electrodes and cantilever tip coating are made of the same material (Pd) we can obtain the difference of Pd and SWCNT work function knowing the contact potential difference between Pd electrode and SWCNT. From our measurements we found that the contact potential difference between Pd electrode and SWCNT is about 160 mV.

In conclusion, SWCNTs were selectively grown on oxidized silicon substrates by low pressure CVD method. Pd electrodes were prepared to SWCNTs to fabricate two terminal structures for SWCNTs resistance measurements. Contact potential difference between Pd electrode and SWCNT was measured using Kelvin mode of Scanning Probe Microscopy.

Acknowledgements

This work has been supported in part by the International Science and Technology Center, grant No. 3836.

References

[1] E. J. Bae *et al*, *Nanotechnology* **18**, 495203 (2007).
[2] H. Li *et al*, *Nano Lett.* **8**, 64 (2008).
[3] Y. Tang *et al*, *Nanotechnology* **18**, 445203 (2007).

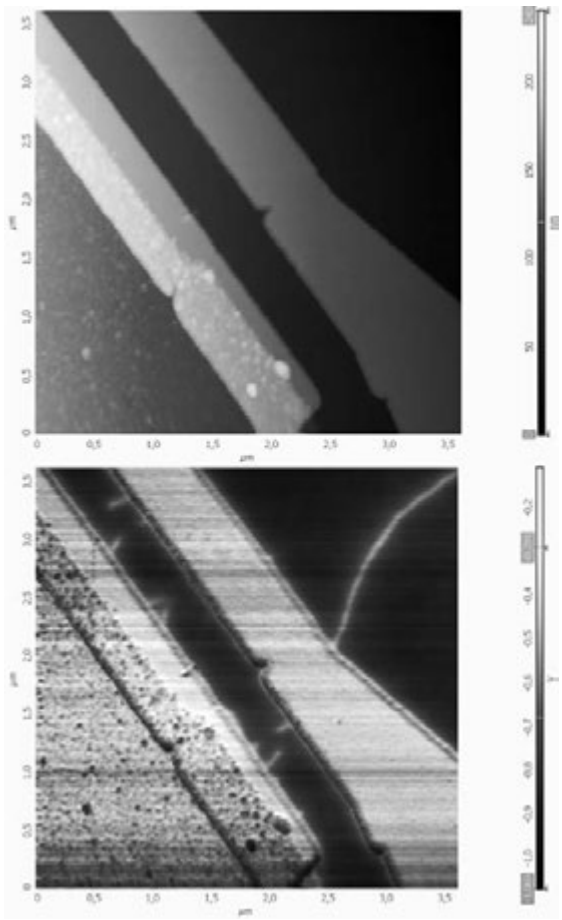

Fig. 3. AFM (top) and Kelvin mode (bottom) images of sample area shown in Fig. 2.

[4] Z. Chen *et al*, *Science* **311**, 1735 (2006).
[5] A. Bachtold *et al*, *Science* **294**, 1317 (2001).
[6] Y. Huang *et al*, *Science* **294**, 1313 (2001).
[7] D. Garcia-Sanchez *et al*, *Phys. Rev. Lett.* **99**, 085501 (2007).
[8] R. F. Gibson *et al*, *Compos. Sci. Technol.* **67**, 1 (2007).
[9] K. A. Dean *et al*, *Appl. Phys. Lett*. 75, 3017 (2001).
[10] K. Matsumoto *et al*, *Appl. Phys. Lett*. **78**, 539 (2001).
[11] M. Lucci *et al*, *Sensors Actuators B* **118**, 226 (2006).
[12] T. Zhang *et al*, *Nanotechnology* 18, 165504 (2007).
[13] M. K. Kumar *et al*, *Sensors Actuators B* **130**, 653 (2008).
[14] K. B. K. Theo *et al*, (Ed.), *Catalytic Synthesis of Carbon Nanotubes and Nanofibers in Encyclopedia of Nanoscience and Nanotechnology* (American Scientific Publishers, New York, 2004), **1**, p. 665.
[15] M. S. Dresselhaus *et al*, (Eds.),*Carbon Nanotubes: Synthesis, Structure, Properties and Applications*, (Topics in Applied Physics) (Springer, Berlin, 2001).
[16] R. H. Baughman *et al*, *Science* **297**, 787 (2002).
[17] Y. A. Kasumov *et al*, *Appl. Phys. A* **88**, 687 (2007).
[18] A. Nojeh *et al*, *Appl. Phys. Lett*. **85**, 112 (2004).

17th Int. Symp. "Nanostructures: Physics and Technology"
Minsk, Belarus, June 22–26, 2009
© 2009 Ioffe Institute

Propagation of Bessel vortices in metamaterials

S. N. Kurilkina and N. S. Kazak
B. I. Stepanov Institute of Physics, NASB, Minsk 220072, Belarus

Abstract. The properties of Bessel vortices propagation and transformation in metamaterials are studied. The possibility is established for unidirectional and opposite directional propagation of Bessel light beams (BLBs) phase and the longitudinal component of its energy flux in metamaterials. It is shown that the transversal part of energy flux of TE and TH polarized high-order Bessel beams has only azimuthal component. It is evidence of the existence of spiral energy fluxes in such beams. The problem is solved by reflection and refraction of vectoral BLBs containing embedded vortices on the boundary of a usual medium and metamaterial. The reflection and refraction coefficients of arbitrary Bessel beam are represented as superposition of linear combinations of reflection and refraction ones of TE and TH polarized Bessel beams. It is established that during crossing the boundary of the usual medium and metamaterial the change of directions of energy flow rotation and orbital angular momentum of a high-order Bessel light beam on the opposite one takes place.

Introduction

Over 30 years ago, V. Veselago [1] suggested that in an isotropic media with a negative dielectric permittivity ε and negative magnetic permeability μ, named as metamaterials, the situation can be realized when a Pointing vector is opposite to the wave vector $\vec{k}$. The predictions of V. Veselago have stimulated appearance of many theoretical and experimental papers in recent years (see, for example, [2–4]). However, as a rule, authors investigate the properties of plane monochromatic wave propagation in metamaterials. During the last decade, Bessel light beams (BLBs), which are characterized by a suppressed diffraction of their central part, have been under extensive consideration owing to wide application for manipulation of microparticles, probing the technical and biological objects, in photolithography [5–7]. In the present paper the properties of Bessel beams of higher orders (or Bessel vortices) propagation in metamaterials are studied.

1. Circularly polarized Bessel vortices in metamaterials

The transverse component of the right circularly polarized electromagnetic field propagating in a medium can be represented as a superposition of TE and TH modes in the form:

$$\begin{aligned}&\vec{E}_\perp(R) = (\imath/\sqrt{2})\exp\left[\imath((m-1)\phi + k_z z)\right]\\&\left\{A^{\mathrm{TE}}\left[J_{m-1}(q\rho)\vec{e}_+ + J_{m+1}(q\rho)\exp(2\imath\phi)\vec{e}_-\right]\right.\\&\left.+A^{\mathrm{TH}}\cos\gamma\left[J_{m-1}(q\rho)\vec{e}_+ - J_{m+1}(q\rho)\exp(2\imath\phi)\vec{e}_-\right]\right\}.\end{aligned} \tag{1}$$

Here $A^{\mathrm{TE,TH}}$ are the constants, γ is the half-cone angle of BLB in the medium, k_z is z-projection of the wave vector, $\vec{e}_\pm = (\vec{e}_1 \pm \imath\vec{e}_2)/\sqrt{2}$ are the unit circular vectors. If electromagnetic wave is reflected (refracted) on the boundary of ordinary medium and metamaterial, $A^{\mathrm{TE,TH}} = Ar^{\mathrm{TE,TH}}$ ($A^{\mathrm{TE,TH}} = At^{\mathrm{TE,TH}}$); $r^{\mathrm{TE,TH}}$, $t^{\mathrm{TE,TH}}$ are reflection and transmission coefficients for TE and TH BLBs, respectively, which can be determined using the boundary conditions:

$$\begin{aligned}t^{\mathrm{TE}} &= \frac{2n_i\cos\gamma_i}{n_i\cos\gamma_i - \sqrt{(\varepsilon_t/\mu_t)}\cos\gamma_t};\\ r^{\mathrm{TE}} &= \frac{n_i\cos\gamma_i + \sqrt{(\varepsilon_t/\mu_t)}\cos\gamma_t}{n_i\cos\gamma_i - \sqrt{(\varepsilon_t/\mu_t)}\cos\gamma_t};\end{aligned}$$

$$\begin{aligned}t^{\mathrm{TH}} &= \frac{2n_i\cos\gamma_i}{n_i\cos\gamma_t - \sqrt{(\varepsilon_t/\mu_t)}\cos\gamma_i};\\ r^{\mathrm{TH}} &= \frac{-n_i\cos\gamma_t - \sqrt{(\varepsilon_t/\mu_t)}\cos\gamma_t}{n_i\cos\gamma_t - \sqrt{(\varepsilon_t/\mu_t)}\cos\gamma_i}.\end{aligned}$$

Index "t''"("i''") denotes metamaterial (ordinary medium). It follows from Eq. (1) that if a right curcularly polarized Bessel light beams falls to the "ordinary medium-metamaterial" interface, transmitted BLB is elliptically polarized (Fig. 1).

Note that for numerical simulation here and further we used the metamaterial with $\varepsilon_t(\nu) = 1 + (25/(0.81 - \nu^2)) + (100/(132.25 - \nu^2))$; $\mu_t(\nu) = 1 + (9/(0.813604 - \nu^2))$, where ν is the frequence measured in GHz (in our case $\nu = 1$).

One can obtain from (1) for the longitudinal component of the Pointing vector of incident $S_{i,z}$, reflected $S_{r,z}$ and transmitted $S_{t,z}$ Bessel beam:

$$\begin{aligned}S_{i,z} &= (c/2\pi)\,n_i\left[\left(1+\cos^2\gamma_i\right)F_{1m}(\rho) + \cos\gamma_i F_m(\rho)\right],\\ S_{r,z} &= -(c/2\pi)\,n_i\left[\left(1+\cos^2\gamma_i\right)r^{\mathrm{TE}}r^{\mathrm{TH}}F_{1m}(\rho)\right.\\&\quad\left.+cos\gamma_i\left[\left(r^{\mathrm{TE}}\right)^2 + \left(r^{\mathrm{TH}}\right)^2\right]F_m(\rho)/2\right],\end{aligned} \tag{2}$$

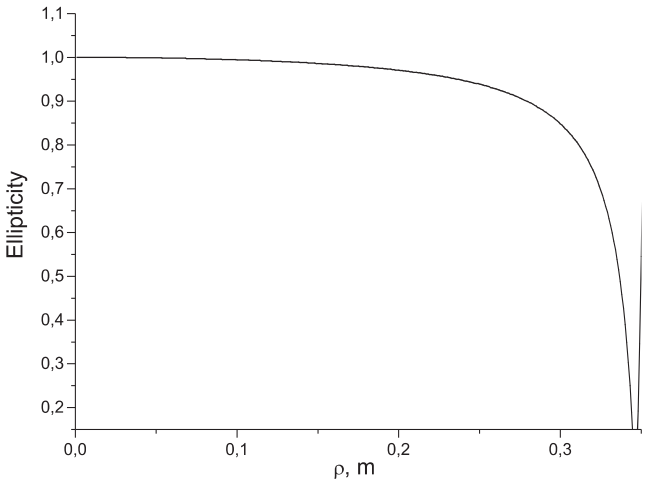

Fig. 1. Ellipticity in transversal section of the Bessel light beam transmitted through metamaterial. Conicity angle of incident right circularly polarized BLB is 20°.

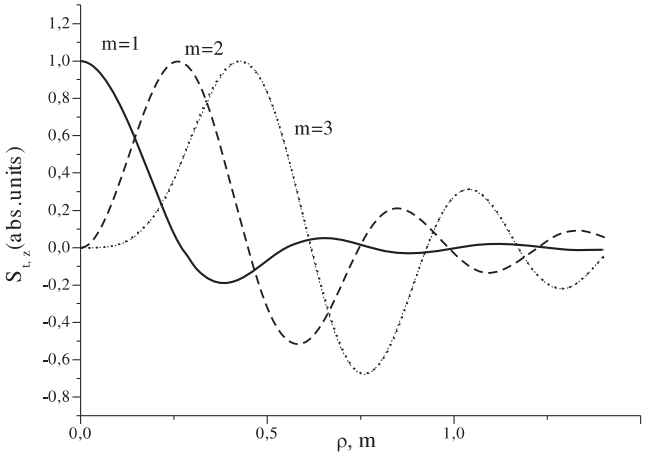

Fig. 2. Radial dependence of longitudinal component of the Pointing vector for transmitted Bessel light beam. Conicity angle of incident right circularly polarized BLB is 20°.

$$S_{t,z} = -(c/2\pi)\sqrt{(\varepsilon_t/\mu_t)}\left[\left(1+\cos^2\gamma_t\right)t^{\mathrm{TE}}t^{\mathrm{TH}}F_{1m}(\rho) + cos\gamma_t\left[\left(t^{\mathrm{TE}}\right)^2+\left(t^{\mathrm{TH}}\right)^2\right]F_m(\rho)/2\right]. \quad (3)$$

Here $F_{1m}(\rho) = (m/q\rho)J_m(q\rho)J'_m(q\rho)$. Calculations made in accordance with (3) show that the longitudinal component of the Poynting vector for TE and TH BLB is positive and opposite to the direction of the propagation of the beam, but in the case of circularly polarized incident Bessel light beam this component can vary direction (Fig. 2).

Thus, it is possible as unidirectional as opposite directional propagation of BLB phase and longitudinal component of its energy flux in metamaterials. This effect takes place for Bessel vortex beam having any topological charge even for small conicity angles. Note, that the Poynting vector forms some rings inside which its longitudinal component is collinear to the propagation direction of BLB, but the larger the narrower and lower intensive these rings. If the conicity angle of incident BLB increases, the region of unidirectional propagation of phase and energy flux decreases. It takes place for any order of Bessel vortex (see, for example, Figs. 3,4).

It follows from (1),(2) that in the case of TE and TH polarized Bessel vortex beam, propagating in metamaterial, the transversal part of energy flux has only azimuthal component. It is evidence of the existence of spiral energy fluxes in such beams. At that the direction of the rotation of energy fluxes is opposite as compared with ordinary medium. By this, while during crossing the boundary of the ordinary medium and metamaterial the change of the direction of orbital angular momentum of a high-order light beam on the opposite one takes place.

Thus, it has been studied the properties of Bessel vortices transformation in metamaterials. The possibility is established for unidirectional propagation of Bessel light beams phase and the longitudinal component of its energy flux in metamaterials. It has been predicted the phenomenon of changing the directions of energy flux rotation and orbital angular momentum of a high-order BLB on the opposite one during crossing the boundary of the ordinary medium and metamaterial. Results obtained can be used while elaborating the elements for controlling Bessel light beams on the base of metamaterials.

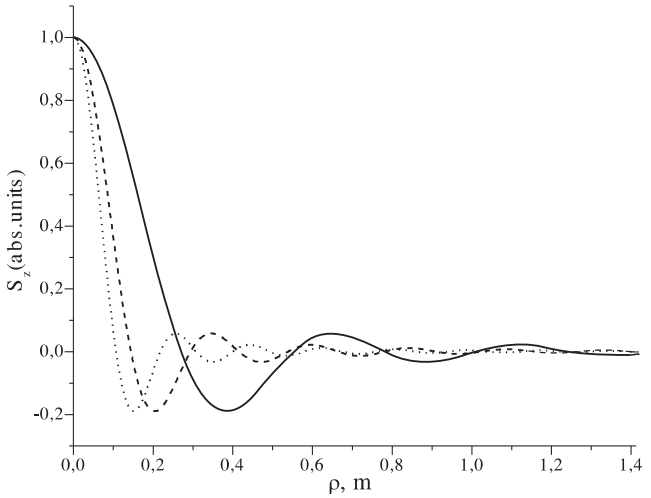

Fig. 3. Radial dependence of longitudinal component of the Pointing vector for transmitted Bessel light beam. Conicity angle of incident right circularly polarized 0-th order BLB is 20° (solid line), 40° (dash line), 60° (dotted line).

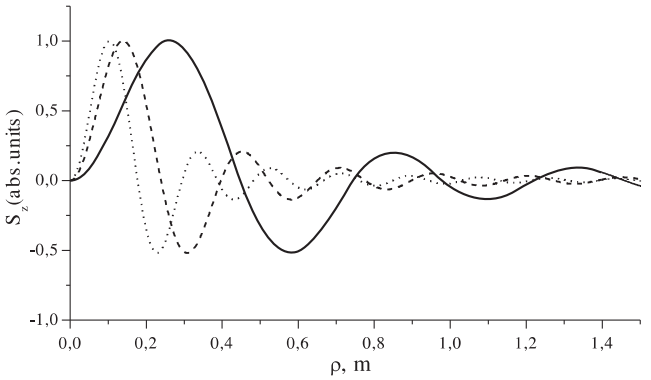

Fig. 4. Radial dependence of longitudinal component of the Pointing vector for transmitted Bessel light beam. Conicity angle of incident right circularly polarized 1-th order BLB is 20° (solid line), 40° (dash line), 60° (dotted line).

References

[1] V. G. Veselago, *Sov. Phys. Usp.* **10**, 509 (1968).
[2] J. Pendy, *Opt. Express* **11**, 639 (2003).
[3] A. Lakhtakia, M. Mccall, *New J. Phys.* **7**, 755 (2005).
[4] D. Smith *et al*, *Science* **305**, 788 (2004).
[5] J. Arlt, K. Dholakia, *Opt. Communs.* **177**, 297 (2000).
[6] N. S. Kazak *et al*, *Proc. Laser Physics and Spectroscopy-1999* **1**, 158 (1999).
[7] N. S. Kazak *et al*, *Proc. SPIE* **6729**, 67290I1 (2007).

17th Int. Symp. "Nanostructures: Physics and Technology"
Minsk, Belarus, June 22–26, 2009
© 2009 Ioffe Institute

Application of complementary analysis for nanotechnology optimisation of epitaxial Fe(001) structures with improved electron transport and magnetic properties

G. M. Mikhailov, L. A. Fomin, I. V. Malikov, S. V. Piatkin and V. Yu. Vinnichenko
Institute of Microelectronics Technology RAS, 142432 Chernogolovka, Russia

Abstract. Complementary analysis of morphology, magnetic and crystalline structures, electron transport and magnetic properties supports developing nanotechnology of epitaxial ferromagnetic conductors with improved electron transport and magnetic properties. Surface morphology essentially affects on epitaxial ferromagnetic conductor properties when singlecrystalline growth in the conductor bulk is observed.

Introduction

Both the bulk and surface structures of a small size conductor have to be considered during optimisation of ferromagnetic nanostructure technology. However, optimal conditions for perfect structure growth in the bulk may be completely far from those for surface structure, in particularly, for flat atomic surface growth during film epitaxy. As far as physical properties of a conductor depend on cooperative effect of many factors influencing also on electrical and magnetic properties, application of the methods carrying complementary information of the subject of investigation is desirable. Sometimes, the choice of the methods is not so evident. In the present work, we applied successfully complementary analysis of surface morphology, magnetic and crystalline structures, electron transport and magnetic properties for optimisation of ferromagnetic epitaxial Fe(001) structures fabrication

1. Experimental

Nanotechnology of epitaxial ferromagnetic structures includes an epitaxial film growth and subtractive microstructurization using electron lithography for nanomask fabrication followed by ion etching [1]. The Fe(001) films were grown by pulse laser deposition technique under ultra high vacuum on singlecrystalline sapphire R-plane substrate. The Mo(001) seed layer of 10 nm thick was used to improve Fe-film surface morphology. For electron mobility characterisation, we used residual resistance ratio to define a residual electron mean free path (L_{eff}), which in integral manner depends on structure-defect density both in the bulk and on the surface. Magnetoresistance measurements were used to characterise magnetic properties. By these data, we measured the coercive forces (H_{c}) and the sharpness of magnetic reversal (ΔH). Surface morphology of Fe(001) structures was investigated using atomic force microscope (AFM) detecting a mean roughness amplitude (S_q) and roughness correlation length (L_{c}). Surface magnetic structures were investigated by magnetic force microscope (MFM) supported by micromagnetic calculation [2] and numerical simulation of magnetic contrast for data interpretation. The bulk structure of the conductors was monitored by X-ray diffraction.

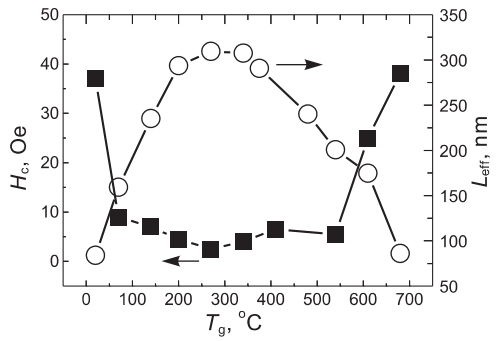

Fig. 1. Dependence of L_{eff} (circles) and coercive forces H_{c} (squares) on the film growth temperature.

2. Results and consideration

Dependence of L_{eff} versus the Fe-film growth temperature (T_{g}) is depicted in Fig. 1 (circles). Residual mean free path increases with the growth temperature till 280 °C. Maximum of the curve is observed in the temperature range 200–400 °C with $L_{\text{eff}} = 320$ nm at $T_{\text{g}} = 280$ °C exceeding film thickness. Further growth temperature rise causes the drop of L_{eff} because of defect density increase. This conclusion is supported by coercive force dependence (Fig. 1 (squares)). Position of H_{c} minimum evidencing of the small pinning centers density is near the position of L_{eff} maximum.

Film morphology evolution with growth temperature is clearly seen in AFM surface imaging. Single crystalline blocks are visualized whose sizes increase with the growth temperature. In temperature range 200–400 °C, the typical roughness correlation length $L_{\text{c}} \sim 50$ nm is found. Near 270 °C growth temperature the strip like morphology is observed indicated on ordered film growth. Under this growth temperature, the X-ray analysis showed the high quality singlecrystalline film growth with small inclination of [001] crystalline axis against the film surface normal related with specific growth mechanism of Mo(001) seed layer on sapphire R-plane [3]. The L_{c} increases in few times and is about 200 nm at growth temperatures 500–700 °C. Most flat film surface with mean roughness amplitude $S_q \approx 0.4$ nm belongs to the films grown near 200 °C (Fig. 2 (squares)). This differs from the optimum temperature value found from the data of Fig. 1. As it follows from the results presented in Fig. 1 and ΔH dependence (Fig. 2 (circles)), the epitaxial Fe(001) films with improved electron transport and magnetic properties were grown at 280 °C. Based on evident correlation of the experimental data collected by different analytical methods (Figs. 1 and 2) and X-ray diffraction analy-

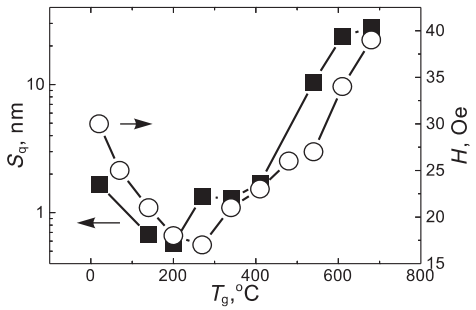

Fig. 2. Dependence of mean roughness S_q (squares) and the width of magnetic reversal ΔH (circles) on the film growth temperature.

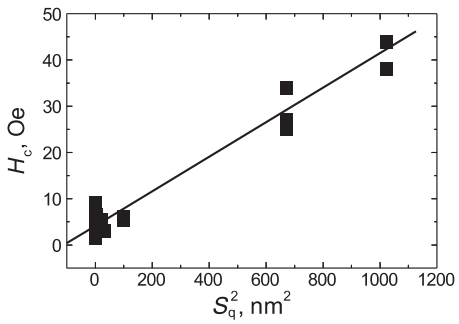

Fig. 3. Coercive forces H_c versus S_q^2 for different Fe(001) films. The straight line is the best fit by Eq. (1).

sis we attribute this discrepancy to the not perfect film growth in the bulk originated at the growth temperatures below 200 °C. As far as the electron mean free path exceeds the film thickness under optimal film growth, most electron scattering and magnetic pinning centers are suited on the film surface because of its roughness irregularities. This causes the correlation between experimental data for coercive forces and roughness amplitude. The straight dependence is observed for H_c versus S_q^2, collected for the film grown under different conditions (Fig. 3). This dependence was predicted theoretically and experimentally investigated in [4,5]. Follow the approach realized in [4], we applied the Eq. (1) to fit experimental data.

$$H_c = \frac{\sigma S_q^2 A^2}{2d^2 L_c M_s} \qquad (1)$$

where σ is domain wall energy per square, d is the film thickness, M_s is saturation magnetic moment and A is anisotropy factor. Substituting the thickness of the films and $L_c = 220$ nm measured by AFM together with the values of $\sigma = 4$ erg/cm^2 and $M_s = 1700$ Gs known for bulk Fe-conductors we found that the best fit by Eq. (1) (Fig. 3) gives the anisotropy factor $A \approx 7$.

Fabricated epitaxial Fe(001) nanostructures by means of subtractive technique that applied to process the films with maximum electron mean free path exhibit regular magnetic structure. It depends on the nanostructure shape, sizes and nanostructure orientation against the axis of easy magnetization (AEM). The MFM magnetic contrast of the Fe(001) epitaxial nanostructure oriented by it's long axis at angle 45° against the AEM (i.e. along in-plane axis of hard magnetization) is presented in Fig. 4(a). It shows complex spatial distribution of magnetic moments. Numerical simulation of magnetic contrast (b) performed in frozen magnetic moments approximation

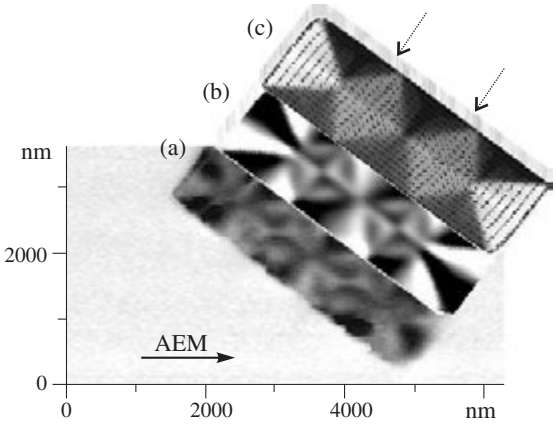

Fig. 4. MFM magnetic contrast of epitaxial Fe(001) nanostructure (a), numerical simulation of magnetic contrast (b) and the result of micromagnetic calculation (c). Direction [010] of the axis of easy magnetisation is depicted.

with use of micromagnetic calculation (c) reveal appearance of three circle-type (in both edges and in the centre of the strip) and two hyperbolic vortexes marked in Fig. 4 by pointed arrows in excellent agreement with experimental data (a).

As the result, application of complementary methods of analysis for morphology, magnetic and crystalline structures, electron transport and magnetic properties characterisation allows developing nanotechnology of epitaxial ferromagnetic Fe(001) conductors with improved electron transport and magnetic properties. Correlation of experimental data collected by different analytical methods supports the most reliable approach for nanotechnology optimisation. Surface morphology essentially affects on epitaxial ferromagnetic nanostructure properties when singlecrystalline growth in the ferromagnetic nanostructure bulk is observed.

Acknowledgements

The work was partly supported by the grant of Russian Academy of Sciences Presidium on Nanotechnology and the RFBR grant 07-07-00119-a.

References

[1] G. M. Mikhailov, L. I. Aparshina, S. V. Dubonos, Yu. I. Koval, I. V. Malikov and A. V. Chernykh, *Nanotechnology* **9**, 1 (1998).
[2] http://math.nist.gov/oommf.
[3] I. V. Malikov, G. M. Mikhailov, *Thin Solid Films* **360**, 278 (2000).
[4] P. Bruno, G. Bayreuther, P. Beauvillain, C. Chappert, G. Lugert, D. Renard, J. P. Renard and J. Seiden, *J. App. Phys.* **68**, 5759 (1990).
[5] M. Li, Y. P. Zhao, G. C. Wang and H. G. Min, *J. App. Phys.* **83**, 6287 (1998).

17th Int. Symp. "Nanostructures: Physics and Technology"
Minsk, Belarus, June 22–26, 2009
© 2009 Ioffe Institute

Optical and magneto-optical studies of atomically thin Fe films on Si(001)

N. I. Plusnin[1,2], V. M. Iliyashenko[1,2], S. A. Kitan'[1,2], S. V. Krylov[1,2], N. A. Tarima[1,2], V. V. Pavlov[3], P. A. Usachev[3] and R. V. Pisarev[3]

[1] Institute of Automation and Control Processes of Far East Branch of RAS, 690041 Vladivostok, Russia
[2] Vladivostok State University of Economy and Service, 690600 Vladivostok, Russia
[3] Ioffe Physical-Technical Institute, St Petersburg, Russia

Abstract. Reflection and transmission optical spectra and the magneto-optical polar Kerr effect have been investigated in ultrathin (0.3–12 Å) Fe films grown on Si(001) surface. This study has been done for Fe surface phase (thickness $d = 0.3$ Å), atomically thin film phase of Fe ($d = 1.2$ Å), ultrathin films of FeSi silicide ($d = 3.0$ Å), FeSi-Fe_3Si silicide mixture ($d = 4.5$ Å), Fe_3Si silicide ($d = 6.0$ Å), and also ultrathin film of Fe deluted by Si ($d = 12$ Å). It has been shown that the atomically thin Fe film ($d = 1.2$ Å) had the largest reflection and the lowest transmission coefficients in the near IR region, and the lowest reflection coefficient in the UV region. Surprisingly, this film demonstrated the largest value of the magneto-optical polar Kerr effect.

Introduction

Atomically thin metal films grown on semiconductor surfaces are very interesting nanomaterials due to a number unique physical phenomena such as interface and quantum-dimensional effects [1]. These effects make ultrathin films a basis for potential applications in spintronics and optoelectronics [2]. In addition, nanodimensional transition metal (like Cr, Fe or Co) films, deposited on semiconductors, may possess unusual crystal, electronic and magnetic structures which significantly differ from those for bulk metals due possible interface phenomena, mismatch effects and growth conditions.

The growth and formation of atomically thin films of transition metals on silicon have been studied in [3,4,5,6,7]. However, optical and magneto-optical properties of atomically thin films of transition metals and, in particular, magnetic Fe, and magnetic silicides FeSi and Fe_3Si on Si(001) have not been investigated so far.

In this paper we present optical and magneto-optical *ex-situ* studies of ultrathin films of Fe on Si(001), which show some unique properties of Fe film nanophase with thickness of 1.2 Å. Up to now attempts to prevent formation of silicide interface layer between Fe and Si failed (see for example [8]). The only known the studies of magnetic properties of Fe on atomically thin Au buffer interlayer were published in [8,9].

1. Experimental methods

All film samples were deposited on silicon substrate Si(001) at room temperature in ultra-high vacuum (UHV) chamber (5×10^{-10} Torr) [10]. Then they were annealed at 523 K under UHV conditions. The deposition was done on single crystal Si wafers doped with P (for details see [10]). After that the films were kept under the normal atmosphere conditions during more than 5 months. Optical reflection and transmission spectra were measured by IR spectroscope based on monochromator and UV spectrometer Hitachi-310. The magneto-optical polar Kerr effect was studied at room temperature using a helium-neon laser (1.96 eV) in the magnetic field range of ±16 kOe. In addition, the films were investigated by the Auger electronic spectroscopy (AES). In order to remove organic contaminations all samples were kept in a toluene vapor atmosphere for about 1 min. In total six film samples grown on Si(001) were studied. They are: 1. Fe surface phase ($d = 0.3$ Å); 2. atomically thin Fe film nanophase ($d = 1.2$ Å); 3. ultrathin films of FeSi ($d = 3.0$ Å); 4. FeSi and Fe_3Si mixture ($d = 4.5$ Å); 5. Fe_3Si ($d = 6.0$ Å); 6. ultrathin film of bulk Fe deluted by Si ($d = 12$ Å).

2. Film composition

Ultrathin Fe film samples were analyzed by the AES. It has been found that C peak prevails in the spectra and only slightly varies in amplitude in comparison with other peaks related to O, Fe and Si. Other peaks were present for different film thicknesses, in particular O peak was observed for $d = 0.3$, 6 and 1.2 Å, Fe peak — for $d = 1.2$ Å, and Si peak — for $d = 0.3$ and 6.0 Å. The low adsorption of O at the Fe film thicknesses $d = 12$, 3 and 4.5 Å is most probably related with proximity of their surface composition to that of FeSi silicide, which has high inertness in relation to O. Invariance of C peak intensity in relation to the film thickness corresponds to the presence of the C layer with the same thickness for all films. Possibly, formation of this layer is related with the procedure of the sample cleaning by toluene. One may estimate the C layer thickness by the value of Fe peak attenuation starting for Fe film thickness of 1.2 Å and by data on the mean free path of electrons [11]. That gives the value of 6–7 Å, which is closed to 2 monolayers of graphene. This method gives an estimation for adsorbed O thickness of 3–4 Å.

3. Optical properties

Visible-UV reflection spectra were measured for all Fe films in the photon energy range of 1.4–6.5 eV (see Fig. 1). Reflection spectra show three strong bands at 3.4, 4.6 and 5.6 eV. With the increase of film thickness the bands at 4.6 and 5.6 eV were shifted to the lower energy side, and intensities at low energy branches about 1.4 eV and at high energy branches about 6.5 eV were shifted up and down, respectively, showing the change of the slope in all spectra.

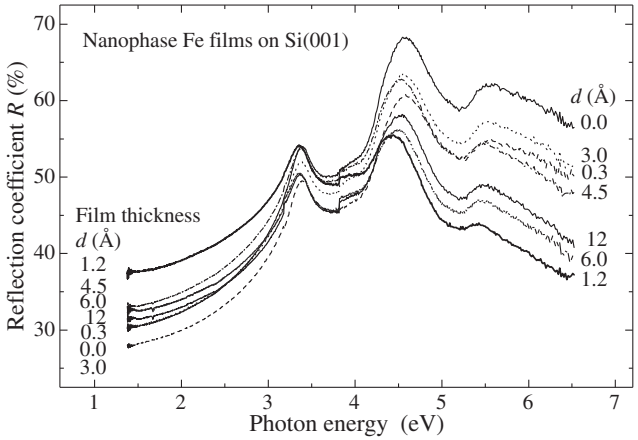

Fig. 1. Reflection spectra as a function of photon energy for Fe films on Si(001) with different film thicknesses.

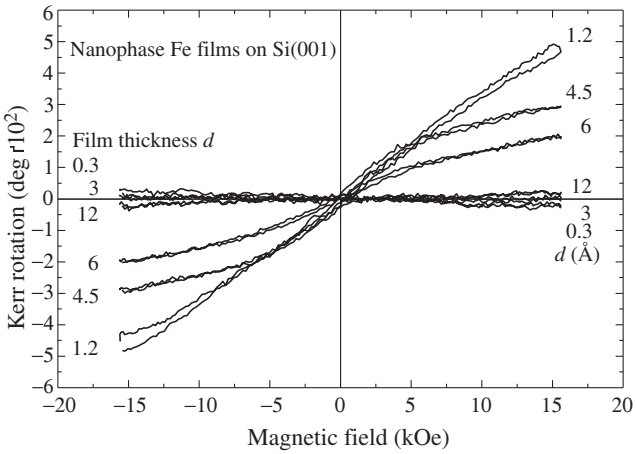

Fig. 2. Magneto-optical Kerr rotation as a function of magnetic field for Fe films on Si(001) with different film thicknesses.

The shift of the bands can be interpreted from the point of view of Si valence *p*-shell change, which arises due to formation of *p-d* silicide bonds and *p-d* hybridization of valence *p*-shell of Si. In Fe films with the thicknesses of 4.5 and 6 Å it takes place due to silicide formation. In films with the thicknesses of 1.2 and 12 Å it takes place due to chemical bonds formation at the interfaces with the substrate (for 1.2 Å) and deluted by Si on the upper surface of the film (for 12 Å).

Possible reason of the spectra slope change is redistribution of valence electrons between the film and the substrate [7]. Obviously, the redistribution of valence electrons at interface between Fe and Si more probably corresponds to the Fe film with the thickness of 1.2 Å. This fact makes the atomically thin Fe film on Si(001) as exceptional in view of its unique optical and other properties. In particular, our studies have shown that Fe film nanophase with thickness of 1.2 Å had minimum transmission coefficient at photon energy near 0.85 eV and minimum reflection coefficient at photon energy near 1.4 and 6.5 eV.

4. Magneto-optical properties

Data on the magneto-optical polar Kerr effect versus the magnetic field value for ultrathin Fe film on Si(001) with different film thicknesses are shown in Fig. 2. As it is seen, magneto-optical Kerr rotation is maximal for the Fe film with thickness of 1.2 Å. It is somewhat smaller for the Fe film with thickness of 4.5 and 6 Å and it vanishes for the Fe film with thickness of 0.3, 3 and 12 Å. We note that the field dependencies for the Fe film with thicknesses of 1.2, 4.5 and 6 Å are of superparamagnetic type. We can suggest that the magnetization disappearance with thickness increase is related with the role of film composition and interface phenomena. The value of Kerr effect is related with the composition of Fe film, which is the pure Fe at the thickness of 1.2 Å (Fe) and silicide mixture (Fe_3Si+FeSi–Fe_3Si) at the thicknesses of 4.5–6 Å, respectively.

Thus, the atomically thin Fe film with the thickness of 1.2 Å showed the largest value of the magneto-optical polar Kerr effect ($\geq 5 \times 10^{-2}$ deg), which was approximately two times larger then the value presented in literature (2.5×10^{-2} deg) for Fe film on Au buffer layer on Si(001) [9]. Such anomalous behavior of the Fe film with the thickness of 1.2 Å can be explained by the presence of resonate states of spin-polarized electrons at the Schottki barrier formed by interface between Fe film and Si substrate (see for example [12]). This can be potentially interesting for novel magneto-optical devices using Schottki barrier.

Acknowledgements

This work is supported by the Ministry of Education and Science, RFBR and the RAS Programs on New materials and Structures, Spintronics and Nanostructures.

References

[1] I. Matsuda *et al*, *e-J. Surf. Sci. Nanotech.* **2**, 169 (2004).
[2] *Metal semiconductor optical device*, United States Patent 5961741.
[3] N. I. Plusnin *et al*, *Phys. Low-Dim. Str.* **9/10**, 129 (2002).
[4] N. I. Plusnin *et al*, *Phys. Low-Dim. Str.* **11/12**, 39 (2002).
[5] V. M. Il'yashenko *et al*, *Phys. Low-Dim. Str.* **2**, 42 (2006).
[6] N. I. Plusnin *et al*, *Tech. Phys. Lett.* **33**, 486 (2007).
[7] N. I. Plusnin *et al*, *Appl. Surf. Sci.* **253**, 7225 (2007).
[8] F. Zavaliche *et al*, *J. Appl. Phys.* **88**, 5289 (2000).
[9] F. Zavaliche *et al*, *J. Phys. D: Appl. Phys.* **36,** 779 (2003).
[10] N. I. Plusnin *et al*, J. Physics: Conf. Ser. **100**, 052094 (2008).
[11] W. Mönch, *Semiconductor Surfaces and Interfaces*, Berlin, Springer Verlag, (1993).
[12] S. Honda *et al*, *Phys. Rev. B* **78**, 245316 (2008).

17th Int. Symp. "Nanostructures: Physics and Technology"
Minsk, Belarus, June 22–26, 2009
© 2009 Ioffe Institute

Structure and optical property of low temperature $Al_xGa_{1-x}As$/GaAs(100) heterostructures

P. V. Seredin[1], A. V. Glotov[1], E. P. Domashevskaya[1], I. N. Arsentyev[2], D. A. Vinokurov[2] and I. S. Tarasov[2]

[1] Solid State Physic and Nanostructures Department, Voronezh State University, 394006 Voronezh, Russia
[2] Ioffe Physical-Technical Institute, St Petersburg, Russia

Abstract. Was shown, that low temperature (LT) $Al_xGa_{1-x}As$ films, as well as disordered homomorphous solid solutions, have sphalerite structure, but as it follows from X-ray diffraction and IR-reflection, the lattice parameter of an LT film increase with growth of concentration of Al atoms in metal sublattice, but it is still has less value than at GaAs, and this fact contradicts to well known Vegard's law.

Introduction

The epitaxial solid solutions of $Al_xGa_{1-x}As$ grown on substrates of GaAs represent the most matched lattice parameter heterostructures which has gained a wide spread occurrence and is one of the most used components in the electronic and optoelectronic industry. Examinations of AlAs-GaAs systems are in progress for quite a long time already and for today all basic properties of its semiconductor solid solutions are studied well. However, influence of various factors, such as nonequilibrium thermodynamic processes in reactors, presence of fields of the strain arising by reason of of the slightest mismatches of lattice parameters of a film and a substrate [1], etc. allows reaching in essence new properties at this type of heterostructures. Thus, production of $Al_xGa_{1-x}As$ solid solutions in the form of chemical compound is an extremely actual problem, and properties of such compounds deserve careful study using various methods. Modification of fundamental properties of the semiconductor systems will inevitably lead to a modification of energy gap width, transition from nondirect to direct band semiconductor, an inverse sequence of energy bands, complicating optical spectra.

1. Sample preparation

The tested samples produced in Ioffe Physical Technical Institute St Petersburg represent $Al_xGa_{1-x}As$/GaAs(100) heterostructures grown with a research objective of processes of autodoping for reaching of the peak concentration of a carbon acceptor. Therefore given experiments were provided at lower temperature and a minimum relation of 5 and 3 groups depending on a composition of a solid solution. Samples were grown by MOCVD installation "EMCORE GS 3/100" in vertical reactor with high speed rotation of substrate holder. The temperature maintain 550 °C, pressure in reactor 77 Torr, substrate holder rotation speed 1000 rpm. As initial reagents were used trimethyl gallium $(Ga(CH_3))_3$, trimethyl aluminum $(Al(CH_3))_3$ and an arsine (AsH_3). Width and composition of grown stratums were calculated proceeding the data received from layers, grown under normal conditions (temperature of growth 600–700 °C, a relation of devices of the fifth and third groups 100-200). Structural quality of samples and definition of lattice parametres of solid solutions were studied with the use of X-ray diffraction on diffractometer ARL X'TRA Thermo Techno with the high angular resolution and using CuKα radiation. IR-reflection spectra from heterostructures have been received with use IR-Fourier spectrometer Vertex-70 Bruker.

2. Experimental results

2.1. X-ray diffraction investigations

Figure 1(a) represents X-ray diffraction pattern from $Al_xGa_{1-x}As$/GaAs (100) epitaxial heterostructure (sample EM1017). The solid solution of this heterostructure is grown by MOCVD method at standard conditions. As it is seen from pattern, diffraction from a plane (600) represents superimposition of two K$\alpha_{1,2}$-doublets: the first, deposed towards smaller angles — from solid solution $Al_xGa_{1-x}As$, second from GaAs (100) monocrystal substrate. Taking into account internal stresses lattice parameter value allows to make the inference that the lattice parameter for solid solution $Al_xGa_{1-x}As$ of sample EM1017 satisfies to linear Vegard law for AlAs-GaAs system. Diffraction (600) patterns of LT heterostructures EM1540, EM1555 and EM1585, decomposed on K$\alpha_{1,2}$-doublets are given at Fig. 1(b)–(d). In homoepitaxial GaAs/GaAs(100) heterostructure, e.g. EM1540 sample, K$\alpha_{1,2}$-doublets from the film and the substrate are clearly matched. Thus the half-width of the general pattern of diffraction from heterostructure EM1540 remains invariable in comparison with the monocrystal GaAs (100) plate used as a substrate for growth of heterostructure. This testifies the presence of nondislocation mechanism of such type of growth and excellent conjugation of lattices for solid solution and a substrate. As it is shown on the figures, diffraction from samples EM1555 and EM1585 also represents superimposition of doublets from GaAs (100) substrate and $Al_xGa_{1-x}As$ solid solution, however unlike EM1017 heterostructure produced using standard procedure has significant difference. This fact includes that K$\alpha_{1,2}$-doublet from LT solid solution $Al_xGa_{1-x}As$ is shifted in comparison with a K$\alpha_{1,2}$-doublet from GaAs (100) towards major angles 2θ. It is a consequence of less $Al_xGa_{1-x}As$ lattice parameter than at GaAs (100). Calculation of lattice parameters of LT heterostructures taking into account internal stresses has been performed using an assumption that for system of $Al_xGa_{1-x}As$ solid solutions produced by such method Poisson coefficients coincide with coefficients for binary compounds $\upsilon_{AlAs} = 0.255$ [1], $\upsilon_{GaAs} = 0.312$ [1]. The analysis of received data allows to make the inference that with increase of Al atoms concentration the lattice parameter of an LT solid solution is also increasing.

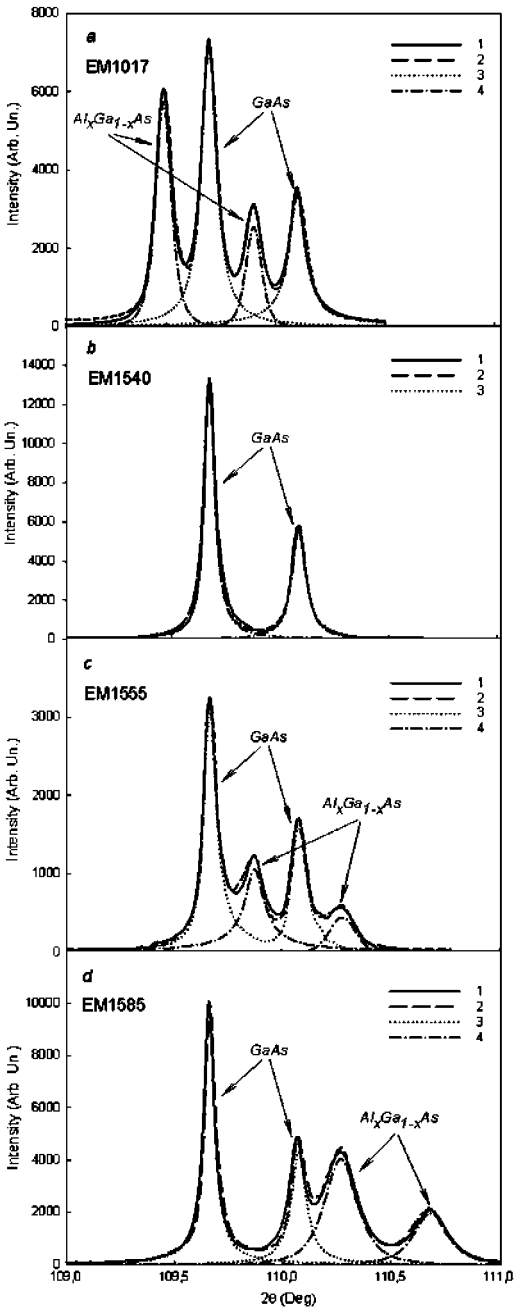

Fig. 1. (600) diffraction pattern from $Al_xGa_{1-x}As$/GaAs(100) heterostructures. Samples: (a) EM1017, (b) EM1540, (c) EM1555, (d) EM1585. Lines on figures: 1 — experimental diffraction, 2 — simulation, 3 — substrate GaAs(100), 4 — solid solution $Al_xGa_{1-x}As$.

2.2. IR-reflection spectra

Regarding that growth of LT $Al_xGa_{1-x}As$ solid solutions with the changed lattice parametres in comparison with disordered homomorphous solid solutions inevitably should be exhibited in character of optical spectra, in the given investigation we undertook examination of IR-reflection spectra of these heterostructures in the field of an single-phonon resonance. Spectra of LT heterostructures of samples EM1555 and EM1585 contain two basic phonon modes Al-As and Ga-As. However, these oscillations do not coincide as on frequencies TO and LO modes, and on intensity with modes of disorder homomorphous solid solutions the same compositions studied in [2]. Besides, dependence on modification of frequencies of longitudinal and transversal modes of the basic oscillations with a alteration of atom concentration in a metal sublattice does not satisfy to the same determined dependences [2]. It is also necessary to mention unusual high reflectance in far infrared at LT heterostructures, and that is more typical for metals than semiconductors.

3. Conclusion

Analyzing the data gathered using methods of X-ray diffraction, scanning electron microscope and IR-spectroscopy, it is possible to make the important deductions about structure of the LT $Al_xGa_{1-x}As$ solid solutions. LT $Al_xGa_{1-x}As$ films, as well as disordered homomorphous solid solutions, have sphalerite structure, that is well enough tracked in case of growth of homoautoepitaxial GaAs/GaAs (100) structures — as from X-ray diffraction results follows, that lattices of solid solution and a substrate are perfectly matched. However essential difference is that the lattice parameter of an LT film though is increased with growth of concentration of Al atoms in a metal sublattice, but it is still has less value, than at GaAs and this fact contradict to well known Vegard's law. This data, obtained from the analysis of effects of X-ray diffraction at first, is also proved by the IR-spectroscopy method, proceeding from data about frequencies and intensities of TO and LO phonons of the basic modes. It is necessary to mention, that the composition of LT solid solutions growing under normal conditions, does not coincide with a certain method of X-ray microanalysis. All these facts testify that thermodynamic requirements of LT growth, lead to that in $Al_xGa_{1-x}As$ solid solutions with $0 < x < 1$ Al and Ga atoms in a metal sublattice take their places not statistically but strictly ordered. I.e. octahedral voids in a sphalerite lattice are filled by atoms of metals layerwise, that leads to occurrence tetrahedral compression along the growing axis and to reduction of lattice parameter of an ordered solid solution. But, if formation of chemical combination $AlGaAs_2$ with superstructural phases has been caused by the kinetic phase transition of solid solution, at LT growth appearance of reorganized structure with development of fundamental properties of major collective of particles is called thermodynamic by type of lability concerning spontaneous partitioning into phases, and the elastic energy putting this mechanism in action, arises owing to the requirement coherent conjugations of divided phases.

Acknowledgements

We acknowledged RFFI for financial support: grant 09-02-97505-r_center_a.

References

[1] E. P. Domashevskaya, P. V. Seredin *et al*, *Semiconductors* **39**, 354 (2005).

[2] Yu. A. Goldberg, *Handbook Series on Semiconductor Parameters. Ed. by M. Levinshtein, S. Rumyantsev, and M. Shur*, (London: World Sci.) Vol. 2, 1999.

17th Int. Symp. "Nanostructures: Physics and Technology"
Minsk, Belarus, June 22–26, 2009
© 2009 Ioffe Institute

Behavior of phonon modes in hexagonal InGaN alloys

A.N. Smirnov[1], V.Yu. Davydov[1], I.N. Goncharuk[1], R.N. Kyutt[1], W.V. Lundin[1], E.E. Zavarin[1], W.J. Schaff[2] and S. Gwo[3]

[1] Ioffe Physical-Technical Institute, St Petersburg, Russia
[2] Department of Electrical and Computer Engineering, Cornell University, Ithaca, New York 14853, USA
[3] Department of Physics, National Tsing-Hua University, Hsinchu 300, Taiwan, ROC

Abstract. We present results of investigations of the behavior of optical phonon modes of InGaN alloys for the entire range of compositions. A strong nonlinearity revealed for the first time in the compositional behavior of the E_2 (high), A_1 (TO) and E_1 (TO) modes in InGaN indicates that the crystal lattice dynamics of this alloy should be investigated more thoroughly, both experimentally and theoretically.

Few studies of the lattice dynamics of $In_xGa_{1-x}N$ have been performed in spite of the fact that they are of not only fundamental importance but also can be efficient for the nanostructure characterization. The crystal lattice dynamics of hexagonal $In_xGa_{1-x}N$ alloys was theoretically analyzed in Ref. [1]. A one-mode type behavior was predicted by the modified random-element isodisplacement model for all Raman active modes. This type of behavior is characterized by a continuous and approximately linear variation of the frequencies of all modes between their values for GaN and InN with varying alloy composition. Experimental investigations of lattice dynamics of $In_xGa_{1-x}N$ alloys were carried out by several groups by using Raman spectroscopy [2–8]. The majority of groups concentrated on the studies of two from six optical phonons allowed in Raman spectra of hexagonal $In_xGa_{1-x}N$ alloys (namely, E_2(high) and A_1(LO) symmetry phonons).

To obtain detailed information on the behaviors of as large a number of Raman allowed phonon modes as possible in a wide compositional range, we have studied a wide set of alloys with the compositions ranging from GaN to InN. The samples were hexagonal $In_xGa_{1-x}N$ epilayers grown on (0001) sapphire substrates. The alloy films in the compositional ranges $0.01 < x < 0.30$ and $0.35 < x < 0.98$ were grown by MOCVD and PA MBE, respectively. All the alloys were nominally undoped films of n-type conductivity with a Hall carrier concentration $n = 1 - 5 \times 10^{18}$ cm^{-3}. The alloy compositions were estimated from the data on Rutherford backscattering of deuterons and high-resolution x-ray diffraction measurements.

Raman process in $In_xGa_{1-x}N$ can be described by different scattering mechanisms depending on the ratio between excitation energy and the $In_xGa_{1-x}N$ band gap that varies from 0.7 to 3.4 eV for samples with different compositions. The Raman measurements were performed at room temperature in a quasibackscattering geometry by using a wide set of excitation energies 1.83–3.81 eV. The use of different excitation energies and scattering geometries where both the surface plane and edge of the samples were examined allowed us to get detailed information on four of six Raman allowed phonon modes.

As an example, Fig. 1 demonstrates Raman spectra of A_1(TO), E_1(TO), E_2(high), and A_1(LO) symmetry modes in the compositional range $0.01 < x < 0.16$. Good agreement between the polarized Raman spectra and the selection rules for the wurtzite structure points to a high crystalline quality of the $In_xGa_{1-x}N$ samples. Figure 2 shows Raman spectra recorded in the $z(xx)\bar{z}$ scattering configuration for the entire set of the

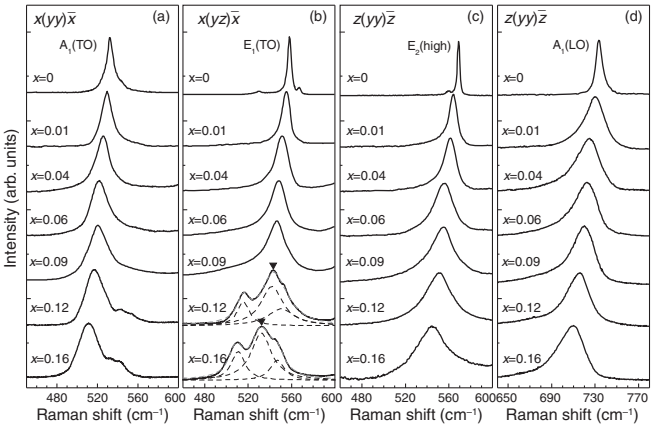

Fig. 1. Room temperature polarized Raman spectra of A_1(TO), E_1(TO), E_2(high), and A_1(LO) symmetry modes of $In_xGa_{1-x}N$ in the compositional range $0.01 < x < 0.16$. The spectra corresponding to different In compositions are normalized to the maxima of the appropriate Raman lines. Here z is the direction of the hexagonal axis of the epilayer.

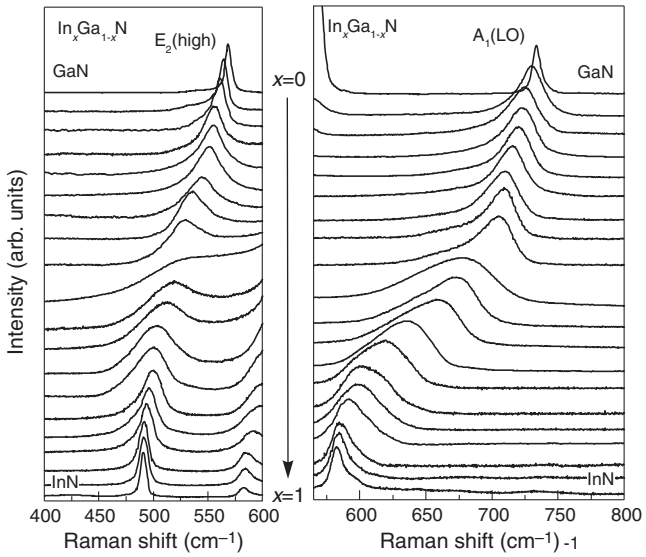

Fig. 2. (a) Room-temperature polarized Raman spectra for the E_2(high) and the A_1(LO) modes of the $In_xGa_{1-x}N$ epilayers with different In contents covering the entire alloy range. The spectra are normalized to the E_2(high) or A_1(LO) intensity.

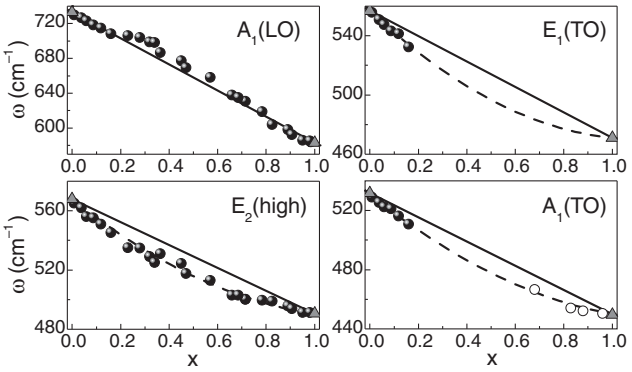

Fig. 3. Frequencies of zone-center phonons in hexagonal $In_xGa_{1-x}N$ versus composition. The solid lines are calculated frequencies [1]. The full circles are experimental data obtained on $In_xGa_{1-x}N$ with low electron concentrations ($n = 1 - 5 \times 10^{18}$ cm^{-3}). The open circles are the positions of L^- mode obtained on In-rich InGaN with high electron concentrations ($n = 7 - 9 \times 10^{19}$ cm^{-3}).

$In_xGa_{1-x}N$ epilayers. In this configuration, only the A_1(LO) and the E_2(high) modes are allowed. As can be seen from Fig. 2, the Raman spectra exhibit only one A_1(LO) peak over the entire composition range. This confirms the theoretical predictions of the one-mode-type behavior of A_1(LO) optical phonon in the $In_xGa_{1-x}N$ alloy [1]. It is evident that the A_1(LO) line is rather narrow for the samples with low concentrations of In or Ga, however this mode exhibits considerable broadening for the samples with intermediate compositions. The line broadening points to a higher lattice disorder and the presence of composition fluctuations in the alloy. It is also seen that for all the compositions x the A_1(LO) band shape is asymmetrical, with a long low-frequency tail and abrupt high-frequency edge. There is no additional high-frequency shoulder of the A_1(LO) mode which is typically related to spinodal decomposition. This suggests that there is no phase separation in the $In_xGa_{1-x}N$ alloys studied, which is consistent with x-ray and PL data (not shown here). The E_2(high) line in the Raman spectra in Fig. 2 is rather narrow for the samples with low In or Ga concentrations and experiences a drastic broadening for the samples with intermediate compositions.

We also studied $In_xGa_{1-x}N$ alloys with a high In content ($0.4 < x < 1$) and a high electron concentration ($n = 7 - 9 \times 10^{19}$ cm^{-3}). The A_1(TO) phonon mode frequencies for In-rich $In_xGa_{1-x}N$ samples can be approximately estimated from the coupled phonon-plasmon L^- mode position because it must be close in the spectra of these alloys to the position of the A_1(TO) phonon mode. Figure 3 compares compositional dependences of the frequencies of zone-center phonons in hexagonal $In_xGa_{1-x}N$ alloys calculated in Ref. [1] and the measured phonon frequencies which are corrected for the strains in $In_xGa_{1-x}N$ layers.

In the case of biaxial strain, the Raman line shift is given by $\Delta\omega = 2a_\omega\varepsilon_\parallel + b_\omega\varepsilon_\perp$, where $\varepsilon_\parallel$ and $\varepsilon_\perp$ are in-plane and normal to plane strain, respectively, in the lattice estimated from x-ray measurements, and a_ω and b_ω are the deformation potentials of the corresponding phonon mode. The a_ω and b_ω parameters were calculated for $In_xGa_{1-x}N$ from the literature data on these parameters for GaN and InN as composition weighted averages: $a_\omega(x) = xa_\omega(\mathrm{InN}) + (1-x)a_\omega(\mathrm{GaN})$ and $b_\omega(x) = xb_\omega(\mathrm{InN}) + (1-x)b_\omega(\mathrm{GaN})$. The deformation potentials of phonon modes A_1(TO), E_1(TO), E_2(high) and A_1(LO) of GaN were taken from [11, 12]. The deformation potentials of E_1(TO), E_2(high) and A_1(LO) modes of InN were taken from [13, 14]. Since no data on phonon deformation potentials of InN for the A_1(TO) mode are available in the literature, the deformation potentials of the A_1(TO) mode of GaN were used to estimate the strain-induced Raman shift for Ga-rich $In_xGa_{1-x}N$ alloys ($0 < x < 0.2$). We did not correct for strain the frequencies of the A_1(TO) mode for In-rich $In_xGa_{1-x}N$ alloys ($0.6 < x < 1$) because these frequencies were estimated from the L^- mode positions of the alloys with high electron concentrations and can be regarded only as tentative.

It can be seen that the measured A_1(LO) phonon frequencies for Ga-rich and In-rich $In_xGa_{1-x}N$ alloys coincide well with the theoretically predicted linear compositional dependence. Note that the linearity in the behavior of the A_1(LO) phonon frequencies is a favorable factor for development of the quantitative method for estimation of the $In_xGa_{1-x}N$ composition via Raman spectroscopy. The dependence of the $In_xGa_{1-x}N$ A_1(LO) phonon mode on In content in the regions $0 < x < 0.2$ and $0.7 < x < 1$ can be approximated as $\omega(A_1(\mathrm{LO})) = 733 - 150x$. A similar expression for the compositional dependence of the A_1(LO) phonon mode of relaxed $In_xGa_{1-x}N$ alloys for $0 < x < 0.3$ was obtained in Ref. [7].

The experimentally observed compositional dependence of the E_2(high) phonon is obviously nonlinear (see Fig. 3). At the same time, there are no signs of the two-mode behavior of this phonon which is typically thought to be responsible for such deviations from linearity. A strong deviation from linearity is also observed for the A_1(TO) and E_1(TO) modes measured for $In_xGa_{1-x}N$ samples in the compositional range $0.01 < x < 0.16$. The behavior of the L^- mode measured for $In_xGa_{1-x}N$ samples in the compositional range $0.4 < x < 1$ is also deviated from linearity.

To summarize, experimental studies of $In_xGa_{1-x}N$ alloys in the entire range of compositions have confirmed a one-mode behavior of LO phonons and have revealed for the first time considerable deviations from the linear dependence for the TO phonons. The compositional dependences of optical phonons we have found can be used for estimation of the $In_xGa_{1-x}N$ composition by Raman spectroscopy.

Acknowledgements

This work is supported by RFBR (Grant 09-02-01280), NSC RFBR (Grant 08-02-92003-HHC), and the Program of RAS "New materials and structures".

References

[1] H. Grille *et al*, *Phys. Rev. B* **61**, 6091 (2000).
[2] G. Kaczmarczyk *et al*, *Phys. Rev. B* **61**, 5353 (2000).
[3] D. Behr *et al*, *Mater. Res. Soc. Symp. Proc.* **468**, 213 (1997).
[4] H. Harima *et al*, *phys. stat. sol. (b)* **216**, 758 (1999).
[5] D. Alexson *et al*, *J. Appl. Phys.* **89**, 798 (2001).
[6] J. W. Ager III *et al*, *Phys. Rev. B* **72**, 155204 (2001).
[7] M. R. Correia *et al*, *Appl. Phys. Lett.* **83**, 4761 (2003).
[8] V. Yu. Davydov *et al*, *phys. stat. sol. (b)* **240** 425 (2003).
[9] A. G. Kontos *et al*, *Phys. Rev. B* **72**, 1555336 (2005).
[10] S. Hernandez *et al*, *J. Appl. Phys.* **98**, 013511 (2005).
[11] V. Yu. Davydov *et al*, *J. Appl. Phys.* **82**, 5097 (1997).
[12] F. Demangeot *et al*, *Phys. Rev. B* **69**, 155215 (2004).
[13] V. Darakchieva *et al*, *Appl. Phys. Lett.* **84**, 3636 (2004).
[14] X. Wang *et al*, *Appl. Phys. Lett.* **89**, 171907 (2006).

17th Int. Symp. "Nanostructures: Physics and Technology"
Minsk, Belarus, June 22–26, 2009
© 2009 Ioffe Institute

Thermooptical properties of polymer nanocomposites based on cadmium sulfide in low density polyethylene

N. M. Ushakov[1,2], D. M. Kulbatskii[1], I. D. Kosobudskii[1,2] and G. Yu. Yurkov[3]

[1] Technical State Universityät Saratov, Russia
[2] V. A. Kotel'nikov Institute of RadioEng. &Electr. of RAS, Saratov Branch, Saratov, Russia
[3] A. A. Baikov Institute of Metallurgy and Materials Science of RAS, Moscow, Russia

Abstract. CdS-containing nanoparticles in low density polyethylene (LDPE) matrix have been produced by thermal decomposition metal-containing compounds in an argon-oxygen atmosphere. Optical absorption factor, dissipation factor and refractive index have been measured from 400 to 900 nm at the temperature field from 20 to 80 °C.

Introduction

One of the important directions of optical materials technology is search and research of new optical mediums having wide functionality for optoelectronics and photonics. At present time optical properties of polymer nanocomposites with d-metal sulphides nanoparticles (SPNC) stabilized in low density polyethylene (LDPE) matrix have been studied for different nanoparticles (NPs) concentration and dimensions in matrix at the room temperature only [1,2]. Nanocomposites based on CdS nanoparticles have a set of perspective applications (for example, see [3]). In this work, we report on results of the investigation of thermo-optical properties of nanocomposites based on 10–30 wt.% CdS nanoparticles in LDPE.

1. Experiment

In present work optical characteristics of nanocomposite thin samples with average thickness 240 microns were measured. Mass concentration of CdS nanoparticles are from 10 to 30 wt.%, and their average sizes are from 2.5 nm up to 20 nm. The particle size of CdS was determined by transmission electron microscopy (JEOL 300B microscope). The accelerating voltage was 75 kV.

The structure of SPNC samples were investigated using X-ray phase analysis method. In Fig. 1 difractogram of the 10 wt.% CdS based on LDPE is presented. Peak No. 1 — CdS (002); peak No. 2 — CdS (001); peak No. 3 — CdS (102) and peak No. 4 — CdS (103) are shown. Experimental results were demonstrated that CdS is the general component of the nano composite.

Optical spectra of investigated samples were measured by a method absorption linear spectroscopy on specially created measuring complex consisting of two beam optical spectrum analyzer based on monochromator MDR-23 (LOMO, Russia) and specially made reception head in range 450–900 nanometers. For comparison absorption a factor for pure high pressure polyethylene was measured. The errors of measurement did not exceed 1%. Two streaming model Kubelka–Munka for calculation of the basic optical factors necessary for the complex description of distribution of light in bulk of the investigated optical material has been chosen [3].

2. Results and discussion

Figure 2 presents the results of measured spectral dependences of optical absorption coefficient for 30 wt.% CdS nanocomposite medium under heating for different temperature.

The results of measurements dependences of optical absorption under heating and cooling for the different temperature are presented in Fig. 3.

As shown in Fig. 3 under heating of samples up to 55 °C optical absorption increasing is observed. Then at the tem-

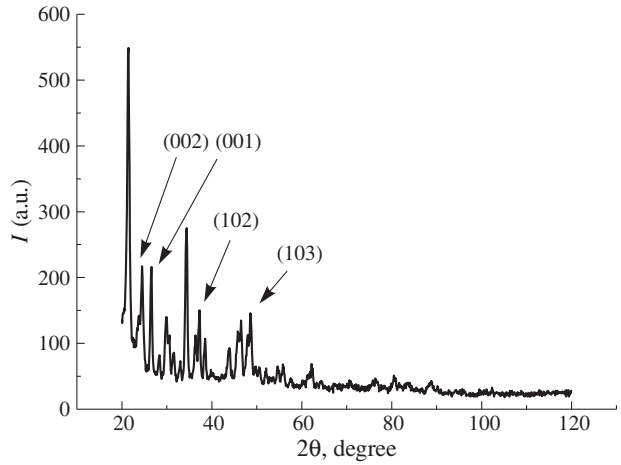

Fig. 1. Difractogram of the 10 mass% CdS-LDPE composite.

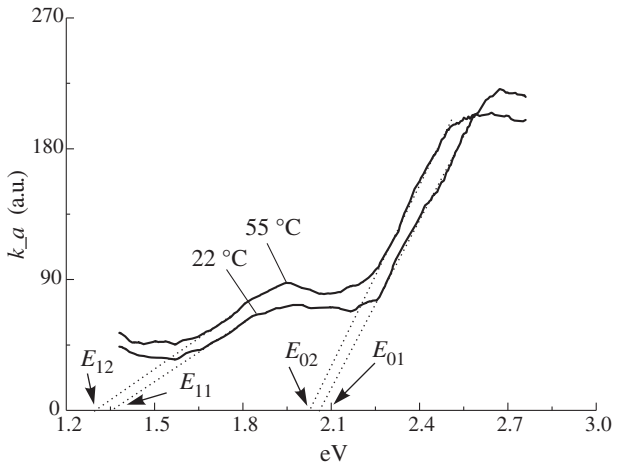

Fig. 2. Spectral dependences of optical absorption coefficient for 30 wt.% CdS nanocomposite medium under heating for 22 and 55 °C.

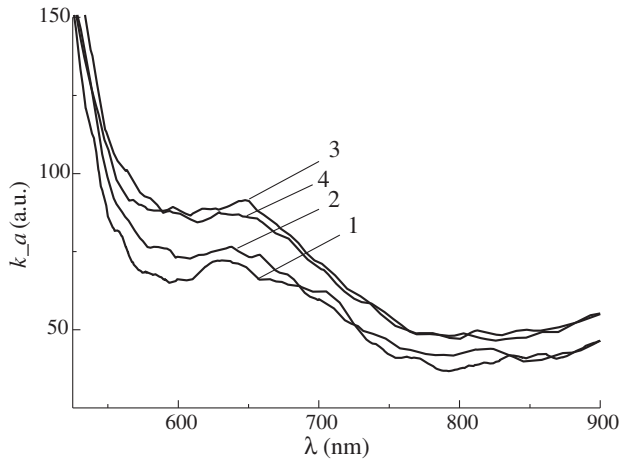

Fig. 3. Spectral dependences of optical absorption coefficient for 30 wt.% CdS nanocomposite medium under heating and cooling from 55 to 70 °C. 1 — 70 °C, 2 — 69 °C, 3 — 64 °C, 4 — 55 °C.

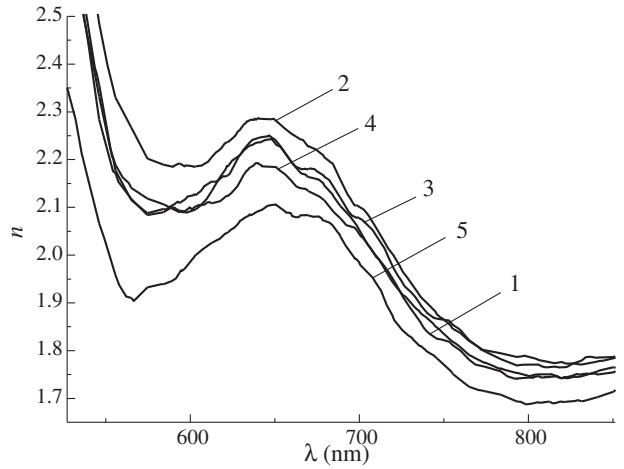

Fig. 4. Temperature dependences of refraction index for the 30 wt.% CdS-LDPE composite sample. 1 — 25 °C, 2 — 47 °C, 3 — 55 °C, 4 — 65 °C, 5 — 77 °C.

perature band from 55 to 77 °C optical absorption decreases. For the temperature region from 55 to 70 °C the optical absorption hysteresis is existed. It is enormous in comparison to what anyone else has done before. In our opinion temperature region from 55 to 70 °C is a very interesting for a development of thermo-optical switches. Most of all the changing of optical absorption at the spectral band from 570 to 700 nm is observed. This spectral band is characteristic for exciton spectra. The rise of exciton peak at the heating can be characteristic by increasing of quantity the excitons. While further temperature increasing exciton collaps exists and medium state replacement to normal state.

Change of refraction index for composites on the basis of nanoparticles CdS reached values $\Delta n = 0.15$ in the range of temperatures from 25 to 77 °C.

Acknowledgements

The work was fulfilled with the financial support of Russian Fund Basic Research (RFBR) (grant 06-08-01011a) and the Ministries of Education and Sciences of the Russian Federation (grant 2.1.1.575).

References

[1] J. O. Winter, Z. Gomez, S. Gatzert *et al*, *Colloids and Surfaces A: Physicochem. Eng. Aspects.* **254**, 147 (2004).
[2] N. M. Ushakov, G. Yu. Yurkov, K. V. Zapsis *et al*, *Optics and Spectroscopy* **100** 3, 414 (2006).
[3] A. Erlacher, *J. of Appl. Phys.* **95**, 2927 (2004).

17th Int. Symp. "Nanostructures: Physics and Technology"
Minsk, Belarus, June 22–26, 2009
© 2009 Ioffe Institute

The influence of the tip induced local anodic oxidation on the conductive atomic force microscopy results

A. Vetushka, A. Fejfar, M. Ledinský, B. Rezek, J. Stuchlík and J. Kočka

Institute of Physics, Academy of Sciences of the Czech Republic v.v.i., Cukrovarnická 10, 162 00, Prague 6, Czech Republic

Abstract. Electrical properties of hydrogenated microcrystalline silicon thin films were studied by conductive atomic force microscopy (C-AFM). Measurement of the local conductivity in ambient conditions is complicated by the presence of thin native oxide layer on the surface of the sample. We report that the tip-induced oxidation changes character of the local current maps even in the scan of a pristine surface. We also show that stripping of the surface oxide by HF etch restores the local currents to values comparable to those measured by C-AFM in ultra high vacuum on in-situ deposited samples.

Introduction

Conductive atomic force microscopy (C-AFM) can measure simultaneously topography and local conductivity [1]. This is of particular importance for hetero-structural materials with nanometer sized features like hydrogenated microcrystalline silicon (μc-Si:H) [2]. The first measurements of μc-Si:H by the Conductive AFM (C-AFM) were done in ultra high vacuum (UHV) on in-situ grown samples to avoid the native surface oxide [3]. But the C-AFM in UHV has two big disadvantages: it is expensive and it is time-consuming. More common and easier way is to use C-AFM in ambient (air) conditions. In turn, in ambient conditions there are other difficulties. Any surface in air is always covered by adventitious contaminants, a layer of condensed water and in case of silicon also a thin native oxide, lowering the observed local currents.

Moreover, it became soon evident that the C-AFM measurement itself can locally modify the Si surface, leading to lowering of the current value in repeated measurements. This so called "memory" effect was observed both in UHV and at ambient conditions. The local current measured can be influenced by charges trapped in the deep states at the sample surface and injected by the tip in a previously sample scan [4] and, in ambient conditions with sufficient positive sample bias, by local anodic oxidation (LAO) of Si surface [5]. In case of LAO the electric field drives the migration of oxyanions from the water meniscus at the tip-surface junction or substrate cations through the surface oxide and leads to the Si surface oxidation, a physical mechanism used for scanning probe lithography.

1. Experiment

Thin films of μc-Si:H were prepared by Plasma Enhanced Chemical Vapor Deposition (PECVD) in a mixture of silane (SiH_4) and hydrogen at the following conditions: discharge frequency 13.56 MHz, the dilution ratio of the gas flows $r_H = [H_2]/[SiH_4]$ around 28, the pressure in the chamber around 70 Pa and substrate temperature 250 $^\circ C$. The film thickness was determined by stylus method using Tencor AlphaStep 100. At the selected conditions we were close to the boundary between the amorphous and microcrystalline growth, which means that there were relatively few large conical microcrystalline grains in the films surrounded by the amorphous tissue. The surface area occupied by the grains within the AFM field of view was used to determine the surface crystallinity of the samples. The samples were measured by Veeco Dimension 3100 AFM equipped with the extended TUNA (Tunneling AFM) module for the current detection in the pA range. All AFM results reported below were performed in contact mode using the Cr/Pt coated Si cantilevers (BudgetSensors ContE) with resonant frequency around 13 kHz and force constant 0.2 N/m. Local current flowing through the grounded cantilever was induced by a dc voltage bias applied to the contact underlying the thin film.

The set point of the AFM scan corresponded to the applied normal force around 25 nN and scanning speed was kept constant at 500 nm/s. Results of the AFM measurements were processed with WSxM software [6].

2. The neighboring line oxidation artifact

The oxide growth induced by the AFM tip (during LAO) proceeds not only vertically, but also laterally. We have determined the width of the oxide line by scanning the sample in a zig-zag pattern at +10 V and then observing the oxidized pattern by the local current map at −2.5 V. The scanning tip at oxidizing bias left behind an oxide line which influenced the local current within a cca 50 nm wide band, in agreement with the minimal line widths in LAO based lithography [5].

Thus the oxidized line is several times wider than the distance between the individual lines in the typical AFM scans:

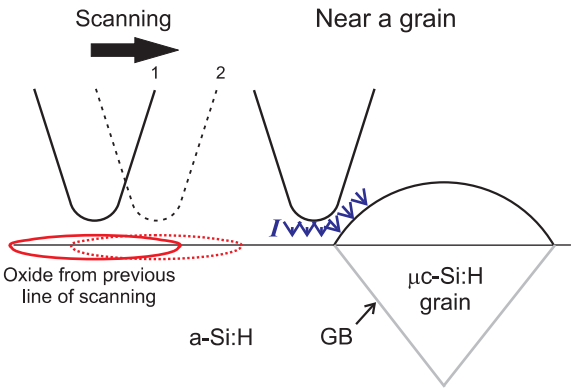

Fig. 1. Schematic picture of the C-AFM measurement illustrating the role of tip-induced anodic oxidation during scanning as well as possible geometrical and electronic effects of the microcrystalline grain edges on the current measurement and the local anodic oxidation.

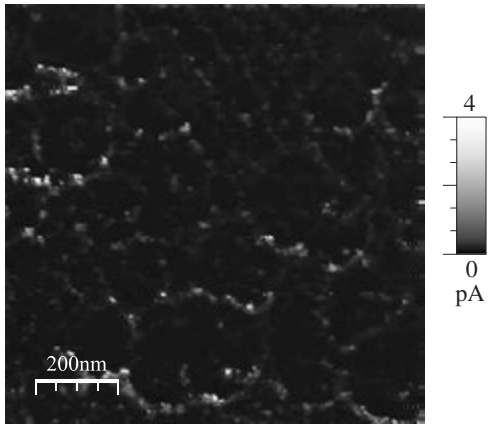

Fig. 2. Artifacts of conductive rings in the ambient C-AFM image of the very first local current scan on the μc-Si:H (voltage +10 V).

commonly used 256 lines per image lead to 8 nm between scan lines for a 2 μm wide field of view (a typical scale for AFM characterization of mixed phase Si). This means that at oxidizing conditions only the first line actually scans the pristine surface and all subsequent neighboring lines record the local current values on already locally oxidized surface (as illustrated in the Fig. 1).

For some reasons the grain edges oxidize less then either amorphous surface or the surface of microcrystalline grains. As a result, the grain edges appear to be more conducting in the C-AFM map shown in Fig. 2. This observation has to be considered a result of the the neighboring line oxidation artifact.

3. HF etching

The local oxidation and related artifacts can be avoided by using the non-oxidizing polarity (sample negative with respect to the tip) and/or keeping the sample dry. However, even for samples with an unknown history the pristine state can be restored by stripping the oxide by a rapid etch in diluted HF acid. Figure 3 compares the local current maps measured on the same sample with a native oxide (left) and after the oxide stripping (right). The color scale for local currents is the same for both measurements. The oxide stripping increased the uniformity as well as the average value of local current registered on the grains. The negative sample polarity and a low bias voltage lead to excellent reproducibility of the local current maps even after four repeated scans.

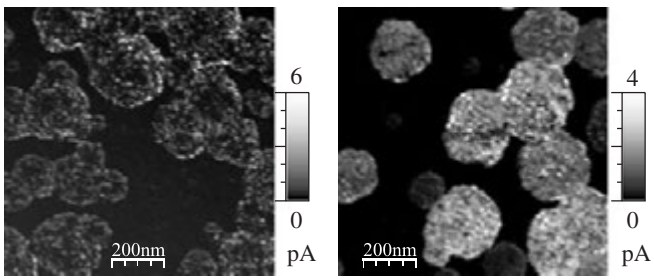

Fig. 3. Comparison of the ambient C-AFM images of local current measured on the μc-Si:H with native oxide (left) and with the surface restored by HF etch (right). The increase of local currents following the HF etch was so large that the applied bias was reduced from −1.5 V (a) to −0.5 V (b).

Acknowledgements

This research was supported by AV0Z 10100521, LC510, LC06040, IAA100100902 and KAN400100701 projects.

References

[1] R. A. Oliver, *Rep. Progr. Phys.* **71**, 076501 (2008).
[2] J. Kočka *et al*, *Sol. Energy Mat. Sol. Cells* **66**, 61–71 (2001).
[3] B. Rezek *et al*, *Appl. Phys. Lett* **74**, 1475–1477 (1999).
[4] B. Rezek *et al*, *Appl. Phys. Lett.* **83**, 1764–1766 (2003).
[5] D. Stiévenard *et al*, *Prog. Surf. Sci.* **81**, 112–140 (2006).
[6] I. Horcas *et al*, *Rev. Sci. Instr.* **78**, 013705 (2007).

17th Int. Symp. "Nanostructures: Physics and Technology"
Minsk, Belarus, June 22–26, 2009
© 2009 Ioffe Institute

Study of photoluminescent properties of anodic aluminum oxide

N. I. Mukhurov, *S. P. Zhvavyi*, I. V. Gasenkova, S. N. Terekhov, A. J. Panarin, V. A. Orlovich, G. K. Zhavnerko

B. I. Stepanov Institute of Physics NASB, Minsk, Belarus

The formation of nanostructures with regularly distributed nanoparticles of a certain size and shape is one of the main directions of progress in nanotechnology. Anodic aluminum oxide (AAO), fabricated by electrochemical oxidation of aluminum in acidic electrolytes has much potential in this sense. The AAO films have regular periodic structure of nanopores which are perpendicular to the substrate surface. Diameter of pores and distances between them can be adjusted by the technological process conditions. Thus the AAO membranes are suitable templates for formation of active silver nanostructures for surface-enhanced Raman scattering (SERS). However, in some cases the luminescent background from alumina can bring significant contribution into SERS-spectra. Investigation of optical characteristics of AAO can give a basis for a choice of optimum conditions for preparation of AAO-based SERS-active substrates.

Porous substrates of the anodic aluminum oxide with 60 μm thickness were prepared by electrochemical anodization of high-purity (99.99%) aluminum foils in a solution of sulfuric acid (20% H_2SO_4) at 13 °C Fourier-transform infrared (FTIR) spectra of the AAO samples were measured on a NEXUS 470 spectrometer at a continuous purge of dry air. Photoluminescence spectra of the AAO films were collected using fluorescence spectrophotometer SDL-2 at 325 nm excitation. The conditions of spectral measurements for all samples were identical.

Freshly prepared substrates of amorphous AAO were modified by annealing on air at different temperatures up to 1200 °C. A choice of temperature and duration of thermal treatment was determined by structural and morphological transformations of anodic aluminum oxide. For instance, a polycrystalline phase, mainly γ-Al_2O_3, is formed at $T > 800$ °C. At increase temperature of annealing more than 1100 °C a new crystal phase α-Al_2O_3 is appeared which mechanical and physical properties are close to aluminum oxide ceramics. Duration of annealing was verified from 10 up to 30 minutes.

Figure 1 shows the top-view AFM image (panel (a)) and Fourier transformation (panel (b)) of the AAO substrate. Fourier transform image consists of six distinct spots on the sides of a hexagon. This is evidence of the perfect ordered lattice pores. Pores diameter and interpore spacing for the obtained AAO nanostructures were 40 and 100 nm, respectively.

Figure 2 presents photoluminescence spectra of AAO substrates under investigation, which were anodized in sulfuric electrolyte. It should be noted, that the intensity of luminescence in this case is much less (approximately by one order of magnitude) in comparison with that for AAO substrates formed in oxalic acid. A narrow band at 390 nm on the broad luminescence contour (curve 1) in spectrum of amorphous AAO can be attributed to oxygen vacancies, grasping two electrons (F-center). High-temperature treatment results in significant reduction of luminescence intensity and appearing of a new band at 480 nm. This band is a result of F-centers aggregation and formation of the F2-centers (two oxygen vacancies with four electrons) via structural reorganization upon γ-Al_2O_3 formation.

IR-spectra of alumina substrates annealed at temperature >800 °C are present in Fig. 2 (panel (b)). The broad intensive band at 2800–3700 cm^{-1} is attributed to H_2O molecular and OH groups stretching vibrations. It is not affected by heat treatment since a hydration of the AAO surface takes place owing to an air exposition.

It is seen that with increase of annealing temperature the band near 1280–1288 cm^{-1} assigned to SO strechings and deformation vibrations of OH-group of ions HSO_4^- decreases. Besides in the range 1000–1100 cm^{-1} the band of stretching

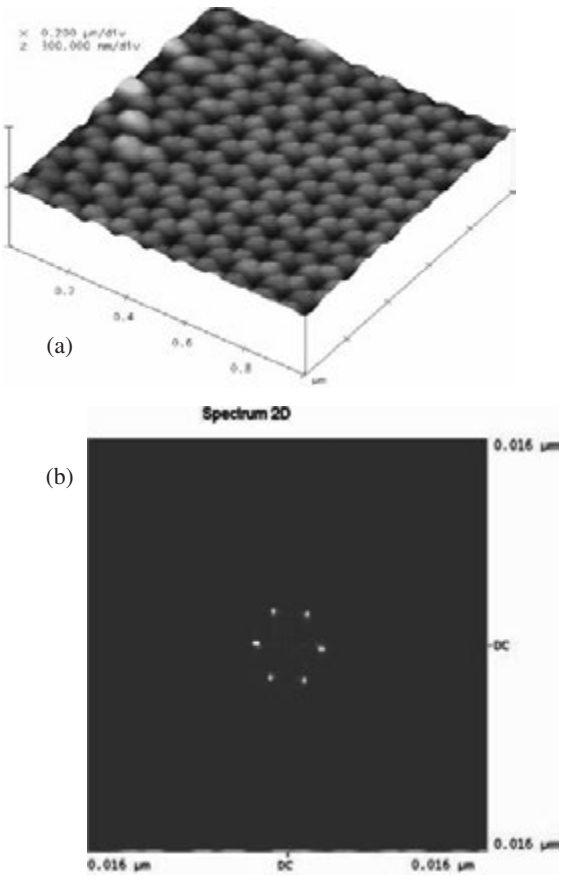

Fig. 1. AFM top view image (a) and Fourier-transform image (b) of porous alumina.

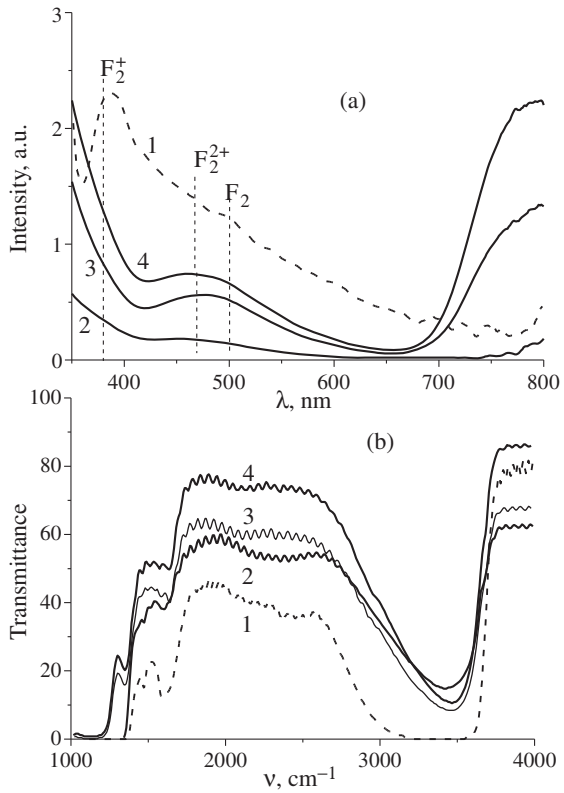

Fig. 2. Photoluminescence (a) and IR (b) spectra of AAO samples formed at anodizing in a sulfuric acid. (1) — amorphous AAO; (2) — $T = 800$ °C, $t = 30$ min; (3) — $T = 1150$ °C, $t = 10$ min; (4) — $T = 1200$ °C, $t = 5$ minutes.

vibrations of HSO_4^- and H_2SO_4 is manifested. Annealing of the AAO results not only in removal of the sulfates-ions, but also to their decomposition. Presence in IR spectrum of the band at 1380 cm^{-1} testifies to the presence of SO_3 groups.

The experimental results obtained reveal that before preparation of SERS-active substrates on the base of AAO matrixes it is necessary to carry out their annealing at temperature <800 °C for essential reduction of the photoluminescence intensity.

Acknowledgements

This work has been supported by the Belarusian Republic Foundation for Fundamental Research (Grant F08-012 and F08 MC-011).

17th Int. Symp. "Nanostructures: Physics and Technology"
Minsk, Belarus, June 22–26, 2009
© 2009 Ioffe Institute

Q-DLTS studies of quantum confinement levels in SiGe quantum wells

M. S. Kagan[1], I. V. Antonova[2], E. P. Neustroev[3], S. A. Smagulova[3], P. S. Alekseev[4] and J. Kolodzey[5]

[1] Institute of Radio Engineering and Electronics, RAS, 125009 Moscow, Russia
[2] Institute of Semiconductor Physics, RAS, Novosibirsk, Russia
[3] Yakutsk State University, Yakutsk, Saha Republik, Russia
[4] Ioffe Physical-Technical Institute, St Petersburg, Russia
[5] University of Delaware, Newark, DE 19716, USA

Abstract. The recharging of quantum confinement levels in single-quantum-well Si/SiGe/Si structures was studied by charge deep-level transient spectroscopy (Q-DLTS). The set of levels were observed as the different slopes at the Arrhenius plot for the same Q-DLTS peak in different temperature ranges. These activation energies were compared with the calculated energies of quantum confinement levels in the QW and attributed to a thermally activated tunneling of holes from the SiGe QW.

Introduction

At present there is considerable interest in studying the electronic capture-emission properties of Si/SiGe/Si quantum well heterostructures, suitable, e.g., for Tera-Hertz lasers [1]. Deep-level transient spectroscopy is a powerful tool to probe the electronic properties of QW systems [2]. The main problem in studies of Si/SiGe/Si QW structures is the relatively small thickness of the Si cap layer. Due to residual positive charge at surface states, the near-surface layers including the SiGe QW are depleted. To diminish the surface charge, we passivated the Si cap layer surface by an organic monolayer deposition [3]. In this report we present the results of Q-DLTS measurements on passivated Si/SiGe/Si heterostructures with different Ge contents in QW, which directly indicate the emission of holes from ground and excited levels in valence band of QWs.

1. Experimental

Si/SiGe/Si structures different Ge contents x in the $Si_{1-x}Ge_x$ layers (designated as SiGe-1, SiGe-2 and SiGe-3 for $x = 0.07$, 0.10 and 0.15, respectively) have been studied. The structures were MBE grown on n-Si(100) substrates at the temperature of 400 °C. The SiGe layers of 14 nm thickness were δ-doped in the middle with boron with a concentration of 6×10^{11} cm^{-2}. Two additional boron-doped δ-layers with the same concentration were positioned within the buffer and cap layers (one each). The thickness of the Si buffer and cap layers was 80 and 38 nm, respectively. The background concentration of holes in the MBE-grown layers did not exceed 3×10^{15} cm^{-3}. To provide low surface charge and high carrier concentration in the SiGe quantum wells, the surface was passivated with organic monolayers of 1-octadecene [3].

Passivated samples were characterized by high frequency (1 MHz) capacitance-voltage (C-V) and Q-DLTS measurements. A mercury probe or Ag electrodes deposited on the surface were used as electrical contacts. The Q-DLTS measuring system employed kept the sample temperature T fixed and scanned the rate window τ_m, where $\tau_m = (t_2 - t_1)/(\ln(t_2/t_1))$, and t_1 and t_2 are the moments of recording the Q-DLTS signal $\Delta Q = Q(t_2) - Q(t_1)$. The expression

$$e_T \sim T^{1/2} \exp(-E_a/kT), \quad (1)$$

where E_a is the activation energy, and k is the Boltzmann constant, was used for description of the emission rate e_T of carriers from confined energy levels in the QWs [4–6].

2. Results and discussion

The Q-DLTS spectra for structure SiGe-2 are given in Fig. 1(a). The position of the main peak A in the spectra demonstrated the activation behavior vs T. Note that peak A was observed only in the passivated structures. One more peak B was appeared only at short enough filling pulse at $\tau_m = 5 \times 10^5$ μs; it was observed for non-passivated structures, too [2]. The amplitude of peak B increased with decreasing filling pulse duration, whereas amplitude of peak A in this structure does not depend significantly on filling pulse duration (Fig. 1(b)). The activation energy of peak B increased with Ge content in the SiGe alloy: it was 0.18 eV for SiGe-1 structure and 0.27 eV for SiGe-3 structure.

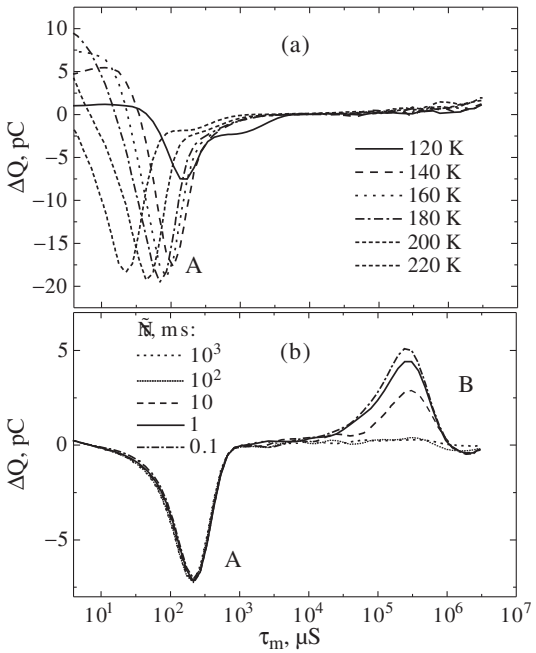

Fig. 1. Capacitance versus voltage curves for the passivated structures SiGe-1 and SiGe-3.

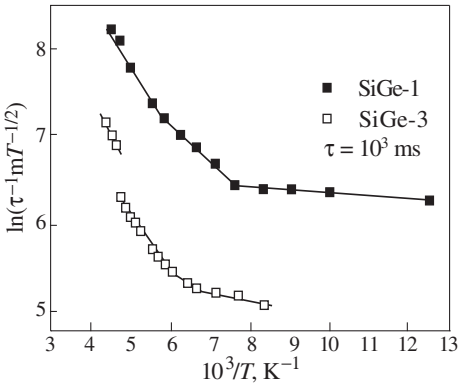

Fig. 2. Arrhenius plots for structures SiGe-1, SiGe-3 in the temperature range of 80 to 300 K, τ is duration of filling pulse.

Fig. 2 shows Arrhenius plots for the peak values of τ_m on $1/T$ for peak A. The peak values of tm gave directly the characteristic times of discharging corresponding electronic states. With decreasing T from 220 to 100 K, the times for peak A changed from 20 to 100 μs for SiGe-1, and from 7 to 70 μs for SiGe-2.

The activation energies were extracted from these plots using expression (1). To determine the origin of the activation energies, the simulation of confined level spectra in strained p-SiGe QW was performed. The method used was an analogue to that in Ref. [7], but with taking into account the spin-orbit interaction by using a 6×6 Luttinger Hamiltonian. The spin-orbit interaction was shown to give considerable contribution to the energy of excited states with index $n > 2$.

It turns out that the experimental activation energies don't agree with the calculated energies of size quantization in QW. However, they can be fitted by taking into account a band bending between the QW and Si cap and buffer layers in the passivated structures, which form triangle barriers. In this case, the activation energy should be the difference between the confined state energy and the energy E_0 of optimal thermo-stimulated tunneling. E_0 for a triangle barrier was found as a maximum of the sum of exponents of thermal emission rate and tunneling probability. It can be expressed (see, e.g., (10.20) in Ref. [8] as $E_0 \sim a + b/T_2$, a and b are constants depending on the barrier shape and confined level parameters. The fitting of the experimental values of E_0 by this expression confirms the model suggested.

Acknowledgements

The work was supported by the RFBR (grants Nos. 08-02-00 351, 08-02-00221, 08-02-01464, 08-02-91323, 07-02-00857), RAS Program "Basic research in nanotechnology and nanomaterials", and RFBR-NSF grant DMR-0601920.

References

[1] M. S. Kagan *et al*, *ECS Transactions* **3**, 745 (2006).
[2] I. V. Antonova *et al*, *Phys. Stat. Solidi C* **2**, 1924 (2005).
[3] I. V. Antonova *et al*, *Appl. Phys. Let.* 91, 102116 (2007).
[4] P. A. Martin *et al*, *J. Appl. Phys.* **54**, 4589 (1983).
[5] K. Schmalz *et al*, *Phys. Rev. B* **54**, 16799 (1996).
[6] N. Debbar *et al*, *Phys. Rev. B* **40**, 1058 (1989).
[7] A. A. Prokofiev, M. A. Odnoblyudov, I. N. Yassievich, *Towards the first silicon laser*, edited by L. Pavesi, S. Gaponenko, L. Dal Negro, Dordrecht, The Netherlands: Kluwer Academic Publishers, 2003.
[8] V. N. Abakumov, V. I. Perel, I. N. Yassievich, Nonradiative Recombination in Semiconductors, *Modern Problems in Condensed Matter Sciences*, **33**, edited by V. M. Agranovich and A. A. Maradudin, Amsterdam, The Netherlands, 1991.

17th Int. Symp. "Nanostructures: Physics and Technology"
Minsk, Belarus, June 22–26, 2009
© 2009 Ioffe Institute

Strong to weak localization transition in 2D quantum dot array driven by disorder and interaction

N. P. Stepina, E. C. Koptev, A. V. Dvurechenskii and A. I. Nikiforov
Institute of Semiconductor Physics, Lavrenteva 13, 630090 Novosibirsk, Russia

Abstract. The crossover from strong to weak localization in a two-dimensional array of Ge/Si quantum dots is observed for the first time. To approach the transition, the wave function spreading was enhanced by variation of the number of holes in dots, by an increase of the quantum dot areal density and annealing of heterostructure at temperatures, which allows to change the islands size and composition. The analysis of temperature dependence of conductance, conductance nonlinearity and checking the scaling theory were carried out to establish the transport mechanism. Two-parameter scaling was found to describe the transport in QDs structure, with the disorder and the interaction being the factors that determine the system state.

Introduction

A high-density array ($1-4\times10^{11}$ cm^{-2}) of Ge/Si quantum dots (QDs) with the lateral size ~10–20 nm is characterized by strong tunnel coupling between dots. The random distribution of dots and quite inhomogeneous dot sizes lead to a strong localization of the electronic states in space. It was shown [1] that the electrical charge transfer in such a system at low (<20 K) temperatures is due to the hole hopping between dots. It was demonstrated also that the conductance and localization radius is essentially depends on the filling factor of QDs with holes and reaches the maximum value at half-integer number of holes in dots. Further increase of the localization radius is expected to cause the changing of the transport behavior due to delocalization of the carrier wave function.

Three ways to vary the disorder, the hopping integral, and the interaction force, all inducing changes in the conductance and in the ξ value, were proposed and realized in this work. First, the average number of holes in Ge QD, grown in Stranskii–Krastanov mode, was varied by the boron concentration in the δ-doped Si layer inserted 5 nm below the QD layer. Second, to enhance the hopping integral I and the interaction, the QD array density value was increased from 4×10^{11} cm^{-2} (single density samples (SD)) to 8×10^{11} cm^{-2} (double density samples (DD)) by changing the growth regimes. Third, annealing at $T=480-625$ °C for SD samples was employed to modify the size and composition of the Ge islands, which was expected to enhance the overlap of carrier wave functions without seriously affecting the e-e interaction in the system. To reveal the influence which the e-e interaction has on the transport behavior of the QD systems under study, we used samples in which the long-range Coulomb potential was screened with a metal plane located close to the QD layer.

1. Results and discussion

The typical temperature dependencies of conductance $G(T)$ in e^2/h units are shown in Fig. 1 as Arrhenius plots for non-annealed SD and DD samples with different dot filling factor. One can see that the conductance of SD sample is much less than that for DD sample and changes with the filling factor ν. The G values of DD samples lie in the range typical for the diffusive regime. Dependence of $G(\nu)$ for the sample with QDs double density is very weak and monotonous. Moreover, the annealing of all SD samples at 480–625 °C leads to an increase of the conductance with annealing temperature.

The samples under study were analyzed in the frame of hopping theory and theory of quantum corrections to conductance. In first case the Efros–Shklovskii law [2] was shown to well described the temperature dependence of the unannealed SD samples. However, the $G(T)$ for the DD samples and for SD samples with $\nu=2.5$ and 2.85 annealed at 600–625 °C is possible to describe by this law but with poor accuracy. Nevertheless, the same procedure was carried out for all samples and both T_0 and localization length ξ were determined. After 625 °C annealing of SD samples, as well as for all DD samples the formally determined values of ξ was shown to be about of some micrometers. The large ξ magnitude, poor accuracy in the simulation of $G(T)$ by the variable-range hopping (VRH), high value of conductance ($\sim e^2/h$) and weak temperature dependence of conductance suggest that the theory of quantum correction can be applied for describing the transport behavior in this kind of samples.

The quantum corrections to the conductance due to the interaction and interference of elastic-scattered electrons lead to the logarithmic decrease of the conductance with decreasing the temperature $\Delta G\propto\ln T$. When analyzed the samples under study in the framework of the quantum correction theory, we found that the conductance for DD samples is well described (Fig. 2) by the logarithmic law up to 20 K and $\Delta G\sim1-4\times10^{-5}$ Ω^{-1} that is the typical value for the quantum corrections [3]. As for SD samples, the $G(T)$ de-

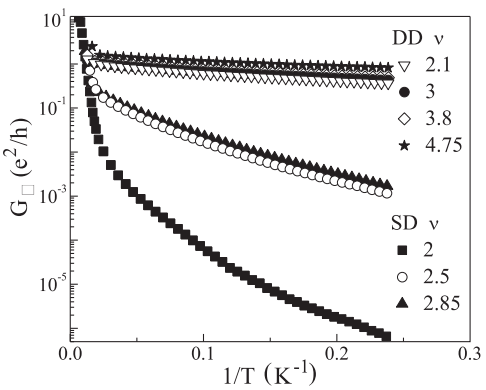

Fig. 1. Temperature dependence of conductance for the samples with different areal density and filling factor ν.

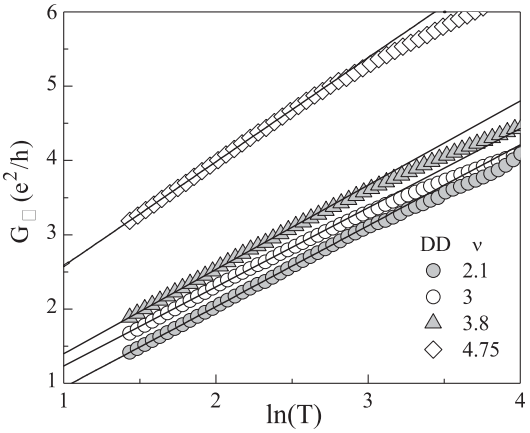

Fig. 2. Conductance of DD samples in dependent on $\ln T$. Lines are the logarithmic approximations of the experimental data.

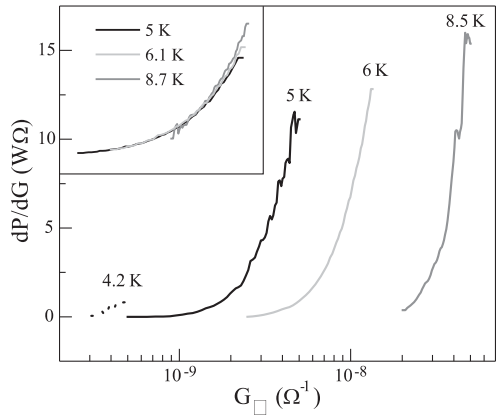

Fig. 3. $dP/dG(G)$ dependencies measured at different lattice temperature for the SD samples with VRH and (inset) for the sample with logarithmic dependence $G(T)$.

pendencies fall into the logarithmic law for the sample with $\nu = 2.5$ only after annealing at $T \geq 600$ °C and for the sample with $\nu = 2.85$ after annealing at 625 °C. The SD sample with $\nu = 2$ never shows the $\Delta G \propto \ln T$ dependence and the conductance of this sample is changed in some orders with temperature. Such a behavior is not a typical for the weak-localization regime, in which ΔG should be of the same order of the conductance itself [3]. Thus, the hopping transport and quantum correction approaches give the non-contradictory description of conductance regimes and allow to distinguish the samples with strong and weak-localization behavior.

To confirm this result, the transport regimes were tested using the method, proposed in Ref. [4]. This method is based on the analysis of power P injected to the sample. As long as the conductance remains diffusive, the dP/dG dependencies measured at different lattice temperatures T_l have to fall on common curve and this property has to disappear when the conductance becomes hopping. We have found that dP/dG-versus-G data obtained for different lattice temperatures fall on a common curve (inset to Fig. 3) for the high-conductance sample with logarithmic temperature dependence of G. On a contrary, for the sample in which the temperature dependence of G described by VRH, the approximation of the electron temperature fails (Fig. 3). Thus, the result of the non-linear conductance analysis confirms the transport behavior of the

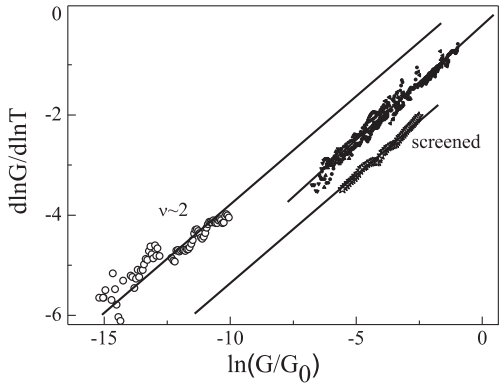

Fig. 4. β-function for the samples under study.

system determined from the measurements of the $G(T)$ dependencies and testifies to the crossover from hopping to diffusive transport in quantum dots array.

To check whether one- or two-parameter scaling correctly describes our system, we analyzed the $G(T)$ dependencies of all used samples in the frame of classical scaling theory.

The $d \ln G/d \ln T$ (β-function) versus $\ln G$ dependencies are analyzed for the samples with hopping transport behavior and the results are shown in Fig. 4. The middle curve demonstrates the results of β calculations for the samples with different filling factor of dots with holes, different structural parameters of dots and after different annealing of samples. The only sample with $\nu = 2$ has a upward deviation from this universal curve. We suggest that namely Coulomb interaction that reaches the maximum value at full filling of QDs ground state ($\nu = 2$) can be a second parameter besides the conductance that determined the system behavior.

To obviously check the influence of long-range interaction to the system behavior, we use the screening of the interaction putting the metal plate on the vicinity of QDs parallel to the dot layer. The β-function for screened samples (bottom curve) is also shown to the Fig. 4. One can see that the β of sample with screening Coulomb interaction is downward shifted from the middle curve. This result is the direct indication that not only disorder but also interaction determine the system behavior and confirms two-parametric scaling in the interacting 2D systems. Independent contribution of these parameters into scaling has never been observed experimentally before.

Acknowledgements

This work was supported by RFBR (Grant No. 08-02-12095-OFI).

References

[1] A. I. Yakimov, A. V. Dvurechenskii, V. V. Kirienko, Yu. I. Yakovlev, A. I. Nikiforov, C. J. Adkins, *Phys. Rev.* **B 61**, 10868 (2000).

[2] B. I. Shklovskii and A. L. Efros, *Electronic Properties of Doped Semiconductors*, Springer Series in Solid-State Sciences (Springer-Verlag, New-York, 1984).

[3] V. F. Gantmakher, in *Electrons in non-ordered medium*, (Fizmatlit, Moscow, 2003).

[4] G. M. Minkov, A. A. Sherstobitov, O. E. Rut, A. V. Germanenko, *Physica E* **25**, 42 (2004).

17th Int. Symp. "Nanostructures: Physics and Technology"
Minsk, Belarus, June 22–26, 2009
© 2009 Ioffe Institute

Kinetics of shallow acceptor impact ionization and recombination in p-Ge

S. K. Paprotskiy, I. V. Altukhov, V. P. Sinis and M. S. Kagan
Institute of Radio Engineering and Electronics, RAS, Moscow, Russia

Abstract. The transient current through the Ge⟨Ga⟩ samples in pulsed electric fields was studied at different uniaxial pressures. The coefficients of impact ionization and capture for shallow acceptors were determined from these data.

Introduction

Stimulated THz emission has been observed in uniaxially strained p-Ge with an optical resonator [1–3]. The origin of the THz emission was attributed to intra-center optical transitions between resonant and localized acceptor levels. A population inversion in the p-Ge RSL occurs for states of a shallow acceptor split under pressure. If the strain is high enough, a split-off acceptor state enters a light-hole branch of the valence band and creates a resonant state. An applied electric field depopulates the ground acceptor state because of impact ionization and accelerates free holes up to the energy of the resonant state, which acts as a trap for holes. As a result, a population inversion of resonant states with respect to the impurity states in the gap is then formed and THz lasing may occur. The frequency of the RSL can be tuned by pressure by a factor of more than 4 without any noticeable change in power. As was shown, p-Ge RSL can also operate in continuous wave regime.

The possible frequency band of modulation of the THz emission is determined by relaxation times of conductivity that is the relaxation times of carrier distribution function and of non-uniform distributions of current (current filaments caused by impurity breakdown) and field (electric domains formed at negative differential conductivity caused by carrier redistribution between different valence band branches with different effective masses), which can arise in strained p-Ge. The latter reasons give the longest characteristic times.

1. Experimental

Ga-doped p-Ge crystals with Ga concentration of 3×10^{13} to 3×10^{14} cm^{-3} were studied at the liquid He temperature. The match-like samples of a square cross section of 0.5 to 1 mm $^{-2}$ and 6 to 10 mm long were cut in the [111] crystallographic direction. The uniaxial pressure P and electric field E were applied along the sample in this direction. Voltage pulses of 0.2 to 1 μs duration were applied to two contacts deposited on the long (lateral) facet of the sample spaced by 4 to 9 mm. The time evolution of current through the sample at the leading front of voltage pulse obeyed an exponential law with at least two different characteristic times (Fig. 1).

The shorter time was attributed to the electric field ionization of shallow acceptors (Ga). The field dependence of impact ionization coefficient was determined from these data (Fig. 2).

$$\frac{dp}{dt} = \beta(E)\,(N_A - N_D - p)\,p - \alpha(E)\,(N_D + p)\,p, \quad (1)$$

$$p(t) = \frac{p_{st}\exp\left(\frac{t}{\tau(E)}\right)}{\left(\exp\left(\frac{t}{\tau(E)}\right) + \frac{p_{st}}{p_0} - 1\right)}, \quad (2)$$

where $\beta(E)$ — impact ionization coefficient, $\alpha(E)$ — capture coefficient, N_A — acceptor concentration, N_D — donor concentration.

$$p_0 = p(t=0), \quad p_{st} = p_{t\to\infty}, \quad \tau = \beta(N_A - N_D) - \alpha N_D.$$

The longer time was referred to the current filament formation caused by instability of S-shaped current — voltage characteristics of initially uniform sample at the impurity breakdown.

The current relaxation at the back front of voltage pulse (Fig. 3) had also the exponential character resulted from a free carrier capture at shallow acceptors. The recombination time

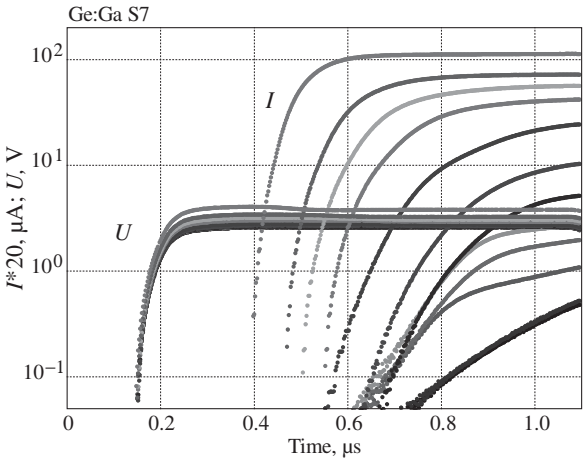

Fig. 1. Current and voltage pulse shapes.

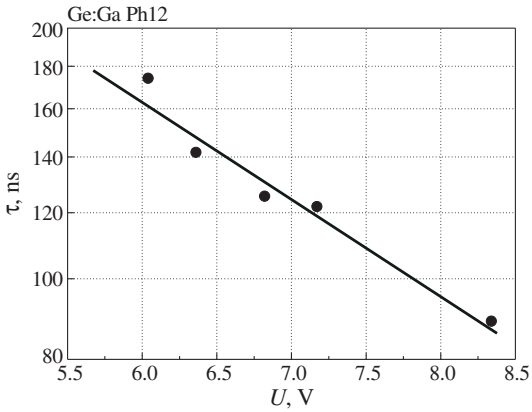

Fig. 2. Characteristic time of impact ionization vs voltage.

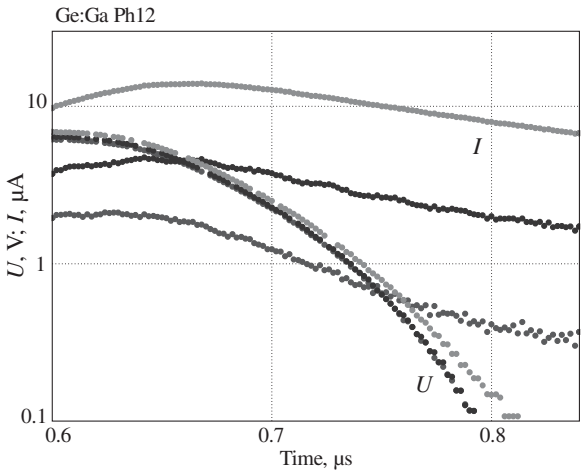

Fig. 3. Current relaxation due to recombination.

was found from the current decay; it was 10^{-7} s at zero pressure for Ga concentration of 10^{14} cm^{-3}.

In summary, studies of time evolution of current at impurity breakdown give the possibility for direct determination of characteristic times of impact ionization and capture for shallow acceptors.

Acknowledgements

The work is supported by RFBR grants 07-02-00857, 08-02-01464 and RAS programs "Basic research of nanotechnology and nanomaterials" and "Modern problems of radiophysics".

References

[1] M. S. Kagan *et al*, *Towards the first silicon laser, NATO Science Series*, editors: L. Pavesi, S. Gaponenko, and L. Dal Negro, Kluwer Academic Publishers, 359 (2003).

[2] M. S. Kagan *et al*, *Journal of Communications Technology and Electronics* **48**, 1047 (2003).

[3] M. S. Kagan *et al*, *ECS Transactions* **3**, 745 (2006).

17th Int. Symp. "Nanostructures: Physics and Technology"
Minsk, Belarus, June 22–26, 2009
© 2009 Ioffe Institute

Bonding-antibonding ground-state transition in double Ge/Si quantum dots

A. I. Yakimov, *A. A. Bloshkin* and A. V. Dvurechenskii
Rzhanov Institute of Semiconductor Physics, Siberian Branch of the RAS, Novosibirsk, Russia

Abstract. We investigate theoretically the two lowest single-particle hole states in the double quantum dots made of two identical, vertically stacked, Ge/Si nanoclusters. The bonding-antibonding molecular ground-state transition in coupled quantum dots is observed. We conclude that a correct description of the ground-state symmetry in Ge/Si quantum dots requires taking into account the presence of strain.

The three-dimensional quantum confinement of conduction electrons or valence holes in quantum dots (QDs) leads to formation of a discrete carrier energy spectrum, resembling that of an atom. Two coupled quantum dots represent another example of zero-dimensional system, in which the interdot coupling extends the analogy between QDs and natural atoms to artificial and natural molecules. Many specific phenomena, which are absent in single QDs, have been predicted for quantum-dot molecules. One of the most intriguing result is the discovery of antibonding molecular ground states for holes in Ge/Si [1], InGaAs/GaAs [2,3], and InAs/GaAs [4] vertically coupled QDs. The existence of this effect is important for basic condensed matter physics since it has no analogue in natural molecules. The electronic coupling between QDs brought close together arises from the process of quantum-mechanical tunneling and appears as a formation of bonding σ_S and antibonding σ_{AS} molecule-type orbitals by an analogy with the covalent bonds in natural molecules. The bonding state corresponds to the symmetric combination of individual dot's wave functions, while the antibonding state is formed by the antisymmetric orbital. The molecular ground state always remains bonding (symmetric) and the first excited state is antibonding (antisymmetric). The energy splitting between the σ_S and σ_{AS} states corresponds to the doubled tunneling matrix element, which is always positive. This is the conventional quantum-mechanical approach used to describe the formation of molecular orbitals in natural molecules and in a system of identical tunnel-coupled QDs containing electrons. However, recent calculations [1,2,4,3] have demonstrated that this is no longer true for hole states. Namely, it has been observed that, with increasing interdot distance, the effective matrix element becomes negative and the hole ground state changes its spatial symmetry from almost symmetric to almost antisymmetric. Several explanations for the bonding-antibonding ground-state transition have been proposed [1,3,2,4], but a complete understanding of this phenomenon has not been achieved to date. The main aim of this paper is to clarify the effects responsible for appearance of antibonding ground state.

We consider two *identical* vertically aligned pyramidal Ge nanoclusters with four {105}-oriented facets and a (001) base embedded into the Si matrix as shown in Fig. 1. Each pyramid lies on a 4 ML Ge wetting layer. The nanoclusters are separated by a Si barrier of thickness d measured from wetting layer to wetting layer. The pyramid base length l is varied from 10 nm to 20 nm in different calculations; the pyramid aspect ratio h/l is fixed and equal to 0.1.

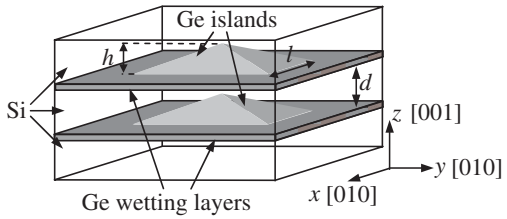

Fig. 1. Schematic representation of a Ge/Si double quantum dot used for simulation of hole states.

To establish the effect responsible for reordering of bonding and antibonding states, we calculate the two lowest hole states in three different levels of approximations

(i) We first study a more realistic situation when both Si matrix and Ge nanoclusters are inhomogeneously strained due to the lattice mismatch between Si and Ge. The finite element calculations of three-dimensional spatial distribution of strain components $\varepsilon_{\alpha\beta}$ are performed using the package COMSOL MULTIPHYSICS.

(ii) In level-2 theory, we neglect the non-uniformity of strain fields and consider the pseudomorphic Ge QDs with $\varepsilon_{xx} = \varepsilon_{yy} = -0.04$ and $\varepsilon_{zz} = 0.03$ buried in unstrained Si crystal. All off-diagonal components are zero. The strain tensor elements are subsequently used as input to a strain-dependent Hamiltonian.

The main difference between electrons and holes arises from the complicated valence-band structure, which is governed by multiple spin-orbit coupled bands rather than the single band for electrons. Here we use a six-band $\mathbf{k}\times\mathbf{p}$ approximation, based on the method of Bir and Pikus [5], which includes spin-orbit and strain effects. The resulting hole eigenstates are six-component objects associated to different Bloch functions $|J, J_z\rangle$, where $|J, J_z\rangle$ are the eigenstates of the total angular momentum J and its projection J_z.

(iii) In the third level of approximation, we ignore the strain-induced term in the Hamiltonian putting all $\varepsilon_{\alpha\beta} = 0$.

Hole binding energies calculated with a level-1 model for QDs of different sizes l are presented in Fig. 2. The bonding-antibonding molecular ground-state transition is observed at $d > d_c = (3.8 - 4.8)$ nm. The critical distance for the transition d_c increases with the increase of the dot size. The reduction of hole energies below the value of the single dot seen in Fig. 2 is due to strain relaxation upon dot stacking accompanied by the strain-induced reduction of the hole confinement potential [6].

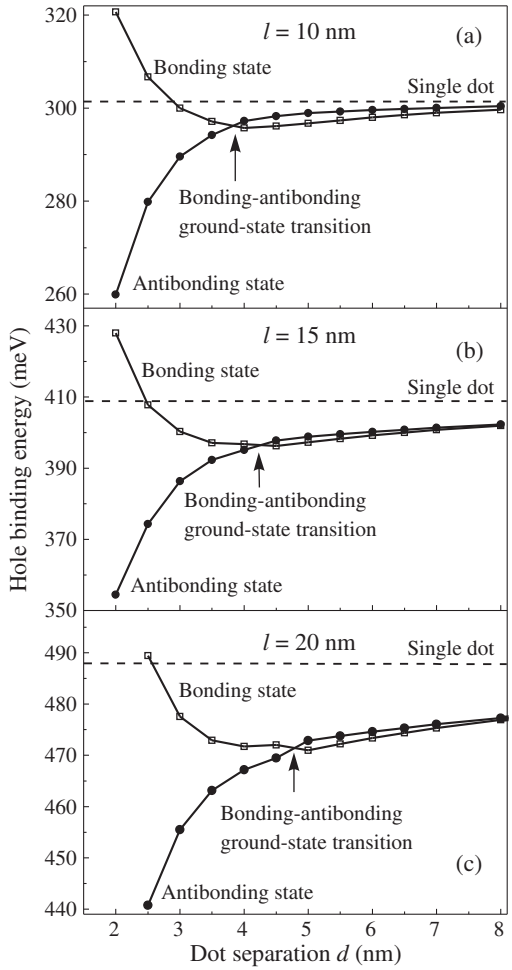

Fig. 2. Evolution of hole binding energy in bonding (symmetric) and antibonding (antisymmetric) states as a function of the distance between inhomogeneously strained QDs, calculated with a 6×6 $\mathbf{k}\times\mathbf{p}$ model for different dot sizes l. As reference, also the hole ground-state energy of isolated single dot is shown by horizontal line. All energies are counted with respect to the valence-band edge in bulk Si.

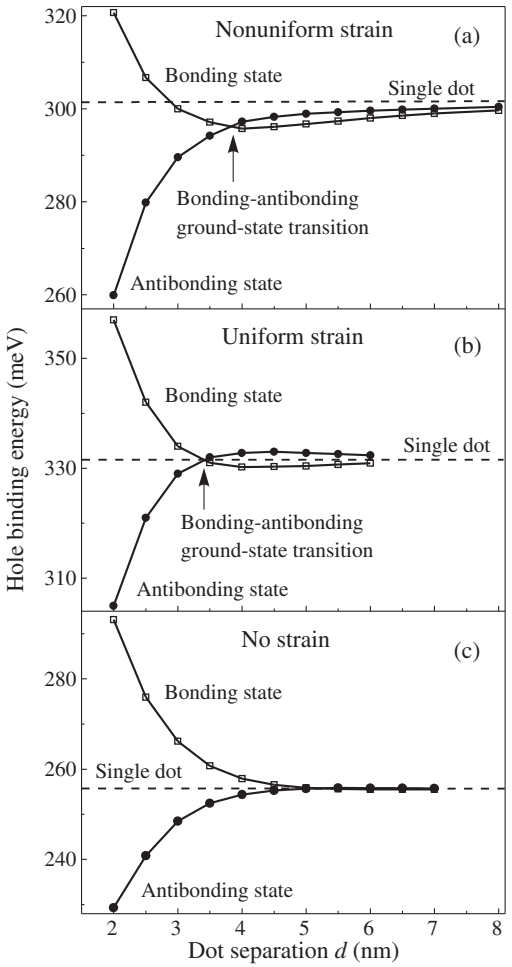

Fig. 3. Hole energy levels as a function of the distance between QDs, calculated for (a) inhomogeneously strained, (b) pseudomorphic, and (c) unstrained QDs. Here $l = 10$ nm.

Figure 3 represents the hole binding energy in the ground and excited states of 10-nm QDs as a function of interdot distance d. Panels (a), (b) and (c) show the energy levels calculated for inhomogeneously strained, pseudomorphic, and unstrained QDs, respectively. For all dot-dot distances of unstrained system, the ground state corresponds to symmetric (bonding) state, while the excited state is antisymmetric (antibonding). However, for strained dots, the change in d causes crossing between the energy levels corresponding to bonding and antibonding orbitals. As a result, at $d > d_c = (3.5 - 3.8)$ nm, the antibonding ground state appears. It follows unambiguously from Fig. 3 that the reversal of the hole ground-state symmetry cannot be understood without invoking strain effects.

Acknowledgements

This work has been supported by RFBR (Grant No. 09-02-00050). A. A. B. acknowledges financial support from Dynasty Foundation.

References

[1] A. I. Yakimov, A. A. Bloshkin, and A. V. Dvurechenskii, *Phys. Rev. B* **78**, 165310 (2008).

[2] G. Bester, A. Zunger, and J. Shumway, *Phys. Rev. B* **71**, 075325 (2005).

[3] J. I. Climente, M. Korkusinski, G. Goldoni, and P. Hawrylak, *Phys. Rev. B* **78**, 115323 (2008).

[4] W. Jaskólski *et al*, *Phys. Rev. B* **74**, 195339 (2006).

[5] G. L. Bir and G. E. Pikus, *Symmetry and Strain-Induced Effects in Semiconductors*, (New York: Wiley) 1974.

[6] A. I. Yakimov *et al*, *JETP Lett.* **85**, 429 (2007).

17th Int. Symp. "Nanostructures: Physics and Technology"
Minsk, Belarus, June 22–26, 2009
© 2009 Ioffe Institute

Photoconductivity of Si/Ge/Si structures with Ge layer thickness 1.5 and 2 ML

O. A. Shegai, V. I. Mashanov, A. I. Nikiforov, V. V. Ulyanov and O. P. Pchelyakov
Institute of Semiconductor Physics, 630090 Novosibirsk, Russia

Abstract. A photoconductivity (PC) of Si/Ge/Si structures with narrow Ge layer thickness 1.5 and 2 monolayers (ML) on interband light intensity have been investigated for the different values of lateral voltage U, and temperature T. In contrast to the Si/Ge structure with 2 ML, where only monotonous PC growth on light intensity was registered, for the 1.5 ML structure a stepped and fluctuated PC were observed. Mechanisms of such behavior are discussed.

Investigation of low dimensional Si/Ge structures it is interesting due to possible applications in Si based technology. Early our studies of lateral photoconductivity (PC) of Si/Ge structures with self-organized quantum dots (QDs) allowed observing a stepped PC as a function of interband light intensity [1,2]. Stepped and fluctuated PC of Si/Ge structures with narrow Ge layer (4 ML) have been observed recently [3]. In this work results of PC studies of narrower Ge layers with 1.5 and 2 ML structures are reported. Studied Si/Ge structures were grown be molecular beam epitaxy. Firstly on Si (100) KDB 2.5 substrate a buffer Si layer with thickness 60 nm at $T = 700$ °C was grown, then a Ge layer ($T = 450$ °C), and capped Si layer with 20 nm at $T = 300$ °C were deposited. Detailed Ge layer width was controlled in situ by reflection of high energy electron diffraction (RHEED). In Fig. 1 RHEED oscillations arise during Ge layers growth are shown. An atomic clear surface leads to maximum of intensity, whereas roughness surface gives a minimum of intensity due to electron beam scattering on 2-dimetional islands with 1 ML height. Arrows in Fig. 1 shows start of Ge growth and its finish at 1.5 and 2 ML, respectively.

PC measurements were carried out by two contact method, a distance between contacts is about 2 mm and illuminated area is $\approx 2 \times 2$ mm^2. Additional experimental details can be found elsewhere [1]. For the Si/Ge structure with 2 ML Ge layer only monotonous PC growth on light intensity was registered in wide interval of temperatures and lateral voltages U. In Fig. 2 typical PC curves for Si/Ge structure with 1.5 ML Ge layer at $T = 22.5$ K and U in interval of 12–15.5 V are shown. In addition to stepped PC (with its number reaches four) a fluctuated PC was observed. Position of steps shifts to low light intensity with increase of U, a like behavior is registered for the growth of T. These features are appeared in the temperature interval of 15–25 K. Besides, step amplitude is not change with the growth of U, but they only shifts to low light intensity. For larger U interval of possible PC values is narrow, in which PC increases slightly. PC fluctuations are appeared at relatively large U and T as a rule on the edge of steps and they amplitude is about the amplitude of each step. The PC fluctuations are registered in some interval of light intensity, which very sensitive to the value of U and it increase with growth of U.

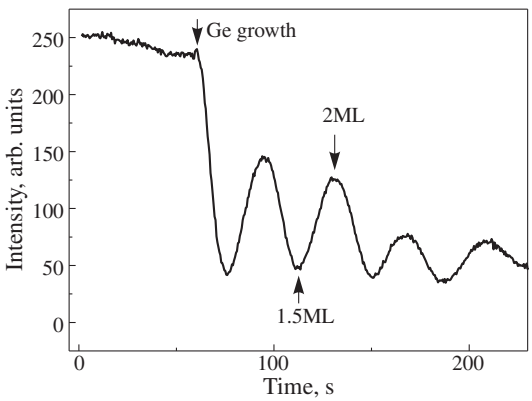

Fig. 1. RHEED oscillations of Ge layer growth; arrows show the start and the finish Ge growth at 1.5 and 2 ML, respectively.

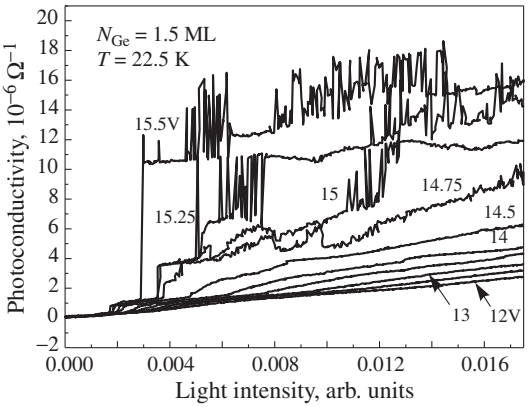

Fig. 2. Photoconductivity of Si/Ge/Si structure (nominal thickness of Ge layer is 1.5 ML) on light intensity for the different lateral voltages; $T = 22.5$ K.

Assuming that the studied Si/Ge structures are related to type II structures and for structure with 1.5 ML Ge layer a degree of roughness is maximal, photoexcited carriers are separated as vertically and laterally: holes are localized in Ge and electrons in Si regions, respectively. Stepped PC is appeared when the carriers reach a percolation level [4]. A few PC steps can be determined by such transition from localized states to the conductive states on each ground and excited electron sublevels induced by the Coulomb potential of holes situated in the narrow Ge layer.

PC fluctuations are appeared near the PC step and can be explained by electron-hole recombination near the percolation level. Electron and hole transport via disordered system of 1.5 ML structure is spatially separated. On the border these two regions Coulomb attraction leads to carriers recombination, which is possible due to disorder allowed escape the problem of indirect semiconductors (Si, Ge), for which interband

transitions without phonons are forbidden. Suppression of PC fluctuation for the large light intensities is due to so increasing Fermi-quasilevel above a percolation level, that the degree of disorder is diminished so, that recombination is forbidden again.

Acknowledgements

This work was supported by RFBR (#07-02-01106).

References

[1] O. A. Shegai, V. A. Markov *et al*, *Phys. Low Dim. Struct.* **1–2**, 261 (2002).
[2] O. A. Shegai, V. A. Markov *et al*, *Phys. Sol. St.* **46**, 74 (2004).
[3] O. A. Shegai, V. I. Mashanov *et al*, *Int. Conf. on Elect. Prop. of 2D Syst. and Mod. Semicond. Struct.* (MSS 13), Genova, Italy, July 15–20, 152 (2007).
[4] B. I. Shklovskii and A. L. Efros, *Electronic Properties of Doped Semiconductors*, (Berlin: Springer), 1984.

17th Int. Symp. "Nanostructures: Physics and Technology"
Minsk, Belarus, June 22–26, 2009
© 2009 Ioffe Institute

Study of the plastic relaxation onset in SiGe islands on Si(100)

V. A. Zinovyev[1], R. Gatti[2], A. Marzegalli[2], F. Montalenti[2] and L. Miglio[2]

[1] Institute of Semiconductor Physics, 630090 Novosibirsk, Russia
[2] Dipartimento di Scienza dei Materiali, Universita di Milano-Bicocca, via Cozzi 53, 20125 Milano, Italy

Abstract. A detailed investigation of plastic relaxation onset in heteroepitaxial SiGe islands on Si(100) is presented. The strain field induced by a straight misfit-dislocation segment is modeled by finite-element-method (FEM) calculations in three dimensions, fully taking into account the interaction with the multifaceted free surfaces of realistic islands. The total elastic energies before and after the placement of a 60^0-dislocation segment in the most favorable position are therefore evaluated by a full FEM approach, for different island sizes and compositions. The critical volumes with composition for inserting the dislocation are finally obtained and successfully compared with the experimental data.

Introduction

Deposition of Ge on Si(100) leads to a Stranski–Krastanow growth mode: after the formation of a thin pseudomorphic wetting layer (WL), coherent three dimensional (3D) islands appear on the substrate. The nanometric size of such 3D structures immediately attracted considerable attention, in view of possible exploitation in the nanofabrication of ordered array of quantum dots, due to the relatively simple chemistry of the system and, obviously, to the wide technological importance of Si-based devices [1].

In-depth experimental analysis of Ge/Si islands revealed a very fascinating physics, in particular for what concerns the morphological evolution during growth of the 3D structures. As the Ge deposition increases, islands change from shallow (prepyramids and pyramids) to steeper (domes and barns) morphologies [2,3], according to a larger strain relaxation and to a reduction in surface to volume ratio. This evolution can be understood in simple thermodynamic terms. Islands with a large height-to-base aspect ratio allow for a better volumetric strain relaxation while involving a larger energy cost in terms of extra exposed surface (with respect to a flat WL). Evolution toward higher aspect ratios, however, is abruptly interrupted by the opening of an alternative plastic channel for strain relaxation. Misfit dislocations are eventually injected, deeply influencing evolution at larger volumes. An intriguing cyclicgrowth regime is actually observed, involving a periodic flattening of the island shape each time a new dislocation nucleates in the island [4].

The issues influencing the critical size for plastic relaxation onset are the shape and the intermixing of the deposited Ge, with Si popping up from the substrate, which has been shown to decrease the Ge content with increasing growth temperatures. Since alloying contributes to strain reduction, by lowering the effective lattice misfit, it competes with plastic relaxation [5] effectively delaying the dislocation nucleation. Interestingly, the same kind of effect lowering of the effective misfit and delaying of the dislocation injection was recently observed for growth on suitably pit-patterned substrates [6].

1. Modeling of the dislocated island

This work devotes to detailed study of the plastic relaxation onset in SiGe islands on Si(100) substrate. New strategy was proposed to calculate a critical volume for the dislocation injection in 3D island. This approach takes into account the realistic shape of SiGe islands and the dependence of the dislocation energy on the position inside the island. We use the finite-element method (FEM) calculation starting from the stress field of a dislocation segment in an infinite body. The main idea is the construction of final solution for the mechanical stress in the dislocated island as a superposition of analytical and numerical parts. The analytical part includes a singularity (divergence) of the stress field near the dislocation core, when the numerical part takes into account the interaction of the dislocation stress field inhomogeneous strain field inside the island and satisfies also the finite-body boundary conditions for free surfaces and interfaces. On the base of FEM approach the stress distributions at the different positions of 60^0 -misfit dislocation in three dimensional island were calculated (Fig. 1).

It allows us to calculate equilibrium dislocation position in the island and critical island dimensions for the dislocation nucleation. The critical island volume is determined by equating the energy cost for introducing one dislocation (i.e., the distortion energy produced by the dislocation itself in a fully relaxed island) to the energy gain produced by the dislocation in a strained island (i.e., the interaction energy between the inhomogeneous misfit stress in the island and the strain field of the dislocation itself). It was found, that dome-like islands (island height to base width, $h/l = 0.2$) is more stable against the dislocation injection than barn-like islands ($h/l = 0.3$). Results of the modeling are in good agreement with the experimental dependence of a critical island base for the onset of plastic relaxation in three dimensional SiGe islands on Ge

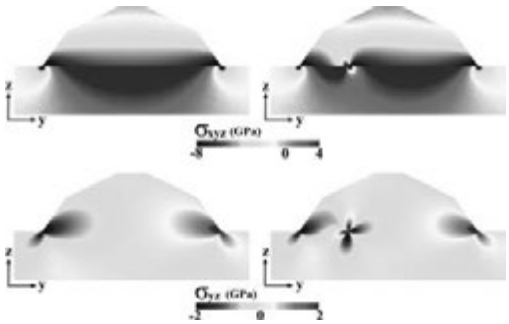

Fig. 1. Hydrostatic (upper panel) and shear (bottom panel) stress components in the coherent barn-like SiGe island on the Si(100) substrate. The left panels show the case of a coherent island, while the right panel show the same system when 60°-misfit dislocation at the island — substrate interface is introduced.

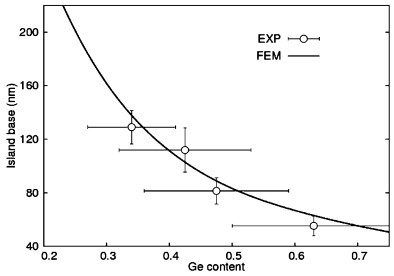

Fig. 2. Critical SiGe island bases as calculated by FEM and compared with the experimental data of Ref. [5].

content [5] (Fig. 2).

Acknowledgements

This work has been supported by Russian Foundation of Basic Research (grant 09-02-00882-a), Europen Union (contract No. 012150, Strep Project D-DOT-FET) and Cariplo Foundation (MANDIS project).

References

[1] K. Brunner, *Rep. Prog. Phys.* **65**, 27 (2002).
[2] M. Stoffel, A. Rastelli, J. Tersoff, T. Merdzhanova, and O. G. Schmidt, *Phys. Rev. B* **74**, 155326 (2006).
[3] G. Medeiros-Ribeiro *et al*, *Science* **276**, 353 (1998).
[4] F. M. Ross, J. Tersoff, M. C. Reuter, F. K. LeGoues, and R. M. Tromp, *Microsc. Res. Tech.* **42**, 281 (1998).
[5] A. Marzegalli, V. A. Zinoviev, F. Montalenti, A. Rastelli, M. Stoffel, T. Merdzhanova, O. G. Schmidt and Leo Miglio, *Phys. Rev. Lett.* **99**, 235505 (2007).
[6] Z. Y. Zhong, W. Schwinger, F. Schaffler, G. Bauer, G. Vastola, F. Montalenti and Leo Miglio, *Phys. Rev. Lett.* **98**, 176102 (2007).

17th Int. Symp. "Nanostructures: Physics and Technology"
Minsk, Belarus, June 22–26, 2009
© 2009 Ioffe Institute

Peculiarity of nonlinear optical effects in heterogeneous liquid-phase Al_2O_3 nanocomposites

Yu. N. Kulchin, V. P. Dzyuba, A. V. Shcherbakov and S. S. Voznesensky
Institute of Automation and Control Processes, Far East Division RAS, Vladivostok, 690041 Russia

Abstract. The results of the study of low-threshold optics nonlinear effects in heterogeneous liquid-phase Al_2O_3 nanocomposites are presented. The determining factors of the nonlinearity are polarization of nanoparticle medium in case of generation of nonequilibrium charge carriers or excitation of charge carriers conditions as well as radiation defocusing effect which is much less dependent on wavelengths then on material of the liquid-phase matrix are shown. The defocusing effect is caused by negative temperature dependence of refractive index of heterogeneous medium (immersion oil based on cedar oil).

The last studies [1–5] have shown that heterogeneous liquid-phase nanocomposites (HLPN) based on high energy-gap semiconductor nanoparticles and dielectric nanoparticles are effective for realization of low-threshold nonlinear optical effects in the visible range of light. Usage of such composites gives us an ability to modify nonlinear optical characteristics by changing matrix type as well as concentration, size and shape of nanoparticles. This idea is proved by the results of experimental studies of passing the laser radiation with $\lambda = 532$ nm and $\lambda = 633$ nm wavelengths through a plane-parallel layer of HLPN. For liquid-phase matrices of HLPN we selected such transparent media as VM-4 vacuum oil with refractive index $n \sim 1.5$ and immersion oil with refractive index $n \sim 1.4$ which have linear optical characteristics in infrared range of light as well as in visible one. HLPN was based on Al_2O_3 (corundum) high energy-gap semiconductor nanoparticles with refractive index $n \sim 1.7$. The crystal of corundum has hexagonal symmetry and its energy gap width is from 6.2 up to 8 eV according to different sources. Mass concentration was from 0.03 up to 0.3%. Maximal average size of nanoparticles was between 40 and 50 nm. The surface of Al_2O_3 nanoparticles is not plane but it has complex multipeak pyramidal shape (Fig. 1). The measured spectrum of light transmission through the Al_2O_3 nanoparticles array in the dielectric matrix based on VM-4 vacuum oil is shown in Fig. 2.

Analyze of the energy spectrum of both free charge carriers and charge carriers bound in exciton pairs in the nanoparticle shows what taking into account the natural and thermal broadening of levels, we can state that the exciton's spectrum in the nanoparticles under consideration is formed by a practically continuous 0.1-eV-wide band adjoined to the bottom of the onduction band from below and by discrete levels localized deeply in the band

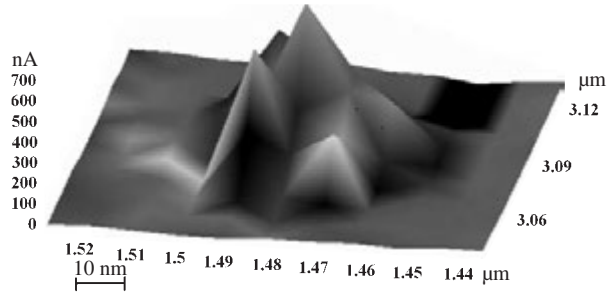

Fig. 1. Photograph of the AFM image of the Al_2O_3 nanoparticle.

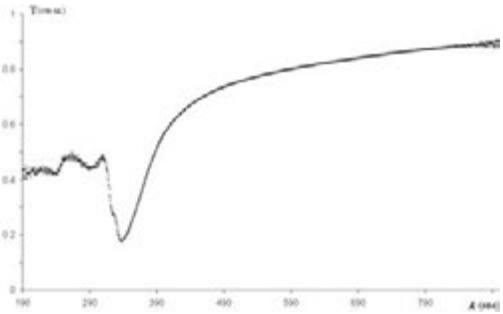

Fig. 2. The transmittance T of the array of Al_2O_3 nanoparticles on the radiation wavelength. Solid and dashed lines show the experimental and simulated tansmittance spectra respectively.

gap at the energies 0.2 eV and larger below the bottom of the conduction band. The energy spectrum of charge carriers in the conduction band also can involve the discrete levels. The studies of laser radiation transmission through a plane-parallel layer of HLPN have revealed low-threshold nonlinear optical effects which are caused by interaction of laser radiation with nanoparticles — liquid-phase matrix complex. These effects are evident as selfinteraction of the light (Fig. 3) or as nonlinear interaction between collinear beams of light with different wavelengths (Fig. 4). The effects discovered are caused by nonlinear changes of effective refractive index of the HLPN medium under the influence of the radiation passed. Effective nonlinear refractive index $n(I)$ of the HLPN medium can be described with consideration for its cubical nonlinearity by using the next model equation [2]: $n(I) = n_0 + n_1 I + n_2(I)$, where I — intensity of radiation passing through nanocomposite, n_0 — refractive index of the matrix medium, n_1 — the factor which is caused by nonlinear characteristics of nanoparticle material and which depends upon nanoparticles' shape and size, n_2 — the factor which describes the dependence of refractive index of matrix medium on temperature. The values of n_1 and n_2 depend on material of nanoparticle, intensity and wavelength of radiation, and they can be positive when $\lambda = 633$ nm as well as negative when $\lambda = 532$ nm. In this case the value of $n(I)$ can exceed the value of n_0 or be lower than $n(I)$, it will cause clearly demonstrated nonlinear optical effects presenting as selfinteraction of laser radiation (Fig. 3) or as nonlinear interaction between collinear laser beams with different wavelengths (Fig. 4).

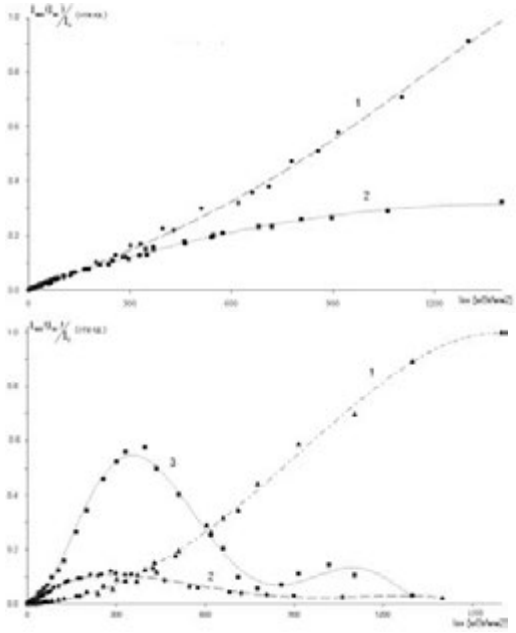

Fig. 3. The dependencies of normalized laser radiation intensity in the HLPC output I_{out} on laser radiation intensity in the HLPC input I_{in} obtained for: a) HLPC based on VM-4 oil (curves 1, 2 obtained when $\lambda = 633$, 532 nm respectively), HLPC based on immersion oil (curves 1–3 obtained when $\lambda = 633$, 532, 633 nm respectively).

Thus, as a result of interaction of laser radiation with nanoparticles — liquid-phase matrix complex on can observe low threshold nonlinearity of effective refractive index of composite medium which is evident as dependence of radiation transmittance of the medium on radiation wavelength. The nonlinearity depends upon characteristics of material of liquid-phase matrix. The determining factors of the nonlinearity are polarization of nanoparticle medium in case of generation of nonequilibrium charge carriers or excitation of charge carriers conditions as well as radiation defocusing effect which is much less dependent on wavelengths then on material of the liquid-phase matrix. The defocusing effect is caused by negative temperature dependence of refractive index of heterogeneous medium (immersion oil based on cedar oil).

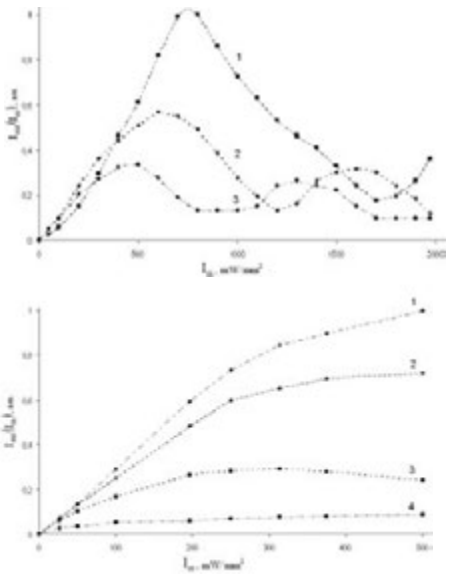

Fig. 4. The $I_{out}(I_{in})$ dependencies normalized to its maximum value and obtained when: a) $\lambda = 633$ nm, curves 1–3 obtained when controlling radiation ($\lambda = 532$ nm) intensity $I = 0$, 250, 500 mW/mm^2 respectively; b) $\lambda = 532$ nm, curves 1–4 obtained when controlling radiation ($\lambda = 633$ nm) intensity $I = 0$, 500, 1500 mW/mm^2 respectively.

These mechanisms are responsible for effective nonlinear interaction between collinear laser beams with different wavelengths in heterogeneous liquid-phase composite.

References

[1] O. P. Mikheeva *et al*, *Tech. Phys* **49**, 739 (2004).
[2] Yu. Kulchin *et al*, *Quan. Electronics* **38**, 154 (2008).
[3] J. A. Ferrari *et al*, *Opt. Eng* **45**, 065001 (1–4), (2006).
[4] V. A. Trofimov *et al*, *Opt. and Spectr.* **99**, 967 (2005).
[5] Yu. N. Kulchin *et al*, *Semiconductors* **43**, 331 (2009).

17th Int. Symp. "Nanostructures: Physics and Technology"
Minsk, Belarus, June 22–26, 2009
© 2009 Ioffe Institute

Silicon on insulator nanowire transistors for bio-medicinal applications

O. V. Naumova[1], L. N. Safronov[1], B. I. Fomin[1], D. A. Nasimov[1], N. V. Dudchenko[1], E. D. Zhanaev[1], V. P. Popov[1], A. V. Latyshev[1], A. L. Aseev[1], Yu. D. Ivanov[2], S. E. Nikitina[2] and A. I. Archakov[2]

[1] Institute of Semiconductor Physics, SB RAS, Novosibirsk, Russia
[2] Research Institute of Biomedical Chemistry, Moscow, Russia

Abstract. Nanowire transistors on the base of the silicon on insulator (SOI) structures were fabricated for bio-medical applications. The sensitivity of SOI nanowire transistors was shown as high as 1 femtomoles with using model protein BSA molecules. Minimal effective charge of proteins adsorbed on the free surface of nanowires was found as 5×10^{-11} cm^{-2}. It was also shown with using gate characteristics of SOI transistors that the sign of the effective charge of immobilized BSA molecules can change depending on the state (functionalization) of the nanowires surface.

Introduction

Silicon on insilator (SOI) based nanowires with ohmic contacts provided at their ends present an analogue to field-effect MOS transistors and can be considered as SOI nanowire transistors (SNWT), with the substrate used as a gate, and the burried dielectric, as a gate oxide. Charge from particles absorbed on the surface of NW induces a compensating charge in the nanowire that modulates its conductance and, hence, the current that flows between the two (source and drain) electrodes. Thus the device acts as a double-gate field-effect transistor, with adsorbed charged species acting as the "top gate" [1–6].

Currently SNWTs are the most promising biosensor elements, having more than 1 to 2 orders of magnitude higher sensitivity over traditional systems of protein diagnosis. Among the overwhelming merits SNW transistors are compatible with modern CMOS technology, which allow creating highly integrated nanobiosystems-on-chip using unified technological basis. Moreover, unlike other types nanowire sensors which use only change of conductivity for detection of particles [7–10], SNWTs allow to determine the effective charge of the particles adsorbed on the NW surface when the gate (substrate) characteristics of SOI-transistors are measuremed.

In the present work, the high setsitivity of SNWTs is demonstrated with the example of bovin serum albumin (BSA) protein molecules. The gate characteristics of SNWTs have been applied to definition of the effective charge of adsorbed bioparticles. Two types of states of the SNWT surface were used: (i) with natural (2–3) nm oxide and (ii) with the free surface (natural oxide was removed before immobilizing of BSA molecules). On this example we have shown the possibility of using the gate characteristics of SNWTs for monitoring/detecting the interaction of adsorbed particles with the sensor surface.

1. Experimental

SNWTs were produced using optical and electronic lithography and technological processes very similar to the standard CMOS chip technologies. Homemade ultra thin (UT) SOI wafers with n-type Si layer were used (the concentration of electrons in the top Si layer was $\sim 6 \times 10^{16}$ cm^{-3}). SNWT chips with the following parameters were obtained:

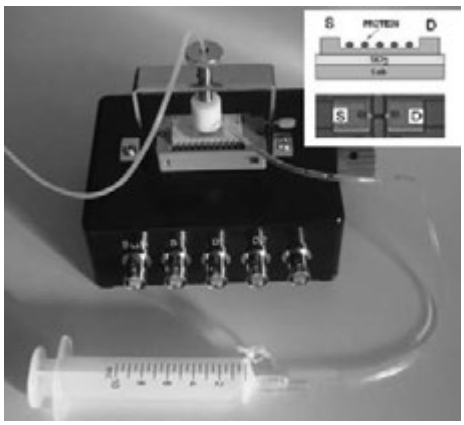

Fig. 1. Test module with fluid cell and packaged biochip (in the insert — a scheme of immobilizing for BSA molecules on the surface of SOI nanowire with optical image of single SNWT).

- the thickness of the SOI films — 10–30 nm,
- the width of the nanowires — 50–500 nm,
- the length of the nanowires — 10 μm,
- the number of SNWTs — 12 on the chip.

Test SNWTs were isolated from each other using protective deposited dioxide layers (TEOS), allowing multiple measurements by test module (Fig. 1) in the various chemical solutions and biological liquids, as well as providing the reproducibility for measurements of test protein molecules of bovine serum albumin content in PBS (KH_2PO_4 with $pH = 7.4$) buffer solutions in the range 10^{-16}–10^{-4} Moles.

Figs. 2 and 3 show, respectively, the source-drain and drain-gate characteristics of different SNWTs before and after immobilizing of BSA molecules with various content in the solution. One can see that confirmed measured sensitivity to the model BSA molecules was not less than 1 femtoMole (about 10 molecules per 1 cubic mm of liquid). Practically parallel shift of gate characteristics along the voltage axis (Fig. 3) was observed for SNWTs with increasing content BSA when the adsorption was curried out on the free SOI surface (after removal of natural oxide from SOI NW).

The total charge accumulated on the surface of NW was calculated from the flatband voltage shift (ΔV_{fb}) of measured

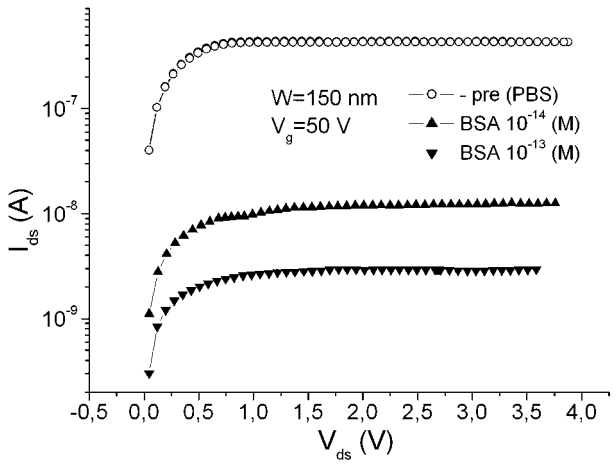

Fig. 2. Source — drain (I_{DS}-V_{DS}) characteristics at the operating point at $V_g = 50$ V for the SNWT with 150 nm width before and after immobilizing of BSA molecules with different content in the solution.

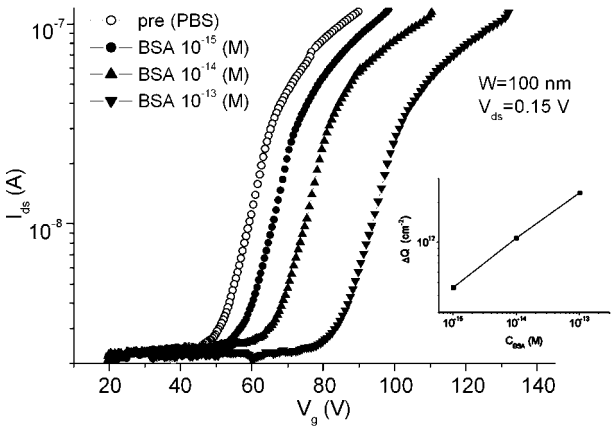

Fig. 3. I_{DS}-V_g characteristics for the SNWT with 100 nm width before and after immobilizing of BSA molecules. Native oxide was removed with SOI NW surface. The insert shows the accumulated negative charge versus BSA concentration.

I_{ds}-V_g characteristics of SNWT (like the conventional MOSFET), as

$$\Delta Q_{\mathrm{ox}} = \Delta V_{\mathrm{fb}} C_{\mathrm{BOX}}/q.$$

Here, C_{ox} is the buried-oxide capacitance, and q is the electron charge.

The density of charge accumulated on the free SNWT surface was $\sim 5 \times 10^{11}$ cm^{-2} at the minimal BSA content in the solution $C_{\mathrm{BSA}} = 10^{-15}$ M.

The sub-threshold slope of the $I_{ds} - V_g$ curves (Fig. 3) is almost independent of C_{BSA}. On the contrary, the change of the sub-threshold slope of $I_{ds} - V_g$ curves was observed in the case of SNWT. Change of the sub-threshold slope obviously specifies on recharging of surface states of SNWT. As result, the BSA molecules get an effective positive charge, as shown in the insert of Fig. 4.

Thus registration of the sub-threshold slope of gate characteriscics SNWTs during adsorption of molecular biological species seems to be a crucial point in the development of electrochenmical nanobiosensors and may be use as method making it possible to identify the ionization and/or depolarization susceptibility of various particles.

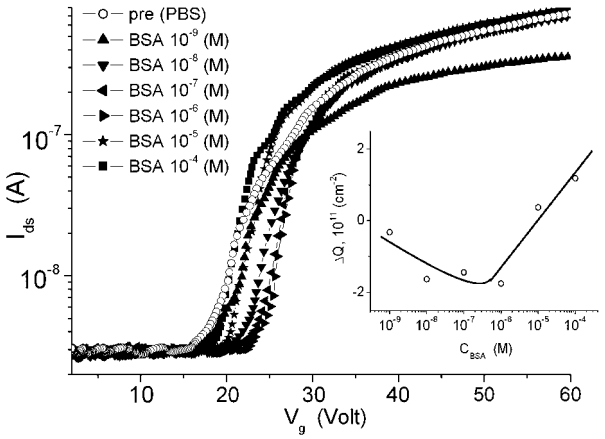

Fig. 4. I_{DS}-V_g characteristics for the SNWT with natural oxide on the NW surface before and after immobilizing of BSA molecules. The insert shows the accumulated charge versus BSA concentration.

Acknowledgements

This work was supported by FCNTP (Grant No. 02.513.11. 3057 and Grant No. 02.512.11.2176).

References

[1] Y. Cui, Q. Wei, H. Park and C. M. Lieber, *Science* **293**, 1289 (2001).
[2] F. Patolsky, G. Zheng, O. Hayden, M. Lakadamayali and X. Zhuang, *Proc. Nat. Acad. Sci. USA* **101**, 14017 (2004).
[3] J. Hahm and C. M. Lieber, *Nano Lett.* **4**, 51 (2004).
[4] Z. Li, Y. Chen, X. Li, T. I. Kamins, K. Nauka and R. S. Williams, *Nano Lett.* **4**, 245 (2004).
[5] M. G. Nikolaides, S. Rauschenbach and A. R. Bausch, *J. Appl. Phys* **95**, 3811 (2004).
[6] E. Stern, J. F. Klemic, D. A. Routenberg, P. N. Wyrembak, D. B. Turner-Evans, A. D. Hamilton, D. A. LaVan, T. M. Fahmy and M. A. Reed, *Nature* **445**, 519 (2007).
[7] A. M. Morales and C. M. Lieber, *Science* **279**, 208 (1998).
[8] J. L. Liu, S. J. Cai, G. L Jin, S. G. Thomas and K. L. Wang, *J. Cryst. Growth.* **200**, 106 (1999).
[9] S. Sharma, T. I. Kamins and R. S. Williams, *J. Cryst. Growth.* **267**, 613 (2004).
[10] T. I. Kamins, X. Li, R. S. Williams and X. Liu, *Nano Lett.* **4**, 503 (2004).

17th Int. Symp. "Nanostructures: Physics and Technology"
Minsk, Belarus, June 22–26, 2009
© 2009 Ioffe Institute

The peculiarity of nanotopography and AFM-based estimation parameters of lead and zinc toxic action on erythrocyte membrane

D. S. Filimonenko[1], A. Ya. Khairullina[1], V. M. Yasinskii[1], E. I. Slobozhanina[2] and N. M. Kozlova[2]

[1] B. I. Stepanov Institute of Physics, NASB, Minsk 220072, Belarus
[2] Institute of Biophysics and Cell Engineering, NASB, 220072 Minsk, Belarus

Abstract. The atomic force microscope (AFM) has been used to study the surface topography of erythrocyte membranes to reveal the most relevant and informative parameters of toxic action on erythrocyte's surface fine structure and to find dependence between fine structure of erythrocyte membranes subjected by action of zinc and lead ions and functional state of some components of membrane composition. The obtained results demonstrate that correlation length of the normalized autocorrelation functions is an informative parameter, in order to estimate degree of toxic action.

Introduction

It is well known that heavy metals are crucial components of proteins and enzymes and allow us to maintain a broad spectrum of functions that are vital for the cell physiology. Nevertheless, the absorption of heavy metals in abundance gives rise to different toxic effects depending upon the peculiarity of the metal and of the cell. The toxic effect on biological cell of exposure to heavy metals has been an issue of primary importance by now because of probable serious consequences on human health produced by growing environmental pollution [1].

The plasma membrane of the cell is one of the primary targets for heavy metals, in that way alteration of membrane surface structure represents an important sign of the interaction between a red blood cell and heavy metal ions. As described in [2,3], high concentrations of lead and zinc can change the physicochemical state of proteins and lipids in erythrocyte membranes. This is due to changes in microviscosity of membrane lipid bilayer and structural modification of the core integral membrane protein — the band 3.

The aim of this study was to find dependence between fine structure of erythrocyte membranes subjected by action of zinc and lead ions and functional state of some components of membrane composition; and to reveal the most relevant and informative parameters of toxic action on erythrocyte's surface fine structure. For that purpose the atomic force microscope (AFM) has been used as a powerful tool that provides high resolution visualization of a membrane's surface.

1. Materials and methods

In investigations, we used blood from healthy donors, which was taken from the Republican Theoretical and Practical Center of Hematology and Blood Transfusion, (Minsk, Belarus). Blood samples contained glugicirum as a preserving agent.

Erythrocytes were separated from plasma by centrifugation of blood at $3000g$ within 15 min. The obtained centrifugate was washed three times either in a solution of NaCl (155 mM/l) or in a sodium phosphate buffer (5 mM/l, pH 7.4) containing NaCl (150 mM). For AFM analysis, samples of a suspension of erythrocytes (20% hematocrit) subjected to the action of zinc (0.2 mM, 0.5 mM, 1 mM, 2 mM of ZnSO4) and lead ions (2 mcM, 5 mcM, 10 mcM of lead acetate) along with a sample of the initial suspension were fixed with two-percent solution of glutaraldehyde, incubated for 2 h at room temperature, diluted with distilled water to 10% hematocrit, and washed two times in distilled water. Finally, the samples were placed on a coverslip and air dried, to allow a detailed AFM analysis during several days, which required to accumulate a statistically significant data group for each sample.

Measuring was conducted in contact mode by AFM NT 206 (ODO Mikrotestmashiny, Belarus) in a small imaging region, using standard silicon tips (from MikroMash) in the static (CSC21 tips) and dynamic (NSC21 tips) regimes. The lateral resolution of the microscope is 20–30 nm, and the vertical resolution is 0.5 nm.

2. Results of AFM investigations

In this study, we investigated the metal induced changes of erythrocytes membrane exposed to subhemolytic concentrations of zinc and lead using an AFM. Two-dimensional image allow us to reveal more clearly that the typical structure of erythrocyte surface consists of large number of nanosized particles (from several to tens nanometers). As a result, it was found that surface profiles of the unmodified erythrocytes membrane have notably more uneven structure in comparison with erythrocytes modified by zinc and lead, moreover the surface roughness increased with concentration of metal. Observable peculiarities of erythrocyte membrane surfaces after action of zinc ions with different concentrations is the result of clustering of the protein band 3, the separation of vesicles from membrane surface and changes in microviscosity of the lipid bilayer of membranes.

To gain a better understanding of the merely topographic effect of metal doping on erythrocytes, the mean value of topographic parameters such as the membrane's mean roughness, root mean square deviation, correlation length of the normalized autocorrelation functions were calculated from a population of at least 40 cells for each concentration of metal.

Since the profile of an erythrocyte membrane represents a typical random process, we chose the normalized autocorrelation function $K_0(r)$ and the root mean square deviation P_q of irregularity profiles as a deterministic function of the random process.To calculate the normalized autocorrelation function

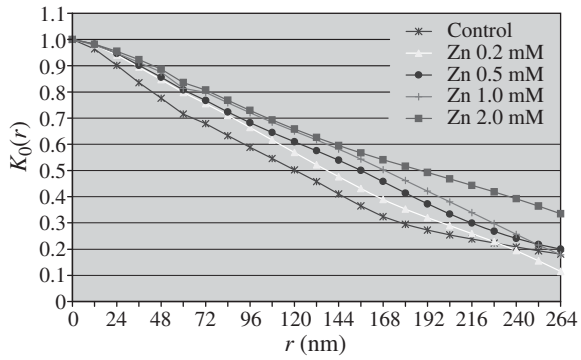

Fig. 1. Normalized autocorrelation functions of unmodified erythrocytes surface profile of erythrocytes, modified by zinc ions of different concentration.

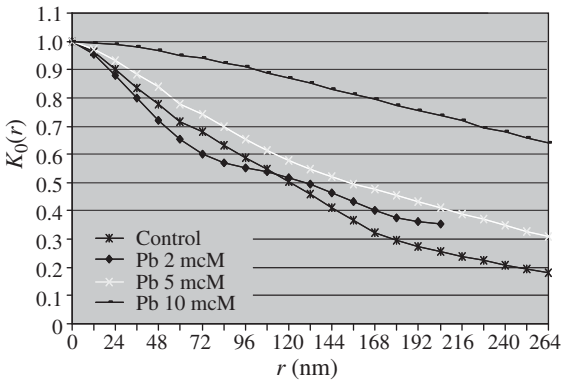

Fig. 2. Normalized autocorrelation functions of unmodified erythrocytes surface profile, of erythrocytes, modified by lead ions of different concentrations.

$K_0(r)$ and the root mean square deviation P_q of irregularity profiles obtained from discrete readings of the atomic force microscope, the standard formalism of the theory of random functions is used [4]. The above-indicated parameters of the structure under study are defined as

$$K_0(r) = \frac{\sum_{i=1}^{N-k}\left[\xi(P_i)-\overline{\xi(P)}\right]\left[\xi(P_i+r)-\overline{\xi(P)}\right]}{\sum_{i=1}^{N}\left[\xi(P_i)-\overline{\xi(P)}\right]^2}, \quad (1)$$

$$P_q^2 = \frac{\sum_{i=1}^{N}\left[\xi(P_i)-\overline{\xi(P)}\right]^2}{N}, \quad (2)$$

where $\xi(P_i)$ is the i-th value (reading) of the random quantity, and

$$\overline{\xi(P)} = \frac{\sum_{i=1}^{N}\xi(P_i)}{N}.$$

Since the experimentally obtained autocorrelation functions are approximated by exponentials, in accordance with [5] correlation length L of profile irregularities is a representative quantity of the random process and is calculated as

$$K_0(L) = \exp(-1). \quad (3)$$

It turned out, that zinc and lead treatment produce correlation length increase with increasing of concentration of metal (Figs. 1,2), while the metal induced changes quantitated by mean roughness and root mean square deviation were found not to explicitly increase with increasing of metal concentration.

In other words these parameters are less informative, and their behavior do not allow us to conclude pronounced interrelation with concentration of heavy metal. Maximal correlation length of the normalized autocorrelation functions of erythrocyte surface profile, which approximated by an exponent for unmodified erythrocyte is 149 nm, for erythrocyte, modified by zinc and lead ions are 245 nm and 564 nm accordingly. Thus the cytotoxicity of lead exceeds the cytotoxicity of zinc.

Taken as a whole, the presented results demonstrate that correlation length of the normalized autocorrelation functions is an informative parameter, in order to estimate degree of toxic action, helpful in diagnostics of diseases linked to disbalance of microelements in human organism. Observable evening-out of rough edges on AFM images of erythrocyte membranes modified by lead and zinc allows us to propose an approach of early disease detection using pre-clinical manifestation of toxic metal action on erythrocytes and also to pursue research into the action of different factors on biological cells.

References

[1] P. A. Olsvik *et al*, *Comp Biochem Physiol.* **128**, 189 (2001).
[2] E. I. Slobozhanina *et al*, *J. Appl. Toxicol.* **25**, 109 (2005).
[3] A. Ya. Khairullina *et al*, *Opt. and Spectr.* **105**, 154 (2008).
[4] S. M. Rytov, *Introduction to Statistical Radiophysics*, (Moscow: Nauka) 404, 1966.
[5] V. A. Bakulin *et al*, *Opt. and Spectr.* **71**, 579 (1991).

17th Int. Symp. "Nanostructures: Physics and Technology"
Minsk, Belarus, June 22–26, 2009
© 2009 Ioffe Institute

In situ research of electronic structure of DNA nucleobases and their transformation under irradiation

Yu. S. Gordeev[1], *V. M. Mikoushkin*[1], V. V. Shnitov[1], F. Alvarado[2], R. Morgenstern[2], T. Schlatholter[2], S. L. Molodtsov[3] and D. V. Vyalikh[3]

[1] Ioffe Physical-Technical Institute, St Petersburg, Russia
[2] KVI, Rijksuniversiteit Groningen, 9747 AA Groningen, The Netherlands
[3] Institut fur Festkorperphysik, Technische Universitat Dresden, D-01062 Dresden, Germany

Abstract. Photoemission spectra of thin films of DNA nucleobases — thymine and adenine — were studied in situ using synchrotron radiation. Extremely low radiation stability of these objects was revealed. In spite of this, density of states of valence electrons of these bio-nanomolecules was measured. Modification of the molecules induced by low and high intensity radiation was studied. Transformation of the density of states and enormous shift of electron states were revealed. It was shown that the modification is accompanied by detachment of nitrogen and oxygen atoms. Mechanism of the modification was shown to include excitation of molecules by photoelectrons and secondary electrons.

Introduction

DNA can be considered as one of the widely spread natural nanostructures consisting of polymeric wire with attached organic nanoclusters or biomolecules called nucleobases. Knowing electronic structure of DNA is important in research of fundamental properties of this object. In addition, DNA is considered to be a promising material for designing molecular nanoelectronic devices [1]. Therefore increasing activity is observed in the research of different kinds of DNA by photoelectron spectroscopy — one of the most effective methods for studying electronic structure of matter [2,3,4,5]. Unfortunately, using this high vacuum and surface sensitive method in the research of bio-molecules faces a number of problems. Samples are usually prepared in air by drying solutions, which makes questionable the atomic purity of studied objects. The contribution of different DNA building blocks makes analysis of photoelectron spectra being difficult. And finally, possible radiation instability of bio-molecules under diagnostic beams must be taken into account by researchers. There was a lack of information about the influence of diagnostic x-ray beams on DNA and their building blocks. But it is known that low energy electrons can drastically modify bio-molecules [6,7]. The aim of this work was to study the elec-tronic structure of important DNA nucleobases — thymine ($C_5N_2O_2H_6$) and adenine ($C_5N_5O_2H_5$) — by photoelectron spectroscopy *in situ* that is just after fabrication of the films directly in the high vacuum chamber.

1. Experimental details

The experiment has been carried out at BESSY synchrotron radiation storage ring using the experimental facilities of the Russian-German laboratory. Experimental technique of in vacuum fabrication of thymine and adenine films was developed. Films of several nm thickness were grown on the silicon (100) surface cleaned by annealing up to 1100 ° C. Photoelectron spectra of the films were measured using monochromatic synchrotron radiation (SR) with photon energy $h\nu = 150$ eV. To study the influence of radiation on the electronic structure, the films were repeatedly exposed to different doses of low intensity ($I_0 < 6 \times 10^{11}$) monochromatic x-rays $h\nu = 150$ eV) and high intensity non-monochromatic SR ($h\nu \sim 0 - 1500$ eV) provided by a "zero-order" mode of the monochromator.

2. Transformation of photoelectron valence band spectrum of thymine under SR

Modification of thymine and adenine was revealed under irradiation. Fig. 1 shows photoelectron spectrum of valence electrons of thymine at different stages of transformation under irradiation by monochromatic x-rays. Spectrum 1 corresponds to pristine film. Spectra 2–4 relate to the film irradiated with increasing doses. Fig. 1 demonstrates drastic (3.5 eV) rigid shift of all of the molecular peaks to higher binding energies (to the left) and essential decreasing (1.75 times) the density of the nitrogen (N2s) and some of the carbon derived states (2 and 3).

Modification of of the valence-band photoelectron spectrum of thymine under much more intensive "zero-order" SR is shown in Fig. 2. Spectrum 1 is the reference curve corresponding to the film irradiated by monochromatic SR (curve 4 in Fig. 1). Spectra 2–5 were measured after irradiation with increasing doses of "zero-order" SR. One can observe drastic line shift to the lower binding energy that is to the opposite direction as compared to the monochromatic irradiation case. Redistribution of the line intensities evidencing for loosing nitrogen, and oxygen atoms is also seen. Finally, contribution of quasi-continuous background, new carbon-derived line (C^c) and quasi-metallic shape of photoelectron spectrum at the Fermi level arise. This background and new lines are related to the phase of some kind of conductive amorphous carbon, which is confirmed by the appearance of the satellite line in the C1s core-level spectrum corresponding to C=C bonds (is not shown here).

3. Mechanism of radiation induced modification of nucleobases

Dependencies of the line shifts and nitrogen content on the dose of monochromatic x-ray irradiation were revealed to consist of two stages and to be similar. Therefore the conclusion

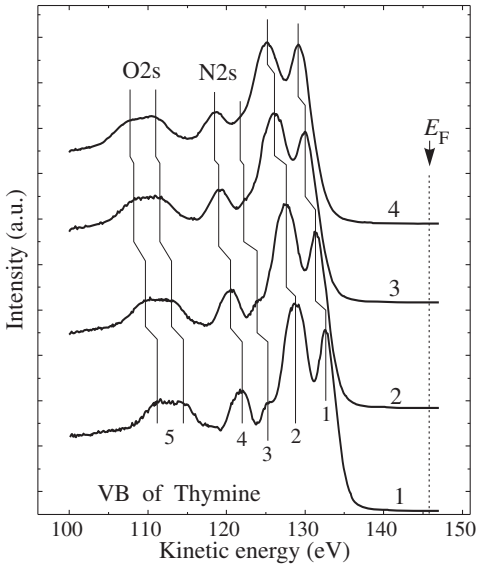

Fig. 1. Photoelectron valence-band spectra of thymine corresponding to pristine (1) film and films irradiated by monochromatic x-rays $h\nu =$ 150 eV (2–4).

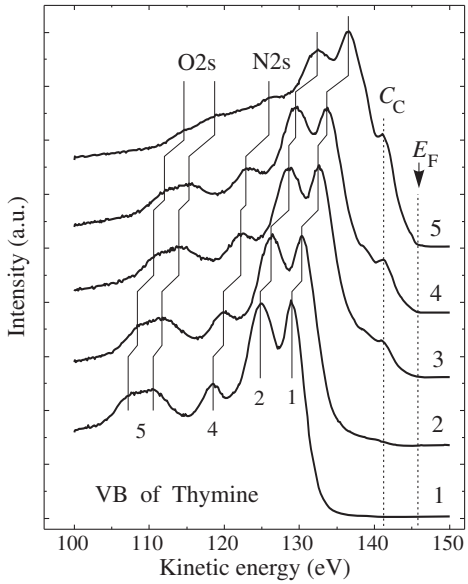

Fig. 2. Photoelectron spectra of the thymine valence band. Curve 1 corresponds to the film irradiated by monochromatic x-rays. Curves 2–5 correspond to increasing "zero-order" irradiation doses.

was made that the observed line shift is connected with loosing nitrogen atoms, some of which can remain in the film as interstitial atoms. As a result, the ring hexagon structure of the molecule must be broken and can be transformed into pentagon ring. New states affecting the position of the Fermi level can be created, which can be one of the reasons of the observed line shift. Taking into account the direction of the shift, these states are the n-type states possibly related to N- interstitial atoms. Creation of the p-type states (e.g. C-interstitial atoms) and diminution of static charging due to formation of the phase of amorphous carbon might be the reasons of the line shift to the opposite direction in the case of intense "zero-order" SR.

The first stage of the dose dependence is finished at the value of about $Q \sim 1 \times 10^{15}$ ph/mm^2. Taking into account the cross section of the valence electron photoionization $\sigma \sim 2 \times 10^{-19}$ cm^2, the portion of ionized atoms was estimated to be less than 1%. Therefore x-ray can not be a direct cause of the observed modification with loosing of about 20% of nitrogen atoms. Indeed, x-ray can not neither directly eject molecular atoms no directly excite valence electrons to initiate the first step of the molecular fragmentation. Thus thymine is modified by photoelectrons and large number of secondary electrons. Contrary to monochromatic x-rays, "zero-order" SR can directly excite valence electrons by ultra-violet and indirectly by photoelectrons of higher energies.

4. The density of states of thymine

Photoelectron spectrum (1) of intact thymine is represented in Fig. 1 in the scale of the photoelectron kinetic energy $E_k = h\nu - E_b - e\varphi - E_s$, were E_b — binding energy relative to the Fermi level E_F, $e\varphi$ — work function, and E_s — electrostatic charging the film due to photoemission. The energy of x-ray quanta $h\nu = 150$ eV is high enough in order the valence photoelectron to reach the continuous region of the vacuum final states. Therefore the spectrum directly characterizes the density of initial states (DOS) of valence electrons. In the case of conductive samples static charging $E_s = 0$. Thymine is a dielectric material with the band gap $\Delta = 5.2$ eV. Therefore spectrum of pristine film (curve 1) is additionally shifted to higher binding energies (to the left) due to positive charging $E_s > 0$. The value E_s can be estimated taken into account positioning the Fermi level in the middle of the band gap of DNA [4]. Then the position of the valence band top is (top) $E_b = \Delta/2 = 2.6$ eV relative to the Fermi level, the line shift associated with charging is $E_s = 5.0$ eV and the binding energies of the molecular peaks can be obtained.

5. Conclusions

Density of states of valence electrons of intact thymine and adenine was measured in spite of the extremely low radiation stability of these objects. Modification of these DNA building blocks and transformation of their electronic structure was revealed under irradiation even of low intensity x-rays. The modification is accompanied by generation of defects and detachment of atoms. Mechanism of the modification by x-rays include excitation of molecules by photoelectrons and secondary electrons.

Acknowledgements

The research was supported by the Russian-German Laboratory at BESSY and by the Program "Quantum physics of condensed matter" of the Russian Academy of Sciences.

References

[1] E. Macia, *Phys. Rev. B* **75**, 035130 (2007).
[2] E. Macia, *Phys. Rev. B* **74**, 245105 (2006).
[3] H. Wadati *et al*, *Appl. Phys. Lett.* **86**, 023901 (2005).
[4] H. S. Kato *et al*, *Phys. Rev. Lett.* **93**, 086403 (2004).
[5] L. Wang *et al*, *Appl. Phys. Lett.* **89**, 013902 (2006).
[6] G. Hanel *et al*, *Phys. Rev. Lett.* **90**, 188104 (2003).
[7] S. Denifl *et al*, *Chem. Phys. Lett.* **377**, 74 (2003).
[8] H. Abdoul-Carime *et al*, *Phys. Rev. Lett.* **92**, 168103 (2004).

17th Int. Symp. "Nanostructures: Physics and Technology"
Minsk, Belarus, June 22–26, 2009
© 2009 Ioffe Institute

Computer modeling of distributions of laser radiation intensity inside homogeneous and core-shell nanoparticles during laser irradiation

L. G. Astafyeva[1], V. K. Pustovalov[2], K. König[3] and W. Fritzsche[4]

[1] B. I. Stepanov Institute of Physics, NASB, pr. Independency, 68, Minsk, 220072, Belarus
[2] Belarusian National Technical University, pr. Independency, 65, Minsk, 220013, Belarus
[3] Saarland University, Saarbruecken, 66123, Germany
[4] Institute for Photonic Technology, 07702, Jena, Germany

Abstract. Theoretical investigation of the distributions of laser radiation intensities inside spherical gold, silver and core-shell silver-gold and gold-silver nanoparticles with radiuses in the range 5–100 nm during laser irradiation for wavelengths 400, 532, 800 nm was carried out. Distributions of laser intensity are inhomogeneous for some ranges of nanoparticle sizes and values of laser wavelengths. These results can be applied for explanation of some experimental data of laser-induced fragmentation, evaporation and formation of nanonetworks as a result of laser action on nanoparticles and for laser technologies of nanoparticles.

Introduction

During the past years many research efforts have been focused on metal nanoparticles because of their unique size-dependent physical and chemical properties. Metal nanoparticles are used in many different fields of research and technology including catalysis, nanophotonics and nanoelectronics, novel materials and nonlinear devices. In particular, gold and silver nanoparticles have been studied aiming at a variety of medical applications, such as laser biomedicine and cancer research, biosensors. Their optical, electronic and thermodynamic properties are totally different from bulk material and also of great fundamental interest.

It is very important to prepare metal nanoparticles with definite sizes, shapes and to control and change their size distribution for all these applications. Several attempts have been made on metal nanoparticles in a solution by means of lasers having various performances [1–7]. Attempts have been made to fabricate nanoscale materials of scientific and industrial interest in a size- and geometry-controlled manner. Recently, a physical method — laser ablation has been used to prepare metal nanoparticles in solution. In combination with the laser ablation method, a laser-induced preparation of metal nanoparticles and nanostructures having a narrow diameter distribution with a small average diameter is one of the most promising methods. To establish these methods it is necessary to elucidate the mechanism of how the preparation proceeds. The processes of absorption of laser radiation by nanoparticles and distribution of laser intensity inside nanoparticles will determine the mechanisms and results of laser-nanoparticle interaction.

Absorption and scattering properties of metal nanoparticles were investigated in different papers.The investigation of distributions of laser radiation intensities inside spherical gold, silver and core-shell silver-gold and gold-silver nanoparticles with radiuses in the range 5–100 nm during laser irradiation for wavelengths 400, 532, 800 nm will be carried out in this report. These results can be applied for explanation of some experimental data of laser-induced fragmentation, evaporation and formation of nanonetworks as a result of laser action on nanoparticles.

1. Results of computer modelling

In the last years much efforts had been invested in synthesizing two-dimensional and three-dimensional well-arrayed nanostructures, in which size-selected metal nanoparticles are connected to each other with some bounds. Under laser irradiation nanoparticles in solution aggregate into groups with formation of interconnected networks with a size of tens of nanometers with maintaining their individual geometries. The nanoparticles in the agglomerates are further heated by the laser pulse and form network structures by encounter and coagulation. Existed nonthermal [8] and thermal [9] models can not explain the formation of nanonetworks and strings under laser pulse action on metal nanoparticles. Thus the most of the questions about mechanisms of laser induced fragmentation and formation of nanonetworks and nanostrings still remain to be answered. One of possible mechanism of the formation of nanonetworks could be the influence of internal distributions of laser intensity and laser energy deposition inside nanoparticle on thermal processes.

There are four characteristic distributions of internal intensity inside gold, silver and core-shell silver-gold and gold-silver nanoparticles for laser wavelengths 400, 532, and 800 nm: a) approximate homogeneous distribution of intensity inside nanoparticle, b) maximum of intensity lies at irradiated surface of nanoparticle, c) maximum of intensity lies at shadow surface of nanoparticle, and d) maximum intensity lies simultaneously at irradiated and shadow surfaces of nanoparticle.

The distributions of radiation intensity with wavelength 400 nm inside gold spherical nanoparticles along main diameter are presented in Fig. 1. Situation a) of approximate homogeneous distribution of intensity inside gold nanoparticle is realized for radii $r_0 \leq 20$ nm for all wavelengths mentioned above with accuracy of about 20–30%. In this case it could be used theoretical model [9] for description of laser heating of gold nanoparticles.

Situation b) when the maximum of intensity lies at irradi-

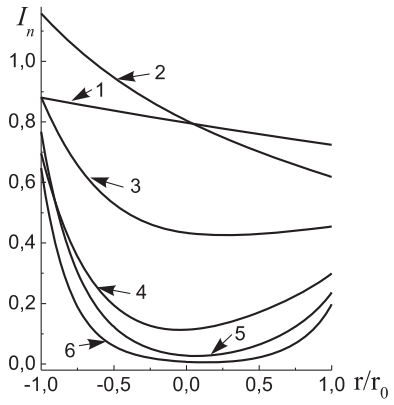

Fig. 1. Distributions of normalized intensity I_n (arbitrary units) of laser radiation with wavelength 400 nm inside spherical gold nanoparticles with radiuses $r_0 = 5\,(1), 20\,(2), 40\,(3), 60\,(4), 80\,(5), 100\,(6)$ nm along the main diameter of nanoparticle. Radius r is the radius of spherical system of coordinates in the center of nanoparticle. The direction of laser radiation propagation is from left to right and value of $r/r_0 = -1$ is equivalent of radius on the irradiated surface of nanoparticle.

ated surface of nanoparticle is realized for radii in the range 40–100 nm for 400 nm.

Situation c) when the maximum of intensity lies at shadow surface of nanoparticle is realized for for radii in the range 40–100 nm for 532 nm.

Situation d) when the maximum of intensity lies simultaneously at irradiated and shadow surfaces of nanoparticle is realized for radii in the range 40–100 nm for 800 nm.

Cases a) and d) when the approximate homogeneous distribution of intensity at the surface of gold nanoparticle with intensive homogeneous surface evaporation could be realized with decreasing of nanoparticle radiuses.

For core-shell silver-gold and gold-silver nanoparticles more complicated situations can be realized depending not only on radius and laser wavelength, but on thickness of shell. In the cases b) and c) the overheating of the metal at irradiation and shadow surfaces can occur and inhomogeneous intensive evaporation and projection of some part of metal (gold vapour and liquid gold) can form the gold strings. We clearly see in the experimental formation of long string only from one point on the surface of parent nanoparticle. The possibility of creation of region at one side of nanoparticle with increased value of intensity up to 2–4 times in comparison with value of intensity at opposite surface can lead to very interesting consequences. First of all it can be inhomogeneous heating of nanoparticles by short (pico-and femtosecond pulses) without smoothing of temperature inside nanoparticle during laser pulse action. After achievement of evaporation temperature it can be realized inhomogeneous surface evaporation of nanoparticle with possible formation of nanonetworks [1–5]. Increasing of laser intensity may lead to realization of optical breakdown on one side of nanoparticle and fragmentation with movement of fragments in definite direction. These possibilities can be used for special aims in selective nanophotothermolysis and laser medicine, in laser nanotechnologies. For example, for formation of special nanonetworks, for movement of fragments of nanoparticle in definite direction, for movement of parent nanoparticle because of evaporation and the action reactive force on it, for heating of concrete surface of nanoparticle, for movement of nanoparticle with conjugated biological object inside cell and so on.

2. Conclusions

Computer modeling of the distributions of laser radiation intensities inside spherical homogeneous gold and silver and core-shell gold-silver and silver-gold nanoparticles with radiuses in the range 5–100 nm during laser irradiation with wavelengths 400, 532, 800 nm was carried out. Distributions of laser intensity are inhomogeneous for some ranges of nanoparticle sizes and values of laser wavelengths. In some cases intensity will be concentrated in thin layer adjoining to external surface of nanoparticle. These results can be applied for explanation of experimental data of surface melting and evaporation, laser-induced fragmentation and formation of nanonetworks as a result of laser action on nanoparticles and for laser technologies of nanoparticles [1–7].

References

[1] F. Mafune *et al*, *J. Phys. Chem. B* **106**, 8555 (2002).
[2] F. Mafune *et al*, *J. Phys. Chem. B* **107**, 12589 (2003).
[3] S. Inasawa *et al*, *Jpn. J. Appl. Phys.* **42**, 6705 (2003).
[4] S. Inasawa *et al*, *J. Phys. Chem. B* **109**, 9404 (2005).
[5] Z. Peng *et al*, *J. Phys. Chem. B* **109**, 15735 (2005).
[6] A. Csaki *et al*, *Nanoletters* **7**, 247 (2007).
[7] F. Garwe *et al*, *Nanotechnology* **19**, 055207 (2008).
[8] P. V. Kamat *et al*, *J. Phys. Chem. B* **102**, 3123 (1998).
[9] V. K. Pustovalov, *Chem. Phys.* **308**, 103 (2005).

17th Int. Symp. "Nanostructures: Physics and Technology"
Minsk, Belarus, June 22–26, 2009
© 2009 Ioffe Institute

Optical properties and heating of spherical gold and silica-gold nanoparticles for laser combined imaging and photothermal treatment of tissues

L. Astafyeva[1], V. Pustovalov[2] and B. Jean[3]

[1] B. I. Stepanov Institute of Physics, NASB, pr. Independency, 68, Minsk, 220072, Belarus
[2] Belarusian National Technical University, pr. Independency, 65, Minsk, 220013, Belarus
[3] Tuebingen University, Experimental Ophthalmic Surgery, Tuebingen, 72072, Germany

Abstract. The results of computer modeling of optical absorption and backscattering properties and laser heating of gold and silica-gold spherical nanoparticles for laser combined imaging and photothermal treatment of cells and tissues conjugated with nanoparticles are presented. The efficiencies of nanoparticle heating and backscattering by nanoparticles depending on their radii, structure and optical properties of metal were investigated. The possibility to use for laser wavelengths 532, 800 nm spherical gold and silica-gold nanoparticles in determined ranges of radii for the purposes of laser combined imaging and photothermal treatment of cells and tissues is established.

Introduction

Recently, several groups of investigators (Anderson, Halas, Zharov, El-Sayed, and their co-workers) demonstrated, through pioneering results, the great potential of laser thermal therapy of cells and tissues conjugated with gold nanoparticles. It was proposed also to use combined diagnostics and therapy on the base of the nanoparticle selection for achievement of efficient contrast for laser imaging applications, as well as for photothermal therapy. Much of the promise for nanotechnology in biology and medicine has focused on the development of multifunctional agents for integrated diagnosis and therapy. Among different nanostructures, silica-gold and gold NPs are the most promising candidates as artificial optical and photothermal agents because they are strong absorbers and scatterers, photostable, nontoxic, easily conjugated to antibodies or proteins, and have adjustable optical properties. Their superior properties coupled with recent advances in nanoparticle (NP) synthesis and conjugation can be used for photonics, biomedical applications and laser nanotechnologies.

Current optical diagnostic techniques in biology and biomedicine rely strongly on optically contrast agents to stain/label specific targets in order to overcome the problem of weak optical signals of endogeneous natural chromophores and to increase spectral differences between targets and ambience. NPs provide an alternative possibility to enable dual imaging/therapy applications as they can be engineered to simultaneously provide both absorption and backscattering properties at specific laser wavelengths, optical contrast for improved diagnostic imaging and, at higher laser intensity, rapid heating for photothermal treatment.

Biomolecules, proteins, antibodies, tumor cells and other targeting components can be readily conjugated to the surface of NPs. Imaging modalities of backscattering radiation such as confocal reflectance microscopy, laser scanning microscopy, spectrofotometry, and optical coherent tomography offer high-resolution approaches to early cancer and other disorders detection. In addition, NPs can be designed to strongly absorb visible and near-infrared radiation providing a novel modality to mediate photothermal therapy. When NPs are irradiated by short laser pulses, their temperature rises very quickly creating many photothermal and accompanied phenomena which may lead target (e.g., abnormal cell) damage [1]. Main problem now is the determination of optimal parameters of NPs (such as sizes, structure, material, optical properties, etc.) that can be used for these purposes.

However, the current understanding of the relationship between nanoparticle optical properties (absorption, backscattering) and the thermal efficiency of combined imaging and therapy is limited. Unfortunately backscattering of laser radiation by NPs has not been investigated and as a result the real efficiency of the use of NPs as backscatterers for reflection imaging is unknown yet. Efficiency absorption factor K_{abs} determines the absorption of laser energy by NP. The heating efficiency and achievement of some maximal temperature of NP depends not only from K_{abs} but also from particle radius r_0, other particle and radiation parameters. We need to perform simultaneous analysis of backscattering properties and heating efficiency of NP depending on laser and NP parameters.

The purpose of this report is to perform computer modeling of optical absorption and backscattering properties of gold and silica-gold spheres in the range of sizes 5–100 nm for widely used laser wavelengths 532 and 800 nm. The efficiencies of NP heating and backscattering by NPs depending on their radii and optical properties of gold and silica-gold spheres were simultaneously investigated. The possibility to use spherical gold and silica-gold NPs in the determined ranges of radii for wavelengths 532 and 800 nm for the purposes of laser combined imaging and photothermal treatment of cells and tissues is established.

1. Backscattering of laser radiation and heating efficiency of NPs by laser pulses

Computer calculation of efficiency factors of absorption K_{abs}, scattering K_{sca} and extinction K_{ext} was carried out on the base of Mie theory for a homogeneous spherical NP with radius r_0 and complex refractive index $m_0 = n_0 - i\kappa_0$ of NP material (gold) located in infinite medium (water).

A two-layered particle consists of a spherical homogeneous core of radius r_0 with the complex refractive index $m_0 = n_0 - i\kappa_0$ of core material (silica), enveloped by the spherically symmetric homogeneous shell of radius r_1 with the com-

plex refractive index $m_1 = n_1 - i\kappa_1$ of shell material (gold). The particles are located in the homogeneous nonabsorbing medium with a refractive index n_m Calculation of the optical properties of layered spherical NPs for some fixed sizes of NP and for some material (silica, gold) was made on the base of extended Mie theory. The expressions for the characteristics of light scattering by two-layered sphere (absorption, scattering and extinction efficiency factors) are expressed in terms of the amplitude coefficients given by the theory of diffraction of electromagnetic radiation on two-layered spherical particle [1–3]. We consider only independently scattering, randomly positioned particles. This means that particles are separated widely enough, so that each particle is in the far-field zone of all other particles, and that scattering by different particles is incoherent.

Main factor that will determine the efficiency of backscattered optical diagnostics is the share (part) of backscattered radiation in all amount of scattered radiation (asymmetry factor of scattered radiation indicatrix). Amount of backscattered radiation from NP should produce considerable part of all amount of scattered radiation. The value of backscattered by particle energy (or backscattered intensity) will be determined by optical detector and used for diagnostics of distribution and concentration of NPs. Shares (parts) of integrated radiation intensity scattered along the radiation direction propagation in the forward hemisphere I_+ (from $\vartheta = 90°$ till $\vartheta = 270°$) and backscattered radiation in backward hemisphere I_- (from $\vartheta = 270°$ till $\vartheta = 90°$).

The values of I_+ and I_- are practically equal each other in the radii interval of $5 < r_0 < 40$ nm for $\lambda = 532$ nm. Values of T_+ sharply increase and values of I_- decrease with increasing of particle radius for $r_0 > 40$ nm for $\lambda = 532$ nm. Values of I_+ and I_- for $\lambda = 800$ nm weakly depend on r_0 in the range $5 < r_0 < 100$ nm and values of I_- are higher than values of I_+.

The following condition should be fulfilled for achievement of successful laser combined diagnostics and thermal treatment — parameters $\Delta T_0/I_0$ and T_- should have maximal values simultaneously for some range of NP radii and for concrete wavelength. Parameter $\Delta T_0/I_0$ [4,5]:

$$\frac{\Delta T_0}{I_0} = \frac{(T_{\max} - T_\infty)}{I_0} = \frac{K_{\text{abs}} r_0}{4k_\infty}\left[1 - \exp\left(\frac{3k_\infty t_{\text{p}}}{c_0 \rho_0 r_0^2}\right)\right] \quad (1)$$

can be viewed as efficiency parameter of NP heating for concrete values of NP radius r_0, efficiency factor of absorption of K_{abs}, wavelength λ, density and heat capacity of NP material respectively ρ_0, c_0, pulse duration t_{p} and coefficient of heat conduction of ambient tissue k_∞ under action of radiation intensity I_0, ΔT_0 — temperature of overheating of NP, T — initial temperature, $T_{\max}$ — maximal value of NP temperature. This parameter determines the increase of particle temperature under action of laser radiation with intensity value is equal 1 W/cm^2 and depends only on particle and ambient tissue parameters and pulse duration t_{p}.

Systematic computer modeling of the optical properties was made for two different classes of NPs — spherical gold and core-shell (two-layered) silica-gold NPs. Optical absorption and backscattering of laser radiation with wavelengths 532, 800 nm by these NPs was investigated. Efficiency parameter of NP heating under action of radiation intensity I_0 was investigated and determined. Definite ranges of spherical gold and silica-gold NPs were determined with realization of maximal values of backscattering and heating efficiency inside them. We can select NPs for the purposes of combined diagnostics and thermal therapy on the base of our results and approximate condition for the ranges of NPs radii, where $I_- \geq 0.3$ and simultaneously variation of parameter $\Delta T_0/I_0$ should be smaller than order of magnitude for all values of t_{p}.

We can select NPs for the purposes of combined diagnostics and thermal therapy on the base of our results. In this case the use of gold NPs in the range of $10 < r_0 < 75$ nm for laser radiation pulses with wavelength 532 nm and pulse duration in the range $t_{\text{p}} = 10^{-6}$–10^{-12} s is better for the purposes of combined imaging and photothermal therapy than for the wavelength of 800 nm. Our results confirm confirm the possibility to use silica-gold NPs in the range of $5 < r_0 < 40$ nm for $\lambda = 532$ nm and in the range of $30 < r_0 < 100$ nm for $\lambda = 800$ nm for the same purpose as well.

2. Conclusion

NPs and lasers can be used for combined imaging and treatment of cells and tissues conjugated with NPs by backscattering and photothermal methods, where NPs act as specific absorbers and backscatterers. Diagnostics allows to determine actual or time resolved localization, assessment of dimensions and shape of an anatomical target (disorder tissue), concentration of drug biomolecules, antibodies, protheins, etc. Therefore, NPs should be designed to strongly backscatter and absorb visible and near-infrared radiation, providing a novel means to mediate diagnostics and photothermal therapy in a truly selective manner.

Laser imaging and treatment options of cells and tissues conjugated with NPs require the analysis of backscattering optical properties and heating efficiency of NPs, depending on NPs and laser radiation parameters. This includes compromise between maximal value of backscattering signal and maximal value of NP heating efficiency. In order to determine and quantify this compromise, the simultaneous analysis of maximal values of NP heating efficiency and backscattering of incident laser radiation has been carried out in this report.

This method can be applied in cancer treatment, ophthalmology, dermatology, etc. Combined diagnostics and thermal treatment at early stage of cancer can be very important. In ophthalmology, imaging of molecules, functional proteins, drugs or antibodies in vivo in the transparent media of the eye is one of the central goals for future diagnosis for many types of highly endemic and age related diseases. Nanoparticles, conjugated to them and acting as optical markers, allow to asses their local and time resolved distribution in the course of a disease. As specific absorbers they can principally enable true selective laser therapy beyond our present means. Benefits may be expected for many highly endemic, socio-economically very relevant age related retinal and other eye diseases.

References

[1] V. A. Babenko, L. G. Astafyeva and V. N. Kuzmin, *Electromagnetic Scattering in Disperse Media*, Springer-Praxis, 2003.
[2] G. W. Kattawar *et al*, *Appl. Opt.* **15**, 1996 (1976).
[3] R. Bhandari, *Appl. Opt.* **24**, 1960 (1985).
[4] V. K. Pustovalov, *Chem. Phys.* **308**, 103 (2005).
[5] V. K. Pustovalov, *Las. Phys. Lett.* **5**, 775 (2008).

17th Int. Symp. "Nanostructures: Physics and Technology"
Minsk, Belarus, June 22–26, 2009
© 2009 Ioffe Institute

Propagation of ultra-short laser pulses through biological and biomimetical nanocomposites

A. V. Bezverbny[1], Yu. N. Kulchin[1], Yu. A. Shchipunov[2], S. S. Voznesensky[1], S. S. Golik[1], A. Yu. Mayor[1], I. G. Nagorny[1] and I. V. Postnova[2]

[1] Institute of Automation and Control Processes of Far Eastern Branch of RAS, 690022 Vladivostok, Russia
[2] Institute of Chemistry of Far Eastern Branch of RAS, 690022 Vladivostok, Russia

Abstract. The transmission of laser femtosecond pulses by spicules of marine glass sponges and monolithic nanocomposite silica biomaterials synthesized on the basis of natural polysaccharides (alginate and hyaluronate) has been experimentally investigated. The strong non-linear optical properties of these biominerals have been revealed in spectral characteristics of transmitted ultra-short pulses.

Introduction

Hexactinellida (Porifera) glass sponges represent a group of the most ancient multicellular organisms dwelling mostly in deep sea areas of the oceans at a depth from 30 m to 5 km. The skeleton of such sponges is composed of siliceous six-ray spicules. The dimensions of such spicules, depending on their kind and age, vary considerably: diameter ranges from 0,01 to 30 mm, length — from some millimeters to several meters. Microscopic investigation reveals that spicules are formed around a central protein filament 1–2 μm in diameter built up from 50 to 120 nm silicon dioxide particles which then combine together to form micron-sized particles making up a solid layer of silicon dioxide. The spicules are present complex composite formations with a central channel surrounded by 100–400 nm thick cylindrical silicon dioxide layers with nano-sized protein layers between them (Fig. 1).

The multi-layer cladding of glass sponge spicules has an obvious analogy with some contemporary artificial microstructured optical fibers. Specifically, our researches have shown that the core diameter and cladding layers thickness of the spicules of *Hyalonema sieboldi* and *Pheronema sp.* glass sponges are appropriate to cause photonic bandgaps in the infrared, visible, and ultraviolet wavelength regions. This enables singlemode waveguide and Bragg light propagation regimes in the spicules [1]. Also comparative analysis of the earlier transmission spectra of ultra-short pulses (USP) reveals that spicules exhibit much stronger non-linear optical properties than quartz optical fibers [1].

Recently new monolithic nanocomposite silica biomaterials were synthesized on the basis of various natural polysaccharides and completely water-soluble precursor tetrakis(2-hydroxyethyl) orthosilicate (Si-precursor) [2]. The polysaccharides radically changed the structure of biomaterials. In

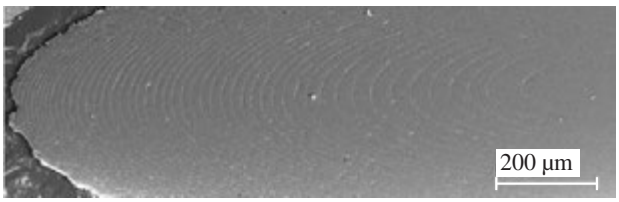

Fig. 1. SEM photo of a slanted polished end-face of *Hyalonema sieboldy* spicule.

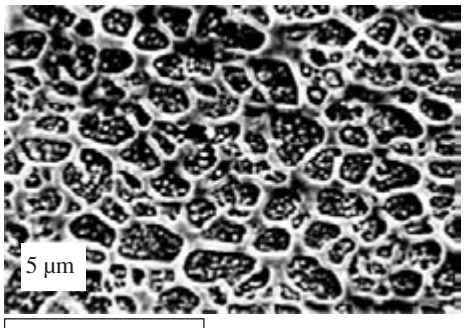

Fig. 2. SEM photo of biomaterials with concentration of polysaccharide (cat-HEC) of 1 wt.%.

place of the cross-linked nanoparticles, there was a three-dimensional network from crossed or branched fibers and uncrossed spherical particles that filled the mesh space (Fig. 2). The density of network, thickness of fibers, and properties of synthesized biomaterials depended on the polysaccharide type, charged degree of their macromolecule, and concentration.

The investigations of the dynamics of propagation of intensive ultra-short pulses through such biological and biomimetical nanocomposites is of substantial interest in terms of creating a new, low-temperature technology for optical fiber production [3], as well as developing novel functional elements for photonics applications [4].

1. Experimental

Laser complex Spitfire Pro 40F (Spectra Physics, USA) with femtosecond Ti:Sapphire oscillator was used in our experiments on propagation through short samples of spicules ($L =$ 5 mm) and cylindrical patterns of nanocomposite silica biomaterials with various natural polysaccharides. Input pulse duration amounting to $T_0 < 40$ fs was controlled by a standard technique of nonlinear autocorrelation with second harmonic generation. Other parameters of USP were as follows: maximum pulse energy $\sim$1 mJ, light beam diameter $d \sim 10$ mm, repetition rate – 100 Hz. Pulse spectrum was centered at 800 nm with $\Delta\lambda_{\mathrm{FWHM}} = 35$ nm.

The shape of spectrums on Fig. 3 demonstrates major changes indicating the broadening and formation of dip due to self-phase modulation (SPM) along with formation markedly strong anti-Stokes component in the output spectrum of transmitted

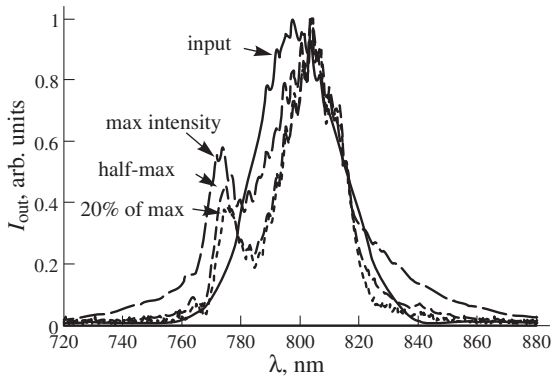

Fig. 3. Spectrums of the input USP and the various energy non-focused pulses transmitted through short sample of *Hyalonema sieboldy* spicule.

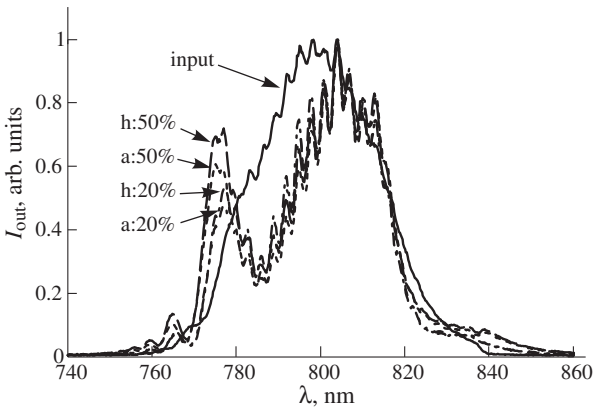

Fig. 4. Spectrums of the input USP and the various energy non-focused pulses transmitted through two patterns of nanocomposite silica biomaterials: a — synthesized on the basis of alginate of Na; h — on the basis of hyaluronate of Na. 50% and 20% — degree of intensity maximum of USP.

USP through short sample of *Hyalonema sieboldy* spicule. Both the dispersion and SPM have significant effect under the experimental layout. The peak input intensity of non-focused beam comes to $I = 7 \times 10^{10}$ W/cm^2. The effect of such non-stationary nonlinear optical effects as generation of optical "shock wave" at the back edge of the light pulse which brings about intensification of the higher-frequency part of the pulse spectrum, multiphoton absorption, spatial self-focusing, noninstantaneous contribution to the nonlinear refractive index increase dramatically. This conclusion also follows from our numerical simulations by applying finite difference method to the envelope evolution equation for $A(z, t)$ in Kerr media [5]:

$$\frac{\partial A}{\partial z} + \beta_1 \frac{\partial A}{\partial t} + \frac{i}{2}\beta_2 \frac{\partial^2 A}{\partial t^2} - \frac{1}{6}\beta_3 \frac{\partial^3 A}{\partial t^3} + \frac{\alpha}{2}A = i\gamma |A|^2 A - \frac{2\gamma}{\omega_0}\frac{\partial \left(|A|^2 A\right)}{\partial t} - i\gamma T_R A \frac{\partial |A|^2}{\partial t},$$

where z is the distance of pulse propagation, ω_0 is the central frequency of the pulse, $\beta_{1;2;3}$ are the coefficients of propagation constant β expansion in Taylor's series in the vicinity of ω_0 (β_2 is the group-velocity dispersion), α is absorption factor, γ is the coefficient of nonlinearity, T_R is the lag time of media response (polarization) to the pulse.

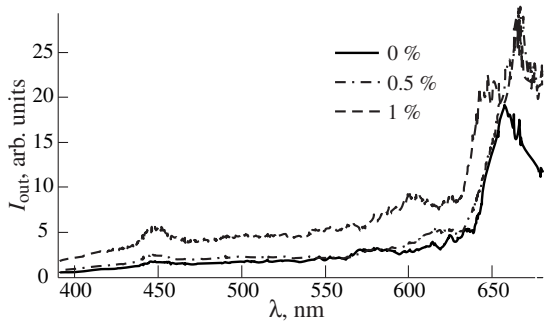

Fig. 5. SC spectrums of USP transmitted through patterns of biomaterials, synthesized on the basis of hyaluronate of Na with different values of weight concentrations of the polysaccharide.

The shock formation due to space-time focusing and self-steepening leads to the appearance of an extremely broad pedestal in the blue part of the transmitted pulse spectrum, and the transformation of input pulse into supercontinuum (SC) generation was observed in our experiments extending to the visible region up to $\lambda_{min} \sim 400$ nm.

The transmitted spectrums of USP through various cylindrical patterns of nanocomposite silica biomaterials with $d = 3$ mm and $L \sim 1$ cm demonstrate more significant non-linear optical properties (Fig. 4). Most efficient transformation of infrared USP into anti-Stokes component of the output spectrum and very efficient generation of SC correspond with the pattern synthesized on the basis of Na hyaluronate. These SC spectrums depend on concentrations of polysaccharides (Fig. 5) and extend to the region up to $\lambda_{min} \sim 200$ nm.

Thus the carried out studies have showed that the nature combination of spongin protein with silicon dioxide extracted from seawater by silicatein protein in glass sponge spicules and monolithic nanocomposite silica biomaterials are biological and biomimetical nanocomposite materials with unique optical properties. These results provide exciting prospects of using the materials for the development of fundamentally new integrated optical elements based on their non-linear optical properties of such structures, e.g. for implementation of active optoelectronic devices such as optical fiber amplifiers and lasers.

Acknowledgements

This work has been supported in part by the RFBR through 06-02-96902-r-ori, 07-02-01442-a.

References

[1] Yu. N. Kulchin *et al*, *Optics and spectroscopy*, (2009), in print.
[2] Yu. A. Shchipunov. / In Eds. Ruiz-Hitzky E., Ariga K., Lvov Yu. M., Bio-inorganic hybrid nanomaterials, Weinheim: Wiley. 2007. P. 75–117.
[3] H. C. Schröder *et al*, *Nat. Prod. Rep.* **25**, 455 (2008).
[4] Yu. N. Kulchin *et al*, *Quantum Electronics* **38**, 51 (2008).
[5] Y. Kodama, A. Hasegawa, *IEEE Journ. of Quant. Electronics* **23**, 510 (1987).

17th Int. Symp. "Nanostructures: Physics and Technology"
Minsk, Belarus, June 22–26, 2009
© 2009 Ioffe Institute

The natural nanostructured materials as promising material for biomimetic simulation

S. S. Voznesenskiy, A. N. Galkina and Yu. N. Kulchin
Institute of Automation and Control Processes FEB RAS, Vladivostok, Russia

Abstract. The studies of structure, element composition of the natural nanostructure minerals — the spicules of the sea glass sponge *Pheronema raphanus* (Pheronematidae; Hexactinellida) by the methods of the optical inverted, scanning electron microscopy (SEM), of the Thermogravimetric differential analysis (TG/DTA), and also OF UV-IR spectroscopy and energy-dispersion microanalysis (EDX) are given. The basic regularity of the physicochemical, optical and structural properties of the spicules, and correlation of the phase state change of spicules material during the modification are established. The detection of the different degree silica condensed its metastable state in the cross section of spicules made to assume the possibility of modification of spicules material of in vitro which makes the spicules of sea sponges as promising material for biomimetic simulation.

Materials for studies were collected by dredging during expeditions of "Academic Oparin" into the South China sea in 2007. The glass deepsea sponges *Pheronema raphanus* (Pheronematidae; Hexactinellida) was selected by dredging from depths 140–300 m on the northeastern slope of the ladd reef, South China sea (8°41.206 N and 111°42.336 E). Spicules from the sponge skeleton were selected: pentactines (Fig. 1a) and diactines.

The scanning electron microscopy (SEM) analyses of the structural organization of glass sponge *Pheronema raphanus* showed that sizes and the geometry of the spicules of sponge varies depending on their functional designation and locations in the sponge; however, the principles of organization persist [1–4]. The sponge are the thin extensive fiber formations, which have uniaxial symmetry, extent from 5 to 8 cm and thickness 150–170 μm. Each spicule has dense central cylinder and thin siliceous concentric layers around it [1–4] outside covered with the laminating shell with the developed surface. From microscale to nanoscale the structural organization of the spicules is strictly hierarchic, and have three-dimensional periodic structure, which consists of the organic matrix and the amorphous silica (Fig. 1(b–d)).

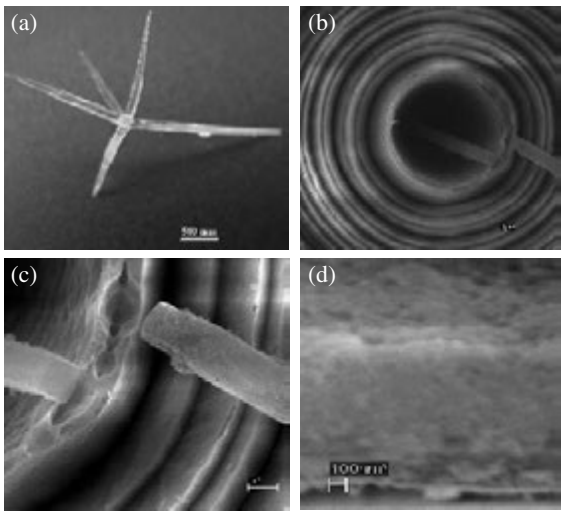

Fig. 1. The hierarchical structuring of the pentactines spicule of glass sponge *Pheronema raphanus*. a — photograph of pentactines, scale 500 μm; SEM analysis of spicule cross section after treatment by the hydrofluoric acid; b — the surface of the spicule cross section, scale 2 μm; c — the section of the of spicules central cylinder, scale 1 μm; d — the nanoparticulate silica, scale 100 nm.

The results of the studies by the method of electron-probe X-ray microanalysis (EDX) testify about composite nature of the spicules and confirm the presence in their composition of the high concentrations of the oxide of silicon and organic compounds, which will agree with the results, obtained for *Euplectella aspergillum* [1], *Hyalonema sieboldy* [2] and *Monorhaphis chuni* [3–4]. The center section of the spicule (axial thread, central dense cylinder and the first layers around it) contain the smallest quantity of silicon and a maximum quantity of carbon of organic origin. An increase in the content of silicon and a reduction of carbon content is observed in proportion to removal from the center of spicule to its shell. The external laminating cladding of spicule consists, predominantly, from the oxide of silicon and it does not contain the connections of carbon. For the spicules of *Pheronema raphanus* are indicated the potassium forms of the silica, with different degree of its polycondensation.

The morphology and phase states of natural biominerals under the influence of different temperatures and mediums are investigated. The thermogravimetric differential and X-ray phase analysis are shown that the additional hydration or the removal of the adsorbed water from the material of spicules changes chemical nature of their silica skeleton, which has an effect on the nature of the thermal-oxidative degradation of the spicules material, and it is also capable of initiating inside the spicules the processes of the phase transition of the polymorphous silica into the quartz.

The detection of the different degree silica condensed its metastable state in the cross section of spicules made to assume the possibility of modification of spicules material of in vitro. The process of the evaporation of the structural and adsorbed water in the material of the *Pheronema raphanus* and the influence of temperature action on their structural, mechanical and optical properties was studied. The results of studies testify about the structural stability and the significant contribution of geometric parameters to the spectral characteristics of spicule material (Fig. 2). The stability of the transmission in the range

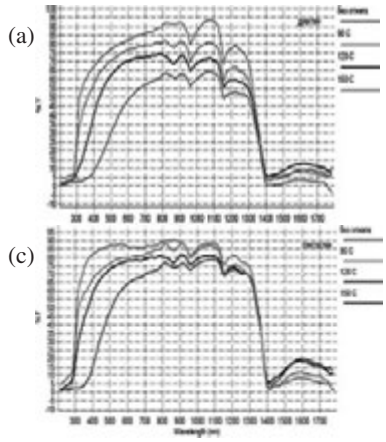

Fig. 2. Spectral characteristics of the spicules *f* glass sponge *Pheronema raphanus* according to the thermal treatment: (a) — diactine, (b) — pentactine.

of wavelengths from 300–1400 nm for all models of spicules, independently of their functional designation, is shown. The nature of the spectral characteristics of the spicules material before and after heating (on 40–90 °C) practically coincide, with exception of section in the long-wave region 800–1400 nm.

With the subsequent heating, in the spicules is observed the decrease of the intensity of transmission, due to packing of the center section of the spicule as a result of compression and sublimation of the hydrated silica. The heating to the temperature of 120 °C occurs the decrease of the intensity of transmission to 14–18% throughout the wavelength range. A similar phenomenon is possible with the formation of spicules structural imperfections in the process of their thermal treatment, on which occurs the dissipation of radiant energy. The structural imperfections can be attributed the coaxial fragmentation of central cylinder, and also the expansion of zone with the low degree of silica condensation and the shift of this zone to the spicules periphery. Further spicules heating up to 150 °C the decrease of the transparency of the material of spicules and the partial fragmentation of the laminating layers is recorded. In this case the intensity and the nature of the transmission of the models of spicules substantially changes. The shift of the minimum of transmission with 300 nm into the region 380–400 nm is observed, and the intensity of transmission with 500–1400 nm is reduced to 50% from the intensity of the transmission of prototype. Similar changes in the nature of transmission are explained by packing of the layers of the silica, by increase in the size of the globules due to the condensation of polymer, and also by partial combustion of the organic matrix of spicules.

The investigations are shown nanocomposite threedimensional periodic structure in the spicules. The presence of the nanostructural hierarchy of the spicules sponge material and the hierarchical control, which is observed during the deposit of minerals in the period of shaping of spicules are established. In this case the feature of the biomaterial of is different degree of the hydration of the oxide of silicon over the cross section of spicules.

The obtained results allow to assume that observed in the spicules of glass sponges laminar silicon structure it leads to the appearance of periodic three-dimensional modulation of dielectric constant with the period, compared with the wavelength of luminous radiation, which makes with their similar to the known microstructured fiber lightguides. It is experimentally shown that the spectral range of the material of spicules is moved into the short-wave region to the wavelength 300 nm, which is of interest for systems and devices for photonics [5–6]. The detection of the phenomenon of different degree of policondensation of the silica in the cross section of spicules and its metastable state made it possible to assume the possibility of the modification of the material of spicules in vitro which makes the spicules of sea sponges with promising material for the biomimetic simulation [7].

Acknowledgements

This work has been supported by grants from the RFBR Nos. 07-02-01442_a, 09-021-98506-p_vostok_a.

References

[1] J. Aizenberg *et al*, *PNAS* **101**, 3358–3363 (2004).
[2] W. E. G. Müller, K. Wendt *et al*, *Biosensors and Bioelectronics* **21**, 1149–1155 (2006).
[3] W. Müller, Xiao-Hong Wang *et al*, *Journal of Structural Biology* **161**, 188–203 (2008).
[4] Wang Xiao-Hong, Li Jin-He *et al*, *Acta Zoologica Sinica* **53**, 557–569 (2007).
[5] Yu. N. Kulchin, S. N. Bagaev *et al*, *Opt. Mem. and Neural Networks* **16**, 189 (2007).
[6] Yu. N. Kulchin *et al*, *Quantum Electronics* **38**, 51–54 (2008).
[7] Peter Fratzl, *Journal of Royal Soc. Interface* **4**, 637–642 (2007).

17th Int. Symp. "Nanostructures: Physics and Technology"
Minsk, Belarus, June 22–26, 2009
© 2009 Ioffe Institute

Temperature dependence of the Coulomb pseudogap in electron tunneling between Landau-quantized two-dimensional gases

V. G. Popov[1,2], S. Wiedmann[3] and J.-C. Portal[3,4,5]

[1] Institute of Microelectronics Technology of RAS, Institutskaya st. 6, Chernogolovka, Moscow region 142432, Russia
[2] Department of Physical and Quantum Electronics of Moscow Institute of Physics and Technology, Institutskiy per. 9, Dolgoprudniy, Moscow region 141700, Russia
[3] GHMFL, CNRS, BP 166, F-38042, Grenoble Cedex 9, France
[4] INSA, 135 Avenue de Rangueil, F-31077, Toulouse Cedex 4, France
[5] Institut Universitaire de France, 103 Bd. St. Michel, F-75005, Paris, France

Abstract. The vertical electron tunneling has been studied experimentally between two-dimensional electron gases in the high magnetic field directed perpendicular to the gases planes. The magnetic field produces Landau levels in the electron spectrum and suppresses the electron tunneling at the low energy inducing the Coulomb pseudogap. We have investigated this pseudogap at the high magnetic fields and the wide range of temperatures. In particularly the anomalous temperature dependence of the Coulomb pseudogap has been revealed below 2 K at the fields when the cyclotron energy exceeds the intersubband splitting in the gas with the higher electron concentration. This effect is considered in the model in which the intersubband plasmons take part in the pseudogap formation and their spectrum is modified by the electron exchange interaction at the low temperatures.

Introduction

The pseudogap is common effect for the tunnel structures with two-dimensional layers. It is revealed as in the high-T_C superconductors [1] so in the semiconductor heterostructures [2]. Experimentally the pseudogap is observed as a suppression of the tunnel current at the low bias voltage [3] or an additional high voltage shift of the resonant current peak in the I–V curve [4, 5]. In this case no signature of the gap is revealed in the lateral electron transport in the two-dimensional electron gas (2DEG). The origin of the pseudogap is still under investigation. Similar to the pseudogap in the superconductors there is one theoretical model considering inhomogeneous states of the 2DEG [6]. In this case the 2DEG is segregated on two phases with different integer filling factors due to the screened Coulomb interactions of the electrons. The electron spectrum is very different in the each phase due to the different value of the exchange enhancement of the Landau levels (LL) spin-splitting. Hence in the average tunnel spectrum one should to observe two maxima corresponded to the spin-split LL. This model can explain the resonance splitting but not resonance high-voltage shift observed in the tunnel junction between 2DEGs with different electron concentrations [4, 5]. Others models consider the electron relaxation effects in the 2DEGs. In particular the electron tunneling is considered as an instant event in compare with the energy relaxation of the whole 2DEG. Such relaxation can take place through the collective excitations that requires some energy. This means the tunneling electron should have some extra energy to organize its relaxation. Therefore the tunnel current is suppressed near zero voltage. Several types of the collective relaxations had been considered such as composite fermion scattering and magnetoroton excitations [7], magnetoplasmons [8]. As for the temperature dependence of the pseudogap it was not observed as for the I–V curve the temperature effect was observed as a smearing of the split and shifted resonance peaks [9]. In this report we show the temperature effect causes resonance shift that indicates on the temperature depended pseudogap.

1. Experimental

The investigated tunnel diodes were made of a single-barrier heterostructure by the conventional photo-lithography and the wet-etching technique. They represent circular mesa structures with diameters of 100 μm. The heterostructure was grown by the molecular-beam epitaxy on a n^+-Si-doped (the Si-donor concentration is $n_D = 2 \times 10^{18}$ cm^{-3}) GaAs substrate. Briefly speaking it has a single 20 nm thick layer of $Al_{0.3}Ga_{0.7}As$ which is doped in the middle. The donors in this barrier are ionized and supply electrons in the adjacent GaAs layers where the 2DEGs accumulate (see insert in Fig. 1). The barrier adjacent layers are separated from the n^+-GaAs layers with slightly doped GaAs spacer layers of the 70 nm thickness. The preliminary measurements [5] had shown that the resistance of the spacers is negligible in compare with the serial resistance of the tunnel $Al_{0.3}Ga_{0.7}As$ barrier. The 2D electron concentrations are 4×10^{11} cm^{-2} and 6×10^{11} cm^{-2} that corresponds to the single ground-subband E_{01} population and to the beginning of the population of the first excited subband E_{12} (see insert in Fig. 1) accordingly.

Measurements of the I–V curves carried out in the variable temperature ^{4}He and ^{3}He cryostats in temperature range from 0.35 K up to 10 K. In the I–V curves the current peak, corresponded to the first resonance i.e. when $E_{01} = E_{11}$, has been observed at the positive voltage. We determine the voltage positions V_r of the first resonant current peak as a voltage position of the minimum in the second current derivative. This allows us to decrease the influence of the non-resonant background current. The voltage dependencies of the second current derivative at different magnetic fields and the temperature of 1.5 K are

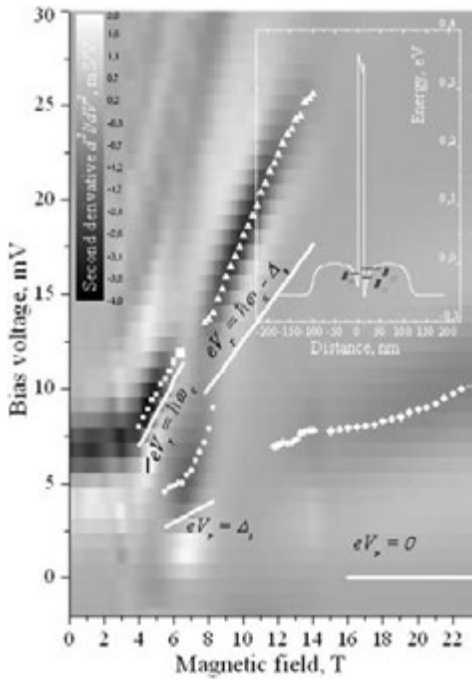

Fig. 1. Current second derivative in the dependence upon the magnetic field and the bias voltage. The experimental values of the V_r are shown with symbols. The symbols are different in accordance with different equations describing the V_r and shown in the figure. In the insert the schematic profile of the conductance-band bottom is shown with the subband levels.

shown in Figure 1 in the grey-scale plot. It is interesting that in the magnetic field higher 12 T the current peak is shifted and split close to zero voltage similar to that it was observed in the case of the identical 2DEGs [3]. The shift and splitting had been explained as the pseudogap effect that was confirmed by the temperature smearing of the current suppression near zero voltage at the temperatures higher 4.5 K [10]. Here we report results of the pseudogap study at temperatures below 2 K. In particularly the remarkable voltage shift of the current peak has been observed in magnetic field higher 12 T.

2. Discussion

The voltage V_r has non-monotonic magnetic dependence. Such behaviour had been successful explained early in the model of the LL pinning accompanied by the enhanced LL spin-splitting and Coulomb pseudogap [5]. Briefly speaking the voltage V_r can be easy determined in the single-particle approximation if one suppose the upper partial filled LLs pined to the Fermi levels in the n^+-contacts. In this case eV_r is simply energy difference of the pined LL. Numbers of the pined LL can be determined from the LL filling factors. The expected single-particle values of the V_r are plotted as the solid lengths in Fig. 1. The used equations are also shown in Fig. 1 where $\hbar\omega_c$, Δ_s are the cyclotron and spin-splitting energies. There is a remarkable high-voltage shift of the experimental values of V_r. This shift associates with Coulomb pseudogap and is shown in Fig. 2 for the two temperatures $T_1 = 0.35$ K (see filled symbols in Fig. 1) and $T_2 = 1.5$ K (see empty symbols in Fig. 1). As it can be seen in Fig. 2 the temperature effect becomes significant at fields higher $B_0 = 12$ T. It is worth noting that at this field

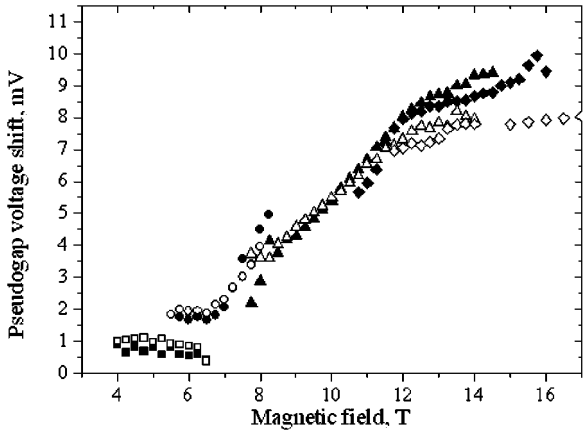

Fig. 2. Pseudogap voltage shift versus magnetic field for the two temperatures $T_1 = 0.35$ K and $T_2 = 1.5$ K. The values for T_1 and T_2 are shown as filled and empty symbols accordingly.

the cyclotron energy becomes equal to the intersubband energy $\Delta E = E_{12} - E_{11}$. Moreover at this fields the voltage position of the second resonance becomes also temperature depended. This is allowed us to conclude that intersubband excitations play significant role in the pseudogap formation in this fields.

Acknowledgements

This work has been supported in part by RFBR (grant number is 07-02-00487).

References

[1] T. Timusk and B. Statt, *Rep. Prog. Phys.* **62**, 61 (1999).
[2] R. C. Ashoori *et al*, *Phys. Rev. Lett.* **64**, 681 (1990).
[3] J. P. Eisenstein *et al*, *Phys. Rev. Lett.* **69**, 3804 (1992).
[4] J. G. S. Lok *et al*, *Phys. Rev. B* **56**, 1053 (1997).
[5] V. G. Popov *et al*, *JETP* **102**, 677 (2006).
[6] M. M. Fogler *et al*, *Phys. Rev. B* **54**, 1853 (1996).
[7] S. He *et al*, *Phys. Rev. Lett.* **71**, 777 (1993).
[8] I. L. Aleiner *et al*, *Phys. Rev. Lett.* **74**, 3435 (1995).
[9] N. Turner *et al*, *Phys. Rev. B* **54**, 10614 (1996).
[10] Yu. V. Dubrovskii *et al*, *Phys. of Low-Dim. Struct.*, **3**, 1–242 (1999).

17th Int. Symp. "Nanostructures: Physics and Technology"
Minsk, Belarus, June 22–26, 2009
© 2009 Ioffe Institute

Low-dimensional effects and electron transport in the ordered network of Si nanocrystals

I. V. Antonova[1], M. S. Kagan[2], V. A. Skuratov[3], J. Jedrzejewski[4] and I. Balberg[4]

[1] Institute of Semiconductor Physics, SB RAS, Lavrentieva 13, Novosibirsk 630090, Russia
[2] Institute of Radio Engineering & Electronics, RAS, 11 Mokhovaya, 125009 Moscow, Russia
[3] Joint Institute for Nuclear Research, Dubna, 141980, Russia
[4] The Racah Institute of Physics, the Hebrew University, 91904, Jerusalem, Israel

Abstract. Modification of films containing Si nanocrystallites (NCs) embedded in SiO_2 by irradiation with high-energy ions was found to induce peaks in their low frequency capacitance-voltage characteristics. Considering the NC spatial distribution that follows the ion tracks we interpret these peaks as due to the charge capture on isolated NC in vicinity the percolation network. Recharging of these NCs is taking place through "bottlenecks" between them and neighboring chains. Electron transport in crystals modified by irradiation is also drastically changed in comparison to the non irradiated samples.

Introduction

The study of materials composed of silicon nanocrystalites dispersed in a SiO_2 matrix (NC-SiO_2 layer) is an issue of high importance due to various optoelectronic and electronic applications (optoelectronic and memory devices, single electron devices that are operated at room temperature and other). Recently, MeV ion irradiation of NCs starts to be used as a tool to tailor the shape of nanoscale and microscale structures [for example, 1]. We have demonstrated that irradiation with high energy ions of arrays of silicon nanocrystals embedded in SiO_2 matrix creates the ordered distribution of the nanocrystals along the ion tracks [2] which accompanied with change in their electrical properties. Modification of a percolation network of the Si nanocrystals by irradiation was found to induce peaks in their low-frequency capacitance-voltage characteristics and to change mechanism of electron transport through the layer. Thus, irradiation of the NC-SiO_2 layers with high-energy ions can serve as a tool for the fabrication of vertical nanostructures with low-dimensional properties.

1. Experimental

For studies we have used mixed Si and SiO_2 (here SiO_x) layers with a thickness of 700–1000 nm by co-sputtering then from a Si and a SiO_2 sources that were separated by a distance of 100 mm, onto a Si-wafer substrate. The silicon content in the SiO_x layer varies along the 100 mm substrate from 5 to 94 volume %. Following a high temperature (1140 °C) annealing the layers are found to consist of Si nanocrystals (NCs) that are embedded in an amorphous SiO_2 matrix. Variation of layer content allows us to determine the content ranges in which NC arrays exhibits photoluminescence (PL), charge storage, conductivity and other. Then the samples were irradiated by either Kr, Xe or Bi ions with energies of 90, 130, 670 MeV, respectively. The dose ranged in the interval 10^{12}–10^{13} cm^{-2}. The ion projected ranges were 16, 17 and 43 μm for Kr, Xe and Bi ions, respectively. Hence, the ions penetrated into the substrate far beyond the NC-SiO_2 layer, so that the main portion of the defects was introduced in the silicon substrate. Subsequent annealing at 800 °C was performed for removal the electrically active centers in the Si substrate.

2. Electron transport through NC-SiO_2 layer

We have measured the I–V characteristics for different values of the silicon phase content x on the reference non irradiated sample as well as on the irradiated samples. The resistivity R at an applied voltage of 5 V of the NC-SiO_2 layers as a function of x is shown in Fig. 1. For the reference sample SiO-1 a percolation transition with a threshold at about $x = 40$ vol.% is found to yield a resistivity increases of about 6 orders of magnitude. The resistivity above the percolation threshold was weakly dependent on the Si-phase content. It is consistent with the usual percolation theory. However, the conductivity of irradiated samples was almost by two orders of magnitude larger than that of non-irradiated samples. This is believed to be due to significantly higher conductivity of a percolation network formed by NC chains arisen along the ion tracks.

Temperature dependences of current (80–300 K) through the NC-SiO_2 layer for different Si-phase contents higher then percolation threshold were measured on the reference and the irradiated samples In the reference sample the current demonstrates the variable range hopping conductivity for $T < 230$ K and activated conductivity for high temperatures. After irradiation another mechanisms of conductivity was found instead the hopping conductivity observed in the same samples before irradiation.

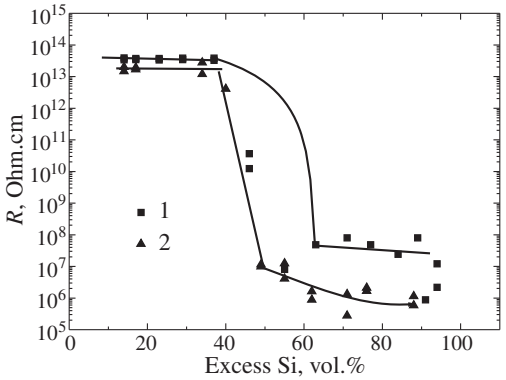

Fig. 1. The resistivity (for an applied bias of 5 V) as a function of the Si-phase content (vol.%) for (1) the reference sample and (2) the sample irradiated with 670 MeV Bi ions (dose was 10^{12} cm^{-2}).

3. Electron transport through NC-SiO_2 layer

In Fig. 2 we show the C–V characteristics of our irradiated structure. As seen, two remarkable capacitance peaks at low frequencies appear after irradiation. These results are typical for the Si-phase in the range of 60–80 vol.%. The magnitudes of the capacitance peaks 1 and 2 as a function of the frequency $\omega = 2\pi f$ can be described as

$$C(\omega) = \frac{C_{\max}}{\sqrt{(1+\omega\tau)^2}}.$$

Hence, the frequency dependence of the peak amplitude allows one to estimate the time constant τ of the NC charging process. The best fitted τ values as derived for Si content of 72% are around 1.5×10^{-5} s and 5×10^{-6} s. The above observation is similar to peaks found in thin layers that include two-dimensional arrays of Si NCs, which are generally attributed to the charging of different energy levels of the NCs [2] and, correspondingly, the peak spacing (in V) is assumed to be associated with the energy spacing (in eV) between states in NCs. Using the τ values we have found a correlation of the bias values of the capacitance peaks with resonant tunneling between the quantum-confined levels and the charging (Coulomb blockade) energies of the single NC. The probability of the carrier tunneling through the barrier is a function of the energy level in the NC. For the above values of τ_1 and τ_2 the NC diameter W is estimated to be 3.3 nm for the expected barrier thickness of 3 nm. The value of W is in very good agreement with the TEM values of 3–5 nm.

Increase in the Si content NC-SiO_2 layer leads in to increase in NC size W extracted from values of τ_1 and τ_2. In the case of non irradiated samples C–V characteristics have no any peaks and $C(\omega)$ dependencies give the same τ values for different voltages.

The NCs in the chains are not able to capture the charge due to the high electric conduction between NCs. So, only isolated NCs in the cells outside the conductive network formed by the chains can retain the charge and recharging of these NCs is penetrated through "bottlenecks" (DBTJ) between them and neighboring chains. Independent of the bottleneck positions, their resistance and the resistance of the rest of the cluster are statistically very similar in different chains and thus the applied voltage is divided between the chain and these "relatively isolated" DBTJ. In the case of the randomly distributed NC clusters in non-irradiated structures, the distance between isolated NCs and the net cells, as well as cell sizes are random. So, no capacitance peaks are possible. Thus, the ion irradiation of the above three-dimensional system appears to be useful then for the fabrication of nanostructures, which have also properties of low-dimensional arrays.

For another sample the bias dependences of real (G) and imaginary (C) parts of the admittance of films, which were irradiated with Xe ions, demonstrates the capacitance peaks that we divided into two groups of peaks according to their bias positions. The voltage difference between the neighboring capacitance peaks within the groups is equal to ~0.5 V and the voltage difference between these groups is ~2.6 V. The G-V curves exhibit only two less pronounced peaks at the same voltages. We have examined our model for a consistency with the

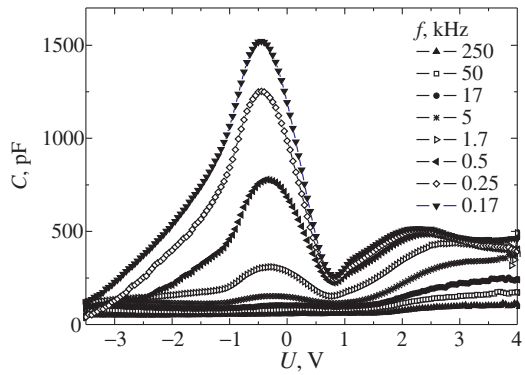

Fig. 2. C–V characteristics measured at room temperature and various frequencies for the structure with Si-phase contents of 69% irradiated with 90 MeV Kr ions (dose was 10^{12} cm^{-2}).

analysis typically used for the two-dimensional NCs arrays [3]. The position of the photoluminescence peak observed in the studied samples corresponds to QDs size of 3.3 nm. The energy distance between the first and exited levels in such a QD is estimated as $\Delta E = 103$ meV according to standard equation. Voltage difference between groups of peaks can be represented as $\Delta V = eK\Delta E$, where K is the coefficient depended on a geometry of QD/matrix system. In our case $\Delta V = 2.6$ eV and it corresponds to K value of 0.048. Charging energy can be estimated from $\Delta E_e = K\Delta V_e$, and we have $\Delta E_e = 24$ meV for the same K. On the other hand, $\Delta E_e = e/C_{NC}$, where C_{NC} is the capacitance of the nanocrystal. The capacitance of NC was estimated as 8 aF which is reasonable value for the NC with the size ~3 nm.

In more details frequency dependence of capacitance and other properties of the NC-SiO_2 layer modified by the irradiation of high energy ions are presented in the Ref. [2,4].

Acknowledgements

This study was supported, in part, by the Russian Foundation of Basic Research (Grants 08-02-00221, 08-02-00351, 08-02-01464), grant of Analytic Task Program 2.1.1/2612, and in part by the Israel Science Foundation and the Israeli Ministry of Science and Technology.

References

[1] R. Giuline, P. Kluth, D. J. Sprouster, L. L. Araujo, A. Byrne, M. C. Rydgway, *Nucl. Instr. Meth. B* **226**, 3158 (2008).

[2] I. V. Antonova, M. B. Gulyaev, A. G. Cherkov, D. V. Marin, V. A. Skuratov, J. Jedrzejewski, I. Balberg, *Nanotechnology* **20**, 095205 (2009).

[3] L. W. Yu, K. J. Chen, L. C. Wu, M. Dai, W. Li, X. F. Huang, *Phys. Rev. B* **71**, 245305 (2005).

[4] I. V. Antonova, A. G. Cherkov, V. A. Skuratov, M. S. Kagan, J. Jedrzejewski, I. Balberg, *Nanotechnology* **20**, in press (2009).

17th Int. Symp. "Nanostructures: Physics and Technology"
Minsk, Belarus, June 22–26, 2009
© 2009 Ioffe Institute

Peculiarities in the current flow near the edge of the tunnel Schottky contact with the delta-doped GaAs layer

I. N. Kotel'nikov[1], N. A. Mordovets[1] and M. N. Feiginov[2]

[1] Institute of Radioengineering and Electronics of the RAS, 125009 Moscow, Russia
[2] Technische Universität Darmstadt, 64283 Darmstadt, Germany

Abstract. We have observed non-monotonous behavior of the differential resistance $R_{\delta g}$ with increase of the "depleting" bias $U_{\delta g}$ between the Al gate and the ohmic contact to the 2D channel in the tunnel Al/delta-GaAs structure. The effect was observed at 4.2, 77 and 300 K, while at liquid-helium temperatures at $U_{\delta g} > U_{\delta g}^{\rm cr}$ we have also observed some hysteresis features. We have shown that the most probable reason for the observed effect is the increase in the channel resistance at the gate edge and/or between the gate and the ohmic contact.

Introduction

The transistor structures with 2D electron gas (2DEG) became of particular interest in the last years due to the possibility of their use for generation and detection of the THz radiation [1,2]. In the HEMT structures used for that purpose, the excitation of 2D plasmons in the gated part of 2DEG plays the major role. Nevertheless, not only plasmons are important in such structures. It was suggested [3] that when the excitation of 2D plasmons is accompanied by a strong nonlinearity of the tunnel current between the channel and the gate then this can lead to significant features in the HEMT high-frequency linear and nonlinear characteristics. Additionally, we have recently shown [4] that it should be possible to achieve negative differential conductance (NDC) in the tunnel current between the gate and channel in the HEMT-like structures. If achieved, NDC should contribute to instability of 2D plasmons [5] and possibly to improve the characteristics of the HEMT plasma THz generators and detectors. I.e., the tunnel properties of the structures might play an important role. The present work is devoted to investigation of the characteristics of such tunnel structures.

We report on the first results of investigation of the 2D tunnel Al/δ-GaAs structures at high channel-depleting biases at the Schottky gate. In such MBE grown structures one can achieve high density of the 2DEG in the near-surface δ-doped GaAs layers [6]. Owing to high quality of the MBE-grown Al-GaAs interface, we could observe many-particle effects [7,8,9] in the tunnel spectra of the Al/δ-GaAs structures. Such tunnel experiments were done at relatively low biases ($\pm$100 mV) between the gate and the channel, when the tunnel resistance $R_{\rm tun}$ was much higher than the resistance of the 2D channel $R_{\rm ch}$. Therefore, we could neglect by the voltage drop along the 2D channel and by the influence of the gate voltage on the electron concentration in the channel. With increase of the bias between the Al gate and the channel, $R_{\rm tun}$ drops exponentially and becomes comparable to $R_{\rm ch}$, that should inevitably lead to the inhomogeneity in the distribution of the gate-channel voltage and of the electron concentration in the channel. Additionally, when $R_{\rm tun} \sim R_{\rm ch}$, the total bias applied to the structure should be divided between the gated and not-gated parts of the channel.

Results and discussion

In our experiments, we were using an MBE grown Al/δ-GaAs structure with the 2D electron concentration of 2–4$\times 10^{12}$ cm^{-2} and two filled subbands in the channel. The samples were prepared in the form of a Hall bars with the width of the 2D channel of 0.5 mm and the full length of 1.5 mm. We had two types of samples. One is with two tunnel gates of the length of 10 μm close to the ends of the Hall bar (sample "d"), the another one (sample "e") had practically the whole Hall bar covered by the gate, the gate length was 1.3 mm in this case. The rho-contacts where between the gates in the first case and under the gate in the second one. The distance between the gate edges and the nearest ohmic (current) contacts was 100 μm. In the sample "e" owing to the rho-contacts, we could measure the potential distribution under the gate, when the bias is applied between the gate and the ohmic contact.

For the channel-depleting biases ($U_{\delta g} < 0$), we have observed that the differential resistance $R_{\delta g}$, measured between the gate of the sample "d" and the nearest ohmic contact at $T = 4.2$ K is non-monotonous (see Fig. 1, the electron density at zero bias in the two filled subbands was 3.6×10^{12} cm^{-2} for the sample). For the "enriching" biases ($U_{\delta g} > 0$), we observe the expected monotonous behavior with the saturation region coinciding with the resistance of the non-gated part of the channel, its length is 0.1 mm and the resistance is $R_{\rm ch} = 1.1$ kOhm. With the increase of the depleting voltage, we see a minimum in the dependence $R_{\delta g}(U_{\delta g})$, after which $R_{\delta g}$ is increasing by an order of magnitude. We observe this type of behavior for different gate areas (Fig. 1). Qualitatively-similar dependencies $R_{\delta g}(U_{\delta g})$ were also observed in the other samples with the electron concentration in the range $(2-4) \times 10^{12}$ cm^{-2}. The dependence $R_{\delta g}(U_{\delta g})$ did not change at $T = 77$ K (except the steps at small biases, arising due to the onsets of tunneling to different subbands [6]) and qualitatively it did not change even at room temperature (Fig. 1). For the biases $|U_{\delta g}| < 1.5$ V the dependencies $R_{\delta g}(U_{\delta g})$ stay the same independent of the direction of $U_{\delta g}$ sweep. We note, that for higher biases a hysteresis was observed in the dependence $R_{\delta g}(U_{\delta g})$. The potential difference $U_{\delta g}(X)$ between the gate and an X point in the channel was saturating with increase of $|U_{\delta g}|$ for all X, where X is the coordinate along the gate, counted from the gate edge nearest to the ohmic contact. For the sample in Fig. 1, the potential

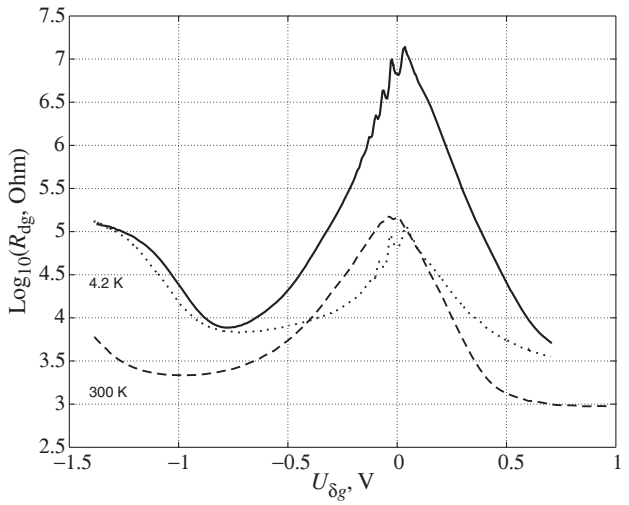

Fig. 1. $R_{\delta g}(U_{\delta g})$ dependences for the "d" (continues and dashed lines) and "e" (dots) samples with the electron concentration of 3.6×10^{12} cm^{-2}.

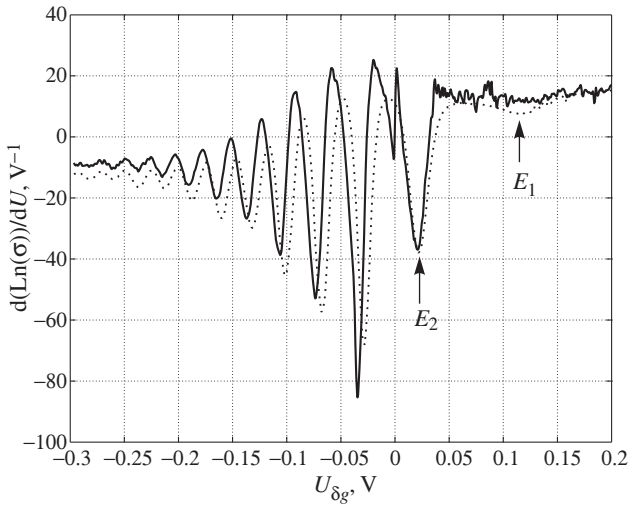

Fig. 2. The tunnel spectrum $d(Ln(\sigma))/dU$ ($\sigma = 1/R_{\rm tun}$) measured in the region of low biases (when $R_{\rm tun} \gg R_{\rm ch}$) at $T = 4.2$ K for "d" sample (continues line) and the results of the self-consistent calculations (dots) [4]. The arrows indicate the positions of the filled subbands: $E_1 \approx 120$ meV and $E_2 \approx 20$ meV relative to the Fermi level in the channel.

difference at $X_{\rm min} = 10$ μm was apprtoaching the value of $U_{\delta g}(X_{\rm min}) = -0.74$ V. The self-consistent calculations [4] for the sample measured in Fig. 1 has shown that the electron concentration under the gate stays relatively high ($\sim 10^{12}$ cm^{-2}) at $U_{\delta g}(X_{\rm min}) = -0.74$ V. I.e., the full depletion of the channel under the gate was not reached in our samples at such bias. The good agreement between the measured and calculated tunnel spectra in the range of biases where $R_{\rm tun} \gg R_{\rm ch}$ (see Fig. 2) indicate the reliability of the calculations.

Starting from the biases of $\sim$1 V, the tunnel resistance $R_{\rm tun}$ becomes small and the growth of the total resistance of the structure should be due the peculiar behavior of the δ-layer resistance under the gate and (or) in the narrow region between the edge of the gate and the ohmic contact. The finite value of $R_{\rm ch}$ should lead to the inhomogeneity of the current under the gate (along X-coordinate). In this case, the magnitude of the current flowing through the gate will saturate far away from the ohmic contact. Only the parts of the structure that are close to the ohmic contact will contribute to the growth of the current with bias. To verify the model, we were comparing the calculated values of $U_{\delta g}(X)$ with the measured ones for different values of the total bias applied to the structure $U_{\delta g}$: in the structures with the long gate, we were measuring $U_{\delta g}(X)$ at two rho-contacts under the gate; in the short structures, we were measuring $U_{\delta g}(X)$ only at the most remote from the ohmic contact point.

Our calculations show, that one can describe the data presented in Fig. 1 and the dependencies $U_{\delta g}(X)$ only in the model that $R_{\delta g}$ is increasing (when $|U_{\delta g}| > 0.7$) due to the channel resistance change in close vicinity to the gate edge or due to the change in $R_{\rm ch}$ between the gate and the ohmic contact. The resistance could be growing due to the heating effects (or transitions to the L valley [10]) and also due to the significant depletion of the channel under the gate edge at high biases. The latter should lead (see, e.g., [11]) to rather slow (hyperbolic) decrease of potential towards the ohmic contact. We can discard the contribution of the DX centers, since the effect (the impedance growth at high negative biases) is observable also at room temperatures. The further experiments should clarify the mechanism of the observed effect.

Acknowledgements

The work was supported by RFBR and RAS Presidium.

References

[1] M. I. Dyakonov, *FTP* **42**, 998 (2008).
[2] D. Veksler, F. Teppe, A. P. Dmitriev *et al*, *Phys. Rev. B* **73**, 125328 (2006).
[3] A. Satou, I. Khmyrova, V. Ryzhii, M. S. Shur, *Semicond. Sci. Technol.* **18**, 460 (2003).
[4] M. N. Feiginov and I. N. Kotel'nikov, *Appl. Phys. Lett.* **91**, 083510 (2007).
[5] M. N. Feiginov and V. A. Volkov, *JETP Lett.* **68**, 662 (1998).
[6] I. N. Kotelnikov, S. E. Dizhur, M. E. Feiginov, N. M. Mordovets, *FTP* **40**, 839 (2006).
[7] I. N. Kotel'nikov, V. A. Kokin, Yu. V. Fedorov *et al*, *JETP Letters* **71**, 387 (2000).
[8] S. E. Dizhur, I. N. Kotel'nikov, E. M. Dizhur, *Radiotekhnika i Elektronika* **51**, 625 (2006).
[9] E. M. Dizhur, A. N. Voronovskii, A. V. Fedorov *et al*, *JETP Letters* **80**, 433 (2004).
[10] M. Shur, *GaAs. Device and Circuits*, Plenum Press, New York, 1987.
[11] A. Ya. Shik, *FTP* **29**, 1345 (1995).

17th Int. Symp. "Nanostructures: Physics and Technology"
Minsk, Belarus, June 22–26, 2009
© 2009 Ioffe Institute

Quantum states in periodically-driven nanostuctures

M. V. Entin[1] and *M. M. Mahmoodian*[1,2]

[1] Institute of Semiconductor Physics, SD RAS, Novosibirsk, 630090, Russia
[2] Novosibirsk State University, Novosibirsk, 630090, Russia

Abstract. We study different one-dimensional systems with local vibrating potential. In particular, free electrons interacting with a potential of "step+vibrating δ-function" and the Dirac model with vibrating δ-functional potential are analyzed. The conductance and stationary photocurrent are found. The high-frequency blockade states are discussed. An optical analogue of the Dirac model is considered.

The system with vibrating local potential attracted attention as possible quantum pumps [1–7]. The quantum pump is treated as a one dimensional system with local vibrating potential which can produce a stationary current across the system. It is very interesting that at some conditions the potential with limited measure can ideally reflect electrons and induce "high-frequency blockade states" [8, 9, 6, 7]. The blockade leads to appearance of very narrow resonances (quasilocal states in continuum) in transmission and conductance. We have found [10] that such systems can be realized, e.g. using curved quantum wires, where acting component of high-frequency field becomes essentially inhomogeneous.

The purpose of the present study is widening of the field of previous works to other potentials and electron spectrum. In particular, we consider here free electrons propagating in the potential of "step+oscillating well" :

$$V(x) = V_0\theta(x) + (u + v\cos(\omega t))\,\delta(x). \qquad (1)$$

Another problem is the potential $V(x) = (u + v\cos(\omega t))\delta(x)$ acting on electrons with the Dirac spectrum

$$\varepsilon = \pm\sqrt{p^2 + \Delta^2}. \qquad (2)$$

In connection to semiconductors the problem is formulated as follows. Let we have a single-mode quantum wire with oscillating potential applied to some part of which. We suppose that the frequency ω is high enough and comparable with the Fermi energy E (we set electron mass $m = 1$, $\hbar = 1$). The width of the oscillating potential well is small as compared with the electron wavelength. In these assumptions the considered models are valid.

We have studied the problems both numerically and analytically. The wave functions were found for propagating electrons. They were utilized to find the stationary conductance and the photocurrent. The specific blockade states were found also.

The problem "step+oscillating well" has asymmetric potential and hence possesses photovoltage unlike the case with $V_0 = 0$ studied earlier. Different situations can be considered. First, the Fermi level in one contact may be above the bottom, while in other contact being below the bottom. This situation resemble the external photoeffect. In this case the current at low temperature appear due to excitation of electrons by single or many photons of oscillating field.

Another situation occurs when both contacts are the Fermi seas. In that case the alternating signal affects the conductance or causes the stationary photocurrent. These effects are presented in the Fig. 1. Earlier, we have studied another asymmetric system with two oscillating delta-functional wells; as compared with that case no splitting of blockade states is observed.

The specific character of the Dirac problem is that no high-frequency blockade states with real energy exist. This behavior is contrary to free-electron and tight-binding problems and originates from the multiphoton transition of electrons through the energy gap. Nevertheless, the limit remains, where the states are approximately blocked. This is the case $\Delta \gg \omega$. This limit is close to the case of free electrons where the blockade states exist. In that case an electron with energy above the gap incident to the well needs too many photons emission to get into the hole sheet of spectrum. This suppresses the width of the blockade states like $v^{2\Delta/\omega}$. The Fig. 2 demonstrates the appearance of quasiblockade states (the bottom of the valley).

The Dirac problem has an optical analogy, namely, optical fiber, where propagating photons has Dirac-like spectrum for all but the lower modes. Modulation of the dielectric constant in some part of the wire results in the effective oscillating "potential" for photons. The modulation of optical properties can be done via non-linear constants of material by external light crossing the waveguide with quadratic non-linearity. The other way is electrical modulation of an active layer with quantum wells.

We have demonstrated the existence of the blockade or quasi-blockade states in more complicated systems than in the systems with δ-function potential. It is desirable to find general condition for the blockade states manifestation. In our cases the matrix of Hamiltonian is band-like with $(n, n \pm 1)$

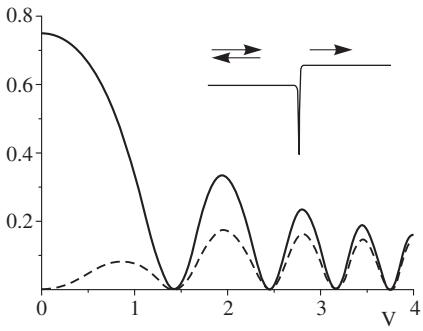

Fig. 1. Insert: sketch of considered potential "step+oscillating δ-well". Main figure: Pattern of conductance (solid) and derivative of the photovoltage with respect to the Fermi energy E (dashed) for $u = 0$, $V_0 = 0.8$, $E = 0.9$. All parameters are measured in units of ω, the functions are measured in units of conductance quantum.

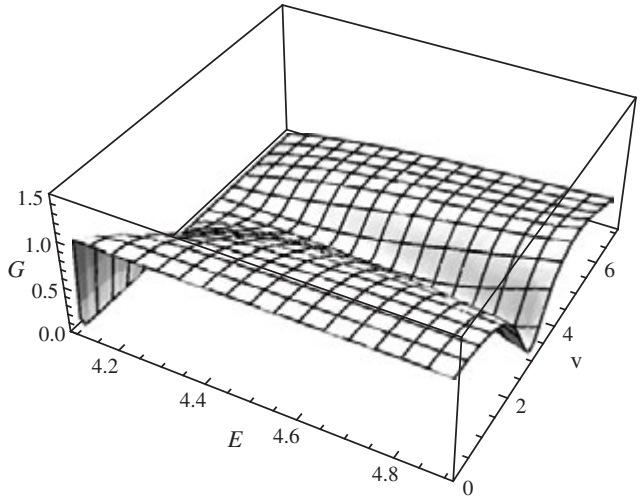

Fig. 2. The conductance of the problem (2). The values of parameters are chosen $\Delta = 4.1\omega$, $u = 0$.

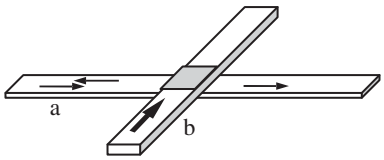

Fig. 3. The sketch of the optical analogue. The weak electromagnetic wave of frequency ω propagates along the waveguide a crossed by a waveguide b with strong wave of frequency Ω. The crossing possesses quadratic non-linearity. The frequency ω is above the threshold frequency ω_t of the waveguide a. If $\omega_t \gg \omega$ the quasiblockade exists with very weak transmission.

non-zero matrix elements (n marks the number of absorbed or emitted photons). Besides, the transition to very large negative n is limited because the spectrum is limited from below. In this case to block the excitation to large energies it is sufficient to select the parameters to vanish two of the nearest wave function coefficients: the subsequent coefficients will vanish automatically. The interference of channels makes this possible. And *vice versa*, in the systems with infinite spectrum in both direction (Dirac case) the blockade states occur to be quasistationary. Hence, the needed conditions are two-step recurrence, finite from one side non-perturbed spectrum and strong enough perturbation.

Acknowledgements

The work was supported by grant of RFBR No. 08-02-00506, the grant of the President of the Russian Federation No. MK-271.2008.2 and the grant of the Russian Science Support Foundation.

References

[1] M. Moskalets and M. Büttiker, *Phys. Rev. B* **66**, 205320 (2002).
[2] S. W. Kim, *Int. J. Mod. Phys. B* **18**, 3071 (2004).
[3] L. S. Braginsky, M. M. Mahmoodian, M. V. Entin, *JETP* **100**, 920 (2005).
[4] M. M. Mahmoodian, L. S. Braginsky, M. V. Entin, *Phys. Rev. B* **74**, 125317 (2006).
[5] M. M. Mahmoodian, M. V. Entin, *Europhys. Lett.* **77**, 67002 (2007); cond-mat/0610832.
[6] M. M. Makhmudian, M. V. Entin, and L. S. Braginskii, *JETP* **105**, 495 (2007).
[7] M. M. Mahmoodian, M. V. Entin and L. S. Braginsky, *Physica E* **40**, 1205 (2008).
[8] O. A. Tkachenko, V. A. Tkachenko, and D. G. Baksheev, *Phys. Rev. B* **54**, 13 452 (1996).
[9] D. F. Martinez and L. E. Reichl, *Phys. Rev. B* **64**, 245315 (2001).
[10] M. V. Entin, M. M. Mahmoodian, *Europhys. Lett.* **84**, 47008 (2008).

17th Int. Symp. "Nanostructures: Physics and Technology"
Minsk, Belarus, June 22–26, 2009
© 2009 Ioffe Institute

Ballistic contributions to unitary localization length

A. A. Greshnov, G. G. Zegrya and E. N. Kolesnikova
Ioffe Physical-Technical Institute, St Petersburg, Russia

Abstract. The divergent at $\omega = 0$ quantum correction to conductivity $\delta\sigma_2(\omega)$ of the leading order in $(k_\mathrm{F}l)^{-1}$ has been calculated neglecting Cooperon-type contributions suppressed by moderate or strong magnetic field. In the so-called diffusion approximation this quantity is equal to zero up to the second order in $(k_\mathrm{F}l)^{-1}$. More subtle treatment of the problem shows that $\delta\sigma_2(\omega)$ is non-zero due to ballistic contributions neglected previously. Knowledge of $\delta\sigma_2(\omega)$ allows to estimate value of the so-called unitary localization length as $\xi_\mathrm{u} \approx l\exp(1.6g^2)$ where Drude conductivity is given by $\sigma_0 = ge^2/h$. This estimation underpins the statement of the linear growth of σ_{xx} peaks with Landau level number n in the integer quantum Hall effect regime [1] at least for $n \leq 2$ and calls Pruisken–Khmelnitskii hypothesis of universality [2] in question.

Introduction

It is well-known since 1979 that conductivity of the non-interacting 2D electronic systems is equal to zero at $T = 0$ [3,4] (if spin-orbit interaction can be neglected). However, typical experimental temperatures allow quantum corrections to conductivity to be comparatively small in the sufficiently clean systems where dimensionless Drude conductivity is large $g = k_\mathrm{F}l \gg 1$. Two-dimensional localization length to be compared with the typical inelastic scales is given by $\xi_0 \approx l\exp(\pi g/2)$ [4]. Quantum correction to conductivity of the first order in $(k_\mathrm{F}l)^{-1}$ usually called weak localization correction is almost fully suppressed in sufficiently strong (kilogauss) magnetic fields which makes magnetoresistance measurements the most important experimental tool for this field. In higher (tesla) magnetic fields the situation is much more complicated since Landau quantization plays a crucial role.

In the present study we consider intermediate range of magnetic fields where both Landau quantization and Cooperon-type corrections to conductivity can be neglected. Under these conditions quantum correction to conductivity of the second order in $(k_\mathrm{F}l)^{-1}$, $\delta\sigma_2(\omega)$, comes to the front. It is generally believed [5,6] that $\delta\sigma_2(\omega)$ determines value of the so-called unitary localization length ξ_u even in high magnetic fields (corresponding to the regime of the integer quantum Hall effect) and restricts dramatically the validity area of the numerical results obtained in Ref. [1].

Although almost three decades have passed since seminal paper of Gor'kov, Larkin and Khmelnitskii [3] only minor success has been achieved in the problem of interest so far. If Ref. [3] it was stated that $\ln^2(\omega\tau)$ terms vanish up to the second order in $(k_\mathrm{F}l)^{-1}$. In Ref. [7] and Ref. [8] the problem was treated using diffusive non-linear σ-model and mutually contradictory answers were obtained. Later K. Efetov withdrew [9] zero value of β-function obtained in Ref. [7] in favor of that of Ref. [8]. Below we show that zero answer of Efetov, Larkin and Khmelnitskii is in line with the so-called diffusion approximation used in Refs. [7, 8] whereas proper consideration of the ballistic contributions is essential. It is also shown that anomalous (short-wavelength) contributions similar to those studied in Refs. [10] cancel out. Our estimation of the unitary localization length gives hard ground under the numerical results obtained in Ref. [1] and calls Pruisken–Khmelnitskii hypothesis of universality [2] in question.

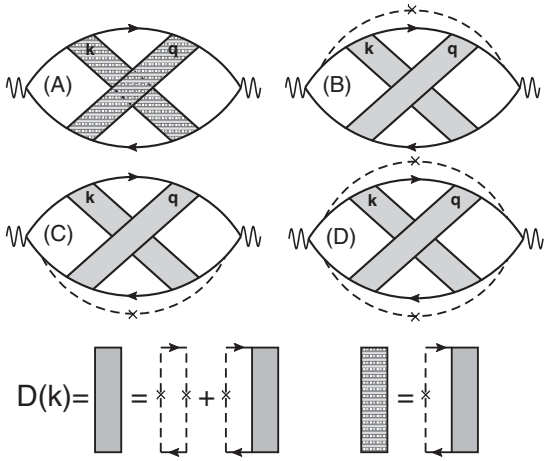

Fig. 1. Ballistic contributions with 2 Diffusons.

Theory

We apply usual impurity diagram technique to the problem of 2D short-range elastic scattering at $T = 0$ and pick out relevant (divergent at $\omega = 0$) diagrams of the second order in $(k_\mathrm{F}l)^{-1}$ containing one, two or three Diffusons as presented in Figs. 1–3. The contributions of Figs. 1,2 were depicted (in slightly unusual manner) and studied previously in Refs. [3,7,8] in the so-called diffusion approximation, i.e. exact Diffuson mode

$$D(k) = \frac{1}{\sqrt{(1 - i\omega\tau)^2 + (kl)^2} - 1} \qquad (1)$$

was substituted for all values of k by approximate expression

$$D_0(k) = \frac{1}{(kl)^2/2 - i\omega\tau} \qquad (2)$$

valid only for $kl \ll 1$. As it was shown in Ref. [3] squared-logarithm contribution coming from 2-Diffuson diagrams (A)–(D), viz. $-\ln^2(\omega\tau)(k_\mathrm{F}l)^{-1}/(2\pi)^2e^2/h$, is cancelled by the contribution of 3-Diffuson diagrams (E)–(M). Using "diffusion approximation" it is easy to show that the terms of the first order in $\ln(\omega\tau)$ cancel out as well. Also note that the diagrams in Fig. 3 were not considered in preceding works.

It is convenient to introduce transparent dimensionless notations of the individual contributions so that

$$\delta\sigma_2(\omega) = \frac{\Sigma}{\pi^2}\,\frac{\ln(\omega\tau)}{k_\mathrm{F}l}\,\frac{e^2}{h}, \qquad (3)$$

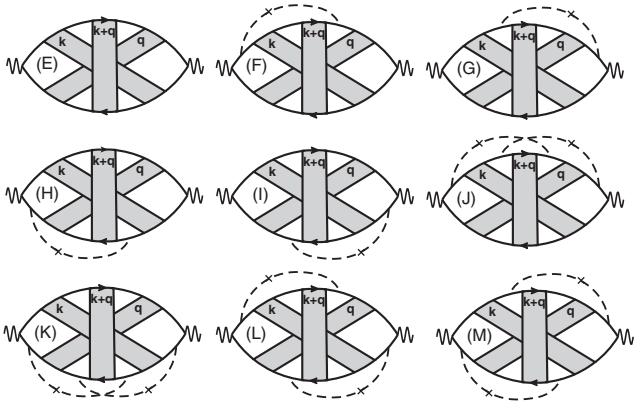

Fig. 2. Ballistic contributions with 3 Diffusons.

$\Sigma = \Sigma_1 + \Sigma_2 + \Sigma_3$, $\Sigma_1 = A + \ldots + D$, $\Sigma_2 = E + \ldots + M$, $\Sigma_3 = a + \ldots + n$. Since divergent (at $\omega = 0$) contributions to conductivity are due to the diffusion processes characterized by arbitrary long scales it is essential to discriminate the areas of small ($\ll l^{-1}$) values of k, q and $|\mathbf{k} + \mathbf{q}|$. Using this trick we are able to calculate all the diagrams depicted in Fig. 1 and Fig. 2, viz.

$$A = \frac{31}{8}, \; B = C = -\frac{3}{4}, \; D = 1, \tag{4}$$

$$\Sigma_1 = \frac{27}{8}, \tag{5}$$

$$E = \frac{3}{4}\ln 2 - \frac{15}{8}, \; F = G = H = I = \frac{3}{8}\ln 2 + \frac{1}{24}, \tag{6}$$

$$J = K = -\frac{3}{4} + \frac{3}{4}\ln 2, \; L = M = \frac{3}{8} - \frac{3}{8}\ln 2, \tag{7}$$

$$\Sigma_2 = 3\ln 2 - \frac{59}{24}, \tag{8}$$

$$\Sigma_{12} = \frac{11}{12} + 3\ln 2 \approx 2.996. \tag{9}$$

Whereas the contributions in Figs. 1,2 have ballistic nature, it is not the case for those presented in Fig. 3. Correct evaluation of these diagrams demands consideration of electron motion on much smaller (λ_F) scale [10]. However, explicit calculation shows that all the "wavelength" contributions cancel out ($a = b = -c = -d$, $e = f = g = h = -i = -j = -k = -l$, $m = -n$), so that overall value of $\delta\sigma_2(\omega)$ is given by Eqs. (3),(9). Now it is easy to find the unitary localization length from the standard condition $\delta\sigma_2(\omega) = -\sigma_0$ [4]:

$$\xi_u \approx l \exp\left(\frac{\pi^2 g^2}{2\Sigma}\right). \tag{10}$$

Previously it was argued [5] that $\xi_u \approx l\exp(\pi^2 g^2)$ that corresponds to $\Sigma = 0.5$. We have shown that the actual value of Σ is almost one order of magnitude higher. In order to apply our result to the case of high magnetic fields corresponding to the regime of the integer quantum Hall effect we substitute g by the "bare" peak values of longitudinal conductivity due to Ando, $g_n = (2n+1)/\pi$ [1]. After this trick we obtain the following expression for the Landau level number dependent unitary localization length ξ_n:

$$\xi_n \approx a_H \exp\left(\frac{(2n+1)^2}{2\Sigma}\right), \tag{11}$$

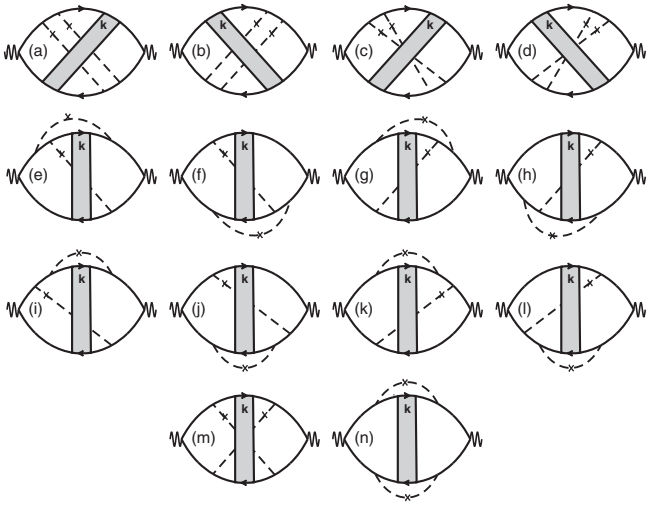

Fig. 3. "Wavelength" contributions (containing 1 Diffuson).

where a_H is magnetic length. For the three lowest Landau levels the values of ξ_n,

$$\xi_0 \approx 1.2a_H, \; \xi_1 \approx 4.5a_H, \; \xi_2 \approx 65a_H, \tag{12}$$

are smaller than the maximum sample length ($L = 100a_H$) used in the numerical calculations of Ref. [1]. Thus we assert that the statement of the linear growth of σ_{xx} peaks with the Landau level number n conjectured from the numerical results of Ref. [1] lies on the hard ground.

Acknowledgements

This work has been supported by RFBR (08-02-01337), Federal Programme on Support of Leading Scientific Schools and RAS Programme. A. A. Greshnov is grateful to V. Yu. Kachorovskii for valuable discussions.

References

[1] A. A. Greshnov, G. G. Zegrya, *Physica E* **40**, 1185 (2008); A. A. Greshnov, G. G. Zegrya, E. N. Kolesnikova, *JETP* **107**, 491 (2008); A. A. Greshnov, G. G. Zegrya, Proc. 15-th Int. Symp. "Nanostructures: Physics and Technology", Novosibirsk, 2007.
[2] H. Levine, S. B. Libby, A. M. M. Pruisken, *Phys. Rev. Lett.* **51**, 1915 (1983); D. E. Khmelnitskii, *JETP Lett.* **38**, 454 (1983).
[3] L. P. Gor'kov, A. I. Larkin, D. E. Khmelnitskii, *JETP Lett.* **30**, 248 (1979).
[4] P. A. Lee, T. V. Ramakrishnan, *Rev. Mod. Phys.* **57**, 287 (1985).
[5] B. Huckestein, *Rev. Mod. Phys.* **67**, 357 (1995); S. Kettemann, *Phys. Rev. B* **69**, 035339 (2004).
[6] Private communications with I. S. Burmistrov, A. D. Mirlin, M. A. Skvortsov.
[7] K. B. Efetov, A. I. Larkin, D. E. Khmelnitskii, *JETP* **52**, 568 (1980).
[8] S. Hikami, *Phys. Rev. B* **24**, 2671 (1981).
[9] K. B. Efetov, *Adv. Phys.* **32**, 53 (1983).
[10] Similar contributions (but convergent at $\omega = 0$) were revealed previously among the usual weak-localization diagrams, see A. P. Dmitriev, V. Yu. Kachorovskii and I. V. Gornyi, *Phys. Rev. B* **56**, 9910 (1997); N. S. Averkiev, L. E. Golub, S. A. Tarasenko and M. Willander, *Phys. Rev. B* **64**, 45405 (2001).

17th Int. Symp. "Nanostructures: Physics and Technology"
Minsk, Belarus, June 22–26, 2009
© 2009 Ioffe Institute

Extended five-stream model for diffusion of implanted dopants in crystalline silicon during fabrication of ultra-shallow p-n junctions

B. B. Khina[1], V. A. Tsurko[2] and G. M. Zayats[2]

[1] Physico-Technical Institute, NASB, 220141 Minsk, Belarus
[2] Institute of Mathematics, National Academy of Sciences, 220072 Minsk, Belarus

Abstract. Ion implantation of dopants into monocrystalline silicon with subsequent thermal annealing is used for fabrication of ultra-shallow p-n junctions in VLSI technology. Decreasing the junction depth is hindered by the phenomenon of transient enhanced diffusion, which is ascribed to the interaction of diffusing species with non-equilibrium point defects. In this work, an extended five-stream model for dopant diffusion in silicon, which takes into account all the possible charge states of both point defects and diffusing pairs "point defect-dopant atom", is presented. Novel initial conditions to the set of nonlinear reaction-diffusion equations are formulated.

Introduction

Ultrashallow p-n junctions (USJ) in modern VLSI circuits are produced by low-energy ($\sim$1$-$10 keV) high-dose ion implantation of dopants into a monocrystalline silicon waver with a subsequent rapid thermal annealing (RTA), the latter is intended to heal the defects generated by implantation and activate the dopant atoms. Decreasing the junction depth permits minimizing the short-channel effect. However, further downscaling the USJ depth (below 40 nm) is hampered by the phenomenon of transient enhanced diffusion (TED): the apparent diffusion coefficient increases by several orders of magnitude, and near the outer surface uphill diffusion takes place [1–3]. Typically, TED is ascribed to the interaction of diffusing species with non-equilibrium point defects (vacancies V and silicon self-interstitials I) accumulated due to ion damage. Solving the intricate problem of TED suppression is impossible without mathematical modeling of this complex phenomenon. However, modern software package SUPREM-IV (by Silvaco Data Systems), which employs the five-stream approach [4–6], encounters difficulties in describing TED. Thus, the goal of this work is to develop an extended five-stream model and formulate new initial conditions to the nonlinear reaction-diffusion problem basing on the experimental concentration profile of dopant after implantation measured by SIMS.

1. Model formulation

1.1. Reaction-diffusion equations

In crystalline silicon, diffusion of dopant atoms proceeds via indirect mechanisms: by pairs "dopant atom-vacancy" (AV) and "dopant atom-silicon self-interstitial" (AI), which exist in several charge states $(\mathrm{AI})^\alpha$, $\alpha = 0, \pm1$ [7]. Also, the diffusion of free point defects X≡V,I, which exist in multiple charge states X^γ, $\gamma = 0, \pm1, \pm2$, takes place [4–6] and is accompanied by interaction between dissimilar diffusing species (generation and recombination of pairs). We consider one-dimensional diffusion of an acceptor impurity, viz. boron (B^-), hence the free charge carries in doped silicon are holes (p). The model consists of four reaction-diffusion equations for diffusing point defects I and V and pairs AV and AI (A≡B^-), which account for the effect of built-in electric field on the diffusion of charged species and include the sink/source terms describing the interaction of dissimilar species:

$$\partial C_\mathrm{I}/\partial t = -\mathrm{div}\, J_\mathrm{I} - R_\mathrm{I\text{-}V} + R_\mathrm{A\text{-}I} + R_\mathrm{AV\text{-}I}, \quad (1)$$

$$\partial C_\mathrm{V}/\partial t = -\mathrm{div}\, J_\mathrm{V} - R_\mathrm{I\text{-}V} + R_\mathrm{A\text{-}V} + R_\mathrm{AI\text{-}V}, \quad (2)$$

$$\partial C_\mathrm{AV}/\partial t = -\mathrm{div}\, J_\mathrm{AV} + R_\mathrm{A\text{-}V} - R_\mathrm{AV\text{-}I} - R_\mathrm{AV\text{-}AI}, \quad (3)$$

$$\partial C_\mathrm{AI}/\partial t = -\mathrm{div}\, J_\mathrm{AI} + R_\mathrm{A\text{-}I} - R_\mathrm{AI\text{-}V} - R_\mathrm{AV\text{-}I}. \quad (4)$$

Since the dopant atoms in the lattice sites are immovable [4–6], the balance equation is written as

$$\partial C_\mathrm{A}/\partial t = R_\mathrm{AI\text{-}V} + R_\mathrm{AV\text{-}I} + 2R_\mathrm{AV\text{-}AI} - R_\mathrm{A\text{-}I} - R_\mathrm{A\text{-}V}. \quad (5)$$

Eqs.(1)–(5) are supplemented with the condition of local electroneutrality:

$$\beta C_\mathrm{A} + \sum_{\alpha=\pm1} \alpha C_{(\mathrm{AI})^\alpha} + \sum_{\alpha=\pm1} \alpha C_{(\mathrm{AV})^\alpha} + \sum_{\gamma=\pm1,\pm2} \gamma C_{\mathrm{I}^\gamma} + \sum_{\gamma=\pm1,\pm2} \gamma C_{\mathrm{V}^\gamma} + p - n_i^2/p = 0. \quad (6)$$

Here C_Y, Y ≡ I,V,AI,AV, is the volumetric concentration of diffusing species (point defects and pairs), which are defined as a sum over all the possible charge states, $C_\mathrm{Y} = \sum_\alpha C_{\mathrm{Y}^\alpha}$, where $\alpha = 0, \pm1$ for pairs AI and AV, $\alpha = 0, \pm1, \pm2$ for point defects; C_A is the concentration of dopant atoms (A ≡ B^-) in the lattice sites and $\beta = -1$ is their charge; α and γ are the charges of pairs and point defects; p is the concentrations of holes; $R_\mathrm{Y-Z}$, Y, Z ≡ I,V,A,AI,AV, Y ≠ Z, are the reaction rates for interaction between dissimilar species; n_i is the intrinsic concentration of free charge carries.

1.2. Diffusion fluxes

The expressions for diffusion fluxes J_Y are obtained using the first Fick's law and Einstein's formula for the mobility of charged species in the built-in electric field assuming that the diffusivity of point defects is independent of their charge [5–7]. Then

$$J_\mathrm{X} = -D_\mathrm{X}\left(\nabla C_\mathrm{X} - \frac{C_\mathrm{X}}{p}\chi_\mathrm{X}\nabla p\right), \quad (7)$$

$$\chi_{\rm X} = \frac{1}{\psi_{\rm X}} \sum_{\alpha=-2}^{+2} \alpha K_{{\rm X}^\alpha} \left(\frac{p}{n_i}\right)^\alpha, \quad \psi_{\rm X} = \sum_{\alpha=-2}^{+2} K_{{\rm X}^\alpha} \left(\frac{p}{n_i}\right)^\alpha,$$

where $D_{\rm X}$, X $\equiv$ V, I, is the diffusion coefficient of point defects, $K_{{\rm X}^\alpha}$ are the equilibrium constants of ionization reactions ${\rm X}^0 + \alpha e^- \leftrightarrow {\rm X}^\alpha$, $K_{{\rm X}^0} = 1$. The values of parameters $D_{\rm X}$ and $K_{{\rm X}^0}$ are known in literature in the Arrhenius form.

Expression for the diffusion flux of pairs AX, X $\equiv$ V, I, are formulated taking into account a difference in the diffusion coefficients of differently charged pairs $({\rm AX})^\alpha$, $\alpha = 0, \pm 1$:

$$J_{\rm AX} = -D_{\rm AX} \left(\nabla C_{\rm AX} + \frac{C_{\rm AX}}{p} \frac{\eta_{\rm X}}{\xi_{\rm X}} \nabla p\right), \tag{8}$$

$$D_{\rm AX} = \frac{1}{\xi_{\rm X}} \sum_{\alpha=-1}^{+1} D_{({\rm AX})^\alpha} K_{{\rm A}^-{\rm X}^{\alpha+1}} K_{{\rm X}^{\alpha+1}} \left(\frac{p}{n_i}\right)^{\alpha+1},$$

$$\xi_{\rm X} = \sum_{\alpha=0}^{+2} K_{{\rm A}^-{\rm X}^\alpha} K_{{\rm X}^\alpha} \left(\frac{p}{n_i}\right)^\alpha,$$

$$\eta_{\rm X} = K_{{\rm A}^-{\rm X}^0} - K_{{\rm A}^-{\rm X}^{++}} K_{{\rm X}^{++}} \left(\frac{p}{n_i}\right)^2, \ {\rm X} \equiv {\rm V, I}.$$

Here $K_{{\rm A}^-{\rm X}^\alpha}$ are the equilibrium constants of pairing reactions ${\rm A}^- + {\rm X}^{\alpha+1} \leftrightarrow ({\rm AX})^\alpha$, $\alpha = 0, \pm 1$; $K_{{\rm A}^-{\rm X}^{\alpha+1}} = C^*_{({\rm AX})^\alpha} / (C^*_{{\rm A}^-} C^*_{{\rm X}^{\alpha+1}})$, where upperscript "*" denotes the equilibrium concentration, i.e. the concentration corresponding to the equilibrium state of the pairing reaction for a particular charge α.

1.3. Kinetic terms

The sink/source terms $R_{{\rm Y}-{\rm Z}}$, Y, Z $\equiv$ I,V,AI,AV, Y $\neq$ Z, are derived using the mass action law and assuming a small deviation from the local equilibrium for a corresponding bimolecular reaction. Summarizing over all charge states, we obtain the following formulas:

$$R_{{\rm I}-{\rm V}} = 4\pi a_0 (D_{\rm I} + D_{\rm V}) \varphi_{{\rm I}-{\rm V}} \left(\frac{C_{\rm I}}{\psi_{\rm I}} \frac{C_{\rm V}}{\psi_{\rm V}} - C^*_{{\rm I}^0} C^*_{{\rm V}^0}\right),$$

$$\varphi_{{\rm I}-{\rm V}} = \psi_{\rm I} + \psi_{\rm V} - 1, \tag{9}$$

$$R_{{\rm A}-{\rm X}} = 4\pi a_0 D_{\rm X} \varphi_{\rm X} \left(C_{\rm A} \frac{C_{\rm X}}{\psi_{\rm X}} - \frac{C_{BX}}{\xi_{\rm X}}\right),$$

$$\varphi_{\rm X} = \sum_{\alpha=0}^{+2} K_{{\rm X}^\alpha} \left(\frac{p}{n_i}\right)^\alpha, \quad {\rm X} \equiv {\rm I, V}, \tag{10}$$

$$R_{{\rm AX}-{\rm Y}} = 4\pi a_0 (D_{\rm Y} + D_{\rm AX}) (C_{\rm AX} C_{\rm Y} - C_{\rm A} C^*_{\rm Y} C^*_{{\rm X}^0} \xi_{\rm X},$$

$${\rm X, Y} \equiv {\rm I, V}, \quad {\rm X} \neq {\rm Y}, \tag{11}$$

$$R_{{\rm AV}-{\rm AI}} = 4\pi a_0 (D_{\rm AV} + D_{\rm AI}) (C_{\rm AV} C_{\rm AI} - C^2_{\rm A} C^*_{{\rm I}^0} C^*_{{\rm V}^0} \xi_{\rm I} \xi_{\rm V}) \tag{12}$$

where $C^*_{\rm X} = \sum_\alpha C^*_{{\rm X}^\alpha}$ is the equilibrium concentration of point defects.

1.4. Boundary and initial conditions

In domain $x \in [0, L]$, the first-kind boundary conditions are posed to Eqs. (1),(2) for diffusion of point defects and the second-kind conditions to Eqs. (3),(4) for diffusion of pairs:

$$C_{\rm X}(x = 0) = C_{\rm X}(x = L) = C^*_{\rm X},$$

$$J_{\rm AX}(x = 0) = J_{\rm AX}(x = L) = 0, \quad {\rm X} \equiv {\rm I, V}. \tag{13}$$

This is motivated by the following considerations. At the outer surface of crystalline silicon ($x = 0$) fast recombination of excess point defects to their equilibrium concentrations can be assumed, while in contact with pure bulk silicon ($x = L$) the concentrations of both vacancies and silicon self-interstitials correspond to the equilibrium values at a given temperature.

Formulation of the initial conditions to Eqs.(1)–(4) is a non-trivial task. The concentration profile of as-implanted dopants is measured experimentally using the second-ion mass spectrometry (SIMS) method ($C^{\rm (SIMS)}_{\rm A}$), while the distribution of point defects after implantation and annihilation of the Frenkel pairs (the so-called "net vacancies" and "net interstitials" $C^{\rm (net)}_{\rm X}$) can only be calculated by Monte Carlo simulation using the "+1" or "+n" model where n is the effective plus-factor [8,9]. Upon heating to the annealing temperature, the pairs AI and AV are formed quickly. Thus, at the attainment of the annealing temperature (at $t = 0$) the total concentration of dopant atoms A, which was measured by SIMS, will include the concentration of these atoms both in pairs ($C_{\rm AI}$ and $C_{\rm AV}$) and in the lattice sites $C_{\rm A}$. Then we can formulate the following set of non-linear algebraic equations [10]:

$$C^{\rm (net)}_{\rm I} = C_{\rm I} + C_{\rm AI}, \quad C^{\rm (net)}_{\rm V} = C_{\rm V} + C_{\rm AV},$$

$$C^{\rm (SIMS)}_{\rm A} = C_{\rm A} + C_{\rm AI} + C_{\rm AV}. \tag{14}$$

Assuming a small deviation from equilibrium, for pairing reactions of acceptor atoms (${\rm A}^- + {\rm X}^{\beta+1} \leftrightarrow ({\rm AX})^\beta$, $\beta = 0, \pm 1$) at the onset of anneal ($t = 0$) we can write:

$$C_{\rm AV} = C_{\rm A} C_{\rm V} \xi_{\rm V} \psi_{\rm V}, \quad C_{\rm AI} = C_{\rm A} C_{\rm I} \xi_{\rm I} \psi_{\rm I}. \tag{15}$$

Thus, the initial conditions $C_{\rm Y}(x, t = 0)$, Y $\equiv$ I,V,AI,AV are determined by solving Eqs. (14),(15) together with the condition of local electroneutrality (6) [10].

Conclusion

An extended five-stream model for diffusion of implanted dopants during thermal annealing, which is used for the fabrication of in modern VLSI technology, is formulated taking into account all the possible charge states of the diffusing species. Novel initial conditions for the profiles of point defects X and pairs AX, X $\equiv$ I, V, are derived. Computer simulation for particular systems will permit determining the optimal regimes of ion implantation and subsequent RTA for obtaining a desirable profile of dopants and holes and hence for optimizing the electrical characteristics of USJ.

References

[1] S. C. Jain *et al*, *J. Appl. Phys.* **91**, 8919 (2002).
[2] S. Solmi *et al*, *J. Appl. Phys.* **94**, 4950 (2003).
[3] M. Ferri *et al*, *J. Appl. Phys.* **99**, 113508 (2006).
[4] A. Ural *et al*, *Phys. Rev. B* **65**, 134303 (2002).
[5] M. D. Giles, *IEEE Trans. Comp.-Aided Design* **8**, 460 (1989).
[6] S. T. Dunham *et al*, *IEICE Trans. Electron.* **E82C**, 800 (1999).
[7] P. M. Fahey *et al*, *Rev. Modern Phys.* **61**, 289 (1989).
[8] G. Lulli *et al*, *J. Appl. Phys.* **82**, 5958 (1997).
[9] G. Hobler *et al*, *J. Electrochem. Soc.* **147**, 3494 (2000).
[10] B. B. Khina, *Defect Diffus. Forum* **277**, 107 (2008).

17th Int. Symp. "Nanostructures: Physics and Technology"
Minsk, Belarus, June 22–26, 2009
© 2009 Ioffe Institute

Hybrid Josephson junctions with s/d-wave symmetry of order parameter for elements of quantum computing systems

Y. V. Kislinskii[1,2], K. Y. Constantinian[1], G. A. Ovsyannikov[1,3], A. V. Shadrin[1], I. V. Borisenko[1], P. V. Komissinskiy[1,4], N. V. Klenov[5] and V. K. Kornev[5]

[1] Kotelnikov Institute of Radio Engineering and Electronics, Mokhovaya 11-7, 125009 Moscow, Russia
[2] Shubnikov Institute of Crystallography, Leninskii prospect 59, 119333 Moscow, Russia
[3] Chalmers University of Technology, SE-412-96, Goteborg, Sweden
[4] University of Darmstadt, Darmstadt, Germany
[5] Physics Department of Moscow State University, MSU 119992 Moscow, Russia

Abstract. Hybrid s/d Josephson junctions Nb/Au/$Ca_{1-x}Sr_xCuO_2$/$YBa_2Cu_3O_7$ were made. I_CR_N products of 100–200 μV were independent on $Ca_{1-x}Sr_xCuO_2$ (CSCO) layer thickness. The second harmonic of current — phase relation up to 40 percent was observed. By estimations, a microscopic quantum tunnelling regime of the junctions may be observed at temperature of 1 K, which is promising for qubit applications.

Introduction

A qubit — two quantum level system with macroscopically distinguished quantum states can be realised as a dc superconducting quantum interference device, which consists of Josephson junctions with nonsinusoidal current phase-relation (CPR). For first and second harmonic in the relation between superconducting current I_S and phase difference across the junction φ, one obtain [1]:

$$I_S(\varphi) = I_{C1}\sin(\varphi) + qI_{C1}\sin(2\varphi). \quad (1)$$

where q is porion of the second harmonic. The device is called as "quiet qubit" because it is stable to magnetic flux fluctuations [2]. Qubit operation can be realised at temperatures below of the junction noise crossover temperature T^*. For $T > T^*$, thermal noise dominates. For temperatures less than T^*, a microscopic quantum tunnelling process is realised and noise current becomes independent on temperature. For d/d bicrystal grain boundary junctions in $YBa_2Cu_3O_7$ (YBCO) d — wave superconductor, the temperature $T^* = 0.05$ K was observed [3]. A source of additional noise in d/d junctions is tunnelling of normal (not superconducting) carriers in nodal direction of d-wave superconductor through a zero energy bound states. According to calculations in article [4], temperature T^* in presence of the tunnelling in nodal directions is so low as 0.025 K. For Nb/Au/YBCO junctions with s — superconductor Nb, the nodal tunnelling is suppressed at low temperatures by s-wave energy gap, and T^* of 0.3 K was calculated [5]. Here we present properties of Nb/Au/$Ca_{1-x}Sr_xCuO_2$/$YBa_2Cu_3O_7$ junctions.

1. Experimental

Josephson junctions Nb/Au/CSCO/YBCO were made from YBCO superconductor 100 nm in thickness, insulator CSCO layer with thickness $d_C = 12$–80 nm, and 10 nm Au film. The three layers were deposited by laser ablation in-situ. By ion etching and evaporation a Nb superconducting layer on the top-square junctions with size $L^2 = 10^2 - 50^2$ μm^2 were made (Fig. 1). Nb and YBCO were superconducting at 4.2 K and four point I-V curves measurements were made. Detector responses were measured by modulation — demodulation technique.

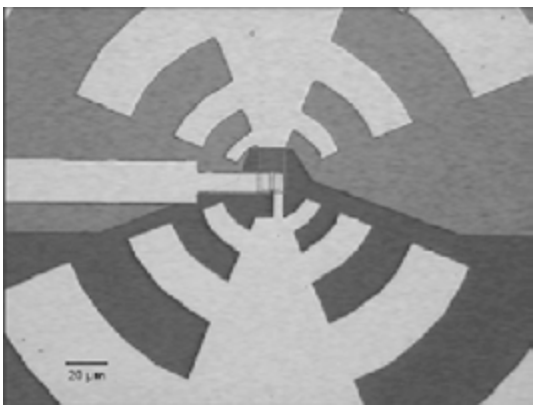

Fig. 1. Hybrid junction, $L = 10$ μm. Au/CSCO/YBCO layers — in upper half, and Nb — in bottom falf of picture.

2. Results and discussion

It is known that junction with sinusoidal CPR shows integer Shapiro step and detector response V_1 under microwave radiation with frequency f at voltage $V_1 = hf/2e$. If the second harmonic of CPR exists half-integer step and response at $V_{1/2} = hf/4e$ appears [6]. Integer at and half-integer responses are shown in Fig. 2.

According to [7] portion of the second harmonic q:

$$q = \frac{1}{2}\sqrt{\frac{\eta_{\frac{1}{2}}R_{D1}}{\eta_1 R_{D\frac{1}{2}}}} \quad (2)$$

where $\eta_{1/2}$ is the difference between maximum and minimum of $\eta(V)$ for half integer response, η_1 the difference for integer one, R_{D1} differential resistance at V_1 and $R_{D1/2}$ the resistance at $V_{1/2}$. The formula is valid in high frequency limit $V_1 \gg I_CR_N$. The q value is 0.3 for data in Fig. 2. By model of resistively

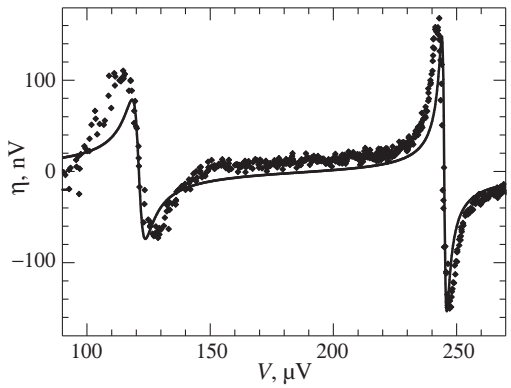

Fig. 2. Junction detector response with $d_C = 20$ nm, $L = 10$ μm on $f = 119.5$ GHz. Points are experimental data, line — RSJ model fit. Integer response is at 245 μV and half-integer — at 121 μV.

shunted junction (RSJ) the line halfwidth of Josephson junction self generation is:

$$\Delta V = 40\ \text{MHz} \times \frac{hR_D^2}{2eR_N} \times \left(1 + \frac{I_C^2}{2I^2}\right), \qquad (3)$$

where I is the junction current. The experimental line width is 2 times wide, than calculated one by the model. We examined critical current density $j_C = I_C/L^2$ versus thickness and observed a decrease with d_C and $R_N L^2$ increase exponentially with d_C as shown in Fig. 3.

Experimental dependency $j_C(d_C)$ was exponential:

$$j_C\,(d_C) = A_j \times \exp\left(-\frac{d_C}{\xi_j}\right), \qquad (4)$$

$A_j = 730$ A/cm^2 and $\xi_j = 7.1$ nm are evaluated from experimental data. Resistances increase with d_C exponentially too:

$$R_N L^2(d_C) = A_R\, exp\left(\frac{d_C}{\xi_R}\right). \qquad (5)$$

From data in Fig. 2 we obtain: $A_R = 0.12$ $\mu\Omega$cm^2 and $\xi_R = 6.9$ nm. Having $\xi_j \cong \xi_R$ the products of $I_C R_N$ do not decrease with CSCO layer thickness at least in 12–50 nm range. At upper temperature of quantum tunneling a deviation of phase difference , which is activated by temperature, is less than a microscopic quantum tunneling deviation. Using this approach from [5] we estimate T^*:

$$T^* = \frac{e}{k_b}\sqrt{\frac{hI_C}{4\pi eC}}, \qquad (6)$$

where k_b — Boltsman constant and C is the junction capacitance. By the estimation formula we obtain for typical hybrid junctions with $I_C = 50$ μA and $C = 2$ pF, the temperature T^* in order of 1 K. Note, that hybrid junctions with c-oriented YBCO have no zero bias conductance peak, so zero energy bound states was not observed in it. Our approximation does not take into account noise from dissipative current of normal carriers through an intrinsic shunt resistance of the junction. Accurate numerical calculations, which consider the shunt resistance [5], gives T^* value of 3 times smaller than the estimation formula for Nb/Au/YBCO. But the $R_N L^2$ of our hybrid

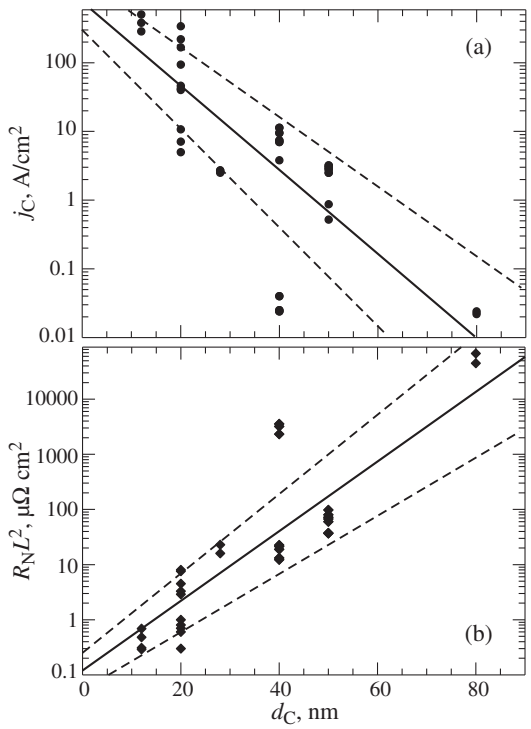

Fig. 3. Dependencies of current density (a) and normal surface resistance (b) versus CSCO layer thickness d_C. Exponential fits for the values are solid lines. Prediction bands with 0.67 probability are shown as dashed lines.

junctions were at least two order large than the reistances of Nb/Au/YBCO, which was considered in [5]. The value of temperature of microscopic tunneling in our c-oriented hybrid junctions was not reported until now and is a subject of future experimental measurements and calculations.

Acknowledgements

The work was supported by President grant for scientific school NSh-5408.2008.2, RFBR 08-02-00487, NMP3-CT-2006-033 191 project and ISTC 3743.

References

[1] M. H. S. Amin *et al*, *Phys. Rev. B* **71**, 064516 (2005).
[2] N. V. Klenov *et al*, *Physica C* **435**, 114 (2006).
[3] T. Bauch *et al*, *Phys. Rev. Lett.* **94**, 087003 (2005).
[4] Ya. V. Fominov *et al*, *JETP Letters* **77**, 691 (2003).
[5] S. Kabawata *et al*, *Phys. Rev. B* **76**, 064505 (2007).
[6] I. V. Borisenko *et al*, *JETP* **99**, 1223 (2004).
[7] P. Komissinskiy *et al*, *Phys. Rev. B* **78**, 024501 (2008).

17th Int. Symp. "Nanostructures: Physics and Technology"
Minsk, Belarus, June 22–26, 2009
© 2009 Ioffe Institute

Electric-field control of electron interference effects in semiconductor 1D nanostructures

V. A. Petrov and A. V. Nikitin
Institute of Radio Engineering and Electronics, Russian Academy of Science, Moscow, 125009, Russia

Abstract. Effects of spatial reproduction for the probability current density $j_x(x, z)$ (or quantum-mechanical current density $ej_x(x, z)$, e being an electron charge) in semiconductor 1D nanostructures in the form of joints in the direction of propagation of the electron wave (the x-axis) of narrow rectangular and wide parabolic (on the z-axis) quantum wires (QWRs) and the possibility to control these effects by the transverse constant electric field in the region of the wide parabolic QWR have been theoretically studied.

Introduction

At present, advances in nanotechnology allow to create semiconductor nanostructures in which linear dimensions 1D or 2D of the conductive channel in the direction of propagation of the electron wave are smaller than the mean free path of the electron. In such a channel particles move in a ballistic regime that allows to study experimentally the effects of ballistic transport in such structures, in particular, various electron interference effects [1]. A large number of theoretical works were devoted to the investigation of electron quantum ballistic transport in 1D and 2D nanostructures whose common feature is the presence in quantum channels of regions of a sharp (nonadiabatic) variation either of the channel's geometry or a potential relief in it [2–4].

The basic objective of our work is to theoretically investigate effects of spatial nonhomogeneity for the probability current density $j_x(x, z)$ (or $ej_x(x, z)$) in semiconductor 1D nanostructures in the form of joints in the direction of propagation of the electron wave (the x-axis) of narrow rectangular and wide parabolic (on the z-axis) quantum wires (QWRs) (z-axis being the axis of the quantization). It is suggested that such structure are constrictions in a 2D electron system (x-z plane). It will be shown that the transverse distribution $j_x(0, z)$ existing at the entry of the wide QWR is reproduced with some accuracy at a definite distance X_1 from the joint (reproduction). This picture is reproduced periodically in cross-sections $X_q = qX_1$ (where q are integer numbers). In this work we also studied theoretically the influence of the transverse (along z-axis) constant electric field strength F in the wide parabolic QWR on these effects in symmetric 1D nanostructures. We have recently presented a detailed numerical analysis of these effects at $F = 0$ for symmetric and asymmetric structures on the basis of 2D parabolic [5] and 2D rectangular [6] quantum wells.

1. Results

We considered the problem of scattering of a monochromatic unit-amplitude electron wave propagating along the lower quantum-dimensional subband ($m = 1$) from narrow rectangular QWR_1 ($x < 0$, $a = 50$ Å) to wide parabolic QWR_2 ($x > 0$) in a 1D nanostructure that is symmetric with respect to the z-axis and that has the parameters of GaAs ($m^* = 0.067m_0$, where m_0 is the mass of a free electron). The interference effects of interest take place in the wide QWR_2.

In this paper, we consider two nanostructures based on a sequence of two such quantum wires: a symmetric nanostructure (Fig. 1a) and an asymmetric nanostructure (Fig. 1b) in which asymmetry is provided by a constant transverse electric field with strength F applied in the region of the wide parabolic quantum wire. The particle motion along all the coordinates is assumed to be separated, and a particle wave vector is directed along the x-axis. We also assume that the potential energy in each of the QWRs does not depend on x varying jump-wise at the point of the joint of the QWRs ($x = 0$). Assuming that the QWRs are defined by a infinite-height-wall potential along the z-axis, the energetic spectrums in this direction are completely discrete.

We have obtained analytical expression for the longitudinal component of the probability current density $j_x(x, z)$ in the QWR_2:

$$j_x(x, z) = \frac{\hbar}{2m^*}\left\{\sum_{n,t} C_n C_t^* \varphi_n(z)\varphi_t^*(z)\left(k_n + k_t^*\right)\exp\left[i\left(k_n - k_t^*\right)\right]\right\}. \quad (1)$$

Here, $\{\varphi_{n,t}(z)\}$ are eigenfunctions of the Schrödinger equations in the parabolic quantum wires at $F = 0$ or $F \neq 0$, $C_{n,t}$ are constant coefficients defining the amplitudes of the waves passed to the QWR_2 through the subbands $E_{n,t}$; $k_{n,t} = [2m^*(E - E_{n,t} - E_d)]^{1/2}/\hbar$ are the wave numbers corresponding to the motion of the particle along the x-axis in the QWR_2. The energy is counted from the conduction band bottom E_d in the 2D system. Let as note that if $E - E_d > E_{n,t}$ then $k_{t,n}$ are real, and the waves corresponding to them are spreading; at inverse inequality $k_{n,t}$ are imaginary, and the waves are damped, with typical lengths of $l_{n,t} = |k_{n,t}|^{-1}$. For the considered structures coefficients B_j and C_n are defined from the system of equations following from boundary conditions for wave functions and their derivatives in point $x = 0$.

Further on, while calculating the $j_x(x, z)$ we will only be interested in undamped at $x \to \infty$ waves with real k in the QWR_2. If all the differences in the exponents of Eq. (1) can be represented in the form $k_n - k_t = q_{n,t}\Delta$, where $q_{n,t}$ are integers, then $j_x(X_1, z) = j_x(0, z)$ for the cross-section $X_1 = 2\pi/|\Delta|$. In this ideal case an initial current profile would be exactly reproduced in cross-sections $X_q = qX_1$, $q = 1, 2, \ldots$ This situation can be approximately realized if the electron energy is much higher than the energy of the lowest levels in the QWR_2:

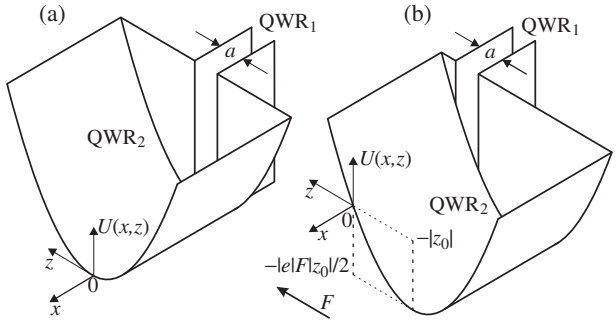

Fig. 1. Schematic diagram of a symmetric 1D nanostructure based on successive narrow rectangular (QWR_1) and wide parabolic (QWR_2) quantum wires in the absence of an electric field ($F = 0$) (a) and in the presence of an electric field ($F \neq 0$) (b).

$E \gg E_n$. Indeed, keeping in expansion of $k_{n,t}$ terms up to the second order over the small parameter E_n/E, we obtain $k_n - k_t \approx (m^*/2E)^{1/2}(E_t - En)/\hbar$. For a number of important cases the differences $(E_t - E_n)$ are proportional to integers.

The complete probability current density (or the complete quantum-mechanical current density) along the x-axis $J_x = \int j_x(x, z)dz$ as a consequence of the orthonormalized character of the functions $\{\varphi_{n,t}(z)\}$ has no coordinate dependence from x, as in Eq. (1) there are only terms with $n = t$ where the terms of the sum corresponding to subbands with $E_{n,t} > E$ and imaginary $k_{n,t}$ are equal to zero. It should be noted that the conductance of the structure $G = |J_x/V|$ does not depend on x.

For the parabolic QWR the difference $(E_t - E_n) = \hbar\omega_0(t - n)$, where $(t - n)$ is always an integer; the profile of the initial distribution $j_x(0, z)$ at the entry to the parabolic QWR_2 is reproduced in an asymmetric QWR_2 on the x-axis at the points $X_q = qX_1$, where X_1 is given by

$$X_1 = \frac{4\pi}{\omega_0}\left(\frac{E_x}{2m^*}\right)^{1/2}. \qquad (2)$$

In the symmetric structure, the synphase sections are found twofold as often as in an asymmetric structure. The frequency $\omega_0 = (K/m^*)^{1/2}$ is controlled by the curvature of the parabola K; this curvature depends on the parameters of the nanostructure.

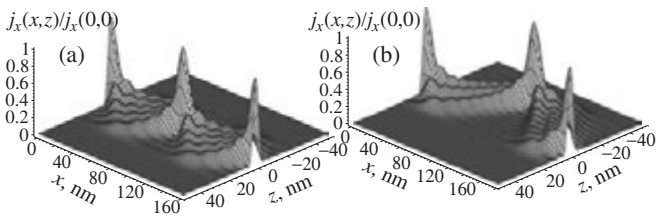

Fig. 2. Spatial distribution of normalized probability current density $j_x(x, z)/j_x(0, 0)$ in parabolic QWR_2 for a symmetric 1D nanostructure with GaAs parameters demonstrating reproduction effects in the cross sections $x = X_1$ and $x = X_2$ at $F = 0$ (a) and during modification of these effects at $F = 1 \times 10^5$ V/cm (b). Calculation was performed for $a = 50$ Å (QWR_1) and a distance $\hbar\omega_0 = 30$ meV between the bottoms of subbands in parabolic QWR_2.

Figure 2a shows the spatial distribution of normalized probability current density $j_x(x, z)/j_x(0, 0)$ in the wide QWR_2 in the x-z plane for a symmetric 1D nanostructure demonstrating (in these approximations) the reproduction effects in the cross sections corresponding to $x = X_1$ and $x = 2X_1$.

Let us consider the situation in the presence of a constant transverse electric field with strength F. The field is applied in the region of the wide parabolic quantum wire and is directed along the z-axis. After application of the electric field, reproduction period X_1 increases owing to the appearance of asymmetry in the structure — the shift of the parabola along the z-axis by z_0 and becomes dependent on F owing to the energy shift of the oscillator spectrumin.

Figure 2b shows the results of calculation of a modification of reproduction effects for normalized probability current density $j_x(x, z)/j_x(0, 0)$ in the wide parabolic QWR_2 in the x-z plane for $F = 1 \times 10^5$ V/cm in the approximation of expanded and real k_x.

Acknowledgements

The authors would like to thank V. G. Baru for useful discussions.

References

[1] D. K. Ferry and S. M. Goodnick, *Transport in Nanostructures*, Cambridge Univ. Press, Cambridge 1997.
[2] E. Tekman, S. Ciraci, *Phys. Rev. B* **43**, 7145 (1991).
[3] Fernando Sols, M. Macucci, U. Ravaioli, and K Hess, *J. Appl. Phys.* **66**, 3892 (1989).
[4] O. Olendski and L. Mikhailovska, *Phys. Rev. B* **66**, 035331-1 (2002).
[5] V. A. Petrov and A. V. Nikitin, *Fizika i Tekhnika Poluprovodnikov* **39**, 436 (2005) [*Semiconductors* **39**, 412 (2005)].
[6] V. A. Petrov and A. V. Nikitin, *Radiotekhnika i Elektronika* **52**, 1387 (2007) [*Journal of Communications Technology and Electronics* **52**, 1286 (2007)].

17th Int. Symp. "Nanostructures: Physics and Technology"
Minsk, Belarus, June 22–26, 2009
© 2009 Ioffe Institute

Numerical simulation of single electron transport in disordered Cr granular films

V. A. Krupenin[1], *V. O. Zalunin*[1,4], S. A. Vasenko[1] and A. B. Zorin[2,3]

[1] Laboratory of Cryoelectronics, Moscow State University, 119899 Moscow, Russia
[2] Physikalisch-Technische Bundesanstalt, 38116 Braunschweig, Germany
[3] Nuclear Physics Institute, Moscow State University, 119899 Moscow, Russia
[4] Mirantis Inc, 107023, Moscow, Russia

Abstract. New results of the numerical study of single electron transport in two dimensional Cr granular films are presented in this paper. The model based on two-dimensional array of Coulomb-blockade islands is used to perform Monte-Carlo simulations. This model allows to discover the stable discrete charge states in both Coulomb Blockade and conducting regions. Also, it describes the nature of sharp current jumps early reported experimentally [1].

Introduction

Granular films are the promising candidates to replace lithographically defined islands and the tunnel barriers in various single-electron devices. Typical size of grains in such structures is in the range of 2–20 nm, which enables these devices to operate at temperatures higher than 4.2 K. The properties of granular single-electron devices strongly depend on their parameters like: self capacitance of islands (grains), mutual capacitance and resistance between grains, operation temperature, etc. These granular films with the intergrain capacitance much higher than the self capacitance of the grains have been studied before in both ways: numerical and experimental [1,3]. In this paper we present the results of numerical modeling of single-electron transport in these Cr granular films which allows us to describe the fundamentals of sharp current jumps (which had not been investigated before).

1. Experimental samples

The experimental samples based on Cr granular films (numerical modeling of which is presented in this paper) have the size of 500 × 100 nm, their thickness is 7–8 nm and are connected to the conducting leads. The pronounced Coulomb Blockade region with the threshold voltage about 3–4 mV are observed at the I–V characteristics of these samples measured at the low temperature T_{bath}: $T_{\text{bath}} \approx 25$ mK (see Fig. 1). Moreover, the switch between the blockade and the conducting region are accompanied by sudden current jump of an amplitude about 200–900 pA. One can find the fabrication and measurement details in [1].

2. Numerical modeling results

It is assumed that the experimental results presented in the previous section can be caused by the influence of the local charge traps formed by the inhomogeneities of the granular film. A model of uniform two dimensional array of conducting island [2] separated by the tunnel junctions with the localized inhomogeneities is used to perform a numerical study of single-electron transport in this structure. The size of the array is chosen as $m \times n = 11 \times 50$ islands to be according to the experimental samples.

According to the results of numerical computations of potential profile [3], the inhomogeneity forms a local trap (potential well). When the first electron enters the array, it is captured in this trap and forms local potential maximum. As the size of this potential maximum (the polarization screening length) $\Lambda \approx 5$–6 is comparable with the width of the array $m = 11$, it forms an additional potential barrier placed at the inhomogeneity. While the bias voltage increasing, it becomes more energetically favorable for the system to have the charge configuration with more than one excess electron. The next electrons entering this array are blocked by the influence of the potential barrier formed by the first electron. Therefore, they fill up the potential well formed by both: the left boundary of the array and and this potential barrier. These electrons form the configuration when one of the electrons is always located at the center of inhomogeneity while others form one of discrete number of stable shapes depending on the applied bias voltage. Fig. 2 shows the example of such configurations and corresponding potential distribution. In general, inhomogeneity can be placed in an arbitrary position and have an arbitrary form. Fig. 2 shows one of them (inhomogeneity consisted of 5 islands which have ohmic contact and placed at the center of array). Also, this figure shows the system in five different charge distributions at the following bias voltages V_b: 5.81 mV, 5.91 mV, 6.01 mV, 6.16 mV, 6.23 mV. Note that these num-

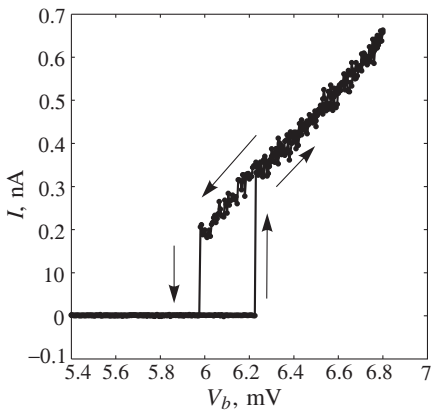

Fig. 1. Experimental example of the sharp current jumps between the blockade and conducting states. Arrows denote changing the current at increasing/decreasing bias voltage.

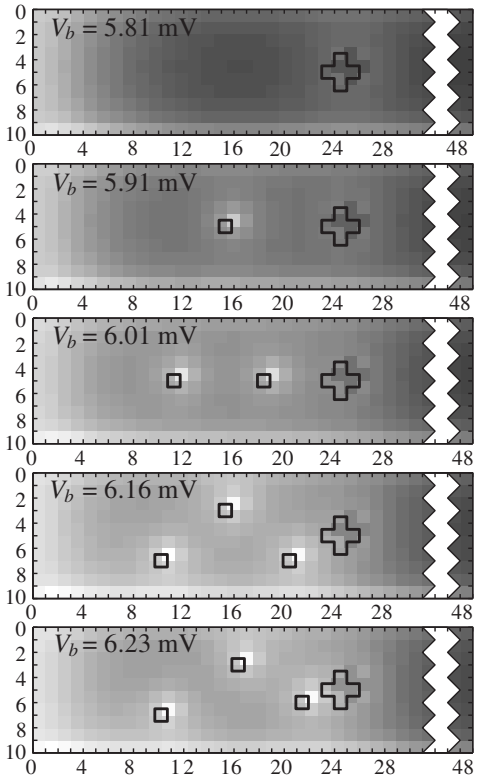

Fig. 2. Stable charge configuration formation example. The lighter color corresponds to higher potential. Areas bounded by the black solid curve corresponds to islands, where excess charges are located. Different panels corresponds to different bias voltages.

bers, indeed, represent the centers of the segments where these configurations are realized. When the bias voltage reaches the Coulomb Blockade threshold (for this example, it equals to 6.25 mV), the stable states are no longer energetically favorable and the current starts to flow through the film.

In the conducting region the studied system also can be found at the different states. Each of these states is characterized by the spatial distributions of the film charge and current. In contrast with the Coloumb Blocakade region, in the conducting region several different states can coexist simultaneously at a fixed value of bias voltage. Fig. 3a shows the distribution of time between two subsequent events of electrons tunneling out from the array to the leads. There are two distinct branches on this plot, each of them is characterized by the tunneling time; and, they correspond to one of the charge/current states. The lower branch in Fig.3a corresponds to the fully conducting state, while the upper one represents the short-term blockade of the electron transport through the array. Slightly above the Coulomb Blockade threshold (represented by vertical dashed line on Fig. 3a) the intensity of the lower, conducting branch is negligibly small and system spent almost all the time in the short-term blockade state. But then, with the increasing of the bias voltage V_b the time spent in lower conducting branch increases. With the increasing of the bath temperature T_{bath} the influence of the thermal fluctuation increases, allowing the system to form new charge/current states. As one can see on Fig. 3b, the increasing of the bath temperature results in new branches in the tunneling time distribution, which indicates the new charge/current states.

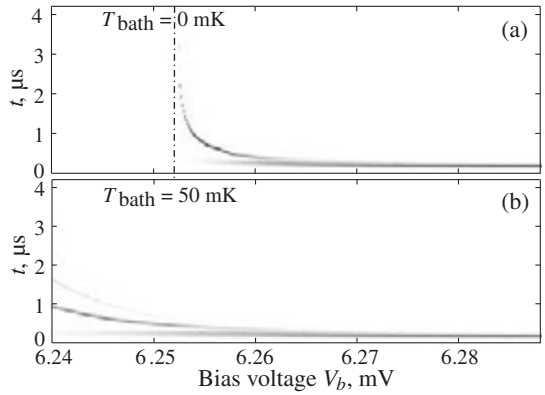

Fig. 3. The 2D plot of tunneling time distribution versus the bias voltage representing 3D figure by color intensity (white color corresponds to zero number of tunneling events, black — maximum value depends on each V_b).

It is well known that in the different materials at the temperature below 1 K, the coupling between electron and phonon gases becomes small. In case of the structure considered in this paper (where the conducting islands separated by tunnel barriers) hot electrons tunneling through the barrier heat the electron gas up to the temperature T_e, which is much higher than the temperature of phonon gas T_{ph} and the substrate temperature T_{sub}. When the system is in the blockade state, the current is equal to zero and no heat is dissipated. So, $T_e = T_{ph} = T_{sub}$. Slightly above the Coulomb blockade threshold the transport current is low and heat dissipation is low too. Once the system switches to the conducting state (lower branch in the tunneling time distribution), hot electrons which tunnels through the barriers start to heat up the electron gas of the islands. At the same time, the increasing of T_e causes the increasing of the transport current. So, the more time system is in the conducting state, the lower the probability of returning back to short-term blockade state. Once it hits the certain temperature the system can not switch back to lower partially blockade branch. This process describes the current jumps observed during the experiment on I–V curves [1].

Acknowledgements

This work has been supported in part by the grant "Program of Fundamental Research of Presidium of RAS #27".

References

[1] V. A. Krupenin , V. O. Zalunin and A. B. Zorin, *Microelectronic Engineering* **81** , 218 (2005).

[2] N. S. Bakhvalov, G. S. Kazacha, K. K. Likharev, S. I. Serdyukova, *Sov. Phys. JETP* **68**, 581 (1989).

[3] V. A. Krupenin, V. O. Zalunin, S. A. Vasenko, A. B. Zorin, *Proc. of 15th Int. Symposium "Nanostructures: Physics and Technology"* (2007), Ioffe Institute, 2007.

17th Int. Symp. "Nanostructures: Physics and Technology"
Minsk, Belarus, June 22–26, 2009
© 2009 Ioffe Institute

Self-action of laser beam at resonant excitation of the basic exciton transition in colloidal quantum dots

V. S. Dneprovskii[1], T. Wumaier[1,2], E. A. Zhukov[1] and S. Dau[1]

[1] Physics Faculty of M. V. Lomonosov Moscow State University, 119991 Russia
[2] Xinjiang Technical Institute of Physics and Chemistry, CAS, China

Abstract. We have explained the revealed self-action of ultrashort powerful laser pulses in highly absorbing colloidal solution of CdSe/ZnS quantum dots (QDs) in the case of one-photon resonant excitation of the basic exciton transition by saturation of absorption (creating of the transparency channel and limiting aperture), strip-effect, and self-diffraction.

Highly luminescent semiconductor Green 545 CdSe spherical core capped with epitaxial ZnS shell and surface trioctylphosphine hydrophobic layer QDs were fabricated by NFM LTD corporation (republic Belarus). To achieve the resonant excitation of the basic exciton optical transition in CdSe/ZnS colloidal QDs by single 30-picosecond pulse of the second harmonic (2.33 eV) of mode-locked Nd^{3+} YAG — laser QDs of appropriate size (radius) for resonant excitation of excitons have been choosed using the transmission and photoluminescence (PLE) excitation spectroscopy methods.

The modified method of PLE spectra measurement has been utilized. The traditional way is the selection of a narrow band from the inhomogeneously broadened luminescence spectrum of QDs and measurement of the luminescence intensity at different wavelength of the exciting light. The application of Cooled Pixis 256 CCD camera possibilities has allowed us to measure a great number of photoluminescence spectra using in each case excitation by the light beam step by step at different wavelength with $\Delta\lambda \approx 1$ nm. Thus PLE spectra at different registration wavelength (for QDs of different size) can be received using this ensemble of PL spectra. The PLE spectrum at 552 nm PL wavelength is shown in Fig. 1. This photoluminescence wavelength corresponds to QDs with maximum absorption in ensemble of QDs with size dispersion. The splash at 552 nm is the track of the exciting light beam at the wavelength of the luminescence spectrum maximum. In CdSe QDs the emitting state is different from the absorbing one. The Stokes shift (the observed 80 meV shift of the maximum of luminescence spectrum compared with the maximum of absorption spectrum) arises in QDs due to the crystal field in the hexagonal lattice, nonspherical shape and electron-hole exchange interaction [1–3]. The latter effect follows R^{-3} dependence and is strongly enhanced by spatial confinement in small QDs. The exchange interaction induces splitting of exciton transition in the optically active absorbing state and optically passive emitting state ("dark-exciton"). Optically passive dark-exciton is responsible for the LO-assisted luminescence of CdSe QDs. We have defined the radius of QDs (2.5 ± 0.4 nm) comparing the energy of the basic $1S_{3/2}(h) - 1S(e)$ electron-hole (exciton) transition (the energy of the minimum of transmission and the maximum of luminescence excitation spectra, and the half width of the transmission spectrum) with the theoretical [4] dependencies of discrete energy transitions in CdSe QDs on their radius. The density of QDs in toluene was about 10^{18} cm^{-3}. The measured linear transmission of the sell with colloidal solution of QDs was less than 0.02.

The transmitted intensity profile has been measured in the case of resonant excitation of the basic exciton optical transition by focused Gaussian laser beam in which the intensity falls down fluently from its centre to periphery. Only at high input intensities of the laser beam the circular like distributions of the output intensity with maximum or minimum intensity in

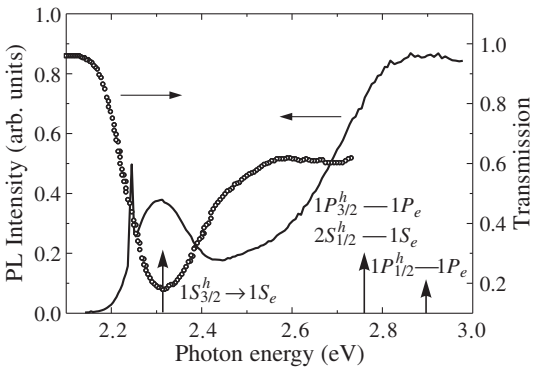

Fig. 1. Transmission (circles) and photoluminescence excitation (solid line) spectra of CdSe/ZnS QDs.

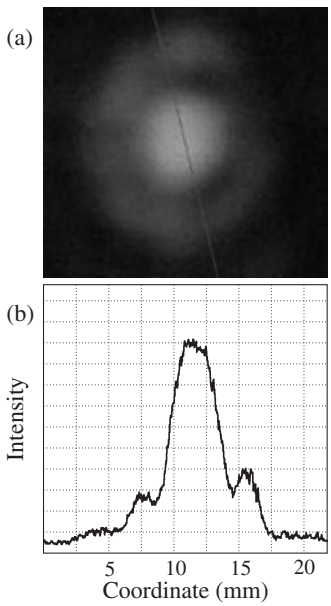

Fig. 2. The transmitted intensity profile of the laser beam (a) and radial distribution of the transmitted intensity (b) along the shown in (a) line in the case of input intensity 1.0 GW/cm^2.

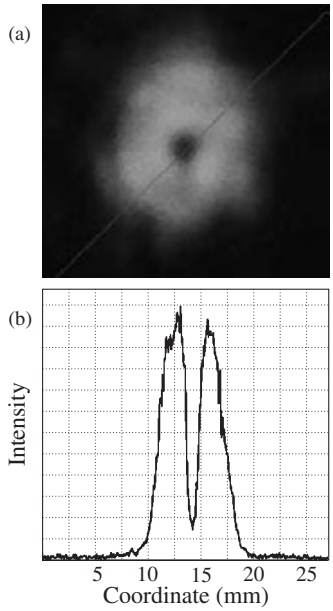

Fig. 3. The transmitted intensity profile of the laser beam (a) and radial distribution of the transmitted intensity (b) along the shown in (a) line in the case of input intensity 1.2 GW/cm^2.

the centre were observed (Fig. 2 and 3).

The observed distribution of the transmitted intensity at different intensity of the exciting laser beam (Fig. 2 and 3) may be explained by propagating of the cross-section limited powerful laser beam in nonlinear media with parameters depending upon the intensity of light. Several processes coexist in the case of resonant excitation of the basic exciton optical transition of colloidal CdSe/ZnS QDs.

Firstly — efficient *state-filling (saturation)* effect. The observed bleaching of laser excited semiconducting QDs was explained in [5] by state filling, and the data were fit to the saturable absorption of two-level system model with saturable α_0 and nonsaturating background α_B absorption:

$$\alpha = \alpha_B + \frac{\alpha_0}{(1 + I/I_S)},$$

where I is the intensity of exciting laser beam and I_S is an invariable saturating intensity. As it was shown in [6], at high input laser intensities it is necessary to take into account the dependence of saturating intensity on the relaxation time τ of the exciton excited state ($I_S \propto 1/\tau$). The relaxation time τ is invariable at moderate intensities and decreases at high intensity ($\tau \propto I^{-2}$) because of the efficient Auger recombination [7]. The decreasing of τ must be taken into consideration: $I_S = I_S^c + \eta I^2$, where I_S^c is invariable part of saturating intensity. Thus the equation for numerical computation in which the relaxation time dependence upon the intensity of the laser beam is taken into account:

$$\frac{dI}{dz} = -\alpha_B - \frac{\alpha I}{1 + \frac{I}{I_S^c + \eta I^2}}. \qquad (1)$$

Nevertheless in our case even at high laser exciting intensities strong saturation effect arises in spite of the fact that the saturation intensity increases. The measured dependence of colloidal CdSe/ZnS transmission on the laser exciting intensity is shown in Fig. 4. The saturation parameter is still great: $I/I_S > 10$.

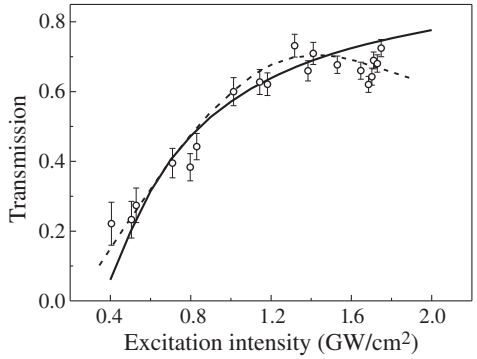

Fig. 4. The measured (open circles) and calculated (using Eq. (1)) dependence of CdSe/ZnS QDs' transmission vs the intensity of exciting laser pulse: $I_S = 30$ MW/cm^2, $\eta = 0$ (solid line) and $I_S = 30$ MW/cm^2, $\eta = 30$ cm^2/MW (dashed line).

Secondly, in the case of great linear absorption and efficient resonant saturation of the basic exciton optical transition in CdSe/ZnS QDs the laser beam creates the channel of transparency in which the absorption is small due to strong saturation. Thus the Gaussian laser beam can penetrate through colloidal solution of QDs losing its external layers of lower intensity for which the saturation is weakened. The latter process is called *"strip-effect"*.

Thirdly, due to the saturation and strip effects *Fresnel self-diffraction* by induced masking aperture may arise. The diameter of masking aperture may be tuned by changing the laser input intensity. Thus the cross-section of the output intensity (Fig. 2 and 3) depends upon the number of the opened Fresnel zones.

Acknowledgements

This work was supported by Russian Foundation for Basic Research (grants 08-02-00205 and 08-02-90102).

References

[1] A. L. Efros *et al*, *Phys. Rev.* **B 46**, 7448 (1992).
[2] A. L. Efros, A. Rodina,*Phys. Rev.* **B 47**, 10005 (1993).
[3] M. Nirmal, D. Norris, M. Kuno, M. Bawendi, A. L. Efros, and M. Rosen, *Phys. Rev. Lett.* **75**, 3728 (1995).
[4] A. I. Ekimov, F. Hashe, M. C. Schanne-Klein, D. Ricard, C. Flytzanis, I. A. Kudryavtsev, T. V. Yaseva, A. V. Rodina, and A. L. Efros, *J. Opt. Soc. Am.* **B 10**, 100 (1993).
[5] N. Peighambarian and S. W. Koch *Semiconductor Nonlinear Materials* in *Nonlinear Photonics* H. M. Gibbs, G. Khitrova, N. Peighambarian (Eds): Springer-Verlag Berlin Heidelberg, 1990.
[6] V. Dneprovskii, D. Kabanin, V. Lyascovskii, T. Wumaier and E. Zhukov, *phys. stat. sol.* **(c) 5**, 2503 (2008).
[7] V. Dneprovskii, A. Efros, A. Ekimov, V. Klimov, I. Kudriavtsev, M. Novikov, *Solid State Commun.* **74**, 555 (1990).

17th Int. Symp. "Nanostructures: Physics and Technology"
Minsk, Belarus, June 22–26, 2009
© 2009 Ioffe Institute

Excitons and magnetic polarons in type-II ZnMnSe/ZnSSe QWs

A. S. Brichkin[1], A. V. Chernenko[1], V. D. Kulakovskii[1], S. V. Sorokin[2] and S. V Ivanov[2]

[1] Institute of Solid State Physics, RAS, 142432, Chernogolovka, Russia
[2] Ioffe Physical-Technical Institute, St Petersburg, Russia

Abstract. Time-resolved and CW photoluminescence spectra of ZnMnSe/ZnSSe MQWs measured at temperatures 2–20 K in the magnetic field up to 10 T in Faraday and Voigt geometries revealed that excitons and excitonic magnetic polarons coexist in photoexcited samples. Their kinetics and dependence on various parameters are studied. The in-plane size of excitonic magnetic polaron and its variation with magnetic field are obtained from the analysis of LO-phonon replicas of the polaron line. Two mechanisms of magnetic polaron formation consistent with experimental results are proposed.

Introduction

Type II semimagnetic (diluted magnetic) QWs are very attractive objects to study formation of excitonic magnetic polarons and their kinetics because of long, ns range, excitonic life-time caused by the spacial separation of electrons and holes. One of the most interesting questions is the dynamics of excitonic magnetic polarons (EMPs') formation and their temporal evolution. We report about magnetophotoluminescence CW and time resolved measurements of excitons and polarons in semimagnetic ZnMnSe/ZnSSe MQWs.

1. Experiment

Two MBE grown samples containing 10 periods of $Zn_{0.9}Mn_{0.1}$ Se[8 nm]/$ZnS_{0.16}Se_{0.84}$[18 nm] (sample A) and $Zn_{0.84}$ $Mn_{0.16}$ Se[8 nm]/$ZnS_{0.16}Se_{0.84}$[18 nm](sample B) QWs' are used for measurements. Photoluminescence (PL) spectra under CW excitation shown in Fig. 1 and 2 revealed two relatively broad lines with FWHM about 12–15 meV separated by 20 meV. The LO-phonon and 2LO-replicas of a lower line is well resolved in the spectra, whereas the LO-replicas of a upper line are invisible. Detailed studies allow us to attribute the high and low energy lines to recombination, respectively, of weakly localized excitons and excitonic magnetic polarons (EMPs). The intensity of the lower energy line quickly decreases with the increase of temperature within the range of 2–12 K in both samples, whereas the intensity of the upper line increases with T. The fast temperature decrease of the intensity of lower energy line is related with dissipation of EMP.

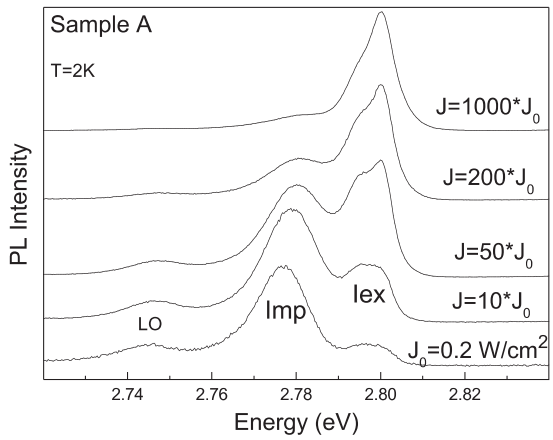

Fig. 1. PL spectra of the sample A with $x = 10\%$ Mn recorded at $B = 0$ T and various levels of excitation power.

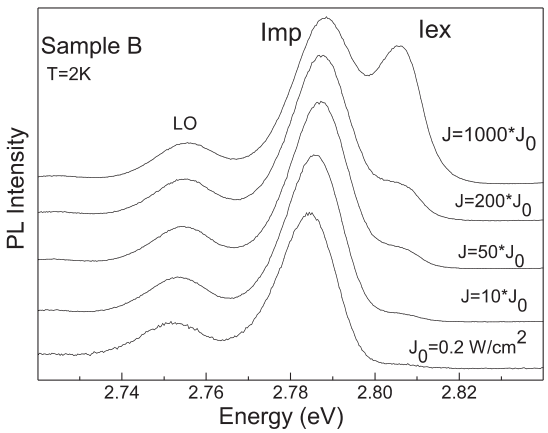

Fig. 2. PL spectra of the sample B with Mn content ($x = 16\%$ Mn) recorded at $B = 0$ T and various levels of excitation power.

The EMP line dominates in PL spectra at low excitation power ($J = 0.2$ W/cm^2) in the sample A as it is shown in Fig. 1. The intensity of the exciton line quickly increases with J whereas the increase of EMPs' line is much smaller. The EMP line demonstrates saturation with the increase of excitation power so that the exciton line dominates in spectra at J higher than 10 W/cm^2. Contrary to this, in sample B the EMP line dominates in whole range of J and only at the highest excitation power $J = 200$ W/cm^2 the intensity of exciton line becomes comparable to that one of EMP line (see Fig. 2).

In the magnetic field $B \parallel Oz$ both lines exhibit substantial redshift and becomes σ^+ polarized. The exciton line shifts faster than EMP line and at high magnetic filed $B = 6 - 10$ T these lines coincide so that the only line remains in the spectrum. The intensity of the exciton line increases with the increase of B in the sample A, whereas the EMP line and its phonon replicas disappear from the spectra at B higher than 3 T. In the sample B EMP line and the 1LO-phonon replica dominates in spectra up to magnetic field $B = 10$ T. The presence of the LO-phonon replicas in PL spectra of the sample B indicates the presence of EMP even in high magnetic fields, whereas disappearance of LO-phonon replicas in sample A confirms the EMP suppression by magnetic field $B \parallel Oz$. In both samples LO-phonon replicas are stronger in Voigt geometry then in the Faraday one.

EMP effects are much more pronounced in the sample B with the higher Mn content. The main difference in spectra of

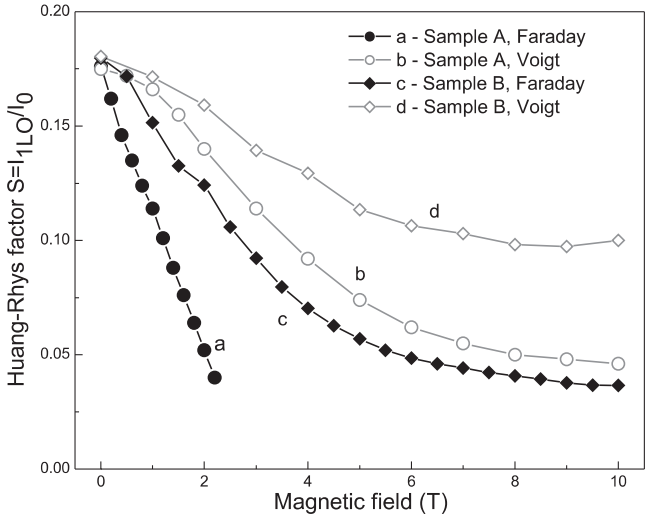

Fig. 3. The ratio of the intensities of the 1LO-phonon replica and the no-phonon (NP) EMP line (Huang–Rhys factor) for both samples recorded in Faraday and Voigt geometries.

samples is related to the different amount of EMP formation centers. One of important characteristics of EMPs is its effective volume. To estimate the EMP volume and its change with B the magnetic field dependences of the ratio of intensities of LO and no-phonon EMP emission lines are investigated both in Faraday and Voigt geometries. The localization volume determines the range of allowed k-space for emitting LO phonons. As a consequence the relative intensity of the LO-phonon replicas or Huang–Rhys factor decreases approximately proportional to the EMP localization radius as it is shown in Fig. 3. The value of EMP localization radius $r_{\rm loc} = 3-4$ nm are found for both samples. In the sample B $r_{\rm loc}$ increases weakly, less than 2 times at the in-plane magnetic field $B = 10$ T, and about 5 times at magnetic field of 10 T normal to the QW's plane. In the sample A the increase of $r_{\rm loc}$ is much stronger: about 4 times at $B = 10$ T in the Voigt geometry and nearly ten-fold in the magnetic field of 3–4 T in the Faraday geometry.

Time-resolved spectra of both samples are measured under above band gap pulsed excitation with pulse duration and pulse repetition are 1.5 ps and 80 MHz, respectively, for detailed studies of EMP kinetics. These measurements reveal a fast kinetics of weakly localized excitons with lifetime $\tau \sim 100$ ps and slow one of EMPs with 5 ns which is comparable to the distance between the exciting pulses.

The EMP emission demonstrates two formation kinetics. The fast one has a characteristic time $\tau_1^{\rm EMP} \sim 30 - 50$ ps whereas the slow one continues $\tau_2^{\rm EMP} \sim 150 - 200$ ps. The fast kinetics results in an increase of the EMP emission just at the spectral position of the EMP line whereas the slow one starts from the emission of delocalized excitons and is followed by a monotonic shift of the emission (∼15 meV) to the EMP position. The slow process is the typical EMP formation process. It starts from a hole localization on potential fluctuations with subsequent gradual alignment of Mn ion spins due to p–d exchange interaction. The fast process demands the holes to be captured by potential fluctuations with spin polarized Mn ions. Such fluctuations appear after the EMP recombination. The relaxation of macroscopic magnetic moment of EMP is quite slow process which provides their living during several ns till the next exciting pulse. Note that this process provides a nearly half of photoexcited EMP at the pulse repetition of 12 ns.

2. Conclusions

Time-resolved and CW photoluminescence studies of ZnMnSe/ZnSSe MQWs at various levels of optical excitation, temperatures, magnitude and direction of magnetic fields revealed coexistence of excitons and excitonic magnetic polarons. The interrelations between PL lines of these qusiparticles are studied. These studies allow one to estimate the in-plane size of EMP and its dependence on magnetic field. Two types of EMP formation kinetics, fast and slow, are proposed in order to explain experimental results.

Acknowledgements

This work was supported by RFBR grants.

17th Int. Symp. "Nanostructures: Physics and Technology"
Minsk, Belarus, June 22–26, 2009
© 2009 Ioffe Institute

Exciton localization and sp-d energy transfer in CdMnTe/CdMgTe nanostructures with ultrathin narrow-gap magnetic layers

V. F. Agekyan[1], P. O. Holtz[2], G. Karczewski[3], E. S. Moskalenko[4], A. Yu. Serov[1] and N. G. Filosofov[1]

[1] V. A. Fock Institute of Physics of St Petersburg State University, 198504 St Petersburg, Russia
[2] IFM Material Physics, Linköping University S-581 83 Linköping, Sweden
[3] Institute of Physics of the Polish Academy of Science, 02-668 Warsaw, Poland
[4] Ioffe Physical-Technical Institute, St Petersburg, Russia

Abstract. Exciton and Mn^{2+} $3d$ intracenter luminescence (Mn^{2+}IL) was studied from series of CdMnTe/CdMgTe periodic systems with various thicknesses of CdMnTe thin narrow-gap inclusions and CdMgTe barriers. The spectra of localized excitons and their temperature transformation account for the real layer profiles. The intensity of Mn^{2+} IL in CdMnTe layers decreases in magnetic field due to the spin conservation restrictions on the energy transfer from the band states to the manganese $3d$-shell.

Introduction

MBE grown II–VI structures with specifically arranged ultrathin planes of a narrow-gap component are interesting for the optical studies and offer promise for practical applications. The inclusions with the nominal thickness from tenth of monolayer (ml) to several mls are intermediate between small size defects and narrow quantum wells. Of importance are the narrow-gap layer thickness and elemental composition as well as the spacing between the layers. The II–VI matrices containing the thin layers of dilute magnetic semiconductors (DMS) exhibit strong magnetic properties including high and controllable magnetic anisotropy which are of interest for spintronics.

The objective of this work is to investigate 1) the luminescence spectra of excitons localized on the ultrathin narrow-gap CdMnTe layers and 2) magnetic-field effect on the rate of energy transfer from the band states to $3d$-shell of Mn^{2+} ions.

1. Experimental

By MBE on the GaAs (100) substrate we grew the 4 μm CdTe and 1.4 μm CdMgTe buffer layers, CdMnTe/CdMgTe superlattices, and cap CdMgTe layers with no interruption of growth at the interfaces. We studied three series ##1–3 of structures containing the periodically embedded narrow-gap CdMnTe layers with the following nominal parameters:

#1. 0.5 ml $Cd_{0.75}Mn_{0.25}Te$ / 50 ml $Cd_{0.7}Mg_{0.3}Te$;
1.5 ml $Cd_{0.75}Mn_{0.25}Te$ / 50 ml $Cd_{0.7}Mg_{0.3}Te$;
3.0 ml $Cd_{0.75}Mn_{0.25}Te$ / 50 ml $Cd_{0.7}Mg_{0.3}Te$.

#2. 1.0 ml $Cd_{0.9}Mn_{0.1}Te$ / 4 ml $Cd_{0.6}Mg_{0.4}Te$;
1.0 ml $Cd_{0.9}Mn_{0.1}Te$ / 8 ml $Cd_{0.6}Mg_{0.4}Te$;
1.0 ml $Cd_{0.9}Mn_{0.1}Te$ / 15 ml $Cd_{0.6}Mg_{0.4}Te$;
1.0 ml $Cd_{0.9}Mn_{0.1}Te$ / 40 ml $Cd_{0.6}Mg_{0.4}Te$.

#3. 6 ml $Cd_{0.9}Mn_{0.1}Te$ / 30 ml $Cd_{0.6}Mg_{0.4}Te$;
3 ml $Cd_{0.9}Mn_{0.1}Te$ / 30 ml $Cd_{0.6}Mg_{0.4}Te$;
3 ml $Cd_{0.9}Mn_{0.1}Te$ / 4 ml $Cd_{0.6}Mg_{0.4}Te$ /
3 ml $Cd_{0.9}Mn_{0.1}Te$ / 30 ml $Cd_{0.6}Mg_{0.4}Te$;
3 ml $Cd_{0.9}Mn_{0.1}Te$ / 12 ml $Cd_{0.6}Mg_{0.4}Te$.

2. Results and discussion

Series #1. Exciton luminescence of the island-like 0.5 ml thick $Cd_{0.75}Mn_{0.25}Te$ layers exhibits one band whereas the spectra from 1.5 ml and 3.0 ml thick $Cd_{0.75}Mn_{0.25}Te$ layers show three bands depicted in Fig. 1. The spectra of localized excitons and their temperature behavior account for several localization levels.

Series #2. The exciton luminescence depends strongly on the spacing between 1.0 ml thick $Cd_{0.9}Mn_{0.1}Te$ layers. Emission spectra are simple where a width of $Cd_{0.7}Mg_{0.3}Te$ barrier is much larger or much less as compared to the size of exciton. The emission spectra are complex and reveal a considerable broadening in the intermediate cases.

Series #3. The luminescence spectra which contain three exciton bands (three localization levels) as well as the excitation luminescence spectra are indicative of a roughness of $Cd_{0.1}Mn_{0.9}Te$ layers embedded in $Cd_{0.7}Mg_{0.3}Te$ matrices at

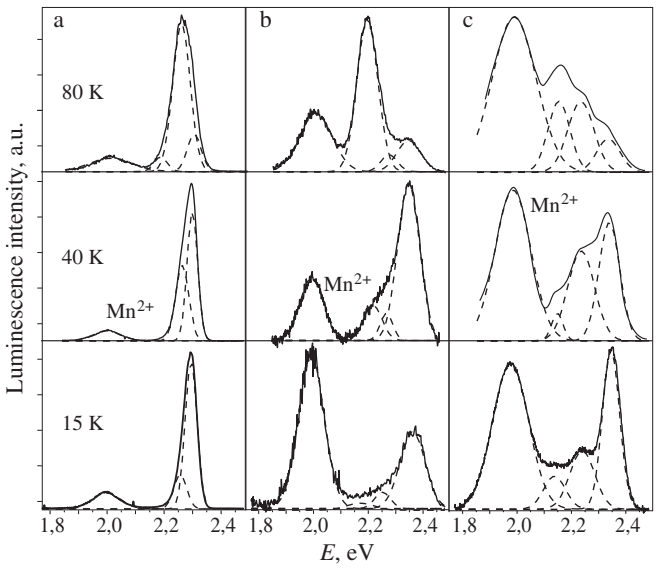

Fig. 1. Emission spectra of excitons and $3d$-shell of Mn^{2+} in 0.5 ml (a), 1.5 ml (b) and 3.0 (c) thick $Cd_{0.75}Mn_{0.25}Te$ layers.

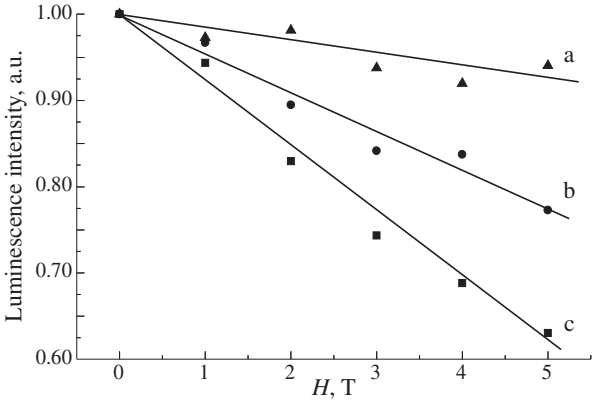

Fig. 2. Intensity of Mn^{2+} IL versus magnetic field for 0.5 ml (a), 1.5 ml (b) and 3.0 (c) thick $Cd_{0.75}Mn_{0.25}Te$ layers, $T = 5$ K.

the scale of exciton size.

Fig. 2. presents the magnetic field dependence of the Mn^{2+} IL ($^6A_1 - ^4T_1$ transition) for the 0.5, 1.5 and 3.0 ml thick $Cd_{0.75}Mn_{0.25}Te$ layers. The decrease of the Mn^{2+} IL intensity is accompanied by enhancement of the exciton emission. The reason for the radiation intensity repartitioning is a slowing down of the energy transfer from the extended barrier states and localized excitons to the Mn^{2+} $3d$-shell in DMS under the increasing magnetic field [1]. The lowest levels of electrons, $+1/2$ and holes, $-3/2$ become mostly populated in $H = 5$ T at liquid helium temperature in $Cd_{0.6}Mg_{0.4}Te$ barriers. As for the excitons localized on the ultrathin $Cd_{0.75}Mn_{0.25}Te$ magnetic layers, their levels are subjected to even bigger Zeeman splitting due to the alignment of the Mn^{2+} magnetic moments under the external field. Magnetic field splits the $3d$-levels too, the distance between the magnetic sublevels of Mn^{2+} term $^6A_1$ being about 0.1 meV at $H = 1$ T according to Raman spin-flip and ESR data [2,3]. Thus the magnetic splitting of the bands and $3d$-levels reduces at low temperature the number of sublevel combinations which satisfy the spin conservation selection rules.

It was shown [4] that the magnetic field dependence of the energy transfer efficiency from band states to the Mn^{2+} $3d$-shell is expected to be much smaller for the antiferromagnetic pairs and clusters as compared to the single Mn^{2+} ions. We have also taken into account our previous studies of picosecond exciton luminescence kinetics [5] and exciton Zeeman splitting [6] in DMS quantum wells. Their results testify that the lifetime of band states is too short to achieve the total thermal equilibrium for spin alignment. In Fig. we show that the magnetic-field induced decrease of Mn^{2+} IL intensity is most pronounced for the 3.0 ml thick $Cd_{0.75}Mn_{0.25}Te$ layer. It may be concluded that the power of magnetic layer is a decisive factor to ensure the spin polarization and efficiently suppress the band $3d$-shell energy transfer in the external field.

References

[1] H. Falk, W. Heimbrodt, P. J. Klar, J. Hubner, M. Oestreich, W. W. Rule, *Phys. Stat. Sol. B* **221**, 781 (2002).
[2] J. Stuhler, G. Schaaks, M. Dahl, A. Waag, G. Landwehr, K. V. Kavokin, and I. A. Merkulov, *J. Cryst. Growth* **159**, 1001 (1996).
[3] J. Lambe and C. Kikuchi, *Phys. Rev.* **119**, 1256 (1960).
[4] M. Nawrocki, Yu. G. Rubo, J. P. Lascaray and D. Coquillat, *Phys. Rev. B* **52**, R2241 (1995).
[5] V. F. Agekyan, I. Akai, N. G. Filosofov, T. Karasawa, G. Karczewski, A. Yu. Serov, and N. N. Vassiliev, *Proceed. 14th Int. Symp. Nanostructures: Physics and Technology. St Petersburg, Russia, July 26–30*, 2006.
[6] V. N. Katz, V. P. Kochereshko, V. F. Agekyan, L. Besombes and G. Karczewski, *Proceed. 16th Int. Symp. Nanostructures: Physics and Technology. Vladivostok, Russia, July 14–18*, 2008.

17th Int. Symp. "Nanostructures: Physics and Technology"
Minsk, Belarus, June 22–26, 2009
© 2009 Ioffe Institute

The elementary collective excitations in the system of two-dimensional Bose–Einstein Condensed magnetoexcitons

S. A. Moskalenko[1], M. A. Liberman[2] and *E. V. Dumanov*[1]

[1] Institute of Applied Physics of the Academy of Sciences of Moldova, Academic Str. 5, Chisinau, MD2028, Republic of Moldova
[2] Departmant of Physics, Uppsala University, Box 530, SE-751 21, Uppsala, Sweden

Abstract. The collective elementary excitations of a system of two-dimensional magnetoexcitons in a state of Bose–Einstein condensation(BEC) with arbitrary wave vector was investigated in Hartree–Fock–Bogoliubov approximation. The breaking of the gauge symmetry of the Hamiltonian was introduced following the idea proposed by Bogoliubov in his theory of quasi-averages. The chains of equations of motion for a set of Green's functions describing the exciton-type excitations as well as the plasmon-type excitations were deduced. The energy spectrum of the collective elementary excitations is characterized by the interconnection of the exciton and plasmon branches, because the plasmon-type elementary excitations are gapless and are lying in the same spectral interval as the exciton-type elementary excitations.

Introduction

Properties of atoms and excitons are dramatically changed in strong magnetic fields, such that the distance between Landau levels $\hbar\omega_0$, exceeds the corresponding Rydberg energies R_y and the magnetic length $l = \sqrt{\hbar c/eH}$ is small compared to their Bohr radii [1,2]. Even more interesting phenomena are exhibited in the case of two-dimensional (2D) electron systems due to the quenching of the kinetic energy at high magnetic fields, with the representative example being integer and fractional Quantum Hall effects [3–5]. Properties of the symmetric 2D electron-hole (e-h) system, with equal concentrations for both components, with coincident matrix elements of Coulomb electron-electron, hole-hole and electron-hole interactions in a strong perpendicular magnetic field also attracted a great attention during last two decades [6–13]. The collective states such as the Bose–Einstein condensation (BEC) of two-dimensional magnetoexcitons and the formation of metallic-type electron-hole liquid (EHL) were investigated in [6–13]. The search for Bose–Einstein condensates has became a milestone in the condensed matter physics [14]. The remarkable properties of super fluids and superconductors are intimately related to the existence of a bosonic condensate of composite particles consisting of an even number of fermions. In highly excited semiconductors the role of such composite bosons is taken on by excitons, which are bound states of electrons and holes. Furthermore, the excitonic system has been viewed as a keystone system for exploration of the BEC phenomena, since it allows to control particle densities and interactions in situ. Promising candidates for experimental realization of such system are semiconductor quantum wells (QWs) [15], which have a number of advantages compared to the bulk systems. The coherent pairing of electrons and holes occupying only the lowest Landau levels (LLLs) was studied using the Keldysh–Kozlov–Kopaev method and the generalized random-phase approximation [11]. The BEC of magnetoexcitons takes place in a single exciton state with wave vector k, supposing that the high density of electrons in the conduction band and of holes in the valence band were created in a single QW structure with size quantization much greater than the Landau quantization. In the case a new metastable dielectric liquid phase formed by Bose–Einstein condensed magnetoexcitons was revealed [11,12]. The importance of the excited Landau levels (ELLs) and their influence on the ground states of the systems was first noticed by the authors of the papers [7–10]. The influence of the excited Landau levels (ELLs) of electrons and holes was discussed in details in paper [12,13]. In this work we determined the energy spectrum of the collective elementary excitations arising in the presence of Bose–Einstein condensation (BEC) of magnetoexcitons, when the excitations of the quasiparticles take place in the frame of the lowest Landau levels (LLLs) and in the absence of their kinetic energy.

1. Elementary excitations of the Bose–Einstein condensed magnetoexcitons in collinear geometry

The collective elementary excitations of a system of two-dimensional magnetoexcitons in a state of Bose–Einstein condensation (BEC) with arbitrary wave vector was investigated in Hartree–Fock–Bogoliubov approximation as well as beyond it taking into account the correlation energy. The breaking of the gauge symmetry of the Hamiltonian was introduced following the idea proposed by Bogoliubov in his theory of quasi-averages. The equations of motion were written in the frame of the starting electron and hole creation and annihilation operators. The chains of equations of motion for a set of Green's functions describing the exciton-type excitations as well as the plasmon-type excitations were deduced. Their disconnections were introduced using the perturbation theory with a small parameter of the theory proportional to the filling factor multiplied by the phase space filling factor. This deconnection procedure permits to obtain an enclosed set of four Dyson equations with self-energy parts Σ_{ij} with $i, j = 1, 2, 3, 4$ forming a 4×4 matrix as follows

$$\det \left| \Sigma_{ij} \left(\overrightarrow{P}, \omega \right) \right| = 0, \qquad \overrightarrow{P} = \overrightarrow{k} + \overrightarrow{Q}. \tag{1}$$

It can be essentially simplified in collinear geometry, when the wave vectors $\overrightarrow{P}$ of the elementary excitations are parallel or antiparallel to the Bose–Einstein condensate wave vector $\overrightarrow{k}$. We will represent the wave vectors $\overrightarrow{P}$ in the form $\overrightarrow{P} = \overrightarrow{k} + \overrightarrow{q}$,

accounting them from the condensate wave vector $\overrightarrow{k}$. The relative wave vector $\overrightarrow{q}$ will be also collinear to $\overrightarrow{k}$, In this case the projections of the wave vector products $\left[\overrightarrow{P} \times \overrightarrow{k}\right]_z$ as well as all coefficients proportional to $Sin\left(\left[\overrightarrow{P} \times \overrightarrow{k}\right]_z l^2/2\right)$ and a half of the matrix elements $\Sigma_{ij}(\overrightarrow{P}, \omega)$ in the equation (1) vanish. The determinant equation (1) disintegrates in two independent equations. One of them concerns only to optical plasmons and has a simple form

$$\Sigma_{33}\left(\overrightarrow{k} + \overrightarrow{q}, \omega\right) = 0, \qquad \left[\overrightarrow{q} \times \overrightarrow{k}\right]_z = 0, \qquad (2)$$

whereas the second equation contains only the diagonal self-energy parts Σ_{11}, Σ_{22} and Σ_{44} and the quasi-average constant η

$$\Sigma_{11}\left(\overrightarrow{k} + \overrightarrow{q}, \omega\right)\Sigma_{22}\left(\overrightarrow{k} + \overrightarrow{q}, \omega\right)\Sigma_{44}\left(\overrightarrow{k} + \overrightarrow{q}, \omega\right)$$
$$-2\eta^2\left(\Sigma_{11}\left(\overrightarrow{k} + \overrightarrow{q}, \omega\right) + \Sigma_{22}\left(\overrightarrow{k} + \overrightarrow{q}, \omega\right)\right) = 0.$$

The energy spectrum of the collective elementary excitations is characterized by the interconnection of the exciton and plasmon branches, because in 2D electron-hole liquid in a strong perpendicular magnetic field the plasmon-type elementary excitations are gapless and are lying in the same spectral interval as the exciton-type elementary excitations. The presence of the condensate of excitons with the given density gives rise to the appearance of the quasi-energy branches of the spectrum, so as side-by-side with the exciton branch of spectrum supplementary exciton quasi-energy branch of the spectrum does appear. It is similar with the case of the laser radiation interacting with electron-hole pairs in semiconductor and leading to different optical Stark effects. The moving condensate with the group velocity of the 2D magnetoexcitons leads to the existence a supplementary term in the energy spectrum considered in the laboratory reference frame. It is proportional to the product of the group velocity multiplied by the wave vector of the elementary excitation in the reference frame moving with the condensate. In the collinear geometry the optical plasmon branch is separated from another three branches which in the starting variant consist from the usual exciton branch, from the quasi-energy exciton branch and from the acoustical plasmon branch. The energy spectrum was investigated in two approximations. In zero order approximation on the concentration contributions the energy spectrum consists from three branches which depend essentially on the condensate grout velocity. The exciton branch has positive energy and a gap because the chemical potential of magnetoexcitons is negative and to liberate the exciton from condensate it is necessary to transmit it a lot of energy. The quasi-energy exciton branch is negative and is so situated on the drawing of the dispersion law, that it can be obtained from the exciton energy branch by two consecutive symmetry operations around two coordinate axes of the drawing.

The third energy branch representing the acoustical plasmon has not its own dispersion law without concentration terms and its dispersion is determined only by the laboratory reference frame. The taking into account of the concentration contributions was made in two approximations, one of them in Hartree–Fock–Bogoliubov approximation(HFBA) and another one beyond HFBA with the correlation corrections. The correlation corrections are important at filling factors about 0.28 when the metastable dielectric liquid phase can appear and are not important when the filling factor is ten times smaller. The concentration terms gives rise to the proper dispersion law for the acoustical plasmon branch as well as add some terms to the excitonic branches. But it is very important that the excitonic branches are doubled because these contributions are added with different signs. The doubling of the excitonic branches can be explained by the formation of exciton-plasmon complexes.

Acknowledgements

This research was supported by the joint grant of the Russian Foundation for Fundamental Research and of the Academy of Sciences of Moldova (08.820.05.033RF). One of the authors (S. A. M) greatly appreciate support of the Wenner–Gren Foundation during his stay in Uppsala, where this work has been completed. E. V. D. thank the Academy of Sciences of Moldova for financial support (08.819.05.07F).

References

[1] M. A. Liberman and B. Johanson, *Uspekhi Fiz. Nauk* **165**, 121 (1995).
[2] Dong Lai, *Rev. Mod. Phys.* **73**, 629 (2001).
[3] H. L. Stormer, *Rev. Mod. Phys.* **71**, 875–889 (1999).
[4] Perspectives in Quantum Hall Effects, edited by S. Das Sarma, and A. Pinczuk (John Wiley & Sons, Inc., New York, 1997).
[5] E. I. Rashba, *Pure and Applied Chem.* **67**, (1995) 409.
[6] I. V. Lerner and Yu. E. Lozovik, *Zh. Eksp. Teor. Fiz.* **78**, 1167 (1980).
[7] I. V. Lerner and Yu. E. Lozovik, *J. Low Temper. Phys.* **38**, 333 (1980).
[8] I. V. Lerner and Yu. E. Lozovik, *Zh. Eksp. Teor. Fiz.* **80**, 1488 (1981) [Sov. Phys. — *JETP* **53**, 763 (1981)].
[9] A. B. Dzyubenko and Yu. E. Lozovik, *Fiz. Tverd. Tela* (Leningrad) **25**, 1519 (1983); 26, 1540 (1984) [*Sov. Phys. Solid State* **25**, 874 (1983); **26**, 938 (1984)]; *J. Phys. A* **24**, 415 (1991).
[10] D. Paquet, T. M. Rice, and K. Ueda, *Phys. Rev. B* **32**, 5208 (1985); T. M. Rice, D. Paquet and K. Ueda, *Helv. Phys. Acta* **58**, 410 (1985).
[11] S. A. Moskalenko, M. A. Liberman, D. W. Snoke, and V. Botan, *Phys. Rev. B* **66**, 245316 (2002);
[12] S. A. Moskalenko, M. A. Liberman, D. W. Snoke, V. Botan and B. Johansson, *Physica E* 19, 278 (2003); V. Botan, M. A. Liberman, S. A. Moskalenko, D. W. Snoke and B. Johansson, *Physica B* **346–347 C**, 460 (2004).
[13] S. A. Moskalenko, M. A. Liberman, P. I. Khadzhi, E. V. Dumanov, Ig. V. Podlesny and V. Botan, *Sol. State Comm.* **140/5**, 236 (2006).
[14] Bose–Einstein Condensation, edited by A. Griffin, D. W. Snoke, and S. Stringari (Cambridge University Press, Cambridge, 1995).
[15] L. V. Butov, A. L. Ivanov, A. Imamoglu, P. B. Littlewood, A. A. Shashkin, V. T. Dolgopolov, K. L. Campman, and A. C. Gossard, *Phys. Rev. Lett.* **86**, 5608 (2001).

17th Int. Symp. "Nanostructures: Physics and Technology"
Minsk, Belarus, June 22–26, 2009
© 2009 Ioffe Institute

Temperature dependence of the photoluminescence intensity in SiN_x:H films with Si nanoclusters: evidence for two processes involved in nonradiative relaxation of photoexcitations

T. T. Korchagina[1], V. A. Stuchinsky[1], V. A. Volodin[1,2], A. A. Popov[3] and M. Vergnat[4]

[1] Institute of Semiconductor Physics of SB RAS, pr. ak. Lavrentjeva 13, Novosibirsk 630090, Russia
[2] Novosibirsk State University, Pirogova street, 2, 630090, Novosibirsk, Russia
[3] Yaroslavl Department of FTI RAS, University ave., 21, Yaroslavl, Russia
[4] Laboratoire de Physique des Materiaux, Nancy-Universite, CNRS, Boulevard des Aiguillettes B.P. 239, 54506 Vandouvre les Nancy, France

Abstract. The temperature dependence of the photoluminescence intensity in SiN_x:H films grown on Si substrates by low-frequency PECVD at temperatures 100 and 380 °C was analyzed versus the film stoichiomery. For the first time, involvement of two different processes in nonradiative relaxation of photoexcitations has been demonstrated. These processes are tentatively identified as thermal dissociation of nanocluster-bound excitons and tunnel migration of such excitons as a whole to nonradiative sites.

Silicon nitride films with amorphous or crystalline Si clusters show promise as a material for optoelectronic and flash-memory applications [1,2]. In the present study, optical properties of SiN_x:H films deposited onto Si substrates by PECVD were examined to analyze the temperature dependence of the photoluminescence (PL) intensity in such films.

The temperature dependence of the PL intensity I_{PL} in silicon nitride or oxide films with Si nano-inclusions is known to arise from the competition between a thermally activated radiative process and a temperature-dependent nonradiative process that proceeds via migration of tunneling excitations to nonradiative sites [3,4]. At sufficiently high temperatures the latter process, whose rate increases with temperature T, starts dominating over the radiative channel, which results in a characteristic dependence of I_{PL} on T with a maximum at $T \approx 60$ K [4,5]. Previously, the temperature dependence of the nonradiative process was analyzed in terms of the so-called Berthelot-type dependence whose origin still lacks clear understanding [4]. In the present work, we show for the first time that the nonradiative process involves two different paths for excitations whose relative intensity depends on T, and report on the kinetic characteristics of both paths.

Table 1. Specifications, growth conditions, thickness d and stoichiometry parameter x of examined SiN_x films.

Sample	T, °C	NH_3/SiH_4 flow ratio	d nm	Stoichiometry parameter x
611	100	5	240	1.3
612	100	2.6	400	1.2
613	100	1.5	400	1.0
614	100	0.9	450	0.7
615	100	0.5	450	0.6
621	380	5	280	1.3
622	380	2.6	430	1.2
623	380	1.5	430	1.0
624	380	0.9	510	0.7
625	380	0.5	510	0.6

Two series of experimental samples, 611 to 615 and 621 to 625, were prepared by depositing SiN_x:H films onto (100) Si substrates in a low-frequency PECVD process at temperatures 100 and 380 °C. The stoichiometry parameter x was varied in the range $x = 0.6$ to 1.3 via varying the NH_3/SiH_4 flow ratio from 0.5 to 5 in the growth process (see Table 1). PL spectra of as-grown films were measured at temperatures 78 to 350 K to analyze the temperature dependence of I_{PL} in the samples.

Additionally, Raman spectra were registered to identify the structure, amorphous or crystalline, of Si inclusions in the samples. The stoichiometry parameter x was estimated from the film refractive indexes and from the red shift of optical gap in the films.

According to Raman scattering data (see Fig. 1), the SiN_x:H films with $x < 4/3$ contained amorphous Si clusters whose density increased with rising the film growth temperature from 100 to 380 °C.

Measured PL spectra were found to depend substantially on the film stoichiometry, showing a red shift of PL maxima with increasing amount of excess Si in the samples (Fig. 2). The latter observation was indicative of the formation of larger Si nanoclusters in samples with higher Si supersaturation. With

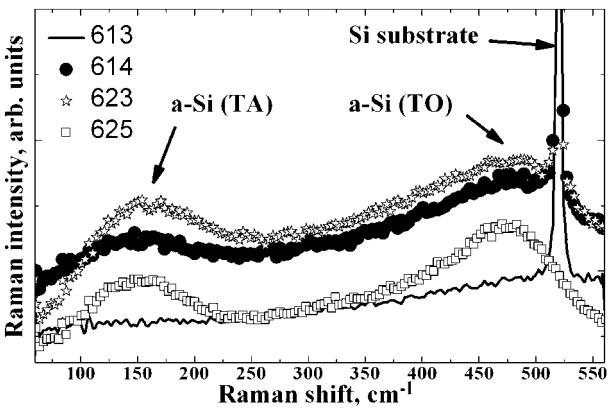

Fig. 1. Raman spectra of some samples.

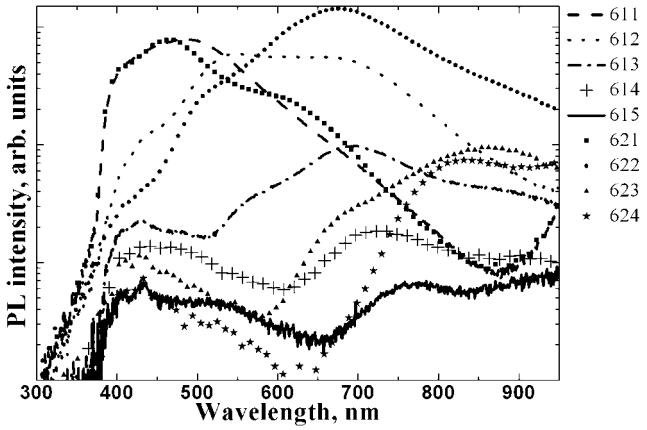

Fig. 2. PL spectra of all samples measured at $T = -190$ °C.

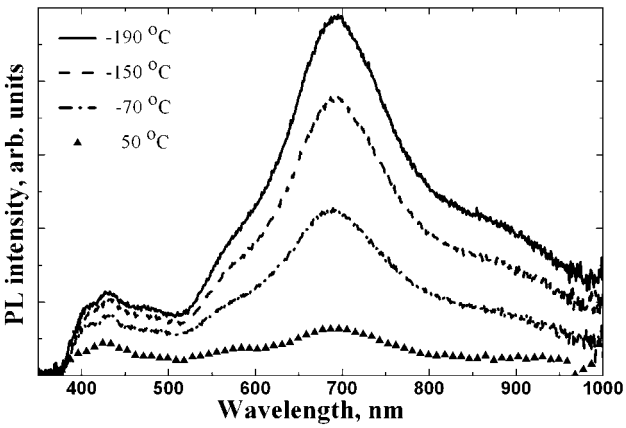

Fig. 3. PL spectra of sample 613 at different temperatures.

increasing the measurement temperature from 78 to 320 K the PL intensity measured at fixed wavelength decreased, while the general shape of the spectrum in each individual sample remained roughly unchanged (see Fig. 3).

Figure 4 shows the curves of $I_{\mathrm{PL}}(T)$ at the PL intensity maximum in each spectrum. The kink at $T = 200$ K, especially clearly seen in the semi-logarithmic plots of the curves, points to the existence of two processes contributing to the nonradiative decay of excitations.

Thus, the existence of three thermally activated processes, one radiative and two nonradiative, can be assumed. With all the three processes proceeding in parallel at characteristic rates $e_1 = v_1 \exp(-E_1/kT)$, $e_2 = v_2 \exp(-E_2/kT)$, and $e_3 = v_3 \exp(-E_3/kT)$, the PL intensity is defined, apart from the total number N of bright Si nanoclusters, by the relative rate of the radiative process, $I_{\mathrm{PL}} \propto N\, e_1(T)/[e_1(T)+e_2(T)+e_3(T)]$. In view of this, the curves of $I_{\max}(T)$ were fitted with dependences

$$I_{\mathrm{PL}} \propto \frac{1}{1 + f_1 \exp\left(\frac{E_1-E_2}{kT}\right) + f_3 \exp\left(\frac{E_1-E_3}{kT}\right)},$$

where $f_2 = v_2/v_1$ and $f_3 = v_3/v_1$ are relative frequency factors of the two nonradiative processes. The varied parameters were f_2, f_3, E_2, and E_3. For the energy E_1, a value 1.6 meV was adopted [5]. The values of E_2, E_3, f_2, and f_3 were found in different samples. The energy E_3 being close to the exciton binding energy in Si nanocrystals [6], it can be hypothesized that the second process proceeds via hops of most

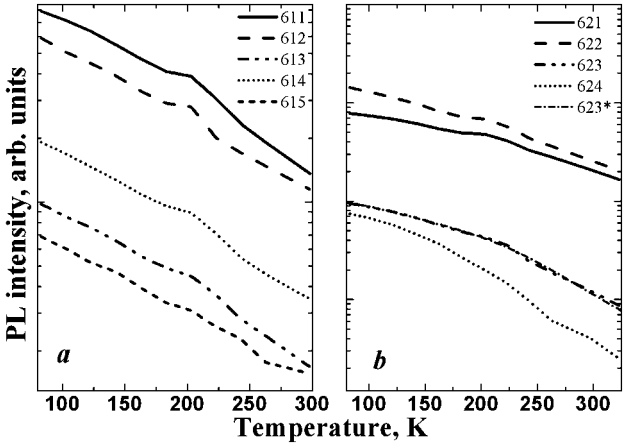

Fig. 4. Maximum PL intensity versus temperature in the spectra of samples grown at $T = 100$ °C (a) and 380 °C (b). To illustrate the fitting quality, curve 623* is shown, calculated by formula (1) to fit the experimental data for sample 623.

mobile carriers, electrons, to neighboring Si nanoclusters after their thermal pre-activation by energy E_3 required for the electrons to overcome the polarization electric field due to the hole left behind. Estimates of typical electron and hole hopping times between neighboring nanoclusters made with the use of known values of energy offsets ($E_{\mathrm{e}} \approx 2$ eV for electrons and $E_{\mathrm{h}} \approx 1.5$ eV for holes [7]) show that, throughout the whole temperature range 80 to 300 K an electron jump into neighboring Si nanocluster ends, with high probability, in exciton dissociation. The estimated probability of uncorrelated simultaneous hops of free electron and freehole into neighboring nanocluster being low, we tentatively identify the second process as tunnel migration of excitonic states over the system of Si nanoclusters. The factors f_2 and f_3 in the samples with different x behave similarly (if the factor f_2 grows in value, so does the factor f_3), pointing, in line with the adopted interpretation of the experimental data, to similar influence of film structural characteristics on the rates of both nonradiative processes. In addition, the frequency factors f_2 and f_3 have higher values in samples 611–615 compared to samples 621–625. All these observations comply with the general concept of tunneling phenomena according to which the migration of tunneling excitations over the system of Si nanoclusters becomes more intense as the nanoclusters in the system grow in size with simultaneous decrease of the separation between them.

To summarize, the obtained data are indicative of the existence of two processes involved in nonradiative relaxation of excitations optically generated in Si nanoclusters embedded in SiN_x:H. These processes were tentatively identified as nondissociative migration and dissociation of tunneling excitons ($E_{\mathrm{act}} = 30$ and 130 meV, respectively).

References

[1] Nae-Man Park *et al*, *Phys. Rev. Lett.* **86**, 1355 (2001).
[2] V. A. Gritsenko. *Phisics-Uspehi* **178**, 727 (2008).
[3] H. Rinnert *et al*, *Physica E* **16**, 382 (2003).
[4] M. Kapoor *et al*, *Phys. Rev. B* **61**, 1941 (2000).
[5] A. Yu. Kobitski *et al*, *Phys. Rev. B* **63**, 115423 (2001).
[6] T. Takagahara *et al*, *Phys. Rev. B* **46**, 15578 (1992).
[7] V. A. Gritsenko *et al*, *Electronic Structure of Amorphous Dielectrics in MOS Structures.* Nauka, (1993), 280 p.

17th Int. Symp. "Nanostructures: Physics and Technology"
Minsk, Belarus, June 22–26, 2009
© 2009 Ioffe Institute

The localization of excitons and trions on longitudinal fluctuations of quantum wire parameters

M. A. Semina, R. A. Sergeev and R. A. Suris
Ioffe Physical-Technical Institute, St Petersburg, Russia

Abstract. By means of the variational method, we study theoretically the effect of electron and hole localization along quantum wire axis on the states and energies of simplest electron-hole complexes. Trial functions with a few variational parameters that let one calculate ground state binding energies of complexes in wide range of structure parameters and carrier effective mass ratios are suggested. The general form of these functions is independent of the specific form of the fluctuation. The applicability of our method is illustrated by calculation of binding energies of quantum wire exciton, X^+ and X^- trions, localized on 1D parabolic potential.

Introduction

Experimental and theoretical studies of the bound states of the simplest electron-hole complexes such as excitons (electron-hole pairs) and trions (charged excitons) in semiconductor quantum wires (QWRs) that determine the spectral features in the vicinity of the fundamental absorption band edge is of significant interest [1–4].

To calculate binding energies of free excitons and trions in thin QWRs one can use the simple variational method with trial function with a small number of trial parameters as it had been done in [1] for wires with logarithmically small radius. Another option is to use complicated numerical methods allowing to calculate not only the complexes binding energy with very high accuracy but also their wavefunctions [3,4]. In our recent work [5] it was shown that the results of works [3,4] can be described with rather good accuracy by means of the simple variational calculation.

The comparison between results of theoretical calculations and experimental measurements shows that experimentally determined values of trions binding energies exceed significantly the theoretical predictions [2]. That effect can be explained by localization of the electron-hole complexes on fluctuations of the QWRs lateral dimensions as it happens in quantum wells [6].

It is reasonable to describe the effect of longitudinal localization of 1D electron-hole complexes in much the same way as it had been done in our work [7] for 2D systems with lateral inhomogeneity, by using variational functions with small number of trial parameters.

1. Trial function for electron-hole complexes

We consider the QWRs with high barrier and small radius so we can separate the coordinates of charge carriers along the structure axis and in plane perpendicular to it. Here we use the 3D Rydberg $Ry = \mu e^4/2\varepsilon^2\hbar^2$ as a unit of energy and 3D exciton Bohr radius $a_B = \hbar^2\varepsilon/\mu e^2$ as a unit of length, $\sigma = m_e/m_h$ with m_e (m_h) being electron (hole) effective mass, ε is the static dielectric constant. The effects of complex structure of valence band are disregarded. We describe the Coulomb attraction between oppositely charged carriers by the following widely used effective potential [6]:

$$\widehat{V}_{\text{eff}}(z, a) = -\frac{2}{\sqrt{z^2 + a^2}}. \qquad (1)$$

Here z is the relative coordinate and a is the effective QWR radius. To describe the Coulomb repulsion between the charge carriers of the same type we use effective potential which differs from (1) by only its sign.

We characterize the interaction of electrons and holes with a fluctuation of a QWR radius by independent single-particle attractive 1D potentials of arbitrary shape $U_e(z_e)$, $[U_h(z_h)]$ for electrons (holes), where z_e and z_h are the 1D coordinates of an electron and a hole along the QWR axis.

The structure of the electron-hole complexes, localized on QWR longitudinal fluctuation is determined by competition between interaction the charge carries with the fluctuation potential and with each other. Following the general method developed in Ref. [8] for quantum wells with interface fluctuations we introduce three characteristic energy parameters: the typical value of the electron-hole Coulomb interaction energy E_c, and E_e (E_h) the interlevel separations for non-interacting electrons (holes), localized on fluctuation. The quantity relations

$$W_e = \frac{\Delta E_e}{E_c}, \qquad W_h = \frac{\Delta E_h}{E_c}. \qquad (2)$$

define the basic structure of the complex. There are only two qualitatively different limiting cases, where electron-hole complex Schrodinger equation can be reduced to several simpler independent equations for systems with smaller number of particles. If both W_e, $W_h \ll 1$ the structure of the complex is determined mostly by Coulomb interaction between the charge carriers. So its wavefunction reduces to the product of the center-of-mass function and the wavefunction depending on the relative coordinates. In the opposite limit, where $W_e \gg 1$ or $W_h \gg 1$, one can separate the motion of different types of the carriers. In such a case the whole wavefunction can be recast as a product of wavefunctions of electron and hole subsystems.

We represent the trial function for localized 1D electron-hole complex as:

$$\Psi = \left[\Psi^{\text{C.M.}}\right]^{\alpha_R} \left[\Psi^{\text{int}}\right]^{\alpha_\rho} \left[\Phi^{e}\right]^{\alpha_e} \left[\Phi^{h}\right]^{\alpha_h}, \qquad (3)$$

where $\Psi^{\text{C.M.}}$ is the wavefunction of the complex center of masses quantized in effective fluctuation potential, Ψ^{int} is the function describing relative motion of electrons and holes in a free 1D complex, $\Phi^{e(h)}$ is the wavefunction of the ground state of electrons (holes) in the sum of the fluctuation potential and the averaged effective Coulomb potential of the holes (electrons). Values α_R, α_ρ, α_e, α_h are the trial parameters, see Ref. [7] for details. Coordinates of respective subsystems are

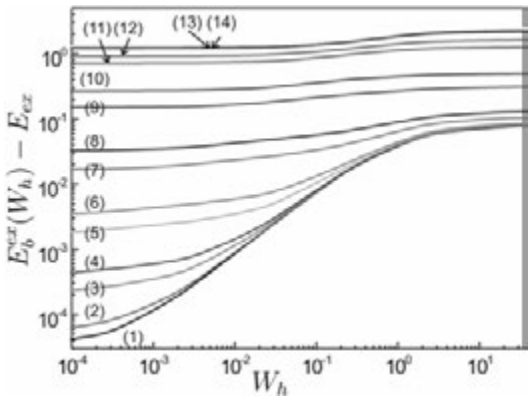

Fig. 1. Exciton binding energy $E_{\rm b}(W_{\rm h})$ as a function of $W_{\rm e}$, calculated for $\ln(a_{\rm B}/a) = 1$ and $\sigma = m_{\rm e}/m_{\rm h} = 0.1$. $E_{\rm ex}$ is the binding energy of free 1D exciton. Curves 1–14 corresponds to: 1) $W_{\rm e} = 1.7\times10^{-5}$, 2) 3.4×10^{-5}, 3) 1.7×10^{-4}, 4) 3.4×10^{-4}, 5) 1.7×10^{-3}, 6) 3.4×10^{-3}, 7) 1.7×10^{-2}, 8) 3.4×10^{-2}, 9) 1.7×10^{-1}, 10) 3.4×10^{-1}, 11) 1.7, 12) 3.4, 13) 17, 14) 34.

omitted in Eq. (3). We note that all of the wavefunctions in Eq. (3) are to be found independently from the solution of the simpler Schroedinger equations with smaller number of variables.

2. Results and discussion

In order to illustrate our approach, we consider the case of exciton, X^+ and X^- trions localized along QWR axis on the parabolic longitudinal potential. We assume the effective fluctuation potentials for electron and holes to be attractive parabolic potentials written as:

$$U_{\rm e} = \frac{1}{4}\,(1+\sigma)\,W_{\rm e}^2 E_{\rm ex}^2 z_{\rm e}^2,\; U_{\rm h} = \frac{1}{4}\left(1+\frac{1}{\sigma}\right) W_{\rm h}^2 E_{\rm ex}^2 z_{\rm h}^2. \quad (4)$$

Here $E_{\rm ex}$ is the binding energy of free 1D exciton. In our calculation we assume electron to hole mass ratio being $\sigma = 0.1$ and logarithm of the effective QWR radius being $\ln(a_{\rm B}/a) = 1$ (it corresponds to QWR effective radius being approximately 45 Å in GaAs-based structures).

Figure 1 shows the exciton binding $E_{\rm b}^{\rm ex}$ energy referred to the free 1D exciton binding energy as a function of $W_{\rm e}$ and $W_{\rm h}$. One can see an increase of the binding energy with an increase of $W_{\rm e}$ and $W_{\rm h}$ due to increasing of efficiency of the electron-hole interaction.

Figures 2 and 3 show the binding energies of X^- and X^+ trions as functions of fluctuation potential parameters. One can see that unlike exciton binding energy binding energies of trions can demonstrate nonmonotonic behavior. This can be explained by interplay of exchange interaction and Coulomb repulsion of identical particles. Increase of the longitudinal potential for the identical particles at first results in increasing of the exchange interactions, while the further increase of this potential results in dominance of Coulomb repulsion. Moreover, in certain parameter range the binding energies of trions can be even negative. It takes place at $W_{\rm e} \gg W_{\rm h}$ for the X^- trion and at $W_{\rm e} \ll W_{\rm h}$ for X^+ trion, respectively. Physically, a significant growth of the fluctuation potential for the identical carriers with fixed potential for the only particle of the other type leads to an increase of their repulsion. Despite the fact that the binding energy for such a trion is negative (and its

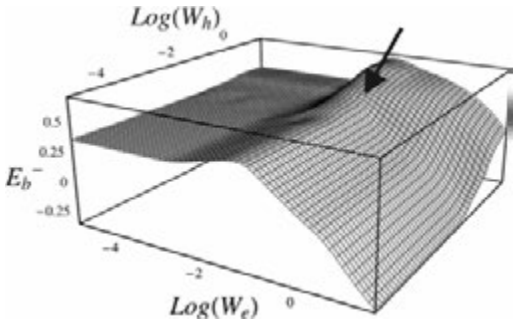

Fig. 2. X^- trion binding energy $E_{\rm b}^-$ as a function of electron and hole potential parameters ($W_{\rm e}$ and $W_{\rm h}$), calculated for $\sigma = 0.1$ and $\ln(a_{\rm B}/a) = 1$.

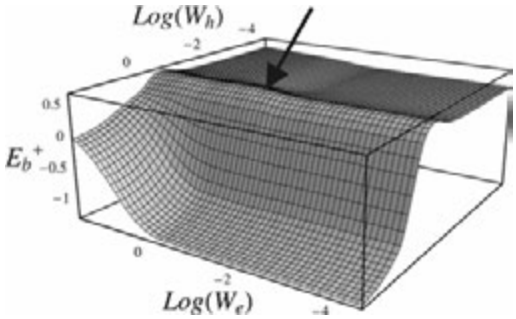

Fig. 3. X^+ trion binding energy $E_{\rm b}^+$ as a function of electron and hole potential parameters ($W_{\rm e}$ and $W_{\rm h}$), calculated for $\sigma = 0.1$ and $\ln(a_{\rm B}/a) = 1$.

emission line lies above that of an exciton), all three carriers are still localized due to the fluctuation potential.

For the sake of an estimation, let us consider the QWR with $\ln(a_{\rm B}/a) \sim 1$ and fluctuation potential with realistic parameters $W_{\rm e} = 0.22$ and $W_{\rm h} = 0.075$ (this point is shown by arrow in Figures 2 and 3). Binding energies of trions localized on such potential increase by 40% for X^+ trion and by almost a factor of 2 for X^- trion in agreement with the experimental data of Ref. [2]. Therefore, a strong increase of trion binding energies in realistic quantum wires can be explained by the localization of electron-hole complexes on quantum wire radius fluctuations.

To conclude, we have generalized a general formalism developed in [7] for 1D structures. So we can build a simple and physically reliable trial functions for electron-hole complexes localized on the QWR longitudinal fluctuation. The binding energies of exciton, X^+ and X^- trions were calculated in a wide range of one-particle potential parameters. It was shown that for realistic fluctuation the significant increase of trion binding energy can be achieved.

Acknowledgements

The work is supported by RFBR, grant 08-02-01337-a, and Federal program on support of leading scientific schools grant 3415.2008.2

References

[1] A. V. Chaplik, *Phys. Low-Dim. Struct.* **9/10**, 131 (1999).
[2] T. Otterburg *et al*, *Phys. Rev. B* **71**, 033301 (2005).
[3] B. Szafran *et al*, *Phys. Rev. B* **71**, 235305 (2005).
[4] Y. Sidor *et al*, *Phys. Rev. B* **77**, 205413 (2008).
[5] M. A. Semina *et al*, *Semiconductors* **42** (12), 1427 (2008).
[6] R. A. Sergeev *et al*, *Eur. Phys. J. B* **47**, 541 (2005).
[7] M. A. Semina *et al*, *Semiconductors* **40** (11), 1338 (2006).

17th Int. Symp. "Nanostructures: Physics and Technology"
Minsk, Belarus, June 22–26, 2009
© 2009 Ioffe Institute

AlGaA/GaAs photovoltaic cells with InGaAs quantum dots

S. A. Blokhin[1,2], A. V. Sakharov[2], A. M. Nadtochiy[1,2], A. S. Pauysov[2], M. V. Maximov[1,2], N. N. Ledentsov[1,2], A. R. Kovsh[3], S. S. Mikhrin[3], V. M. Lantratov[2], S. A. Mintairov[2], N. A. Kaluzhniy[2] and M. Z. Shvarts[2]

[1] St Petersburg Physics and Technology Centre for Research and Education RAS, St Petersburg, Russia
[2] Ioffe Physical-Technical Institute, St Petersburg, Russia
[3] Innolume GmbH, Konrad-Andenauer-Allee 11, 44263 Dortmund, Germany

Abstract. We studied the different carrier kinetic mechanisms involved into the interband absorption of quantum dots (QDs) by photocurrent spectroscopy. It was shown that in vertically coupled "shallow" InGaAs QDs an effective carrier emission, collection and separation of photogenerated carriers take place due to minizone formation. The possibility for the incorporation of vertically-coupled QDs into solar cells (SC) without any deterioration of structural quality of p-n-junction has been shown. An increase (∼1%) in short-circuit current density for the QD SC-devices has been demonstrated for the first time. The maximum efficiency was 18,3% for 1 Sun air-mass 1.5 global non-concentrated solar spectrum.

Introduction

Photovoltaic (PV) devices, so called solar cells, are promising alternatives to traditional fuel resources. However, the low power conversion efficiency caused by the non-zero contributions of different loss mechanisms prevents widespread application of solar cell technology [1]. The common approach to improve the efficiency of PV devices is based on stacking layers with different band gap together in multiple heterojunction cells [2]. However, the need in the lattice matching and tunnel junctions significantly limit the maximum achievable conversion efficiency (up-to-date 41%) [3]. Recently, self-assembled quantum dots were proposed for using in solar cells, providing an approach complementary to the multi-junction solar cells [4,5,6].

In this paper we report on detailed study of physical processes of energy conversion in In(Ga)As QD media and the critical issues related to optimization of QD structures for effective photovoltaic conversion.

Design

The use of QDs provides much more freedom in absorption band and strain engineering as compared to the case of bulk material. The spectral characteristics of In(Ga)As QDs and the carrier localization in QD arrays can be precisely controlled by changing the QD size and shape. Quite low absorption level in QDs can be overcome by vertical staking technique. However, the real QD density (especially for case of vertical coupling technique) is limited by the critical QD size at which the misfit dislocation nucleates. Our additional investigations showed that the average In composition in QDs should be decreased to achieve high optical quality of high-dense In(Ga)As QDs without use of any strain reduce technology. Thus, we focused on InGaAs QDs grown in submonolayer deposition mode. Two *p-i-n*-PV structures based on InGaAs QDs with the ten stacked QD planes with the GaAs spacer thickness of 30 nm (sample A) and 10 nm (sample B) has been grown. To estimate the future perspectives of the QD media in photovoltaic, single-junction AlGaAs/GaAs solar cells with back n-AlGaAs potential barrier and thin wide band gap p-AlGaAs window were used (see inset in Fig. 2). The solar cell (SC) structures have been grown in two configurations: with 10 layers of vertically coupled InGaAs QDs (QD-SC) in i-GaAs region and without QDs keeping the i-region width of 130 nm (ref-SC). The details of design and fabrication have been described in [7].

Results and discussion

Fig. 1 depicts the results of photocurrent spectroscopy over wide temperature range for two *p-i-n*-PV samples based on the 10 stacked InGaAs QD layers with different GaAs spacer thickness. For uncoupled QDs (sample A), the decrease in temperature leads not only to the shift of absorption, but also to the spectra shape transformation — the sequential disappearing of contribution from ground state (GS), excited states (ES) and even from wetting layer (WL) of vertically stacked uncoupled QDs (see Fig. 1a). Such behaviour is caused by the transition from nonequilibrium to equilibrium carrier distribution in QD array at about 100 K. The probability of thermal activation for the carriers localized in QDs at low temperature is quite low, and the tunnelling becomes the only feasible mechanism of carrier emission. However, due to higher effective mass the escape rate of the holes is 10-times lower than that of the electrons, which together with the high recombination probability of photogenerated carriers in QDs significantly decreases the QD contribution in total photocurrent. The thermal activated

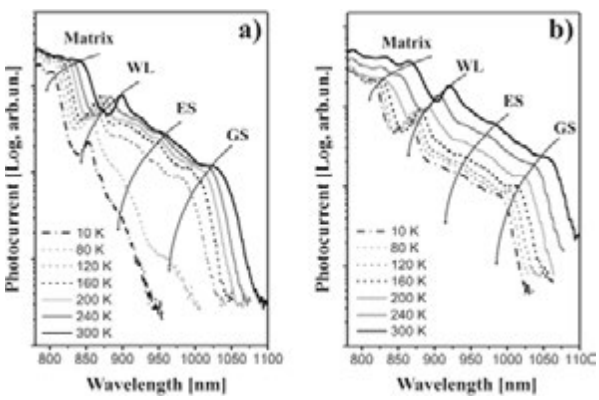

Fig. 1. Temperature evolution of photocurrent spectra for *p-i-n*-PV-structures based on stacked InGaAs QDs with the spacer thickness of 30 nm (a, sample A) and 10 nm (b, sample B).

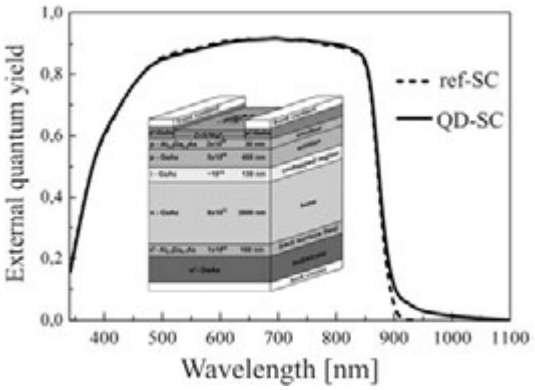

Fig. 2. External quantum efficiency of single-junction AlGaAs/GaAs solar cells with (QD-SC) and without (ref-SC) QD arrays in *i*-region. Inset: schematic view of AlGaAs/GaAs single *p-i-n*-junction multiplayer solar cell.

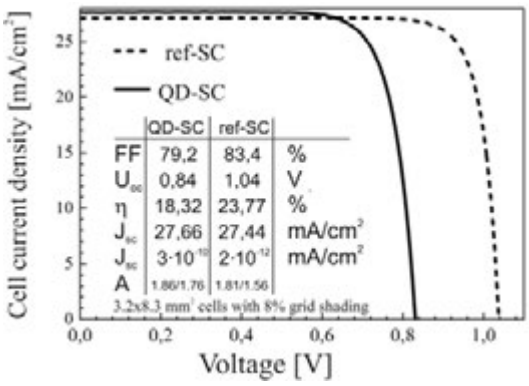

Fig. 3. Light-current-voltage characteristics of investigated PV devices under the 1 sun AM1.5G solar spectrum.

carrier escape process becomes more intensive with the temperature increasing, and, thus, a mixed mechanism of carrier emission — thermal-assisted tunnelling takes place, where the electrons are thermally activated into QD excited states with subsequent tunnelling to matrix, while the holes are directly thermally activated into valence band due to their weaker localization energy. In case of vertically coupled QDs, the high level of light absorption and carrier emission for present QD-media type were surprisingly observed even at helium temperatures, as shown in Fig. 1b. Moreover the contribution to total current for sample B is slightly higher then that for sample A even at room temperature. We believe that such effective carrier emission, collection and separation of photogenerated carriers from QD array can be attributed to the formation of a minixones [8].

Fig. 2 shows spectral dependencies of external quantum efficiencies for both investigated solar cells. QD-SC devices demonstrate a wider absorbing spectral range up to 1100 nm as compared to that for reference-SC device. The matching of photosensitivity spectra for both solar cells in the visible spectral range is evidence of dislocation-free growth of vertically coupled QDs as well as of high structural quality of *p-n* junction.

The current-voltage characteristics of the investigated solar cells measured under simulated 1 Sun air-mass 1.5 global (AM1.5G) spectra are shown in Fig. 3. For the first time, the QD-PV cells demonstrated 1% increase in current density (J_{sc}) owing to QD absorption in the long-wavelength range of solar spectrum under effective separation of photogenerated charge carriers. However, the insertion of QD-media results in noticeable reduction of open-circuit voltage (U_{oc}), which in combination with slightly smaller fill factor of light current-voltage characteristic (FF) limits the maximum achievable efficiency (η) at the level of 18.3% for developed QD-SC cells.

To understand the origins of this effect, the dark current measurements were carried out. In reference-SC devices, the mixed current flow mechanism takes place with the domination of recombination process (diode factor, $A \sim 1.81$) under low exposure level and with the domination of diffusion processes ($A \sim 1.56$) under concentrated solar exposure. The insertion of QD array into *i*-region of SC-device results in domination of recombination mechanism ($A \sim 1.86$ and $A \sim 1.76$ under low and high exposure level, correspondingly) with sufficiently higher reverse saturation current density (100-fold) as compared to that for reference-SC devices. Thus, the drop of open-circuit voltage and efficiency in QD-SC is associated with the radiative recombination in narrow-band gap material of InGaAs QDs. We believe that this problem can be solved by moving QD array from *i*-region into base and by using distributed Bragg reflector instead of back potential barrier.

Conclusion

The photovoltaic devices with self-assembled In(Ga)As QDs have been fabricated and studied. It was observed that the vertically coupled InGaAs QDs are the most promising medium for solar cells as compared to other types of self-organized QDs. For the first time QD-based solar cells demonstrated 1% increase in short circuit current due to QD absorption in the long-wavelength optical region of solar spectrum and effective separation of photogenerated carriers through minizones. The radiative recombination in narrow-band gap material of InGaAs QDs is responsible for the drop of open-circuit voltage and efficiency in QD-SC cells.

Acknowledgements

The work was supported in different parts by the Partner Project ISTC 3781p, Grant from St Petersburg Scientific Centre RAS, Program of fundamental studies of Presidium RAS "Fundamental studies of nanotechnologies and nanomaterials" and Purpose-oriented program of Russian Federal Agency of education "Development of scientific potential of higher education institutions (2009-2010)".

References

[1] V. M. Andreev *et al*, *Photovoltaic Conversion of Concentrated Sunlight*, (John Willey & Sons Ltd.) 1997.
[2] C. H. Henry, *J. Appl. Phys.* **51**, 4494 (1980).
[3] R. R. King *et al*, *Proc. of the 23th European Photovoltaic Solar Energy Conference*, Valencia, Spain (2008) pp. 24–29.
[4] V. Aroutiounian *et al*, *J. Appl. Phys.* **89**, 2268 (2001).
[5] A. Luque *et al*, *J. Appl. Phys.* **99**, 094503 (2006).
[6] S. M. Hubbard *et al*, *Appl. Phys. Lett.* **92**, 123512 (2008).
[7] S. A. Blokhin *et al*, *Fizika i Tekhnika Poluprovodnikov* **43**, 537 (2009).
[8] N. N. Ledentsov *et al*, *Phys. Rev. B.* **54**, 8743 (1996).

17th Int. Symp. "Nanostructures: Physics and Technology"
Minsk, Belarus, June 22–26, 2009
© 2009 Ioffe Institute

Resistance switching mechanism in yttrium-based cuprate films

S. Yu. Larkin[1], I. V. Boylo[2], M. A. Belogolovskii[2], T. Plecenik[3], M. Tomášek[3], M. Gregor[3], J. Noskovic[3], M. Zahoran[3], T. Roch[3], P. Kúš[3], A. Plecenik[3], M. A. Moskalenko[4], M. Španková[5] and Š. Chromik[5]

[1] Scientific and Industrial Concern "Nauka", 03148 Kyiv, Ukraine
[2] Donetsk Institute for Physics and Engineering, NASU, 83114 Donetsk, Ukraine
[3] Department of Experimental Physics, Comenius University, 84248 Bratislava, Slovak Republic
[4] State Scientific Research Center "Phonon", 03148 Kyiv, Ukraine
[5] Institute of Electrical Engineering, SAS, 84104 Bratislava, Slovak Republic

Abstract. Heterostructures formed by an Ag counter-electrode and epitaxial yttrium-based cuprate films have been fabricated and their current-voltage characteristics as well as the differential conductance were measured at temperatures from 4.2 to 300 K. A physical mechanism driving the resistance switching phenomenon, the sudden change of the resistance by the application of a strong electric field, is discussed. We propose a simple one-dimensional model which assumes that the switchings occur in a nano-scale poor-conducting region in close proximity to the metal/perovskite interface, where the oxygen vacancies content changes in time and in space. The model predictions are compared with experimental data.

Introduction

Resistive random access memory (RAM), which uses a reversible resistive switching effect in transition-metal oxides by the application of a strong electric field, is now believed to be one of the most promising candidates for nonvolatile data storage devices with improved performance characteristics. Comparing with magnetic tunneling junctions, employing a magnetic field for magnetization switching of the tunneling resistance, resistive RAM allows fully electronic programming and thus can avoid many problems of programming power and disturbs that are expected, for example, for magnetic RAMs. It has been shown that a number of different oxides exhibit resistive switching [1,2]. However, the underlying microscopic mechanism of the effect is still debated, especially, in complex transition-metal oxides like perovskites. In the latter case the main disputes are concentrated on two issues: (i) whether the resistance change comes from the oxide bulk or it is an interface effect, and (ii) if it is a result of an atomic rearrangement or is caused by specific features of highly correlated electron systems.

In this contribution we report on our experimental investigations of current-voltage $I(V)$ characteristics of heterostructures formed by an Ag strip and epitaxial yttrium-based cuprate $YBa_2Cu_3O_{7-x}$ (YBCO) samples, present a simple model which relates the switching phenomenon to electric field-induced oxygen ion migration that piles up the oxygen vacancies in the nano-scale vicinity of the metal/oxide interface and compare the model predictions with the measured experimental data. In contrast to a recent paper [3] dealing with YBCO ceramics we were studying high-quality epitaxial YBCO films and have realized two new ways of monitoring the switching effect: first, we used a special time current profile control in order to reveal the presence of diffusion processes in the heterostructures studied and, second, we measured the contact differential conductance $G(V) = dI(V)/dV$ at 4.2 K in order to observe a fine structure corresponding to the superconducting energy gap and to study the nature of a transition region between the two conducting electrodes.

1. Experimental

Single-crystalline $LaAlO_3$ (001) substrates offering small lattice (within ∼1%) and thermal mismatches with YBCO have been used in order to obtain high-quality cuprate films with low surface resistance. Epitaxial YBCO films were deposited applying high pressure on-axis dc magnetron sputtering from a stoichiometric ceramic target. The sputtering was carried out at an oxygen pressure of 240 Pa, heater temperature of 815 °C, and a dc power of 200 W. After the deposition, the YBCO films were subsequently annealed in O_2 (10^4 Pa) at 500 °C for 30 min and then the temperature was lowered down to ambient one with a rate of 15 °C/min. Then the lift-off photolithography was used in order to fabricate micro-structures for 5, 10, and 15 μm wide Ag strips across the YBCO layer. After additional ion beam etching for 10 minutes, 110 nm thick Ag upper electrodes was deposited by thermal evaporation and photoresist was removed. Transport measurements have been done in a standard four-contact setup up to 4.2 K with Keithley 220 Programmable Current Source.

In Fig. 1 we present typical $I(V)$ curves with two branches corresponding to the two internal low-resistive "ON" and high-resistive "OFF" states. Characteristics were measured at 100 K in the current-source mode with time current profiles

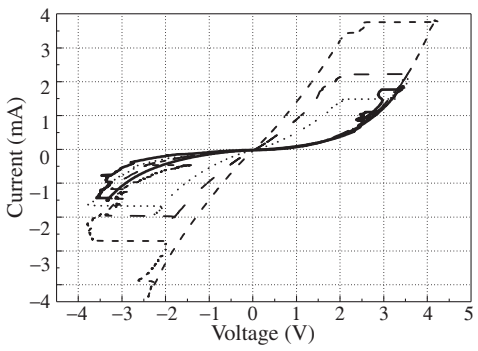

Fig. 1. Typical current-vs-voltage characteristics of the Ag/YBCO heterostructures at 100 K.

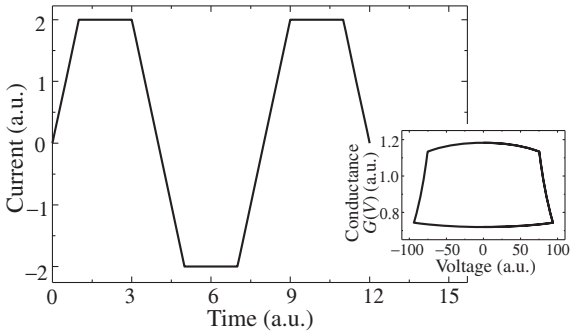

Fig. 2. The time current profile used in the simulations. The inset shows model conductance-vs-voltage characteristic for $c_{\text{bulk}} = 0.2$, $c_0 = 0.8$.

similar to that shown in Fig. 2. Namely, in the high-resistance state after decreasing the dc current to a certain value $\bar{I}$ its value remained constant during the time interval sufficient to transfer the device into the "ON" state (the voltage across the device changed while the current was constant). Then the dc current was increased till switching again into the "OFF" state. With increasing the $\bar{I}$ value the "ON" resistance was going down. Temperature also strongly influenced on the current-voltage curves increasing absolute values of switching parameters with lowering T.

To further characterize the switching mechanism, we investigated the voltage dependence of the contact resistances in both states at 4.2 K when the yttrium-based cuprate was superconducting. Besides the overall behavior, showing the presence of two resistive states, at $|V| < 20$ meV, i.e., at voltages below the YBCO superconducting energy gap, the state "ON" exhibited a fine structure typical for a high-transparency contact between a normal counter-electrode and a superconductor whereas for the state "OFF" we usually observed a quasi-linear background with signs of the gap structure typical for tunnel junctions with a potential barrier between the electrodes [4] (Fig. 3). The gap-induced structure for strongly degraded YBCO surfaces was totally absent in both cases. As is known from the conventional theory of the electron tunneling spectroscopy in MIM heterostructures [4], the transformations observed in Fig. 3 are caused by changes of the transition interlayer between the metallic electrodes on nanometer scales. It proves that the effect we are dealing with appears to be a result of local modifications of the YBCO resistivity in the nano-size vicinity of the metal/cuprate interface.

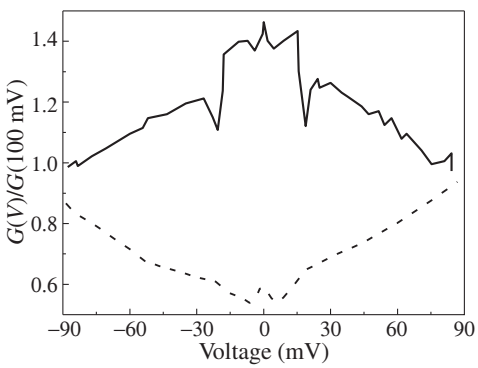

Fig. 3. Conductance-vs-voltage characteristics of the Ag/YBCO heterostructures at 4.2 K.

2. Model

Our oversimplified one-dimensional model assumes that the switching effect occurs in a poor-conducting region of the thickness d in close proximity to the metal/perovskite interface where the content of oxygen vacancies changes in time and in space whereas the rest of the YBCO ($z < 0$) plays the role of their reservoir. The total device resistance is equal to $R(t) = R_0 + \int_0^d dz\rho\,(z,t)$, where $\rho\,(z,t) = \rho_0 \exp(x(z,t)/x_c)$ [5] with fitting parameters R_0 and ρ_0, $x(z,t)$ being the oxygen deficiency index, $x_c \sim 0.2$ [5]. Let us introduce the oxygen concentration $c(z,t) = 1 - x(z,t)$ satisfying a one-dimensional diffusion equation

$$\frac{\partial c(z,t)}{\partial t} = D(c)\frac{\partial^2 c(z,t)}{\partial z^2}, \tag{1}$$

with the diffusion coefficient $D(c) = (1-c)a^2 w$, a being the lattice parameter, and w being the probability of oxygen motion per second. The diffusion quation (1) can be solved with appropriate initial and boundary conditions: in the active region $0 < z < d$ we impose a uniform initial oxygen concentration $c = c_0$ at $t = 0$ and $c(0,t) = c_{\text{bulk}}$, $c(d,t) = 1$.

Without electric field the rates of an ion to overcome the potential barrier U between two neighboring sites 1 and 2 are equal to $r_{1\to2} = r_{2\to1} = \nu \exp(-U/k_{\text{B}}T)$ with ν, the attempt frequency. When the local electric field $E(z,t) = I(t)\rho\,(z,t)$ is applied, the jumps in the $1 \to 2$ direction occur with an enhanced probability comparing with those going back $r_{1\to2(2\to1)} = \nu \exp(-(U \mp eaE)/k_{\text{B}}T)$, where e is the elementary charge. As a result, an average drift velocity w of charged oxygen vacancies in the field direction is

$$w = r_{1\to2} - r_{2\to1} = 2\nu \exp\left(-\frac{U}{k_{\text{B}}T}\right)\sinh\left(-\frac{eaE}{k_{\text{B}}T}\right). \tag{2}$$

For sufficiently small electric fields $eaE \ll k_{\text{B}}T$ from Eq. (2) we get a standard formula for a linear ionic drift with an average ion mobility $\mu = 2ea^2\nu(k_{\text{B}}T)^{-1}\exp(-U/k_{\text{B}}T)$. The inset in Fig. 2 shows the voltage dependence of the contact conductance calculated for a time current profile presented in Fig. 2. It qualitatively describes the experimental data given in Fig. 3 with the exception of the energy-gap region as the superconducting effect has not been included in the model.

Resuming, our experimental data obtained for heterostructures formed by an Ag counter-electrode and epitaxial yttrium-based cuprate films are consistent with an oxygen-drift model for the resistance switching phenomenon in perovskites. They provide new important arguments proving that the effect is directly linked with local modifications of the YBCO resistivity in the nanometer-scale vicinity of the metal/cuprate interface.

References

[1] R. Waser, M. Aono, *Nat. Mater.* **6**, 833 (2007).
[2] A. Sawa, *Mater. Today.* **11**, 28 (2008).
[3] C. Acha, M. J. Rozenberg, *J. Phys.: Condens. Matter* **21**, 045702 (2009).
[4] E. L. Wolf, *Principles of Electron Tunneling Spectroscopy* (Oxford: Oxford University Press) 1985.
[5] K. Yamamoto, B. M. Lairson, J. C. Bravman and T. H. Geballe, *J. Appl. Phys.* **69**, 7189 (1991).

17th Int. Symp. "Nanostructures: Physics and Technology"
Minsk, Belarus, June 22–26, 2009
© 2009 Ioffe Institute

Room temperature operation of a novel quantum-dot based memory device

A. Marent[1], T. Nowozin[1], J. Gelze[1], M. Geller[1,2] and D. Bimberg[1]

[1] Institut für Festkörperphysik, Technische Universität Berlin, Hardenbergstrasse 36, 10623 Berlin, Germany
[2] Experimentalphysik & CeNIDE, University Duisburg-Essen, Lotharstr. 1, 47048 Duisburg, Germany

Abstract. We demonstrate room temperature operation of a first prototype memory using self-organized semiconductor quantum dots (QDs) as storage units. The prototype consists of InAs QDs embedded in an $Al_{0.9}Ga_{0.1}As$ matrix enabling storage times up to seconds at room temperature. Read out of the stored information was realized by measuring the resistance of a two-dimenional hole gas formed in a GaAs/$Al_{0.9}Ga_{0.1}As$ quantum well embedded below the QD-layer. Write and erase times are in the range of μs.

Introduction

Mainly two memory types dominate the present semiconductor memory market: The DRAM (dynamic random access) [1] and the Flash [2] memories. Both types have distinct advantages concerning access speed, endurance and storage time. DRAMs provide fast access times (below 20 ns) and good endurance ($>10^{15}$ read/write cycles), but the stored information has to be refreshed within ten milliseconds (they are volatile). Flash memories are non-volatile with storage times in the order of 10 years but exhibit a bad endurance ($<10^6$) and a slow write speed ($\sim \mu$s). Development of faster Flash memories with better endurance is at present actively pursued.

One of the promising options is the use of self-organized nanostructures, especially quantum dots (QDs) based on III–V semiconductors. Recently, we proposed a novel memory concept (QD-Flash) based on QDs [4,5], which should enable very fast write times (< ns) independent of the carrier storage time, enabling long storage times (>10 years). The write time in our concept is limited only by the charge carrier relaxation time from the band edge to the QD states, which is below picoseconds at room temperature [6,7], more than four orders of magnitude faster than the write time of a DRAM cell. We demonstrated previously a storage time of seconds at room temperature for InAs QDs with an $Al_{0.9}Ga_{0.1}As$ barrier suggesting more than 10^6 years for GaSb QDs in an AlAs matrix [8]. In addition, a short write time of 6 ns in InAs/GaAs QDs, already in the order of the access time of a DRAM cell was measured [5].

Here, we present a first prototype of a QD-Flash memory with full functionality at room temperature using InAs QDs embedded in $Al_{0.9}Ga_{0.1}As$. Read-out of the stored information at room temperature is demonstrated using a two-dimensional hole gas (2DHG) embedded below the QD-layer.

1. Sample structure and memory operations

The layer structure of the QD-Flash prototype is shown in Fig. 1(a). 135 nm below the surface the InAs QDs are embedded in undoped $Al_{0.9}Ga_{0.1}As$. 15 nm below the QD layer a 2DHG is formed using a GaAs quantum well and a highly p-doped $Al_{0.9}Ga_{0.1}As$ layer which provides the holes to form the 2DHG. This layer structure is designed to store holes in the QDs. The 2DHG acts as a read out detector. Stored holes in

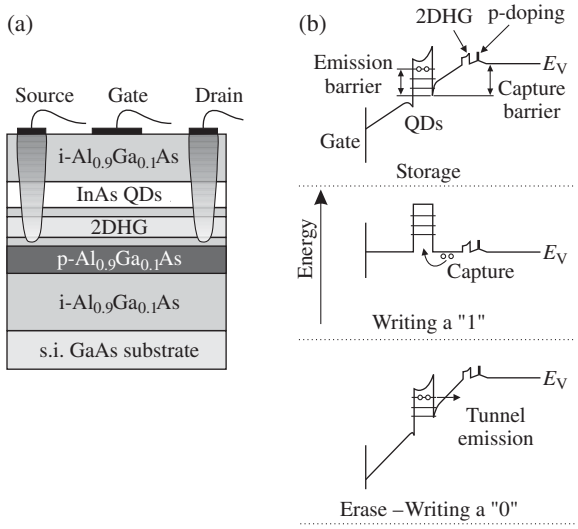

Fig. 1. (a) Layer structure of the QD-Flash prototype with InAs QDs in $Al_{0.9}Ga_{0.1}As$. (b) Memory operations of the QD-Flash concept (storage, writing, erasing).

the QDs deplete the charge density in the 2DHG and, hence, a higher resistance is measured between the source/drain contacts.

Figure 1(b) shows schematically the valence band of the structure for the three different operation modes of a memory: storage, writing, and erasing. At the storage position the localization energy of holes in the QDs represent an emission barrier needed to store a logical '1' state. To store a '0' state a capture barrier is necessary. It is formed by the band-bending of the depletion region of the gate's Schottky barrier. To write a '1' state a forward bias is applied to eleminate the capture barrier and holes can directly relax in the QD states. To erase the information, the depletion region is expanded and tunneling in a high electric field occurs. Read out is done by resistance measurements of the 2DHG.

2. Performance of the QD-Flash prototype

Figure 2 displays the switching between the two logical states by a hysteresis curve of the resistance in the 2DHG at room temperature (295 K). At a gate bias of more than -0.5 V the QDs are fully occupied with holes ('1' state). If the gate bias is now swept to the storage position (e.g. -2.5 V), the QDs

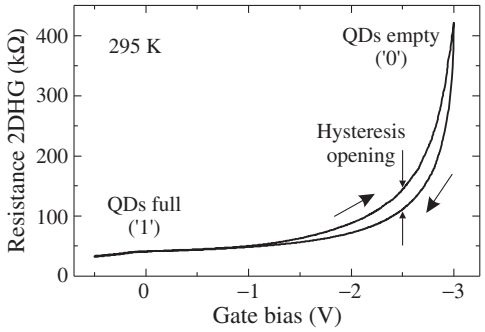

Fig. 2. Resistance sweep of the QD-Flash prototype at 295 K.

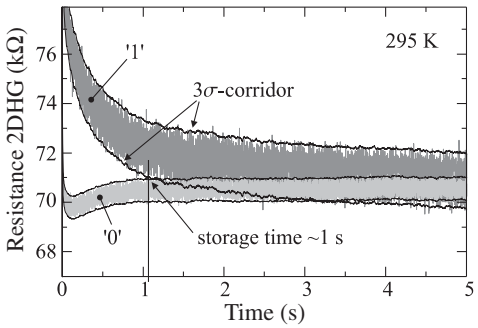

Fig. 3. Time resolved resistance measurements of the 2DHG for initially fully occupied QDs (upper transient) and initially empty QDs (lower transient). The 3σ-corridors of both transients start to overlap at a time of about 1 s defining the storage time of the prototype.

are full and a larger resistance is observed. If the gate bias is swept to -3 V, holes tunnel out of the QDs ('0' state) and a smaller resistance is observed upon sweeping back to the storage position. The maximum of the hysteresis opening as the difference between the resistance values for '0' and '1' states is more than 34% of the resistance measured for empty QDs.

2.1. Storage time

The storage time of a memory is defined as the time until which the two logical states '0' and '1' can be clearly distinguished (here via a resistance measurement of the 2DHG). We measured time resolved the resistance of the 2DHG at a storage position of -2 V after applying a write pulse of 1.5 V as well as applying an erase pulse of -3 V. The observed resistance transients at the storage position are shown in Fig. 3. The upper transient in Fig. 3 represents the change of the resistance of the '1' state. Due to hole emission out of initially fully occupied QDs, the resistance decreases on equilibrium state. The lower transient in Fig. 3 represents the '0' state. Here, the resistance increases as holes are captured into initially empty QDs until equilibrium state is reached. The two logical states cannot longer be distinguished when both transients start to overlap. Including a standard deviation of 3σ we obtain a storage time at 295 K of about 1 s. Recently, we have determined the hole storage time in $InAs/Al_{0.9}Ga_{0.1}As$ QDs to 1.6 s at 300 K using capacitance spectroscopy measurements [8]. The storage time of the prototype is in good agreement with these results. This supports the assumption that the QDs act as the storage unit.

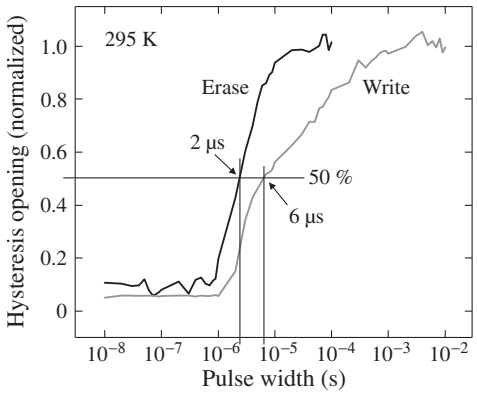

Fig. 4. Hysteresis opening for varying write/erase pulse widths.

2.2. Write and erase time

To study the limits of the write and erase times, series of write/erase pulses were applied with decreasing pulse widths down to 10 ns. The measurement starts with a write/erase pulse of 3 V and -4 V, respectively. Then, the hysteresis opening at a storage position of -1 V is determined. A shortening of the write/erase pulse width leads to a decrease of the hysteresis opening if the QDs are not sufficiently charged/decharged anymore. We define the write/erase time limit as a drop in the hysteresis opening to 50 of its maximum. The normalized hysteresis opening is plotted versus the write/erase pulse width in Fig. 4. A minimum write time of 6 μs and a minimum erase time of 2 μs is obtained. The write/erase times are at the moment still limited by the experimental setup and the parasitic cutoff frequency of the RC low pass of the device. Much faster write/erase times should be feasible for improved structures having higher external cutoff frequencies.

Acknowledgements

This work was partly funded by the QD-Flash project in the framework of ProFIT of the Investmentbank Berlin (IBB) and by DFG Grant No. BI 284/29-1.

References

[1] R. Waser, Microelectronics and Information Technology, Wiley-VCH, Berlin, 2003.

[2] P. Pavan, R. Bez, P. Olivo, E. Zanoni, *Proc. of the IEEE* **85** (8) 1248–1271 (1997).

[3] L. Geppert, *IEEE Spectrum* **40** (3), 48–54 (2003).

[4] M. Geller, A. Marent, D. Bimberg, Speicherzelle und Verfahren zum Speichern von Daten, German patent application No. 10 2006 059 110.0, Germany, 27.10.2006.

[5] M. Geller, A. Marent, T. Nowozin, D. Bimberg, N. Akç ay, N. Öncan, *Appl. Phys. Lett.* **92** (9), 092108 (2008).

[6] M. Geller, A. Marent, E. Stock, D. Bimberg, V. I. Zubkov, I. S. Shulgunova, A. V. Solomonov, *Appl. Phys. Lett.* **89** (23), 232105 (2006).

[7] T. Müller, F. F. Schrey, G. Strasser, K. Unterrainer, *Appl. Phys. Lett.* **83** (17), 3572–3574 (2003).

[8] A. Marent, M. Geller, A. Schliwa, D. Feise, K. Potschke, D. Bimberg, N. Akç ay, N. Öncan, *Appl. Phys. Lett.* **91** (24), 242109 (2007).

17th Int. Symp. "Nanostructures: Physics and Technology"
Minsk, Belarus, June 22–26, 2009
© 2009 Ioffe Institute

Silicon nanowire Field Effect Transistor as a core element for the bio- and chemical femtomolar sensors

V. A. Krupenin[1], D. E. Presnov[2], *V. S. Vlasenko*[1] and S. V. Amitonov[1]

[1] Laboratory of Cryoelectronics, Moscow State University, 119991 Moscow, Russia
[2] Nuclear Physics Institute, Moscow State University, 119991 Moscow, Russia

Abstract. In this work authors offer simplified fabrication method of Silicon nanowire field effect transistor (FET) which does not involve doping and activation. Interfaces of the electrode metal contacts (Ti) with source and drain of transistor form two Schottky's barriers that could be used to control a bias current with the gate electrode. Voltage-current characteristics of the experimental structures were measured over a wide range (−10 V to +10 V) of the gate voltages. The possibility of using of the silicon nanowire FET as a supersensitive field/charge sensor was analyzed.

Introduction

Recent advances in nanoscale fabrication technologies and crossdisciplines researches allow to develop original devices, such as nanowire based field effect transistors, which can be used not only in physical experiments and electronic schemes but also in a wide variety of biological and chemical applications, for example, as ultra small bio- and chemical sensors [1] with femtomole sensitivity to the certain type of objects [1–5]. Modification of the nanowire (it serves as a conductive channel of the transistor) surface with special molecules, which can selectively bind the objects of interest (such as viruses [2–3], DNA [4–5], etc.), allows to construct brand new devices which can detect even a single virus or molecule (Fig. 1) [3]. This could be vital step in problems of early medical diagnostics, harmful biological substances detection in bioterrorism protection and biowarfare.

1. Samples fabrication

In this work we used technology that is based on a reactive ion etching of required structures pattern through the metal mask. Experimental structures were fabricated from silicon-on-insulator (SOI) film. We used SOI material with 110 nm thick silicon layer with the p-type doping and 200 nm insulating SiO_2 layer placed on a silicon substrate. After e-beam lithography for the structure patterning a metal mask was formed by deposition of Al thin film. Then using the reactive ion etching of SOI film through the Al mask we made nanowires approximately 120 nm in width and 1.5 μm in length (Fig. 2). After lift-off of the Al mask contact pads of the nanowires were made with a consecutive deposition of Ti (15 nm) and then Au (50 nm) through another resist mask. The backside of the substrate serves as a gate electrode for all the structures on the same sample.

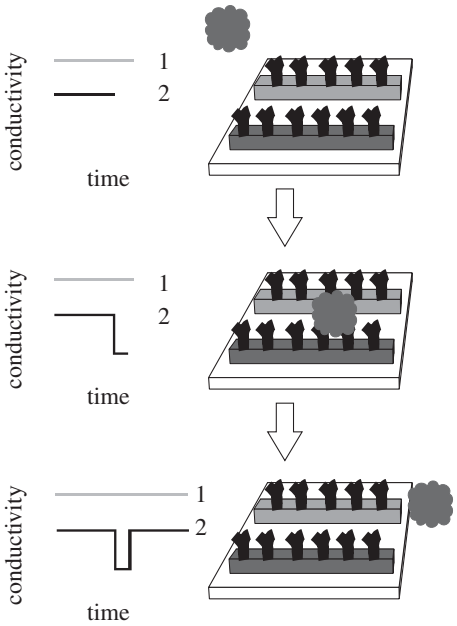

Fig. 1. Working principles of Nanowire transistor as an ultra sensitive biological sensor.

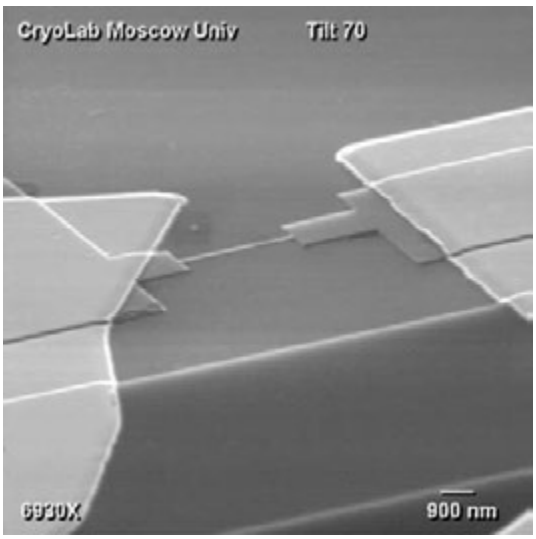

Fig. 2. Nanowire transistor structure (SEM image).

2. Results

In source/drain contacts interface with a doped Si nanowire a Schottky barrier occurs [6]. At high gate voltages electrons could tunnel through the barrier as its width decreases. For the positive gate voltages the width of the barrier for electrons is sufficiently low to form an inverse conductive channel in a nanowire.

We have observed IV-characteristics of the Si nanowire FET structures by applying source-drain voltage and measuring the current at different gate voltages (Fig. 3). All the devices show

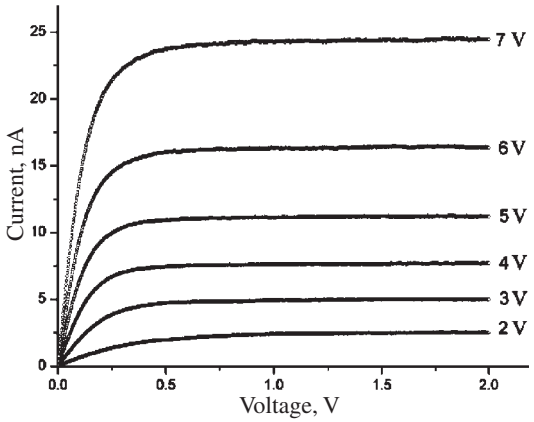

Fig. 3. IV-characteristics of Si nanowire FET at different gate voltages.

enhancement-mode operation for positive gate biases (inverse electron channel) with saturated drain current. Even at high negative gate voltages (up to the -10 V) p-type conductivity was too low hereby no close investigations were carried out.

Conductivity of transistor channel depends on the electric field applied to the Si nanowire. Even a local disturbance of the electric field around the nanowire could change its conductivity notably. This enables to register any small charged particles which are attached to (detached off) the surface of Si nanowire channel: molecules, nanoparticles, viruses, DNA etc.

3. Conclusions

Fabricated Si nanowire FET discussed above shows the capability to serve as a very good core element of the bio- and chemical sensors. Modification of its surface with the selectively binding molecules and radicals could provide us a nanoscale femtomolar selective sensor. Introduced technology offers great reproducibility and high quality of the fabricated structures.

Acknowledgements

Authors wish to express their gratitude to professor M. Yu. Kupriyanov for assistance provided during this work discussion and preparation.

References

[1] Yi Cui, Qingqiao Wei, Hongkun Park, Charles M. Lieber, *Science* **293**, 1289–1292 (2001).

[2] Eric Stern, James F. Klemic, David A. Routenberg, Pauline N. Wyrembak, Daniel B. Turner-Evans, Andrew D. Hamilton, David A. LaVan, Tarek M. Fahmy and Mark A. Reed, *Nature* **445**, 519–522 (2007).

[3] Fernando Patolsky, Gengfeng Zheng, Oliver Hayden, Melike Lakadamyali, Xiaowei Zhuang and Charles M. Lieber, *PNAS* **101** 39, 14017–14022 (2004).

[4] Wayne U. Wang, Chuo Chen, Keng-hui Lin, Ying Fang, and Charles M. Lieber, *PNAS* **102** 9, 3208–3212 (2005).

[5] Jong-in Hahm and Charles M. Lieber, *Nano Letters* **4** 1, 51–54 (2004).

[6] Sang-Mo Koo, Monica D. Edelstein, Qiliang Li, Curt A. Richter and Eric M. Vogel, *Nanotechnology* **16**, 1482–1485 (2005).

17th Int. Symp. "Nanostructures: Physics and Technology"
Minsk, Belarus, June 22–26, 2009
© 2009 Ioffe Institute

Planar InGaAs/InAlAs avalanche photodiode with gain-bandwidth product over 100 GHz

A. L. Chizh, S. A. Malyshev and Y. G. Vasileuski

B. I. Stepanov Institute of Physics, NASB, pr. Independency, 68, Minsk, 220072, Belarus

Abstract. Numerical simulation of planar InGaAs/InAlAs/InP avalanche photodiode is performed. Simulation results of spatial electric filed distribution, current-voltage, and bandwidth-gain characteristics are discussed.

Introduction

A great activity is being carried out worldwide to develop avalanche photodiodes including materials, fabrication, and its application. Vertical illuminated planar InGaAs/InP avalanche photodiodes with separated $In_{0.53}Ga_{0.47}As$ absorption layer, InGaAsP graded charge sheet and InP multiplication layer are widely used for optical fiber communication systems operating near 1300 and 1550 nm wavelength due to the internal gain provided by impact ionization. However impact-ionization rate for holes in InP is greater than that for electrons up to 2 times, therefore today, $In_{0.52}Al_{0.48}As$ holds interests as avalanche material with electron-injection structure and ionization coefficient ratio up to 3, which allows avalanche photodiodes based on InGaAs/InAlAs to enlarge gain-bandwidth product and decrease excess noise factor [1–2].

In this paper, we report theoretical investigation of performance of InGaAs/InAlAs separated absorption, charge, and multiplication avalanche photodiodes with thin multiplication region based on 2D numerical simulation.

1. Avalanche photodiode structure

A schematic cross section of an InGaAs/InAlAs avalanche photodiode based on a guardring-free planar structure is shown in Figure 1. Photodiode structure consists of 700 nm thick p^+-region with doping concentration of 5×10^{18} cm^{-3}, formed in 600 nm thick top i-InP layer, 1200 nm thick i-InGaAs absorption layer, 100 nm thick p-InAlGaAs graded transition layer and 50 nm p-InAlAs charge sheet with doping density of 3×10^{12} cm^{-2}, 200 nm thick i-InAlAs multiplication layer, n^+-InAlAs buffer layer and n^+-InP substrate with doping concentration of 2.5×10^{18} cm^{-3}. Outer diameter of the modeling structure (die diameter) is 300 μm, while diameter of the p^+-region equals to 25 μm.

Numerical model, used for simulation, is based on drift-diffusion scheme and piecewise harmonic balance method and well presented elsewhere [3–6]. For $In_{0.52}Al_{0.48}As$ material we have used a single set of parameters that satisfied the exponential model independent of the multiplication-region width [7].

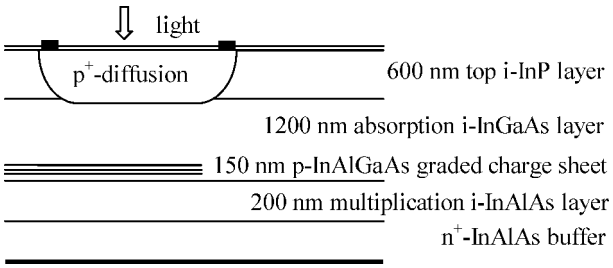

Fig. 1. Cross section of the planar InGaAs/InAlAs avalanche photodiode.

Figure 2 shows electric field profile of the avalanche photodiode. Due to highly doped p-InAlAs charge sheet electric field exceeds 650 kV/cm in multiplication layer and is about 100 kV/cm in absorption layer at avalanche mode. At the periphery of the diffused p^+-region the smooth electric field perturbations could not cause tunneling or impact ionization edge breakdown.

2. Avalanche photodiode characteristics

Figure 3 shows current-voltage and gain-voltage characteristics for the avalanche photodiode under 100 optical power. As can be seen, breakdown voltage is about 29 V, and multiplication gain exceeds 100. At the 13 V reverse bias voltage dark current is 11.3 nA and sensitivity at the 1550 nm wavelength and unity gain is 0.95 A/W, which meet experimental data [1–2,8].

The 3-dB bandwidth-gain characteristic, shown in Figure 4, has been calculated for 50 Ω load resistance and 100 nW optical power. Figure shows that maximum bandwidth of the avalanche photodiode is 7.5 GHz, observed at a gain of 6. At higher gains, the bandwidth decreases, limited by the avalanche buildup time. In this mode, the gain-bandwidth product (GBP) equals 100 GHz.

Figure 5 illustrates the influence of absorption and multiplication layer thickness on gain-bandwidth product. One can see that, as for conventional p-i-n photodiode, there is a trade-off between bandwidth and quantum efficiency. In spite of this trade-off, it is possible to simultaneously achieve near 100% quantum efficiency and gain-bandwidth product over 100 GHz by nanometer scaling of the multiplication layer thickness. The

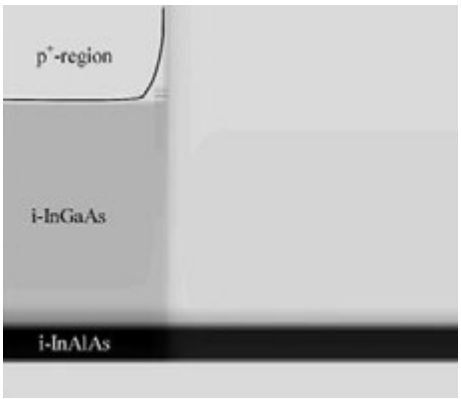

Fig. 2. Electric field distribution.

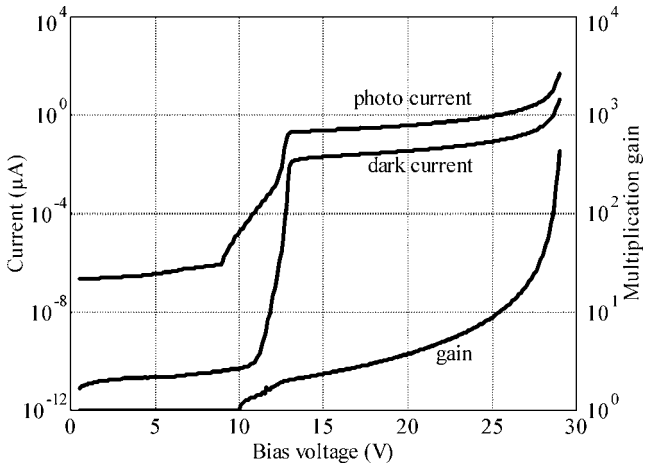

Fig. 3. Dark current, photocurrent, and multiplication gain versus bias voltage at 100 nW optical power.

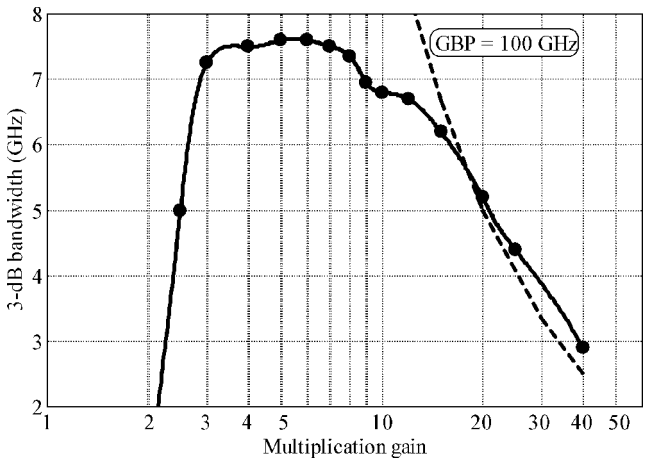

Fig. 4. 3-dB bandwidth versus multiplication gain.

gain-bandwidth product of the InGaAs/InAlAs avalanche photodiodes is over 30 GHz and can be up to 180 GHz.

It should be noted that gain-bandwidth product does not depend on InGaAs absorption layer thickness when multiplication layer is thicker than 500 nm. In this case InGaAs/InAlAs avalanche photodiode frequency response is determined rather by avalanche build-up time than by transient time or RC-time.

3. Conclusion

We have simulated characteristics of avalanche photodiode based on $In_{0.53}Ga_{0.47}As/In_{0.52}Al_{0.48}As$ heterostructure. It is found that frequency response of such photodiode is limited by avalanche buildup time, and it is possible to simultaneously achieve near 100% quantum efficiency and gain-bandwidth product over 100 GHz by nanometer scaling of the multiplication layer thickness. Such photodiodes can be used in fiber-optic communication systems and for single photon counting applications.

References

[1] E. Yagyu *et al*, *IEEE Photon. Technol. Lett.* **19**, 765 (2007).
[2] A. Rouvie *et al*, *IEEE Photon. Technol. Lett.* **20**, 455 (2008).
[3] S. Malyshev *et al*, *Semiconductors* **40**, 1116 (2006).
[4] S. Malyshev *et al*, *Proc. of EUROCON-2007* Warsaw, Poland, 2047 (2007).

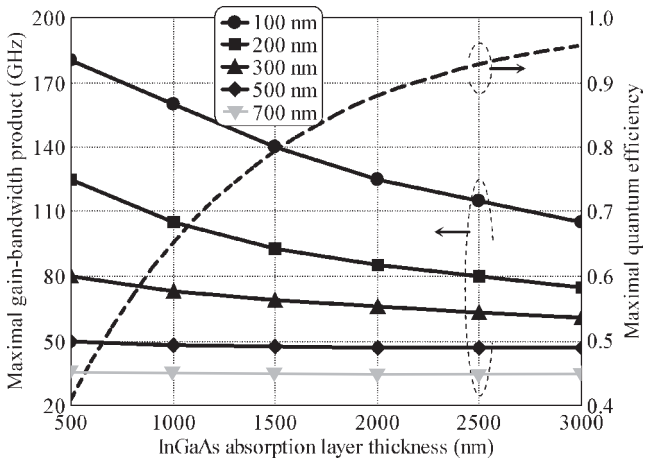

Fig. 5. Maximal gain-bandwidth product and quantum efficiency at the wavelength 1500 nm versus InGaAs absorption layer thickness for different InAlAs multiplication layer thicknesses.

[5] S. Malyshev *et al*, *Proc. of NUSOD-2008* Nottingham, Great Britain, 81 (2008).
[6] S. Malyshev *et al*, *J. of Lightwave Technol.* **26**, 2732 (2008).
[7] M. Saleh *et al*, *IEEE Trans. on Electron Devices* **48**, 2722 (2001).
[8] E. Yagyu *et al*, *IEEE Photon. Technol. Lett.* **18**, 76 (2006).

17th Int. Symp. "Nanostructures: Physics and Technology"
Minsk, Belarus, June 22–26, 2009
© 2009 Ioffe Institute

Physics and technology preparation of planar x-ray waveguide-resonator

E. V. Egorov and V. K. Egorov
IMT RAS, Chernogolovka, Moscow district, 142432 Russia

The invention of planar X-ray waveguide-resonator (PXWR) is the great present for nanotechnology and the direct challenge for x-ray synchrotron facilities [1]. PXWR is a very simple device but it allows to form thread X-ray beams with width 7–200 nm characterized by an enhanced radiation density and a low flux angular divergence. These devices have beautiful perspectives for fundamental material researches and wide practical application. So, it is very important to pay attention to the waveguide-resonator physical background and the technological peculiarities of it's preparation.

The waveguide-resonator is formed by couple planar dielectric reflectors placed opposite each other on distance, which must be smaller as the coherence length of the quasimonochromatic X-ray radiation transported by the device. The taking into account the fundamental radiation parameter — it's coherence length leads to the principle difference of the waveguide-resonance mechanism for X-ray beam propagation through the planar nanosize slit clearance from the multiple total reflection one. The radiation coherence length defines possibilities of the waveguide-resonance mechanism arising and by such manner limits the critical distance between reflectors formed PXWR. PXWR has the width of slit clearance smaller as the critical size. The width is defined by the thickness of strips deposited on edges of one reflector in the couple. Accordingly to our opinion, the deposit technology must supply very high thickness uniformity on all length of the strips [2]. But for the practical purposes it is very important to know the critical value for the strips thickness nonuniformity. The work is devoted to discussion of the new type mechanism physics and the technological thickness inaccuracy at the strips deposition and to evaluation of permissible non-parallelism between reflectors forming the waveguide-resonance channel. There are presented the experimental results supported the new mechanism idea and demonstrated that the standard inaccuracy typical for conventional methods of long coating deposition $l \approx 100$ mm is acceptable for PXWR preparation. There are discussed features of X-ray waveguide-resonator and possibilities of PXWR using for elaboration of new devices for X-ray fluorescence analysis and diffractometry of nanostructures. Directions for PXWR properties modifications are pointed.

References

[1] V. K. Egorov *et al*, *X-ray Spectrometry* **36**, 381 (2007).
[2] V. K. Egorov *et al*, *Thin Solid Films* **398-399**, 405 (2001).

17th Int. Symp. "Nanostructures: Physics and Technology"
Minsk, Belarus, June 22–26, 2009
© 2009 Ioffe Institute

Ultrafast e-h plasma response in semiconductor nanomaterials

S. A. Tikhomirov[1], O. V. Buganov[1], V. V. Stankevich[1], *M. V. Ermolenko*[1], A. S. Shulenkov[2] and S. V. Gaponenko[1]

[1] B. I. Stepanov Institute of Physics, NASB, Minsk 220072, Belarus
[2] Minsk Research Institute of Radiomaterials, Minsk 220024, Belarus

Abstract. Ultrafast nonlinear properties of semiconductor Bragg nanostructures were studied. Optical properties of GaAs/$(AlGa)_xO_y$ heterostructures were examined using interband excitation by 150 fs laser pulses. The mean decay time for nonlinear wideband response in heterostructures ranges from 1.0 to 2.5 ps. The possibility of 1.5 μm ultrafast all-optical modulator realization is discussed.

Introduction

The thermalization and cooling of electron-hole (e-h) plasma in semiconductors and their heterostructures are of crucial importance for most optoelectronic devices. Application of heterostructures in a single circuit board or a single chip promotes to scale down the dimensions of the latter. Utilization of various ultrafast nonlinear properties of semiconductor materials will possibly increase data transfer rate in the future.

Because of high standards of data transfer rate (nowadays they are tens gigahertz per channel) design and integration of ultrafast optical modulators have become the barest necessity. A number of ultrafast all-optical and electro-optical devices [1–6] have been proposed to date. However, due to high energy consumption and dissipation, complexity of production process and on-chip integration, none of these devices is used extensively.

In the present article, effects of e-h plasma thermalization and cooling in multilayer heterostructures are proposed as one way of operating principles of light modulators. In case if one of the materials constituting the heterostructure is nonlinear than it is possible to substantially modify transmission and reflection spectra by intense laser radiation. Heterostructures should be constructed in such a way that by insignificant change of refractive index it would be possible to substantially change the reflection/transmission spectra. To strongly modify reflection/transmission spectra the contrast of refractive indices of the constituting materials should be as large as possible. One more essential condition is sufficient band-gap energy difference of both sublattices to have possibility of only one sublattice excitation. In this case pronounced modification in transmission and reflection spectra is feasible. To produce high-performance structures with low number of defects, compatibility of lattice constants for the materials used is necessary as well. In spite of heterostructures design there is one more important factor influencing on performance of optical modulator. That is nonlinear response of e-h plasma. A nonlinear material should possess ultrashort relaxation/recombination times of e-h plasma. The shorter relaxation/recombination times the faster light modulator can be produced.

Summing up suggested light modulator represents a sharp-edge interference filter based on multilayer heterostructure which has one nonlinear sublattice with ultrafast response of e-h plasma under the condition of intense laser excitation. The wavelength of transmission/reflection maximum of such filter should correspond to wavelength of interest (e.g. 1.5 μm). Under intense laser excitation this maximum gives place to minimum. The sharper edges of maximum the greater modulation can be achieved. This idea was realized with GaAs/$(AlGa)_xO_y$ based heterostructures in the present work.

1. Experimental

GaAs and $(AlGa)_xO_y$ pair satisfies in the best way all primary requirements. GaAs has become a model system for the studies of ultrafast dynamics in semiconductors because of its scientific and technological relevance. Nonlinear properties of GaAs are well known for a long time. Besides strong nonlinearities GaAs has large refractive index. $(AlGa)_xO_y$ has notably smaller refractive index and greater band-gap energy depending on oxygen concentration. GaAs/$(AlGa)_xO_y$ multilayer heterostructures are formed from GaAs/$Al_xGa_{1-x}As$ ones by lateral selective etching in water vapour of $Al_xGa_{1-x}As$ layers with high concentration of AlAs [7]. By selective oxidation of AlGaAs in atmosphere saturated with water vapor GaAs/Al_xO_y periodic heterostructure could be produced. Refractive indices of the materials of such a pair differ by about two times.

Transient spectroscopy experiments were performed with pump-probe spectrometer [8] based on a home-made original femtosecond Ti:saphire pulsed oscillator and a regenerative amplifier system operated at 10 Hz repetition rate. The Ti:sapphire master oscillator was synchronously pumped with doubled output of feedback controlled mode-locked picosecond pulsed Nd:YAG laser. The pulse width and energy of Ti:sapphire system after the amplifier were 150 fs and 0.5 mJ, respectively, tunable over the spectral range 760–820 nm. The fundamental output of the Ti:sapphire system (790 nm output wavelength was set for present study) split into two beams in the ratio 1:4. The more intense beam passed through a controlled delay line and was utilized for sample pumping. The second beam of fundamental frequency was used for generation of a femtosecond supercontinuum (by focusing into a 1 cm path length cell with water or into a sapphire plate) which served as the probe radiation. The continuum probe light was split with a beam splitter into two pulses (reference and signal), identical in intensity, and was focused on the sample by mirror optics. The spectra of both reflected pulses were recorded for every laser

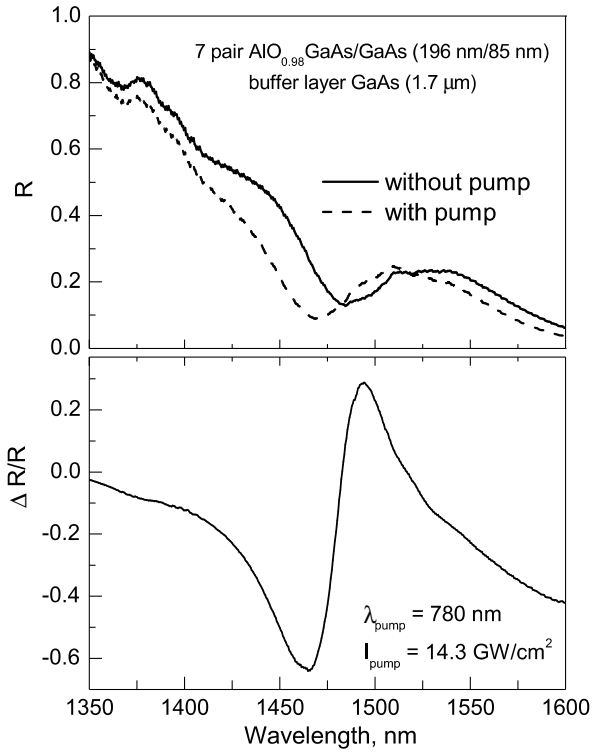

Fig. 1. Reflection spectrum of a 7-period GaAs/$(AlGa)_xO_y$ Bragg structure (top), its modification under excitation at 795 nm in terms of relative differential reflection (bottom).

flash by a polychromator equipped with silicon CCD matrix and transferred to the computer. Time resolution of the setup is limited by the pump and probe pulse duration and estimated as 0.2 ps. For measurements in spectral range 1–1.6 μm a IR array detector based on InGaAs was used.

2. Results

The experiments were performed for a 7-period GaAs/$(AlGa)_xO_y$ heterostructures grown on a GaAs substrate. This sample was excited by the fundamental harmonic of the Ti:sapphire laser at room temperature. In all experiments a strong ultrafast wideband nonlinear response was observed both near absorption onset of GaAs and in spectral range (Fig. 1) where both materials have negligible absorption (up to 1,6 μm). The short component of the response time varies from 1.0 to 2.5 ps (Fig. 2). As it was shown in previous investigations [9–11] the nonlinear response extends far from the fundamental absorption edge in region of material transparency, the mean response time being approximately equal in the whole measured spectral range except vicinity of the fundamental absorption edge. Responses in the range of material transparency and in the vicinity of the absorption edge are due to essentially different phenomena.

Nonlinear response near absorption onset of GaAs results from band gap renormalization caused by free carries in the bottom of the conduction band and in the top of the valence band. Response far from the fundamental absorption edge in the region of material transparency is defined only by dense e-h plasma excited in the GaAs sublattice.

As a result of intense excitation high concentration of free carries is established which in turn leads to approaching of

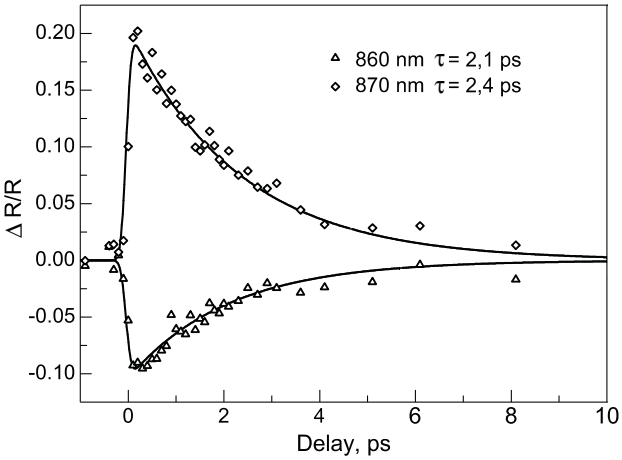

Fig. 2. Nonlinear reflection kinetics for a 7-period GaAs/$(AlGa)_xO_y$ heterostructure (dots) recorded at different probe wavelengths. Curves correspond to fitting.

plasma frequency to VIS-IR spectral range. It means that concentration of free carries is large enough to noticeably change refractive index, absorption factor still being negligible.

The considerable shift ($\sim$25 nm) of reflectance spectrum was obtained at $\sim$1.5 μm. Maximal change of reflectivity in this spectral range was about 10%. More considerable changes could be achieved in case of heterostructure with sharp-edge reflection spectrum.

3. Conclusion

In conclusion, we have demonstrated the possibility of design of the ultrafast light modulator based on semiconductor Bragg reflectors. In case of GaAs/$(AlGa)_xO_y$ heterostructure we observed a strong spectrally wide nonlinear response with the relaxation time of 1.0–2.5 ps in the spectral range where both materials have negligible absorption. These short times correspond to e-h plasma relaxation time. By designing the structure possessing reflection/transmission spectrum with sharper edges it is possible to obtain a considerably deeper modulation of reflectivity.

References

[1] D. Cotter *et al*, *Science* **286**, 19 (1999).
[2] T. Asano *et al*, *Appl. Phys. Lett.* **79**, 4509 (2001).
[3] X. Yang *et al*, *Opt. Comm.* **236**, 329 (2004).
[4] A. Liu *et al*, *Nature* **427**, 615 (2004).
[5] V. R. Almeida *et al*, *Opt. Lett.* **30**, 2733 (2005).
[6] R. S. Jacobsen *et al*, *Nature* **441**, 199 (2006).
[7] N. A. Maleev *et al*, *Semiconductors*, **39**, 487 (2005).
[8] A. P. Blokhin *et al*, *Zh. Prikl. Spektrosk.* **70**, 66 (2003).
[9] V. V. Stankevich *et al*, *Appl. Phys. B* **81**, 257 (2005).
[10] M. V. Ermolenko *et al*, *Photonics and Nanostructures* **5**, 101 (2007).
[11] M. V. Ermolenko *et al*, *Proc. of SPIE* **7138**, 71381Y (2008).

17th Int. Symp. "Nanostructures: Physics and Technology"
Minsk, Belarus, June 22–26, 2009
© 2009 Ioffe Institute

Colour centers in nanostructured diamond — perspective resource for quantum informatics

S. Ya. Kilin[1], A. P. Nizovtsev[1], A. L. Pushkarchuk[2], F. Jelezko[3] and J. Wrachtrup[3]

[1] B. I. Stepanov Institute of Physics NASB, 220072 Minsk, Belarus
[2] Institute of Physical Organic Chemistry NASB, 220072 Minsk, Belarus
[3] Institute of Physics, University of Stuttgart, 70550 Stuttgart, Germany

Abstract. We are presenting results of recent investigations (including our ones) of structural, photophysical, spectral, spin and dynamical characteristics of single colour centers in bulk and nano-sized diamond. As well, recent progress in diamond material engineering and nano-structuring is reviewed and perspectives to implement various diamond-based quantum information applications are discussed.

Introduction

The field of quantum information is rapidly growing towards its practical implementations [1]. New achievements in the investigations of different candidates for prototypes of quantum information (QI) hardware (qubits, gates, scalable quantum processors, quantum memories, repeaters, etc.) are emerging in a short time scale. Well-recognized leader in the "Quantum Information Race" is the group of "solid state participants" which has evident advantages among other candidates for QI technological applications. Among them, defects in wide band-gap semiconductors, particularly defect colour centers in diamond, are becoming more and more attractive [2, 3]. For example, it has been suggested [4] that single electron and nuclear spins in these systems can be used as qubits to implement quantum computing. Another practically important application of single colour centers in diamond is to generate single-photons on demand [5] for quantum cryptography. Precise characterisation and understanding of quantum properties of single colour centers in diamond is still under progress. A great variety of colour centers and complex environment conditions together with strict limitations posed on candidates for QI applications make the characterisation of these defects an important and hard problem.

1. NV center-based QI hardware

The mostly investigated potential candidate for spin-based qubit applications is the negatively charged nitrogen-vacan-cy defect center ($[\text{N-V}]^-$ center) in diamond, consisting of the substitutional N atom and the vacancy in an adjacent site of a diamond lattice. The center exhibits a strong dipole-allowed optical transition with a zero-phonon line at 1.945 eV ($\lambda = 637$ nm) originating from optical transition ^{3}A-^{3}E between ground ^{3}A and excited ^{3}E electronic states which are both the spin triplets ($S = 1$). The ground ^{3}A state is split by 2.88 GHz into the lower $m_S = 0$ level and the upper $m_S = \pm 1$ levels. Analogous fine structure strongly influenced by stresses in diamond crystal presents in the excited ^{3}E state. Additionally, the center has the metastable singlet states ^{1}A and ^{1}E [6].

The center can be individually isolated and optically detected [7], thus opening the excess to long-lived single spin $S = 1$ in the ground ^{3}A state which can be physical carrier of qubit. The first step for coherent single spin manipulation is to prepare a pure state of the spin. For the $[\text{N-V}]^-$ center, spin state preparation can be achieved by optical pumping with a polarized laser beam tuned above the absorption band [8, 9]. Decay from the ^{3}E level via optical emission dominates but conserves spin. On the other hand, decay via the singlet levels ^{1}A and ^{1}E is slower since it does not conserve spin. Competition between those two processes leads to a spin polarization of the ^{3}A ground level with preferential population transfer to the $m_S = 0$ spin sublevel [8, 9]. Once polarized, the electronic spin can be manipulated using microwave resonant fields [7]. Read-out of the spin state is achieved optically because the fluorescence occurs predominantly when the spin state is $m_S = 0$ for both ^{3}A ground and ^{3}E excited energy levels [10, 11, 12]. Due to weak interaction with very hard surrounding diamond lattice the electron spin coherence time is rather long even at room temperature. In the material, limitation of coherence time arises from local magnetic field fluctuations induced by nearby defects (mostly, by flipping nitrogen electron spins $S = 1/2$). Respectively, the need for ultra-pure diamond samples was highlighted and it was demonstrated that in pure diamond samples the coherence time ~0.65 ms can be achieved [13].

Along with the electronic spins of the NV centers, nuclear spins of surrounding atoms are also envisaged as carriers of quantum information thanks to their very long coherence time, going up to seconds. In diamond, nuclear spins of an isotopic ^{13}C carbon atom having nuclear spin $I = 1/2$ can be naturally coupled to the electron spin of the neighbor NV center, leading to a hyperfine structure in the center energy levels which can be distinguished optically. Such spin coupling leads directly to a two-qubit quantum gate. One of them (CROT gate) has been demonstrated experimentally in [14] with fidelity of nearly 90% using a single $[\text{N-V}]^-$ center coupled to a single ^{13}C nuclei disposed in the first coordination sphere near the vacancy of the center. Most recently [15], the entangled two-spin Bell and three-spin Greenberger–Horne–Zeilinger (GHZ) states have been created and studied in the system consisted of the electronic spin of the NV center and two ^{13}C nuclear spins being nearest neigbor to the vacancy of the NV center. Such spin systems can be used as a quantum computer register with optical excess to its states [16, 17]. Additionally, spin-entanglement was generated for two electron spins belonging to closely spaced pairs of $[\text{N-V}]^-$ ($S = 1$) and substitutional nitrogen defects ($S = 1/2$) [13]. These realisations of few-qubits entangled states were an important next step towards realistic quantum processors on a long spin chain or 2-D arrays [2, 3].

Thus, accessibility of single spins for a manipulation even at room temperature, coherent control and read-out, demonstrated by the investigations of the $[\text{N-V}]^-$ colour centers, together with the proposals of application of these centers for room-temperature quantum computer [4], single-photon emitters [5], quantum cryptography [18], quantum memory and quantum repeaters [19, 20], made this center to be one of the most perspective candidate for QI applications. During last 10 years there was an impressive progress in understanding of its non-trivial photophysics based on both experimental and theoretical activities. In particular, in our works [11, 12, 21] made in tight collaboration with experimental group by prof. J. Wrachtrup (Institute of Physics, Stuttgart University, Stuttgart, Germany) there was shown that a wide range of experimental observations on single centers can be interpreted in a consistent way. Moreover, we performed quantum-chemical *ab initio* simulation of diamond nanoclusters containing the $[\text{N-V}]^-$ center elucidating the geometrical structure of relaxed nanoclusters and distributions of electronic and spin densities over the nanocluster atoms [22, 23]. The isotropic and anisotropic hyperfine coupling constants for ^{14}N ($I = 1$) and ^{13}C ($I = 1/2$) nuclei at various positions in relaxed lattice have been calculated for a first time and show reasonable coincidence with the experiments [16, 17] being important for implementation of quantum registers with $[\text{N-V}]^-$ center and surrounding ^{13}C nuclear spins.

2. Other colour centers in diamond for QI applications

The $[\text{N-V}]^-$ center is not the only defect with a potential use for QI processing applications in diamond. Moreover, in some applications (e.g., single-photon emission) this center has far from ideal properties. Meanwhile, CVD diamond growth and material post processing offers a whole new spectrum of defects with potential to stock the diamond quantum tool box. Nickel [24, 25] and silicon [26] related defect centers in diamond have been demonstrated to act as single-photon sources (SPS) in the infrared. More than 30 new colour centers have been identified recently in single crystal CVD diamond. Promising candidates include the vacancy-hydrogen and nitrogen-vacancy-hydrogen defects, as well as Xe-related defects [27, 28, 29]. They display luminescent properties at 1358, 1382, 1456 and 812 nm, but their performance as SPSs has not yet been measured. Considerable effort should be focused on detailed understanding of the optical and spin physics of these prospective defects. We carried out quantum-chemical simulation of structural, electronic and spin properties of the new nickel-related NE8 center consisting of Ni atom in the semi-vacancy position surrounded by four N substitutional atoms in nearest

lattice positions. For the purpose the positively charged hydrogen-passivated cluster $C_{33}H_{24}N_4Ni^{+1}$ having a spindoublet ($S = 1/2$) ground state has been studied. After simulation of the relaxed structure of the clusters, calculations of electronic and spin properties have been performed. It was shown that in accordance with experiment the spin density is localized mainly (80%) at Ni atom and at the six atoms (two carbon and four nitrogen atoms) that are the nearest neighbors to the Ni atom. Again, the isotropic and anisotropic hyperfine coupling constants for ^{61}Ni atom ($I = 3/2$), as well as for ^{14}N and ^{13}C nuclei of the relaxed cluster have been evaluated. Recently the center was identified to be a source of single photons in the infrared, emitting at $\sim$ 800 nm with a room temperature linewidth of 1.5 nm (FWHM) and short photon emission lifetime [24]. In the context of a single-photon source for fiber optic communications, this colour center displays properties which are in many respects superior to the [N-V]$^-$ colour center. Furthermore, it has been shown that these defects can be fabricated by chemical vapour deposition [30] and that the host diamond crystal can be grown directly on the surface of the core of an optical fiber for photon waveguiding [31]. Such properties pave the way to daylight open-air single-photon QKD as well as fiber-based schemes.

Colour centers in diamond were also suggested to be used for implementation of the quantum repeater protocol [19]. Specific sequences of laser, radiofrequency and microwave pulses that implement all repeater stages within the NV+^{13}C center are discussed in [32]. Numerical simulation reported there shows high efficiency of such a repeater. Recent finding of the non-spin-conserving transitions for [N-V]$^-$ centers in strained samples of diamonds [33] gives a new support for a very demanded idea to make all-optical control of single spins and to transfer quantum state of photons on long-lived nuclear spin states realizing quantum memory.

3. Diamond material improvement and nano-engineering of diamond samples

The demonstrated high potential of the diamond-based systems for QI applications has shown that primary task for further advances of the systems is material improvement allowing control of the nitrogen and carbon isotopes contents as well as nano-engineering of diamond samples. Fortunately diamond material engineering has matured quite substantially during recent years. It has become possible to reduce the N content in diamond samples grown by chemical vapor deposition (CVD) to below a ppb (parts per billion carbon atoms) [27] and, moreover, reduce the ^{13}C isotopes content up to 0.5% [35] instead of natural abundance of 1.1%.

Potentially useful colour centers can be created in diamond with submicron spatial resolution via irradiation with focused electron or ion beam [36, 37]. Paramagnetic transition metal impurity centers (especially nickel) grown into high temperature and pressure synthetic diamonds and other irradiation damage systems that form paramagnetic defect centers also show properties attractive for QI processing. Additionally, the progress in synthesis of diamond nanocrystals has also been recently made. It has been shown [38] that stable colour center exhibiting strong photoluminescence at room temperature can exist naturally in nanodiamonds or they can be created and activated by electron irradiation and annealing.

Important unavoidable problem for diamond-based QI devices is creating of photonic microstructures in diamond samples including micromirrors, microwaveguides, etc. The breakthrough in diamond material processing consists of three-dimensional micromachining of free-standing single-crystal diamond using an ion-beam lift-off technique [39,40]. This technique allowed for the construction of an all-diamond optical waveguide structure. Additionally, planar microcavities can be fabricated by adding mirrors above and below diamond thin films and diamond nanocrystals or diamond photonic crystals can be created and used to provide nano-engineering of the photon emission by embedded colour centers and to collect more effectively the emitted photons. Detailed studies of these structures are needed to optimize them. Preliminary results of such simulation for [N-V]$^-$ centers in nanostructured diamond can be found in [41] where it was shown that in one-dimensional finite diamond photonic-crystal, having two geometrical defects, coherent control of light localization is possible. This result is important for implementation of optical read-out and optical initialization of two micrometer spaced [N-V]$^-$ centers in nano-structured diamond.

In conclusion, the above reviewed demonstrations of qubit manipulation, based on the ground-state spin of colour centers in diamond and on surrounding nuclear spins, of single-photon emission from centers for quantum cryptography, along with the progress in synthesis of the highest purity single crystal diamond, in production and functionalization of diamond nanocrystals, as well as recent breakthrough in lithographic creation of individual defect centers and construction of the first all-diamond optical waveguide give the hope that the time is ripe to push diamond onto the central stage for quantum information.

Acknowledgements
This work has been supported in part by EU under the project of the 6FP program "Engineered Quantum Information in Nanostructured Diamond" (EQUIND).

References

[1] *Quantum Information Science and Technology Roadmap. Part 1: Quantum Computation, Advanced Research and Development Activity (ARDA)*, http://qist.lanl.gov
[2] J. Wrachtrup and F. Jelezko, *J. Phys.: Condens. Matter* **18**, S807 (2006).
[3] A. D. Greentree *et al*, *J. Phys.: Cond. Matter* **18,** S825 (2006).
[4] J. Wrachtrup, S. Ya. Kilin and A. P. Nizovtsev, *Optics and Spectroscopy* **91**, 429 (2001).
[5] C. Kurtseifer *et al*, *Phys. Rev. Lett.* **85**, 290 (2000).
[6] L. Rogers *et al*, *New J. Phys.* **10**, 103024 (2008).
[7] A. Gruber *et al*, *Science* **276**, 2012 (1997).
[8] J. Harrison, M. J. Sellars and N. B. Manson, *J. Luminescence* **107**, 345 (2004).
[9] J. Harrison, M. J. Sellars and N. B. Manson, *Diamond & Related Materials* **15**, 586 (2006).
[10] A. P. Nizovtsev *et al*, *Optics and Spectroscopy* **94**, 895–905 (2003).
[11] A. P. Nizovtsev *et al*, *Physica B: Physics of Condensed Matter* **340–342**, 106 (2003).
[12] N. B. Manson, J. P. Harrison and M. J. Sellars, *Phys. Rev. B* **74**, 104303 (2006).
[13] T. Gaebel *et al*, *Nature Phys.* **2**, 408 (2006).
[14] F. Jelezko *et al*, *Phys. Rev. Lett.* **93**, 130501 (2004).
[15] P. Neumann *et al*, *Science* **320**, 1326 (2008).
[16] L. Childress *et al*, *Science* **314**, 281–5 (2006).
[17] M. V. Gurudev Dutt *et al*, *Science* **316**, 1312 (2007).
[18] R. Alleaume *et al*, *New Journal of Physics* **6**, 92 (2004).
[19] L. Childress *et al*, *Phys. Rev. Lett.* **96**, 070504 (2006).
[20] P. van Loock *et al*, *Phys. Rev. Lett.* **96**, 240501 (2006).
[21] A. P. Nizovtsev *et al*, *Optics and Spectroscopy* **99**, 248 (2005).
[22] V. A. Pushkarchuk *et al*, *Optics and Spectroscopy* **99**, 245 (2005).
[23] V. A. Pushkarchuk *et al*, *J. Appl. Spectr.* **74** (2007) 87.
[24] T. Gaebel *et al*, *New J. Physics* **6**, 98 (2004).
[25] E. Wu *et al*,*Opt. Express* **14**, 1296 (2006).
[26] C. Wang *et al*, *J. Phys. B: At. Mol. Opt. Phys.* **39**, 37 (2006).
[27] C. Glover *et al*, *Phys. Rev. Lett.* **92**, 135502 (2004).
[28] C. Glover *et al*, *Phys. Rev. Lett.* **90**, 185507 (2003).
[29] A. M. Zaitsev *et al*, *Phys. Stat. Sol. (a)* **203**, 638 (2006).
[30] J. R. Rabeau *et al*, *Appl. Phys. Lett.* **86**, 131926 (2005).
[31] J. R. Rabeau *et al*, *Appl. Phys. Lett.* **86**, 134104 (2005).
[32] A. A. Bukach and S. Ya. Kilin, *Opt. Spectrosc.* **103**, 181 (2007).
[33] Ph. Tamarat *et al*, *Phys. Rev. Lett.* **97**, 083002 (2006).
[34] Ph. Tamarat *et al*, *New J. Phys.* **4**, 045004 (2008).
[35] D. Twitchen and M. Markham, *XII Int. Conf. on Quant. Opt. and Quant. Inf. (ICQO-2008, 23–23 Sept. 2008, Vilnius, Lithuania)*, Su21C(Z)2.
[36] J. Martin *et al*, *Appl. Phys. Lett.* **75**, 3096 (1999).
[37] J. R. Rabeau *et al*, *Appl. Phys. Lett.* **88**, 023113 (2006).
[38] Y. Sonnefraud *et al*, *Opt. Lett.* **33** 11 (2008).
[39] A. D. Greentree *et al*, *Phys. Rev. A* **73**, 013818 (2006).
[40] S. Tomljevic-Hanic *et al*, *Optics Express* **14**, 3556 (2006).
[41] A. S. Maloshtan and S. Ya. Kilin, *Opt. Spectr.* **103**, 335 (2007).

17th Int. Symp. "Nanostructures: Physics and Technology"
Minsk, Belarus, June 22–26, 2009
© 2009 Ioffe Institute

Growth and crystal phase of III–V nanowires

M. N. Lubov[1,2], Yu. V. Trushin[1,2], D. V. Kulikov[1,2], V. G. Dubrovskii[1,2] and N. V. Sibirev[1]

[1] St Petersburg Physics and Technology Centre for Research and Education RAS, St Petersburg, Russia
[2] Ioffe Physical-Technical Institute, St Petersburg, Russia

Abstract. Theoretical model for the GaAs nanowire growth under catalyst droplet accounting nucleation on the triple line and catalyst droplet volume variation is proposed. Numerical calculations of GaAs nanowires growth are performed. Crystal phase transformations on the initial stage of growth and after Ga flux "turn off" are demonstrated. The results of calculations are in good agreement with experimental data.

Introduction

Nanowires are wirelike nanocrystals that have high ratio of their length L_W ($1-10\ \mu$m) to radius R_W (10–100 nm). Nanowires have unique physical properties and a lot of applications in nano- and optoelectronics [1].

Semiconductor nanowires (GaAs, InP) usually are grown by chemical vapor deposition [2] or by molecular beam epitaxy [3] on the surfaces activated by catalyst droplets. Nanowire growth occurs according to vapor-liquid-solid mechanism: atoms from vapor adsorb on the catalyst liquid droplet surface and then build into the top facet of nanowire crystal.

Nanowire crystal structure influences on material properties and so properties of electronic devices made of it. In III–V nanowires crystal structure can differ from bulk form. Recent studies show that these nanowires usually adopt wurtzite (WZ) crystal structure, while in bulk they have zinc-blende (ZB) structure [4]. Also in GaAs nanowires crystal phase transformations are observed [4,5]: on the initial stage of the growth, and after "turn off" of Ga flux. And therefore it is very important to investigate growth mechanism of nanowires and influence of growth conditions on crystal structure.

In this work we propose theoretical model of III–V nanowires growth accounting processes on the substrate and in the liquid droplet. Consideration of nanowire growth is carried out for GaAs.

1. Theoretical model

Let us consider an ensemble of Au catalyst droplets distributed uniformly with density ρ_W on the GaAs substrate. Deposition of Ga, As "turns on" at time $t = 0$. Deposited atoms adsorbs by droplets surface or by substrate. One part of adsorbed by the substrate atoms diffuse to the droplets or growing nanowires, another part builds in surface resulting its growth and last one evaporates from the surface. Introduce the following assumptions.

1. Nanowires grow independently of each other.
2. During growth process, the nanowire radius R_W is constant and equal to the initial droplet radius $R_d(t = 0)$.
3. Catalyst droplet is a segment of sphere with radius $R_d(t)$, contact angle $\beta(t)$ and volume $V_d(t)$.
4. All surface atoms reached the nanowire side facet diffuse to the liquid droplet with no evaporation.
5. Nanowire grows layerwise. In the beginning of monolayer formation, 2D solid nucleus is formed and then it overgrows top facet, as molecules of GaAs join to it.
6. Amount of Ga and As atoms in the droplet is constant, and nucleation on the top facet of the nanowire is defined by Ga concentration $C_{Ga}(t)$, $C_{Ga}(t) = n_{Ga}(t)/Vd(t)$. Here $n_{Ga}(t)$ — amount of Ga atoms in the droplet.
7. In the case of small nanowire radius (several tens of nanometers) nucleation can be treated as monocentric.

Based on the assumptions the system of kinetic equations can be written for physical quantities characterizing growth process: gallium surface concentration $N_{Ga}(t)$, amount of gallium atoms in the droplet $n_{Ga}(t)$, droplet radius $R_d(t)$ and free energy of critical nucleus $F_\sigma(n_c)$ with structure σ ($\sigma =$ ZB, WZ), where n_c — number of GaAs molecules in critical nucleus.

For the gallium surface concentration $N_{Ga}(t)$ following equation can be written:

$$\frac{dN_{Ga}(t)}{dt} = g - q - 2\pi\langle R_W\rangle\rho_W J_W - \frac{N_{Ga}(t)}{\tau^s}. \qquad (1)$$

Here g — deposition flux, q — substrate growth flux, $\langle R_W\rangle$ — average radius in nanowires ensemble, J_W — diffusion flux to the nanowire, τ^s — lifetime of the Ga atom on the surface. Diffusion flux J_W has the following form:

$$J_W = D_{Ga}\frac{N_{Ga}(t)}{a},$$

here D_{Ga} — Ga adatom diffusion coefficient, a — length of diffusion jump of Ga atom on the surface. Equation (1) could be solved analytically. Similar equation can be written for the amount $n_{Ga}(t)$ of gallium atoms in the droplet:

$$\frac{dn_{Ga}(t)}{dt} = g_d + J_d - J_{ev} - J_n. \qquad (2)$$

Here g_d — deposition flux from the source, $g_d = 2\pi R_d^2(t)g$; J_d — diffusion flux from the substrate, $J_d = 2\pi R_W J_W$; J_{ev} — evaporations flux from the droplet; J_n — flux to the top facet of the nanowire. In equation (2) J_{ev} is proportional to the gallium droplet concentration and area of the droplet surface. J_n is defined by nucleation rate $I(n_{Ga}(t), R_d(t))$ on the top facet of the nanowire, which intern depends on the supersaturation in the droplet and free energy of critical nucleus $F_\sigma(n_c)$ of structure σ. In article [5] it was suggested to calculate free energy of such nucleus accounting its position: at the triple line "vapor-droplet-nanowire", or in the "center" of the top facet of the nanowire. According to this assumption free energy of the

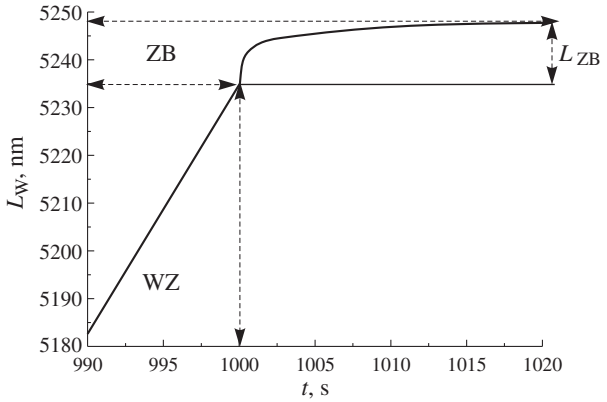

Fig. 1. GaAs nanowire length L_W time dependence, calculated for the conditions of experiment [4] (see Fig. 4a). Nanowire radius R_W = 20 nm. L_{ZB} — length of the top part of nanowire, formed after Ga flux "turn-off".

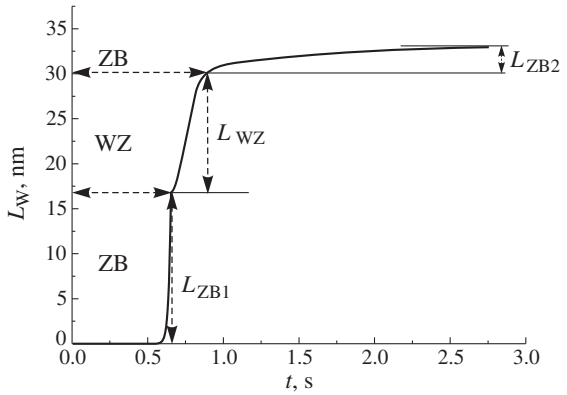

Fig. 2. GaAs nanowire length L_W time dependence, calculated for the conditions of experiment [5]. Nanowire radius R_W = 25 nm. L_{ZB1} — length of the lower part of nanowire, L_{WZ} — length of the middle part of nanowire, L_{ZB2} — length of the top part of nanowire, formed after Ga flux "turn-off".

critical nucleus can be estimated as:

$$F_\sigma(n_c) = \left(\frac{\chi a}{2}\right)^2 \frac{\left[\omega\left(\gamma_{ev}(\sigma) - \gamma_{dv} R_W R_d^{-1}(t) - \gamma_{ed}\right) + \gamma_{ed}\right]}{h_\sigma \Delta\mu_{ls} - \gamma_{nw}(\sigma)}.$$

Here χ — coefficient accounting nucleus geometry; ω — part of nucleus perimeter bounded with vapor; γ_i — specific boundary energies, $i = ev$ — "nucleus edge-vapor", dv — "droplet-vapor", ed — "nucleus edge-droplet", nw — "nucleus-nanowire", h_σ — height of nucleus with structure σ; $\Delta\mu_{ls}$ — difference in chemical potentials in liquid and solid phases. In this difference Gibbs–Thomson effect must be accounted. Equation for the droplet radius $R_d(t)$ can be found from geometrical considerations. Length L_σ of the nanowire layer with structure σ grown up during the time t in the case of monocentric nucleation is determined by nucleation rate $I(n_{Ga}(t), R_d(t))$:

$$L_\sigma(t) = h_\sigma S_\sigma \int_{t_1}^{t_2} I_\sigma\left(n_{Ga}(t'), R_d(t')\right) dt'.$$

Here t_1, t_2 — times of begining and ending of the layer with structure σ growth, S_σ is area where nucleation takes place. Total length L_W of the nanowire is the sum of all layers length.

2. Results and discussion

To find nanowire length and crystal structure, one should solve system of the kinetic equations for $N_{Ga}(t)$, $n_{Ga}(t)$, $R_d(t)$, $F_\sigma(n_c)$ taking into account crystal structures formation probability, $p_\sigma = S_\sigma exp(-F_\sigma(n_c)/kT)$, where k is Boltzmann constant. This probability determines most favorable crystal structure in the nanowire. In Fig. 1 and Fig. 2 nanowire length time dependencies are presented. Depositions rate was 1 ML/s [3] for the first calculation and 0.4 ML/s for the second.

Formation of ZB structure on the initial stage of GaAs nanowire growth is caused by low gallium concentration in the droplet and substrate crystal structure (ZB). During the growth gallium concentration (and also number of gallium atoms) increases and wurtzite nuclei formation become more energetically favorable. Ga flux "turn off" on the last stage of growth leads to gallium concentration decrease and zinc-blende structure forms again. For the GaAs nanowire with radius R_W = 20 nm, length L_W lies in the range obtained in [6] and is equal to 5248 nm. Length L_{ZB} of upper part of nanowire (see Fig. 1) is equal 13.2 nm, and in experiment 13.6 nm (see Fig. 4a [4]). For the GaAs nanowire with radius R_W = 25 nm (see Fig. 2) calculated values of layers lengths are L_{ZB1} = 17.2, L_{WZ} = 13 nm, L_{ZB2} = 3 nm. These values are close to the experimental ones [5]: 17.6 nm, 13.5 nm, 3 nm respectively.

Presented theoretical model allows to reproduce all principal stage of the nanowire growth process. Obtained quantitative values are in good agreement with experimental data.

Acknowledgements

This work was supported by the Russian Foundation for Basic Research (projects Nos. 07-02-01052-a, 08-02-01337-a.)

References

[1] F. Quang *et al*, *Nano Lett.* **4**, 1975 (2004).
[2] W. Seifert *et al*, *J. Cryst. Growth.* **272**, 211 (2004).
[3] V. G. Dubrovskii *et al*, *Phys. Status Solidi B* **241**, R30 (2004).
[4] I. P. Soshnikov *et al*, *Sol. State Phys. Lett.* **47**, 2213 (2005).
[5] F. Glas *et al*, *Phys. Rev. Lett.* **99**, 146101 (2008).
[6] G. E. Cirlin *et al*, *Semiconductors* **39**, 587 (2005).

17th Int. Symp. "Nanostructures: Physics and Technology"
Minsk, Belarus, June 22–26, 2009
© 2009 Ioffe Institute

Electrical properties of MOS structures with dysprosium and yttrium thin oxide films as high-k dielectrics

N. V. Babushkina[1], *S. A. Malyshev*[1], A. A. Kovalevsky[2], D. V. Zhygulin[1], L. I. Romanova[1]

[1] B. I. Stepanov Institute of Physics, NASB, Minsk, Belarus
[2] Belorussian State University of Information and Radioelectronics, Belarus

Abstract. MOS structures with dysprosium and yttrium thin oxide films were prepared and investigated. MOS structures are characterized by low total surface charge, interface states density and hysteresis of C-V curves (<0.1 V). The equivalent oxide thickness (EOT) is 2.2–2.4 nm. MOS structures with dysprosium oxide based films have considerably less leakage current in accumulation than SiO_2 films with the same electrical thickness. It is shown that dysprosium and yttrium thin oxide films are suitable for application as high-k dielectrics in Si nanocrystal nonvolatile memory.

Introduction

The continual miniaturization of the metal-oxide-semiconductor (MOS) devices requires the replacement of the SiO_2 gate dielectric by new dielectrics with a high dielectric constant (high-k) to decrease the gate leakage (tunneling) current. The review of these problems can be found e.g. in reference [1]. Moreover high-k dielectrics replace SiO_2 in Si nanocristal nonvolatile memory. It was shown that dysprosium (Dy_2O_3) and yttrium (Y_2O_3) oxides as the alternative gate dielectrics are the promising candidates for the achievement less than 1.0 nm equivalent oxide thickness [2–5]. Dy_2O_3 and Y_2O_3 films are characterized by relative wide band gap of 4–5 eV, the moderately high dielectric constant of 12–15.5 for Dy_2O_3 and 17–18 for Y_2O_3, the thermal stability in contact with silicon, the low moisture degradation and suitable electrical characteristics including low leakage current. MOS field-effect transistors with Dy_2O_3 and Y_2O_3 as the gate dielectric demonstrate the good reliability properties and the effective electron mobility of 339 and 210 cm^2/Vs, respectively [3,5]. In this work, we investigated electrical properties of MOS structures with Dy_xO_y and Y_xO_y films prepared by thermal annealing metallic dysprosium or yttrium films as well as MOS structures with germanium-doped silicon nanocrystals and Dy_xO_y or Y_xO_y films as tunneling and control films.

1. Experimental

Si wafers with (100) orientation were used as substrates with the standard RCA treatment. Dysprosium and yttrium oxide films (Dy_xO_y and Y_xO_y) were obtained by the thermal vacuum evaporation of metallic dysprosium or yttrium and deposition onto non-heated Si substrates. Thermal annealing of films was conducted at the temperature $T_{ox} = 400 - 600$ °C during 7–30 min in a dry oxygen stream. The direct oxidation of deposited dysprosium or yttrium films to form oxide films is a simple method similar to conventional thermal SiO_2 in contrast to chemical vapor deposition (CVD), sputtering or atomic layer deposition (ALD). Germanium-doped silicon nanocrystals were deposited by CVD method. MOS capacitances were fabricated with oxide films to investigate capacitance-voltage (C-V) at 1 MHz and current-voltage (J-V) characteristics.

2. Electrical properties of MOS structures

It is shown that MOS capacitances with thin Dy_xO_y and Y_xO_y films are characterized by similar electrical properties. There are the positive total surface charge on p-type Si with the density $(3-5) \times 10^{11}$ cm^{-2} and the negative charge on n-type Si with the density $(1-3) \times 10^{11}$ cm^{-2}. The interface states density is $(1-3) \times 10^{11}$ eV^{-1} cm^{-2}. The hysteresis of C-V curves is <0.1 V.

Measured and simulated high-frequency C-V curves of the In-Dy_xO_y-pSi MOS capacitor are presented in Fig. 1. The physical thickness of the Dy_xO_y film is 5.0–5.2 nm. The indicated equivalent oxide thickness (EOT) of $d_{eq} = 2.2 - 2.4$ nm has been extracted using Berkeley simulated program, taking into account the quantum mechanical correction [6]. The equivalent (electrical) oxide thickness is defined as the thickness extracted from accumulation capacitance of the C-V curve assuming that the permittivity k of the film is that of SiO_2 ($k = 3.9$). The good agreement between measured and simulated C-V curves indicates the low interfacial traps at the Dy_xO_y-Si interface. There is a small hysteresis ($V < 0.1$ V) in the C-V curve. The leakage current is found to be about 3×10^{-3} A/cm^2 at the $V_g - V_{fb} = -1$ V. The leakage current decreases to about 5.6×10^{-5} A/cm^2 after Dy_xO_y film annealing in nitrogen. The leakage current of SiO_2films with the same physical thickness is about 8×10^{-4} A/cm^2.

To characterize the possibility of Dy_xO_y based films us-

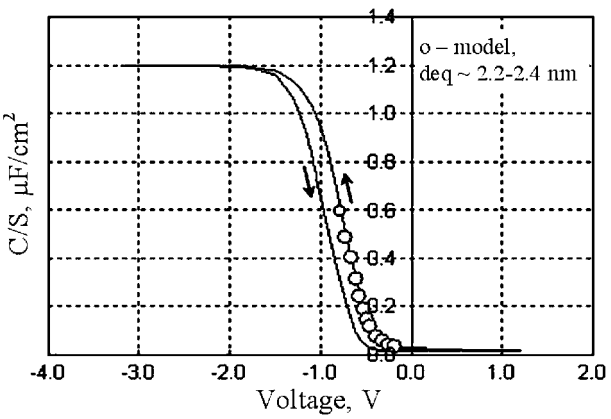

Fig. 1. Measured and simulated high frequency (1 MHz) capacitivity versus gate voltage of In-Dy_xO_y-pSi capacitor.

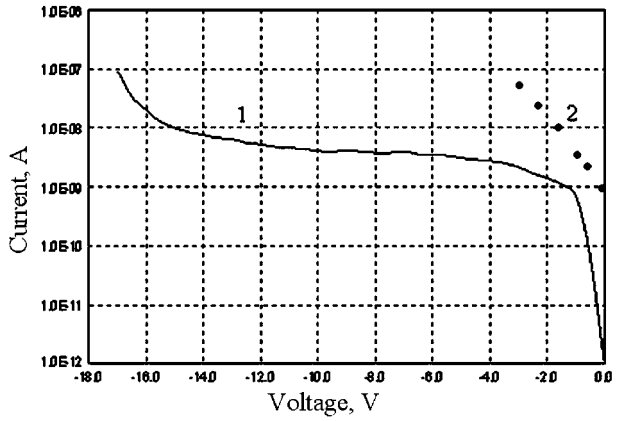

Fig. 2. Current-voltage characteristics of MOS structures with Dy_xO_y based film (1) and SiO_2 film (2).

ing instead of SiO_2 in the nonvolatile Si nanocrystal memory, MOS capacitances with Dy_xO_y based film and SiO_2 film are compared. The equivalent oxide thickness of Dy_xO_y based film is 5.0 nm. The physical thickness of SiO_2 film is 5.2 nm. The MOS capacitances have approximately the same electrical properties. However the leakage current in accumulation is less for Dy_xO_y based film because it has more physical thickness as compared with SiO_2 film (Fig. 2). The leakage current influences on the storage time of the Si nanocrystal nonvolatile memory.

MOS structures with germanium-doped Si nanocrystals and Dy_xO_y or Y_xO_y films as tunneling and control films were prepared. It is shown that these structures are characterized by large hysteresis of C-V characteristics: 1.0 to 1.5 V for Dy_xO_y films and 0.5 to 1.0 V for Y_xO_y films. Therefore, Dy_xO_y and Y_xO_y films are suitable for application as high-k dielectrics in Si nanocrystal nonvolatile memory.

References

[1] H. J. Osten, *Proc. 5th International Conf. on ASDAM-98*, Smolenice Castle, Slovakia, 155 (2004).

[2] S. Ohmi, H. Yamamoto, J. Taguchi, K. Tsutsui, and H. Iwai, *Jpn. J. Appl. Phys.* **43**, 1873 (2004).

[3] H. Yu-ren, C. I. Yin-ku, W. Ving-strong, L. J. Ya-min, *Integrated Ferroelectrics* **97**, 111 (2008).

[4] S. Guha, E. Cartier, M. A. Gribelyuk, N. A. Bojarczuk, and M. C. Copel, *Applied Physics Lett.* **77**, 2710 (2000).

[5] L.-A. Ragnarsson, S. Guha, M. Copel, E. Cartier, N. A. Bojarczuk, and J. Karasinski, *Applied Physics Lett.* **78**, 4169 (2001).

[6] "QM CV simulator", UC Berkeley Device Group, http://www-device.eecs.berkeley.edu/qmcv/index.html.

17th Int. Symp. "Nanostructures: Physics and Technology"
Minsk, Belarus, June 22–26, 2009
© 2009 Ioffe Institute

III-nitride heterostructures with quantum well channel on heat conducting substrates for power microwave transistors

S. I. Petrov, A. N. Alekseev, A. E. Byrnaz, V. P. Chaly, D. M. Krasovitskiy, M. V. Pavlenko, M. Yu. Pogorelsky, A. P. Shkurko, I. A. Sokolov and M. A. Sokolov
JSC "Svetlana–Rost", St Petersburg, Russia

Abstract. DHFETs based on HS with QW GaN channel on saphire with gate width 0.48 mm demonstrate DC current density of 1.0 A/mm and RF power 1.8 W at 10 GHz (power density 3.8 W/mm). The saturation current of test devices produced from heterostructures on Si and AlN/SiC substrates is similar to that on sapphire; at the same time current slump due to thermal effects at large of operating voltage doesn't observed.

Introduction

AlGaN-based double heterostructure field effect transistors (DHFET) can provide an order of magnitude higher power densities as compared with GaAs. The key issue for the development of nitride based high power devices is the electron confinement which is directly effects on transistors cut off and leakage [1]. Besides, hot electrons spillover under high gate-source bias takes place and limits maximum current and thus power density. The latter essentially contributes to the so called "RF-current collapse" due to electron trapping in buffer and upper barrier layers. Leakage can be minimized by compensation doping of GaN buffer layer with impurities producing deep levels, such as Fe, C, Mg etc. [2]. To reduce current collapse related to surface traps, various passivation techniques are used [3]. Nevertheless, above methods can not prevent electron trapping in thick buffer GaN layer, moreover, the problem seems to be accented because an additional traps are produced by compensation doping of buffer layer. Alternatively, better electron confinement without electron trapping can be obviously provided in double heterostructures (DHS), containing wider bandgap semiconductor material underneath an active GaN channel. A number of publications reporting successful realization of DHS field effect transistors (DHFET) based on AlGaN/GaN/AlGaN [4,5] are available, and device parameters are competitive to ones obtained on "classic" heterostructures GaN/AlGaN. We also previously reported DHFET with GaN channel layer thickness of 100 nm demonstrating current density up to 1 A/mm in DC-mode [6]. To improve electron confinement and so device performance, GaN thickness should be further decreased. Another important technological issue in nitride based power microwave transistors production is a heat sink because dissipated power from such devices is tens of watts. Among substrates used until recent times for nitride heterostructure growth (Al_2O_3 and SiC) best results in correlation of operating frequencies and power densities are achieved on semi insulating SiC substrates. The central failures of such substrates are high cost and trade restrictions for a variety of reasons caused by practically monopolistic market position of principal producers. The overcoming of the problem of heterostructure cracking and using of relatively low cost high-resistance Si substrates ($\approx 10^4\ \Omega$ cm) make for rapidly development of the GaN technology on Si substrates [7] mainly for communications. The alternative approach proposed by japanese company Fujitsu is based on application of rather thick transitional insulating AlN layers grown on relatively low cost n-type SiC substrates used for GaN light emitting devices mass production over the world. The combination of high thermal conductivity, relatively low cost, large diameter and reduced threading dislocations densities enables to produce on such semi insulating SiC/AlN substrates the next generation of nitride high power microwave transistors [8]. Here we report DC and RF parameters of DHFETs with quantum well (QW) GaN channel layer thickness of 5 nm on sapphire, Si and AlN/SiC substrates.

1. Experimental

Nitride heterostructures were grown using specialized nitride MBE system STE3N2 (SemiTEq). The main peculiarities of this system are extremely high (up to 1200 °C) growth temperatures and V/III ratios (up to 1000), combined with all the traditional opportunities of molecular beam epitaxy system. The main peculiarities of structure design is 0.2 μm thick AlN template, grown at 1100–1200 °C directly before heterostructure within the same epitaxy process [6]. Properties of grown samples were studied using AFM, XRD, C-V and Hall measurements and test transistors were fabricated.

2. Results and discussion

It was found that mobility drastically decreases in double heterostructures when GaN channel thickness layer is reduced due to following main reasons. First, relaxation above critical thickness may be accompanied by formation of various defects, contributing to an additional carrier scattering; so narrowing the channel to thickness close to this defect region results in mobility degradation. Second, polarization induced parasitic hole conductivity appears near bottom interface AlGaN/GaN at high aluminum content in AlGaN buffer layer (analogous to two-dimensional electron gas formation near upper GaN/AlGaN interface). It was found that parasitic hole conductivity is not formed when Al mole fraction at bottom interface AlGaN is lower than 0.15, however polarization induced distortion band diagram is enough for quantum confinement even at quite low Al mole fraction in AlGaN buffer layer of 0.1. Critical thickness of relaxation for Al mole fractions in 0.1–0.2 range was estimated to be 15–20 nm. So for optimum design of heterostructures with (QW) channel, buffer

layer should be finished by AlGaN with 0.1 Al fraction and channel thickness should be 5 nm. Because of polarization induced bowing of bandgap, making electron concentration lower, we also optimized Al content in cap layer. Thus, Al mole fraction of 0.4–0.45 instead of commonly used 0.25–0.35, give an increase from the common values of $(0.9-1.1)\times 10^{13}$ cm^{-2} up to $(1.3-1.5)\times 10^{13}$ cm^{-2} while keeping mobility in the range of 1100–1300 cm^2/V s. DHFETs based on these MHS with gate width 0.48 mm demonstrate DC current density up to 1.0 A/mm and power 1.8 W on 10 GHz (power density 3.8 W/mm). In spite of the fact that electrophysical parameters of the heterostructures practically correspond to state of the art world level and high frequency current collapse was minimized due to the double electron confinement, values of power obtained without of heat sink optimization are closed to possible limit. By optimization of growth conditions we succeeded in minimizing of macroscopic cracks number while growth on Si substrates. The application of AlN template allows to practically reproduce basic device properties in spite of rather rough surface of initial AlN/SiC substrates. The saturation current of test devices produced from heterostructures on Si and AlN/SiC is compared with analogous parameter of devices on sapphire substrates (0.6–1.0 A/mm) at the same time current doesn't reduce at large value of operating voltage.

References

[1] Y. K. Su *et al*, *Mat. Sci. Eng.* **B 110**, 172 (2004).
[2] H. Tang *et al*, *Solid-State Electronics* **44**, 2177 (2002).
[3] A. E. Vertiatchikh *et al*, *Elec. Lett.* **38**, 388 (2002).
[4] G. Simin *et al*, *Jpn. J. Appl. Phys.* **40**, L1142 (2001).
[5] C. Q. Chen *et al*, *Appl. Phys. Lett.* **82**, 4593 (2003).
[6] A. N. Alekseev *et al*, *Tech. Phys. Lett.* **31**, 846 (2005).
[7] http://gaasmantech.org/Digests/2005/2005papers/4.3.pdf.
[8] http://gaasmantech.org/Digests/2006/2006Digests/12A.pdf.

17th Int. Symp. "Nanostructures: Physics and Technology"
Minsk, Belarus, June 22–26, 2009
© 2009 Ioffe Institute

Electromagnetic effects in carbon nanotubes: modeling and device applications

S. A. Maksimenko and G. Y. Slepyan
Institute for Nuclear Problems, Belarus State University, 220030 Minsk, Belarus

Abstract. A general approach to electromagnetism of carbon nanotubes (CNTs) is presented. A strong slowing down of surface waves is demonstrated in the IR and THz ranges. An analysis of the scattering pattern and the absorption cross-section of finite-length CNTs is reported. The comparison with experiment allows physical interpretation of the observed THz absorption peak. Antenna properties of CNTs are described and the concept of CNT as a thermal antenna is proposed. Prospective problems of electrodynamics of CNTs are discussed.

Introduction

A great progress has been achieved during last two decade in the synthesis and fabrication of different nano-structured artificial materials with fascinating mechanical, electronic and optical properties. Accompanied by the impressive parallel development of the characterization techniques and measurement instrumentation, this process necessitates the revision of traditional concepts of physics and chemistry of condensed matter, significantly extending our knowledge of the nature of solids and our capabilities to control their properties. In particular, promising potentiality of nano-structured elements for transmission and processing RF and light signals motivates active studying electromagnetic response properties of nanostructures. Thus, a new branch of physics of nanostructures-nanoelectromagnetics — is currently emerging. In this regard, researchers face new problems, while the traditional electromagnetics (see e.g. [1]) gain new life in their application to the new objects.

Among others, carbon nanotubes (CNTs) have been the subjects of intensive research in the area of nanotechnology for about 15 years [2], yet understanding of their fundamental physics is far from complete. One topic under intensive investigation is their electromagnetic response. In particular, CNTs have been proposed to fabricate several different integrated-circuits elements and electromagnetic devices, such as transmission lines [3–5], interconnects [6–8], and nanoantennas [9–15]. References [16–19] demonstrate the potential of CNTs as emitters of terahertz and infrared radiation.

In this talk, we give an overview of peculiar electromagnetic problems in the nanoscale focusing mainly on specific electromagnetic effects in carbon nanotubes and CNT-based composites. The talk covers problems of carrier transport and linear electrodynamics of carbon nanotubes and touches upon radiative processes in nanotubes, see [19–21].

1. Basic formalism of electrodynamics of CNTs

A CNT is a plane mono-atomic graphitic layer (*graphene*) rolled up into a cylinder [2]. In terms of the lattice basic vectors $\mathbf{a}_1$ and $\mathbf{a}_2$, the geometric configuration of CNTs can be classified by a dual index (m, n) that has the form $(n, 0)$ for *zigzag* CNTs and (n, n) for *armchair* CNTs; m and n are integers. Typically, CNTs are 0.1–10 μm in length, their cross-sectional radius varies within the range 1–5 nm.

Physical transport mechanisms and interaction between charged quasi-particles and periodic potential in nanotubes and in three-dimensional media express themselves in a significantly different manner because of the quasi-one-dimensional conductivity of CNTs and transverse quantization of the quasi-momentum. The account for the transverse quantization yields the CNT dispersion law, which essentially differs from the dispersion law of graphene [2].

Our approach is based on the method of effective boundary conditions (EBCs), originally developed in antenna theory (see e.g. [1]) for periodical structures with the period small compared with the free-space wavelength. The basic idea of the EBC method is that a smooth homogeneous surface is considered instead of a periodic structure, and appropriate EBCs for the electromagnetic field are stated for this surface. These conditions are chosen in such a way that the spatial structures of the electromagnetic field due to an effective current induced on the homogeneous surface, and the electromagnetic field of the real current in the lattice turn out to be identical some distance away from the CNT surface. The lattice parameters are included in coefficients of the EBCs. For a CNT, the EBCs take the form as follows [3]:

$$\begin{aligned} &E_{\varphi,z}\big|_{\rho=R_{\rm cn}+0} - E_{\varphi,z}\big|_{\rho=R_{\rm cn}-0} = 0,\\ &H_z|_{\rho=R_{\rm cn}+0} - H_z|_{\rho=R_{\rm cn}-0} = 0,\\ &H_\varphi\big|_{\rho=R_{\rm cn}+0} - H_\varphi\big|_{\rho=R_{\rm cn}-0} = \frac{4\pi}{c}\,\sigma_{zz}(\omega)\; E_z|_{\rho=R_{\rm cn}}\,. \end{aligned} \quad (1)$$

Here $\sigma_{zz}(\omega)$ is the CNT axial conductivity. Note that the boundary conditions are analogous to the Weinstein–Sivov boundary condition for grid structures in electrodynamics of microwaves. However, unlike to the electrodynamics of microwaves, which deals with either metals or dielectrics, the CNT conductivity is a complex function of entire parameters. Theoretical modeling of the CNT conductivity is the crucial problem in the electrodynamics of nanotubes. In general case, this problem is analyzed by the system of kinetic equations for the density matrix [3,22], which describes the dynamics of electrons in a nanotube imposed to external electric field and takes into account both intraband and interband transitions.

2. Electromagnetic effects in CNTs

The problem of the surface waves propagation along an isolated infinite CNT in free space is similar to the eigenwave

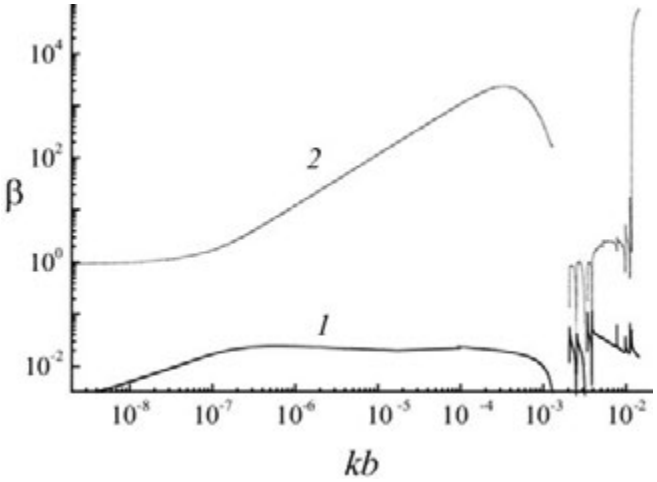

Fig. 1. The slow-wave coefficient in a (9,0) metallic zigzag CNT for relaxation time $\tau = 3$ ps and $T = 295$ K. 1 — Re (β); 2 — Re (β)/Im (β) [3].

problem for microwave slow-wave helical structures [1]. Using the radiation conditions in the limit $\rho \to \infty$, we express the electromagnetic field scalar Hertz potential in terms of the modified cylindrical Bessel functions. Then the dispersion relation for the surface wave in a CNT is obtained:

$$\left(\frac{\kappa}{k}\right)^2 I_l(\kappa R_{\rm cn})\, K_l(\kappa R_{\rm cn}) = \frac{ic}{4\pi k R_{\rm cn}\sigma_{zz}}\left[1-\left(k^2+\kappa^2\right)\right]. \quad (2)$$

Figure 1 shows the slow-wave coefficient $\beta = k/h$ for the axially symmetric ($l = 0$) surface wave in the metallic CNT. At low frequencies ($kb < 10^{-7}$) the nanotube demonstrates strong attenuation, while in the THz and IR regimes ($10^{-5} < kb < 10^{-3}$), permits the propagation of slowly decaying surface waves with almost frequency-independent β and the phase velocity $v_{\rm ph} = {\rm Re}\,(\omega/h)$. Therefore, a wave packet will propagate in CNT without significant distortions and much slower then light in vacuum, $v_{\rm ph}/c \approx 0.02$. Thus, we can conclude that metallic CNT in IR and THz range is [3]:

— a dispersionless nanowaveguide of surface waves, and
— a nano-scale electromagnetic slow-wave structure.

These properties make CNTs perspective for *the design of IR and THz nanoantennas* [11], and allow explanation*of experimental results on THz absorption in CNT-based composites* and, in combination with the ballisticity of the electron motion in CNTs, lead to the concept of CNT as nano-sized traveling wave tube [18–19]. Also, dramatic enhancement of the spontaneous decay rate of an atom placed in the vicinity of a CNT is shown to exist [20].

The Leontovich–Levin equation for optical scattering by a finite-length CNT has been formulated in [11] based on a quantum-mechanical microscopic model of the conductivity [3]. Solution yields the surface current density distribution and scattering pattern. The CNT polarizability in low-frequency range and the scattering pattern in the range of optical interband transitions and in the vicinity of plasmon resonance have been calculated. Geometric resonances of strongly retarded surface waves emerge in the THz range, see Fig. 2 [11].

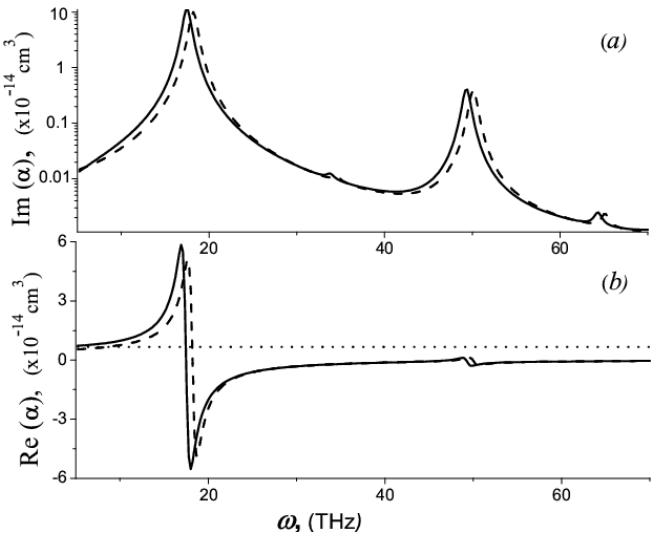

Fig. 2. Frequency dependencies of (a) the imaginary and (b) the real parts of the polarizability scalar of a (9,0) zigzag metallic CNT of length $L = 1$ μm [11].

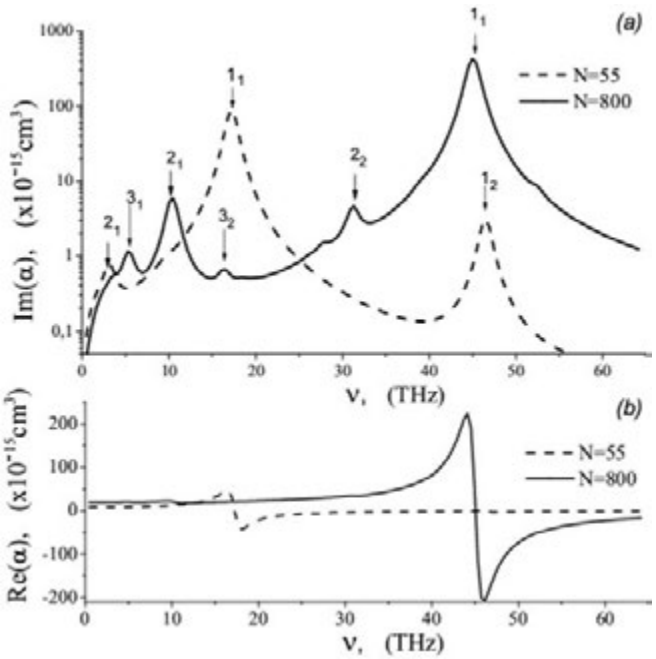

Fig. 3. Frequency dependence of (a) the imaginary and (b) the real parts of the polarizability scalar of a bundle of CNTs of length $L =$ 500 nm for two values of N [14].

Further analysis has been performed for closely packed bundles of metallic CNTs by means of an equivalent-multishell approach [14]. Antenna resonances of CNT bundles are depicted in Fig. 3 [14]. The coefficient β for azimunthally symmetric guided waves increase with the number of metallic CNTs in the bundle, tending for thick bundles to unity, which is characteristic of macroscopic metallic wires. Therefore, thick CNT bundle, in spite of the strongly imperfect conductivity of their components, have electromagnetic response in far-field region the same as a rod with near perfect conductivity [14], what is in agreement with experimental results [9].

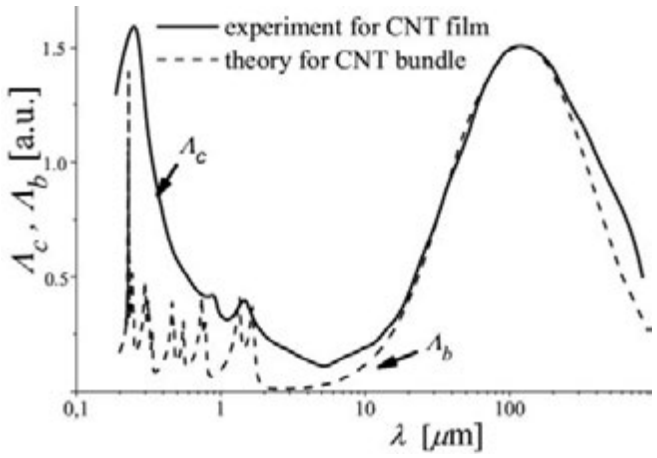

Fig. 4. Comparison between experimentally observed normalized absorbance of single-walled CNT film [26], and calculated normalized absorption cross-section of CNT bundle [23].

Numerical simulation of the wave scattering by multi-wall CNTs accounting for the interband conductivity resonances lying in the visible range and allowing the quantitative comparison with [9] has been presented in [15].

Calculations of antenna resonances in single- and multi-wall CNTs and in CNT bundles can be used for the qualitative interpretation of experimentally observed THz features in the response characteristics of CNT-based composites [24–29]. The experimentally registered by Hu *et al*, [26] normalized absorbance of a film comprising a sparse disordered array of finite-length bundles of single-walled CNTs is depicted in Fig. 4 by solid line. In [26], the CNT bundles were found to have average diameter 2.7 nm and length $L < 2$ μm. The dashed curve in Fig. 4 shows calculated absorption cross-section of a bundle of three tubes with chiral vectors (13,0), (12,0) and (11,0). The semiconductor nanotubes (13,0) and (11,0) have been chosen to fit the experimentally observed extremums in the high-frequency part of the absorption spectrum, as it is seen in Fig. 4. The low-frequency pick on the theoretical curve is due to geometrical resonance in metallic CNT, whereas the contribution of semiconductor CNTs in this frequency range is negligibly small. Position of the peak on the frequency axis is determined by the CNT length, while its width is dictated by the electron free-path time τ. In Fig. 4 both parameters have been chosen to provide the best correlation with the experimental plot: $L = 1.2$ μm and $\tau = 22$ fs.

The thermal radiation from an isolated finite-length CNT has been theoretically investigated in Ref. [21]. The formation of the discrete spectrum in metallic CNTs in the terahertz range is demonstrated due to the reflection of strongly slowed-down surface-plasmon modes from CNT ends, sees Fig. 5. Presence of the discrete structure of the thermal radiation allows the concept of CNT as a thermal nanoantenna for THz range.

3. Conclusion

We have shown that the emergence of CNTs as key building block of nanoelectronic and nanophotonic devices has extended to nanoscale such classical problems of the circuit theory as operational properties and electromagnetic compatibility

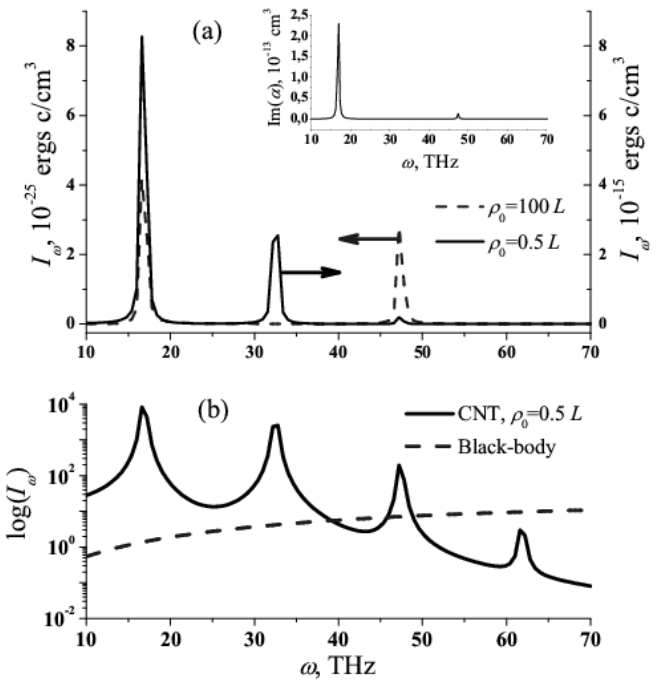

Fig. 5. (a) Thermal radiation spectra of metallic (15,0) CNT at different distances from the CNT The inset presents the CNT's polarizability. (b) Thermal radiation from CNT in the near-field zone compared to the black-body radiation [21].

of circuit elements, noise control, and so on. However such an extension implies radical modification of the basic approaches to the principles of circuit design, which rely on macroscopic electrodynamics. Nanoelectromagnetics provides necessary tools for solving of that novel class of problems.

Acknowledgements

This research was partially supported by IB BMBF (Germany) under project BLR 08/001, the EU FP7 project FP7-230778 TERACAN and the Belarus RFFR under project F07F-013.

References

[1] S. Ilyinsky, G. Ya. Slepyan, and A. Ya. Slepyan, *Propagation, Scattering and Dissipation of Electromagnetic Waves*, London: Peregrinus, 1993.

[2] S. Reich, C. Thomsen, and J. Maultzsch, *Carbon Nanotubes. Basic Concepts and Physical Properties*, Berlin: Wiley-VCH, 2004.

[3] G. Ya. Slepyan, S. A. Maksimenko, A. Lakhtakia, O. Yevtushenko, and A. V. Gusakov, *Phys. Rev. B* **60**, 17136 (1999).

[4] M. J. Hagmann, *IEEE Trans. Nanotechnol.* **4**, 289 (2005).

[5] J. Rybczynski *et al*, *Appl. Phys. Lett.* **90**, 021104 (2007).

[6] A. Raychowdhury and K. Roy, *IEEE Trans. CAD Integrat. Circ. Syst.* **25**, 58 (2006).

[7] A. Maffucci, G. Miano, and F. Villone, *Int. J. Circ. Theory Appl.* **36**, 31 (2008).

[8] H. Li, W.-Y. Yin, K. Banerjee, and J.-F. Mao, *IEEE Trans. Electron Devices* **55**, 1328 (2008).

[9] Y. Wang *et al*, *Appl. Phys. Lett.* **85**, 2607 (2004).

[10] G. W. Hanson, *IEEE Trans. Antennas Propagat* **53**, 3426 (2005).

[11] G. Ya. Slepyan, M. V. Shuba, S. A. Maksimenko, and A. Lakhtakia, *Phys. Rev. B* **73**, 195416 (2006).

[12] P. J. Burke, S. Li, and Z. Yu,*IEEE Trans. Nanotechnol.* **5**, 314 (2006).

[13] G. Miano and F. Villone, *IEEE Trans. Antennas Propagat.* **54**, 2713 (2006).
[14] M. V. Shuba, S. A. Maksimenko and A. Lakhtakia, *Phys. Rev. B* **76**, 155407 (2007).
[15] M. V. Shuba, G. Ya. Slepyan, S. A. Maksimenko *et al*, *Phys. Rev. B* **79**, (2009), to be published.
[16] J. A. Misewich *et al*, *Science* **300**, 783 (2003).
[17] O. V. Kibis and M. E. Portnoi, *Tech. Phys. Lett* **31**, 671 (2005).
[18] K. G. Batrakov, P. P. Kuzhir, and S. A. Maksimenko, *Proc. SPIE* **6328**, 63280Z (2006).
[19] K. G. Batrakov, S. A. Maksimenko, P. P. Kuzhir and C. Thomsen, *Phys. Rev. B* **79**, 125408 (2009).
[20] I. V. Bondarev, G. Ya. Slepyan, and S. A. Maksimenko, *Phys. Rev. Lett.* **89**, 115504 (2002).
[21] A. M. Nemilentsau, G. Ya. Slepyan, S. A. Maksimenko, *Phys. Rev. Lett.* **99**, 147403 (2007).
[22] G. Ya. Slepyan, A. A. Khrutchinski, A. M. Nemilentsau, S. A. Maksimenko, J. Herrmann, *Int. J. Nanosci.* **3**, 343 (2004).
[23] M. V. Shuba, S. A. Maksimenko and G. Ya. Slepyan, *J. Comput. Theor. Nanosci.* **6**, (2009), to be published.
[24] F. Bommeli *et al*, *Sol. State Commun.* **99**, 513 (1996).
[25] A. Ugawa *et al*, *Phys. Rev. B* **60**, R11305 (1999).
[26] H. Hu *et al*, *J. Am. Chem. Soc.* **125**, 14893 (2003).
[27] F. Borondics *et al*, *Phys. Rev. B* **74**, 045431 (2006).
[28] C. Kang *et al*, *Phys. Rev. B* **75**, 085410 (2007).
[29] T. Kampfrath *et al*, *phys. stat. sol. (b)* **244**, 3950 (2007).

17th Int. Symp. "Nanostructures: Physics and Technology"
Minsk, Belarus, June 22–26, 2009
© 2009 Ioffe Institute

Control of sub-Kelvin hole spin dynamics in high-mobility two-dimensional hole systems

T. Korn, M. Kugler, A. Wagner, S. Fehringer, R. Schulz, C. Gerl, M. Kubová, D. Schuh, W. Wegscheider and C. Schüller

Institut für Experimentelle und Angewandte Physik, Universität Regensburg, D-93040 Regensburg, Germany

Abstract. We have observed spin dynamics of resident holes in high-mobility 2-dimensional hole systems in GaAs/$Al_{0.3}Ga_{0.7}As$ single quantum wells (QW) by time-resolved Faraday rotation and time-resolved Kerr rotation (TRFR/TRKR), at temperatures down to 400 mK. The strong temperature dependence of the long-lived hole spin dynamics indicates that hole localization is crucial for hole spin coherence. In a series of samples with different QW width, we observe that the hole spin dephasing time increases as the well width decreases. By applying a gate voltage to our samples, we are able to tune the observed hole g factor by more than 50 percent.

Introduction

In the emerging field of semiconductor spintronics, one focus has been the investigation of electron spin dynamics in various material systems, in bulk and in reduced dimensions. Hole spin dynamics, however, have been studied with far less intensity. Several recent advances in materials science further an interest in hole spin dynamics: (a) in diluted magnetic semiconductors (DMS) like Ga(Mn)As, the ferromagnetic coupling is mediated by free holes [1]. (b) carbon p-modulation doping now allows for very high hole mobilities in 2-dimensional structures, offering a clean model system for studying hole properties [2]. In bulk GaAs, the heavy-hole (HH) and light-hole (LH) valence bands are degenerate. Any momentum scattering of holes may therefore change the hole state from HH to LH and destroy the hole spin orientation, as HH and LH states have different angular momentum [3]. In a quantum well (QW), however, the degeneracy between LH and HH is lifted due to the confinement along the growth direction, leading to longer hole spin dephasing times of typically a few picoseconds [4]. Long-lived hole spin precession was observed at very low sample temperatures and weak excitation in n-doped QW structures by time-resolved photoluminescence measurements [5,6], and very recently in p-doped QW structures by time-resolved Faraday rotation (TRFR) [7].

Here, we investigate the hole spin dynamics in single-sided p-modulation-doped QWs by time-resolved optical spectroscopy techniques. We study the influence of sample temperature and magnetic field, as well as the effect of a varying growth-axis potential applied by a gate voltage. We observe long-lived hole spin dynamics in our samples at sub-Kelvin temperatures. These hole spin dynamics are strongly suppressed as the sample temperature is increased and vanish at liquid-Helium temperature, indicating that hole localization is crucial for long hole spin dephasing times. In a series of samples with different QW width, we observe that the hole spin dephasing time increases as the well width decreases. In a gated sample, we observe that the hole spin precession frequency can be tuned at a fixed in-plane magnetic field by changing the applied gate voltage.

1. Sample design and experimental technique

Our samples are single-sided p-modulation doped GaAs-AlGaAs QWs containing a 2-dimensional hole system (2DHS) with relatively low hole density and high hole mobility, grown by molecular beam epitaxy (MBE) on [001] substrates. Sample data are listed in Table 1. For TRFR measurements, the samples are first glued onto a sapphire substrate with optically transparent glue, then the semiconductor substrate is removed by grinding and selective wet etching, leaving only the MBE-grown layers. Semitransparent top gates are fabricated by thermal evaporation of a thin NiCr layer through a shadow mask onto the sample surface. The 2DHS is contacted from the top via Indium alloying. The optical measurements are performed in an optical cryostat with ^{3}He insert, allowing for sample temperatures below 400 mK and magnetic fields up to 11.5 Tesla. In the TRFR and time-resolved Kerr rotation (TRKR) measurements, near-resonant excitation from a Ti:Sapphire laser system (pulse length 600 fs, spectral width of the laser pulses 3–4 meV) is used. A circularly polarized pump pulse creates electron-hole pairs, and a time-delayed, linearly polarized probe pulse detects the growth-axis component of the spin polarization within the sample via the Faraday/Kerr effect. We use an optical bridge detector and lock-in-detection to increase detection sensitivity.

Table 1. Sample data. Density and mobility were determined from magnetotransport measurements at 1.3 K.

Sample	width (nm)	density p (10^{11} cm^{-2})	mobility μ (10^6 cm^2/Vs)
A	15	0.9	0.50
B	11	1.0	0.36
C (gated)	10	1.1	0.53

2. Sub-Kelvin hole spin dynamics

We first investigate the temperature dependence of the hole spin dynamics. Figure 1(a) shows TRFR traces of sample A taken with an in-plane magnetic field of 10 Tesla at various sample temperatures. For the highest temperature (4.5 K), a fast oscillation of the TRFR signal is visible. As the temperature is lowered to 1.2 K, a second, long-period oscillation

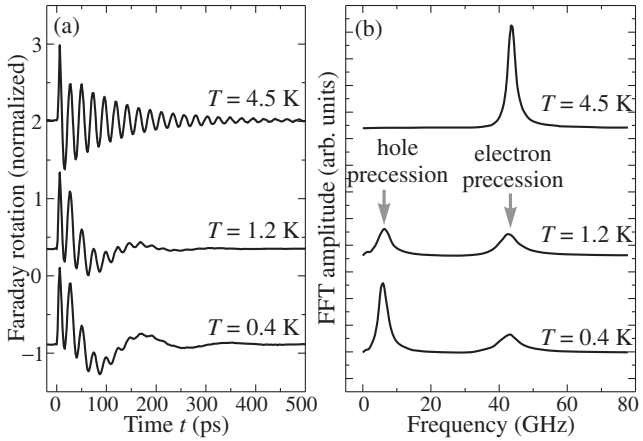

Fig. 1. (a) TRFR traces for sample A for different sample temperatures. A 10 Tesla in-plane magnetic field was applied during the measurements. (b) Fourier transform traces of the data from (a). The electron and hole spin precession frequency peaks are marked by the grey arrows.

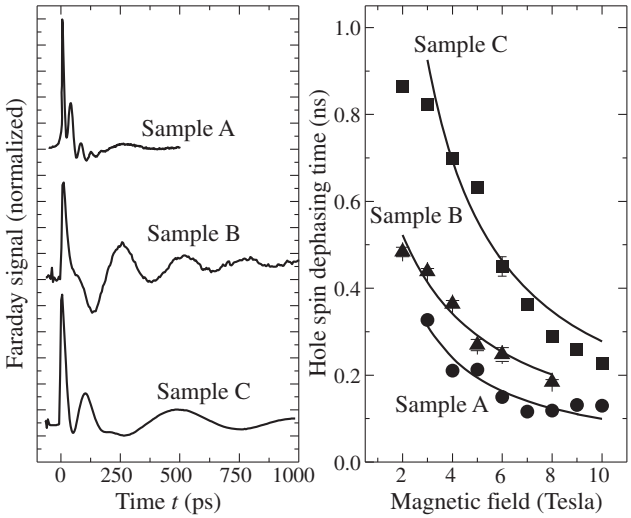

Fig. 2. (a) TRFR traces for all three samples, measured with an in-plane field of 6 Tesla. (b) Hole spin lifetime for samples A (dots), B (triangles) and C (squares) as a function of the in-plane magnetic field. The lines represent a $1/B$ dependence.

becomes apparent, superimposed on the fast oscillation. This long-period oscillation becomes even more pronounced at the lowest sample temperature of 0.4 K. By performing a Fourier transform analysis of the TRFR traces (shown in Figure 1(b)), we can determine both, the oscillation frequencies, and the decay constants of these oscillations. By performing these measurements for different in-plane magnetic fields, we determine the dispersion of both oscillations (see [8]). A linear fit to these dispersions yields the g factors. The g factor corresponding to the fast oscillation is $|g_e| = 0.28$, which is in good agreement with the electron g factor for GaAs QWs of similar width [9]. Interestingly, the damped electron spin precession decays more quickly as the sample temperature is lowered. We attribute this to a reduction of the photocarrier lifetime at lower sample temperatures. As the samples are p-doped, electron spin precession can only be observed during the lifetime of the photocreated electrons. The g factor of the low-frequency oscillation is $|g_h| = 0.038$. It was predicted by Winkler *et al*, [10] that the in-plane hole g factor for QWs grown in the [001] direction should be close to zero, and very low values between 0.012 and 0.05 were found experimentally [6,7]. We therefore identify this long-lived, low frequency precession as the precession of resident holes within the QW, which persists even after photocarrier recombination.

The Fourier transform data in Figure 1(b) demonstrates the very strong temperature dependence of the hole spin dephasing time: by increasing the sample temperature from 0.4 to 1.2 K, we observe a decrease of the hole spin dephasing time from 165 to 120 ps, while at 4.5 K, no long-lived hole precession is observed. We note that to our knowledge, the measurement at 0.4 K represents the first time-resolved spin dynamics measurement in the sub-Kelvin regime. From this temperature dependence, we infer that the main mechanism for the increased hole spin dephasing time is hole localization. As all samples show a very high hole mobility, we may identify two possible causes for localization: (a) potential fluctuations due to the statistical distribution of the ionized remote acceptors. (b) monolayer fluctuations of the quantum well width. The main mechanism for the increase of hole spin dephasing time due to localization is as follows: only at $k = 0$, the HH and LH bands have a well-defined character. For $k > 0$, there is a finite admixture between LH and HH [11]. Therefore, momentum scattering may still cause hole spin relaxation in a QW. Localization significantly reduces the hole quasimomentum, keeping the hole in a well-defined HH state.

3. Quantum well width dependence of hole spin dephasing time

Next, we study hole spin dynamics as a function of the QW width. Figure 2(a) shows TRFR traces for all three samples measured with an in-plane field of 6 Tesla. All samples show fast electron spin precession, which dies out in the first 100 ps after excitation. We note that the *electron* g factor strongly depends on the QW width [9], therefore the electron precession frequency is different for the samples. Superimposed on the electron spin precession, we observe the slower hole spin precession. It is clearly visible that the hole spin precession decays most quickly for the widest sample A (150 ps), and three times more slowly for the narrow sample C (445 ps). The different observed hole spin precession frequencies are due to slight tilting of the samples with respect to the applied magnetic field (see inset in Figure 3). It has been predicted [10] and recently shown experimentally [7] that the hole g factor measured in TRFR/TRKR is in fact a geometric sum of the in-plane ($g_{h,\perp}$) and growth-direction ($g_{h,||}$) hole g factors: $g_h = \sqrt{g_{h,\perp}^2 \cos^2\alpha + g_{h,||}^2 \sin^2\alpha}$.

The significant increase in hole spin dephasing time can be attributed to an increased HH/LH splitting, which reduces the admixture of the LH band to the top of the HH band, where the resident holes reside. In a first approximation, this energy splitting ΔE is proportional to 1 over the well-width L squared:

$$\Delta E \approx \left(\frac{1}{m_{LH}} - \frac{1}{m_{HH}}\right) \frac{\hbar^2\pi^2}{2L^2}$$

. For all samples, the hole spin lifetime decreases with increasing magnetic field, as Figure 2(b) shows. This decrease is

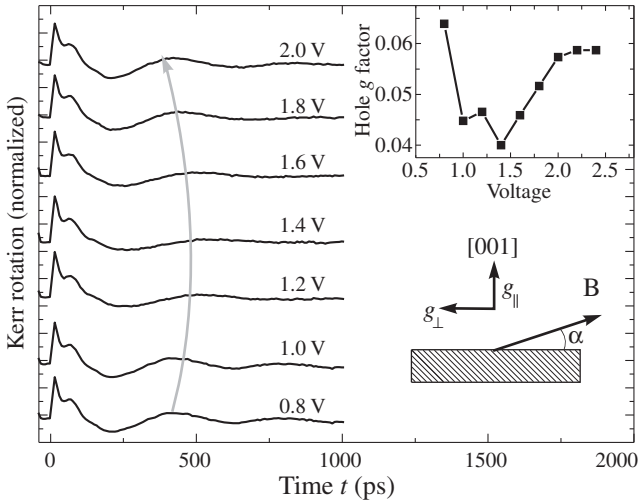

Fig. 3. TRFR traces for sample C for different applied gate voltages, measured with an in-plane field of 6 Tesla. The grey arrow traces the position of the first hole spin precession maximum. The inset shows the modulus of the hole g factor as a function of the applied gate voltage. A sketch of the magnetic field geometry and the hole g factor components is shown below.

governed by the hole g factor inhomogeneity: for larger magnetic fields, the hole spin ensemble dephases more rapidly due to the spread of g factors [12]. We note that due to the rapid photocarrier recombination, at zero and low magnetic fields, no significant resident hole spin polarization may be created in the system [14].

4. Hole g factor tuning by a gate voltage

Finally, we investigate the effect of a gate voltage on the hole spin dynamics. Figure 3 shows TRKR traces measured on sample C with a **constant** in-plane magnetic field of 6 Tesla. In these measurements, the gate voltage was varied. It is clearly visible how the hole spin precession changes its frequency, the grey arrow serves as a guide to the eye. From these measurements, the hole g factor was extracted, and as the inset in the same figure shows, it has a pronounced minimum for a gate voltage of 1.4 Volts. This behavior may be explained by the growth-axis displacement of the hole wave function depending on the QW potential. For a symmetric QW, the wave function is localized mostly within the GaAs, while for an asymmetric potential, a significant part of the wave function leaks into the AlGaAs barrier. For holes, like for electrons, where electrical g factor control has been demonstrated [13], the g factor depends on the semiconductor material. For holes, both, the in-plane($g_{\mathrm{h},\perp}$) and growth-direction ($g_{\mathrm{h},||}$) hole g factors change as a function of the applied voltage. In fact, calculations show that the growth-direction g factor undergoes a sign change at about 1.2 Volts [8]. As the measured hole g factor is a geometric sum, however, total suppression of hole spin precession via compensation of $g_{\mathrm{h},\perp}$ and $g_{\mathrm{h},||}$ is not observed in our experiment.

Conclusion

In conclusion, we have investigated the spin dynamics of resident holes in a series of high-mobility 2-dimensional hole systems. At low temperatures, we observe long-lived hole spin precession, which is strongly suppressed as the temperature is increased. The hole spin dephasing time increases as the quantum well width is decreased, due to a larger splitting between the light and heavy hole states. In a gated sample, electrical tuning of the hole g factor is observed. It is caused by a growth-axis displacement of the hole wave function, which changes both, the in-plane ($g_{\mathrm{h},\perp}$) and growth-direction ($g_{\mathrm{h},||}$) hole g factors, as the hole wave function partly leaks into the barrier material.

Acknowledgements

The authors would like to thank T. Andlauer and P. Vogl for fruitful discussion. Financial support by the DFG via SPP 1285 and SFB 689 is gratefully acknowledged.

References

[1] H. Ohno *et al*, *Appl. Phys. Lett.* **69**, 363 (1996).
[2] C. Gerl *et al*, *Appl. Phys. Lett.* **86**, 252105 (2005).
[3] D. J. Hilton *et al*, *Phys. Rev. Lett.* **89**, 146601 (2002).
[4] T. C. Damen *et al*, *Phys. Rev. Lett.* **67**, 3432 (1991).
[5] B. Baylac *et al*, *Solid State Commun.* **93**, 57(1995).
[6] X. Marie *et al*, *Phys. Rev. B* 60, 5811 (1999).
[7] M. Syperek *et al*, *Phys. Rev. Lett.* **99** 187401 (2007).
[8] M. Kugler *et al*, in preparation.
[9] M. J. Snelling *et al*, *Phys. Rev. B* **44**, 11345 (1991).
[10] R. Winkler *et al*, *Phys. Rev. Lett.* **85** 4574 (2001).
[11] S. Pfalz *et al*, *Phys. Rev. B* **71**, 165305 (2005).
[12] D. R. Yakovlev and M. Bayer, "Coherent Spin Dynamics of Carriers", chapter in "Spin Physics in Semiconductors" Springer (2008).
[13] G. Salis *et al*, *Nature* **414**, 619 (2001).
[14] T. Korn *et al*, in preparation.

17th Int. Symp. "Nanostructures: Physics and Technology"
Minsk, Belarus, June 22–26, 2009
© 2009 Ioffe Institute

Tamm–Dirac states in graphene

V. A. Volkov and I. V. Zagorodnev
V. A. Kotelnikov Institute of Radioengineering and Electronics of RAS, 125009, Moscow, Russia

Abstract. The quantum-mechanical behavior of the massless 2D Dirac fermion near the lateral edge of graphene is analysed. From the symmetry considerations, the boundary conditions for the envelope wave functions on a straight edge of graphene are derived. Solving the Dirac equation for the envelope functions with the derived boundary conditions, we get analytically 1D electron spectrum of the Tamm-type edge states in graphene. In simplest case these Tamm–Dirac states are described by a single phenomenological parameter, which depends on edge microscopics.

Introduction

An electron in graphene has an ultrarelativistic spectrum, that a charged 2D neutrino would have, if existed. This spectrum is twice valley-degenerated, the centers of valleys are being spaced by vector $2\vec{K}_0$ in Brillouin zone. The envelope wave functions in each valley obey the two-component Weyl-Dirac equation for spinor $\psi = (\psi_1, \psi_2)^T$:

$$\tau v \vec{\sigma}\,\vec{p}\psi = E\psi, \tag{1}$$

where T is the transposition operation, $v = 10^8$ cm/c, $\tau = \pm 1$ is the valley number, and

$$\vec{\sigma}\,\vec{p} = \begin{pmatrix} 0 & -i\hbar\frac{\partial}{\partial x} - \hbar\frac{\partial}{\partial y} \\ -i\hbar\frac{\partial}{\partial x} + \hbar\frac{\partial}{\partial y} & 0 \end{pmatrix} \tag{2}$$

To describe a number of effects, including the abnormal quantum Hall effect, size quantization in nanoribbons and quantum dots, it is necessary to know the behavior of electrons or holes near the edge of graphene, i.e. to derive the boundary conditions (BCs) for envelope wave functions. In general case the BCs have rather complicated form [1]. Therefore the model BCs [2,3] are generally in use. Armchair and zigzag edges are usually considered and the BCs are derived from the nearest neighbour tight-binding approximation [4]. The results are sensitive to the choice of model of the edge [5,6]. In this work a behaviour of the massless 2D Dirac fermion near the edge of graphene is analysed. The problem is a generalization of the intrinsic surface states problem (Tamm problem) for the Dirac electron [7], that's why we named the intrinsic edge states in graphene Tamm–Dirac states.

1. Boundary conditions for the massless 2D Dirac fermion

Consider the straight graphene edge (S), making an angle α with the armchair orientation (Fig. 1). From the symmetry considerations (Hermiticity and T-invariance of the boundary problem), the BCs for the envelope wave functions are derived. For simplicity let us neglect the intervalley scattering. In this simplest case the graphene edge (S) appears to be described by a real parameter a:

$$\left(\psi_1 + ia^\tau e^{-i\alpha}\psi_2\right)\Big|_S = 0. \tag{3}$$

The value a depends on the edge structure microscopics.

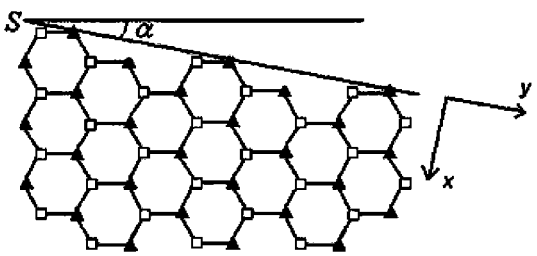

Fig. 1. Edge orientation (S) of semi-infinite graphene lattice.

2. Tamm–Dirac states spectra

Solving (1) with the BC (3) we get 1D spectrum of the Tamm–Dirac edge states in graphene $E(k_y)$:

$$E_\tau(k_y) = \frac{2avk_y\tau}{a^2+1}, \tag{4}$$

where

$$k_y\left(1 - a^{2\tau}\right) > 0. \tag{5}$$

The electron momentum along the sample edge (k_y) is measured from the projection of the valley center on the direction of the sample edge, $\pm K_{0y}$. The edge states band is represented with the rays (Fig. 2) beginning at the center of each valley and located in one of the quadrants E vs. k_y, depending on the sign of a and $(1 - a^2)$. For the value $a = 0$ the known dispersionless spectrum for zigzag edge is obtained [3,4]. For all values of a there are edge states with linear dispersion. For $a = 0.2$ the result agrees with the next nearest neighbors tight-binding calculation [5].

In quantizing magnetic fields, allowing $a \neq 0$ in the BC (3) qualitatively change the known magnetic edge states spectrum. Fig. 3 can be treated as a result of superposition of the spectra

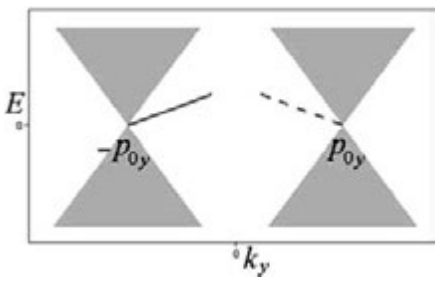

Fig. 2. Intrinsic edge states ("Tamm–Dirac states") spectra for $a = 0.2$. Intervalley scattering is neglected.

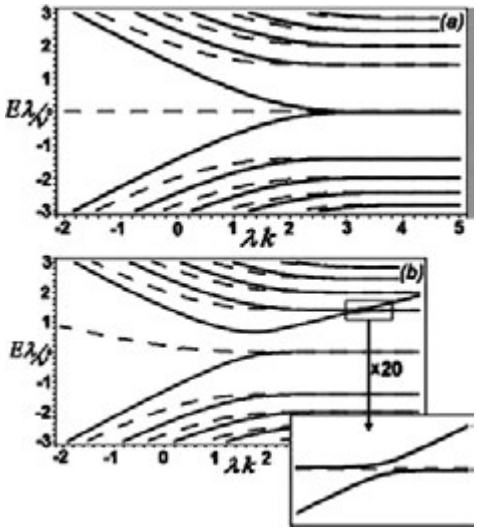

Fig. 3. Spectra of magnetic edge states in the left (the solid curve) and in the right (the doted) valleys for different meanings of the parameter a (Fig. 3a: $a = 0$, Fig. 3b: $a = 0.2$), λ is the magnetic length. Intervalley scattering is neglected.

(4),(5) and the spectra of the usual magnetic edge states taking into account the anticrossing.

An effect of inter-valley scattering of the Tamm–Dirac states also is considered. The effect leads to anticrossing of the edge spectra branches shown in Fig. 2.

Acknowledgements

This work is supported in part by the INTAS (grant No. 05-1000008-8044), and the RFBR (grant No. 08-02-00206).

References

[1] E. McCann and V. I. Fal'ko, *J. Phys. Condens. Matter.* **16**, 2371 (2004).
[2] M. V. Berry and R. J. Mondragon, *Proc. R. Soc. Lond.* **A412**, 53 (1987).
[3] L. Brey and H. A. Fertig, *Phys. Rev. B* **73**, 235411 (2006).
[4] K. Nakada, M. Fujita, G. Dresselhaus, M. S. Dresselhaus, *Phys. Rev. B* **54**, 17954 (1996).
[5] N. M. Peres, F. Guinea, A. H. Castro Neto, *Phys. Rev. B* **73**, 125411 (2006).
[6] A. R. Akhmerov and C. W. J. Beenakker, *Phys. Rev. B* **77**, 085423 (2008).
[7] V. A. Volkov, T. N. Pinsker, *Sov. Phys. Solid State* **23**, 1022 (1981).

17th Int. Symp. "Nanostructures: Physics and Technology"
Minsk, Belarus, June 22–26, 2009
© 2009 Ioffe Institute

g-Factor of low mobility 2D GaAs electron gas from strong magnetic field experiments

A. V. Germanenko[1], N. Kozlova[2], G. M. Minkov[1,3], J. Freudenberger[2], O. E. Rut[1], A. A. Sherstobitov[1,3] and I. V. Soldatov[1]

[1] Ural State University, 620083 Ekaterinburg, Russia
[2] Leibnitz Institute for Solid State and Material Research Dresden, IFW Dresden, D-01171 Dresden, Germany
[3] Institute of Metal Physics, 620041 Ekaterinburg, Russia

Abstract. We study low-mobility 2D electron gas in GaAs quantum well in tilted magnetic field up to 45 T. Analyzing the behavior of the Shubnikov-de Haas (SdH) oscillations we obtain the value of g-factor, $|g| = 0.9 \pm 0.1$, which is noticeably larger than that predicted theoretically and obtained from optical experiments. Possible reasons of the discrepancy are discussed.

Introduction

One of the widely used method for determining the value of g-factor in two-dimensional (2D) systems is study of the SdH oscillations in tilted magnetic field. The method is based on the fact that the spin splitting of the Landau levels is controlled by the total magnetic field (B) while the orbit quantization is sensitive only to the normal component:

$$\begin{aligned} E &= \left(n+\frac{1}{2}\right)\hbar\omega_c \pm \frac{1}{2}g\mu_B B \\ &= \left(n+\frac{1}{2}\right)\frac{\hbar eB}{m}\cos\theta \pm \frac{1}{2}g\mu_B B, \end{aligned} \qquad (1)$$

where θ is the angle between the magnetic field and the direction normal to the 2D plane, m is the effective mass. The g-factor determining the conduction band spin splitting can be found by rotating the sample in the magnetic field to identify the angle θ_0 at which the spin splitting is equal to the half of the cyclotron energy [1]. When the sample is in such a position, the SdH oscillations amplitude passes through zero, and their phase changes by π. Once, such orientation angle, θ_0, is found, the effective g-factor can be determined as

$$g = \frac{e\hbar}{2\mu_B m}\cos\theta_0 \qquad (2)$$

provided that the effective mass is known for the same sample. This method works well for the high-mobility systems, in which the oscillations are observed starting from the very low magnetic fields, and for the systems with the relatively high value of g-factor. In the dirty systems with the relatively low mobility and/or with small value of g-factor the vanishing of the oscillations amplitude is not observed under usual experimental conditions, and more delicate approach is needed. The theory of the SdH effect for 2D systems in the tilted magnetic fields has been developed in [2].

In the present work we report the results of the experimental study of the 2D GaAs electron system in the tilted magnetic field up to 45 T. We demonstrate that the value of the g-factor can be experimentally obtained from the analysis of the angle dependence of the amplitude of the SdH oscillations even for the case of the low-mobility samples.

1. Experimental

Results for $Al_{0.7}Ga_{0.3}As/GaAs/Al_{0.7}Ga_{0.3}As$ single quantum well structure grown by MBE are reported. It consists of a 250 nm-thick undoped GaAs buffer layer grown on semiinsulator GaAs, a 50 nm $Al_{0.7}Ga_{0.3}As$ barrier, a Si δ layer, a 6 nm spacer of undoped $Al_{0.7}Ga_{0.3}As$, a 8 nm GaAs well, a 6 nm spacer of undoped $Al_{0.7}Ga_{0.3}As$, a Si δ layer, a 50 nm $Al_{0.7}Ga_{0.3}As$ barrier, and 200 nm cap layer of undoped GaAs. The electron density and mobility are 1.8×10^{16} m^{-2} and 1.5 m^2/V s, respectively. The samples were mesa etched into standard Hall bars. The measurements have been performed using the DC technique in the Laboratory for pulsed high magnetic fields of the Institute for Metallic Materials, IFW Dresden.

2. Results and discussion

The magnetic field dependences of the resistance measured for different angles θ are presented in Fig 1. The spin split oscillations maxima are clearly evident for $\theta = 0$. They, however, are shifted to the inaccessible magnetic field with the change of the tilt angle. The low magnetic field oscillations remain periodic

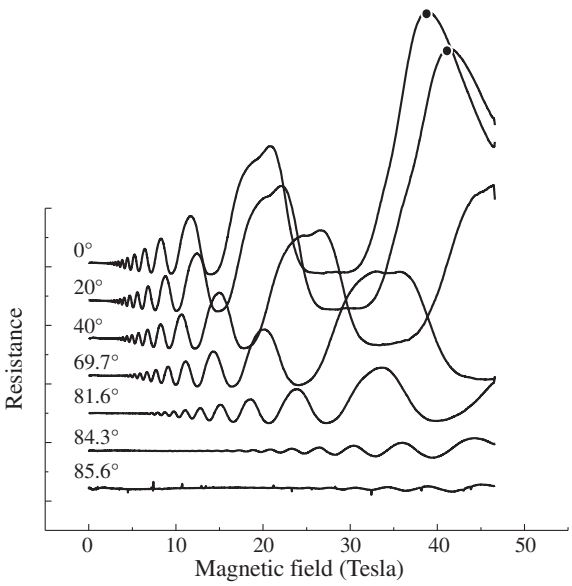

Fig. 1. The SdH oscillations for various orientation of the magnetic field, $T = 4.2$ K.

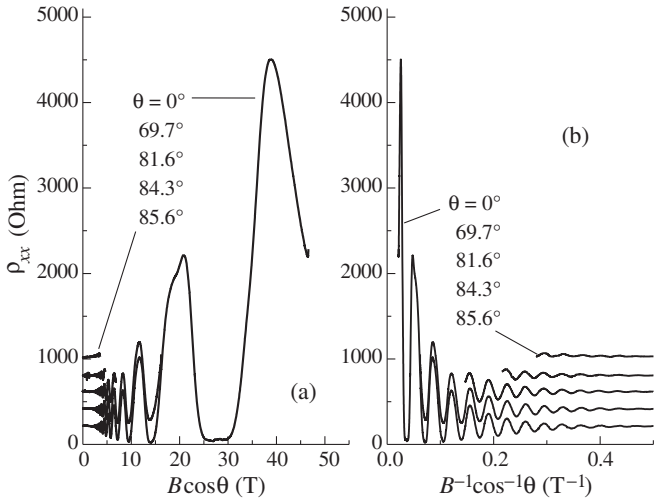

Fig. 2. The oscillations plotted against $B_\perp$ (a) and $B_\perp^{-1}$ (b) for different values of the tilt angle.

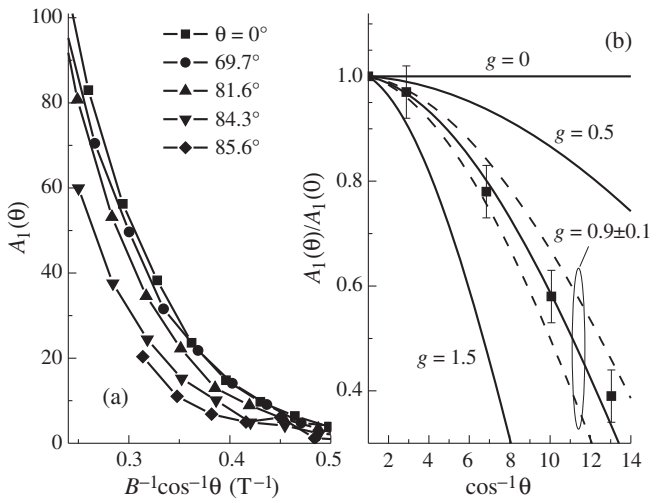

Fig. 3. (a) — The $B_\perp^{-1}$ dependence of the amplitude of the 1-st harmonic of the SdH oscillations for the different angles θ. (b) — The $A_1(B,\theta)$ to $A_1(B,0)$ ratio as a function of $1/\cos\theta$. Symbols are the data, the lines are calculated from Eq. (3) with the different values of g-factor and $m/m_0 = 0.067$.

and all the oscillations curves measured for different angles coincide with each other being plotted against the perpendicular component of the magnetic field, $B_\perp = B\cos\theta$ (Fig. 2).

To obtain experimentally the value of g-factor we have analyzed the magnetic field dependence of the SdH oscillations measured for different θ. Theoretically, the amplitude of the s-th harmonic of the oscillations measured in tilted magnetic field is connected with that measured at $\theta = 0$ via the simple expression

$$\frac{A_s(\theta)}{A_s(0)} = \cos\left(\frac{\pi s}{2}\,\frac{g}{\cos\theta}\,\frac{m}{m_0}\right)\Big/\cos\left(\frac{\pi s}{2}\,g\,\frac{m}{m_0}\right). \qquad (3)$$

One can see that the $A_s(B,\theta)$ to $A_s(B,0)$ ratio should not depend on the magnetic field, and its angle dependence is fully determined by the value of g-factor.

In Fig. 3, the experimental data are compared with the expression (3). Each experimental point in this figure is obtained by averaging over the magnetic field range in which the oscillations amplitude is rather small. Just the variation of $A_s(B,\theta)$ to $A_s(B,0)$ ratio in this $B_\perp$ range is indicated by the error bar. The best agreement is achieved for $|g| = 0.9 \pm 0.1$. This value is significantly larger than that calculated theoretically and observed in optical experiments. The value of g-factor on the bottom of the conduction band for this structure is predicted close to -0.15 in the framework of $\mathbf{k}\times\mathrm{P}$ model [3]. At the Fermi energy, $E_\mathrm{F} \simeq 25$ meV, its value is still less due to nonparabolicity of the conduction band, it can be estimated as $g \simeq 0 \pm 0.05$.

The taking the exchange interaction into account [4,5] does not improve the situation due to relatively low value of the gas parameter $r_s = \sqrt{2}/k_\mathrm{F}a_\mathrm{B}$, where k_F is the Fermi quasimomentum, a_B is the effective Bohr radius; it is about 0.4 in the sample investigated. Our estimations show that the exchange-induced enhancement of g-factor at the Fermi energy should be under 10%, while $r_s < 1$.

Another possible reason for discrepancy is the anisotropy of the effective g-factor. Although the "low-field" g-factor of the 2D electrons is practically isotropic [3], it is not the case when the magnetic field is relatively strong. Namely, when the magnetic length, L, becomes less than the width of the quantum well, d, the longitudinal g-factor ($\theta = 90°$) should be close to that of the balk material, $g_\parallel \simeq g = -0.44$, whereas g-factor responsible for the Zeeman splitting for $\theta = 0$ is close to zero as mentioned above. In our case the minimal L value corresponding to $B = 45$ T is about 3.8 nm, that is nearly twice as small as $d = 8$ nm. This mechanism, however, does not allow us to describe the experimental data quantitatively, suggesting further work is needed.

Acknowledgements

This work has been supported in part by the RFBR (Grant 08-02-91962) and DFG (Grant No. KO 3743/1-1).

References

[1] T. Ando *et al*, *Rev. Mod. Phys.* **54**, 437 (1982).
[2] S. A. Tarasenko, *Physics of the Solid State* **44**, 1769 (2002).
[3] P. Pfeffer and W. Zawadzki, *Phys. Rev. B* **74**, 233303 (2006).
[4] J. F. Janak, *Phys. Rev.* **178**, 1416 (1969).
[5] C. S. Ting *et al*, *Phys. Rev. Lett.* **34**, 870 (1975); T. K. Lee *et al*, *ibid*, **35**, 1048 (1975).

17th Int. Symp. "Nanostructures: Physics and Technology"
Minsk, Belarus, June 22–26, 2009
© 2009 Ioffe Institute

Magnetic moment of a two-dimensional electron gas in the presence of spin-orbit interaction

V. A. Margulis and V. A. Mironov
Institute of Physics and Chemistry, Mordovian State University, 430005 Saransk, Russia

Abstract. Explicit analytical expression for the magnetic moment of a two-dimensional electron gas (2DEG) in the presence of a perpendicular magnetic field and of Rashba spin-orbit interaction (SOI) is derived. The magnetic moment is investigated as a function of the magnetic field strength. We have compared our results with the recent experimental data on observation of the magnetization.

Introduction

Theoretical and experimental investigations of the energy spectrum of the two-dimensional electron gas in the presence of Rashba SOI show that two stairs of Landau levels appear in the system in external magnetic field. This modification of energy spectrum leads to significant changes of the transport and equilibrium properties of low-dimension structures.

Central problem to the understanding of physics of two-dimensional electron systems (2DES) is a detailed knowledge of the density of states (DOS) between Landau levels [1]. In particular, the absence of discontinuous jumps in the magnetization observed in the series of experiments was interpreted by a finite DOS between Landau levels [1,2]. The experimental results [1,3] reported the observation of discontinuous jumps in the magnetization where interpreted by absence of finite DOS between Landau levels. This specific feature of the magnetization was predicted by Peierls [4] for the ideal 2DES. It should be noted, the magnetization at fixed number N of particles in the system is an oscillating function of filling factor ν. It is the sawtooth periodical function of reversed magnetic field $(1/B)$, and the magnetization jumps at even integer ν are very sharp [1,3,5].

1. Evaluation of magnetization

We consider 2DEG in the xy plane in a uniform perpendicular magnetic field B. The energy spectrum of the system in the presence of Rashba SOI is determined by the formula [6]

$$E_s^{\pm}=\hbar\omega_c\left[\left(s+\frac{1}{2}\pm\frac{1}{2}\right)\mp\sqrt{\delta^2+\left(s+\frac{1}{2}\pm\frac{1}{2}\right)\gamma}\right], \quad (1)$$

where $s = 0, 1, 2, \ldots$, $\delta = (1 - gm^*/(2m_0))/2$, g is the Zeeman factor, $\gamma = 2\alpha^2 m^*/(\hbar^3\omega_c)$, α is the strength of the SOI, ω_c is the cyclotron frequency, m^* is the effective electron mass, m_0 is the free electron mass.

The magnetic moment of 2DEG at fixed number of particle in the system is very interesting to study, because this case is more adequate for a variety of real experimental situations [5]. Shoenberg [7] reported that in this case at $T = 0$ the Fermi energy coincides with the energy of the uppermost filled level, but this level is partially occupied, and its occupation increases from 0 to $D = 1/2\pi l_c^2$ when magnetic field decreases. Here D is the degeneracy of Landau level per unit area and $l_c = \sqrt{\hbar/m^*\omega_c}$ is the magnetic length. Thus the chemical potential μ corresponds to uppermost filled Landau level. Therefore μ is sawtooth function of B.

Energy levels are crossed when magnetic field is changed (Fig. 1). Since two cases of evaluation of the magnetic moment M exist. In the first one the uppermost filled level is partially occupied level and it corresponds to Landau levels for electron with energy E_n^+. In the other stair uppermost filled level E_m^- is full occupied, that is $E_n^+ > E_m^-$. In this case the magnetic moment $(M = M_1)$ is given by

$$\begin{aligned}\frac{M_1}{\mu_B^*} = &-\frac{m^*\omega_c}{\pi\hbar}\left\{n(n+1)+m(m+1)+2\delta+\frac{3\sqrt{\gamma}}{2}\right.\\
&\times\left[\zeta\left(-\frac{1}{2},1+n+\frac{\delta^2}{\gamma}\right)-\zeta\left(-\frac{1}{2},1+m+\frac{\delta^2}{\gamma}\right)\right]\\
&+\frac{\delta^2}{2\sqrt{\gamma}}\left[\zeta\left(\frac{1}{2},1+n+\frac{\delta^2}{\gamma}\right)-\zeta\left(\frac{1}{2},1+m+\frac{\delta^2}{\gamma}\right)\right]\\
&+2\left(\frac{N}{2D}-(n+m+1)\right)\left(n+1-\sqrt{\delta^2+(n+1)\gamma}\right)\\
&\left.+\frac{1}{2}\left(\frac{N}{D}-(n+m+1)\right)\frac{\gamma(n+1)}{\sqrt{\delta^2+(n+1)\gamma}}\right\}. \quad (2)\end{aligned}$$

Here $\zeta(z, a)$ is the generalized Riemann ζ-function.

The second case is opposite $E_n^+ \le E_m^-$, here the level E_m^- is partially occupied level, and E_n^+ is the completely occupied level. Thus the magnetic moment $(M = M_2)$ is determined by

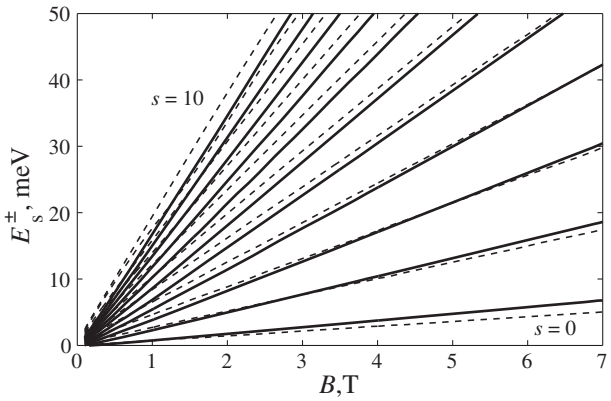

Fig. 1. Dependence of the energy spectrum (1) of Rashba's model on the magnetic field for $0 \le s \le 10$. The energy E_s^+ are represented by solid line, E_s^- are represented by dashed line. $\alpha = 1.2 \times 10^{-11} eVm$, $g = 5$, $m^* = 0.067m_0$.

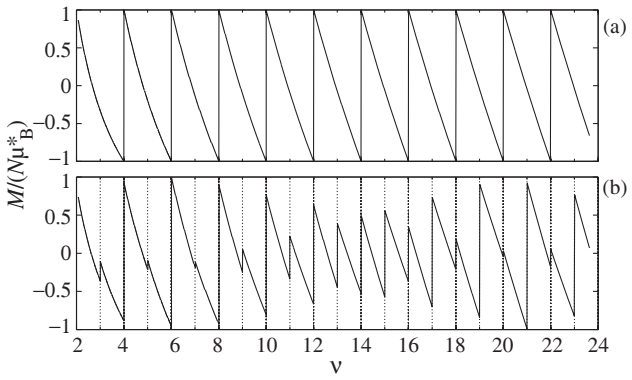

Fig. 2. Dependence of the magnetic moment per electron on the filling factor at $T = 0$ and $N = \text{const}$: (a) without of SOI and the spin-splitting ($\alpha = 0$, $g = 0$), (b) in the presence of SOI at $\alpha = 0.8 \times 10^{-11} eVm$, $g = 5$. $m^* = 0.067 m_0$, $n_s = 4 \times 10^{11} \text{cm}^{-2}$.

the formula

$$\frac{M_2}{\mu_B^*} = -\frac{m^*\omega_c}{\pi\hbar}\Big\{(2+n)(1+n) + m(m-1) + 2\delta + \frac{3\sqrt{\gamma}}{2}\left[\zeta\left(-\frac{1}{2}, 2+n+\frac{\delta^2}{\gamma}\right) - \zeta\left(-\frac{1}{2}, m+\frac{\delta^2}{\gamma}\right)\right] + \frac{\delta^2}{2\sqrt{\gamma}}\left[\zeta\left(\frac{1}{2}, 2+n+\frac{\delta^2}{\gamma}\right) - \zeta\left(\frac{1}{2}, m+\frac{\delta^2}{\gamma}\right)\right] + 2\left(\frac{N}{2D} - (n+m+1)\right)\left(m + \sqrt{\delta^2 + m\gamma}\right) - \frac{1}{2}\left(\frac{N}{D} - (n+m+1)\right)\frac{\gamma m}{\sqrt{\delta^2 + m\gamma}}\Big\}, \quad (3)$$

where μ_B^* is the effective Bohr magneton. Note, that in both situations total number $n + m + 1$ of completely filled levels is equal to integer part of ratio N/D.

We emphasize that the magnetic moment M at $N = \text{const}$ is described by equation (2) if the uppermost partially occupied level belong to stair E_s^+ and is described by equation (3) if the uppermost partially occupied level belong to stair E_s^-.

Conclusion

As follows from (2) and (3), the magnetic moment of 2DEG in the presence of SOI is periodical oscillating function of the reversed magnetic field. In addition, it oscillates periodically with ν. The amplitude of oscillations changes with ν (see Fig. 2b, where n_s is electron density). Formation of these oscillations is stipulated by variable number of electrons on the uppermost partially occupied Landau level. It is noted in the previous section, that this level may belong to various stairs of Landau levels depending on magnetic field, number of particles and parameters of energy spectrum. Comparison of the dependence on Fig. 2a with Fig. 2b indicates that accounting of SOI in calculation of the magnetic moment gives rise to discontinuous jumps at odd filling factor. It is in agreement with experiments [1, 3, 5], which observed the magnetization of 2DES in AlGaAs/GaAs. Since the parameters of 2DEG used in our calculation are very similar to those of the devise used in the experiment [1], we can compare our calculated magnetic moment in Fig. 3b with the experimental results [1] shown in Fig. 3a. It can be seen that our calculated magnetic moment

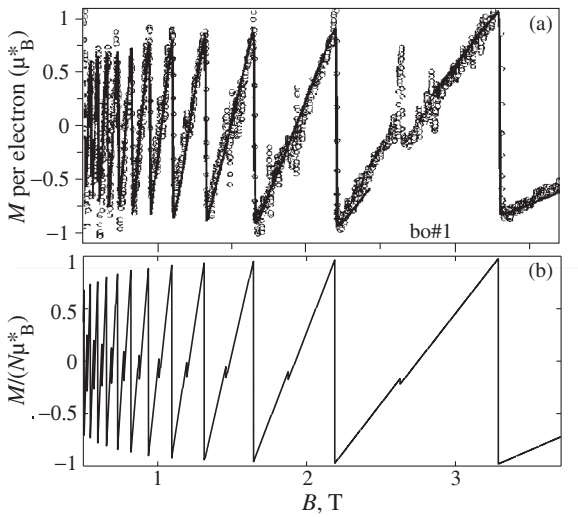

Fig. 3. Comparison of the experimental data [1] observation of magnetization (a) with our results (b) for magnetic moment at $T = 0$ in the presence of SOI. $\alpha = 0.25 \times 10^{-11} eVm$, $g = -0.44$, $m^* = 0.067 m_0$, $n_s = 3.18 \times 10^{11}$ cm^{-2}.

have reproduced the main features of the experimental results, such as dependence of oscillation amplitude on the magnetic field and presence of additional discontinuous jumps in the magnetization (on the background of general jumps, predicted by Peierls [4]) at odd filling factor ν.

Acknowledgements

This work was supported by the Russian Foundation for Basic Research (Grant No. 08-02-01035).

References

[1] M. A. Wilde *et al*, *Phys. Rev. B* **73**, 125325 (2006).
[2] N. Ruhe *et al*, *Phys. Rev. B* **74**, 235326 (2006).
[3] S. A. J. Wiegers *et al*, *Phys. Rev. Lett.* **79**, 3238 (1997).
[4] R. Peierls, *Z. Phys.* **81**, 186 (1933).
[5] M. P. Schwarz *et al*, *Phys. Rev. B* **65**, 245315 (2002).
[6] E. I. Rashba, *Sov. Phys. Solid State* **2**, 1109 (1960).
[7] D. Shoenberg, *Magnetic oscillations in metals*, (Cambridge) 1984.

17th Int. Symp. "Nanostructures: Physics and Technology"
Minsk, Belarus, June 22–26, 2009
© 2009 Ioffe Institute

Wide range tunneling current noise spectra singularities formed by charged localized states

V. N. Mantsevich, N. S. Maslova, A. I. Oreshkin and V. I. Panov
Moscow State University, Faculty of Physics, Chair of Quantum Electronics, Moscow, 119991, Russia

Abstract. We report the results of theoretical investigations of tunneling current noise spectra in a wide range of applied bias voltage in vicinity of individual impurity atoms on semiconductors and metallic surfaces. It was found that power law exponent of tunneling current noise spectra strongly differs for measurements above flat surface and above impurity atom. Obtained results can be explained by switching ON and OFF of Coulomb interaction of conduction electrons with one or two charged localized states in tunneling junction which results in power law singularity of low-frequency part of tunneling current noise spectrum $1/f^{\alpha}$ and also results on high frequency component of tunneling current spectra (singular peaks appear).

Introduction

In this work we discuss one of the possible reasons for the tunneling current noise formation in the STM/STS junctions. Up to now a great amount of experimental works devoted to the problem of $1/f^{\alpha}$ noise study can be found [2–4] but microscopic origin of this phenomenon is still unknown. Theoretical study of noise spectra in two-level system was carried out in [5]. We have found only a few works where high frequency region of tunneling current spectra is studied [6]. Our main goal was to study theoretically one of the possible microscopic origins of $1/f^{\alpha}$ noise in tunneling contact and to analyse how different impurity atoms on the surface or subsurface layers influence tunneling current noise spectra in a wide range of applied voltage.

1. Experimental results

We have found experimentally [1] that both for $InAs_S$ (n-type bulk conductivity, 1.5×10^{18} cm^{-3}) and $InAs_{Mn}$ (p-type bulk conductivity, 1.4×10^{16} cm^{-3}) the power law exponent is different for measurements above defect free surface area and above impurity atom. For $InAs_S$ the power law exponent α measured above clean surface is equal to 0.89 whereas above dopant atom it has value 1.16. For $InAs_{Mn}$ the power law exponent α measured above clean surface is equal to 1.04 whereas above dopant atom it has value 0.75. One can see the difference in the behavior of the power law exponent in cases of $InAs_S$ and $InAs_{Mn}$. While moving from impurity atom to the clean surface α is decreasing for $InAs_S$ sample. Opposite situation was observed for $InAs_{Mn}$ surface. Our simple model gives an opportunity to analyze one of the possible microscopic origins of $1/f^{\alpha}$ noise formation.

2. The suggested model and main results

When electron tunnels to or from localized state, the electron filling numbers of localized state rapidly change leading to appearance of localized state additional charge and sudden switching "on" and "off" Coulomb interaction. Electrons in the leads feel this Coulomb potential.

The model system (Fig. 1) of tunneling through two localized states can be described by hamiltonian $\hat{H}$. One of the localized states is formed by impurity atom in semiconductor and the other one by tip apex localized state.

$$\begin{aligned}
\hat{H} &= \hat{H}_0 + \hat{H}_{\mathrm{T}} + \hat{H}_{\mathrm{int}},\\
\hat{H}_0 &= \sum_k (\varepsilon_k - eV)\, c_k^+ c_k + \sum_p \varepsilon_p c_p^+ c_p + \sum_{i=1,2} \varepsilon_i a_i^+ a_i,\\
\hat{H}_{\mathrm{T}} &= \sum_{k,i} T_{ki} c_k^+ a_i + \sum_{p,i} T_{pi} c_p^+ a_i + T \sum a_1^+ a_2 + \mathrm{h.c.},\\
\hat{H}_{\mathrm{int}} &= \sum_{k,k'} W_1 c_k^+ c_{k'} a_1 a_1^+ + W_2 c_k^+ c_{k'} a_2 a_2^+,
\end{aligned}$$

$\hat{H}_0$ describes free electrons in the leads and in the localized states. $\hat{H}_{\mathrm{tun}}$ describes tunneling transitions between the leads through localized states. $\hat{H}_{\mathrm{int}}$ corresponds to the processes of intraband scattering caused by Coulomb potentials W_1, W_2 of localized states charges.

Operators $c_k^+(c_k)$ and $c_p^+(c_p)$ correspond to electrons in the leads and operators $a_i^+(a_i)$ correspond to electrons in the localized states with energy ε_i.

Current noise correlation function is determined as:

$$\begin{aligned}
(\hbar/e)^2 \times S(t,t') &= \langle I_{\mathrm{L}}(t) \times I_{\mathrm{L}}(t')\rangle\\
&= \sum_{k,k',i,j} T_k^2 \langle c_k^+(t') a_i(t') a_j^+(t) c_{k'}^+(t)\rangle.
\end{aligned}$$

The current noise spectra is determined by Fourier transformation of $S(t,t')$: $S(\omega) = \int S(\tau) d\tau \times e^{i\omega\tau}$.

When the applied bias voltage become close to energy level of impurity atom we obtain low frequency tunneling current spectrum. So we have to put $eV = \varepsilon_1 = \varepsilon_2$. Some low

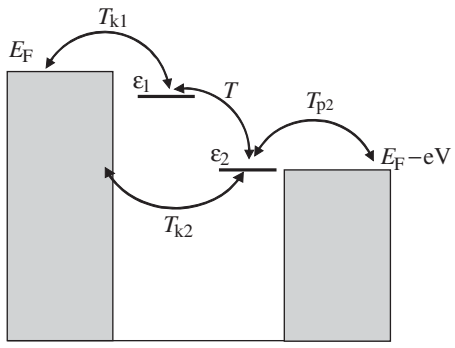

Fig. 1. Schematic diagram of tunneling through states localized on impurity atom and on the STM tip apex.

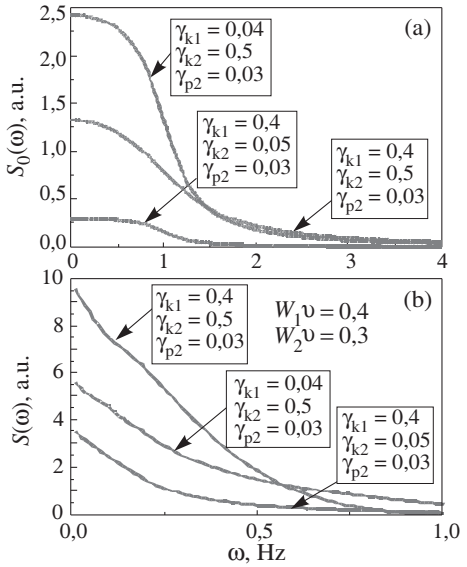

Fig. 2. Typical low frequency tunneling current noise spectra for different values of dimensionless kinetic parameters for two localized states in tunneling contact ($eV = \varepsilon_1 = \varepsilon_2 = 1$). a) In the absence of Coulomb re-normalization of tunneling vertexes. b) In the presence of Coulomb re-normalization of tunneling vertexes.

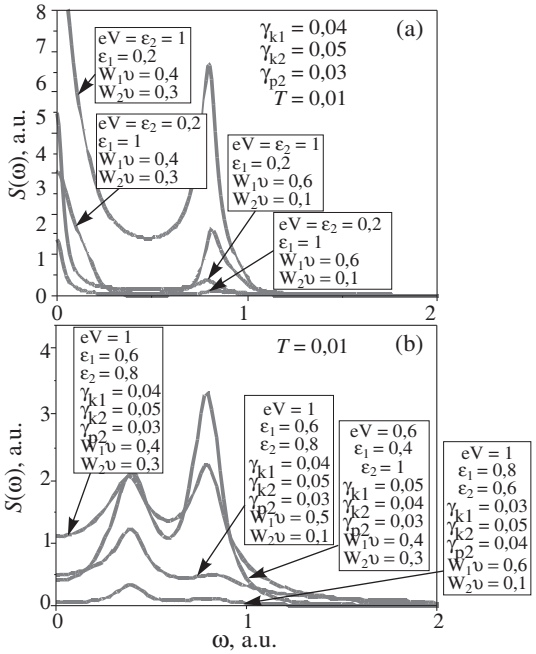

Fig. 3. Typical low frequency tunneling current noise spectra for different values of dimensionless kinetic parameters for two localized states in tunneling contact in the absence of Coulomb re-normalization of tunneling vertexes. a) $eV = \varepsilon_2 \neq \varepsilon_1$. b) $eV \neq \varepsilon_2 \neq \varepsilon_1$.

frequency spectra without Coulomb re-normalization of tunneling vertexes for different values of dimensionless kinetic parameters in the case of resonance tunneling are shown on (Fig. 2a). It is clearly evident that when frequency approaches zero, tunneling current spectra approaches constant value. We have found that typical power law singularity in low frequency tunneling current noise spectra (Fig. 2b) is a result of tunneling matrix element re-normalization by switched "on" and "off" Coulomb interaction of charged impurities with electrons in the leads of tunneling contact. This effect can be qualitatively understood by the following way: apart from the direct tunneling from the localized state to the state with momentum k in the lead of tunneling contact described by the amplitude T_k, the electron can first tunnel into any other empty state k' in the lead and then scatter to the state k by Coulomb potential. So the appearance of even a weak Coulomb interaction significantly modifies the many particle wave function of the electron gas in the leads.

Let's analyse the case of non-resonance tunneling. In our case of weak interaction between localized states ($T < \gamma_{k1}$, γ_{k2}, γ_{p2}) tunneling transfer amplitude T plays an important role in kinetic processes in the tunneling junction but weakly influences on the energy spectra. Tunneling current spectra without Coulomb re-normalization have the form equal to the un-re-normalized spectra in the resonance case shown on Fig. 2a. Tunneling current spectra with Coulomb corrections to the tunneling vertexes are shown on the Fig. 3. In the case of two localized states in tunneling junction when energy level of one of the localized states is connected with the tip apex and is not equal to energy level of the impurity atom localized state on the surface ($eV = \varepsilon_2 \neq \varepsilon_1$) we can see typical power law dependence for the low frequency part of tunneling current spectra and singular peak in the particular high frequency region of tunneling current spectra determined by the localized states energy levels deposition in the tunneling junction (Fig. 3a). In the non-resonance case of the cluster on the surface ($eV \neq \varepsilon_2 \neq \varepsilon_1$) (Fig. 3b) we have found two singular peaks in the high frequency region of tunneling current noise spectra and when frequency aspire to zero tunneling current spectra aspire to constant value. In this case there is no power law singularity in a low frequency part of tunneling current spectra. Singular peaks in high frequency region of tunneling current spectra are caused by the singularities on the difference frequencies. So our results demonstrate that changing of the applied bias voltage leads to the tuning of tunneling current noise spectra.

Simple estimation gives possibility to analyze the validity of obtained results. For typical composition of tunneling junction parameters in the low frequency region power spectrum of tunneling current corresponds to experimental results. Power spectrum on zero frequency has the form: $S(0) \approx (\gamma_{\text{eff}}\, e/\hbar)^2 (D/\gamma_{\text{eff1}})^{\nu W} (1/\Delta\omega)$.

For typical γ_{eff}, $\gamma_{\text{eff1}} \approx 10^{-13}$, $D \approx 10$, $W\nu \approx 0.5$ $S(0) \approx 10^{-18}$ A^2/Hz [1].

Acknowledgements

This work was supported by RFBR grants and Grants for technical regulation and metrology 01.648.12.3017 and 154-6/259/4-08.

References

[1] A. I. Oreshkin *et al*, *JETP Letters* **85**, 46 (2007).
[2] R. Moller *et al*, *Appl. Phys. Lett* **55**, 2360 (1989).
[3] T. Tiedje *et al*, *J. Vac. Sci. Technol. B* **A6**, 372 (1988).
[4] M. Lozano *et al*, *Europhys. Lett.* **30**, 537 (1995).
[5] L. S. Levitov *et al*, *JETP Letters* **55**, 534 (1992).
[6] A. Nauen *et al*, *Phys. Rev. B* **70**, 033305 (2004).

17th Int. Symp. "Nanostructures: Physics and Technology"
Minsk, Belarus, June 22–26, 2009
© 2009 Ioffe Institute

Spatial oscillations of the density of states near domain boundaries on the Ge(111) 2×1 surface studied by LT STM/STS

S.V. Savinov[1], D.A. Muzychenko[1], V.N. Mantsevich[1], N.S. Maslova[1], V.I. Panov[1], K. Schouteden[2] and C. Van Haesendonck[2]

[1] Faculty of Physics, Moscow State University, 119991 Moscow, Russia
[2] Laboratory of Solid-State Physics and Magnetism, BE-3001 Leuven, Belgium

Abstract. We present the results of low-temperature scanning tunneling microscopy and scanning tunneling spectroscopy investigations of the spatial oscillations of the local electron density of states on clean Ge(111) 2×1 surfaces. The oscillations appear in the vicinity of the boundaries between domains with different atomic arrangements. We introduce a tight-binding based model, which consistently explains the observed experimental features in terms of the formation of two-dimensional surface states within the surface band gap due to the breaking of the translational symmetry at the domain boundaries.

Introduction

Electronic properties of elemental semiconductor surfaces have attracted a lot of interest due to their crucial importance both for technological applications and for fundamental scientific issues. The Ge(111) surface with 2×1 reconstruction is among the most intensively investigated. Already in the eighties of last century photoemission studies [1] of heavily doped Ge single crystals as well as theoretical calculations [2] revealed the existence of separate occupied and non-occupied bands for the surface electrons. Until now, there were no direct observations of effects that are connected with the non-occupied surface states band of the Ge(111)2×1 surface. Here, we show that the existence of non-occupied surface states induces the appearance of spatial oscillations in the local density of states (LDOS) of the surface electrons at domain boundaries that appear on the reconstructed Ge(111)2×1 surface.

Experiment and results

The main goal of our STM investigation at low temperatures was to clarify the details of the Ge(111)2×1 surface electronic structure. Consequently, we intensively used the STS modes of the STM operation. Spectroscopic measurements were performed using harmonic detection by means of lock-in amplification for measuring the spatial variation of the differential conductance $\mathrm{d}I/\mathrm{d}V$ (closed feedback loop) at selected values of the tunneling bias voltage V. This spatial variation corresponds to a map of the LDOS at energy eV with respect to the Fermi energy. Everywhere in the text the tunneling bias voltage V refers to the sample voltage, while the STM tip is virtually grounded.

The investigated Ge samples are doped with Ga at a doping level of 2×10^{16} cm^{-3}, resulting in a p-type bulk conductivity. Ge slabs with size $5 \times 3 \times 1$ mm^3 and long axis aligned with the (111) direction were cleaved *in-situ* at room temperature in the UHV preparation chamber at a pressure about 5×10^{-11} mbar. Within 5 minutes after cleaving the samples were transferred to the low-temperature STM chamber, where the pressure was about 4×10^{-12} mbar for the reported STM and STS measurements.

The results of our combined STM and STS experiments for the Ge(111)2×1 surface can be summarized as follows.

— Spatial oscillations of the electron density were observed on the Ge(111)2×1 surface for both n-type (results are not shown here) and p-type bulk conductivity in the vicinity of DBs (see Fig. 1). The oscillations become visible in LDOS maps as well as in the CITS data.

— Within the experimental error, the wavelengths of the spatial oscillations originating from different type of DBs are the same.

— The oscillation wave fronts are aligned with the direction of the domain boundary and not with the direction $[01\bar{1}]$ of the π-bonded chains (Fig. 1(b–e)).

— Perturbations of the spatial oscillations by local 0D defects (Fig. 1(d)) occur in the direction $[01\bar{1}]$ of the π-bonded chains.

— The spatial oscillations can be best described in terms of a decaying sine wave oscillation superimposed upon a smooth non-monotonic background. The oscillation amplitude exponentially decays with increasing distance from the DB.

— The spatial oscillations can be observed only within the range of bias voltages between 0.23 V to 0.85 V, where surface states are the only states that are able to carry the tunneling current.

Discussion

Our experimental observations can be consistently interpreted in the framework of a model relying on the presence of Tamm surface states. The basic idea can be described as follows. It is well known that the breaking of the 3D translational symmetry at the surface of a 3D solid induces the appearance of p-orbital derived surface states that are localized within a narrow surface layer. The Tamm states are decaying exponentially into the vacuum, while they reveal an oscillating decay into the bulk. While the presence of a 2D surface on a 3D solid results in the appearance of 2D surface states, a 1D surface defect (a DB in our case) of the 2D surface causes in a similar way the appearance of 1D surface states.

In order to achieve a quantitative description of the experimental observations we performed analytical calculations within a tight-binding approach. The Ge(111)2×1 surface is modeled by linear atomic chains, separated by b distance, consisting of two inequivalent atoms 1/2 located at the distance a along chain with energy levels $\varepsilon_1/\varepsilon_2$ and tunneling matrix elements T ($1 \rightarrow 2$ tunneling) and t ($2 \rightarrow 1$ tunneling). This

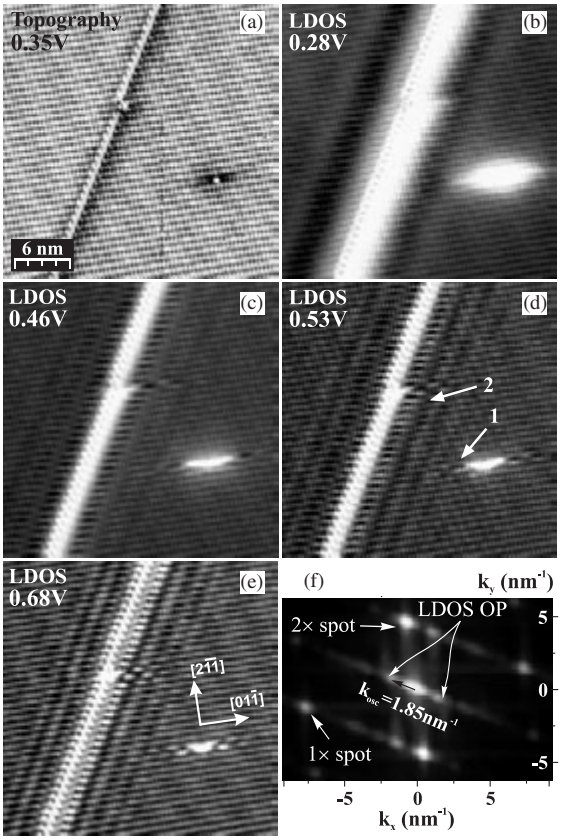

Fig. 1. (a) — STM constant current image of Ge(111)2 × 1 surface. (b–e) — LDOS maps of the same surface area. The value of the tunneling bias voltage values at which the measurements were performed is indicated on each of the images. The setpoint for the tunneling current I is 400 pA and the image size is 24 × 24 nm^2 for all images. (f) — 2D Fourier transform of the LDOS map in (e). The Fourier peaks resulting from both the 2 × 1 surface reconstruction and the spatial oscillations of the LDOS are indicated by the white arrows. The wave vector for the LDOS oscillations caused by the type-B domain boundary is represented by the black arrow in the center.

is a reasonable assumption if one bears in mind the fact that the Ge(111)2 × 1 surface consists of *up/down* atom dimers. The unperturbed energy levels ε_1 and ε_2 reside in the filled π_{VB} and empty π^*_{CB} surface states band, respectively. The interaction between atomic chains is described in terms of a tunneling amplitude τ, which has the same value for all atoms in the chain. The potential introduced by the domain boundary is modeled in terms of a hard wall potential W. All possible relaxation processes are described using one single parameter γ. The local density of surface states can be obtained from a formalism based on the Green's functions diagram technique. First, we calculate the LDOS for a single atomic chain. Next, we use the calculated LDOS for a single atomic chain to add the influence of the inter-chain interaction τ and of the relaxation γ. Finally, we add the scattering at the domain boundary. In the framework of proposed model the dependence of the the LDOS of the surface states on the distance in a direction perpendicular to the DB is given by

$$\rho(x,\,y) = \frac{1}{\pi}\mathrm{Tr}\Big(\mathrm{Im}\sum_{\vec{\kappa},\vec{\kappa_1}}\hat{G}^{\mathrm{R}}(\vec{\kappa},\vec{\kappa_1},\omega)e^{i\vec{\kappa}x}e^{-i\vec{\kappa_1}y}\Big).$$

The results of numerical calculations based on this equation

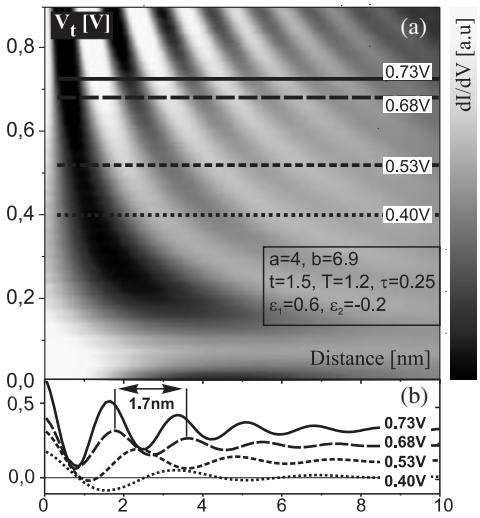

Fig. 2. (a) — Calculated quasi-3D map of the LDOS of the surface electrons in the vicinity of a DB. The abscissa corresponds to the distance from the DB, while the ordinate corresponds to the tunneling bias voltage. A few hyperbola-like branches are clearly visible. The value of the parameters, which have been used for the calculations are shown. (b) — Cross-sections of the color map in (a) at the values of tunneling bias voltage that are indicated in (a). For the cross-section at $V = 0.68$ V it is illustrated how the wavelength can be determined. The value of the parameters, which have been used for the calculations are shown.

are presented in Fig. 2. The gray scale map in (a) gives the 2D spatial variation of the local density of surface states $\rho(\vec{r}, eV)$ in the vicinity of a DB. DB is located at vertical axis. The abscissa corresponds to the distance from the DB, while the ordinate corresponds to the value of tunneling bias voltage. In panel (b) of Fig. 2 we illustrate the 1D variation of the LDOS of the surface states versus distance from the DB in the direction perpendicular to the DB at the bias voltages indicated in both (a) and (b). The 1D graphs in Fig. 2 (b) correspond to cross-sections of the 2D LDOS at the selected tunneling bias voltages that are indicated by the horizontal colored dashed lines in Fig. 2. The low-frequency background has been filtered out from the cross-sections. The link between experiment and the theory are cross-sections. Each cross-section in Fig. 2(b) at certain bias voltage $\mathrm{V_t}$ corresponds to cross-section of experimental LDOS map, taken at mentioned bias, in direction (aa') in Fig. 1(a), which is perpendicular to DB. The overall agreement between experimental data and theoretical predictions is very good.

As one can see the value of inter-chain interaction τ is comparable with values of inter-atomic matrix elements t and T. That is why our system should be treated not as purely one dimensional (with electrons localized along π-bonded chain rows), but as quasi two-dimensional.

Acknowledgements

This research in Moscow has been supported by the RFBR's grants. The research in Leuven has been supported by the Fund for Scientific Research - Flanders (Belgium) as well as by the Interuniversity Attraction Poles (IAP) research program.

References

[1] J. N. Nicholls *et al*, *Phys. Rev. Lett.* **54**, 2363 (1985).
[2] J. E. Northrup *et al*, *Phys. Rev. B* **27**, 6553 (1983).

17th Int. Symp. "Nanostructures: Physics and Technology"
Minsk, Belarus, June 22–26, 2009
© 2009 Ioffe Institute

Low-temperature scanning tunneling microscopy of ring-like surface electronic structures around Co islands on InAs(110) surfaces

D.A. Muzychenko[1], S.V. Savinov[1], N.S. Maslova[1], V.I. Panov[1], K. Schouteden[2] and C. Van Haesendonck[2]

[1] Faculty of Physics, Moscow State University, 119991 Moscow, Russia
[2] Laboratory of Solid-State Physics and Magnetism, BE-3001 Leuven, Belgium

Abstract. We report on the experimental observation by STM at low temperature of ring-like features that appear around Co metal clusters deposited on a clean (110) oriented surface of cleaved p-type InAs crystals. These features are visible in spectroscopic images within a certain range of negative tunneling bias voltages due to the presence of a negative differential conductance in the current-voltage dependence. A theoretical model is introduced, which takes into account non-equilibrium effects in the small tunneling junction area. In the framework of this model the appearance of the ring-like features is explained in terms of interference effects between electrons tunneling directly and indirectly (via a Co island) between the tip and the InAs surface.

After the pioneering work of Tsui [1], two-dimensional (2D) electron systems have been intensively investigated. The 2D electron gas provides an excellent playing ground for studying the physical properties of low-dimensional systems [2]. Here, we present the results of local STM/STS measurements of the electronic properties of a 2D system, which consists of metal Co islands deposited *in situ* on the (110) oriented surface of InAs that is obtained by cleavage in ultra-high vacuum (UHV) of a single crystal.

The investigated InAs samples are doped with Mn at a doping level of 5×10^{17} cm^{-3}. Mn in InAs is expected to act as a shallow acceptor with ionization energy around 28 meV. InAs slabs with size $5 \times 2 \times 2$ mm^3 were cleaved *in-situ* at room temperature in the UHV preparation chamber (base pressure is about 5×10^{-11} mbar). Co islands were deposited by means of electron-beam evaporation. All the reported STM/STS experiments are performed at liquid helium temperature ($\simeq$4.5 K). Tunneling bias voltage V_t refers to the sample voltage.

According to our STM measurements, Co atoms tend to form small clusters on the InAs(110) surface despite the low substrate temperature during deposition. Surprisingly, some clusters are surrounded by ring-like features on the STM images. We have also performed spatially resolved spectroscopic measurements above the same surface area where the STM image was obtained (Fig. 1(a)). In a first set of experiments, we relied on imaging based on harmonic detection with a lock-in amplifier. The results are shown in Figs. 1(b),(c),(d) and (f). Each image corresponds to a map of tunneling conductance proportional to LDOS.

From our analysis of the results shown in Fig. 1 we conclude that:

(i) sharply defined dark rings appear in the differential conductance (LDOS) images around some of the clusters within a certain range of negative tunneling bias voltages,

(ii) the size of the dark rings is shrinking when the absolute value of the tunneling bias voltage is decreased,

(iii) the LDOS has an almost constant value above the Co-InAs surface except for the clusters and the immediate vicinity of the dark rings,

(iv) the differential conductivity has negative (NDC) value on the dark rings.

Most probably the presence and the different diameters of the dark rings around the different clusters is caused by the different bonding of the clusters to the InAs substrate.

The large grid size that has been used for acquiring the CITS data allows us to present the data in another interesting way. Figure 2 gives a 2D map of the variation of the normalized tunneling conductance data along the cross-section bb' in Fig. 1(a). The horizontal axis corresponds to the spatial coordinate, while the vertical axis corresponds to the tunneling bias voltage, and the color intensity corresponds to LDOS.

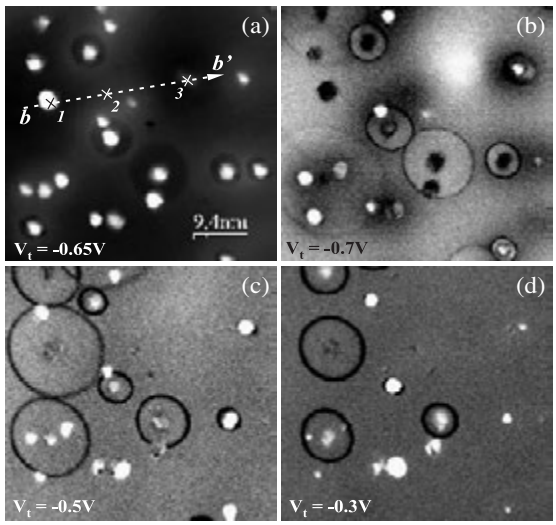

Fig. 1. (a) Experimental constant current topographical STM image of the Co-InAs(110) surface with a Co coverage of about 0.02 ML obtained at $V_t = -0.65$ V and $I = 400$ pA. The image size is 47×47 nm^2. (b),(c) and (d) are maps of the measured differential conductance $dI/dV_t(x, y, V_t)$ for the same surface region as in (a) at different tunneling bias voltage. The tunneling current setpoint is $I_t = 150$ pA, while the tunneling bias voltage is indicated at the bottom of the maps. Ring-like features, whose appearance is strongly affected by the applied negative bias voltage, can be observed.

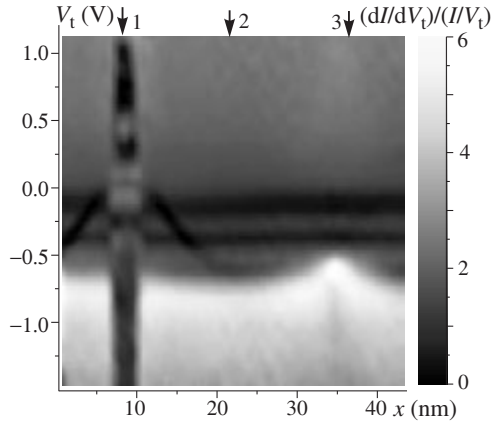

Fig. 2. 2D representation of the normalized differential tunneling conductance, extracted from the CITS data (see text) along the line bb' indicated in Fig. 1(a). The horizontal axis corresponds to the spatial coordinate, while the vertical axis corresponds to the tunneling bias voltage. The color contrast in the image corresponds to the value of the differential tunneling conductance as given by the color scale on the right hand side.

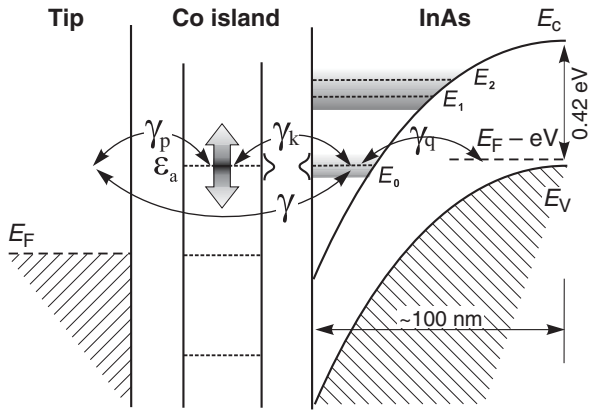

Fig. 3. Schematic representation of the tunneling processes occurring in the system consisting of the STM tip, a Co cluster and the InAs(110) substrate. ε_a is the Co cluster energy level that is participating in the tunneling. E_0 is the first 2D subband, which has a non-zero but narrow width, as indicated by the gray stripe. A gray stripe is also used to mark the presence of the higher 2D subbands, which form a continuum of states due to their broadening. The system is shown at non-zero bias voltage when ε_a and E_0 are aligned and a dark ring appears around the Co cluster in the maps of the differential tunneling conductance.

From Fig. 2 it is clear that a Co cluster affects the LDOS in the conduction and valence bands only very locally. Except for a limited voltage range near $V_t = 0$, the influence of a cluster on the LDOS is very rapidly decaying outside the cluster. Inside the cluster, the conductivity in the valence band is considerably suppressed. Some of the energy levels of the Co cluster become visible in the voltage range corresponding to the band gap and the conduction band. In Fig. 2 there are two tilted dark lines that approximately start from the peak in the normalized tunneling conductance of the cluster and that extend over a distance of about 8 nm into the defect free surface area. These two dark lines directly reflect the presence of the dark rings around the clusters as well as the dependence of the ring diameter on the tunneling bias voltage, which is clearly non-linear.

Another important observation related to Fig. 2 is the influence of the Mn impurity atoms below the Co-InAs(110) surface on the tunneling spectra. In the vicinity of a Mn atom the LDOS is affected deep inside the conduction and valence bands. Additionally, an intense peak appears in Fig. 2 near the valence band top and most probably this peak reflects the energy position of the Mn acceptor band. We note that the spatial extent of this peak is relatively large, about 7 nm.

In order to describe the observed effects consistently one needs to take into account the presence of non-equilibrium and interference effects in the small tunneling junction [3], which can be described using the Keldysh diagram technique. Two main peculiarities of the ring-like features observation have to be explained. First, the presence of the NDC region in the tunneling conductivity curves has to be accounted for. Second, the limited spatial extent of the circular features requires an explanation. The model structure of InAs-Co-STM tip structure is depicted in Fig 3.

Co cluster on the surface acts as a donor, and consequently it is positively charged. In case of non-equilibrium, the energy ε_a of the cluster level, which is participating in the tunneling (see Fig. 3), depends on the electron filling number $\langle n_a \rangle$ of this level: $\varepsilon_a = \varepsilon_0 + U(n_0, -\langle n_a \rangle)$, where ε_0 is the unperturbed position of the cluster energy level, n_0 is the equilibrium cluster level filling number, and U is the Coulomb interaction energy of the localized charges [3]. At certain conditions this can lead to the appearance of negative slope area on I(V) dependence.

The most probable physical mechanism causing the formation of narrow (of the order of the interatomic distance) ring-like features in real space is some kind of resonant tunneling. When the STM tip changes its spatial position, localized energy levels that participate in the tunneling processes are coming out of resonance or even are falling outside the tunneling window $[E_F, E_F - eV_t]$. This leads to variations of the cluster level filling number, and consequently to changes in the cluster level energy.

In conclusion, by means of LT STM/STS measurements, we have been able to identify the presence of ring-like features around Co metal clusters on a p-type InAs(110). These features become clearly visible in the maps of the differential conductance for a certain range of negative tunneling bias voltages, due to the presence of a NDC region in the $I(V_t)$ dependence. The diameter of the rings is decreasing when decreasing the absolute value of the tunneling bias voltage.

A theoretical model was developed, which takes into account the non-equilibrium effects that occur in the small STM tunneling junction. In the framework of the model the appearance of the ring-like features is accounted for by the interference of direct and indirect (via a Co cluster) tunneling between the STM tip and the InAs surface.

Acknowledgements

This research in Moscow has been supported by the RFBR's grants. The research in Leuven has been supported by the Fund for Scientific Research — Flanders (Belgium) as well as by the Interuniversity Attraction Poles (IAP) research program.

References

[1] D. C. Tsui, *Phys. Rev. Lett.* **24** 7, 303 (1970).
[2] V. Yu. Aristov *et al*, *Phys. Rev. B* **47**, 2138 (1993).
[3] P. I. Arseev *et al*, *JETP Lett.* **68** 4, 320 (1998).

17th Int. Symp. "Nanostructures: Physics and Technology"
Minsk, Belarus, June 22–26, 2009
© 2009 Ioffe Institute

Response time and negative conductance of resonant-tunneling-diode beyond resonant-state-lifetime limit

M. N. Feiginov[1] and D. Roy Chowdhury[2]

[1] Technische Universität Darmstadt, 64283 Darmstadt, Germany
[2] Universitaet Duisburg-Essen, 47057 Duisburg, Germany

Abstract. We show, first, that the charge relaxation (response) time of resonant-tunneling diode (RTD) can be significantly shorter or longer than the resonant-state lifetime, depending on RTD operating point and RTD parameters. Coulomb interaction of electrons is responsible for the effect. Second, we demonstrate that the operating frequencies of RTDs are limited neither by resonant-state lifetime, nor by relaxation time; particularly in the RTDs with heavily doped collector, the differential conductance can stay negative at the frequencies far beyond the limits imposed by both time constants. We provide experimental evidences for both effects.

Introduction

Resonant-tunneling diodes (RTDs, see Fig. 1) are the most simple structures with resonant tunneling. Such structures were intensively studied in the last several decades, they are used for studies of fundamental aspects of tunneling and they are also attractive for practical applications. E.g., RTDs belong to the fastest [1] operating devices nowadays and their negative differential conductance (NDC) is useful for high-frequency oscillators [2, 3]. The question that arises in connection with any electronic device: what is limiting its response time and its operating frequencies? The response of RTD is connected to population and depopulation of the resonant states in the quantum well (QW) of the diode. Therefore, it is typically accepted [4, 5] that the inherent response-time limitation of such structures should be determined by the resonant-state lifetime (τ). Also it is also intuitively expectable [5] that the current and conductance of the structure should tend to zero, when $\omega\tau \gg 1$.

One of us has shown theoretically previously that the intuitive picture is not generally correct [6, 7, 8]. The objective of the present work is to demonstrate that experimentally. We show that the response time or, equivalently, the time constant of charge-relaxation processes ($\tau_{\rm rel}$) can be significantly shorter than τ. Such behavior is the consequence of the Coulomb interaction between the charge carriers in the structures [6, 7]. We also show that, under certain conditions, the Coulomb interaction can lead to the opposite effect, when $\tau_{\rm rel}$ becomes longer than τ. Additionally, we demonstrate that, as predicted [8], the resonant-tunneling conductance can stay large and it can stay even negative in RTDs, when $\omega\tau \gg 1$ and $\omega\tau_{\rm rel} \gg 1$. Such effects have not been observed till recently [9].

1. Experimental

For the experimental demonstration of the above effects, we were studying InGaAs/AlAs RTDs with heavily doped collector specially designed (see subscript to Fig. 1) to have approximately equal effective thicknesses (including the screening and depletion lengthes) of the emitter (d) and collector (l) barriers. $l \approx d$ is a necessary condition to achieve NDC when $\omega\tau_{\rm rel} \gg 1$ and $\omega\tau \gg 1$ [9]. Without loss of generality of the obtained results and for the sake of ease of measurements only, the barriers of RTDs were made thick (≈3.5 nm), so that the value of τ is ≈100 ps. For such diodes, the conditions $\omega\tau \gg 1$ and $\omega\tau_{\rm rel} \gg 1$ are already well satisfied at the frequencies below 10 GHz and the effects we are looking for could be demonstrated with standard microwave measurement techniques.

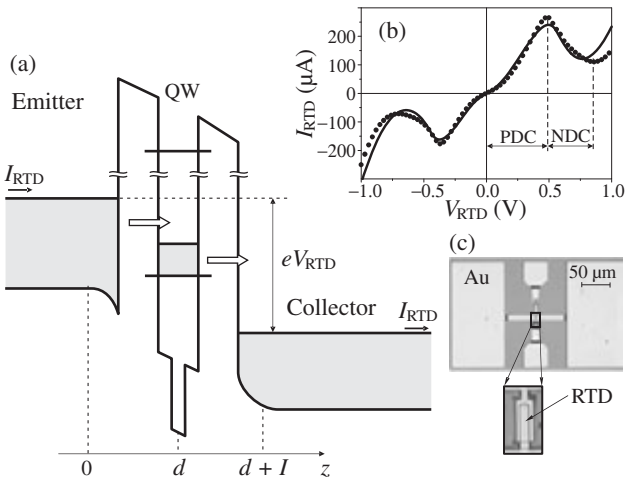

Fig. 1. (a) Schematic band diagram of the fabricated RTD. Panel (b) shows measured (dots) and simulated (solid line) room-temperature I–V curves of 3 × 15 μm^2 RTD with the following layer sequence: QW with 1.4 nm $In_{0.53}Ga_{0.47}As$ 3.0 nm $In_{0.68}Ga_{0.32}As$ 1.4 nm $In_{0.53}Ga_{0.47}As$ layers is sandwiched between ≈3.5 nm (nominal value) AlAs barriers and $In_{0.53}Ga_{0.47}As$ emitter and collector regions n-doped at the level of 10^{18} cm^{-3} with 1.5 nm spacers close to the barriers. (c) The photograph of fabricated RTDs with connecting circuitry for microwave-probe measurements.

The layout of the fabricated RTD structures is shown in Fig. 1c. RTD is connected via air bridges and other metal lines to the contact pads for the standard microwave-probe measurements. The admittance of RTD with the surrounding parasitic circuitry has been measured with a conventional vector network analyzer. To determine the contribution of the parasitic circuitry, the additional short and open structures were fabricated and measured, where RTD is replaced by a short (for the measurement of the inductive contribution) or open (for the capacitive contribution) circuits. The parasitic parameters measured in such a way are supported by simulation results (with CST Microwave Studio). When the parasitic contributions to

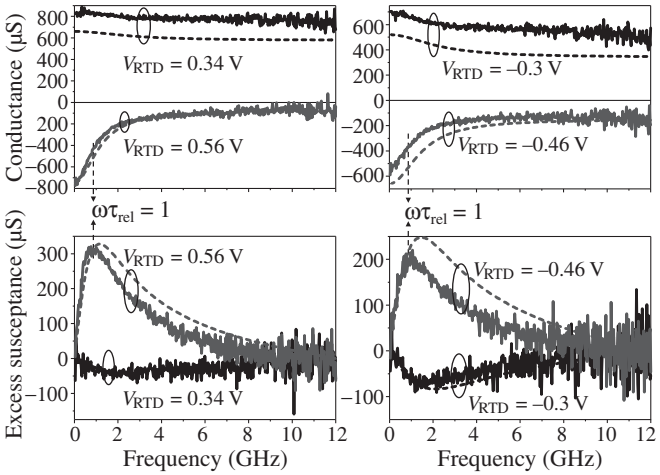

Fig. 2. The plots of measured (solid lines) and simulated (dashed lines) RTD conductances (Re (G)) and excess susceptances (Im (G) − ωC_{RTD}) for forward (0.34 V and 0.56 V) and reverse (−0.3 V and −0.46 V) biases, C_{RTD} is the geometrical RTD capacitance. The biases of 0.34 V and −0.3 V are in the PDC region of the I–V curve (see Fig. 1b) and those of 0.56 V and −0.46 V are in NDC region. The RTD was designed in such a way that the values of $1/2\pi\tau$ and $1/2\pi\tau_{rel}$ in NDC region are close to 1 GHz. The plots of RTD conductance at 0.56 V and −0.46 V show that the conductance stays negative, even when $\omega\tau_{rel} \gg 1$ and $\omega\tau \gg 1$: $\omega\tau_{rel} \approx 12$ and $\omega\tau \approx 8$ at 12 GHz.

the measured admittance are excluded, we get the resultant "pure" RTD admittance, see Fig. 2. The plots of conductance in the NDC region clearly show that RTD conductance stay negative in the whole measurement range of 12 GHz, where the conditions $\omega\tau_{rel} \gg 1$ and $\omega\tau \gg 1$ are satisfied.

Further, we simulate the static and dynamic characteristics of RTDs. The sequential-tunneling approximation is used in our self-consistent static simulations, we take into account the nonparabolicity in the barriers, finite (room) temperature, thermionic emission over the barriers, tunneling through the second subband in QW. The simulated curves are in very good agreement with the measured ones, they describe well the peak and valley regions of the I–V curves both for the forward and reverse biases applied to RTD (see Fig. 1b). The RTD parameters used in the simulations (the barrier thicknesses are 3.3 and 3.2 nm) are in good agreement with the nominal MBE growth parameters and the parameters of the layers determined by X-ray diffraction on the calibration test structures (the barriers were 3.6 and 3.5 nm). Further, the AC characteristics of RTD have been calculated relying on our previously developed theory [7,8]. The simulated and measured AC admittances are in good agreement with each other both in the positive differential conductance (PDC) and NDC regions and also for the forward and reverse biases, see Fig. 2.

Knowing the RTD parameters from the simulations and comparison with experimental data above, we calculate τ and τ_{rel} for our diodes, Fig. 3. The values of τ_{rel} can be also determined from the admittance plots (Fig. 2). As it has been shown by one of us theoretically [7,8], the characteristic conductance roll-off frequency and the peak in the excess susceptance (see Fig. 2) correspond to the condition $\omega\tau_{rel} = 1$. The experimental values of τ_{rel} determined in such a way are also plotted in Fig. 3. The figure shows that τ_{rel} determines the roll-off of the AC

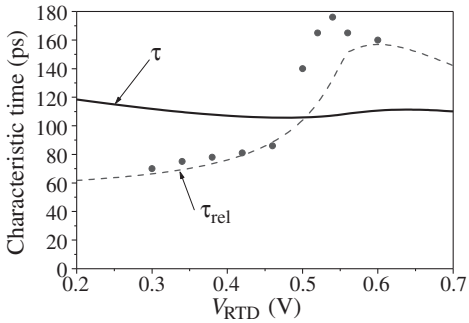

Fig. 3. The plots for simulated values of τ (solid line) and τ_{rel} (dashed line) for forward bias. The values of τ_{rel} determined from the experimental RTD conductance and susceptance data (see Fig. 2) are marked with dots.

characteristics of RTD, while τ has even qualitatively different behavior. The value of τ is decreasing with bias as a consequence of the decrease of the collector-barrier height, whereas τ_{rel} is increasing, as a consequence of the Coulomb-interaction effects [6,7], when one goes from PDC to NDC region of the I–V curve. The experimental and theoretical values of τ_{rel} are in quantitative agreement with each other. Both the simulations and measurements do indeed show that τ_{rel} is by a factor of ≈ 2 shorter (longer) than τ in the PDC (NDC) regions.

Although the measurements presented here are done at relatively low frequencies, the same effects should be observable also at much higher frequencies. E.g., the same RTDs with 1.5 nm barriers would have $\tau \approx 0.5$ ps and $1/2\pi\tau \approx 300$ GHz. One of the practical consequences of the presented results is that the frequency range, where the differential conductance of RTD stays negative and realization of RTD oscillators is possible, should be limited neither by τ nor by τ_{rel} in RTDs with heavily doped collectors. Such diodes should allow one to overcome the upper frequency of ≈0.7 THz achieved [2,3] with RTD oscillators till now. Additionally, although we present in this work the data on the most simple resonant-tunneling structure and at relatively low frequencies, the observed effects (Coulomb shortening of the relaxation time and conductance beyond the resonant-state-lifetime limit) are also expected in the more complicated structures (multi-barrier structures, single-electron-transistor-like structures, quantum-cascade lasers, etc.) and at the frequencies much higher than those covered in the present work and even in the THz frequency range.

Acknowledgements

The financial support of DFG and the Alexander von Humboldt Foundation are gratefully acknowledged.

References

[1] J. S. Scott *et al*, *Appl. Phys. Lett.* **64**, 1995 (1994).
[2] E. Brown *et al*, *Appl. Phys. Lett.* **58**, 2291 (1991).
[3] M. Asada *et al*, *Jpn. J. Appl. Phys.* **47**, 4375 (2008).
[4] T. C. L. G. Sollner *et al*, in *Physics of Quantum Electron Devices*, edit. by F. Capasso, Vol. 28 (Springer-Verlag, New York, 1990).
[5] E. R. Brown *et al*, *Appl. Phys. Lett.* **54**, 934 (1989).
[6] M. N. Feiginov, *Appl. Phys. Lett.* **76**, 2904 (2000).
[7] M. N. Feiginov, *Nanotechnology* **11**, 359 (2000).
[8] M. N. Feiginov, *Appl. Phys. Lett.* **78**, 3301 (2001).
[9] M. N. Feiginov *et al*, *Appl. Phys. Lett.* **91**, 203501 (2007).

17th Int. Symp. "Nanostructures: Physics and Technology"
Minsk, Belarus, June 22–26, 2009
© 2009 Ioffe Institute

Spin Faraday, Kerr and ellipticity effects in quantum dots

M. M. Glazov[1], I. A. Yugova[2], E. L. Ivchenko[1] and Al. L. Efros[3]

[1] Ioffe Physical-Technical Institute, St Petersburg, Russia
[2] Institute of Physics, St Petersburg State University, 198504 St Petersburg, Russia
[3] Naval Research Laboratory, Washington DC 20375, USA

Abstract. We develop a theory of two color pump-probe Faraday and Kerr rotation and ellipticity signals for singly charged quantum dot ensembles. The theory describes generation of spin polarization in the quantum dots by short pump pulses of circularly polarized light with the carrier frequency lying in the vicinity of a trion resonance. The response of quantum dots on a weaker, linearly polarized probe pulse is calculated. The expressions for Faraday, Kerr and ellipticity signals are derived. These signals have a different spectral sensitivity which reveals itself in the time-resolved pump-probe waveforms.

Introduction

Spin Faraday and Kerr effects observed under pump-probe conditions are commonly used efficient methods of the spin dynamics exploration in bulk semiconductors [1], quantum wells [2] and quantum dot (QD) systems [3]. Despite the tremendous success of the pump-probe Faraday and Kerr rotation measurement techniques, their microscopic theoretical description for QD structures is absent to the best of our knowlegment.

Qualitatively, the pump-probe spectroscopy of electron spins is based on the following principles. The sample is subject to a strong circularly polarized pump pulse which, according to the optical selection rules, creates spin polarization of charge carriers in the system. The time dependence of this polarization is probed later by a weak linearly polarized pulse. For the probe pulse, the sample acts as an optically active medium and the polarization plane of the reflected (Kerr effect) or transmitted (Faraday effect) probe experiences rotation, see Fig. 1(a). In addition, both reflected and transmitted signals acquire a certain degree of ellipticity.

Here we present a theory of spin Kerr, Faraday and ellipticity signals for single and multiple layers of n-type QDs containing single resident electrons.

1. Spin coherence generation

In what follows we consider a planar array of QDs where the lowest in energy hole states are those with the momentum projection $\pm 3/2$ on the growth axis z. The QD state is conveniently described by a four component wavefunction $\Psi = [\psi_{1/2}, \psi_{-1/2}, \psi_{3/2}, \psi_{-3/2}]^{\mathrm{T}}$, where $\psi_{\pm 1/2}$ determine the spin states of resident electron while $\psi_{\pm 3/2}$ determine the spin states of the singlet trion which are labelled in accordance with the hole spin projection.

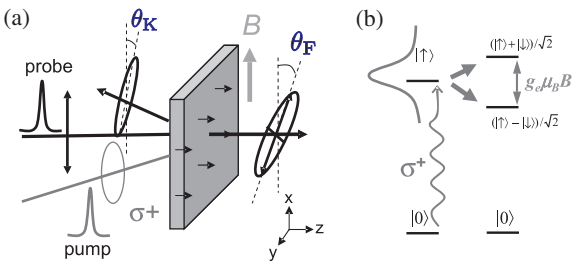

Fig. 1. Schematic illustration of (a) the pump-probe Faraday and Kerr rotation measurement technique and (b) a coherent superposition created by a short pulse of σ^+ polarized light from the two spin states split in a transverse magnetic field.

Let $\mathbf{S}^- = [S_x^-, S_y^-, S_z^-]$ and $\mathbf{S}^+ = [S_x^+, S_y^+, S_z^+]$ be the electron spin components before pump pulse arrival and just after the pulse end, respectively. One can show that after the pulse of the σ^+-polarized light with the carrier frequency ω_{P} tuned close to the trion resonance frequency ω_0 they are related by

$$S_z^+ = \frac{Q^2-1}{4} + \frac{Q^2+1}{2} S_z^-, \tag{1a}$$

$$S_x^+ = Q\cos\Phi S_x^- + Q\sin\Phi S_y^-, \tag{1b}$$

$$S_y^+ = Q\cos\Phi S_y^- - Q\sin\Phi S_x^-, \tag{1c}$$

where the values of Q and Φ lie in the intervals $0 \le Q \le 1$, $0 \le \Phi < 2\pi$ and are determined by the pump pulse shape, power and detuning between the trion resonant frequency and the carrier frequency of the pump pulse, $\omega_{\mathrm{P}} - \omega_0$. Here we assumed that the repetition period of pump pulses exceeds by far the trion radiative lifetime in a QD τ_{QD}. For the σ^- circular polarization pump pulses, one should invert signs of the first term in Eq. (1a) and of Φ in Eqs. (1b) and (1c).

It is seen from Eqs. (1) that the circularly polarized pump pulse leads to (i) generation of z-spin component of the resident electron (see Fig. 1b) and (ii) the rotation of in-plane components of electron spin.

2. Formation of spin Kerr, Faraday and ellipticity signals

In order to calculate the polarization plane rotation and ellipticity of the weak linearly-polarized probe pulse with the carrier frequency ω_{pr} which arrives on the sample with a certan delay Δt after the pump pulse we use the non-local dielectric-response theory [4]. Calculation for the case of a sample containing a planar array of QDs shows that the Faraday rotation $\mathcal{F}$ and ellipticity $\mathcal{E}$ signals are given by

$$\mathcal{F} = \frac{3\pi}{q^2\tau_{\mathrm{QD}}} N_{\mathrm{QD}}^{2d}(S_z - J_z) I_{\mathrm{pr}} \,\mathrm{Im}\,\{G(\Omega)\}, \tag{2}$$

$$\mathcal{E} = \frac{3\pi}{q^2\tau_{\mathrm{QD}}} N_{\mathrm{QD}}^{2d}(S_z - J_z) I_{\mathrm{pr}} \,\mathrm{Re}\,\{G(\Omega)\}. \tag{3}$$

Here q is the light wavevector inside the sample, N_{QD}^{2d} is the two-dimensional density of the QDs, $I_{\mathrm{pr}} = |E_{\mathrm{pr}}|^2$ is the probe

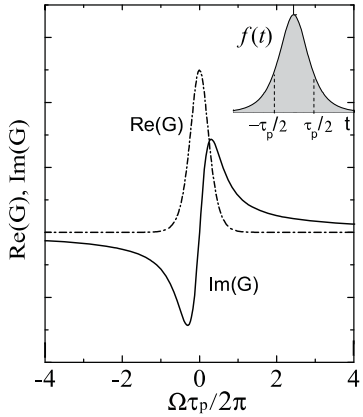

Fig. 2. The real and imaginary parts of $G(\Omega)$ (dash-dot and solid curves, correspondingly), $f(t) = \cosh(\pi t/\tau_p)$ [Eq. (4)].

intensity. The z-components of the electron, S_z, and trion, J_z, spins are functions of the pump-probe delay. Function $G(\Omega)$ where $\Omega = \omega_{\rm pr} - \omega_0$ is the detuning between the probe frequency and QD resonance frequency can be expressed via the envelope function of the probe field $f(t)$ as

$$G(\Omega) = \int_{-\infty}^{\infty} {\rm d}t \int_{-\infty}^{t} {\rm d}t' f(t) f(t') {\rm e}^{i\Omega(t-t')}. \qquad (4)$$

It is worth noting, that the Kerr rotation signal $\mathcal{K}$ is a linear superposition of Faraday and ellipticity signals, in general, because it is determined by the phase acquired by the probe pulse in the cap layer of the sample.

The real and imaginary parts of the function G are shown in Fig 2. One can see, that the Faraday signal is odd function while ellipticity signal is even function of the detuning, Ω. Therefore, the sensitivity of ellipticity has a maximum at $\Omega = 0$ while the Faraday signal is most sensitive for $|\Omega|\tau_p \sim 1$. Moreover, QDs on higher and lower energies sides on probe energy contribute to the Faraday signal with the opposite signs.

3. Manifestations of spin dynamics

In order to calculate the polarization plane rotation or ellipticity of the probe pulse as a function of time delay between pump and probe pulses, we assume that the QD array is subject to a periodic sequence of the pump pulses following with the repitition period $T_{\rm rep}$. The number of pump pulses is assumed to be infinite, so that the steady-state distribution of electron spins is reached. The spin dynamics of electrons is determined from the self-consistent solution of the spin-dependent kinetic equation allowing for the spin precession in the external magnetic field **B** (applied in the QD plane) and Eqs. (1) which describe pump effects. Such an approach takes into account resonant spin amplification and mode-locking effects [1,3,5].

In the numerical calculation we assumed that, in the QD ensemble, the inhomogeneous broadening of the trion resonance frequency ω_0 is much wider than τ_p^{-1} so only a narrow subsystem of QDs with the resonance frequencies around $\omega_{\rm P}$ is excited by the pump pulse. The distribution of electron g-factors over QDs was related to the corresponding resonance frequency by $g(\omega_0) = g(\omega_{\rm P}) + g'(\omega_0 - \omega_{\rm P})$ [3].

The results of calculation are shown in Fig. 3. Each panel presents the ellipticity and Faraday rotation signals as functions

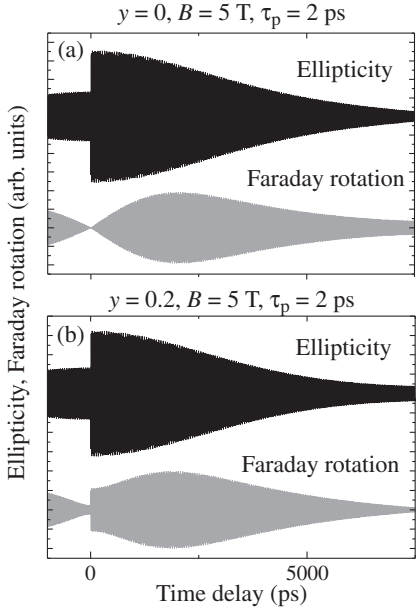

Fig. 3. Faraday and ellipticity signals as functions of pump-probe delay. Top: degenerate pump and probe, bottom: detuning, $y = \Delta\omega\tau_p/2\pi = 0.2$. Repitition period $T_{\rm rep} = 13.2$ ns, electron spin relaxation time $\tau_{\rm s,e} = 3 \times 10^3$ ns, $\bar{g} = 0.556$. Shaded areas are oscillations smoothed due to their small period ∼10 ps.

of the pump-probe delay shifted vertically relative to each other. Top panel corresponds to degenerate pump and probe, bottom panel corresponds to a nonzero detuning $\Delta\omega$ between pump and probe carrier frequencies.

The spin Faraday and ellipticity signals as functions of pump-probe delay are qualitatively different: the envelope of ellipticity is monotonous function while that of Faraday rotation is not. This is a result of different spectral sensitivity of the Faraday and ellipticity effects, see Fig. 2. The ellipticity is determined by the total spin of the QD ensemble while Faraday rotation is proportional to the imbalance of electron spins at energies higher and lower than probe resonant energy. Such an imbalance of electron spins results from the correlation between resonance frequency of a QD and resident electron g-factor.

To conclude, a quantitative theory of pump-probe spectroscopy of electron spins in QDs is developed. It describes (i) spin orientation by short pump pulse, (ii) spin precession in the external magnetic field, and (iii) polarization plane rotation of the probe pulse and rise of its ellipticity.

Acknowledgements

This work was financially supported by the RFBR, "Dynasty" Foundation — ICFPM (MMG), the Office of Naval Research and Alexander-von-Humboldt Foundation (ALE).

References

[1] J. Kikkawa, D. Awschalom, *Phys. Rev. Lett.* **80**, 4313 (1998).
[2] E. A. Zhukov *et al*, *Phys. Rev. B* **76**, 205310 (2007).
[3] A. Greilich *et al*, *Science* **313**, 341 (2006).
[4] E. L. Ivchenko, *Optical Spectroscopy of Semiconductor Nanostructures*, (Alpha Science, Harrow UK, 2005).
[5] M. M. Glazov, E. L. Ivchenko, *Semiconductors* **42**, 951 (2008).

17th Int. Symp. "Nanostructures: Physics and Technology"
Minsk, Belarus, June 22–26, 2009
© 2009 Ioffe Institute

Spin-dependent phenomena in CdMnSe/ZnSe nanostructures as studied by optically detected magnetic resonance

N. G. Romanov[1], *D. O. Tolmachev*[1], P. G. Baranov[1], R. A. Babunts[1], B. R. Namozov[1], Yu. G. Kusrayev[1], S. Lee[2], M. Dobrowolska[3] and J. K. Furdyna[3]

[1] Ioffe Physical-Technical Institute, St Petersburg, Russia
[2] Department of Physics, Korea University, Seoul, Korea
[3] Department of Physics, University of Notre Dame, Notre Dame, Indiana 46556, USA

Abstract. Fine structure of isolated Mn^{2+} ions in CdMnSe/ZnSe sub-monolayer quantum wells is revealed by optically detected magnetic resonance recorded by monitoring both exciton emission and intra-Mn luminescence. A large decrease of exciton photoluminescence intensity and an increase of the Mn^{2+} photoluminescence intensity under EPR conditions for Mn^{2+} ions was observed. Based on these results, a spin-dependent energy transfer from excitons to the intra-Mn excitation is suggested to occur.

Introduction

The most extensively studied semimagnetic semiconductors are II–VI compounds in which a fraction of the group-II sublattice is replaced at random by Mn [1]. The band structure of these semiconductors is modified by an *sp-d* exchange interaction of the localized Mn^{2+} magnetic moments with band electrons. This exchange interaction influences physical phenomena which involve electrons in the conduction and valence bands, leading, e.g., to a giant Zeeman splitting of electronic states in both conduction and valence bands [2,3]. Even a small content of Mn introduced in II–VI semiconductors can strongly suppress excitonic photoluminescence (PL) if the semiconductor energy gap exceeds the energy of the internal Mn transitions. Photoexcitation of carriers in II-Mn-VI materials results in the luminescence of excitons, as well as in intra-Mn luminescence due to internal transitions of the $3d^5$ electrons of Mn^{2+} ions. The intensity of the emission of excitons localized in CdMnSe/ZnSe nanostructures strongly depends on magnetic field and temperature. At liquid He temperatures a large increase of the integrated PL intensity with magnetic field was observed, along with a shift of the PL maximum [4,5]. The energy of exciton emission in QD's depends on both the *sp-d* interaction and on the thermal average of the Mn^{2+} spin $\langle S_z \rangle$ in the magnetic field direction z, i.e., on the Mn spin temperature. The PL is extremely sensitive to the polarization of the Mn^{2+} ions. The increase of PL intensity with magnetic field was explained to be evoked by the suppression of the spin-dependent Auger process in individual Mn^{2+} ions [4,5].

Electron paramagnetic resonance (EPR) is a method of choice for the study of transition metal ions [6]. However, direct measurements of EPR in nanostructures are difficult because of the small total number of spins; and therefore optically detected magnetic resonance (ODMR) is much better suited for the magnetic resonance measurements in such systems [7]. ODMR was applied to several Mn doped II–VI compounds [8]. However, no anisotropy of Mn ODMR was reported until our recent publication [9], in which the axial fine structure with a strong positive zero-field splitting for Mn^{2+} ions in CdMnSe/ZnSe quantum dots (QDs) was revealed due to their low dimensionality. In spite of the isotropic g-factor of the Mn^{2+} ions, anisotropic behavior of the center of gravity of the resonance has been observed because of the high Boltzmann factor at 35 GHz and 2 K.

In this paper, the EPR spectra of the individual Mn^{2+} ions in CdMnSe/ZnSe sub-monolayer QW's are investigated by the ODMR method.

1. Experimental

CdMnSe/ZnSe sub-monolayer quantum well structures were grown by MBE on GaAs(100) substrates, consisting of a ZnSe buffer layer and 7 periods of 0.3 monolayers (ML) of CdMnSe (20% of Mn) and 10 ML of ZnSe. Photoluminescence was excited far above the band gap of ZnSe using a 405 nm semiconductor laser, and detected with a grating monochromator and a photomultiplier (PM) tube at a temperature of $T = 2$ K. ODMR was studied using a 35 GHz ODMR spectrometer supplying microwave power up to 1W and magnetic field up to 4.5 T. The sample was mounted on a rotating sample holder, which enables ODMR measurements at different orientations of the magnetic field. ODMR was detected as microwave-induced variations of the PL emission intensity using on-off modulation of microwaves and lock-in amplification.

2. Results and discussion

Fig. 1 shows the PL spectra in zero magnetic field and in magnetic field of 2 T recorded at 2 K in the Faraday geometry ($\theta = 0°$). The spectra consist of the ZnSe band edge emission at 443 nm and of exciton emission in CdMnSe quantum wells, which shifts towards lower energies and strongly increases in intensity when magnetic field is applied. ODMR signals recorded on this emission correspond to a decrease in emission intensity with increasing field. The observed broad ODMR line shifts to lower fields as the sample is rotated in the (110) plane away from [001] ($\theta = 0°$), as shown in Fig. 2(a).

In addition, a weak luminescence in the red spectral range was observed, exhibiting ODMR as an increase of its intensity (see Fig. 2(b)). The spectral dependence of ODMR shown in the insert in Fig. 2(b) coincides with the Mn^{2+} emission corresponding to the ${}^4T_1 \leftrightarrow {}^6A$ transition. The positions and the line widths of the ODMR signals recorded at different orientations coincide within experimental error with ODMR detected in exciton and in Mn emissions. The angular dependences of ODMR for these two cases are plotted in Fig. 2(c). ODMR

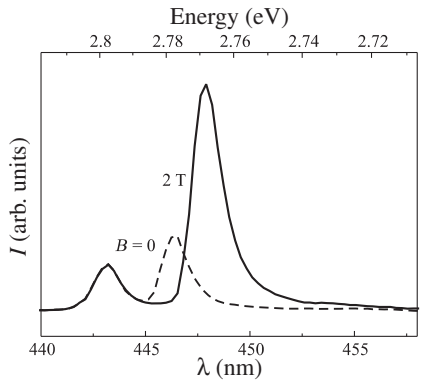

Fig. 1. Photoluminescence spectra recorded at $T = 2$ K in zero magnetic field (dashed curve) and $B = 2$ T (solid curve) in CdMnSe/ZnSe sub-monolayer quantum wells.

signals are definitely connected with Mn^{2+} ions. The g-factor of individual Mn^{2+} ions is known to be isotropic and close to $g = 2$, and therefore cannot give rise to an anisotropy of the ODMR signal. For $\theta = 0°$ the effective g-factor of the observed ODMR is much smaller (1.98). It should be pointed out that the observed anisotropy of optically detected EPR spectra exclude any possible effects of exchange interaction with band electrons, which could lead to a line shift of the EPR spectra of Mn^{2+} as suggested in Ref. [10].

Recently we have found an anisotropy of Mn ODMR in CdMnSe QDs [9]. The axial fine structure with a strong positive zero-field splitting $D = 200 \times 10^{-4}$ cm^{-1} led to the conclusion that it is caused by the low dimensionality of the structure. We believe that the fine structure splitting of Mn is the reason for the observed behavior of ODMR. The anisotropy of the center of gravity of the ODMR spectra appears because of the large Boltzman factor characteristic of high magnetic fields at low temperatures. At thermal equilibrium the lowest fine-structure levels of Mn^{2+} are more populated and this results in an angular variation of the $M_S = -5/2 \leftrightarrow M_S = -3/2$ EPR transition that dominates the spectrum. The symmetry of the fine-structure splitting, which is due to the crystal field is consistent with the [001] growth direction. The estimated value of the zero-field splitting for the structures under study ($D = 50 \times 10^{-4}$ cm^{-1}) is much smaller than that obtained for CdMnSe QDs investigated in [9]. The spin-lattice relaxation time T_1 of Mn^{2+} was found to be about 40 μs from the modulation frequency dependence of ODMR.

In conclusion, under EPR conditions for Mn^{2+} we have observed a large decrease of the intensity, and a simultaneous increase of the PL intensity associated with internal Mn^{2+} transitions. Based on this, a spin-dependent energy transfer from excitons to an intra-Mn excitation was suggested to occur.

Acknowledgements

This work was supported by the Programs of RAS "Spin-Dependent Effects in Solids and Spintronics", "Support of Innovations and Elaborations", and "Basic Researches of Nanotechnologies and Nanomaterials"; by the RFBR projects 09-02-00730-a and 09-02-01409-a; by the U.S. Civilian Research & Development Foundation Cooperative Grants Program; and by Russian Federal Agency for Science and Innovations under Contract No. 02.513.12.3031.

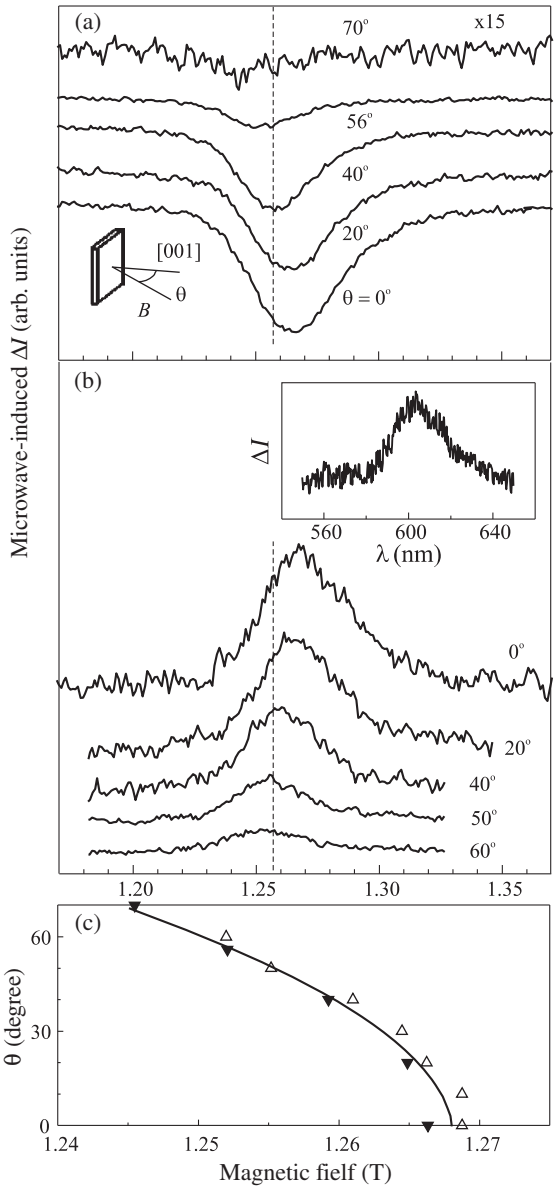

Fig. 2. 35 GHz ODMR in CdMnSe/ZnSe sub-monolayer quantum wells recorded at $T = 2$ K via the PL intensity of excitons (a) and Mn^{2+} (b) for different orientations of magnetic field. Dashed lines mark magnetic field corresponding to $g = 2$. Inset in (b) shows the spectral dependence of ODMR amplitude in the Mn emission region. (c) — angular dependences of ODMR detected via the PL intensity of excitons (black triangles) and Mn^{2+} (open triangles).

References

[1] J. K. Furdyna, *J. Appl. Phys.* **64**, R29 (1988).
[2] A. V. Komarov *et al*, *Sov. Phys. JETP* **46**, 318 (1977).
[3] T. Wojtowicz *et al*, *Phys. Rev. B* **59**, R10437 (1999).
[4] A. V. Chernenko *et al*, *Phys. Rev. B* **72**, 045302 (2005).
[5] P. R. Kratzert *et al*, *Appl. Phys. Lett.* **79**, 2814 (2001).
[6] A. Abragam and B. Bleaney, *Electron Paramagnetic Resonance of Transition Ions*, Oxford University Press, Oxford, 1970.
[7] P. G. Baranov, N. G. Romanov, *Appl. Magn. Reson.* **21**, 165 (2001).
[8] M. Godlewski, *Opt. Applicata* XXXVI, 271 (2006).
[9] P. G. Baranov *et al*, *JETP Lett.* **88**, 631 (2008).
[10] G. Yang *et al*, *Phys. Rev.* **59**, 2768 (1999).

17th Int. Symp. "Nanostructures: Physics and Technology"
Minsk, Belarus, June 22–26, 2009
© 2009 Ioffe Institute

Dynamics of nuclear spin polarization in InGaAs/GaAs quantum dots studied by time-resolved Hanle effect

S. Yu. Verbin[1,2], R. V. Cherbunin[1,2], I. Ya. Gerlovin[1], I. V. Ignatiev[1,2], D. V. Vishnevsky[1], D. Reuter[3], A. D. Wieck[3], D. R. Yakovlev[2] and M. Bayer[2]

[1] Physics Department, St Petersburg State University, 198504 St Petersburg, Russia
[2] Experimentelle Physik II, Technische Universität Dortmund, 44221 Dortmund, Germany
[3] Angewandte Festkörperphysik, Ruhr-Universität Bochum, 44780 Bochum, Germany

Abstract. Degree of circular polarization of InGaAs/GaAs quantum dot photoluminescence is experimentally studied as a function of magnetic field applied perpendicular to the optical excitation direction (Voigt geometry). The measurements are performed using various protocols of modulation of polarization and intensity of the excitation. The experimental data obtained allow us to estimate the characteristic times of polarization and relaxation processes for nuclear spin system in the heterostructure studied.

Introduction

The hyperfine interaction of electron and nuclear spins in semiconductor quantum dots has become recently a matter of extensive theoretical and experimental research. The electron spin dynamics is found to depend sensitively on the state of the nuclear system. On the other hand, oriented electron spin can generate a dynamical nuclear polarization (DNP) through hyperfine interaction. Steady-state properties of DNP are studied at least three decades, however experimental and theoretical studies of the dynamics of DNP are developed only the last several years. It is found that the dynamics in quantum dots (QDs) is substantially complicated [1] and the nuclear spin relaxation time appears to be considerably shorter in some particular cases [2] than it was assumed earlier.

Most experimental data about the DNP in QDs are obtained in magnetic field applied along the optical axis of excitation and of signal detection (Faraday geometry) [2]. The presence of magnetic field prevents the nuclear spin system from the angular momentum leakage due to the dipole-dipole interaction of nuclear spins. Such experiments provide with the results which allow straightforward analysis of the processes studied.

In the magnetic field perpendicular to the optical axis (Voigt geometry), polarization of the electron spin decreases due to its precession about the field (Hanle effect). Strong optical pumping accompanied by relaxation processes in nuclear spin system gives rise to effective DNP field aligned along the external magnetic field and, correspondingly, across to the direction of optical orientation. The presence of DNP field may considerably modify the Hanle curve [3].

In present work, we report on results of first experimental observations of the time-resolved Hanle effect for InGaAs/GaAs quantum dot ensemble. These results allow us to estimate the characteristic times of processes occurring in the nuclear spin system.

1. Experimental details

A heterostructure containing 20 layers of self-assembled (In,Ga)As QDs sandwiched between n-delta modulation doped GaAs barriers is studied. Donor ionization supplies every dot with on average a single resident electron.

Photoluminescence (PL) was excited by a continuous-wave Ti:Sapphire laser. Special timing protocols for the optical excitation were developed to study the dynamics of nuclear polarization, as described in more detail in the next section and shown in Figs. 1–2. The PL polarization was measured using a photoelastic modulator operated at a frequency of about 50 kHz and a multi-channel photon counting system.

The electron spin polarization was determined from the degree of circular polarization of the QD PL excited at the wetting layer optical transition.

2. Experimental results

To study the dynamics of nuclear polarization rise we have measured a set of Hanle curves at modulated polarization of the ex-

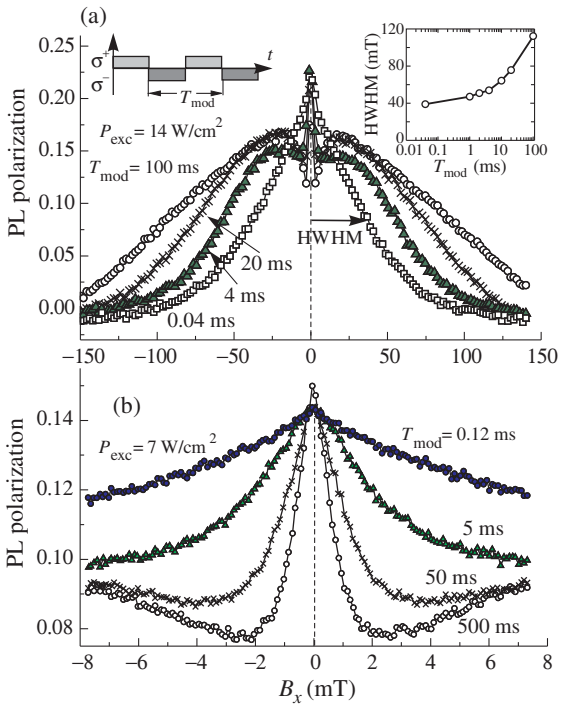

Fig. 1. Transformation of Hanle curves at the change of polarization modulation period in the large (a) and small (b) magnetic fields. Left inset shows modulation protocol; right inset shows the change of HWHM of the Hanle curves with T_{mod}.

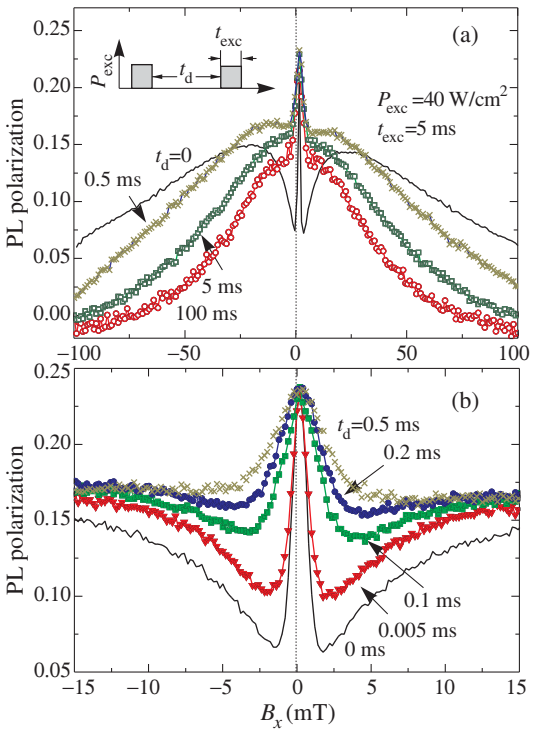

Fig. 2. Hanle curves measured at modulated intensity of excitation: (a) overview, (b) details in small magnetic field. Inset shows the excitation protocol.

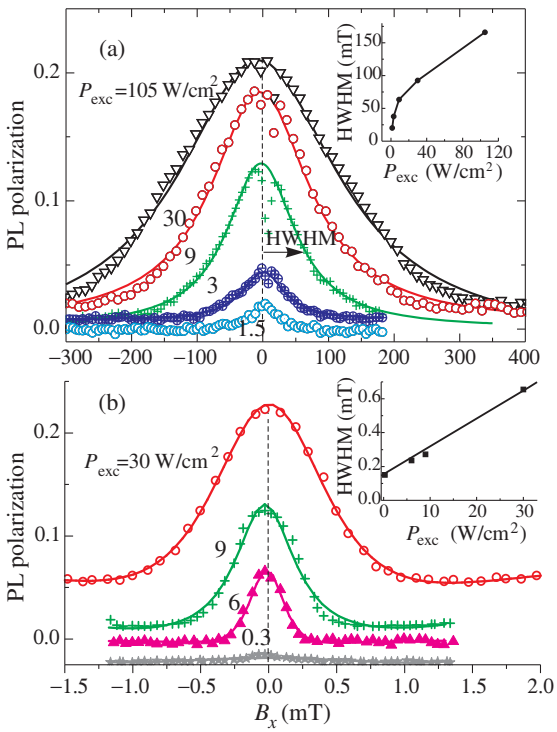

Fig. 3. Hanle curves measured in CW regime at different excitation densities (a) overwiev, (b) details in small magnetic field. Insets show the dependence of HWHM of the Hanle curve (a) and of the central peak (b) on excitation density.

citation. The modulation period was varied in the large range. In the limit of continuous-wave (CW) measurements, the Hanle curve has a w-shape with narrow central peak [see Fig. 1(a)]. At large modulation period ($T_{mod} > 100$ ms), the Hanle curve is found to almost coincide with that for continuous-wave (CW) measurements. Decrease of the period is accompanied by remarkable modification of the curves in the range of small fields. As seen on Fig. 1(b), the width of the central peak increases, the symmetrical dips around the peak are smoothed, and the curve approaches to the standard form for Hanle curve. According to Ref. [3], the w-shape of Hanle curve with narrow central peak is caused by DNP whose effective magnetic field is directed along the external magnetic field. Our results show that, at the excitation conditions used, the DNP is developed in the time range of about 100 ms.

To study the relaxation of DNP, we used the amplitude modulation of optical excitation keeping the helicity of polarization as it is shown in the inset of Fig. 2(a). The duration of light pulse was kept fixed ($t_{exc} = 5$ ms) while the dark interval, t_d, is varied from microseconds to fractions of second. As seen, the Hanle curve measured at the modulated excitation becomes similar to that measured in CW regime only at very small dark interval. With increase of the dark interval, the Hanle curves become narrower and the dips near the central peak disappear. These transformations of the Hanle curves indicate the noticeable relaxation of DNP at the time intervals about of units of microseconds. We would like to note that so fast decay of the nuclear field did not observed so far.

In Fig. 3, the Hanle curves measured in CW regime at different pump powers are shown. As seen, the pump power increase is accompanied by the increase of both the amplitude and the HWHM of the curves. At the maximal excitation power $P_{exc} = 100$ W/cm^2 used in the experiment, HWHM exceeds 150 mT [see inset in Fig. 3(a)] and almost four times larger than that obtained in the absence of DNP [compare with Fig. 1(a), $T_{mod} = 0.04$ ms]. We believe that the HWHM increase is related to the DNP field rise and its value exceeds 100 mT at the largest power density used.

3. Conclusion

The experimental data obtained clearly demonstrate the dynamics of the nuclear spin polarization and relaxation in the conditions when the axis of optical pumping is perpendicular to that of external magnetic field.

Acknowledgements

This work has been supported by the Russian Foundation for Basic Research and the Ministry of Education and Science of the Russian Federation.

References

[1] H. Christ, J. I. Cirac, and G. Giedke, *Phys. Rev. B* **75**, 155324 (2007).

[2] P. Maletinsky, A. Badolato, and A. Imamoglu, *Phys. Rev. Lett.* **99**, 056804 (2007).

[3] D. Paget, G. Lampel, B. Sapoval, V. I. Safarov, *Phys. Rev. B* **15**, 5780 (1977).

17th Int. Symp. "Nanostructures: Physics and Technology"
Minsk, Belarus, June 22–26, 2009
© 2009 Ioffe Institute

Spin relaxation of electrons in two-dimensional quantum dot arrays with different shape of nanoclusters

A. F. Zinovieva[1], A. V. Dvurechenskii[1], N. P. Stepina[1], A. I. Nikiforov[1], L. V.Kulik[2] and A. S. Lyubin[3]

[1] Institute of Semiconductor Physics, 630090 Novosibirsk, Russia
[2] Institute of Chemical Kinetics and Combustion, 630090 Novosibirsk, Russia
[3] Novosibirsk State University, 630090 Novosibirsk, Russia

Abstract. Two-dimensional heterostructures with Ge/Si quantum dots (QDs) of different shape (hut- and dome-clusters) were studied by conventional continuous wave (*cw*) EPR and spin-echo methods. We obtain the different orientation dependence of EPR line width for heterostructures with single shaped QDs (hut-clusters) and heterostructures with two groups of QDs, namely hut- and dome-clusters. The observed effect can be explained by different localization degree of electrons in investigated structures. The spin echo measurements confirm the model of spin relaxation through the precession in the effective magnetic field during tunneling between QDs.

Introduction

A dimensionality reduction leads to the appearance of new effects, many of them are governed by symmetry of nanostructures. In particular, the symmetry of nanostructure has a crucial impact on the spin dynamics. The spin-orbit (SO) coupling in asymmetrical quantum well structures gives the possibility to manipulate with spins of carriers [1,2], but it serves as main source of spin relaxation [3,4]. The longitudinal spin relaxation time and coherence time of two-dimensional electrons are controlled by effective in-plane fluctuating magnetic fields, arising from the SO interaction and the broken inversion symmetry at the heterostructure interface [5]. The confinement of electrons in all three dimensions switch off the efficient mechanism of the spin relaxation and the spin coherence time has to increase. Then the electron localization in QD is one of promising way to preserve the spin orientation. However in high density two-dimensional QD array, where the electron transitions between QDs are possible, the spin relaxation can be very intensive due to SO interaction and broken inversion symmetry at the QD array plane. During tunneling between quantum dots the spin rotates around effective magnetic field, whose direction is assigned by tunneling direction $\mathbf{n}$, $H_{\mathrm{QD}} = \alpha_{\mathrm{QD}} \Delta k_{\mathbf{n}} (\mathbf{n} \times \mathbf{e}_z)/g\mu_{\mathrm{B}}$, here $\Delta k_{\mathbf{n}}$ is the uncertainty of electron momentum, $\Delta k_{\mathbf{n}} \sim 1/l$, l is the lateral size of QD, g is the electron g-factor, μ_{B} is the Bohr magneton and e_z is the unit vector in the growth direction. According to results of tight-binding calculations [6] the magnitude of effective magnetic field depends on the aspect ratio of QDs (h/l, where h is the QD height). Then one can suppose that in heterostructures, containing QDs with higher aspect ratio the spin relaxation goes more intensive. Here we report the results of experimental check of this hypothesis. We study by conventional continuous wave (*cw*) EPR and spin-echo methods the QD heterostructures with different shape of nanocusters. The *cw* EPR experiments and spin-echo measurements can provide a full information about spin relaxation in the QD system and can be helpful for understanding of main mechanisms of spin relaxation.

1. Samples and experiment

Samples were grown by molecular-beam epitaxy on n-Si(001) substrates with a resistivity of 1000 Ω cm. The QD structure with single shaped QDs (hut-clusters) was optimized with the aim to enlarge the electron binding energy E_{b} in the Si potential well near a QD. The vertical stack of four Ge QDs layers has been grown. The accumulation of the strain from different QD layers in the stack leads to an increase of the potential well depth. The stack of Ge QDs layers was inserted into the 0.6 μm epitaxial n-Si layer (Sb concentration 4×10^{16} cm^{-3}) at a distance of 0.3 μm from the substrate. The density of QDs is $\sim 10^{11}$ cm^{-2}. According to the numerical calculations using the effective-mass approximation [7] the electron localization occurs between the second and the third QD layers at the apices of the Ge dots, and the electron binding energy amounts to 60 meV.

The QD structure with different shape of nanoclusters (huts and domes) contains 6 layers of QDs separated by 30 nm Si spacer layers. Each QD layer are formed by deposition of 7 ML Ge at the temperature $T = 550$°C. On top of the structure a 0.3 μm epitaxial n-Si layer (Sb concentration 4×10^{16} cm^{-3}) is grown, the same layer is grown under QDs layers. The scanning tunneling microscopy of structure with single QD layer uncovered by Si shows the bimodal distribution of QDs (huts and domes). The average size of dome-cluster is 50 nm, the average size of hut-clusters is 15 nm. Aspect ratio for domes is 0.2, for huts it is 0.1. The calculations in the effective mass approximation show that the electron localization near the apex of dome-cluster is more effective than the localization near the hut-clusters. The electron binding energy can reach 80 meV (the calculations are performed for $Si_{1-x}Ge_x$ dome-cluster with $x = 0.6$, the height of domes $h = 10$ nm, lateral size $l = 50$ nm).

Measurements were performed with a Bruker Elexsys580 X-band EPR spectrometer using a dielectric cavity Bruker ER-4118 X-MD-5 and a helium flow cryostat (Oxford CF935). The spin echo measurements carried out for the magnetic field $\mathbf{H} \parallel Z$, where Z is the [001] growth direction of the structure.

2. Results and discussion

In the *cw* EPR experiments on the single-shaped QD structures, a EPR-line with the principal values $g_{zz} = 1.9995$ and $g_{xx} = g_{yy} = 1.9984$ is observed. An analysis of the obtained g-tensor values confirms an electron localization in the strain-

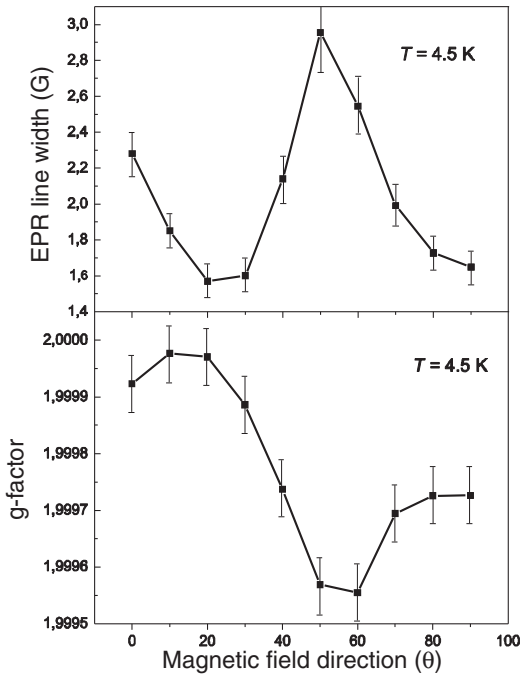

Fig. 1. The angular dependence of EPR-line width and electron g-factor for heterostructure with dome-clusters. For $\Theta = 0$ the magnetic field is parallel to the growth direction of the structure.

induced potential wells in Si in the vicinity of the Ge dots. The observed EPR-line has the minimal width $\Delta H_{pp} \approx 0.8$ G at the magnetic field $\mathbf{H} \parallel Z$, where Z is the [001] growth direction of the structure. On the deviation of the magnetic field from the Z-axis the EPR-line becomes broader and weaker, and the maximal line width $\Delta H_{pp} \approx 3$ G is observed at $\mathbf{H} \perp Z$.

The EPR signal of QD structure with dome-clusters has more complicated angular dependence. The EPR-line width has minimum at $\Theta = 30°$ and maximum at $\Theta = 60°$, Θ is the angle between direction of magnetic field and Z-axis (see Fig. 1). The g-factor behavior completely correlates with EPR line width change. In the magnetic field perpendicular to the plane of QD array the g-factor value is $g = 1.9999 \pm 0.0001$. At the deviation of magnetic field from Z-axis the g-factor value slightly grows up to $g = 2.0000 \pm 0.0001$, then at $\Theta = 60°$ the minimal g-factor value is observed, and in the end the g-factor value increases and practically returns to its initial value $g = 1.9999 \pm 0.0001$.

The angular dependence of the EPR-line width can be explained in terms of an effective magnetic field lying in the plane of the QD array. Spin relaxation comes from the precession of the electron spin in the effective magnetic field during certain tunneling events. Such a mechanism of spin relaxation has been discussed in detail in the Ref. [6,8].

Let us discuss the reason of the observed difference between two types of structure. In the first case of stacked structure with hut-clusters the localization of electron is more effective than in the second case of structure with dome-clusters (this is confirmed by g-factor values). During growth of Si cover layer the dome-clusters lose their height due to Si and Ge interdiffusion. Then the strain near the apex of dome-clusters is reduced, and the depth of potential well for electron decreases. As result the localization of electrons in the second type structure is

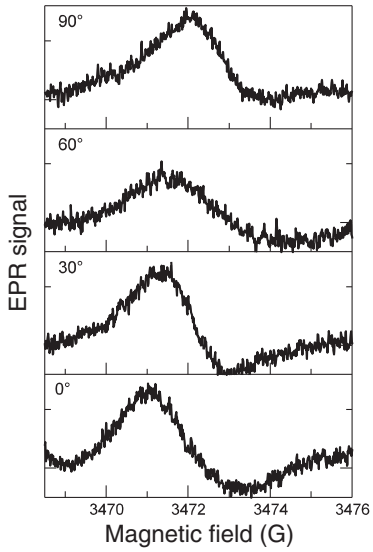

Fig. 2. EPR signal from heterostuctures with dome-clusters at the different magnetic field orientation.

weaker. The external magnetic field can affect the localization of electrons through the effect of the in-plane wave function compression. In the second type structure this effect is more pronounced, while in the first type structure the effect of wave function compression is negligible. In the second type structure at the deviation of magnetic field from growth direction the compression is reduced and the electron localization becomes weaker. The electron transitions between quantum dots can occur easier and this leads to line narrowing, providing the minimum at $\Theta = 30°$. The maximum at $\Theta = 60°$ can be explain by exponential dependence of the transition probability P between QDs on the external magnetic field, $P \sim \exp(-\text{const} \times H)$.

The measurements of spin echoes confirm the model of spin relaxation through the precession in effective magnetic field during tunneling between QDs. According to this model the spin relaxation is anisotropic [8] and the transverse spin relaxation time has to be two times larger than longitudinal time ($T_2 = 2T_1$) for the magnetic field $\mathbf{H} \parallel Z$. From results of spin echo measurements we can conclude that in studied structures there are a few groups of carriers with different spin relaxation times. However in all groups, except one, the unusual relation $T_2 > T_1$ is observed. The difference in the spin relaxation time we explain be difference of tunneling rates between QDs. The electron group with higher transition rate between QDs has the shorter spin relaxation time. The exceptional group has $T_2 \approx T_1 \approx 2\ \mu$s and can be attributed to the non-tunneling electrons, whose spin relaxation is governed by another mechanism.

Acknowledgement

This work was supported by RFBR (Grant 08-02-00121).

References

[1] S. Datta and B. Das, *Appl. Phys. Lett.* **56**, 665 (1990).
[2] J. Schliemann, J. C. Egues, and D. Loss, *Phys. Rev. Lett.* **90**, 146801 (2003).
[3] A. M. Tyryshkin *et al*, *Phys. Rev. Lett.* **94**, 126802 (2005).
[4] Z. Wilamowski *et al*, *Phys. Rev. B* **66**, 195315 (2002).
[5] A. Bychkov and E. I. Rashba, *J. Phys. C* **17**, 6039 (1984).
[6] A. F. Zinovieva *et al*, *Phys. Rev. B* **71**, 033310 (2005).
[7] A. I. Yakimov *et al*, *Phys. Rev. B* **73**, 115333 (2006).
[8] A. F. Zinovieva *et al*, *Phys. Rev. B* **77** (2008).

17th Int. Symp. "Nanostructures: Physics and Technology"
Minsk, Belarus, June 22–26, 2009
© 2009 Ioffe Institute

Magnetoresistance and transport properties of manganite-based magnetic junctions on grain boundary of [100]-tilt type

I. V. Borisenko[1], G. A. Ovsyannikov[1,2], A. M. Peterzhik[1] and V. A. Shakhunov[1]
[1] Kotel'nikov Institute of Radio Engineering and Electronics, RAS, Moscow, Russia
[2] Chalmers University of Technology, SE-412-96, Göteborg, Sweden

Abstract. Magnetic bicrystal contacts were made of manganite $La_{0.67}Ca_{0.33}MnO_3$ films on bicrystal substrates with a misorientation of the $NdGaO_3(110)$ basal planes on an angle of $\pm 14°$ around the bicrystal boundary line. The temperature dependence of the contact electrical resistance was studied, and the magnetoresistance was measured in fields of up to 200 mT. It is shown that the suppression of ferromagnetic correlations near the bicrystal boundary leads to the formation of a layer having a substantially lower Curie temperature. Magnetoresistance of 150% was measured at T=4.2 K in a magnetic field of about 50 mT and at a characteristic electrical resistance of the boundary of 3×10^{-6} $Omega$cm^2. It is found that slight orthorhombic distortions of a $La_{0.67}Ca_{0.33}MnO_3$ film due to a lattice mismatch with the $NdGaO_3(110)$ substrate crystal structure lead to the formation of biaxial magnetic anisotropy in the $La_{0.67}Ca_{0.33}MnO_3$ film.

Introduction

Magnetic tunnel junction (MTJ) as basic device in the field of spintronics have attracted many interest both as physical phenomenon and due to their potential application in electronics. As was recently proved in experiments [1] manganites ($La_{1-x}A_xMnO_3$, where A — Ca, Sr, Ba,… and x is around 0.33) have nearly 100% spin polarization in the ferromagnetic state that makes this material very attractive as a base for MTJ. However due to complex metaloxide nature of manganites fabrication of multilayer MTJ encounter serious problems related with degradation of ferromagnetic properties in the vicinity of interfaces. Recently several works were published where properties of artificial grain boundary MTJ on [001]-tilt bicrystal substrates were studied [2,3]. As it was shown in [4] for high-Tc superconducting Josephson junctions using bicrystal substrates of [100]-tilt type more suitable for making high quality metaloxide tunnel junctions than bicrystals of [001]-tilt type and they show higher $I_C R_N$ product and lower resistance. The aim of the present work is to study transport, magnetoresistive and microwave properties of manganite based MTJ on [100]-tilt bicrystal substrate.

1. Experimental

50-nm-thick $La_{0.67}Ca_{0.33}MnO_3$ (LCMO) epitaxial films were grown by the laser ablation technique on $(110)NdGaO_3$ (NGO) bicrystal substrates with $\pm 14°$ misorientation of their axes about the $[1\bar{1}0]$ direction (Fig. 1). For LCMO grown on NGO substrates, the following epitaxial relations were satisfied: LCMO(001)‖NGO(110) and LCMO[100]‖NGO $[1\bar{1}0]$. The LCMO pseudocubic lattice parameter $a_L = 3.858$ Å, and the NGO(110) lattice parameters (orthorhombic unit cell with $a = 5.426$ Å, $b = 5.502$ Å, and $c = 7.706$ Å) along the [001] and $[1\bar{1}0]$ directions are $a_N = 3.853$ Å and $b_N = 3.863$ Å, respectively. Since $a_N < a_L < b_N$, stresses of opposite polarity arise in an LCMO film, namely, compressive stresses along NGO[001] and tensile stresses along NGO$[1\bar{1}0]$.

Films were grown by laser ablation in an oxygen atmosphere at a pressure $P = 0.2$ mBar at a substrate temperature $T = 750$ °C with subsequent annealing in oxygen at a pressure of 1 Bar. In a film, 7 μm-wide bridges intersecting the bicrystal boundary were formed by ion-beam etching using a photoresist mask.

All electrophysical measurements were carried out by the four-probe method using platinum contact areas deposited by rf sputtering through a metallic mask. During epitaxial growth, the bicrystal-substrate crystalline structure is reproduced in an LCMO film and a bicrystal boundary is formed in the film. The translation symmetry is broken at the boundary. As a result, the electronic state is transformed, which, in turn, leads in manganites to the occurrence of a thin separation layer with high resistivity (Fig. 1).

2. Results and discussion

The dependence of the electrical resistance on magnetic field was measured at 4.2 K in fields of up to 150 mT for three mutually perpendicular directions of the magnetic field: along the normal to the substrate plane (axis Z), along the bicrystal boundary line (axis Y),and along the normal to the bicrystal boundary plane(axis X, Fig. 1). The relative magnetoresistance (MR) was calculated from the formula $MR = (R_{AP} - R_P)/R_P$,

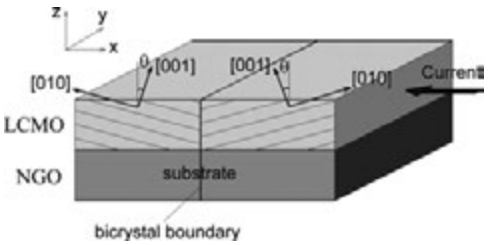

Fig. 1. Bicrystal boundary in an NGO substrate and an LCMO film (schematic). The X,Y, and Z axes coincide withthe directions along which an external magnetic field was applied when measuring the magnetoresistance. The crystallographic directions in the LCMO film are indicated by the arrow pairs. The external current is passed in the substrate plane perpendicular to the boundary.

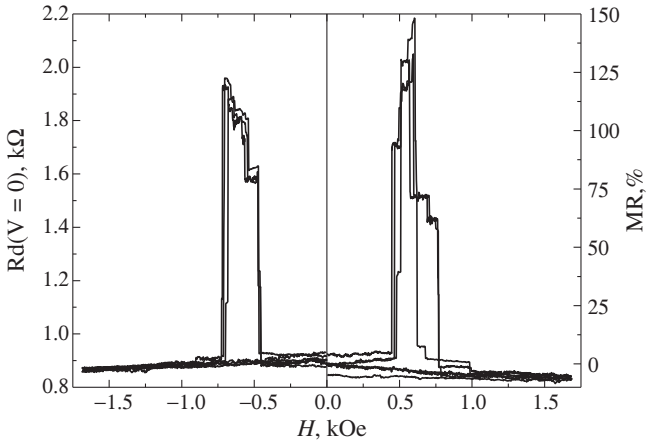

Fig. 2. Magnetoresistance of a bicrystal boundary in an LCMO film measured at $T = 4.2$ K as a function of external magnetic field applied along Z axis. The differential resistance of the bicrystal boundary at a zero stress (on the left) and its variation in percent (on the right) are shown.

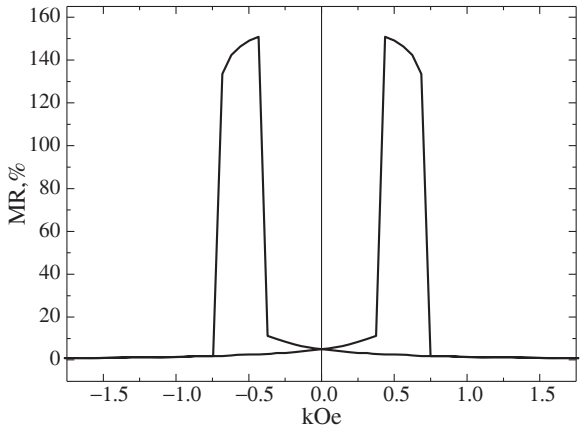

Fig. 3. Field dependence of the magnetoresistance obtained from simulating the magnetization reversal in magnetic field directed along the Z axis.

where R_{AP} and R_P are the electrical resistances measured at low voltages for the antiparallel and parallel mutual orientations of the magnetizations in the contact banks, respectively. The maximum magnetoresistance was nearly 150% (Fig. 2), which substantially exceeds the values of about 30% found earlier on bicrystal contacts with the axes rotated in the substrate plane [2,3]. The magnetization reversal in magnetic fields applied along the Y and Z axes is accompanied by a jump in resistance within relatively narrow magneticfield ranges 75 and 300 Oe wide, respectively (Fig. 2), which demonstrates a sharp reorientation of the magnetization in the film near the bicrystal boundary. In magnetic fields applied along the X axis, the dependence of the electrical resistance on magnetic field is smooth, which corresponds to the coherent magnetization rotation in the contact banks (Fig. 2).

The results of the simulation for magnetic fields applied along the Z and X axes are presented in Fig. 2. The magnetization obtained for an LCMO film (400 emu/cm^3) by fitting the experimental data agrees well with that of epitaxial films measured by a SQUID magnetometer. The best fit to the experimental data is obtained when the easy magnetization axis is deviated from the normal to the film surface through angles of $\pm 14^\circ$ and coincides with the [001] direction of the LCMO film. Moreover, the measurement of the magnetoresistance along the Y axis shows that there is another easy magnetization axis coinciding with the [100] direction in the LCMO. The study of the influence of stresses on the magnetic anisotropy in manganite films grown on SrTiO3 and LaAlO3 substrates having cubic lattices showed that the compressive stress in the (001) plane causes the appearance of an easy magnetization axis along the LCMO[001] direction (for LaAlO3) and that the tensile stress in the LCMO(001) plane creates in-plane easy magnetization axes along the [110] and [1$\bar{1}$0] directions (for SrTiO3). Although the effect of stresses on the magnetic anisotropy of LCMO films on NGO substrates has not been studied, we can conclude, based on the data for SrTiO3 and LaAlO3 substrates, that tensile stresses in the direction LCMO[100]$\|$NGO[1$\bar{1}$0] and compressive stresses in the direction LCMO[010]$\|$NGO[001] create easy magnetization axes along the LCMO [100] and LCMO[001] directions.

3. Conclusions

We have shown experimentally that magnetic contacts prepared on a bicrystal substrate with the inclined basal planes exhibit high magnetoresistance of up to 150% in magnetic fields of up to 1 kOe. However, the prepared contacts have a fairly high characteristic electrical resistance of the bicrystal boundary, which hampers the study of their dynamic properties and the effects of the high-current injection of spin-polarized carriers. It is likely that the use of bicrystal substrates with small misorientation angles could permit one to solve this problem. Based on the established dependence of the magnetic anisotropy of manganite films on the substrate crystallographic orientation and on the relationship between the lattice parameters of the film and the substrate, one can create magnetically sensitive elements with predetermined properties by properly choosing these parameters.

Acknowledgements

This work was supported by programs of the Presidium and the Department of Physical Sciences of the Russian Academy of Sciences, a grant of the President of the Russian Federation (project No. NSh-5408.2008.2), a program of the European Union (project NMP3 -CT-2006-033191), and the International Scientific and Technical Center (project 3743).

References

[1] M. Bowen, M. Bibes, A. Barthe *et al*, *Appl. Phys. Lett.* **82**, 233 (2003).
[2] N. D. Mathur, G. Burnell, S. P. Isaac *et al*, *Nature* **387**, 266 (1997).
[3] R. Gunnarsson, M. Hanson, *Phys. Rev. B* **73**, 014435 (2006).
[4] I. V. Borisenko, I. M. Kotelyanski, A. V. Shadrin *et al*, *IEEE Trans. Appl. Supercond.* **15**, 165 (2005).
[5] I. V. Borisenko and G. A. Ovsyannikov, *Physics of the Solid State* **51**, 309 (2009).

17th Int. Symp. "Nanostructures: Physics and Technology"
Minsk, Belarus, June 22–26, 2009
© 2009 Ioffe Institute

Spin Hamiltonian and *ab initio* simulation of quantum register on single NV center and set of nearby ^{13}C in nanodiamond

A. P. Nizovtsev[1], S. Ya. Kilin[1], A. L. Pushkarchuk[2], V. A. Pushkarchuk[3], S. A. Kuten[4], F. Jelezko[5] and J. Wrachtrup[5]

[1] B. I. Stepanov Institute of Physics NASB, 220072 Minsk, Belarus
[2] Iinstitute of Physical Organic Chemistry NASB, 220072 Minsk, Belarus
[3] BSUIR, 220013 Minsk, Belarus
[4] Institute for nuclear problems, 220050 Minsk, Belarus
[5] Institute of Physics, University of Stuttgart, 70550 Stuttgart, Germany

Abstract. Spin systems consisted of single electronic spin of the NV center in diamond and few nearby ^{13}C nuclei spins in diamond lattice which can be used to implement a register of quantum computer with optical access are studied using spin Hamiltonian method in combination with *ab initio* (DFT) calculations of the characteristics of super hyperfine interactions between the spins. New experimental spectra of optically detected magnetic resonance for various "NV+few ^{13}C" spin systems are described well without fitting parameters.

Introduction

It is now widely acknowledged that one of the most promising systems for quantum computation is an array of (electronic or nuclear) spins associated with impurities in solid matrix. Nitrogen-vacancy (NV) center in diamond is among the recognized candidate for solid-state quantum computing technology because of its unique properties [1, 2]. In diamond crystal lattice, nuclear spins like ^{13}C carbon can be coupled via hyperfine interaction to the electron spin of neighboring NV center. This coupling leads to a hyperfine structure in the colour center energy levels which has been proposed [3] as the basis of a scalable quantum processor built with the help of two-qubit quantum gates, formed by the NV colour center and a set of neighboring ^{13}C nuclear spins. It was shown [4,5,6] that optical read-out of the electron spin state gives access to the single nuclear spin state and allows to implement a two-qubit CROT quantum logical gate. As a further step, few ^{13}C nuclei located in the first and the next coordination shells around individual NV center can be detected and manipulated by means of microwave (MW) and radiofrequency (RF) fields [7, 8, 9]. It means that their states can be used as a register for quantum logical gates. To implement different gates with this register, full understanding of its spin properties is necessary. Here we have studied the spin properties of such quantum register using spin Hamiltonian method in combination with *ab initio* calculations of the characteristics of super hyperfine interactions (*shfi*) between NV center and ^{13}C nuclear spins located in various positions around the center.

1. Spin properties of quantum registers

Strong super hyperfine interactions between electronic spin $S = 1$ of ground-state ^{3}A of the NV center and the ^{13}C nuclear spins (isotropic *shfi* constants consisted of ∼150 MHz and ∼10 MHz for the spins belonging to first and third coordination shells of the NV center, respectively [10,11,12,13]) along with spin-selective photophysics of the NV center [4] provide the unique opportunity to initiate and read-out the nuclei spin states optically at room temperature, while manipulating them with microwave/radiofrequency pulse series [7,8,9]. Recently such spin systems have been studied experimentally [9] by observing optically detected magnetic resonance (ORMR) on single NV centers in ^{13}C-enriched diamond samples (∼8% and ∼20% content of ^{13}C). The ODMR spectra have been monitored for single NV centers having one, two and three ^{13}C atoms in positions being nearest neighbor (NN) to the vacancy of the NV center. Moreover, the entangled two-spin Bell and three-spin Greenberger–Horne–Zeilinger (GHZ) states have been created and studied in the spin systems. Analogous ODMR spectra have also been observed and studied recently for spin system consisted of the single NV center and few ^{13}C nuclear spins located in more distant positions.

To elucidate the spin properties of a system of coupled spins and describe new experimental ODMR data we have considered spin Hamiltonian of the "NV + few ^{13}C" center $H = g_e\beta_e S \times B + S \times D \times S + \sum_n S \times A^{(n)} \times I^{(n)}$ where the first term describes the interaction of electronic spin S with magnetic field B and the second one takes into account zero-field splitting of the ground triplet state of the center. D is the diagonal tensor with elements $D_{XX} = D/3$, $D_{YY} = D/3$, $D_{ZZ} = -2D/3$, $D = 2.88$ GHz [10] in the principle axes coordinate system (PACS) of the center, wherein the Z axis lies along [111] direction of diamond lattice. The third term describes *shfi* of the electronic spin S with ^{13}C nuclear spins, where $A^{(n)}$ are *shfi* tensors for various ^{13}C atoms, assigned conventionally as diagonal tensors in the PACSs $(xyz)^{(n)}$ being specific for each n-th ^{13}C atom. Usual way to determine these $A^{(n)}$ tensors is the EPR method. For single ^{13}C atom in NN position to the vacancy of the NV centers such information has been obtained in experiment [10]. Isotropic $a = 150.5$ MHz and anisotropic $b = 27$ MHz *shfi* constants have been determined along with the directional cosines of the ^{13}C PACS with respect of the NV PACS.

Here we performed quantum-chemical (DFT) simulation of diamond nanoclusters containing the NV center to calculate distributions of electronic and spin densities over the atoms of nanocluster and to determine the $A^{(n)}$ tensors for various ^{13}C atoms in nanoclusters. The nitrogen atom and vacancy

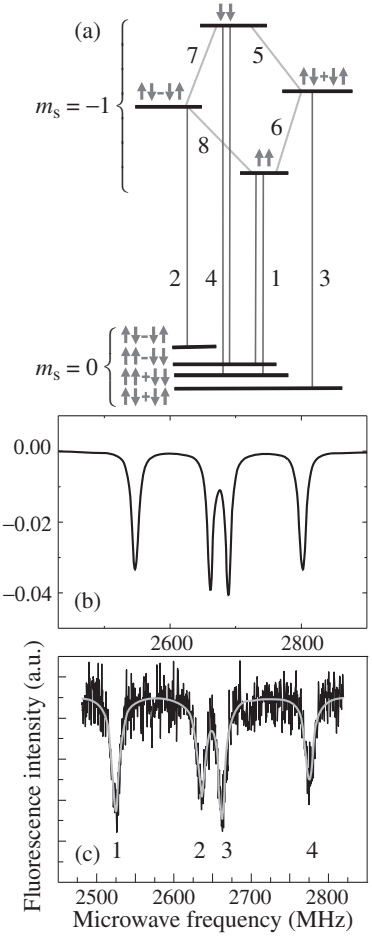

Fig. 1. a) Energy levels, spin wavefunctions (arrows up and down mean $\pm 1/2$ projections of ^{13}C nuclear spins) and possible EPR (1–4) and RF (5–8) transitions for the NV center having two ^{13}C in the NN positions at non-zero magnetic field $B = 78.5$ gauss ($B \parallel [111]$). b) ODMR spectrum of the spin system obtained using the *shfi* tensors for two ^{13}C atoms calculated with *shfi* parameters simulated by DFT for the cluster $C_{84}H_{78}NV$. c) Respective experimental ODMR spectrum.

forming the $[NV]^-$ defect center were placed in the center of the clusters. Calculations of the optimized geometrical structure of clusters as well as calculations of spin density distributions were carried out within frameworks of the semi-empirical quantum-mechanical PM3 and DFT methods using the GAMESS [14] and CAChe [15] software packages. The calculations have been performed for singly negatively charged clusters in the triplet ground state. More specifically, we have simulated the $C_{33}H_{36}NV$, $C_{69}H_{84}NV$ and $C_{84}H_{78}NV$ clusters. To unify and simplify the analysis we calculated the *shfi* tensors for various ^{13}C atoms in the same coordinate system coinciding with the PACS for the NV center. Clearly, the $A^{(n)}$ tensors in the NV PACS were non-diagonal. Both isotropic *(ishfi)* and anisotropic (*ashfi*) parts of the $A^{(n)}$ tensors for ^{13}C nuclei at various positions in relaxed clusters have been calculated.

The calculations confirmed that most part of spin density is localized at three carbon atoms being NN to the vacancy resulting in maximal values of *shfi* tensors elements for the ^{13}C atoms in these positions. In particular, for the largest studied $C_{84}H_{78}NV$ cluster the diagonal elements of the diagonalized *shfi* tensors (in respective n-th PACSs $(xyz)^{(n)}$) had maximum values at these three C atoms, equal $\sim$126.1 MHz for A_{xx}, A_{yy} and 193.5 MHz — for A_{zz}. The calculated elements of *shfi* tensors for C atoms belonging to the second coordination shells around the NV center were negative and ranges about $(\pm)3-9$ MHz while those for the third shell are again positive with A_{xx}, $A_{yy} \sim 7.0-8.5$ MHz and $A_{zz} \sim 11.1-12.9$ MHz. These findings are in good agreement with experimental data of [7,8] and *ab initio* simulation of [13].

The *shfi* $A^{(n)}$ tensors calculated by DFT in the NV PACS were inserted into the above spin Hamiltonian and the latter was diagonalized numerically to determine eigenenergies and eigenstates of the considered "NV + few ^{13}C" spin systems and, further, to fit the available experimental ODMR spectra for such systems both in zero- and non-zero external magnetic field. The examples of calculations are shown in Fig. 1 for the case of the presence of two ^{13}C nuclei in the NN positions to the vacancy along with the respective experimental ODMR spectrum for this case. The figure exhibits very good coincidence with the experimental data of [9] showing characteristic splitting $\Delta \sim 130$ MHz due to *shfi* to the NN nuclear spins. Analogous coincidence between calculated and experimental ODMR spectra for the NV + NN ^{13}C centers was obtained for three ^{13}C nuclei in the NN positions at non-zero and zero magnetic field.

In the cases of the presence of ^{13}C nuclei in more distant positions from the vacancy the calculated ODMR spectra were also are in reasonable qualitative coincidence with the experimental ones but quantitatively the simulated spectra show slightly smaller *shfi* splitting equal $\sim$11 MHz for the largest cluster $C_{84}H_{78}NV$ in comparison with the experimental splitting $\sim$13 MHz. The reason for this divergence is evidently in the size of the simulated carbon cluster which was not sufficiently large for simulation of *shfi* parameters for distant ^{13}C nuclei located in the third coordination shell of the NV center.

Acknowledgements

This work has been supported in part by EU under the project of the 6FP program "Engineered Quantum Information in Nanostructured Diamond" (EQUIND).

References

[1] J. Wrachtrup and F. Jelezko, *J. Phys.: Condens. Matter* **18**, S807 (2006).
[2] A. D. Greentree *et al*, *J. Phys.: Cond. Matter* **18**, S825 (2006).
[3] J. Wrachtrup, S. Ya. Kilin and A.P. Nizovtsev, *Optics and Spectroscopy* **91**, 429 (2001).
[4] A. P. Nizovtsev *et al*, *Optics and Spectroscopy* **94**, 895 (2003).
[5] F. Jelezko *et al*, *Phys. Rev. Lett.* **92**, 076401 (2004).
[6] F. Jelezko *et al*, *Phys. Rev. Lett.* **93**, 130501 (2004).
[7] L. Childress *et al*, *Science* 314, 281–5 (2006).
[8] M. V. Gurudev Dutt *et al*, *Science* **316**, 1312 (2007).
[9] P. Neumann *et al*, *Science* **320**, 1326 (2008).
[10] J. H. N. Loubser, J. A. van Wyk, *Diamond Research* **11**, 11 (1977).
[11] V. A. Pushkarchuk *et al*, *Optics and Spectroscopy* **99**, 245 (2005).
[12] V. A. Pushkarchuk *et al*, *J. Appl. Spectr.* **74**, 87 (2007).
[13] A. Gali, M. Fyta and E. Kaxiras, *Phys. Rev. B* **77**, 15506 (2008).
[14] http://www.msg.ameslab.gov/GAMESS/pcgamess.shtml.
[15] http://www.cachesoftware.com.

17th Int. Symp. "Nanostructures: Physics and Technology"
Minsk, Belarus, June 22–26, 2009
© 2009 Ioffe Institute

DFT modeling of atomic and spin structure of single NV$^-$-centers near nanodiamond surface

V. A. Pushkarchuk[1], A. B. Filonov[1], A. P. Nizovtsev[2], S. Ya. Kilin[2], V. A. Pushkarchuk[3] and S. A. Kuten[4]

[1] Belarusian State University of Informatics and Radioelectronics, Brovki 6, 220013 Minsk, Belarus
[2] B. I. Stepanov Institute of Physics, NASB, Nezavisimosti 68, 220072 Minsk, Belarus
[3] Institute for Physical-Organic Chemistry, NASB, Surganova 13, 220072 Minsk, Belarus
[4] Institute for Nuclear Problems, Belarusian State University, Bobruiskaia 11, 220030 Minsk, Belarus

Abstract. Modeling of the atomic structure and spin properties of a NV$^-$-center formed close to a (111) surface of nano-diamond has been carried out by using quantum-chemical PM3 and DFT methods. We consider the case where the nitrogen atom of the NV$^-$-center is located in the near-subsurface atomic layer of a (111) facet. The relaxations of the surface atoms relative to their initial position are studied. The calculated spin densities for the considered clusters were compared with those ones for the clusters having the NV$^-$-center in the bulk. It was shown that as distinct of the NV$^-$-center in the bulk diamond where the spin density is located mainly on C atoms being the nearest neighbors to the vacancy, in the case of nanodiamonds there is the redistribution of spin density resulting in its major allocation at the three C atoms being the nearest neighbors to the N atom and forming just the first atomic layer of the (111) surface.

Introduction

At the top of systems proposed for the processors of quantum computers, there are the systems in which electronic and nuclear spins of various defects and impurities in diamond are used as stationary qubits [1,2]. Single NV$^-$-centers having electronic spin $S = 1$ in the ground electronic state are the most promising [3]. To improve optical read-out of such spin-states, various three-dimensional nanostructures in diamond such as micro resonators, waveguides, photon-crystal structures, etc. [1,4,5] are being developed. Besides, the methods of NV$^-$-center implantation with high accuracy of positioning in diamond were developed [6,7] to create scalable quantum processors.

Electronic and spin properties of NV$^-$-centers in such nanostructured diamond samples are not yet studied. The first theoretical results obtained with the use of quantum chemical methods are reported below. For modeling of the NV$^-$-center in diamond nanostructures, the clusters $C_xH_y[NV]^-$ were used. In this paper we study the influence of the surface of nanodiamonds containing NV$^-$-centers on their structural and spin properties.

1. Modeling results

Modeling of $C_{33}H_{30}[NV]^-$ and $C_{66}H_{72}[NV]^-$ clusters was carried out. We got similar qualitative results for both clusters, so here we presents detailed results only for cluster $C_{33}H_{30}[NV]^-$. Structural, electronic and spin characteristics of diamond nanoclusters with the surface completely saturated with hydrogen were considered elsewhere [8,9]. Here we analyze a role of the free (111) surface on the above mentioned characteristics. The cluster $C_{33}H_{30}[NV]^-$ was built on the basis of $C_{33}H_{36}[NV]^-$ cluster by removal of six H atoms on the (111) crystal face (see Fig. 1). Calculations of partial and fully optimized atomic geometry of the cluster as well as calculations of the spin properties were carried out by using the semi-empirical quantum-chemical PM3 method and the density functional method (DFT) with the B3LYP1 functional and

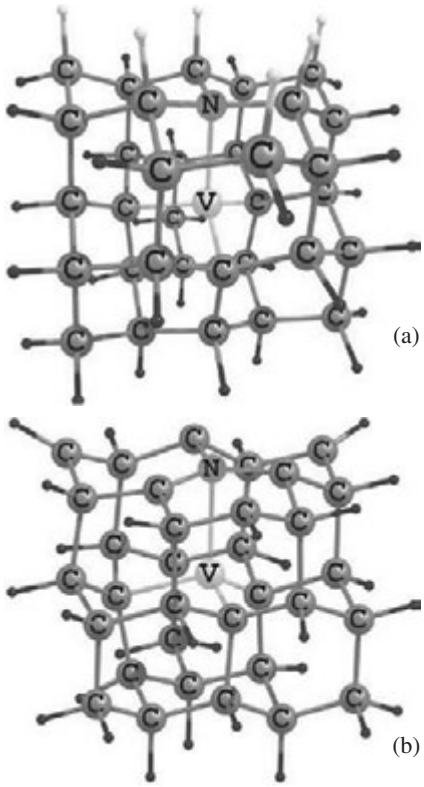

Fig. 1. Modeling of the (111) surface: a) initial $C_{33}H36[NV]$-cluster, b) $C_{33}H_{30}[NV]$-cluster with the free (111) surface (six white H atoms were removed).

the MINI and 6-311G* basic functions. The software packages GAMESS [10] and CAChe [11] were used. The calculations were carried out for the negatively charged cluster with the triplet ground electronic state ($S = 1$).

In this model the N atom of the NV$^-$-center belongs to the second subsurface layer. Partial and complete optimization of the geometry was carried out for the $C_{33}H_{30}[NV]^-$ cluster. For the first case, the relaxation of only N and C atoms, being the first and the second neighbors to N atom forming the first and

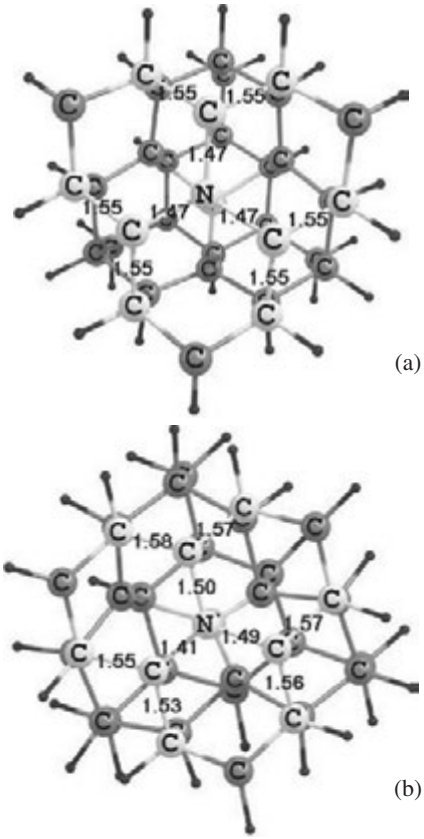

Fig. 2. Distances between the surface atoms (white color) in the $C_{33}H_{30}$[NV]-cluster before (a) and after (b) relaxation. The ⟨111⟩ direction is perpendicular to the figure plane.

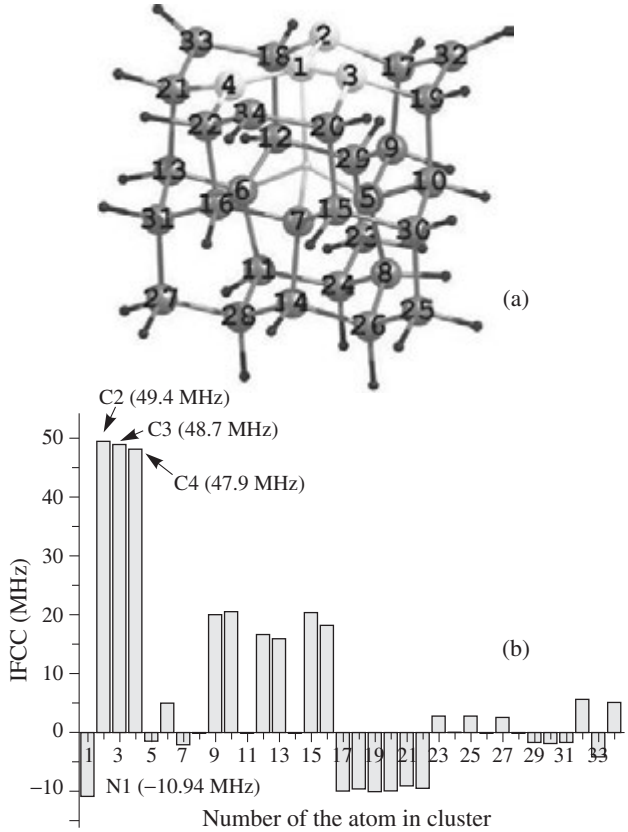

Fig. 3. Spin properties of partially relaxed $C_{33}H_{30}$[NV]-cluster: a) cluster structure; white — ^{13}C and ^{15}N atoms with higher IFCC, b) IFCC distribution.

the second subsurface atomic layers was taken into account. All the other atoms of the cluster were fixed. The starting and relaxed distances for the C-C and C-N pairs are presented in Fig. 2.

Fig. 3 demonstrates partially relaxed atomic structure of the $C_{33}H_{30}[NV]^-$-clusters and distribution of isotropic Fermi contact coupling (IFCC) in it, calculated within DFT with 6-31G* basis set. In our previous calculations [8,9], it was shown that the spin density is located mainly at the three C atoms, which are the nearest neighbors to the vacancy of the NV^--center.

It is evident that, in the case when a NV^--center is formed in an immediate proximity to the surface, the redistribution of the spin density and IFCC occurs. The spin density is located mainly at C atoms that form the first atomic layer of the (111) surface of the nanocrystal.

2. Conclusion

After the atomic relaxation of clusters $C_{33}H_{30}[NV]^-$ and $C_{66}H_{72}[NV]^-$ in the ground state tended to have a diamond-like atomic structure.

It was shown that the diamond surface graphitization occurs independent on the NV^--center localization. For partially relaxed diamond nanocrystals in the case of the NV^--center located in the immediate proximity to the surface, the spin density is localized at the three surface C atoms being the nearest neighbors to the N atom, while the spin density have more complicated redistribution for the completely relaxed nanocrystals.

Acknowledgements

The work was done with partial support from the State Complex Research Program “Nanomaterials and nanotechnology”, the Belorussian Republican Fund of Fundamental Research and project EQUIND of the 6-th EU framework program.

References

[1] A. D. Greentree *et al*, *J. Phys. Condens. Matter* **18**, 825 (2006).
[2] J. Wrachtrup, F. Jelezko, *J. Phys. Condens. Matter.* **18**, 807 (2006).
[3] L. Childress *et al*, *Science* **314**, 281 (2006).
[4] P. Olivero *et al*, *Adv. Mater.* **17**, 2427 (2005).
[5] J. Meijer *et al*, *Appl. Phys. Lett.* **87**, 261909 (2005).
[6] J. R. Rabeau *et al*, *Appl. Phys. Lett.* **88**, 23113 (2006).
[7] V. A. Pushkarchuk, S. Ya. Kilin, A. P. Nizovtsev, A. L. Pushkarchuk, A. B. Filonov, V. E. Borisenko, *Optics and Spectroscopy* **99**, 245 (2005).
[8] V. A. Pushkarchuk, S. Ya. Kilin, A. P. Nizovtsev, A. L. Pushkarchuk, A. B. Filonov, V. E. Borisenko, *J. of Appl. Spectroscopy* **74**, 101 (2007).
[9] http://www.msg.ameslab.gov/GAMESS/pcgamess.shtml.
[10] http://www.cachesoftware.com.

17th Int. Symp. "Nanostructures: Physics and Technology"
Minsk, Belarus, June 22–26, 2009
© 2009 Ioffe Institute

Simulation of the structural, electronic and spin properties of the Eu@C_{60} and Eu@C_{82} clusters by the DFT method

A. L. Pushkarchuk[1], A. A. Khrutchinsky[4], S. A. Kuten[4], V. A. Pushkarchuk[3], S. Ya. Kilin[2], A. P. Nizovtsev[2] and I. V. Bondarev[5]

[1] Institute for Physical-Organic Chemistry, NASB, Surganova 13, 220072 Minsk, Belarus
[2] B. I. Stepanov Institute of Physics, NASB, Nezavisimosti 68, 220072 Minsk, Belarus
[3] Belarusian State University of Informatics and Radioelectronics, Brovki 6, 220013 Minsk, Belarus
[4] Institute for Nuclear Problems, Belarusian State University, Bobruiskaia 11, 220030 Minsk, Belarus
[5] Physics Department, North Carolina Central University, 1801 Fayetteville Str., Durham, NC 27707, USA

Introduction

Metallofullerenes are widely used in various applications from technology to biomedicine. One important area of their applications is the development of the new generation of materials that may host quantum coherent states for a long time. Many metal atoms can be encapsulated into fullerene cages to form metallofullerene complexes. That is why much attention has been paid recently at the electronic and structural properties of endohedral metallofullerenes with partly occupied f-electron shells, such clusters as Ce@C_{82}, Pr@C_{82}, Gd@C_{82}, Tm@C_{82}, etc. (see [1–11] and refs. therein). The advantage of getting a rear-earth atom isolated from its environment has made endohedral fullerenes attractive for many applications. One such application is quantum information processing (QIP), where the isolated electron spin on the metal atom is used as a nano-sized quantum bit (qubit) for quantum computation [12,13]. Our goal here is to study the Eu@C_{82} and Eu@C_{60} endohedral structures as possible candidates for spin qubits in quantum computer applications.

1. Results of DFT simulation

Using computational methods of quantum chemistry, we study a possibility to create coherent quantum states in complexes of rear-earth Eu atoms and fullerenes. We consider the structures Eu@C_{82} and Eu@C_{60} containing the endohedral Eu atom inside the fullerene. Calculations are performed for the system in its ground spin state $S=7/2$ within ROHF and UHF approaches. Geometry optimization was done within the framework of the quantum chemical density functional method (DFT) with the use of the B3LYP1 functional in MINI basis. We used PC GAMESS computational software packages in our calculations [14].

C_{60} and three C_{82} isomers were under study. Initial coordinates of the carbon atoms in the fullerenes were calculated using Nanotube Modeller software. After the Eu atom introduction inside the fullerene cage, the geometry configurations of the Eu@C_{82} and Eu@C_{60} complexes were optimized. The complexes were exposed to annealing, i.e. they were allowed to relax to new equilibrium states under control of the corresponding program. After such an optimization, the Eu atom shifted towards the wall from the fullerene cage center (Fig. 1).

The distances between the Eu atom and carbon atoms vary in the range of 3.0 Å to 5.6 Å for the Eu@C_{82} complex. Annealing increases the C-C bonds for both complexes. This approximately corresponds to their transformation from the one-and-half bonds for unrelaxed structures to the single bonds for the relaxed ones.

The calculated charge distribution shows that the Eu atom loses two electrons which become uniformly distributed over the carbon atoms of the fullerene. The charge distribution of the Eu@C_{82} complex corresponds to the formula $Eu^{+2}C_{82}^{-2}$, similar to what happens in the Sc@C_{82} complex [13].

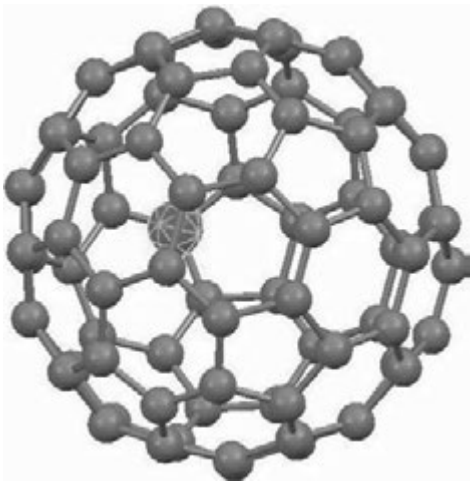

Fig. 1. Relaxed Eu@C_{82} cluster after annealing.

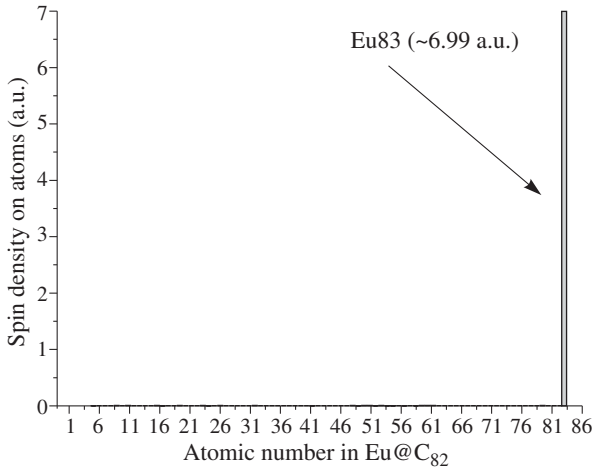

Fig. 2. Spin Density Distribution over all atoms in the Eu@C_{82} complex.

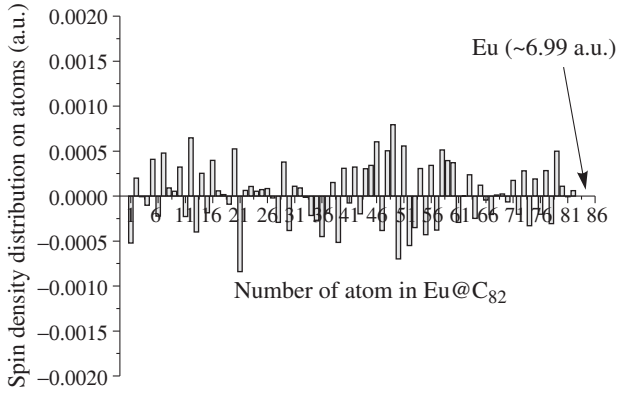

Fig. 3. Spin Density Distribution for C atoms in the Eu@C_{82}.

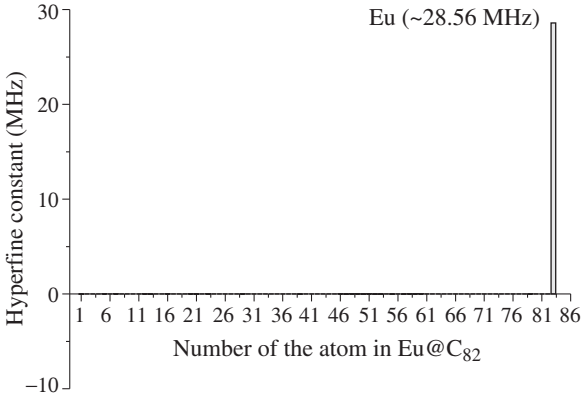

Fig. 4. IFCC of all atoms in the Eu@C_{82}.

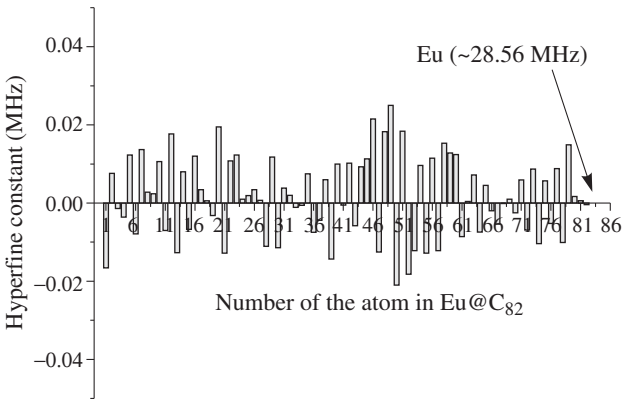

Fig. 5. IFCC of C atoms in the Eu@C_{82}.

The analysis of the localization of the α- and β- HUMO orbitals shows that almost all the unpaired electrons are localized on the Eu atom. Fig. 2 demonstrates the spin density distribution in the Eu@C_{82} complex (calculated within the DFT method with MINI basis set).

Fig. 3 shows the spin density distribution for the carbon atoms only in the Eu@C_{82} complex. Comparing Fig. 3 with Fig. 2, we see that about 80% of the Eu@C_{82} complex spin density is located on europium.

Fig. 4 demonstrates the calculated distribution of the isotropic hyperfine (Fermi) contact coupling (IFCC) (calculated within DFT with MINI basis set) in Eu@C_{82}. IFCC is representative of the electron density on the nucleus. Fig. 5 shows the IFCC distribution for the C atoms only. We see that most of the electrons are localized on the Eu nucleus.

To summarize, the spin density localized on the Eu nucleus is two orders of magnitude larger than that distributed over the carbon shell. The value of IFCC on the Eu nucleus is about 29 MHz. Obviously, the complex exhibits the strong localization of the spin density on the Eu nucleus, which is one of the basic necessary requirements to be a good candidate for spin qubits realization.

References

[1] T. Wakahara *et al*, *Chem. Phys. Lett.* **360**, 235 (2002).
[2] L. Senapati *et al*, *Nano Lett.* **4**, 2073 (2004).
[3] L. Wang *et al*, *Nano Lett.* **5**, 2340 (2005).
[4] L. Senapati *et al*, *Nano Lett.* **5**, 2341 (2005).
[5] E. Nishibori *et al*, *Phys. Rev.* **B69**, 113412 (2004).
[6] N. Mizorogi *et al*, *Chem. Phys. Lett.* **431**, 110 (2006).
[7] T. Kodama *et al*, *J. Am. Chem. Soc.* **124**, 1452 (2002).
[8] H. Shinohara, *Rep. Prog. Phys.* **63**, 843 (2000).
[9] C. Ton-That *et al*, *Phys. Rev.* **B71**, 045419s (2005).
[10] K. Muthukumar and J. A. Larsson, *J. Mater. Chem.* **18**, 3347 (2008).
[11] K. Muthukumar and J. A. Larsson, *J. Phys. Chem.* **A112**, 1071 (2008).
[12] D. Suter, K. Lim, *Phys. Rev.* **A65**, 052309 (2002).
[13] G. W. Morley *et al*, *Nanotechnology* **16**, 2469 (2005).
[14] msg.ameslab.gov/GAMESS/pcgamess.

17th Int. Symp. "Nanostructures: Physics and Technology"
Minsk, Belarus, June 22–26, 2009
© 2009 Ioffe Institute

Dynamics of nuclear spin polarization in quantum dots: graded box model approach

M. Yu. Petrov, G. G. Kozlov, and I. V. Ignatiev
Physics Department, St Petersburg State University, 198504 St etersburg, Russia

Abstract. We report on the numerical simulations of the dynamics of nuclear spin polarization in a quantum dot (QD) in framework of graded box model. It is shown that, at the initial stage of polarization, the system can be well described by the exactly solvable box model. Simulation of further polarization of nuclei requires more precise graded models whose solutions coincide with exact dynamics of nuclear spins in time range of nuclear spin relaxation time. It is also shown that the peripheral nuclei in the QD are polarized not only by direct interaction with the spin-oriented electron but also by spin-diffusion from the middle of the QD.

Introduction

The physics of electron-nuclear spin system in semiconductor quantum dots (QDs) has been under intensive investigation in recent years [1,2]. The enhanced hyperfine interaction strongly couples the spin of resident electron with large number of nuclei spins due to strong localization of electron in the QD. The hyperfine interaction with unpolarized nuclear spins is the main electron-spin decoherence mechanism in QDs [3,4]. This relaxation mechanism can be efficiently suppressed by external magnetic field [5] as well as by the nuclear spin polarization (NSP) [6] because of stabilizing of the electron spin along the preferential direction.

Due to very large number of nuclei in a QD interacting with the electron spin $N \propto 10^5$ the exact solution of the quantum mechanical problem of electron-nuclear spin dynamics is impossible neither analytically nor numerically. This is why the exactly solvable models are of particular interest even when the exact solution is obtained at the expense of assumptions whose plausibility cannot be reliably evaluated.

The simplest model allowing an exact electron-nuclear spin dynamics solution is a "box model" where the space dependence of hyperfine interaction is ignored [7,8]. The main drawback of this model is that it cannot explain a high values of the NSP observed experimentally [9].

Here we report on further generalization of the box model previously reported in Ref. [10] and on the numerical calculations of the NSP dynamics in framework of "graded box model" in which the spatial non-uniformity of the hyperfine interaction is taken into account.

1. Graded box model

The contact Fermi interaction of resident electron-spin $\hat{\mathbf{S}}$ with nuclear spins $\hat{\mathbf{I}}_j$ in a QD in the first order of perturbation theory can be described by Hamiltonian [4]

$$\hat{\mathcal{H}}_{\rm hf} = v_0 \sum_j A_j \left|\psi(\mathbf{R}_j)\right|^2 \left(\hat{\mathbf{S}} \times \hat{\mathbf{I}}_j\right), \qquad (1)$$

where v_0 is the volume of unit cell, A_j is the hyperfine coupling constant, and $\psi(\mathbf{R}_j)$ is the electron envelope wave function at the nuclear site $\mathbf{R}_j$. The sum in Eq. (1) goes over all nuclei in the QD electron localization volume.

We approximate smooth electron-density distribution $|\psi(\mathbf{r})|^2$ by step-like function with n levels $|\psi_k|^2$, $k = 1, \ldots, n$, so that: $0 = |\psi_0|^2 < |\psi_1|^2 < \ldots < |\psi_n|^2 = |\psi|^2_{\max}$. The nuclei of the layer with electron density lying in the range $|\psi_{k-1}|^2 < \left|\psi(\mathbf{R}_j)\right|^2 < |\psi_k|^2$ can be referred to kth group and considered to be equally coupled with the electron spin. In this way, we obtain n groups of equivalent nuclei. Then, we can introduce the average hyperfine coupling constants $\mathcal{A}^{(k)}$ for each group of nuclei so that: $v_0 \sum_{j\in(k)} A_j \left|\psi(\mathbf{R}_j)\right|^2 / N_k = \mathcal{A}^{(k)} |\psi_k|^2$, where sum goes over all N_k nuclei in kth group. Using the total nuclear spin for each group defined as $\hat{\mathcal{I}}^{(k)} = \sum_{j\in(k)} \hat{\mathbf{I}}_j$, $k = 1, \ldots, n$, Hamiltonian (1) can be rewritten as

$$\hat{\mathcal{H}} = \sum_{k=1}^{n} \mathcal{A}^{(k)} |\psi_k|^2 \left[\hat{S}_z \hat{\mathcal{I}}_z^{(k)} + \frac{1}{2}\left(\hat{S}_+ \hat{\mathcal{I}}_-^{(k)} + \hat{S}_- \hat{\mathcal{I}}_+^{(k)}\right)\right], \qquad (2)$$

where $\hat{S}_\pm$ and $\hat{\mathcal{I}}_\pm^{(k)}$ are rising and lowering operators which increase and decrease the spin z projections $\hat{S}_z$ and $\hat{\mathcal{I}}_z^{(k)}$, respectively. The accuracy of such description will be improved with increasing number of groups of equivalent nuclei. Also, the model with one group corresponds to box model. The example of the models is shown in Fig. 1.

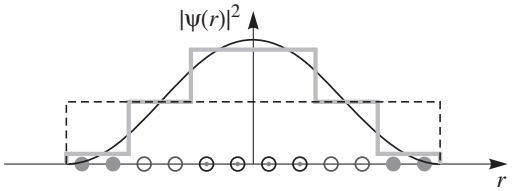

Fig. 1. Approximation of cosine-squared-like electron density (thin solid line) by step-like function in graded box model. Example for 12 nuclei and three equivalent-nuclei groups is shown by thick solid line. The nuclei belonging to one group are represented by the one-type circles. The approximation in the simple box model where all nuclei are supposed to be equivalent is represented by dashed line.

The Hamiltonian (2) cannot be diagonalized exactly but can be represented in block-diagonal form using the basis of functions $|\Upsilon\rangle = |S_z\rangle|\ell^{(1)}, \ell_z^{(1)}, \ldots, \ell^{(n)}, \ell_z^{(n)}, \beta\rangle$ where $S_z = \pm 1/2$ is the electron-spin z projection, $\ell^{(k)}$ and $\ell_z^{(k)}$ are the quantum numbers of total momentum and its z projection for each kth nuclei group, respectively, and β is the set of other quantum numbers needed for the state to be uniquely specified. Then, each block in the Hamiltonian matrix can be diagonalized independently using divide-and-conquer algorithm for block-tridiagonal matrices [11] in a numerically stable way.

2. Dynamics of nuclear spin polarization

To describe the dynamics of NSP in the QD ensemble we have used the density matrix formalism. First, we discuss the protocol of nuclei spin polarization. In the initial state, all the nuclei

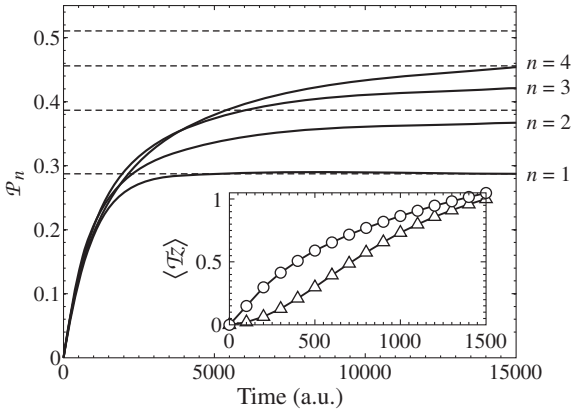

Fig. 2. Dynamics of nuclear spin polarization degrees (solid lines) calculated for the QD model with 24 nuclei having spins $I = 1/2$ and different number n of the approximation grades. The dependencies repeat each other at the initial stage and then are saturated at different steady-state values (dashed lines) corresponding to different achievable values of NSP at different approximations. Inset shows the dynamics of z projections of the nuclear momenta in the QD middle (circled line) and in the peripheral areas of the QD (triangled line) calculated in the model with $n = 3$ groups of nuclei.

are unpolarized, so that the nuclear density matrix is proportional to unity matrix $\rho_n \sim \mathbb{1}$ (high-temperature state). At the moments $T_m = 0, \Delta t, \ldots, m\Delta t$, short laser pump-pulses transfer the electron spin into strictly defined states with density matrix $\rho_e(T_m) = \begin{bmatrix} \cos^2\phi & 0 \\ 0 & \sin^2\phi \end{bmatrix}$ where the degree of polarization is determined by angle ϕ. The laser pulses are so short that they do not change the nuclear-spin state during their actions, so that ρ_n is continuous at each T_m moment and can be extracted from the total electron-nuclear density matrix ρ at the moment T_m by averaging over electron-spin states. In this way the total density matrix describing the system immediately after mth orientation event is

$$\rho(T_m + 0) = \langle \rho(T_m - 0) \rangle_e \otimes \begin{bmatrix} \cos^2\phi & 0 \\ 0 & \sin^2\phi \end{bmatrix} \qquad (3)$$

Between the moments of electron spin orientation, the electron-nuclear system coherently evolve according to the von Neumann equation which solution is

$$\rho(T_m + t) = e^{-i\hbar\hat{\mathcal{H}}t}\rho(T_m + 0)e^{+i\hbar\hat{\mathcal{H}}t} \qquad (4)$$

where $\hat{\mathcal{H}}$ is defined by Eq. (2). We note here, that the coherent evolution of the electron-nuclei spin system is broken by the electron spin orientation events. At each event, the angular momentum obtained from previous pump-pulse remains in the nuclei spin system.

Each different block of the Hamiltonian (2) represents the interaction of electron spin with nuclear spins which are in the specific state described by the set of quantum numbers $\mathcal{J} = \{\ell^{(1)}, \ell^{(2)}, \ldots, \ell^{(n)}\}$. The probability of realization of the state with given set $\mathcal{J}$ is $w_{\mathcal{J}} = \prod_{k=1}^{n} \Gamma_{N_k}(\mathcal{I}^{(k)})$ where $\Gamma_{N_k}(\mathcal{I}^{(k)})$ is the number of ways to obtain angular momentum $\mathcal{I}^{(k)}$ by summing N_k elementary spins I. These functions can be calculated for different elementary nuclear spins $I = 1/2$, $I = 3/2$, $I = 9/2$ [10]. Similarly to the Hamiltonian matrix, the density matrix can be also divided into independent blocks $\rho_{\mathcal{J}}$. In this case, dynamical equations (3) and (4) can be applied to the different blocks of density matrix independently. In this work we are interested in calculation of NSP degree which is the ratio of the average nuclear spin z projection to its maximal value $\mathcal{P}_n = \langle \mathcal{I}_z \rangle_\Sigma / (NI)$ where $\langle \mathcal{I}_z \rangle_\Sigma = \sum_{k=1}^{n} \sum_{\mathcal{J}} w_{\mathcal{J}} \mathrm{Tr}[\rho_{\mathcal{J}} \times \mathcal{I}_z^{(k)}]$.

To illustrate the polarization protocol we have calculated the dynamical equations (3) and (4) numerically in the models with different number of equivalent groups of nuclei. The results of such modeling are shown in Fig. 2. As seen, the time dependencies of NSP degree repeat each other at the initial stage of polarization and are saturated at steady-state values, $\mathcal{P}_n^{ss}$, which are different for different models. The steady-state values correspond to the independent polarization of nuclear states with each given $\mathcal{J}$ in each of density matrix block $\rho_{\mathcal{J}}$ and can be estimated by $\mathcal{P}_n^{ss} = \mathcal{P}_1^{ss}(N)\sqrt{n}$ where $\mathcal{P}_1^{ss}(N)$ is the steady state polarization calculated in framework of box model $\mathcal{P}_1^{ss}(N) \approx 0.92\sqrt{I+1}/\sqrt{NI}$ [10]. Important result of this modeling is that, at the initial stage, the NSP dynamics can be well described by the exactly solvable box model. After the initial stage, the polarization is slowed down in all the models but with different rates. We believe that real dynamics is developed according to exact model with $n = N$ but time of such calculations with macroscopic number of nuclei exponentially grows with N. In reality, the graded box model with $n \ll N$ can be used if it describes the exact dynamics at timescale not exceeding the time of nuclear-spin relaxation. For example, if the relaxation time corresponds to 5000 units in Fig. 2 the model with $n = 3$ can be used.

The dynamics of polarization of central and peripheral nuclei in the QD is illustrated in inset of Fig. 2. At the initial stage, when all the nuclei in QD are unpolarized, the rate of NSP is mainly determined by the value of electron density on the nuclear sites. Therefore the nuclei in the QD middle are polarized more rapidly than the peripheral nuclei. An important physical reason of large possible values of polarization of peripheral nuclei is the spin diffusion from the center to the peripheral areas via hyperfine interaction of different nuclei with the electron spin.

Acknowledgements

This work has been supported by RFBR.

References

[1] *Spin Physics in Semiconductors*, ed. by M. I. Dyakonov (Springer-Verlag, Berlin Heidelberg 2008).
[2] *Semiconductor Quantum Bits*, ed. by F. Henneberger and O. Benson (Pan Stanford Publishing, Singapore 2009).
[3] A. V. Khaetskii *et al*, *Phys. Rev. Lett.* **88**, 186802 (2002).
[4] I. A. Merkulov *et al*, *Phys. Rev. B* **65**, 205309 (2002).
[5] P.-F. Braun *et al*, *Phys. Rev. Lett.* **94**, 116601 (2005).
[6] R. Oulton *et al*, *Phys. Rev. Lett.* **98**, 107401 (2007).
[7] S. M. Ryabchenko and Yu. Semenov, *Sov. Phys. JETP* **57**, 825 (1983) [*Zh. Eksp. Teor. Fiz.* **84**, 1419 (1983)].
[8] G. G. Kozlov, *JETP* **105**, 803 (2007) [*Zh. Eksp. Teor. Fiz.* **132**, 918 (2007)].
[9] P.-F. Braun *et al*, *Phys. Rev. B* **74**, 245306 (2006).
[10] M. Yu. Petrov, G. G. Kozlov, and I. V. Ignatiev, *Proc. of the 16th Int. Symp. "Nanostructures: Physics and Technology"*, p. 226, St Petersburg 2008.
[11] W. Gansterer *et al*, *SIAM J. Sci. Comput.* **25**, 65 (2003).

17th Int. Symp. "Nanostructures: Physics and Technology"
Minsk, Belarus, June 22–26, 2009
© 2009 Ioffe Institute

Electron spin decoherence in semimagnetic quantum wells

P. M. Shmakov, A. P. Dmitriev and V. Yu. Kachorovskii
Ioffe Physical-Technical Institute, St Petersburg, Russia

Abstract. We study electron spin dynamics in diluted magnetic quantum wells. The electrons are coupled by exchange interaction with randomly distributed magnetic ions polarized by magnetic field **B**. This coupling leads to both spin relaxation and spin decoherence, having characteristic times T_1 and T_2, respectively. In this presentation, we demonstrate that even very small spatial fluctuations of quantum well width dramatically increase rate of decoherence. Depending on the strength of exchange interaction two different regimes are realized: inhomogeneous decoherence (strong coupling) and homogeneous decoherence (weak coupling). Both cases are described analytically. In the regime of homogeneous decoherence, the transverse (with respect to **B**) component of electron spin decays on the short time scale as $\exp(-t/T_2)$, while the long-time spin dynamics is non-exponential demonstrating long-lived power law tail. In the inhomogeneous case, the transverse spin component decays exponentially with the exponent quadratic in time: $S \sim \exp(-\omega_0^2 t^2)$.

Introduction

In diluted magnetic semiconductors, the exchange interaction couples the itinerant carrier spins with the spins of magnetic impurities. This leads to two effects: the increase of the electron spin precession frequency (up to the order of magnitude) due to average exchange field created by spin-polarized ions and the decay [1,2] of electron spin modes caused by the fluctuations of exchange field around the average value. For the 2D case, the theory of this decay was developed in Ref. [3]. It was demonstrated that delta-correlated fluctuations of ion concentration lead both to electron spin decoherence and spin relaxation with characteristic frequencies $1/T_2 \sim 1/T_1$. However, decoherence rate observed in 2D diluted magnetic semiconductors [1,2] turned out to be higher by at least one order of magnitude than the theoretically predicted value, which implies that another mechanism is relevant. In this presentation, we demonstrate that even very small fluctuations of quantum well width dramatically increase the rate of decoherence $1/T_2$. Our estimates show that this mechanism might explain the experimental data [1,2].

1. Theory

We consider the 2D electron gas interacting with the magnetic ions randomly distributed with the concentration n_J, which is assumed to be relatively high, so that $n_J a^3 \gg 1$, where a is the quantum well width. The system is placed into perpendicular magnetic field which leads to Zeeman splitting of both electron and ion spin levels with frequencies ω_e and ω_J, respectively.

The Hamiltonian of the system is given by

$$\hat{H} = \hat{H}_e + \hat{H}_J + \hat{H}_{Je}, \tag{1}$$

where

$$\hat{H}_e = \frac{\hat{\mathbf{p}}^2}{2m} + U(\mathbf{r}) + \hbar\omega_e \hat{s}_z, \tag{2}$$

$$\hat{H}_J = \hbar\omega_i \sum_k \hat{J}_{kz}, \tag{3}$$

$$\hat{H}_{Je} = \alpha\hat{\mathbf{s}} \sum_k \hat{\mathbf{J}}_k \delta(\mathbf{r} - \mathbf{R}_k)|\Psi(z_k)|^2. \tag{4}$$

Here $\hat{H}_e$ is the Hamiltonian of an electron in a random potential $U(\mathbf{r})$ and the external magnetic field, $\hat{H}_J$ is the Hamiltonian of the ions and $\hat{H}_{Je}$ represents the exchange interaction between electron spin $\mathbf{s}$ and the spins $\mathbf{J}_k$ of the ions located at points $(\mathbf{R}_k, z_k)$. Here $\Psi(z)$ is the wave function of the lowest electron level in the well and α is the interaction constant. $\hat{H}_{Je}$ can be rewritten as follows

$$\hat{H}_{Je} = \langle \hat{H}_{Je} \rangle + \delta\hat{H}_{Je}, \tag{5}$$

where the angular brackets mean averaging over ions' positions.

The term $\langle \hat{H}_{Je} \rangle$ leads to significant renormalization of electron spin precession frequency

$$\omega = \omega_e + \alpha \langle J_z \rangle n_J / 2\hbar. \tag{6}$$

Typically, $\alpha\langle J_z\rangle n_J/\hbar \gg \omega_e$ [1,2], which means that the electron spin precession frequency is mostly determined by the effective magnetic field, created by polarized ions.

The fluctuations of the effective field $\delta\hat{H}_{Je}$ arising due to delta-correlated fluctuation of ion concentration,

$$\langle \delta n_J(\mathbf{r}, z)\delta n_J(\mathbf{r}', z')\rangle = n_J \delta(\mathbf{r} - \mathbf{r}')\,\delta(z - z'), \tag{7}$$

lead to both electron spin relaxation and decoherence. The analysis of these processes based on perturbation theory shows that in 2D case the longitudinal and transverse (with respect to B) components of the electron spin decay exponentially with the characteristic times [3]:

$$\frac{1}{T_1'} = \frac{3\alpha^2 m n_J}{2a\hbar^3}\langle J_x^2\rangle, \quad \frac{1}{T_2'} = \frac{3\alpha^2 m n_J}{4a\hbar^3}\left(\langle J_z^2\rangle + \langle J_x^2\rangle\right). \tag{8}$$

Here angular brackets mean quantum-mechanical and thermodynamical averaging of ion spin operators. It is seen that T_1' is of the same order as T_2'. Comparing these equations with the recent experimental data [2] (see also more recent publication [1]), one can see that experimentally observed decoherence rate is much higher (about order of magnitude) than the one predicted by Eq. (8). This implies that delta-correlated density fluctuations can not provide sufficient fluctuations of the exchange field.

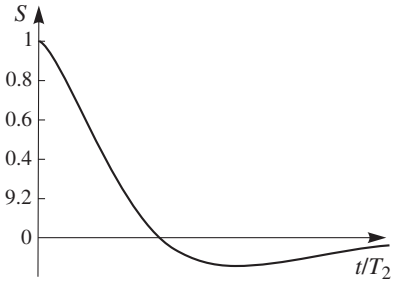

Fig. 1. Decay of the spin component, perpendicular to magnetic field.

In this presentation, we suggest another mechanism of decoherence, which is due to spatial fluctuations of quantum well width, and demonstrate that at certain conditions it can lead to significantly shorter T_2. Physically, this happens because the well width fluctuations causes the long-range fluctuations of the 2D ion concentration. Consequently, the effective magnetic field acting on the electron spin becomes spatially dependent:

$$\omega(\mathbf{r}) = \omega + \delta\omega(\mathbf{r}),\ \delta\omega(\mathbf{r}) \approx \frac{\alpha\langle J_z\rangle n_J}{2\hbar}\frac{\delta a(\mathbf{r})}{a}, \qquad (9)$$

where $\delta a(\mathbf{r}) = a - a(\mathbf{r})$. We assumed fluctuations of $\delta a(\mathbf{r})$ are Gaussian with the spatial scale d. The correlator has the following form:

$$\langle\delta\omega(\mathbf{r})\delta\omega(\mathbf{r}')\rangle = 2\omega_0^2 e^{-(\mathbf{r}-\mathbf{r}')^2/d^2},$$

where $\omega_0 = \alpha\langle J_z\rangle n_J \delta a_0/\hbar a\sqrt{8}$, and δa_0 is the amplitude of well width fluctuations.

The dynamics of the transverse spin components obeys the following kinetic equation

$$\frac{\partial s_+}{\partial t} + \mathbf{v}\frac{\partial s_+}{\partial \mathbf{r}} - i\omega(\mathbf{r})s_+ = \mathrm{St}\, s_+, \qquad (10)$$

where $s_+ = s_x + is_y$ represents the transverse spin density and $\mathrm{St}\, s_+$ is the collision integral describing elastic scattering with the mean free path l.

Equation (10) was analyzed in different regimes. For relatively strong exchange interaction ($\omega_0 \gg v_F/d$ in a case $d \ll l$, and $\omega_0 \gg v_F l/d^2$ in a case $d \gg l$), the decoherence is inhomogeneous and the total transverse spin $S_+(t) = \int s_+ d^2\mathbf{r} d^2\mathbf{v}$ is given by

$$S_+(t) = e^{i\omega t}\langle e^{-i\delta\omega(\mathbf{r})t}\rangle = e^{i\omega t}e^{-\omega_0^2 t^2}. \qquad (11)$$

For $d \ll l$, $\omega_0 \ll v_F/d$, the decoherence process is homogeneous and electron motion is ballistic (for $\omega_0 \gg v_F/\sqrt{ld}$) or diffusive (for $\omega_0 \ll v_F/\sqrt{ld}$) on the scale of the decoherence time. Both in ballistic and in diffusive case one finds

$$S_+(t) = e^{i\omega t}e^{-t/T_2},\ \frac{1}{T_2} = \frac{\sqrt{\pi}\,\omega_0^2 d}{v_F}. \qquad (12)$$

In the case $d \gg l$, $\omega_0 \ll v_F l/d^2$, the decoherence is also homogeneous, the electron motion is diffusive and the spin dynamics is given by

$$S_+(t) = S(t)\exp(i\omega t),$$

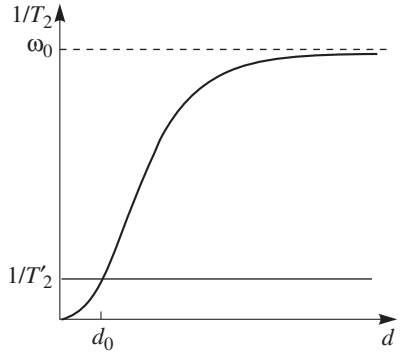

Fig. 2. Decoherence time as a function of the spatial scale of quantum well width fluctuations. For $d > d_0$ mechanism related to fluctuations of the well width dominates.

where $S(t)$ has the following asymptotics (see Fig 1):

$$S(t) \sim \begin{cases} \exp\left[-\dfrac{\omega_0^2 d^2 t}{D}\ln\left(\dfrac{D}{\omega_0 d^2}\right)\right] & \text{for } t \ll \frac{D}{\omega_0^2 d^2}, \\ -\dfrac{D}{\omega_0^2 d^2 t\,\ln^2\left(Dt/d^2\right)} & \text{for } t \gg \frac{D}{\omega_0^2 d^2}. \end{cases} \qquad (13)$$

Here $D = v_F l/2$ is the diffusion coefficient. We see that in this case spin dynamics on the long time scales is essentially non-exponential and long-lived power-law tail appears in the transverse spin polarization.

2. Conclusions

We see that increasing correlation radius d decreases T_2 both in ballistic and diffusive regimes. The maximal value of $1/T_2$ is on the order of ω_0. One can show that $\omega_0 T_2' \gg 1$ for typical values of parameters [2] which implies that suggested mechanism dominates already at relatively small d ($d > d_0$, see Fig. 2) and might be responsible for short values of decoherence time observed in the experiment [2]. The parameter d_0 (Fig. 2) is estimated as follows: $d_0 \sim k_F a/n_J\delta a_0^2$, for $l \gg d$ and $d_0 \sim \sqrt{ak_F l/n_J\delta a_0^2}$, for $l \ll d$ regime. Assuming that δa_0 is on the order of couple of lattice constants, for typical values of experimental parameters [2] we find that $d_0 \approx 10$ nm.

Acknowledgements

The work was supported by RFBR, by grant of Russian Scientific School, and by programmes of the RAS. V. Yu. K. was supported by Dynasty foundation.

References

[1] F. J. Teran, *et al*, *Phys. Rev. Lett.* **91**, 077201 (2003).
[2] M. Vladimirova, *et al*, *Phys. Rev. B* **78**, 081305 (2008).
[3] Y. G. Semenov, *Phys. Rev. B* **67**, 115319 (2003).

17th Int. Symp. "Nanostructures: Physics and Technology"
Minsk, Belarus, June 22–26, 2009
© 2009 Ioffe Institute

Pd/Fe/GaAs/InGaAs quantum structure for electron spin detection

O. E. Tereshchenko[1,2], T. S. Shamirzaev[1,2], A. M. Gilinsky[1], A. I. Toropov[1], D. V. Dmitriev[1], D. Lamine[3], Y. Lassailly[3], D. Paget[3] and J. Peretti[3]

[1] Institute of Semiconductor Physics, 630090 Novosibirsk, Russia
[2] Novosibirsk State University, 630090 Novosibirsk, Russia
[3] Laboratoire de Physique de la Matière Condensée, Ecole Polytechnique, 91128 Palaiseau, France

Abstract. We have used transport measurements and electroluminescence to characterize the Pd/Fe/GaAs/InGaAs/GaAs(001) structure. Pd/Fe overlayers have been deposited on clean reconstructed GaAs(001) surfaces. In view of demonstrating a spin polarimeter based on the spin filter effect in the magnetic Fe, suitable magnetic and transport properties have been obtained, and the dependence of the polarized electroluminescence on the spin dependent electron injection has been observed.

Introduction

The magnetic and spin transport properties of the Fe/GaAs system have been extensively studied because of numerous potential applications to spintronics and spin injection. One possible practical application of such structures consists in the realization of an electron spin-detector for free electrons based on the spin filter effect [1]. It was found that above a given critical thickness of the order of 4 ML, the Fe is magnetic, with a magnetization in the surface plane and a strong magnetic anisotropy, with a magnetic moment similar to that of bulk Fe. Injection of spin polarized electrons from the Fe layer into the semiconductor was also successfully achieved [2]. Spin dependent transmission across a magnetic material, a phenomenon also called the spin filter effect, has also been demonstrated for the Fe/GaAs heterostructure [1]. Because of the latter effect, the same system has attractive potentialities for measuring electronic spin in vacuum. Such properties, as well as the transport properties of the Fe/GaAs heterostructure, have been comparatively little investigated. However, with respect to the usual Mott polarimeter, it can be anticipated that spin polarimeters based on Fe layers should be more compact and with a similar figure of merit. Further, the presence of a Pd overlayer, initially aimed at protecting the Fe from oxidation in air ambient, induces impact ionization processes which strongly enhance the spin sensitivity [3]. The present work is an investigation of Pd/Fe/GaAs/InGaAs system with the goal of building a spin polarimeter based on the optical registration of the spin filter effect.

1. Experimental

For the starting surface before Fe evaporation, we used clean reconstructed (001) surfaces obtained by treating the naturally oxidized GaAs surface by a HCl-isopropanol solution, and by annealing after introduction into vacuum to temperatures of 450 and 540 °C, respectively. These annealings are known to produce the c(2 × 8) As rich surface and the c(8 × 2) Ga-rich one [4]. The surface composition, structure and electronic properties of the starting surfaces were studied by means of x-ray photoelectron spectroscopy, low energy electron diffraction, high resolution electron energy loss spectroscopy and photoreflectance. The electron transport and electronic properties of the Schottky structures were characterized by current-voltage (I–V) and electroreflectance measurements. The magnetism of the Fe layer was characterized by a magneto-optic Kerr (MOKE) experiment in air.

We have fabricated spin light emitting diode (LED) designed to provide injection of spin-polarized electrons from epitaxial Fe film contacts into GaAs/InGaAs quantum well LED structure. The LED heterostructures were grown by molecular beam epitaxy in a Riber 32 system. The 4 nm thick Fe capped by 4 nm of Pd film was grown with the substrate at RT to minimize intermixing at the GaAs interface. The Fe forms a Schottky barrier contact, which is tailored to provide a tunnel barrier for electrical injection of spin polarized electrons under reverse bias. The light emitted perpendicular the surface normal from the cleaved side of the heterostructure is analyzed for polarization $\sigma+$ and $\sigma-$ spectroscopically resolved using a quarter wave plate and linear polarizer followed by a spectrometer. The EL spectra were measured at liquid nitrogen temperature.

2. Results and discussion

The main results are promising for future electron polarimeters, both from the point of view of magnetism, electron transport and optical properties. The magnetization of the Pd/Fe layers was found close to that of a bulk Fe layer of equivalent thickness and isotropic for Fe layers deposited on clean GaAs surfaces and anisotropic for magnetic layers grown on oxide covered surfaces. For Schottky barriers prepared by Fe deposition on the reconstructed GaAs(001) surfaces the ideality factors and barrier heights were found in the range 1.02–1.2 and 0.70–0.8 eV, respectively. The dependence of build-in surface electric field as a function of applied voltage was measured by electroreflectance and discussed in terms of Fermi level pinning by surface states at the interface metal/semiconductor.

The circular polarization $P_{\mathrm{circ}} = (I^+ - I^-)/(I^+ + I^-)$ is shown in Fig. 1 as a function of wave length. I^+ and I^- are the EL component peak intensities when analyzed as $\sigma+$ and $\sigma-$, respectively. We observed a difference in the intensity of the EL spectrum when analyzed as $\sigma+$ and $\sigma-$, corresponding to 7% percent of unpolarized light intensity. The quantum selection rules provide a quantitative link between the measured P_{circ} and the spin polarization of the carriers which radiatively

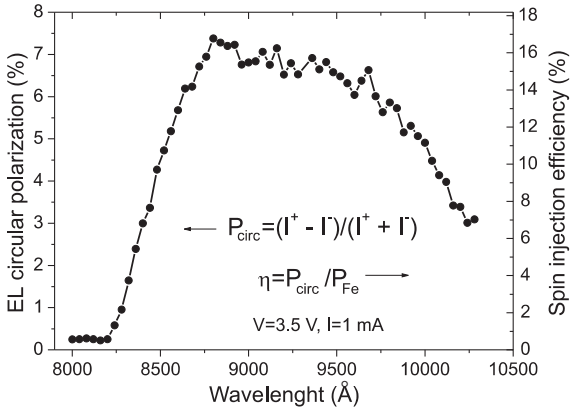

Fig. 1. The spectrum of the circular polarization P_{circ} and the corresponding spin injection efficiency $\eta = P_{\mathrm{circ}}/P_{\mathrm{Fe}}$.

recombine in the QW. For the case here in which only the heavy hole levels participate, $P_{\mathrm{circ}} = P_{\mathrm{spin}}$. The spin injection efficiency η from the Fe contact through the Schottky tunnel barrier and into the QW can be calculated as $\eta = P_{\mathrm{circ}}/P_{\mathrm{Fe}}$, where P_{Fe} is the spin polarization of the Fe contact near the Fermi level. Using $P_{\mathrm{circ}} = 7\%$ from Fig. 1, and $P_{\mathrm{Fe}} = 0.44$ [5] we obtain $\eta = 16\%$ at 78 K. This is comparable to the injection efficiencies reported using a wetting layer system [6]. Thus, the Pd/Fe/GaAs/InGaAs is a promising system for a spin polarimeter based on the optical registration of the spin filter effect [3].

Acknowledgements

This work was partly supported by the SBRAS (grant No. 22) and INTAS (grant No. 06-1000014-6147).

References

[1] A. Filipe, H.-J. Drouhin, G. Lampel, Y. Lassailly, J. Nagle, J. Peretti, V.I. Safarov, and A. Schuhl, *Phys. Rev. Lett.* **80**, 2425 (1998).

[2] I. Zutic, J. Fabian, and S. das Sarma, *Modern Physics*, **76**, 323 (2004) and references therein.

[3] N. Rougemaille, D. Lamine, G. Lampel, Y. Lassailly, and J. Peretti, *Phys. Rev. B* **77**, 094409 (2008).

[4] O. E. Tereshchenko, S. I. Chikichev, A. S. Terekhov, *J. Vac. Sci. Technol. A* **17**, 2655 (1999).

[5] R. J. Soulen, J. M. Byers, M. S. Osofsky, B. Nadgorny, T. Ambrose, S.-F. Cheng, P. R. Broussard, C. T. Tanaka, J. Nowak, J. S. Moodera, A. Barry, and J. M. D. Coey, *Science* **282**, 85 (1998).

[6] C. H. Li, G. Kioseoglou, A. T. Hanbicki, R. Goswami, C. S. Hellberg, and B. T. Jonker, M. Yasar and A. Petrou, *Appl. Phys. Lett.* **91**, 262504 (2007).

17th Int. Symp. "Nanostructures: Physics and Technology"
Minsk, Belarus, June 22–26, 2009
© 2009 Ioffe Institute

Formation of graphene-like structures on the surface of nickel crystal

M. A. Britch[1], K. V. Dobrego[1] and L. I. Krasovskaya[2]

[1] Heat and Mass Transfer Institute, 220072 Minsk, Belarus
[2] Technological University, Minsk, Belarus

Abstract. The dynamics of carbon atoms deposited on a nickel crystal is investigated by means of the molecular dynamics modelling. It has been shown that the dominant process is a migration of carbon atoms along the crystal surface with subsequent association of the atoms to form a regular graphene-like structure.

Introduction

Last time graphene has attracted much attention due to its remarkable properties making them the material with promising applications in various fields, especially in nanoelectronics [1]. Alongside the exfoliation procedure [2], the epitaxial growth on solid substrates is used for production of graphene monolayer [3].

Despite numerous studies, the detailed mechanisms of carbon nanostructure formation remain to be unclear. Recent advances in in situ observations of the catalytic formation of carbon nanostructures on nickel crystals [4] revealed the key role of the migration of carbon atoms over the crystal surface [4,5].

Here we present the results of the molecular dynamics modelling of interaction of carbon components with the surface of nickel crystal. It has been shown that such a process can lead to the formation of graphene-like structures.

The results presented are in good agreement with the recently published results obtained by other method [6].

1. Method

The system considered was constituted by several atomic layers of Ni crystal at given temperature and a set of carbon atoms depositing on the crystal surface with a predefined rate.

The energy of C-C interaction in the modelling of the dynamics of atoms was approximated with the Brenner's potential function [7], Ni-Ni interactions — by expressions from [8]. For description of Ni-C bonds, we have extended the expressions from [8,9] by the additional terms to take into account both the dependence of the Ni-C bond energy on the degree of saturation of valence bonds of the carbon atom, and the reduction of C-C bond strength caused by surrounding Ni atoms.

2. Results

In general, the features of the system behaviour are following.

Most of the influx carbon atoms adsorb on the crystal surface. The atoms undertake heat vibrations in the vicinity of

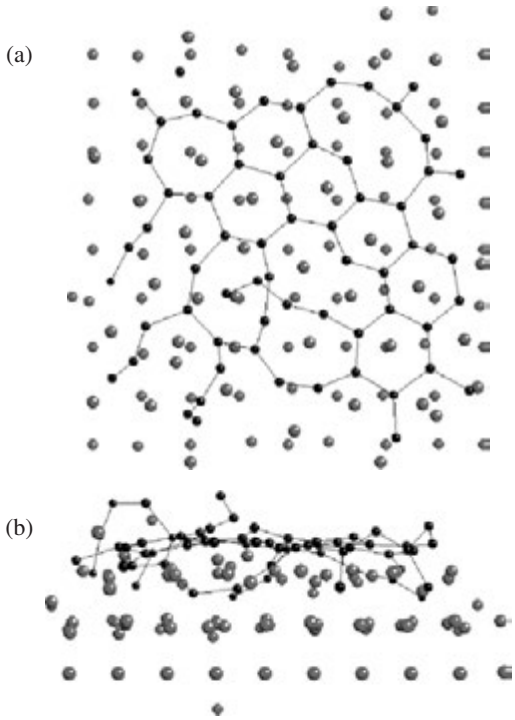

Fig. 1. Snapshot of the configuration of Ni and C atoms ($T = 1200$ K, $t = 200$ ps after beginning of the process; Ni atoms in grey, C atoms in black; only C-C bonds are shown): (a) plane view; (b) side view.

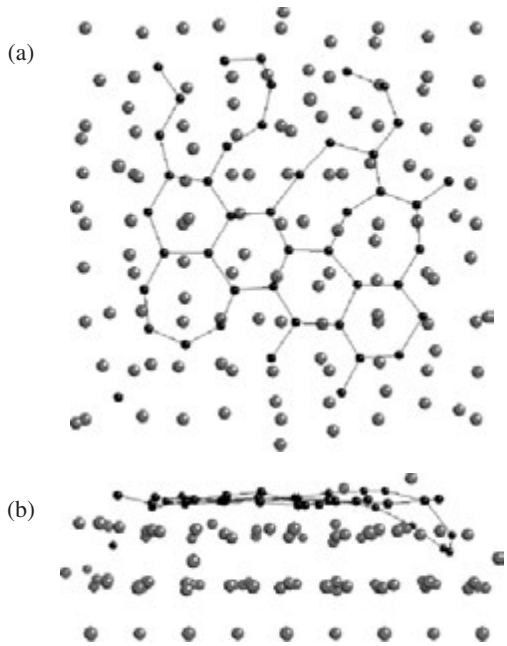

Fig. 2. Snapshot of the configuration of Ni and C atoms ($T = 1000$ K, $t = 200$ ps after beginning of the process; Ni atoms in grey, C atoms in black; only C-C bonds are shown): (a) plane view; (b) side view.

equilibrium positions, and occasionally they undertake random transitions from one position to another (transitions of the carbon atoms take place more often than those of the nickel atoms). Carbon atoms dominantly move along the crystal surface, occasionally they penetrate under the surface layer of Ni atoms. When carbon atoms become enough close to each other, the strong covalence bond is established. Bonded carbon atoms form two-dimensional clusters (chains and rings). When a number of the adsorbed carbon atoms increases, these clusters grow, become multibranched, rebuild and associate to form a graphene-like structure, including polygons with various number of sides (Fig. 1, 2). This relatively fast stage is followed by slow relaxation process, when the hexagons become dominating in these structures as the most stable formation.

So, as a result of interaction of the nickel crystal surface with the flux of carbon atoms, the tendency to the formation of the regular graphene-like nanostructures is observed. The character of the structures obtained depends on the temperature of the system (compare Fig. 1 and Fig. 2).

References

[1] A. K. Geim *et al*, *Physics Todey* August issue, 35 (2007).
[2] K. S. Novoselov *et al*, *Science* **306**, 666 (2004).
[3] A. Banerjee *et al*, *Nanotechnology* **19**, 365303 (2008).
[4] S. Helveg *et al*, *Nature* **427**, 426 (2004).
[5] F. Abild-Pedersen *et al*, *Phys. Rev. B* **73**, 115419 (2006).
[6] H. Amara *et al*, *Phys. Rev. B* **79**, 014109 (2009).
[7] D. W. Brenner, *Phys. Rev. B* **42**, 9458 (1990).
[8] Y. Yamaguchi *et al*, *Eur. Phys. J.* **9**, 385 (1999).
[9] Y. Shibuta *et al*, *Chem. Phys. Lett.* **382**, 381 (2003).

17th Int. Symp. "Nanostructures: Physics and Technology"
Minsk, Belarus, June 22–26, 2009
© 2009 Ioffe Institute

Spontaneous polarization role in the formation of the energy diagram for the heterojunctions based on the SiC polytypes

S. Yu. Davydov
Ioffe Physical-Technical Institute, St Petersburg, Russia

Abstract. The role of spontaneous polarization of the noncubical component for the SiC based heterojunction is considered. It is shown that the account of spontaneous polarization changes significantly the energy structure and the quantum well level positions.

Introduction

The thorough study of the spontaneous polarization (SP) effects on SiC based heterostructures is now of great interest. Different calculations have demonstrated that the SP $P_{\rm sp}$ of the noncubical polytypes is of the order of 10^{-2} C/m^2. The corresponding polarization electric field $F_{\rm sp} = P_{\rm sp}/\varepsilon_0\varepsilon_1$, where ε_0 is the dielectric constant and ε_1 is the static dielectric function of noncubical polytype, has an order of 10^6 V/cm and must be taken into account in the bands line-up scheme [1]. Here we consider the $n_1 - N{\rm H}/p_2$-3C heterojunction, where NH stands for the hexagonal SiC polytypes with $N = 4, 6, 8$.

1. SP effects on the energy structure of the heterojunction

We have begun with the heterojunction consist of the hexagonal and cubic components occupping $x \le 0$ and $x \ge 0$ domains correspondingly. It can be shown that the resulting electric field $F(x) = -(d\tilde{\varphi}(x)/dx)$, where $\tilde{\varphi}(x)$ is the electrostatic potential with account of SP, can be approximately separated to the SP electric field $F_{\rm sp}(x)$ and the contact field $F_{\rm c}(x)$ contributions. Introducing the dimensionless potential energy (potential) $\tilde{\psi}(x) = e\tilde{\varphi}(x)/k_{\rm B}T$, where e is the electron charge, $k_{\rm B}$ is the Boltzmann constant and T is the temperature, with the aim of the Poisson equation we get

$$\frac{d\tilde{\psi}_1}{dx} = -L_{n1}^{-1}\sqrt{e^{-\Delta} - e^{-\psi_1} + \Delta - \psi_1} - \frac{\tilde{P}_{\rm sp}}{\varepsilon_1}, \quad x \le 0,$$
$$\frac{d\tilde{\psi}_2}{dx} = -L_{p2}^{-1}\sqrt{e^{\tilde{\psi}_2} - \tilde{\psi}_2 - 1}, \quad x \ge 0, \qquad (1)$$

with the boundary conditions $\tilde{\psi}_1(0) = \tilde{\psi}_2(0) = \tilde{\psi}_s$, $\varepsilon_1(d\tilde{\psi}_1/dx)_{x=0} = \varepsilon_2(d\tilde{\psi}_2)_{x=0}$ and additional requirements $\psi_1(-\infty) = \Delta$ and $P_{\rm sp}(-\infty) = 0$. Here and in what follows $\tilde{\psi}_i$ and ψ_i $(i = 1, 2)$ mean the dimensionless potential with and without account of the spontaneous polarization,

$$L_{n1(p2)} = \sqrt{\varepsilon_0\varepsilon_{1(2)}k_{\rm B}T/2e^2n_1(p_2)}$$

is the corresponding Debye length and $\tilde{P}_{\rm sp}(x) = eP_{\rm sp}(x)/\varepsilon_0 k_{\rm B}T$. The first term on the right hand side of Eq. (1) corresponds to the contact field $F_{\rm c}(x)$ (with the opposite sign), and the second one corresponds to the polarization field $F_{\rm sp}(x)$. We have supposed that the SP can be approximated as $P_{\rm sp} = P_0\exp(x/L_{\rm sp})$, $(x \le 0)$, where $L_{\rm sp}$ is the SP decay length. This expression for $P_{\rm sp}(x)$ is a rather general. In the limit $L_{\rm sp} \to \infty$ we have $P_{\rm sp}(x) = {\rm const}$. If we assume, that the SP field at the left end of the hexagonal heterojunction component, located at $x \to -\infty$, is somehow compensated (say, by the chemisorption of the appropriate species), than we have to consider $L_{\rm sp}$ as a finite value. Since below we will consider mainly the SP effects in the cubical 3C domain, the particular interpretation of the $P_{\rm sp}(x)$ is of no importance.

Assume that the potentials can be written as $\tilde{\psi}_i(x) = \psi_i(x) + \chi_i(x)$ (i =1,2). Taken the boundary conditions into account we have obtained

$$\sqrt{e^{-\Delta} - e^{-\psi_s} + \Delta - \psi_s} + \Pi_0^* = \sqrt{\eta(e^{\psi_s+\chi_s} - \psi_s - \chi_s - 1)}, \qquad (2)$$

where $\Pi_0^* = eL_{n1}P_0/\varepsilon_0\varepsilon_1k_{\rm B}T$, $\eta = (\varepsilon_2 p_2/\varepsilon_1 n_1)$. The nondimensional SP parameter Π_0^* depends on the Debye length L_{n1}. Therefore, varying the electron concentration n_1, it is possible to change the parameter Π_0^* value continuously.

The analyses of the Eq. (2) have shown that for the case of $\Pi_0^* > 0$ both contact $F_{\rm c}$ and polarization $F_{\rm sp}$ field components are positive, that give s$F = F_{\rm c} + F_{\rm sp}$. Therefore, the $\psi^+ = \tilde{\psi}_s(\Pi_0^* > 0)$ function increases monotonically with the parameter Π_0^*. Otherwise, for the $\Pi_0^* < 0$ case resulting electric field $F = F_{\rm c} - F_{\rm sp}$, that manifests itself in the decrease of the $\psi^- = \tilde{\psi}_s(\Pi_0^* < 0)$ function. At some value of $\Pi_0^* = \bar{\Pi}_0^*$, that can be easily defined from Eq. (2), function ψ^- becomes equal to zero. The following increase of the $|\Pi_0^*|$ leads to the change of the bend-bending slope from the positive to negative one. The sign of the SP is fixed by the nature of the hexagonal polytype surface (Si or C), connected with the 3C one. As has been shown earlier, the Si-atom plane is positively charged while the C-atom plane is charged negatively. So, we accept $\Pi_0^* > 0$ for the Si-plane and $\Pi_0^* < 0$ for the C-plane.

2. SP effects on the quantum well energy levels

We have also considered the SP effect on the energy of the electron ground state $\bar{\varepsilon}_0$ in the quantum well (QW), which can be formed near the heterojunction within the 3C domain. We approximate real QW by the well known triangular potential well model. Within the scope of this model $\bar{\varepsilon}_0 \propto (F')^{2/3}$. We have taken for F' the value of the $F_0 = -(d\tilde{\varphi}(x)/dx)_{x=0}$. The analyses of the relations $\zeta_+ = \bar{\varepsilon}_0(\Pi_0^* > 0)/\bar{\varepsilon}_0(\Pi_0^* = 0)$ and $\zeta_- = \bar{\varepsilon}_0(\Pi_0^* < 0)/\bar{\varepsilon}_0(\Pi_0^* = 0)$ dependences on the $|\Pi_0^*|$ value have shown that for the different values of η the ζ_+ functions are practically identical and increases with the Π_0^* value, while the ζ_- functions differ only at $|\Pi_0^*| \to \bar{\Pi}_0^*$, where they come

to zero The origin of such a dependence arises from the fact that the parameter η has only a small effect on electric field $F_0^0 \equiv F_0(\Pi_0^* = 0)$, while the electron concentration n_1 is of importance.

Acknowledgements

This work is partly supported by the grant of the Russian Foundation for the Basic Research (RFBR project No. 07-020063a), RAS Presidium program "Quantum Physics of Condence Matter" and the Russian National Project "Development of the Scientific Russian Federation High School Potential" (RFMES, project No. 2.1.1/2503).

References

[1] A. A. Lebedev, *Semicond. Sci. Technol.* **21**, R17 (2006).

17th Int. Symp. "Nanostructures: Physics and Technology"
Minsk, Belarus, June 22–26, 2009
© 2009 Ioffe Institute

Composites based on nanostructured oxides and noble metals: Optical and sensor properties

A. Ya. Khairullina[1], T. V. Olshanskaya[1], A. N. Kudanovich[1], T. N. Vorobyova[2], O. N. Vrublevskaya[2] and D. S. Filimonenko[1]

[1] B. I. Stepanov Institute of Physics, NASB, 220072, Minsk, Belarus
[2] Research Institute for Physical Chemical Problems of Belarusian State University, 220030, Minsk, Belarus

Abstract. The absorption spectra of NiO, WO_3 and also the layers of these oxides doped with noble metal particles on Al_2O_3 substrate are investigated in red and near IR spectral range. The correlation between the optical, gas sensor properties of composites on NiO base and their structural parameters has been revealed. Pilot investigations of photo-electric properties of composites consisted from oxides doping noble metals were realized.

Introduction

The interest in investigation of the optical and photoelectrical properties of the composites on the base of multi component oxide and metal-oxide systems in visible and IR spectral range is being governed by the search for materials that are promising to fabricate the effective IR detectors, components for optics, gas selective optical sensors with the improved characteristics as compared to the composites currently available. The environmental safety, thermal steadiness, stability to deterioration, and a low cost of proposed materials and structures are the important parameters of the systems on base of oxides. Rather poor data there currently exist concerning absorption and photoconductivity of the structures formed by oxides and island-like metal-oxide films in the red and near IR spectral bands. That is why optical and photoelectric properties of nanostructures from different materials produced by physical or chemical methods are the subject of numerous investigations [1–3].

It is well known that the most of semi-conductive oxides absorb electromagnetic radiation in UV region owing to the sufficient band-gap due to high ionicity of the chemical bond between metal and oxygen atoms. Nevertheless, in some cases the absorption band is situated in the visible region or even reaches the infrared region.

1. Materials and methods

We used the three stage method for fabrication of NiO and WO_3 films doped with a metal on Al_2O_3 substrate. At the first stage metal films were formed by a vacuum sputtering of a metal onto anodic alumina substrates. At the second stage the method of metal film thermal oxidation was used to obtain metal oxides. The X-ray photoelectron spectroscopy has shown that these oxide films consist of NiO and WO_3. The oxide films have a thickness about 300 nm and a grained structure. The mean sizes of nickel and tungsten oxide grains on the surface are about 8 and 50 nm. Grains are grown up into aggregates consisting from several to ten particles. The next stage was the deposition of noble metal particles obtained by the reduction of metal ions in solutions.

Absorption coefficients in the infrared spectral range were calculated from the transmission and reflection coefficients and from the diffuse transmission and reflection coefficients over the spectral range from 320 to 740 nm.

2. Results of investigations

The absorption spectra of NiO, WO_3 and also the layers of these oxides doped with noble metal particles on Al_2O_3 substrate are given in Fig. 1. We observed optical absorption in 650–730 (I) and 1800–2500 (II) spectral range for NiO layers. According to data [1] the first band is due to the electric dipole *d–d* transition, complicated by contribution of surface states. The second broad band is a magnetic dipole in nature. The gold nanoparticles increase the absorption at 500–730 nm and 1800–2000 nm inherent to NiO and WO_3 layers. The silver nanoparticles increase the absorption of WO_3 in a wide spectral range from 500 to 1800 nm. Optical absorption of metal-oxide composites and oxides in the IR spectral region is rather large that makes this fact important for the interpretation

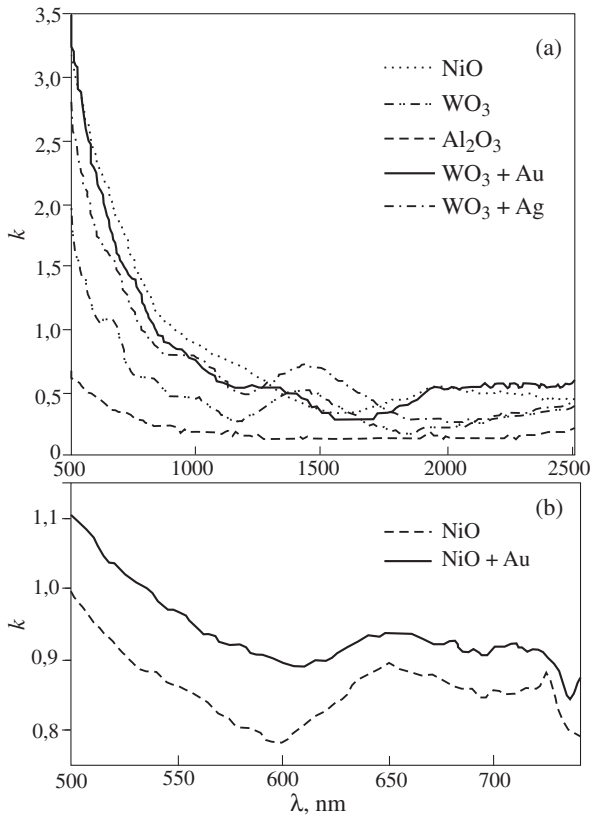

Fig. 1. Absorption spectra of NiO, WO_3 layers and modified by noble metals a — IR spectral region; b — visible spectral region.

Table 1. Values of He–Ne laser optical response (F_s/F_0) before and after the action of carbon monoxide, of the diffuse reflection coefficient (R_{dif}) at the band I and of the mean size (H_{mean}) of nickel oxide aggregates.

No.	F_s/F_0 before action	F_s/F_0 after action	R_{dif}	H_{mean}, nm
1	0.125	0.117	0.23	67.3
2	0.092	0.135	0.156	57.4
3	0.099	0.115	0.174	64.0

and prediction of photoelectric characteristics of composites.

The data of the Table reveal the correlation between the optical, sensor properties of composites and their structural parameters. The revealed narrow band at 650nm for NiO monolayer with the layer thickness 3 nm make this structure perspective for optic gas sensor in visible spectral range. Pilot investigations of photo-electric properties of composites consisted from oxides doping noble metals give hope.

References

[1] V. V. Volkov, Z. L. Wang, B. S. Zou, *Chem. Phys. Lett.* **337** 117 (2001).

[2] A. P. Boltaev, N. A. Penin, A. O. Pogosov, F. A. Pudonin, *J. Exp. Theor. Phys.* **23** (5), 1057 (2003), (in Russ.)

[3] A. Ya. Khairullina, T. V. Olshanskaya, V. A. Babenko, D. A. Yavsin, V. M. Kozhevin and S. A. Gurevich, *Opt. Spectrosc.* **98** (1), 96 (2005).

17th Int. Symp. "Nanostructures: Physics and Technology"
Minsk, Belarus, June 22–26, 2009
© 2009 Ioffe Institute

Features of hot hole transport in 6H-SiC

V. I. Sankin, P. P. Shkrebiy and A. A. Lepneva
Ioffe Physical-Technical Institute, St Petersburg, Russia

Abstract. In materials with a small degree of ionicity ranging 10–15%, such as in SiC, carrier scattering on polar optical potential is plausible. In this work possible mechanisms contributing to the J-F characteristics are considered: scattering on ionized impurities; impurity breakdown due to Al acceptors; hole transport in the light valence subband; and dielectric breakdown related to polar optical scattering.

Introduction

At the present time, the developments of the SiC electronics are based on materials with electron conductivity. This seems natural, since the electron mobility is an order of magnitude higher than the hole mobility in hexagonal SiC. However, effects of Wannier–Stark localization (WSL) in strong electric fields critically limit the region of reliable functioning of electronic devices. On another hand, there exist grounds to believe that conditions for WSL are absent in the valence band. Furthermore, it is known that in materials with a small degree of ionicity ranging 10–15%, such as in SiC, polarization arises due to longitudinal optical vibrations of the lattice when positive ions shift as a whole in respect to negative ones. Carriers of charge experience scattering on alternate electric field of such vibrations. At strong external electric fields, when the carrier energy is higher than the energy of the optical phonon, carrier velocity increases so much that the intensity of scattering on polar lattice vibrations begins decreasing, which may cause a sharp increase of drift velocity. It has been shown theoretically that such process leads to a dielectric breakdown (DB), which is similar to an electrical breakdown, but instead of an avalanche increase of carrier concentration, an abrupt increase of mobility takes place. In the current density — electric field (J-F) characteristics there appears a region of negative differential conduction (NDC), where the current density J increases while the electric field F decreases. DB has not been observed experimentally up to now because of inter-valley scattering and band-to-band impact ionization (II). Therefore, in order to realize the DB effect, it is necessary to ensure the following conditions:

— Carrier transport study at the condition of one valley, i.e. an optimal case of a band having its extremum in the k-space at $k = 0$.

— The field ranges of DB and II must be essentially separated. It can be assumed then, that under these actualities the effect of DB will be possibly realized in the transport of hot holes in SiC.

1. Experimental results and discussion

In this work, I–V characteristics of hot holes transport in 6H-SiC have been studied at electrical field 1–300 kV/cm. The measurements were performed on P^+–P–P^+ experimental structures. The first P^+-layer was grown on an N-type 6H-SiC Lely substrate, followed by the formation of the P-layer. Both layers were deposited by sublimation epitaxy. The top P^+ layer, which was used as a contact layer, was accomplished by ion implantation each of the three layers was doped by aluminum, however to a different extent. The free hole concentration and hole mobility at 300 K in the P^--layer were determined from Hall effect and conductivity measurements, being $2 \times 10^{15}\ cm^{-3}$ and 50 cm^2/V s, respectively. For higher temperatures these parameters were extracted from Ref. [3]. The mesa-structures with a diameter 100 μm were made by dry etching. As a contact to mesa-structures was used a sputtered Al. A common contact area of $S = 4$ mm^2 was located on the epitaxial P^+-layer. Electrical measurements were carried out in static and pulse regimes in a temperature range 77–600 K. I–V characteristic as shown in Fig. 1, consists of an ohmic region and exponential region. The last one started at more than 100 kV/cm. Saturation of current and drift velocity was not observed in contrast to I–V characteristics for electrons in SiC [4]. Values of the drift velocity up to 10^8 cm/s were measured. With increasing temperature the drift velocity decreased, but the character of the I–V curves did not change, which is evidence that we deal with scattering on polar optical potential in strong electrical fields, and that impurity (e.g. Al) related breakdown effect is absent. Additional experiments on a P (Al)-doped layer with $N_a - N_d \sim 10^{18}$ cm^{-3} at 77 K allowed us to estimate that the threshold field for a breakdown due to the Al doping was near 40 kV/cm. In the I–V characteristics a region with NDC was observed at ∼200 kV/cm, which can be possibly attributed to DB. In summary, the ob-

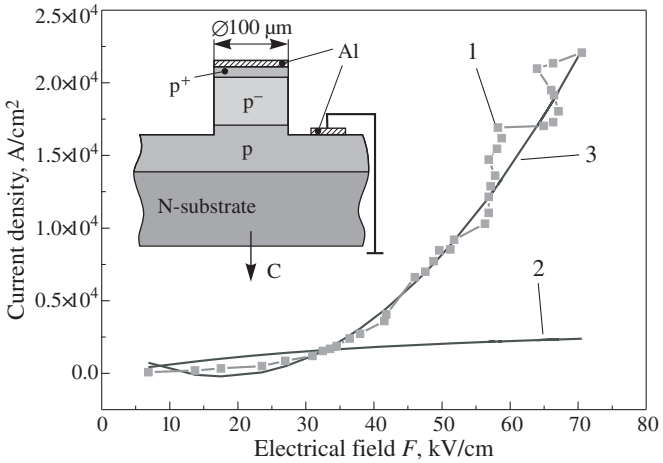

Fig. 1. J-F characteristics of a P-type 6H-SiC (Al) epitaxial layer with $N_a - N_d \sim 5 \times 10^{17}$ cm^{-3}, $F \parallel C$, $T = 300$ K. 1 — experiment, 2 — theory, 3 — approximation $v/v_{ds} \sim f(F^2)$). The cross section of a mesa is shown on the inset.

tained results showed the complicated character of the hot hole transport in 6H-SiC. A comparative analysis of experimental results with the theory of carrier scattering processes allowed assuming the basic mechanisms of I–V characteristic formation: i) in the range of 10–40 kV/cm — scattering on ionized impurities; ii) the range of 40–64 kV/cm — scattering on optical polar potential in the sub-band of light holes; iii) the range of 65–70 kV/cm — dielectric breakdown. From a practical point of view, a key finding in this study is the decrease of the deferential resistance of the P^+–P–P^+ structures more than 50 times in a range of electric fields 0.1–70 kV/cm.

Acknowledgements

The work was partially supported by Russian Foundation of Basic Researches (project No. 08 - 02 -00565). We thank our colleagues Dr. Mokhov E. N. and Dr. Zelenin V. V. for technological support, Dr. Poloskin D. S. for the Hall measurements, Misharina M. V. for the preparation of samples.

References

[1] V. I. Sankin, P. P. Shkrebiy, and A. A. Lepneva and M. S. Ramm, *Materials Science Forum Vols.* **556–557**, 431–434 (2007).

[2] M. Glicsman and W. A. Hicinbothem, *Phys. Rev.* **129**, 1572 (1963).

[3] G. A. Lomakina, Yu. A. Vodakov, E. N. Mokhov, V. G. Oding and G. F. Choluyanov *Fiz. Tverd. Tela* **12**, 2918 (1970).

[4] I. A. Khan and J. A. Cooper: *Proceedings ICSCIII-N' 97, Stockholm, August 31–September* **5**, 57 (1997).

17th Int. Symp. "Nanostructures: Physics and Technology"
Minsk, Belarus, June 22–26, 2009
© 2009 Ioffe Institute

Properties of zinc oxide nanostructures formed during electrical discharge in liquids

N. V. Tarasenko[1], V. S. Burakov[1], M. I. Nedelko[1], E. I. Mosunov[2] and A. A. Nevar[1]

[1] B. I. Stepanov Institute of Physics, NASB, 68 Nezalezhnasty Ave., 220072 Minsk, Belarus
[2] Institute of Machine Mechanics and Reliability, NASB, 12 Akademichnaya Str., 220072 Minsk, Belarus

Abstract. Zinc oxide nanoparticles were synthesized by submerged electrical discharge technique in water and aqueous ammonia solution with further deposition on the silicon substrates. The composition, morphology, growth mechanisms, absorbance and luminescent properties of the formed structures were studied. The study revealed that films of high structural and optical quality can be prepared and the developed method can be extended for preparation of doped ZnO nanocrystals.

Introduction

Last years, ZnO nanostructures have been found to have many novel properties and wide potential applications. Zinc oxide (ZnO) is a wide-bandgap semiconductor that has a stable wurtzite structure. The specific physical and chemical properties of zinc oxide make it a promising candidate for applications in blue/UV light emitting diodes, varistors, piezo-electric transducers, gas sensors, etc. [1]. In some respects, the semiconducting properties of ZnO compare favorably to those of the GaN system. ZnO has higher exciton binding energy (60 meV), more radiation hard and is multifunctional (piezoelectric, ferroelectric and ferromagnetic).

To date several fabrication methods, such as the thermal decomposition [2], chemical vapor deposition [3], wet chemical synthesis, spray pyrolysis, sol-gel method, molecular beam epitaxy, etc. have been reported for the preparation of ZnO nanoparticles and films.

Recently plasma assisted techniques based on electrical discharges in liquids have become a focus of many studies for fabrication of nanoparticles [4,5]. The capabilities of this technique for fabrication of zinc oxide nanocrystals are discussed in the present paper. Material composition, optical and electrical properties of the formed products were studied.

1. Experimental

Several experimental conditions were tested to synthesize nanoparticles of different composition and morphology. The electrical discharge between two zinc electrodes immersed in distilled water was used to produce ZnO nanoparticles. To elucidate a possibility of synthesis of N-doped and In-N co-doped ZnO nanocrystals and fabrication of p-type ZnO we used electrical discharge between Zn-Zn and Zn-In electrodes immersed into the 10% aqueous ammonia solution.

The experimental apparatus and the experimental procedure for forming nanoparticles by the electric erosion method have been described earlier in [5,6]. Metallic rods with diameters of 6 mm were employed as electrodes. The discharge was stable as long as a cathode-anode gap was less than 1 mm. The power supply provides AC and DC discharge regimes at the repetition rate of 100 or 300 Hz with 60 A and 10 A peak current, 50 μs and 5 ms duration pulses in the spark and arc regimes, respectively. The discharge current was monitored by means of the current viewing resistor. Voltage and current were recorded utilizing a digital oscilloscope. The discharge was initiated by applying a high-frequency voltage of 3.5 kV.

The synthesized particles were obtained as colloidal solutions. The formed nanoparticles were characterized by optical absorption and photoluminescence spectroscopy for monitoring the changes in the absorption characteristics and luminescence properties, transmission electron microscopy (TEM) and X-ray diffraction (XRD) in order to determine the powder composition, its crystalline structure, lattice parameters and grain size. Nanopowders for XRD measurements were obtained after the drying of the colloidal solutions. The X-ray diffractometer D8-Advance (Bruker, Germany) was used for XRD measurements.

The elemental composition of the powder deposited on the substrate was detected using energy dispersive X-ray (EDX) spectrometer attached to the scanning electron microscope (SUPRA 55WDS, Carl Zeiss, Germany).

The luminescence spectra of the deposited samples were measured with a spectral resolution of 1 nm on a Solar SFL-1211A spectrometer with a Xe lamp as excitation source.

2. Results and discussion

The optical absorption spectra (Fig. 1) of as-prepared colloidal solutions (in both liquids) were rather featureless. The typical absorption spectrum of the colloid exhibited a broad absorption band edge in the UV spectral range. From the absorption coefficient data the optical band-gap (E_g) was determined using the relation $khv = (hv - E_g)^{1/2}$ ($hv > E_g$), where hv

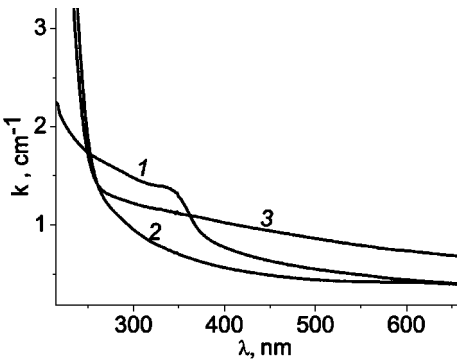

Fig. 1. Optical absorption spectra of zinc oxide nanoparticles prepared in Zn-Zn discharge in water (1), Zn-Zn discharge in NH_3 solution (2) and Zn-In discharge in NH_3 solution (3).

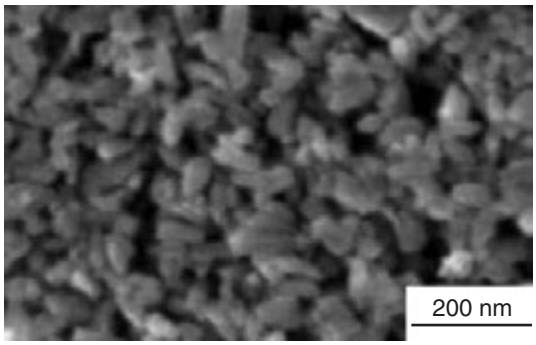

Fig. 2. SEM micrograph of ZnO nanoparticles prepared by electrical discharge in water.

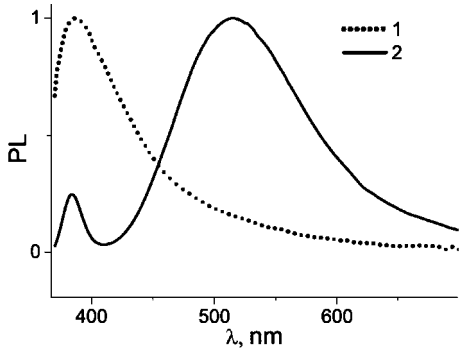

Fig. 3. Photoluminescence spectra of ZnO nanoparticles prepared by spark discharge between two zinc electrodes immersed in water (1) and of commercial ZnO powder (2).

is the photon of energy. The direct optical band-gap energy was evaluated from a straight-line plot of $(kh\nu)^2$ against photon energy $h\nu$ extrapolated to $k = 0$. The estimated optical band-gap values for both the ZnO:N and ZnO:(In,N) samples were found to be shifted slightly to lower energies compared to that for the undoped ZnO ($E_g = 3.38$ eV).

The SEM micrograph presented in Fig. 2 shows the typical morphology of the formed nanoparticles revealing loosely aggregated clusters consisting of rod-like grains with average diameter of about 30 nm and 80–100 nm in length.

Structural identification of the ZnO nanopowders was investigated using XRD in the range of 2θ between 2°–100°. XRD analysis indicated that the ZnO nanopowders had a crystalline structure. The lattice parameters and grain size of the formed powders were determined from their XRD diffraction. As it followed from the XRD patterns (not shown here) the product synthesized in water was composed of hexagonal ZnO with lattice constants $a = 0.325$ nm and $c = 0.521$ nm, which is in agreement with the JCPDS card for ZnO. The measured c/a ratio (1.621) was in good agreement with that for the ideally close-packed hexagonal structures ($c/a = 1.633$). From the width of the (002) peak by using the Scherrer formula, the mean size of crystallites forming the grains was determined as 25 nm.

The position of XRD peaks is expected to be shifted with varying the composition of dopants. Such experiments are in progress and their details will be discussed.

Measurements of photoluminescence (PL) can be very useful for the determination of structural defects and impurities in oxide nanostructures. The typical room-temperature luminescence spectrum recorded for a sample prepared from solution formed during spark discharge between Zn-Zn electrodes in water is presented in Fig. 3. For comparison, a spectrum of the sample prepared from the commercial ZnO powder (bulk ZnO) with characteristic crystallite size of 0.5 μm is also shown. Before a deposition a small amount of this powder was ultrasonically dispersed in water and then dropped onto a silicon substrate

The luminescence spectrum of ZnO samples synthesized by electrical discharge reveals the prominent UV-band at 380 nm and exhibits relatively weak violet emissions. For the sample prepared from the commercial ZnO powder, two peaks are observed in the PL spectrum: the relatively weaker UV band at 383 nm and a broad green emission band at about 515 nm. The UV photoluminescence peak is attributed to near band edge excitonic emissions. The mechanism of visible emission is suggested mainly due to the present of various point defects, either extrinsic or intrinsic, which can easily form recombination centres.

3. Summary

The results presented above prove that an electrical discharge in liquid technique is a simple, rapid, and low cost synthesis route for producing nanocrystalline ZnO powders with good crystallinity and optical properties. This method can be also extended for preparation of doped ZnO nanocrystals and fabrication of p-type ZnO.

References

[1] Z. L. Wang, "Nanostructures of zinc oxide", *Materials Today* **6**, 24 (2004).
[2] S. Labuayai *et al*, *Appl. Phys. A* **94**, 755 (2009).
[3] B. P. Zhang *et al*, *Chem. B* **108**, 10899 (2004).
[4] V. V. Podkropivny *et al*, *Tech. Phys. Let.* **33**, 88 (2007).
[5] V. S. Burakov *et al*, *J. of App. Spect.* **75**, 114 (2008).
[6] V. S. Burakov *et al*, *Tech. Phys. Let.*, **34**, 679 (2008).
[7] B. D. Yao *et al*, *Appl. Phys. Lett.* **81**, 757 (2002).

17th Int. Symp. "Nanostructures: Physics and Technology"
Minsk, Belarus, June 22–26, 2009
© 2009 Ioffe Institute

Physics of microcavity: nonlinear-optical properties

V. V. Kabanov
Institute of Physics, National Academy of Sciences of Belarus, Nezavisimosty Ave. 68, Minsk 220072, Belarus

Along with the progress in nanostructure physics and technology, the role of optical microdevice investigations is of importance at present. First of all, optical microcomponents are the basis of not merely optical microsystems making, but they are combined with electronic, mechanical and sensor components in complex microsystems. The particular type of optical microsystems are microcavities. In addition to small geometry size, low power requirement and good processing speed (response time), such systems have to be possessed of high cavity quality factor. These characteristics are essential both for the diminutive effective laser sources making and for the creation of unique nonlinear optical microelements.

Some expectations in the field of microcavities development are related to utilization of three-dimensional microcavities with different geometries (sphere, cylinder, ring and other). The main advantage of such microcavities is the possibility to form three-dimensional close-packed arrangement of high quality modes by means of total internal reflection effect. The quality factor rises with the mode order increasing, e.g. it reaches the value of $\sim 10^{10}$ for sphere microcavity with mode lifetime of about $\sim 10^{-5}$ s [1]. This quality factor value is several orders greater than Q-factor of the best quasi-one-dimensional cavity. The high microcavity Q-factor may be achieved by means of high precision cavity formation and low internal losses related with the possibility to create high active medium homogeneity within small volume.

The high close-packed arrangement of microcavity modes leads to effective realization of many nonlinear phenomena and allows us to talk about new nonlinear optical properties of electromagnetic radiation under interaction with nonlinear medium within microcavity. For example, nonlinear change of refractive index of InP disk injection microlaser results in the shift of mode frequency to the blue spectral side with injection current increasing [2]. More complex situation is observed under investigation of the temperature regime of InAs/InAsSbP disk microlaser lasing ($\lambda = 3.03$–$3.06\,\mu$m). In particular, there is temperature range (with)in which two shifted each other lasing lines (bands) are realized simultaneously [3].

It is of interest also to display nonlinear properties of interaction of whispering-gallery modes within a spherical microparticle. Spherical microparticles provide, for example, good conditions for a laser generation [4], stimulated Raman scattering [5], and stimulated Brilouin scattering [6]. The realization of a nonlinear structure as a set of vector spherical harmonics interacting with an induced change of the equilibrium condition of the microcavity's medium allows to reckon on the appearance of quantum mechanical properties [7,8] and the observation of new regimes of a nonlinear dynamics and a self-organization [9] of such object as a nonlinear structural resonance. A set of spherical harmonics can under certain conditions form spherically symmetric structure of a soliton type in a small volume of a homogeneous isotropic nonlinear medium [10]. A spherically radial-gradient distribution of refractive index induced in the nonlinear medium acts as a microcavity in this case, and the total internal reflection inside this cavity ensures the existence of the spherically symmetric structure of electromagnetic field [7]. Such system of electromagnetic field and induced by it changes of nonlinear medium's parameters is named the structural resonance. The obtaining of the spherical structural resonance with the properties mentioned above is connected with stability of such system, and with an excitation of a plasmon structure in the volume of the microcavity. At that unlike the laser excitation of plasmons in thin films and metals surface layers [11] in the case in question the main subject is a spherical plasmon excitation in the volume of the micron size cavity [12]. Nonlinear properties and mechanism of the interaction of laser radiation within microparticles are discussed. Realizing conditions of the induced plasmon structure in the volume of the spherical microcavity filled with a low-temperature electron plasma is analyzed.

References

[1] I. S. Grudinin, A. B. Matsko and L. Maleki, *Optics Express* **15**, 3390 (2007).
[2] P.-Y. Bourgeois, V. Giordano, *IEEE Transactions on Microwave theory and techniques* **53**, 3185 (2005).
[3] V. V. Kabanov, Y. V. Lebedok, A. G. Ryabtsev *et al*, *Semiconductors* **43**, 522 (2009).
[4] G. Chen, D. Q. Chowdhury, R. K. Chang, W.-F. Hsieh, *J. Opt. Soc. Amer. B* **10**, 620 (1993).
[5] H.-M. Tzeng, K. F. Wall, M. B. Long, R. K. Chang, *Optics Letts* **9**, 499 (1984).
[6] J.-Z. Zhang, R. K. Chang, *J. Opt. Soc. Amer. B* **6**, 151 (1989).
[7] V. V. Kabanov, *Quantum Electron.* **6**, 820 (1996).
[8] V. V. Kabanov, *Lithuanian Journal of Physics* **39**, 275 (1999).
[9] V. V. Kabanov, *Chaos, Solitons and Fractals* **17**, 425 (2002).
[10] V. V. Kabanov, *Nonlinear Phenomena in complex systems* **4**, 302 (2001).
[11] C. Max, F. Perkins, *Phys. Rev. Lett.* **27**, 1342 (1971).
[12] V. V. Kabanov, V. A. Sobolevsky, *Nonlinear phenomena in complex systems' 2002*, Minsk, 356 (2002).

Author Index